Hard Rods on Lattices between Two and Three Dimensions: Nonequilibrium, Equilibrium, and Machine Learning

DISSERTATION

der Mathematisch-Naturwissenschaftlichen Fakultät
der Eberhard Karls Universität Tübingen
zur Erlangung des Grades eines
Doktors der Naturwissenschaften
(Dr. rer. nat.)

vorgelegt von
MIRIAM D. KLOPOTEK
aus Boston, Vereinigte Staaten von Amerika

Tübingen
2020

Gedruckt mit Genehmigung der Mathematisch-Naturwissenschaftlichen
Fakultät der Eberhard Karls Universität Tübingen.

Tag der mündlichen Qualifikation: 17.03.2021

Stellvertretender Dekan:	Prof. Dr. József Fortágh
1. Berichterstatter:	Prof. Dr. Martin Oettel
2. Berichterstatter:	PD Dr. Johannes Bleibel
3. Berichterstatter:	Prof. Dr. Matthias Schmidt

Für meinen Vater,

meine Familie,

und meine „Adoptiv-Familie."

In Erinnerung an Nikolaos.

Abstract

This thesis explores the statistical mechanics of idealized model systems of hard-core rods and "sticky" hard rods, as well as the behavior of a machine learning algorithm. Rods are constrained to square and cubic-type lattices: in monolayer confinement ((2+1)D), in the three-dimensional bulk (3D), and in full confinement to two dimensions (2D).

We study rods in (2+1)D in a basic model system for early stages of thin film growth with anisotropic particles. We write, develop, and execute a very large array of kinetic Monte Carlo (KMC) simulations of the nonequilibrium dynamics. The physics of monolayer growth with sticky hard rods is extremely rich. The bounty of phenomena on metastable phases and complex phase transition kinetics we find has not been addressed before by comparable simulation or analytical models. We identify at least five different phase transition scenarios; the different dynamical regimes are traceable in the 2D plane ("map") spanned by the reduced temperature (or attraction strength) and deposition-flux–to–diffusion ratio. The rod-length as well as simple substrate potentials further shift these regimes and alter the topology of the "map", i.e. the set of phase transition scenarios. The specific model choice for microscopic rotational dynamics of rods is another, surprisingly important factor altering the kinetics and, therewith, the morphological evolution.

For the limiting case of purely hard-core rods, we find excellent agreement between KMC simulations and a corresponding lattice dynamical density functional theory formulated for monolayer growth. The latter is based on a lattice fundamental measure theory formulated for our hard-core rods on lattices. Deviations to KMC simulations are most visible near jamming transitions. In the same, purely hard-core limit, we compare the lattice rods to a continuum model of hard spherocylinders – first in equilibrium, then under growth conditions. These show strong qualitative similarities, despite entailing different "equation-of-states" (virial coefficients).

We simulate 3D and 2D systems of hard and sticky hard rods in the grand canonical ensemble to characterize their phase behavior, focusing on the isotropic–nematic orientational transitions. The nature of 3D nematic ordering is very different when compared to e.g. liquid crystal models in the continuum. We find this transition is only weakly first-order in the purely hard-core limit. Moreover, for rod-lengths 5 and 6, ordering is realized when one orientation is *suppressed* rather than dominant – a unique feature of the fully discretized degrees of freedom. We present the 3D bulk phase diagrams for sticky hard rods at multiple rod-lengths, and another for full 2D confinement. In the latter, a heightened competition between isotropic–nematic and vapor–liquid ordering transitions leads to presumably tricritical behavior.

We train beta-variational autoencoders (β-VAEs) – an unsupervised and generative machine learning algorithm – on configurations of the 2D sticky-hard-rod model in order to better understand their learning capabilities and limits. The algorithms appear to "coarse grain" the configurations of the hard rods. The upper limit on the resolution, i.e. how detailed the reconstructed or generated configurations appear, is set by the chosen latent-space dimension. The specific level-of-resolution is also sensitive to the hyperparameter β, where mode collapse occurs past a threshold value. We interpret the latent variables

as fluctuating collective variables in the rod system. Intriguingly, at the threshold state of β, these form a broad, "disentangled" coarse-graining hierarchy. The first two latent variables are identifiable with the 2D thermodynamic order parameter of the rod system. The paired encoding on latent space – the means and variances for the multivariate Gaussian model posterior – renders highly sensitive information to thermodynamic (Boltzmann-Gibbs) states of the rod system. The full generative model appears to (approximately) represent a critical state that could be expected for a finite-sized system. However the interpretability of the model remains limited as it does not represent a true thermodynamic state.

Zusammenfassung

Diese Arbeit beschäftigt sich mit der statistischen Physik idealisierter Modellsysteme harter als auch attraktiver Stäbchen und dem Lernverhalten von maschinellen Lernalgorithmen. Als Modellsysteme werden quadratische und kubische Gittersysteme verwendet: Stäbchen in 2D eingeschränkter Geometrie, in der (2+1)D-Monolage und im 3D „bulk“. Um fundamentale Erkenntnisse über das Dünnschichtwachstum anisotroper Partikel zu gewinnen, modellieren wir die Physik mit einem (2+1)D Stäbchensystem. Zu diesem Zweck wurden im Rahmen dieser Arbeit kinetische Monte-Carlo (KMC) Simulationen entwickelt, durchgeführt und deren Ergebnisse analysiert. Diese Simulationen sind speziell dafür konzipiert, die Nichtgleichgewichtsphysik dieser Systeme zu untersuchen. Im Falle attraktiver Stäbchen ist die beobachtete Physik sehr vielfältig, beinhaltet metastabile Zwischenphasen und daraus resultierend eine komplexe Phasenübergangskinetik. Wir finden eine große Anzahl von physikalischen Phänomenen, die bisher nicht in vergleichbaren Studien untersucht wurden. Wir identifizieren und charakterisieren fünf unterschiedliche Phasenübergangsszenarien, die verschiedene dynamische Regime definieren. Diese können in einer speziellen zeit-, temperatur- und quenchratenabhängigen Orientierungsordnungsparameterkarte identifiziert werde. Die Topologie dieser Karte kann mit Hilfe der Stäbchenlänge und einem attraktiven Substratpotential modifiziert werden: Phasenübergangsszenarien können verschoben oder gar entfernt werden. Ein weiterer wichtiger Stellparameter ist die spezifische mikroskopische Dynamik der Stäbchenrotation, die überraschenderweise einen enormen Einfluss auf die Phasenübergangskinetik hat.

Für den Fall des Monolagenwachstums mit rein harten Stäbchen finden wir eine hervorragende Übereinstimmung zwischen der KMC-Simulation und einer speziell für dieses Problem formulierten dynamische Dichtefunktionaltheorie. Unterschiede können nahe am Einfrieren der Dynamik („jamming“) identifiziert werden. Ein analoger Vergleich mit einer Kontinuumssimulation von Sphärozylindern zeigt für beide Simulationen qualitativ dieselbe Physik, obwohl ihnen unterschiedliche „Zustandsgleichungen“ (Virialkoeffizienten) zu Grunde liegen.

Um das Gleichgewichtsphasenverhalten dieser Stäbchensysteme in 2D und 3D zu charakterisieren, haben wir spezielle Simulationen im Großkanonischen Ensemble durchgeführt, wobei der Fokus auf den isotrop-nematischen Orientierungsübergang gelegt wurde. Die Natur des 3D-Orientierungsübergangs in den Gittersystemen unterscheidet sich signifikant von dem in Flüssigkristallmodellen. Der in Gittermodellen beobachtete isotrop-nematische Übergang ist ein Phasenübergang von sehr schwacher erster Ordnung. Darüber hinaus konnte beobachtet werden, dass die Orientierungsordnung für Stäbchen der Länge 5 und 6 dadurch realisiert wird, indem eine der möglichen Orientierungen unterdrückt wird. Final präsentieren wir Phasendiagramme für 3D-Systeme attraktiver Stäbchen und ein weiteres für ein 2D-System. Im letzteren führt die Konkurrenz zwischen dem isotropisch-nematischen und dem Gas-Flüssig Übergang zu einem tri-kritischen Verhalten.

Um das Lernverhalten einer speziellen Klasse nicht-unterwiesener und generativer maschineller Lernalgorithmen („beta-variational-autoencoders“ – β-VAEs) zu erforschen, zu verstehen und somit eindeutiger interpretieren zu

können, wurde diese Algorithmen mit den physikalischen Konfigurationen eines ausgiebig untersuchten 2D Systems harter Stäbchen trainiert. Wir kommen zu dem Schluss, dass die Algorithmen die Komplexität der Stäbchenkonfigurationen im Sinne eines physikalischen „coarse-graining“ reduzieren. Die obere Grenze der Auflösung – d.h. wie „grobkörning“ die rekonstruierte oder generierte Konfiguration erscheint - wird dabei von der Dimension des latenten Raums bestimmt. Desweiteren beeinflusst der Hyperparameter β diese Auflösung: Wird der β-Parameter oberhalb eines bestimmten Schwellwertes justiert, hat dies einen „mode collapse“ zur Folge. Ein wichtiges Ergebnis ist, dass sich die latenten Variablen mit den kollektiven Variablen des physikalischen Stäbchensystems identifizieren lassen. Interessanterweise formen die latenten Variablen eine „entwirrte“ Hierarchie, wenn β einen Wert knapp unterhalb des Schwellwert annimmt. Die ersten beiden latenten Variablen können generell mit dem thermodynamischen 2D-Ordnungsparameter des Stäbchensystems identifiziert werden. Die „paarweise“ Kodierungen im latenten Raum, die über die Mittelwerte und Varianzen des Gaußschen Modells gegeben sind, liefern sensitive Informationen über die thermodynamischen (Boltzmann-Gibbs) Zustände des Stäbchensystems. Wenn das gesamte generative Modell hingegen keinen wahren thermodynamischen Zustand repräsentiert, ist es nicht eindeutig interpretierbar.

Contents

List of Figures

List of Tables

List of Abbreviations

2D	two- (**2**-)**d**imensional *or* two (**2**) **d**imensions
3D	three-(**3**-)**d**imensional *or* three (**3**) **d**imensions
(2+1)D	two-plus-one-((**2+1**)-)**d**imensional *or* two-plus-one (**2+1**) **d**imensions
MCMC	**M**arkov-**c**hain **M**onte **C**arlo
MC	**M**onte **C**arlo
KMC	**k**inetic **M**onte **C**arlo
GCMC	**g**rand-**c**anonical **M**onte **C**arlo
SUS	**s**uccessive **u**mbrella **s**ampling
RSA	**r**andom **s**equential **a**dsorption
OMBD	**o**rganic **m**olecular **b**eam **d**eposition
DFT	**d**ensity **f**unctional **t**heory
DDFT	**d**ynamic **d**ensity **f**unctional **t**heory
FMT	**f**undamental **m**easure **t**heory
PCA	**p**rincipal **c**omponent **a**nalysis
VAE	**v**ariational **a**uto**e**ncoder
β**-VAE**	**beta**- *or* β- **v**ariational **a**uto**e**ncoder

Danksagung

Ich möchte mich zu erst bei meinem Hauptbetreuer Martin Oettel für die Möglichkeit zur Promotion in seiner Arbeitsgruppe ganz herzlich bedanken. Die letzten Jahren waren für mich eine aufregende aber auch enorm herausfordernde Zeit, geprägt von verschiedensten Erfahrungen, und ich bedanke mich bei ihm für die stetige Unterstützung in vielerlei Hinsicht – insbesondere bei meinem Wunsch, mir ein komplett neues Themenfeld zu erarbeiten. Ebenfalls möchte ich mich bei meinem Zweitbetreuer Frank Schreiber für seine Unterstützung, Hilfe sowie für die unterliegende Motivation meiner Arbeit zum Dünnschichtwachstum bedanken. Dies hat mir die Möglichkeit gegeben, mir die Physik weg vom Gleichgewicht zu erarbeiten. Dieser extrem faszinierende Bereich der Vielteilchenphysik hat mein Physiker-Leben sehr bereichert. Weiterhin möchte ich mich bei Tanja Schilling für die Kollaboration und ihre Unterstützung herzlich bedanken, sowie die Inspiration, tiefgehende Fragen zu stellen. Positiv in Erinnerung ist der Besuch bei ihre ehemalige Arbeitsgruppe in Luxembourg, wo ich sehr warmherzig empfangen wurde. Mein Dank für die konstruktive Zusammenarbeit geht auch an ihren ehemaligen Doktoranden Mohit Dixit.

Darüber hinaus möchte ich mich vornehmlich bei meinem Kollegen Hans Joachim Schöpe für ausserordentlich hilfreiche Diskussionen, Hinweise zu meiner Arbeit, und für Korrekturarbeiten bedanken. Dasselbe möchte ich an meinem Kollegen Johannes Bleibel richten. Darüber hinaus bedanke ich mich bei ihm, dass er immer offen war, "verrückte" Ideen von mir anzuhören, sowie auch für die spassige und fruchtbare Zeit bei der Gestaltung von "Numerical Techniques II". Ich danke auch Hendrik Hansen-Goos für die zielführende Kollaboration. An alle drei möchte ich mich auch für ihre moralische Unterstützung und Freundschaft bedanken. Dasselbe gilt für meinem Büro-Kollegen Shang-Chun Lin, bei dem ich zusätzlich sehr schätze, dass wir die Abendteuerlust im Bereich des maschinellen Lernens gemeinsam teilen. Die erfolgreiche Zusammenarbeit mit (ehemaligen) Kollegen Paul Quiring, Axel Gschwind, Eelco Empting, Chris Mony, und Manuel Maeritz und die Mitbetreuung ihrer Abschluß-Arbeiten bereiteten mir viel Freude. Ich weiss ihr Talent und Vertrauen zu schätzen. Einen weiteren Dank geht auch an Yuding Ai, für seine Sommer-Praktikumsarbeit bei mir in Tübingen. Ich möchte mich bei der restlichen Arbeitsgruppe von Martin Oettel und dessen ehemaligen Mitgliedern ganz herzlich für die offene, neugierige, und bodenständige Arbeitsatmosphäre, aber auch für ihre Kollegialität und Freundschaft bedanken. Dasselbe reiche ich auch an diverse (ehemalige) Kollegen der Arbeitsgruppe von Frank Schreiber weiter.

Ich bin froh, ein Willkommensein innerhalb des Fachbereichs in Tübingen genossen zu haben, insbesondere schätze ich die motivierende Unterstützung und Kollegialität von Roland Roth und Sabine Andergassen. Ich spreche ferner einen Dank an Michal Rolinek, Georg Martius, und Matthias Bauer (ehemalig) vom MPI für Intelligente Systeme für Hinweise zu den VAEs sowie für anregende Gespräche aus. Anschliessend möchte ich mich bei den vielen Wissenschaftlerinnen und Wissenschaftlern aus der Community bedanken, die mir hilfreiche Fragen und Diskussionen zu meiner Arbeit, oder einfach motivierende Worte gegeben haben – unter Anderem Sabine Klapp, Nicola Kleppmann, Daniel de las Heras, Matthias Schmidt, Sebastian Wetzel, Bill van Megen, Alexander Hartmann, und Kollegen aus dem Exzellenzcluster "Machine Learning

for Science" in Tübingen. Meine engsten Freunde und meine Familie, die immer hinter mir stehen, waren in dieser Zeit und bleiben für mich unersetzlich.

"Imagination is more important than knowledge"

Albert Einstein

Part I

Introduction and Theory

Chapter 1

Introduction

Fools ignore complexity. Pragmatists suffer it. Some can avoid it. Geniuses remove it.

Alan Perlis

This thesis addresses the physics of classical many-body systems of rod-like particles, as well as machine learning pertaining to one class of algorithms. We study the statistical mechanics of simple, highly-idealized model systems of hard rods constrained to square and cubic-type lattices: in the bulk (3D), in full two-dimensional confinement (2D), as well in monolayer confinement ((2+1)D), the latter of which is depicted in Fig. 1.1. This thesis also studies unsupervised and generative machine learning by training specific algorithms upon configurations of these hard-rod systems in 2D.

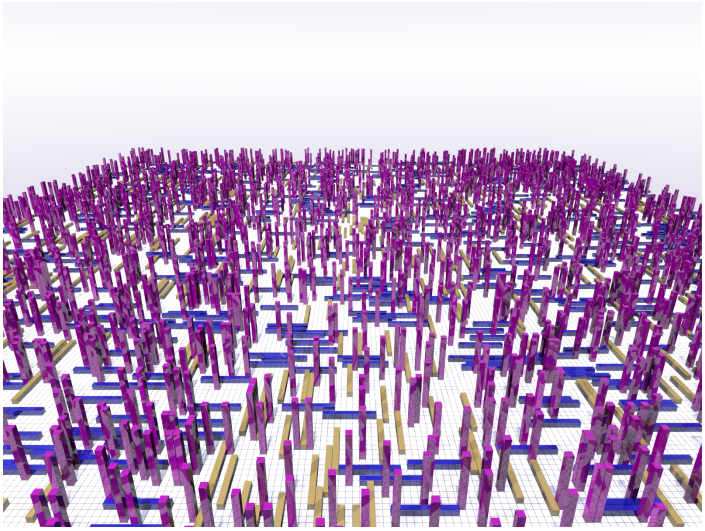

FIGURE 1.1: Artist's depiction of the lattice model of hard-core rods, shown for the case of (2+1)D monolayer confinement, which we investigate in part II of this thesis (please see main text). A cubic-type lattice (also in 3D) allows for only three possible rod orientations: standing (magenta) and two lying (yellow and blue) orientations. In full 2D confinement, the lattice constraint allows for only two possible rod orientations.

We will consider hard (and "sticky") rods in monolayer confinement (maximally one layer at a substrate) in order to better understand the nonequilibrium dynamics of a generic model system for thin film growth with anisotropic particles. We will perform a very large array of kinetic Monte Carlo simulations

that we designed, wrote and developed for this research purpose, which we shall motivate in the following paragraphs.

In current times, a large body of research studies thin film growth with rod-like organic molecules, where fundamentals for many modern materials are being explored and established [1–6]. Producing films of organic molecules with custom structural properties is a promising prospect: They have a huge potential owing to their larger number of degrees of freedom (they are anisotropic and entail complicated interaction potentials). Thus, various crystalline or even amorphous states can occur at initial and throughout later stages of growth [7–16]. In principle, the scales of resulting coherent structures could be modified if the phase transition kinetics during self-assembly were fully understood. Yet, there is a dearth of understanding to this end. For one thing, each molecular system entails different thermodynamically stable as well as metastable structures, generally speaking. Moreover, whichever form of kinetics will depend on control parameters of the growth experiment – the simplest are temperatures and flux rate of newly deposited particles. In this driven nonequilibrium setting of a constant deposition influx of new particles, the system can end up visiting states that are non-ergodic. Therefore, the full story is very complicated, and simple model systems are absolutely necessary for a fundamental understanding.

We will discuss how organic molecular thin film systems can be understood as situated in-between typical colloidal systems [17–19] and atomic systems [20, 21]. Their strong directional interactions generate highly ordered (i.e. crystalline) structures, which may admit the use of a coarse-grained model with discretized degrees of freedom.[1] Our simple, dynamical, on-lattice model system of anisotropic particles will demonstrate that the nonequilibrium physics of thin film growth is very rich. It entails complex phase transition kinetics involving metastable phases. Very basically, the orientational and translational degrees of freedom will be coupled in highly nontrivial ways, leading to collective reorientation processes and a competition between the growth of differently-oriented structures. Kinetic Monte Carlo (KMC) simulation methods that we employ are perfectly attuned for lattice systems, and are event-driven [22–24], allowing us to vary the dynamics across seven to eight orders of magnitude. The phenomena and effects we will present have not been addressed by comparable simulation or analytical approaches before.[2]

In many soft matter model systems, the limit of very high temperatures (in equilibrium) represents the case of purely hard-core interactions [25, 26]. This is generally true when attractions remain short-ranged, which may be denoted "sticky". Purely-hard-core interacting systems are amenable to state-of-the-art analytical approaches for complex liquids in equilibrium, i.e. fundamental measure theory (FMT) [27–30], which belongs to the broader scope of classical density functional theory (DFT) [26, 31–33]. Moreover, dynamical density functional theory (DDFT) is a dynamical extension to the equilibrium theory (see also Refs. [31, 34–37]). It incorporates correlations, at least approximately, into an effective equation-of-motion – of density distributions in nonequilibrium conditions. Therefore, we will also present a detailed study on this limiting case of monolayers of purely hard-core rods, comparing equilibrium [38] as well as nonequilibrium (KMC) simulations to these analytical theories.

[1] A discussion thereof is found in Ch. 2.4.

[2] Please see the latter Sec. 1.2 for a more detailed discussion.

Important for predicting structures grown in thicker, multi-layer films is a good understanding of the bulk phase diagrams. However, these are often not known, and molecules in solution can entail different phase behavior than in thin films,[3] which are typically grown under (ultra-high-)vacuum conditions [1, 3, 6]. If we introduce a new model for thin film growth, then understanding the multilayer phase behavior (in semi-confinement with a substrate wall) would be desirable, as well. In this thesis, we study the extreme limiting case – the 3D bulk – of the same model we have introduced for thin film growth: hard and "sticky" rods on cubic lattices.

From another viewpoint, although particle anisotropy has long been known to induce orientational ordering in a bulk system, i.e. a nematic transition [26, 39–42], the effect of constraining anisotropic particles to lattices is not fully-understood. This is true despite the fact that though lattice systems have traditionally held a special place in theory development [43–49]. Simple models in the literature studying orientational transitions in the bulk are either only discretized in rotational degrees of freedom, or are spin-like models on lattices (no hard-core interactions). In this thesis, we contribute to both soft matter physics as well as a broader field of statistical mechanics by characterizing the isotropic–nematic transition and corresponding phase diagrams of systems of hard, as well as sticky hard rods constrained to cubic (3D) and square (2D) lattices.

Finally, we aim to explore the currently booming field of machine learning by studying one particular unsupervised and generative algorithm – (beta-) variational autoencoders [50–52]. In order to understand their capabilities and limits better, we observe their learning behavior when trained upon configurations of a well-characterized (well-understood) many-body model system: the same model system of sticky hard rods in 2D confinement that we will have characterized beforehand in this thesis. The so-called generative capabilities of the algorithm originate from learning a probabilistic (approximative) model of the observed data. In an exploratory study with some statistical-physics "reverse engineering", we attempt to understand *what* (beta-) variational autoencoders are learning about the physical model system. For example, we are interested in whether they are learning the most important macroscopic properties like order parameters. We also hope to gain insight on the physical meaning of the probabilistic model that is learned, i.e. whether it can be interpreted in terms of thermodynamic (equilibrium) states of the system.

We have written this thesis out of a number of projects, where each addressed scientific questions that require different methodical approaches, but also belong to different bodies of knowledge: We will investigate both equilibrium and nonequilibrium physics, as well as machine learning in this thesis. Therefore, in the following motivation, Sec. 1.1, we will try to set the stage at a very generic level. An introduction to each, specific research topic will follow thereafter.

[3] Most basically, this can be understood as owing to the confinement setup. Please see discussion in Ch. 2.2.

1.1 A theoretical motivation

Idealizations in physics are the aim "*to find the point of view from which the subject appears in the greatest simplicity*," as Gibbs once said.[4] In physics, we transcribe the complex world into ideal (mathematical) entities and look for analogies between seemingly disparate systems. Surely, we can "undo" some of the loss of complexity by gradually adding details back, extending models step-by-step. But, more importantly, we must be wary not to remove the very things in a model that are giving it its realistic properties in the first place. To put it in the famous words of Einstein, "*Everything must be made as simple as possible. But not simpler.*" The dance between idealization – to be able to make practical use of intelligible and actionable models – and the constant re-assessment of their success and limitations sums up the daily business of (classical many-body) physics. This thesis exemplifies this method-of-action and process, in which we introduce and study the physics of very simple model systems of anisotropic particles in equilibrium and nonequilibrium contexts.

Statistical mechanics attempts to connect the macroscopic world of systems composed of many bodies with the microscopic physics of inter-particle interactions. Arguably, the concept of a "body" in classical physics awakens a platonic notion of a geometric object with well-defined boundaries. In this sense, we are compelled to understand the behavior of a macroscopic system of *discernible* objects. Uncovering the laws governing dense assemblages of *extended* bodies is the core of liquid state theory [26], which attempts to address, most fundamentally, the effects of particle exclusion (hard-core repulsion), as well as "extra" inter-particle interactions, usually presumed to be simple in character.

Colloidal systems can realize this platonic notion – of assemblages of microscopic, idealized bodies – in "real-world" experiments. The inter-particle interactions are short-ranged and weak enough to allow for the study of particle dynamics and self-assembly kinetics in real time due to the relatively large particle size (their response to forces is "slow"). Therefore, colloidal model systems provide a place to look for *how* and *why* matter re-arranges into macroscopic objects. They can aid us with a better understanding of the basic mechanisms behind crystallization of atomic matter, where in the latter, particle rearrangement dynamics are so fast that what are deemed as "many-body" effects are virtually invisible. In contrast, in the realm of slower, soft-matter or colloidal systems, subtler distinctions between "entropy-driven" versus "energy-driven" effects are possible. Yet, even the platonically most simple of soft matter systems – that of hard spheres – continues to challenge our current theoretical understanding in some of the most important questions: The full statistical problem in equilibrium has not been solved exactly to date (in the case of our two- or three-dimensional world), neither has that of the dynamics in nonequilibrium conditions.

Phase transitions are probably the most poignant example of complex behavior in many-body systems, and are at the heart of the study of condensed matter out-of-equilibrium. Lattice models have been pivotal, historically, for opening up theoretical study thereof. "*Why study a simple model like the Ising* [43] *model?*", as Kadanoff puts it [53]. It had been used to prove that spontaneous magnetization was an emergent phenomenon [54, 55]. The simplicity behind it (and other lattice models) has enabled us to formulate elementary

[4] Quoted in A. L. Mackay, *Dictionary of Scientific Quotations*, London (1994).

questions: Under which conditions do phase transitions occur? What happens upon changing the details of the microscopic model? It appears that many, if not most systems showing critical behavior can be organized into particular *classes* [44, 48, 56–58]. Only a few, simple aspects turn out to be relevant for critical behavior, such as the range of inter-particle interactions, dimensionality of the system, and symmetry – and not on many other details about a material. Along these lines, lattice models can be considered the "fruit-flies" of statistical physics, offering a steady place to work and return to foundational questions.

In contrast, many of the models studied in liquid state theory and soft matter entail continuous degrees of freedom, in particular those exemplifying entropy-driven orientational ordering: Colloidal systems of rods or liquid crystals showcase a transition where individual particles become aligned, on average, in the same direction: the *isotropic–nematic* transition in three-dimensional bulk [25, 26, 39, 40, 42, 59, 60]. Thus, orientational ordering is typically understood in terms of continuous rotational degrees of freedom.

As to lattice models, orientational degrees of freedom have traditionally been incorporated via spin-type interaction Hamiltonians (e.g. XY models) [49, 58]. However, these are fundamentally different, as these interaction potentials are not hard-core-repulsive. A hard-body interaction implies a model of *extended bodies*, where particles exclude volumes of space from other particles during their motion – the basis of all entropy-driven phenomena. Lattice-model counterparts to hard-body models from the continuum are lesser-known or studied in the literature: We make a contribution in this thesis by investigating systems of (long) hard rods on square and cubic lattices.

One question arises immediately – can lattice models be used as aliases for soft matter systems, in particular when the particles are anisotropic? Clearly, lattice and continuum models express fundamentally different *symmetries*. A theoretical procedure to convert a continuum model of a rod to a discretized version is not known, let alone may even be impossible. Nevertheless, knowing the phase diagrams in each case is imperative. Markov-Chain Monte Carlo simulation methods [38, 61–63] are key in this regard. They render formally exact estimates of observables in equilibrium (after properly accounting for finite-size effects and statistical (sampling) errors). We study the phase behavior of lattice models of hard rods in part III, as well as within part II of this thesis. In part II, we compare lattice and continuum hard-rod systems *directly* in monolayer confinement. In part III, we will find on-lattice models of hard rods behave very differently, indeed, compared to well-known systems from the continuum.

Complementary information can be gained when studying each system under nonequilibrium conditions. There, collective dynamical phenomena can occur such as (metastable) gelation, glassy behavior, or dynamical arrest. We compare the nonequilibrium dynamics of hard rods in monolayer confinement to a continuum model directly in part II of this thesis. While the continuum model is simulated to undergo Brownian dynamics at local scales, the lattice model presumes Markovian dynamics at the smallest relevant scale of treatment, using the KMC approach. We will discuss these presumptions again in a chapter on theoretical fundamentals, Ch. 3. Collective dynamical phenomena like arrest and gelation will become strongly apparent in the lattice model, in particular after the addition of "sticky" attractions.

In our investigations of physics with simple model systems, we become part of a larger quest: to search for effective physical laws at intermediate scales of space and time. In statistical mechanical theory of equilibrium, time loses its meaning. All relevant statistical relationships (in infinite time) are encapsulated in a partition function or free energy function(al). If we can treat a density distribution of particle occupation in space, as in density functional theory, a free energy functional thereof is minimized in equilibrium (with a static external potential or constraint), rendering a unique solution. In this picture, the relevant laws of physics can be expressed, formally, in terms of *stationary*, average quantities with fluctuations. Correlation functions are expressible as higher-order derivatives of the functional [26, 58, 64–67].

However, finding a tractable solution to the generating functional (free energy functional or partition function) of *interacting* many-body systems poses one of the greatest intellectual challenges in condensed matter and statistical physics that, in the context of classical systems, remains unsolved for nearly all two- and three-dimensional systems. Traditionally, mean-field approximations have been utilized with some notable success – e.g. for producing approximate phase diagrams, predicting scaling behavior, or even for modeling near-equilibrium dynamics (which is another story worth discussing) [49, 65, 68]. As they fail to capture correlations correctly, relevant effects at mesoscopic scales may be left out.

Systems of particles that entail both translational and rotational degrees of freedom at the one-body scale (like hard rods) are particularly difficult cases. The long-range correlative effects of hard-core repulsions in liquids are a major challenge against mean-field approaches. Fundamental measure theory (FMT) makes an astute attempt at incorporating correlations, specifically designed for the case of hard-core repulsions [27–30, 32, 33, 69]. Fortunately, as long as attractions remain short-ranged, these can be treated on an effective level – they can be mapped to repulsive forces due to a depletant, at least for systems in equilibrium conditions [70–72]. In this thesis in part II, we compare simulations against FMT formulated for hard rods on lattices, both in the purely-hard-core case, as well as for additional, short-ranged ("sticky") attractions.

On the other side of the spectrum, systems far-from-equilibrium are more than just intriguing, they are fundamental to our own existence: Life itself [73] as well as computers and computation [74, 75] are inherently highly nonequilibrium phenomena. A more tangible concept is pattern formation which we observe in nature – ripples formed on sand due to wind or water, crystals, or patterns generated by lifeforms, e.g. camouflage. Nonlinearities are inherent in all these examples, which is why dynamics of nonequilibrium many-body systems are so nontrivial [76, 77]. Patterns are synonymous with *regularities*, thus with a reduction of complexity to something simpler and partially coherent. If we seek to generate these simpler patterns, then, we may only need to apply a few, simple rules recursively (which is how fractals form). The point is however, that Nature comes up with the simpler rules herself, like a "blind watchmaker".[5] (We can speak here, broadly, of emergent phenomena [79, 80].) Therefore, nonequilibrium phenomena (such as thin film growth) challenge us to uncover the "rules", transcribable onto equations of motion for the important system variables, whatever these may actually be.

[5] We borrow the phrase Richard Dawkins coined [78] to portray biological evolution via natural selection.

While dynamical systems theory [81–84] and nonlinear dynamics [85] can carve out necessary, basic conditions for asymptotic limits like thermodynamic equilibrium or steady states to be reached after infinite time, this is only partly satisfying. Beginning at a microscopic level, we are hit with the reality of an enormous number of degrees of freedom (of "possibilities"), all of which are coupled (correlated) in nontrivial ways in a many-body system. Nonequilibrium statistical mechanics as a body of knowledge suffers from a long-standing failure at finding a unified, principled approach. An "all-purpose" recipe to extract a reduced (let alone tractable) set of equations of motion is still lacking. The highly coupled nature of motion in a many-body system means, in practice, assumptions are imposed in top-down fashion, and the approximations on the dynamics may be uncontrolled. The problem is no less easy for cases where particles are anisotropic in shape (hard-core repulsion). Moreover, strong confinement requires especial attention, as it can additionally generate (or, conversely, destroy) correlative effects in fluids.

We explore a system combining all these aspects, where particles are both anisotropic and confined to a monolayer, as well as treated in nonequilibrium conditions.

Notably, the founders of statistical mechanics had attempted to explain equilibrium phenomena from dynamical (or kinematic) considerations [86–88]. Yet, historically, a different route was taken that postulated stationarity of probability distributions (ensembles) in equilibrium, tied deeply to the ergodic hypothesis [64, 89, 90]. This concept is at the basis of optimization principles like that in density functional theory, developed much later. In contrast, variational approaches for nonequilibrium are not well-developed or standard in the field [91, 92]. Dynamical simulations are thus crucially important for any particular system of interest, and is often the only tool available.

From a theoretical point-of-view, the difficulty with nonequilibrium lies in the non-Markovian nature of the dynamics of observables. The state of a system becomes conditioned on its previous history, far back in time [93–97]. In fact, outcomes can quickly change given a few, subtle adjustments of parameters (temperature, speed of a driving protocol, experimental waiting times, slight modifications in the microscopic constituents of the many-body system, number of particles, form of confinement, and any systematic or preparation errors). In other words, systems far-from-equilibrium may be mercurial with respect to such controllable (or uncontrollable) parameters. Yet, correlations in many-body systems introduce coherence, generated via particle collisions, which can ultimately steer the system towards its equilibrium state. Although involving an intricate competition between internal and external forces, taking place at various length- and time-scales, root causes for large-scale re-ordering may be thermodynamic in nature if, for example, phase separation is involved. Thus, *typical* behavior can indeed be ascribed to a nonequilibrium evolution, often phenomenologically; the system may go though different epochs or regimes.

In thin film growth, the physics of the first monolayer is characteristically different than that of later stages, where the system transitions from a quasi-2D system to a multi-layer system [20, 21]. Within the sub-monolayer regime itself, initial kinetics involving island nucleation are different from those later, when e.g. island ripening and coalescence occurs. To our surprise, however, we find in this thesis that even island-formation kinetics can vary dramatically upon adjusting basic parameters. (The evolution of a growing monolayer of rod-like particles goes well beyond the scope of

standard, so-called "atomistic" models for submonolayer growth.) This liability can be attributed in part to the anisotropic shape of rods as well as to the confinement of the system, which introduces a number of metastable states.

Today, much of nonequilibrium behavior remains markedly ominous and unpredictable, accompanied by a vast body of phenomenology that is growing with ever more types of systems explored. Each can hold new surprises, which, in turn, calls for a better understanding of the underlying physical principles. The growth of thin films with rod-like particles is a particular example, relevant for materials science, and e.g. the development of novel semiconductors and optical devices [1–6]. As these technological developments reside at the edge of our current understanding, simulations are remarkably *empowering*, in particular when starting with simple model systems, giving us possibilities to "reverse engineer" the effective laws we have been seeking in the first place. We can vary and control parameters that may otherwise be very difficult or practically impossible to do in experiments. Of course, the downside is that all simulated models contain assumptions that can (unknowingly) break down at some point, especially in nonequilibrium situations. Despite this, we can be sure of one thing: the equilibrium versus nonequilibrium physics should be consistent at long–time or quasistationary limits.

Throughout this thesis, we attempt to harmonize the above point, performing analysis of the same structural observables in nonequilibrium as well as in equilibrium conditions. In this way, we may be able to judge how far from equilibrium a system is located along in its trajectory. A system will retain many of its equilibrium properties under *quasiequilibrium* dynamical conditions. In most other situations, however, like near phase boundaries, where ergodicity will be lost, new sets of mesoscopic and macroscopic states emerge in a highly intricate process difficult to capture with current theories (for general cases). Crucially, the states visited are thermodynamically unstable or, at best, metastable, which means the phase diagrammatic information will not help us predict the short- or intermediate-timescale evolution. Dynamical arrest such as jamming can occur, which is not accessible via analytical approaches based on thermodynamical equilibrium, as far as we can tell. Nonequilibrium conditions "store" a high potential for complexity in the often largely unpredictable set of trajectories a system will take. The complexity is reduced upon converging to the next thermodynamically stable state. In this way, we can call nonequilibrium a "creative process". Our concrete studies of a driven, nonequilibrium system of hard, sticky rods (for monolayer growth) in Ch. 5 should make this figurative description clearer, where we will discover a bounty of surprising phenomena; *despite* a very high degree of model simplicity.

Machine learning algorithms – where a large number of free parameters of the learning system are optimized – are complex systems in and of themselves, and will be subject to emergent phenomena [98, 99]: The process of learning is known to involve phase transitions and threshold behavior. However, we can also think of machine learning as finding a coherent and reduced model of the world. Algorithms could be able to find coarse-grained versions of a complex, intractable many-body system, for example. These ideas are highly intriguing, and have motivated us to study the learning behavior of one algorithm, a *variational autoencoder* [50–52], in Ch. 7 of this thesis. Arguably, if we were to

understand exactly how to construct algorithms that model and predict the dynamics or detailed properties of a physical many-body system correctly, under quite general conditions and up to a controlled level of approximation, we would succeed both in theory on learning as well as open up a new chapter (era) in theoretical physics. This thesis tries to take a first, preliminary step by investigating the capabilities of current, refined machine learning methods to model complex, Boltzmann-distributed configurations of a many-body system of hard rods.

Random properties: From thermal equilibrium to nonequilibrium and machine learning

Established theories of statistical physics of classical many-body systems view these systems from a probabilistic point-of-view, representing the large number of degrees of freedom as random variables. More than just a means to an end in our descriptions of the universe, it is up to debate whether probability, or, better, randomness, is an inherent property of the universe itself [100–102].

Aside from these semi-ontological questions, to use the techniques offered by classical statistical physics in or near equilibrium, we often begin by coupling a large assemblage of identical particles to a thermal bath. This allows them to fluctuate and move randomly in space in time. As already alluded to, the power of established theory lies in the simple notion that the relevant variables have stationary statistics in equilibrium. Fluctuations, which are fundamental to the stochastic dynamics, are "simply" extractable from an equilibrium generating function (linear response theory). Thus, in principle, a minimized free energy (functional) (or maximized entropy for purely hard-core particles) is the governing principle for the calculation of any quantity in equilibrium, which takes on the form of expectation values. Crucially, estimates suffer dependent on the (in-)accuracy of the free energy functional.

Equilibrium properties calculated in this manner do not explicitly consider the sharp, microscopic trajectories of particles. The ergodic hypothesis guarantees that contributing information of "sharp" particle trajectories will eventually be "annealed out", given we wait long enough. This prompts the Markovian character underlying the dynamics of macroscopic observables in equilibrium. In thermal systems, the annealing process is driven by the thermal bath. Yet, when the temperature is sufficiently cool or the density of particles breaks past a critical value, the system of interest will not be able to anneal away these variables quickly enough, i.e. will not be able to forget its history. We now enter the realm of nonequilibrium physics that is distinct in both phenomenology and theoretical approachability. An extreme form – when the annealing processes cease – renders long-lasting, *quenched* randomness, which is "never forgotten". Such quenched randomness emerges spontaneously in jamming transitions, for example, where the particles become arrested due to frustration in overly crowded particle packings. Even less-severe variants of nonequilibrium dynamics still imply that the ability to "anneal out" or relax all relevant variables in the system is limited significantly. Synonymous is a loss of ergodicity, which can be restored if a system is allowed to relax (when driving forces are turned off or the system becomes thermally isolated).

Randomness in nonequilibrium dynamics entails a different meaning, possibly: A system can take on one of many trajectories of the system given particular constraints (driving forces, temperature, volume, etc.) from a particular

initial condition. Ergodicity can be broken (even transiently) [103–107]; all trajectories that abide to constraints (both on dynamics including initial or at intermediate conditions where external forces are applied) are (equally) possible. In contrast, in equilibrium, all possible *states* abiding to static constraints are explorable (and therewith equally justified) after infinite waiting or measurement time, irrespective of the initial condition.

Modern machine learning algorithms that are *generative* are based on probabilistic models of data, i.e. the data at hand is only a subset of all *possible* data [51, 98, 108–111]. The learning challenge is to "figure out", i.e. infer, a way to represent the full set of data, given a few model presumptions. The optimal or stationary solution to the objective function can be thought of as finding an equilibrium with constraints. Yet, the constraints can frustrate the system during the optimization process. We argue that a studying how an algorithm learns when "fed" data that represents a model system from statistical mechanics may be fruitful – for understanding and interpreting their generally complicated behavior, defining limits on their learning capabilities, and finding ways to improve them. One example may be whether the learned models sufficiently capture basic, physical quantities within datasets, such as order parameters, as well as functional dependencies such as measures of energy. This constitutes the heart of our investigations within this thesis, where we apply generative algorithms to data distributions of hard-rod configurations.

* * *

In the following sections, we introduce the specific studies of this thesis, while providing a literature review: Sec. 1.2 introduces our study of nonequilibrium thin-film growth with a lattice model in part II of this thesis. We study the equilibrium properties of bulk systems of hard rods constrained to lattices in III, which we introduce in Sec. 1.3. In Sec. 1.4 we introduce the study of part IV, where we apply an unsupervised machine learning algorithm to configurations of the two-dimensional system of hard rods. At the end of this chapter in Sec. 1.5 , we provide a complete overview of the further organization of this thesis – of chapters and corresponding scientific topics. Within the same section, we will address the issue of co-authorship: This thesis presents the work of multiple co-authored manuscripts that are readily published. Thereafter, we will make a few statements on the scope of the numerical work done by the author of this thesis, for all of this thesis.

1.2 A lattice model for monolayer growth with rod-like particles at substrates

In part II of this thesis, we explore a very basic statistical-mechanical model system under *nonequilibrium* conditions: One of hard-core, rod-like particles on lattices confined to maximally one monolayer. In this particular dynamical model set-up, the system is *driven* (or, in other terms, gradually *quenched*) by the monotonic deposition of new particles from a virtual reservoir, emulating the growth of a single film on a surface. We seek to understand the conditions under which particular types of structure form, or which phase separation kinetics are possible. In Ch. 5, our generic model system of sticky hard rods – that we implement within kinetic Monte Carlo simulations – is defined by

a very limited number of control parameters. However, these are more than enough to generate a very rich variety of effects, i.e. multiple phase transition scenarios and therewith many possibilities for the structural and dynamical evolution during monolayer growth. The limiting case of purely hard-core rods is studied, first, in Ch. 4, where we additionally compare the simulations of growth to dynamical density functional theory.

Our motivation is twofold, to some degree: The first is rather pragmatic in nature, aimed at a better theoretical understanding of the growth of thin films at substrates with anisotropic molecules, tied to a large body of research with multifarious phenomenology. The second, "ultimate" aim is exploring nonequilibrium statistical mechanics of systems where orientational degrees of freedom play a central role. In the specific set-up, the system is exposed to a driving force – the monotonic deposition of new particles. This is interesting from the fundamental perspective of phase transition kinetics. As we will see, Ch. 5, the deposition–to–diffusion rate together with the (reduced) temperature (or "sticky" attraction strengths) control the *types* of phase transition scenarios in the monolayer. Every one of these can be characterized by a particular kind of competition between metastable and stable phases having different particle orientation.

As we shall discuss more deeply in Ch. 2.1 and Ch. 2.3, confinement will induce various correlative effects: The phase behavior and dynamics in the rod-systems will be fundamentally altered compared to bulk, and many otherwise unstable states can become metastable or longer-lived.

Equilibrium information about these systems necessarily completes a full understanding of the statistical mechanics of these systems. We study the equilibrium properties of the limiting case of purely hard-core interactions in Ch. 4. These are compared to those predicted by fundamental measure theory. For the "sticky"-rod monolayer systems, we will also estimate the (stable-phase) vapor–liquid binodals using grand-canonical Monte Carlo (GCMC) simulations.

The deposition of particles at surfaces represents the most basic mechanism for the growth of thin films. Widely known systems are, for example, Langmuir monolayers [112–117], i.e. amphiphilic molecules on a liquid water surface. Orientational transitions of films of anisotropic particles at surfaces is of general theoretical interest (e.g. Refs. [118–122]), where self-assembled monolayers (SAMs) [123–126] can be regarded as prototypical cases. A generic feature in SAMs is that they entail a transition between a "lying"- (λ-)phase and a "standing"- (σ-)phase in a monolayer, the appearance of which depends on the level of coverage. These orientational phases are associated with qualitatively different dynamics and kinetics of the system during (nonequilibrium) growth [127]. Specifically, (depending on growth conditions) the λ-phase appearing first with the σ-phase subsequently indicates a change in the kinetics of growth and gives rise to (at least) two regimes.

These lying and standing phases, and transitions thereof, are also reported to occur in thin films of organic molecules grown at at substrates. Thin films of organic semiconductors [128] are notable examples systems [2, 3, 5]. Almost all of the typically-employed organic molecules are anisotropic (except for e.g. C60), some of which are displayed in Fig. 1.2, and films of rod-like molecules like pentacene, diindenoperylene and others are utilized in e.g. organic electronic devices and optical devices [9, 129–131]. Clearly, the scientific studies on organic molecular films, as well as SAMs and Langmuir monolayers are

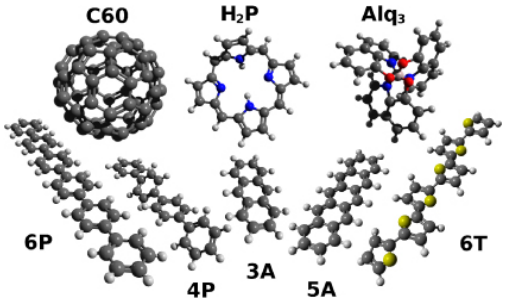

FIGURE 1.2: Depiction of various organic molecules used in organic molecular thin films. Source: Ref. [1].

strongly motivated by applications: Smooth surface coatings, functionalized surfaces, or rough interfaces in films of mixed organic molecules can be desirable, for example. Organic molecules seem particularly suited for tailored photonic and optoelectronic properties (efficient solar cells) [2, 132–135]. Yet, these experimental systems also allow the exploration of questions on structure formation away from equilibrium at a more fundamental level.

Organic molecular beam deposition (OMBD) [1, 3, 6] is a technique with which pristine thin films of these organic molecules are grown within a vacuum chamber: particles are continually adsorbed onto a substrate via a vapor reservoir. As particles become mobile on the substrate, undergoing predominantly random motion, they self-assemble into compact structures that grow, and may further transform or even disappear during the nonequilibrium evolution. (A brief introduction is given further below.)

Important for the motivation and context of this work is the following observation: the growth of organic molecular films is markedly distinct from that of atomic crystalline films in the richer phenomenology involved. Grown thin films with organic molecules entail a large variety of orientationally-ordered (crystalline) states due to the particle anisotropy or, in other terms, highly directional forces between the molecules [1, 3, 9, 127, 136]. Phases with differing molecular orientations co-occur or transform into one another at the submonolayer and "ultra-thin-film" regimes [7, 137–148]. (Some of these may even be metastable [13, 149–152].) Monolayer and thin-film phases distinguish themselves from the crystal phases and associated film morphology dominating at later stages of film growth [11, 15, 16] We provide a review on the literature around the monolayer stage in Sec. 1.2.1 below.

Early-stage kinetics of thin film growth with isotropic particles have been approached analytically in terms of rate equations of time-dependent islands number and sizes. The growth of islands are assumed to be driven by monomer attachment-detachment kinetics [20, 21, 153, 154]. Yet, these traditional approaches come from the context of atomic crystallization from a vapor phase, and are mean-field in character. Therefore, many-body correlative effects, such as collective re-ordering processes, are not taken into account in any explicit way. Moreover, potential intermediary phases are not considered; the conversion from a vapor to a crystal phase is considered direct. However, organic molecular films are described as having a pronounced, "soft-matter" character [155]. We shall discuss this separately in Ch. 2.4, but, mention a few effects here: "Liquid-like"-like wetting layers, a competition between and co-occurrence of various crystalline phases, wetting transitions, and multiple phase separation

processes are possible at various stages. In this view, self-assembly with organic molecules may be better characterized as more "entropy-driven" due to particle extent and anisotropy, as well as effectively weaker bonding, in contrast to the fast, "energy-driven" phase transformations involved in atomic matter.

This notion makes a study of the interplay between the equilibrium phase diagram/equation-of-state and the dynamics of film formation for systems of anisotropic particles particularly worthwhile. Already in 3D bulk rod-like particles exhibit numerous phases (liquid, nematic, smectic of various kinds, columnar and crystalline) (we also study 3D bulk systems of rod systems constrained to lattices in this thesis, part III).[6] Importantly, *confinement* can completely "change the game" drastically regarding both the phase behavior and dynamics (discussed more generally in Ch. 2.2). The high sensitivity of organic molecular thin films to even small changes in molecular structure [156] or to the type substrate [8] attests to the notion that confinement amplifies subtle differences between systems: theoretical studies of monolayer systems of anisotropic particle systems have concluded that that the details in the microscopic interactions are crucially important to the ordering behavior [157], where even the basic particle shape biaxiality can alter the entropy-driven behavior [158]). At a most basic level, the coupling of translational and orientational degrees of freedom is key to understanding complex fluids, and dimensional confinement can select and enhance particular many-body aspects.[7]

In part II, we take a "soft-matter" approach to thin film growth with rod-like particles, aiming to extract generic principles on the statistical mechanics of these systems. We introduce an idealized, microscopically "coarse-grained" model system amenable to KMC simulations. The numerical advantages are clear: We can simulate large systems over long times, i.e. up to high coverages of the monolayer. Further, the extreme model simplicity allows us to employ classical density functional theory and dynamical density functional theory.

A main feature of the idealized model is the locality of the configurational Hamiltonians – rods are hard-core repulsive, and (later) have simple, nearest-neighbor attractive interactions. The second main feature is that rods are constrained to a (simple cubic) lattice. The full model only contains a handful of free parameters: (1) particle aspect ratio, (2) the attraction strengths between rods (the case of sticky hard rods), (3) the strength of a simple substrate potential that biases an orientation of particles, (4) simple microscopic diffusion rates of translational and rotational degrees of freedom (in the ideal-gas limit), (5) and a constant particle influx (in the case of nonequilibrium film growth).

In investigating the equilibrium properties as well as the nonequilibrium growth trajectories systematically, we attempt to provide a holistic view of the phase separation kinetics and possible pathways taken from an empty substrate towards a full monolayer. In addition to simulations, we explore the capabilities of density functional theory in the form of fundamental measure theory [28, 30, 32, 33, 69, 159, 160] for analytical approaches of the purely hard-core systems in equilibrium. Notably, this is an inherently many-body approach, as FMT can express many-body correlation functions in the form of functional derivatives. Further, we compare dynamical density functional

[6] Please see the introductory Sec. 1.3.

[7] A follow-up, deeper discussion is found in Ch. 2.

theory (DDFT) [34, 35, 37, 161, 162] with KMC simulations [22–24, 163] in describing nonequilibrium dynamics of structural observables for the case of purely hard-core rods.

The next section discusses and reviews the phenomenology of organic molecular thin film growth around the monolayer stage. Section (Sec. 1.2.2) motivates and discusses our approach in more detail. A brief review of related simulation studies is also provided.

1.2.1 Phenomenology of monolayer-stage film growth with organic molecules

Thin film growth

In OMBD (and general molecular beam deposition), thin films are grown onto a substrate surface within ultra-high vacuum chambers, of a given vacuum pressure, emanating from a vaporizing (hot) source of particles, and depositing (condensing or sublimating) onto a (cooler) substrate with whichever chosen material properties. Thin-film growth is a dynamical nonequilibrium phenomenon, where many processes – single or many-body in nature – compete in an out-of-balance manner. In nonequilibrium, relative rates amongst all processes render a way to measure the imbalance of forces in the system, which drives the growth (or disappearance) of various structures. Figure 1.3 shows a schematic of the basic processes assumed to play the most fundamental role in the evolution of so-called "atomistic"-type of multilayer thin film growth – with particles (atoms) that lack any anisotropy, e.g. metallic systems [20, 153, 163]. A deposition flux of rate F drives forward (increases) the number of parti-

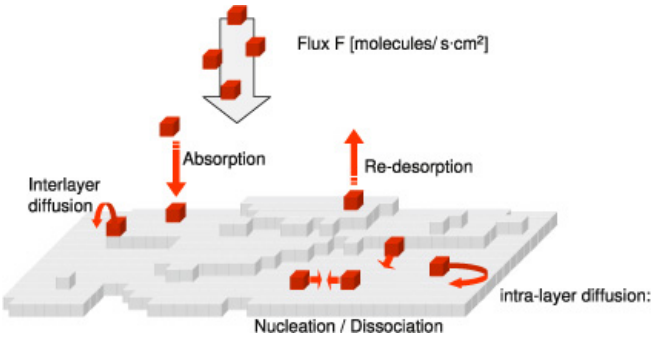

FIGURE 1.3: Schematic of the basic processes involved in the nonequilibrium evolution of thin film growth for atomistic systems (no particle anisotropy). Source: Ref. [6].

cles on the substrate system. Diffusive processes (translational diffusion of rate D) drive the system towards a global equilibrium, and inter-particle attractions generally favor a localization of structures. (Evaporation or other dynamics such as particle-swapping can also occur, generally, and multi-layer growth models also consider intra-layer transport processes.) In Ch. 2 we provide a more thorough discussion on the main driving forces during growth from the standpoint of generic fluid systems.

The submonolayer stages of film growth entails the initial self-assembly that will affect the subsequent growth kinetics at later stages, ultimately determining the macroscopic properties of multi-layer films [164, 165]. It is usually described in terms of island formation and growth under deposition, and a later

ripening and coalescence thereof. However, the case of elongated particles is more complex owing to pronounced coupling of translational and orientational degrees of freedom, hiding a greater potential for various self-assembly trajectories during monolayer growth. We will review phenomena on monolayers with organic molecules further below.

Macroscopic features such as thick islands and mounds or smooth layers [20] are visible during later stages of growth. A combination of growth modes, where both occur, may be possible [149]. These features may be tunable, in part, via the flux [166] or temperature [167]. However, intermediate and later stages of growth are not treated in the context of this thesis.[8] We mention here that the (real-time) evolution of morphology of thicker films is very often quantified using x-ray scattering techniques. This can allow one to characterize the size distribution and correlation lengths of domains within a film, as well as the roughness of the film [9, 169].[9]

Around the monolayer stage of film growth: various phases and competing structures

As mentioned, SAMs are known to show lying and standing phases [125, 127, 171]. Single-component monolayer films of organic molecules[10] are known to entail different crystal phases, appearing at various stages during the submonolayer stages of growth, for example flat-lying, side-lying, and standing dense phases [176–178]. Disordered or liquid-like phases [10, 13, 144, 147, 179–183] also appear at higher coverages of the monolayer. A number of counterintuitive effects can occur, for example, island morphology varies with temperature in an inverted manner compared to that predicted by diffusion-limited aggregation [178, 183].

Some of these structures are clearly unique to the monolayer: "thin film", "ultra-thin film", "monolayer" or "bilayer" structures are reported for various organic molecular thin films. Many of them are believed to be metastable [141, 147, 149, 155, 181, 183–186], and the molecular order appears poor (disordered) [12, 150, 180], reported as having a "liquid-like" character [13]. Heating (and cooling cycles) applied to pentacene in the submonolayer regime changes the mean orientations in an *irreversible* way [182, 187], such that phases do not reappear in the reverse cycle. "Annealing away" [12, 178, 180, 187–190] such metastable or nonequilibrium phases into stable orientations is possible in these cases. These metastable states are associated with kinetically trapped or arrested particle re-orientation dynamics, where re-ordering may be enabled on a many-body (collective) scale only [13, 182, 188]. These findings resemble those of our studies of monolayer growth with sticky hard rods on lattices (Ch. 5), where a standing-up transition may occur after a metastable, disordered state decays that entails dynamic arrest, or when a stable phase nucleates out of

[8] This is investigated in a complementary piece of work parallel to this thesis (Ref. [168]). A simulation code for multilayer growth with sticky hard rods was developed during the work of this thesis, which we mention in the outlook of Ch. 5 and discuss again in the closing part of this thesis.

[9] With grazing incidence x-ray scattering, one can obtain information on lateral spatial correlation lengths, whereupon island sizes and shapes can be extracted [170].

[10] See also Refs. [146, 172–175] for additional single-component monolayer-film studies, in addition to others cited in the main text.

it. (We discuss more on general self-assembly in nonequilibrium and the soft-matter-nature of monolayers of organic molecules in Ch. 2.4.) Clearly, then, the state of the monolayer will affect subsequent growth kinetics [13, 191, 192].

We mention here another category of monolayer systems: That of mixtures of organic molecules. These have enjoyed attention in recent years [169, 193–200]: these systems can behave quite perplexedly at submonolayer densities. For example, a single component may form 3D islands, while the other forms more regular crystals [201]. The phase behavior is much richer, naturally: Ref. [202] reports at least three well-defined thermodynamically-stable mixed phases in heteromolecular monolayers. The submonolayer phases of a single-component system is disturbed by the second material, leading to a certain level of disorder [203]. To this end, Ref. [204] compares different substrates, and [156] compares different, but similar substances in bilayer formation. See also Refs. [195, 196, 205–207].

The flux-versus-self-diffusion-rate F/D is a fundamental control parameter for the size and frequency of compact structures in the system. This will determine the particular shape of islands, i.e. they will change as a function of temperature [178, 208, 209], coverage, and deposition flux rate [210]. However, in colloidal fluid systems, a metastable phase is postulated to precede the crystallization or aggregation of a stable crystal phase in many systems. Quite interestingly, we find this in our lattice model for thin film growth in Ch. 5, and this metastable phase can even form compact islands at sufficiently low temperatures. To this end, Ref. [211] reports on coexisting islands dependent on temperature, hinting at a critical temperature above which one type of morphology is observable during growth. (Coexisting islands of two types have also been reported in Ref. [147], one of which includes a disordered, lying phase that appears metastable.) Therefore, the temperature T is crucial for the type of kinetics and structures that can occur, but, a higher F/D will prefer the first phase, extending its lifetime towards later stages of monolayer growth. A dynamical asymmetry persists between the two phases (see further discussion on this aspect in Ch. 2.3.). This kind of "effect" of the flux has been reported for rubrene [212]. A (disordered or line-like) lying phase was reported only to occur for very low temperatures [11, 152, 181] or high flux rates [213] for tetracene.

As to control of structures, the self-assembly involving metastable phases in the monolayer have been ascribed to disordered structures emerging, rather than compact islands [12, 212, 213]. Therefore, the level of disorder versus order seems to be connected to the degree of (thermodynamic) stability, which is why a characterization of thermodynamic properties (phase diagrams) in these systems is pertinent. The nonequilibrium evolution can be understood as coming from intricate ties between equilibrium phase boundaries and dynamics, where the parameters F, D, and T, which adjust a competition among various phases and (collective) processes at the monolayer regime. The specific choice of substrate will also be a third key factor, as it changes the phase diagrams, as well.

The modes of growth (see Fig. 1.4), crystal structures, phase transitions or structural frustration occurring at the next stages are a function of the monolayer state, which can be seen as a template, in effect, for the future evolution of the system. At later times (higher total coverage), competing surface free energies of the film structures above can be cause for strain, which can relax via dewetting transitions: Metastable monolayer phases can survive until the

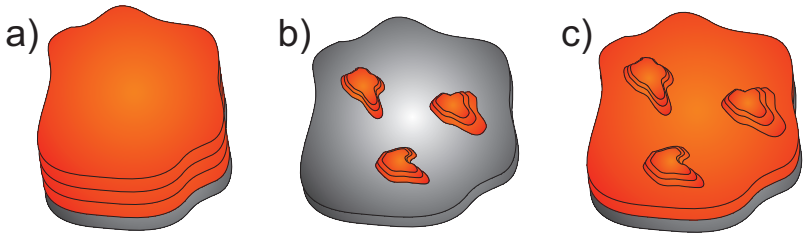

FIGURE 1.4: Schematic representation of (multilayer) thin film growth modes in the standard classification, see e.g. [20]: (a) Frank-van-der-Merwe (layer-by-layer), (b) Vollmer-Weber (3D islands), and (c) Stranski-Krastanov (islands-on-layers) growth. Courtesy of C. Frank (Ref. [214]).

.

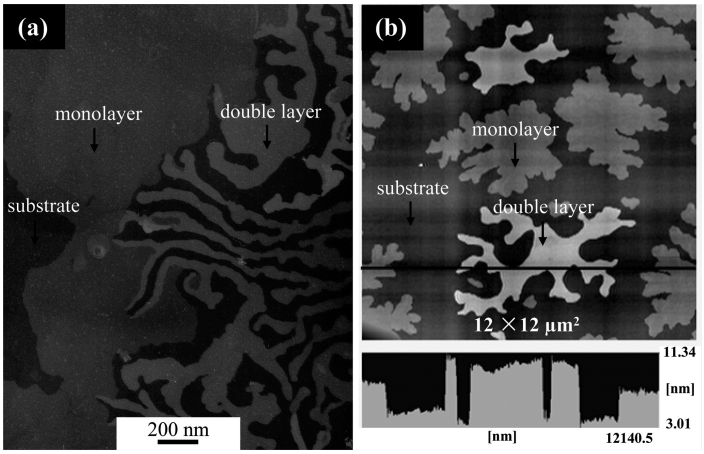

FIGURE 1.5: Co-occurrence or competition of phases during growth of p-6P (para-sexiphenyl) at near-monolayer packing: (1) A stable "bilayer" crystal phase forms during growth at the same time as a "liquid-like" monolayer-phase. (b) A second type of phase separation kinetics, where two island species appear, can occur upon annealing. Source: Ref. [13].

monolayer is completely filled [213]. A relaxation may first occur once the second layer forms: Fig. 1.5(a) shows of co-occurrence of "monolayer" and "bilayer" phases at near-monolayer packing, where the "monolayer" phase is assumed metastable [183]. The monolayer phase may be "liquid-like", starkly different from the bilayer phase, and is suppressed with a higher substrate temperature. Annealing the film (Fig. 1.5(b)) causes the monolayer phase to transform in a dewetting transition, where a new regime of self-assembly and kinetics begins. A co-occurrence of islands of different phases is also possible. Such dewetting of the monolayer-phase is reported in many places, see e.g. Refs. [12, 13, 142, 147];[11] this could be behind a change in growth modes that may appear counterintuitive [216].

The above discussion should make clear that the self-assembly processes around the monolayer stage of growth are far from simple, and a more fundamental understanding with a generic model seems necessary. A generalized

[11]Notably, nematic thin films show similar features [122], and models of hard rectangles in strong confinement confirm the possibility for two different out-of-plane ordering in one or two "layers" [215].

"map" of possible mesoscopic morphological structure formation during submonolayer growth, and control thereof, is a desirable goal, in these respects – one that investigates the role of inter-molecular attractions and repulsion, particle shape, substrate potentials, as well as dynamical control parameters like diffusion constant D and flux rate F. (Refs. [190, 217–219] provide rough examples of phase diagrams as a function of coverage and temperature, yet, lack in detail and will not be universal. Ref. [220] presents a diagram in much more detail, but treats heteromolecular monolayer systems. Ref. [221] reproduces a variety of monolayer phases in small-scale, specialized Monte-Carlo simulation models.) Apart from equilibrium considerations, full-blown dynamical information (to cite Ref. [149]) is required to capture all potential metastable phases as well as other reproducible features that express inherently nonequilibrium states (e.g. kinetic arrest). Understanding these intermediary states is crucial for optimizing (and understanding) the material functionality of the organic films [8, 156, 184, 194, 196, 201, 222–224], and is absolutely necessary for a coherent picture of thin film growth with organic molecules. With our model system (see below), we attempt to address this desire, in which we explore the effects of a wide range of controllable parameters on dynamics and energetics of the system during the nonequilibrium evolution of monolayer growth. The simplicity and idealization of the model express an attempt to remain maximally generic in order to gain broader insight into the statistical mechanics of these monolayer systems.

Beyond the specific context of thin film growth, the self-assembly of complex molecules or particles at surfaces has a broader context and motivation for modern materials engineering [132, 225]. An avoidance of metastable phases may alone be of considerable interest for self-assembly [133, 226]. Molecular gels in confinement could offer mechanically flexible photovoltaic devices [134], for example. Monolayer *nanoparticle* systems [227, 228] may be further relevant for developing drug delivery or modeling biological systems [229]. Photonic quasicrystals have been developed with rod-like nanoparticles [230]. Polymeric films – those of long, flexible, chained molecules – likewise show complex phase behavior at surfaces. These are other, basic classes of systems of interest [231] with which some analogies to our model can be found.[12] Thus, we may extend the scope of our model system of hard rods on lattices to general self-assembly in quasi-2D or extreme confinement [225].

1.2.2 A "soft matter" approach to monolayer growth with an idealized model system

Generic, large-scale simulations of thin film growth of rod-like particles growth within or beyond the first monolayer in large-scale simulations, particularly those on lattices, are rare [4, 233, 234]. Due to the computational bottleneck of modeling a many-body system with processes having vastly different timescales, on-lattice models are a "must" if we want to understand self-assembly involving large numbers of particles. Even so, event-driven algorithms like kinetic Monte Carlo are algorithmically much more complex when considering anisotropic particles. Another difficulty, theoretical in nature, is that nonequilibrium systems may be highly sensitive to fine details of a model, which we will

[12] Phase transformations with multiply coexisting or competing phases also is a topic of interest for the design of multi-component alloy materials [232].

be demonstrated by the model system we study in this thesis. Any constraints on the local dynamics (particular rotational symmetries) and the energy scales of interactions, as well as particular rates (energy barriers) of processes can fundamentally alter the evolution. (We demonstrate this point in Ch. 5). Not knowing which particular local particle "moves" should be employed for anisotropic particles is an outstanding issue, particularly for multi-layer growth, where traditionally "solid-on-solid"-like models are employed [21, 163]. Moreover, the exact rates of e.g. translational or rotational diffusion are not known, generally, for any organic molecular thin film system. Other factors like desorption rates or effective inter-particle interaction strengths remain somewhat elusive (We discuss more in Sec. 1.2.1 below).

We take these uncertainties, technical challenges, and outstanding issues into our hands in part II of this thesis. Only after understanding the full premises of the model – by characterizing the equilibrium properties as well as effects of changes in microscopic dynamics, by observing the nonequilibrium evolution over e.g. seven to eight orders of magnitude in dynamics as well as over a wide range of energetic parameters – can we become convinced of its genericness and explanatory power. In doing so, we provide a uniquely in-depth and broad study of monolayer growth with rod-like particles.

In Ch. 4, we first explore the case of purely-hard-core rods as a first step towards more complex models, but also to initiate and investigate the accuracy of analytical approaches using density functional theory. The questions we initially focus on are: What are the conditions under which orientational transitions arise in monolayer of hard rods, and when do these correspond to thermodynamic transitions? What role does rod length play in the thermodynamic behavior? How does a substrate potential that biases an orientation change the properties and character of growth in this model? Is a quasiequilibrium description of growth possible? How does the flux–to–rotational-rate of particles modify the nearness to quasiequilibrium? How does this model compare to an off-lattice model?

In Ch. 5, we explore the lattice model system of monolayers of hard rods with additional "sticky" attractions between rods. We attempt to address the following questions: What is the role of rod length and strength of the short-ranged attractions (or reduced temperature) on phase separation kinetics during growth? Under which conditions can we still quantify "quasiequilibrium"? Can we identify different dynamical regimes, where one type of phase separation kinetics dominates? Which phase transformation processes might produce the bounty of phenomenology reported in experimental systems? What role does the substrate potential play in these systems? How does the choice of microscopic dynamics ("moves") of rods in the KMC model change the morphological and dynamical evolution? To which extent can we find analogies of these systems to other soft matter model systems?

Quite generally, the existence of various stable and metastable phases can give rise to various co-occurring or competing structures under highly nonequilibrium conditions [116]. We will see in Ch. 5 that the nonequilibrium growth of monolayers of hard, sticky rods is highly complex, indeed, owing to multifarious (multi-step) phase separation processes involving metastable phases that form dynamically arrested states. Thus, we find various "soft matter" features such as a precursor-phase that can form a "gel" or "wetting layer" under suitable dynamical and energetic conditions. We report on organic molecular thin

films at the sub-monolayer stage showing potentially similar soft-matter-like features in Ch. 2.4.

The evolution at the initial stages of growth with rod-like molecules is fundamentally different from the picture painted by simple, atomistic models of island nucleation-and-growth. A different, mesoscopic approach that correctly accounts for the pronounced coupling of translational and orientational degrees of freedom may be needed. Some results of this thesis could aid in theoretical development to this end, which we discuss in the conclusion of Ch. 5 and in Ch. 8.

An idealized model

A natural starting point for a generic model is when the anisotropic particles (rods) are purely hard-core. The role of additional attractions can be studied afterwards, an approach which is typical when using colloidal model systems to study ordering phenomena. The case of purely hard-core rods has a particular advantage, as alluded to earlier already: its density functional is tractable with fundamental measure theory. One can obtain all equilibrium quantities of interest by minimizing the density functional. We formulate the lattice DFT of hard rods both in monolayers (also applicable for bulk and 2D systems of part III) in Ch. 4. A dynamical extension of DFT in a near-equilibrium-type of approach is dynamical density functional theory. In Ch. 4, we formulate the lattice DDFT and compare the results to the kinetic Monte Carlo (KMC) simulations. The theoretical interpretation of these lattice DDFT equations (in the form of *master equations*) is discussed much more thoroughly in Ch. 3, as well as kinetic Monte Carlo simulation methods and equilibrium versus nonequilibrium dynamics. Further, we address the case of sticky hard rods in Ch. 5 of this thesis, for which a lattice FMT for sticky rods was developed in parallel to this thesis using the depletion effect for effective attractions (an Asakura–Oosawa model) in Ref. [72].

A second main form of idealization that we incorporate is the constraint of the particles (rods) to a *lattice*. One motivation is the computational ease in modeling such systems. The computational bottleneck in more faithful, molecular dynamics simulations of thin film growth [4, 235–237] hinders large-scale investigations, and are not trimmed for revealing generic effects. Kinetic Monte Carlo is a perfect candidate for idealized models as soon as these entail discrete translational degrees of freedom, where a well-defined set of local particle "moves" can be defined. Yet, this modeling approach implies drastic coarse-graining of both the particle-particle interactions as well as orientations, which are restricted to a set of solely three, namely, one perpendicular and two parallel orientation with respect to a substrate. Nevertheless, historically, lattice models have played a central role in all branches of condensed matter physics and field theory, and we can be confident that such a model will enable us to explore basic questions around the self-assembly of thin films with anisotropic particles.

An on-lattice model of hard rods may, in fact, in fact, have a somewhat stronger affinity to organic molecular thin film systems due to the discretization of degrees of freedom to a lattice. As mentioned, molecular orientational degrees of freedom are likely highly *selectively* directional and nearly discrete in translational degrees of freedom due to the energy minima on the energy landscape provided by the surrounding substrate and islands. This may take

the form of strong multipolar interactions, which has been shown in coarse-grained simulations to produce a multitude of orientation and translational order on periodic substrates [140, 238]. We model purely hard-core rods in Ch. 4, which is arguably more "colloidal-like", and sticky hard rods in Ch. 5.

To gauge the genericness of our fully on-lattice statistical model of rods, we compare it directly to a continuum model of spherocylinders for the purely-hard-core case in Ch. 4. Differences between lattice and continuum models are not clear up front, pertaining to the bulk phase behavior that we study depth in part III of this thesis. Restrained degrees of freedom do *not* imply simpler phase behavior in any way or form: Restricted-orientation models of hard-core rods show a rich phase diagram [239] – also true for the case of confinement [240]. In (semi-) confinement, qualitative similarity to unrestricted-orientation models [241] is found. We discuss more on lattice constraints and dimensional confinement in Ch. 2.

On a related note, it has been observed that Langmuir monolayers (having no underlying lattice of the substrate) and e.g. SAMs of thiols on gold (having an underlying lattice) show different phase behavior [112, 125, 127]. The crystallinity of the substrate obviously introduces additional constraints and a potential having a periodic corrugation. Differences in their phase diagrams are apparent, but both have in common that multiple phases with different tilt structure are possible. Hence, whether an on-lattice model system will capture main features in both cases is unclear up-front. Yet, strong directional forces between molecules, such as in the case of organic molecules, may effectively confine molecules locally, leading (rather quickly) to various well-ordered crystalline phases during self-assembly; a lattice restriction within a simple model may be justifiable. We will discuss this aspect again further below.

In our idealized, "soft-matter" approach, we stick with simple particle attractions: the rods studied in Ch. 5 entail short-ranged, "sticky" attractions. Similarly, the interaction potentials with the substrate are also sticky, which we investigate in Chs. 4 and Ch. 5. Attractions must be put in relation to $k_\mathrm{B}T$, hence we can tune a reduced temperature in the model, moving the system across different points in the phase diagram. Phase diagrams will be deformed by the specific substrate interaction potential, as well, discussed in Ch. 2. A final factor that modifies the thermodynamic aspects of the model system is the rod-length (particle anisotropy), therewith adjusting the degree of energetic and entropic contributions (a generic discussion is found in Ch. 2). Complex phase separation kinetics during monolayer growth is directly tied to complex phase diagrams of the confined systems.

Unfortunately, surface phase diagrams of the molecular systems are not known, generally (see Refs. [190, 217–219]), and, may be highly particular to each thin film system. Knowledge of binding energies are somewhat limited, but a few studies can help us: Ref. [11] recently calculated single-particle binding energies of tetracene (an "aspect ratio" of possibly $\sim 3 \ldots 4$) with the substrate of around $(8 \ldots 30)k_\mathrm{B}T$ (room temperature) on silicon, depending on the lying or standing orientation. As they calculated a total energy with substrate and a monolayer, using a gross lattice model we can say that $\epsilon \sim -(3 \ldots 4)k_\mathrm{B}T$ and a biasing potential of the substrate (not adhesion energy, but regarding the lying-standing energetic difference at the substrate) $\epsilon_\mathrm{sub} \sim -(7 \ldots 10)k_\mathrm{B}T$. This substantial difference between orientations hints at a clear "lying"-preference at the submonolayer stage (from a *single*-particle point-of-view).

Dynamics is our model are assumed locally Markovian, i.e. the "internal" dynamics of rods on the substrate can be considered diffusion-like (on a lattice). We simulate hopping diffusion and random rotations, whose ideal-gas-rates ("attempt" rates) constitute part of the basic dynamical parameters.[13] The particle influx from a reservoir is modeled to deposit particles at a fixed "attempt" rate, as well, completing the dynamical model specifications. By varying the ratio of the flux–to–diffusion rates over many orders of magnitude, we can surmise to be able to capture many of the relevant kinetics in the system.

Arguably, the self-assembly of crystal-phase structures with large length-scales requires "sufficient" particle diffusion [145]. However, the exact self-diffusion rates (translational and rotational) of the molecules at the substrates are often not known. Dynamics have been characterized for specific molecule–substrate combinations in Refs. [185, 242, 243].[14,15] Ref. [243] showed that diffusion rates (and general character of the microscopic dynamics) of organic molecules at substrates are highly sensitive to the particular interaction potentials, i.e. the substrate-particle interaction. As to the nature of the dynamics, such translational motion is strongly coupled to the rotational motion [185, 242–244, 246]. In fact, the diffusive dynamics are also reported to be "1D-like", depending strongly on the substrate (metal, molecular, amorphous silicon) [247] (apart from temperature). Note that motion on an amorphous or quasicrystalline substrates generally causes deviation from "free" 2D diffusion, even for colloidal particles [248, 249]. This kind of 1D motion favors the formation of *rows* [250], which are clearly visible in some reported studies [10, 14]. In other cases, this could lead to "need-like" islands forming.[16]

In terms of a generic model, particularities like that of "1D-like" motion befuddle which aspects are relevant for the formation of large-scale structures, as well as which type of order appearing. Such details can usually be added in later, on top of a generic model, in order to see their explicit effects.

We foreshadow that the choice of a *coupled* rotational- and translational-diffusion "move"-set will have significant effects on evolution of morphology in the monolayer. Yet, the main driving forces behind the phase separation kinetics during growth remain thermodynamic in origin (in addition to the external particle flux). This leads us to the following (general) discussion on the role of thermodynamics in understanding and controlling self-assembly during thin film growth.

Role of equilibrium in nonequilibrium, generally

By modifying the "attempt" rates of microscopic processes in the system (self-diffusion rates D in translation and rotation, deposition flux F) and temperature, we adjust the *likelihoods*, in effect, of each phase appearing during monotonous growth. Assuming Arrhenius laws are valid, the temperature directly adjusts the strength of (free) energy barriers involved in the formation of mesoscopic structure, which means it can suppress or prefer such structures with particular different orientational order. The ratio of the "attempt" rates

[13] As a note to the keen reader, we match these rates from the simulations to the transport rates of the DDFT equations.

[14] We note here that Ref. [12] estimates a maximal diffusion rate of $2 \cdot 10^{-9} cm^2 s^{-1}$ for a 2D gas phase for the specific system investigated.

[15] See also Refs. [244, 245].

[16] For more on "needle-like" islands, please consult to references within Ref. [251].

adjust the relative power with which diffusive motion or the particle influx will move the system from or towards the next global equilibrium state. The flux will ultimately drive a monolayer across coexistence (stable) points in a phase diagram. It also plays an important role in favoring the creation of coherent structures (phases) at various mesoscopic scales (we discuss these topics more extensively in Ch. 2.)

Our studies in Ch. 5 shall make clear that the emergence, transformation, or disappearance of structure are related to the current position in the phase diagram, as well as on the ratio D/F. In the highly non-Markovian evolution during a phase transformation, the exact state depends crucially on the entire *history* of the trajectory. Therefore, a large variety of characteristically different trajectories are possible between beginning and end-states – of empty and full monolayers. To illustrate this point in more detail, monolayer growth is, in essence, a very "long" phase transition between two stable phases – a gas and a dense ("crystalline") phase at full density. *How* the system moves between these stable end-points depends on the system parameters of dynamical rates, attractions (temperature), as well as rod-length, the substrate potential, and even choice of modeled microscopic dynamics (how rotations are implemented). For any given system, the main control axes are the ratio D/F and reduced temperatures, i.e. attraction strengths, which we allude to more closely in Ch. 2.3.1. We will show that these axes unveil a dividing line between two major dynamical regimes, where within each a prominently different type of phase separation kinetics occurs.

In practice, by observing sufficiently many variations of nonequilibrium trajectories, "hidden" phase boundaries underneath binodals of the gas and dense-phase can be unveiled, as well as dynamically arrested states. (Notably, metastable phase boundaries are only detectable in out-of-equilibrium conditions.) This has implications for tailed self-assembly. Pattern formation, generally, can be controlled once phase separation and phase transformation properties are understood in full [252, 253]. For customized self-assembly, then, an experimenter could tune macroscopic properties such as temperature before or during, or after the self-assembly process (annealing or cooling). He or she could also interrupt the deposition process intermittently [254]. Further, the ratio of deposition and *desorption* rates (which is shifted by the substrate potential strength) adjusts the supersaturation at the surface [166]. We discuss such experiments – by means of simulations we performed preliminarily – in Ch. 5. Further, a change of the substrate potential will alter the behavior dramatically, which may even cause metastable phases to become stable if these potentials strongly favor lying orientations of rods (we will show this effect in Ch. 5).

From the theory side, equilibrium information is necessary for quasi-stationary and local-equilibrium approximations to equations-of-motion, which may remain valid if the system is exposed to slowly varying forces. We demonstrate this principle in Ch. 4 for the dynamics of monolayer growth of purely hard-core rods, which almost always remain near-equilibrium except for conditions of very fast deposition and strong substrate potentials favoring a lying orientation. Further, in order to be able to be consistent with thermodynamic equilibrium, a simulation or theoretical model on dynamics must provide a well-defined equilibrium limit. Our studies in part II are trimmed towards this requirement by the use of kinetic Monte Carlo, as well as dynamical density functional theory that treats (local) balance conditions leading the system to equilibrium (if the driving forces are turned off). (See

Ch. 2.3 and Ch. 3). In our studies, we make use of fundamental measure theory, which captures correlations during the evolution. This means the *response* of the system to thermodynamic forces during growth might be modeled much more faithfully than other mean-field approaches.

Related simulation studies

We briefly review here other simulation studies trimmed at modeling thin film growth with anisotropic organic molecules at the monolayer stage. A popular choice is molecular dynamics [4, 138, 139, 235–237, 255, 256], which, however, restricts the number of particles and simulation times massively, as it is generally only coarse-grained with respect to inter-atomic potentials. Simulations like that of Ref. [4, 235] are situated towards the fine-grained-end of the spectrum; these all-atom approaches model pentacene film growth on a substrate of C_{60} (fullerene) with about 100 particles. Even so, evidence for a lying–standing transition has been found. Ref. [139] addresses two potential growth modes at the submonolayer stage depending on molecule-molecule and molecule-substrate interactions. However, they simulated circa 10 pentacene molecules on amorphous SiO_2. Nevertheless, the results hint at a reorientation transition even with such small number of molecules. Ref. [236] finds that a pentacene molecules persist in "disordered aggregates" of a lying orientation before attaching to a standing crystalline phase. A transition point (density) is indicated,[17] whereupon a lying phase disappears. Unfortunately, only a single curve is provided without a variation of kinetic parameters.) Ref. [237] likewise attests to the different molecular morphologies appearing on substrates, including crystal phases. Ref. [256] hints at a network-like structure of pentacene rods at low submonolayer densities on a C_{60} substrate, as well as a low-ordered structure of pentacene at higher submonolayer densities (Fig. 2 in the reference). Ref. [138] models 6T (sexithiophene) monolayers grown through a sequence of deposition and annealing steps. Post-deposition wetting effects were studied in Ref. [142], which notes that the reported lying phase at the substrate may be a precursor to stable island formation.

Systematic investigations including relations to thermodynamic phases have been investigated more systematically in less generic models. Rod-like molecules with multipolar interactions were modeled in a mixed lattice-continuum model using kinetic Monte Carlo of 6P (sexiphenyl) molecules on patterned substrates in Ref. [140, 257, 258], see also Ref. [250]. The simulations by Kleppmann *et al.* have explored the feasibility of such hybrid models for reproducing experimental phenomena for specific systems. (See also simulations of more generalized particles with quadrupolar interactions in [238].)

Full lattice models, like the one studied in this thesis, allow for much larger systems to be investigated, numerically. Lattice models for thin film growth with rods have already been modeled in the cases of dimers and "trimers" possessing short-ranged attractions (Refs. [233, 234]). In Ref. [233], different the inter-particle interaction type and strengths were simulated in an exploratory fashion for generating various forms of islands and ordered states therein. In Ref. [234], the energetic parameters employed were tailed to thiophene molecules on different substrates, motivated by quantum chemical calculations.

[17] Fig. 1 in Ref. [236]

Although various patterns were observed to appear during the growth simulations, upon variation of temperature and substrate type, the relation to equilibrium phases was not investigated. A clear explanation of the phenomenology is lacking and many of the quantitative results are difficult to interpret. An older lattice study (Ref. [120]) treats the phase behavior in monolayers from an equilibrium perspective. It models non-hard particles with a head and tail that are mobile on substrate, with the head confined to the substrate. They address the equilibrium lying–standing transition at different conditions of substrate potentials, densities or chemical potentials, and inter-particle interactions. Notably, they detect liquid-vapor separation involved in the formation of lying and standing states, where these two transitions are seen to be successive (in density).[18] The study clearly hints at complex behavior within monolayers, seen even in most simple models. Ref. [259] studies growth kinetics around step edges by utilizing a dimer model. Lastly, the effect of anisotropic interactions was studied in a lattice system in Ref. [260], where particles are $1 \times 1 \times 1$ in extent and entail anisotropic pair potentials, contrasting the behavior to atomistic growth models.

* * *

The next section introduces the next topic of this thesis, where we continue to explore our generic lattice model of hard (and sticky) rods in other contexts: We study the phase behavior around the isotropic–nematic transition in 3D bulk as well as in 2D (full) confinement.

1.3 Phase behavior of hard (and "sticky") rods on square and cubic lattices

In part III of this thesis, we will explore the bulk phase behavior of an extremely idealized version of fluids composed of elongated particles. While the behavior of e.g. liquid crystals is well-established, much less is known about the ordering behavior of rods in on-lattice models. We aim to understand the effect of discretizing the full degrees of freedom by characterizing the phase behavior with Monte Carlo simulations – around the isotropic–nematic transition. This will come with a few surprises. From the technical side, we employ Markov-Chain Monte Carlo simulations in the grand-canonical ensemble. As mentioned earlier and in the context of the previous section, we will compare our phase diagrams to those predicted by fundamental measure theory (FMT) on the lattice [159, 160] (more references are listed further in the discussion below).

After a motivation in the next few paragraphs, we will introduce the basic physics of bulk systems of rod-like particles in the continuum, specifically, their orientational-ordering transitions. We also introduce some aspects of the phase behavior of rods in 2D confinement. The ordering transition in partly-discretized models (with continuous translational degrees of freedom) are reviewed thereafter. Finally, we will discuss what has been understood about ordering behavior in fully discrete models of hard rods prior to the work in this thesis.

[18] reminiscent of orientational behavior in SAMs discussed at the beginning of this section.

Can a hard-core interaction between anisotropic particles induce long-ranged, so-called nematic order, where large domains of (nearly-)parallel rods distinguish themselves from the isotropic phase of the fluid? This question has laid at the heart of a long history of studied on systems of rod-like particles beginning in the middle of the last century. Indeed, systems with anisotropic, hard or semi-flexible particles undergo a range of possible phase transitions that induce preferred orientations. These are fundamentally entropy-driven, due to the hard-core repulsion of the particles. Upon increasing the packing fraction (number density) from an isotropic phase, a nematic transition occurs. At higher packing fractions, smectic ordering of various kind occur, before a crystalline phase is ultimately reached.

The phase behavior of continuum models of spherocylinders is well-established. However, much less is known about lattice models of hard rods, in particular for 3D systems. In part III of this thesis, we study the isotropic–nematic transition of hard rods confined to lattices in 3D bulk with Markov-Chain Monte Carlo (MCMC) simulations of equilibrium. Further, we characterize the phase diagrams of sticky hard rods in 3D and 2D, for densities around the isotropic-nematic transitions, A basic motivation of this (and all!) parts of this thesis is the idea that lattice hard rods might provide alternative, workhorse models for studying orientationally-induced order-disorder transitions in soft matter physics. Their genericness put aside, lattice models are certainly *computationally* less expensive to simulate. One must ask, naturally, how well on-lattice hard rods may *actually* serve as "aliases" for bulk nematic systems. Self-evidently, discrete systems have symmetries fundamentally different from those in the continuum. We allude to some underlying issues in coming sections below, reviewing the known phase behavior of rod-like model systems in the continuum, as well as in the studied examples of (partially-) discretized models of rods.

The exact effects of discretizing both translational and orientational degrees of freedom on the phase behavior are not clear up front. Prior to our first published study on 3D systems of hard lattice rods, there had been no simulation studies on lattice systems of hard rods in the 3D bulk. Therefore, in in Ch. 6 of this thesis, we investigate the transitions of 3D bulk systems of hard, as well as hard and sticky rods.[19] The 2D systems of purely hard-core rods on lattices have enjoyed much more attention in the last two decades. With our studies, we fill a gap in the literature. Further, we will compare our simulation results with lattice fundamental measure theory. Lattice variants of FMT have been less popular, in general, as well [159, 160, 262–266], which also applies to lattice DFT, more broadly [267–280]. Our direct comparison may aid future theoretical developments for lattice density functionals.

A further motivation is to fully understand the possible phases of the systems of rods in (2+1)D monolayer confinement. These are the model systems for early stages of thin film growth with anisotropic molecules, the topic of part II of this thesis, and are introduced in Sec. 1.2. 2D systems of rods can be considered a limiting case where an infinitely strong substrate potential biases the lying orientation. We characterize the phases of 2D systems of very long, sticky rods in part III. Multilayer thin films "live" in the realm between

[19] We note up-front that during the time our research was done, Ref. [261] also investigated the model of hard rods, with one complementary finding that we mention in the corresponding chapter.

the monolayer and 3D bulk. Therefore, the bulk 3D is another limiting case whose phase behavior would complete a full understanding of surface films (surface phases). Simulations of multilayer thin film growth with lattice rods is an outlook of this thesis, and this thesis will provide a solid theoretical bedrock towards work in this direction.

1.3.1 Bulk systems of rods in the continuum

Liquid crystals are probably the most famous kind of nematic systems [39, 281–283]. Nematic systems engulf in a broader class of anisotropic, rod-like particles that may entail various kinds of interactions in addition to steric repulsion (e.g. paramagnetic, electrostatic, ferromagnetic, van der Waals, and depletion interactions). Clearly implied by their name, all showcase the isotropic-nematic transition that is in focus in part III of this thesis. Yet, hard-core spherocylinders (e.g. in colloids) can show the same phases seen in many liquid crystal systems (isotropic, smectic phases), without the need of added external forces of special electrostatic of magnetic interactions, see Fig. 1.6 [42, 59, 60, 284]. Hard-bodied

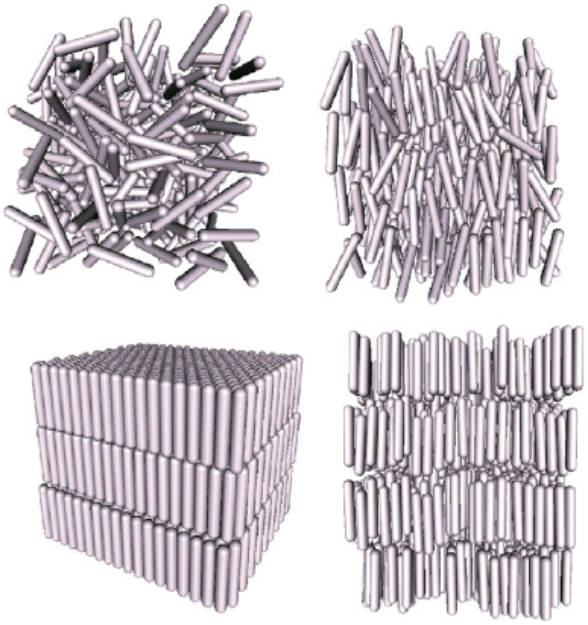

FIGURE 1.6: Example configurations of different ordered phases in a system of hard spherocylinders. Clockwise from upper left: isotropic, nematic, smectic-A and ordered crystal phases of a system of hard spherocylinders. Source: Ref. [26, Ch. 12].

models of bulk liquid crystals are further reviewed in Refs. [40] and [26, Ch. 12.7].[20]

There is general agreement from the theoretical side about the behavior of infinitely thin rods in the 3D continuum: It all started with Onsager's pioneering study on the existence of a first-order transition between an isotropic and a nematic state in a hard-rod fluid in the limit of infinitely long rods [41]. This was an early, clear example of an entropy-driven phase transition. In the meantime, the phase behavior of hard rods in the continuum has been fully established by

[20] Relatedly, see Ref. [25] for an overview of diverse hard-core colloidal systems.

Bolhuis and Frenkel, see Refs. [18, 42]. Nematic ordering starts from a critical aspect ratio L/D (ratio between length and diameter) of about 3.8. Symmetry arguments and mean-field theory predict the transition to be first order, but an associated density gap is hard to detect near the critical aspect ratio. This becomes clearly visible for $L/D = 5$ [285] and reaches the Onsager limit already for $L/D \gtrsim 15$. Colloidal bulk systems of spherocylinders [286] show strong similarities to the phase diagram calculated by Bolhuis and Frenkel.[21]

The most accurate density functionals for hard, anisotropic particles have been derived from Fundamental Measure Theory [292–298].[22] Wittmann et al. used mixed measures to derive a functional that is exact in the low-density limit; for higher densities, typical FMT approximations were employed [296]. The corresponding phase diagram for hard spherocylinders showed almost quantitative agreement with Ref. [42]. However, the FMT results showed an almost constant density jump between the coexisting isotropic and nematic states for aspect ratios starting from $L/D \gtrsim 3.5$. Thus, the transition is strongly first order for all aspect ratios.

In part III, we will see that the lattice model of purely hard-core rods entails at best a *weak* first order isotropic–nematic transition, in stark contrast to the models in the continuum. Further the lattice FMT that we employ will reproduce a wide density gap – a clear sign of weakness of the lattice FMT. Further, the *nature* of the "nematic" phase on the lattice will be very different: It will not be long-ranged; rather, it will show a mean orientational dominance in one of three possible orientations (or, a directional *suppression* for the cases of $L = 5, 6$). Albeit, the *specific* nematic direction fluctuates over the course of Monte-Carlo time (on time-scales longer than other, "internal" fluctuations). We presume this represents the same class of Ising "demixing" transitions that characterizes 2D restricted-orientation models of rods. The latter will be discussed in Sec. 1.3.2 further below.

Attractive rods in bulk

The case of rods with additional attractions has been studied mainly in the context of the Asakura–Oosawa (AO) model, appropriate for systems of hard rods where the addition of non-adsorbing polymers provides tunable attractions through the depletion effect. Here, the concentration of polymers corresponds to an inverse temperature. Mean-field theories such as free volume theory for the AO model of rods and polymers [59, 60] predict a continuous and substantial widening of the isotropic-nematic density gap.

In the case of small polymers (corresponding to short-ranged attractions), the transition smoothly crosses over to a transition between an isotropic vapor and a nematic liquid. This scenario is basically confirmed in simulations, but, the nematic transition becomes metastable with respect to the isotropic vapor–crystal transition in those cases [60, 285]. The widening of the coexistence

[21] Further experimental studies of colloidal systems of hard rods (though not addressing bulk phase diagrams) include Refs. [287–291].

[22] For completeness, we mention here some older studies from the theoretical side of hard-core (spherocylinder) bodies in the 3D continuum. Scaled-particle treatments of the hard-core systems include Refs. [299–304]. Virial expansions were calculated by Frenkel et al., see the review in Ref. [305]. Other approaches include Refs. [306–312]. Density-functional treatments of spherocylinders were initiated by e.g. Refs. [313, 314].

density gap has been observed experimentally in mixtures of fd-virus and dextrane polymer mixtures [315][23] and in ones of boehmite rods and PDMS or PS polymers [284], although arrested states appearing further complicates matters.

Confinement to a two-dimensional continuum

History on the theory of two-dimensional systems of liquid crystals has not progressed in a strictly straightforward manner. Straley (1971) [320] used a theory based on the lowest-order approximation to the virial expansion of the free energy (the Onsager limit) to determine whether nematic ordering exists, but, was inconclusive. The existence of this phase transition was long put up for debate, as an isotropic to nematic transition requires the breaking of the symmetry of the continuous group of rotations. There were reasons to believe that "true" phase transitions, involving the breaking of a continuous symmetry, cannot take place in two dimensions [321]. Nevertheless, various theoretical approaches were developed, and e.g. Chakravarty and Woo (1975) [322, 323] suggested that even further smectic and crystalline phases can be constructed by taking short-range correlations explicitly into account. However, when treating hard ellipses, Cuesta *et al.* (1989) argued that the first-order isotropic–nematic transition known from 3D actually becomes continuous in 2D [324]. Such a "destruction" of first-order phase transitions is typical for dimensional confinement [325] (see discussion in Ch. 2.2). An integral-equation study on hard ellipses with density functional theory thereafter [326] also excluded the possibility of the transition being first order. Later studies also suggested that the isotropic–nematic transition is always continuous [327], and occurs for aspect ratios $L/D \geq 7$ in spherocylinders [327]. (The case of ellipses is a more subtle [328, 329], and may even first occur for $a \geq 3$.) In contrast, other forms of 2D liquid crystal models [330] show first order transitions, which bear analogy to spin-like models that we discuss further below. Ref. [331] investigated the crossover between the continuous and first order transition in *off-lattice* 2D liquid crystal models. These, however, are not hard-core. The model of hard rods studied in this thesis can "bridge" both sides – it has a tricritical crossover between continuous or first order transitions, depending on the attraction strength between hard-core rods, and is an *on-lattice* model.

Since the translational degrees of freedom are continuous, fluctuations in the average orientation may destroy the long-range order of a nematic state (leading to a *quasinematic* state), decaying algebraically. However, anisotropic hard particles (for which position and orientation degrees of freedom are coupled) may still exhibit true, nematic long-ranged order, see the discussion in Ref. [332]. Thus a continuous isotropic–quasinematic transition of Kosterlitz–Thouless type [333–335] is possible, as well as an isotropic–nematic transition of first order. Interestingly, both types had been found in the hard ellipse system [328] (first-order for aspect ratio 4 and continuous for aspect ratio 6), though, Ref. [336] contradicts this and finds only continuous transitions. Further 2D simulations of hard rods [327, 337] and hard ellipses in Refs. [329, 338] seem to confirm algebraic decay (see also Ref. [339]; Ref. [340] confirms this is for experimental systems of ellipsoids in quasi-2D confinement). Nevertheless, some topics may still be open.

[23] Further studies with the fd-virus include Refs. [316–319].

Notably, then, the *quasinematic* phase transition in 2D liquid crystals is related to the problem of melting hard-sphere crystals in 2D [341], which is described by the KTHNY (Kosterlitz-Thouless-Halperin-Nelson-Young) mechanism [342]; a hexatic phase appears (see early Monte Carlo studies in Ref. [343]) and the transition is topological. The planar spin models (XY) also show such behavior [344]. Generally speaking, rod models like any other are exposed to "pathological" problems encountered during dimensional crossover from 3D to 2D. The lattice models of 2D sticky rods studied in part III of this thesis will also show quite "different" behavior from the 3D bulk, in that the weak first-order isotropic-nematic transition at the purely-hard-core limit will be "destroyed", turning into a continuous transition. In doing so, the "sticky"-rod phase diagram for the 2D system will entail a tricritical point.

We discuss confinement more generally in Ch. 2.2. Below, we discuss known effects of discretizing degrees of freedom of rods on the isotropic–nematic transition.

1.3.2 Lattice models of hard rods

The effect of constraining a system to a lattice on nematic ordering is not clear up-front. "True" nematic ordering is *long-ranged* and represent the breaking of a continuous symmetry. In analogy to the discussion of dimensional confinement above, but also in Ch. 2, constraining degrees of freedom to a lattice is like filtering out particular (Fourier) modes, which might destroy long-range ordering in its "own" way. Indeed, in our study of the ordering transition of long rods on lattices in 3D likely belongs to the Ising universality class (a gas-liquid transition): a discrete symmetry is broken instead. Correlated domains with orientational order fluctuate strongly amongst the discrete set of realizations of orientational order; the domains are always "short-ranged".

Despite these subtleties, lattice models have often been introduced to take up the role of a simplified version of a continuum model of interest, in the hope they retain the basic physics, e.g. the type of phase transition. Most famously, the Ising model enabled the understanding of liquid-vapor transitions.[24] Other well-known examples are lattice polymer models, which attempt to reduce the vast configurational space of "true" polymers in the continuum.

For 2D systems, the Lebwohl-Lasher / XY-models [334, 346, 347] have early taken on the role as basic models for phase transitions in liquid crystals. Also, the Potts model in 2D or 3D (with discrete spin-orientation degrees of freedom) [46] may serve as an approximate analogy to liquid crystals in the respective dimensions [330]. However, the examples mentioned all share one common feature: They are *on-lattice*, but have anisotropic potential-type interactions that do *not* stem from local, steric-repulsion due to particle shape. They are "spin-like" models.

On the other hand, in the broad scope of soft matter systems [348, 349], steric repulsions play the central role (see Ch. 2) for crystallization, as well as for other phase transformation processes and phase behavior [350–354]. In this context, basic anisotropic-particle systems like liquid crystal models have long been studied in addition to famous hard-sphere systems. However, these

[24] Note that, serendipitously, lattice models can sometimes be mapped onto each other: the Ising model can be mapped onto to the linear XY model with an external field; the 2D dimer problem (dimers) is equivalent to the ground state of a generalized XY-model [345].

are essentially always treated in the continuum. Therefore, we argue that on-lattice models of *sterically* anisotropic particles complement both the palette of well-studied soft-matter model systems, as well as that of "spin"-type model systems on the lattice.

Discretized orientations: Zwanzig models

The *Zwanzig model* [355] describes the model where the possible orientations of the rods are discrete, pointing in the three Cartesian directions in 3D. Yet the Zwanzig model allows for continuous translational degrees of freedom. A density-functional treatment of the Zwanzig model for hard rods in three dimensions (3D) using fundamental measure theory (FMT) shows many qualitative similarities in the phase diagram generated compared to the one for continuum rods [239], but, additional phases do appear. Fundamental measure theory for the Zwanzig model is described in Ref. [33]. Simulation results for the phase diagram of the continuum Zwanzig model in 3D are not known to us, neither are studies on the influence of additional attractions between the rods.

When regarding the bulk behavior of 3D spherocylinders discussed above, it is important to notice the following fact: rods constrained to a cubic lattice in 3D will *not* take on a continuum limit of hard spherocylinders simply by making the lattice "denser". This "dense" limit of the lattice renders the Zwanzig model. Zwanzig found that rods that are long and hard render virial coefficients that scale very differently with their aspect ratio from those of hard-rod models with unrestricted orientations. If a "conversion" between models is at all possible poses a nontrivial theoretical question: They entail different rotational symmetry groups, locally, which then couple to translational degrees of freedom once particles are in mutual vicinity, a topic we discuss in Ch. 2 more generally. Consequently, a second-virial approximation is not sufficient to locate the isotropic-nematic transition even in the limit of long rods. Zwanzig's argument about the virial coefficients should similarly apply to the 3D lattice model, which we discuss in Ch. 6 when comparing to a model of continuous spherocylinders.

The "isotropic–nematic" transition in the 2D Zwanzig model was shown to be of a liquid-gas *demixing* type [356], presumably of the Ising universality class. An early work with Monte-Carlo simulations also suggested such order-disorder transitions when studying an on-lattice model of rods in Ref. [357]. Therefore, the correlations of orientations in the restricted-orientations 2D model are even shorter-ranged than in 2D liquid crystals (algebraic decay). We may conclude that in 2D lattice and continuum models show qualitatively very different behavior with respect to the type of phase transition.

Fully discrete models

Theoretical studies of the bulk phase of the lattice models in 2D and 3D were sparked by DiMarzio [358], having approached the problem from the context of polymer theory. Their solutions are based on combinatorial considerations. DiMarzio calculated the number of possible packings of rods—thus evaluated the entropy – through approximating the probability of inserting a new rod into a system already containing other rods. The approximation consists of

treating all rods orthogonal to the rod that is to be inserted in a typical mean–field fashion: one such orthogonal rods (of length L) is considered a 'cloud' of L independently–distributed obstacles (of size 1×1 in 2D and $1 \times 1 \times 1$ in 3D) for the rod to be inserted. DiMarzio, however, did not evaluate the bulk state explicitly by maximizing the entropy. This appears to have first been done by Alben [359] for the 3D model, who found a strong first order nematic transition for rod lengths $L \geq 4$. Notably, the DiMarzio entropy corresponds to the exact solution on Bethe-like lattices [360] (see also the much earlier Ref. [361] regarding such a connection).

As mentioned, the 2D Zwanzig rod has a *demixing* transition in 2D between the two oriented states allowed [356]. This aspect and the associated critical exponents are discussed in Refs. [362–364]. Therefore, a 2D mixture of rods can be viewed as a binary system of particles (rods oriented in x– and y–direction, respectively). The simulation studies show that the critical packing fraction for the onset of demixing scales approximately as $4.8/L$ for large L [363, 365]. Alben's solution [359] to the 2D lattice problem is in contrast to simulations [366], which found demixing for $L \geq 7$: Alben predicts demixing of the two rod species occurs for $L \geq 4$ above a critical packing fraction $\eta_c(L) = 2/(L-1)$.

At very high packing fractions $\eta \approx 1$, theoretical arguments predict a reentrant transition from the demixed to a disordered state bearing some characteristics of a cubatic phase on a lattice [366]. This transition has been studied in more detail using simulations in Refs. [367, 368]. For rods with extensions $mL \times m$ (where mL, m are integer and L may be non-integer), the phase diagram has been investigated in Refs. [365, 369], where (for $m > 1$) it is shown that a columnar phase appears between the demixed and high-density disordered phase (see also very early, related work on hard squared in 2D in Refs. [370, 371]). Ref. [372] studied bidispersed systems, where further interesting effects occur: When both the rod lengths are larger than 6, they observe the existence of two ordering transitions at full packing, upon varying the composition. See also the thesis of Kundu [373]. Ref. [374] studies a dimer lattice gas model with nearest-neighbor exclusion.[25]

We will show in part III that in addition to the known effect of orientational "demixing" 2D systems, 3D systems of hard rods on the lattice demix in a unique way: We will show how "nematic" phase corresponds to an excess of *any* of three species, though the specific direction is transient and switches via intermittent relaxation events. For intermediate rod lengths, this nematic "excess" actually turns into a "deficiency" of one rod species, a completely unique feature of the fully discretized model, which has not been reported before. Indeed, the nematic phase appears only for rod-lengths $L \geq 5$, below which a "normal" liquid–vapor transition between two isotropic states persists. Further, in addition to the hard-core isotropic-nematic transition being discovered

[25] A mathematical proof of the existence of "nematic" orientational ordering on discrete lattices was motivated by the conjecture of Heilmann and Lieb [375, 376] who originally considered mixed systems of monomers and dimers. Directional ordering transitions [363, 366] has been proven in agreement with the simulations, [377–379], additionally for polydisperse systems [380]. Notably, relationships between planar spin (XY) models and dimer models had long been discussed [345]. Yet, as collinearity of very short rods at low temperatures is predicted (for hard-core systems mixed with monomers, a direct relevance for the model (or thermodynamic ensembles!) employed in this thesis remains unclear.

in 3D in simulation, we characterize the effect of attractions on the isotropic–nematic phase transition for a large range of rod-lengths. As to 2D systems, we investigate a large range of attraction strengths – much more than previously investigated in the literature, providing a much "wider" view on the phase diagram. We study the exemplary case of $L = 10$.

* * *

In the next section, we introduce the third major topic of this thesis, machine learning. We will use our gained knowledge of the 2D behavior of sticky hard rods to better understand an unsupervised machine learning algorithms – by training it on configurations of the model system and observing its ability to extract thermodynamically-relevant information.

1.4 Unsupervised-machine-learning a "sticky" hard-rod system in 2D

In this thesis in part IV, we study the learning behavior of a generic, unsupervised, and generative learning algorithm – β-variational autoencoders (β-VAEs). In an autodidactic-style approach, we train the algorithm on configurations of a statistical system of "sticky" hard rods in 2D – whose thermodynamic properties we understand. We characterize the phase behavior of physical system in part III aforehand. In this way, we aim to find out more about the limits and capabilities of the algorithm with an alternate viewpoint from statistical mechanics.

The work in part IV is exploratory in character, hence, will render a number of surprises. For example, we find that β-VAEs "coarse grain" configurations. As we characterize the learning behavior over a wide range of parameters (β and number of latent variables), we find the learning algorithm *itself* undergoes a phase transition. This occurs upon a critical or threshold value β, whereafter the effective level of coarse-graining is changed. The *latent variables*, which we interpret as (fluctuating) collective variables in the rod system, become "disentangled" and form a broad hierarchy at this critical state of β, after which certain variables collapse. (This intriguing behavior may bear some analogy to solidification of amorphous systems or to the appearance of goldstone modes [381, 382].) We will find out that the first few variables express the global order parameters in the system, i.e. the quantities reflecting the symmetry in the system that is broken upon a thermodynamic phase transition. Higher-order variables seem to express further "modes" in e.g. a fluid or a solid. These algorithms thus learn a reasonable model system, to some extent. Yet, we will see that their generative capacities are limited in their interpretability, and suggest a few ways forward.

In the next section, Sec. 1.4.1, we will motivate machine learning more generally, thereafter alluding to deeper theoretical connections to statistical physics. We will then foreshadow that our approach taken in this thesis will reveal intriguing learning behavior, which connect to a very fundamental topics: on compression, critical phenomena, and coarse-graining. We provide a brief review of current applications of learning algorithms to statistical physics, which is a rapidly moving field. We describe β-VAEs very briefly in Sec. 1.4.2, as well as review the limited number of applications to statistical physics that we have found in the literature.

1.4.1 Introduction to machine learning

Machine learning [383–390] is having dramatic effects on many areas of technology and science, being one of the most rapidly growing technical fields. Algorithms can complete specialized tasks that we may deem as "complex", in the sense that we do not know (or want to know) how to formulate the exact rules leading to a 'correct' answer. The key is that algorithms are capable of learning rules implicitly, not imposed explicitly by human engineers [391]. Most dominant in recent years is the broad class of learning algorithms that embody *deep learning* [108], which, however, has its origins date back to the mid and latter part of the last century. Deep-learning is a form of *representation learning* with multiple levels. With enough transformations chained on top of one another, very complex functions can be learned [391]. Thus, deep learning as well as many other machine learning algorithms can, loosely, "abstract away" unimportant details in datasets. They discover underlying regularities or recurring variables (patterns), the basis for making predictions on the data-sets. One can say they try to "make sense" of large, complex data-sets, especially if we impose a *probabilistic model* on the data, fundamental to the philosophy behind VAEs that we study in part IV of this thesis.

Standard learning setups

As stated in Ref. [392, Ch. 1.1], most, if not all, known facets of intelligence can be formulated as driven towards a *goal*, which can be stated generally as, "*Approximate a target concept given a bounded amount of data about it*" [393]. In whichever way the target concept is to be understood, striving towards a goal can be formulated as an optimization problem, generally [393]. A sharp distinction should be made between learning generic features of datasets in the learning problem and reproducing training data in a memorized fashion: This is the central idea behind the *generalization* ability of an algorithm.

The "type" and meaning of the objective function depends on the class of learning problem: they come in three main variants [383, 388, 389, 391, 394, 395]. In most applications, a more appropriate categorization is a mixture of these. The first and most common, *supervised learning*, is the most intuitive, arguably. Prototypical examples are classification and regression. In classification, a machine learning algorithm learns to map data to categories distinguished by *labels* (e.g. "cat" or "dog"), which augment the raw data (e.g. images), *both* of which are passed to the algorithms during training. In this way, the correct answer is given to the learning agent during training. The machine then provides predictions – probabilities – for each category of possible answers. Supervised learning is specialized to the particular task and dataset, especially when compared to unsupervised or reinforcement learning (see below). It is probably the farthest from any general form of intelligence. Nonetheless, much of the practical successes on representation learning have arisen in supervised settings.

Yet, there is a deep desire to develop algorithms capable of performing well without the need to label data. This leads to the class of *unsupervised learning*, where a learning agent finds an internal representation of the data, discovering hidden relationships within it. One can say they find natural "partitions" of the data, given a few, basic model assumption. Most generally, correct answers are not provided to the machine. The crux of these (seemingly) "free" algorithms

is that model assumptions are required in order to be able to organize the data into partitions, at all [396]. For example, in *clustering*, the data is rearranged onto a low-dimensional manifold, abiding to a model that governs statistical distances between data-points.[26] In linear dimensional reduction techniques like *principal component analysis* (PCA), the covariance matrix over data is diagonalized and the eigenvectors with the highest variance are selected. As we will discuss in Ch. 3.6, this is akin to presuming a (global) Gaussian field theory of the data. We mention that PCA represents a limiting case of VAEs [397]. VAEs are also unsupervised algorithms, which are discussed separately below.

The third class encompasses *reinforcement learning*, which can be placed somewhere in between supervised and unsupervised learning. We will not describe them in detail. We only mention that unsupervised learning is more "lax" about the goal of a learning task than with full supervision.

The deep connection to statistical physics

Alongside the "use and abuse" of deep learning methods and amidst their striking success, there is an urgent intellectual desire to understand the "*why's*" and "*how's*" of algorithmic learning from fundamentals. One of the lessons of modern machine learning is that the most flexible (generic) learning systems render the best predictive performance, especially when learning from large data sets [390]. Physics-informed or physics-inspired algorithms [398–402] – as well as methods to *test* algorithms – may offer new ways forward. The latter case represents our approach in this thesis, in which we test an algorithm on a well-understood and sufficiently idealized many-body system. In this way, we can reveal what the algorithm is learning about the physics of the many-body system, i.e. thermodynamic properties, fluctuations, or phase transition boundaries, thereupon, we can judge model presumptions in the algorithms.

The deep *theoretical* ties between machine learning (information theory) and statistical physics are associated with the many-body nature of the problem: a large number of degrees of freedom that a system can explore with given, physical constraints. Citing Kirkpatrick *et al.* (1983) [403] in their seminal work utilizing the Markov-Chain Monte-Carlo methods of Metropolis *et al.* [404] for hard optimization problems,[27] "*There is a deep and useful connection between statistical mechanics (the behavior of systems with many degrees of freedom in thermal equilibrium at a finite temperature) and multivariate or combinatorial optimization (finding the minimum of a given function depending on many parameters) . . . This connection . . . exposes new information and provides an unfamiliar perspective on traditional optimization problems and methods.*" Statistical thermodynamics provides principles for assessing the entropic and energetic costs of manipulating information [75]. (See also Ch. 3.5.2 later in this thesis.) Moreover, theory on frustrated many-body systems, i.e. spin glass theory [405], represented the context in which learning theory was developed and understood in the 1980s–1990s [406–415]. From a very general standpoint, then, statistical physics could provide insight and clarification on basic questions [75, 102, 416–419]. In this thesis in part IV, we aim to take a step in this direction.

[26] The model can consist of a few low-dimensional Gaussian distributions, and the number of clusters is given by the user (it is a hyperparameter, i.e. a free model parameter (usually in the cost function) that is fixed prior to the training or optimization procedure).

[27] a method well-known as *simulated annealing*

As to physics-inspired methods, we note that canonical methods from statistical field theory like variational mean field theory have been imported directly into machine learning (e.g., see Ref. [420]). The VAEs we study in this thesis utilize this approach, which we will explain in more detail in Ch. 3.

Compression, coarse-graining, and critical phenomena

Deep learning is traditionally described as finding a complex, parametrized map between data and hidden representations. For a learning problem, the true map may be unknown, hence learning is a type of inverse problem, where arbitrary functions should be approximated. Nonlinearities in the networks are known to be key to their representation power and expressibility.

It may be of no surprise, then, that learning entails critical phenomena. Notably, criticality and scaling appear naturally in biological or neuronal systems [73, 421–426]: Systems poised at criticality may be "optimal" in response to biological or evolutionary adaptation pressures. Hence, *optimal* forms of learning may be tied to a learning situated at a critical point [393, 427–430]. In this thesis in part IV, we find that a β-variational autoencoder set at a threshold state of its hyperparameter (i.e. a free model parameter in the cost function that is fixed prior to the training or optimization procedure) learns a hierarchy of coarse-grained variables in the rod system. The level-of-detail of the reconstructed or generated images suffers after crossing the threshold, which is due to mode collapse.

Trade-offs in the representation ability have long been known in other contexts [431–433], where a characteristic power-law frequency of variables is captured at an optimal (threshold) state.[28] The ultimate goal of deep learning seems to be a trade-off between capturing *predictive information* and finding representations that are maximally "relevant"[29] while being maximally compressed. Heuristically, it should separate "signal" from "noise" [438–440]. More specifically, an optimal trade-off state[30] may imply, for example, that every bit of compression in the representation is equivalent to doubling the training data (when regarding the impact on the generalization error) [449].

Though these topics may sound quite abstract, we see evidence for critical or threshold phenomena, due to frustration or trade-offs, in our simple experimentation with β-VAEs in part IV. We we apply them to configurations of the 2D sticky-hard-rod system, where, specifically, the training dataset spans widely across phase boundaries, i.e. is in an out-of-equilibrium state itself (or approximately "critical"). Notably, the critical *learning* behavior will be tied to learning a hierarchical "coarse-graining" of the configurations, which is quite interesting from a theoretical perspective. A series of works has alluded to connections between (deep) learning (or even PCA) and renormalization group methods: These algorithms seem to work by realizing a hierarchical coarse-graining procedure [417, 418, 427, 450–457]. The issue of *symmetry* is further important, as this reduces the amount of independent parameters. In our studies,

[28] We note that a broad the frequency distribution of variables is characteristic for the observation of *Zipf's law* in various forms in nature and data, see Refs. [428, 434].

[29] Specifically, the predictive information is the *mutual information* between the training set and an infinite test set [435], which quantifies the amount of information that the training data provides about the underlying generative process. It is essentially a measure for the complexity of such a process [436–438].

[30] Please refer to information bottleneck theory by Tishby and coworkers [441–446]. See also Refs. [429, 447, 448].

we will see that a data representation that provides a basis for the broken global symmetries in the physical system is key to successful, as well as interpretable learning. In our case, these will correspond to the three-fold degenerate, global states that coexist (co-occur) at the tricritical point. Finally, we will see that the learning systems can only compress the information in configurations at the cost of coarse-graining them, where the upper limit on resolution upon coarse-graining corresponds to the level of compression. We will see that changing the architecture from a simple VAE to a deep-convolutional VAE does not necessarily improve the results. We think the training data sets of the sticky-hard-rod systems seems to pose a very difficult learning problem, i.e. they have to a high level of complexity or a low level of irreducibility, especially as they span across phase boundaries. Therefore, many open issues we will encounter are highly stimulating from a theoretical perspective.

Applications of machine learning, generally, within statistical physics

Complementary to basic machine learning research, using algorithms as a *tool* for physics [458] has become very popular in recent years, in the hope to "accelerate" physics research [394, 449]. In the realm of statistical physics, much of literature in the past few years has reported on automatic classification of ("self-assembled") structures, or on automatic "detection" of phase boundaries,[31] including topological phase transitions.[32] Lattice spin models have been the most popular choice for most of the works listed above – off-lattice and anisotropic-particle systems have been explored in e.g. Refs. [485, 486]. There has been a noticeable dominance towards *quantum* many-body systems [487]. The infamous, intrinsically difficult problem of fully representing the many-body wave functions is at the heart of many endeavors using artificial neural networks.[33]

Machine learning algorithms may become useful for physics on a much more abstract level, as well. Discovering new physical concepts [501–503], identifying new experimental questions [502, 504], or even detecting consistencies among different theories [505] are very attractive ideas that could be possible. However, more "down-to-earth" applications to statistical field theory have already found success: Extracting analytical forms of order parameters (generally of polynomial type) like with support vector machines may aid in theory development of many-body model systems, which for the vast majority are intractable [506–511].[34] Machine learning has also been used in the context of liquid state theory or classical density functional theory [513–515]. Approximating intractable statistical models, predicting, and generating properties thereof – without the need for expensive (Monte Carlo) simulations – are very attractive prospects [459, 512, 516–521].[35] To this end, VAEs, which we apply and investigate in this thesis, could be viewed as a possible method for approximating an intractable partition function or free energy; however, under restrictive conditions. We introduce the algorithm below on a very generic level, and report on

[31] See, for example, Refs. [352, 459–479] on automatic classification of structures and "detection" of phase boundaries.

[32] See e.g. Refs. [480–484] for examples where topological transitions were detected.

[33] See e.g. Refs. [479, 488–500] for examples where many-body wave functions are represented in neural nets.

[34] Other "explainable" AI methods used in this regard are reported in Refs. [510, 512].

[35] Other applications head towards overcoming finite-size scaling problems of in simulated lattice systems [522, 523], or in identifying extensive parameters of statistical systems [524].

related work in the context of applying them to statistical model systems from physics.

1.4.2 Beta-variational autoencoders (β-VAEs)

To understand how variational autoencoders are set up, let us begin with a standard autoencoder. An autoencoder attempts to reconstruct an input "as best as possible": input data is passed though an encoder through a bottleneck layer, which is much lower-dimensional than the original data. This is where the compressed representations of the data are encoded. A decoder maps these back to the original space, outputting a reconstructed image of the input (see schematic in Fig. 1.7). The basic objective function is "only" the reconstruction error, which is a measure for the accuracy of the output for a given input.

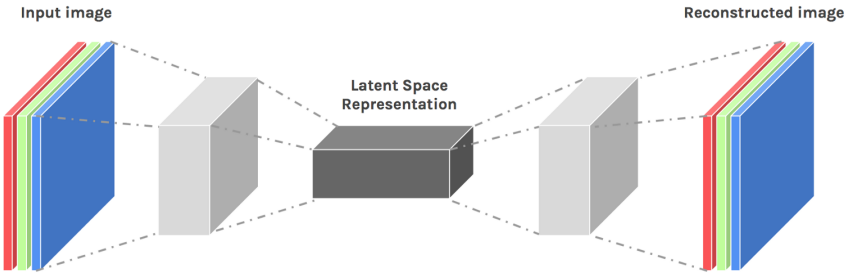

FIGURE 1.7: A schematic of how an autoencoder neural network is built up. An input image (here with three color channels) is passed through an encoder into a bottleneck layer, where the latent space representation of the data is encoded (compressed). The latent code is then passed through the decoder network, which outputs an approximate reconstruction of the image. Encoder and decoder implementation is fully flexible (fully-connected layers, convolutional layers, etc.), and the optimization problem is to minimize the reconstruction error. Source: Ref. [525].

In contrast to the deterministic autoencoders, (beta-) variational autoencoders (VAEs) [50–52] are neural networks that provide a probabilistic model of the data. It is a *generative* model. Figure 1.8 provides a first view of how the probabilistic model is realized by a neural network: An encoder network maps an input $\boldsymbol{x}$ onto the *latent space* spanned by $\boldsymbol{z}$, and represents the conditional probability distribution, the model (approximate) *posterior* of the latent variables, $p_\phi(\boldsymbol{z}|\boldsymbol{x})$. "$\phi$" represents the trainable (free) parameters of the encoder neural network. In the standard VAE model, this approximate posterior presumed to follow a fixed (tractable) form: A multivariate Gaussian, in fact, a *diagonal* one. Hence, each image is encoded in terms of the multidimensional *means* $\boldsymbol{\mu}$ and *variances* $\boldsymbol{\sigma}$ of this distribution. A sampler network that draws a random value $\boldsymbol{z}$ from this encoded distribution, and sends it to the probabilistic decoder neural network, whose free parameters are denoted "θ". The decoder represents the probability distribution of observing $\boldsymbol{x}$ $p_\theta(\boldsymbol{x}|\boldsymbol{z})$ conditioned on specified latent variable $\boldsymbol{z}$. The output $\boldsymbol{x}'$ is a probabilistic "reconstruction" that is compared to the input $\boldsymbol{x}$ in the same manner as with an autoencoder. However, the VAE cost function will contain an "extra" term that judges how well

the posterior $p_\phi(z|x)$ matches a prior distribution (a unit Gauss), i.e. a VAE minimizes the so-called *variational free energy* to learn the (approximative) model of the data. We will explain this notion and the full β-VAE algorithm in more detail in Ch. 3.6.

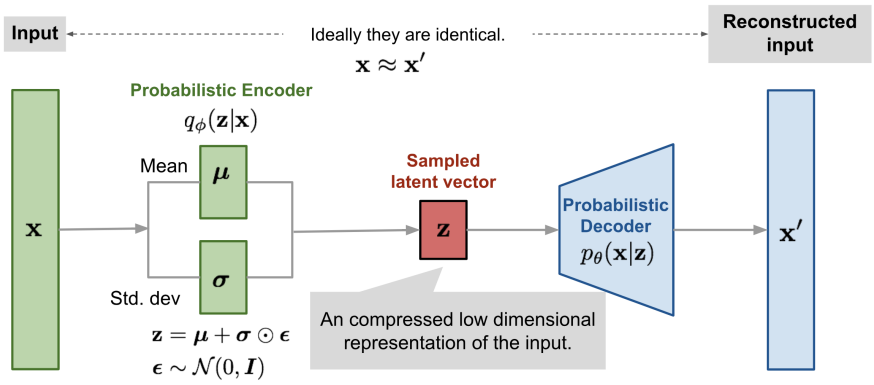

FIGURE 1.8: A schematic of a variational autoencoder with input x, output x' and latent variables z. Please see main text for a more detailed description. Source: Ref. [526].

VAEs are praised because they "work" for many types of data and are highly robust (they are stable compared to GANs, for example). Yet, they, too, show idiosyncratic behavior [527–529]: posterior collapse or "mode collapse" [530, 531] occurs. Whether they are capable of "disentangling" representations in latent space [532, 533] is a topic receiving quite a bit of attention in recent years. Further, the images generated by VAEs are typically "fuzzy", hence they are less competitive with GANs for generating realistic images of faces, for example. Therefore, many issues around VAEs remain open, and we aim to judge their capabilities in our own way by applying them to physical data of a model system we understand well – the configuration of sticky hard rods, in Ch. 7.

Applications of VAEs to statistical physics

Applications of VAEs to statistical-physical systems is remarkably recent, given their invention in the computer-science community in 2013–2014 [50, 51]. A very brief application of VAEs was performed in 2017, which was compared to other "dimensional reduction" and unsupervised methods [463]. VAEs were employed in a customized architecture for quantum many-body systems in Ref. [495] in 2018. In 2020, Ref. [534] further demonstrated the capability of VAEs on the Ising model (apart from Ref. [463]), and Ref. [535] that on spin glasses. Ref. [536] likewise utilizes generative aspects of VAEs for modeling complex systems from quantum mechanics. VAEs were employed in Ref. [537] to generate a reduced version of many-body dynamics in an application for biophysics. (Related is the work of Ref. [538] using standard autoencoders.) The detection of phase boundaries with unsupervised learning and discovery of collective variables are related topics for which we provided a brief literature review in Sec. 1.4.1. We note further that principal component analysis (PCA) is conceptually related to VAEs [397, 527], representing a limiting case.

Applications of PCA are quite popular, as it is much easier, numerically and algorithmically: PCA was applied to configurations of lattice models in Refs. [460, 462–464], as well as off-lattice models in Refs. [485, 486].

1.5 Overview and organization of this thesis

The remaining two chapters (Ch. 2 and Ch. 3) of part I of this thesis prepare and engage the reader with underlying themes and the deeper physics behind the research presented in subsequent parts of thesis. This includes a description and assessment of the specific methods applied in this thesis.

We begin by discussing the physics of complex fluids of anisotropic particles in Ch. 2, where the pronounced coupling between the large number of orientational and translational degrees of freedom makes way to intricate phase behavior in bulk and in confinement. Moreover, this coupling leads to a large number of possibilities of structure and dynamics in nonequilibrium, where self-assembly occurs. We report on a "soft-matter" affinity of organic molecular thin films, as well.

Chapter 3 provides a deeper theoretical backdrop on equilibrium and nonequilibrium statistical mechanics, discussing probabilistic descriptions in both cases. Quite generally, time- and spatial scales in a system reflect the static and dynamical information of a fluid. *Coarse-graining* aims to provide levels-of-descriptions when particular time and spatial scales are deemed "relevant", although the case of nonequilibrium dynamics requires care. At the end of the day, limited or partly available information necessitates a probabilistic description, the notion upon which statistical mechanics is founded. This prospect about partial information forms a natural bridge between statistical physics and machine learning, whereby the latter field is rapidly developing and these connections have not been expended in full. Markov-Chain Monte Carlo algorithms – more than mere calculation tools – are rooted deeply in the basic postulates of equilibrium statistical mechanics. KMC is closely related: it characterizes the numerical approach to "solve" the formal, full N-body stochastic dynamics of a nonequilibrium system upon a first level of coarse-graining, still remaining consistent with microscopic causal relationships (action and reaction of particles). We compare and discuss the approach to the nonequilibrium N-body problem with DDFT, whereby equilibrium DFT will also have been be described. With conceptual overlap from statistical field theory, the generative model of VAEs (machine learning) finds an optimized effective model of data, which is probabilistic by necessity and construction.

Part II of this thesis entails two chapters on our work on monolayers of hard rods on planar substrates in an on-lattice model of hard-core rods. This study was introduced in Sec. 1.2. In the first part of monolayers, Ch. 4, we investigate the nematic ordering behavior of *purely* hard-core rods in equilibrium conditions. In the second part of the chapter, we present the corresponding nonequilibrium ordering behavior by programming and employing KMC simulations: The growth of a full monolayer is driven by a deposition flux introducing new particles onto the substrate. We compare the simulations results directly to an analytical approach with DDFT. We also match the nonequilibrium dynamics

in the lattice model with that of the off-lattice spherocylinder system, allowing us to compare the two systems directly.

The second chapter of part II, Ch. 5, addresses the case of "sticky" hard rods in the lattice model. Upon augmentation of our KMC simulation code to account for sticky attractions between rods, we present an extensive study of the evolution and kinetics during monolayer growth for this highly generic and idealized model. The dynamics are varied over seven to eight orders of magnitude and the sticky attraction strengths are varied over a large range. The kinetics are very rich: We identify and discuss multiple phase transition scenarios in the monolayer (related to e.g. metastable phases appearing). This has not been reported elsewhere for comparable models, and there is currently no theory that could predict this behavior, as far as we can reckon. We further find clear effects upon varying rod-length, strength of substrate potentials, and the specific choice of microscopic dynamics in the model regarding the rotations of the rods. Many of our findings seem qualitatively compatible with the reported literature that we introduced in Sec. 1.2, which opens up the possibility for a new and deeper understanding of "real" thin film systems.

Part III of this thesis addresses the equilibrium phase behavior of hard rods constrained to lattice in 3D bulk, as well as 2D. We introduced this piece of work in Sec. 1.3. This part of the thesis contains one chapter (Ch. 6). Using GCMC simulations, we first investigate the isotropic–nematic transition in 3D for hard-core rods, finding a uniquely weak transition that differentiates the lattice systems from off-lattice systems of rods in the bulk. The latter is also true for the nature of the transition: the "nematic" phase entails a clearly different meaning on the lattice, realized in a particularly unusual way owing to the discrete rotational degrees of freedom. Thereafter, we produce phase diagrams for the case of sticky hard rods in 3D and 2D (via GCMC simulations).

Part IV of this thesis addresses the work on machine learning introduced in Sec. 1.4, and contains one chapter (Ch. 7): We investigate beta-variational autoencoders (β-VAEs), an unsupervised and generative machine learning method: We see how these algorithm "learn" configurations of the 2D sticky-hard-rod system of Ch. 6, reinterpreting and discovering intriguing aspects of the algorithm from a physical point-of-view. The learning algorithm can clearly distinguish between different thermodynamic phases, and we can use the latent (hidden) variables to construct alternative order parameters, for example. As it seems VAEs discover collective variables in the configurations, and automatically encode local fluctuations thereof, these algorithms may be useful for e.g. coarse-graining. We also compare the learned representations and quality of a simple, "vanilla" β-VAEs to those of a deep convolutional β-VAEs.

Part V constitutes the closing of this thesis. In Ch. 8, we provide a general discussion across the various projects of Chs. 4–Ch. 7. There, we tie together findings in each research project in a broader context, integrating knowledge gained from all projects. We also reassess the scope and feasibility of certain approaches taken in this thesis to answer some of the original scientific questions. As part of a general outlook, we will discuss the directions in which we sense fruitful ground, both theoretical, as well as applied in nature. The general conclusions of our thesis are consolidated in Ch. 9.

1.5.1 About co-authored publications incorporated into this thesis

We incorporate the work of four readily published manuscripts into Ch. 4 (two manuscripts) and Ch. 6 (two manuscripts) of this thesis. Each and every one is a co-authored piece of work. References to the corresponding pairs of publications are provided at the beginning of Chs. 4 and Ch. 6. Contributions of the author of this thesis to each manuscript are stated therein, as well, including e.g. which figures the author produced.

1.5.2 About programming, simulations, and numerical analysis performed in this thesis

We would like to use this section to provide a rough overview of the numerical work involved in producing and presenting data in this thesis.

Simulation programming and production

The author of this thesis was fully responsible for designing, planning, programming, testing, executing and managing all KMC simulations in this thesis. Everything was written in *C++*, abiding to modern programming standards: The simulation codes are fully object-oriented and utilize modern design patterns, template metaprogramming, as well as diverse compile-time and runtime optimization "tricks". We employed modern *Boost* libraries and even wrote our own libraries. The program is well-tested, flexible and has even been extended and tested for a number of future simulation studies[36] that are out of the scope of this thesis.[37] The volume of the self-written KMC simulation code consists of the order of $25,000 - 30,000$ lines of code (without whitespaces). This includes testing modules, self-written libraries, and the portion of numerical analysis routines that were written in *C++*. (Most "higher level" data analysis codes were written separately in *Python*, see below).

Further, the author aided in the design, testing, and management of the *equilibrium* GCMC (and successive umbrella sampling) simulations in Chs. 4, 5 and 6 that were finally written and executed by other co-authors.[38] We stress that *nowhere* in this thesis were simulation packages utilized: All numerical simulations were generated from self-written program codes.[39]

Machine learning algorithms and training

The machine learning algorithms (β-VAEs) presented of Ch. 7 were all implemented, trained, managed, and fully analyzed by the author of this thesis, in the *Python* programming language. We employed the *Keras* libraries with a *Tensorflow* backend. [40] Excluding a large round preliminary work, we trained ~ 100 neural networks.

[36] We could simulate full 3D dynamics or 3D film growth. Already tested for preliminary results are the following simulations: monolayer evaporation, heating, temperature-quenching or cooling, interrupted growth or evaporation–deposition growth

[37] We also note that the author designed the underlying algorithm for rejection-free KMC algorithms with anisotropic particles herself, and wrote the program code in a most basic form in the context of a Master's thesis.

[38] in the context of co-supervision of student theses and student summer internship projects

[39] *Nota bene*, this includes the codes of other co-authors, as well.

[40] The author greatly thanks colleagues S.-C. Lin, C. Mony, as well as M. Maeritz for assistance in preliminary and exploratory stages of writing or running these types of or related algorithms.

Numerical analysis and plotting

Part of the numerical analysis was performed using *C++* with *self-written routines*, such as cluster detection schemes, morphological analysis routines,[41] and some dynamical analysis routines in Ch. 5, as well as a few statistical analysis routines in Chs. 4. We employed *Python* for the bulk part of the numerical analysis and plots that were produced by the author of this thesis (intensively in Chs. 5, 7). The plots originating from the author in Ch. 4 were produced using *grace*. Apart from regular plotting, mostly done in *Python*, we have also produced a number of "artistic", 3D visualizations in this thesis using the *POV-ray* scripting language and program.

[41] The author thanks colleague J. Bleibel for a helpful code "stub".

Chapter 2

The Mesoscopic Nature of Complex Fluids of Rods

For all bodies are in perpetual flux like rivers, and parts are passing in and out of them continually.

Gottfried Wilhelm Leibniz [Monadology]

This chapter provides a background to some of the basic physic and phenomenology of complex fluids, particularly those of hard rods which we study in forthcoming parts of this thesis. We first address generic topics like importance of strongly coupled rotational and translational degrees of freedom in systems composed of anisotropic particles. We then discuss phase behavior and dynamics (of rods) in dimensional *confinement*, which are important for understanding the rod-systems explored in 2D (part III of this thesis) and (2+1)D monolayer confinement (part II). We also attempt to illustrate potential effects of *discretized* degrees of freedom on phase behavior, which represents a central theme of this thesis and is a novel aspect of the research presented in it. We also touch upon self-assembly or phase separation kinetics in such systems, and become acquainted with the notion of nonequilibrium "driving forces" behind thin film growth studied in part II. In line with our general discussion of complex fluids, we argue and discuss how organic molecular thin films are more soft-matter-like than atomic films and should display a wider range of collective phenomena (associated with a higher variety or more complex phase transition kinetics). We provide evidence from the literature in favor of this position.

Packing problems have fascinated people for millennia,[1] and the study of them has produced a body of literature across many disciplines [353]. In which way can we pack a surface or volume with a given hard-core object of particular shape? Which (combination of) shapes or particle orientations allow for a regular tiling pattern in 2D or 3D? These express in part very old, unresolved questions in discrete geometry (and number theory).[2] Collections of polyhedra display a vast array of such unique structures and packing geometries [228, 540–546], including quasicrystals [547]. Each makes way for different *macroscopic properties* [541], naturally, which can have *novel* electronic, optical, and

[1] with regards to Platonic and Archimedean solids

[2] As a simple example, the packing of ellipsoids can be more efficient than that of spheres [539].

dynamical properties – some of which may be highly desirable for fabricating advanced electronic, photonic [230, 547, 548], and rheological devices.

Apart from practical uses and phenomenology, many deep questions remain unanswered. Understanding *how* macroscopic properties emerge in hard-bodied systems represents a cardinal inquiry that encompasses a wide variety of scientific and practical problems. Below we discuss how rod-like particles that are hard-core will be subject to entropy-driven phenomena; their anisotropy will highlight the important ties between orientational and translational degrees of freedom that are present in in *all* fluids. Certain mesoscopic levels of ordering are inherent in all fluids. These surface most apparently in nonequilibrium, where a broader bandwidth of relevant time-scales (ascribed to various kinetics) spawns the mesoscopic character of structure and dynamics. We venture to understand the formation of ordered structures in nonequilibrium for hard-rod fluids on lattices in part II. Equilibrium phases represent stable, macroscopic states resulting from the complex interplay of many, individual degrees of freedom – we study the phase behavior bulk systems of hard rods on lattices in part III. Finally, unsupervised machine learning is able to discern between different rotationally- and translationally-ordered states of a liquid, which we demonstrate in our study in part IV of this thesis.

2.1 On structure and dynamics in complex fluids

We typically discern various phases of matter using structural arguments. Liquids (and glasses, which are solids) in the continuum of space do not have pronounced long-range translational or orientational order. They are amorphous and *homogeneous* when considering larger time and spatial scales. Yet, a crucial factor is that *locally* in space and time, homogeneous fluids show orientational and translational ordering [352, 549].[3] The key here is that complex fluids are not composed of point-like particles – rather, the spatial extent of the particles is key to the "higher order" structural quantification in fluids in equilibrium, and are at the heart of fluctuations. The inherent coupling of degrees of freedom gives rise to local, transient, coherent structures and dynamics, which are particularly important in nonequilibrium settings such as during phase separation, where ever larger-scaled coherent modes emerge.

2.1.1 Rotational and translational degrees of freedom

Rotational and translational ordering play somewhat different roles in complex fluid systems, which are crucial for understanding the phase behavior, as well as nonequilibrium structure formation, of these systems, particularly in the case of anisotropic particles. Arguably, the breakdown of translational symmetry in liquids takes place intrinsically at a global scale, while the breakdown of rotational symmetry can be local, paraphrasing the discussions in Refs. [352, 549]. Global translational symmetry implies conservation of linear momentum across all mesoscopic (relevant) scales of treatment. Motion of individual particles in translational degrees of freedom are main contributors to "holding up" this symmetry, if the system is ergodic. In contrast, local angular degrees of freedom must couple to translational degrees of freedom in order to

[3] An exception may be e.g. fluid mixtures.

transfer rotational energy along one dimension of space. Arguably, then, owing to this complication, a rotational symmetry is generally "easier" to break. Before crystallization sets on in a metastable fluid of hard sphere colloids, for example, transient clusters belonging to different symmetry groups appear and disappear [550] – local orientational ordering is thus one of the key factors in crystallization [551].

If the coupling between local rotational and these longer-ranged translational modes becomes *strong enough*, a global break of this symmetry is possible (at long ranges):[4] This characterizes the case of the isotropic-nematic transition of long, hard rods in the 3D bulk (see also Ch. 1.3.1). The transition occurs when both a high enough mean density is reached, i.e. when momentum transfer is more efficient, and when rods are long enough, so that they can more easily correlate their orientational states to the farthest reaches of space.

Although this long-ranged ordering transition is abrupt in nature (requiring some amount of work), nematically-ordered fluids preserve much of their liquid-like dynamics in translational degrees of freedom. The global break in translational symmetry (a density gap, and therefore, an interface dividing space) upon this kind of ordering is generally weak when compared to crystallization.[5] Subsequent transitions, at even higher densities, break the remaining continuous rotational symmetries into various smectic phases [39, 282, 283], which, however, still allow for a certain degree of continuous translational degrees of freedom (locally). The final, most difficult transition breaks the global, continuous translational symmetry space – the solid crystal phase – where a long-ranged crystal of discrete translational symmetry emerges. Therefore, orientational ordering will generally occur, much more pronouncedly, before translational ordering, which breaks the homogeneity of space [549, 551].

Fluids composed of many bodies have an innate capacity for a large diversity of ordering phenomena. This owes to the complex coupling of translational and rotational degrees of freedom, which correlate variables within and among various mesoscopic scales, even in equilibrium. A single event of a symmetry break beginning at a local scale, imposed from some outside source, will induce an irreversible sequence of events [552, 553], finding a new organization of the fluid. Self-assembly occurs in these kinds of nonequilibrium scenarios (see Sec. 2.3 later on). Key are the mesoscopic unbalanced forces that characterize its non-Markovian dynamics at those scales, and fundamentally non-local character of the fluid in out-of-equilibrium (we will further discuss such topics in Ch. 3).

Confinement is discussed further on in Sec. 2.2, but we mention here, again, the following aspect of 2D confinement (see also Ch. 1.3): 2D confinement converts a "global", long-ranged break of a continuous symmetry to that over on quasi-long rages (algebraic decay in correlation functions of the order parameter) [321]. A break of a continuous symmetries is generally "easier" in 2D, where many transitions lose their first-order character [325]. As to hard rods, the nematic transition from the bulk becomes a "quasinematic" transition in 2D [332]. Translational and rotational degrees of freedom couple *differently* in confinement, and, therewith the local and global ordering properties change. Determining the exact coupling between all rotational and translational degrees

[4] Note here that long-ranged ordering is only possible in breaking a *continuous symmetry*, as far as theory goes [321].

[5] The packing fractions remain below those required for crystallization, i.e. the free energy difference is weaker.

of freedom is a most fundamental, yet one of the most nontrivial, currently unresolved challenges of liquid state theory for inhomogeneous fluids in our two and three dimensions of space. By the end this thesis, we will be able to discuss the effect of confinement in comparing systems of (sticky) hard rods constrained to lattices in purely 2D confinement, monolayer (2+1)D confinement, and in the 3D bulk.

"Entropy-" versus "energy-driven" phenomena

Energy-driven structure formation is often distinguished, heuristically, from that which is entropy-driven [554]: In the former, we associate the effects of attractive forces to aggregation, for example. Further, attractions are required for *condensation* of a fluid from a gas phase. In contrast, an ordering phenomenon is often considered entropy-driven if the process correlates particles over longer distances. This owes to repulsive forces, fundamentally: Repulsions lead to long-ranged order and large, spatially extended domains (large coherence length). Crystallization of fluid systems is a phenomenon owing to repulsive forces, most famously demonstrated in hard-sphere colloidal systems [555–557]. A particle with spatial extent will exclude a configurational volume from other particles (for a moment in time). We could regard many phenomena in confinement as fundamentally entropy-driven for similar reasons, which we discuss more in Sec. 2.2. Repulsive forces are thus key to the formation of spatially extended structures with *distinguished* order. For this reason, in parts III and part II of this thesis, we spend much of our efforts in studying the fully hard-core repulsive systems of hard rods before investigating the competing role of additional, short-ranged attractions.

A distinction between "energy-driven" and "entropy-driven" can be somewhat misleading under circumstances, as these represent extreme cases. Most generally, a complex interplay of minimizing energy and maximizing entropy characterizes the situation as a whole. One exception worth mentioning might be systems with long-ranged attractive forces [558]. Such fluids appear to be inherently non-ergodic [559–562]. As for short-ranged attractions, it turns out we can map these, in equilibrium fluids, to repulsive forces arising from virtual particles (i.e. analogs of polymers). The latter system is known as the Asakura-Oosawa model [70] of mixtures of colloids with polymers. Then, the attractive forces between nearby colloids are *effective*, arising from many-body interactions. Specifically, the attractive interaction is calculated from an overlap of the excluded volume of space available for polymers quantifies.[6]

2.1.2 Motion in complex fluids

In colloidal suspensions, the liquid in which colloidal particles are dispersed induces the overdamped, Brownian-type motion in equilibrium. The background liquid takes over the task of momentum transfer. This idea is quite central: The motion of a fluid system of N particles through configuration space is "led" by liquid motion of the $M \gg N$ particles in the bath. A foundational idea behind statistical mechanics is that phase space dynamics of isolated systems of interest can be described by flow of an incompressible and immiscible fluid,

[6] As a speculative note, the isotropic-nematic transition, which generally entails a first-order density gap, can maybe be seen as due to an effective attraction between rod midpoints owing to excluded orientational states.

i.e. Liouville's theorem (See Ch. 3). The motion of the particles of interest is modeled and reduced to stochastic, purely Markovian motion in equilibrium. This assumption will be valid as long as $M \gg N$ and enough free volume is offered to the particles (i.e. the concentration of particles is below the jamming transition so that there are no packing constraints). In other words, the bath can be 'integrated out", so that a "sharp" $(N + M)$ probability distribution (of delta-functions) can be reduced to a N-body distribution, which is usually further reduced to a "fuzzy" 1-body distribution in equilibrium settings: The latter is normalized with a canonical partition function (or grand canonical for systems coupled to particle reservoirs), which we discuss in much more detail in the next chapter.

As mentioned, the stochastic motion of one spherical particle in equilibrium with an M-body bath is assumed to be Brownian, which is an inherently "slow" process of transport due to *dissipation*: an essentially continuous spectrum of modes (Gaussian) couples to the degrees of freedom of a single particle. These originate from microscopic collisions with much smaller particles of the surrounding bath. Dynamics of individual colloidal particles are Markovian for equilibrium fluids. As colloidal particles also interact, however, the dynamics entail a "mesoscopic" character even for a global equilibrium state, where the characteristic relaxation times of the dynamics depend on the level-of-treatment (i.e. for a given wave-number in Fourier space). Nevertheless, ergodicity and equilibrium imply that the statistics are self-averaging, which is even tied to the equipartition theorem. In nonequilibrium fluids, however, this is not the case, for example during crystallization from a fluid of hard-core particles. Collective modes of motion (which are damped out in equilibrium) occur at a multitude of scales in the system [555, 557]. Transient, *mesoscopic* features in the fluid become significant that show larger ranges of coherent motion. A broad bandwidth of relaxation times is a dynamical signature of this significant change in the system, almost "foreshadowing" the solid-state-type of motion that will emerge.

The build-up of correlated features over sub-portions of phase space mean that a fluid system gets "stuck" in dynamical traps [563, Ch. 11]. Abrupt changes to structure and dynamics taking place in the fluid can be seen as "escape" events from these traps. Fig. 2.1 illustrates this notion. Therefore, the strong *space-time* dependencies in nonequilibrium hinders a clean separation of length- and time-scales, which is prerequisite for a Markovian description at the relevant scales of these dynamics.[7]

A large bandwidth of relaxation times signals a high degree of variability in the dynamics, which becomes ever larger at critical points, for example (see further discussions in Ch. 3). This is directly related to a highly susceptibility to any disturbance. Clearly, a large variety of possible outcomes is a crucial ingredient for complex self-assembly in nonequilibrium. However, capturing the broadest variety of outcomes is part of an essential tradeoff during machine learning. In other words, the learning challenge can be to predict a specific outcome with high precision while still encompassing a broad variety of possible outcomes in the same model. (See discussion in Ch. 1.4). We will see this effect in in part IV in the form of a phase transition, internally, in the learned representation of data.

[7] In this view, effects associated with with broken ergodicity like anomalous diffusion and *ageing* occur [564, 565].

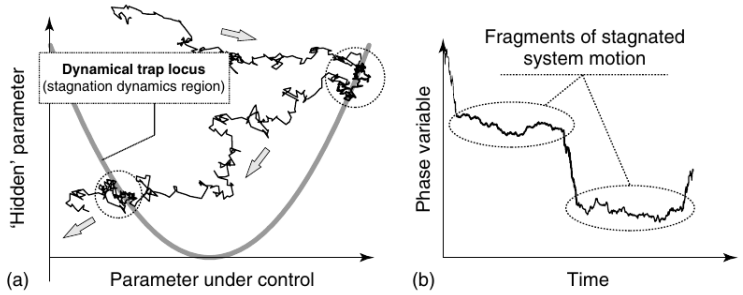

FIGURE 2.1: Illustration of typical nonequilibrium time statistics, here due to the existence of 'dynamical traps': (a) A projection of phase space with the region of the dynamical traps where system motion becomes stagnated; (b) measured time evolution for one of the projected phase state variables (mesoscopic order parameters). Source: Ref. [563, Ch. 11].

Rare "escape" events also occur in Markov-Chain-Monte-Carlo pseudodynamics, i.e. during simulations trimmed at simulating *equilibrium* properties of a system in a given ensemble, once the system is near a critical, tricritical, or at a coexistence point in the grand-canonical ensemble. Under these conditions, each stable thermodynamic phase can be thought of as a *metastable state*, between which the system can "jump" (see also discussion on symmetry-breaking and phase transitions in Ch. 3.2.1, on mesoscopic balance conditions in Ch. 3.3.4, and on mesostates in Ch. 3.221).

2.1.3 Order parameters for complex fluids

Standard approaches to characterize various phases in complex fluids imply quantifying structural order parameters at given time-points. In the case of hard rods, one can measure the density or packing fraction, as well as the global orientational order parameter. In Markov-Chain Monte Carlo (MCMC) simulations, a histogram can be constructed by collecting samples of an order parameter over long MC time. Upon approaching a continuous phase transition point via adjusting an external force or macroscopic control parameter, an initially unimodal distribution will become maximally broad, thereupon "splitting" into two or more peaks, depending on the broken symmetry of the order parameter Q, as well as the order of the transition. See Fig. 2.2.

At *coexistence* in the grand canonical ensemble – considered in part III of this thesis — multiple peaks can co-occur, where each may correspond to the homogeneous and symmetry-broken phase, which depends on the chosen order parameter. For example, one peak may arise for an isotropic phase ($Q = 0$) and two peaks of the two degenerate states of the broken-symmetry phase. In any case, an *abrupt* transition typically entails a density difference between an isotropic and a nematic phase. Hence, the densities ρ should, in theory, split into two peaks. Yet, *weak* first order transitions are very difficult to discern from continuous transitions due to a small density gap. We encounter such a case in Ch. 6 for 3D systems of hard-core rods constrained to lattices. A multi-dimensional order-parameter representation in the style of Fig. 2.3 below are helpful, potentially. This is even more true for *tricritical* behavior, which we will see for the 2D system of rods in Ch. 6.

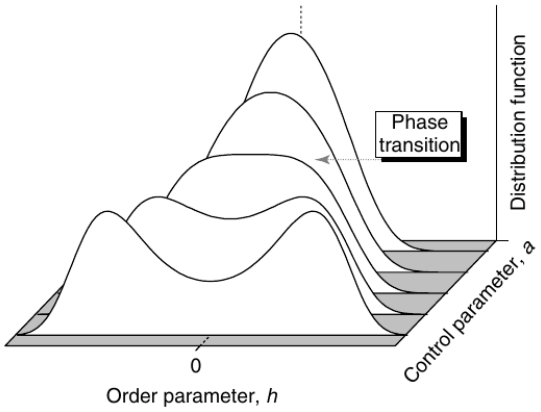

FIGURE 2.2: An example of a "split" histogram of a scalar order parameter into two degenerate states upon a spontaneous break of symmetry by means of adjusting an external field strength. Source: Ref. [563, Ch. 11].

In equilibrium, the second-order moments reflect fluctuations in the system as well as its susceptibility to externally-applied, conjugate fields (see also fluctuation-dissipation theorem in Ch. 3.2). In GCMC simulations, the *variance* of a global order parameter peaks ("diverges") at the transition point. Higher-order moments suffer from sampling error, but can be used to discern between first- and second-order transitions in the form of reduced cumulants [62, 566].

"Collective" variables

A certain *repeatable* or re-occurring local pattern can be thought of as a local, discrete symmetry of the system, and could be captured by a suitable order parameter. An average, nearly-constant-valued order parameter over some region of space can be deemed a "collective" variable. Such mesoscopic ordering of transient structures occur in out-of-equilibrium situations. For example, hard-sphere colloids in the metastable supercooled or supersaturated state show pronounced, transient local order than can be quantified with a bond-directional order parameter denoted by "Q_6" (see also Fig. 2.3).

Machine learning algorithms can be helpful, in these respects [567]: They could help us in an automatized detection of the "relevant" variables in a system (i.e. variables that repeat or represent coherent structures over some portions of space and times). For equilibrium, these may embody order parameters, which was shown for many cases of machine-learning systems applied to statistical model systems (see discussion in Ch. 1.4. We show in part IV of this thesis that unsupervised machine learning automatically finds collective variables of a fluid system, which possess an empirical quality. Each thermodynamic (Boltzmann) distribution of configurations entails a different spectrum thereof, and the algorithm further provides a model for the fluctuations of these variables. Indeed, we show that the broadest spectrum of variables is obtained at an internal critical state of the learning system. At this state, the variables form a spatial coarse-graining hierarchy. Notably, critical behavior seems plausible in this case, as the input data represents out-of-equilibrium statistics, composed of configurations that span across phase boundaries – over

a large section of configuration space sampled from various thermodynamic ensembles.

Very important for the performance and interpretability of this learning algorithm is that the microscopic coupling of translational and rotational degrees of freedom should be properly represented at the microscopic scale – another finding that connects to the most basic properties of complex fluids. We allude to more on this aspect below.

Coupling between translational and rotational order

For a full structural description of a fluid, we must account of the coupling of rotational and translational degrees of freedom at *both* the local, as well as global scales.[8] Two-dimensional or pairwise histograms of an order parameter and density can aid in analysis of the fluid, see e.g. Fig. 2.3 for the example of the local hexagonal order parameter Q_6 and global density for the supersaturated fluid of hard spheres (before crystallization sets in). For a representation of the

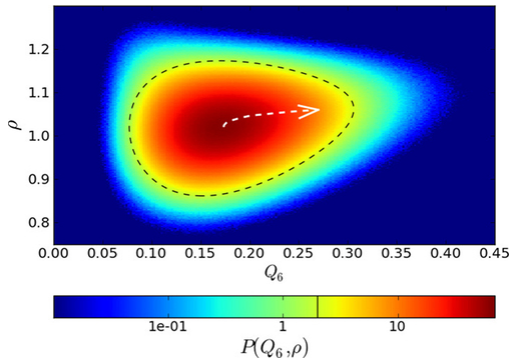

FIGURE 2.3: An example 2D histogram showing the relationship between orientational order and density: Probability distribution for a supersaturated state of hard spheres in the $\rho - Q_6$ space. From Ref. [551].

coupling between translational and rotational order in this example, at least *three* axes would be required, allowing for a distinction between fluid and crystalline translational order [568]. Hard rods on cubic lattices studied in part III necessitate two-dimensional histograms for representing the orientationally ordered ("nematic", or orientationally demixed) phase (the order parameter is two dimensional and distinguishes a three-fold symmetric state). A three dimensional histogram (which we did not investigate, however), would aid in visualizing density gaps between phases, for example.

As it turns out, machine learning algorithms that process configurations of such systems are very sensitive to the choice of representation of rotational and translational order *locally* (per site), which we show in part IV of this thesis. A *two-dimensional* system of sticky hard rods on lattices around the "nematic" (orientational demixing) transition entails a 2D order parameter that shows the coupling between rotational and translational degrees of freedom. We show that the full information on different global symmetries (different thermodynamic states) is represented when each site of the 2D lattice is provided with *at least* a two-dimensional basis – one that assigns the local state of the rotational

[8] See discussion in e.g. Refs. [549, 551].

and translational degree of freedom, the latter in the form of a vacancy or occupancy.[9] Only upon this choice of basis can the algorithms easily and sufficiently distinguish between different thermodynamic phases of matter, particularly when first-order transitions separate these, which involve a density gap. The algorithms are able to learn the analogy of the 2D global order parameter in an unsupervised manner.

2.2 Confinement

Novel phenomena often appear under "finite-size" limitations on the fluid systems [569], known as *confinement*. In its most basic form, confinement is the notion of imposing boundary conditions upon a many-body system (a fluid), realized by walls on two ends (slab geometry) or one one side (semi-confined geometry) as in the case of fluids at a singular surface. In fact, two surfaces with infinite separation from one another represent the limiting case of a single wall, or semi-confinement. These boundaries inherently break the translational symmetry of a bulk system [570]. *Finite-size effects* appear due to the finite width of the capillary [571] that shift the bulk critical points. We discuss these in the context of the critical Casimir effect below.

Confinement fundamentally changes the equilibrium phase behavior of systems. The shift of critical point positions can be substantial, and depend on the inherent symmetries of the system (microscopic degrees of freedom), the geometry of the boundaries (shape), the interaction potentials with the particles, and any inherent patterns (crystal phases) on the walls themselves [124]. Surface films with distinguished order can form, part of general *wetting phenomena* [124, 570, 572–575]:

In fact, the effect of a wall is so fundamental to understanding the physics of complex fluids that the most sophisticated theories like density functional theory[10] are put to the test at a wall. A macroscopically homogeneous liquid of hard-core particles in continuous space exposed to a surface will have its global translational symmetry broken, whereupon local rotational symmetry will be broken. Particles will become localized at the surface, increasing the density locally. Changes to dynamics occur, which we discuss later in Sec. 2.2.1.

The irreversible change can take on the form of a phase transition, the reason behind the wetting phenomena aforementioned. The kinetics of crystallization, for example of hard-core particles are enhanced at a neutral surface, i.e. heterogeneous nucleation [576, 577], which occurs much earlier than in the bulk. In thermodynamic terms, the surface effectively lowers the free energy threshold. More generally, confinement stabilizes phases not seen in equilibrium, i.e. "*more phases are thermodynamically stable*", citing Ref. [578], which depend heavily on the confinement geometry (strength of confinement). These stabilized states in confinement may be considered *metastable* states that disappear when reaching a thermodynamic limit (unconfined systems) [253]. In this line of reasoning, phases with strong order will form at surfaces more easily than in the bulk [579]. Nematic wetting layer or nematic thick film may form at the wall "earlier" than a nematic transition in the bulk.

[9] We emphasize this point because most other examples from the machine-learning literature we are aware of implement scalar values at each site (as a pixel in an image).

[10] More on the topic of DFT is presented in Ch. 3.

Illustration: Critical Casimir effect

A most prominent example of confinement is the *critical Casimir effect*, where effective forces appear when a binary fluid mixture is at its critical point. This is characterized by *universal scaling functions* that depend only on the internal symmetries of the system [571] and not on specific material properties. The fluctuation spectrum, i.e., the energies and forms of the eigen-modes of the fluctuating fluid, is affected by the *geometry* of the system. Introducing surfaces imposes boundary conditions on the fluctuating field and thus determines its mode spectrum: fluctuation modes are effectively "cut off". This was first considered by Casimir in 1948 for the electromagnetic field between electrostatically neutral particles, and was anticipated for critical fluids by Fisher and de Gennes [580, 581].

Colloidal particles are exposed to these forces when suspended in binary liquids near their critical point, even though the colloidal particles themselves may be unconfined (*no wall*) [582, 583]. From a microscopic viewpoint, when two particles are close enough, the fluctuating solvent "notices" it is confined in-between the surfaces. This modifies their effective pair potential interaction. If the Casimir interaction is comparably strong to the thermal energy, then the phase behavior of the colloids can be altered drastically [584, 585], and the interactions become non-additive [586, 587]. Effective "surface forces" are long-ranged in character and are the source of stress on the fluid.

2.2.1 Altering the nature of phase transitions

From the viewpoint of fluctuating fields, a fluid put between two parallel plates at distance M, is exposed to a finite length-scale "cutoff", the maximal *correlation length* ξ that a system can manifest – this is the characteristic, mean length-scale of the relevant order parameter of the fluctuating field or fluid. Exactly at the critical point, $\xi \to \infty$ should diverge, so M provides the only macroscopic length-scale. The correlation length ξ remains finite above the critical point, thus the ratio ξ/M governs the range of correlative forces [588]. The shift of the bulk critical point follows scaling laws on functions of ξ/M [589]. This so-called *finite-size scaling* must be accounted for when simulating bulk systems, which are necessarily confined to a finite simulation box [38, 57, 61, 62, 590] and is related to real-space renormalization techniques [591–593].

The surface tension between coexisting phases may be weakened, as the relative width of the interface with respect to the system size will increase. Indeed, the abrupt nature of first order transitions in 3D bulk can be completely "destroyed" by dimensional crossover to 2D, becoming continuous in nature. In fact, a critical length between two parallel plates may exit whereupon this destruction occurs [325, 578, 594].

Reducing the dimensionality of a system to 2D enhances the thermally-excited long-wavelength elastic modes (those *in-plane*), which dismantle perfect, long-ranged order (paraphrasing Ref. [324]). Therefore, orientational ordering is quasi-long-ranged, associated with algebraic decay in the correlation of order parameters, at least for systems with *continuous* degrees of freedom in 2D. The model at the core of the theoretical development of these transitions that are of the general Kosterlitz-Thouless-type [333, 334], where e.g. a hexatic phase appears during the melting of hard-sphere crystals in 2D [341, 595], has been the planar XY or rotor model [334], showing topological defects in the

form of vortices [335]. Yet the behavior of "nematic" transitions in 2D liquid crystals [342, 596] remained a debated topic for many decades, which we outlined in Ch. 1.3. Indeed, quasinematic transitions of the Kosterlitz-Thouless type occur upon decreasing the distance between the walls confining a bulk system below a critical threshold [597]. We discuss more on anisotropic-bodied fluids below.

Confined fluids of rods

Fluids of rods entail a highly localized coupling between rotational and translational degrees of freedom, as each individual particle has its own rotational degrees of freedom (in an equilibrium fluid). In fluids of hard spheres, for example, one must move to *mesoscopic* variables like small clusters of particles in order to express rotational symmetries. Therefore, the effect of walls on their coupling is pronounced. In general, anisotropic particles like rods in confinement can render intricate structure and phase behavior [598, 599]. Surface-induced effects are also seen in liquid crystal and colloidal rod systems: These include *critical adsorption*, and *wetting* and *layering* [121, 600, 601].

As discussed, an increased density at a wall induces orientational ordering in the fluid that becomes inhomogeneous, macroscopically. Long, hard rods show nematic ordering at a wall [602]: an example for the resulting inhomogeneous ordering is shown in Fig. 2.4 for various fixed "tilt" directions, known as *anchoring* conditions.[11] [12] [13] Sedimentation-diffusion experiments [286, 623] uti-

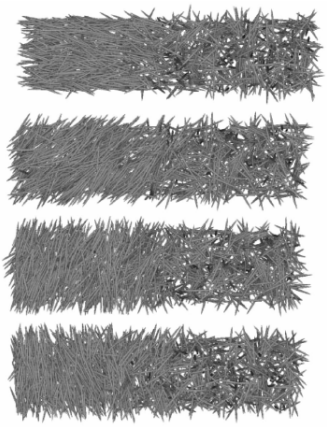

FIGURE 2.4: Depiction of anchoring conditions imposed from a surface. (Top to bottom): Snapshots of simulated configurations in the immediate vicinity of the (broad) nematic-isotropic interface for various anchoring conditions: 0,30,60, and 90 degrees. From Ref. [602].

lize confinement in the presence of gravity by allowing non-gravity-matched colloidal suspensions to settle on a planar surface, generating a gradient in the pressure of the fluid above a hard wall (barometric law). Therewith, a gradual change of phases occurs in the direction normal to the surface, including the interfaces between coexisting phases (isotropic, nematic, and smectic

[11] Experimental techniques for measuring the anchoring transition in e.g. thin films of liquid crystals includes ellipsometry [603–605].

[12] Such systems and others related have been explored in e.g. Refs. [119, 121, 579, 597, 602, 606–616].

[13] Density functional theory of such systems was been applied in Refs. [617–622].

phases).[14] We develop a simulation model inspired by sedimentation-diffusion for hard spherocylinders deposited onto a surface in Ch. 4 as a colloidal thin-film growth model.

A system will visit various metastable phases in various levels of confinement, which then disappear when approaching the idealized thermodynamic limit of an unconfined system [253, 625]. Thus, confined fluids of rod-like particles, like liquid crystal films, can be tuned, in principle, to show a large array of structures. Any particular outcome is a product of the complex interplay of the interfacial properties, applied external fields, and internal, "orientational" torques due to elastic deformations in the bulk of the material above the surface [579, 615, 626]. The particular properties of the particles like the rod length, but also any magnetic moments play a key role [627]. By changing the surface preparation, an external field, or the temperature [579, 600, 610, 611, 616, 628], one can induce transitions between orientation states at the surface; further, the thickness of wetting films can be adjusted. The *topology* of the confining surfaces is also a factor. For example, rods confined to spherical surfaces render significantly different phase behavior [629].

In any case, the continuous nature of the rotational degrees of freedom is another key point in determining the type of ordering and structure. If we discretize the orientational degrees of freedom, we end up with the Zwanzig model, as discussed in Ch. 1.3. The wetting behavior [240, 630, 631] bears strong analogy to that of spherocylinders [606], although the *discrete* rotational symmetry may enhance the distinction between parallel orientations to the surface, inducing a continuous surface phase with local biaxial ordering before first-order nematic ordering or capillary nematization occurs. Indeed, our lattice model of sticky hard rods of Ch. 5 exemplifies how the lying and standing orientations are highly distinguished, the former of which forms a metastable phase in monolayer confinement that competes with the highly-ordered, standing-phase.

Extreme forms of confinement

Although confinement can "destroy" first-order nematic transitions [157] or cause quasi-long ranged order for rod-like systems, an extreme form of confinement can completely rid particular wetting effects: No capillary nematization occurs when the wall separation is smaller than about twice the length of the spherocylinders [606]. Under extreme confinement, the phase behavior of rod systems can be quite surprising: States appear that break anchoring constraints or the symmetry imposed by the surfaces [632]. These states have lower symmetries than those of the corresponding stable states in bulk, analogous to the 2D melting behavior of hard disks mediated by the KTHY mechanism [343, 633] where a two-step and first-order hexatic transition can occur [595]. Indeed, a *three-stage* melting transition has been observed in 2D liquid-crystal films [634] that suggests the possible existence of two phases between the 2D solid and liquid, much like the melting of hard spheres (disk) crystals in 2D: a hexatic phase and, at a higher temperature, an intermediate liquid phase with hexatic-like positional correlations but no long-range orientational order. Similar behavior is found for weakly anisotropic (up to aspect ratio 3) hard rectangular rods in narrow slit-like pores: Up to three differently-oriented macroscopic structures

[14] i.e. "stacking sequences", see e.g. the theoretical work in Ref. [624].

can be observed [215] depending on the width of the confining pore; see also Refs. [158, 635] Further, Ref. [636] reports on the formation of monolayer- versus bilayer-phases in narrow confinement between two walls. Allowing for a bilayer condition appears to change the 2D ordering behavior to a first-order ordering transition [341]. Notably, these findings have spurred on debate [341] and issues may still be open (a situation typical for many strongly confined systems). This notion may compatible, at least, with the abundance of phenomena reported for organic molecules at the submonolayer stage, depending on the specific systems (we introduced them in Ch. 1.2.1 and discuss them further in Sec. 2.4 forthcoming.)

Lattice systems in the form of spin-type models have been studied in confinement beyond the XY or rotor models: e.g. the Blume-Capel model in confinement [637], the 3-state Potts models in confinement [325], or others [157, 346, 638]. In this thesis in part II, we treat an extreme form of confinement, a monolayer system of hard rods in (2+1)-dimensions, as they can have three orientational states, but 2D translational degrees of freedom (the "+1" dimension is exclusive to rotational degrees of freedom). Therefore, the Blume-Capel and 3-state Potts models bear some analogy owing to three orientational degrees of freedom. We discuss more on the effect of constraints of degrees of freedom to a lattice in Sec. 2.2. To this end, the purely-2D setup has been a popular choice for on-lattice hard rod models [362, 363, 366–369].

In this thesis, we study the lattice system of hard rods in (2+1)D monolayer confinement and compare it to likewise confined systems of spherocylinders in Ch. 4. Further, we study the pure 2D system of sticky hard rods in Ch. 6 and the (2+1)D corresponding system under nonequilibrium (growth) conditions in Ch. 5.

Dynamics

Quite basically, the altered dynamics within the system result from the constrained degrees of freedom. An an example, disordered solids in 2D confinement entail different vibrational spectra compared to 3D [639]. Dynamics are more correlated compared to the bulk case, generally [640–642], the degree of which will depend on the confinement setup [643] and on the specific (anisotropic) interactions [644]. Intricate self-assembly phenomena at surfaces such as thin film growth at surfaces (part II of this thesis) are products of the highly correlative nature of dynamics in confinement [188, 221]. Anisotropic fluids are particularly prone to such highly correlative dynamics in confinement owing to their pronounced coupling of orientational and translational degrees of freedom [17, 645–647]. The original isotropy of the rotational states of particles can be broken in various ways depending on the form of confinement and on the substrate potential [648, 649].

Effects like frustration or jamming as well as anomalous diffusion [229, 249, 587, 643, 650, 651][15] are quite natural. Monolayers of spherocylinders or ellipsoids show dynamical heterogeneity [653] and may form glasses [653–655]. Memory and ageing will play a different role compared to the bulk [564, 656].

[15]Effects of frustration may be visible from colloidal experiments of a layer of short hard rods at full packing [652]. The cited experiment avoided gravity matching to the extent that the gravitational torque force on standing particles is likely quite strong. Therefore, the effects seen may be a form of jamming, rather. Further electrostatic forces between the colloidal rods may need to be considered, too.

In light of the above discussion of altered phase behavior, kinetics of phase separation may have a different character [657]. More specifically, the creation of filament-like structures may be an effect pronounced in 2D confinement [658], which, notably, may imply that diffusion-limited aggregation is a likely type of kinetics occurring in strongly confined systems.

2.2.2 Constraints to lattices: Qualitative analogies

As discussed, confinement breaks global symmetries of a bulk, allowing for more thermodynamically stable phases to exist that would otherwise be unstable. For example, a (2+1)D confined system of lattice rods of part II can differentiate between "lying" and "standing" states of rods (under certain conditions) – such states lose their meaning in 3D bulk. Constraint to a lattice might entail some degree of analogy to dimensional crossover, which for the case of rods will alter the position, range and strength of various phase transitions [324]. The possible orientational and translational degrees of freedom are altered in a fundamental way, becoming discrete. The high-frequency spatial modes "finer" than the lattice constant will be cut off, which may allow low-frequency modes to obtain a higher density of states (due to energy conservation).

If we regard the isotropic-nematic interface for hard-core rods, for example, it might be expected to become broader on an cubic lattice than in the 3D continuum, in congruence with the enhancement of low-frequency modes. Indeed, the lattice system of hard rods in 3D bulk has an extremely weak first order isotropic-nematic transition, which is one main result of our studies in part III of this thesis. Additionally, it has been shown in Refs. [659, 660] that the addition of quenched disorder (or site dilution) in systems with a strong first-order transition can significantly weaken this transition. Ironically, then, the constraint to a regular lattice might effectively cause frustration and disorder in the system, owing to the fact that the rods are more than one unit cell in extent. The consequences can be rich: we will show that the behavior of the lattice system in 3D is genuinely unique, as intermediate rod-lengths $L = 5, 6$ render an ordered state of the 3D system that is a pile-up of *nearly* 2D systems.

Closer inspection in the mesoscopic structure of the fluid does show hints of the origin of this geometric "frustration": We will show in part III how a 2D fluid structures of lattice rods (with attractions) is characterized by large, mesoscopic domains of intermediate to high densities of rods – depending on the attraction strength – that are highly incompatible with each other, sterically, due to the discrete nature of the rotational degrees of freedom. If incompatible domains become tightly packed, then "voids" appear at the interface between domains, forming a gas phase. In Ch. 6, we show that this the vapor–fluid gap widens rapidly below a threshold temperature (a tricritical point). In 3D, we will see similar effects, where the widening occurs below a pseudo-tricritical point, i.e. a small region in the phase diagram which looks like a tricritical point if the density gap were to disappear above it. Such widening is predicted for 3D continuum models [42], but the effect may be much stronger in the lattice system.[16]

As in confinement, if the relaxation of translational degrees of freedom (diffusive transport) is hindered by local preferences of orientational order, strain

[16]There are no "mixed" or "in-between" orientations that could make the transition between the isotropic gas (3 directions) and aligned liquid (1 direction) a more gradual transition by varying the density.

can arise, which then leads to dynamical heterogeneity, anomalous diffusion, amorphous solids and jamming [661], gels [662] or glassy behavior [640, 641, 644, 663–668] – mesoscopic structures of varying degrees of symmetry compete. We will see that the occurrence of jamming, as well as gel-like or glassy phases appear in the lattice monolayer systems of rods in part II of this thesis. Indeed, a crystallization process is postulated to be due to a competition of *many* order parameters [551], where these types of order may "fractionate" locally [556, 669], showing local orientational symmetries. Crystallization kinetics or the processes governing cluster formation of a solid phase will be fundamentally altered by particle shape and any constraints on the degrees of freedom such as constraint to a lattice. This is important for understanding thin film growth at the submonolayer stage, which we introduced in Ch. 1.2. We discuss self-assembly in nonequilibrium further in Sec. 2.3.

Analogies to phase behavior of simpler models

As mentioned, other spin-like lattice models, where local orientational order is included, may offer qualitatively similar behavior to our nematic rod models on lattices and are worth mentioning. A planar spin model,[344], the XY-model [334, 347], the Potts model [46], and the Lebwohl-Lasher model [346] are examples of more-or-less well-known spin-type models for 2D systems that may serve as approximate analogies liquid crystals in 2D or 3D [330]. In 2D, the three-state Potts model shows tricritical behavior [670], as well as the Blume-Capel model [671] and Blume-Emery Griffifths model [672, 673]. Generally, multicritical phenomena can arise from a competition of order parameters [674] – in this case, it is the spatial ordering (gas-liquid) that competes with orientational ordering (isotropic-nematic). As mentioned, the 3D Potts model can also show tricritical behavior [675], or weak first-order transitions [659, 660, 676] particularly with site dilution. Precaution is necessary, however, as these models neglect the strong coupling between positional and orientational degrees of freedom due to hard-core exclusion (infinitely strong repulsion).

We can search for even more basic analogies to simple fluid mixture models using mean-field theories: If we presume isotropic-nematic transition is similar enough to *continuous* (Ising) gas-liquid demixing in a symmetrical fluid (which is true particularly in 2D!), then phase diagrams of two-component fluids may help us (AB models). In even such simple models, the critical behavior can meet first-order-transition binodals in nontrivial positions in the phase diagram, inducing tricritical points, a triple point, or critical end-points "right" of the gas-liquid critical density [677], see Fig. 2.5. The 2D system of hard rods becomes ordered via a an Ising-type demixing of orientational states, and we will show that the phase diagram will render the tricritical behavior alluded to here. In fact, in 2D, the two-component rod system might be even more similar to the ABV mixture model of two fluid species plus vacancies [678, 679]. There, a line of critical points will also meet a binodal separating a liquid and gas phase, according to mean-field calculations. Nevertheless, if we consider 3D systems of lattice rods, then it is clear that the three orientations of rods orientations could macroscopically split: Two subgroups can form upon ordering, where one of three species becomes either dominant or suppressed. In this way, the 3D systems might also find analogy to the AB model in its demixing behavior into subgroups of orientations. Indeed, we will see this analogy holds in part. III

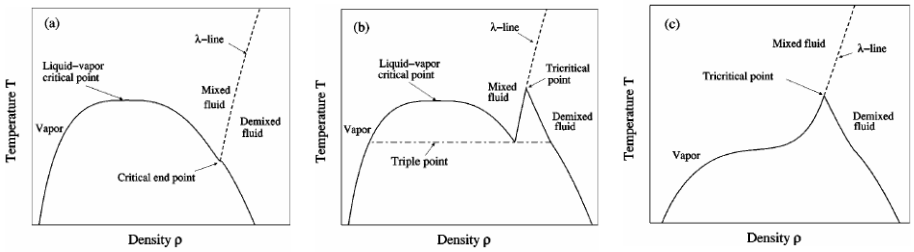

FIGURE 2.5: Potential phase diagrams of a mean-field model of a symmetric binary fluid mixture (AB model). A line of critical points (the "λ-line") influences the gas-liquid binodal in nontrivial ways, leading to tricritical behavior (b) and (c) or critical end-points (a). From Ref. [677].

for the bulk behavior of 3D sticky rod systems of lattices. A notable difference is that the "λ-line" will be realized by a line of weak first order transitions, in accordance with the purely hard-core isotropic–nematic transition.

Furthermore, there may be metastable phases "hidden" beneath a "parent" binodal in the AB model, shown in Fig. 2.6. At short enough lengths for lat-

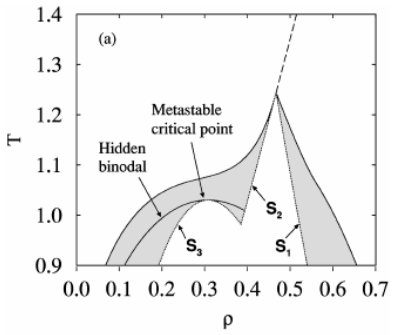

FIGURE 2.6: A simple model of a two-component fluid mixture (AB model) can contain metastable phases. A liquid-vapor "parent" binodal envelops a hidden binodal with a metastable critical point, indicating complex gas-liquid behavior. The spinodal lines are indicated with "S"'s. From Ref. [677].

tice rods in (2+1)D confinement, rods will split into "isotropic","lying" and "standing" mesoscopic and macroscopic states. Indeed, the isotropic–standing transition is the monolayer analogy of the isotropic–nematic transition: If these demix, then we can expect the phase separation to entail metastable phases like in the AB model shown. We will show this type of behavior in Ch. 5, where a "lying" phase is a metastable intermediary to a "standing" dense phase entailing a higher degree of order (is thermodynamically preferred). Therefore, the AB model may be able to serve as a rough analogy for the phase behavior of sticky rods on a simple cubic lattice confined to (2+1)D monolayers.

* * *

As we discussed here (Sec. 2.2), both confinement and a constraint of degrees of freedom to a lattice (the inherent symmetries in a system) changes the phase behavior and dynamics in systems. The exact nonequilibrium behavior of complex fluids will be a function of the model specifics and dimensionality. Nonequilibrium is the topic of the next section.

2.3 Nonequilibrium: emergence of mesoscopic features

As we investigate thin film growth in part II of this thesis (introduced in Ch. 1.2), we would like to discuss a few basic points on nonequilibrium.

Systems will be driven out-of-equilibrium when external, time-dependent, non-conservative forces are applied, e.g. shear forces at the system boundaries.[17] The imbalance of forces, originating at a local scale, generates a system-wide response over the course of time, distributing energy and momentum until a new equilibrium is reached. The way in which a complex system responses to forces is most fundamental, a theme that will come up repeatedly in Ch. 3. If a system is highly susceptible to change, a subtle change in control parameters (external forces (potentials) or those controlling microscopic dynamics, i.e. temperature) can set off a phase transition. In terms of thermodynamic terms, a critical value of temperature, chemical potential, etc. is crossed. Near phase boundaries, fluctuations in the system are dominated by ever more *collective* behavior (See also Chs. 3.2 and 3.5.3), implying time-scales for relaxation are stretched and the bandwidth of all possible processes increases.

At the very bottom of it, "nonequilibrium" means a disbalance of forces generates currents throughout the system, and an arrow of time becomes noticeable. If a stationary state is reached, forces are balanced at all relevant mesoscopic and macroscopic scales. (We discuss more on balance conditions in terms of a master equation for lattice systems in Ch. 3.3.) In equilibrium, all events that occur can and will eventually reversed (although exactly when remains stochastic), given we wait enough time. A balance of probability fluxes will be guaranteed given sufficient integration time and a corresponding spatial level-of-treatment, which is at the heart of the meaning of "coarse-graining".

Self-assembly is the nonequilibrium evolution of a system where structures with a certain form of order emerges with diverse length-scales, a process which may entail various intermediate stages, however. In the most general form, self-assembly of large, coherent structures expresses the fact that phase transition kinetics are underway, i.e. forces of thermodynamic origin play a central role. Soft matter systems and complex fluids show rich self-assembly phenomena, directly related to their often complex equilibrium phase diagrams. We develop on these notions below in Sec. 2.3.2 below. However, beforehand in Sec. 2.3.1, we discuss nonequilibrium dynamics in the case of thin film growth.

2.3.1 Thin film growth

On reversibility versus irreversibility of events

During thin film growth, an external source of particles deposits these onto a substrate, driving the direction of the nonequilibrium evolution of the system: towards a full layer (in the case of monolayer constraint). The degree of "nonequilibrium" versus "equilibrium" dynamics during this evolution is difficult to quantify, generally, especially owing to memory effects. Ratios of the relaxation rates in the system (which change in time) to the deposition rate would, in theory, indicate the momentary competition in the system. However, in most practical cases, we cannot quantify the relaxation rates of diverse processes during the evolution, moreover, the systems may be dynamically

[17] These systems are studied generally, for example, in active matter or driven colloidal systems [17, 354, 680].

heterogeneous. In the realm of our KMC simulation model, we can modify the attempt self-diffusion rate D (defined for ideal-gas limit) and well as the attempt flux F. "Attempt" means the moves will be rejected when a hard-core repulsive interaction prevents a successful event (the dynamics are presumed to remain locally Markovian and independent of other moves, directly). In this way, a large ratio of attempt rates F/D will imply a highly nonequilibrium character of the evolution, which can be understood as entailing a high degree of *irreversibility*.

Random sequential adsorption (RSA) is ordinarily the term for the irreversible process of randomly depositing hard-core particles onto a surface or defined space without any particle diffusion or further moves. This has been explored in diverse lattice models, including for rods [136, 681–686]. The asymptotic packing fraction after which no further insertion can occur, the jamming fraction, is a central quantity of interest. The nonequilibrium critical behavior in these systems can be considered a limiting case for more general models involving additional diffusion. Indeed, jamming transitions [353, 687, 688] occur in both disordered liquid and solids under nonequilibrium conditions [661]. The irreversible nature of the dynamics means every event of a deposition forever constrains the future evolution. Quenched randomness arises from the interplay between the random source of particles and the hard-core repulsive interactions. The randomness is *not* further annealed via a diffusive process, which introduces a second, steady source of randomness in the system. Notably, introducing particle attractions will not change anything, as these are only noticed if the system entails an annealing process (when variables *fluctuate*).

In contrast, diffusive systems are coupled to bath, which provides an annealing process. If the system reaches equilibrium (no deposition), any and all changes to a system can be undone as long as we wait long enough. This is synonymous with the ability to reach all states *from* any other state (the ergodic hypothesis, see Ch. 3). Therefore, states will follow a stationary probabilistic distribution weighted by a Boltzmann factor (with e.g. attractive interactions) only after a very many annealing events have occurred. In these terms, fluctuation of all system variables is the key mechanism in upholding the stationarity of averaged quantities in equilibrium. It expresses the balance of forces in the system, which have a microscopic origin.

Machine learning (which study in part IV of this thesis) is subject to similar principles of balance in stationary conditions. Framed as an optimization problem, learning entails finding a stationary solution to a model equipped with a large number of degrees of freedom. In fact, in enforcing balance, some degrees of freedom may need to be "shut down" (contribute only very faintly) when the model becomes effectively overdetermined. Variational autoencoders (see introductory Sec. 1.4 and Ch. 3.6) show this kind of behavior, which we present in Ch. 7.

In contrast to a balanced system, one which loses its ability to relax (anneal) signals a loss of ergodicity. The ceaseless deposition of particles on a surface – without the ability to reverse this (desorption) – is a clear source of irreversibility behind the clearly nonequilibrium character monolayer thin film growth studied in part II of this thesis. Indeed, very fast deposition can generate partly quenched disorder in the form of jammed or arrested states, which we show in Ch. 4 and Ch. 5. Yet, in most cases of film growth, the system remains partly reversible, as diffusion only halts completely in these extreme cases. Generally, a

higher degree of reversibility implies dynamics are closer to global equilibrium, which can be aided by additional particle desorption [689–691].

Competing forces during monolayer growth

The nonequilibrium evolution in thin films is characterized by a competition of forces in the system that affect variables of various mesoscopic scales of space and time. As alluded to above, the random deposition of particles is the first basic force, the driving force, coming from an external source. Microscopically, the stochastic inflow of particles will first hinder the motion of neighboring particles, correlating structures nearby and generating a higher local density (i.e. a higher local chemical potential, so to speak, that may be highly imbalanced globally). Secondly, random, thermal forces from the substrate (having a fixed temperature) induces thermal motion of particles, i.e. diffusive motion, locally. We may dub these "diffusive forces", which are locally anti-correlative in nature (at low average densities), as they transport particles away from their sources. The induced particle currents eventually restore ergodicity of the system.

The two forces are in competition with each other: the former tends to push the system away from global-scale equilibrium, while the latter pulls it towards global equilibrium, in figurative terms. The continual exertion of both forces throughout the system will generate a complex array of currents. An exception, of sorts, occurs when forces inhibit each other. One such case we have mentioned is dynamical arrest, when particles fail to diffuse, another is *jamming* (of growth), when the successful deposition of particles essentially halts.

The absolute *energy scales* of attractive forces can shift this competition between diffusive and deposition forces. (In thermodynamic terms, only the ratio to $k_B T$ is important, hence we may speak of the reduced temperature of the system instead of attractive energy scales.) Strong attractive forces generate correlated structures quickly at local scales, at the cost of a slowed relaxation at larger scales, at least for fluid systems. Inter-particle attractive forces are thus in competition with the diffusive forces. However, what we avoided mentioning is that diffusive forces, repulsive in nature, drive the building-up of correlations in liquids due to eventual particle collisions. Generally, then, phase separation kinetics and structure formation arise from a 'dance' between between these three types of forces. The processes can be quite intricate. For example, particle deposition correlates densities at a local scale, which mean can *accelerate* island growth kinetics (separating from a vapor) by increasing the supersaturation of the vapor, effectively. On the other hand, a high flux can effectively "freeze out" the competing diffusive mechanism in dense fluids, generating arrested states and partly quenched randomness.

Part of the competition in thin film growth can be reduced to the ratio of the attempt rates of diffusive and particle flux forces, i.e. D/F or F/D, reducing the three main types of forces above to two. The attraction strength ϵ or reduced temperature $T^* = k_B T/|\epsilon|$ is the remaining other axis. F/D generally controls the size-distribution of clusters. However, it also adjusts the likelihood, during, and size-scales of metastable states that can appear during growth, in a manner similar to the effect of T^*, given the system remains within a regime of temperature. In Ch. 5, we will show how these two axes identify a divide of the system into two main dynamical regimes, each dominated by a different form of phase separation kinetics.

Structurally, each regime either shows a "lying" versus a "standing" phase. The former phase is metastable. It entails inherently different dynamics and, therewith, phase separation kinetics. The latter may roughly be described as more aggregation-like (forming network structures and gels), and may not require overcoming an energy barrier. In contrast, the dynamical regime is characterized when the "standing" phase separation kinetics dominate; these are more "nucleation-and-growth"-like. The dynamical asymmetry between both phases means that F/D and T^* can favor of select one or the other, as they effectively shift 'free energy' barriers in the system.

Diffusion-limited aggregation might be regarded as more strongly nonequilibrium than, say phase-ordering processes governed by nucleation-and-growth. The latter may be considered more "near-equilibrium", and require work to overcome a barrier. A strong flux-versus-self-diffusion will favor this aggregation-sort of behavior, as the flux is locally correlative. A weak F/D, on the other hand, will allow for more near-equilibrium phase ordering kinetics to take over. This "closer-to-equilibrium"-type of phase ordering is also visible by smooth interfaces (compact, round islands instead of network structures with some degree of fractality). We note that how flux compensates for the system being at higher temperatures has (long) been recognized experimentally [3, 141] and is part of scaling theories for islands nucleation and growth [153, 692]. Yet, uniquely for the case of rods at the monolayer that we will show in Ch. 5, this mutually compensating behavior between F/D and T^* is also manifested in the adjustment of structure and *persistence* of the metastable phase.

We mention in closing that desorption would constitute another competing force in the system, and would work together with diffusive forces as a competitor to the deposition flux. (We discuss some preliminary results on monolayer growth with desorption dynamics in Ch. 5). The supersaturation at the substrate would be adjusted by the ratio of attempt-desorption-to-attempt-flux ratio, which might even lead to a steady state condition (i.e. grand-canonical equilibrium). Moreover, desorption will generally avoid the formation of metastable states, accelerates the relaxation towards thermodynamic equilibrium (in an open system), therewith favoring thermodynamically-stable phases. (Indeed, similar effects have been reported with regards to aggregate-like structures in organic molecular thin films [691].)

2.3.2 Self-assembly of soft matter systems in nonequilibrium

Understanding the dynamics of complex fluids are fundamentally important for the broad range of phenomena that occur out-of-equilibrium, often dubbed "self-assembly" or "self-organization" processes. Much practical interest is involved, as well applications (proper control of microstructure, e.g. domains sizes, can make way to novel, super-strong materials, for example [693]), but the phenomena manifest a broader, theoretical notion of "emergent properties" of complex systems [694].

Generally speaking, phase boundaries are a prerequisite for the self-assembly of complex structures in the form of compact islands, domains and long-scale correlated structures. Phase separation kinetics [17, 695] generally lay behind slow, collective processes seen in many-body systems. Self-assembly induced by spinodal decomposition is a well-known protocol to create structure having various length-scales. This is usually done via

quenching, where an external variable (mostly temperature) is changed extremely quickly to a new state into an unstable region (the spinodal) of a phase diagram. The nucleation and growth of dense-phase clusters out of a vapor is another mechanism. It should occur near the binodal lines, where the fluids are considered metastable. This expresses the common notion that a large fluctuation is required to initiate a spontaneous nucleation process, which usually happens after waiting certain period of time.

Yet, in describing kinetic pathways to self-assembly, it is easy to jump to conclusions on the exact mechanisms, however: Whether a structure forms via spinodal decomposition or nucleation-and-growth, whether it is precursor-mediated, or aggregation plays a role is not simple to discern [696–699] – even if the model systems appear simple [700] – and require deep analysis [19]. These are topics of basic research at current times. For a given position in the phase diagram, several mechanisms of self-assembly can occur at the same time and, equally important, other mechanisms may be impossible [701].

Disorder and arrest as a means to new order

Disorder and arrest are imminent parts of the nonequilibrium formation of new structures having various length-scales. Long-lived macroscopic structure can arise, generally, if diffusive mechanisms become limited, i.e. kinetically limited. In some cases, aggregation – which generally forms non-compact, fractal-like structures – [702] can lead to gelation [19]. These can span the entire system in a network [703], which may form as the nucleation of fractal-like clusters [704]. (Systems with short-range attractions seems particularly prone to such scenarios [705], as a matter of fact.) These networks are spatially random, in some measures (like partial fractality), and change only slowly [703, 706]. The internal dynamics of gels remains liquid-like in that they are characterized by longitudinal (liquid) vibrational modes [662]. Intriguingly, gels may often be a transient state of matter [707–710], attesting to their inherently nonequilibrium character.

Solids and liquids show similar properties when disorder is introduced by dynamic arrest: When a liquid jams, it undergoes a transition from a flowing to a rigid state [661], and the internal structure remains disordered in the solid as well as the fluid phase. Glassy behavior entails kinetic arrest that is strikingly similar to gelation [711].[18]

The deep relationship between metastable states and complex self-assembly has long been recognized [713]. In fact, it has been postulated that metastable gels are present, universally, in fluid-crystal phase diagrams in the form of hidden binodals [704, 714] (a hidden binodal is depicted for a model 'AB' binary system in Fig. 2.6). In congruency, metastable states of matter may represent necessary *precursors* to crystalline clusters [696, 715, 716]: The precursor represents the first step of "two-step" nucleation of hard-sphere crystals from a metastable melt [669, 717]. As the onset and speed of nucleation has been shown to be highly sensitive to particle polydispersity in hard-sphere fluids [556, 669], we may be alerted to the possibility for even more complex behavior for our systems of sticky hard rods on lattices, which can be thought of as a mixtures of three rod species, to some extent. Confinement of the fluid system

[18]Colloidal systems of rods or liquid crystals, on a side note, show kinetic arrest and glassy structures exist in 3D [667, 668, 712].

may enhance these intrinsic but "hidden" fluid states, which may be why premelting on surfaces is seen in many systems (i.e. surface "quasi-liquids") [7, 718–722]. In Sec. 1.2, we provided some evidence that these kinds effects are 'real' in ultra-thin films of organic molecules at the initial stages of film growth: They could take on the form of liquid-like, disordered phases precluding thermodynamically stable and well-ordered phases, those of which are often seen in a bilayer regime (i.e. "bilayer" phases).

The emergence and evolution of metastable states, frustrated states, gels, or glasses [723] expresses a highly nontrivial coupling of rotational and translational degrees of freedom [662, 724] that diminishes individual particle motion substantially. This will depend on the relative rates of the external change (e.g. a temperature quench) versus rotational and diffusion processes [725]. The same should be true in considering the rate of particle *deposition* versus diffusion rates – a "deposition quench" rate – which characterizes the basic nonequilibrium setup of thin film growth studied in this thesis. Our exploration of the growth of sticky-hard-rod monolayers will show that both arrested dynamics entailing quenched randomness, but also (annealed) collective dynamics like growth of a stable phase cluster occur in the same system: First, kinetic arrest is found during monolayer growth in our lattice model with purely hard-core rods in Ch. 4, when a biasing substrate potential is very strong. Further, we see metastable phases of lying orientation during monolayer growth model of sticky hard rods in Ch. 5. The metastable phase forms disordered, liquid-like structures that are network-forming. We characterize these as gel-like (see further discussion below on viscoelastic fluids). We further see evidence that this lying phase may be a precursor to the nucleation of a standing phase in the monolayer, i.e. the thermodynamically-favored dense phase in the lattice model. The system can become completely engulfed by the lying phase for very long periods of time, in an arrested state that we call a "wetting layer". The conditions under which these phases appear are controllable by the external parameters of deposition flux rate, the internal dynamics, and the system temperature, as well as the external potentials induced by the substrate. Our model system is highly instructive in the sense that it can be used to demonstrate arrest, jamming, gelation, metastable "precursors", and possibly glassy behavior in the nonequilibrium evolution in forming a monolayer of a stable phase. Different dynamical regimes are clearly apparent despite the high simplicity of the model system.

One clear way to guarantee that a broad variety of structures can be formed is an inherently complex phase diagram. Mixtures of components can fulfill this criterion with a certain amount of ease.[19] Pronounced particle anisometry is another method: A larger number of rotational states implies a larger variety of ways to break the rotational symmetries of the system. Confinement plays an additionally key role, as (partially) ordered states that are otherwise unstable in the bulk become metastable or stable in strong confinement. Arising domain patterns can generally be understood as a manifestation of spatially modulated phases, stabilized by competing forces, dependent on the temperature, modulating field, and modulation time-periods (i.e. relative time-scales) [728]. Very generally, then, pattern formation accompanied by thermodynamic instability and external forces renders a vast array of nonequilibrium phenomena on 2D

[19] One striking example is bijels [726, 727], which utilize spinodal decomposition among two components before the third component is trapped at the domain interfaces.

surfaces [729]. 2D phenomena are generally are more quaint (as discussed in Sec. 2.2), owing to e.g. the topological nature of solid-phase transitions of the Kosterlitz-Thouless-type.[20] The salience of confinement is particularly visible in non-equilibrium conditioned, especially with patterned substrates, rendering a complex of self-assembly pathways [248, 249, 731, 732]. With regards to thin films, *evaporation* or drying [227, 733, 734] are examples of nonequilibrium scenarios complementary to film growth that also entail and demonstrate this complexity.

Viscoelastic fluids

Viscoelastic fluids show a rich phenomenology regarding phase separation kinetics, see Refs. [724, 735]. Two or more structures that have a dynamical *asymmetry* can form depending on the dynamical regime of the main processes in the system. A basic model is a fluid composed of fast and slow components. Dynamical asymmetries in viscoelastic fluids are presumed to arise due to either the large size difference or a difference in transition temperatures between the components of a mixture. Phase separation kinetics are complex, where viscoelastic effects play a dominant role. Viscoelastic fluids can form two types of mesoscopic structure: one network-forming and another compact structure depicted in Figure 2.7. Paraphrasing Ref. [724], phase separation will lead to a long-lived network (a transient gel) of the slow component, as long as their attraction strength is strong enough. The reasoning is as follows: A long, inherent relaxation time of one component means that stress that builds up during a phase separation process will split asymmetrically among the components. A network-like or sponge-like structures of the slow component forms in a force-balance condition at these intermediate stages. Clearly, the phase transformation kinetics involving such dynamically asymmetric components will be more complicated than "typical" nucleation-and-growth [735].

The (2+1)D sticky rod model on the lattice with its metastable, gel-forming may be better understood as mixture of fast and slow phase-separating components. Network-like structure of a lying phase as well as compact structures of a standing phase may form, depending on the dynamics of diffusion and rotational rates as well as temperature. In the driven setting of nonequilibrium growth, these will also depend on the external flux rate in our model, i.e. F/D and the temperature are the main control axes.

* * *

In nonequilibrium conditions, surprising and intricate structures at various mesoscopic scales can be generated. One has some element on control, particularly with respect to the external forces applied to such systems. In the case of thin film growth, this would correspond to the flux rate; further control parameters that alter the microscopic dynamics include temperature and diffusion rates. Dynamical arrest can occur in complex fluids brought out of equilibrium, and seem to be part of the palette of possible kinetic pathways towards *solidification*. In the next section, we discuss how organic molecular

[20] Arrested dynamics occur, naturally, in rod-like particle systems in "pure" 2D confinement, as well as quasi-2D or monolayer confinement: Colloidal or liquid crystal particles in quasi-2D confinement clearly show dynamic arrest and glassy phases [171, 730] other rod-like particle systems show the same [653–655].

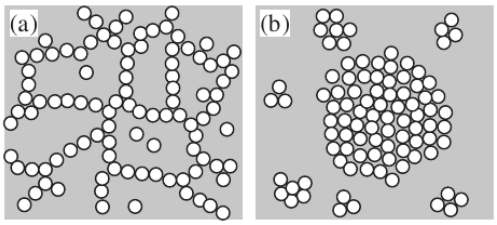

FIGURE 2.7: A depiction of possible two structures formed in viscoelastic phase separation, arising from an inherent dynamical asymmetry between possible liquid states. Citing Ref. [724], "*The change in the particle configuration from an open tenuous (a) to a compact structure (b) for colloidal suspensions. An open structure corresponds to a transient gel. A transient gel state is in a higher energy state and the system tries to lower the energy by increasing the number of the nearest neighbors. Mechanical stress originating from inter-particle attractive interactions stretches the arms of a transient gel and leads to their break-up. In this way, an open structure relaxes to a lower-energy structure, namely, a compact structure.*" Image from Ref. [724].

thin films, too, are likely subject to these kinds of effects, rendering diverse soft matter phenomena during self-assembly. Part II of this thesis will highlight this in the model system we investigate for growth of monolayers with hard (and sticky) rods.

2.4 Organic molecular thin films

Note: This section pertains to our study of a model system for monolayer-stage thin film growth of organic molecules – part II of this thesis. The introduction to the subject matter was given in Sec. 1.2.

Organic molecular films seem to lay somewhere between soft or colloidal matter, and atomic condensed matter with regards to phase transformation behavior during thin film growth. We report on some literature below that shows a commonness of organic molecular thin films to other soft matter systems. The similarity between colloidal and molecular epitaxial *multi-layer* growth has been discussed and quantified in some of the literature, see e.g. Ref. [736–738] for isotropic particles or molecules such as C_{60}.[21]

On a basic level, organic molecules entail a pronounced coupling of orientational degrees of freedom owing to particle shape and potentials, and, therewith, a potential for various entropy-driven phenomena not seen in atomic systems. Rod-like particles from colloidal soft matter are well-known to entail complex phase diagrams in bulk (See Sec. 1.3), and the underlying exclusion effects due to anisometry also "spill over" to distinctive behavior and pattern formation in far-from-equilibrium situations [25, 744]. In particular, the situation of confinement (at the substrate) generally enhances these effects: Anisotropic particles can become caged in a way that localizes their rotational motion, a

[21] Colloidal crystallization on periodic substrates (via crystal-structured epitaxy) have been explored for hard sphere systems [739–743]. The case of anisotropic (spherocylinder) colloids crystallizing on patterned or periodic substrates remains to be shown experimentally and in simulation, as far as we reckon.

prerequisite for dynamical arrest [666, 745]. The phase transition kinetics concurring during growth may bear many similarities to that in soft matter systems of anisotropic particles.

However, the degrees of freedom of organic molecules are more "discrete" in character, arguably, than those of typical colloidal systems with simpler, usually less directional interaction potentials. The locally Markovian dynamics of molecules at substrate assumed to be thermally activated by phonons, in contrast to a mediating fluid in the case of colloidal suspensions. A local vibration at a certain attempt rate induces random hopping events – quite different from Brownian-type motion in the short-time limit, which has a continuous power spectrum. Thus, a lattice-based approach may be more faithful, in fact.[22]

Affinity of organic molecules to "soft matter" behavior

A central reason behind the soft-matter character of organic molecules [155] is the relatively weaker strength and range of interactions [746], compared to, say, metallic matter, and the potential anisotropy of the molecule. The lower relevant temperature scales required for growth (sublimation or melting temperatures) attests to effectively weaker attractions between molecules and with the substrate (compared to $k_{\mathrm{B}}T$): The molecules represent "coarse-grainable" objects with spatial *extent*, and assignment of $\frac{1}{2}k_{\mathrm{B}}T$ thermal energy per degree of freedom makes dynamics more intertwined among the degrees of freedom and, therewith, "soft" than atomic systems. The pronounced coupling of the translational with the rotational degrees of freedom of particles (see Ref. [247]) implies that many-body, collective reorganization processes are likely. The solidification or sublimation process from a vapor will be more 'complex', entailing a larger bandwidth of possible events along the evolution, in light of previous discussion in Sec. 2.1.2. Therewith, the kinetics of self-assembly will be intricate.

The weakened effective binding of the molecules can make growth more prone to desorption and sensitive to subtle changes thereof [141, 145, 149, 689, 691, 747, 748]. The film roughness and quality are reported to be quite sensitive to the specific vacuum pressure during growth [749]. Vapor-phase deposition experiments also attest to this heightened sensitivity [151]. Thermodynamically, this implies a lower surface free energy than metals: estimates confirm this; moreover, the contribution of entropy is likely much larger [750]. Organic molecular films are further sensitive to the roughness, heterogeneousness and cleanliness of the substrate [145, 184, 219, 747, 751]. Lastly, while metals or atomistic systems "need" a well-matched substrate lattice to grow films (these will entail significant strain upon any lattice mismatch, and thick films may not even form at all), the restriction is much looser for organic molecular films. Quite the contrary is observed: weak adhesion to the substrate may even be the key to epitaxial-type growth for organic molecules [16].

As structure at the initial stages of growth is allowed to be much more amorphous (due to the lack of necessity for a crystalline substrate), *long-term memory* in the form of strain can build up gradually in the film, relaxing at later stages of growth in a collective re-ordering process. In other words, *surface phases* or *wetting layers* of a lower degree of crystalline order may form, often

[22] The situation of organic molecules may be even more complex, as diffusive motion on a substrate (with a particular crystal structure) may be nearly 1D [247, 250].

described as "liquid-like" in character, and setting in from the very beginning of growth [10–14, 251]. These are shown to dewet at a later time-point [12, 216]. In fact, wetting transitions in organic molecular films are reported broadly and may occur at quite 'late' stages of growth, see also Refs. [9, 141, 149, 167, 169, 199, 213, 216].[23] [24] The particular choice of substrate interactions, just like in other confined soft matter systems (see discussion in Ch. 2.2), will affect the kinetics and possible self-assembly pathways – through the monolayer, bilayer and multilayer stages of growth [7–9]. (As discussed before on systems in confinement, the substrate effectively "deforms" the bulk phase diagram in equilibrium, and changes the dynamics (kinetics) in nonequilibrium, see e.g. Ref. [151].)

These wetting layers or surface phases at the submonolayer or ultra-thin film stage are generally described as "loose" or "liquid-like". The phenomenon of surface "pre-melting" or "quasi-liquids" is an important topic of discussion for surface phenomena, see Refs. [7, 718–722]). Such behavior could occur for organic molecular systems, as well, see Refs. [10, 141, 212, 236, 237, 752].[25] Monolayers of attractive colloidal spheres [743] or monolayers of binary hard spheres [730] show these kinds of surface effects. Moreover, these dense, disorderly phases may represent surface "precursors" to the formation of the stable-phase crystal, an effect discussed for bulk colloidal crystallization from a liquid [669, 715–717]. In general, then, "soft" phases might be a prominent part of the growth of thin films with organic molecules. These can induce long-ranged orientational correlations in the films. Large discrepancies in size distributions of islands with different orientational order are reported to occur in the monolayer regime [146]. We will see in our simple model for growth in Ch. 5, as well.

Other "soft matter" capabilities at the submonolayer stage such as a dendritic, network-forming structure might occur during sub-monolayer growth on a substrate [753]. More generally, kinetically trapped or arrested state may occur before the crystallization process of stable-phase islands, see e.g. Ref. [188]. Fundamentally, a nontrivial competition between rotational and translational degrees of freedom (in confinement) can render nonergodic, glassy dynamics [665]. Indeed, we see a jammed state in purely hard-core monolayers of hard rods if an external potential favors the lying orientation strongly (in Ch. 4).[26] Kinetic arrest is also found in our model for monolayers of "sticky" hard rods with the spontaneous formation of a transient, gel-like phase or "wetting layer", composed of lying rods only, see Ch. 5. All in all, organic monolayers show phenomenological affinity to other soft matter systems, which differentiates them from atomic thin films. Relating to the discussion in Sec. 2.3, we will expect the emergence and disappearance of differently-ordered states as a function of density (time), temperature [149, 752], and dynamical rates (diffusion, flux) during monolayer growth.

[23] We note here that nematic thin films can only stably wet surfaces after a certain thickness [122], which may help in interpreting various dewetting phenomena that are reported for thin films of organic molecules, in particular at the second layer.

[24] The phenomena with organic molecular thin films that involve a "lying" liquid, as well as 1D-like ordering [10, 14] appear to overlap with those of organic Langmuir monolayers on metal surfaces [115]. Langmuir monolayers can also entail metastable surface phases, seen e.g. upon evaporation [117].

[25] For example 2D "lattice-gas-like" disordered phases are reported in Ref. [220], as well.

[26] See comparable effects of arrest in lattice models in Refs. [663, 664, 754].

As we foreshadowed in the introduction (Ch. 1.2), the phenomenology at the monolayer stage of thin film growth with rod-like particles is rich due to a fundamentally complex interplay of orientational and translational degrees of freedom in confinement. Our studies in part II of this thesis will attest to pronounced "soft-matter" effects during thin film growth.

This chapter discussed the mesoscopic aspects of complex fluids of rod-like particles, regarding both structure and dynamics. We provided therein a broader context of the systems of hard rods on lattices studied in this thesis. In the next chapter, we shall delve deeper into the fundamentals behind statistical mechanics of systems in equilibrium and nonequilibrium. On-lattice systems in nonequilibrium are discussed more deeply, as well, in addition to statistical-physical notions of – and some basics around – machine learning approaches relevant for this thesis.

Chapter 3

On Probabilistic Descriptions of Classical Many-Body Systems

The actual science of logic is conversant at present only with things either certain, impossible, or entirely doubtful, none of which (fortunately) we have to reason on. Therefore the true logic for this world is the calculus of probabilities

James Clerk Maxwell

This chapter will provide us with a fundamental background on statistical mechanics and associated techniques – regarding both equilibrium and nonequilibrium systems – which are relevant for the research on hard-rod models presented in subsequent parts of this thesis. We wish to discuss the *probabilistic approach* taken for classical many-body systems from some of its very basic postulates like ergodicity, which break down in nonequilibrium. Thus, although statistical mechanics is well-developed for equilibrium systems, nonequilibrium systems pose a great challenge, and a unifying approach is lacking (we motivated this is Ch. 1.1 already). We argue that lattice systems of hard rods studied in this thesis (particularly that for nonequilibrium thin film growth in part II) are highly instructive, highlighting the importance dynamical *presumptions* like locally-Markovian dynamics, which allow for nonequilibrium descriptions based on Master equations. On a related note, we discuss the basis of (and describe in more detail) kinetic Monte Carlo and general Markov-Chain Monte Carlo algorithms, which are techniques employed in parts II and III of this thesis. We also introduce density functional theory and discuss dynamical density functional theory employed, as well.

Further, we discuss the connections between "effective" approaches *a la* statistical field theory and machine learning algorithms, the latter of which we employ in part IV, where in both cases variational principles can provide the means to bounded approximations. The algorithms are discussed at the end of this chapter. Aforehand, we illustrate deeper connections between statistical mechanics and information theory, where thermodynamic concepts akin to entropy play basic roles. These ideas are tied to historically famous debates on the "paradox of irreversibility" and generally coarse-grained descriptions of out-of-equilibrium systems.

Many-body systems of interacting particle systems are inherently *complex*, in that in order to exactly predict the dynamical evolution of various emergent phenomena, such as phase transformations, many – if not all – constituents

would need to be taken into account, potentially. The deep nature of this complexity may render even a hypothetically complete description practically useless: it might be unintelligible to a human, as abstraction is at the basis our of cognition and understanding of the world. Only by narrowing our focus to a limited window of length- and time scales can we make reasonable progress toward quantitative understanding of natural phenomena [755]. Hence such an abstraction of the system's microscopic laws governing the motion of individual particles is imperative [756] – an abstraction of the full set of (deterministic) equations-of-motion at the microscopic scale of, say, 10^{12} colloidal particles in a suspension. This realization may also bear greater depth about the nature of physical law itself. To quote P. W. Anderson in his 1972 paper on the philosophy of meso- and macroscopic descriptions in condensed matter physics [757], "*The behavior of large and complex aggregates of elementary particles, it turns out, is not to be understood in terms of a simple extrapolation of the properties of a few particles. Instead, at each level of complexity entirely new properties appear, and the understanding of the new behaviors requires research which I think is as fundamental in its nature as any other.*"

The logical structure is alluded to here: the derivation of the macroscopic laws of physics should, in principle, succeed by means of different coarse-graining stages from microscopic laws. The connection of microscopic physics to the macroscopic laws is usually made in *expectation values* of physical quantities, i.e. observables that quantify mean values. At the macroscopic scale, we are making statements on *typically* realized values of quantities of the system [758, 759]. Predictions are thus always statistical in nature as the science does not deal with individual contributing objects any longer [64, Ch. 1.1]. Gibbs makes this clear: "*The laws of thermodynamics, as empirically determined, express the approximate and probable behavior of systems of a great number of particles, or, more precisely, they express the laws of mechanics of such systems as they appear to beings who have not the fineness of perception to enable them to appreciate quantities of the order of magnitude of those which relate to single particles, and who cannot repeat their experiments often enough to obtain any but the most probable results*" [89, p. viii].

The logic may appear somewhat loose-ended, though, missing a central point about what the theory is about: how can we agree on what is "macroscopic", at all? Quoting Uhlenbeck (1963) [760, Ch. 1], "*There is an element of arbitrariness in the concept of the macroscopic . . . [I]n principle the macroscopic knowledge of the state of the system depends so to say on the zeal of the observer and can therefore not be defined in general. All one can say is that the macroscopic description is a contracted description, which uses much fewer variables than required for the precise microscopic specification. Also, in practice, it usually is clear what the macroscopic variables are, since they are dictated by the experimental phenomena which one tries to explain.*" The problem here is to find an appropriate description of the "effective" or "projected" processes [96, Ch. 2.5]. Once we can agree upon the macroscopic states of interest, we can do the crucial step of clarifying which variables are random [81]. Then, a cruder step is taken: we decide which of these mean values can substitute an entire set of microscopic states (the "contraction" step). By such a partial contraction of information, we project the system onto a certain cross-section of our understanding. An irreversible step is taken into an *idealized* macroscopic world, where mesoscopic quantities are precise with respect to our measurement instruments, i.e. they become "sharp" objects in our models: we describe *mean* (expectation) values and employ statistical *density*

distributions (ensembles).

Yet, a method-of-approach for general, nonequilibrium scenarios constitutes a central, not-fully-resolved challenge of the subject field. Existing formalisms include that of the Zwanzig and Mori [93, 761–763], advanced in light of information theory and geometry by Balian et al. [756]. Yet, in practice, *a prioiri* approximations (presumptions not necessarily based on experimental evidence) are required at some point. "Bottom-up" approaches will not work if we cannot specify a constraint or a known feature at a higher level. Feedback from real-world experiments or simulations at the full N-body level will be absolutely necessary in developing any such theory.

An information-theoretic perspective on many-body systems has been debated and developed [64, 756, 764–766]. Importantly, as the irrelevant variables are eliminated, they become "hidden" [96, p. 70], or *lost*. This is why information is contracted, and the description becomes *incomplete* one. Only partial statistics or typical values of the relevant observables remain. From this viewpoint, then, reconstructing the initial conditions leading to the observable outcome is an ill-posed problem, and these outcomes shall appear random, in spite of deterministic microscopic laws [94, 95]. The necessary information required for reconstructing the exact initial conditions of the system is lost. Such lost information (our lack of knowledge) is quantified by statistical measures of entropy. The more ignorant we become or pretend to be – in stages of coarse-graining or contractions – the greater the information content "locked away" will become. There is a thermodynamic "cost" of erasing details in the search of a less complex description of reality [75, 436, 767].

A caveat remains, however: There is no obvious way to identify these relevant variables that govern the macroscopic evolution. What should one *a priori* choose to measure?[1] How can we know which variables are simple, e.g. Gaussian or follow a Markov process? Each choice renders different fundamental equations of motion, possibilities for mean-field approximations, and even specific definitions of dissipation. It is sobering that most notions of nonequilibrium statistical mechanics and dynamics are thus *relative* [756]. This stands in stark contrast to certain empirical findings, however: many systems display the same, universal behavior when near critical points. Thus, some blatantly oversimplified, "workhorse" models of statistical physics (e.g. the Ising model) owe it to the benevolence of nature for being so "unreasonably" effective, at least with regards to critical behavior [768]. Extremely modern developments in machine learning approached in this thesis in Ch. 7 that could offer a shimmer of hope, as well: they appear well-suited for the task of separating relevant from irrelevant variables, as they are designed to empirically separate "signal" from "noise", to say, by finding those variables that produce reliable and informative statistical guesses. Even so, we may have to assort to "top-down" approaches assuming *a priori* a certain form of dynamics or of statistical dependencies between variables, or doing approximations like perturbation theory, purely for convenience or tractability issues. One can iteratively improve upon these by cross-checking with experiments or simulations. Deviations are undeniably useful: they may be clear signposts of e.g. left-out relevant degrees of freedom at macroscopic scales (collective modes) or microscopic scales (conformational,

[1] Of course, looking at the Hamiltonian could help, especially if the systems is in a stationary state.

internal vibrational modes). Yet, we would not like to understate the level of difficulty of the task.[2]

Probability densities over states are normalized measures; their normalization constant is the partition function. To ensure properness of mesoscopic descriptions in *equilibrium* situations, one would need to preserve the value of the partition function exactly when transitioning between scales, which entails transforming variables; formalisms for partition function(al)s in *nonequilibrium* situations, exist, as well, [91]. Any transformation of a set of variables involves re-defining interactions (couplings) between typically particles or fields into some effective or collective entities. Explicitly *reducing* the total number of random variables, in addition to tracking the effects of their transformation, is the approach taken by the renormalization group (for systems near a critical point), see e.g. [66, 768]. The validity of statistical field theory rests on the *universality* postulate, which means that particular classes of approximations should apply across a variety of different systems in nature [57, 65–67, 769–771]. This may not be limited to physics alone: Structure and dynamics evolve (naturally) in biological systems in many regards. Statistical theories may be one of the most powerful approaches in science in general, arguably best developed and most rigorously testable within the context of physics [96, p. V]. On some level, statistical mechanics offers generic principles that can apply to other fields of sciences and and to physics at different scales of treatment. However, even this theory is incomplete, in part, and the continuation of research thereof is pertinent. By studying simple model systems like those in this thesis, we hope to make a humble contribution to this broad and abstract goal.

3.1 Phase space and thermodynamic equilibrium

As an abstraction that arises from our immediate perceptions of the world, matter and energy in the macroscopic world – as considered, historically in e.g. fluid mechanics, thermodynamics, and electromagnetism – were treated as a continuum. In this view, continuous or piecewise-continuous functions of space coordinates and time are the natural mathematical representation of macroscopic physical quantities, $A(x,t)$. Their evolution is governed by partial-differential equations or by integro–differential equations [94, Ch. 2.1][95, Ch. 2.3].

In stark contrast to the continuum view on nature, the advent of an atomistic theory of matter rendered a very different, microscopic description, namely of many moving and interacting bodies: We begin with an isolated system of N *point-like* particles who move along "sharp" trajectories. These are solutions of the equations of motion of Hamilton [97, Ch. 3][88, Ch. II]. Given that all particles have three translational degrees of freedom, the dynamical state of the system at a given time-point is completely specified by $3N$ coordinates $\boldsymbol{q}^N = \{\boldsymbol{q}_1, \ldots, \boldsymbol{q}_N\}$ and $3N$ momenta $\boldsymbol{p}^N = \{\boldsymbol{p}_1, \ldots, \boldsymbol{p}_N\}$, defining points in phase space. The time evolution for the microstates is given by a trajectory function (phase variables) $\{\boldsymbol{q}^N(t), \boldsymbol{p}^N(t)\}$. The microscopic laws governing the motion are given from the set of $6N$ coupled first-order partial differential

[2] Take the theory of a glass formation, for example [105].

equations of the Hamiltonian $\mathcal{H}(\boldsymbol{p}^N, \boldsymbol{q}^N; t)$

$$\frac{d\boldsymbol{q}_\alpha(t)}{dt} = \frac{\partial \mathcal{H}(\boldsymbol{q}^N, \boldsymbol{p}^N; t)}{\partial \boldsymbol{p}_\alpha} \tag{3.1}$$

$$\frac{d\boldsymbol{p}_\alpha(t)}{dt} = -\frac{\partial \mathcal{H}(\boldsymbol{q}^N, \boldsymbol{p}^N; t)}{\partial \boldsymbol{q}_\alpha};. \tag{3.2}$$

The standard example of a Hamiltonian is one where the particles interact with potential energy Φ and an external field V^{ext}:

$$\mathcal{H}(\boldsymbol{p}^N, \boldsymbol{q}^N) = \sum_\alpha \frac{\|\boldsymbol{p}_\alpha\|^2}{2m_\alpha} + \Phi(\boldsymbol{q}_1, \ldots, \boldsymbol{q}_N) + V^{\text{ext}}(\boldsymbol{q}_1, \ldots, \boldsymbol{q}_N; t) \tag{3.3}$$

with the first term representing the kinetic energy. We can recover Newton's equations of motions:

$$\frac{d\boldsymbol{q}_\alpha(t)}{dt} = \frac{\partial \mathcal{H}(\boldsymbol{q}^N, \boldsymbol{p}^N; t)}{\partial \boldsymbol{p}_\alpha} = \boldsymbol{p}_\alpha / m_\alpha \tag{3.4}$$

$$\frac{d\boldsymbol{p}_\alpha(t)}{dt} = -\frac{\partial \mathcal{H}(\boldsymbol{q}^N, \boldsymbol{p}^N; t)}{\partial \boldsymbol{q}_\alpha} = -\frac{\partial U(\boldsymbol{q}^N)}{\partial \boldsymbol{q}_\alpha} = \mathbf{f}_\alpha(\boldsymbol{q}^N)\,, \tag{3.5}$$

where on the right-hand sides we have m_α as the mass of particle α and $\mathbf{f}_\alpha(\boldsymbol{q}^N)$ as the vectorial force on particle with coordinate vector $\boldsymbol{q}_\alpha$.

These are the usual assumptions of classical mechanics [88, Ch. I-III]. We can be assured that it is possible to know all the positions and momenta of an N-particle system to arbitrary precision at some initial time, and that the motion can be calculated exactly from integrating these equations of motion of the phase variables given initial conditions $(\boldsymbol{q}_\alpha(t_0), \boldsymbol{p}_\alpha(t_0))$. The phase variables represent here the microscopic dynamical states of the system. The number F of conjugate pairs of variables specifies the number of degrees of freedom necessary to completely characterize the dynamical system: If all particles retain their degrees of freedom, then we have $F = 3N$ for 3D space.

3.1.1 Key notions

Degrees of freedom

The standard meaning of "number of the degrees of freedom" F is the number of actually *independent variations* that can be made in the coordinates. Constraints on the system that are inherent, such as two particles bound by a fixed distance, will reduce the number of independent variations. There is a differentiation between holonomic and non-holonomic constraints, where the system is made in such a way that coordinates are connected by relations that hinder their independent variation [88, p. 18]. Degrees of freedom enter the Hamiltonian in a *quadratic* manner (such as those that contribute to a kinetic energy, or of harmonic oscillators). They are in effect "modes"; in equilibrium, the system is *quasiperiodic*,[3] i.e. a superposition of periodic motions. The equipartition of energy says that each such quadratic degree of freedom contributes $1/2 k_B T$ to the average energy for temperature T of the system and Boltzmann constant k_B. Deviations from this theorem arise with nonlinearities in the potential – the

[3] an observation studied by Poincaré (1899) [772, Appendix][760, 773].

definition of degrees of freedom must be modified for nonlinear dynamical systems – and with quantum corrections [774, Ch. 3.5][81]. In any case, variables with a given total number of degrees of freedom can be expressed in a *collective* manner, so that many particles are involved. Finding convenient forms or the most simplifying collective variables is the key to describing many-body, macroscopic states in statics and dynamics (see more below). "Coarse-graining" aims to define constraints in order to reduce the number of degrees of freedom.

From the point of view of any equation of motion – from classical to quantum mechanics, a "free" propagator solution is time-independent (no inhomogeneous part) and reflects the degrees of freedom of the body. Stationary external fields will not affect the number of degrees of freedom, as these couple to the configurational variables only. Hence, momenta are the key parts of phase space that indicates (statistically) independent "axes" along which a system can transfer energy. Apart from this constituting a purely conceptual note, it is key to interpreting machine learning algorithms that we employ in this thesis in part IV, which we motivate later in this chapter in Sec. 3.6.

Integrals of motion: Conserved, invariant quantities

Integrals of motion C_i are quantities that are conserved over trajectories – every trajectory can be characterized by special values c_i of the dynamical variables $C_i(\boldsymbol{q}^N, \boldsymbol{p}^N)$, which are constraints defining the subspace $\boldsymbol{\Gamma}(\boldsymbol{q}^N, \boldsymbol{p}^N; c_i)$ of the phase space accessible ("valid") to the trajectory. Integrals of motion effectively reduce the total number of degrees of freedom F, and can be included in variational approaches via Lagrange multipliers. When $V^{\text{ext}}(\boldsymbol{q}^N; t) = 0$, then one such integral of motion is the total energy E and particle number N. If there is an invariance under choice of coordinate system with respect to displacement and rotation (a symmetry persists), the total linear momentum $\sum_{\alpha=1}^{N} p_\alpha$ and total angular momentum $\sum_{\alpha=1}^{N} \boldsymbol{q}_\alpha \times \boldsymbol{p}_\alpha$ are constants of motion, in accordance with Noether's theorem [775, Ch. 1][776, Ch. 6][765, Ch. 14]. Global symmetries of a system are generally important, as they may be spontaneously broken at phase transitions, which we touch upon later, see Sec. 3.2.1.

The identification of all the symmetries is crucial for constructing any field-theoretic models, i.e. to write down the most generic Lagrangian or effective Hamiltonian (discussed later) compatible with the symmetries of a system. In general, quantities that are nearly conserved up-front may not be obvious, as in some cases may only be determined experimentally [64, Ch. 4.1]

Constancy is an idealization, however: it is a matter of time-scales and of intensity, dependent on the measurement time-window of a many-body system (i.e. of the level of treatment) and on the precision of measurement. A constant total (mean) energy, i.e. systems in thermodynamic equilibrium, means there is no clear direction of time at the macroscopic level. The statistical treatment is thus of stationary quantities (apart from stationary fluctuations) and effectively time-independent (See discussion later about the "paradox" of irreversibility in Sec. 3.5). In nonequilibrium systems, a nearly-constant energy corresponds to e.g. *metastable* states that are long-lived – a direction of time is only very weak. Highly non-stationary solutions of any equation of motion also imply that energy is not conserved in the particular level of treatment.

3.1.2 Impelled probability densities (?)

Apart from the practical and philosophical problem of keeping track of gigantic amounts of details, discussed in the beginning of this chapter, is there some other argument for necessitating many-body physics to be a *statistical* theory [775, Ch. 1.1][90, Ch. I-IV][95, Ch. 2][94, Ch. 2][87, Ch. 1]?

Let us first continue our description of the microscopic world as above, and assume that a property $\mathcal{A}$ takes on a particular (continuous) value at every instant of time along the trajectory. If a measurement is done over a longer time span then the macroscopic, observable quantity is

$$\mathcal{A}_{\text{obs}} = \overline{\mathcal{A}} = \overline{\mathcal{A}(\boldsymbol{q}^N, \boldsymbol{p}^N; t)} = \lim_{T\to\infty} \frac{1}{T} \int_{t=0}^{T} \mathcal{A}(\boldsymbol{q}^N, \boldsymbol{p}^N; t)\, dt \tag{3.6}$$

with T denoting the time interval, and the bar that of a time average. This definition is also the basis for molecular dynamics simulations [777], as well as equilibrium Markov-Chain Monte Carlo methods that we employed in this thesis (see Sec. 3.4). Our experience tells us that the observational value will converge to a *stationary* value, at least for systems we deem to be "in equilibrium". However, we have not answered *why* is there a statistical outcome, in the first place. Naively, if we know the laws of motion are deterministic and we prepare a system in a microscopically exact initial condition, then the outcome should be deterministic, not stochastic.

There are several arguable reasons why the macroscopic behavior is well-describable via stochastic means: (1) It is practically impossible to know (measure) the exact initial state of a system; an ultimate "stop sign" would be quantum uncertainty, yet any imperfect knowledge or measurements in space and time lead to large deviations of the system given sufficient time. (2) Nonlinear dynamical equations (for classical many-body motion) all "suffer" from *dynamical instability* [778], a topic treated in e.g. ergodic theory of chaos [81]. (3) Likewise, it is impossible to perfectly measure the system *during* its evolutionary trajectory: in effect, the "true" trajectory cannot be specified as a singular entity, splitting into others at every moment as time passes. (4) Systems are never fully isolated, and so the degrees of freedom and external influences are uncontrollably ignored in the dynamical equations of motion Eqs. (3.1) and (3.2). All together, we cannot specify the microscopic state to perfection when requiring that macroscopically large spatial and time- spans should be treated. At the end of the day, is a lack of perfect information the reason for the stochastic nature of many-body systems? This more modern viewpoint [64, 766] has been cause for hefty debate for decades.

Still, even if we accept the necessity for probabilities, can we formally obtain the macroscopic *expectation values* of observational quantities from microscopic dynamics? An old question that has been ruminated on since the time of Boltzmann and Gibbs. The older view on statistical mechanics, such as that of Fowler (1936) [87], is that we ought to calculate time averages of dynamical variables (phase variables). This is the standpoint Boltzmann took. Yet, for one thing, infinite-time averages never can be made, and the time-average approach does not leave room for the notion of *rare* or "exceptional" many-body motions or events [779]. It might rule out a discussion at all about non-equilibrium statistics, arguably, a critique that later e.g. Jaynes [766, 780] and Balescu [94]

purported.

As a means to get around the looming problems with averaging observables over dynamics, Gibbs introduced the concept of *ensembles* as phase-space probability densities, which we discuss in the following. Each ensemble imposes unique macroscopic "known" constraints on the possible phase-space trajectories of the system. All "other" microscopic variables are effectively free to vary whilst abiding to microscopic laws (i.e. respect the Hamiltonian). The hope is that the ensemble provides a shortcut to calculating *all* possible outcomes of many-body dynamical systems compatible with the constraints.[4] By taking the mean, the ensemble should render the stationary macroscopic observables that we are seeking. Each ensemble introduces different constraints that reduce the degrees of freedom in the system in different ways.

At the very bottom of it, to be certain of the equivalence of dynamical versus ensemble averages, we would have to prove a postulate called the *ergodic hypothesis*, which we discuss in Sec. 3.1.3 below: The ensemble at every single time-point t_0 in its copies of the system renders a random set of phase variables $\{\mathcal{A}(\boldsymbol{q}^N, \boldsymbol{p}^N; t_0)\}$. The mean of this set is equivalent to that of measuring momentary values of a single system with $\mathcal{A}(\boldsymbol{q}^N, \boldsymbol{p}^N; t)$ over long periods of time $t \in [0, T \to \infty)$. Gibbs' formulation of equilibrium statistical mechanics has stood the test of time with regards to predictions, yet the ergodic hypothesis sitting at the base of the theory has not been proved for general situations.

The central idea of statistical mechanics, therefore, is that distribution functions are the fundamental objects for a macroscopic description of the world. They are "fuzzy" objects, encompassing a whole set of "sharp" *points* (microscopic states) that could be measured. This idea will be developed further in Sec. 3.1. The consistency of the microscopic–to–macroscopic picture fully rests on the presumption of ergodicity [781–784], which we will discuss more in forthcoming.

Classical phase space distribution functions

Gibbs introduced the idea of applying the laws of dynamics to "*a great number of independent systems, identical in nature but differing in phase, that is in their condition with respect to configuration and velocity*" [89]. In other words, the generation of an *ensemble*[5] means we consider an essentially infinite collection of *independent* (non-interacting), individual systems characterized by identical microscopic dynamics and identical macroscopic state variables that are fixed aforehand (number of particles, volume, temperature, energy, etc.), yet differing in their initial conditions [64]. Such a statistical description results from necessity – to express equations explicitly and in a tractable way.

In doing so, we consider the average behavior of a collection of macroscopically identical systems distributed over a range of states (microstates). In this large number of copies, we can consider continuous changes of a particular state when passing to neighboring states. In assigning a probability density in

[4] This is impossible to do, in practice

[5] Prior to Gibbs, Boltzmann [86] introduced the concept of an assembly, which is a collection of weakly interacting systems, in his seminal treatment of the dynamics of dilute gases.

phase space, the implicit assumption is that this density function has continuous partial derivatives with respect to each macroscopic variable.[6] The initial conditions of the distribution function are considered to span the phase space specified by the macroscopic constraints. Then phase space probability density $f^{(N)}(\boldsymbol{q}^N, \boldsymbol{p}^N; t)$ describes a probability (a fraction of systems)

$$f^{(N)}(\boldsymbol{q}^N, \boldsymbol{p}^N; t)\; d\Gamma^N \tag{3.7}$$

of being in a microstate represented by a point $\{\boldsymbol{q}^N, \boldsymbol{p}^N\}$ settled in the infinitesimal surrounding volume $d\boldsymbol{q}^N d\boldsymbol{p}^N \equiv d\Gamma^N$ at time t [775, Ch. I][88, Ch. III]. These we call *representative points*: Each is the instantaneous state of any member system of the ensemble, and the condition of the ensemble as a whole is then given by a 'cloud' of such points. Ensemble averages are expectation values of dynamical variables, computed with respect to the joint probability density function $f^{(N)}(\boldsymbol{q}^N, \boldsymbol{p}^N; t)$ over all possible dynamical states of the system. All macroscopic properties of the system are now calculated as averages of an ensemble, thus over all (virtual) members of an ensemble. For a macroscopic, observable state M, the evolving probability distribution $p_M(t)$ can be interpreted as the fraction of systems in the ensemble that are in the observational state M at time t. In this way, the statistical properties of the system depend crucially on the probability measure, which is determined by constraints of the system as a whole. If there is a higher probability density in a certain region of phase space, then any system chosen at random is more likely to be in a microstate located in that region.

The normalization condition for N corresponds to an integral over the volume in phase space:

$$\int f^{(N)}(\boldsymbol{q}^N, \boldsymbol{p}^N; t)\; d\Gamma^N = 1\,. \tag{3.8}$$

A most natural way to normalize $f^{(N)}(\boldsymbol{q}^N, \boldsymbol{p}^N; t)$ to unity for such N identical particles is by using the integration with the dimensionless volume element

$$d\Gamma^N = \frac{1}{N!(2\pi\hbar)^{3N}} \prod_{\alpha=1}^{N} d\boldsymbol{q}_\alpha d\boldsymbol{p}_\alpha \tag{3.9}$$

where $\hbar$ is Planck's constant. For systems allowed to exchange particles with their surroundings, as in the grand canonical ensemble, the particle number N becomes a discrete random variable. The normalization condition of the distribution function sums over the different possible realizations of the normalization for the N-particle phase-space distribution function, as in the following:

$$\sum_{N=0}^{\infty} \mathrm{e}^{\beta\mu N} \int f^{(N)}(\boldsymbol{q}^N, \boldsymbol{p}^N; t)\; d\Gamma^N = 1\,. \tag{3.10}$$

The factor $\mathrm{e}^{\beta\mu}$ is known as the *fugacity*, a more detailed description of this ensemble is given in Sec. 3.1.4.

[6] Paraphrasing Ref. [97, Ch. 3.3], if the system is Hamiltonian and all trajectories are confined to the energy surface, one eliminates the energy as a variable, and considers the density function defined on a surface of constant energy (effectively reducing the dimensionality of the system). This eliminates the discontinuity when taking a derivative with respect to the energy.

The normalizing factor of the distribution incites the definition of a partition function for the given ensemble, which we describe more in Sec. 3.1.4 below. The latter incorporates all of the relevant information of the system, a topic which will re-arise in following sections, and is the key quantity for statistical physics in equilibrium situations and the field-theoretic notions that follow (see Sec. 3.2). According to the ergodic hypothesis (Sec. 3.1.3), all relevant statistics – those of a measurable, meso- or macroscopic quantity – are stationary in equilibrium, hence probability densities over microstates are time-independent. Due to the constancy of total momenta (integrals of motion), they are usually expressed purely in terms of configuration variables.

The microscopic connection (illustration)

Note: This section goes into further depth regarding the interpretation of the microscopic versus macroscopic viewpoint of classical many-body dynamics, which is not *a central theme of this thesis, but may be interesting from a general perspective; the reader may skip ahead to Sec. 3.1.3, if desired.*

The relationship between the classical laws of motion and a statistical description is somewhat more subtle, where the following illustration is based heavily on Refs. [95, Chs. 2, 3][94, Ch. 2]. Macroscopic quantities $A(\boldsymbol{x}, t)$ are *fields* in *physical space-time*, $(\boldsymbol{x}, t)$, i.e. coordinates $\boldsymbol{x}$ and time t. Microscopic physical quantities (which we will denote later as "a") are *dynamical functions of the phase-space* variables $(\boldsymbol{q}_1, \ldots, \boldsymbol{q}_N, \boldsymbol{p}_1 \ldots, \boldsymbol{p}_N) \equiv (\boldsymbol{q}, \boldsymbol{p})$, and may also depend on the *parameters* $(\boldsymbol{x}, t)$.

Let us begin with a few basic concepts and definitions. The classical equations of motion at the microscopic level treat phase variables, which are $3N$-dimensional dynamical functions, obtained by solving the equations of motion of microscopic trajectories

$$\boldsymbol{q}(t) \equiv \boldsymbol{q}(\boldsymbol{q}(0), \boldsymbol{p}(0); t) \tag{3.11}$$

$$\boldsymbol{p}(t) \equiv \boldsymbol{p}(\boldsymbol{q}(0), \boldsymbol{p}(0); t)\ , \tag{3.12}$$

with the initial conditions at $t = 0$. Their *natural motion* follows the solution of the Hamilton equations-of-motion according to the *time-independent* Hamiltonian $\mathcal{H}(\boldsymbol{q}, \boldsymbol{p})$. Thus, the microscopic dynamical functions representing physical quantities can be written as $a(\boldsymbol{q}, \boldsymbol{p}; \boldsymbol{x}, t)$, whereby the macroscopic space-time coordinates $\boldsymbol{x}$ and t can be considered parameters of these functions.

The *Poisson operator*[7] is defined as

$$[\mathcal{H}] \equiv \sum_{\alpha=1}^{N} \left\{ \frac{\partial \mathcal{H}}{\partial \boldsymbol{p}_\alpha} \frac{\partial}{\partial \boldsymbol{q}_\alpha} - \frac{\partial \mathcal{H}}{\partial \boldsymbol{q}_\alpha} \frac{\partial}{\partial \boldsymbol{p}_\alpha} \right\}\ , \tag{3.13}$$

which acts on the microscopic dynamical variables in the following way:

$$\frac{\partial a(\boldsymbol{q}, \boldsymbol{p}; \boldsymbol{x}, t)}{\partial t} = \sum_{\alpha=1}^{N} \left\{ \frac{\partial a}{\partial \boldsymbol{p}_\alpha} \frac{\partial}{\partial \boldsymbol{q}_\alpha} - \frac{\partial a}{\partial \boldsymbol{q}_\alpha} \frac{\partial}{\partial \boldsymbol{p}_\alpha} \right\} \tag{3.14}$$

$$\equiv [a, \mathcal{H}]\ . \tag{3.15}$$

[7] also called the Liouville operator, e.g. Ref. [26]

Formally, Eqs. (3.14)–(3.15) can be solved by expanding $a(\boldsymbol{q},\boldsymbol{p};t)$ as a power series of t, upon defining $a(\boldsymbol{q},\boldsymbol{p};t)\equiv a(t)$ and $a(\boldsymbol{q},\boldsymbol{p};0)\equiv a$

$$a(t)=\sum_n \frac{1}{n!}t^n b^{(n)}(0)=\sum_n \frac{1}{n!}t^n[\mathcal{H}]^n a\ . \tag{3.16}$$

This corresponds to

$$a(t)=\mathrm{e}^{[\mathcal{H}]t}a\ , \tag{3.17}$$

where $\mathrm{e}^{[\mathcal{H}]t}$ is the *propagator*. Owing to the properties of the Poisson bracket, it acts on the dynamical variables in the following way:

$$a(\boldsymbol{q},\boldsymbol{p};t)=\mathrm{e}^{[\mathcal{H}]t}a(\boldsymbol{q},\boldsymbol{p};0)=a(\mathrm{e}^{[\mathcal{H}]t}\boldsymbol{q},\mathrm{e}^{[\mathcal{H}]t}\boldsymbol{p};0)=a(\boldsymbol{q}(t),\boldsymbol{p}(t);0)\ . \tag{3.18}$$

Returning to the microscopic–macroscopic connection, we wish to describe the world in terms of the fields $A(\boldsymbol{x},t)$, whose expectation values will give us *observables*. We are concerned with the map

$$a(\boldsymbol{q},\boldsymbol{p};\boldsymbol{x},t)\ \longrightarrow\ A(\boldsymbol{x},t)\ . \tag{3.19}$$

In the macroscopic world, to obtain a probability mass density over phase space, we would have to apply *localization* operation $\delta(\boldsymbol{q}_\alpha(t)-\boldsymbol{x})$ on each particle α. The mass density measured for a particle to be at point $\boldsymbol{x}$ in space and time $t=0$ is a delta-function

$$f^{(N)}(\boldsymbol{q}_\alpha,\boldsymbol{p}_\alpha;\boldsymbol{x},0)=m\delta(\boldsymbol{q}_\alpha-\boldsymbol{x})\ . \tag{3.20}$$

This singular function demonstrates the contrast between both viewpoints – the "sharp" trajectories in the microscopic world with a probabilistic description of the macroscopic world. A sum over all of particles renders the N-particle density $f^{(N)}(\boldsymbol{q},\boldsymbol{p};\boldsymbol{x},0)$:

$$f^{(N)}(\boldsymbol{q},\boldsymbol{p};\boldsymbol{x},0)=m\sum_{\alpha=1}^{N} f(\boldsymbol{q}_\alpha,\boldsymbol{p}_\alpha;\boldsymbol{x},0)=\sum_{\alpha=1}^{N} m\,\delta(\boldsymbol{q}_\alpha-\boldsymbol{x})\ . \tag{3.21}$$

To obtain the value of the density an arbitrary *future* time-point t in our coordinate system, we apply the propagator $\mathrm{e}^{[\mathcal{H}]t}$

$$f^{(N)}(\boldsymbol{q},\boldsymbol{p};\boldsymbol{x},t)=\mathrm{e}^{[\mathcal{H}]t}\sum_{\alpha=1}^{N} m\,\delta(\boldsymbol{q}_\alpha-\boldsymbol{x})=\sum_{\alpha=1}^{N} m\,\delta(\boldsymbol{q}_\alpha(t)-\boldsymbol{x})\ . \tag{3.22}$$

In switching to a purely macroscopic description (the world we observe) in physical space-time, we lose the precision of the microscopic trajectories, as we must *integrate out* the phase space variables. Let $f^{(N)}(\boldsymbol{q},\boldsymbol{p})$ be the phase space distribution function, chosen once for all, which defines the macroscopic state of the system.

$$\begin{aligned} a(\boldsymbol{q},\boldsymbol{p};t) \quad &\longrightarrow \quad A(\boldsymbol{x},t) && (3.23)\\ &\equiv \quad \langle a(\boldsymbol{q},\boldsymbol{p};\boldsymbol{x},t)\rangle && (3.24)\\ &\equiv \quad \int d\boldsymbol{q}d\boldsymbol{p}\,a(\boldsymbol{q},\boldsymbol{p};\boldsymbol{x},t)\,f^{(N)}(\boldsymbol{q},\boldsymbol{p})\ . && (3.25) \end{aligned}$$

We note here that the assumption that the macroscopic state of a system is fully defined by $f^{(N)}(\boldsymbol{q},\boldsymbol{p})$ is a basic postulate of statistical mechanics. The macroscopic physical quantity is a *marginalized* one.

Equation (3.25) can now be expressed in a "Heisenberg" picture,

$$A(\boldsymbol{x},t) = \int d\boldsymbol{q}d\boldsymbol{p}\,\{\mathrm{e}^{[\mathcal{H}]t}\,a(\boldsymbol{q},\boldsymbol{p};\boldsymbol{x},0)\}\,f^{(N)}(\boldsymbol{q},\boldsymbol{p})\;. \tag{3.26}$$

which defines the idea that the law of the macroscopic quantities in physical space is induced by Hamiltonian dynamics on phase space. During an averaging process, the dynamical quantities evolve in time while the initial state of system is kept fixed, which is specified by the distribution function $f^{(N)}(\boldsymbol{q},\boldsymbol{p})$. Alternatively, the whole time-evolution can be transferred to the phase space distribution function if we perform the following operation:

$$f^{(N)}(\boldsymbol{q},\boldsymbol{p};t) = \mathrm{e}^{-[\mathcal{H}]t}f^{(N)}(\boldsymbol{q},\boldsymbol{p})\;. \tag{3.27}$$

Then the macroscopic quantity will be defined as:

$$A(\boldsymbol{x},t) = \int d\boldsymbol{q}d\boldsymbol{p}\,a(\boldsymbol{q},\boldsymbol{p};\boldsymbol{x})\,f^{(N)}(\boldsymbol{q},\boldsymbol{p};t) \tag{3.28}$$

where $a(\boldsymbol{q}^N,\boldsymbol{p}^N;\boldsymbol{x}) = a(\boldsymbol{q},\boldsymbol{p};\boldsymbol{x},0)$ In this "Schrödinger" picture, the time dependence is in the distribution function $f^{(N)}(\boldsymbol{q},\boldsymbol{p};t)$. This resolves a nagging problem with the "Heisenberg" representation that requires solving the equation of motion for each separate dynamical function (see the references given at the start of this section). The microscopic quantity $a(\boldsymbol{q},\boldsymbol{p};\boldsymbol{x})$ is now *time-independent*.

The time-dependent distribution function $f^{(N)}(\boldsymbol{q},\boldsymbol{p};t)$ follows a partial differential equation that is known as *Liouville's equation-of-motion*, the basic equation of classical statistical mechanics:

$$\frac{\partial}{\partial t}f^{(N)}(\boldsymbol{q},\boldsymbol{p};t) = [\mathcal{H}(\boldsymbol{q},\boldsymbol{p}),f^{(N)}(\boldsymbol{q},\boldsymbol{p};t)] \tag{3.29}$$

Here we used the Poisson bracket specified in Eqs. (3.14)–(3.15). We will discuss this equation more in the next section.

The conceptual transfer between two levels-of-description of our world is summarized: Microscopic motion is described by "sharp" trajectories; at the macroscopic level, the motion becomes that of a distribution function $f^{(N)}(\boldsymbol{q},\boldsymbol{p};t)$ that is postulated to specify the macroscopic state in full. Yet, comparing microscopically resolved trajectories to probability densities over states is not necessarily straightforward, particularly when in nonequilibrium conditions.

Remark. These considerations should become more complicated for systems coupled to thermal baths, which entail *dissipative* terms in the microscopic Hamiltonian, and for systems in nonequilibrium. Both are exposed to *non-conservative* forces, i.e. there is an explicit time-dependence in the microscopic Hamiltonian $\mathcal{H}(\boldsymbol{q},\boldsymbol{p},t)$, and the notion of time-invariant, *natural motion* does not hold any longer. Statistical mechanics of equilibrium rests upon the microscopic–macroscopic connection in isolated systems that we have illustrated above, before proceeding to describe open systems. We shall discuss the ensembles in forthcoming sections.

3.1.3 Evolution in isolated systems

The general form of a Hamiltonian in Eq. (3.3) contains a time-dependent external potential $V^{\text{ext}}(\boldsymbol{q}_1, \ldots, \boldsymbol{q}_N; t)$. If this loses its time-dependence, then the full Hamiltonian of the N-body system becomes time-independent [775, Ch. 1][88, Ch. II]. The rate of change of the Hamiltonian, in general form, calculated from the equations of motion Eqs. (3.1) and (3.2),

$$\frac{d\mathcal{H}(\boldsymbol{q}^N, \boldsymbol{p}^N; t)}{dt} = \sum_\alpha \left(\frac{d\boldsymbol{p}_\alpha}{dt} \frac{\partial \mathcal{H}}{\partial \boldsymbol{p}_\alpha} + \frac{d\boldsymbol{q}_\alpha}{dt} \frac{\partial \mathcal{H}}{\partial \boldsymbol{q}_\alpha} \right) + \frac{\partial \mathcal{H}}{\partial t} \tag{3.30}$$

vanishes for this case:

$$\frac{d\mathcal{H}(\boldsymbol{q}^N, \boldsymbol{p}^N; t)}{dt} = \frac{\partial \mathcal{H}}{\partial t} = \frac{\partial V^{\text{ext}}}{\partial t} = 0 \, . \tag{3.31}$$

The integrals of motion now include *at least* the energy; they include the total angular and linear momentum, as well, given the corresponding global symmetries of the system. We mentioned this in the first part of Sec. 3.1.

Liouville equation

In this isolated system, the time evolution of the phase space density $f^{(N)}(\boldsymbol{q}^N, \boldsymbol{p}^N; t)$ is governed solely by *Liouville's equation* [88, Ch. III][775, Ch. 1][88, Ch. III][47, Ch. 4][779, 785], which we first introduced in Eq. (3.29),

$$0 = \frac{\partial f^{(N)}}{\partial t} + \sum_\alpha \left(\frac{\partial f^{(N)}}{\partial \boldsymbol{q}_\alpha} \frac{\partial \mathcal{H}}{\partial \boldsymbol{p}_\alpha} - \frac{\partial f^{(N)}}{\partial \boldsymbol{p}_\alpha} \frac{\partial \mathcal{H}}{\partial \boldsymbol{q}_\alpha} \right) \tag{3.32}$$

$$\equiv \frac{\partial f^{(N)}}{\partial t} - \left[\mathcal{H}, f^{(N)} \right] \, , \tag{3.33}$$

which can be written in a more compact way with Poisson brackets as in Eq. (3.33). It depends only on the fact that $f^{(N)}(\boldsymbol{q}^N, \boldsymbol{p}^N; t)$ is a function of phase space points, where the motion is governed by the canonical equations of motion Eqs. (3.1) and (3.2). Written in alternative form,

$$0 = \frac{\partial f^{(N)}}{\partial t} + \sum_\alpha \left(\frac{\partial f^{(N)}}{\partial \boldsymbol{q}_\alpha} \frac{d\boldsymbol{q}_\alpha}{dt} - \frac{\partial f^{(N)}}{\partial \boldsymbol{p}_\alpha} \frac{d\boldsymbol{p}_\alpha}{dt} \right) \tag{3.34}$$

Liouville's theorem states that the motion of the points representing the systems in phase space is similar to the motion of an incompressible fluid, whose volume is preserved. This theorem and its other formal variants play an important role for classical statistical mechanics. We mention here three consequences [47, Ch. 4.1][786, Ch. 7.3].

(1) The right-hand-side of Eq. (3.32) is simply the total derivative of the density in time, $0 = \frac{df^{(N)}}{dt}$; therefore, the density is conserved in phase space. It describes the fact that the representative phase-space points accessed by the ensemble are neither created nor destroyed during its entire evolution. There are no attractors, which do appear in general *dissipative* dynamical systems (Hamiltonian or conservative systems have no dissipation). Dissipation is indeed tied to a loss of information – hence a lack of conservation of such representative phase space points, discussed in Sec. 3.5. Simply, put, if the system is isolated,

not all the phase space is available to it, since the motion is constrained by the conservation of energy.

(2) In accordance with this theorem, any extension in phase space would retain its volume in relative parts, but change shape (get stirred around), which may becomes so 'filamentous' over time. This is related with the notion of *mixing*. Equation (3.33) (or Eq. 3.32) is a $6N$ dimensional analog of the continuity equation of an incompressible fluid.

(3) Because of the conservative nature of the dynamical system, a point in the region between two surfaces of constant energy $(E, E + \delta E)$ will remain in the region forever: Hence the time-evolution of any set of points in this constrained area will remain there. In other words possible trajectories, i.e. N-bodied phase functions $X(t) = X(\boldsymbol{q}_1(t), \ldots, \boldsymbol{q}_N(t), \boldsymbol{p}_1(t), \ldots, \boldsymbol{p}_N(t))$ will lie on the surface $\mathcal{H} = E$ and enable one to define a stationary stochastic process. This is important for a microcanonical ensemble (see below), which embodies a *uniform* phase-space density over a small shell of energies $(E, E + \delta E)$. Accordingly, it remains uniform, which means it is time-independent. Establishing the formal equivalence of time and space averages spawned the development of ergodic theory.

Remark. We point out here that, crucially, the Liouville equation is invariant under time reversal, i.e. to every solution $f^{(N)}(\boldsymbol{q}^N, \boldsymbol{p}^N; t)$, there is a corresponding solution describing the reversed evolution; the same states are visited, just in reverse time-order (See, e.g., [775, Ch. 1.1.4]). The paradox addressed by Loschmidt is that real systems are irreversible in character at meso- or macroscopic scales, i.e. their evolution is time asymmetric (See Sec. 3.5). However, violations of the Second Law of Thermodynamics are observable for small systems [784]. As we have alluded to previously, it is virtually impossible to prepare the exact time-reversed state, and real systems are by no means completely isolated. Thus, we may have to admit here that this Hamiltonian model description of dynamics is condemned approximate, as the coupling to additional degrees of freedom outside the systems. Even very weak coupling may affect the dynamics of individual particles in a way to make the evolution sufficiently unpredictable. The highly nonlinear solutions of the Liouville equation are very sensitive to even a small violation of the time-reversal symmetry [775, Ch. 2].[8] Equilibrium system coupled to baths, i.e. non-isolated equilibrium ensembles (see further below), are affected by dissipative forces. Dissipation is tied to a direction of time [436, 439, 784, 787, 788] as long we track high-resolution dynamics of single particles, i.e. if we are fast enough in our measurements.

Conditions for statistical equilibrium

The condition on an ensemble for equilibrium is that the probability density distribution is preserved by its associated dynamics, so that probabilities of finding phase points in the various regions of space and associated statistics are time-independent. An equilibrium distribution function $f^{(N)} = f^{(N)}(\boldsymbol{q}^N, \boldsymbol{p}^N)$ should remain one forever.[9] What can we say about the density to make it a function of the $\boldsymbol{q}$'s and $\boldsymbol{p}$'s in a manner independent of time for all time at all points?

[8] For a potentially different viewpoint, arguing on the level of quasi-periodic recurrence, see Ref. [71].

[9] Ref. [787, Ch. 4] addresses this rigorously.

From the Liouville Eq. (3.34) we know the rate $\frac{\partial f^{(N)}(\boldsymbol{q}^N,\boldsymbol{p}^N;t)}{\partial t}$ at which the density would be changing in time at any selected point in phase space. Hence a uniform distribution

$$f^{(N)}(\boldsymbol{q}^N,\boldsymbol{p}^N) = \text{const} \tag{3.35}$$

would make the partial derivatives vanish

$$\frac{\partial f^{(N)}}{\partial \boldsymbol{q}_\alpha} = \frac{\partial f^{(N)}}{\partial \boldsymbol{p}_\alpha} = 0 \tag{3.36}$$

for all α, making

$$\frac{\partial f^{(N)}(\boldsymbol{q}^N,\boldsymbol{p}^N;t)}{\partial t} = 0\,. \tag{3.37}$$

More generally, if a the distribution f is a function of any integral of motion of the system $c_i(\boldsymbol{q}^N,\boldsymbol{p}^N)$, which is itself a function of the coordinates and momenta,

$$f^{(N)} = f^{(N)}(c_i)\,, \tag{3.38}$$

then we will get

$$\frac{dc_i}{dt} = \sum_\alpha \left(\frac{\partial c_i}{\partial \boldsymbol{q}_\alpha}\frac{d\boldsymbol{q}_\alpha}{dt} + \frac{\partial c_i}{\partial \boldsymbol{p}_\alpha}\frac{d\boldsymbol{p}_\alpha}{dt} \right)\,. \tag{3.39}$$

The Liouville equation for the density will then render

$$\frac{\partial f^{(N)}(c_i)}{\partial t} = -\frac{df^{(N)}}{dc_i}\sum_\alpha \left(\frac{\partial c_i}{\partial \boldsymbol{q}_\alpha}\frac{d\boldsymbol{q}_\alpha}{dt} + \frac{\partial c_i}{\partial \boldsymbol{p}_\alpha}\frac{d\boldsymbol{p}_\alpha}{dt} \right) = 0\,, \tag{3.40}$$

proving that this distribution will also be permanently maintained.

The microcanonical (N,V,E)–ensemble

As we discussed, a density distribution that is constant over the accessible region of phase space, or one that is explicitly a function of some integral of motion $f^{(N)}(\boldsymbol{q}^N,\boldsymbol{p}^N) = f^{(N)}\left(c_i(\boldsymbol{q}^N,\boldsymbol{p}^N)\right)$, will remain explicitly time-independent during the evolution of an isolated system evolution, i.e. $\partial f^{(N)}/\partial t = 0$. The most natural integral of motion is the total energy $c_i(\boldsymbol{q}^N,\boldsymbol{p}^N) \equiv \mathcal{H}(\boldsymbol{q}^N,\boldsymbol{p}^N) = E$. In the *microcanonical ensemble*, the N-particle system is constrained to a subvolume of phase-space – into an infinitely thin "shell" of width δE where the Hamiltonian takes on values between $(E, E+\delta E)$.

The corresponding density distribution in phase space that we write as $f_{\text{eq}}^{(N)}$ is defined as

$$f_{\text{eq}}^{(N)}(\boldsymbol{q}^N,\boldsymbol{p}^N|N,V,E) = C\delta(\mathcal{H}(\boldsymbol{q}^N,\boldsymbol{p}^N) - E)\,, \tag{3.41}$$

where C satisfies a normalization condition.

Note that the system is supposed to be finite in size (with constant volume V) as to guarantee a finite measure of each energy shell: Such a system would therefore be placed in an idealized container with hard walls, exerting forces

onto the system via purely elastic collisions:

$$V^{\text{ext}}(\boldsymbol{q}^N) = \begin{cases} 0 \text{ if } \boldsymbol{q}_\alpha \in V,\ \alpha = 1 \dots N \\ \infty \text{ else.} \end{cases} \tag{3.42}$$

The total Hamiltonian retains its general form as in Eq. (3.3). Any further integrals of motion (e.g. total angular momentum for isotropic systems and total linear momentum for homogeneous systems) can split up the energy shells into "subshells" with corresponding values of the fixed constants. There are no transitions between subshells. According to the *ergodic hypothesis*, a microcanonical system moves through the whole subshell once it is in this subshell.

If we calculate the ensemble average of the Hamiltonian, the internal energy, then

$$\begin{aligned} U &= \langle \mathcal{H} \rangle && (3.43) \\ &= \int \mathcal{H}(\boldsymbol{q}^N, \boldsymbol{p}^N) f_{\text{eq}}^{(N)}(\boldsymbol{q}^N, \boldsymbol{p}^N | N, V, E)\ d\Gamma^N && (3.44) \\ &= \int \mathcal{H}(\boldsymbol{q}^N, \boldsymbol{p}^N) C\delta(\mathcal{H}(\boldsymbol{q}^N, \boldsymbol{p}^N) - E)\ d\Gamma^N && (3.45) \\ &= E \int C\delta(\mathcal{H}(\boldsymbol{q}^N, \boldsymbol{p}^N) - E)\ d\Gamma^N && (3.46) \\ &= E && (3.47) \end{aligned}$$

This corresponds to a time-average of the Hamiltonian (which remains a constant E), in accordance with our assumption of ergodicity.

An equal probability density in phase space (Eq. (3.41)) – for a sub-volume of a fixed energy– is the basic assumption for the existence of the microcanonical ensemble, and thus for the rest of equilibrium statistical mechanics. This is on par with the Bayesian inference idea that all states are equally probable if we have no prior information (the hypothesis of equal *a priori* probabilities [88]), a viewpoint purported by Jaynes, which we will discuss in Sec. 3.5.2. However, proving this for Hamiltonian systems is far from easy and has led to the development of ergodic theory (see below).

Ergodicity

Formulated by Boltzmann in 1871, the assumption at the foundations of statistical mechanics says that the long time average of the dynamical quantities accessible to measurement is equal to the ensemble average of the same dynamical quantity taken with respect to a microcanonical ensemble (an isolated system).

Formally, the flow of state points on the energy shell is defined *ergodic*, when almost all points move in such a way that they pass through every small finite neighborhood on the energy surface, i.e. each point samples small neighborhoods over the entire surface during the course of its motion [48, App. C]. Additionally important is the property of *mixing* [47, 789], so that the flow reaches many, far-apart points of the system, though with ever "thinning" probability density.

Recall $f^{(N)}d\Gamma^N$ gives the probability of finding phase variables within the element $d\Gamma^N$ of the N-particle phase space of identical particles *a la* Gibbs' ensemble theory. We obtain the mean or ensemble average of dynamical variable $A(\boldsymbol{q}^N, \boldsymbol{p}^N; t)$ of the system of N isolated particles as follows:

$$\langle \mathcal{A}(t) \rangle_{f^{(N)}} = \int A(\boldsymbol{q}^N, \boldsymbol{p}^N; t) f^{(N)}(\boldsymbol{q}^N, \boldsymbol{p}^N; t)\, d\Gamma^N \,. \tag{3.48}$$

The observable $\langle \mathcal{A} \rangle$ could vary at each time-point. However, according to the ergodic hypothesis, the time-dependency of the statistics should disappear for microcanonical equilibrium systems, when the probability densities become stationary: $f^{(N)}(\boldsymbol{q}^N, \boldsymbol{p}^N; t) \to f^{(N)}_{\text{eq}}(\boldsymbol{q}^N, \boldsymbol{p}^N)$ for $t \to \infty$. Hence

$$\langle \mathcal{A}(t) \rangle_{f^{(N)}} \to \langle \mathcal{A} \rangle_{f^{(N)}_{\text{eq}}} \,.$$

Expressed in another way, any single trajectory of the system should render the same statistics in the long-time limit. Rather than following a full probability density, if we follow a *single* trajectory that we can denote formally as $\delta\left(\boldsymbol{q}(t), \boldsymbol{p}(t)\right)$, then we should obtain the same averages as with a stationary (equilibrium) ensemble

$$\lim_{\tau\to\infty} \frac{1}{\tau} \int_{t=0}^{\tau} \delta\left(\boldsymbol{q}(t), \boldsymbol{p}(t)\right) A(\boldsymbol{q}^N, \boldsymbol{p}^N; t)\, dt = \langle \mathcal{A} \rangle_{f^{(N)}_{\text{eq}}} \tag{3.49}$$

The left-hand-side of Eq. (3.49) represents what can be quantified "in practice", i.e. Eq. (3.6).

If the microcanonical ensemble is ergodic, then ergodicity applies to other ensembles as well (in equilibrium): We can apply it to the statistics of coarse-grained, *mesoscopic* states that are manifested, for example, due to a finite resolution of a measurement device, i.e. when $\{\boldsymbol{q}^N, \boldsymbol{p}^N\} \to \{M\}$. A time-series will render stochastic evolution of the system between these meso-states. The occupation probabilities of the mesoscopic states will become stationary given sufficient time – intuitively, because of the "self-averaging" properties of equilibrium systems.

In a grand-canonical ensemble, for example (described in the next Sec. 3.1.4), the number of particles is not fixed. The calculation of the ensemble averages involves a summation over averages obtained from ensembles on the microscopic level:

$$\langle \mathcal{A}(t) \rangle_{f^{(N)}} = \sum_N \int A(\boldsymbol{q}^N, \boldsymbol{p}^N; t) f^{(N)}(\boldsymbol{q}^N, \boldsymbol{p}^N; t)\, d\Gamma^N \,. \tag{3.50}$$

In any case, ergodicity allows for a *repeatability* of measured statistics, so that they do not depend on the time-point or on the measurement frequency, so long as "enough" samples are gathered. The issue of repeatability of measured quantities, having stationary statistics, is intimately tied to these being describable by Markovian dynamics [90, Ch. 1], which we discuss in Secs. 3.3 and 3.3.8. Yet, in nonequilibrium systems (Sec. 3.5.3), the time-windows may never be "long enough", which is associated with a loss of ergodicity.

3.1.4 Gibbs equilibrium ensembles

A system can also be a subsystem of a larger system which is itself in equilibrium, for example, when coupled to a heat bath. Exchanges of energy with the bath cause observables in the subsystem to fluctuate. This is the canonical ensemble. The grand canonical system additionally couples the subsystem to a large bath (source) of particle.

Large, macroscopic environments (baths) lead to statistical constraints on the systems of interest. All other, unconstrained variables of the system fluctuate. Compatible with this viewpoint is the "MaxEnt" approach by Jaynes [790, 791]: all equilibrium ensemble distributions can be derived from the condition that the information entropy functional is maximum; it is subject to constraints imposed on the ensemble. In the canonical ensemble, the average energy is constrained, as well as the normalization constant of the probabilities. In the grand canonical case, the average particle number is additionally constrained. We refer the reader to Refs. [48, 64, 92, 775] for explicit examples.

The canonical (N, V, T)–ensemble

The canonical ensemble [48, 64, 161, 785] is composed of systems of N identical particles that can exchange energy with a large heat reservoir or bath, which is so large that it maintains a constant temperature T for the system; it is denoted (N, V, T). We set $\beta = 1/k_{\mathrm{B}}T$.

The canonical partition function $\mathcal{Z}_N(V, T)$ is defined by

$$\mathcal{Z}_N(V,T) \;=\; \int d\Gamma^N \, \mathrm{e}^{-\beta\mathcal{H}(\boldsymbol{q}^N,\boldsymbol{p}^N)} \tag{3.51}$$

with the phase space measure $d\Gamma^N = \frac{1}{N!h^{3N}} d\boldsymbol{q}^N d\boldsymbol{p}^N$ (Eq. (3.9)).

The phase space density distribution $f_{\mathrm{eq}}^{(N)}$ is the Boltzmann distribution – the occupation probabilities of each microstate is proportional to $\mathrm{e}^{-\beta\mathcal{H}(\boldsymbol{q}^N,\boldsymbol{p}^N)}$, where the value of the energy $\mathcal{H}(\boldsymbol{q}^N, \boldsymbol{p}^N)$ varies:

$$f_{\mathrm{eq}}^{(N)}(\boldsymbol{q}^N, \boldsymbol{p}^N | N, V, T) = \frac{1}{N!h^{3N}\mathcal{Z}_N(V,T)} \mathrm{e}^{-\beta\mathcal{H}(\boldsymbol{q}^N,\boldsymbol{p}^N)} \;, \tag{3.52}$$

with $\beta = 1/\,k_{\mathrm{B}}T$.

In dealing with equilibrium fluid systems, often only the configurational integral $Q_N(T, V)$ is considered by integrating the momenta out of the partition function. This is possible when the kinetic and potential energy terms of the Hamiltonian separately depend on $\boldsymbol{q}^N$ and $\boldsymbol{p}^N$ (Eq. (3.3)), which is only the case in equilibrium. (For homogeneous fluids, $V^{\mathrm{ext}}(\boldsymbol{q}^N)$ is a global constant of the coordinates.) After integration, we are left with the configurational integral

$$Q_N(V,T) \equiv \frac{1}{N!} \int\limits_V d\boldsymbol{q}^N \, \mathrm{e}^{-\beta\Phi(\boldsymbol{q}^N)+V^{\mathrm{ext}}(\boldsymbol{q}^N)} \tag{3.53}$$

which is related to the full partition function by

$$\mathcal{Z}_N(T,V) = \Lambda^{-3N} Q_N(T,V) \;. \tag{3.54}$$

Here, Λ is the de Broglie wavelength that normalizes the momentum space.

Fundamental to statistical mechanics is the partition function. All statistical relationships (correlations) between microstates can be obtained from it. Thermodynamics is recovered by relationship between the partition function and the the Helmholtz free energy in this ensemble:

$$F(N,V,T) = -k_{\mathrm{B}}T \ln \mathcal{Z}_N(V,T) \; . \tag{3.55}$$

Using this, one can derive further relations between thermodynamic state functions. The first derivative of the log-partition function with respect to temperature renders the average "internal" energy, or inner energy U, of the system:

$$\begin{aligned} \left.\frac{\partial \ln \mathcal{Z}}{\partial T}\right|_{N,V} &= \left.\frac{1}{\mathcal{Z}}\frac{\partial \mathcal{Z}}{\partial T}\right|_{N,V} && (3.56)\\ &= \frac{1}{\mathcal{Z}_N(V,T)} \int d\Gamma^N \, \frac{\partial \mathrm{e}^{-\beta\mathcal{H}}}{\partial T} && (3.57)\\ &= \frac{1}{\mathcal{Z}_N(V,T) k_{\mathrm{B}}T^2} \int d\Gamma^N \, \mathcal{H}\mathrm{e}^{-\beta\mathcal{H}} && (3.58)\\ &\equiv \frac{U}{k_{\mathrm{B}}T^2} && (3.59) \end{aligned}$$

where

$$\frac{1}{\mathcal{Z}_N(V,T)} \int d\Gamma^N \, \mathcal{H}\mathrm{e}^{-\beta\mathcal{H}} \equiv U \; . \tag{3.60}$$

We can further derive the entropy from the thermodynamic relation

$$S = -\left.\frac{\partial F}{\partial T}\right|_{N,V} \; . \tag{3.61}$$

Inner energy, entropy, and free energy are related in one, famous equation equation:

$$F = U - TS \; . \tag{3.62}$$

The inner energy will *fluctuate* in the canonical ensemble. This is captured by the specific heat, which depends on second derivatives of the partition function. It can be shown to have the following form:

$$\begin{aligned} C_V &= \left.\frac{\partial U}{\partial T}\right|_{N,V} && (3.63)\\ &= \frac{1}{k_{\mathrm{B}}T^2} \left(\langle \mathcal{H}^2 \rangle - \langle \mathcal{H} \rangle^2 \right) \; . && (3.64) \end{aligned}$$

Systems in these ensembles can show phase transitions (in dimensions greater than one) due to the dissipative nature of the thermal bath. A standard example is the Ising model; there, the specific heat diverges at the critical point (See Sec. 3.2).

The grand canonical (μ, V, T)–ensemble

A grand canonical ensemble [26, 48, 64, 161, 785] is again composed of a system of identical particles in thermal contact with an external reservoir, but can

also exchange particles with an external *particle reservoir* that is considered huge. The state of this particle reservoir is assumed to be exactly controllable by a fixed value of a chemical potential μ, which is a macroscopic variable. This chemical potential is, in view of our ensemble, a conjugate field to the following "internal" variable: N, the particle number, in its *expectation value* $\langle N \rangle$. We explain the interpretation of conjugate fields more in Sec. 3.2 – they couple the microscopic or "internal" degrees of freedom of a system with a macroscopic system, by allowing these to *fluctuate* (have a variance), thereby setting fixed expectation values once the system reaches a stationary solution (equilibrium) under the new conditions. Discussion about these generalized external forces is continued in Sec. 3.3.3) after having introduced probabilistic many-body equations of motion in the form of master equations.

The normalization constant for densities in this ensemble is the grand canonical partition function

$$\Xi(\mu, V, T) = \sum_{N=0}^{\infty} \int d\Gamma^N \, \mathrm{e}^{-\beta(\mathcal{H}-\mu N)} \tag{3.65}$$

$$= \sum_{N=0}^{\infty} z^N \mathcal{Z}_N(V, T) \tag{3.66}$$

with *activity* or *fugacity* $z = \exp(\beta\mu N)$. The phase-space measure is $d\Gamma^N = \frac{1}{N!h^{3N}} d\boldsymbol{q}^N d\boldsymbol{p}^N$ (which entails a combinatorial pre-factor of $1/N!$ in each term within the sum).

The phase space density distribution over microstates of the system, denoted here as Ψ, is

$$\Psi_{\mathrm{eq}}(\boldsymbol{q}^N, \boldsymbol{p}^N | \mu, V, T) = \frac{1}{\Xi(\mu, V, T)} \mathrm{e}^{-\beta\mathcal{H}(\boldsymbol{q}^N, \boldsymbol{p}^N) + \beta\mu N} \, . \tag{3.67}$$

This describes a density over all microscopic phase space points with freely varying number N, i.e over *various* microscopic phase spaces, as each is defined on $(\boldsymbol{q}^N, \boldsymbol{p}^N)$. In this sense, the microscopic system now has a new phase space coordinate (a new degree of freedom), that which allows for a free energy to realize a fluctuating number of particles. The N-body probability density function over this extended phase space is

$$f_{\mathrm{eq}}^{(N)}(\boldsymbol{q}^N, \boldsymbol{p}^N; N | \mu, V, T) = \frac{1}{N! h^{3N} \Xi(\mu, V, T)} z^N \mathrm{e}^{-\beta\mathcal{H}(\boldsymbol{q}^N, \boldsymbol{p}^N)} \, . \tag{3.68}$$

The grand potential function is defined by

$$\Omega = -k_{\mathrm{B}} T \ln \Xi \, , \tag{3.69}$$

which plays the role of the canonical free energy in Eq. (3.55) in full formal analogy.

The average number of particles is given by the first derivative of the log-partition function:

$$\frac{\partial \ln \Xi}{\partial(\beta\mu)} = \frac{1}{\Xi}\frac{\partial \Xi}{\partial(\beta\mu)} \tag{3.70}$$

$$= \frac{1}{\Xi}\frac{\partial}{\partial(\beta\mu)}\sum_{N=0}^{\infty} z^N \mathcal{Z}_N(V,T) \tag{3.71}$$

$$= \frac{1}{\Xi}\sum_{N=0}^{\infty} N z^N \mathcal{Z}_N(V,T) \tag{3.72}$$

$$= \langle N \rangle \tag{3.73}$$

Fluctuations in the particle number can be shown to be the second derivatives of the log-partition function. It is also the derivative of the expectation value of the particle number:

$$\frac{\partial}{\partial(\beta\mu)}\langle N \rangle = \frac{\partial^2}{\partial(\beta\mu)^2}\ln \Xi \tag{3.74}$$

$$= \langle N^2 \rangle - \langle N \rangle^2 \,. \tag{3.75}$$

We employ the grand canonical ensemble in equilibrium studies of hard rods in Ch. 6. It is also the ensemble in which density functional theory is formulated, see below.

3.1.5 Density functional theory

Classical density functional theory (DFT) treats inhomogeneous systems of large numbers of identical particles [30–33, 69, 161, 792, 793][26, Ch. 3]. It was invented in 1964 by Hohenberg and Kohn to describe an inhomogeneous electron gas, which is why DFT is most commonly known in the context of quantum systems. Crucially, they discovered a functional for the internal energy depending solely on the electron density, but is valid for all external potentials. Mermin generalized this to finite temperatures.[10] The paradigm was later adapted to classical systems. DFT is rooted on a formally exact variational principle, where the equilibrium-averaged one-body density profiles come out of functional minimization of the grand potential (the free energy in the grand canonical ensemble); this is for general, inhomogeneous cases of fluids. The theory is thus state-of-the-art for calculating equilibrium properties. The theory operates in the grand-canonical ensemble (μ, V, T). A single-body density is defined by a "classical trace", which is simply an abbreviation for an integral over phase space variables $(\boldsymbol{r}^N, \boldsymbol{p}^N)$ [794, p.252]. For three dimensional space,

$$\mathrm{Tr}_{cl} \equiv \sum_{N=0}^{\infty} \frac{1}{h^{3N} N!} \int\int d\boldsymbol{r}_1 \cdots \int d\boldsymbol{r}_N \int\int d\boldsymbol{p}_1 \ldots d\boldsymbol{p}_N \tag{3.76}$$

which reduces the N-body distribution to one of a single body in the configuration space. The momenta are integrated out because in equilibrium, they can represent integrals of motion (constants) on any level, as long as one averages enough over time. The grand-canonical microstates are distributed with

[10] and references therein

$\Psi_{\rm eq}(\boldsymbol{q}^N, \boldsymbol{p}^N|\mu, V, T)$, according to Eq. (3.67). By defining a density operator

$$\hat{\rho}(\boldsymbol{r}) = \sum_{k=1}^{N} \delta(\boldsymbol{r} - \boldsymbol{r}_k) \tag{3.77}$$

for the position of each particle for an *inhomogeneous* fluid with N particles, we can obtain the averaged one-body density by the grand-canonical ensemble average $\langle\hat{\rho}(\boldsymbol{r})\rangle$:

$$\rho(\boldsymbol{r}) = \mathrm{Tr}_{cl}\left[\Psi_{\rm eq}(\boldsymbol{r}^N, \boldsymbol{p}^N|\mu, V, T)\sum_{k=1}^{N}\delta(\boldsymbol{r} - \boldsymbol{r}_k)\right] . \tag{3.78}$$

The grand-canonical free energy (grand potential) $\Omega([\rho(\boldsymbol{r})]; T, \mu,)$ – at fixed chemical potential μ and temperature T– can first be written, formally as a functional of this reduced one-particle density. There is a unique grand potential functional that becomes minimal for the equilibrium density [31]. The variational problem is therefore expressed as

$$\frac{\delta\Omega([\rho(\boldsymbol{r})]; T, \mu, V)}{\delta\rho(\boldsymbol{r})} = 0 . \tag{3.79}$$

The free energy functional is a Legendre transform of the grand potential:

$$\Omega([\rho(\boldsymbol{r})]; T, \mu, V) = \mathcal{F}([\rho(\boldsymbol{r})]; T) - \mu\int d\boldsymbol{r}\rho(\boldsymbol{r}) . \tag{3.80}$$

It can be split into three contributions:

$$\mathcal{F}[\rho(\boldsymbol{r})] \equiv \mathcal{F}^{\rm id}[\rho(\boldsymbol{r})] + \mathcal{F}^{\rm exc}[\rho(\boldsymbol{r})] + \mathcal{F}^{\rm ext}[\rho(\boldsymbol{r})] , \tag{3.81}$$

where

$$\mathcal{F}^{\rm ext}[\rho(\boldsymbol{r})] = \int d\boldsymbol{r}\,\rho(\boldsymbol{r})V^{\rm ext}(\boldsymbol{r}) \tag{3.82}$$

is the *external* contribution to the free energy functional for a *static* external potential $V^{\rm ext}(\boldsymbol{r})$ that only couples to the configurational degrees of freedom (a basic assumption about conservative fields). $\mathcal{F}^{\rm id}$ is the *ideal* term that represents an ideal-gas contribution, i.e. the entropic contribution from exchanging particle positions over all of space. It is exactly expressed by

$$\beta\mathcal{F}^{\rm id} = \int d\boldsymbol{r}\,\rho(\boldsymbol{r})[\ln(\Lambda^d\rho(\boldsymbol{r})) - 1] \tag{3.83}$$

where Λ is the (irrelevant) de Broglie wavelength (compare Eq. (3.54)). Finally, $\mathcal{F}^{\rm exc}$ is the *excess* free energy stemming from the particle interactions – the most interesting and difficult part to obtain. It represents the part of the functional that contains the full information about particle correlations. The variational problem can now be expressed as

$$\begin{aligned} \frac{\delta\Omega([\rho(\boldsymbol{r})]; T, \mu)}{\delta\rho(\boldsymbol{r})} &= \\ \frac{\delta\mathcal{F}^{\rm exc}([\rho(\boldsymbol{r})]; T)}{\delta\rho(\boldsymbol{r})} + k_BT\left(\ln(\Lambda^3\rho(\boldsymbol{r})) + \beta V^{\rm ext}(\boldsymbol{r}) - \beta\mu\right) &= 0 . \end{aligned} \tag{3.84}$$

At the heart of the theory is the one-to-one correspondence between the density distribution and the position-dependent external potential. The equilibrium density of a fluid under an external is that which uniquely minimizes the grand potential functional given the external potential (as well as temperature and chemical potential). Schematically,

$$V^{\text{ext}}(\boldsymbol{r}) \leftarrow \rho(\boldsymbol{r}) \ ,$$

which implies a few things directly: Any application of an external field to probe the system will generate a different (perturbed) density. One can learn something about two-point correlation functions in the fluid this way. Indeed, one can even "fix" one particle position at the origin and observe the structure of the fluid around it, if desired. And so, *all* equilibrium properties can be obtained given the knowledge of the excess functional – correlation functions are expressed as functional derivatives of the free energy with respect to the density (at equilibrium).

Yet, this presupposes having an exact excess functional, which is typically unknown. The most sophisticated approaches are those of *fundamental measure theory* (FMT) [27–30], which are constructed for *hard-core* particle systems and truly attempt at generating all many-body correlations, not only 2nd-order approximations. These had been formulated for general lattice systems of hard-core particles by Lafuente, Cuesta, and colleagues [159, 160, 262–266]. Some of the exact functionals that have been found are those of FMT, but constrained to zero or one dimensions (one exception is the free energy functional found by Percus for 1D fluids of hard rods [795]). In two and three dimensions, all these functionals are approximate. In this thesis, we compare the quality of an FMT functional for lattice rods in equilibrium in parts II and III.

* * *

In this section, we discussed the fundamentals of (equilibrium) statistical mechanics, including the ansatz of probability densities on phase space and the hypothesis of ergodicity. We introduced Gibbs ensembles, which are relevant for many further parts of this thesis. Specifically, we will work with the grand-canonical ensemble in Ch. 4, in which the fundamental-measure-theory density functional for hard rods in monolayer confinement will be derived. Moreover, we perform Markov-Chain Monte Carlo simulations in the grand-canonical ensemble in Ch. 6 to determine phase boundaries of the "isotropic–nematic" and gas–liquid transitions in 2D and 3D systems of hard (and sticky) rods.

3.2 "Coarse-grained", effective theories

Note: This section was written to provide a deeper understanding of probabilistic descriptions of classical many-body systems. Specifically, it aims to provide physical background behind probabilistic model approaches (variational mean field theory) used in a certain class of machine learning algorithms, variational autoencoders, which are studied in part IV of this thesis. Moreover, the discussion leads to notions of symmetry breaking, as well as phase transitions more generally, in Sec. 3.2.1.

Upon approaching a phase transition, in particular, at a critical point, quantities at all (or, at least, many[11]) mesoscopic scales fluctuate – "collective" properties become pronounced, involving many particles as correlations reach across ever larger portions of space [65]. Can we find "high-level" descriptions that render the correct macroscopic properties (mean values and fluctuations) based on a few phenomenological parameters?[12] As the long-wavelength-contributions are strongest at phase transitions, a "top-down" approach is typically taken, beginning with fluctuations of the global quantities such as order parameters. Scaling of e.g. susceptibility functions upon approaching a critical point quantifies the increasing contributions of ever larger wavelengths to fluctuations in macroscopic state functions. Fortunately, scaling relations are found to be rather universal in many systems observed in experiment. The hypotheses of *universality* and *scaling* provide some "secure footing" on which the construction of generic theories can be backed.

In statistical mechanics, we first distinguish between a microscopic and a statistical state [796]. A *microstate* $\boldsymbol{x}$ is a single point in (N-dimensional) phase space: It is a single "snapshot" of the system. Now, upon coupling this microstate to a thermal bath (a huge system that is itself in equilibrium) with temperature T, the system of interest moves between particular points in phase space in a stochastic manner. x The probability distributions ascribed to these points are the ensembles, which we discussed in Sec. 3.1. Any observable of the microstate of a system – such as the Hamiltonian – ultimately fluctuates.

All thermodynamic properties of this system of interest could be extracted from a partition function constructed by *summing* over all the microscopic states in a weighted manner (Boltzmann weights)

$$\mathcal{Z}(T) = \mathrm{tr}\left[\mathrm{e}^{-\beta\mathcal{H}(\boldsymbol{x})}\right] \tag{3.85}$$

with $\beta = \frac{1}{k_\mathrm{B}T}$, such as already defined in Eq. 3.51; the trace denotes here a general sum-over-microstates. Eq. (3.85) alludes to the fact that many questions in statistical mechanics can be reduced to formulating limit theorems for *properly normalized sums* of random variables with dependencies given by a model [774, p. 5]. The Boltzmann factor gives the probabilities of microstates of the system so that an effective theory can be expressed in terms of new variables, the *field* variables. The underlying uncertainty of the exact microstate of a system (whose knowledge would require a kind of "high-resolution limit") is taken care of in the form of a *new* stochastic, fluctuating field, often defined on a continuum. The new field is then a *coarse-grained* version of the old. We illustrate this with an example:

With an effective theory, i.e. *statistical field theory* [65–67, 768, 770, 797], we could describe the system at a mesoscopic scale, where "important" collective properties (e.g. large-scale fluctuations) are captured to a good approximation. We are seeking for the laws of physics emerging at mesoscopic scales, given knowledge at the microscopic scales.

We can try to invoke a notion of a field $m(\boldsymbol{x}) \equiv (m_1, \ldots, m_N)$ (N-dimensional field), where position is now a continuous variable $\boldsymbol{x} \equiv (x_1, \ldots, x_d)$

[11] in the case of first-order transitions

[12] Note that this is intimately tied to *compression*, i.e., can we extract a compressed version of the complex system? We go back to this when discussing machine learning in Sec. 3.6.

(d-dimensional space). $m(\boldsymbol{x})$ is an *averaged*, *local-scale* order parameter. Then eq. (3.85) can be written as

$$\mathcal{Z}([m(\boldsymbol{x})], T) = \mathrm{tr}\left[e^{-\beta\mathcal{H}}\right] = \int \mathcal{D}m(\boldsymbol{x})\mathcal{W}\left[m(\boldsymbol{x})\right] \ , \tag{3.86}$$

where, tr[] corresponds to a *trace* over all microstates (microscopic realizations), $\mathcal{W}\left[m(\boldsymbol{x})\right]$ are the corresponding probability weights for different microstates, and $\mathcal{D}m(\boldsymbol{x})$ denotes the measure over all possible realizations.[13]

Illustration

Let us consider the prototypical Ising Hamiltonian. The microscopic Hamiltonian is

$$\mathcal{H}(\boldsymbol{s}) = -J\sum_{\langle ij\rangle} \boldsymbol{s}_i\boldsymbol{s}_j \tag{3.87}$$

with J representing a universal coupling constants between spins $\boldsymbol{s}_i$ (which take on values +1 or -1 in the original case, but we write them more generally as vectors here), and $\langle ij\rangle$ denotes nearest-neighbor sums. To solve the full problem, we need to calculate the partition function for the model (in the canonical ensemble), whereby we treat configuration space only (no momenta):

$$\mathcal{Z}([\boldsymbol{s}], T) = \sum_i \mathrm{e}^{-\beta\mathcal{H}(\boldsymbol{s})} \tag{3.88}$$

One should be stroke by the giant challenge that this harmless-looking equation poses: (1) Find a way to account for ("write down") – in closed form – all and every *valid* configuration $\boldsymbol{s}$ (for infinite systems!). This is the central challenge. This is even more difficult when the models entail space-filling units of the fluctuating field that mutually exclude each other, such as hard rods. Imagining this were possible, we could proceed to (2) calculate the proper statistical weights of each of these configurations $\mathrm{e}^{-\beta\mathcal{H}(s)}$ (the Boltzmann factor), i.e. evaluate the Hamiltonian. We certainly would have had to write down all details about the structures at all length-scales in order to evaluate the Hamiltonian. Regarding hard-core particles plus vacancies,[14] the problem would have been fully solved once (1) is completed, as "valid" means abiding to a Hamiltonian with infinite energies for overlaps. All this is impossible in nearly all cases of 2D and 3D systems, gases excluded.

An effective theory of the Ising model begins by imagining a coarse-grained scalar order parameter, the *magnetization field* defined on positions $\boldsymbol{r}$ of spins $\boldsymbol{s}$

$$m(\boldsymbol{r}) = \frac{1}{R^d}\sum_{\|\boldsymbol{r}-\boldsymbol{r}'\|<R} \boldsymbol{s}' \tag{3.89}$$

summing over spins in a ball or radius R in d dimensions. The radius R would

[13] Equation (3.86) is a functional integral of the fields $m(\boldsymbol{x})$, also known as a *path integral*.

[14] The Ising model can be equivalently transformed into the lattice gas model of hard-core particles with unit volume.

set the scale of the coarse-graining. Alternatively, this amounts to a cutoff wave-number Λ in Fourier space:

$$m(\boldsymbol{r}) = m_0 + (2\pi)^{-d} \int\limits_{\boldsymbol{k}<\Lambda} d\boldsymbol{k}\, m_{\boldsymbol{k}} \exp(i\boldsymbol{k}\cdot\boldsymbol{r}) \tag{3.90}$$

where m_0 is the global mean order parameter and $m_{\boldsymbol{k}}$ represents the field value for wave-number k. The two definitions of the coarse-grained magnetization field are equivalent provided $2\pi/\Lambda \sim R$.

Performing an integration explicitly on the basis of the operation Eq. (3.89) is generally intractable.[15] We must postulate that a coarse-grained Hamiltonian can be constructed on basic, global considerations alone.

First, we should agree that a coarse-grained Hamiltonian should depend on the local magnetization and short range interactions, just like at the microscopic scale between spins. This notion is called *locality*. The interactions can then be expressed by gradients ∇m. We then consider the *symmetries* of the system, i.e. translational and rotational (discrete groups), given the system is not exposed to any nonuniform external force fields. Further, we should assure stability of fluctuations around the equilibrium solution, i.e. no linear terms of the fields or derivatives.

For the Ising example, the coarse-grained Hamiltonian will take on the form of an expansion with respect to even powers of the field variables and its gradients. We write it here as $\mathcal{F}[m(\boldsymbol{r})]$ as a d-dimensional integral (the dimensions of space):

$$\beta\mathcal{F}[m(\boldsymbol{r})] = \int d^d\boldsymbol{r} \left[\frac{t}{2}m^2 + \frac{K}{2}(\nabla m)^2 + um^4 + \dots\right] \tag{3.91}$$

where t, K, and u are phenomenological coefficients which, unfortunately, are *nonuniversal*, unknown functions of the original microscopic interactions, as well as external parameters such as pressure and temperature T (since we have to account for the entropy of the short-distance fluctuations lost in the coarse-graining process). This is the "price we have to pay" for by our postulate of the mathematical form of Eq. (3.91). The new weight for a particular configuration of the field $m(\boldsymbol{r})$ is

$$\mathcal{W}\left[m(\boldsymbol{r})\right] = \mathrm{e}^{-\beta\mathcal{H}[m(\boldsymbol{r})]}\,. \tag{3.92}$$

The effective Hamiltonian above (also known as the *Ginzburg-Landau* Hamiltonian) can be regarded as an effective *free energy*: it is obtained by integrating over microscopic degrees of freedom while constraining averages thereof to $m(\boldsymbol{r})$. We develop on this point in the next subsection. Nevertheless, the coarse-grained Hamiltonian (free energy) in Eq. (3.91) is a functional of the field variables $m(\boldsymbol{r})$.[16]

[15] Renormalization group methods can perform an iterative summation for calculating properties near critical points [593, 768, 798, 799]. A key aspect is self-similarity near criticality and that the microscopic Hamiltonian remains fully local, like in the Ising model.

[16] We note that if we add a "kinetic energy" term of $(\frac{\partial m}{\partial t})^2$, then we can model the dynamics (propagation) of long-wavelength variables in the system. This time-dependence can be a useful for modeling the growth of domains during phase separation kinetics [800], for example.

The theoretical "structure" of statistical physics

Living in the macroscopic world, if we wish to understand the many-body processes "behind the curtains" that give rise to our observables, we must probe the system in one way or another. At the end of the day, this amounts to exerting *forces* onto the system, which, when the latter has relaxed to equilibrium, will shift the energies of microscopic states. For any microscopic Hamiltonian, we can add a term that expresses the bias of a *conjugate field variable*. The term can be set to zero when the bias is "turned off". The fields are conjugate to mean values in the system, whereby these mean values can be mesoscopic in nature, i.e. fields over spatial position when treating, say, inhomogeneous systems.

Let us consider our microscopic Ising Hamiltonian further. We modify Eq. (3.87).

$$\mathcal{H}([\boldsymbol{s}]) = -J\sum_{\langle ij\rangle}\boldsymbol{s}_i\boldsymbol{s}_j - \sum_i \boldsymbol{h}_i\boldsymbol{s}_i + \cdots \tag{3.93}$$

with J being the coupling constants between spins $\boldsymbol{s}_i$, and $\boldsymbol{h}$ denoting the site-dependent conjugate fields that couple the to the spin variables, meaning our partition function is now also a function of these fields:

$$\mathcal{Z}([\boldsymbol{s}], \boldsymbol{h}, T) = \sum_i \exp\left(-\beta\ \mathcal{H}(\boldsymbol{s})|_{\boldsymbol{h}=0} - \sum_i \boldsymbol{h}_i\boldsymbol{s}_i\right) \tag{3.94}$$

For homogeneous systems, the simplest biasing field is a constant, i.e. $\boldsymbol{h} \to h$

$$\mathcal{H}([\boldsymbol{s}], \boldsymbol{h} = h) \quad = \quad -J\sum_{\langle ij\rangle}\boldsymbol{s}_i\boldsymbol{s}_j - h\sum_i \boldsymbol{s}_i\ . \tag{3.95}$$

Here is the nontrivial structure of statistical mechanics: the fluctuating variables are both the quantities averaged over to obtain observables and those that generate the statistical outcomes of the observables by being part of the Hamiltonian (Boltzmann weighting).

If we wish to define a *local mean magnetization* field $m = \{m_i\}$ and local *susceptibilities* $\hat{\chi} = \{\chi_{ij}\}$, they express the mean and and variance of the random spin variables (in equilibrium):

$$\begin{aligned}
m_i &\equiv \langle \boldsymbol{s}_i\rangle && (3.96)\\
\chi_{ij} &\equiv \frac{\partial m_i}{\partial \boldsymbol{h}_j} && (3.97)\\
&= \beta\left(\langle \boldsymbol{s}_i\boldsymbol{s}_j\rangle - \langle \boldsymbol{s}_i\rangle\langle \boldsymbol{s}_j\rangle\right) && (3.98)\\
&= \beta\left(\langle \boldsymbol{s}_i\boldsymbol{s}_j\rangle - m_i m_j\right) && (3.99)\\
&\equiv \beta C_{ij} && (3.100)
\end{aligned}$$

where $\langle \boldsymbol{s}_i\boldsymbol{s}_j\rangle$ are correlation functions of the local spins and C_{ij} is the *spin-spin* correlation function.

More generally, partial derivatives of the free energy function generate our local magnetization and susceptibility, i.e. *connected* correlations:

$$m_i = -\frac{\partial F}{\partial \boldsymbol{h}_i} \tag{3.101}$$

$$\chi_{ij} = -\frac{\partial^2 F}{\partial \boldsymbol{h}_i \partial \boldsymbol{h}_j} \tag{3.102}$$

The above expresses the *fluctuation-response theorem*[17] that relates how the statistical variables fluctuate in the presence of these conjugate fields, i.e external stimuli. $\frac{\partial F}{\partial \boldsymbol{h}_i}$ and $\frac{\partial^2 F}{\partial \boldsymbol{h}_i \partial \boldsymbol{h}_j}$ are *response functions* to the external fields.[18]

Equilibrium correlations functions are thus found by taking derivatives of the free energy. By the relation

$$\beta F([\boldsymbol{s}], \boldsymbol{h}, T) = -\ln \mathcal{Z}([\boldsymbol{s}], \boldsymbol{h}, T) \ , \tag{3.103}$$

we could also find that the partial derivatives of the partition function generate correlation functions of the spin variables in powers of β (it is the moment generating function):

$$\frac{\partial \mathcal{Z}}{\partial \boldsymbol{h}_i} = \beta \mathcal{Z} \langle \boldsymbol{s}_i \rangle \tag{3.104}$$

$$\frac{\partial^2 \mathcal{Z}}{\partial^2 \boldsymbol{h}_i \boldsymbol{h}_j} = \beta^2 \mathcal{Z} \langle \boldsymbol{s}_i \boldsymbol{s}_j \rangle \tag{3.105}$$

$$\vdots$$

In principle, one could try to expand the probabilities and conditional probabilities every type of many-body structure in terms of these correlation functions. For this reason we say that the partition function or the free energy functions contains the full information.

The relation in Eq. (3.100), i.e.

$$C_{ij} = k_{\mathrm{B}} T \chi_{ij} \tag{3.106}$$

between two-point correlation functions and susceptibilities is in err for approximate distributions (see sections below). Likewise, it is only valid for the *equilibrium* distribution (linear response regime) of a system. In fact, in the linear response regime (very near or in equilibrium), the so-called *fluctuation-dissipation theorem* holds:

$$\langle \boldsymbol{s}(t) \rangle_{h \neq 0} - m = \beta \left(\langle \boldsymbol{s}(t) \boldsymbol{s}(0) \rangle_{h=0} - m^2 \right) \ . \tag{3.107}$$

Fluctuations of mesoscopic or macroscopic variable near equilibrium are determinable (in principle) by this simple relation (Eq. 3.107). Far from equilibrium, however, fluctuations show a richer anatomy and their analytical form becomes intractable, generally. Unfortunately, finding an approximation needs to be handled on a case-by-case basis, usually requiring some form of a 'hard'

[17] See also Refs. [96, 801–803] for more on the fluctuation-response theorem.

[18] We can also say that the free energy is the cumulant generating function.

presumption on dynamics [93, 96].[19]

Gaussian models

As alluded to above, approximations to partition functions or their logarithms are necessary for calculating statistical properties of many-body systems. Mean-field methods neglect higher-order statistical dependencies among the field variables (correlations), apart from fixing their mean. Landau theory ignores fluctuations altogether.[20] Gaussian models represent a first-order correction, which allow for fluctuations while allowing the variables to remain statistically independent. They are tractable owing to the inherent mathematical simplicity of Gaussian distributions, which are fully determined by their means and variances (covariance matrix). All higher-order cumulants vanish. A Gaussian field theory for the free energy results from keeping the quadratic orders in the Ginzburg-Landau expansion. The partition function under these assumptions for d dimensions of space is

$$\mathcal{Z}_G([m],h) = \int \mathcal{D}m(\boldsymbol{r}) \exp\left\{ -\int d^d\boldsymbol{r} \left[\frac{t}{2}m^2 + \frac{L}{2}(\nabla^2 m)^2 - hm \right] \right\} . \quad (3.108)$$

The free energy (also called the effective Hamiltonian) for homogeneous systems (translational invariance) can be written as

$$\mathcal{F}_G([m]) = \frac{1}{2}\int d^d\boldsymbol{s}\, d^d\boldsymbol{s}'\, m(\boldsymbol{s})\mathcal{H}^{(2)}(\boldsymbol{s}-\boldsymbol{s}')m(\boldsymbol{s}') \quad (3.109)$$

where the microscopic "kernel" $\mathcal{H}^{(2)}(\boldsymbol{s}-\boldsymbol{s}')$ is symmetric, positive, and local. In the simplest examples, it represents a *differential operator*, a polynomial in the laplacian ∇_s^2:

$$\mathcal{H}^{(2)}(\boldsymbol{s}-\boldsymbol{s}') \equiv \mathcal{K}(-\nabla_s^2)\delta^d(\boldsymbol{s}-\boldsymbol{s}') . \quad (3.110)$$

For our Ising model, the microscopic kernels represent nearest-neighbor *laplacians*, i.e. *local curvature functions* of the magnetization field.

Functional integrals like Eq. (3.86) are very often approximated via the *saddle-point approximation*: The largest contributors to the integrals are the saddle points, i.e. those where the first derivatives are zero. A Gaussian-model offers a bounded approximation to the "true" integral (partition function) only when in equilibrium, a point made in the discussion on variational mean field theory below.

The renormalization group [593, 798, 799] provides a fixed-point iterative transformation procedure of the system's Hamiltonian so that the fixed point is the critical point. This relies on the self-similarity of the system at the transition. The renormalization fixed-point effective Hamiltonian (free energy) $\mathcal{H}^*$ for a Gaussian theory is a function of the gradients of the field $m(\boldsymbol{r})$ alone [65]:

$$\beta\mathcal{H}^* \propto \int d^d\boldsymbol{x}\, (\nabla m(\boldsymbol{r}))^2 . \quad (3.111)$$

[19] We note that various *bounds* on fluctuations as well as nonequilibrium work relations have been derived for nonequilibrium steady states [787, 804–806].

[20] See also Refs. [49, 566, 794, 807].

This relation may help in interpreting machine learning algorithms such as PCA and variational autoencoders, which we introduce in Sec. 3.6, as they work with Gaussian models, in effect, over statistical (input) data. The squared-gradients represent eigenvectors of the effective field theory.

Variational mean field theory

Standard variational mean field theory [49, 794] allows one to approximate the free energy of any system as a Gaussian theory of *trial densities*: Using the prototypical Ising example, which is microscopically very easy to define (with two possible states), the microscopic variables are discrete spins $\boldsymbol{s}$. The microscopic Hamiltonian $\mathcal{H}^{\text{mic}}$ is *quadratic* in form and *local*. The equilibrium distribution over the whole state of all spins $\rho^{\text{eq}}(\boldsymbol{s})$ can be approximated by another, tractable distribution. The latter is parametrized in some form, i.e. in terms of a trial density distribution $\rho^{\text{var}}(\{\Theta\};[\boldsymbol{s}])$ with free parameters $\{\Theta\}$, indirectly related to the spins $\boldsymbol{s}$. An optimization problem is now formulated: We minimize the variational free energy with respect to the free parameters of the trial densities.

Remark. We could write, instead, that $\rho^{\text{var}}(\{\Theta\};[\boldsymbol{s}]) \equiv \rho(\{\boldsymbol{m}_\alpha(\boldsymbol{s})\}_\alpha)$, where $\boldsymbol{m}_\alpha(\boldsymbol{s})$ is a multidimensional Hilbert space of *continuous* field variables. These are continuous degrees of freedom that arise from the parametrization $\{\Theta\}$ and are each distinguished by the index of α. This is the basic idea around variational autoencoders, which we describe more precisely later in Sec. 3.6.

The minimized variational free energy is an *upper bound* on the true free energy function in equilibrium situations. If one considers ρ^{eq}, the equilibrium probability density, then the optimized variational mean-field approximation ρ^{var} will entail an error, or deviation about the true density:

$$\rho^{\text{var}} \equiv \rho^{\text{eq}} + \delta\rho \,. \tag{3.112}$$

The correlations between the microscopic spins are calculated with the ensemble average over the trial densities

$$\langle \boldsymbol{s}_i \boldsymbol{s}_j \rangle_{\text{var}} = \int d\boldsymbol{s}\, \rho^{\text{var}}(\boldsymbol{s}) \boldsymbol{s}_i \boldsymbol{s}_j = \int d\boldsymbol{s}\, \rho^{\text{eq}}(\boldsymbol{s}) \boldsymbol{s}_i \boldsymbol{s}_j + \int d\boldsymbol{s}\, \delta\rho(\boldsymbol{s}) \boldsymbol{s}_i \boldsymbol{s}_j \tag{3.113}$$

will be accurate only up to linear order in $\delta\rho$.

However, the free energy will be accurate to *second order* in the deviation $\delta\rho$,

$$\mathcal{F}^{\text{var}} = \mathcal{F}^{\text{eq}} + \sum_{\boldsymbol{s}} \frac{\partial \mathcal{F}}{\partial \rho(\boldsymbol{s})}\bigg|_{\rho^{\text{eq}}} \delta\rho(\boldsymbol{s}) + \frac{1}{2} \sum_{\boldsymbol{s}_i, \boldsymbol{s}_j} \frac{\partial^2 \mathcal{F}}{\partial \rho(\boldsymbol{s}_i) \partial \rho(\boldsymbol{s}_j)}\bigg|_{\rho^{\text{eq}}} \delta\rho(\boldsymbol{s}_i) \delta\rho(\boldsymbol{s}_j) + \ldots \tag{3.114}$$

(As the free energy is an extremum, the second term in the expansion – the linear term – vanishes.) Therefore, *free energy differences* can be represented accurately by the variational free energy, while correlations among variables may not.

The free energy is proportional to the logarithm of the partition function, so it should entail the same topology. In a second order approximation, the saddle points are assumed to be areas with "significant" *local* curvature on the free energy surface, so that higher order terms can be neglected. From Eq. (3.102) we see that this curvature is the susceptibility tensor in *exact* descriptions; in

Gaussian approximate cases, the susceptibility shall contain errors that can be large; yet, the relative *depths* of these minima will be well approximated, similar to a least-squares approximation. The Gaussian approximation is a second-order approximation, and assumes the effective free energy landscape over the field variables is well-described by a distribution of local paraboloids.[21] These considerations are the basis for variational mean-field methods employed in machine learning, i.e. for variational inference. We continue the discussion in Sec. 3.6 and in part IV of this thesis.

3.2.1 Phase transitions

Ehrenfest (1933) [808] classified transitions by sorting them according two which thermodynamic quantities undergo discontinuous jumps. A singularity appears in the free energy and its derivatives, from which discontinuities of physical quantities (e.g. order parameters) emerge upon approaching the transition point. Yet, the mathematical complexity of phase transitions in terms of these singularities is greater than Ehrenfest had postulated, and the effects are more subtle. According to modern classification schemes, of phase transition comes in only two "kinds" [65, 789, 797]: First-order phase transitions [566] are deemed *discontinuous*, where basic macroscopic quantities like an order parameter show a sudden jump as a function of temperature, pressure, or chemical potential. *Continuous* transitions show different behavior in the changes of characteristics of a system: *Critical points* are the positions in phase diagrams where divergences in the susceptibility functions (fluctuations of the order parameter) appear, without a discontinuous jump in the order parameter itself.

Consider a system described by a microscopic configurational Hamiltonian $\mathcal{H}(\boldsymbol{x}, \lambda)$ where $\lambda = \lambda(t)$ represents a *time-dependent* external control parameter that adjusts properties of the system directly at some mesoscopic or macroscopic scale. The control parameter can represent a *conjugate field* that each microstate "feels" (Eq. (3.95)) which would "like to" bias the mean values at the macroscopic scale. For example, the magnetic field or a chemical potential biases the average magnetization or particle number of particles, respectively. The control parameter may also directly control the (inverse) temperature of the system (with respect to a reference temperature T_0), which is, in effect conjugate to the configurational Hamiltonian itself.

A continuous phase transitions occurs when an external control parameter exceeds a certain, critical value λ_c. On approaching this critical point, observed, large-scale dynamics become non-Markovian in character, which is tied to an effect in Markov-Chain Monte Carlo (MCMC) simulations known as *critical slowing down*. Two-time correlation functions (fluctuations) of structural variables diverge (in the thermodynamic limit), as well as spatial fluctuations, captured best by the variance of the most *global* structural variables of the system – the *order parameters*. In our prototypical example of the Ising model, a transition occurs when adjusting the temperature at zero external field conjugate to the magnetization. Upon crossing through the critical point, an ordered (ferromagnetic) phase (of two degenerate possible directions) forms spontaneously from the disordered phase.

This transition can be more easily understood by considering the state of the system "metastable" after the event [552]. The system will "jump" among the

[21] Also, the distribution of minima along the relevant (reaction) coordinates must be 'friendly' enough to guarantee mean behavior.

the degenerate subset of states, metastable "mesostates", which define separate regions of phase space. Thus, ergodicity is not lost from a global point-of-view (global balance). In MCMC simulations (described more in Sec. 3.4), this is seen as "flips" back-and-forth between these regions (by observing the order parameter values) that require very long waiting times to occur (similar to Fig. 2.1). In effect, ergodicity is only lost *transiently* when measurement time is shorter than that of these spontaneous flips.[22]

Symmetry breaking

In spontaneous symmetry breaking of a global-scale symmetry, the system responds to a control field by introducing a nonzero biasing conjugate field to the order parameter of the symmetry. Upon crossing λ_c, the order parameter of the symmetry will now take on a degenerate set of possible "choices" (different mean values). For continuous rotational symmetry breaking (the $\mathbb{SO}(n)$ group), this will mean that directional ordering occurs over *long spatial ranges*, such as in the XY model or nematic transitions. The *Goldstone theorem* states that the order-parameter *response functions* (the fluctuations) will develop a pole if the original state was uniform – the 'Goldstone modes' arise. Discrete symmetry breaking such as the spin group $\mathbb{Z}_2$ will induce an ordering transition where a discrete values of the magnetization is realized.

Symmetries and conservation laws are intimately tied in equilibrium systems, a manifestation of *Noether's theorem* in classical and quantum mechanics. An invariant or conserved quantity of any physical system expresses a symmetry group, and mathematically are related to the Hamiltonian via commutation operations (in quantum systems). In general, then, a break of a symmetry implies that Hamiltonian is not conserved. At continuous transitions, the system can be regarded as *perturbed* from an equilibrium state. In these terms, a spontaneous break of symmetry means the expectation values of the Hamiltonian in terms of "quasi-averages" does not coincide with those of the equilibrium averages (at zero perturbation) [775, Ch. 2]. All correlation functions after the transition entail a non-zero "rest" term in their expectation values that expresses one of the degenerate symmetric states persisting.

We note here that it is generally assumed that continuous symmetry breaking can only occur in $d \geq 3$, where d is the dimension of the system, for short-ranged-interacting systems [321]. Two-dimensional systems are well-known to show quite 'different' phase behavior that e.g. entails only quasi-long-ranged ordering upon the transition [333].

As in many simple fluids, a critical point λ_c marks the beginning of phase separation, below which a line of first-order transitions persists. These *abrupt* phase transitions break the *global translational* symmetry of the model, assuming it began in a homogeneous state. The confinement of the system to a 'corner' of phase space upon this kind of transition will have unavoidable thermodynamic implications (as we have alluded to in Ch. 2.2): Entropy is decreased if the full set of microstates is smaller. This needs to be compensated for via heat dissipation, requiring work – the transition entails a gap in the free energy that is significantly larger than $k_\mathrm{B}T$. Thus, crossing the phase boundary is "harder" than in the case of continuous transitions. A first-order transition connects two thermodynamic equilibrium (stable) states, which entail significant degrees of

[22] Truly "sharp" continuous transitions only really occur in infinite systems [66].

global translational order (spatial homogeneity for fluids, a lattice structure for solids). An example is the isotropic–nematic transition in the continuous bulk, where the nematic phase preserves a "fluid" character regarding the midpoints of rods.

Remark. Order parameters can be seen as collective variables of configuration space, and express the main eigenvalues of a Gaussian (bilinear) part of the free energy. In other words, in a system that shows symmetry breaking (like at coexistence) the largest amount of information about the state of the system is entailed in the order parameters alone – these express the best variable with which to *distinguish between* microstates, among different regions of phase space. (We also mentioned "collective variables" in general contexts of complex fluids in Ch. 2.1.3.) This notion is relevant for interpreting machine learning methods like variational autoencoders, which work with Gaussian 'free energy' models of data, which we employ in part IV of this thesis. These are introduced in more detail in Sec. 3.6.

Remarks on universality

In this thesis, we explore the phase behavior of highly idealized models – hard rods on lattices – from the viewpoint that they may render good analogies for more complicated systems (e.g. molecular). Experimentally shown in the middle of the last century, quantities like T_c (the critical temperature) are sensitive to the details of the inter-particle interactions of a system. In contrast, *critical exponents* can be universal, i.e. depending only on a small number of *generic* features: They are the key quantifiers of the divergence behavior of macroscopically relevant quantities around critical points.[23] This hypothesis of *universality* [65, 66, 770, 809–812] boils down the large variety of critical phenomena observed in systems to a few equivalence classes (*universality classes*). Therefore, universality should ensure that essential features of critical behavior can still be predicted even by rather crude models of physical systems: Though coming from a very different physical context, liquid–vapor transitions, binary mixtures of liquids, as well as many alloys (showing order–disorder transitions) belong to the same *Ising* universality class. In fact, in Ch. 6, we study the bulk order–disorder transition in systems of hard-core rods of lattices in 2D and 3D, which (as far as we can tell) belong to the same universality classes in the respective dimensions.

* * *

In this section we discussed effective theories for systems from a *static*, field-theoretic perspective. Later in this thesis, we will pinpoint ordering transitions in systems of hard rods confined to lattices in part III for the cases of 3D bulk and 2D confinement (using Markov-Chain Monte Carlo methods, described in Sec. 3.4). Further, we will calculate the equilibrium phase behavior of rods in various dimension (2D, 3D, (2+1)D) using *density functional theory*, specifically, fundamental measure theory. This will be derived in Ch. 4. Variational autoencoders (described in detail in Sec. 3.6) are based on the variational mean-field theory ansatz that we motivated in this section – we will employ them in Ch. 7.

[23] For static quantities in the canonical ensemble, for example, we first define the variable $\tau \equiv (T - T_c)/T_c$. The susceptibility χ (Eqs. (3.100) and (3.102)) in the Ising model, for example, diverges upon approaching the critical point (scales) according to $\chi \sim |\tau|^{-\gamma}$, where γ is the associated critical exponent.

We shall now move our discussion to *dynamics* of systems of particles coupled to a thermal bath. The dynamics of the N-body system with short-ranged, as well as hard-core interactions are presumed to be stochastic dynamics on the level of local, individual particle motion: The variables of the bath are effectively "integrated out", incorporated into transition rates of particles randomly "hopping" between lattice sites. Later in this thesis in part II, we will investigate nonequilibrium dynamics (during layer growth), which are modeled at this locally-Markovian level of approximation. More on the loss of ergodicity and inherently non-Markovian character of observed dynamics at larger, meoscopic or macroscopic scales, e.g. during phase transitions, is discussed in Sec. 3.5.3.

3.3 Master equations for dynamics in lattice systems

We mentioned in the last section that correlation functions have stationary, finite values in equilibrium systems. In equilibrium (and ergodic) systems, one should observe a system moving stochastically between well-defined mesoscopic states at some average rate. These dynamics typically express a Markovian character (laid out more specifically in Sec. 3.3.8), and, therefore, can be effectively described by *master equations* upon a first-level coarse-graining procedure. These master equations are the subject of this section in the context of lattice systems, which present a discrete set of states between which the system moves. These equations are also the basis for Markov-Chain Monte Carlo methods, which we introduce in Sec. 3.4 thereafter.

As motivated previously in this chapter, a probabilistic description of a many-body evolution is compatible with ignoring certain dynamical variables on phase space; master equations can be tuned to various levels-of-description. In this section, we focus on a fine-grained description, where the master equations can describe the equations of motion of single bodies coupled to a thermal bath – the probability densities are "sharply" localized on the configuration space of particles, but their momenta are effectively randomized: The motion is presumed locally random (locally diffusive) and locally in equilibrium with a bath. Thus, the dissipative nature of the thermal bath is a microscopic source of uncertainty in this system, driving the basic type of stochastic evolution inherent in all Monte Carlo methods. From this viewpoint, the master equations of N-body systems coupled to a bath can be "solved", numerically, with kinetic Monte Carlo simulations in this thesis (part II). These simulations are described in more detail in Sec. 3.4, but, we shall discuss the *transition rates* in this section (Sec. 3.3.4): At the fine-grained level of particles, we will see that master equations capture the causality of events ("actio=reactio") at a local scale (although entailing some uncertainty to *when* the reaction comes due to the random nature of motion at that scale). This expresses local force balance and, thus, local energy conservation within the smallest 'resolvable' unit of time. In fact, stationary master equations express a continuity equation.

Dynamics following master equations can be perturbed by nonequilibrium driving forces – when these do not interfere directly with the local configurational Hamiltonian. In general, a "weak-coupling limit" means an underlying configurational Hamiltonian is perturbed slightly; this will suffice to determine the evolution of the probability density of state occupations. (The master equation was originally derived for transitions between two states in

atomic systems by Pauli in 1928 [93, Ch. 3.3].) In a simpler model of reality, then, we presume that dynamics at the level of individual particles holds under the condition that external perturbations (like the deposition of new particles during thin film growth) remain statistically independent of the motion of particles (these remain locally Markovian). We discuss more on coarse-graining, a description in terms of "mesostates" in out-of-equilibrium conditions, and the breakdown of Markovian dynamics (at coarse-grained scales) later in Sec. 3.5.

Master equations are differential equations for time-dependent probability densities $p_j(t)$ of enumerable states $\{j\}$ [107, 774, 813, 814],[24] where the transitions between these states (at the relevant level of treatment, also in time) are *Markovian*, i.e. statistically independent of the history of the trajectory. The transition probabilities between states are denoted here as W_{ji}:

$$0 = \sum_j \left(W_{ji}(t) p_j(t) - W_{ij}(t) p_i(t) \right) + \frac{\partial p_i(t)}{\partial t} \, . \tag{3.115}$$

The master equation (Eq. 3.115) shows a trade-off between a gain of probability flux towards state i from states j in the first term of the sum with time-dependent transition rates $W_{ji}(t)$, and a loss of probability flux from state i to state j on the second term in the sum with rates $W_{ij}(t)$, both balanced by the time-derivative of the probability density.

We extend Eq. (3.115) to a more general case (which will be useful for describing a nonequilibrium system of interest) by making the left-hand-side *inhomogeneous*:

$$\frac{dp_i(t)}{dt} = \sum_j \left(W_{ji}(t) p_j(t) - W_{ij}(t) p_i(t) \right) + \frac{\partial p_i(t)}{\partial t} \, . \tag{3.116}$$

where the total change of probability in time to be in state i is entails a net probability flow (the sum on the right-hand-side) between states, and a "source" term $\frac{\partial p_i(t)}{\partial t}$ with the partial derivative of the probability versus time. Note that in most general cases, $W_{ij} \neq W_{ji}$. As we will see, systems that preserve a total probability mean that $\frac{dp_i(t)}{dt} = 0$, and the partial change of a probability in time represents how a system flows between states in equilibrium.

We will see that master equations represent (inhomogeneous) continuity equations found in classical field theories: those of many-body density distributions and respective currents. We shall discuss the ansatz made by classical dynamical density functional theory (DDFT) that was implemented in this thesis in Ch. 4, as well as kinetic Monte Carlo, implemented in Chs. 4 and 5.

Basic considerations: from deterministic motion (no bath) to stochastic motion (with bath)

The probability densities to find any particles in the full N-body phase space is expressed as a *N-body* density distribution $\rho^{(N)}(\boldsymbol{s}^N, \boldsymbol{p}^N, t)$, i.e. for particles in discretized phase space $(\boldsymbol{s}^N, \boldsymbol{p}^N)$. (Please note that $\boldsymbol{s}$ denotes lattice sites,

[24] These probability densities of the state could be considered *fields* $p_j(\boldsymbol{r}, t)$ over configurational space $\boldsymbol{r}$, as well.

and not lattice spins like in Sec. 3.2.) The Hamiltonian can be any general time-independent function of the phase space coordinates like Eq. (3.3). For equilibrium, in general, the external forces must be time-independent, and the inter-particle interactions only depend on coordinates (not momenta).

If all external forces are time-independent, the system is isolated, and the N-body probability density should evolve in accordance with the Liouville equation (Eq. (3.32)): the full motion is purely *deterministic* as long as we retain the *full information* of all coordinates and momenta, as argued in Sec. 3.5. In fact, this equation *is* a master equation for the N-body distribution of all particles $\alpha = 1 \dots N$. It has the form:

$$0 \;=\; \frac{\partial \rho^{(N)}}{\partial t} + \sum_{\alpha} \left(\frac{\partial \rho^{(N)}}{\partial \boldsymbol{s}_\alpha} \frac{d\boldsymbol{s}_\alpha}{dt} - \frac{\partial \rho^{(N)}}{\partial \boldsymbol{p}_\alpha} \frac{d\boldsymbol{p}_\alpha}{dt} \right) . \tag{3.117}$$

Given some initial condition of the phase space coordinates of all particles at $t = 0$, $(\boldsymbol{s}_\alpha(0), \boldsymbol{p}_\alpha(0))$, the density $\rho^{(N)}$ will evolve in a deterministic manner, where each $\frac{d\boldsymbol{s}_\alpha}{dt}$ and $\frac{d\boldsymbol{v}_\alpha}{dt}$ fulfill the Hamilton's equations of motion, Eqs. (3.1) and (3.2). (The Hamiltonian can be any general time-independent function of the phase space coordinates like Eq. (3.3).)

In the next two sections, Secs. 3.3.1 and 3.3.2, we will attempt to motivate and interpret the terms in the master equations for first one-, then N-body systems while treating deterministic motion (no coarse-graining, yet). However, we shall move from the microscopic picture of trajectories, in terms of the derivatives of the phase variables $\boldsymbol{s}_\alpha(t)$ and $\boldsymbol{p}_\alpha(t)$, to a picture in terms of currents $\boldsymbol{j}^{(N)}(\boldsymbol{s}, t)$ and their derivatives: The master equation will then be well-suited for describing systems coupled to thermal baths, where the motion of individual particles becomes *stochastic*, in effect, if we wish to only treat the sub-system of particles (not the bath). Coupling the system to thermal and particle baths are discussed in Sec. 3.3.3 thereafter.

Note: The entire presentation and discussion in the following Secs. 3.3.1–3.3.7 have a heuristic character, and we demonstrate no rigorous proofs or derivations. The aim is to prepare the reader to understand both a DDFT equation of motion for a nonequilibrium growth system of particles on lattices, investigated in Ch. 4, as well as the counterpart, N-body particle simulations (KMC) performed in the whole of part II. We also aim to discuss the general difficulty of describing N-body systems of interacting particles analytically, as well as the fundamental differences between equilibrium and nonequilibrium in the context of dynamics on lattices.

3.3.1 One-body dynamics

Note: Some of the notation in this and following sections is based on the lecture notes, Ref. [162].

To describe the evolution explicitly in terms of a time-dependent distribution over state space and time-dependent transition rates, the simplest place to begin is for non-interacting particle systems, even one that is *thermally isolated* (no bath, at first). Then each system $(\boldsymbol{s}_\alpha, \boldsymbol{p}_\alpha)$ is completely decoupled from all others, and we end up with equations motion for each one-bodied system, separately.

We need to "localize" the particles onto our chosen space-time $(\boldsymbol{s}, t)$. We can use the delta function to localize the configurational phase variable $\boldsymbol{s}_1$

$$\rho^{(1)}(\boldsymbol{s}, t) = \delta(\boldsymbol{s} - \boldsymbol{s}_1(t)) \tag{3.118}$$

we can define the localized particle current operator as

$$\boldsymbol{j}^{(1)}(\boldsymbol{s}, t) = \delta(\boldsymbol{s} - \boldsymbol{s}_1(t))\boldsymbol{v}_1(t) \tag{3.119}$$

where $\boldsymbol{v}_1(t) = \dot{\boldsymbol{s}}_1(t)$ is the velocity variable of a particle. A general, even time-dependent Hamiltonian will generate equations of motion that relate the rate of change of the momenta to *forces* (Eq. (3.5)). Hence we define a localized force field operator for completeness, where $\boldsymbol{f}_1(t)$ is a force at time t:

$$\boldsymbol{f}^{(1)}(\boldsymbol{s}, t) = \delta(\boldsymbol{s} - \boldsymbol{s}_1(t))\boldsymbol{f}_1(t) \tag{3.120}$$

The density operator can be further resolved *spatially*, as it represents a sum over contributions at each lattice site:

$$\rho^{(1)}(\boldsymbol{s}, t) \equiv \sum_i \delta(\boldsymbol{s}_i - \boldsymbol{s}_1(t)) \equiv \sum_i \rho^{(1)}(\boldsymbol{s}_i, t) \ . \tag{3.121}$$

The currents follow the same logic: we can define the localized particle current operator as

$$\boldsymbol{j}^{(1)}(\boldsymbol{s}_i, t) = \delta(\boldsymbol{s}_i - \boldsymbol{s}_1(t))\boldsymbol{v}_1(t) \ . \tag{3.122}$$

and the localized force-field operator as:

$$\boldsymbol{f}^{(1)}(\boldsymbol{s}_i, t) = \delta(\boldsymbol{s}_i - \boldsymbol{s}_1(t))\boldsymbol{f}_1(t) \ . \tag{3.123}$$

The dynamical equation for the density (resolved at each site of the lattice) should be expressible by a master equation because of the conservative nature of probability. We need to relate transition rates W of the generalized master equation (Eq. (3.116)) to the physical quantities defined above, specifically, to the current of Eq. (3.122). The evolution of the density will appear as:

$$\begin{aligned} \frac{d\rho^{(1)}(\boldsymbol{s}_i, t)}{dt} = \sum_{\langle ij \rangle} \left(W_i^{(1)}(\boldsymbol{s}_j, t)\rho^{(1)}(\boldsymbol{s}_j, t) - W_j^{(1)}(\boldsymbol{s}_i, t)\rho^{(1)}(\boldsymbol{s}_i, t) \right) \\ + \quad \frac{\partial \rho^{(1)}(\boldsymbol{s}_i, t)}{\partial t} \end{aligned} \tag{3.124}$$

where n is the local coordination number (in the case of square or cubic lattices, $n = 2d$, d being the dimension) and $\langle ij \rangle$ indicates nearest-neighboring sites, and $i \neq j$. The transition rates of the single-particle distribution will be written in a position-dependent form here, i.e. $W_j^{(1)}(\boldsymbol{s}_i, t) \equiv W_{ij}^{(1)}(t)$. In the section below, we will discuss how to "map" the deterministic motion on a lattice onto the master equation.

Stationarity, transition rates

Crucially, as we first assume the system is completely conservative (and deterministic), and the particles are non-interacting, we know that the velocities

will not change. We can thus reduce $v_i(t) \to v_i$ to a constant. The transition probability should reflect a forward derivative of the density operator in space: a *gradient* of the density, which will fully move from one position $\boldsymbol{s}_i$ to the neighboring one $\boldsymbol{s}_j$ within a unit time fixed by the velocity and lattice spacing. Thus, the transition probability is re-scaled with the constant velocity of the particle, in fact, with its component parallel to the forward direction.

The local unit directions $\boldsymbol{u}_{ij}^{+} = \boldsymbol{s}_j - \boldsymbol{s}_i$ (with j a *positive* spatial direction) allow us to define local gradient operators ∇_{ij}^{+}:

$$\nabla_{ij}^{+}\rho^{(1)}(\boldsymbol{s}_i,t) = \frac{\partial\rho(\boldsymbol{s}_i,t)}{\partial\boldsymbol{u}_{ij}^{+}} \equiv \left.\frac{\partial\rho(\boldsymbol{s},t)}{\partial\boldsymbol{s}_j}\right|_{\boldsymbol{s}=\boldsymbol{s}_i} \tag{3.125}$$

As the particle mass remains local (it does not spread in the fully-resolved, deterministic setting), the full mass moves from one unit cell to the next within a time-step. Then, the local transition flux (the rate times the density) between lattice sites should be proportional to the gradient in the density, $W_j^{(1)}(\boldsymbol{s}_i,t)\rho^{(1)}(\boldsymbol{s}_i,t) \propto \nabla_{ij}^{+}\rho^{(1)}(\boldsymbol{s}_i,t)$. Taking account of the (constant) particle velocity, we can interpret the transition rate as proportional to the local gradient operator

$$W_j^{(1)}(\boldsymbol{s}_i,t) \equiv \boldsymbol{v}^{(1)}\cdot\boldsymbol{u}_{ij}^{+}\nabla_{ij}^{+}\,. \tag{3.126}$$

Now, it is clear that in this case of fully resolved dynamics, the particle can be at *either* position $\boldsymbol{s}_i$ *or* position $\boldsymbol{s}_j$ at a fixed time-point t. So, the "gain" term $W_i^{(1)}(\boldsymbol{s}_j,t)\rho^{(1)}(\boldsymbol{s}_j,t) \equiv 0$ from neighboring sites must vanish. The density propagation in time is a *purely "forward" evolution*. Thus the sum in the master equation (Eq. (3.116)) becomes

$$\sum_{\langle ij\rangle} W_j^{(1)}(\boldsymbol{s}_i,t)\rho^{(1)}(\boldsymbol{s}_i,t) = \sum_{\langle ij\rangle}\boldsymbol{v}^{(1)}(\boldsymbol{u}_{ij}^{+}\nabla_{ij}^{+}\rho^{(1)}(\boldsymbol{s}_i,t) \tag{3.127}$$

$$= \boldsymbol{v}^{(1)}\cdot\nabla^{(\boldsymbol{s}_i)}\rho^{(1)}(\boldsymbol{s}_i,t) \equiv \nabla^{(\boldsymbol{s}_i)}\cdot\boldsymbol{j}^{(1)}(\boldsymbol{s}_i,t) \tag{3.128}$$

where in the last line we applied the definition in Eq. (3.122).

For isolated systems, the master equation is a continuity equation, as mentioned above. In our treatment of non-interacting particles, the master equation governs the motion of singular particles, i.e. it is "resolved" one-body level, over each lattice position $\boldsymbol{s}_i$:

$$\frac{\partial\rho^{(1)}(\boldsymbol{s}_i,t)}{\partial t} = -\nabla^{(\boldsymbol{s}_i)}\cdot\boldsymbol{j}^{(1)}(\boldsymbol{s}_i,t) = 0\,. \tag{3.129}$$

As we have *not* performed any act of coarse-graining, the equation of motion for the one-body density over all sites retains the same mathematical form:

$$\frac{\partial\rho^{(1)}(\boldsymbol{s},t)}{\partial t} = -\nabla\cdot\boldsymbol{j}^{(1)}(\boldsymbol{s},t) = 0\,. \tag{3.130}$$

Notably, stationarity means a *divergence-free* particle current: A lack of *sources* of energy density means a lack of "driving" currents that would introduce a disbalance in the currents of Eq. (3.128). Before developing on this notion, we will formulate the full N-body problem in the next section.

3.3.2 Many-body dynamics

For many-body systems, we first define an operator for the N-body density:

$$\rho^{(N)}(\boldsymbol{s},t) = \sum_{\alpha=1}^{N} \delta(\boldsymbol{s}-\boldsymbol{s}_\alpha) \equiv \sum_{\alpha=1}^{N} \rho_\alpha(\boldsymbol{s},t) \tag{3.131}$$

Similarly, the N-body currents

$$\boldsymbol{j}^{(N)}(\boldsymbol{s},t) = \sum_{\alpha=1}^{N} \delta(\boldsymbol{s}-\boldsymbol{s}_\alpha)\boldsymbol{v}_\alpha(t) \equiv \sum_{\alpha=1}^{N} \rho_\alpha(\boldsymbol{s},t)\boldsymbol{v}_\alpha(t) \tag{3.132}$$

and forces can be defined likewise:

$$\boldsymbol{f}^{(N)}(\boldsymbol{s},t) = \sum_{\alpha=1}^{N} \delta(\boldsymbol{s}-\boldsymbol{s}_\alpha)\boldsymbol{f}_\alpha(\boldsymbol{s},t) \equiv \sum_{\alpha=1}^{N} \boldsymbol{f}_\alpha(\boldsymbol{s},t)\rho_\alpha(\boldsymbol{s},t) \tag{3.133}$$

Following the discussion above, an isolated system with *many*, non-interacting particles will continue to abide to a continuity equation:

$$\frac{d\rho^{(N)}(\boldsymbol{s},t)}{dt} = -\nabla\cdot\boldsymbol{j}^{(N)}(\boldsymbol{s},t) = 0\,. \tag{3.134}$$

Interacting many-body dynamics: Highly correlated

Consider now short-ranged interactions between particles. In this case, we must consider the (imbalance of) currents *locally*, where the interactions play out.

If we want to have fully resolved dynamics, we need to localize the particles at every site, i.e. have "spatially localized" operators for the N-body density ready:

$$\rho^{(N)}(\boldsymbol{s}_i,t) = \sum_{\alpha=1}^{N} \delta(\boldsymbol{s}_i-\boldsymbol{s}_\alpha) \tag{3.135}$$

Similarly, the microscopic N-body currents

$$\boldsymbol{j}^{(N)}(\boldsymbol{s}_i,t) = \sum_{\alpha=1}^{N} \delta(\boldsymbol{s}_i-\boldsymbol{s}_\alpha)\boldsymbol{v}_\alpha(t) \tag{3.136}$$

and microscopic forces can be defined likewise:

$$\boldsymbol{f}^{(N)}(\boldsymbol{s}_i,t) = \sum_{\alpha=1}^{N} \delta(\boldsymbol{s}_i-\boldsymbol{s}_\alpha)\boldsymbol{f}_\alpha(\boldsymbol{s}_i,t)\,. \tag{3.137}$$

Microscopically, the forces exerted on each particle will come from the motion of the surrounding particles. Any external forces that are assumed to decouple from the microscopic dynamics of each particle will contribute, as well.

Unbalanced currents will emerge locally due to these forces. In equilibrium, these currents balance completely over a long-time average. The system

becomes *correlated* in the sense that the many-body density evolution must correctly express an order-of-events at each site $\boldsymbol{s}_i$ at every time-point of the evolution. Therefore, formally, we would have to solve the full time-evolution equations for each spatially localized density distribution at every site $\rho^{(N)}(\boldsymbol{s}_i, t)$. The propagation of one localized density will ultimately affect that of all others. It is clear that this is an impossible task, theoretically, without resorting to approximations (see discussion in Sec. 3.3.6). Simulations like kinetic Monte Carlo are clearly in advantage, in this sense, as they can generate one version of the ordering-of-events per execution (a random trajectory of the N-body system on a lattice coupled to a thermal bath).

Remark. We note additionally that time-ordering of events is lost, in general, when dissipative forces are at play. To be precise about our "fine-grained", N-body description, the exact time when an event (a particle hop) occurs remains uncertain. Upon coarse-graining at a higher level, like in attempting to reduce (perform a partial trace of) a many-body density (see Sec. 3.3.6), dissipative forces are introduced in the act, in effect, as we lose information about individual particle trajectories.

The full set of equations of motion on the N-body level is at hand in a *single, N-body equation-of-motion* when we take the *derivative* of the master equation (Eq. (3.134)) (the inhomogeneous term can be absorbed into the currents),

$$\frac{\partial^2 \rho^{(N)}(\boldsymbol{s}, t)}{\partial t^2} = -\nabla \cdot \frac{d\boldsymbol{j}^{(N)}(\boldsymbol{s}, t)}{dt} \,. \tag{3.138}$$

By the definition of the N-body currents (Eq. (3.132)), we find after some steps of calculation

$$\begin{aligned} \frac{d\boldsymbol{j}^{(N)}(\boldsymbol{s}, t)}{dt} &= \frac{d}{dt} \sum_{\alpha=1}^{N} \rho_\alpha(\boldsymbol{s}, t) \boldsymbol{v}_\alpha(t) && (3.139) \\ &= \sum_{\alpha=1}^{N} \frac{\partial \rho_\alpha(\boldsymbol{s}, t)}{\partial \boldsymbol{s}_\alpha} \frac{d\boldsymbol{s}_\alpha}{dt} \boldsymbol{v}_\alpha(t) + \sum_{\alpha=1}^{N} \rho_\alpha(\boldsymbol{s}, t) \dot{\boldsymbol{v}}_\alpha(t) && (3.140) \\ &= -\nabla \cdot \sum_{\alpha=1}^{N} \rho_\alpha(\boldsymbol{s}, t) \boldsymbol{v}_\alpha(t) \boldsymbol{v}_\alpha(t) + \boldsymbol{f}^{(N)}(\boldsymbol{s}, t)/m \,, && (3.141) \end{aligned}$$

where $\boldsymbol{f}^{(N)}(\boldsymbol{s}, t)/m = \sum_{\alpha=1}^{N} \rho_\alpha(\boldsymbol{s}, t) \dot{\boldsymbol{v}}_\alpha(t)$ is used. Therefore, the rate of change of the many-body current is directly related to the gradient of a kinetic stress tensor (that realizes transport) plus a many-body force.

The master equation for the N-body distribution on the lattice system is a differential equation that is explicitly first-order in time and works on the level of local, effective currents (fluxes). However, the transition rates for a flux are explicitly time-dependent, and these represent first-order derivative objects (velocities, rates). In terms of "Newton's laws" above, we must evaluate the imbalance of forces among the particles in-between time-steps. After a short-time integration step in-between, we arrive at the currents again. The new transition rates express the locally perturbed probability density currents.

On the fully-resolved *microscopic* level, a local divergence of currents, or the difference between "gain" and "loss" terms of the master equation, results from locally *imbalanced* forces – a "source" term of local energy density. A divergence

in the currents (a local imbalance) at a local site $\boldsymbol{s}_i$ could be related by

$$\boldsymbol{f}^{(N)}(\boldsymbol{s}_i, t-\delta t)\cdot\boldsymbol{v} \sim -\nabla\cdot\boldsymbol{j}^{(N)}(\boldsymbol{s},t)\ , \tag{3.142}$$

which, however, is delayed in time if we observe an imbalanced current at time t. The left-hand side of Eq. (3.142) expresses the power of the force fields – the work performed by the many-body forces per unit of time – which induces the imbalanced current at a very brief moment later. Notice that the original perturbation at site $\boldsymbol{s}_i$ must have a response that is non-local in space and in time in order to guarantee an evolution of the system (a time-evolution operator), which is why we must express the right-hand-side equations in terms of the full N-body densities.

Thus, a simple, second-order response to the forces at the same site (in the density variables) might be related to a gradient in density

$$\boldsymbol{f}^{(N)}(\boldsymbol{s}_i, t-\delta t) \sim -\nabla\rho^{(N)}(\boldsymbol{s}_j, t+\delta t) \tag{3.143}$$

which we interpret as "internal" forces (a diffusive term) in the system if the system is isolated. In thermal systems, which we describe further below, this corresponds to a "gradient-diffusion" force, i.e. will generate diffusive motion, locally, in an ideal gas. The response to the current will eventually relax the system towards equilibrium, beginning to even-out the densities in a second-order of δt (in the integration step), which means in a *squared* order in space. This is the basis for diffusive motion, which we describe further below.

Stationarity: Global balance of internal forces

The condition of a net force balance, then, is the sum of Eq. (3.142) over all sites $\boldsymbol{s}_i$. If energy is globally conserved (isolated systems), the sum is zero. Written differently,

$$0 = \nabla\cdot\boldsymbol{j}(\boldsymbol{s},t)\ . \tag{3.144}$$

The time-dependency of the total density is a global loss or gain of total probability. The global current becomes an *integral of motion* (j^{const}), which expresses the possibility for a global *steady state* of the system. Stationarity in the form of a master equation is thus fulfilled when the full sum over currents is zero. This is called *global balance*, discussed further in Sec. 3.3.4.

Indeed, if a system renders an approximately balanced current for *some* of the variables $\{\boldsymbol{s}\}_{i=1}^{m}$, $m < N$, then the system dynamics may be able to be split into stationary and non-stationary contributions, in the style of some near- or quasi-equilibrium approximations. Approaches that express mean fluxes among mesostates – which are related to a mean waiting times – may be applicable. (Please refer to the later discussions in Secs. 3.5.1 and 3.5.2.) We discuss mesoscopic balance conditions in Sec. 3.3.4.

3.3.3 Response to generalized forces

Statistical mechanics is about connecting the microscopic world with a macroscopic description, in terms of particle number densities and current densities (Sec. 3.1.2). To reduce the effective number of degrees of freedom from our *macroscopic* viewpoint, it is useful to imagine the response of the system to

some set of external forces, denoted here as "generalized forces". These couple to the microscopic velocities. In stationary states (for stationary solutions of equations of motion), the "free" momenta define the available *degrees of freedom* of the system (Sec. 3.1.1) – let us say there are F such degrees of freedom.

To repeat a crucial point, without reducing the distribution functions, i.e. without any loss of information about the many-body dynamics in the system, we can be sure the microscopic laws of physics are governed by Hamilton's equations of motion Eqs. (3.1) and (3.1). In non-isolated systems, the Hamiltonian will be time-dependent, and the evolution of the total energy in the form of Eq. (3.30). The external potentials in the Hamiltonian (Eq. (3.3)) are responsible for the time-dependence and generally complex evolution of the system.

For weak disturbances to a system, a dynamical theory can be formulated that is quasistationary in character (also called *adiabatic*): In so-called *linear response theory* [68, 96, 97, 815], equilibrium time-correlation functions suffice in describing a dynamical evolution, and the fluctuation-dissipation theorem, Eq. (3.107), holds. The latter also guarantees that equilibrium will be reached eventually. We will return to transport properties in thermal systems further below, where we will discuss how dissipative forces of "bath" variables relate to the fluctuations or correlations of the system variables.

More generally, however, we can write the Hamiltonian in the form [90, Ch. 1]

$$\mathcal{H}(\boldsymbol{p}_1, \ldots, \boldsymbol{p}_F; \xi_1 \ldots \xi_n) \tag{3.145}$$

for F degrees of freedom (momenta) and ξ_i corresponding to generally-defined *external parameters* (currents outside the system, positions of pistons, etc.) that depend on time in some way or could be controlled. From Eq. (3.30) and (3.145) we obtain

$$\frac{d\mathcal{H}}{dt} = \sum_{i=1}^{n} f_i \frac{d\xi_i}{dt} \,, \tag{3.146}$$

where

$$f_i(\boldsymbol{p}_1 \ldots \boldsymbol{p}_F; \xi_1 \ldots \xi_n) \equiv \frac{\partial \mathcal{H}}{\partial \xi_i} \tag{3.147}$$

is a *generalized force* associated with parameter ξ_i.[25] If, for example, ξ_i is the displacement of a piston, then f_i is the force on that piston. Therefore, the equations of motion within the system will involve the time-varying conjugate forces (parametrized by the changes in ξ_i) coupling to the momenta in some general way; the configurational variables of the "internal" system will evolve according to a local conservation of mass (probability) – a local continuity equation – as long as the forces are not "infinitely" strong.

We can think of this setup as a way to "probe" a many body system with our external, macroscopic world. An experimenter can control (fix!) only some part of the full set of external parameters: The rest will evolve freely in response. The nonequilibrium response within the system to the forces is captured by the fluctuations of the momenta, the current-current correlation functions. The

[25] Notice the general form coming from the right-hand-side of Eq. (3.5) together with Eq. (3.30).

work expended by the experimenter will thus generate nonequilibrium correlations between the "internal" configurational variables in a manner generally beyond linear response theory. Further, a weak "back-response" to the "outside" system might also be measurable in the fluctuations among the external variables, as long as these are fixed to some mean values with a certain variability (they are not completely independent).

The differential work performed on the system around time t is

$$\delta W(t) \equiv \sum_{i=1}^{n} f_i \, d\xi_i(t) \; . \tag{3.148}$$

which is not a total differential for non-conservative forces. This can be related to an increase of nonequilibrium entropy in the system δS (an entropy production) and increase in thermal energy. Indeed, very strong (and fast) forces may induce phase transitions (see Sec. 3.2.1). In such cases, the forces induce abrupt changes in the energetics of the systems and, thus, to the degrees of freedom (the "free" momentum variables) of the internal system. Furthermore, nonequilibrium stationary states can emerge in driven nonequilibrium systems, such as under shear (see Sec. 3.5.3), which completely change the nature of fluctuations and meaning of susceptibility functions within the fluid.

On the other end of the spectrum, weak forces (linear response regime!) may couple most strongly to only a subset of variables, i.e. those with the slowest or fastest relaxation times. In the former, average exchange rates for mesoscopic states (involving many particles) can change, or, in the latter, the microscopic transport coefficients (diffusion rates) can be altered. The latter may represent a slow change in temperature via the Einstein relation (Eq. (3.156)). Both these extreme situations might be suitable for *quasi-stationary* approximations of dynamical equations. For example, we investigate quasiequilibrium dynamics, during "slow" growth of a monolayer of purely hard-core rods in Ch. 4: There, the slowly varying quantity is the total particle number density, a collective quantity, for infinitely slow application of the external force (particle influx).

In any case, quantifying the response of nonequilibrium systems to external forces is the key for any formulation of many-body dynamics. The advent of nonequilibrium fluctuation relations [784, 805, 816–819] as well as the Jarzynski equality [820] have been milestones in this direction, where the latter states the following: work that external forces must perform to switch between between nonequilibrium steady states is directly related to the equilibrium free energy differences of these states.[26] [97, Ch. 9] Current fluctuations signify energy dissipation mechanisms in the system, and account for the global dynamical state of a system.

Particle reservoir coupling (quasistationary treatment)

In equilibrium, the particle reservoirs are expressed as (local) fields conjugate to the (local) particle numbers $N(\boldsymbol{s})$. These are (local) chemical potentials $\mu(\boldsymbol{s})$. The microscopic, perturbed Hamiltonian is

$$\mathcal{H}(\boldsymbol{s}^N, \boldsymbol{v}^N; \boldsymbol{\mu}) = \mathcal{H}(\boldsymbol{s}^N, \boldsymbol{v}^N; N)\Big|_{\boldsymbol{\mu}=0} - \sum_i \mu(\boldsymbol{s}_i) N(\boldsymbol{s}_i) \tag{3.149}$$

[26] These are defined on a mesoscopic level

The equilibrium distribution of microstates $\Psi^{\rm eq}(\boldsymbol{s}^N, \boldsymbol{v}^N|T, \boldsymbol{\mu})$ system represents that of the grand canonical ensemble, i.e. for fixed temperature and chemical potential (Eq. (3.67)). The (partial) derivatives of the free energy with respect to the conjugate fields (see Sec. 3.2) render correlation functions or fluctuations of the densities.

In the macroscopic world of the grand canonical ensemble, the particle number $N(\boldsymbol{s})$ is an expectation value, a spatial integral of the particle number density operator at a localized position in space, Eq. (3.135).

$$\sum_i \mu(\boldsymbol{s}_i)\langle N(\boldsymbol{s}_i)\rangle \;\; = \;\; \sum_{\boldsymbol{s}_i} \mu(\boldsymbol{s}_i) \int d\boldsymbol{s}\, \rho_{\rm eq}^{(N)}(\boldsymbol{s}_i; N|\mu_i) \; . \tag{3.150}$$

The conjugate fields connect the microscopic world (phase space trajectories) described by a microscopic Hamiltonian $\mathcal{H}(\boldsymbol{s}^N, \boldsymbol{v}^N; \boldsymbol{\mu})$ to the macroscopic description (configuration space densities in the grand canonical ensemble).

From the quasi-stationary point-of view, forces ascribed to the time-dependent part of the Hamiltonian are dissipative, and will act on a system in a stochastic manner. We describe this protocol for general thermal systems below. The time-dependent microscopic Hamiltonian couples the generalized forces of the bath to the number densities in each N-bodied system:

$$\frac{\partial \mathcal{H}(\boldsymbol{s}^N, \boldsymbol{v}^N; t)}{dt} \propto \sum_i \frac{\partial \mathcal{H}(\boldsymbol{s}^N, \boldsymbol{v}^N; t)}{\partial N(\boldsymbol{s}_i)} \frac{N(\boldsymbol{s}_i)}{dt} \equiv \sum_i f_\mu(\boldsymbol{s}_i, t) \frac{N(\boldsymbol{s}_i)}{dt} \; . \tag{3.151}$$

Here, $f_\mu(\boldsymbol{s}_i, t)$ are the generalized forces of the bath, which either insert or remove a particle from the coordinate.

The particle reservoir introduces fluxes or currents of particles $\frac{N(\boldsymbol{s})}{dt}$. Localized particle current density operators due to the bath can be expressed as

$$\boldsymbol{j}_\mu(\boldsymbol{s}_i, t) = \sum_\alpha \delta(\boldsymbol{s}_i - \boldsymbol{s}_\alpha) \frac{N(\boldsymbol{s}_i)}{dt} \tag{3.152}$$

in analogy to Eq. (3.136). Crucially, these are *assumed* to be independent from the "internal" currents within the system (under equilibrium conditions). (They are "orthogonal" to the system of interest.) As these "new" currents fluctuate, they enhance dissipation in accordance with the fluctuation-dissipation theorem (Eq. 3.107). In this way, thermodynamically unstable states can decay much more quickly and dynamics will "close in" to a "near-equilibrium" regime more rapidly. We see evidence for this effect when simulating particle evaporation-deposition during a nonequilibrium evolution of thin film growth,[27] discussed in Ch. 5. Particles can be transported across large distances, in effect, accelerating "nucleation-and-growth" kinetics during phase separation, for example. This may also imply that e.g. *spinodal decomposition* is faster than in the canonical ensemble.[28]

It seems obvious, then, that a fluid in the grand canonical ensemble will entail mesoscopic dynamics that are faster than in the canonical ensemble. This idea should have practical consequences for dynamical models "utilizing"

[27] preliminary investigations

[28] To "localize" a density distribution (in space) in the grand-canonical ensemble means we obtain a *mean* density – one over all sorts of many-body systems with variable N, which will entail many different "internal" currents at each site over which an average will be taken.

the grand canonical ensemble even for a canonical system, (e.g. DDFT, see discussion of Sec. 3.3.6). In nonequilibrium, "spurious" currents arising from exchanges from the bath may essentially 'ameliorate' e.g. jamming and any other highly nonequilibrium states, producing systematic errors. As above mentioned, phase separation kinetics may miss crucial features, as well.

On the other side of the same token, localized currents due to the coupling with the bath (Eq. (3.152)) can be used as an 'alias' for diffusive particle motion (one of the "internal" currents), at least for homogeneous fluids near equilibrium. A local diffusive current can be thought of as resulting from a particle (double) exchange event with the bath, describable with a (local) chemical potential difference between two states. The particle exchange motion is then a stochastic analog of hopping motion between sites (deleting a particle and placing it somewhere else is similar to (fast) diffusion, at least in near-equilibrium conditions). This idea is employed in a lattice DDFT (a master equation) formulated in Ch. 4 of this thesis.

Thermal systems (linear response regime)

From the form of the master equation, we can induce that changes in current densities and density distributions, owing to (imbalanced) forces, will propagate (summing over all neighboring states). Therewith, it is easy to understand where a delayed response to an external force comes from, and that this is inherently stochastic (embodied by the transition rates).

If a fluid is homogeneous on the relevant scale of treatment, then we can reduce the many-body density in equilibrium to a (mean) one-body density in equilibrium. The mean two-point density-density correlations are connected to the susceptibility (Eq. (3.106)). Thus, the linear response describes overdamped motion of a mean particle in accordance with the fluctuation-dissipation theorem (Eq. 3.107).

More generally, this expression is also valid for the N-body distribution in equilibrium. Eq. (3.134) holds true for equilibrium systems coupled to a thermal bath – in the long-time limit compared to the time-scale of the dynamics of the bath. Microscopically, the thermal bath acts with dissipative forces on each particle, i.e. the forces are assumed to be describable with stationary, *stochastic* dynamics. In this view, forces act virtually instantaneously on the relevant currents of the system of interest, and in a manner independent of the past. This is a *Markovian* assumption that expresses the notion that the huge bath is in equilibrium, internally, and with the physical system of interest. At the "interface" between the two subsystems, random fluctuations persist, driving the random motion of the system of interest. The forces on each particle can be assumed to be delta-correlated (produce white noise) [96, Ch. 1.3], i.e.

$$\langle \boldsymbol{f}_\alpha(t_1)\boldsymbol{f}_\alpha(t_0)\rangle = \langle \|\boldsymbol{f}_\alpha\|^2\rangle \delta(t_1 - t_0) \tag{3.153}$$

with a constant proportionality factor assumed to be homogeneous in space. A time-homogeneous process is described if the average correlation will not depend on the specific moment in time anymore, only on $\Delta t = t_1 - t_0$. The random forces cause particle motion to be "overdamped" because the responding momenta will be *randomized* locally. (Technically, these exclude any *inertial forces*.) The probability for an effective particle velocity $\boldsymbol{v}_\alpha$ will decay within a

waiting time Δt according to a Poisson process. The ensemble-averaged two-time correlation of these particle velocities will decay exponentially within a waiting time Δt that is long enough to express the overdamped motion

$$\begin{aligned}\langle \boldsymbol{v}_\alpha(t+\Delta t)\boldsymbol{v}_\alpha(t)\rangle &= \left\langle \int_0^{\Delta t} d\Delta t' \boldsymbol{v}_\alpha(t)\cdot\boldsymbol{v}_\alpha(t+\Delta t')\right\rangle \\ &= \langle \|\boldsymbol{v}_\alpha(t)\|^2\rangle \frac{1}{\gamma}\mathrm{e}^{-\gamma\Delta t}\,.\end{aligned} \tag{3.154}$$

The prefactor expresses a mean kinetic energy that must be equal to the thermal energy

$$m\langle \|\boldsymbol{v}_\alpha(t)\|^2\rangle \equiv k_\mathrm{B}T$$

in equilibrium (also when $\Delta t \to \infty$), a manifestation of the equipartition of energy. The characteristic relaxation time $1/\gamma$ indicates, therefore, a time-scale for dissipation of the mean kinetic energy.

Of course, these weak forces only contribute to an evolution of the physical system if it perturbs the system (within the time-scale of measurement) in a moment when the mean velocities (currents) have not yet become stationary. In other words, "overdamped" depends on time-scale of the level-of-treatment. A disturbance that generated a a small, imbalanced current will be related to a gradient in the density ("gradient diffusion"), which is the beginning of Brownian-type diffusive motion with diffusion rate $D(\boldsymbol{s})$:

$$\boldsymbol{j}(t) = -D(\boldsymbol{s})\nabla\rho(\boldsymbol{s},t)\,. \tag{3.155}$$

A relaxation of particle density distribution follows the propagation of this current, which we describe in the next section. The Einstein relation for equilibrium fluids connects the *diffusion coefficient* D, which characterizes the decay of the density fluctuations (see below), to the thermal energy and the random forces:

$$D = Mk_\mathrm{B}T\,. \tag{3.156}$$

The proportionality factor is the particle mobility M, the ratio of a mean particle drift velocity $\langle \boldsymbol{v}_\alpha\rangle$ to the magnitude of the applied force that induces fluctuations in the current, $M = \|\langle \boldsymbol{v}_\alpha\rangle\| \,/\, \|\boldsymbol{f}_\alpha\|$.

Diffusion

We assume a fluid is describable by a one body density that is initially in equilibrium (a constant distribution). We now assume some non-conservative external force $\boldsymbol{f}_\mathrm{ext}(\boldsymbol{s},t)$ perturbs a system at a particular time-point in the 'conservative' evolution of the isolated system.[29] It accelerates the motion of a single particle very briefly, and generates a small, unbalanced current or probability flux at site $\boldsymbol{s}_i$ at a minuscule time-step later. The unbalanced current will spread beyond the originally local summation. If the current has the form $\boldsymbol{j}(\boldsymbol{s},t) = \frac{d\boldsymbol{s}}{dt}\nabla\rho(\boldsymbol{s},t)$,

[29] It could equivalently mean that we "prepare" a system with an initial condition like a delta-function at some point in space.

then the long-time equilibrium limit will follow the global balance condition:

$$0 = \frac{\partial \rho(\boldsymbol{s},t)}{\partial t} - \nabla \cdot (\frac{d\boldsymbol{s}}{dt} \nabla \rho(\boldsymbol{s},t)) \tag{3.157}$$

Before equilibrium is reached, after an initial period, the disturbance will propagate in a way that is *self-similar* in time (it is a *Wiener process*), as a local response to a disturbance force is only "just behind" and will locally relax with a brief time delay (Markovian approximation). The generalized velocity variable $\frac{d\boldsymbol{s}}{dt}$ is a diffusion coefficient $D(\boldsymbol{s}) = D$, homogeneous, isotropic and constant for the simplest kinds of particle interactions. The global balance condition

$$0 = \frac{\partial \rho(\boldsymbol{s},t)}{\partial t} - D\nabla^2(\rho(\boldsymbol{s},t)) \ , \tag{3.158}$$

expresses an equation-of-motion for $\rho(\boldsymbol{s},t)$. The continuous-space and continuous-time solution is a spreading Gaussian distribution, beginning at an initial delta-distribution $\rho(\boldsymbol{s},t=0) = \delta(\boldsymbol{s}-\boldsymbol{s}_0)$:

$$\rho(\boldsymbol{s},t) = \frac{1}{\sqrt{4\pi D t}^d} \exp\left(-\left\|\boldsymbol{s}-\boldsymbol{s}_0\right\|^2 / (2dDt)\right) \ , \tag{3.159}$$

where the d indicates the dimension. These dynamics are purely Markovian and fulfill the following relation of central importance for statistical mechanics:

$$\left\langle \left\|\boldsymbol{s}-\boldsymbol{s}_0\right\|^2 \right\rangle_{\rho(\boldsymbol{s},t)} = \int\limits_{\boldsymbol{s}\in\Gamma} d\boldsymbol{s}\, \rho(\boldsymbol{s},t)\ \left\|\boldsymbol{s}-\boldsymbol{s}_0\right\|^2 = 2dDt \tag{3.160}$$

for long times t, which means that the average variance or spread in the position grows *linearly* with time.

Considering a lattice system with "fine-grained" resolution of densities and currents, we can clearly emulate this diffusive mode of transport over long times by stochastic "jump" processes between lattice sites. KMC simulations (Secs. 3.3.4 and 3.4.1), utilized in part II of this thesis, model diffusive transport of particles at a local level. Overdamped motion is assumed to occur at all times when particles are mobile, otherwise, particles cannot move *at all* if they are locally hindered due to hard-core repulsions. Additional attractive interactions effectively reduce the diffusion rate, locally, by introducing an energy barrier (the rate follows an Arrhenius law). We discuss this in the follows two sections.

3.3.4 Physical constraints on transition rates

In the absence of external time-dependent forces (not including the thermal bath), probability distributions over states should reach the equilibrium stationary state($\rho^{(N)}(\boldsymbol{s}_j,t) \to \rho_{\text{eq}}^{(N)}(\boldsymbol{s}_j)$) from an arbitrary starting state, given we wait long enough ($t \to \infty$). The density $\rho_{\text{eq}}^{(N)}(\boldsymbol{s}_j)$ now expresses that of one of the thermodynamic (Gibbs) *ensembles* discussed in Sec. 3.1.4. A system coupled to a bath with constant (lattice) volume will be represented with the canonical ensemble. The same coupled to a particle reservoir will be describable with a grand canonical ensemble (where N becomes a fluctuating variable).

The equilibrium balance conditions are used to design transition rates for events ("moves") in Markov-Chain Monte Carlo (MCMC) simulations. These *pseudodynamics* in phase space are used to sample the thermodynamic equilibrium (Boltzmann) distribution of N-body configurations: in essence, the chain is a random walk (diffusive-type motion) through configuration space. We shall discuss Markov-Chain Monte Carlo simulations in Sec. 3.4.2.

Global balance

We have discussed how global balance of currents is a property of isolated systems, and is a continuity equation that expresses total energy conservation (Sec. 3.130). Formally, this implies that transitions rates $\{W_i(\boldsymbol{s}_j, t)\}$ must fulfill

$$\sum_i \sum_j \left(W_i(\boldsymbol{s}_j, t)\rho_{\text{eq}}^{(N)}(\boldsymbol{s}_j) - W_j(\boldsymbol{s}_i, t)\rho_{\text{eq}}^{(N)}(\boldsymbol{s}_i) \right) = 0 \tag{3.161}$$

once the distribution reaches equilibrium. There, time t loses its absolute meaning and can be left out of the notation. On the flip side, any transition rates that fulfill this condition will lead a nonequilibrium density $\rho^{(N)}(\boldsymbol{s}, t)$ to global stationary solution (as long as the system is ergodic):[30] Formally, then, a nonequilibrium density representing a stationary state $\rho_{\text{st}}^{(N)}(\boldsymbol{s}_j, t)$ may also fulfill

$$\sum_i \sum_j \left(W_i(\boldsymbol{s}_j, t)\rho_{\text{st}}^{(N)}(\boldsymbol{s}_j, t) - W_j(\boldsymbol{s}_i, t)\rho_{\text{st}}^{(N)}(\boldsymbol{s}_i, t) \right) = 0 \, . \tag{3.162}$$

On another note, sophisticated, high-performance MCMC algorithms for equilibrium sampling have been developed that fulfill global balance, but, break local or detailed balanced (not in this thesis) (see e.g. Ref. [821]).

Local (detailed) balance

Detailed balance imposes the strongest balance condition among every and all pairs of states i and j, namely

$$W_i(\boldsymbol{s}_j, t)\rho_{\text{eq}}^{(N)}(\boldsymbol{s}_j) - W_j(\boldsymbol{s}_i, t)\rho_{\text{eq}}^{(N)}(\boldsymbol{s}_i) = 0 \, , \tag{3.163}$$

in equilibrium. This ultimately means that there is perfect *balance of forces* at the microscopic scale. The equilibrium densities are Boltzmann distributions over microstates

$$\rho_{\text{eq}}^{(N)}(\boldsymbol{s}_j) \propto \exp\left(-\frac{\mathcal{H}(\boldsymbol{s}_j)}{k_{\text{B}}T} \right) \, , \tag{3.164}$$

according to stationary, configurational Hamiltonians, i.e. local equilibrium.

To be more precise with the notion of local equilibrium in nonequilibrium situations, consider the system is at state j in time t. For the next time iteration, we perform a virtual displacement of the particle from $\boldsymbol{s}_j$ to the state $\boldsymbol{s}_i$ within an instantaneous time-scale δt, changing the probability density and Hamiltonian of the system, denoted here as $\tilde{\rho}$ and $\tilde{\mathcal{H}}$, respectively, the latter of which is implied in a changed transition rate $\tilde{W}_j(\boldsymbol{s}_i, t)$. The condition can be formulated

[30] Formally, aperiodicity of the Markov chain must also be fulfilled.

as

$$W_i(\boldsymbol{s}_j,t)\rho^{(N)}(\boldsymbol{s}_j,t) - \tilde{W}_j(\boldsymbol{s}_i,t)\tilde{\rho}^{(N)}(\boldsymbol{s}_i,t+\delta t) = 0\,. \tag{3.165}$$

This clearly guarantees detailed balance in equilibrium for $\rho(\boldsymbol{s},t) \to \rho^{\mathrm{eq}}(\boldsymbol{s})$, when any non-conservative external fields are "turned off". The main assumption about local balance is a *local Markovian* one: the exchange of energy between neighboring microscopic states $\boldsymbol{s}_i$ and $\boldsymbol{s}_j$ occurs faster than between next-neighboring, and all other states of the system. Local equilibrium expresses a *microscopic* continuity equation for short time-periods around time-point t. In fact, local balance presumes the time-independent part of the Hamiltonian governing the system is *local*, i.e. composed of short-ranged particle potentials with *pairwise interactions*, a fundamental ingredient to apply any field-theoretic notions of coarse-graining (Sec. 3.2).[31] The range of two-particle interactions sets the "fine-grained" spatial (and time-scale) limits of local balance of currents: Local balance only at somewhat larger (mesoscopic) scales express "cross-terms" resulting from coupling between orientational states among particles, for example. This connects with our discussion further above.

We assume the local microstates follow an equilibrium Boltzmann distribution for the locally stationary configurational Hamiltonian $\mathcal{H}(\boldsymbol{s}_j,[t])$ around each site $\boldsymbol{s}_j$, depending only *implicitly* on the absolute time-point of the macroscopic evolution. So, within an infinitesimal amount of time δt, the density is:

$$\rho^{(N)}(\boldsymbol{s}_j,t) \propto \exp -\frac{\mathcal{H}(\boldsymbol{s}_j,[t])}{k_{\mathrm{B}}T} \tag{3.166}$$

$$\tilde{\rho}^{(N)}(\boldsymbol{s}_i,t) \propto \exp -\frac{\tilde{\mathcal{H}}(\boldsymbol{s}_i,[t+\delta t])}{k_{\mathrm{B}}T}\,. \tag{3.167}$$

The relevant quantity at the mesoscopic scale (where the dynamics become stochastic) is the *ratio* of these transition rates

$$\frac{W_i(\boldsymbol{s}_j,t)}{\tilde{W}_j(\boldsymbol{s}_i,t)} = \frac{\tilde{\rho}(\boldsymbol{s}_i,t+\delta t)}{\rho(\boldsymbol{s}_j,t)} = \exp\left(-\frac{\Delta_{ji}\mathcal{H}(\boldsymbol{s},[t])}{k_{\mathrm{B}}T}\right)\,. \tag{3.168}$$

For systems with short-ranged attractive configurational Hamiltonians and hard-core repulsion, it is possible to express a forward transition rate by

$$W_i(\boldsymbol{s}_j,t) \;\propto\; \min\left\{1, \exp\left(-\frac{\tilde{\mathcal{H}}(\boldsymbol{s}_i,[t+\delta t]) - \mathcal{H}(\boldsymbol{s}_j,[t])}{k_{\mathrm{B}}T}\right)\right\} \tag{3.169}$$

$$\equiv\; \min\left\{1, \exp\left(-\frac{\Delta_{ji}\mathcal{H}(\boldsymbol{s}_j,[t])}{k_{\mathrm{B}}T}\right)\right\} \tag{3.170}$$

where the minimum condition avoids double-counting the configurational energy barrier between the states $\Delta_{ji}\mathcal{H}(\boldsymbol{s},[t])$ with the reverse process. The minimum condition implies there is a maximal rate for one direction, and a smaller rate for the other direction. The form of Eq. (3.170) is known as the *Metropolis algorithm* for MCMC methods (Sec. 3.4). Otherwise, one can choose

[31] Long-ranged interactions may pose a fundamental problem in that the systems may be non-ergodic, see discussion in Sec. 3.5.3.

to *halve* the effective energy barrier $\Delta_{ji}\mathcal{H}(\boldsymbol{s}_j,[t])$ for each direction,

$$W_i(\boldsymbol{s}_j,t) \quad \propto \quad \exp\left(-\frac{\Delta_{ji}\mathcal{H}(\boldsymbol{s}_j,[t])}{2k_{\mathrm{B}}T}\right) \tag{3.171}$$

Applied to a time-dependent density, local balance will express the *fastest, smallest-scale* fluctuations in the system.

"Mesoscopic" balance (qualitative discussion)

Notice that nonequilibrium stationary states can be stationary of the global-balance condition (Eq. (3.162)), as well. For example, a system can jump between various *metastable* states (i.e. there *is* no single, global minimum). For example, this occurs at coexistence in the grand-canonical ensemble or in a symmetry-broken phase (upon a continuous phase transition). There, the Markov chain still fulfills this global condition, where dynamically-coarse-gained, *rare* events characterize the dynamics *among* the states. (See also discussion on mesostates in Sec. 3.5.1.)

Thus, at the mesoscopic level-of-treatment, transitions occur among *subsets* or sub-partitions of phase space. Schematically, we can think of a partitioning of phase space into mesoscopic states $\Gamma_\alpha \subset \Gamma$. As we presume that the time-scales between transitions among metastable states is much longer than that of local dynamics, we can generally approximate the behavior as "equilibrium" within each metastable state, i.e. forces are approximately balanced.[32] Hence any state $\boldsymbol{s}_i$ states within the subsystem $\boldsymbol{s}_j \in \Gamma_\alpha$, would fulfill local balance (if the subsystem is approximately isolated), i.e.

$$\sum_{\boldsymbol{s}_j\in\Gamma_\alpha}\Big(W_i(\boldsymbol{s}_j,t)\rho^{(N)}(\boldsymbol{s}_j|\boldsymbol{s}_j\in\Gamma_\alpha) - W_j(\boldsymbol{s}_i,t)\rho^{(N)}(\boldsymbol{s}_i|\boldsymbol{s}_i\in\Gamma_\alpha)\Big) \approx 0\,. \tag{3.172}$$

The condition for restoring a global equilibrium state, however, after very long times means this subsystem must still find a transition path to other regions of phase space. Transition rates between coarse-grainable mesostates in this case means the global balance condition is shifted "one level up" in coarse-graining. Situations where mesoscopic balance occurs is at coexistence in the grand canonical ensemble, for example, if we consider each stable phase a "metastable" state in global equilibrium. This can be observed in MCMC simulations at coexistence or upon crossing a critical point – the system will 'jump' between symmetry-broken phases in a rare, abrupt event.

3.3.5 "Attempt" rates and random motion *a la* KMC

The proportionality factor in Eq. (3.170) is something like an "attempt" rate for the transition, i.e. an *a priori* probability for the transition due to thermal motion that decouples from the configurational Hamiltonian. Conceptually, an attempt rate means microscopic motion *faster than the considered level of coarse-graining*: A ratio of kinetic (thermal) energy $k_{\mathrm{B}}T$ versus an energy barrier $-U_b^{(i)}(\boldsymbol{s}_j)$ would

[32] In this way, we can consider the subspace as a *biased* ensemble, part of a general class of numerical "tricks" to accurately sample rare events in MCMC methods – *umbrella sampling*, for example.

render an effective rate

$$W_{ji}^{0} \equiv \exp\left(-\frac{U_b^{(i)}(\boldsymbol{s}_j)}{k_{\mathrm{B}}T}\right) \tag{3.173}$$

for an escape that happens at *intermediate* times of a locally balanced dynamics between lattice sites. Eq. (3.173) is an example of an *Arrhenius law*. Submicroscopically (way below the resolution the fastest processes considered in the master equation), this random motion is due to the coupling with a thermal bath (Sec. 3.3.3). Thus, both the "attempt" motion is inherently stochastic and renders "overdamped" dynamics.

Eq. 3.170 signifies that the random motion at site $\boldsymbol{s}_i$ can be considered a "chain" of events: A successful "attempt" motion, before the local configurational Hamiltonian is evaluated (which sets a lower limit on the local time-scale Δt), and an *uncertain* "acceptance" motion conditioned on the attempt that will slow the motion due to modified energy barriers evaluated at the intermediate state (at Δt). As the acceptance motion has less than one probability, it might hinder the *real* motion completely. As this "motion" is *virtual*, alluded to above in Sec. 3.3.4, it does not hinder the propagation of time $t \to t + \Delta t$. In another sense, the "attempt" motion is also virtual, but as it fixes the average minimal required time-step Δt (see below), we can call it "real" at the local scale. Both the "attempt" motion and the (conditional) "acceptance" motion are inherently overdamped and are suitably modeled by Poisson processes in-between time-steps.

In a kinetic Monte Carlo (KMC) simulation (described more generally in Sec. 3.4), the local random motion in the form of isotropic hopping diffusion with rate $W_i(\boldsymbol{s}_j, t)$ will be emulated by sampling a random *direction* i around $\boldsymbol{s}_j$ with relative probabilities

$$p^{rel}\left(\rho^{(N)}(\boldsymbol{s}_j, t) \to \tilde{\rho}^{(N)}(\boldsymbol{s}_i, t + \Delta t)\right) \equiv \frac{W_i(\boldsymbol{s}_j, t)}{\sum\limits_{i'} W_{i'}(\boldsymbol{s}_j, t)} \tag{3.174}$$

and by sampling a random, (bounded) value of a time-step Δt. This is chosen from a Poisson distribution of waiting times over each direction,

$$\Delta t(t) \sim p^{\mathrm{wait}}(\Delta t) = \exp\left(-\sum_{i'} W_{i'}(\boldsymbol{s}_j, t)\Delta t\right) . \tag{3.175}$$

The time-steps are written here as a function of the time-point t since the transition rates can change over time. In the case of *many* concurrent processes in-between time-steps, the joint Poisson distribution must be considered. Note here that in the assumption of *randomized* motion (momenta) due to a thermal bath, the exact ordering-of-events of concurrent processes is unknown, which we describe as a joint stochastic process. A random process (event or "move")

is sampled according to its relative rate versus the sum over all possible rates:

$$\Delta t(t) \sim p^{\text{wait}}(\Delta t) = \exp\left(-\sum_{kl} W_l(\boldsymbol{s}_k, t)\Delta t\right) \tag{3.176}$$

$$p^{rel}\left(\rho^{(N)}(\boldsymbol{s}_j, t) \to \tilde{\rho}^{(N)}(\boldsymbol{s}_i, t+\Delta t)\right) \equiv \frac{W_i(\boldsymbol{s}_j, t)}{\sum\limits_{k,l} W_l(\boldsymbol{s}_k, t)} \,. \tag{3.177}$$

$W_l(\boldsymbol{s}_k, t)$ lists all processes (e.g. "hopping moves") in the system from sites $\boldsymbol{s}_k$ to $\boldsymbol{s}_l$ that are *physically possible* at time-point t (exclusions are due to hard-core repulsions, for example).

We would like to remark on one detail here. If short-ranged *soft* repulsions between particles are added in the model system, the Arrhenius, attempt rate should absorb the repulsive potential This will shrink the minimal required time-step to resolve the locally "faster" dynamics due to short-ranged and weak repulsion. Away from other particles, the effective "hop" rate will be smaller by shifting the energy barriers in the rates again. We assume that the motion remains overdamped at the scales of the coarse-grained dynamics considered. As mentioned before, it is generally possible to split rates into many contributions if we assume the underlying Hamiltonian is separable (additive). Hence, ("weak") static external potentials are assumed to decouple from the other parts of the Hamiltonian and will not change the local Markovian or "overdamped" character of the dynamics, either. Again, these potentials are included in the (Arrhenius) energy barriers in the attempt rates. Slowly-changing external potentials could be added into the local Hamiltonian of the acceptance rates, as these are evaluated on-the-fly.

Within this locally-Markovian dynamical model of interacting particles, any "fast" or "strong" changes to the system by external means (temperature quenches, confinement potentials, rapid increase in particle number) or due to "thermodynamic forces" (actually, a disbalance of "internal" forces due to an unfavorable initial condition that causes phase separation, for example), break the local balance of "internal" forces, generating currents in the system and, therewith, a nonequilibrium response. Locally coherent structures at various mesoscopic scales emerge ("collective variables") in phase separation, for example, which we observe in Ch. 5 during thin film growth with a system of "sticky" hard rods.

3.3.6 Towards mesoscopic, analytical descriptions for nonequilibrium

Reduced distributions

We discussed the formal N-body dynamical evolution of interacting particles in the form of a master equation on lattices in Sec. 3.3.2. The difficulty lies in the system being highly correlated, and there is no easy way to extract the form of these correlations, even of a reduced set. Formulating equations of mesoscopic or macroscopic variables (order parameters) during the evolution will require some approximations, such as quasi-stationary (thermal or overdamped) motion for at least a subset of variables.

In isolated systems, the microscopic "evolution" is a *natural motion* that is completely reversible in time. In Sec. 3.1.2 we described how a density distribution $\rho^{(N)}(\boldsymbol{q}^N, \boldsymbol{p}^N, t)$ can be defined in a clear way, given the "sharp" microscopic motion of phase variables (phase space trajectories). Unfortunately, if we wish to describe the dynamical evolution in terms of a one-body density system $\rho^{(1)}(\boldsymbol{q}^N, \boldsymbol{p}^N, t)$, then we run into problems: In the thermodynamic limit ($N/V \to \infty$), this amounts to solving an infinite set of coupled integro-differential equations. If particles interact with each other, then we cannot decouple these into a set of one-body equations of motion for the density functions. In fact, the dependencies form a *hierarchy* of reduced s-body distribution functions, known as the *BBGKY* (Bogoliubov–Born–Green–Kirkwood–Yvon) hierarchy [26, 95]: Determining an f particle distribution means we need to know the $(f+1)$ particle distribution.

Knowledge of the one, two, and possibly three-body distribution functions is usually sufficient for calculating relevant *observables*; however, these equations will not form a closed set of two or three equations [95, Ch. 4]. Therefore, dynamical theories of equilibrium that work on the basis of two or three-bodied distribution functions must entail some approximations or *closure* relations. The Boltzmann or Vlasov equations, or even *master equations* of the reduced set are some examples.

The typical master equations discussed in this chapter are valid within thermal systems, which are a bit more subtle, as their form of natural motion in equilibrium is stochastic (locally Markovian, "overdamped" motion).[33] Fluctuations at microscopic scales due to the thermal bath generate a very weak uncertainty of the precise microscopic state at smallest scales treated.

Putting this subtlety aside, these systems will entail the same difficulty in reducing the master equation for the "sharp" N-body distribution from $\rho^{(N)}(\boldsymbol{s}, t)$ to a one-body distribution function $\rho^{(1)}(\boldsymbol{s}, t) \equiv \rho(\boldsymbol{s}, t)$. We speculate this has to do with the lost time-ordering of events when integrating out the (N-1) other equations of motion. We may be forced to consider taking the limit $\Delta t \to 0$ in nonequilibrium conditions, for example, where we will need to "resolve" the dynamics at ever shorter time- and length-scales. Thus, it may be difficult or impossible to find a universal transition rate $W_i(\boldsymbol{s}_j, t)$ between discrete states $\boldsymbol{s}_i, \boldsymbol{s}_j$ at an exact time-point t for *all* realizations of the system. DDFT makes an approximation which is quasistationary and *mean* in character, which we describe below.

Weakly coupled systems can render a closed one-body equation for $\rho^{(1)}(\boldsymbol{s}, t)$ in a mean-field approximation, where correlation functions of order higher than a certain number f can be neglected, while correlation functions of lower order ($\leq f$) can be expressed in terms of the one-particle reduced distribution function [95, Ch. 5]. The resulting equations of motion are considered those of a *kinetic regime*.

Approximation to one-body dynamics: DDFT

In density functional theory, static, *configurational* properties of equilibrium are captured by the mean one-body density $\rho(\boldsymbol{s})$ defined as a grand-canonical ensemble average (a classical "trace" operator (Eq. 3.78)) of a localized one-body

[33] Note, however, that even deterministic motion, i.e. the microcanonical ensemble, can be expressed in terms of a master equation (Liouville equation, or in a piecewise manner [774, Ch. 5].

function $\hat{\rho}(\boldsymbol{s}) \equiv \sum_{\alpha} \delta(\boldsymbol{s} - \boldsymbol{s}_{\alpha})$. This mean density is also a functional derivative of the grand potential functional with respect to an external (static) field:

$$\rho(\boldsymbol{s}) = \left. \frac{\delta \Omega[V^{\text{ext}}(\boldsymbol{s})]}{\delta V^{\text{ext}}(\boldsymbol{s})} \right|_{\mu VT} . \tag{3.178}$$

If we define a "local" chemical potential via

$$\mu_{\text{loc}}(\boldsymbol{s}) = \mu - V^{\text{ext}}(\boldsymbol{s}) \tag{3.179}$$

then we can see that

$$\rho(\boldsymbol{s}) = - \left. \frac{\delta \Omega[\mu_{loc}(\boldsymbol{s})]}{\delta \mu_{loc}(\boldsymbol{s})} \right|_{VT} . \tag{3.180}$$

Further, we can find the relation

$$\left. \frac{\delta^2 \Omega[V^{\text{ext}}(\boldsymbol{r})]}{\delta V^{\text{ext}}(\boldsymbol{s}) \delta V^{ext}(\boldsymbol{s}')} \right|_{\mu VT} = - \left. \frac{\delta \rho(\boldsymbol{s})}{\delta V^{ext}(\boldsymbol{s}')} \right|_{\mu VT} \tag{3.181}$$

$$= \beta \left(\langle \hat{\rho}(\boldsymbol{s}) \hat{\rho}(\boldsymbol{s}') \rangle - \rho(\boldsymbol{s}) \rho(\boldsymbol{s}') \right) \big|_{\mu VT} \tag{3.182}$$

$$= \chi(\boldsymbol{s}, \boldsymbol{s}') \big|_{\mu VT} \tag{3.183}$$

where the right-hand side expresses the response of the density with respect to an external conjugate field at another position in space (See Sec. 3.2). The density response is also known as a susceptibility $\chi(\boldsymbol{s}, \boldsymbol{s}')$. This means that the response is completely expressible in terms of the grand potential functional $\Omega[\rho(\boldsymbol{s}); V^{\text{ext}}(\boldsymbol{s})]$. We can also connect this response to the fluctuation-dissipation theorem (Eq. (3.107)), which means that for weak perturbations from equilibrium, the mean, time-dependent density $\rho(\boldsymbol{s}, t)$ will propagate according to equilibrium response functions (Brownian diffusion).

This is a small motivation for DDFT. On the lattice system, we can begin by assuming a local equilibrium of fluxes (Eq. (3.165)) defined by mean one-body densities $\tilde{W}_j(\boldsymbol{s}_i, [t])\rho(\boldsymbol{s}_i, t)$ and $\tilde{W}_i(\boldsymbol{s}_j, [t])\rho(\boldsymbol{s}_j, t)$ along with some mean transition rates. The relative transition rate between the locations defines the microscopic motion at site $\boldsymbol{s}_i$, and can be considered to arise from a difference in an external potential $\Delta_{ij} V^{\text{ext}}(\boldsymbol{s})$ applied a neighboring site from $\boldsymbol{s}_i$. By Eq. (3.179), we can interpret the disturbance as a disbalance

$$\Delta_{ij} \mu(\boldsymbol{s}) \equiv \mu(\boldsymbol{s}_j) - \mu(\boldsymbol{s}_i) \tag{3.184}$$

in the local chemical potential. The local chemical potential is related to the free energy by a functional derivative

$$\mu(\boldsymbol{s}_i) = \frac{\delta \mathcal{F}(\boldsymbol{s}_i)}{\delta \rho(\boldsymbol{s}_i)} \tag{3.185}$$

$$= \frac{\delta \mathcal{F}^{\text{exc}}[\rho(\boldsymbol{s})]}{\delta \rho(\boldsymbol{s}_i)} + \frac{\delta \mathcal{F}^{\text{id}}[\rho(\boldsymbol{s})]}{\delta \rho(\boldsymbol{s}_i)} \equiv \mu^{\text{exc}}(\boldsymbol{s}_i) + \mu^{\text{id}}(\boldsymbol{s}_i) \tag{3.186}$$

The "external field" disturbance is thus due to a local excess chemical potential difference $\Delta_{ij}\mu^{\text{exc}}(\boldsymbol{s})$ between the sites.[34]

In terms of a local configurational "Hamiltonian" $\tilde{\mathcal{H}}(\boldsymbol{s},[t])$ that depends on the moment of the evolution implicitly, we have the local balance condition in analogy to that of the full N-body evolution in Eq. (3.170):

$$\frac{\tilde{W}_j(\boldsymbol{s}_i,[t])}{\tilde{W}_i(\boldsymbol{s}_j,[t])} = \frac{\rho(\boldsymbol{s}_j,t)}{\rho(\boldsymbol{s}_i)}\exp\left(-\beta\Delta_{ij}\tilde{\mathcal{H}}(\boldsymbol{s},[t]) + \beta\Delta_{ij}\mu^{\text{exc}}(\boldsymbol{s},[t])\right) . \tag{3.187}$$

However, density functional theory is a *mesoscopic* theory, working with mean values of densities over a grand canonical ensemble. From its viewpoint, statistics are obtained by long-time observation or an integration over phase space variables – concepts we illustrated in Sec. 3.5.1. The microscopic character has already been "integrated out", and the local "Hamiltonians" will take on the same value, to first order in space and time, so $\Delta_{ij}\tilde{\mathcal{H}}(\boldsymbol{s},[t]) \approx 0$. In this approximation, the ratio of the transition probabilities results from a difference in excess chemical potentials:

$$\frac{\tilde{W}_j(\boldsymbol{s}_i,[t])}{\tilde{W}_i(\boldsymbol{s}_j,[t])} = \frac{\rho(\boldsymbol{s}_j,t)}{\rho(\boldsymbol{s}_i,t)}\exp\left(\beta\Delta_{ij}\mu^{\text{exc}}(\boldsymbol{s},[t])\right) \tag{3.188}$$

$$\equiv \exp\left(\beta\frac{\delta\mathcal{F}_{\text{eq}}^{\text{exc}}[\rho(\boldsymbol{s},t)]}{\delta\rho(\boldsymbol{s}_j,t)} - \beta\frac{\delta\mathcal{F}_{\text{eq}}^{\text{exc}}[\rho(\boldsymbol{s},t)]}{\delta\rho(\boldsymbol{s}_i,t)}\right) . \tag{3.189}$$

The DDFT ansatz in Eq. (3.189) says that the free energy functional that defines the local excess chemical potential is that of equilibrium, only we evaluate it for the nonequilibrium density. This means the response of the density function will follow Eqs. (3.181) and (3.182).

The Eq. (3.188) allows for an *a priori* probability or an "attempt" rate that can set a diffusion constant (particle mobility), for example, completely analogous to the "attempt" rates for KMC simulations. Notice that we need not express a minimum condition like in the general form of Eq. (3.170) since we can, in effect, absorb the excess chemical potential differences into the "attempt" rate. The ratio of the transition rates will render the difference in excess chemical potentials.

Further, the assumption that the effective "Hamiltonians" take on the same value at nearby lattice sites is only valid for simple hopping diffusion of point particles. If the lattice objects are extended in space (like rods), then a transition can occur over extended regions of space, depending on the motion ("move") considered. One must account for the possibility that certain lattice sites will remain "blocked" during this local equilibrium period. This means we need to define a (minimally) *mesoscopic balance* equation, i.e. fluxes will not follow detailed balance (which is strictly pairwise and presumes all degrees of freedom can be decoupled completely), but, from a sum rule. This may lead to a transition rate that has multiple terms in the exponent for one direction of motion, while only one term in the exponent for another direction.

These are the general forms of the lattice DDFT equations that we shall explore in the context of a lattice model of hard rods in Ch. 4, with one further

[34] It appears unnecessary to treat the ideal part of the chemical potential in the DDFT transition rates, which we find empirically in Ch. 4; we argue here that in integrating out the microscopic character (see next few sentences), their local difference becomes approximately zero.

simplification: For homogeneous systems, we make the assumption that the master equation only depends on particle orientation (which represent the indexed mesoscopic states), but not position $\boldsymbol{s}$.

The downside of effective approximations: limited "bandwidth"

Assuming that the microscopic structure and dynamics (governed by an underlying microscopic Hamiltonian $\tilde{\mathcal{H}}$ of the "sharp" N-body description) have been "integrated out" comes with one important consequence: In the spirit of "effective field theories (Sec. 3.2), an "effective" Hamiltonian $\tilde{\mathcal{H}}$ will always take on *larger* values than the mean of the microscopic Hamiltonian:[35]

$$\beta\Delta\tilde{\mathcal{H}} \approx -\ln\langle \mathrm{e}^{-\beta\Delta\mathcal{H}}\rangle \geq -\langle \ln \mathrm{e}^{-\beta\Delta\mathcal{H}}\rangle \equiv \beta\langle\Delta\mathcal{H}\rangle \tag{3.190}$$

We presumed that $\Delta\tilde{\mathcal{H}} \approx 0$, hence the "true" relative rates can, at times, be much faster or slower than than that offered by Eq. (3.188), which acts as a *lower bound* on the possible relative transition rates: The *bandwidth* of rates (time-scales differences) will be larger within the true system. The consequence is that the time-evolution in the "true" system will be much slower. This is an effect we see in KMC simulations in Ch. 5 when approaching phase boundaries, at the point when the bandwidth of rates in the system is largest. Then, the propagation of time slows, measurable in smaller required time-steps to resolve all the time-ordering events in the N-body dynamics, i.e. $\Delta t \propto \frac{1}{\sum \mathcal{W}_{kl}}$ where W_{kl} represents the rates. A larger bandwidth about a mean total rate $\sum \mathcal{W}_{kl} \approx \langle W\rangle + \Delta W$ will imply the "extra" events must relax – with relaxation time $\frac{1}{\Delta W}$ – *in between* events accounted for in the "mean" dynamics. Thus, a whole series of events that are propagated in terms of the "mean" time-scales are effectively cut out of the evolution.

Therefore, the DDFT evolution via Eq. (3.188) might be too *too fast* (locally, in time) as a nonequilibrium system can entail a larger heterogeneity of energetically-activated processes, especially if particles are anisotropic. Another point is the *level of localization*, or the level of coarse-graining attempted. The larger the spatial coarse-graining scale, the narrower the bandwidth of events considered, capping the ability to capture highly nonequilibrium stages of an evolution.[36] We see this effect to some extent in Ch. 4 once a system is brought to a highly nonequilibrium state entailing a high degree of dynamic arrest (the case of *jamming* in a monolayer). The DDFT appears "too fast", in the sense of too "efficient" at dissipation. This is especially the case when the (simulated) dynamics couple individual-particle rotational with translational degrees of freedom.

[35] like constructing a 'partition function' over probable states, but, locally in time and space in a "mesostate"

[36] A related topic is that of choosing a "grid" length in numerical solvers or more generally for a lattice model, at least for equilibrium systems. In nonequilibrium, excluding events due to an 'uncontrolled' cutoff time-scale can change the future evolution drastically. We see will see these effects, indirectly, in Ch. 5, where a different *choice* of local-scale dynamics of rods (coupling the rotational and translation "moves" directly) on a lattice leads to different phase separation kinetics, and, thus a different morphological and dynamical evolution of a system.

3.3.7 Suggested improvements (speculative discussion)

In light of the above discussion, we suggest an improvement the DDFT Eq. (3.188) that, however, remains purely speculative at this point. The uninterested reader can proceed to Sec. 3.3.8.

We may effectively *increase* the bandwidth of the rates if we include higher-order functional derivatives of the free energy, during a minuscule time-step δt in-between a 'mesoscopic' transition time-scale Δt.[37] The additional term to the excess chemical potential (perturbation field) might be written as

$$\Delta^{(2)}_{ij}\mu^{\mathrm{exc}}(t) \propto \frac{\delta\mathcal{F}[\rho(\boldsymbol{s},[t])]}{\delta\rho(\boldsymbol{s}_i,t-\delta t)\delta\rho(\boldsymbol{s}_j,t-\delta t)}\,, \tag{3.191}$$

for any "internal" dynamics like rotational or translational (effective) motion of particles. The second derivatives of the free energy represent *correlations* of excess chemical potentials in equilibrium.

Arguably, by employing correlation functions from derivatives of an equilibrium free energy functional (the central ansatz of DDFT), we seem to be implying that the fluctuation-dissipation theorem from equilibrium is fulfilled, locally. It would be interesting in to explore in the future how well the amount of dissipation is estimated with this ansatz.

Saddle points in the free energy are particularly interesting. They represent locally *stationary points* of the free energy surface (see Sec. 3.2, utilized in Gaussian approximations and variational mean field theory). There, second order gradient terms of the free energy – like in Eq. (3.191) – are nonzero, but first-order gradient terms disappear.

Thus, although detailed balance is broken in nonequilibrium, we may still be able resort to a "*metastable*" form of balance, which would reinstate approximate continuity and energy conservation at a mesoscopic level. The saddle-points contained in a second-order correction term might allow for the dynamics to enter quasi-stationary (transient) states during the evolution, increasing the effective bandwidth of events (effectively correlating the system in more ways locally), potentially "slowing down" the dissipation. In other words, such a correction term may introduce a small *separation* of time-scales in the dynamics. Therefore, phase separation kinetics may be captured more accurately by including these saddle points, in particular the entry to and exit from metastable phases.

Self-consistent approaches (?)

Perturbative approximations like cumulant expansions are not necessarily self-consistent and can violate conservation laws. An expansion should act, ideally, as a *bound* on the (variational) free energy [822] or whatever other generating functional is central to the approximation.[38] For dynamics, it seems we would need to quantify a limit with respect to a local *power* or dissipation rate, likely related to entropy production rates [804–806, 817, 823, 824]. Theoretical approaches that begin with a functional form of dissipation rates and power

[37] This idea may bear resemblance to numerical integration with the so-called leap-frog scheme.

[38] Please see a description of variational mean field theory in Sec. 3.2.

like *power functional theory* [825, 826] may be promising, in line of our discussion. There, densities are found after obtaining nonequilibrium currents (from the functional minimization) by means of a continuity equation, i.e. the approach is self-consistent and abides to a conservation law at relevant scales.

On a general note, if we do not correctly account for self-consistency (preservation of energy per unit time) in the evolution of dynamics, then we modify a most fundamental aspect of dynamics: the *causal structure* of relevant events occurring at the considered scales (see discussion in e.g. Refs. [784, 827]). Causality is related to a visible "arrow" of time at the considered scale [788, 818, 828], and is at the heart of irreversible dynamics (see further discussion in Sec. 3.5). A loss of causal relations implies a fundamental loss of information, as time-ordering of events is lost (a "smearing out" of probability densities). A coarse-grained model has less ways in which events can occur, and thus, be reordered. Therefore, the reduction of dynamical complexity (bandwidth) in nonequilibrium will need to be highly adaptive along the evolution.

Remark. Dissipation protocols can also be regarded as gauging the many-body processes during an evolution, involving various number of variables or particles. In accordance with our discussion of dynamical coarse-graining in Sec. 3.5.1, a transition between two many-body mesostates m, m' can be associated with a 'free energy' barrier:

$$W_{m,m'} \propto \exp\left(-\beta \Delta_{m,m'} F\right) \ . \tag{3.192}$$

For first-order phase transitions to occur dynamically, then, the dissipative power of the external forces must be sufficient to overcome such a energetic barrier within a certain interval of time, in comparison to competing processes. The rates provided by our initial DDFT formulation, Eq. (3.188) may not provide a correct bound on the "internal" dissipation rate or entropy production in between local time-steps – the first-order term of the chemical potential difference represents an unstable 'drift' term, and not a saddle point. We need to consider correlations of chemical potential differences when transitioning among differently-oriented states of *anisotropic* particles, which amounts to finding a mesoscopic balance condition.

3.3.8 Formal properties of Markovian dynamics

Any theory of equilibrium or nonequilibrium must address the question of how a system initially in equilibrium responds to external stimuli in time, which means we look at two-time correlation functions. A two-time autocorrelation function is defined as

$$f_A(t, t') = \frac{\langle A(t'+t)A(t)\rangle_{t'} - \langle A(t')\rangle_{t'}^2}{\langle A(t')^2\rangle_{t'} - \langle A(t')\rangle_{t'}^2} \ . \tag{3.193}$$

The observable $A(t')$ is usually some kind of configurational average (an order parameter) at time t', making it one of the slowest variables in the dynamics. The autocorrelation function may decay in a non-exponential manner that could indicate a number of things: Stretched exponential decays are common when approaching a liquid-solid transition in hard-sphere systems, for example [557], and can indicate that the system entails a broad variety of relaxation processes; on the other hand, the system may not yet be in equilibrium (often

indicating that e.g. sampling is not good enough), or may have begun at a highly nonequilibrium state and entails *memory*. (The latter would quantifiable by varying the laboratory time t in relation to the time-difference $\Delta t = t' - t$.) However, in the simplest of cases of Markovian dynamics, an exponential relaxation will be observable, and the relaxation time $\tau_{\exp}$ can be fit by the ansatz

$$f(\Delta t) \approx a \exp(-\Delta t/\tau_{\exp}) \tag{3.194}$$

for sufficiently long time differences (waiting times) Δt.

Markov chains

For a stochastic chain of events in time to be *Markovian*, formally, the conditional probability for the system to transition to state j at time-point $t + \Delta t$ must depend only on our last observation of the system in state i at time t rather than on the full history $\{\boldsymbol{s}_i(t')\}_0^t$:

$$p(\boldsymbol{s}_j(t+\Delta t)|\{\boldsymbol{s}_i(t')\}_0^t) = p(\boldsymbol{s}_j(t+\Delta t)|\boldsymbol{s}_i(t)) \tag{3.195}$$

We can say the dynamics of such a system that are *local in time*, and the evolution proceeds in discrete time-steps Δt. However, Markovian dynamics of many-particle systems must also be *local in space*: Assuming the states are already coarse-grained, we impose the condition of statistical independence to all other states, their history included

$$p(\boldsymbol{s}_j(t+\Delta t)|\boldsymbol{s}_i(t), \{\boldsymbol{s}_{k\neq i}(t')\}_0^t) = p(\boldsymbol{s}_j(t+\Delta t)|\boldsymbol{s}_i(t)) \ , \tag{3.196}$$

too.

The transition probability has to satisfy [774, Ch. 5]

$$p(\boldsymbol{s}_j(t+\Delta t)|\boldsymbol{s}_i(t)) \to \delta(\boldsymbol{s}_j(t) - \boldsymbol{s}_i(t)), \ \Delta t \to 0 \ . \tag{3.197}$$

The next term in the expansion with respect to the time-step entails the transition rate $W_i(\boldsymbol{s}_j)$:

$$\begin{aligned} p(\boldsymbol{s}_j(t+\Delta t)|\boldsymbol{s}_i(t)) = (1 - a(\boldsymbol{s}_i(t))\Delta t)\, \delta(\boldsymbol{s}_j(t) - \boldsymbol{s}_i(t)) \\ + \Delta t W_i(\boldsymbol{s}_j) + \mathcal{O}((\Delta t)^2) \end{aligned} \tag{3.198}$$

The factor $a(\boldsymbol{s}_i(t)$ is determined from the normalization condition for the conditional probability, for $t > t'$, $\Delta t > 0$:

$$1 = \sum_i p(\boldsymbol{s}_j(t+\Delta t)|\boldsymbol{s}_i(t)) \tag{3.199}$$

$$= 1 - a(\boldsymbol{s}_i(t)\Delta t + \Delta t \sum_i W_i(\boldsymbol{s}_j) + \mathcal{O}((\Delta t)^2) \ , \tag{3.200}$$

i.e.

$$a(\boldsymbol{s}_i(t) = \sum_i W_i(\boldsymbol{s}_j) \tag{3.201}$$

Eq. (3.198) implies that for small time-step Δt, the system will either proceed into the same state with a certain probability, or proceed to another state with

a complementary probability. A trajectory of the random variable ($\boldsymbol{s}(t)$) will appear constant on longer time-scales, interrupted by random jumps.

A transition rate $W_i(\boldsymbol{s}_j)$ thus characterizes the number of jumps – in changing between states i to $j \neq i$ – over a certain time-period Δt.

If the value of the changes within Δt is variable, but follows a stationary mean, this stochastic chain-of-events effective dynamics can be expressed as Poisson processes. The Poisson process is characterized by a waiting time distribution between events (transitions) that render a mean number of events. The probability to be waiting to transition to $\boldsymbol{s}_i$ within a time-interval Δt, given the system is in $\boldsymbol{s}_j$, is an exponential decay:

$$p^{\text{wait}}(\boldsymbol{s}_j \to \boldsymbol{s}_i, \Delta t) = \exp(-W_i(\boldsymbol{s}_j)\Delta t) \ . \tag{3.202}$$

Notably, if many Poisson processes co-occur in the system, one needs to consider a *joint* Poisson process. We cover this in Sec. 3.4 for kinetic Monte Carlo, an algorithm that propagates time via Poisson waiting time distributions like Eq. 3.202.

3.4 Markov-Chain Monte Carlo methods

Highly idealized systems – such as lattice models – are perfect candidates for simulation methods based on Markov chains. Up front, the lattice models of particle systems must readily be "coarse grained" on some basic level, spatially and in dynamics, the latter of which can be presumed locally Markovian, i.e. thermal motion of particles due to coupling with a thermal bath. These are arguably one of the simplest possible types of local dynamics, and the N-body system of simple particles following such dynamics is describable, in theory, by the kind of N-body master equation motivated in Sec. 3.3. Kinetic Monte Carlo (KMC) simulations emulate exactly these kinds of dynamics, in-equilibrium, but also nonequilibrium conditions. In the latter case, we must assume the external perturbation driving the nonequilibrium evolution do not affect the local-scale dynamics of the system *directly*, i.e the dissipative part of the Hamiltonian does not couple to external perturbations and the Hamiltonian remains local. We describe this method in Sec. 3.4.1 below.

Crucially, master equations describe an irreversible evolution of probability fluxes towards the equilibrium end-state as soon as any such external perturbations are "turned off". In equilibrium, balance conditions should hold for any relevant scale of treatment. As equilibrium guarantees various self-averaging properties, dynamics will also appear Markovian at these various scales. In fact, we can come up with our own, "make-pretend" version of system dynamics at a microscopic level –single-particle "moves"– or mesoscopic level many-particle, collective "moves" – as long as we are certain these lead to a globally balanced state (and are ergodic, of course). Equilibrium Markov Chain Monte Carlo algorithms utilize this "trick" for simulation equilibrium *pseudodynamics*. We describe these in Sec. 3.4.2.

3.4.1 Kinetic Monte Carlo simulations

We employ kinetic Monte Carlo algorithms [22, 24] in this thesis in part II for exploring nonequilibrium dynamics in a lattice model of hard rods. KMC (also

called the "n-fold-way algorithm" [23, 163]) numerically solves the master equation that would describe the effective dynamics of particles with short-range interactions coupled to thermal baths, where temperature is clearly-defined. It is usually performed for discrete systems, i.e. on lattices, but can be used for continuum systems in a coarse-grained approach, too (which we will not discuss here). Random motion is inherent, therefore, owing to the thermal bath, where an *attempt rate* quantifies microscopically diffusive or random-walk-type of motion in the low-density limit.

KMC models the *full* N-body dynamics, where microscopic dynamics are modeled as *Poisson processes*, i.e. locally Markovian dynamics. Thus, between simulation time-steps, the full system is described by the full set of *rates* $\{W_i(\boldsymbol{s}_j, t)\}$ of the system. The simulation propagates time by the *joint* Poisson process that describes the full system – it is inherently stochastic, then, and each run of the simulation will generate a unique trajectory of the system that is compatible with these assumptions (and with local physical laws enforced by inter-particle interactions).

In any case,at each time-step, any *possible* processes can occur at any moment because we assume they are statistically independent. 'Processes' are random, abrupt, discrete "events" that are distributed with a Poissonian prior. In a Poisson process, abrupt events occur with a random *waiting time* between events, the mean value of which is the reciprocal of the characteristic *rate* of the process [829]. In a system with *many* independent Poisson processes (a joint process), the characteristic waiting time for *any* event to occur is the reciprocal of the *sum* over the individual rates.

Consider the set of possible transitions (with their rates) $\{W_i(\boldsymbol{s}_j, t)\}$ between any pair $i \neq j$ of states. The full waiting distribution before the next follows

$$p^{\text{wait}}([t], t' | \{W_i(\boldsymbol{s}_j, t)\}) = \exp\left(-\sum_{i \neq j} W_i(\boldsymbol{s}_j, t)\, t' \right) \tag{3.203}$$

for $t' > t$. Therefore, the waiting time $t' - t \equiv \Delta t(t)$ can be sampled from this distribution at every time-step t of the KMC simulation:

$$\Delta t(t) = \frac{1}{\sum\limits_{i \neq j} W_i(\boldsymbol{s}_j, t)} \ln u \tag{3.204}$$

for $u \sim \text{Uniform}(0, 1]$ is a random number in the unit interval. The total rate

$$W^{\text{tot}}(t) = \sum_{i \neq j} W_i(\boldsymbol{s}_j, t) \tag{3.205}$$

sets the time-scale at which the system is next expected to evolve forward (when a "move" will next happen).

As discussed in Sec. 3.3.4, in an interacting many-body system, the transition rates will change in time with the evolving configurations, i.e. the Poisson processes in the joint distribution are only independent *between* time-steps. The "true" rates must be adjusted *ad hoc* after every forward evolution of the system (after every time-step). In essence, we are updating the posterior probabilities for events in the system at every time-point.

In the local Markovian assumption, these rates are adjusted to fulfill the local-balance condition (Eq. (3.170)): The transition rate can be expressed, most

generally, as

$$W_i(\boldsymbol{s}_j, t) = W_{ji}^0 \min\left\{1, \exp\left(-\frac{\Delta_{ji}\mathcal{H}(\boldsymbol{s}, [t])}{k_{\mathrm{B}}T}\right)\right\} \tag{3.206}$$

where W_{ij}^0 represents the "attempt" rate to transition between two positions (or orientations, in the case of rods), $(\boldsymbol{s}_i, \boldsymbol{s}_j)$, and the "min" expression represents a *posterior* probability for the event to occur, according to a (local equilibrium) Boltzmann distribution. Typically, the attempt rates are independent of absolute position $\boldsymbol{s}$ (for a uniform substrate potential, for example, in the case of thin film growth with rods studied in this thesis). In line with our discussion in Sec. 3.3.4, Eq. (3.206) sets the magnitude of the current generated by local *forces*, which are a product of the configurational part of the Hamiltonian $\mathcal{H}(\boldsymbol{s}, [t])$ at the time-point t and the (unchanging) dissipative part of the Hamiltonian that drives the thermal, random motion. (The subtlety here is that thermal systems are dissipative (Sec. 3.3.3.)

The relative probability for a particular event to occur, i.e. that a particular particle "hops" or e.g. rotates into a neighboring site(s), among all possible events $\{W_{i'}(\boldsymbol{s}'_j, t)\}$ at time t, is given by the ratio of its rate with the total rate $W^{\mathrm{tot}}(t)$:

$$p^{\mathrm{rel}}(W_i(\boldsymbol{s}_j, t)|\{W_{i'}(\boldsymbol{s}'_j, t)\}) \equiv \frac{W_i(\boldsymbol{s}_j, t)}{W^{\mathrm{tot}}(t)} \,. \tag{3.207}$$

The algorithm must choose a random event according to this relative probability at each time-step.

In its most general form, KMC is implemented to avoid *rejection* steps completely while sampling the trajectories of the system, unlike "standard" Metropolis-Hastings Monte Carlo algorithms. Only *valid* "moves" are calculated in-between time-step. A KMC simulation is thus "event-driven", propagating time only when something *moves* (when an event occurs). Instead of evaluating Eq. 3.206 after sampling a potential move from a *prior* (i.e. any particle in the system can move in any direction), we update all rates *in-between* time-steps (calculate the posterior probabilities) by evaluating Eq. 3.206. This, however, comes at a cost of algorithmic-design complexity as well as run-time complexity. The "updating" steps are nontrivial and rather involved for anisotropic particles, such as long, hard rods (particularly in full 3D, which we have implemented, along with rods in monolayer confinement). Rods are non-local (extended in space), and affect a much larger range of potential events, let alone their affect on each other is not symmetric. (See part II of this thesis). We had to design a new, customized algorithm for this purpose, the basic ideas of which are illustrated farther below.

We employed an adaptive method [830] that allows us to reduce the computational overhead to some extent: Possible events are updated only according to the hard-core potential between particles (whether or not they are 'blocked'). By ignoring the attractive interactions, at first, we reduce the number of updating "checks" significantly between time-steps. However, we are required to sample the correct (relative) rates later in an "accept-reject" Metropolis step. Let us explain in more detail.

For hard-core systems with attractive forces the minimum-condition can be split into two conditions – one for the hard-core part of the local Hamiltonian

change, and one for the attractive part:

$$W_i(\boldsymbol{s}_j, t) \propto \min\left\{1, \exp\left(-\frac{\Delta_{ji}\mathcal{H}^{\text{hard}}(\boldsymbol{s}_j, [t])}{k_{\text{B}}T}\right)\right\} \times \min\left\{1, \exp\left(-\frac{\Delta_{ji}\mathcal{H}^{\text{att}}(\boldsymbol{s}_j, [t])}{k_{\text{B}}T}\right)\right\} \quad (3.208)$$

The hard-core potential seen from site $\boldsymbol{s}_j$ is defined by the occupation probability (which is binary at the "fully-resolved" level of each particle) of the neighboring lattice site $\boldsymbol{s}_i$:

$$\Delta_{ji}\mathcal{H}^{\text{hard}}(\boldsymbol{s}_j, t) = \begin{cases} 0, & \text{if } \rho^{(N)}(\boldsymbol{s}_i, t) = 0 \\ \infty, & \text{otherwise} \end{cases} \quad (3.209)$$

The product of the minimum conditions implies, algorithmically, that second conditions can be evaluated subsequently to the first during the simulation: The hard-core repulsion is tracked at every moment using an algorithm that suitably searches for the correct "free volume" for a particle (an "inverted event-list index"), which we developed for hard rods on lattices. Together with the attempt rate, the "hard-core" transition rate constitutes an *upper limit* on the correct transition rate. Secondly, the "attractive" component, which needs to evaluate the local energy around two different local configurations, is evaluated *a posteriori*, after the *upper limit* of the rate has been used for the full N-body time-propagation step (in the calculation of the total rate in Eq. 3.205 and in selecting any one of these random events with relative rate in Eq. 3.207). Whenever an event has been chosen, the event is randomly accepted with a probability $\min\left\{1, \exp\left(-\frac{\Delta_{ji}\mathcal{H}^{\text{att}}(\boldsymbol{s}_j, t)}{k_{\text{B}}T}\right)\right\}$ for the "attractive" part of the rate. We employ this "hybrid" KMC method method in Ch. 5 for a system of "sticky" hard rods.

As the N-body transition rates are evaluated between time-steps, the stochastic equations of motion are effectively second-order in time. KMC is thus a "*full*" dynamical N-body solver of the equations of motion, given that a Markovian dynamics holds at the smallest scales considered (at the level of each particle). Technically speaking, the evolution proceeds according to a "forward" master equation, i.e. the *unbalanced* current that renders a forward equation of motion.

$$\frac{d\rho^{(N)}(\boldsymbol{s}_i, t)}{dt} = -\sum_j W_{ij}(t)\rho^{(N)}(\boldsymbol{s}_i, t) \quad (3.210)$$

(The inhomogeneous part of the master equation Eq. (3.116) can be absorbed into the sum over transition rates.) In the absence of external perturbations or away from any phase transitions, the simulations will emulate motion of an N-particle system in equilibrium system as long as Eq. 3.205 is properly calculated (local balance). In nonequilibrium, where detailed balance is ultimately broken owing to an external perturbation, the KMC algorithm will generate a possible trajectory of the N-body system.

3.4.2 Equilibrium MCMC sampling

The broader class of Markov Chain Monte Carlo methods is usually aimed at equilibrium systems [38, 61–63][794, Ch. 6][57, Ch. 7]. The simulations offer efficient methods for obtaining estimates of statistical quantities of the system in equilibrium, which are formally exact. The accuracy of these estimates are limited by the quality of the sampling.[39]

The ergodic hypothesis means that any dynamics that explore all of phase space will ultimately render the same, static properties in the long time limit. Consequently, we can generate the correct statistics using "fake" dynamics, as long as these converge to equilibrium. We do not necessarily need to try to emulate how "real-world" systems move. For example, molecular dynamics simulations are more "faithful" in the dynamics to the motion of classical bodies, but, are computationally too costly for exploring a long evolution of a large system. The "point" of Markov Chain Monte Carlo (MCMC) methods is to obtain high quality statistics of equilibrium *structural* quantities like order parameters.

Quite simply, the Markov chain samples the equilibrium (Boltzmann) distribution of configurational states through simulated time (MC "pseudo"-time), corresponding to the number of simulation steps. The convergence of this chain to equilibrium is only then guaranteed if the algorithmic motion through phase space ("moves") fulfills the local (detailed) balance condition when reaching a Boltzmann distribution. The *proposal* and *acceptance* probabilities of the "moves", which are to be executed in the simulation, must be carefully crafted when implementing the algorithm, which we will explain below. In addition, all states in phase space must be accessible (ergodicity of the system), and the algorithm must be *aperiodic* (will not get "caught" in a repeatable loop).

The transition probability can be split into two parts: a probability for an event to be chosen – the *proposal* probability π_{ij} that is usually "time"-independent – and an *acceptance* probability $\pi_{ij}(t)$ that will change with the evolving configuration. This is completely analogous to the "attempt" and "acceptance" motion discussed in the context of KMC simulation of dynamics. Formally, then, the transition rates from state i to j can be reformulated as

$$W_j(\boldsymbol{s}_i, t) = \pi_j(\boldsymbol{s}_i) \cdot \alpha_j(\boldsymbol{s}_i, t) \; . \tag{3.211}$$

To fulfill local equilibrium, then,

$$\pi_j(\boldsymbol{s}_i)\alpha_j(\boldsymbol{s}_i, t)p(\boldsymbol{s}_i, t) = \pi_i(\boldsymbol{s}_j)\alpha_j(\boldsymbol{s}_j, t)p(\boldsymbol{s}_j, t) \tag{3.212}$$

implies that the acceptance rate (probability) can be formulated as

$$\alpha_j(\boldsymbol{s}_i, t) = \min\left\{1, \frac{\pi_i(\boldsymbol{s}_j)p(\boldsymbol{s}_j, t)}{\pi_j(\boldsymbol{s}_i)p(\boldsymbol{s}_i, t)}\right\} \; . \tag{3.213}$$

This is known as the *Metropolis-Hastings* sampling algorithm [404, 831].

[39] And finite-size effects, which, with more effort can be "scaled out" at phase transitions.

Grand Canonical Monte Carlo (GCMC)

The form of $p(i,t)$ can be Boltzmann-distributed according to the current Hamiltonian or free energy of a system in the local equilibrium approximation. For grand-canonical ensembles, then, the global system variable $N(t)$, or the number of particles, will also enter the form of the probability

$$p(\boldsymbol{s}_i, t|\mu) \equiv p(\boldsymbol{s}_i, t; N(t)|\mu) \propto \frac{1}{N(t)!} \mathrm{e}^{-\beta\mathcal{H}(\boldsymbol{s}_i,[t])+\beta\mu N(t)} \tag{3.214}$$

given a fixed chemical potential μ. In such simulations, we introduce a *combination* of MC moves that are asymmetrical in their *a priori* probabilities, which is why the Metropolis-Hastings algorithm is so useful. In these cases, we introduce global "insertion" moves and "deletion" moves on the configuration of the system:

$$W^{\mathrm{ins}}_{N+1}(N,t|\mu) = \pi^{\mathrm{ins}}\, \alpha^{\mathrm{ins}}_{N+1}(N,t|\mu) \tag{3.215}$$

The prior for the insertion move is

$$\pi^{\mathrm{ins}} = \frac{1}{2}\frac{1}{V}\frac{1}{\nu}\,,$$

given there are ν species of particles (orientations) in the system, for example. The inverse deletion move (only valid for $N \geq 1$)

$$W^{\mathrm{del}}_{N-1}(N+1,t|\mu) = \pi^{\mathrm{del}}\, \alpha^{\mathrm{del}}_{N}(N+1,t|\mu) \tag{3.216}$$

has an even simpler prior,

$$\pi^{\mathrm{del}} = \frac{1}{2}$$

if we choose to track a list of particles of size $N(t)$ at all times that will *certainly* be attempted to be deleted.

We employ these MCMC moves for grand canonical Monte Carlo (GCMC) simulations in various chapters, particularly in part III on this thesis.

Remark. Cluster algorithms [38, 61–63] accelerate Monte Carlo simulations massively by decreasing the time intervals needed between samples for independent statistics. Cleverly constructed cluster updates change a configuration at collective scales rather than at local ones, meaning the Markov Chain explores different parts of configuration space more quickly. [40] Yet the challenge remains to construct proper updates. Typically, one relies on local symmetries in the system. For example, in the Ising model, a local spin can be flipped, rendering a different, physically valid configuration. When flipping entire clusters of spins having the same spin direction, the same logic holds. Unfortunately for hard rods, one cannot locally rotate a rod without producing particle collisions, generally, violating the physical rules. Therefore, in Ch. 6, we resort to the "default" of using local updates exclusively. Options for other optimized algorithms are discussed in the outlook of Ch. 6.

* * *

[40] Notably, the dynamic universality class of a cluster algorithm (the scaling of e.g. susceptibilities with time) is different than that of local updates; moreover, these classes can differ among cluster algorithms (i.e. the Swendsen-Wang [832] versus the Wolff [833] variant) [834].

Now that we have described the dynamics of lattice systems in terms of master equations, and have discussed simulations thereof with KMC and MCMC methods, we turn to more general discussion on the conceptual difficulties in expressing the time-evolution of many-body systems, both in an out-of equilibrium, whereby the meaning of "coarse graining" will be illuminated.

* * *

We have discussed Markov-Chain Monte Carlo methods, master equations, as well as aspects of DDFT in the preceding sections. These topics have direct relations to the research in this thesis. The next section is aimed at illustrating fundamental concepts, very general in nature. We will provide a broader view of the concept of coarse-graining in equilibrium and near equilibrium. Conceptual ties to information theory will be discussed, and concepts relevant for machine learning will be given a broader setting. Finally, we discuss the breakdown of Markovian dynamics in nonequilibrium. A discussion of the machine learning algorithms and concepts for part IV of this thesis will proceed in Sec. 3.6 thereafter.

3.5 Irreversible dynamics and the role of coarse-graining

The success and aesthetics of equilibrium statistical mechanics lies in how a single formula allows for the calculation of all thermodynamical quantities given the input of a Hamiltonian, which is what determines in a nutshell the evolution of the particles of a system.[41] Its simplicity is based ultimately on the ergodic hypothesis, were we can replace dynamical averages with ensemble averages. Uniquely in equilibrium, we are allowed to lose the sense of time. However, if we ask *how* this equilibrium is reached from an arbitrary starting point, then there is no extraordinary simplicity any longer. It is the transition from the well-defined beginning and end-states that is so enormously complex. Thermal systems undergo irreversible dynamics, and describing the dynamical evolution is at least as hard as correctly describing the static properties of the system.

We discussed in Sec. 3.1 the underlying equations of motion of isolated classical many-body systems, described by Hamilton's canonical equations, or for general probability densities, that of Liouville (for isolated systems). These are completely *time-reversible*. Our experience in the macroscopic world stands in stark contrast to this, as systems clearly evolve in one direction of time, most pronouncedly towards an equilibrium end-state: How is it that macroscopic dynamics *breaks* this time-symmetry, and entropy remorselessly increases, in line with the second law of thermodynamics? This is the *paradox of irreversibility* [82, 83, 758, 759, 764, 779, 835–838][789, Ch. 4], which has been a heated point of debate for statistical physics. This point was first observed in the last century (Loschmidt, Zermelo, Gibbs) and still creates controversy in current times. Thermodynamics would not exist as it stands without irreversibility, making this a pertinent issue.

Strictly speaking, no paradox arises if we only stick to calculating *equilibrium* values: These are assumed stationary, hence time-independent. On the

[41] paraphrasing Balescu [95, p. 1]

other hand, behavior far from equilibrium is not time-symmetrical. A real contradiction would arise if we could derive the asymmetrical equations from the underlying symmetrical ones. We are therefore forced to accept that there is some additional postulate looming around – show asymmetry in time and non-dynamical in nature – that must be conjoined with the time-symmetrical, internal, microscopic dynamical laws [90, Ch. 1]. However, although time reversibility may appear locally, the boundary conditions are not reversible: the state of the system is fixed at its initial conditions, paraphrasing Ref. [101, p. 95]. Thus even a deterministic system, like cellular automata, that is highly complex will take on a different evolution depending on these *a priori* conditions. Indeed, *causality* at the microscopic scale, may lead to irreversible behavior at the macroscopic scale if we can presume ergodicity (see Ref. [784].) The "extra" postulate is causality in this case, where we leave the debate open to the reader.

Attempts to trace this irreversibility back to the microscopic level go back far to the beginnings of modern statistical mechanics. In some approaches to the matter, the devil is hidden in the details: "sufficiently unstable" dynamical systems might allow for the definition of an ensemble of states, see the work in Refs. [839, 840]. Ref. [841] showed (1980) that, roughly, partitioning the continuum of space in to *disjoint* cells – no matter how finely [82] – renders a "strongly" irreversible stochastic Markov process towards a stationary state (equilibrium). Specifically, so-called Lyapounov variables that grow monotonically in time can be found. These allow one to define a dynamical entropy function, thus an "arrow of time" [841–843]. Refs. [84, 836] also outlined conditions for being able to map a Liouvillian equation of motion to a probabilistic, Chapman-Kolmogorov equation [774, 813] that defines a stochastic process. [42]

Taking a step back, however, we postulate[43] "all we need to do" is to solve the formally exact Liouville equation. This should offer a natural starting point for nonequilibrium dynamics.[44] Completing an approach with Liouville is easier said than done, however. Nobody ever solved a nontrivial Liouville equation *exactly* for interacting systems, which is a fundamental problem.

Typical *dissipative* dynamical systems [840] (which per definition are not isolated!) do follow irreversible evolution towards *chaotic attractors*, which can represent the equilibrium end-points. Arguably, then, we might try to "include" randomness into the evolution of classical phase space distribution functions by assuming some part of the dynamics is due to a stochastic process, rendering stochastic versions of the Liouville equation [96, Ch. 2.2][763]. The challenging question remains, however, under which conditions this would be a valid assumption. Energy transfer with an external system (a bath) would break the preservation of phase-space densities on the subsystem we are trying to describe, hence of Liouville's theorem. The non-conservation of probability makes way to an increase in entropy: This is an argument for incorporating an external system when describing a nonequilibrium system with a clear end-point (equilibrium).

Thus fundamentally unresolved is how to develop a stochastic description "simply" by algebraically transforming reversible, deterministic microscopic equations of motion, paraphrasing Ref. [813, p. 251]. For many decades,

[42] Ref. [844] further discusses obtaining Markov chains from chaotic, deterministic dynamics.
[43] paraphrasing Ref. [96, Ch. 22]
[44] using the words of Zwanzig [761]

nonequilibrium descriptions have been tailored to specific systems, where assumptions about e.g. a separation of time-scales are introduced *a priori* (such as nucleation theories for island growth in phase-transforming systems). More- or less-well-understood "top down" stochastic approaches include Langevin, master, or Fokker-Planck equations.

Intuitively, one can imagine that if an isolated system undergoes sufficiently unstable dynamics, then a small perturbation (a measurement, or a weak coupling with an external system) should induce the complex dynamics that differ from the initial condition in each instance. If a fundamental uncertainty (a partitioning) in phase space is all that is needed to irreversibly march towards equilibrium, then surely *any* act of coarse graining will induce irreversible behavior. Specific information about a system (its initial state) is lost, which is why the notions around Shannon information entropy are further useful. In attempting to describe the system with an initial probability density, parts of it will "leak away" into variables that are not covered by the distribution. A monotonic increase of a quantity that is regarded as entropy will be visible, which necessitates an explicit time-dependency of a probability density distribution in order to guarantee normalization. We discuss more on dynamical coarse-graining near- or in-equilibrium later in Sec. 3.5.1.

Gibbs Entropy: Measure over coarse-grained states

Gibbs originally introduced the concept of coarse-graining phase space into cells in an attempt to reconcile the irreversible approach of macroscopic states to an equilibrium state. Boltzmann attempted to prove this with his famous *H-theorem* for the Boltzmann equation [88, 765, 838], transport equations for certain classes of gases.[45] One can envision coarse-graining dynamics by dividing phase space into some cells, on which one can describe mean or typical (maximally likely) values of occupation during a system evolution [789]. This view was dwelled upon by Gibbs [836]:

In considering a system of N identical particles, we assume that available volume of phase space Γ can be partitioned into a number $\Omega(M)$ of equal-volume cells in congruency with some mesoscopic constraints; the mesoscopic states $\{X_m\}$ are here enumerable. We associate now an N-body density on phase space to one on a *reduced* set of *mesoscopic* variables [845, Ch. 2][846]

$$\rho^{(N)}(\boldsymbol{p}^N, \boldsymbol{q}^N) \to \rho^{(N)}(\boldsymbol{X}_m) \ .$$

First let us consider the case when the cell volumes are constant: $|\Gamma_m| = |\Gamma|/\Omega(M)$. For each cell center, $\boldsymbol{X}_m \equiv (Q_m, P_m)$ (representatives of each mesoscopic state m), the Gibbs entropy for the equilibrium distribution over *coarse-grained* phase space is

$$S_G = -\sum_{m\in\Omega(M)} \rho^{(N)}(\boldsymbol{X}_m) \log \rho^{(N)}(\boldsymbol{X}_m) \ . \tag{3.217}$$

The above reduces to the Boltzmann-Planck formula of entropy as logarithm of the total number of coarse-grained states

$$S_B = k_B \log \Omega(M) \ . \tag{3.218}$$

[45] Yet, these already base on the existence of (reduced) density distributions on phase space [95].

Thus, entropy gives a measure of a countable number of mesostates in a system.

For a fully microscopic (*fine-grained*) description of phase space – in the microcanonical ensemble – the entropy for an equilibrium density is generalized[46] as

$$S_{\text{fine}} = k_B \int d\Gamma^N \rho_{\text{eq}}^{(N)}(\boldsymbol{x}) \ln \frac{c}{\rho_{\text{eq}}^{(N)}(\boldsymbol{x})} \,, \tag{3.219}$$

with c denoting a constant that varies from system to system, but can usually be set as $c = 1$.[47]

For quantum mechanical systems, this quantity in equilibrium is given by the von Neumann entropy [764, 847] given phase space density operators D with a countable dimension:

$$S(D) \equiv -k_B \text{Tr} D \ln D \,. \tag{3.220}$$

In classical mechanics, these operators are the "sharp", fully localized N-body distributions $\rho_{\text{eq}}^{(N)}(\boldsymbol{x})$ that we treated in Sec. 3.3. The von Neumann entropy provides the lowest, most "fine-grained" limit on a measure of entropy in phase space, equivalent to Eq. (3.219).

Equation (3.218) emerges after-the-fact that entire regions of phase space have collapsed to single points, associated with representatives $\boldsymbol{X}_m$. Therefore, conversely, Boltzmann postulated that an entropy can be associated with every phase space point. In this view, a coarse-grained mesostate $\boldsymbol{X}_m$ has an intrinsic amount of entropy:

$$S_B(\boldsymbol{X}_m) = k_B \ln(c/|\Gamma_m|) \tag{3.221}$$

A such definition can also be extended to non-equilibrium systems, which we describe further below.

Information entropy

Shannon uncovered the information entropy in 1948 Ref. [848] by analyzing messages transmitted across channels. The information that comes out of a message-generating process[48] is quantified by a weighted summation of contributions from uniquely identifiable distributions. Intuitively, the more ordered a system, the shorter the required length of description to fully characterize its current or typical state. The Shannon entropy quantifies this a measure of the "information content" and order [47, 92, 766, 849–851],

$$S_{\text{sh}}[p(\boldsymbol{x})] = -\sum_{\boldsymbol{x}\in\Gamma} p(\boldsymbol{x}) \log p(\boldsymbol{x}) \tag{3.222}$$

which is regarded as the mean of the logarithmic *likelihood* of state $\boldsymbol{x}$ to occur, from a frequentist point-of-view. If we write the Shannon entropy in terms of the coarse-grained states $\boldsymbol{X}_m$, instead, then by comparing Eqs. (3.217) and

[46] mostly thanks to Boltzmann and Gibbs

[47] This general form for equilibrium can be extended to other ensembles, that are non-isolated, as well, as phase space is thus already "coarse-grained" or projected out (regarding the degrees of freedom of the bath).

[48] A Markovian one

(3.222) we see that the coarse-grained Boltzmann-Gibbs entropy is the special case of the Shannon (information) entropy.

Conversely, Shannon's quantification of information can be used to express that the true microscopic state $\boldsymbol{x}$ of a system is hidden from us if we observe only the mesoscopic or macroscopic world. A mesoscopic state $\boldsymbol{X}_m$ can be associated with a bounded region of phase space Γ: Thus, the conditional probability $\rho^{(N)}(\boldsymbol{x}|\boldsymbol{X}_m)$ expresses a density constrained by this boundary. The information in the conditional density

$$S(\rho^{(N)}(\boldsymbol{x}|\boldsymbol{X}_m)) = -k_B \int d\Gamma^N \, \rho^{(N)}(\boldsymbol{x}|\boldsymbol{X}_m) \ln(\rho^{(N)}(\boldsymbol{x}|\boldsymbol{X}_m)) \; . \tag{3.223}$$

could be regarded as that "hidden" in the mesoscopic state.

The information entropy also opens up the possibility for quantifying relative levels of information. The *Kullback-Leibler divergence* (KL-divergence) [849–851] after a work by its authors 1951 (Ref. [852]), or *cross-entropy*

$$D_{KL}\left(p(\boldsymbol{x})||q(\boldsymbol{x})\right) = \int \mathcal{D}\boldsymbol{x} \, p(\boldsymbol{x}) \log\left(\frac{p(\boldsymbol{x})}{q(\boldsymbol{x})}\right) \geq 0 \tag{3.224}$$

is the *relative entropy* in physics and is strictly non-negative. (The integration measure $\mathcal{D}\boldsymbol{x}$ is written here in continuous form, but can be discrete.) For example, $q(\boldsymbol{x})$ may be a *prior* probability (a steadfast reference) and $p(\boldsymbol{x})$ might represent a *posterior* probability, i.e. the probability distribution of states after measuring the system in a concrete state.

The relative entropy of a particular mesoscopic state can be considered as the KL-divergence of the constrained density versus that in equilibrium:

$$D_{KL}\left(\rho^{(N)}(\boldsymbol{x}|\boldsymbol{X}_m)||\rho^{(N)}_{\mathrm{eq}}(\boldsymbol{x})\right) = k_B \int d\Gamma^N \, \rho^{(N)}(\boldsymbol{x}|\boldsymbol{X}_m) \ln \frac{\rho^{(N)}(\boldsymbol{x}|\boldsymbol{X}_m)}{\rho^{(N)}_{\mathrm{eq}}(\boldsymbol{x})} \; . \tag{3.225}$$

This will be illustrated more further below.

3.5.1 Irreversible march towards equilibrium (illustrative)

This section is an illustration on 'coarse-graining' in nonequilibrium situations. We would like to continue our discussion of coarse-graining from the viewpoint of probability densities on phase space. A nonequilibrium density irreversibly evolves towards the equilibrium stationary density – a rigorous description of which, however, turns out to be a nontrivial task. We outline basic ideas on the continual increase in entropy, dating back to Boltzmann and Gibbs [86, 88, 90, 764, 765, 779, 847]. We also discuss entropy production rates and a few "entropy-like" quantities important for nonequilibrium. These are well-defined for systems with Markov-chain dynamics (which assume microscopically Markovian dynamics) like those studied in part II of this thesis. When such a "Markovianization" of nonequilibrium dynamics is possible is discussed thereafter.

Dynamical entropy

The *fine-grained* dynamical entropy of a normalized time-dependent distribution function in phase space $\rho^{(N)}(\boldsymbol{q}^N, \boldsymbol{p}^N, t)$ is the analogy of Eq. (3.219):

$$S_{\text{fine}}(t) = k_B H_G(t) \tag{3.226}$$

$$H_G(t) = -\int d\boldsymbol{p}^N d\boldsymbol{q}^N / h^{6N} \rho^{(N)}(\boldsymbol{q}^N, \boldsymbol{p}^N, t) \log \rho^{(N)}(\boldsymbol{q}^N, \boldsymbol{p}^N, t) \tag{3.227}$$

The entropy for nonequilibrium distributions is always larger than that of Eq. (3.218), maximizing when thermal equilibrium at a *macroscopic* state is reached.[49] During a nonequilibrium evolution, then, the "highest resolution" entropy of the underlying Liouville dynamics governed by Eq. (3.220) or Eq. (3.227) will remain constant, and the *H-function* $H_G(t)$ or Boltzmann-Gibbs entropy will not decrease. In case the dynamics of a system with a *master equation*, the non-decrease of the H-function can be shown explicitly [88, 779].

This implies that nonequilibrium evolution will always sample more states locally (in space and time) than a Liouville distribution would cover in equilibrium – the relative volume of sampled states will grow. The nonequilibrium Boltzmann entropy can be expressed as [779]

$$S_B(t) = k_B \ln(c\Omega(t)) \tag{3.228}$$

describing the growth of a number of differentiable states $\Omega(t)$ covered by the nonequilibrium distribution. Nonequilibrium dynamics of time-dependent distributions can be interpreted as "error propagation" of local uncertainties in phase space (the growth of a relative volume over microstates), generating an increase in total "uncertainty" or entropy. This expresses a fundamental loss of information about the microscopic state of the system. The heuristics of this argument are illustrated in Fig. 3.1.

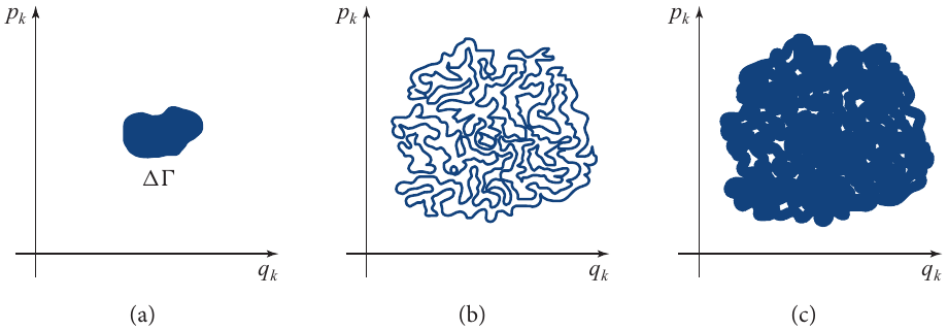

FIGURE 3.1: Coarse-grained trajectory from a clear initial condition (a): the "propagation" of an uncertainty of the microscopic state of a system eventually increases the total volume of the coarse-grained trajectory (b) even if the underlying trajectory is a Liouville evolution (c). Source: Ref. [789, Ch. 4].

[49] A basic assumption of statistical thermodynamics is that the equilibrium Boltzmann-Gibbs entropy is the thermodynamic entropy [853].

Irreversible evolution with master equations (illustrative)

Master equations are basic aliases for a conversion between different levels of coarse-graining: from "fine-grained", microscopic dynamics among states in phase space to *mesoscopic* dynamics, and finally to macroscopic equilibrium (if the system is allowed to equilibrate). In terms of phase space, then, master equations can describe the evolution of any (nonequilibrium) probability density.

Let us consider a probability density initially in equilibrium. The master equation describes the conservative flow of probability among "sharp" states. In the lattice system, this "sharp" evolution is analogous to Liouville dynamics, as we described in Sec. 3.3. However, if the microscopic state of the system suddenly becomes uncertain at some point in time,[50] i.e. is not *sharp* locally, then the dynamics following will be irreversible, will make the probability density "smear out", and express an inevitable increase in entropy. This evolution is inherently *nonequilibrium*.

At some future point, the visitation of microstates becomes independent of any "previous" state – it is as if the system draws random samples of microstates from a prior distribution: the macroscopic equilibrium distribution. The transitions between microscopic states might as well occur simultaneously, over many different microscopic trajectories, implying that the true realization of microscopic motion becomes hidden from us.

In nonequilibrium, we should be able to explicitly quantify the so-called *entropy production rate*, which is always nonnegative in agreement with the second law of thermodynamics [806, 854, 855]. In describing the motion of a single body (in a Langevin picture), we expect the surrounding bath to contribute to one part, and the stochastic movement of particles to another. The entropy production is indeed *linear* in time [856], apart from fluctuations, and this increase is proportional to the effective diffusion constant. The entropy production will disappear at the maximum entropy state – after the densities "hit the walls", i.e. once the finite system size becomes noticeable.

The entropy production rate of a density $\rho^{(N)}(\boldsymbol{s}, t)$ evolving according to a master equation (Eq. (3.124)) can be calculated as

$$\dot{\sigma}(\rho(\boldsymbol{s}_i, t)) = -\frac{1}{2} k_B \sum_{j \neq i} \Big(W_i(\boldsymbol{s}_j, t)\rho^{(N)}(\boldsymbol{s}_j, t) - W_j(\boldsymbol{s}_i, t)\rho^{(N)}(\boldsymbol{s}_i, t) \Big) \times \ln \left(\frac{W_j(\boldsymbol{s}_i, t)\rho^{(N)}(\boldsymbol{s}_i, t)}{W_i(\boldsymbol{s}_j, t)\rho^{(N)}(\boldsymbol{s}_j, t)} \right) \geq 0 \,. \quad (3.229)$$

Therefore, a nonequilibrium evolution entails unbalanced fluxes exist and *persist* in the system over long time-periods. If these fluxes decay to zero everywhere, then Eq. (3.229) is exactly zero, and the probability density reaches equilibrium. We refer the reader to the references listed above for an explicit calculation. The entropy production rate can thus quantify *dissipation*, which ultimately guides the system towards equilibrium.

Using the same terms describe local balance conditions (Sec. 3.3.4), at the fine-grained level, the transitions differ by a "virtual" time step taken δt to evaluate the local Hamiltonian at any time-point t (Eq. 3.170). Defining the

[50] According to the discussion in Sec. 3.3.3, the initial uncertainty means that the system must have been exposed to non conservative forces.

local "forward" flux as $p^+(\boldsymbol{s}_i, \boldsymbol{s}_j, t) = W_j(\boldsymbol{s}_i, t)\rho^{(N)}(\boldsymbol{s}_i, t)$, and a local "backward" flux as $p^-(\boldsymbol{s}_i, \boldsymbol{s}_j, t+\delta t) = W_i(\tilde{\boldsymbol{s}}_j, t)\tilde{\rho}^{(N)}(\tilde{\boldsymbol{s}}_j, t+\delta t)$. and the definition of the Kullback-Leibler divergence (Eq. 3.224), we can write that locally, the entropy production

$$\dot{\sigma}(\rho(\boldsymbol{s}_i, t)) = \\ \frac{1}{2}\left(D_{KL}\left(p^+(\boldsymbol{s}_i, \boldsymbol{s}_j, t)||p^-(\boldsymbol{s}_i, \boldsymbol{s}_j, t+\delta t)\right) + D_{KL}\left(p^-(\boldsymbol{s}_i, \boldsymbol{s}_j, t+\delta t)||p^+(\boldsymbol{s}_i, \boldsymbol{s}_j, t)\right)\right) \tag{3.230}$$

is the symmetrized Kullback-Leibler divergence of the "forward" and "backward" fluxes. However, the KL-divergence is only defined when all entries are non-zero, which poses a problem for hard-core repulsive particles. Hence, we can use the continuous version of the KL-divergence instead, the so-called *Jensen-Shannon divergence*,

$$D_{JS}(p^+(\boldsymbol{s}_i, \boldsymbol{s}_j, t)||p^-(\boldsymbol{s}_i, \boldsymbol{s}_j, t+\delta t)) \equiv \\ \frac{1}{2}\left(D_{KL}\left(p^+(\boldsymbol{s}_i, \boldsymbol{s}_j, t)||P^{+-}(\boldsymbol{s}_i, \boldsymbol{s}_j, t)\right) + D_{KL}\left(p^-(\boldsymbol{s}_i, \boldsymbol{s}_j, t+\delta t)||P^{+-}(\boldsymbol{s}_i, \boldsymbol{s}_j, t)\right)\right) \tag{3.231}$$

with $P^{+-}(\boldsymbol{s}_i, \boldsymbol{s}_j, t) \equiv \frac{1}{2}(p^+(\boldsymbol{s}_i, \boldsymbol{s}_j, t) + p^-(\boldsymbol{s}_i, \boldsymbol{s}_j, t+\delta t))$, which, by the way, can "show" the arrow of time in Markov-chain dynamics (see e.g. Refs. [788, 857]).

In a coarse-grained description, the forward and backward fluxes will eventually equalize, expressing equilibrium. In the maximally fine-grained description, all microscopic transition fluxes will never become fully equalized, locally, which could be interpreted as the thermal motion (fluctuations) of equilibrium. This is what KMC simulations will capture (Sec. 3.4.1)– it will evolve the system forward in time even in equilibrium. Yet, at that point, the localized Jensen-Shannon divergence should level out to zero. Interestingly, as soon as transition fluxes are balanced at a mesoscopic level (via a sum-over-states), the mean local Jensen-Shannon divergence will obtain a minimal value that is nonzero. A proper summation over many sites (an act of coarse-graining) should alleviate this aspect, but highlights the coupling of microscopic degrees of freedom in equilibrium (Ch. 2) – such as for fluids of long rods with rotational and translational degrees of freedom.

Discussion: A "Markovianization" of dynamics

"Proper" dynamical coarse-graining is not an easy task, at all, generally. As in any quantitative description of a system in nature, the first thing to do is to specify the degrees of freedom on which we focus our attention, while ignoring all others. In this general take on the problem [96, Ch. 2][756, 858], we seek to separate an ensemble of trajectories (phase variables) into a "relevant" part and an "irrelevant" one. The probability distribution of the "irrelevant" variables must be preserved by the dynamics of the rest and are thus *stationary* among themselves [763]. (They undergo a stationary dynamics in a sub-process [786, Ch. 7].) Formally, we would apply operators that "project out" these irrelevant variables from the full problem. However, the key diffuculty is knowing the "correct" relevant variables.

If we do a "Markovianization" protocol, probability distribution functions only change at the particular (coarse-grained) time-point t, and not with its history [95, Ch. 6.2, 9]. At the level of the Markovian dynamics, a *simultaneous* separation of length-and time-scales is possible [96]. A "Markovianization" implies, then, that the system entails quasi-stationarity to some degree, where local Boltzmann statistics can be assumed. Markov-chain dynamics follow this prescription, i.e. the dynamics of KMC employed for a lattice model of hard rods in this thesis. The locally "overdamped" motion of particles means the particle finds thermal equilibrium, locally, with a thermal bath – possible when there is a huge separation of intrinsic time-scales between the motion of the bath and that of the particles. The local equilibrium approximation is behind the local (detailed) balance governing the transition rates, see Sec. 3.3.4). The first "relevant" degree of freedom arises on the level of "escape" events to a neighboring site, i.e. "hopping" events. These "mesoscopic" states are defined after a first level of time-scale and length-scale separation.

In many practical situations, it may be helpful to describe general, out-of-equilibrium "mesostates" with thermodynamic concepts like entropy and free energy. For example, information theory and machine learning methods make use of thermodynamic concepts for a large array of variational optimization problems. Heuristically, if we wish to constrain a *model* about the world (or data) to *evidence*, we will be exposing the model system (described by a probability distribution) to effective, external "forces". In the quasistationary approximation, this is similar to the effect of *conjugate fields* on an equilibrium system, which we described and discussed in Secs. 3.2 and 3.3.3. Protocols as well as *bounds* on how well a probabilistic model can adjust to evidence will be *thermodynamic* in character. Specifically in many probabilistic machine learning methods (which we discuss later in Sec. 3.6) quantifying the "mismatch" between a model prior (and "in-equilibrium" distribution) and a model posterior (and "out-of-equilibrium", perturbed system) will be necessary. We attempt to illustrate a few of these concepts below, given everything else we have discussed so far.

3.5.2 Ties to information theory and machine learning

The following discussion aims to illustrate concepts central for the generative machine learning model of variational autoencoders employed in this thesis, remaining in the subject of equilibrium-versus nonequilibrium, as well as coarse-graining. Many parts presented below are based heavily on Ref. [859]. The ideas are part of a framework of stochastic thermodynamics, where thermodynamic-like relationships (inequalities, bounds, etc.) can be formulated for out-of-equilibrium systems. Therein, information theory (i.e. computation and learning [74, 75]) can be formulated and quantified in statistical-physical terms. We refer the interested reader to the corresponding literature for in-depth discussions.

"Mesostates", relative entropy and alike (illustrative)

We can define a "mesostate" (see Refs. [859, 860]) in an out-of-equilibrium system if we observe it remaining there for a very long period of time. The state itself may be a binned average or coarse-grained particle positions, for example.

Assume that any microstate $\boldsymbol{x} \in \Gamma$ is assumed to belong to only one mesostate represented by $\boldsymbol{X}_m$. This should be true for the period of time we measure the system over its trajectory $X(t)$. An infinitely long trajectory average would generate equilibrium statistics and render the likelihood or probability of each mesostate $\boldsymbol{X}_m$

$$\lim_{\tau\to\infty}\frac{1}{\tau}\int_0^\tau dt\delta_{X(t)}\delta_{X,\boldsymbol{X}_m} \equiv p(\boldsymbol{X}_m)\ , \tag{3.232}$$

which by *presuming* ergodicity can be compared to an ensemble average over states belonging to the mesostate:

$$p(\boldsymbol{X}_m) = \sum_{\boldsymbol{x}\in\Gamma_m} \mathrm{e}^{-\beta(\mathcal{H}(\boldsymbol{x})-F)} \equiv \mathrm{e}^{-\beta(F_m-F)}\ . \tag{3.233}$$

where F is the equilibrium free energy of the system with microscopic Hamiltonian $\mathcal{H}(\boldsymbol{x})$.

$$F = -\frac{1}{\beta}\ln\sum_{\boldsymbol{x}\in\Gamma}\mathrm{e}^{-\beta\mathcal{H}(\boldsymbol{x})} = -\frac{1}{\beta}\ln\sum_{\boldsymbol{x}\in\Gamma}p(\boldsymbol{x})\ . \tag{3.234}$$

The right-hand-side of Eq. (3.233) is a way to *estimate* a 'free energy' of the mesostate state F_m via empirical data collection. Conceptually, the mesostate can represent a set of states of a system biased or confined by external means

The internal energy of the mesostate $U_m = \frac{\partial}{\partial\beta}(\beta F_m)$ is a weighted inner energy

$$U_m = \sum_{\boldsymbol{x}\in\Gamma} p(\boldsymbol{x}|\boldsymbol{X}_m)\mathcal{H}(\boldsymbol{x}) \equiv \langle\mathcal{H}(\boldsymbol{x})\rangle_{p(\boldsymbol{x}|\boldsymbol{X}_m)} \tag{3.235}$$

over conditional probabilities

$$p(\boldsymbol{x}|\boldsymbol{X}_m) = \frac{\mathrm{e}^{-\beta(\mathcal{H}(\boldsymbol{x})-F)}}{p(\boldsymbol{X}_m)} = \mathrm{e}^{-\beta(\mathcal{H}(\boldsymbol{x})-F_m)}\ . \tag{3.236}$$

The *Shannon entropy* over these conditional probabilities is

$$\begin{aligned} S_m &= \beta^2\frac{\partial F_m}{\partial\beta} = -\sum_{\boldsymbol{x}\in\Gamma}p(\boldsymbol{x}|\boldsymbol{X}_m)\ln p(\boldsymbol{x}|\boldsymbol{X}_m) && (3.237)\\ &= -\beta F_m + \beta U_m\ . && (3.238)\end{aligned}$$

A relative entropy of the mesostate (compared to equilibrium) can be expressed by the Kullback-Leibler divergence (Eq. (3.224))

$$\begin{aligned} S_m^{\mathrm{rel}} \equiv D_{KL}(p(\boldsymbol{x}|\boldsymbol{X}_m)||p(\boldsymbol{x})) &= \sum_{\boldsymbol{x}\in\Gamma}p(\boldsymbol{x}|\boldsymbol{X}_m)\ln\frac{p(\boldsymbol{x}|\boldsymbol{X}_m)}{p(\boldsymbol{x})} && (3.239)\\ &= \beta F_m\sum_{\boldsymbol{x}\in\Gamma}p(\boldsymbol{x}|\boldsymbol{X}_m) = \beta F_m \geq 0 && (3.240)\end{aligned}$$

which is equivalent to βF_m if $p(\boldsymbol{x}|\boldsymbol{X}_m)$ is normalized. The relative entropy is always greater than zero, so, constraint to a mesostate (for example when coarse-graining states) implies an excess (positive) 'free energy'.

The above notions may help interpret variational autoencoders (Sec. 3.6.2),

which employ a variational free energy model that includes a relative entropy term much alike Eq. 3.239. Specifically, if we might think of input data as mesostates $\boldsymbol{X}_m$ constraining an equilibrium, unconstrained system of hidden (latent) variables ($\{\boldsymbol{x}\}$). In many probabilistic machine learning methods, the task is to find the optimal latent variables that minimizes the relative entropy. We might interpret this as minimizing the 'free energy' of a "hidden" model exposed to the constraints of the data.

We would like to illustrate another concept important for variational autoencoders, which can be derived and understood within the (same) framework of stochastic thermodynamics. an out-of-equilibrium 'free energy' functional can be defined, over the constrained densities (we refer the interested reader to Ref. [436] on more precise clarification):

$$\begin{aligned} \mathcal{F}_{\text{neq}}[p(\boldsymbol{x}|\boldsymbol{X}_m)] &\equiv \langle E(\boldsymbol{x},\boldsymbol{X}_m)\rangle_{p(\boldsymbol{x}|\boldsymbol{X}_m)} + \beta^{-1}\langle \ln p(\boldsymbol{x}|\boldsymbol{X}_m)\rangle_{p(\boldsymbol{x}|\boldsymbol{X}_m)} \quad (3.241)\\ &\equiv \langle E(\boldsymbol{x},\boldsymbol{X}_m)\rangle_{p(\boldsymbol{x}|\boldsymbol{X}_m)} - \beta^{-1}S_m \quad (3.242)\end{aligned}$$

(where we used the definition in Eq. (3.238)). The "energy" function $E(\boldsymbol{x},\boldsymbol{X}_m)$ that the joint distribution $p(\boldsymbol{x},\boldsymbol{X}_m)$ is presumed to follow an exponential ansatz as follows:

$$p(\boldsymbol{x},\boldsymbol{X}_m) = p(\boldsymbol{x}|\boldsymbol{X}_m)p(\boldsymbol{X}_m) = \mathrm{e}^{-\beta(\mathcal{H}(\boldsymbol{x})-F)} \equiv \mathrm{e}^{-\beta E(\boldsymbol{x},\boldsymbol{X}_m)} \tag{3.243}$$

(using Bayes' theorem in the first step). With this expression, we can re-write this out-of-equilibrium 'free energy' functional as

$$\begin{aligned} \mathcal{F}_{\text{neq}}[p(\boldsymbol{x}|\boldsymbol{X}_m)] \equiv &-\beta^{-1}\langle \ln p(\boldsymbol{x},\boldsymbol{X}_m)\rangle_{p(\boldsymbol{x}|\boldsymbol{X}_m)} \\ &+\beta^{-1}\langle \ln p(\boldsymbol{x}|\boldsymbol{X}_m)\rangle_{p(\boldsymbol{x}|\boldsymbol{X}_m)} \end{aligned} \tag{3.244}$$

which turns out to express, formally, the negative *evidence lower bound* at the heart of the variational mean-field-theory ansatz in variational autoencoders, shown later in Sec. 3.6.2 e.g. Eq. (3.274). In the variational problem, this out-of-equilibrium 'free energy' functional should be minimized – with respect to a "hidden" model (defined over free parameters).

Assuming mesostates are independent from each other, a free energetic difference between these two can be inferred as

$$\Delta_{m,m'}F = F'_m - F_m = -\beta^{-1}\ln\left(\frac{p(\boldsymbol{X}'_{m'})}{p(\boldsymbol{X}_m)}\right) . \tag{3.245}$$

Yet, independence (microstates can belong to only one mesostate over the course of very long periods) implies that these two mesostates will have to emerge during a system dynamics after the first state has fully relaxed. In this case, the fluxes between the two states should balance

$$p(\boldsymbol{X}'_m,t'|\boldsymbol{X}_m,t)p(\boldsymbol{X}_m) = p(\boldsymbol{X}_m,t|\boldsymbol{X}'_m,t')p(\boldsymbol{X}'_m) . \tag{3.246}$$

which means we can express transition rates (when expanding for small time-differences $t'-t$) with a familiar exponential or Arrhenius relationship

(Sec. 3.3.8):

$$\frac{W(\boldsymbol{X}_m \to \boldsymbol{X}'_m)}{W(\boldsymbol{X}'_m \to \boldsymbol{X}_m)} = \mathrm{e}^{-\beta\Delta_{m,m'}F} = \mathrm{e}^{-\beta\Delta_{m,m'}U+\Delta_{m,m'}S} \tag{3.247}$$

where

$$W(\boldsymbol{X}_m \to \boldsymbol{X}'_m) = \frac{\partial}{\partial t'} p(\boldsymbol{X}'_m, t'|\boldsymbol{X}_m, t)\Big|_{t'=t} .$$

The waiting time for the transition to state $\boldsymbol{X}'_m$, given the system starts fully in state $\boldsymbol{X}_m$, is thus describable by an Arrhenius law

$$p^{\text{wait}}(\boldsymbol{X}_m \to \boldsymbol{X}'_m, t) = \mathrm{e}^{-\beta\Delta_{m,m'}Ft} \tag{3.248}$$

The above relations will fail to hold if the dynamics become non-Markovian at the mesoscopic scale of treatment. 'Spatial' or time-like separation is then ill-defined, and a *coupling* between the mesostates may become visible in the form of wide, and non-exponential relaxations or broad-banded statistics of relaxation times. Such broadening is seen in many cases where ergodicity is lost, examples are liquids with long-ranged interactions or the transition to a glass [68, 352, 861]. We discuss more on topics of nonequilibrium dynamics in Sec. 3.5.3. We also find this kind of 'broadening' of spectra in machine learning systems – within variational autoencoders – when it approaches a transition point (in its internal state), see Ch. 7.

Foundational principles from information theory

As we investigate machine learning from a "statistical mechanics" point-of-view in this thesis, we feel necessitated to discuss some of the better-known and deepest ties between information theory and statistical mechanics. We have seen that if we attempt to coarse-grain a physical system in equilibrium, information-theoretic notions quantify, most generally, the statistical relationships between variables among and across different levels. Jaynes [790, 791] regarded statistical physics as a way to draw inferences – the probability distributions – from limited data, such as the measured average energy per particle in an assembly of particles, so that these is the least possible bias regarding all other degrees of freedom [92]. The more biased a probability law, the more information it carries [847].

In Jaynes' *maximum entropy* (*MaxEnt* [92, 766, 790, 791]) procedure, one maximizes the Shannon-Gibbs entropy of a probability distribution function $p(A)$ on a set of (general) microstates $\boldsymbol{x}$. The aim is to solve following variational problem

$$S[p(\boldsymbol{x})] = -k_B \sum_{\boldsymbol{x}} p(\boldsymbol{x}) \ln p(\boldsymbol{x}) - \sum_i \lambda_i \mathcal{C}[\boldsymbol{x}] = \max \tag{3.249}$$

subject to additional constraint functions $\mathcal{C}[\boldsymbol{x}]$ that define Lagrange multipliers $\{\lambda\}$ in the variational problem. They may fix expectation values such as the average energy given by a Hamiltonian on the states, which is typically an indication of large baths [92]. Probability conservation is fixed via a normalization constant (ultimately rendering the partition function). These can be used to derive the stationary ensembles for thermodynamic equilibrium, as

we mentioned in Sec. 3.1.4. Note that as with any variational approach, (thermodynamic) predictors are only valid *after* the maximization procedure of the entropy functional.

In this view on statistical laws, any other law compatible with the data would entail a smaller statistical entropy (more than the minimal amount of information required). By choosing probabilities by means of maximum entropy, we keep all the available information of a system while discarding any other irrelevant information [847]. This agrees with a Bayesian *inference* viewpoint frequently adopted in machine learning. In this way, statistical physics could be a science about partially unknown (unmeasurable) states of a system (at whatever level of resolution), given constraints on what *is* known. i.e. mean values or known macroscopic constants of a system.

Kullback [851, Ch. 3] had theorized in 1959 that minimizing the Kullback-Leibler divergence or *relative entropy* ("minimum discrimination information") can be a general principle when prior information is at hand. Maximizing Shannon entropy is a special case when the prior is uniform, i.e. when we only know the number of possible states.[51] The Kullback-Leibler divergence (Eq. 3.224) was derived by Shore and Johnson ([863, 864]) (1980-81) as the minimizing functional (apart from a pre-factor) that is self-consistent with measurement outcomes, *without* having to assuming anything about Shannon's function beforehand.

Yet, in physics, entropy extremization principles are typically only associated with equilibrium systems. Formulations for time-dependent systems, in particular nonequilibrium systems, have been proposed in various contexts (e.g. Ref. [865]), but have not found universal acceptance. A generating functional [91, 775, 803] for dynamics should, in theory, allow one to derive nonequilibrium current fluctuations. A time-dependent extremization principle might be discussed in terms of parametrized paths of a system [92, 803, 854, 866]. We refer the reader to the references for further discussion. In any case, lattice systems following a discrete-time master equation are excellent candidates for developing and testing theory on nonequilibrium. Significant progress has been made in the last decades in the framework of Markov chain models [817, 819, 820, 855, 857, 859, 867, 868].

The relative entropy or Kullback-Leibler divergence has been a key quantity in this context. It can be an indicator for the "arrow of time" in nonequilibrium [784, 788, 805, 818, 828]). (It is also directly related to the Fisher information matrix, an important quantity within quantum many-body theory.) Variational autoencoders, a machine learning algorithm explored in part IV of this thesis, minimize a Kullback-Leibler divergence (the relative entropy in Eq. 3.239) to find a stationary solution to a variational problem. The variational problem can be formulated more specifically as minimizing the out-of-equilibrium 'free energy functional' defined in Eq. 3.244. We described the algorithm employed in this thesis in more detail in Sec. 3.6.

3.5.3 Breakdown of Markovian dynamics in nonequilibrium

Unsuitable places to attempt to coarse-grain a system are where ergodicity is lost – around phase transitions, and in other far-from-equilibrium situations

[51] A uniform prior as being appropriate in such a case of ignorance is something Jaynes showed using transformation group arguments in Ref. [862].

where events in the system irreversibly change the future properties of the system at various mesoscopic and macroscopic scales. On the other hand, these are some of the most interesting places in physics, arguably, which may be no accident. In this thesis, we investigate nonequilibrium dynamics in part II for a model of thin film growth. Moreover, MCMC simulations (done in part III of this thesis) trimmed at extracting equilibrium statistics are exposed to nonergodic behavior at phase transitions. We see hints of 'frustration' during training in a machine learning algorithm studied in part IV, which is likely related to a loss of ergodicity, as well. Therefore, we aim to provide a general, qualitative discussion below.

Generally: Broken ergodicity

Problems arise when a system begins to 'fractionate' its characteristic time-scales for relaxation processes. Once some of these relaxation processes occur on time-scales longer than the observation time, ergodicity will be lost. In these terms, ergodicity can be an *observed* property, and its degree if breaking is related to the amount of observational information that can be collected. Moreover, it is related to whether system variables fluctuate in our time- and space-window of observation. A gradual breakdown occurs, for example, during the formation of a glass [105, 106]. During the formation of a glass in colloidal systems, for example, the strong space–time coupling can be seen in the characteristic time-scales for a relaxation in the fluid, which becomes strongly length-scale dependent [104]. Metastable hard-sphere fluid states, where particles get "caged", also show a loss of ergodicity of the colloidal particles prior to the onset of crystallization [103]. Systems with long-ranged forces are quite unique cases in that they seem to be inherently non-ergodic – stationarity may be a nonequilibrium steady state rather than Boltzmann equilibrium [558–562].

A system out-of-equilibrium lives in the realm of surprising (*non-typical, rare*[52]), intricate, and unforeseeable characteristics (i.e. instabilities) [76]; the evolution of our entire universe today included [869]. Nature's talent to generate such intricacies when highly out-of-equilibrium (non-ergodic) is exemplified by our model system for thin film growth with hard rods (part II): In Ch. 4, we uncover dynamic arrested, "jammed" states with unique structure. In Ch. 5 we study the highly diverse array of kinetics and structure formation with "sticky" rods in a nonequilibrium evolution between two stable, equilibrium states: from a low-density vapor phase to a high-density liquid phase (in the lattice model).

In any case, time-dependent correlation functions in highly nonequilibrium systems are different from those in equilibrium [870], and a broad distribution of waiting times (or frequencies of events) can indicate a loss of ergodicity. These are characteristic features of critical dynamics (see Sec. 3.2.1) and scaling, which can occur observable in in a variety of machine learning problems (discussed also in Ch. 1.4). The case of variational autoencoders are investigated in Ch. 7.

For Brownian dynamics (fully Markovian), a relationship exists between space (a mean-squared displacement) $\|\Delta \boldsymbol{r}\|^2$ and waiting time Δt persists:

$$\left\langle \|\Delta \boldsymbol{r}\|^2 \right\rangle_{\Delta \boldsymbol{r} \sim \rho(\Delta \boldsymbol{r}, \Delta t)} = 2dD\Delta t \tag{3.250}$$

[52] in the sense of equilibrium

where the brackets indicate an ensemble average, d is the dimension. The proportionality between an area (second degree in space), and time, is given by the diffusion constant D. Note that the dynamics in the continuum can be coarse-grained into a discrete-space and time- Markovian processes, e.g. with a continuous-time random walk, which represents the same type of dynamics on lattices. This proportionality between area and time (Eq. (3.156)) will disappear when an equilibrium fluid falls out-of-equilibrium, where e.g. anomalous diffusion occurs [107, 871]: the relationship between area and time may be $\propto \Delta t^{\alpha}$, for some $\alpha < 1$. The system will show ageing and memory, and effective equations of motion of the integro-differential kind will have to include *memory kernels*, for example. The non-Markovian character of a nonergodic system cannot be 'rid of' via a sum-over-states, i.e. any attempt to 'Markovianize' or coarse-grain the system will be systematically in err.

Although we do not treat nonequilibrium steady states in this thesis, they highlight inherent "space-time-" couplings that occur in nonequilibrium, generally, even for the arguably simplest of fluids. Nonequilibrium steady states are the 'next best thing' to equilibrium, from a theoretical point-of-view, as the macroscopic (static) state of the system is stationary. They may arise due to an external, time-dependent driving force, e.g. a slowly oscillating field. Although mean densities can be constant, for example, the striking difference to equilibrium becomes apparent when looking at the internal dynamics of the fluid (see e.g. Ref. [872]). Fluids in nonequilibrium steady states can entail long-ranged correlations that are *Coulombic* in their extent, i.e. proportional to $\sim \frac{1}{r}$ in 3D, and $\sim \ln\left(\frac{1}{r}\right)$ in 2D [68, Ch. 5][873–875]. Clearly, a "sufficient" decay of correlations is fundamental for equilibrium and Markovian dynamics.

Phase transformation

The emergence of new structures when crossing a binodal line is an expression of an internal transformation of the *dynamics* of the system. In Sec. 3.2.1 we described that thermal energy must be dissipated due to the work required from the outside to cross the phase boundary. New modes of energy and momentum transfer are opened up, and all remain coupled until the system reaches a new equilibrium after long times. Initially, correlations become increasingly 'stretched' and decays can become power-law-like [68, 555], indicating a broad spectrum of processes in the system, analogous to the behavior upon approaching a critical point (see next paragraph). New structures appear throughout the system and become increasingly large (i.e. "nucleation and growth"). Although it will be difficult to coarse-grain the full dynamics, it is possible that certain sub-sets of variables reach equilibrium faster than others, possibly is some kind of hierarchical cascade.[53] We observe the nonequilibrium dynamics of diverse structural variables during phase separation in part II of this thesis by modeling thin film growth in monolayers.

In Sec. 3.2.1 we described how a continuous phase transition through a *critical* (point) is tied to a loss of ergodicity in a violent, singular event. Upon approaching the critical point, the dynamics modeled by Markov chains will

[53] Effective dynamical field theories (of the Ginzburg-Landau type or Cahn-Hilliard equations) can be used for describing the spatially extended (low-wavelength) variables during phase separation kinetics [17, 68, 800]. These are mean-field based (see Sec. 3.2), providing an evolution equation of an order parameter field.

become increasingly detailed at ever finder time-scales, slowing down the sampling of independent states in the simulation. This effect is denoted *critical slowing down* [876], which is a bit misleading, as much more happens than ever before: One needs ever more fine time-windows to capture the increasingly broad spectrum of processes (which is directly calculated in kinetic Monte Carlo, Sec 3.4). This shrinking of a characteristic time-window shows that any attempt at coarse-graining the dynamics ultimately fails exactly at a true critical point, which is defined for infinite systems. There, time- and length-scales are governed by power laws (scaling theory describes the divergence of correlation fluctuations). See remark below. For finite systems, such as those simulated in MCMC methods, the phase transitions are not sharp, as these pathological power laws are reduced down to "broad" spectra. The system dynamics can become Markovian again after sufficiently long waiting times, as the split between differently ordered macroscopic states is only metastable (see Sec. 3.2.1).

Remark. Ref. [877] proved that such power-law decays cannot arise from purely Markovian processes. They analyze the mutual information between random variables generated by a general Markov process arising at two points in time t_1 and t_2. This quantity decays exponentially for large separation $|t_2 - t_1|$ in the sense that it is possible to bound the mutual information by an exponential. This illustrates again the deep tie between equilibrium dynamics (that of *observational states* of the system [90]) and Markovian descriptions (i.e of a possibility to map it to a Markov chain).

* * *

We have discussed probabilistic approaches in equilibrium and nonequilibrium statistical mechanics. We illustrated and discussed the most fundamental ideas behind equilibrium statistical mechanics, and discussed concepts relevant for further parts of this thesis. We have also discussed the Markov-Chain Monte Carlo methods relevant for the next two parts of this thesis. These can be used to explore nonequilibrium dynamics of simple model systems under the assumption that the dynamics of individual particles are Markovian at the microscopic scale (KMC simulations) – this concerns part II of this thesis. At any larger scale-of-treatment, however, the highly correlative nature of nonequilibrium dynamics is related to an inability to separate length- and time-scales and non-ergodicity. Finding an effective treatment of highly nonequilibrium systems is a great challenge, and may even be impossible with a (partially) Markovian prescription for general cases. Approaches that may be 'near-equilibrium' (to quite some extent) like DDFT were also discussed in the context of master equations for lattice systems. Finally, we motivated connections between statistical mechanics and information theory, as well as the use of statistical-physical concepts within probabilistic machine learning methods.

We close our discussion about equilibrium and nonequilibrium physics with one point about the divergences of length- and time-scales at phase transitions: Essentially any empirical observable that is a function of the configurations (linear sums or nonlinear transformations), if sampled over sufficiently many steps during system dynamics, will entail the largest variance at phase transition points. Generally speaking, machine learning algorithms aim at being able to capture a broad spectrum of possible states while still being able to

accurately predict or distinguish a concrete state from the 'rest'. The latter is essentially an impossible task if the states (data) come from a system near or at a critical point. This may be important for why machine learning algorithms can "detect" phase transitions in physical data-sets – or, rather, distinguish between phases – so well, which has been reported numerous times in the literature.

We shall discuss more general aspects of probabilistic modeling for machine learning in the next section, Sec. 3.6. Therein we shall also introduce variational autoencoders which are explored in this thesis.

3.6 Probabilistic modeling with machine learning

Many frontiers in modern machine learning research involve formulating probabilistic models for data that incorporate known information [386, 390, 878, 879]. An abstract *origin* of data (an "unknown" stochastic generating process) is tied our *observations* thereof (the dataset at hand). Specifically, probability densities to observe data allow us to estimate how *likely* a specific example may be. An ability to estimate statistical relationships of variables beyond just an expectation (mean) value is another argument in favor of such "fuller", inference models of the world. Moreover, if we can infer a generative (stochastic) *process* underlying observed data, then we can use this to produce similar data.

Aside from utilitarian aspects, the case could be made that learning to generate data (that is convincing in multiple measures) is an ultimate "litmus test" of the algorithm's ability to capture generic features in the given dataset, all the while having formulated a synthetic model of reality. This goes back to the intuitive idea that if enough samples are seen during training, it should be possible to extract something like the "essence" of the data – We should be able to make predictions as well as capture all possible states that make up the dataset. This is a much stronger statement than being able to making good *estimates* of specific quantities in the data, i.e. "fitting" data, and represents a *Bayesian* view on machine learning [390, 394, 850, 880].

Latent variable models, Bayesian modeling

A probabilistic model for data is expressed through the density $p_{\text{model}}(\boldsymbol{x})$ with the introduction of unknown, *hidden* or *latent variables* $\boldsymbol{z}$ that are responsible for some underlying features in the data, left unspecified [108, 394]. The formal relationship between the observable data set $\boldsymbol{x}$ and these features is the integral

$$p_{\text{model}}(\boldsymbol{x}) = \int\limits_{\Omega(z)} d\boldsymbol{z} p(\boldsymbol{z}) p_{\text{model}}(\boldsymbol{x}|\boldsymbol{z}) \,, \tag{3.251}$$

where the conditional probability, the *likelihood function* $p(\boldsymbol{x}|\boldsymbol{z})$, represents the probability of observing the dataset or sample $\boldsymbol{x}$ given the set of (unknown) variables $\boldsymbol{z}$. $\Omega(\boldsymbol{z})$ is the domain of the here continuous variables, typically $\Omega(\boldsymbol{z}) \equiv \mathbb{R}^d$ with d being the dimensionality of the latent space. The *prior distribution* on these latent variables is expressed by $p(\boldsymbol{z})$. This prior can be arbitrary, but is often set as a unit Gaussian. (In contrast, a uniform prior reflects the hypothesis of *equal a priori probabilities on phase space* of statistical mechanics.) Although Eq. 3.251 may seem trivial at first, it is the basis for a wide variety

of sophisticated machine learning methods. The next paragraph attempt to illustrate the genericness of the above relation.

Equation (3.251) expresses a key notion: The hidden variables – also known as *latent variables* – are other ways to represent the data: This so-called *representation learning* [109, 391] can be of great utility for a physicist, as these variables are a concrete characterization of a physical system: Representations that are further tied to a probabilistic model, like in variational autoencoders (see below), can model a process that generates the data, which us useful if we do not know where the data came from or how to generate it (without e.g. MC methods). In the other case that the underlying physical, generative process is *known*, then these representations are an interesting alternative – at the very least – for describing the system formally. In the best case, the variables are *interpretable* and might follow some systematics, such as a coarse-graining hierarchy, that can be incorporated into an analytical description. This appears to be the case in our study with applying machine learning in Ch. 7. Probabilistic machine learning models can thus serve as sophisticated, automatic "feature extractors" or "representation vendors" for physical data.

Another interpretation of Eq. (3.251) is that the hidden variables are intermediaries, interacting with visible degrees of freedom in a possibly simple manner, but rendering complex correlations between the visible degrees of freedom when integrated out (*marginalized over*). One can also interpret the hidden variables as the degrees of freedom remaining after an integration, forming an effective field theory of the data (see Secs. 3.2 and 3.5, as well as the introductory discussion in Ch. 1.4). We find this is consistent with collective variables found by variational autoencoders in Ch. 7. This could make latent variable models candidates for building analytical theories if these methods are applied to a physical system, a crucial point of outlook discussed in the corresponding chapter.

By the basic relation $p_\theta(\boldsymbol{z})p_\theta(\boldsymbol{x}|\boldsymbol{z}) = p_\theta(\boldsymbol{x},\boldsymbol{z})$, we see that eq. (3.251) is expressing a *marginal likelihood* or *model evidence* of observable variables (data) when taken as a function of parameters θ:

$$p_\theta(\boldsymbol{x}) = \int\limits_{\Omega(\boldsymbol{z})} d\boldsymbol{z} p_\theta(\boldsymbol{x},\boldsymbol{z}) \,, \tag{3.252}$$

where $p_\theta(\boldsymbol{x},\boldsymbol{z})$ is a so-called *deep latent variable model* or *deep generative model* over both observable and latent variables. Further relationships can be expressed in terms of the *posterior distribution*

$$p(\boldsymbol{z}|\boldsymbol{x}) = \frac{p(\boldsymbol{z})p_{\text{model}}(\boldsymbol{x}|\boldsymbol{z})}{\int\limits_{\Omega(\boldsymbol{z})} d\boldsymbol{z} p(\boldsymbol{z})\ p_{\text{model}}(\boldsymbol{x}|\boldsymbol{z})} \,, \tag{3.253}$$

The posterior in Eq. (3.253) represents the probability to observe a particular set of latent variables after a set of inputs arrives.

Eq. (3.253) holds true because of *Bayes' theorem*, which in simpler form expresses a basic relationship between (unknown) probability distributions and *certain information*: A general conditional distribution $p(\boldsymbol{x}|\boldsymbol{z})$ is related to the conditional distribution (the posterior) $p(\boldsymbol{z}|\boldsymbol{x})$, which may be a "measurable

quantity", for example via

$$p(\boldsymbol{x}|\boldsymbol{z}) = \frac{p(\boldsymbol{z}|\boldsymbol{x})p(\boldsymbol{x})}{p(\boldsymbol{z})} \,. \tag{3.254}$$

where $p(\boldsymbol{x})$ is the marginal probability of observing $\boldsymbol{x}$ and $p(\boldsymbol{z})$ likewise for the hidden variable $\boldsymbol{z}$ – the prior.

Equations (3.251) and (3.253) are merely formal: A term such as $p_{\text{model}}(\boldsymbol{x}|\boldsymbol{z})$ may, in fact, be modeled by a stochastic neural network that is optimized in parameters θ with respect to a particular objective function, written as $p_\theta(\boldsymbol{x}|\boldsymbol{z})$. This is the case for *variational autoecoders* (see corresponding section below). As an illustrative example, $p_\theta(\boldsymbol{x}|\boldsymbol{z})$ may be assumed to be Gaussian, and if $\boldsymbol{z}$ is discrete, then $q_\phi(\boldsymbol{z}|\boldsymbol{x})$ – now a model for $p(\boldsymbol{z}|\boldsymbol{x})$ – becomes a mixture of Gaussian distributions. In other cases, one assumes a Bernoulli form of $p_\theta(\boldsymbol{x}|\boldsymbol{z})$. For continuous values of $\boldsymbol{z}$, which is more convenient and can be realized a the so-called *reparametrization trick*, the marginal likelihood $p_\theta(x)$ can be seen as an infinite mixture, which, in practice, could be more powerful than discrete mixtures [878, Ch. 1.6].

This general, Bayesian type of approach allows for a full probabilistic model at one's disposition, rather than the first (at most few!) moments of a distribution (e.g. fitting). In principle, then, inference can be used to predict any of the variables given any of the other variables by expressing their conditional probabilities. Moreover, the features extracted in the latent space should be telling us something generic about the dataset.[54] In Ch. 7 we find that if data is Boltzmann-Gibbs distributed, i.e. is composed of equilibrium configurations, then a probabilistic latent-variables model (VAEs) can discover *collective variables* of the physical system (many-body features). The full set of these variables can be used to distinguish between thermodynamic phases, for example. Further, for the probability to detect a certain feature in the data, this model provides *variances* that can relate to the physical *susceptibility* of the system.

Tractability issues: Variational methods

A tractable posterior distribution $p(\boldsymbol{z}|\boldsymbol{x})$ might be lacking, which means that $p_\theta(\boldsymbol{x})$ is intractable. Hence we cannot differentiate it with respect to its parameters and optimize it, as can be done using *maximal likelihood estimation* on fully observable models. Approximation of $p_\theta(\boldsymbol{x})$ with a *model inference* distribution $q_\phi(\boldsymbol{z}|\boldsymbol{x})$ becomes a necessary technique – we assume a particular analytical, tractable form. This then allows for obtaining a tractable expression for $p_\theta(\boldsymbol{x})$. This describes the situation for variational autoencoders (which we describe further below). One then optimizes an objective function with respect to the parameters ϕ of the model. This may be deemed a "point-wise variational free energy" $F(\boldsymbol{x})$ that provides a tractable lower bound on the underlying, unknown (log-) probability distribution of data $p(x)$. The underlying methods come from variational mean field theory (See Sec. 3.2).

Remark. Quite obviously, some vocabulary has been adopted from physics: *Energy-based models* assume that the (generally unknown) distribution over data $\boldsymbol{x}$ follows a Boltzmann distribution, $p(\boldsymbol{x}) \sim \exp(-E(\boldsymbol{x}))$, where $E(\boldsymbol{x})$ is a scalar function, i.e. part of the exponential family of probability distributions. These

[54] Clearly, the exact origin of a generic feature is an ill-defined inverse problem, as features are found throughout entire 'ensembles' of data.

are also called *Gibbs distributions* in the field, in analogy to Gibbs ensembles that we discuss in Ch. 3.

Generative modeling

Infamous architectural examples of generative models – those where we can generate fake examples of data closely resembling the training set – include variational autoencoders (VAEs) (see below) and generative adversarial networks (GANs) [111]. These architectures are 'idiosynchratic' in their behavior, i.e. latent variables may "collapse" that cause generated images to be of one particular "type" only (GANs are more susceptible to this [881]). The question of why generative models may or may not succeed for arbitrary datasets, and which considerations about the sources of the data are necessary, play a central role in current machine learning research.

The development of *generative methods* stems from a basic desire to find methods that can represent data in *many* ways, i.e. flexible learning systems that are useful for many tasks. In figurative terms, a learning systems should gain a *generic* "understanding" about the data, i.e. should find a universal representation of it. In contrast, while "standard" representation learning – like standard autoencoders – is clearly useful and somewhat insightful, it still depends on the end-task for which it will be applied for, i.e. on the specific input–output setup. We need a different kind of setup where an algorithm could, in principle, find "generalized" representations that would be useful out-of-task. This means we first need to understand what fundamental, generic properties a learning agent will try to "reverse engineer" when exposed to sample input data. In order to venture towards "generalized" learning in all earnestness, then, we may need to question deeply into the nature of physical reality [109]. Let us explain.

From a more pragmatic point-of-view, generative algorithms should "generate" data (images) "just like" the training set, but, consistent with underlying probabilistic model (the *source* that generates it). For VAEs, we will be forced to impose a model for the data in an approximate posterior distribution (see further below). The *meaning* behind these assumption, and even how well these are founded, is part of what we explore in this thesis. As we apply the algorithms to a statistical-mechanical model systems, we will be in a uniquely privileged position to scrutinizing such model assumptions about the world – in this case, the *physical* world.

Regarding ontological questions of generative modeling, we should probably presume that data is generated by or organizable according to a hierarchical principle [417]. "Information" in data will also reflect some form of temporal and spatial coherence [882]. Symmetry (and the breaking thereof) is another, very fundamental principle that seems unavoidable for learning "reasonable" representations, see e.g. Ref. [532]. We discussed this in Ch. 1.4.1. The machine learning literature discusses so-called "generating" or "salient factors of variation" in datasets that should be represented (learned) in a "disentangled" fashion by the learning agent [108, 109]. We are not sure about the *physical* definition or meaning of this elusive notion. Nonetheless, our studies with VAEs in part IV of this thesis might contribute to similar foundational ideas about generative modeling, arguing that we can test the compatibility of models and representations with *physical laws*.

3.6.1 Principal Component Analysis (PCA)

Principal component analysis (PCA) is an unsupervised method for dimensionality reduction [388, Ch. 15] [386, Ch. 13][883, Ch. 10][389, Ch. 12][394][384, Ch. 6]. In this utilitarian view, PCA provides a simple means for projecting data onto two- or three-dimensional space, where we can use our intuition to further interpret or process data. In contrast to clustering methods such as *t-stochastic neighbor embedding* (t-SNE) (see e.g. [394]), PCA is a linear method, which is one of its basic limitations, as any significant variations that embody a nonlinear 'distortion' in the data will be at best approximated with covariances. It can be extended to a nonlinear mapping via a kernel transformation of the data in *kernel Principal Component Analysis*, which is out of the scope of this discussion, however.

PCA decomposes a dataset into eigenmodes via a diagonalization (rotation) of the covariance matrix of the data. The basic assumption is that there is a single Gaussian model (of high dimension) of the data (the mean is set to zero). Thus, its can be viewed a projecting data onto a high-dimensional manifold of uniform curvature in each direction, the curvature inversely related to the variance of the data.

Viewpoint from statistical field theory

Note: We provide here a brief, unconventional discussion on PCA based heavily on Ref. [454].

We can imagine that the dataset is a physical system with N variables $\{\phi_i\}_{i=1}^N$, where N is large. For simplicity, we assume the means of these variables is zero. As in standard field-theory approaches, we assume their fluctuations are nearly Gaussian, hence for their joint probability density, following the exponential of an effective Hamiltonian or action,

$$p(\{\phi_i\}) = \frac{1}{Z} \exp\left(-\frac{1}{2} \sum_{i,j} \phi_i K_{ij} \phi_j - \frac{1}{4!} g \sum_i \phi_i^4 + \dots \right) . \tag{3.255}$$

The coefficient g represents a weak kurtosis of the random variables. Eq. (3.255) is also the maximum entropy density constrained to a covariance of the variables (second moment) and mean kurtosis (fourth moment), which makes it arguably generic. The system is determined by a Gaussian if $g = 0$, where the matrix K_{ij} is the inverse of the covariance matrix defined by $C_{ij} = \langle \phi_i \phi_j \rangle$.

The eigenvalues λ_ν and eigenvectors $\{u_i(\nu)\}$ of the matrix K fulfill

$$\sum_j K_{ij} u_j(\nu) = \lambda_\nu u_i(\nu) \tag{3.256}$$

and allow the variables $\{\phi_i\}$ to be decomposed into modes $\{\tilde{\phi}_\nu\}$

$$\phi_i = \sum_\nu u_i(\nu) \tilde{\phi}_\nu . \tag{3.257}$$

If $g = 0$, the modes are precisely the principal components. The Gaussian part of the effective Hamiltonian is then

$$\frac{1}{2}\sum_{i,j}\phi_i K_{ij}\phi_j = \frac{1}{2}\sum_{\nu}\lambda_\nu\tilde{\phi}_\nu^2 \,. \tag{3.258}$$

The variance of each such mode is determined by the inverse eigenvalue $\langle\tilde{\phi}_\nu^2\rangle = 1/\lambda_\nu$. Further, in the limit of large N, the spectral density distribution of eigenvalues $\rho(\lambda) = \frac{1}{N}\sum_\nu \delta(\lambda - \lambda_\nu)$ becomes a continuous function. There is a largest eigenvalue Λ: the average variance of any variable is calculated as

$$\frac{1}{N}\sum_i \langle\phi_i^2\rangle = \frac{1}{N}\sum_\nu 1/\lambda_\nu \;\longrightarrow\; \int_0^\Lambda d\lambda\rho(\lambda)\frac{1}{\lambda} \,. \tag{3.259}$$

In applying this formalism to datasets with many degrees of freedom, we have no access to the underlying matrix K. However, we can estimate K with the inverse of the covariance matrix as long as the dataset is close to following a Gaussian, and as long as it is large enough. However, importantly, in systems with symmetries such *translation invariance*, the eigenvectors of C should turn out to be those of K. In fact, if the variables live in positions $\mathbf{r}$ in a d-dimensional Euclidean space, a "kinetic energy" term induces correlations among the variables ϕ, enforcing similarity among neighbors, as in the Ginzburg-Landau effective Hamiltonian or free energy (see [65]),

$$\frac{1}{2}\sum_{i,j}\phi_i K_{ij}\phi_j \;\longrightarrow\; \int d\mathbf{r}(\nabla\phi(\mathbf{r}))^2 \tag{3.260}$$

The eigenvectors of this Gaussian field theory are divergence operators or (Fourier) modes, thus the local Hamiltonian "kernel" is a *laplacian*, as mentioned in sec. 3.2. These can be indexed by a wave vector $\mathbf{k}$, and the eigenvalues are $|\mathbf{k}|^2$. If the original space has a lattice spacing a, then the maximum eigenvalue is $\Lambda \sim (\pi/a)^2$, in line with the ground harmonic state having one-half wavelength.

Of course, it is not clear *a priori* whether or not this is the case. Closer inspection on the eigenvalue spectrum of PCA provides partial answers. It can first be used to order the degrees of freedom along an axis (in the Gaussian case by the wave-numbers). If the spectrum of the covariance matrix entails a limited number of low eigenvalues (with highest variance) that differ substantially from the rest, then one can say that the system is genuinely low-dimensional. Usually there is a continued variation in the magnitude of the eigenvalues; there may even be power-law behavior, which is difficult to verify, however.

In such a broader-spectrum case, one can then "coarse grain" the model by eliminating (averaging out) the modes that have small variance, i.e. those with $\lambda < \Lambda$, which amounts to decreasing the limit Λ of the integral in eq. (3.259). Though this might appear a trivial task, the joint probability density of the remaining variables may be highly nontrivial, of which one could measure e.g. fourth-order moments, in practice, to characterize such a progressive coarse-graining transformation. This is at the heart of renormalization group analysis. Hence, using PCA, we can ignore microscopic details in data that are irrelevant for a more global model, "zooming out" to the stochastics of macroscopic,

collective variables that are ranked in importance by their Gaussian-expected fluctuations. The effective number of degrees of freedom upon this coarse-graining is

$$N_{\text{eff}} = N \int_0^\Lambda d\lambda \rho(\lambda) \, . \tag{3.261}$$

The average of the quadratic term in the effective Hamiltonian is automatically proportional to this, as would be required for the entropy to grow extensively with N_{eff}.

Ref. [454] further discusses higher-order terms in the effective theory (e.g. fourth order), whose contributions could become increasingly important in each coarse-graining step if these terms represent relevant operators. Theoretically, a scaling function of re-scaled couplings $\tilde{g}$ differentiates both possibilities. We simply mention this point and refer the interested reader to the reference.

3.6.2 Variational autoencoders

A variational autoencoder (VAE) is a method that combines neural networks with (approximative) inference [878, Ch. 2][386, Ch. 20], using an ansatz stemming from variational mean field theory (which we discussed in Sec. 3.2). A neural network maps data in a nonlinear way to a latent variable space; another maps latent space variables back to our physical space. We investigate the learning behavior of these algorithms in part IV of this thesis when trained on physical data, namely configurations of hard, "sticky" rods in 2D (from a biased Boltzmann-Gibbs distribution). We review very briefly the main concepts of the algorithm in this section.

VAEs are known to reproduce the same kinds of results of PCA given the neural networks are linear [397, 527]; however, PCA does not entail a statistical model of the data in an explicit way. Moreover, the form of VAEs – in that it maps data to a latent space and back – mimics standard autoencoder neural networks (AEs). However, the maps in VAEs are *stochastic*, i.e. are not deterministic, and are expressed in terms of probability densities. Hence, more than employing just "added noise", variational autoencoders provide a full generative model of the data. We will discover in part IV that the process of learning configurations is akin to discovering a hidden 'energy landscape', where e.g. partly separated regions of latent space correspond to "mesostates" of symmetry-broken phases.

The method was developed by Rezende (2014) [51], and by Kingma and Welling (2013/2014) [50]. In terms of the machine learning literature, a VAE is a latent variable model (a generative model) $p_\theta(\boldsymbol{x}, \boldsymbol{z})$ of observable variables $\boldsymbol{x}$ (the data) and hidden, latent variables $\boldsymbol{z}$. The model is specified by trainable parameters θ. The VAE is composed of two parts, which in practice are implemented as neural networks:

- An approximate posterior is used (the *inference model*) with additional parameters ϕ, modeled by a stochastic neural network called the *encoder*

$$q_\phi(\boldsymbol{z}|\boldsymbol{x}) \approx p_\theta(\boldsymbol{z}|\boldsymbol{x}) \tag{3.262}$$

- A *decoder* (also a stochastic neural network) models $p_\theta(\boldsymbol{x}|\boldsymbol{z})$, mapping points from the latent space to the observable (data) space.

Figure 3.2 depicts the VAE in its neural-network setup, while Fig. 3.3 depicts the probabilistic model of variational autoencoders. Generally, the data comes from some complex, unknown distribution $p_{\mathcal{D}}$, whose samples we observe empirically by the existence of data in a dataset $\mathcal{D}$. The hidden variables are assumed to take on a *simple* form, expressed by the prior $p(\boldsymbol{z})$.[55] The generative model that is learned is

$$p_\theta(\boldsymbol{x}, \boldsymbol{z}) = p_\theta(\boldsymbol{x}|\boldsymbol{z})p(\boldsymbol{z}) \tag{3.263}$$

The variational lower bound – as its name implies – is a formal lower bound on the "true" log-likelihood of the data, and is to be maximized during training of the encoder and decoder parameters $\{\phi, \theta\}$ (see following sub-sections).

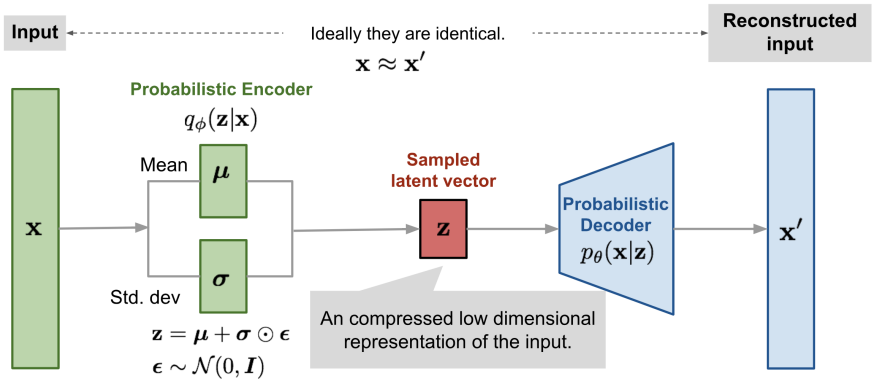

FIGURE 3.2: A schematic of a VAE implemented as a neural network (duplicated from Ch. 1.4.2, Fig. 1.8). An input image $\boldsymbol{x}$ passes through an encoder network (flexible architecture) that represents the approximate posterior $q_\phi(\boldsymbol{z}|\boldsymbol{x})$, where the latent variables $\boldsymbol{\mu}$ and $\boldsymbol{\sigma}$ are learned. A sample latent vector $\boldsymbol{z}$ is drawn from the distribution, and sent through the decoder network (flexible architecture) that represents $p_\theta(\boldsymbol{x}|\boldsymbol{z})$, rendering a probabilistic outcome for $\boldsymbol{x}'$ (a particular "reconstructed" input). Source: Ref. [526].

Central to the VAE method is a first assumption (I) that $\boldsymbol{x}$ is a stochastic variable. Each *empirical* input $\boldsymbol{x} \in p_{\mathcal{D}}(\boldsymbol{x})$ from data will still be modeled by a probability distribution. One can sample "fake" variants of a single instance of data on the input side (as well as sampling from the latent-space prior faking *any* kinds of similar data). The method models the probability of finding $\boldsymbol{x}$ conditioned on latent variables $p(\boldsymbol{x}|\boldsymbol{z})$, hence a *distribution of outputs* when marginalizing (sampling) over $\boldsymbol{z}$. The latter $p(\boldsymbol{x}|\boldsymbol{z}) = p_\theta(\boldsymbol{x}|\boldsymbol{z})$ is the *decoder* – either *Bernoulli* or of *Gaussian* distributions in standard cases. In practice, this means the output values of the pixels of an input image (which are binary) will follow a *distribution*, and will then take on values between 0 and 1 in the output (if not sampled from the range). During training (see below), the parameters θ are optimized (with constraints that involve the assumptions governing the other parameters of the encoder ϕ) via a *reconstruction loss* term: The input and

[55] It is up to debate whether that more complex priors improve VAEs [529].

(many) outputs are compared via either the binary cross-entropy function[56] or e.g. a *mean-squared error* (these are the standard cases).

The second central assumption (II) is that the approximate posterior in latent space $q_\phi(\boldsymbol{z}|\boldsymbol{x})$ is assumed to be a *diagonalized* multivariate Gaussian over n-dimensional variables $\boldsymbol{z}$:

$$q_\phi(\boldsymbol{z}|\boldsymbol{x}) \equiv \mathcal{N}\left(\boldsymbol{z};\, \boldsymbol{\mu}[\boldsymbol{x}], \Sigma^{kk'}[\boldsymbol{x}]\delta_{kk'}\right) \,, \tag{3.264}$$

where the covariance matrix $\boldsymbol{\Sigma}$ is diagonal with a vector of eigenvalues $\boldsymbol{\sigma}$ and $\boldsymbol{\mu}$ is the mean vector. These are both implicitly functions of $\boldsymbol{x}$. The latent variables are thus *assumed* to be uncorrelated in the hypothetical model:

$$q_\phi(\boldsymbol{z}|\boldsymbol{x}) \equiv \prod_{k=0}^{n} q_\phi(z_k|\boldsymbol{x}) \tag{3.265}$$

where z_k is the kth latent (field) variable. In practice, the algorithm will try to enforce the diagonality across the latent variable dimensions given empirical data $\boldsymbol{x} \in p_{\mathcal{D}}(\boldsymbol{x})$.

Both assumptions (I+II) together fix the functional form of the optimization problem. Neither the reconstruction nor the assumption of uncorrelated latent variables will be fulfilled *strictly*; the optimization should provides a "best fit" between both (to second order in a "free energy" function), which, we will discuss in our case study in Ch. 7, may make way for nontrivial competition as soon as the dataset is highly unstructured, i.e. entails a high amount of information (related to irreducible symmetries of the set).

Remark. We note that the assumption of a diagonal matrix can be loosened, which, however, may not change much, qualitatively, as any non-diagonal Gaussian can be diagonalized with a series of orthogonal transformations – with a rotation matrix. The exact advantage has been reported to be unclear. In practice, a non-diagonal covariance matrix amounts to an additional diagonalization step within each training step and, thus, more overhead. A deeper exploration of the full-covariance-matrix Gaussian posterior of VAEs was not investigated in this thesis.

In the discussion on PCA in the previous section, we saw that the eigenvalues of the covariance of the data, measured 'directly', are inversely related to the variance expected by a Gaussian part of the effective free energy of the data. VAEs are conceptually similar to PCA, except for two points: (1) The VAE entails a Gaussian model of the original data *after some nonlinear transformations* via the encoder neural networks. Generally, then, it should be more adept at finding a suitable Gaussian part of an "effective free energy" – for whatever variables best store the information of a Gaussian model. These latent or "hidden" Gaussian variables need not at all be linear functions of the data. (2) One can directly generate new data by sampling either from the approximate posterior around all empirical data points $q_\phi(\boldsymbol{z}|\boldsymbol{x})$ (the distribution of which will only slightly differ from the original dataset) or, better, via the prior $p(\boldsymbol{z})$, which should express the full (abstract) breadth of nonlinear features among the data (via the generative model of the VAE). PCA cannot perform such a generative step in any direct way, and only fits the mean and variance over all

[56] that abides more faithfully to the pixel-wise Bernoulli assumption

of the empirical data, without a probability distribution over each individual empirical data point.

Optimization: maximize the *evidence lower bound*

The *variational* or *evidence lower bound* (ELBO) – a lower bound on the log-likelihood of the data in variational inference approximations – can be derived using *Jensen's inequality* for convex functions [850, p. 35][849, Ch. 2] directly, but we demonstrate another derivation [878, Ch. 2.3]:

For an arbitrary inference model $q_\phi(\boldsymbol{z}|\boldsymbol{x})$ parametrized by (a set) ϕ arbitrarily, we can write

$$\log p_\theta(\boldsymbol{x}) = \left\langle \log p_\theta(\boldsymbol{x}) \right\rangle_{\boldsymbol{z}\sim q_\phi(\boldsymbol{z}|\boldsymbol{x})} \tag{3.266}$$

$$= \left\langle \log \frac{p_\theta(\boldsymbol{x},\boldsymbol{z})}{p_\theta(\boldsymbol{z}|\boldsymbol{x})} \right\rangle_{\boldsymbol{z}\sim q_\phi(\boldsymbol{z}|\boldsymbol{x})} \tag{3.267}$$

$$= \left\langle \log \frac{p_\theta(\boldsymbol{x},\boldsymbol{z}) q_\phi(\boldsymbol{z}|\boldsymbol{x})}{q_\phi(\boldsymbol{z}|\boldsymbol{x}) p_\theta(\boldsymbol{z}|\boldsymbol{x})} \right\rangle_{\boldsymbol{z}\sim q_\phi(\boldsymbol{z}|\boldsymbol{x})} \tag{3.268}$$

$$= \left\langle \log \frac{p_\theta(\boldsymbol{x},\boldsymbol{z})}{q_\phi(\boldsymbol{z}|\boldsymbol{x})} \right\rangle_{\boldsymbol{z}\sim q_\phi(\boldsymbol{z}|\boldsymbol{x})} + \left\langle \log \frac{q_\phi(\boldsymbol{z}|\boldsymbol{x})}{p_\theta(\boldsymbol{z}|\boldsymbol{x})} \right\rangle_{\boldsymbol{z}\sim q_\phi(\boldsymbol{z}|\boldsymbol{x})} \tag{3.269}$$

$$\equiv \mathcal{B}_{\theta,\phi}(\boldsymbol{x}) + D_{KL}(q_\phi(\boldsymbol{z}|\boldsymbol{x})||p_\theta(\boldsymbol{z}|\boldsymbol{x}))\,, \tag{3.270}$$

Eq. (3.266) is possible because $p_\theta(\boldsymbol{x})$ is completely independent of $\boldsymbol{z}$, hence the right-hand-size is a trivial statement. The quantity $\mathcal{B}_{\theta,\phi}(\boldsymbol{x})$ denotes the ELBO and $D_{KL}(q_\phi(\boldsymbol{z}|\boldsymbol{x})||p_\theta(\boldsymbol{z}|\boldsymbol{x}))$ is the Kullback-Leibler- (KL-) divergence (*relative entropy*) between the approximate and true posterior distributions, introduced in eq. (3.224). Importantly, the KL-divergence is always nonnegative[57]:

$$D_{KL}(q_\phi(\boldsymbol{z}|\boldsymbol{x})||p_\theta(\boldsymbol{z}|\boldsymbol{x})) \geq 0 \tag{3.271}$$

rendering zero when the two distributions are identical. Now, reordering equation (3.270),

$$\mathcal{B}_{\theta,\phi}(\boldsymbol{x}) = \log p_\theta(\boldsymbol{x}) - D_{KL}(q_\phi(\boldsymbol{z}|\boldsymbol{x})||p_\theta(\boldsymbol{z}|\boldsymbol{x})) \tag{3.272}$$

$$\leq p_\theta(\boldsymbol{x})\,. \tag{3.273}$$

The ELBO is thus clearly a lower bound of the log-likelihood of data, thus the task during training of the neural network is to *maximize* this lower bound. The negative of the lower bound (which we denote as $\mathcal{L} \equiv -\mathcal{B}$) is also called the *variational free energy* from variational mean field theory (see Sec. 3.2), which should be *minimized*.

Here, the discrepancy between the true- and approximate-posteriors will be reduced by the KL-divergence term when maximizing the ELBO. So, the size of the gap ("tightness-of-bound") between the ELBO and the marginal log-likelihood of the data will be reduced the better the approximation of the distribution $p_\theta(\boldsymbol{z}|\boldsymbol{x})$. This is a central notion around advanced improvements

[57] It satisfying the so-called *Gibbs-inequality*, a central inequality for information theory [850, p. 34] that is also underlies the variational principles for density functional theory [793]

for VAEs – to make the approximate posterior more expressive and flexible via, e.g. *inverse autoregressive flow*, see Ref. [884].

The ELBO $\mathcal{B}_{\theta,\phi}(\boldsymbol{x})$ can be re-written as [51, 386, 878]

$$\mathcal{B}_{\theta,\phi}(\boldsymbol{x}) = \left\langle \log p_\theta(\boldsymbol{x},\boldsymbol{z}) - \log q_\phi(\boldsymbol{z}|\boldsymbol{x}) \right\rangle_{\boldsymbol{z}\sim q_\phi(\boldsymbol{z}|\boldsymbol{x})} \ . \tag{3.274}$$

The first term represents a negative "inner energy" function, while the second the negative Shannon entropy of the approximate posterior, given a specific $\boldsymbol{x}$. Therefore, the name "pointwise free energy" is fitting; we interpret it as a local free energy difference in an energy landscape.

Yet, to estimate the ELBO given empirical data, we need to reformulate it once more in terms of the prior distribution: Since we can now write $p_\theta(\boldsymbol{x},\boldsymbol{z}) = p_\theta(\boldsymbol{x}|\boldsymbol{z})p(\boldsymbol{z})$, we find

$$\begin{aligned}
\mathcal{B}_{\theta,\phi}(\boldsymbol{x}) &= \left\langle \log p_\theta(\boldsymbol{x}|\boldsymbol{z}) + \log p(\boldsymbol{z}) - \log q_\phi(\boldsymbol{z}|\boldsymbol{x}) \right\rangle_{\boldsymbol{z}\sim q_\phi(\boldsymbol{z}|\boldsymbol{x})} && (3.275)\\
&= \left\langle \log p_\theta(\boldsymbol{x}|\boldsymbol{z}) - \log\left(\frac{q_\phi(\boldsymbol{z}|\boldsymbol{x})}{p(\boldsymbol{z})}\right) \right\rangle_{\boldsymbol{z}\sim q_\phi(\boldsymbol{z}|\boldsymbol{x})} && (3.276)\\
&\equiv \left\langle \log p_\theta(\boldsymbol{x}|\boldsymbol{z}) \right\rangle_{\boldsymbol{z}\sim q_\phi(\boldsymbol{z}|\boldsymbol{x})} - D_{KL}(q_\phi(\boldsymbol{z}|\boldsymbol{x})||p(\boldsymbol{z})) && (3.277)
\end{aligned}$$

The first term in Eq. (3.277) is the so-called *reconstruction error*, and the second term the Kullback-Leibler divergence between the approximate posterior and prior on latent space. Eq. (3.277) is the practical form of the ELBO that can be optimized during training of VAEs, i.e. during optimization of the parameters $\{\theta,\phi\}$.

Reparametrization

We note that during optimization of the neural network via the standard *backpropagation* algorithm for neural networks, it is necessary to make every parametrization differentiable. The approximate posterior is the distribution function $q_\phi(\boldsymbol{z}|\boldsymbol{x})$ assumed to be a Gaussian. The "reparametrization trick" was developed in Ref. [51] that, when used with *stochastic gradient descent* [389, Ch. 5] [387, Ch. 4][385, Ch. 3] – which essentially samples changes in global states within small batches – means derivatives are defined and the algorithm is extremely fast, even requiring only single samples to be generated per update. Schematically, it means there is a "parallel" split of the neural network in the layer that represents the latent variables, and *every* instance of input $\boldsymbol{x}$ is associated with a parametrized random or stochastic *field* variable $\boldsymbol{z}$ over the data

$$\boldsymbol{z}([\boldsymbol{x}];\phi) = \boldsymbol{\mu}[\phi(\boldsymbol{x})] + \epsilon\boldsymbol{\sigma}[\phi(\boldsymbol{x})] \ . \tag{3.278}$$

Here, ϵ is an n-dimensional *random number* that is normally distributed, where n is the dimension of the latent space. The first term is the *mean* of the Gaussian and the second is the root variance of the Gaussian defined by the approximate posterior. The parameters of the neural network ϕ are optimizable and thus define a deterministic mapping function of the data $\boldsymbol{x}$ after training. The notation $\phi(x)$ is thus clear. Fig. 3.2 shows this reparametrization in the basic setup of the VAE as a neural network.

Some initial remarks

Notice, also, that many inputs may produce the same value of z upon sampling, given they are "close enough" in latent space and have overlapping Gaussian distributions – in this way, the VAEs are able to model similarities in the data, loosely speaking.

Notice that the number n of latent variables (the dimension of latent space) is a hyperparameter. Thus, VAEs *must* operate on principles of compression (the latent space is low-dimensional) given constraints (*implied* by competing terms within the ELBO). We suspect there is an optimal trade-off between compression ("global", "ensemble" predictability) and reconstruction ("local", sample-wise predictability) – though we did not find formal investigations on this in the literature. The (Shannon) information in the generative model of the dataset is supposed to *preserved* in a best way while also finding a best "useful" (tractable) representation in a latent space with finite degrees of freedom. As this will never work perfectly except for data that *is* Gaussian (i.e. noise), there will be some loss of information necessary in one way or another. First of all, a finite number of independent degrees of freedom in latent space should be related to compression, and will likely limit the level of "local" predictability. An original image will never be perfectly encoded (lossy encoding!) into the latent space of a VAE that aims in detecting generic features. Thus, *why* particular representations emerge in the latent space is a subject still open in the literature. We shed significant light on this topic in the results of this thesis in part IV.

In general, it is recommended to implement the encoder and decoder as *deep* neural networks in order to increase the expressivity in the mappings between both spaces, and to aid in extracting the "relevant" features in the data (see introductory discussion on deep learning in Ch. 1.4, as well). However, in this thesis, find that shallow neural networks may actually do job better if one extends the dimension of latent space to very large number, i.e. wide-and-shallow neural networks. (An additional factor must be considered in terms of another hyperparameter β of the *β-VAEs* that we employ, which we shall discuss in part IV.)

β-VAEs

The ELBO on Eq. (3.277) can be modified once more:

$$\mathcal{B}_{\theta,\phi}(\boldsymbol{x};\beta) \equiv \langle \log p_\theta(\boldsymbol{x}|\boldsymbol{z}) \rangle_{\boldsymbol{z}\sim q_\phi(\boldsymbol{z}|\boldsymbol{x})} - \beta D_{KL}(q_\phi(\boldsymbol{z}|\boldsymbol{x})||p(\boldsymbol{z})) \tag{3.279}$$

where β is a hyperparameter fixed at the beginning of training. This formulation of VAEs [52] allows one to shift the tradeoff between the two terms in the loss or *cost* function

$$\mathcal{L}_{\theta,\phi}(\beta) \equiv -\left\langle \mathcal{B}_{\theta,\phi}(\boldsymbol{x};\beta) \right\rangle_{\boldsymbol{x}\sim p_{\mathcal{D}}(\boldsymbol{x})} \tag{3.280}$$

that is estimated over some minibatch of data from the empirical distribution $p_{\mathcal{D}}(\boldsymbol{x})$. In recent years, much attention has been given to the phenomenon of "disentanglement" of latent variables that can be adjusted via emphasis on the KL-term [533]. We shed light on the topic in part IV of this thesis, where we uncover a phase transition upon varying the hyperparameter β; at its vicinity,

the latent representations become maximally decoupled and form a hierarchy of sorts.

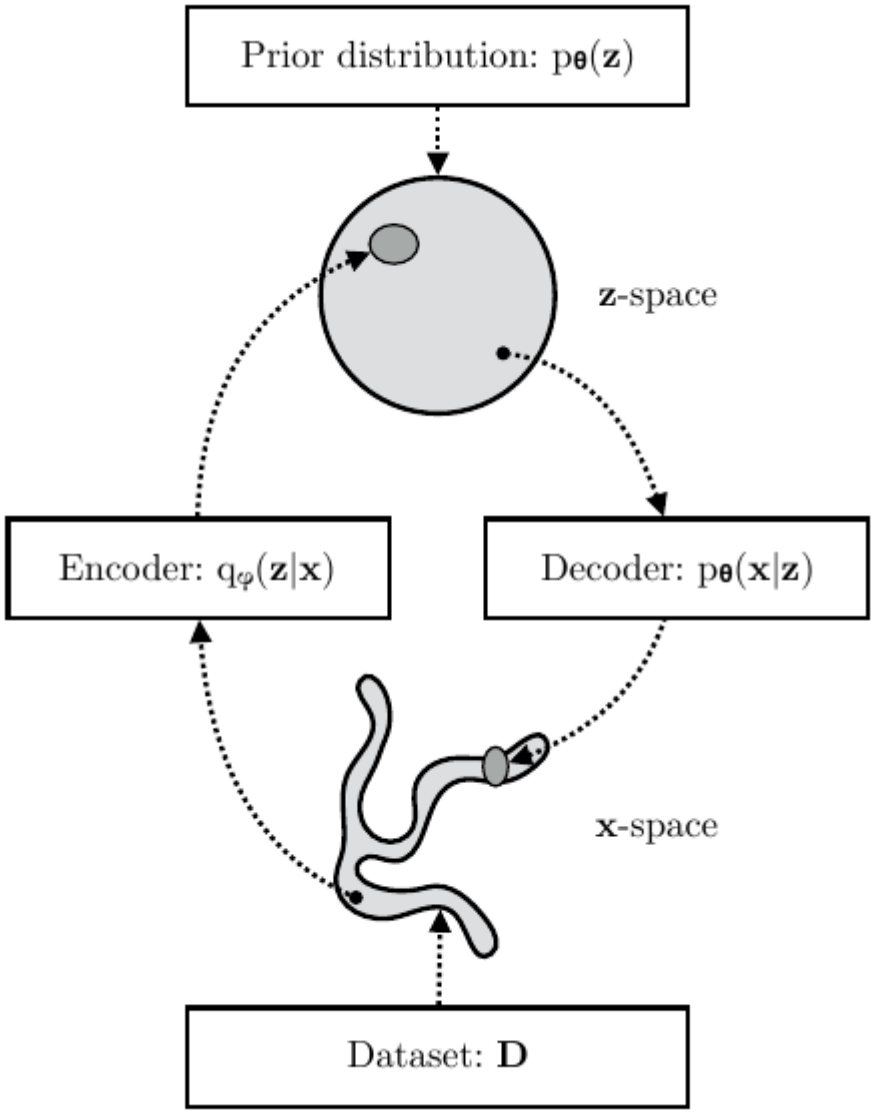

FIGURE 3.3: Depiction of the probabilistic model of a VAE: It learns a stochastic map between the data space $\{\boldsymbol{x}\}$, which is observable, and the latent (hidden) space of variables $\{\boldsymbol{z}\}$. The complex, empirical data distribution is $p_{\mathcal{D}}(\boldsymbol{x})$, the *a priori* distribution of latent variables $p_\theta(\boldsymbol{z})$ is a unit Gaussian. The *decoder/generator* function (a neural network) embodies $p_\theta(\boldsymbol{x}|\boldsymbol{z})$, so that the joint probability distribution $p_\theta(\boldsymbol{x}, \boldsymbol{z}) = p_\theta(\boldsymbol{x}|\boldsymbol{z})p(\boldsymbol{z})$ is the generative model learned. The exact posterior distribution (the inference model) $p_\theta(\boldsymbol{z}|\boldsymbol{x})$ is intractable and hence modeled by an approximative distribution $q_\phi(\boldsymbol{z}|\boldsymbol{x})$, which is implemented as a stochastic neural network, the *encoder*. See Ref. [878, Ch. 2] (image taken from there).

This chapter has reviewed and thoroughly discussed fundamental concepts of probabilistic approaches to describing classical many-body systems in- and out-of-equilibrium – with focus on the meaning of "coarse-graining", the fundamental presumptions (and some debate) around equilibrium statistical mechanics, dynamical equations in the form of master equations (which are intuitively illustrated when considering *on-lattice* systems), and Markov-Chain Monte Carlo methods. The validity of Markovian or "coarse-grainable" assumptions are challenged in nonequilibrium or nonergodic systems – many open issues remain, as there is currently no unifying (or agreed-upon) formalism for nonequilibrium systems.

In any case, the statistical behavior of a (highly correlated) system can be quantified by information-theoretic measures, even in nonequilibrium e.g. for dynamics following Markov chains (microscopically Markovian dynamics). Apart from offering generic methods for statistical characterization, these measures quantify and may even manifest some of the most basic presumptions about the physical world on which equilibrium statistical mechanics is based, i.e. Jaynes' principle of maximum entropy, to mention a famous example. Machine learning "utilizes" these measures in defining a learning problem (objective functions), where we motivated the "*variational free energy*" and Kullback-Leibler divergence in the context of "*mesostates*" visited by an essentially near-equilibrium (*biased*-ensemble) system following Markovian dynamics.

The fields of physics and machine learning relate in much more general ways, too. Learning seems to follow the same principles of finding effective, coarse-grained field theories (about data). Behavior of unsupervised machine learning algorithms like PCA and variational autoencoders might be understood in an alternative way, which is part of our motivation behind our exploratory work in part IV of this thesis.

The end of this chapter marks the end of part I of this thesis. The next parts will cover the scientific studies that have been introduced in this first part. We will provide an outlook that ties together the topics covered in this theoretical chapter with all of the results in part V.

Part II

Hard Rods in (2+1)D Confinement: Monolayer Growth

Chapter 4

Monolayer Systems of Purely Hard-Core Rods: Equilibrium Theory and Growth Dynamics

Nothing is more practical than a good theory.

Ludwig Boltzmann

This part (part II) of this thesis has been motivated in Ch. 1.2: We aim to characterize and explore an idealized model system for thin film growth with rod-like particles at the submonolayer stage of growth. The model we present is that of hard rods in simple cubic lattices confined to maximally one monolayer ((2+1)D). In this chapter, we treat only the limiting case of purely hard-core rods. The general case of added attractions will be addressed in the latter Ch. 5.

The research aims behind the results presented in this chapter can be characterized as the desire for methodical control, stemming from sophisticated, equilibrium and near-equilibrium theory: classical density functional theory and dynamical "extensions" thereof. Kinetics of phase separation processes during layer growth will not be addressed, as no thermodynamic phase transitions occur in purely hard-core systems of rods (which we will discover). This purely hard-core case studied in this chapter is not a faithful models for organic molecular thin film growth – the next chapter will address the more generic case of "sticky" hard rods. Nonetheless, the purely hard-core case is an important limit, i.e. "high-temperature" behavior (in confinement).

We shall explore the equilibrium properties of the purely hard-core model of rods, which is amenable to state-of-the-art analytic theory: Fundamental measure theory (FMT) is formulated for the lattice rods. This theory is compared to equilibrium Monte Carlo simulations in the grand canonical ensemble. In order to obtain a fuller picture of the physics of hard-core rods in monolayer confinement, we compare the lattice model to that of a continuum model – hard spherocylinders.

After studying equilibrium, we shall explore the nonequilibrium and quasi-equilibrium dynamics of the many-body systems during the deposition of new particles (which represents an external driving force), measured in terms of the evolution of global order parameters. We write, develop, and employ kinetic Monte Carlo (KMC) simulations specifically for hard-core rods, as well as for the monolayer-growth setup. As we remain in the purely hard-core limiting case, the nonequilibrium growth of monolayers can be formulated analytically within the framework of dynamical density functional theory (DDFT) on the lattice based on the lattice FMT presented in the first half.

A systematic, direct comparison to the KMC simulations is presented. Within the same context of monolayer growth, we compare directly the trajectories of global observables in the lattice model to those in continuum models with hard spherocylinders.

The concepts we discuss here connect to much of those introduced and discussed the previous part I of this thesis. We discussed fundamentals of the physics of complex fluids of rods in Ch. 2.1; in particular, we stressed that their pronounced coupling of rotational and translational degrees of freedom is the key for ordering phenomenology. A broad motivation behind this thesis is that lattice models are often useful to study a simpler version of a more complex reality. This general idea was discussed in the introduction, Ch. 1.1. The lattice model was originally conceptualized as a "coarse-grained" model of organic molecules at substrates. The validity of this model assumption is what we aim to find out, ultimately. We discuss this and other issues later in the closing part (part V) of this thesis. The constraint of complex fluids of rods to lattices was discussed preliminarily in Ch. 2.2.2 at a qualitative level. The general idea of effective theories was described in the broad context of field theoretical approaches in Ch. 3.2, while "coarse-graining" was discussed in Ch. 3.5: it is tied to finding Markovian dynamics at the relevant level of description, i.e. a quasi- or near-equilibrium description of an effective process (which may be a "sub-process" in a system if the time-scales are sufficiently separated). As a monolayer system represents a confined 3D fluid (to maximally one layer), we have discussed basic aspects of confinement on phase behavior and dynamics in Ch. 2.2.

This chapter addresses a theoretical treatment of monolayers by the use of sophisticated methods for equilibrium fluids, in which we minimize a grand potential functional of the one-body density distribution. The latter is classical density functional theory (DFT), for which we provided a background in Ch. 3.1.5. Specifically, fundamental measure theory (FMT) is employed, whose construction aims at a capacity for many-body correlations within the analytical description. Fundamentals of equilibrium statistical mechanics were discussed in Ch. 3.1. Equilibrium ensembles like the grand canonical ensemble – in which DFT is defined – were discussed in Ch. 3.1.4. We shall compare the DFT results to Markov-Chain Monte Carlo simulations in the grand canonical ensemble, i.e. GCMC simulations, which we were discussed in Ch. 3.4.2.

We discussed nonequilibrium layer growth and self-assembly on a general note, in the context of soft matter or complex fluids in Ch. 2.3. The irreversible nature of nonequilibrium dynamics was discussed in Ch. 3.5, and fundamentally non-Markovian dynamics in far-from-equilibrium scenarios – for example in dynamically arrested states – were discussed in Ch. 3.5.3. We motivated, illustrated and discussed fundamentals on the nonequilibrium N-body dynamics of hard-core particles on lattices in Ch. 3.3, which are describable in terms of inhomogeneous master equations. Within that section (Ch. 3.3.6), we discussed the ansatz made by dynamical density functional theory (DDFT), which is an analytical approach attempting to include two-body correlative effects into a reduced, one-body description of dynamics, albeit using a functional that is well-defined in equilibrium only. Within Ch. 3.3.5 and more concisely in Ch. 3.4.1, we discussed kinetic Monte Carlo (KMC) simulations that generate example trajectories of the N-body system, where underlying dynamics are presumed Markovian at the microscopic scale (the dynamics are coarse-grained at

a first level of treatment, i.e. that of the lattice). This simulation method is at the heart of our study of nonequilibrium layer growth below. The organization of this chapter is found below after making a few statements on published work.

4.1 Published work

This chapter is based heavily on the following two publications, where multiple authors were involved:

> M. Oettel, M. Klopotek, M. Dixit, E. Empting, T. Schilling, and H. Hansen-Goos, "Monolayers of hard rods on planar substrates. I. Equilibrium". In: *The Journal of Chemical Physics* 145.7 (July 2016), p. 074902. DOI: 10.1063/1.4960618.

> M. Klopotek, H. Hansen-Goos, M. Dixit, T. Schilling, F. Schreiber, and M. Oettel, "Monolayers of hard rods on planar substrates. II. Growth". In: *The Journal of Chemical Physics* 146.8 (Jan. 2017), p. 084903. DOI: 10.1063/1.4976308.

Contributions of author (MK)

We have decided to include all results of these publications in this chapter in order to preserve the coherence of the scientific story, i.e. to offer a fuller picture of monolayer growth with rods in the hard-core-particle limit. We state the contributions of the author of this thesis ("MK") below:

J. Chem. Phys. ***145****, 074902 (2016)*:
MK contributed to research via writing and running the first simulations of this lattice model system of rods. MK contributed to the research, development, and writing of the grand canonical Monte Carlo (GCMC) simulations in the context of co-supervision of a student thesis (bachelor). MK produced a schematic and 3D visualizations (Figs. 4.2 and 4.6, respectively, in this thesis), and contributed to editing the manuscript.

J. Chem. Phys. ***146****, 084903 (2017)*:
MK contributed substantially to research, collaboration, simulation development, data visualization, data production, and writing the paper. All kinetic Monte Carlo (KMC) simulations codes were written, developed, managed and executed by MK. All plots, as well as many schematics and visualizations were produced by MK. In many or most sections, MK was the main author of the text. Exceptions are: the introduction (paper Sec. I), the description and analysis of the DDFT (paper Sec. II), and summary/conclusions (paper Sec. VI). MK was responsible for all final editing and the full journal submission process. MK corresponded with editors and reviewers.

The first part of the results in this chapter (as of Sec. 4.4) presents the work that is published in *J. Chem. Phys.* ***145****, 074902 (2016)*, where we characterize the equilibrium properties of hard-rod monolayers, using theoretical methods but also simulations. The second part of this chapter (Sec. 4.8) presents the work published in *J. Chem. Phys.* ***146****, 084903 (2017)*, where we explore the (nonequilibrium) growth of monolayers using simulations as well as theoretical methods. Note that in certain places, we have modified the text, as

well as added to the original text of the publication. Throughout the course of the chapter, we will indicate where we have contributed and in which manner at the beginning of main sections. Also, we have completely re-written, as well as massively extended and broadened the introduction to the model system, aims of the study, and literature reviews in part I of this thesis (particularly in Ch. 1.2.) We have also written our own conclusions, as well as an extended discussion in Sec. 4.13.

An outline of the sections and corresponding topics of this chapter is provided in the next section.

4.2 Organization of this chapter

In Sec. 4.3, we will present the basic, *static* model definition of hard-core rods in monolayer confinement, as well as the global-scale, thermodynamic orientational order parameters investigated. In Sec. 4.4, we will describe the lattice version of fundamental measure theory (FMT) for hard rod mixtures, as well as illustrative examples like monolayer confinement, as well as 2D and the 3D bulk. We study the properties of the monolayer systems in equilibrium via the lattice FMT and comparative simulations for equilibrium conditions in Sec. 4.5. In Sec. 4.6, we briefly describe our equilibrium Monte Carlo simulation method in the grand canonical ensemble. Sec. 4.7 discusses and compares the equilibrium behavior of monolayers in the lattice model to that of a continuum model of hard spherocylinders. After the end of the section, we will review briefly the most important results of the first chapter.

The second half of this chapter investigates the growth of monolayers with dynamical models. It begins in Ch. 4.8, where we describe very briefly the kinetic Monte Carlo (KMC) method for simulating hard rods on lattices with diffusive-type motion and a deposition flux. Thereafter, in Sec. 4.9 a lattice dynamical density functional theory (DDFT) is formulated for monolayer growth with hard rods, based on the equilibrium fundamental measure theory that we presented in the first part of the chapter. We will then proceed to compare the DDFT to "ground truth" KMC simulations in Sec. 4.10, discussing mostly the quality of the analytical DDFT approach as well as its (in-)consistency with the simulation, but also exploring the dynamics of a number of global-scale (particle-averaged) observables during growth. A quasiequilibrium growth description is possible in the monolayer of hard-core rods, as there are no phase transitions for intermediate rod-lengths. Further, in Sec. 4.11, we will have derived an expression for the effective 2D diffusion rate for "tumbling" rods, which couple transitional as well as rotational degrees of freedom (these out-of-plane rotational dynamics were implemented in the KMC model). In Sec. 4.12, we shall present a lengthy comparison between dynamical models of monolayer growth on the lattice (KMC) and continuum models employing spherocylinders. Two such models are implemented and compared to the lattice model.

A summary and our conclusions are written in Sec. 4.13, where we also provide an additional discussion.

4.3 Static model definition of hard rods confined to monolayers ((2+1)D)

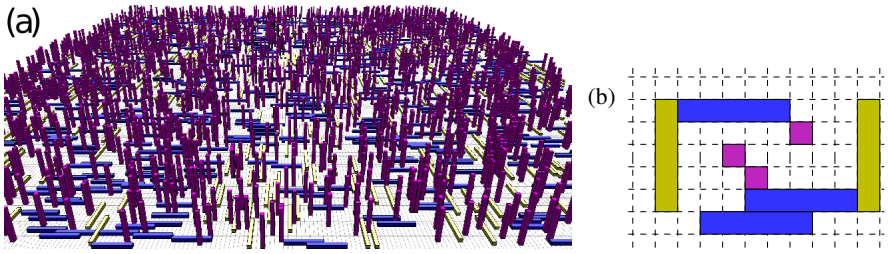

FIGURE 4.1: Illustration of our lattice model for hard-rod monolayers, as seen (a) in 3D and (b) projected on the x–y–plane. Blue rods are oriented in x–direction, yellow rods in y–direction and magenta rods in z–direction.

In the lattice model (Fig. 4.1) of (2+1)D monolayers, the rods can take on three discrete orientations on a planar, square lattice – two lying and one standing. The three population densities are quantified as ρ_1, ρ_2, and ρ_3, given as a number per volume (area). All equilibrium properties in the form of order parameters are calculated as a function of (average) total number density of rods $\rho = \rho_1 + \rho_2 + \rho_3$, which fluctuates about a mean in equilibrium in the grand canonical ensemble.

The (global-scale) *orientational* order parameters that characterize the system are

$$\begin{aligned} Q &= \frac{\rho_3 - \frac{\rho_1+\rho_2}{2}}{\rho_1+\rho_2+\rho_3}\,, \\ S &= \frac{\rho_1-\rho_2}{\rho_1+\rho_2}\,. \end{aligned} \tag{4.1}$$

$Q \neq 0$ signifies an excess ($Q > 0$) or depletion ($Q < 0$) of particles in the z–direction (nematic state) while $S \neq 0$ signals order in the x–y–plane orthogonal to the nematic director (biaxial state). We will see that i.e. the nematic ordering continually increases (with a nonzero slope) with increasing density. The biaxiality does not play a role for rods of intermediate lengths $L < 13$ (at least as predicted by the FMT, see corresponding Sec. 4.5). Therefore, the main global orientational order parameter in focus will be Q. In this (2+1)D confined system, the packing fraction

$$\eta = L(\rho_1 + \rho_2) + \rho_3 \tag{4.2}$$

also offers information on the global orientational state of the system, as the contribution of lying rods (species 1 and 2) and standing rods (species 3) is *asymmetric*.

* * *

Now that we have defined the model, we begin the next section with the formulation of an equilibrium approach to the behavior of the monolayer systems of hard rods: Fundamental measure theory.

4.4 Density Functional Theory for hard rods on lattices (equilibrium)

4.4.1 Fundamental measure theory

The rod model used in this work is formulated, generally at first, on a simple cubic lattice in d dimensions. A lattice point $\mathbf{s}$ is specified by a set of d integers ($\mathbf{s} = (s_1, ..., s_d)$). The lattice constant a is the unit of length. Hard rods are lines (1D), rectangles (2D) or parallelepipeds (3D) with corners sitting on lattice points and thus their geometry is specified by their extent in the Cartesian directions which are again sets of d integers. The position of a rod is specified by the corner whose lattice coordinates are minimal each (see Fig. 4.2). Hard rods are not allowed to overlap (but they may "touch", i.e. share surfaces), thus the interaction potential for two rods $\mathcal{L}_i$ and $\mathcal{L}_j$ of species i and j at positions $\mathbf{s}_i$ and $\mathbf{s}_j$ with extensions $\mathbf{L}_i = (L_{i,1}, ..., L_{i,d})$ and $\mathbf{L}_j = (L_{j,1}, ..., L_{j,d})$ is given by

$$u_{ij}(\mathbf{s}_i, \mathbf{s}_j) = \begin{cases} \infty & (f_{ij} = 1) \\ 0 & (f_{ij} = 0) \end{cases} \tag{4.3}$$

Here, $f_{ij} = f(\mathbf{s}_i, \mathbf{s}_j, \mathbf{L}_i, \mathbf{L}_j)$ is the rod overlap function given by

$$f(\mathbf{s}_i, \mathbf{s}_j, \mathbf{L}_i, \mathbf{L}_j) = \prod_{k=1}^{d} \theta(s_{i,k}, s_{j,k}, L_{i,k}, L_{j,k}) \tag{4.4}$$

$$\theta(s_{i,k}, s_{j,k}, L_{i,k}, L_{j,k}) = \begin{cases} 1 & (s_{j,k} = \{s_{i,k} - (L_{j,k} - 1), ..., s_{i,k} + (L_{i,k} - 1)\}) \\ 0 & (\text{otherwise}) \end{cases} \tag{4.5}$$

The overlap function is 1 whenever there is overlap in all lattice dimensions, meaning that the rods are disjunct for $f = 0$ (see. Fig. 4.2). Note that due to the chosen convention for the rod location the overlap function is not symmetric in the rod locations $\mathbf{s}_i$ and $\mathbf{s}_j$.

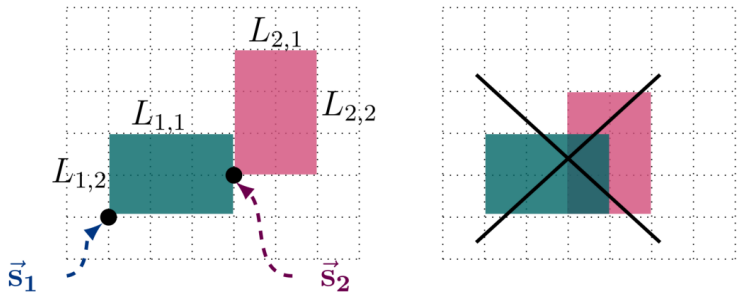

FIGURE 4.2: Definitions for the example of hard 2x3–rods in $d = 2$. Rod location is specified by the position of the lower left corner (i.e., the corner whose lattice coordinates are minimal). Rods may "touch" (left picture) but not overlap (right).

In the following we consider such a rod mixture with ν species subject to external fields $V^{\text{ext}}(\mathbf{s}) = \{V_1^{\text{ext}}(\mathbf{s}), ...V_\nu^{\text{ext}}(\mathbf{s})\}$ where $V_j^{\text{ext}}(\mathbf{s})$ acts on rod species j. At lattice site $\mathbf{s}$, the number density of rods per lattice site is specified by $\rho(\mathbf{s}) = \{\rho_1(\mathbf{s}), ..., \rho_\nu(\mathbf{s})\}$ where $\rho_j(\mathbf{s})$ is the density of rod species j, i.e. the probability of a given site to be occupied by the lower left corner of a particle.

In density functional theory, all equilibrium properties of a rod mixture in external fields are obtained by minimizing the grand potential functional

$$\Omega[\rho(\mathbf{s})] \;=\; \mathcal{F}^{\mathrm{id}}[\rho(\mathbf{s})] + \mathcal{F}^{\mathrm{ex}}[\rho(\mathbf{s})] - \sum_{i=1}^{\nu}\sum_{\mathbf{s}}(\mu_i - V_i^{\mathrm{ext}}(\mathbf{s}))\,\rho_i(\mathbf{s}) \qquad (4.6)$$

with respect to the particle densities $\rho(\mathbf{s})$. The chemical potential for rod species $i = 1...\nu$ is denoted by μ_i If different species belong to the same type of rod in different orientations, the corresponding chemical potentials must be equal in equilibrium. $\mathcal{F}^{\mathrm{id}}[\rho(\mathbf{s})]$ denotes the ideal gas contribution to the free energy functional, given by

$$\mathcal{F}^{\mathrm{id}}[\rho(\mathbf{s})] \;=\; \sum_{i=1}^{\nu}\sum_{\mathbf{s}}\rho_i(\mathbf{s})(\ln\rho_i(\mathbf{s}) - 1)\;. \qquad (4.7)$$

Energies are measured in units of $k_{\mathrm{B}}T$ throughout this chapter.

The exact form of the excess free energy functional $\mathcal{F}^{\mathrm{ex}}$ is in general unknown, in this work we will approximate it within the fundamental measure approach. For lattice models of hard rods, this approach has been worked out in Refs. [159, 160], resulting in an approximative form for $\mathcal{F}^{\mathrm{ex}}$ which we apply in the present study (Lafuente-Cuesta functional).

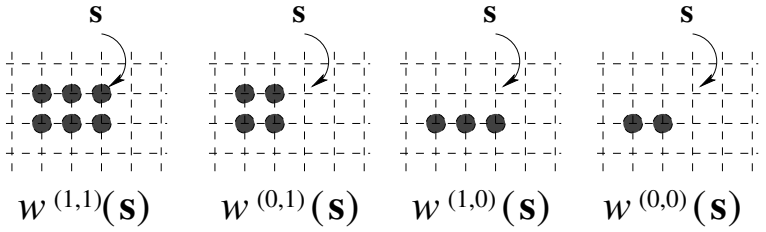

FIGURE 4.3: The four FMT weight functions for a rod with edge lengths $\mathbf{L} = (3, 2)$. The lattice point at which the weight functions are evaluated is denoted by $\mathbf{s}$. The thick points indicate on which lattice points the weight function is 1.

The class of free energy functionals derived in Refs. [159, 160] makes use of weighted densities $n^{\alpha}(\mathbf{s})$ which are defined as convolutions of densities $\rho(\mathbf{s})$ with weight functions $w^{\alpha} := \{w_1^{\alpha}, ..., w_{\nu}^{\alpha}\}$:

$$n^{\alpha}(\mathbf{s}) \;=\; \sum_{i=1}^{\nu}\rho_i \otimes w_i^{\alpha}\,(\mathbf{s}) \qquad (4.8)$$

Convolutions ($\otimes$) on the lattice are defined as

$$(f \otimes g)\,(\mathbf{s}) \;=\; \sum_{\mathbf{s}'} f(\mathbf{s}')g(\mathbf{s} - \mathbf{s}')\;. \qquad (4.9)$$

The d–dimensional index $\alpha = (\alpha_1, ...\alpha_d)$ specifies different weight functions w_i^{α}, with allowed values $\alpha_i = 0, 1$ only. The weight functions w_i^{α} (specific for species i) have the meaning of defining a support of rods $\mathcal{K}_i^{\alpha}$ with edge lengths $\mathbf{K}_i^{\alpha} = (K_{i,1}^{\alpha_1}, ..., K_{i,d}^{\alpha_d})$, i.e. they are 1 on points covered by $\mathcal{K}_i^{\alpha}$ and 0 otherwise. This can be formalized using the θ–function already employed for defining rod

overlap (Eq. (4.5)),

$$w_i^{\alpha}(\mathbf{s}) \quad = \quad \prod_{k=1}^{d} \theta(0, s_k, \alpha_k, K_{i,k}^1) \; . \tag{4.10}$$

The edge lengths of rods $\mathcal{K}_i^{\alpha}$ are related to those of the rods $\mathcal{L}_i$ as follows:

$$K_{i,k}^{\alpha_k} = L_{i,k} - (1 - \alpha_k) \qquad (k = 1, ..., d) \; , \tag{4.11}$$

i.e. whenever the index α_j is 0, the edge length of $\mathcal{K}_i^{\alpha_i}$ in the dimension j is shortened by 1 compared to the corresponding edge length of $\mathcal{L}_i$, otherwise ($\alpha_j = 1$) the edge length is identical. In particular, for $\alpha = (1, ..., 1)$ all rods $\mathcal{K}_i^{\alpha_i}$ are identical to $\mathcal{L}_i$. The meaning of the corresponding weighted density $n^{(1,...,1)}(\mathbf{s}) = \eta(\mathbf{s})$ is a local packing or volume fraction of rods at point $\mathbf{s}$. Fig. 4.3 illustrates the four possible weight functions for a rods with edge lengths $\mathbf{L} = (3, 2)$ on a 2D lattice.

As a second ingredient, the Lafuente-Cuesta functional needs the excess free energy of a zero–dimensional (0d) cavity, Φ^{0d}, i.e. a restricted domain on the lattice which can only hold one particle at a time. Such a cavity may consist of more than one point where the rod is positioned. Furthermore, for a mixture the set of points $\{s_{\text{cav},i}\}$ specifying the allowed location of species i does not need to coincide with the corresponding set $\{s_{\text{cav},j}\}$ for species j. Note that the sets $\{s_{\text{cav},i}\}$ and $\{s_{\text{cav},j}\}$ are not independent since the 0D cavity property is required to hold globally for the mixture, and not just for the individual components. The free energy $\Phi^{0d}(\eta)$ of such a cavity is a function only of the total packing fraction $\eta \equiv \eta_{\text{cav}} = \sum_{i=1}^{\nu} \sum_{\mathbf{s} \in \{s_{\text{cav},i}\}} \rho_i(\mathbf{s})$ in the cavity,

$$\Phi^{0d}(\eta) \quad = \quad \eta + (1 - \eta) \ln(1 - \eta) \; . \tag{4.12}$$

Using this 0d free energy, the Lafuente–Cuesta excess free energy functional is given by

$$\mathcal{F}^{\text{ex}} \quad = \quad \sum_{\mathbf{s}} \mathcal{D}_{\alpha} \Phi^{0d}(n^{\alpha}(\mathbf{s})) \; . \tag{4.13}$$

Remember that α is a d–dimensional index with entries $\{0, 1\}$ only. In Eq. (4.13), $\mathcal{D}_{\alpha} = \prod_{i=1}^{d} D_{\alpha_i}$ and D_{α_i} is the difference operator acting on a function $f(\alpha_i)$ according to $D_{\alpha_i} f(\alpha_i) = f(1) - f(0)$.

It can be shown that $\mathcal{F}^{\text{ex}}$ as defined above yields the correct excess free energy, Eq. (4.12), for *any* 0D cavity [159, 160]. In order to assess the accuracy of the expression for situations of less severe confinement, we evaluate explicitly the properties of different bulk systems in the forthcoming Ch. 6. In a first step, however, we illustrate the construction of the Lafuente-Cuesta functional by applying it to different mixtures in 1D, 2D, and 3D.

4.4.2 Special cases

Here we give the explicit functionals for some special mixtures. The equilibrium properties of examples (b) and (c) (2D and 3D systems) will be discussed in Ch. 6 and those of example (d) (monolayer) in Sec. 4.5 below.

(a) $d = 1$: Mixture of hard rods in one dimension. The excess free energy functional is given by

$$\mathcal{F}^{\text{ex}} = \sum_{\mathbf{s}} \left(\Phi^{0d}(n^{(1)}(\mathbf{s})) - \Phi^{0d}(n^{(0)}(\mathbf{s})) \right) . \tag{4.14}$$

This is the well-known exact solution for the 1d lattice hard rod mixture, derived in Ref. [159] following the recipe from Ref. [885], which treats the 1D continuum hard rod mixture. Another yet different derivation can be found in Ref. [278].

(b) $d = 2$: A system of rods with length L and width 1 corresponds to the binary mixture with rod lengths $\mathbf{L}_1 = (L, 1)$ and $\mathbf{L}_2 = (1, L)$. The excess free energy functional is given by

$$\mathcal{F}^{\text{ex}} = \sum_{\mathbf{s}} \left(\Phi^{0d}(n^{(1,1)}(\mathbf{s})) - \Phi^{0d}(n^{(0,1)}(\mathbf{s})) - \Phi^{0d}(n^{(1,0)}(\mathbf{s})) \right) . \tag{4.15}$$

The weighted densities are given by

$$\begin{aligned} n^{(1,1)}(\mathbf{s}) &= \rho_1 \otimes w_1^{(1,1)}(\mathbf{s}) + \rho_2 \otimes w_2^{(1,1)}(\mathbf{s}) , \\ n^{(0,1)}(\mathbf{s}) &= \rho_1 \otimes w_1^{(0,1)}(\mathbf{s}) , \\ n^{(1,0)}(\mathbf{s}) &= \rho_2 \otimes w_2^{(1,0)}(\mathbf{s}) . \end{aligned} \tag{4.16}$$

Note that the weights $w_2^{(0,1)} = w_1^{(1,0)} = 0$ since they correspond to the support of rods with width 0. Likewise $w_1^{(0,0)} = w_2^{(0,0)} = 0$.

(c) $d = 3$: A system of rods with length L and height/width 1 corresponds to the ternary mixture with rod lengths $\mathbf{L}_1 = (L, 1, 1)$, $\mathbf{L}_2 = (1, L, 1)$ and $\mathbf{L}_3 = (1, 1, L)$. The excess free energy functional is given by

$$\begin{aligned} \mathcal{F}^{\text{ex}} = \sum_{\mathbf{s}} \Big(& \Phi^{0d}(n^{(1,1,1)}(\mathbf{s})) - \Phi^{0d}(n^{(0,1,1)}(\mathbf{s})) - \Phi^{0d}(n^{(1,0,1)}(\mathbf{s})) \\ & - \Phi^{0d}(n^{(1,1,0)}(\mathbf{s})) \Big) . \end{aligned} \tag{4.17}$$

The weighted densities are given by

$$\begin{aligned} n^{(1,1,1)}(\mathbf{s}) &= \rho_1 \otimes w_1^{(1,1,1)}(\mathbf{s}) + \rho_2 \otimes w_2^{(1,1,1)}(\mathbf{s}) \\ &\quad + \rho_3 \otimes w_3^{(1,1,1)}(\mathbf{s}) , \end{aligned} \tag{4.18}$$

$$\begin{aligned} n^{(0,1,1)}(\mathbf{s}) &= \rho_1 \otimes w_1^{(0,1,1)}(\mathbf{s}) , \\ n^{(1,0,1)}(\mathbf{s}) &= \rho_2 \otimes w_2^{(1,0,1)}(\mathbf{s}) , \\ n^{(1,1,0)}(\mathbf{s}) &= \rho_3 \otimes w_3^{(1,1,0)}(\mathbf{s}) . \end{aligned} \tag{4.19}$$

Similarly to case (b), the weights $w_i^{(\alpha_1,\alpha_2,\alpha_3)} = 0$ whenever $\alpha_j = 0$ and $i \neq j$ since they correspond to the support of rods with width 0.

(d) $d = 3$ (confined), the monolayer: A system of rods with length L and height/width 1 whose positions are constrained to a 2D–plane corresponds to a 2D ternary mixture with rod lengths $\mathbf{L}_1 = (L, 1)$, $\mathbf{L}_2 = (1, L)$ (rods lying in–plane) and $\mathbf{L}_3 = (1, 1)$ (rods standing up). The excess free

energy functional is given by formally the same functional as in (a),

$$\mathcal{F}^{\mathrm{ex}} = \sum_{\mathbf{s}} \left(\Phi^{0d}(n^{(1,1)}(\mathbf{s})) - \Phi^{0d}(n^{(0,1)}(\mathbf{s})) - \Phi^{0d}(n^{(1,0)}(\mathbf{s})) \right) , \quad (4.20)$$

but now the weighted densities are given by

$$\begin{aligned} n^{(1,1)}(\mathbf{s}) &= \rho_1 \otimes w_1^{(1,1)}(\mathbf{s}) + \rho_2 \otimes w_2^{(1,1)}(\mathbf{s}) + \rho_3 \otimes w_3^{(1,1)}(\mathbf{s}) , \\ n^{(0,1)}(\mathbf{s}) &= \rho_1 \otimes w_1^{(0,1)}(\mathbf{s}) , \\ n^{(1,0)}(\mathbf{s}) &= \rho_2 \otimes w_2^{(1,0)}(\mathbf{s}) . \end{aligned} \quad (4.21)$$

* * *

In the following section, we shall present the results for the equilibrium behavior (static properties) of monolayers of hard rods obtained from the lattice FMT. We also compare these results with equilibrium simulations in the grand canonical ensemble.

4.5 Results of lattice FMT for monolayers ((2+1)D)

Note: The author of this thesis contributed substantially in this section to research and development of the simulations and corresponding data presented below (i.e. the Monte Carlo simulations for the lattice rods in the grand-canonical ensemble). This encompasses Sec. 4.6, as well.

In the lattice model for the monolayer, we have a 2D ternary mixture of rod lengths $\mathbf{L}_1 = (L, 1)$, $\mathbf{L}_2 = (1, L)$ (rods lying in–plane) and $\mathbf{L}_3 = (1, 1)$ (rods standing up).

The total density is $\rho = \rho_1 + \rho_2 + \rho_3$ and the total packing fraction in the plane is $\eta := n^{(1,1)} = L(\rho_1 + \rho_2) + \rho_3$. The order parameters Q and S are the same as in Eqs. (4.1). $Q > 0$ signifies an excess of particles "standing–up" (nematic state) while $S \neq 0$ signals demixing of "lying–down" particles (biaxial state, if additionally $Q \neq 0$). In the bulk free energy density, $f_{3d,\mathrm{conf}}(\rho, Q, S) = f^{\mathrm{id}}_{3d,\mathrm{conf}} + f^{\mathrm{ex}}_{3d,\mathrm{conf}}$, one can identify $f^{\mathrm{id}}_{3d,\mathrm{conf}} = f^{\mathrm{id}}_{3d}$ whereas the excess part becomes

$$\begin{aligned} f^{\mathrm{ex}}_{3d,\mathrm{conf}} = \Phi^{0d}(L(\rho_1 + \rho_2) + \rho_3) - \Phi^{0d}\left((L-1)\rho_1\right) - \\ \Phi^{0d}\left((L-1)\rho_2\right) . \end{aligned} \quad (4.22)$$

At fixed total density ρ, the minimization of the free energy with respect to Q and S gives the following picture. For "small" rod lengths $L \leq 12$ there is no biaxial state ($S = 0$, no demixing in the plane) but the "nematic" order parameter Q monotonically and smoothly grows from 0 to 1 when the total density varies between 0 and 1 (close-packed state of rods standing up). Results for $L = 4 \ldots 10$ are shown in Fig. 4.4(a) which demonstrates that for increasing L the rods quickly "stand up". The FMT results show excellent agreement with Monte Carlo simulation results [120] on the same confined model for $L = 4$ and 6. For larger rod lengths ($L = 8$ and 10) the agreement with our grand canonical Monte Carlo (GCMC) simulations (see end of this section) is only slightly worse.

For $L \geq 13$, FMT predicts reentrant demixing in the plane, i.e. in a certain interval $[\rho_{\mathrm{low}}(L), \rho_{\mathrm{up}}(L)]$ for the total density the biaxiality parameter will

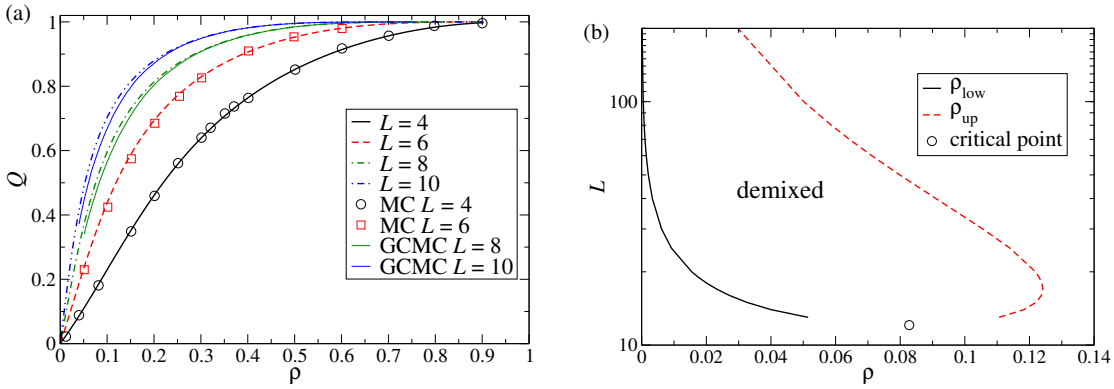

FIGURE 4.4: (a) Order parameter Q for rods standing up vs. total density. Lines are results from FMT and symbols are results from Monte Carlo simulations reported in Ref. [120]. Thin lines are results from our GCMC simulations where a running average of 20 points on density intervals of 0.04 has been taken. (b) Phase diagram from FMT showing a reentrant behavior for mixing ($S = 0$) and demixing ($S \neq 0$) in the plane. The rod length L is treated as a continuous variable. The critical point occurs for a rod length of $L_c \approx 12.077$ at a density of $\rho_c \approx 0.0828$.

be nonzero, $S \neq 0$. This reentrant behavior is qualitatively understood as follows. In the $d = 2$ model it was found that the critical density of demixing of planar rods is $\rho_1 + \rho_2 = 2/(L(L-1))$. For increasing L one therefore expects $\rho_{\text{low}}(L) \to 0$. On the other hand, for a certain L but increasing ρ the fraction of planar rods initially grows, reaches a maximum and becomes smaller again since the rods stand up, see Fig. 4.4(a). Therefore, if there exists a lower demixing density $\rho_{\text{low}}(L)$ then one would expect the existence of a higher remixing density $\rho_{\text{up}}(L)$ owing to the reduction of the planar rod density. As in the $d = 2$ model, the demixing transition is continuous and therefore the densities $\rho_{\text{low}}(L), \rho_{\text{up}}(L)$ can be found by the following argument: Let $\mu_Q(\rho, Q, S) = \partial f_{3d,\text{conf}}/\partial Q$ and $\mu_S(\rho, Q, S) = \partial f_{3d,\text{conf}}/\partial S$ be chemical potentials for the order parameters Q and S. For a mixed state ($S = 0$), we define $Q_{\text{eq}}(\rho)$ through $\mu_Q(\rho, Q_{\text{eq}}, 0) = 0$. As before, we may expand

$$\mu_S(\rho, Q, S) \approx \mu_{1,S}(\rho, Q)S + \mu_{3,S}(\rho, Q)S^3 + \ldots \tag{4.23}$$

At the de-/remixing densities one has the condition

$$\mu_{1,S}(\rho, Q_{\text{eq}}(\rho))|_{\rho=\rho_{\text{low[up]}}} = 0, \tag{4.24}$$

which needs to be solved numerically. The results are shown in Fig. 4.4(b), showing the onset of demixing at $L = 13$ and a maximum density interval for the demixed state at around $L = 20$.

The continuous behavior of $Q(\rho)$ and the reentrant demixing are in fact very similar to the behavior found in the FMT study of the restricted-orientation model with continuous translational degrees of freedom [635]. There biaxial ordering sets in at larger rod lengths, $L \geq 21.34$.

The results of Fig. 4.4 suggest $Q \propto \rho$, i.e. the continuous nematic ordering sets in at $\rho = 0$. This can be understood easily in a low-density expansion of the FMT excess free energy (4.22) which is exact up to second order. Assuming

no biaxiality ($S = 0$) and combining ideal and excess part we find for the free energy derivative with respect to Q:

$$\mu_Q = \frac{\partial f_{3d,\mathrm{conf}}}{\partial Q} \approx \frac{2}{3}\rho \ln\frac{1+2Q}{1-Q} + \frac{2}{9}\rho^2\left([2-L-L^2]+[L-1]^2Q\right) + \mathcal{O}(\rho^3)\,. \tag{4.25}$$

Note that in the excess part of μ_Q, at fixed density, there is a constant term driving the system to $Q > 0$ for $L \geq 2$. This differs from the 2D and 3D bulk systems where the constant term is absent and thus $Q > 0$ (for low densities) is always unfavorable in terms of free energy cost. The equilibrium solution $\mu_Q = 0$ at $Q = Q_{\mathrm{eq}}$ is found to be

$$\rho = \frac{3\ln\frac{1+2Q_{\mathrm{eq}}}{1-Q_{\mathrm{eq}}}}{[L^2+L-2]-[L-1]^2Q_{\mathrm{eq}}} \quad \rightarrow \quad Q_{\mathrm{eq}} \approx \frac{1}{9}(L^2+L-2)\rho\,. \tag{4.26}$$

Hence, for large L the lattice model predicts a scaling $Q_{\mathrm{eq}} \propto \rho L^2$.

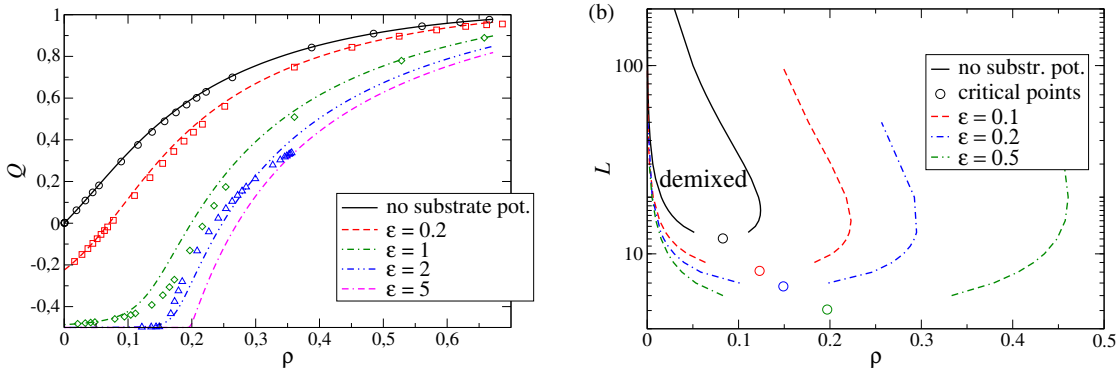

FIGURE 4.5: (a) Order parameter Q for rods standing up vs. total density subject to a substrate potential (rod length $L = 5$). The substrate potential is parametrized as $-\epsilon$ per unit length such that $v_3 = -\epsilon$, $v_0 = -L\epsilon$ and, thus, $v_Q = (2/3)(L-1)\epsilon$. Lines are DFT results, symbols results from GCMC simulations (see end of this section). The error is smaller than the symbol size. (b) FMT phase diagram (for nonzero substrate potential) showing the reentrant behavior for mixing ($S = 0$) and demixing ($S \neq 0$) in the plane. The critical points $\{L_c, \rho_c\}$ are located at $\{8.12, 0.123\}$ for $\epsilon = 0.1$, $\{6.72, 0.149\}$ for $\epsilon = 0.1$, and $\{5.06, 0.197\}$ for $\epsilon = 0.5$.

4.5.1 Finite substrate potential

One may ask whether a finite substrate potential could alter the continuous transition found above. It is natural to assume that the substrate potential acts equally on the flat-lying species 1 and 2 and differently on the upright species 3. Hence the external contribution to the free energy becomes

$$f^{\mathrm{ext}} = \sum_{i=1}^{3} V_i^{\mathrm{ext}}\rho_i = v_0(\rho_1+\rho_2) + v_3\rho_3 = \frac{\rho}{3}(2v_0+v_3) + \frac{2}{3}\rho Q(v_3-v_0)\,. \tag{4.27}$$

Therefore the free energy derivative with respect to Q is modified as $\mu_Q \to \mu_Q + \rho v_Q$ with $v_Q = \frac{2}{3}(v_3 - v_0)$. For the ideal gas limit this implies an initial ordering on the substrate with order parameter

$$Q_{\mathrm{id}} = \frac{\exp(-3v_Q/2) - 1}{\exp(-3v_Q/2) + 2} \,. \tag{4.28}$$

If the substrate is strongly attractive for the flat–lying species 1 and 2 ($v_Q \gg 0$), then we find $Q_{\mathrm{id}} \to -1/2$. At nonzero densities, the solution of $\mu_Q = 0$ (Eq. 4.25 with the external contribution) is obtained in the form $\rho(Q)$. For small deviations from equilibrium, $Q_{\mathrm{eq}} = Q_{\mathrm{id}} + \delta Q$, we can invert this function and obtain

$$\delta Q \approx \frac{3}{2}\rho \, \frac{\alpha - \beta Q_{\mathrm{id}}}{2(1 + 2Q_{\mathrm{id}})^{-1} + (1 - Q_{\mathrm{id}})^{-1}} \tag{4.29}$$

with $\alpha = 2(L^2 + L - 2)/9$ and $\beta = 2(L-1)^2/9$. Although the range of validity is very limited, it implies that the qualitative behavior for $\rho \to 0$ is unchanged since the slope of $\delta Q(\rho)$ is always positive. Thus the transition stays continuous. However, for increasing v_Q the "standing up" transition of the monolayer becomes increasingly steep at *moderate* densities, see Fig. 4.5(a) where we show the $Q(\rho)$ behavior for $L = 5$. For these moderate densities the expansion up to second order is not valid anymore. Especially for the case $\epsilon = 5$ the behavior near $\rho = 0.2$ looks as if $Q(\rho)$ has a bifurcation point here, similar to the demixing transition in the 2D bulk system discussed in teh forthcoming Ch. 6. The density $\rho = 0.2 = 1/L$ at which this apparent transition occurs is the close–packing density for rods lying flat. However, for finite potentials it is not a phase transition since $Q(\rho)$ maintains its linear behavior of $Q(\rho)$ with nonzero slope at very small densities.

A finite substrate potential has a marked influence on the reentrant transition for demixing in the plane. The location of the phase boundaries has been calculated using Eq. (4.24), with the condition $\mu_Q(\rho, Q_{\mathrm{eq}}, 0) = -\rho v_Q$ for Q_{eq}. Fig. 4.5(b) shows the phase boundaries for the demixed phase for substrate potentials $\epsilon = 0.1$, 0.2 and 0.5 in comparison with the case $\epsilon = 0$. With increasing substrate potential, the density range for the demixed phase widens considerably and the critical point moves to smaller rod lengths.

4.6 Equilibrium grand-canonical Monte Carlo simulations for lattice model

The simulation results for the lattice monolayer system were obtained using grand canonical Monte Carlo (GCMC) simulations on an $M \times M$ lattice. We treated the rods with a fixed orientation as a distinct species with corresponding particle number N_i ($i = 1 \ldots 3$). The chemical potential μ was equal for all three species. In each GCMC step, insertion or deletion of a rod was chosen with probability 1/2. Then, the species on which the insertion/deletion is performed, was chosen with probability 1/3. For the insertion move $N_i \to N_i + 1$, a random lattice site was chosen. If no overlap with the existing rods occurs, the move was accepted with probability

$$\alpha_{\mathrm{ins}} = \min\left(1, M^2/(N_i + 1)\, z\, \exp(-\Delta V^{\mathrm{ext}})\right) \,, \tag{4.30}$$

where $z = \exp(\mu/(k_B T))$ and ΔV^{ext} is the change in external energy upon insertion of the rod. For the deletion move $N_i + 1 \to N_i$, a particle from species i was chosen randomly and removed with probability

$$\alpha_{\text{del}} = \min\left(1, (N_i + 1)/M^2\, z^{-1}\, \exp(+\Delta V^{\text{ext}})\right) . \tag{4.31}$$

We used lattices with $M = 256$ and 10^7 single moves for a data point with no or small external potential. For stronger external potentials, we used 10^8 moves ($\epsilon = \{1, 2\}$).

* * *

In the following section, we will investigate the equilibrium behavior of a monolayer of hard spherocylinders that constitutes a continuum model. This shall serve as a comparison to the lattice model so that the effects of discretization the degrees of freedom shall be made explicit, at least with respect to the equilibrium behavior of static, *global* quantities like the nematic order parameter.

4.7 Equilibrium monolayer systems of hard spherocylinders

Note: The author contributed to the results in this section by generating Fig. 4.6.

For the lattice monolayer discussed in the previous section it does not matter which rod point or segment is actually fixed to the plane since all choices lead to the same effective 2D model. Physically, fixing the end point corresponds to the case of rods on a hard substrate while fixing some other rod point (e.g. in the middle) applies to Langmuir monolayers. For a continuous model of hard rods, there should be a difference between the two cases which is not expected to be qualitative (with regard to the type of transition). As can be seen below, the low-density behavior of long rods with large aspect ratios is actually insensitive to the choice of confining plane. We will thus present simulation results below only for the case of fixed mid-points.

4.7.1 DFT in an expansion up to second order in density

We consider hard spherocylinders with length L and diameter D whose centers or ends are fixed on a plane. In order to investigate the nature of the orientation transition, we consider a low-density expansion of the free energy. For the well-studied model of hard rods in 3D, this method was used to establish the onset of nematic order as a bifurcation and the nature as a first order transition [886]. The free energy density up to second order in density, including the

contribution from an external potential, is given by

$$\mathcal{F} = \mathcal{F}^{\mathrm{id}} + \mathcal{F}^{\mathrm{ex}} + \mathcal{F}^{\mathrm{ext}} \tag{4.32}$$

$$\mathcal{F}^{\mathrm{id}} = \int d^2r \int d\Omega\, \rho(\mathbf{r},\Omega)(\ln(\rho(\mathbf{r},\Omega)\Lambda^2) - 1) \tag{4.33}$$

$$\mathcal{F}^{\mathrm{ex}} = \frac{1}{2}\int d^2r \int d\Omega \int d^2r' \int d\Omega'\, \rho(\mathbf{r},\Omega)\rho(\mathbf{r}',\Omega')\omega(|\mathbf{r}-\mathbf{r}'|,\Omega,\Omega') \tag{4.34}$$

$$\mathcal{F}^{\mathrm{ext}} = \int d^2r \int d\Omega\, \rho(\mathbf{r},\Omega)V^{\mathrm{ext}}(\mathbf{r},\Omega) \tag{4.35}$$

Here, $\rho(\mathbf{r},\Omega)$ is an inhomogeneous particle density in two dimensions and units of [length]$^{-2}$ which depends on the space point $\mathbf{r}$ and the orientation of the rod $\Omega = (\theta,\phi)$, specified by the polar angle θ and the azimuthal angle ϕ. The integral over orientations is defined as

$$\int d\Omega = \frac{1}{4\pi}\int_0^{\pi} \sin\theta d\theta \int_0^{2\pi} d\phi\ . \tag{4.36}$$

Λ is the thermal de-Broglie length. $\omega(r,\Omega,\Omega')$ is the overlap function between rods for given orientations of and distance r between the particles. It is 1 if there is overlap, otherwise zero. The external (substrate) potential $V^{\mathrm{ext}}(\mathbf{r},\Omega)$ is measured in units of $k_{\mathrm{B}}T$.

We consider only orientation-dependent substrate potentials, $V^{\mathrm{ext}}(\Omega)$, and bulk states, i.e. no spatial dependence of the density and introduce the orientation distribution $f(\Omega)$:

$$\rho(\mathbf{r},\Omega) = \rho_0 f(\Omega)\ . \tag{4.37}$$

Then the ideal, excess and external part of the free energy per particle ($a = a^{\mathrm{id}} + a^{\mathrm{ex}} + a^{\mathrm{ext}}$) become:

$$a^{\mathrm{id}} = \int d\Omega f(\Omega)(\ln(\rho_0\Lambda^2 f(\Omega)) - 1)\ , \tag{4.38}$$

$$a^{\mathrm{ex}} = \frac{\rho_0}{2}\int d\Omega \int d\Omega'\, f(\Omega)f(\Omega')\beta(\Omega,\Omega')\ , \tag{4.39}$$

$$a^{\mathrm{ext}} = \int d\Omega\, f(\Omega)V^{\mathrm{ext}}(\Omega)\ . \tag{4.40}$$

Here, $\beta(\Omega,\Omega') = \int d^2r\omega(r,\Omega,\Omega')$ is the excluded area between the rod centers (or ends) with fixed orientations of the rods.

In equilibrium, $f(\Omega)$ minimizes a. From $\delta a/\delta f = 0$ we obtain

$$\ln f(\Omega) = -\ln C - V^{\mathrm{ext}}(\Omega) - \rho_0 \int d\Omega'\, \beta(\Omega,\Omega')f(\Omega')\ , \tag{4.41}$$

where C is a constant ensuring that f is properly normalized, i.e. $\int d\Omega\, f(\Omega) = 1$. It is determined by exponentiating Eq. (4.41) and integrating over Ω:

$$f(\Omega) = \frac{1}{C}\exp\left(-V^{\mathrm{ext}}(\Omega) - \rho_0\int d\Omega'\, \beta(\Omega,\Omega')f(\Omega')\right)\ , \tag{4.42}$$

$$C = \int d\Omega \exp\left(-V^{\mathrm{ext}}(\Omega) - \rho_0\int d\Omega'\, \beta(\Omega,\Omega')f(\Omega')\right)\ .$$

The orientation-dependent substrate potential gives rise to a non-constant orientational distribution in the ideal-gas limit:

$$f_{\mathrm{id}}(\Omega) = \frac{\exp(-V^{\mathrm{ext}}(\Omega))}{\int d\Omega \exp(-V^{\mathrm{ext}}(\Omega))} , \tag{4.43}$$

which is normalized to 1. We introduce the small deviation $f_1(\Omega) := f(\Omega) - f_{\mathrm{id}}(\Omega)$ and linearize Eq. (4.42) in f_1:

$$\begin{aligned} \frac{f_1(\Omega)}{f_{\mathrm{id}}(\Omega)} &= C_1 - \rho_0 \int d\Omega' \beta(\Omega,\Omega')(f_{\mathrm{id}}(\Omega') + f_1(\Omega')) \\ C_1 &= \rho_0 \int d\Omega \int d\Omega' f_{\mathrm{id}}(\Omega)\beta(\Omega,\Omega')(f_{\mathrm{id}}(\Omega') + f_1(\Omega')) . \end{aligned} \tag{4.44}$$

The constant C_1 ensures the necessary normalization condition $\int d\Omega f_1(\Omega) = 0$. If one expands f_1 in powers of ρ_0 then one finds the leading order solution

$$\begin{aligned} f_1(\Omega) \approx \rho_0 \, f_{\mathrm{id}}(\Omega) \Bigg(\int d\Omega \int d\Omega' f_{\mathrm{id}}(\Omega)\beta(\Omega,\Omega') f_{\mathrm{id}}(\Omega') \\ - \int d\Omega' \beta(\Omega,\Omega') f_{\mathrm{id}}(\Omega') \Bigg) . \end{aligned} \tag{4.45}$$

This expression is equivalent to Eq. (4.29) in the lattice model and shows that any deviations from the ideal gas distribution are continuous and proportional to the density ρ_0.

In the absence of a substrate potential ($f_{\mathrm{id}} = 1$), we can proceed further. Without loss of generality, we put rod 1 at the coordinate center with orientation (director) $\mathbf{u}_1 = (\sin\theta_1, 0, \cos\theta_1)^T$. Rod 2 has the director $\mathbf{u}_2 = (\sin\theta_2\cos\phi_2, \sin\theta_2\sin\phi_2, \cos\theta_2)^T$. The excluded area depends in general on the three angles $\theta_1, \theta_2, \phi_2$. If we consider only nematic order without biaxiality, $f(\Omega) \equiv f(\theta)$, then we can define the integrated overlap area

$$\frac{1}{2\pi} \int d\phi_2 \beta(\theta_1,\theta_2,\phi_2) =: \beta_\phi(\theta_1,\theta_2) . \tag{4.46}$$

If we take the polar angle (with respect to the interface normal) in the interval $[-\pi/2, \pi/2]$, symmetry considerations give us $\beta_\phi(\theta_1,\theta_2) = \beta_\phi(-\theta_1,\theta_2) = \beta_\phi(\theta_1,-\theta_2) = \beta_\phi(-\theta_1,-\theta_2)$. Since also $f(\theta) = f(-\theta)$, the integration domain over θ can be restricted to $[0, \pi/2]$. The nematic order parameter in the monolayer is defined by

$$Q_{\mathrm{nem}} = \int_0^{\pi/2} d(\cos\theta) P_2(\cos\theta) \, f(\theta) , \tag{4.47}$$

where $P_2(x)$ is the second of the Legendre polynomials $P_i(x)$. It is also useful to introduce the Legendre coefficients of the excluded area:

$$B_{ij} = \int_0^{\pi/2} d(\cos\theta) P_{2i}(\cos\theta) \int_0^{\pi/2} d(\cos\theta') P_{2j}(\cos\theta') \, \beta_\phi(\theta,\theta') . \tag{4.48}$$

Owing to the symmetry of the excluded area, projections only onto even Legendre polynomials are nonzero. Using these definitions, the nematic order parameter in the case of no substrate potential is obtained by projecting with P_2

onto the solution for f_1 in Eq. (4.45):

$$Q_{\rm nem} \approx -\rho_0 B_{10} \tag{4.49}$$

This is an interesting result since it tells us that $Q_{\rm nem} \propto \rho_0$ as long as the leading off-diagonal Legendre coefficient of the excluded area is nonzero. This is precisely the case in the monolayer system (see below), whereas in 3D this coefficient vanishes. The linearity $Q_{\rm nem} \propto \rho_0$ is completely equivalent to the linearity found in the lattice model in the absence of a substrate potential (see Eq. (4.26)).

The linearized equation (4.44) is connected to an approximated free energy per particle $a_{\rm lin}$ through $\delta a_{\rm lin}/\delta f_1 = 0$. $a_{\rm lin}$ is quadratic in f_1 and is defined to give the the difference to the isotropic state:

$$\begin{aligned} a_{\rm lin} &= \frac{1}{2}\int_0^{\pi/2} d(\cos\theta) f_1(\theta)^2 + \\ &\quad \frac{\rho_0}{2}\int_0^{\pi/2} d(\cos\theta)\int_0^{\pi/2} d(\cos\theta')\beta_\phi(\theta,\theta')(2+f_1(\theta))f_1(\theta')\ . \end{aligned} \tag{4.50}$$

For the leading order solution (4.45), the free energy can be explicitly evaluated. It is convenient to use the Legendre expansion of the solution: $f_1 = \sum_{i=1}^{\infty} f_{1,i} P_{2i}(\cos\theta)$ with $f_{1,i} = -(2i+1)\rho_0 B_{i0}$. Using furthermore $B_{i0} = B_{0i}$ one finds

$$a_{\rm lin} \approx -\frac{1}{2}\sum_{i=1}^{\infty}(2i+1)\rho_0^2 B_{i0}^2\ , \tag{4.51}$$

i.e. the free energy in the anisotropic state is always lower than in the isotropic state.

For hard spherocylinders in the limit $L/D \to \infty$ the excluded area does not depend on whether the rod centers or ends are fixed to the plane. Through geometric arguments (see next section below) we find

$$\begin{aligned} \beta(\theta_1,\theta_2,\phi_2) &= \frac{2LD}{\cos\theta_{\rm min}}|\sin\gamma|\ , \\ &\quad \theta_{\rm min} = \min(|\theta_1|,|\theta_2|) \\ &\quad \cos\gamma = \cos\theta_1\cos\theta_2 + \sin\theta_1\sin\theta_2\cos\phi_2\ , \end{aligned} \tag{4.52}$$

where γ is the angle between the rods. Thus, we see that for long rods a scaling $Q_{\rm nem} \propto L\rho_0$ is predicted, which is different from $Q \propto L^2\rho$ found in the lattice model. The numerical evaluation of the Legendre coefficient in Eq. (4.49) gives

$$Q_{\rm nem} \approx 0.45\ LD\rho_0 \qquad (L/D \to \infty)\ . \tag{4.53}$$

4.7.2 Excluded area for hard spherocylinders in the limit $L/D \to \infty$

Here we briefly derive Eq. (4.52). The geometric definitions are given in Fig. 4.6. For infinitely thin hard rods, the (maximum) distance of closest approach $d/2$ is given by

$$d/2 = \frac{(L/2)}{\cos\theta_{\rm min}}\sqrt{\cos^2\theta_1 + \cos^2\theta_2 - 2\cos\theta_1\cos\theta_2\cos\gamma}\ . \tag{4.54}$$

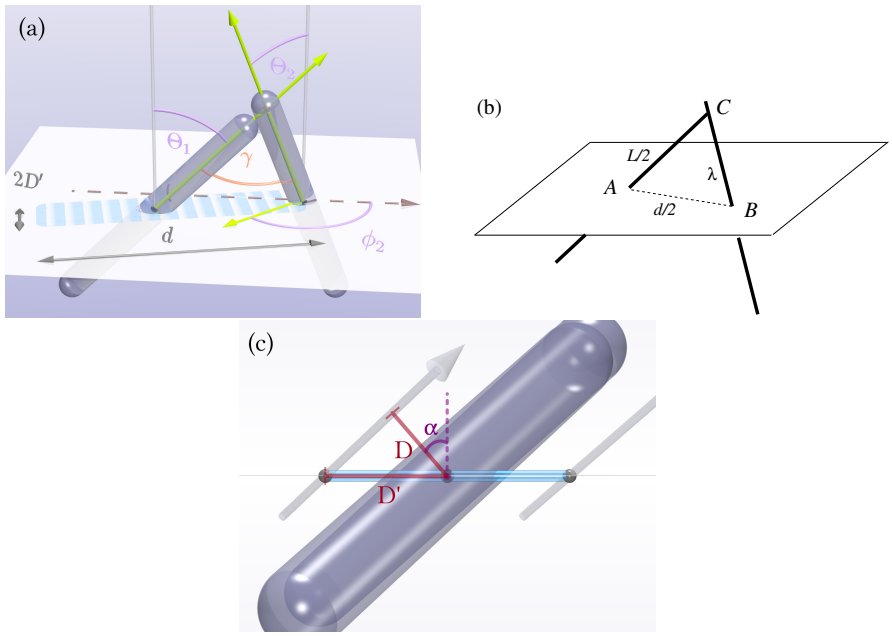

FIGURE 4.6: (a) and (b): Hard rods (spherocylinders) with their mid points fixed on the substrate plane. The area enclosed in dashed lines is the excluded area and can be approximated by a rectangle with side lengths d and D' in the limit $L/D \to \infty$. (c): Side view on the two hard rods from a perspective where rod 2 is exactly hidden behind rod 1.

This is obtained from the law of cosines in the triangle ABC (see Fig. 4.6(b)) where $\lambda = (L/2)\cos\theta_{\max}/\cos\theta_{\min}$ and $\theta_{\min[\max]} = \min[\max](|\theta_1|, |\theta_2|)$. If we consider now a finite, small thickness D of the rods then rod 2 may slide past rod 1 at a distance D' to either side of rod 1 along the direction of d. This defines the excluded area (enclosed in dashed lines in Fig. 4.6(a)). It is a rectangle with side lengths d and $2D'$. According to Fig. 4.6(c), the distance D' is given by

$$D' = \frac{D}{\sin\alpha}\,, \tag{4.55}$$

where α is the angle of $\mathbf{e}_z$ with the normal vector $\mathbf{n}$ to the plane spanned by the two rods. This normal vector is given by

$$\mathbf{n} = \frac{\mathbf{u}_1 \times \mathbf{u}_2}{|\sin\gamma|}\,, \tag{4.56}$$

where $\mathbf{u}_i$ is the normalized director of rod i. Thus

$$\cos\alpha = \mathbf{n}\cdot\mathbf{e}_z = \frac{\sin\theta_1 \sin\theta_2 \sin\phi_2}{|\sin\gamma|}\,. \tag{4.57}$$

Insertion into Eq. (4.55) and some manipulations give

$$D' = D\,\frac{|\sin\gamma|}{\sqrt{\cos^2\theta_1 + \cos^2\theta_2 - 2\cos\theta_1\cos\theta_2\cos\gamma}}\,, \tag{4.58}$$

such that finally the excluded area becomes

$$\beta(\theta_1, \theta_2, \phi_2) \approx 2D'd = \frac{2LD}{\cos\theta_{\min}} |\sin\gamma| \,. \tag{4.59}$$

4.7.3 Comparison to MC simulations

In order to validate the predictions from the previous section, we have performed Monte Carlo (MC) simulations of hard spherocylinders (cylinders of length L capped with two hemispheres of diameter D on either end) whose centers are restricted to move within a plane (off lattice) while the orientation vectors can take any direction in three-dimensional space. A cuboid simulation box with periodic boundary conditions and dimensions $L_x \times L_y \times (L + D)$ is used. Configurations have been generated using single particle displacement and rotations via the Metropolis scheme [404] as well as a specialized move for small densities that forces particles to come close to each other. We pick two random particles. If they are further apart than $(L + D)$, we move one into a circle of radius $(L + D)$ around the center of mass of the other. To fulfill detailed balance, the acceptance criterion of the inverse move (i.e. to remove one particle from the proximity of another and to place it somewhere in the plane) is simply multiplied by the ratio between the area of the simulation plane ($L_x \times L_y$) and the area of that circle ($\pi(L + D)^2$). We generated configurations for a fixed particle number N while varying the dimensions of the plane $L_x \times L_y$ to change the area number density of the rods ρ_0. After equilibration, we generated at least 10^6 independent configurations for each value of L/D, N and ρ_0 to evaluate the nematic order parameter Q_{nem}.

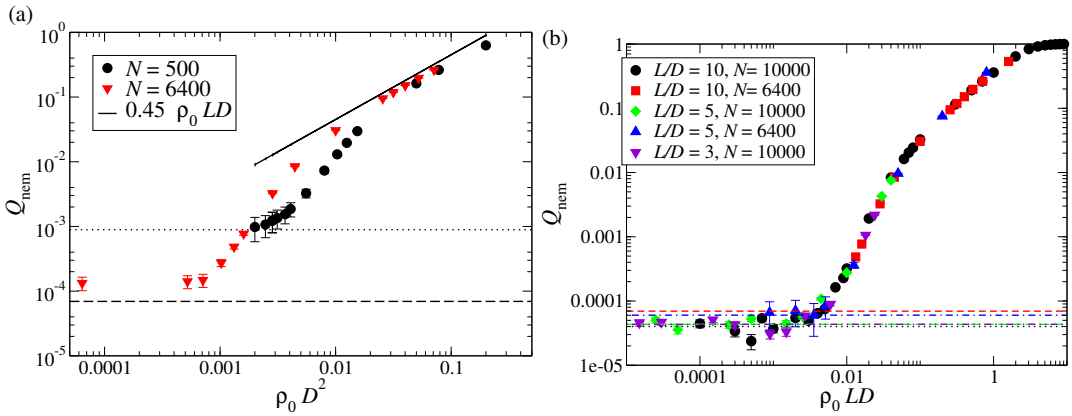

FIGURE 4.7: (a) Finite system size analysis, rod length $L/D = 10$. The dashed and dotted horizontal lines are Q_{nem} values obtained for a system of freely penetrable rods for particle numbers N = 6400 and 500, respectively, while the solid line is the DFT result (Eq. (4.53)). (b) Order parameter Q_{nem} vs. $\rho_0(L/D)$ plot for different aspect ratios L/D and numbers of rods N. The horizontal lines are as in (a).

At low densities, the simulations are subject to strong finite–size effects, which produce artifacts that might be misinterpreted as traces of a phase transition. In Fig. 4.7(a), we show $Q_{\text{nem}}(\rho_0)$ at low densities for two different N. Here, the horizontal lines mark the Q_{nem}–values obtained in simulations of freely penetrable rods. For an infinite number of particles, this value would be

zero. However, since in the simulations we sum the orientational order tensor over a finite number of particles its eigenvalues are not exactly zero and, therefore, the largest eigenvalue, corresponding to Q_{nem}, is always larger than zero. (This problem is not solved by the common strategy of taking twice the middle eigenvalue instead of the largest eigenvalue. It is inherent in the restriction to finite particle numbers [887].) The horizontal lines thus mark the limit of detection of a Q_{nem} that truly signals orientational anisotropy for a given number of particles N. For a given N, there appears a first (lower) density above which orientational order is detectable, and a second (larger) density where the theoretically expected behavior $Q_{\mathrm{nem}} \propto \rho_0$ sets in. These two densities are particle number dependent and shift towards zero with increasing N, and thus are not signatures of an additional phase transition. The solid line in Fig. 4.7(a) is the DFT result (Eq. (4.53)) derived in the previous section. For densities beyond the second density, the simulation results are very close to the DFT result and the density range where this occurs becomes larger with increasing system size.

The linearity $Q_{\mathrm{nem}} \propto \rho_0$ can also be seen in numerical results for a monolayer of ellipsoids [888] (Fig. 4 therein, for an aspect ratio of 10). The density functional used in Ref. [888] reduces to Eq. (4.34) in the low–density limit and should therefore comply with the present analysis, however, explicit expressions have not been given in Ref. [888]. Corresponding Monte-Carlo simulation results in Ref. [888] show agreement with the DFT results but low densities have not been considered.

In Fig. 4.7(b), we show Q_{nem} vs. $\rho_0(L/D)$, which is independent of the aspect ratio L/D. System sizes are very similar here such that the finite size effect discussed above is not visible.

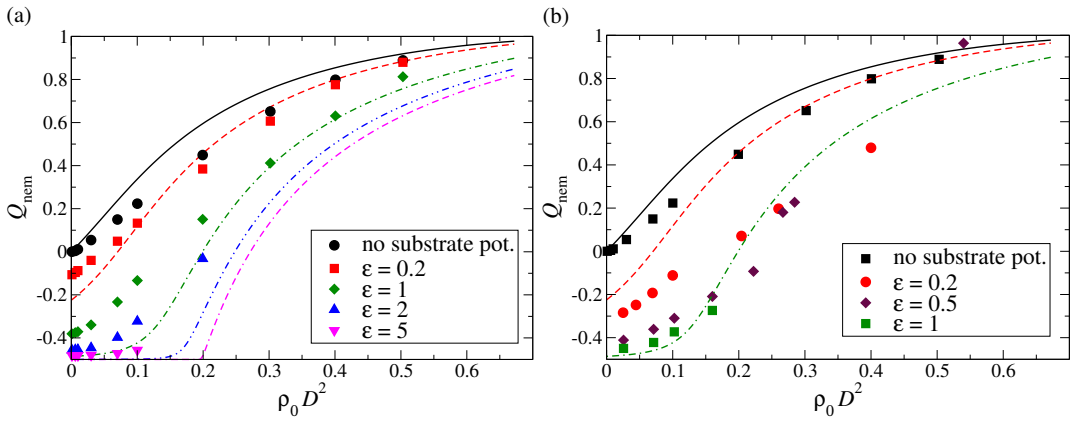

FIGURE 4.8: Order parameter Q_{nem} vs. number density $\rho_0 D^2$ for rods subject to an attractive substrate potential ($L/D = 5$). The dashed lines are the results from the lattice model shown in Fig. 4.5 while data points correspond to the off-lattice simulation (errors smaller than symbol size). The substrate potential is orientation–dependent defined by (a) $V^{\mathrm{ext}} = -\epsilon(L/D)\sin\theta$ and, (b) $V^{\mathrm{ext}} = -\epsilon(L/D)\sin^2\theta$, where θ is the angle between rod director and the substrate normal.

In the presence of an attractive substrate potential (Fig. 4.8), we qualitatively observe the same behavior as in the lattice model (in Fig. 4.5). We compare two different potentials (a) $V^{\mathrm{ext}} = -\epsilon(L/D)\sin\theta$ and, (b) $V^{\mathrm{ext}} = -\epsilon(L/D)\sin^2\theta$, where θ is the angle between rod director and the substrate normal. Both choices drive the system toward nematic order (rods “standing up"), with

choice (b) the external free energy per particle (Eq. (4.40)) becomes

$$a^{\text{ext}} = \int_0^{\pi/2} d\theta\, f(\theta) V^{\text{ext}}(\theta) = \frac{2}{3}\,\epsilon\,\frac{L}{D}\,(Q_{\text{nem}} - 1)\,. \tag{4.60}$$

Similar to the choice of the external potential in the lattice model (Eq. (4.27)), the corresponding free energy contribution (apart from an additive constant) is proportional to the nematic order parameter. The plots show qualitative agreement with the lattice model as Q_{nem} remains continuous and the "standing up" transition becomes steeper with increasing substrate potential parameter ϵ.

For the moderate aspect ratios investigated here (between 3 and 10 in the case of no substrate potential and 5 for the attractive substrate) no transition to a biaxial state has been found. Such a biaxial state would correspond to the demixing in the plane investigated in the lattice model. In Ref. [888], the biaxial transition was investigated in more detail for their system of ellipsoids on a plane and an effective substrate attraction mimicked by a restriction of the polar angle to values between a nonzero limiting angle and $\pi/2$. Using DFT, the authors find that the occurrence of a biaxial transition is very sensitive to the limiting angle: for zero angle (no substrate potential) no transition has been found in simulations for aspect ratios up to 20 whereas small nonzero angles induce this transition.

* * *

The first half of this chapter explored the equilibrium, static properties of monolayers of purely hard-core rods in terms of a global order parameter Q (orientational order) as a function of monolayer number density ρ. The focus was on developing and exploring the capabilities of analytical theory, where equilibrium simulations in the grand canonical ensemble provided the "ground truth" comparison. As the systems remain purely hard-core in this section, we were able to formulate a lattice FMT for rods of geometry $L \times 1 \times 1$. We found no thermodynamic phase transitions for the moderate rod-lengths explored ($L = 4 \ldots 10$) in this form of confinement: the "standing up" behavior of rods from an isotropic vapor at low densities proceeds continually upon increased number density, and is entropy-driven. For very long rods, $L \geq 13$, FMT does predict a phase transition – reentrant demixing in-plane (among the two lying orientations) – but, we have not checked this against simulations. Additional substrates that bias the lying orientation do not induce a phase transition, but, for e.g. $L = 5$, a very narrow width of densities exists in which the order parameter increases steeply – hence, we may dub this effect as a "pseudo-phase-transition": In the next section, we will see for longer rod-lengths that dynamical arrest appears, we which suspect are associated with these regions of high 'free energy curvature'. We also compared the systems of hard rods in the (2+1)D lattice model to a monolayer system of spherocylinders. We have found qualitative agreement in their equilibrium phase behavior, yet, the models entail different "equation-of-states" (virial coefficients) and are thus physically incompatible. There is no way to convert one model into the other. This was evidenced in the scaling of the second-virial coefficient of the spherocylinder model, which does not seem to exist for the lattice.

In the next sections, we shall move on to exploring monolayer growth under nonequilibrium conditions in models including dynamics.

4.8 Growth of monolayers: From quasi-equilibrium to nonequilibrium dynamics

Note: The author contributed majorly to the next half of this chapter. All kinetic Monte Carlo simulations were written, developed, and executed by the author. All data plots and schematics were generated and put into final form by the author, as well. Exceptions are Figs. 4.17 and 4.20. We will make additional notes about our contribution at the beginning of sections where this may not be clear, i.e. where contributions are a mixture among different co-authors.

As of this section, we will investigate the nonequilibrium evolution of hard-rod monolayers – with regards to macroscopic static properties such as the total particle density ρ, packing fraction η, and nematic order parameter Q, in as much analogy as possible to the investigations of equilibrium properties of the last section. We first describe the simulations with kinetic Monte Carlo (KMC) in Sec. 4.8.1. A dynamical DFT (DDFT) will be formulated for growth and then cross-checked with the KMC simulations; it is first described in Sec. 4.9, and the direct comparisons to the KMC simulations are presented in Sec. 4.10. We also provide a derivation of the long-time translational diffusion rate of "tumbling" rods, which were implemented in the KMC model, within the ideal gas limit in Sec. 4.11. Finally, we investigate the behavior of growing monolayers of hard spherocylinders (in the continuum) in Sec. 4.12. We shall first discuss how to match the dynamics between models, and afterwards present quantitative results, whereby we will explore two different continuum-model realizations for monolayer growth.

4.8.1 Kinetic Monte Carlo Simulations

Note: This section represents text written by the author herself, and has been modified and extended compared to the passages written in the corresponding (second) publication.

We introduced kinetic Monte Carlo in Chs. 3.3.5 and 3.4.1 for the first time. We discuss more technical aspects of the algorithm here for hard rods. To refresh the basic concepts, KMC is suited for simulating dynamical systems that can be characterized by a finite number of elementary processes occurring with different rates (denoted 'events'). An underlying assumption is that each event j having a rate k_j occurs via a Poisson-process with mean waiting time $1/k_j$. As events occur independently, the total random process of waiting for *any* among all events is also Poisson-distributed with a mean waiting time $1/\sum_j k_j$. Specifically, this probability distribution of waiting times has the form $P^{\text{wait}}(t) = e^{-\sum_j k_j/t}$.

In each KMC iteration step, a single, currently allowed event having rate k_i is chosen randomly among all such events with a relative probability $\frac{k_i}{k_{\text{tot}}(\{\mathcal{C}\})}$, $k_{\text{tot}}(\{\mathcal{C}\}) = \sum_j k_j$, where $\{k_j\}_j\big|_{\{\mathcal{C}\}} \ni k_j$ is the full list of allowed events at this configuration. (Note that this list *could* include *forbidden* events [830], but at the computational cost of rejecting them.) KMC is therefore effectively "rejection-free", at least in the variant of the algorithm used here, first proposed in Ref. [23]. The waiting time since the last event, i.e. the increment of time, is chosen according to the distribution $P^{\text{wait}}(\Delta t, \{\mathcal{C}\})$, employing $\Delta t = -1/k_{\text{tot}}(\{\mathcal{C}\}) \ln u$, with $u \in (0, 1]$ chosen randomly and uniformly. The

chosen event is executed. The list of allowed events must be updated according to the new configuration by adding newly–allowed events and removing forbidden ones.

This tracking of allowed and forbidden events makes KMC non-trivial, illustrated here for the case of hard-core particles: An event might become forbidden, for example, if a nearest neighbor rod is blocking the hopping or tumbling move of a rod. Also, a new event must be added to the list once the nearest neighbor(s) in the way moves away from the rod. We implement a detection system that tracks proper neighborhood patterns. Such a system becomes increasingly complex the higher the degree of anisotropy of the particles. Our algorithmic approach (see below) can be extended to general hard-core lattice systems. As one sees, the rejection-free bonus of KMC comes at the cost of algorithmic complexity to eliminate forbidden moves.

The kinetics of our lattice model (square lattice in the $\boldsymbol{x}$–$\mathbf{y}$-plane [substrate] with unit length u, size $M \times M = 256^2$, periodic boundary conditions) is characterized by the rates of the allowed single–particle processes. The first rate is k^0_{hop} for an explicit hopping process of a rod of orientation i ($i = 1..3$) on the substrate, translating it by one lattice site in any of 4 directions. This process may occur regardless of the orientation, and the rates are identical. The second rate k_{tum} is ascribed to a tumbling process, which changes the orientation of a rod. Here, the rod is assumed to rotate around one of its ends. Specifically, the tumbling process is split into two types – the first, a tumble 'upward' into the $\boldsymbol{z}$-direction from a lying orientation ($i = 1, 2$) to a standing one ($i = 3$). This rate is denoted $k^{\text{u}}_{\text{tum}}$. The second is a tumble 'downward' into the $\boldsymbol{x}$–$\mathbf{y}$-plane from a standing orientation to a lying one. This is denoted $k^{\text{d}}_{\text{tum}}$. The third rate $k_{1\leftrightarrow 2}$ is the in-plane rotation between orientations 1 and 2 about the rod midpoints. This constrains our investigations to rod-lengths L of odd number. All rates are in units of inverse time. The final rate (orientation-specific) is k^{ins}_i for a random influx of rods of orientation i, in units of inverse time multiplied by u^2. This influx of rods (corresponding to the insertion rate in the DDFT model) is implemented as a random appearance of rods of orientation i at constant rate k^{ins}_i per lattice site, whereby the move is rejected if overlap occurs, i.e. the rod "disappears". There is hence a monotonic, but nonlinear relationship between number density ρ and simulated time (see Fig. 4.15(a) below).

Novel, rejection-free algorithmic implementation for anisotropic particles

We implement a rejection-free KMC algorithm developed in the spirit of Bortz et al. [23] for highly anisotropic hard particles. We use a detection system for tracking all allowed/forbidden events in current configurations that is (1) on–the–fly during simulation and (2) localized around the change in configuration during each MC step. We restrict our discussion in the following to purely hard–core interactions between particles, although these considerations may be extended to finite-ranged interaction potentials. Viewing the kinetics from the point–of–view of a particle, a neighbor may exclude one of the particle's elementary moves (translations or rotations) if the neighbor gets close enough. A similar statement holds from the point–of–view of the neighbor. According to the KMC method, any of their excluded moves are removed from the current list of possible events. The opposite may also be true – moves may suddenly become possible if the particles have moved apart. These moves must be added to

the current list of events. The act of forbidding or allowing the moves of a neighbor is not commutative for anisotropic particles, in general.Fig. 4.9 shows this situation for rotations of hard rods about their endpoints. This asymmetrical

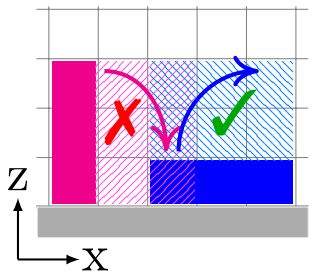

FIGURE 4.9: Illustration (out–of–plane) of two neighboring rods and the space they need for rotations about their ends. The left rod is blocked by the right rod, while the right rod is free to rotate: their blockage is not symmetrical.

relationship between neighbors makes neighbor-lists unsuited for implementation. We outline a characteristically different method using what we denote as 'inverted list indices' below.

We first take advantage of one feature unique to lattice systems: sites can be tabulated. We implement a field over the lattice that represents the state of occupancy at each site. Given this setup, each particle need only know the local neighborhood pattern of occupancy around it. To clarify, a move by a particle is only possible if a minimal finite volume around it is unblocked by other particles. In addition, if simulations are not restricted to a plane, for example, a move may also require particular sites around it to be occupied (such as in multilayer growth with rods, where a particle may only rotate and translate with occupied sites beneath it as to exclude forming overhangs). Hence, each move by a particle needs this particular pattern around the particle in order to be considered *allowed*; else, the move is *forbidden*. The abstract object representing the tracker for this neighborhood pattern is the inverted list index—it acts as a local field over the lattice, moving with the particle and switching with the particle's orientation, accordingly (see Fig. 4.10). Any change occurring on the lattice is evaluated by the affected inverted list indices, and if one changes its state (*allowed* to *forbidden*, or vice versa) the inverted list index removes its 'index' from the list of allowed events. We note that we adapt the nomenclature of inverted lists from computer science; for the case of (1×1) particles, Ref. [889] illuminates the situation: A list of events $\{e_k\}$ is stored, and a particular event e_k is executed at spatial index (i, j) on the lattice (position of a particle). An inverted list $\{e_{(i,j)}\}$ should allow one to quickly access index in memory of the event occurring at position (i, j). This is useful when doing updates locally around the place of each event. Our inverted list indices differ in that they exhibit spatial extent and are rather more sophisticated; they perform their updates themselves, i.e. they may add or remove their own indices from the events list. They are merely called to re–evaluate their state if an occupancy has changed within their local field.

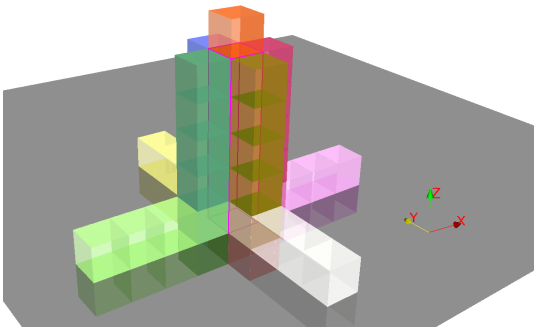

FIGURE 4.10: Visualization of the inverted list indices for the event-driven KMC algorithm for hard rods, here for the moves of a standing rod with $L = 5$. Represented are their fields over discrete space, each colored differently. The moves correspond to rotations downwards about the rod-end on the substrate (gray), as well as translational hops to nearby planar sites. Spurious pattern-checking above and beneath the plane is done since the implementation was originally developed for multilayer growth.

4.9 Dynamical DFT on a lattice

Note: The author's contribution to the results of this section are in generating the plots and the KMC data points in Fig. 4.11, to editing the text, as well as to research. The author contributed substantially to the preliminary research and results that initiated the following work. The development and execution of the quasiequilibrium theory, the DDFT theory, and execution of the numerical codes thereof are outside of the scope of the author's direct contributions.

FMT for monolayers: A refresher

In the present work, we only need the free energy functional for the homogeneous case for the monolayer. Rods with dimensions $1 \times 1 \times L$ (in lattice units) are confined to a substrate plane (square lattice) with their lower left corner (see Fig. 4.1(a)). Thus, the monolayer becomes a 2D ternary mixture of $1 \times L$ rectangles with two possible orientations in the substrate plane and 1×1 squares representing the upright rods (Fig. 4.1(b)). The bulk number densities per unit square on the lattice are denoted by ρ_1, ρ_2 ($1 \times L$ rods with orientation in x– and y–direction, respectively), and ρ_3 (1×1 rods). The total density is $\rho = \rho_1 + \rho_2 + \rho_3$. The free energy density is given as a sum of an ideal gas part, excess part and external part:

$$f = f^{\mathrm{id}} + f^{\mathrm{ex}} + f^{\mathrm{ext}} \qquad \text{with} \tag{4.61}$$

$$\beta f^{\mathrm{id}} = \sum_{i=1}^{3} \rho_i \ln \rho_i - \rho \,, \tag{4.62}$$

$$\beta f^{\mathrm{ex}} = \Phi^{0d}(L(\rho_1 + \rho_2) + \rho_3) - \Phi^{0d}\left((L-1)\rho_1\right) - \Phi^{0d}\left((L-1)\rho_2\right) \tag{4.63}$$

$$\beta f^{\mathrm{ext}} = \sum_{i=1}^{3} \rho_i V_i^{\mathrm{ext}} \,. \tag{4.64}$$

Here, $\beta = 1/(k_B T)$ is the inverse temperature which will be set to 1 from now on, and

$$\Phi^{0d}(\eta) \quad = \quad \eta + (1-\eta)\ln(1-\eta)\,. \tag{4.65}$$

is the excess free energy of a zero–dimensional cavity (which can hold no or only one particle) depending on its average occupation $\eta \in [0,1]$. The substrate potential is specified by the three constants V_i^{ext} which can be different from each other, in general.

4.9.1 Setup

The goal of our dynamic lattice DFT is to provide an equation for the time evolution of the observables ρ_1, ρ_2, and ρ_3 (or, equivalently, ρ, Q, and S) in a system driven out of equilibrium by particle deposition at constant rates. We limit our description to this tractable set of observables, i.e., a given configuration of the system specified by these three observables stands for a much larger set of different microstates of the nonequilibrium system. Thus we cannot expect to reproduce trajectories of the system exactly. However, it is conceivable to gradually improve the description by refining the set of observables, thereby allowing for better discrimination of non-equilibrium configurations [890].

Within the framework provided by the observables ρ_1, ρ_2, and ρ_3 the following formally–exact dynamic equations are readily obtained:

$$\frac{\partial \rho_i}{\partial t} = \alpha_i^{\text{ins}} p_i^{\text{ins}} + \sum_{j\neq i} \alpha_{j\to i}\rho_j p_{j\to i} - \sum_{j\neq i} \alpha_{i\to j}\rho_i p_{i\to j}\,, \tag{4.66}$$

where $i = 1,2,3$. The constants α_i^{ins} correspond to the deposition rates of the individual orientation into an empty system. The parameters $\alpha_{i\to j}$ characterize the particle mobilities, i.e., the probability for a single particle of orientation i in an otherwise empty system to change its orientation and become a particle of orientation j is given by $\alpha_{i\to j}dt$. The complexity of the dynamics is contained in the probabilities p_i^{ins} and $p_{i\to j}$, which denote the probability that an attempted particle deposition or orientational transition, respectively, is successful in a non–dilute system evolving along a certain non-equilibrium trajectory. These probabilities depend on the history of the system and generally cannot be expressed as functions of the ρ_i.

Expressions for the probabilities p_i^{ins} and $p_{i\to j}$ can be obtained by employing equilibrium-like approximations, applicable for a situation where the deposition rates α_i^{ins} are very small compared to particle mobilities $\alpha_{i\to j}$. Using the excess chemical potential μ_i^{ex} of orientation i,

$$\mu_i^{\text{ex}} = \frac{\partial f^{\text{ex}}}{\partial \rho_i} \tag{4.67}$$

from Eq. (4.63), we use the thermodynamic definition of an insertion probability,

$$p_i^{\text{ins}} = e^{-\mu_i^{\text{ex}}} = \begin{cases} \frac{(1-\eta)^L}{(1-(L-1)\rho_i)^{L-1}} & \text{for } i = 1,2 \\ 1-\eta & \text{for } i = 3\,, \end{cases} \tag{4.68}$$

where $\eta = L(\rho_1 + \rho_2) + \rho_3$ denotes the packing fraction of the system, equivalent to the surface fraction of the substrate covered by a monolayer.

For the calculation of $p_{i\to j}$ we need to specify exactly how the orientation of a rod is changed under the given dynamics. To this end, we first consider a model where a change in orientation from i to j is realized in two steps. First, a rod with orientation i is removed from the system and, second, a rod with orientation j is inserted into the system at a random lattice site. We refer to these somewhat unrealistic dynamics as UNCO, denoting that removal and insertion of a rod are spatially *uncorrelated*. The quasi–equilibrium limit of $p_{i\to j}$ under the UNCO dynamics is readily obtained as $p_{i\to j} = p_j^{\text{ins}}$. It can easily be checked that with these probabilities Eq. (4.66) yields an equilibrium state with $\rho_i \propto e^{-\mu_i^{\text{ex}}}$ for $t \to \infty$, provided that no particles are deposited, i.e., $\alpha_i^{\text{ins}} = 0$. These are precisely the equilibrium particle densities following a minimization of the free energy $f = f^{\text{id}} + f^{\text{ex}}$ using Eqs. (4.62) and (4.63), w.r.t. the ρ_i.

In order to compare the UNCO dynamic equations with our KMC simulations we make use of the fact that the equilibrium phase diagram obtained from Eqs. (4.62) and (4.63) does not feature biaxiality for $L \leq 12$ (Sec. 4.5). We, therefore, make the assumption that $\rho_1 = \rho_2$ also holds for the non–equilibrium setting of the rod–lengths studied in the simulations (with $L = 5$ and 9 investigated below). We consider two different modes of particle deposition: (i) perpendicular deposition and (ii) isotropic deposition. The corresponding deposition rates are (i) $\alpha_1^{\text{ins}} = \alpha_2^{\text{ins}} = 0$, $\alpha_3^{\text{ins}} = \alpha_{\text{ins}}$ and (ii) $\alpha_1^{\text{ins}} = \alpha_2^{\text{ins}} = \alpha_3^{\text{ins}} = \frac{1}{3}\alpha_{\text{ins}}$. Time is measured relative to particle mobility, which we assume to be isotropic with $\alpha_{i\to j} = 1$, where $i \neq j$. Results of the UNCO model are obtained by solving the set of differential equations numerically for an initially empty system. Figure 4.11 shows the UNCO trajectories of the system for different deposition rates α_{ins} in the (η, Q) plane resulting from perpendicular and isotropic deposition. Since the behavior for different rod–lengths $L \leq 12$ is found to be qualitatively the same in the model, we limit ourselves at this point to the case $L = 5$. Results for rod–lengths $L = 9$ are shown in Sec. 4.10.2, where we compare the dynamic DFT results to KMC simulations.

It is interesting to note that in the long-time limit $t \to \infty$ the UNCO dynamics do not necessarily generate a configuration in which all the rods stand up, i.e. for sufficiently fast deposition we find $Q < 1$ while $\eta \to 1$. This is reflected in the UNCO dynamic equations being stationary for $\eta = 1$, irrespective of the value of Q, thereby allowing for a fully–covered surface with a certain fraction of rods still in the λ orientation (i.e. lying down). While somewhat counter–intuitive, this behavior is rooted in the non–locality of the UNCO dynamics. Once a λ rod is chosen for a change in orientation, these particular dynamics attempt to insert the rod after reorientation at a *random* site of the lattice. For sufficiently large η this insertion is almost always impossible, even for a rod in the σ orientation (i.e. standing up). As a result, the rod chosen to perform the move remains at its initial site in λ orientation. Consequently, the system can remain locked in a fully–packed configuration, preventing it from switching out all the rods in the system to those with a perpendicular orientation (to the surface).

More realistic *local* dynamics is provided by the CORR model, which performs changes in orientation locally and takes *correlations* at the given site into account. It is based on the simple observation that if a transition from a λ to σ orientation is done locally, the move is always accepted since a rod lain down

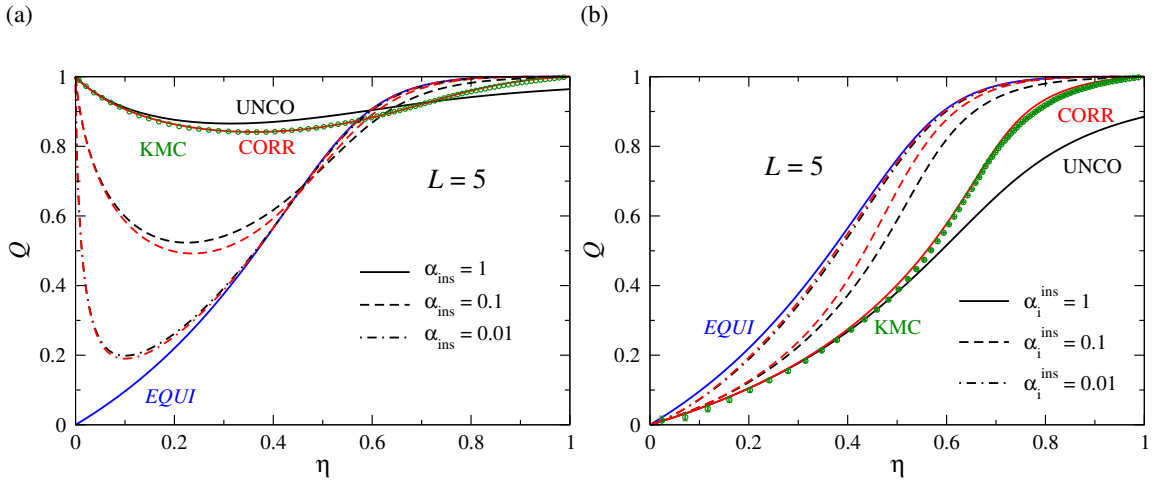

FIGURE 4.11: (a) Trajectories of the deposition of a monolayer of hard rods of length $L = 5$ represented in the (η, Q) plane, where η denotes the covered surface fraction and Q denotes the degree of nematic order in the monolayer. The system is initially empty ($\eta = 0$) and rods are deposited with different rates $\alpha_{\rm ins}$ measured relative to their rotational mobility. Rods are perpendicular to the substrate upon deposition. The blue curve corresponds to thermodynamic equilibrium. Results were obtained using the UNCO (black) and CORR (red) dynamic lattice DFT (see text). KMC simulations matched to the dynamics of $\alpha_{\rm ins} = 1$ (fastest deposition) were performed (green circles, for a description see below). Their error bars are smaller than the symbols. (b) Same analysis, but for deposition with random orientations $i = 1 \ldots 3$ inserted with equal rates $\alpha_i^{\rm ins}$ (isotropic deposition). Error bars for KMC simulations (green) are displayed.

on the substrate automatically guarantees room for it to stand up at the same location. Hence, in the CORR model, we employ $p_{1\to3} = p_{2\to3} = 1$. In order to recover the correct equilibrium behavior in the stationary state without particle deposition, we must have $p_{3\to i} = e^{-\mu_i^{\rm ex}+\mu_3^{\rm ex}}$, where $i = 1, 2$. The remaining transition probabilities are the same as in the UNCO model. Assuming no biaxiality ($S = 0$), results are obtained by solving the set of differential equations numerically for various depositions rates, considering both perpendicular and isotropic deposition. In Fig. 4.11 we show results of the CORR model for rods of length $L = 5$. In particular, the theory predicts $Q = 1$ in the limit $\eta = 1$, meaning that in the long–time limit with full surface coverage all the rods are in σ orientation. It can easily be shown from the dynamic equations that, in contrast to the UNCO model, stationarity in the CORR model requires $\eta = 1$ *and* $\rho_1 = \rho_2 = 0$. This implies $\rho_3 = 1$ and, therefore, $Q = 1$.

Figure 4.11 includes data from KMC simulations (Sec. 4.8.1) with matching dynamic parameters (Sec. 4.10.1 below). We note that for the error bars, here and everywhere else, KMC data is first averaged into bins; thereafter the binned data is averaged over six independent runs. Exceptions are for $\alpha < 10^{-3}$, where data is collected from a single run; they are otherwise noted. The CORR model appears to give an excellent description of the dynamics of rods of lengths $L = 5$, particularly in the case of perpendicular deposition. Sec. 4.10.2 compares the dynamic DFT results with our KMC simulations further for rod-length

$L = 9$.

4.9.2 Finite substrate potentials

We consider the case where the substrate interacts via an attractive potential of strength ϵ per segment touching the substrate:

$$V_i^{\text{ext}} = \begin{cases} -\epsilon & (i = 3) \\ -L\epsilon & (i = 1, 2) \end{cases} . \tag{4.69}$$

Here, the rotational mobilities $\alpha_{i\to j}$ have to be partially modified. While the mobilities in the substrate plane remain unchanged (i.e. unity in the present normalization) the attractive interaction suppresses transition from a λ to σ orientation, and within the present dynamics we have $\alpha_{i\to 3} = e^{-\epsilon(L-1)/2}$ for $i = 1, 2$. On the other hand, a transition from a σ to λ orientation is promoted, leading to modified mobilities $\alpha_{3\to i} = e^{\epsilon(L-1)/2}$ for $i = 1, 2$. In both the UNCO and the CORR models, these modified mobilities lead to stationary points for $\alpha_{\text{ins}} = 0$, which are identical to the equilibrium properties obtained by minimization of the free energy functional with the appropriate external potential in Eq. (4.69). Note that we will study the scenario of an attractive substrate only in the case of perpendicular deposition, which means we may leave the insertion rate unmodified.

4.9.3 Quasiequilibrium growth

When the flux rate is infinitely slow compared to all other kinetic parameters in the monolayer, every moment of growth is fully described by thermodynamic equilibrium. The change in density of species j through deposition within time step dt is proportional to the flux rate as

$$d\rho_j^{\text{dep}} = \alpha_j^{\text{ins}} e^{-\mu_j^{\text{ex}}} dt \, , \tag{4.70}$$

The deposited particles become redistributed instantaneously ($d\rho_j^{\text{dep}} \to d\rho_j$) with conservation of the total number of particles,

$$d\rho^{\text{dep}} = \sum_j d\rho_j^{\text{dep}} = \sum_j d\rho_j = d\rho \, , \tag{4.71}$$

such that the total chemical potential $\mu = \mu_j$, as well as the increments $d\mu = d\mu_j$, are constant and equal among all species. Here, $\mu_j = \ln \rho_j + \mu_j^{\text{ex}}$. $r_{ij} = \frac{\partial \mu_i}{\partial \rho_j}$ and, thus,

$$d\mu = d\mu_i = \sum_{j=1}^{3} r_{ij} d\rho_j \qquad (i = 1..3) \, . \tag{4.72}$$

In our system $\rho_1 = \rho_2$. Solving for the two independent density increments we obtain

$$d\rho_i \;\; = \;\; A_i d\rho \qquad (i = 1, 3) \tag{4.73}$$

where $A_1 = \frac{r_{13} - r_{33}}{2r_{13} + r_{31} + r_{32} - r_{11} - r_{12} - 2r_{33}}$, $A_3 = 1 - 2A_1$ and $d\rho$ is defined through Eqs. (4.70) and (4.71). The total time increment in $d\rho$ can be re–scaled, $dt^\star =$

$\alpha_{\text{ins}}dt$, such that the coupled system of equations in (4.73) does not depend on the total flux α_{ins} anymore. The solutions $\rho_i(t^\star)$ can then be found through numerical integration.

4.10 Comparison between KMC simulations and theory (DDFT)

Note: The author contributed substantially to all parts of this section: in writing almost all of the text, to deriving the 2D translational coefficient for "tumbling" rods and therewith to matching the dynamics between KMC and DDFT, to generating all plots as well as being responsible for all of the KMC simulations.

4.10.1 Matching KMC to DDFT

In the following we only consider the case where $k^{\text{u}}_{\text{tum}} = k^{\text{d}}_{\text{tum}} \equiv k_{\text{tum}}$ (no biasing substrate potential). The rates for the tumbling and deposition process are related to the rates defined in the DDFT equation (4.66) as follows:

$$\alpha_{i\to j} \;\leftrightarrow\; 2k_{\text{tum}} \qquad \text{all combinations with } i \neq j \tag{4.74}$$

$$\alpha^{\text{ins}}_i \;\leftrightarrow\; k^{\text{ins}}_i \,. \tag{4.75}$$

where the relation means equality up to the same constant factor. The first relation holds since we have fixed $\alpha_{i\to j} = 1$ in DDFT globally. The factor two arises from the fact that the rods can rotate into each orientation in one of two rotational directions. Since one of the rates can be used to define the time scale, a growth process only depends on ratios of rates. As introduced before, we consider vertical deposition ($\alpha^{\text{ins}}_i = \alpha_{\text{ins}}\delta_{i,3}$) or isotropic deposition ($\alpha^{\text{ins}}_i = \frac{1}{3}\alpha_{\text{ins}}$) with the total deposition rate α_{ins}; the same deposition rate holds for the KMC model via $k_{\text{ins}} = \sum_i k^{\text{ins}}_i$. We also assume isotropic transition rates $\alpha_{i\to j}$ (see Sec. 4.9), analogous to $k^{\text{u}}_{\text{tum}} = k^{\text{d}}_{\text{tum}} = k_{\text{tum}} = k_{1\leftrightarrow 2}$ in KMC. DDFT predicts that there is no dependence of our observables on k^0_{hop}. This is indeed what we also observe in KMC (see Fig. 4.12). Our matching condition is hence set by the single independent variable α characterizing the growth dynamics:

$$\alpha := \frac{k_{\text{ins}}}{2k_{\text{tum}}} = \frac{\sum_i k^{\text{ins}}_i}{2k_{\text{tum}}} \equiv \frac{\sum_i \alpha^{\text{ins}}_i}{\alpha_{i\to j}} = \frac{\alpha_{\text{ins}}}{1} \,. \tag{4.76}$$

This variable is different from the single variable, commonly denoted F/D, characterizing growth with isotropic particles, where F is the incoming flux rate and D is the diffusion constant in the substrate plane. For our KMC model, the translational diffusion constant $D \equiv D^{\text{latt}}_{\text{2D}}$ in the dilute limit (monolayer density close to zero) is determined by both k^0_{hop} and k_{tum}:

$$D^{\text{latt}}_{\text{2D}}/u^2 = \left(\frac{1}{2}k^{\text{u}}_{\text{tum}} + \frac{1}{1+2\frac{k^{\text{d}}_{\text{tum}}}{k^{\text{u}}_{\text{tum}}}}\left(k^{\text{d}}_{\text{tum}} - \frac{1}{2}k^{\text{u}}_{\text{tum}}\right)\right)\frac{(L-1)^2}{4} + k^0_{\text{hop}} \tag{4.77}$$

$$\equiv \qquad k_{\text{hop}} + k^0_{\text{hop}} \,, \tag{4.78}$$

which is derived in the subsequent Sec. 4.11. One sees that hopping and tumbling (through an effective hopping rate k_{hop}) contribute to diffusion independently.

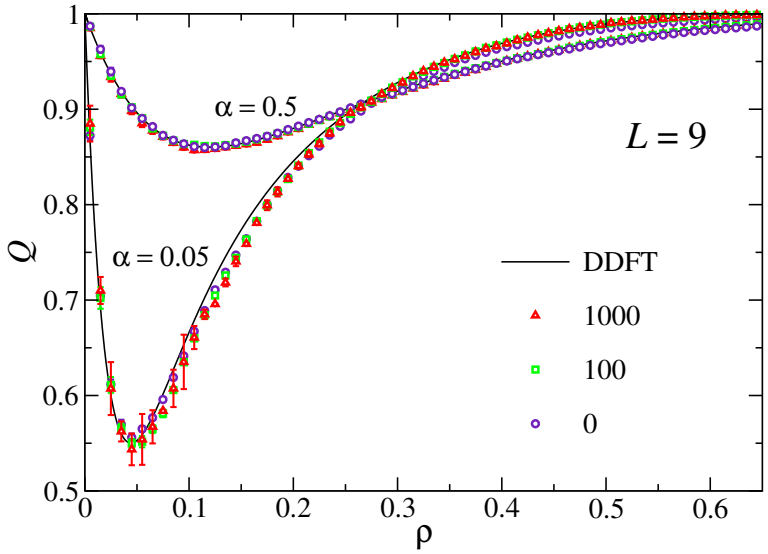

FIGURE 4.12: Dependency of growth dynamics of the monolayer of hard rods on the kinetic parameter k^0_{hop}: There is virtually none. The total number density is ρ and Q denotes the degree of nematic order in the monolayer. Data with error bars is from KMC simulations with $L = 9$, perpendicular deposition, and two cases of the growth parameter $\alpha = 0.5, 0.05$ (Eq. (4.76)) and different values of $k^0_{\text{hop}}/k_{\text{tum}}$. The solid curves are calculated by DDFT (CORR). The data set $\{k^0_{\text{hop}}/k_{\text{tum}} = 1000, \alpha = 0.05\}$ is averaged over two independent runs instead of six.

4.10.2 Results: DDFT vs. KMC

The case $k^{\text{u}}_{\text{tum}} = k^{\text{d}}_{\text{tum}}$ (no substrate potential)

We calculate the dynamics via KMC and DDFT for $L = 9$. Since the total density ρ grows during the deposition process, $Q(\rho)$ is an indirect way to visualize the time dependence of the nematic order $Q(t)$, but in contrast to $Q(t)$, $Q(\rho)$ can be directly compared with the equilibrium curve. In Fig. 4.13 we compare KMC and DDFT (CORR) with varying degrees of growth; we employ both perpendicular as well as isotropic deposition. There is very gratifying agreement between theory and simulation, although with a small deviation only in the isotropic deposition case. This is highlighted when we plot the order parameter against the surface packing fraction η in Fig. 4.14. The deviation of DDFT from KMC with isotropic deposition appears to amplify with long rods; compare these results to $L = 5$ in Fig. 4.11(b) with $\alpha = 3$. This is likely a combination of effects: the density functional is less precise for longer rods (Sec. 4.4), and the packing fraction $\eta (= L\rho_{12} + \rho_3)$ is particularly sensitive to resulting errors in the number density $\rho_{12} = \rho_1 + \rho_2$; so, the error in η scales with L. Apart from this, isotropic deposition with its random insertion of rod species $i = 1, 2$ appears to emphasize errors in the calculation of ρ_{12}. Fig. 4.15(a) shows satisfactory correspondence between DDFT and KMC for total number

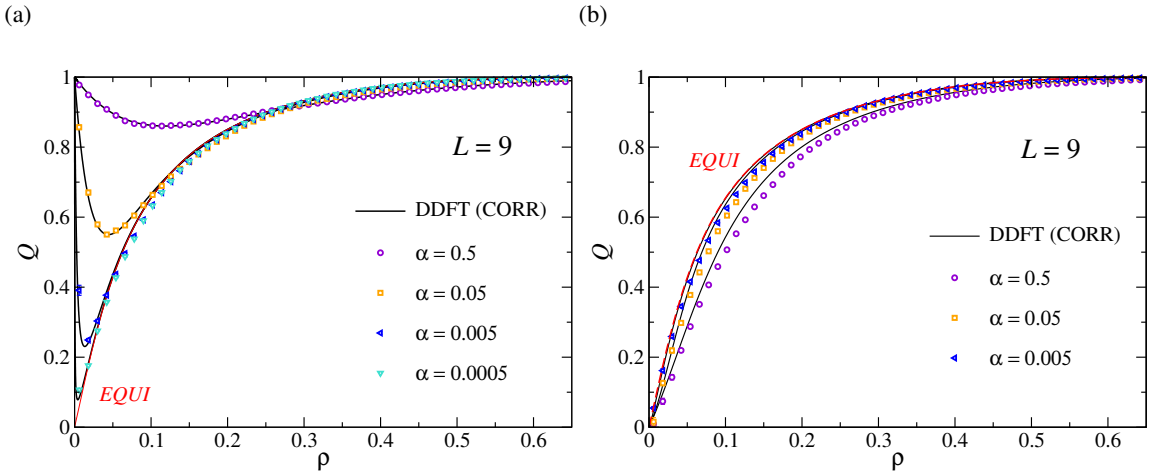

FIGURE 4.13: Trajectories of the deposition of a monolayer of hard rods of length $L = 9$ represented in the (ρ, Q) plane, for a varying growth parameter α. Plotted are calculations with KMC (symbols with error bars) and DDFT (CORR) (black lines) with (a) perpendicular deposition and (b) isotropic deposition. The red curves (EQUI) correspond to solutions from equilibrium DFT.

density ρ for both deposition types, while Fig. 4.15(b) highlights the errors when observing ρ_{12} alone.

The explicit evolution of observables in time such as in Fig. 4.15 can be compared directly between DDFT and KMC if the kinetic rates, rather than their ratios, are matched explicitly. We set $k_{\text{tum}} = \frac{1}{2}\alpha_{i\to j} = \frac{1}{2}$, as well as $k_{\text{ins}} = \alpha_{\text{ins}}$ and observe the evolution of number densities during growth. If we re-scale the time variable with the flux rate $t^\star = \alpha_{\text{ins}} t$, the evolution of number densities can be compared for different growth rates. Naturally, for decreasing flux rate these curves converge to a single curve, the quasiequilibrium growth curve obtained by the solution of Eq. (4.73). From Fig. 4.15(a) one sees that the time evolution of the total density is very well-described by the quasiequilibrium curve for all deposition rates. Since the quasiequilibrium curve is essentially determined by the equation of state (through $\mu(\rho_i)$), a measurement of $\rho(t)$ can be regarded as an effective measurement of the equation of state. This is different for $\rho_{12}(t)$ (Fig. 4.15(b)) where the results for the fastest deposition rate deviate considerably both in shape and magnitude from the quasiequilibrium curve.

One may compare these results to a very simple generalization of the Langmuir growth model. The latter is formulated for the adsorption of isotropic particles, corresponding to our lattice model with perpendicular rods only. The insertion probability is proportional to the free substrate area, i.e. the time development of the density is governed by $\dot{\rho} = \alpha_{\text{ins}}(1-\rho)$ with the solution $\rho(t) = 1 - \exp(-\alpha_{\text{ins}} t) = 1 - \exp(-t^\star)$. It describes our solution for perpendicular deposition reasonably well.

The case $k^{\text{u}}_{\text{tum}} < k^{\text{d}}_{\text{tum}}$: attractive substrates

From the perspective of kinetics, the potential induces an additional energy barrier for the rods to stand up, where the activated dynamics is described

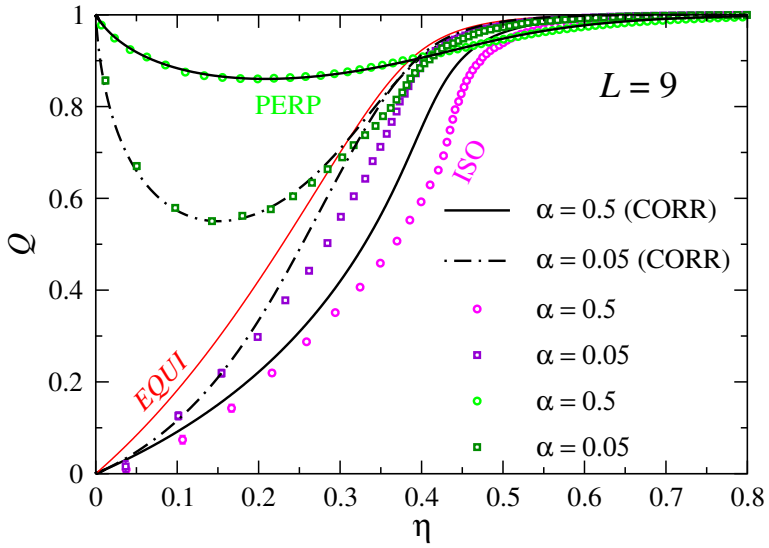

FIGURE 4.14: Trajectories of the deposition of a monolayer of hard rods of length $L = 9$ represented represented in the (η, Q)–plane for $\alpha = 0.5, 0.05$. Curves are DDFT (CORR), symbols are KMC data; green (PERP) indicates perpendicular deposition, pink/violet (ISO) indicates isotropic deposition. The red curve (EQUI) corresponds to solutions from equilibrium DFT.

by an Arrhenius law.[1] The corresponding rates employed follow the DDFT modeling (see Sec. 4.9.2):

$$k^{\mathrm{u}}_{\mathrm{tum}} = k_{\mathrm{tum}} e^{-(L-1)\epsilon/2} \tag{4.79}$$

$$k^{\mathrm{d}}_{\mathrm{tum}} = k_{\mathrm{tum}} e^{(L-1)\epsilon/2} \tag{4.80}$$

Figure 4.16 shows the resulting dynamics from both KMC and DDFT calculations for the nematic order parameter $Q(\rho)$.

A key feature distinguishes the dynamics on attractive substrates from the one on neutral substrates: the kinetic parameter k^0_{hop} contributing to translational diffusion comes into play (compare Fig. 4.12). It appears that for large $k^0_{\mathrm{hop}}/k_{\mathrm{tum}}$ the $Q(\rho)$–curves converge to a single one which is approximately described by the DDFT result. Now that tumbling moves are very rare events soon after a rod is introduced, this parameter alone controls local equilibration of the translational degrees of freedom. This likely means strong configurational jamming (dynamical arrest) occurs when rod translations cannot contribute to relaxation. Figure 4.16(b) shows that the surface becomes fully packed at $\eta = 1$ at rather low densities ρ, illustrated in Fig. 4.16(d). In an unusual change in character, the dynamics at full packing fraction is dominated by the rare events of rods standing up with (perpendicular) deposition taking place at the vacancies generated.

[1] We model the effect of an energy barrier only on rotational motion – the substrate does not influence translational motion directly.

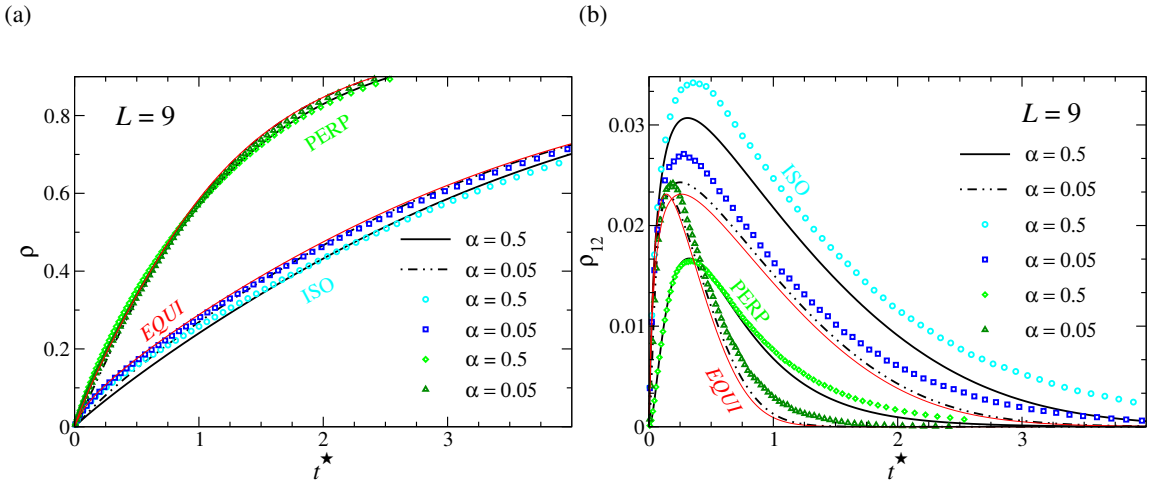

FIGURE 4.15: Evolution of number densities during growth in a monolayer of hard rods of length $L = 9$ with growth parameters $\alpha = 0.5, 0.05$; perpendicular– (PERP, green) as well as isotropic–deposition growth (ISO, cyan/blue) is calculated via KMC (symbols with error bars) and DDFT (CORR) (black lines). (a) Total number density ρ and (b) number densities of lying rods $\rho_{12} = \rho_1 + \rho_2$ versus time re-scaled with the flux rate $t^\star = \alpha_{\text{ins}} t$. The red curves (EQUI) – shown for both deposition types correspond to infinitely-slow, quasiequilibrium growth calculated from DFT.

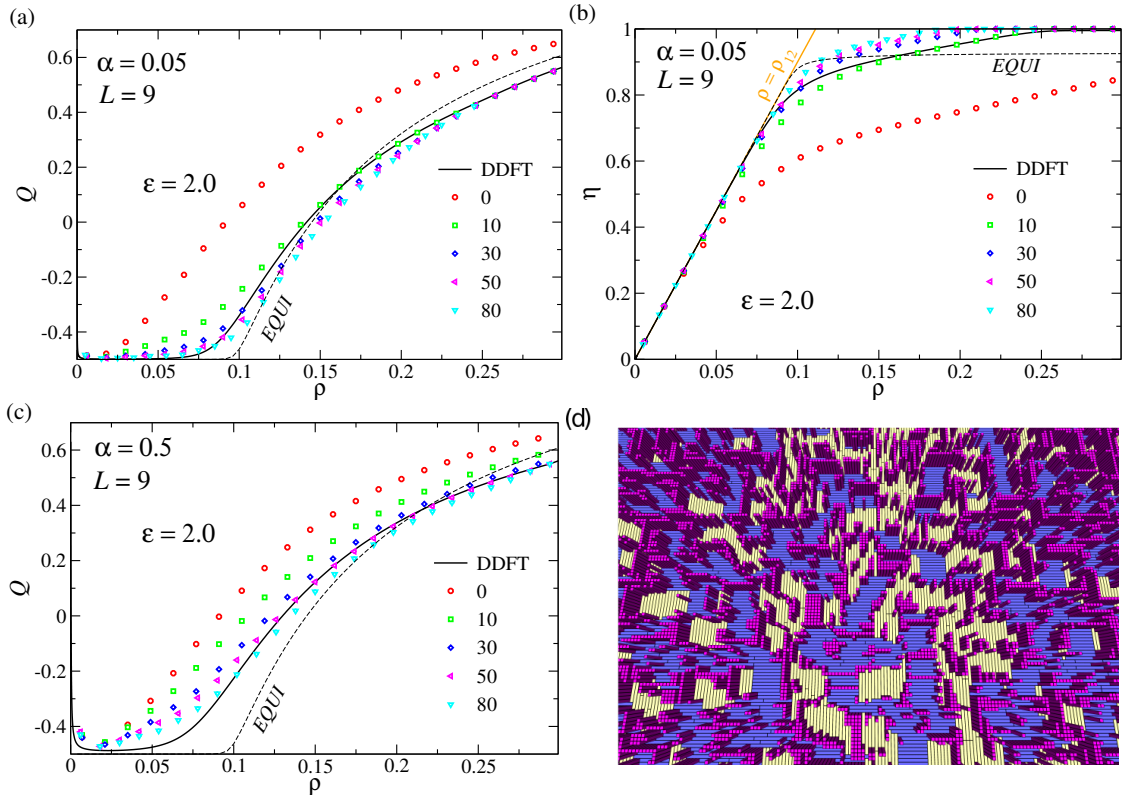

FIGURE 4.16: Growth of a monolayer of hard rods with lengths $L = 9$ on attractive substrates under perpendicular deposition: Dependency of growth dynamics on translational diffusion. Indicated in the legend are values of the kinetic parameter $k^0_{\mathrm{hop}}/(2k_{\mathrm{tum}})$ (symbols with error bars). Shown additionally are DDFT calculations (black curves) as well as results from equilibrium DFT (black dashed curves). The substrate strength $\epsilon = 2.0$. Growth with comparably small rate $\alpha = 0.05$ is represented (a) in the (ρ, Q), and (b) in the (ρ, η) plane, where it is seen that full packing is reached at relatively low densities. The limiting case of all rods lying on the substrate ($\rho \equiv \rho_{12}$) is drawn in orange. (c) Same as (a), but for faster growth $\alpha = 0.5$. Data points represent binned averages within single runs. (d) Illustration of a fully–packed configuration ($\eta = 1$) at intermediate density. The color code is the same as in Fig. 4.1.

* * *

Up to now, we have compared the KMC results of the growth of a monolayer for purely hard-core rods on a lattice with the approach of DDFT. Quasiequilibrium growth is possible at neutral substrates for a slow growth rate α. We see strong qualitative overlap between DDFT and the simulations at situations further from equilibrium at neutral substrates, i.e. for fast growth rates, while errors or idiosyncrasies of the DDFT become conspicuous for non-neutral substrates. The KMC simulations show us an onset of a dynamic arrest (or a transient jamming transition) for strong substrate potentials, where the growing monolayer becomes fully-packed $\eta \to 1$ at number density $\rho < 1$ and remains at this kind of state for a very long period of time until the final state of $\rho \to 1$ is reached. The DDFT we developed here does not consider an explicit dependence of the rotational and translational degrees of freedom, which becomes important in far-from-equilibrium situations (highly non-Markovian dynamics) like when dynamical arrest sets in. We reiterate that all investigations considered structural observables at a global scale like orientational order parameter, packing fraction and number densities.

In the next section, we venture on to comparing the lattice model for growth at neutral substrates with that of the continuum model of spherocylinders, analyzed in equilibrium previously in Sec. 4.7. As in the equilibrium case, we will discover qualitative overlap in the behavior of global structural order (the order parameters Q and Q_{nem}, respectively to each model).

4.11 Derivation of $D_{\mathrm{2D}}^{\mathrm{latt}}$ in the dilute limit

Note: This section is a direct contribution of the author of this thesis.

We begin by writing down the master equation describing the change of a population density $\rho_i(t)$ ($i = 1..3$) over time within the dynamics of an ideal lattice gas of tumbling rods (pure hopping does not change the number of rods in any orientation):

$$\frac{d\rho_i(t)}{dt} = \sum_{j \neq i} -\rho_i(t) T(i \to j) + \rho_j(t) T(j \to i) \,, \tag{4.81}$$

where $T(i \to j)$ is the transition rate for a rod to go from orientation i to j. We are interested in steady–state ensemble properties—hence, we enforce that for all i the left hand side of Eq. (4.81) is zero and the populations reach a stationary state $\{\rho_1, \rho_2, \rho_3\}$. This leaves us with the following condition for the transition rates:[2]

$$\sum_{j \neq i} \rho_i T(i \to j) = \sum_{j \neq i} \rho_j T(j \to i) \,. \tag{4.82}$$

The transition rates are simply $T(1 \to 2) = T(2 \to 1) = 2k_{1 \leftrightarrow 2}$, $T(1 \to 3) = T(2 \to 3) = 2k_{\mathrm{tum}}^{\mathrm{u}}$, and $T(3 \to 2) = T(3 \to 1) = 2k_{\mathrm{tum}}^{\mathrm{d}}$, where the factor 2 arises because the rods can rotate into each orientation with positive and negative rotation directions. One can easily show that the only linearly

[2] which can be interpreted as global balance in a Markov–chain Monte Carlo algorithm

independent equation that remains is the following:

$$(\rho_1 + \rho_2) k_{tum}^{u} = 2\rho_3 k_{tum}^{d} \tag{4.83}$$

Notice that any dependency on the in–plane rotations with rate $k_{1\leftrightarrow 2}$ drops out of the equations. Defining $\rho_{12} := \rho_1 + \rho_2$, we obtain $\rho_{12} = \rho_3 \frac{2k_{tum}^{d}}{k_{tum}^{u}}$. Since the total density is preserved, $\rho = \rho_{12} + \rho_3 = \text{const.}$, we find for the stationary state:

$$\frac{\rho_3}{\rho} = \frac{1}{1 + 2\frac{k_{tum}^{d}}{k_{tum}^{u}}} \tag{4.84}$$

$$\frac{\rho_{12}}{\rho} = 1 - \frac{1}{1 + 2\frac{k_{tum}^{d}}{k_{tum}^{u}}} \,. \tag{4.85}$$

These equations will be useful in steps that follow.

Returning to expressing the diffusion constant on an infinite 2D lattice, we first consider the motion of the rods of length Lu only along one axis. The first contribution to diffusion comes from a tumbling move in an average time $1/k_{tum}$ (where k_{tum} is k_{tum}^{u} or k_{tum}^{d}) which displaces the center–of–mass of the rods by $(L-1)/2$ in units of u. According to Fick's law for 1D diffusion with diffusion constant D, $\langle |\Delta x|^2 \rangle = 2Dt$ we obtain the 1D contribution to translational diffusion from tumbling as $D = \frac{1}{8} k_{tum} (L-1)^2 u^2$.

We next consider specifically the tumbles contributed by upright rods ($i = 3$): The mean waiting time for the propagation to this mean–squared–displacement is $1/k_{tum}^{d}$, as before. Therefore, this part of the 1D diffusion, is $\frac{\rho_3}{\rho} \frac{(L-1)^2}{8} k_{tum}^{d} u^2$, where we included the probability ρ_3/ρ for a rod being upright. Similarly, upward tumble moves of lying–down rods ($i = 1, 2$) occur at timescales of $1/k_{tum}^{u}$. In this case, however, only one–half of the ρ_{12} population (on average) contributes to the diffusion in 1D (that half aligned along the corresponding 1D axis).

The second contribution to translational diffusion along a line is simply the rate $\frac{1}{2} k_{hop}^{0}$ since, as before, the mean waiting time for the propagation of $1u^2$ is $1/k_{hop}^{0}$ (and the same rate is assigned for all populations ρ_i).

In summary, the 1D–translational diffusion coefficient on a lattice in units of space u is:

$$D_{1D}^{latt}/u^2 = \frac{1}{2} \left(\left(\rho_3 k_{tum}^{d} + \frac{1}{2} \rho_{12} k_{tum}^{u} \right) \frac{(L-1)^2}{4\rho} + k_{hop}^{0} \right) \,, \tag{4.86}$$

where in 1D, the stationary densities are $\frac{1}{2}\rho_{12} = \rho_1 = \rho_3$. Inserting (Eqs. 4.84) and (4.85) for the density ratios and observing that diffusion in 2D is simply twice the diffusion in 1D,[3] we obtain:

$$D_{2D}^{latt} = \left(\frac{1}{1 + 2\frac{k_{tum}^{d}}{k_{tum}^{u}}} k_{tum}^{d} + \frac{1}{2} \left(1 - \frac{1}{1 + 2\frac{k_{tum}^{d}}{k_{tum}^{u}}} \right) k_{tum}^{u} \right) \frac{(L-1)^2}{4} + k_{hop}^{0} \,, \tag{4.87}$$

[3] The MC moves occur with the same rates in both axes $\hat{x}, \hat{y}$; we effectively add the independent Poisson processes together to a process twice as fast in propagating the mean–squared displacement.

which can be rearranged straightforwardly to the form of Eq. (4.87).

Verification

We verify the form of Eq. (4.87) via KMC simulations of a ideal gas (no interaction energy) of hard rods on an infinite 2D lattice doing hopping and tumbling moves with input parameters $L = 9$ and various relations of rates $\{k^0_{\text{hop}}, k^{\text{d}}_{\text{tum}}, k^{\text{u}}_{\text{tum}}\}$. The translational diffusion is measured by fitting a line through the ensemble–averaged mean–squared–displacement over simulated time, given $2 \cdot 10^4$ rods and some 2^{23} MC steps (depending on the relative rates) *after* a certain equilibration time during which each ρ_i reaches a stationary average value. The fit is weighted with the error bars of the data, the error–of–the–mean (ensemble average). The fitted slope corresponds to 4 times the translational diffusion constant, in accordance with Fick's law in 2D. A series of such fitted slopes are measured over a few independent trials and the agreement is excellent. The averaged fitted diffusion rate matches that of Eq. (4.87) to within error bars. The 1D case was verified, as well, where the fitted slope corresponds to twice the diffusion constant.

4.12 On-lattice rod model vs. continuum (hard spherocylinders)

Note: The author contributed substantially to all parts of this section in writing almost all of the text, in generating all plots as well as being responsible for all of the KMC simulations, to planning or designing the comparison continuum simulation models I and II, and to matching the dynamics between models. Writing and execution of the Monte-Carlo simulation codes of hard spherocylinders are outside of the scope of the author's contribution.

Similarly to our investigation of equilibrium monolayers in Sec. 4.7, we will explore the possibility to match our lattice results in the dynamic case to corresponding results for a continuum model with hard spherocylinders. One has to bear in mind, though, that the lattice model does not result from a systematic coarse-graining procedure applied to the continuum model. Rather, we attempt to match basic dynamic parameters (i.e. characteristic microscopic times) and compare results.

We have performed MC simulations off-lattice (with small displacement and rotation moves) of hard spherocylinders with length L_{sph}, diameter D_{sph} and aspect ratio $\kappa := L_{\text{sph}}/D_{\text{sph}}$ in the continuous 2D plane in a way analogous to those of Sec. 4.7. The minuscule MC moves induce pseudodynamics that on larger timescales (where time is measured by the number of MC sweeps) that represent translational and rotational diffusive motion (over longer times). As shown in Refs. [891–893], it is possible to define a unique MC time scale being independent of the size of the MC change of any degree of freedom, and to relate such an MC time scale to that of Brownian dynamics. As a matter of fact, in our case we only need to relate the MC time scale to that of KMC for the lattice model. Apart from the Brownian translational and rotational motion, the continuum model also includes an external flux for introducing (depositing) rods into the system.

To compare growth between the lattice and continuum models it is necessary to map the characteristic times of their microscopic dynamics (rates). We proceed to do so in the case of a dilute gas)ideal-gas limit) of rods. In the continuum model, these are $\{1/(FD_{\rm sph}^2), \tau_{\rm diff}, \tau_{\rm rot}\}$ (with F denoting the influx or deposition rate per area and a unit area is chosen by $D_{\rm sph}^2$, $\tau_{\rm diff}$ the translational self-diffusion time and $\tau_{\rm rot}$ a rotational relaxation time) – these must be matched to the three characteristic times $\{1/(k^{\rm ins}u^2), 1/k_{\rm tum}, 1/k_{\rm hop}^0\}$ in the lattice model (unit $u = 1$). We discuss this matching procedure generally below before applying it to two specific continuum growth models in Secs. 4.12.3 and 4.12.4. Note here that as in Sec. 4.7, the order parameter used in the continuum model is the largest eigenvalue, $Q_{\rm nem}$, of the nematic order tensor. Furthermore, we address only the case of neutral substrates in these investigations.

4.12.1 Matching translational diffusion

In the continuum model, the translational self–diffusion time over a distance $D_{\rm sph}$ is given by

$$\tau_{\rm diff} = \frac{D_{\rm sph}^2}{D_{\rm 2D}^{\rm cont}} \, . \tag{4.88}$$

The equivalent time in the lattice model would be the translational self–diffusion time over a distance u (lattice unit). Matching these gives

$$\frac{D_{\rm sph}^2}{D_{\rm 2D}^{\rm cont}} = \frac{u^2}{D_{\rm 2D}^{\rm latt}} \, . \tag{4.89}$$

For a dilute system of rods in the lattice model, the translational diffusion constant is given by $D_{\rm 2D}^{\rm latt}/u^2 = k_{\rm hop}^0 + k_{\rm hop}(k_{\rm tum}^{\rm d}, k_{\rm tum}^{\rm u})$ (see Eqs. (4.77),(4.78) and the next subsection below), where $k_{\rm hop}^0$ accounts for the explicit translational move and $k_{\rm hop}$ is due to the tumbling move. For vanishing substrate potentials ($k_{\rm tum}^{\rm d} = k_{\rm tum}^{\rm u} \equiv k_{\rm tum}$) the contribution from tumbling becomes

$$k_{\rm hop}\big|_{k_{\rm tum}^{\rm d}=k_{\rm tum}^{\rm u}} = \frac{2}{3}\frac{(L-1)^2}{4} k_{\rm tum} \, . \tag{4.90}$$

This value is fixed for a given tumbling rate and rod–length L.

In the continuum model (with given translational and rotational moves), we measure $D_{\rm 2D}^{\rm cont}$ directly in a separate simulation where rods behave like an ideal gas and the diffusion constant is extracted from the slope of the mean-square displacement of a rod versus simulated time. In this way, the diffusion rate from the translational move in the lattice model can be fixed to

$$k_{\rm hop}^0 = D_{\rm 2D}^{\rm cont}/D_{\rm sph}^2 - k_{\rm hop}(k_{\rm tum}) \, . \tag{4.91}$$

The tumbling rate $k_{\rm tum}$ entering the equation above is fixed by a concrete rotational relaxation time (see below).

However, in Sec. 4.10.1 we showed that the dynamics does not depend on $k_{\rm hop}^0$ in the lattice model as long as there is no external potential. As our investigation is restricted to this condition, the particular value of $k_{\rm hop}^0$ does not play any role for evolution of the total density and the orientational order and

is put to zero. For a closer investigation of the case of finite substrate potential, one would need to take the condition in Eq. ((4.91)) into account.

4.12.2 Matching rotational diffusion

In the continuum model, the rotational relaxation time τ_{rot} can be defined by the relaxation time for nematic order, i.e. the characteristic decay time in the autocorrelation function $\langle Q_{\mathrm{nem}}(t)Q_{\mathrm{nem}}(0)\rangle$ in a dilute system. We obtain this decay time by recording the autocorrelation function in a system of spherocylinders with no interactions and fitting it to an exponential ($\propto \exp(-t/\tau_{\mathrm{rot}})$).

In the lattice model, the corresponding autocorrelation function $\langle Q(t)Q(0)\rangle$ can be obtained analytically in the ideal-gas limit and the characteristic decay time is $\tau_{\mathrm{rot}}^{\mathrm{latt}} = (6k_{\mathrm{tum}})^{-1}$. For given rotational moves in the continuum simulation, the tumbling rate k_{tum} is determined by matching these times.

Instead of using the characteristic decay time of orientational (nematic) order, one might think of matching the rates for a transition from a standing–up to a lying–down rod. In the lattice model, this would be affected by 4 possible discrete moves, each with rate k_{tum}. Thus, this transition time is $1/(4k_{\mathrm{tum}})$. In the continuum model, this transition time would be the first passage time for a rotation from standing to lying, which we also determined in a simulation with ideal spherocylinders. However, this first passage time is about 100 times larger than the decay time for nematic order. Through the comparison of lattice and continuum results (see below) we find that matching the decay time for nematic order is sensible and matching the first passage time leads to grossly different results. The reason is that in the autocorrelation function measures a continuous change of order. A certain change ΔQ in the lattice model comes about by a fraction of rods reorienting in the lattice model, whereas for a corresponding change ΔQ_{nem} in the continuum model, the spherocylinders need (on average) to reorient the same amount. The corresponding time needed is much smaller than the first passage time for a rotation from standing to lying.

Deposition time and growth parameter

The characteristic time for deposition on the unit area for a dilute system does not depend on the diffusional properties and is simply given by $1/k^{\mathrm{ins}}$ (lattice, $u = 1$) and $1/(FD_{\mathrm{sph}}^2)$ (continuum). Hence the growth parameter α must be matched between lattice and continuum in the following way:

$$\alpha = \frac{k^{\mathrm{ins}}}{2k_{\mathrm{tum}}} = k^{\mathrm{ins}}(3\tau_{\mathrm{rot}}^{\mathrm{latt}}) = (FD_{\mathrm{sph}}^2)(3\tau_{\mathrm{rot}}^{\mathrm{cont}}) \; . \tag{4.92}$$

4.12.3 Model I: Deposition as random 'appearance' of rods

In this model, the midpoints of the hard rods are constrained to a continuous 2D plane of size $l_{\mathrm{Box}}^2 = 200 \times 200 D_{\mathrm{sph}}^2$ with periodic boundary conditions. They rotate freely and diffuse along the substrate via small MC moves as to approximate Brownian dynamics. Rotational moves are performed as described in Ref. [894]. New rods are introduced to the monolayer (they 'appear') with a global rate $r_{\mathrm{ins}} = F\, l_{\mathrm{Box}}^2$. As in the lattice model, hard–core repulsion between the rods means an attempt at inserting a rod at some position and with a certain orientation is *rejected* if it overlaps with another. Time progresses also for

these unsuccessful deposition attempts, causing the number density of rods to depend on time in a monotonic, but nonlinear way, see Fig. 4.19 below. As in the lattice model, we employ two deposition conditions: one where rods are deposited in a vertical orientation and another in random, isotropically-distributed orientations. Results are presented below, whereby the parameters are also indicated.

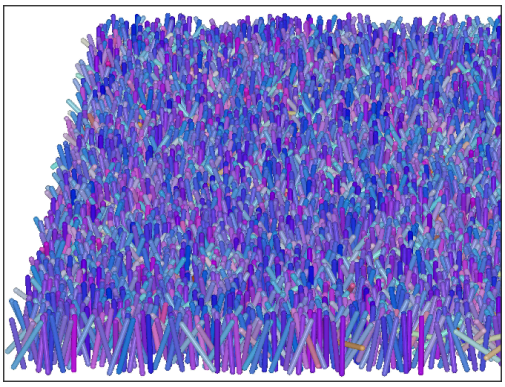

FIGURE 4.17: Illustration of continuum Model I for a monolayer of hard spherocylinders.

Our investigations are performed for rods of length $L = 9$ (lattice) and aspect ratio $\kappa = 8$ (continuum) since the spherocylinders have total length $L_{\mathrm{sph}} + D_{\mathrm{sph}}$. We note that results for $\kappa = 9$ are very similar and will not be shown.

Results for model I

In Model I (see illustration in Fig. 4.17), where new rods 'appear' within the monolayer, one might expect the evolution of the order parameters Q (lattice) and Q_{nem} (continuum) with the total number density ρ to look similar to Fig. 4.13. Indeed, this is what we find in Fig. 4.18, where we varied the growth parameters α over two decades. All continuum data are running averages over a single run, and equilibrium data points for the lattice model are obtained via Grand Canonical Monte Carlo simulations. Most striking in the figure is the similar form of the curves for growth under perpendicular deposition with respect to the equilibrium curve (Fig. 4.18(a)). In both models, the downward dip of the order parameter and subsequent approach to the equilibrium curve happens at about the same value of Q (Q_{nem}), but it is shifted to higher densities in the continuum. For dilute systems, the shift in densities can be attributed to the different two-body excluded volumes in the lattice and the continuum model. If the lattice densities are multiplied by the ratio of the volumes, which is approximately given by $\frac{L^2+L-2}{9\cdot 0.45L}$ (≈ 2.5 for $L = 9$) (Sec. 4.7), the agreement between the lattice and continuum models is quite good for continuum densities $\rho D_{\mathrm{sph}}^2 < 0.2$, yet differences remain for higher densities.

Fig. 4.19 displays the dynamics of the total number density ρ versus the re–scaled time $t^\star = k^{\mathrm{ins}} t$ (lattice) and $t^\star = (F D_{\mathrm{sph}}^2) t$ (continuum), respectively. The quasi-equilibrium growth curve for the lattice model (see Sec. 4.9.3) is also shown in Fig. 4.19(b). For the continuum model with isotropic deposition (Fig. 4.19(a)), there is little variation of $\rho(t^\star)$ with α (as in the lattice model), and the results seem to be well-described by a quasiequilibrium growth curve,

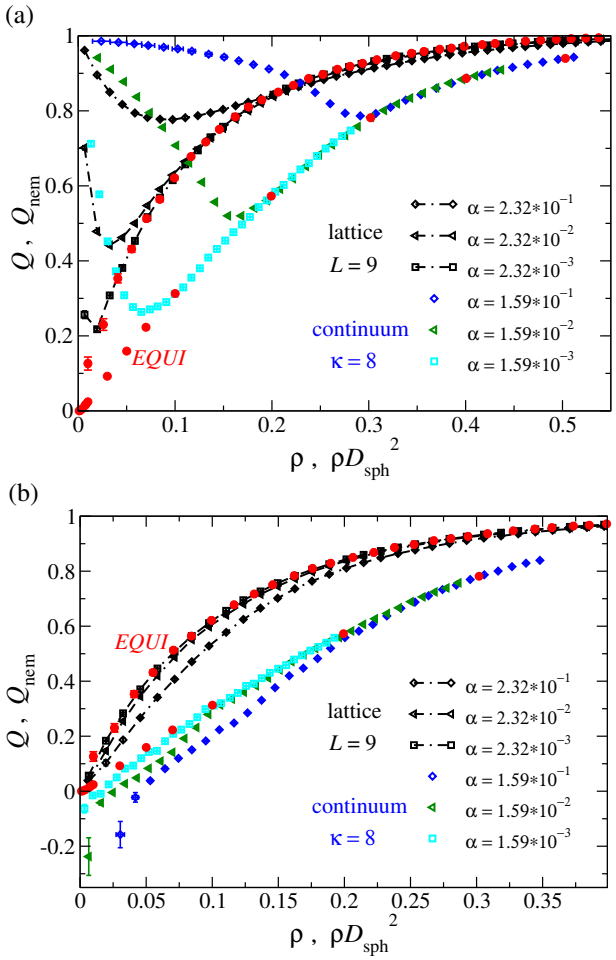

FIGURE 4.18: Growth of a monolayer of hard spherocylinders ($\kappa = 8$) using Model I (appearing rods) represented in the $(\rho, Q_{\rm nem})$ plane: comparison to lattice model (black) with matched kinetics. Monolayers are grown with perpendicular deposition (a) and isotropic deposition (b). Red data points correspond to thermodynamic equilibrium in the lattice (steep curve) and continuum (shallow curve) models.

which would be attained for $\alpha \to 0$. For perpendicular deposition, the results for the highest growth rate ($\alpha \approx 0.16$) are different from those for the two lower growth rates, but they converge for later times $t^\star \gtrsim 20$. We point out a strong difference when comparing these growth curves for the lattice and continuum: In the continuum model, the density increases only very slowly beyond the dilute limit ($t^\star \gtrsim 0.1$). Since the quasiequilibrium growth curve is determined only by the equation of state (through $\mu(\rho(\theta))$ where θ is the polar angle), this indicates the equations of state in the lattice and continuum model, respectively, are very different already for moderate densities. The continuum equation of state for the full density range is not known. In Sec. 4.7 we only analyzed a virial expansion up to second order. Already at this order we found a different scaling of the second virial coefficient: it is $\propto L_{\rm sph} D_{\rm sph}$ for the continuum model and $\propto L^2$ for the lattice model.

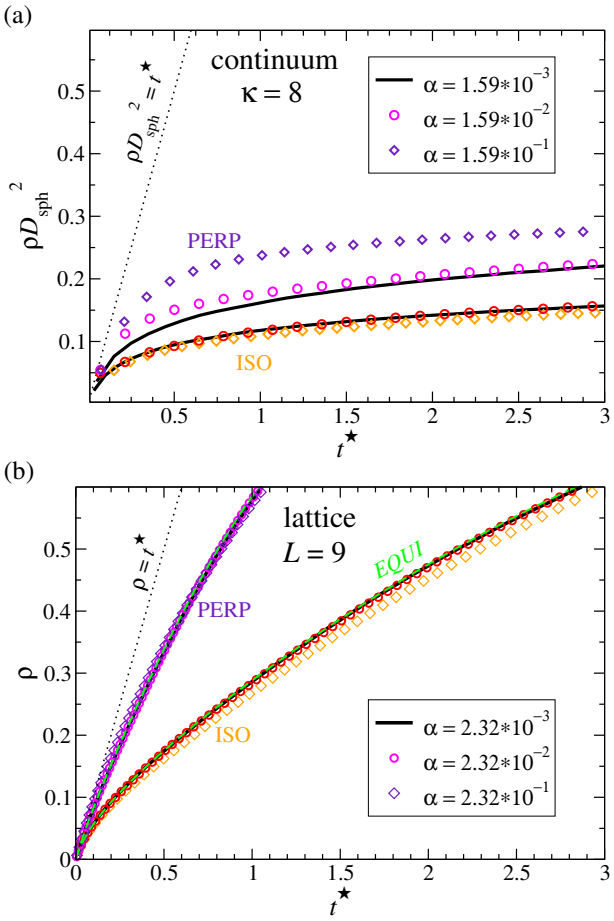

FIGURE 4.19: Evolution with re–scaled time $t^\star$ of number densities ρ during monolayer growth in continuum Model I and lattice. Perpendicular deposition (PERP) is shown in purple, while isotropic deposition (ISO) is shown in orange. Same symbol shapes/line–style refer to the same growth parameter α. (a) Continuum, $\kappa = 8$. (b) Lattice, $L = 9$. The green dashed curves (EQUI) correspond to quasiequilibrium growth calculated with DFT. Deposition of a vapor of rods in the ideal-gas limit (dotted lines) describes the initial slope in $\rho(t^\star)$.

4.12.4 Model II: Deposition as sedimentation caused by a constant force-field ("gravity")

In this model, the hard rods move in 3D space via small rotations about their midpoints and translation moves in 3D. They fall onto a square-well attractive substrate (well depth $= 50k_BT$, width $= 0.05D_{sph}$) in a box with periodic boundary conditions in the substrate plane. The attractive substrate is not of the sort described in Sec. 4.10 – rather, it acts as an "adherent" where the rod experiences the well (with the orientation–independent depth) only if the surface–to–surface distance to the substrate is less than the width of the square-well potential. Thus it serves as a strong barrier against rods desorbing. Rods diffuse and rotate by the same MC moves as in Model I, even though, now, midpoints are unconstrained above the substrate and diffusion moves are generated in 3D. Rods are generated with random positions and orientations at the top of the box ($l^2_{Box} \times l_z = 50 \times 50 \times 100 D^3_{sph}$) and inserted at a fixed rate r_{ins};

hence we only investigate isotropic deposition. They 'fall' to the bottom of the substrate under an artificial gravitational force g. In order to disentangle gravity and the adhesive substrate potential, we switch–off the gravity when the z-coordinate of the rod midpoint is less than half a rod-length $(L_{\mathrm{sph}} + D_{\mathrm{sph}})/2$, where z is normal to the substrate. This model qualifies for 3D multilayer growth, emulating thin film growth with, say, OMBD more closely; however, we investigate only exemplary cases as the 3D nature of this model deviates significantly from the lattice system in focus.

In order to match the characteristic deposition time, we need to determine the deposition rate per unit area (flux) F. Our MC pseudodynamics result in a net drift of the rods towards the substrate with velocity $v = \Gamma g$, where the mobility Γ is determined by the translational diffusion constant in 3D $D_{\mathrm{3D}}^{\mathrm{cont}}$ through $\Gamma = D_{\mathrm{3D}}^{\mathrm{cont}}/k_{\mathrm{B}}T$. The flux is then given by $F = \rho_{\mathrm{3D}} v = D_{\mathrm{3D}}^{\mathrm{cont}}/k_{\mathrm{B}}T\rho_{\mathrm{3D}}g$, where ρ_{3D} is the 3D number density of rods well-above the substrate. In the simulations, we fix $\rho_{\mathrm{3D}} = 10^{-4}/D_{\mathrm{sph}}^3$ and measure $D_{\mathrm{3D}}^{\mathrm{cont}}$ through the slope in the mean–squared displacement vs. time. Matching the flux between lattice and continuum is achieved by appropriately choosing g.

For matching the self-diffusion time, we measure the diffusion rate $D_{\mathrm{2D}}^{\mathrm{cont}}$ (see Sec. 4.12.1), but, this time for an ideal gas of rods adhering to the substrate. Note that although the MC moves for translations continue in 3D, the substrate potential almost always causes a Metropolis rejection for a move escaping the potential barrier. As this barrier is very thin ($0.05D_{\mathrm{sph}}$), the restricted 3D diffusion is effectively 2D diffusion. Similarly, we match the rotational relaxation time by measuring the autocorrelation function for nematic order. We note that orientational diffusion of rods in model II arises from a combination of midpoint rotation moves and vertical moves since the rods must remain close to the adhering substrate. This leads to an autocorrelation of Q_{nem} not describable by a single exponential. For determining τ_{rot}, we fitted the initial decay.

Our monolayer orientational observables are calculated strictly for rods adhering to the substrate, with the number density in the monolayer denoted by ρ_{subs}. We additionally analyze the total density across the z-direction, in particular as a 'second layer' may form.

Model II is depicted in Fig. 4.20.

Results for model II

Figure 4.21(a) displays growth of the monolayer in the $(\rho_{\mathrm{subs}}D_{\mathrm{sph}}^2, Q_{\mathrm{nem}})$ plane, where Q_{nem} is calculated for all rods adhering to the substrate (i.e. those contributing to ρ_{subs}). The equilibrium curve shown corresponds to that of rods with fixed midpoints, i.e. the system in model I. For the two smaller growth rates ($\alpha = 10^{-6}$ and 10^{-5}) the nematic order in the monolayer is close to the equilibrium curve, similar to model I. On the other hand, faster growth (cyan squares, $\alpha = 10^{-4}$) shows different behavior: the nematic order is noticeably lower, an effect also seen in the isotropic–deposition growth of model I (Fig. 4.18(b)). Furthermore, at higher densities the monolayer does not converge to a fully–ordered state. Q_{nem} drops, instead. This is an effect of particles accumulating on top of the first layer.

Figure 4.21(b) shows $\rho(t^\star)$ for model II. The initial, linear behavior characteristic of deposition on a dilute layer is similar to model I; however, for

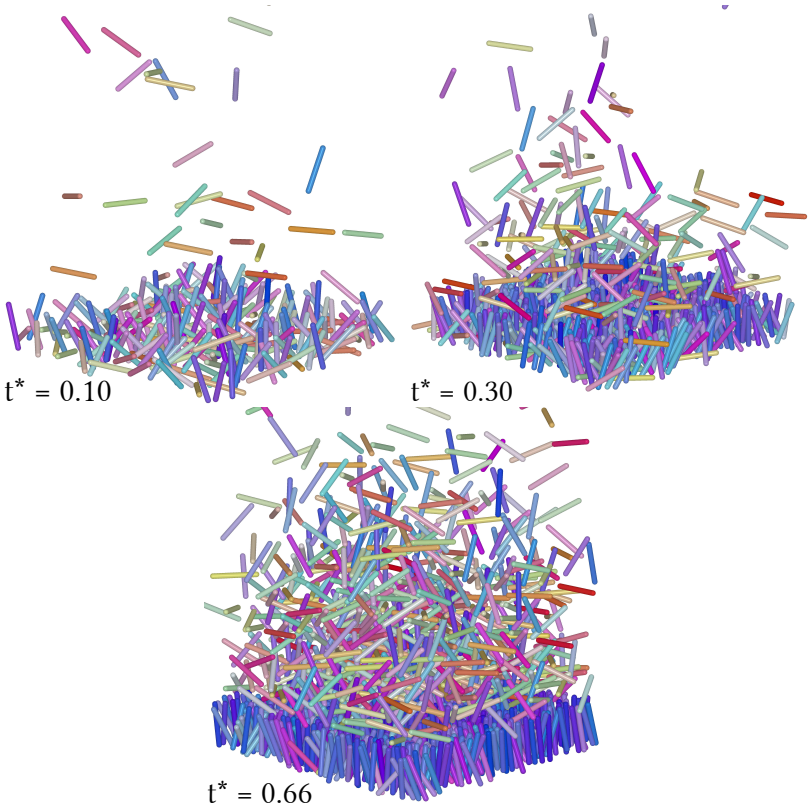

FIGURE 4.20: Snapshots of growth in Model II of growth of monolayers of spherocylinders for aspect ratio $\kappa = 8$ and growth parameter $\alpha = 10^{-5}$.

$\rho_{\text{subs}} D_{\text{sph}}^2 \gtrsim 0.2$ significant deviations appear. There, growth in model I becomes very slow (see Fig. 4.19(a), ISO curves). In model II, new rods increasingly 'hover' above the monolayer, breaking the single–layer assumption and leading to enhanced adsorption in the first layer. Convergence to a quasi–equilibrium growth curve for low α can be seen only up to $\rho_{\text{subs}} D_{\text{sph}}^2 \approx 0.3$.

In the monolayer growth regime, two major differences between model I and II can be observed. (i) The curve $\rho(t^\star)$ in model I quickly bends over and stays near $\rho D_{\text{sph}}^2 = 0.15$ for a long time. This is not so in model II. Apparently almost all the rods that are in the vicinity of the substrate reach it within a short time–period. This happens since rods diffuse around in the vicinity of the substrate and finally reach it after multiple "attempts". The fluxes employed are small so that diffusion is a reasonably fast process. (For the lowest α, the first rods reach the substrate not by the sedimentation drift but by bulk 3D diffusion). (ii) The growth parameters used to study model II are well in the quasi–equilibrium growth regime for model I. Nevertheless, we see these values of α generating clearly non–equilibrium behavior that also differ significantly in character to model I. We conjecture that an effective α for model II is actually higher than reported owing to the aforementioned bulk 3D diffusion.

In the regime past the monolayer, we comment on a few preliminary findings: As aforementioned, in the vicinity of reduced densities of 0.6 in the monolayer, the nematic order drops due to a population of rods building up above the monolayer, jamming up space for rods in the first layer. An exemplary distribution of rods versus vertical height for this regime is shown in Figure 4.21(c).

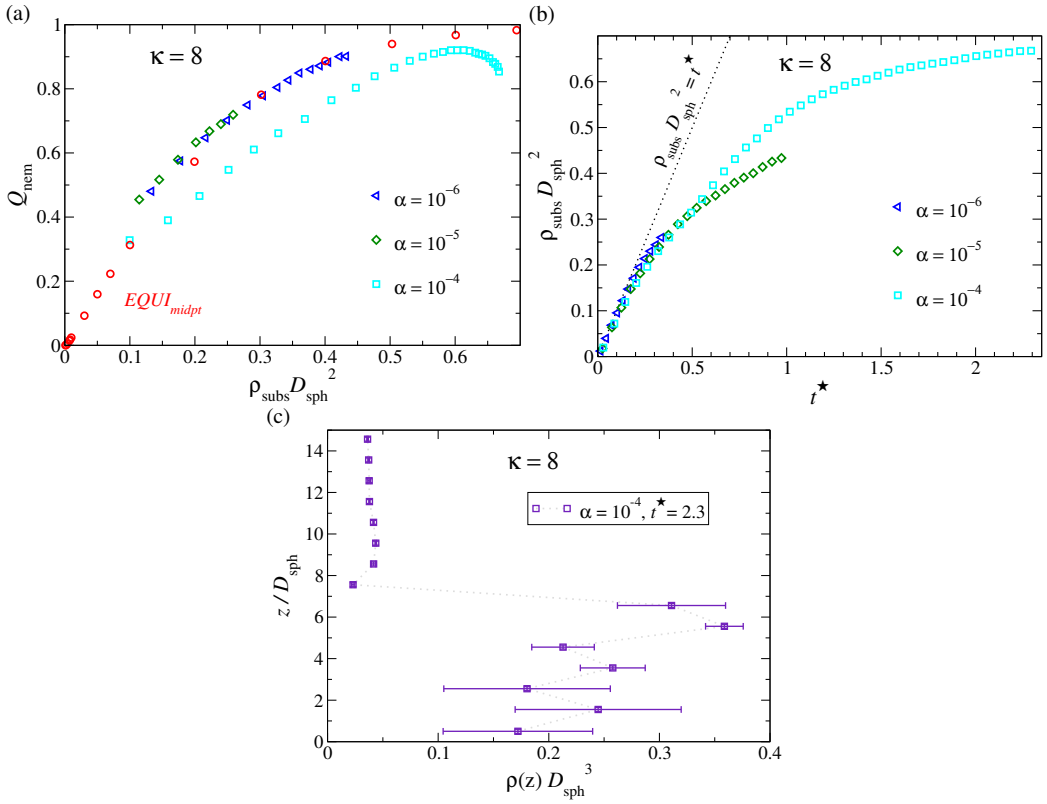

FIGURE 4.21: (a) Nematic order vs. density in the first grown layer of hard spherocylinders (aspect ratio $\kappa = 8$) using model II (rod sedimentation) for different values of α. Red data points correspond to thermodynamic equilibrium in the continuum model with fixed midpoints. (b) Evolution of the density in the first grown layer ρ_{subs} with re–scaled time $t^\star$. The deposition curve for ideal gas particles (dotted lines) means that (on average) all drifting particles reaching the substrate will stick to it. (c) Height above substrate versus 3D rod density for a growth parameter $\alpha = 10^{-4}$ and $t^\star = 2.3$, corresponding to the last point in (a). The increased density for $z/D_{\text{sph}} > 4.5$ signals the formation of a disordered second layer.

Rods in the monolayer contribute to the measured density $\rho(z)$ only up to $z/D_{\text{sph}} = 4.5$; thus, increased density for larger z belongs to a second layer. This second layer is very disordered as corresponding snapshots suggest (see Fig. 4.20).

4.13 Summary, conclusions and discussion

Note: The following text is the author's writing (she re-wrote, shifted the focus of, and extended the conclusions written in the two publications). We have also added a discussion, addressing some points for an outlook of this chapter, in Sec. 4.13.2 below.

4.13.1 Summary and conclusions

In the first half of this chapter, we analyzed the equilibrium properties of hard rods constrained to a cubic lattice in (2+1)D confinement (maximally one layer),

where rods entail only three orientations and discrete translational degrees of freedom. Their geometry is $L \times 1 \times 1$. The case studied in this chapter was exclusively in the *purely hard-core limit* of particle interactions. We developed and performed formally-exact Monte-Carlo simulations in the grand canonical ensemble (GCMC), which served as a test for density functional theory (DFT) in which the properties were explored. (Specifically, lattice fundamental measure theory (FMT) was formulated for the rod system.) We find a continual "standing-up" of rods with increasing density, which is *not* a thermodynamic phase transition – both with the FMT and in the GCMC simulations. An attractive substrate that biases "lying" rods: does not change the continual "standing-up" behavior, but, attractive energies per unit rod length which are of the order of $5\,k_{\mathrm{B}}T$ or larger induce near-"kinks" in the nematic order Q upon increasing density ρ. These resemble ("pseudo-") second-order transitions. (A truly second-order transition is found, for instance, in the fully-2D-confined system, which we discuss more in Ch. 6.) Monte Carlo simulations seem to agree, although in these case, the systems were difficult to equilibrate (also in the continuum model, see below). This may hint at the dynamically arrested states ('jamming') at we find in dynamical simulations for monolayer growth (see further below).

In order to better gauge the effects of restricted translational and orientational degrees of freedom, we also compared the on-lattice model to a continuum model with hard spherocylinders, which have unrestricted in-plane-translational and orientational degrees of freedom. The continuum model also shows the same, continual, entropically-driven "standing-up" behavior; guaranteed at least from a DFT for the spherocylinders in a virial expansion. Corresponding Monte-Carlo simulations seem to agree for large system sizes, but results are masked by strong finite-size effects. The central difference between lattice and continuum models is that they follow inherently different "equation-of-states" regarding orientations versus number density. In the continuum model, the order parameter Q scales with ρLD where L and D are length and diameter of the rods (which was found out by the scaling of the second virial coefficient). The lattice model does not show such scaling behavior, which points at the fact that these models represent fundamentally different systems.

In the second half of this chapter, we investigated (nonequilibrium) monolayer growth with long rods on lattices in monolayer confinement, in the same purely hard-core limit. In the dynamical model on the lattice, a dynamical N-body ("sharp") distribution evolves according to an inhomogeneous master equation, where microscopic dynamics in every time-step are presumed microscopically Markovian – "diffusive" in the ideal gas limit. However, the nontrivial part of the macroscopic, many-body dynamics (in purely hard-core systems) arises when microscopic dynamics becoming arrested – "moves" become "forbidden" – in-between time-steps due to hard-core repulsive forces. After specifying the microscopic "attempt" rates of basic "moves", these dynamics are simulated formally-correctly by kinetic Monte Carlo (KMC). However, we implemented KMC as a *rejection-free* algorithm: It is event-driven, propagating time forward only when something in the system actually moves. The simulations we wrote and developed "from scratch" were conceptualized, first, with a novel algorithmic implementation for hard-core, anisotropic particles. In fact, the original conceptualization was meant for the more complex and general

case of 3D growth simulations. In the monolayer, the long rods "move" via in-plane and out-of-plane rotations, as well as translational hops to nearest-neighboring sites (the full set of possible "moves" in the monolayer is much smaller than for the generalized case of 3D growth.)

For a wide range of particle deposition rates, we find that monolayer growth with hard rods can be described by "quasi-equilibrium" growth dynamics; at least, when observing the global-scale order parameter mean-values only. Quasi-equilibrium means that every value of Q as a function of the density ρ corresponds to that for equilibrium. Deviations from quasi-equilibrium become more pronounced when imposing an asymmetric "initial condition" on rod orientation, i.e. when rods are deposited in the "standing" orientation only. The underlying reason for this affinity to equilibrium in driven conditions is very likely the lack of thermodynamic phase transitions in the monolayer. For the same reason, the fluid system of rods (probably) remains homogeneous, more-of-less, during the evolution. Therefore, we found the most relevant dynamical parameter (for the range of parameters investigated) was the deposition-flux–to–rotational-diffusion-rate ratio.

We also found that a proper scaling variable of the deposition–diffusion dynamics is the re-scaled time $t^\star = Ft$, where F is the deposition "attempt" flux (rejections occur due to hard-core repulsion), and t is simulated time. We explored dynamics of particle number-densities ρ_{12} of lying rods as a function of re-scaled time, as well as that of standing rods. In employing global-scale, thermodynamics order parameters, where time plays no role in equilibrium, the deviations from equilibrium-type growth are most visible when plotting the nematic order Q against the packing fraction η. In the latter, "lying" and "standing" orientations contribute asymmetrically and, thus, render more detailed information than ρ. (This representation will be important for the next chapter, where the system dynamics become heavily nonequilibrium.)

One focus of the study was in testing the quality of a lattice dynamical density functional theory (DDFT), which was formulated for the lattice system of purely hard-core rods. It is based on the FMT that was investigated in the first half of the chapter. It was formulated for the case of a homogeneous fluid (more "near-equilibrium", no phase-separation), i.e. no spatial dependencies were accounted for. Implied, also, is an independence of translational from rotational degrees of freedom in the system. This seems to be the case, when tested against KMC, as long as dynamics remains near-equilibrium. In the case of strongly attractive substrates, the system loses ergodicity – dynamical arrest occurs in the form of a (possible) nonequilibrium "jamming" transition. We did not explore the physics of this case further, but, remark that the translational and rotational degrees of freedom of the nonequilibrium 'fluid' appear highly coupled in these cases: There is a clear, explicit dependence of the macroscopic evolution on the hopping rate. The DDFT would need extensions to capture this variability, and in its current form, appears to emulate the case of very large hopping rate. Therefore, it seems to predict too "fast" dynamics (in other words, high dissipation) and heads closer towards the quasi-equilibrium limit – as far as we can tell from the data we presented. Exploring quantities relevant for the dynamics in the system such as two-time and two-point correlation functions, or currents – rather than macroscopic, (structural) mean quantities — would be important in the future. This applies both to testing and developing the DDFT, but, more generally, to understanding the loss of ergodicity in these systems of highly anisotropic particles.

Another focus of the study was to compare the nonequilibrium evolution of the lattice model during monolayer growth to that of the continuum model of hard spherocylinders. (We realized deposition with two different protocols in the continuum model, accordingly). As the microscopic dynamics between lattice and continuum models are fundamentally different, we first performed a matching procedure: We matched the characteristic times for diffusion, relaxation of nematic order and deposition between lattice and continuum models in ideal-gas limits. The results on the time-evolution of the nematic order shows qualitative agreement between both models, much like in the equilibrium case. The evolution of the total monolayer density is mainly determined by the quasi-equilibrium "equation-of-state", which differs between lattice and continuum.

4.13.2 Extra discussion and outlook

For this simple system, we have reached a good 'methodological control' with the lattice and continuum treatments, allowing for the study of equilibrium, dynamic effects and their interplay. However, we suspect that much of the qualitative and semi-quantitative overlap between continuum and lattice models, as well as KMC and DDFT might owe to the following: With only hard-core interactions, as far as we have seen, the systems of rods with intermediate rod-lengths do not entail any thermodynamic phase transitions in the monolayer. Thus, most of the nonequilibrium dynamics remain "quasi-equilibrium-like". We had to impose a particular initial condition – "perpendicular" deposition – in order to see any deviations on global order parameters at early stages. Once the monolayer densities reached some intermediate values, the global-scale, structural order parameters are essentially equilibrated.

We also would like to comment that the purpose of event-driven kinetic Monte Carlo simulations is to simulate over long time-scales when many different relaxation times in the system co-occur – it is a method that should help us understand highly nonequilibrium systems, where collective as well as heterogeneous dynamics occur on the many-body scale (arising nonetheless from individual particle motion with microscopically Markovian dynamics). For example, the method can simulate long time-scales and many-particle systems during a phase transition or in nonequilibrium steady states. They are key for gaining insight where ergodicity is lost and where equilibrium and detailed balance breaks down, e.g. into dynamically arrested states, phase transition kinetics, and possibly glassy behavior. The author spent a very long time on algorithmic conceptualization (a rejection-free KMC algorithm for anisotropic particles was unknown to the literature before), early-stage and late-stage development, writing, debugging, systematically testing, optimizing, and running the simulation codes (all done alone and "from scratch").

The near-equilibrium character of the systems studied in this chapter will break down in the next chapter. Therefore, "methodically well-controllable" descriptions of dynamics based on equilibrium presumptions will very likely become invalidated: With additional "sticky" attractions, monolayer growth with hard rods will be characterized by highly complex and intricate phase transition kinetics, i.e from an isotropic vapor to a "standing" liquid, entailing various metastable, intermediate states. In this chapter, the fluid was presumed by the DDFT to remain "homogeneous" at all states, and the principal ratio we found for these "near-equilibrium" dynamics was the growth parameter α that measures the flux–to–rotational-rate. The only exception we found was

when dynamical arrest (jamming) occurred, which became visible upon introducing a strong substrate potential. There, the system dynamics (kinetics) depended explicitly on the hopping dynamics. In the next chapter, the principal dynamical ratio will be the flux–to–translational-diffusion rate F/D during monolayer growth: As monolayer growth will constitute the long and complex phase transition (driven by a deposition "quench") from an isotropic gas to a "standing" liquid, the system loses its homogeneous character, and becomes heterogeneous in dynamics and structural properties.

In this chapter, we unfortunately did *not* explore dynamical properties such as structural fluctuations, currents (from the rates obtainable in KMC) and their fluctuations: In other words we did not study two-time and two-point correlation functions. A quantification thereof would present an advanced method-of-study on the meaning of nonequilibrium-versus-"near-equilibrium", as well as on understanding how rotational and translational degrees of freedom couple in the many-body system. From a practical point-of-view, this would provide a better method of scrutinizing a DDFT against KMC simulations, as well as the lattice-versus-continuum models. Information on the inherently different dynamics between models is complementary to characterizing structural differences like their different "equation-of-states" of global-scale (mean) order parameters.

Conditions where *ergodicity is lost* states offer a setup in which to scrutinize the accuracy of the DDFT model. We found the monolayer growth systems entail transient jamming transitions when a substrate potential is strong. We emphasize that these are highly interesting: They seem to be directly associated with the "pseudo-phase-transition" points in the phase diagram (seen in the equilibrium FMT). Thus, a high curvature of the free energy (in equilibrium) seems related to non-ergodic, dynamically arrested states in nonequilibrium. In retrospect, then, analyzing space- and time-dependent correlation functions will be absolutely necessary for a better, fundamental understanding.

At extremely high deposition rates and strong substrate potentials (and for very long rods), the possibility for visiting a *series* of arrested or jammed states cannot be excluded. In fact, in the next chapter, we find evidence for other types of arrested states that occur when particles are additionally attractive.

In this chapter, we explored the most basic form of an idealized model system for monolayer growth of systems with rod-like particles – the case of purely hard-core rods. This limiting case has been amenable to sophisticated theoretical methods based on equilibrium theory. However, because of the lack of thermodynamic phase transitions in monolayer confinement, the nonequilibrium growth dynamics of monolayers was *de facto* rather "near-equilibrium" in the parameter range we explored. The dynamics of order parameters (at the coarse-grained, global scale) were well-describable by their equilibrium values (quasiequilibrium growth), or, better, via a linear-response-like theory based on an equilibrium functional (dynamical density functional theory). The one exceptional case we found – of jamming or arrest (i.e. a loss of ergodicity) during growth under the influence of an attractive substrate potential – leaves open many questions and opportunity for the future.

In the next chapter, we will be occupied with cases when monolayer systems of rods go go far beyond such "near-equilibrium" conditions; we will be able

to demonstrate the efficaciousness of our kinetic Monte Carlo simulations for modeling the physics over many orders of magnitudes in the dynamical control parameters. As simple addition of "sticky" attractions between rods induces extremely rich many-body behavior during monolayer growth (not reported elsewhere in comparable literature), where the system dynamics become heterogeneous, complex, and definitely can be called "highly nonequilibrium".

Chapter 5

Growth of Monolayers with "Sticky" Hard Rods

Loveliest of lovely things are they
On earth that soonest pass away.
The rose that lives its little hour
Is prized beyond the sculptured flower.

William Cullen Bryant

The future influences the present just as much as the past.

Friedrich Nietzsche

In this chapter, we explore the nonequilibrium evolution of confined systems of hard rods on lattices with "sticky" (short-ranged attractions): we explore the behavior during monotonic growth, investigating the manifestation of lying–standing transitions in the monolayer under varying nonequilibrium conditions. This is an extension of the system studied in Ch. 4, yet the simple addition of attractive interactions changes the game completely for the self-assembly process. Our model now presents a many-body system that evolves under *highly* nonequilibrium conditions, even at slower deposition. It shows heightened sensitivity to any universal change in local dynamics (the parameters that govern these). As we discussed and foreshadowed in Ch. 2.3, the inherently complex phase diagrams provide a large bandwidth of processes during a nonequilibrium evolution; here, this is realized upon crossing (multiple) thermodynamic phase boundaries into non-stable regions during layer growth.

The self-assembly of a full monolayer from a vapor phase entails an end-state – a dense phase of upright-standing rods (a consequence of entropy, as we saw in the previous chapter). The pathways towards the dense-phase end-state state are manifold. We will encounter various metastable phases and transient states along the way. The monolayer system of rods unfolds a remarkably large diversity of pathways, making them quite interesting from a theoretical perspective. We see strong similarities to phenomena reported in the literature on organic molecular thin film growth at the monolayer stages. We reviewed these in the introduction in Ch. 1.2, as well as in Ch. 2.4.

The system of purely-hard-core rods of the previous chapter 4 represents a limiting case of the monolayer, where, according to the equilibrium analysis,

only *thermodynamically stable* states dominate the character of the evolution. The only exception we found is a quasi-stationary, long-lived nonequilibrium states in the form of jamming near a *pseudo-phase-transition* point, where the curvature of the free energy is strong. These appear when the substrate potential of strength u_{sub} strongly biases a lying orientation of the rods, an effect even more pronounced for long rods like $L = 9$.

Sticky-hard-rod monolayers studied in this chapter entail an additional attraction strength ϵ, where, in equilibrium, only its relation to $k_{\mathrm{B}}T$ is relevant for equilibrium information. Therefore, we denote $T^* \equiv k_{\mathrm{B}}T/|\epsilon|$ as the reduced temperature (see Sec. 5.1 below). In our emulation of a thin-film growth experiment, the self-assembly of compact structures from a vapor phase (i.e. islands and other morphological forms) is now possible, representing what happens in the vapor–solid (sublimation) or vapor–liquid coexistence region. Note that in this simple lattice model, the stable dense phase is captured by a dense, upright-oriented, quasi-2D liquid on the substrate. The most basic thermodynamic parameters T^* and ρ span a two-dimensional phase diagram in confinement. During layer growth, the system is pushed through this thermodynamically non-stable region of the phase diagram via the deposition flux. Depending on the basic rates of processes in the system and on the strength of ϵ and u_{sub}, the evolution will pick up on various "in-between" quasistationary states that are metastable and (or) dynamically arrested. Phase diagrams for the monolayer lattice model predicted from density functional theory indicate a vapor–high-density-liquid transition for low enough temperatures, as well as metastable intermediate states.

During the nonequilibrium evolution of layer growth, the most basic dynamical parameters are the particle flux F, and the hopping self-diffusion rates D (k_{hop}) along with the rotational rates k_{rot}, which represent "attempt" rates during the MC dynamics (the maximal possible rates, please refer to Ch. 2.3 and Ch. 3.3.5). In the last chapter the systems remained rather homogeneous at macroscopic scales. Therefore, the relevant reduced parameter was the flux-to-out-of-plane-rotational-rate α.[1] However, in "sticky" monolayers, the systems become highly inhomogeneous. The translational self-diffusion rate D plays a central role, determining the structural length-scales of dense phases separating from a vapor, as well as the kinetics (i.e. the likelihoods of these phases over times). This is true even for self-assembly scenarios without deposition, i.e. upon a *temperature quench*, see Sec. 5.8. The relevant reduced parameter for the growth kinetics during deposition is the deposition-flux-to-diffusion-rate $F/D_{\mathrm{hop}} \equiv F/D$. The rotational self-diffusion rate plays a subordinate role, at first, for a most general understanding. However, the exact microscopic dynamics (the realization of MC moves) – which we can vary in our model – plays a significant role for the shape of compact islands and the kinetics, which we demonstrate, as well (Sec. 5.6).

The monolayer systems entail multiple phases with inherent, dynamical asymmetries which are cause for highly distinguished types of trajectories of the system during growth. In the nonequilibrium evolution, the three main dynamical control parameters are T^*, D, F, which shift the likelihood and endurance of particular mesoscopic states during deposition, as we discussed

[1] The translational degrees of freedom express more "global"-scale ordering that is harder (in the sense of free energy) to realize than the more "local-scale" ordering inherent to orientational degrees of freedom (see generic discussion in Ch. 2.1).

quite generally in Ch. 2.3. The flux rate F represents the rate with which external non-conservative forces are applied. It is locally correlative in its effect on the fluid, similar to the effect of adjusting the attraction strength ϵ between rods, or the reduced temperature T^*. A clear dichotomy in the kinetics will become visible, related to the occurrence of a gel-forming, lying phase that appears metastable. Complex self-assembly pathways occur even for the most basic case of neutral substrates. With substrate potentials, dynamical regimes are shifted, and certain transitions may even become thermodynamically stable. We also explore the effects of rod-length as well as the choice of microscopic dynamics in the model, which will ultimately change the phase transition kinetics in the system (certain dynamical regimes may be excluded, for example.)

The organization of this chapter is as follows: In Sec. 5.1 we introduce and specify the dynamical simulation model of sticky hard rods in more detail. Sec. 5.2 provides information on the equilibrium phase behavior of sticky-hard-rod monolayers in the lattice model, obtained from GCMC simulations and density functional theory. In Sec. 5.3, we provide an overview and general description of various self-assembly scenarios with respect to lying and standing orientations in the growing monolayer. We focus on $L = 3$ as the most basic system before moving to other cases. We discuss and list the various phase transition scenarios that we find in this model at the end of the corresponding section.

The effect of attractive substrates on systems with rods of length $L = 3$ is studied in Sec. 5.5. Results for longer rods ($L = 5$) are presented in Sec. 5.4. A further finding is that the self-assembly is strongly sensitive to the chosen microscopic dynamics – particularly of the out-of-plane rotations. This is presented in 5.6. We present results on the dimer model $L = 2$ in Sec. 5.7, including the effect of attractive substrates. Other potential simulated experiments with monolayers – like annealing, quenches, or evaporation – are briefly discussed in Sec. 5.8. We provide a general discussion in Sec. 5.9. Finally, we provide our conclusions and outlook of our study in this chapter in Sec. 5.10.

5.1 Model and methods

We study a dynamical model of sticky hard rods of dimensions $L \times 1 \times 1$ on a neutral, planar substrate, whereby the rods take on three-dimensional orientations in space that is defined as a lattice, i.e. two lying orientations and one standing are defined. Apart from hard-core repulsion forbidding them to overlap, the rods have a short-range attraction between them that is proportional to their mutually adjacent area a_{ij} (in units of lattice area) for two rods i and j,

$$U_{ij} = a_{ij} \frac{\epsilon}{k_\mathrm{B} T} \,, \tag{5.1}$$

where $\epsilon < 0$ is the unit attractive energy and $k_B = 1$ the unit Boltzmann constant. We define the *reduced temperature* as $T^* \equiv k_\mathrm{B} T / |\epsilon|$, as only the relation to $k_\mathrm{B} T$ is a relevant variable, thermodynamically. Figure 5.1 depicts the sticky attraction between two adjacent, lying rods. Note that two standing rods will have adjacent area $a_{ij} = L$, two lying rods of the same orientation will have area $1 \leq a_{ij} \leq L$ depending on the positioning. Adjacent rods of different orientations $\omega \in \{1, 2, 3\}$ will always have $a_{ij} = 1$. As $U_{ij} \propto \epsilon$, adjusting the

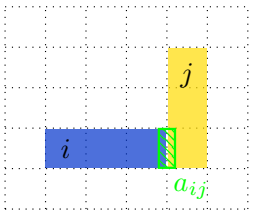

FIGURE 5.1: Schematic on the "sticky" attraction between lattice rods: Two lying rods of lengths $L = 3$ will have a 'sticky' attraction proportional to their adjacent area $a_{ij} = 1$, sown here for a single, unit area. This can be greater than 1 for parallel adjacent rods. Two adjacent, *standing* rods (not shown) will entail $a_{ij} = L$, i.e. binding energies are maximal when two rods are perfectly aligned in parallel orientations.

reduced temperature $T^* \equiv k_B T/|\epsilon|$ in the system changes the local attractive energy, accordingly.

The microscopic dynamics of these particles are presumed to be locally Markovian, hence nearest-neighbor hops and particle rotations are the main "ingredients" for the "internal" dynamics of these on-lattice rod systems, which we simulate with kinetic Monte Carlo (see below).

5.1.1 Dynamical model via kinetic Monte Carlo

The dynamical model is defined as follows: As in the last chapter, we apply the external driving force of *monotonic deposition* of rods with rate F for an attempt to deposit a rod at a random position. If the position is occupied, the move is rejected. We employ the "isotropic" deposition mode, where all three orientations are attempted at the same rate. The rods undergo translational (hopping) diffusion, with an attempt rate that reflects the self-diffusion of an ideal gas of non-rotating rods, $D^{\text{hop}} = k^0_{\text{hop}}$. The rotational rates apply to "in-plane" and "out-of-plane" rotational moves, which can be defined in various ways. Each choice will deflect the full translational diffusion rate D on the substrate (in an ideal gas of rods). For odd-valued rod-lengths $L = 3, 5, \ldots$, we chose rotations that are are decoupled from the hopping moves ("central rotations"), unlike in the last chapter, where we implemented "tumbling" rotations in the out-of-plane direction. The in-plane rotations are defined around rod-centers, and are fixed to $k_{1\leftrightarrow 2} = 10$ (unless otherwise noted). Similarly, the out-of-plane rotations are set to $k^{\text{u}}_{\text{rot}} = 10$ and $k^{\text{d}}_{\text{rot}} = 10$ for "upward" and "downward" rotations, accordingly.[2] The values will be adjusted depending on the strength of the substrate potential u_{sub}, which biases either move (this will be explained in further text). In other words, "initial" rates are universally set as $k^{\text{u}}_{\text{rot}} = k^{\text{d}}_{\text{rot}} = 10 \equiv k_{\text{rot}}$ for neutral substrates, unless otherwise noted. We specify a dimensionless parameter γ, which represents the ratio of the translational diffusion attempt rate to that of rotational diffusion in the out-of-plane direction. It is defined by $\gamma \equiv k^0_{\text{hop}}/(2k_{\text{rot}})$ for neutral substrates. On non-neutral substrates, the upward rotational rate $k^{\text{u}}_{\text{rot}} < k^{\text{d}}_{\text{rot}}$ (see below), hence this parameter captures the downward rate only, i.e. $\gamma \equiv k^0_{\text{hop}}/(2 * k^{\text{d}}_{\text{rot}})$.

[2] For "central" rotations, the full rotational rates are $2k^{\text{u}}_{\text{rot}}$ and $2k^{\text{d}}_{\text{tum}}$, accordingly.

For even-valued rod-lengths $L = 2, 4, \ldots$, a different rotational set is employed, where the rods rotate around end-points *both* out-of-plane (like in the last chapter, Ch. 4), as well as *in-plane*, the latter case of which we call "*shuffling*". The translational and rotational "moves" now couple in the ideal-gas limit. We have provided expressions for the long-time 2D translational self-diffusion rates for all these scenarios, including for substrate potentials that break the symmetry of the rates in the out-of-plane directions, in Sec. 5.1.2).

Modification of rejection-free algorithm for hard-core rods to "sticky" rods

We employ the same algorithm we developed for hard-core rods, described extremely briefly in Ch. 4 using objects we denote as "inverted indices". Let us review this: Each particle "move" (translation, rotation) is associated with an extended structure on the lattice (an inverted event-list index) that detects whether or not the move is blocked or free ("allowed"). Other particles that move in the system can change the allowance state of any of such moves via their hard-core "blocking" action. Any changes to the binary "allowance" state then is forwarded, either removing or adding the changed-state move to the corresponding list of all valid moves in the system. The main KMC algorithm then propagates motion and time forward in the system (according to locally Markovian dynamics, i.e. locally Poisson statistics of random, abrupt events) when one such valid event is then selected from the list of all valid events, using the relative probability weighted with each move's "attempt" rate). The time-step — *when* this selected event occurs — is chosen randomly according to the joint Poisson process of all valid processes (using the sum of all rates) in the system. We remind the reader that we had discussed KMC algorithms more generally within Ch. 3.

The "sticky" interaction goes into the calculation of the local transition rates (moves). We employ a Metropolis step using a local equilibrium approximation (discussed within Ch. 3), where, once chosen, a local particle move ν is accepted with probability

$$p^{\text{sticky}} = \min\left\{1, \exp(-\Delta_\nu U_{sticky}/k_\text{B}T)\right\} \ . \tag{5.2}$$

The local change in the attractive part of the local Hamiltonian upon the *potential* move is denoted here as $\Delta_\nu U_{\text{sticky}}$. As the KMC algorithm is event-driven for *hard-core* repulsion, like in the previous chapter, we apply this Metropolis accept-or-reject step for the attractive part only – our KMC algorithm is a *hybrid* of purely event-driven KMC and Metropolis-Hastings Monte Carlo.

This works well for local attractive interactions, as the maximal possible rate of each move is that for free particle with no neighbors. (Other forms of local repulsion would shift this maximal possible rate.) The advantage of our "hybrid" approach – where events that will be rejected are left in the KMC event lists [830] – is a reduction of overhead and run-time complexity: A nearly $O(1)$ operation is *calculating the total rate* $K^{\text{tot}} = \sum_i k_i$. Selecting a random event is another $O(1)$ operation, and, importantly, the *insertion* and *removal* of events from the lists are also $\sim O(1)$ operations when using optimized containers (i.e. hash maps). We note that "standard" KMC algorithms are usually rejection-free, but, updating all rates in the system would become computationally overly complex for long, anisotropic rods: The "sticky" energies would have to be re-calculated for all possibly affected particles in every time-step. Moreover, with

a "standard" KMC approach, one would typically resort to using tree-like data structures (as there are so many possible values of rates of various events in the system), where the calculation of the total rate K^{tot} and removing or adding particles would much slower, computationally. We note here that the largest computational bottleneck we typically encounter is either a dense, fluid-like system where particles remain highly mobile, or, when the system encounters a fully globally arrested state, where the monolayer growth process is hindered as the packing fraction becomes nearly unity (because the deposition events are also calculated in an attempt–accept-or-reject manner).

In this chapter, non-neutral substrates are defined by an external "sticky" potential $u_{\mathrm{sub}} < 0$ that acts per unit area "touching" the substrate, in the same spirit as in Ch. 4. The "downward" and "upward" rotational attempt rates become asymmetrical under the influence of this external field. We note on a slight modification in the implementation of the rates compared to the last chapter, while retaining local balance: Here, the "downward" rotational rate remains $k^{\mathrm{d}}_{\mathrm{rot}} \equiv k_{\mathrm{rot}}$, while the "upward" rate is reduced according to a Boltzmann factor: $k^{\mathrm{u}}_{\mathrm{rot}} = k_{\mathrm{rot}} \exp\left(-(L-1)|u_{\mathrm{sub}}|/k_{\mathrm{B}}T\right)$, where the exponential argument has units of $k_{\mathrm{B}}T$ (which we set to unity).

We provide an overview of the default KMC rates of rod "moves" in Tab. 5.1. Further, we provide a list of the relevant dynamical and energetic sets of parameters that fix the nonequilibrium model system in Tab. 5.2.

RATE	VAL[3]	MEANING AND NOTES
F	$0.1 - 1 \times 10^{-6}$	Deposition flux rate (per lattice site)
k^0_{hop}	1,10,60	Translational hopping rate, value for any of 4 directions
$k^{\mathrm{u}}_{\mathrm{rot}}$	10	Out-of-plane, "central" rotation upwards[4]
$k^{\mathrm{d}}_{\mathrm{rot}}$	10	Out-of-plane, "central" rotation downwards[5]
k_{rot}	10	Out-of-plane rotation rate $(= k^{\mathrm{u}}_{\mathrm{rot}} = k^{\mathrm{d}}_{\mathrm{rot}})$ (neutral substrates), separate for any direction
k_{tum}	10	Out-of-plane, "tumbling" rotation rate in any direction $= k^{\mathrm{d}}_{\mathrm{tum}} = k^{\mathrm{u}}_{\mathrm{tum}} \equiv k_{\mathrm{rot}}$ (neutral substrates), for odd- or even-valued L, implemented in Secs. 5.7, 5.6[6]
$k_{1\leftrightarrow 2}$	10	In-plane rotation rates around *rod-centers*, requires L *odd*, value defined for either direction[7]
k_{shuff}	5	In-plane rotation rates around *rod-ends*, principally for any L, implemented in Sec. 5.7, value defined for either direction[8]

TABLE 5.1: Overview of moves and default "attempt" rates that are implemented in KMC models for sticky hard rods of various variety. (The choices of rotational "moves" — $k^{\mathrm{d}}_{\mathrm{tum}}$ versus $k^{\mathrm{d}}_{\mathrm{rot}}$ or k_{shuff} versus $k_{1\leftrightarrow 2}$ — will change throughout this chapter, and will be noted accordingly.)

NOTATION	MEANING
D	Ideal-gas translational self-diffusion rate
F	Deposition attempt flux rate
F/D	Deposition–to–diffusion rate (one main "axis")
$\gamma \equiv {}^{D}/_{2k^{\mathrm{d}}_{\mathrm{rot}}}$	Diffusion–to–out-of-plane-rotational rate
ϵ	"Sticky" attraction strength, $\epsilon^* = \epsilon/k_{\mathrm{B}}T$ is dimensionless
$T^* \equiv k_{\mathrm{B}}T/\lvert\epsilon\rvert$	Reduced temperature (another main "axis")
$1/\lvert\epsilon\rvert$	Inverse "sticky" attraction strength, often interchanged with $1/\lvert\epsilon^*\rvert$ (dimensionless)
u_{sub}	Substrate potential attraction strength (a "third" axis) often interchanged with $u^*_{\mathrm{sub}} = u_{\mathrm{sub}}/k_{\mathrm{B}}T$ (dimensionless)
L	Rod-length (a "fourth", implicit axis)

TABLE 5.2: Overview of the relevant dynamical and energetic parameters for a nonequilibrium evolution in the KMC model. We note which basic parameters which consider the main "axes" adjusting the self-assembly kinetics. The reduced quantities ϵ^* and u^*_{sub} are often used interchangeably in this chapter with ϵ and u_{sub}: All energetic quantities are to be understood in units of $k_{\mathrm{B}}T$. Likewise, all rates are to be understood as the occurrences of events per unit time (diffusion and flux rates are also to be understood in terms of unit area).

Note on diffusion rates

In most experimental systems, one can only adjust the self-diffusion rate via lowering the temperature, as diffusion hopping process is generally presumed to be thermally activated. Therefore, standard approaches vary the "attempt" translational self-diffusion rate D with temperature according to an Arrhenius law, i.e. $D(T) = D_0 k_{\mathrm{B}}T \exp(-{}^{E_D}/_{k_{\mathrm{B}}T})$, where E_D is some (fixed) diffusion barrier depending on the material properties of the substrate, and D_0 is an "attempt". Unfortunately, changing the diffusion rate via increasing the temperature also changes the position in the phase diagram. This complicates the general picture of possibly dynamical scenarios (phase transition kinetics) that can occur. Therefore, in our simulation model system, we decouple the "attempt" self-diffusion rates from the attraction strength and vary the attraction strength independently.

[3]Default values or range of values

[4]The full rotation upwards from a lying orientation is actually implemented to be $2k^{\mathrm{u}}_{\mathrm{rot}}$ for "central" rotations, requires odd-valued L.

[5]The full rotation downwards from a standing orientation is actually implemented to be $2 * k^{\mathrm{u}}_{\mathrm{rot}}$ for "central" rotations, requires odd-valued L.

[6]alluded to here for neutral substrates only ($k^{\mathrm{d}}_{\mathrm{tum}} = k^{\mathrm{u}}_{\mathrm{tum}}$)

[7]The full rotation rate in-plane is thus $2k_{1\leftrightarrow 2}$.

[8]The full rotation rate in-plane is $4k_{\mathrm{shuff}}$.

5.1.2 Expressions for D_{2D} for any choice of rotational moves and substrates

In this section, we provide analytical expressions for the effective 2D translational diffusion rate $D_{2D} \equiv D$ of an ideal gas of rods on lattices that perform hops as well as rotations *not along the rod centers*: The latter propagate the center-of-masses of rods across space, which implies that translational and rotational degrees of freedom are *coupled* at the one-body scale. This section is an extension of our derivation of D_{2D} in Ch. 4.11 that treated the case of "tumbling" rotations on neutral substrates. We now consider the generalized case where $k^{u}_{tum} \neq k^{d}_{tum}$ (i.e. substrate potentials). Further, we provide the diffusion rate when particles can "shuffle" in-plane, as well (e.g. the case of dimers studied in this chapter).

Hopping diffusion

The first rate that contributes to translational motion is k^{0}_{hop} for an explicit hopping process of a rod on the substrate, in any of 4 directions. For an ideal gas of rods performing *only* hopping moves in a 2D plane, the relation between the hopping rate and the diffusion constant can be shown to be

$$D^{hop} = k^{0}_{hop} \, . \tag{5.3}$$

Out-of-plane tumbling

Now, if we let rods rotate about their ends in the out-of-plane direction, we speak of "tumbling" rotations, denoted by k_{tum}. This process can be split into a tumble 'upward' with rate k^{u}_{tum}, and one 'downward' with k^{d}_{tum}. There is a twofold degeneracy of each of these processes between orientations $i = 3$ and $i = 1, 2$ due to each orientation having two possible directions to rotate into. This case was utilized in Ch. 4. These tumbles occur alongside in-plane rotations about the rod-center with rate $k_{1\leftrightarrow 2}$, which do not contribute to translational diffusion.

Following the logic in the derivation of Ch. 4.11, an ideal gas of rods only tumbling has the following diffusion constant in a projected 1D dimension:

$$D^{tum}_{1D}(L, k^{u}_{tum}, k^{d}_{tum}) = \frac{1}{2}\left(\frac{\rho_3}{\rho}k^{d}_{tum} + \frac{1}{2}\frac{\rho_{12}}{\rho}k^{u}_{tum}\right) \times \begin{cases} \dfrac{L^2}{4} \, , & \text{L even} \\ \dfrac{(L-1)^2}{4} \, , & \text{L odd} \end{cases} . \tag{5.4}$$

The previous derivation treated populations of rods in each orientation in a stationary state (equilibrium) where $\frac{d\rho_i}{dt} = 0$ for $i = 1..3$. One can easily show that the following relations arise from the stationarity condition $\frac{d\rho}{dt} = 0$:

$$\frac{\rho_3}{\rho} = \frac{1}{1 + 2\frac{k^{d}_{tum}}{k^{u}_{tum}}} \tag{5.5}$$

$$\frac{\rho_{12}}{\rho} = 1 - \frac{1}{1 + 2\frac{k^{d}_{tum}}{k^{u}_{tum}}} \tag{5.6}$$

Here, $\rho_{12} = \rho_1 + \rho_2$. Hence the final form for the diffusion rate in 2D, which is simply twice the diffusion rate along one projected axis, is

$$D^{\text{tum}}(L, k^{\text{u}}_{\text{tum}}, k^{\text{d}}_{\text{tum}}) = \left(\frac{1}{2}k^{\text{u}}_{\text{tum}} + \frac{1}{1+2\frac{k^{\text{d}}_{\text{tum}}}{k^{\text{u}}_{\text{tum}}}}\left(k^{\text{d}}_{\text{tum}} - \frac{1}{2}k^{\text{u}}_{\text{tum}}\right)\right) \times \times \begin{cases} \frac{L^2}{4}, & \text{L even} \\ \frac{(L-1)^2}{4}, & \text{L odd} \end{cases}. \tag{5.7}$$

The default case of neutral substrates is ascribed through $k^{\text{d}}_{\text{tum}} = k^{\text{u}}_{\text{tum}} = k_{\text{tum}} = 2k_{\text{shuff}}$. Eq. 5.7 becomes

$$D^{\text{tum}}(L, k_{\text{tum}}) = \frac{2}{3}k_{\text{tum}} \times \begin{cases} \frac{L^2}{4}, & \text{L even} \\ \frac{(L-1)^2}{4}, & \text{L odd.} \end{cases} \tag{5.8}$$

In-plane shuffling (combined with out-of-plane tumbling)

Another set of possible rotations are when rods pivot at their ends *in plane*. These microscopic kinetics are suited for simulations with rods of even lengths $L = 2, 4, 6 \ldots$, which have no well-defined center, but can be used for any rod length.

With respect to the in-plane rotations denoted here as k_{shuff} — the rods "shuffle" along the substrate in doing pivots around their ends — these have a fourfold degeneracy for each orientation $i = 1, 2$. To match the rates of the in-plane rotations $k_{1\leftrightarrow 2}$ for even-L cases, one must consider the total rate of in-plane rotations per orientation: $2k_{1\leftrightarrow 2} = 4k_{\text{shuff}}$.

The full diffusion constant on the substrate in the dilute limit has an additional term compared to Eq. 5.7 due to shuffling in-plane. To see this, one first considers half of the population ρ_{12}, e.g. the ρ_1 population that can displace its center-of-mass during one event. There are indeed two directions that the rod propagates in simultaneously, hence $||\Delta\vec{r}|| = \frac{\sqrt{2}L}{2}$ (even L) or $\frac{\sqrt{2}(L-1)}{2}$ (odd L) after a shuffle move. This process can be done in one step in two ways: by rotating clockwise and counterclockwise, which defines the unit time-step of the propagation: $\Delta t = (2k_{\text{shuff}})^{-1}$. Following Fick's law $\langle||\Delta\vec{r}||^2\rangle = D^{\text{shuff}}\Delta t$, and the fact that are two populations of lying rods that contribute to the mean-squared displacement, which doubles the left-hand-side,[9] we solve for the shuffling diffusion constant:

$$D^{\text{shuff}}(k_{\text{shuff}}, [\rho_{12}]) = \left(\frac{\rho_{12}}{\rho}2k_{\text{shuff}}\right) \times \begin{cases} \frac{L^2}{4}, & \text{L even} \\ \frac{(L-1)^2}{4}, & \text{L odd.} \end{cases}. \tag{5.9}$$

We have written this implicitly as a function of ρ_{12}, as we are considering the ideal gas on a whole. The full contribution will depend on the in- and outflux

[9] Eq. 5.6 still holds for this case because in-plane rotations are assumed to be isotropic (i.e. there is no demixing in-plane)

of orientations, which are fixed by $k^{\mathrm{u}}_{\mathrm{tum}}$ and $k^{\mathrm{d}}_{\mathrm{tum}}$ (for the case of out-of-plane tumbles). Using Eqs. 5.5 and 5.6, the final result for the long-time translational diffusion rate due to shuffling in-plane and out-of-plane tumbles is

$$D^{\mathrm{shuff+tum}}(L, k^{\mathrm{d}}_{\mathrm{tum}}, k^{\mathrm{u}}_{\mathrm{tum}}, k_{\mathrm{shuff}}) = 2k_{\mathrm{shuff}} \left(1 - \frac{1}{1 + 2\frac{k^{\mathrm{d}}_{\mathrm{tum}}}{k^{\mathrm{u}}_{\mathrm{tum}}}} \right) \times \times \begin{cases} \dfrac{L^2}{4}, & \text{L even} \\ \dfrac{(L-1)^2}{4}, & \text{L odd.} \end{cases} \tag{5.10}$$

For the simpler case of *neutral substrates*, we set $k^{\mathrm{d}}_{\mathrm{tum}} = k^{\mathrm{u}}_{\mathrm{tum}} = k_{\mathrm{tum}} = 2k_{\mathrm{shuff}}$. The full diffusion rate for an ideal gas $L = 2$ becomes

$$D(L, k_{\mathrm{tum}} = 2k_{\mathrm{shuff}}) = D^{\mathrm{hop}} + \frac{4}{3} k_{\mathrm{shuff}} \times \begin{cases} \dfrac{L^2}{4}, & \text{L even} \\ \dfrac{(L-1)^2}{4}, & \text{L odd.} \end{cases} \tag{5.11}$$

Summary

The full 2D diffusion rate for *hops + central rotations* is simply

$$D(k^0_{\mathrm{hop}}) = D^{\mathrm{hop}} , \tag{5.12}$$

which represents the *default* case in this chapter.

The full 2D diffusion rate for *hops + tumbles* is

$$D(L, k^{\mathrm{u}}_{\mathrm{tum}}, k^{\mathrm{d}}_{\mathrm{tum}}, k^0_{\mathrm{hop}}) = D^{\mathrm{hop}} + D^{\mathrm{tum}}(L, k^{\mathrm{u}}_{\mathrm{tum}}, k^{\mathrm{d}}_{\mathrm{tum}}) , \tag{5.13}$$

which characterizes the cases of $L = 3, 5, 9$ at neutral substrates ($k^{\mathrm{u}}_{\mathrm{tum}} = k^{\mathrm{d}}_{\mathrm{tum}}$) presented in Sec. 5.6.

The full 2D diffusion rate for *hops + tumbles + shuffles* is likewise

$$D(L, k^{\mathrm{u}}_{\mathrm{tum}}, k^{\mathrm{d}}_{\mathrm{tum}}, k_{\mathrm{shuff}}, k^0_{\mathrm{hop}}) = D^{\mathrm{hop}} + D^{\mathrm{shuff+tum}}(L, k^{\mathrm{u}}_{\mathrm{tum}}, k^{\mathrm{d}}_{\mathrm{tum}}, k_{\mathrm{shuff}}) , \tag{5.14}$$

which characterizes the case of dimers ($L = 2$) in Sec. 5.7.

5.2 Information on equilibrium phase diagrams from other methods

Phase diagrams from lattice FMT (for neutral substrates)

Before moving on to the results from our KMC simulations, we will discuss the phase diagrams predicted by FMT in Ref. [72], reproduced in Fig. 5.2:

For $L = 3$ at *neutral* substrates, Fig. 5.2(b), a first-order vapor–liquid transition characterizes the phase separation of an isotropic gas and a "standing" liquid state (a distinction between a solid or a liquid "standing" state cannot be made in this lattice model), where the binodal is indicated by the solid

black line. This "parent" binodal engulfs further binodals that are metastable, enabling liquid-liquid phase separation in the system. The metastable critical point is labeled "$T_{\mathrm{cr},2}$" in the phase diagram; we denote it inversely as "$\epsilon_{\mathrm{crit,\,meta,\,denem}}$". Displayed are two binodals that nearly coincide up to their right-hand-sides at higher densities: The green-dotted indicates what *would* correspond to an isotropic-vapor–isotropic-liquid transition. (Note that for the green-dotted line, the isotropy was enforced in the functional minimization. It is supposed to show that the purple dot-dashed line "nearly" corresponds to a transition between isotropic states.) The purple dot-dashed line marks the metastable binodal between two low-ordered states. In our simulation results during growth, it is difficult to discern exactly between low-ordered states, as some of them are metastable and the phase transformation process occurs quite rapidly from the beginning. Yet, as we will present in the coming sections, we find evidence for a lying fluid (nearly $Q < 0$), a nearly $Q \approx 0$ mixed fluid state, and a standing fluid ($Q > 0$), which may be the candidates for this metastable phase separation process. Hence the metastable lines computed by FMT in the phase diagrams are only *partly* helpful, at least for making us aware of a wide variety of phenomena that are possible, in particular metastable *critical points*.

At very low temperatures, a metastable reentrant demixing in the substrate plane is also predicted by FMT, in the red dot-dashed line. We do not see "2D" demixing at all during growth in a wide variety of circumstances (apart from very long rods, $L = 9$): it is an artifact of the DFT. The FMT also predicts another metastable critical point ($T_{\mathrm{cr,nem}}$, which we denote inversely with "$\epsilon_{\mathrm{crit,\,meta,\,nem}}$") below which a first-order "nematic–nematic" transition occurs between two differently-ordered states, at high densities. We think the interpretation during growth, where phase separation kinetics are ongoing, may be different: We find a standing-up transition that occurs from a lying "wetting layer", especially enhanced for slightly attractive substrates, within certain dynamical regimes defined by (F/D and $1/|\epsilon|$ or reduced temperature T^*). In nonequilibrium conditions, it seems very difficult to determine the densities of metastable transitions one phase separation sets in. During growth, we see this specific example of standing up at densities past $\rho > 1/L$ (neutral substrates). *Critical points* of metastable transitions, however, may be spotted from a wide variety of trajectories explored. The phase behavior regarding stable binodals for longer rods $L > 3$ is predicted to be similar topologically to the case of $L = 3$. The metastable binodals or transitions may be altered by the length of the rods, according to the FMT, i.e. the "nematic–nematic" transition in the black dashed line might become stable for longer rods. We think that an additional, strongly attractive substrates makes this transition stable, which we will present later in this chapter.

For $L = 2$ at neutral substrates, two critical points in the system are stable. The vapor–standing-liquid transition analogous to that of $L = 3$ is indicated in the solid black lines. FMT predicts an overlap of two binodals that become metastable, after the black binodal, when sufficiently extending below from a stable critical point $T_{\mathrm{cr},2}$ in Fig. 5.2(a). The two binodals (green dotted and purple dashed) are the analogs of those for $L = 3$, i.e. a gas–isotropic–liquid transition and a vapor–"denematic"-liquid transition between two low-ordered states. Indeed for neutral substrates, we see an isotropic fluid with intermediate density forming during growth, a feature we cannot find for $L = 3$. Yet, just like with $L = 3$, a preciser interpretation from our simulation results remains difficult.

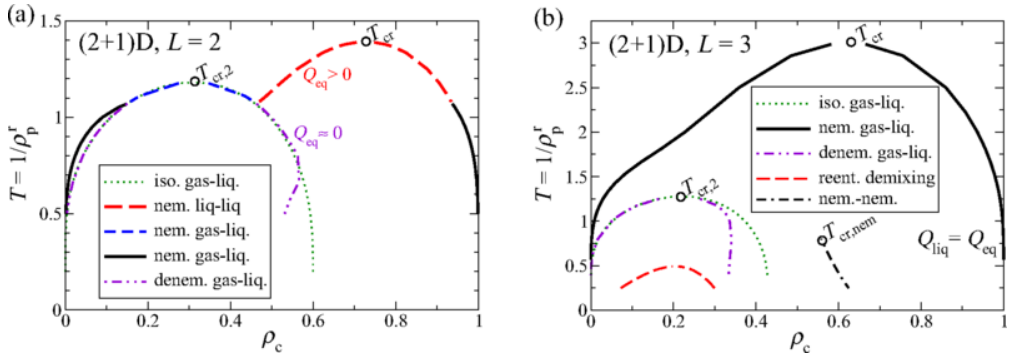

FIGURE 5.2: Phase diagram for sticky hard rods with length $L = 2$ (a) and $L = 3$ (b) calculated with a lattice-FMT for the "sticky" monolayer systems we study in this chapter: The "sticky" attractions implemented in an Asakura-Oosawa-type model, where "polymers" induce short-range attractions. See text for a description. Taken from Ref. [72]. The temperature T corresponds to our reduced temperature T^*.

Stable binodals from GCMC simulations (for neutral substrates)

Figure 5.3 displays our simulation estimates of the "parent" binodal – of the demixing of an isotropic gas and a "standing", high-density phase – for rod-lengths $L = 3, 4, 5$ at neutral substrates. We employed GCMC simulations for this purpose, just like in the last chapter, employing "sticky" attractions here.[10] See Ch. 3 for a general description of the GCMC method. Note that no finite-size analysis was performed. For $L = 3$, we see that the "parent" binodal is lower

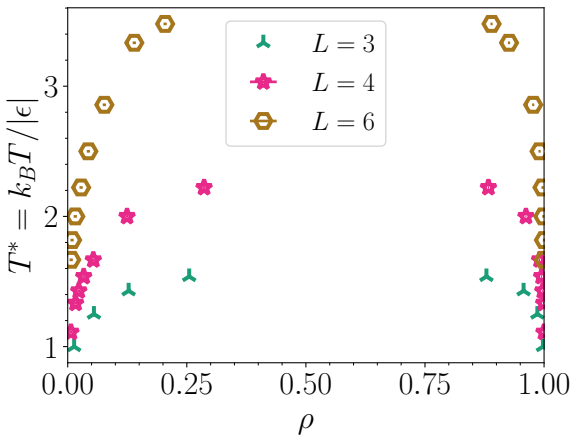

FIGURE 5.3: Estimates of the isotropic-vapor–standing-liquid binodals obtained from GCMC simulations for rod-lengths $L = 3, 4, 6$: Reduced temperature T^* versus global mean density ρ of the monolayer. The used simulation box size is 256×256 and no finite-size analysis was performed. Estimated errors in the density are smaller than the symbols.

than that predicted by FMT, at least for the low- and high-density regimes. The exact position of the critical point is not known, but we have estimated it to be around $\epsilon = -0.625$ from our simulations on 256×256 lattices.[11]

[10] Produced data are courtesy of E. Empting and P. Quiring.
[11] This information is courtesy of P. Quiring.

* * *

In the coming sections, our KMC simulations will unveil a vast number of ways in which structure and dynamics evolve in nonequilibrium conditions – during monolayer growth, on the way to a full monolayer. This seems tied to the complexity of the phase diagram (predicted by the FMT) that we discussed in this section. Note that the KMC simulations of the forthcoming sections were specified in Sec. 5.1.1.

In the following section (Sec. 5.3), we will first focus on the monolayer growth behavior of rods with $L = 3$ on neutral substrates. FMT predicts that the equilibrium behavior with slightly longer rods should be qualitatively similar to that for $L = 3$. Longer rods and neutral substrates can change the onset of metastability of various transitions, which is why these are treated thereafter. We will treat the case of dimers quite later in this chapter, after studying a series of systems with even-valued rod-lengths L. We will discuss the metastable phases in these systems in a retrospective manner at the end in Sec. 5.9 at the end of this chapter.

5.3 Results on monolayer growth for rod-lengths $L = 3$

We shall present and discuss the findings for monolayer growth with rods of length of $L = 3$ in this section. We present selected results for growth with rods of length $L = 5$ in Sec. 5.4. Growth with sticky dimers is presented in Sec. 5.7 afterwards. The effects of substrate potentials that bias lying rods are discussed in Sec. 5.5 for $L = 3$ and in Sec. 5.7.2 for $L = 2$.

5.3.1 Different phase transition scenarios and categorization

Monolayer growth with $L \geq 3$ shows a wide variety of behavior depending on F/D as well as the reduced temperature $T^* \equiv k_B T/|\epsilon|$. For the latter, we will adopt the convention of discussing the (inverse) attraction strength ϵ or $1/|\epsilon|$, instead.

We find five different phase transition scenarios in the monolayer depending on these two "axes", which we list below. As a 'disclaimer' of prior to presenting the results, we wish to make clear that any conclusions or categorical distinctions we draw are based on careful study over a wide variety of parameters. We additionally integrate knowledge obtained under slightly modified conditions (an additional external potential, slightly longer rods) that are presented in later sections.

Due to historical reasons, in writing this chapter, we will often describe the phenomenology in terms of "ϵ-regimes" (I-III). However, this categorization does not integrate the dependency of the (complex) phase transition kinetics on F/D. This categorization was motivated from an equilibrium standpoint, i.e. from the point-of-view of describing the systems relative to critical points in the phase diagram whose positions we can only infer with high uncertainty. The (approximate) FMT, described in Sec. 5.2, predicts at least three critical points, at least two of which represent metastable transitions.

We will discover a very rich variety of phase transition scenarios characterizing the kinetics of monolayer growth. These are function of the reduced temperature $T^* \sim 1/|\epsilon|$ and the relative rate of flux-to-diffusion, F/D. In fact,

F/D can be thought of as a *deposition quench rate*, analogous to a gradual temperature quench experiment. We shall adopt this term in forthcoming sections of this chapter. The scenarios we categorize are the following:[12]

(A) "Hard–rod–like" growth of a monolayer[a]

(B) Isotropic–fluid–to–standing transition via "nucleation" and growth of clusters

(C) Competition of lying- and standing-cluster formation

(D) Low-density-lying-gel and standing-cluster formation

(E) Formation of standing clusters out of a dense, lying–gel phase

[a] This involves no thermodynamic phase transition, see Sec. 5.3.2.

These scenarios can be shifted in the $(1/|\epsilon|, D/F)$–parameter-space for longer rods, which we present in Sec. 5.4, as well as for shorter rods (dimers), which we present in Sec. 5.7 much later. This is also true when adding substrate potentials to the system, which we present in Sec. 5.5. Finally, some of these scenarios may "drop out" when the rod dynamics are defined with a different set of microscopic "moves", which we present in Sec. 5.6.

We will first discuss our observations phenomenologically, tracing three ϵ-regimes (I-III) by means of analyzing a large number of observables during growth, and by varying a large number of dynamical parameters. In the next few sections, we will focus on Q (nematic order parameter), ρ (number density of the monolayer), ρ_{12} (lying number density) and ρ_3 (standing number densities. In Sec. 5.3.7 thereafter, we will introduce our cluster analysis methods, and extract cluster number densities, cluster sizes, morphological measures in the form of Minkowski functionals, as well as percolation probabilities. We will analyze observables pertaining to the dynamics of the nonequilibrium systems in Sec. 5.3.8, i.e. the number densities of mobile particles, the nematic order of the mobile subsystem, and rotational and translational fluxes in the system in the form of relative rates. We have provided a table of the observables presented in this section in Tab. 5.3. By combing through this large number of observables, we will then be able to identify and fully characterize the scenarios (A)–(E). The detailed discussion thereof is found at the end of this section, Sec. 5.3.9. Beforehand, we will collect evidence for regions in the $(1/|\epsilon|, D/F)$–parameter-space where these scenarios show up.

We also note here that almost all data-points presented in the plots of this chapter stem from a single run on a $M \times M = 256 \times 256$ grid.[13] The focus of our studies has been to explore behavior over a widest possible range of dynamical parameters (F/D, long simulated times) rather than quantitative precision. All points in plots represent binned (running) mean values, whose often invisible error bars are calculated with a standard errors within bins.

[12] These scenarios describe the most "basic" case of $L = 3$ at neutral substrates, simulated with the "standard" set of microscopic "moves" defined in Sec. 5.1.1. See further text on changes thereof.

[13] exceptions include the case of $\epsilon = -0.33$ for $L = 3$, performed on a 512×512 grid.

OBSERVABLE	DESCRIPTION
Q	Nematic order parameter
ρ	Number density of rods on the substrate
ρ_{12}	Lying number density
ρ_3	Standing number density
η	Packing fraction (coverage of monolayer)
n/M^2	Number density of clusters
$\langle i \rangle$	Mean cluster size ("mass" of clusters)
W_0	Minkowski functional: total "outline" of connected regions
W_1	Minkowski functional: total *area* of connected regions
χ	Euler characteristic: (positive:) number of separate *clusters* and (negative:) number of *holes in* connected regions
Perc. prob.	Probability that any cluster percolates
$\rho_{\text{mob., trans.}}$	Number density of rods that are translationally mobile (in at least one direction)
$\rho_{\text{mob., rot. down}}$	Number density of *standing* rods that are rotationally mobile (in at least one direction)
$Q_{\text{mob, trans.}}$	Nematic order of translationally mobile rods
$Q_{\text{mob., rot.}}$	Nematic order of out-of-plane-rotationally mobile rods
$J_{\text{trans., rel.}}$	Total translational flux relative to total "internal" motion flux
Accept. ratio α	"Sticky" acceptance ratio of all "internal" moves that can be rejected due to "sticky" binding energies only

TABLE 5.3: Overview of observables measured during monolayer growth that are presented in this entire section (Sec. 5.3). See Sec. 5.3.7 for details on Minkowski functionals and cluster analysis, as well as Sec. 5.3.8 for details on the dynamical observables (bottom 6 rows).

5.3.2 ϵ-Regime I: "Hard–rod–like" monolayer growth

At high reduced temperatures, no phase transition should occur according to thermodynamics: With very weak attractions, i.e. at $\epsilon \approx -0.33, -0.4$, we can describe the dynamics during monolayer growth as "hard-rod-like", which we categorize as ϵ-regime I.[14] We have provided a few further quantitative results in App. A.1, but, the nonequilibrium dynamics in this regime are not in the focus of this thesis. Briefly, a subtle transition from quasiequilibrium behavior to nonequilibrium behavior of globabl obervables can be observed in Fig. 5.4 with increasing F/D, where the nematic order parameter is plotted versus the surface packing fraction. The subtlety bears strong analogy to that seen in the last chapter at high rates $\alpha = F/(2k_{\text{rot}})$ for the iostropic ("ISO") deposition mode (Ch. 4). Interestingly, even at these weak values of ϵ, we observe that the lying orientation of rods is favored over the standing orientation for the highest values of F/D, especially visible when analyzing the structure of the fluid using nearest-neighbor cluster-detection schemes. These are explained later in Sec. 5.3.7. In particular, there is a peak in the size of the lying regions in Fig. 5.5, which corresponds to a density (not shown) around $\rho \approx 0.33$, which will

[14]Notation: ϵ is used here as a dimensionless quantity in units of $k_B T$, i.e. it represents the reduced quantity $\epsilon^* = \epsilon/k_B T$.

reappear as a density at which global dynamic arrest occurs for lower values of ϵ or reduced temperature. (Please refer to App. A.1 for more figures. The former foreshadows a lying phase that will emerge for lower $1/|\epsilon|$ (discussed further below).[15]

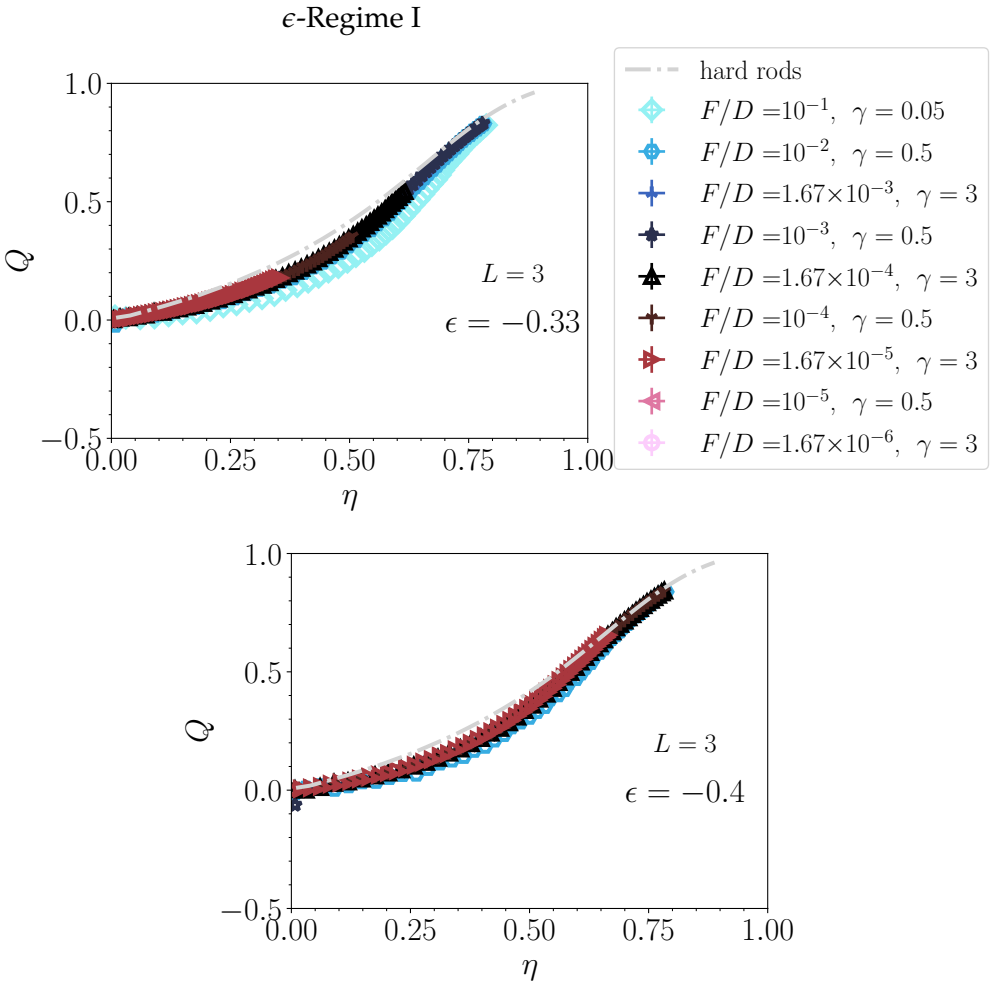

FIGURE 5.4: Nematic order parameter Q versus packing fraction (coverage) during growth of a monolayer for ϵ-regime I at varying F/D ($L = 3$): shown for $\epsilon = -0.33$ (top) and $\epsilon = -0.4$ (bottom). It seems quasiequilibrium growth is possible for low values of F/D. The gray dashed curve represents quasiequilibrium growth for *purely* hard-core rods ($\epsilon = 0$), from which both sets of trajectories deviate only mildly over the large range of F/D's explored. Note that the $\epsilon = -0.33$ system was simulated on a larger lattice of $M \times M = 512 \times 512$.

[15]The kinetics of (potential) jamming transitions, which we saw for hard-core rods at attractive substrates, are not studied here, but would be worthy of attention for a more complete dynamical picture of the monolayer rod systems.

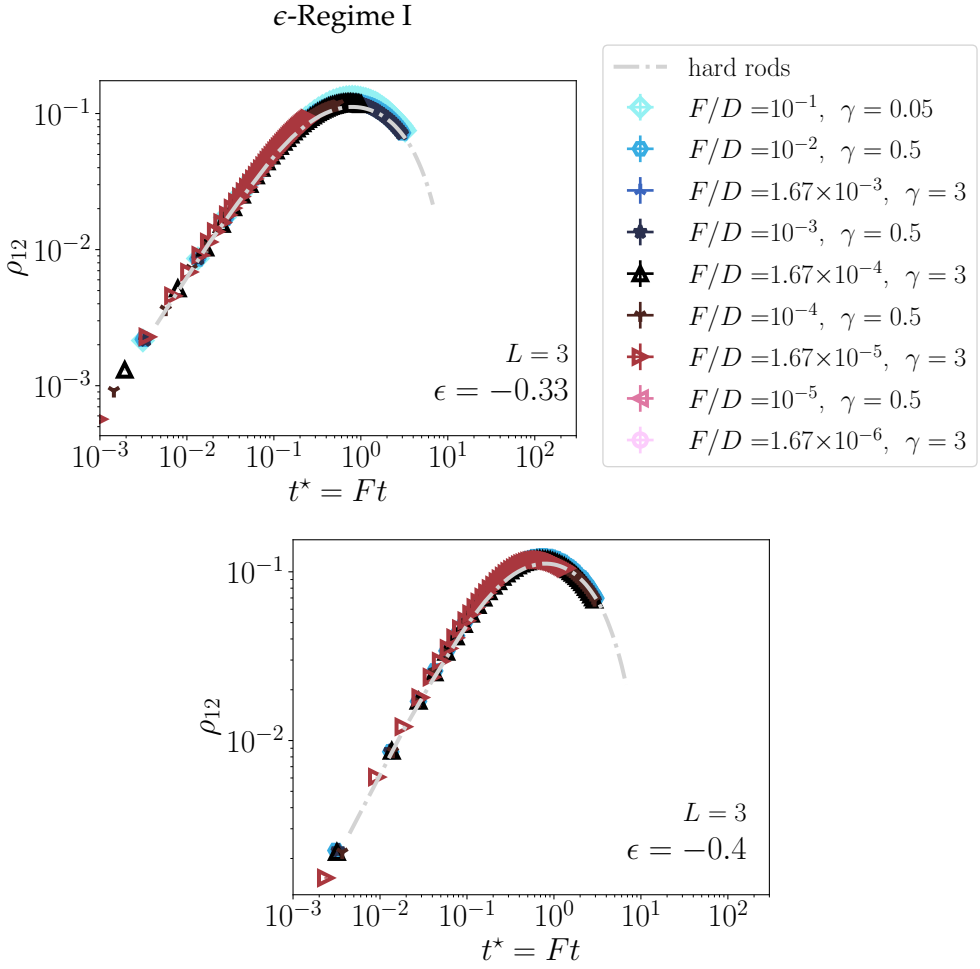

FIGURE 5.5: Lying number density ρ_{12} versus re-scaled time $t^\star \equiv Ft$ during growth of a monolayer for ϵ-regime I at varying F/D ($L = 3$): shown for $\epsilon = -0.33$ (top) and $\epsilon = -0.4$ (bottom). It seems quasiequilibrium growth is possible for low values of F/D. The gray dashed curve represents quasiequilibrium growth for *purely* hard-core rods ($\epsilon = 0$), from which both sets of trajectories deviate only mildly over the large range of F/D's explored.

5.3.3 Around the critical point: The role of fluctuations and F/D

Spatial fluctuations (heterogeneity) in the orientational order become noticeably amplified upon approaching a vapor–liquid critical point, which we estimate lies in the interval $0.4 < |\epsilon_{\text{crit}}| < 0.7$, very roughly estimated to be near $|\epsilon_{\text{crit}}| \approx 0.62$ for neutral substrates via GCMC simulations.[16] Our simulated case of $\epsilon = -0.5988$ seems to be very near a critical point, where we have analyzed the kinetics from the time traces of various observables more extensively. (We will encounter these in later parts of this chapter). Such amplified local structures are visible in configuration snapshots shown in Fig. 5.6, shown for rather low F/D. In App. A.1, we additionally compared cases of very weak

[16] This information is courtesy of P. Quiring, but, we cannot estimate how large the uncertainty is at the current moment.

attractions ($\epsilon = -0.33$) with the system near the critical point (see results below for the latter).

Local, transient structures (what we dub as nonequilibrium spatial fluctuations) are a strong function of F/D. Those entailing a lower degree of local ordering are effectively "pulled up" by the nonequilibrium driving force, the *deposition quench rate* F/D: Local structures with a standing orientation are much smaller and are suppressed over lying local structures that are favored in these nonequilibrium conditions. Hence, the global order parameter Q drops for high F/D, which can be seen in Fig. 5.7. In the figure, we have plotted the nematic order parameter Q versus the monolayer packing fraction η (surface coverage) along a growth trajectory. A high F/D (a fast deposition quench rates) effectively freezes out these energetically unfavorable structures, i.e. the relaxation of structures in the fluid is clearly hindered, and dynamical arrest begins to play a very important role for the kinetics.

To support this we have performed structural analysis of simulation snapshots using cluster-detection routines (nearest-neighbor connected regions), the analysis of which is found in App. A.1. Growth at ϵ near the critical point ϵ_{crit}, we find that lying connected regions are larger for nonequilibrium growth conditions (a higher F/D) compared to those for low-F/D growth trajectories. In contrast, standing connected regions are much smaller on average. In particular, there is a peak in the size of the lying regions around $\rho \approx 0.33$, which will reappear as a density at which global dynamic arrest occurs for lower values of ϵ (or reduced temperature).

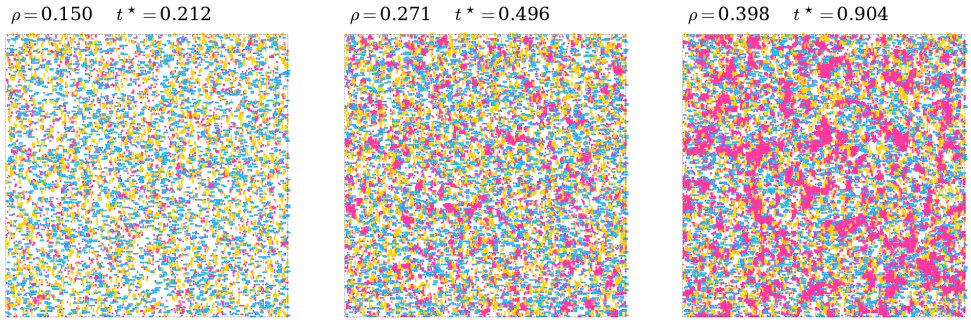

$\epsilon = -0.5988$, near critical point ϵ_{crit}, $F/D = 1.67 \times 10^{-4}$

FIGURE 5.6: Snapshots of configurations of the monolayer during growth for $\epsilon = -0.5988$, projected to be very near the first critical point ϵ_{crit}. The monolayer fluid entails strong spatial fluctuations in density and order. Yet, dynamics in this example are for a *low* deposition quench rate, when local lying structures are allowed to relax ($F/D = 1.67 \times 10^{-4}$ and $\gamma = 3$). Colors: standing rods (magenta), lying rods (blue and yellow).

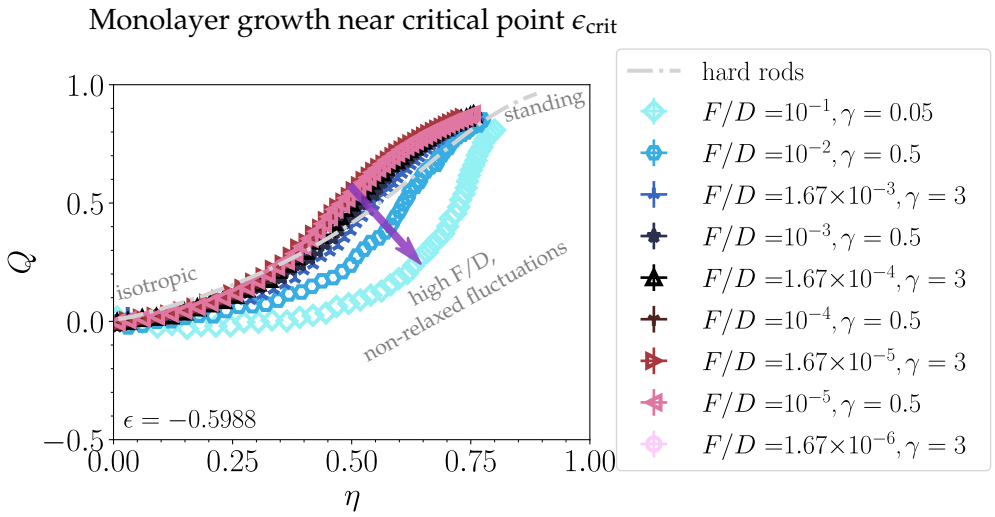

FIGURE 5.7: Nematic order parameter Q versus packing fraction (coverage) during growth of a monolayer for ϵ-regime I at varying F/D ($L = 3$): shown for $\epsilon = -0.5988$. Compared to low values of F/D, at high F/D local structures (spatial "fluctuations") of *lying* order, whose relaxation is hindered by the driving force (*not* visible in the lower F/D-case in Fig. 5.6). The gray dashed curve represents quasiequilibrium growth for *purely* hard-core rods ($\epsilon = 0$), serving as a general reference in forthcoming plots alike.

5.3.4 ϵ-Regime II: Large, standing islands forming from surrounding

At lower reduced temperatures, we find new behavior that motivates us to categorize ϵ-regime II, which we associate with the region $-1 \cdots -0.8 \lessapprox \epsilon \leq \epsilon_{\text{crit}} \approx -0.6$: Compact clusters "nucleate" and grow, separating from a "vapor" or thin fluid, and end up forming large, *standing* islands (scenario (B)). At very low F/D, this represents vapor–liquid separation between a thin fluid with isotropic orientational order and an upright-standing ("nematic") dense phase. A visualization of the growth (or coarsening) of such standing clusters during monolayer growth within this regime is seen in the top two rows of Fig. 5.8 (magenta clusters).

A subtle distinction can be made between standing, compact clusters that form in regime II and regime IIIa (see next Sec. 5.3.5): The standing islands are more "fuzzy" in character in regime II – less compact and fluctuating more strongly at their interface to the surrounding vapor or fluid.

(Although we provide results for this regime further below, additional plots to this regime are found in App. A.2.)

Quite a different scenario of the inevitable standing-up of rods is displayed in Fig. 5.11: A highly nonequilibrium, arrested state of mixed orientation eventually begins to stand up after reaching some maximal packing fraction near $\eta \to 1$. This aggregate forms during rapid monolayer growth (high F/D, such as $F/D = 10^{-1}$).

The nematic order parameter Q versus packing fraction η is seen in Fig. 5.9 to take on much more extreme paths compared to ϵ-regime I for the same range of F/D's, entailing a broader bandwidth of dynamics at various scales:

In the driven setup with monotonic deposition, the monolayer is continually "quenched" into thermodynamically unstable regions in the phase diagram – we can call F/D a *deposition quench rate*. Phase separation between a vapor of thin fluid and a standing, dense fluid sets in somewhat delayed after crossing the predicted binodal density, see Fig. 5.10, albeit this or any transition will be "smeared out" due to the dynamical nature of the system. An unavoidable dilation time is an expression of the (nonequilibrium) response of structural variables to changes in the dynamical state (i.e. applied forces to the system). The delayed effect is particularly pronounced for high deposition quench rates F/D that are comparable or faster than the structural re-ordering process at the given state.[17] We remind the reader that we have separately estimated the binodal densities for intermediate attraction strengths for $L = 3, 4, 6$ at neutral substrates with equilibrium GCMC simulations, see Fig. 5.3.

We will give a detailed overview and description of *all* observed phase transition scenarios for sticky monolayers of rods with $L = 3$ at neutral substrates in Sec. 5.3.9 at the end of Sec. 5.3.

[17] A delay time before nucleation-and-growth is to be expected upon crossing a binodal, as the fluid is metastable.

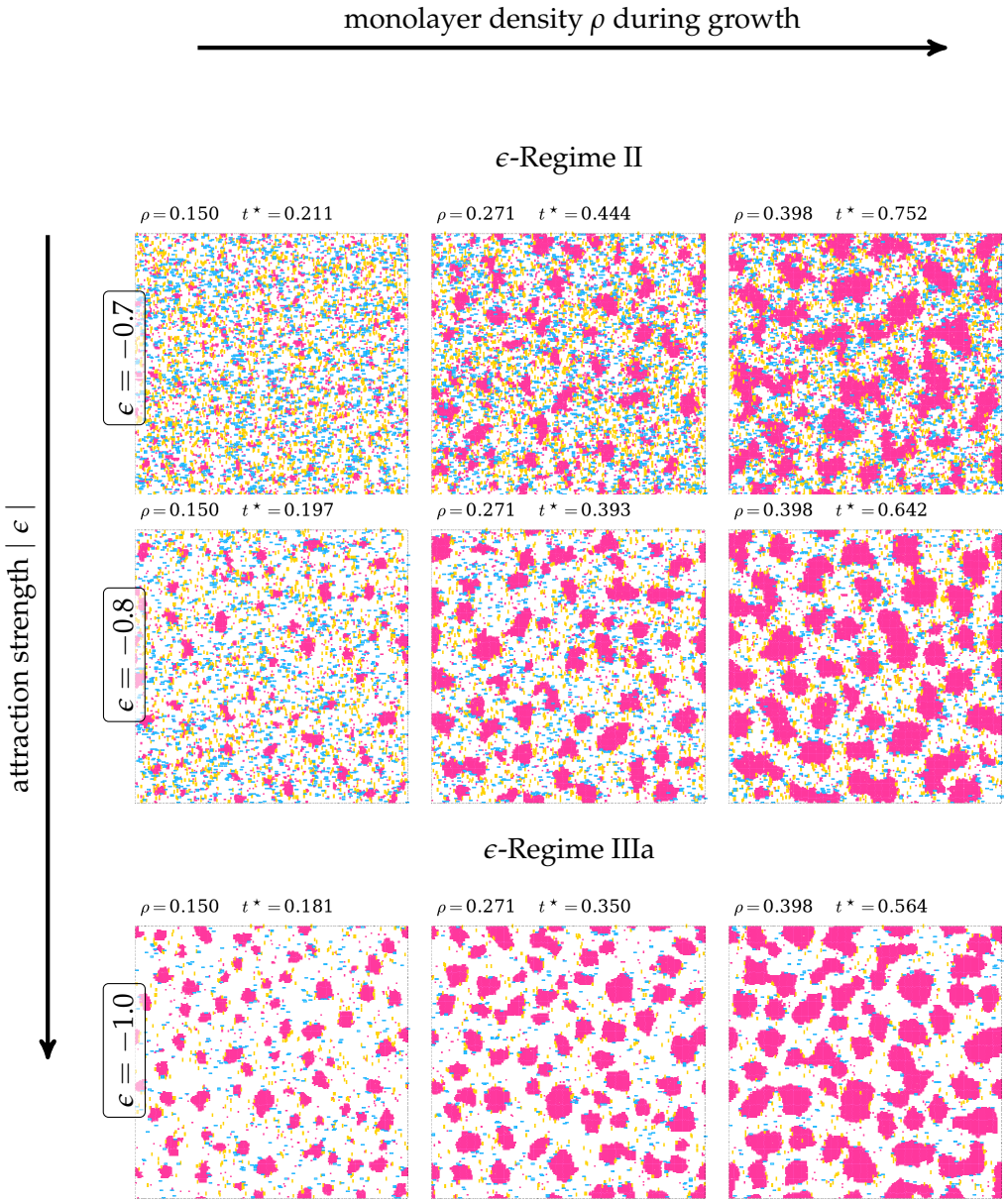

FIGURE 5.8: Configuration snapshots at three densities during monolayer growth in ϵ-regime II and the crossover region of ϵ-regime IIIa (see Sec. 5.3.5) for varying ϵ at neutral substrates. Here, $F/D = 1.67 \times 10^{-5}$ and $\gamma = 3.0$ are fixed. The monolayer density ρ as well as re-scaled time $t^\star \equiv Ft$ increases from left-to-right, specific values can be found on top of each snapshot. From top-to-bottom, the values of the attraction strength are $\epsilon \in \{-0.7, -0.8, -1.0\}$. In regime II, large, standing-phase (magenta) islands may grow, depending on F/D. These are more "fuzzy" in comparison to the standing islands that form in ϵ-regime IIIa. An isotropic "vapor" phase surrounding the clusters is composed of both standing and lying rods (depicted as blue and yellow).

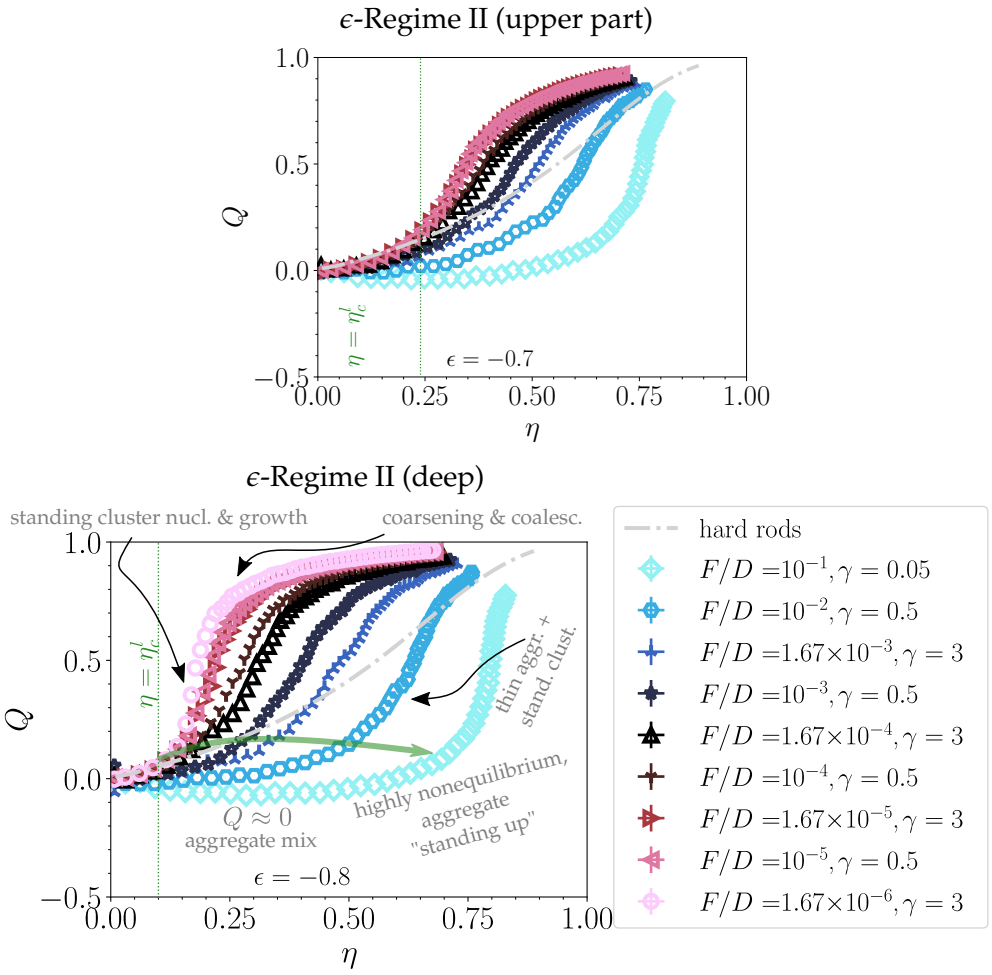

FIGURE 5.9: Nematic order parameter Q versus packing fraction during growth of a monolayer for ϵ-regime II [$\epsilon = -0.7$ (top), $\epsilon = -0.8$ (bottom)] at different F/D conditions, as indicated in the legend ($L = 3$). The green lines indicates the equilibrium packing fractions η_c^l at the left binodals, estimated from GCMC simulations. The gray dashed curve represents quasiequilibrium growth for purely hard-core rods ($\epsilon = 0$). Compare to regime I in Fig. 5.4.

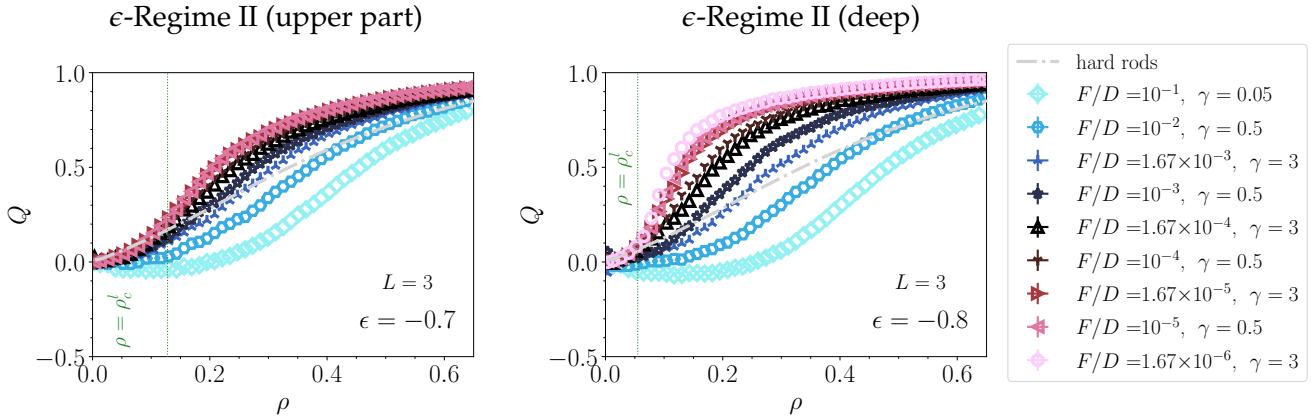

FIGURE 5.10: Global order parameter Q versus global density ρ at fixed attraction strengths for a sweep over F/D ($L = 3$) within regime II [$\epsilon = -0.7$ (left), $\epsilon = -0.8$ (right)]. Green lines indicate the left binodal densities estimated from GCMC simulations (right binodals are very near $\rho = 1$).

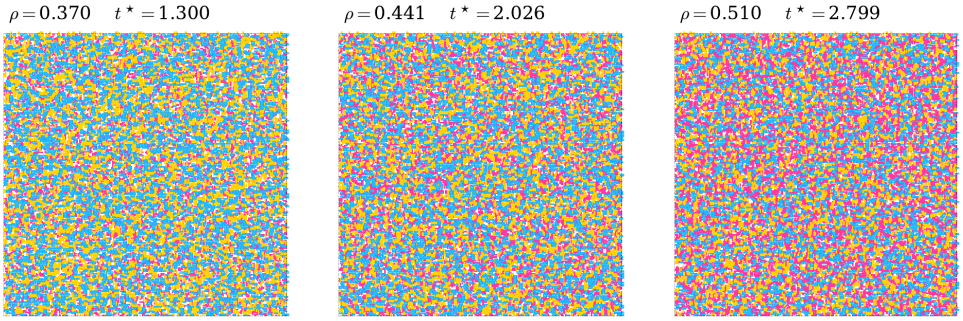

$\epsilon = -0.8$, regime II (deep), $F/D = 1 \times 10^{-1}$

FIGURE 5.11: Visualized snapshots of a highly nonequilibrium system, grown rapidly, within ϵ-regime II in a mixed-orientation aggregate or arrested state at high packing with $Q \approx 0$, thereupon standing up in into a $Q > 0$ system with small structural length-scales. Magenta depicts standing rods, while yellow and blue depict lying rods. Here, $\epsilon = -0.8$ and $L = 3$. The dynamical parameters are $F/D = 1 \times 10^{-1}$ and $\gamma = 0.05$.

5.3.5 ϵ-Regime III: Lying "gel" or "wetting layer" before standing islands

We categorize ϵ-regime III ($\epsilon \lessapprox -1$) when we suspect that a second, metastable critical point is crossed, as predicted by the FMT. We first estimate it to be situated around $\epsilon_{\text{crit, meta, denem}} \approx -1$ for neutral substrates, and will return to another estimation later in Sec. 5.3.9, after exploring this regime and various forms of quantitative analysis more thoroughly in coming sub-sections. Characteristic for this regime is that a conspicuous, lying dense phase grows and ripens during the monolayer growth evolution – we discover it can be either in a loosely-packed for or a thick form depending on ϵ and F/D. Phase transition scenarios (C), (D) and (E) will be involved in $1/|\epsilon|$-regime III, which we summarize and tie together at the end of this main section (Sec. 5.3.9).

The lying dense phase be seen quite easily in the simulation snapshots shown in Figs. 5.12 and 5.13 (the blue–yellow areas), representing the change in the nonequilibrium evolution by varying ϵ and the deposition quench rate F/D. The lying phase phase is transient, i.e. it will decay under unfavorable dynamical conditions: it fails to appear or survive long for low F/D, pointing at its inherent metastability. We also performed experiments with "interrupted growth" and temperature quenches from a "hot" monolayer (see discussion in Sec. 5.8), which demonstrates a decay of the lying phase at fixed density (no driving deposition). The phase of matter has a higher degree of spatial and 2D orientational disorder compared to the standing liquid seen during growth, entailing a lower packing fraction, as well. As discussed in Sec. 5.3.2, local structures with a lying orientations are favored in nonequilibrium conditions, as the "entropic" barrier for visiting this phase is likely lower. (We note here that additional plots to this regime can be found in App. A.2.)

We observe that initial clusters (see Figs. 5.12, 5.13, and 5.14) have a lying orientation, highly amorphous in shape (have a low degree of ordering), and quickly form network-like structures. The latter may ultimately percolate under proper conditions of F/D or $1/|\epsilon|$ – see the visualization of monolayer growth at three snapshots in Fig. 5.12 for the deepest shown attraction strength in regime III. As aforementioned, the (percolating) network (regions with blue and yellow rods in the figure) ripens or coarsens, appearing to form a "gel"-like phase of matter. We note here that network-forming gels in colloidal systems arise when a colloid-poor suspension separates from a colloid-rich solution. In any case, we find that the thermodynamically favorable standing phase is hindered by the lying phase, growing later see lower left corner of Fig. 5.12. (We will explain phase transition scenarios (C) and (D) in more detail later on, as mentioned.) The standing phase is seen to compete with with the network-forming lying phase, and eventually "eats" it up.

All in all, the growth of monolayers in regime III is characterized by a competition and (or) co-occurrence of lying and standing phases, the latter of which is thermodynamically stable and forms stable clusters even at higher reduced temperatures in regime II. This competition can be tuned by varying the attraction strength ϵ (reduced temperature T^*) as well as the deposition quench rate F/D. A stronger ϵ or a larger F/D delays the appearance of the standing phase (see Fig. 5.14, and Fig. 5.9 of regime II). In turn, a high F/D favors the appearance of the thermodynamically unfavorable, but *locally* favorable (in space and time) lying phase, as shown in Figs. 5.12–5.14. This phase seems to appear prior to the standing phase universally, quickly forming out

of lying aggregates. It entails a lower degree of spatial order with respect to translational as well as orientational degrees of freedom. The "nucleation-and-growth" behavior of the thermodynamically favored, standing islands with higher degree of order is hampered or delayed by the formation and growth of this lying phase. We infer a "two-step" nucleation process from preliminary temperature quenching experiments at constant densities, as well (see Sec. 5.8). We will present quantitative analysis providing strong evidence for nontrivial phase separation kinetics in coming sub-sections.

Extreme cases of the lying phase occurs in ϵ-regime III upon very fast deposition quench rate F/D (upper-rightmost image in Fig. 5.13) and for very strong attraction strengths $|\epsilon|$ (bottom-rightmost image in Fig. 5.12), where the monolayer becomes nearly fully-packed ($\eta \to 1$) with a clearly negative order parameter (Fig. 5.14). At very high deposition quench rates F/D, the resulting structure is fine-grained in its microstructure, which we can characterize as a nonequilibrium arrested state. It can also be considered a densely-packed gel, or a "wetting layer", especially for stronger $|\epsilon|$. Subtle distinctions depending in the degree of translational and rotational order between these nearly-fully-packed $Q < 0$-states may exist, but, the kinetics (which we summarize later in Sec. 5.3.9) will appear similar. We describe these in forthcoming sub-sections.

Nevertheless, we have categorized ϵ-regime III into *regime IIIa* (around $\epsilon \approx -1$) and *regime IIIb* ($-1.5 > \epsilon$) partly due to the density and level of orientational order of the "gel" that we can see both from simulation snapshots and in global observables like Q, which we describe more below. The case of $\epsilon \approx -1.5$ seems to be near a crossover case, which we denote as *regime IIIab*. We speculate that the differences between IIIa and IIIb may be due to another metastable critical point, from the thermodynamic point-of-view. The FMT (Sec. 5.2) predicts "$T_{\text{cr,nem}}$" (i.e. the reduced $T^*_{\text{cr,nem}}$) in Fig. 5.2(b), below which a nematic–nematic transition between two highly dense liquids of different nematic order should occur. This lies somewhat below the first metastable critical point in the reduced-temperature- (or ϵ-) representation.

The variables F/D and $|\epsilon|$ are visibly analogous to one another from the snapshots in Figs. 5.12 and 5.13. We discussed in Ch. 2.3 how they are both locally correlative, in effect. In Fig. 5.12, we varied the attraction strength $|\epsilon|$ at fixed F/D, finding an appearance of a lying phase at stronger attraction strengths. In the latter figure, we varied F/D for a fixed value of ϵ within ϵ-regime IIIb ($\epsilon = -2$), where a lying phase can form aggregates as well as clusters alongside standing islands. In both figures, the extreme cases of highly compact standing islands as well as a fully-packed monolayer of nearly 2D character (with nematic order near $Q \to -0.5$) are possible. Notably, selecting an ϵ in regime II would not display this inverse relationship, as a lying phase does not occur.

ϵ-Regimes IIIa and IIIab

As we find the behavior of $\epsilon = -1$ subtly different from that of deeper ϵ during growth: The lying arrested state that forms in Fig. 5.14 at high F/D begins to "stand up" in a steep, nearly vertical increase in Q at nearly fixed η (or a noticeably increase when plotted against ρ in Fig. 5.16 (top)) after reaching a maximal packing fraction – somewhat less sharply than in stronger-$|\epsilon|$ cases (for fast F/D), see the later Figs. 5.15 and 5.16 for comparison. The case of $\epsilon = -1.5$ is probably a crossover case between regime IIIa and regime IIIb, which

is why we call this case "regime IIIab)". It is able to form a densely-packed gel or wetting layer, where $\eta \to 1$ for e.g. $F/D = 1 \times 10^{-1}$ in Fig. 5.14 (bottom). In what we deem as clearly regime IIIa ($\epsilon = -1$), we only see maximally a looser gel forming in competition with standing islands at moderate F/D (scenario (D) described later in Sec. 5.3.9). Extreme cases for high F/D show a $Q < 0$ state with high packing fraction. This stands in contrast to regime IIIb (below), where this lying phase becomes a pronounced, thick gel which can persist for a long portion of the evolution. More evidence for differences in kinetics will be visible in quantitative analysis of the next subsections.

ϵ-Regime IIIb

At lower reduced temperatures, $1/|\epsilon| \lessapprox 0.5$ (which we categorize as ϵ-regime IIIb shown in Fig. 5.15), the lying "gel" phase can become very dense. The densely-packed arrested state becomes a "wetting layer" (this arrested state becomes more pronounced for longer rods and attractive substrate potentials which we discuss later in this chapter). Via visual inspection, we can report that the dynamics therein appear to remain "liquid-like", as we observe perpetual fluctuations (random motion) at local scales by visual inspection. This globally arrested state – a densely-packed gel or wetting layer – seems to persist very long, even longer than reasonable computational time at deep values of $1/|\epsilon|$. The time-scales for which the lying phase persists are partly to be estimated or extrapolated from Figs. 5.17 and 5.18 for the global density ρ and the global lying density ρ_{12} during growth, correspondingly: The lifetime of a "wetting layer" for regime IIIb (e.g. $\epsilon = -2$, $F/D \sim 10^{-2}$) is likely to be around at least $\Delta t^* \propto 10^1 - 10^2$ units for $t^* \equiv Ft$ corresponding to the re-scaled time variable that we introduced in the last chapter.

We note that a long lifetime gives credence to the notion of overcoming a metastable "free energy" barrier (under driven conditions) in order to induce the new (standing) dense phase.[18] If this is true, then the *escape* from this wetting layer could involve a first-order transition, where standing islands nucleate and grow out of the wetting layer. Hints for this scenario can be seen in Fig. 5.16 (top right): There is an abrupt increase in Q upon crossing the critical density $\rho \sim 1/L$ at high deposition quench rates, visible for data on $\epsilon = -2$. However, it is difficult to distinguish whether this transition has thermodynamic origins. In any case, we can say the dynamics are arrested. Moreover, for many other explored parameters in ϵ-regime IIIb, our simulations got "stuck" at the $\eta \approx 1$ state, and the simulation time expired before this transition scenario was captured.

Evidence for a first-order-type of thermodynamic transition existing in the monolayer growth systems (phase transition scenario (E) discussed in Sec. 5.3.9) mounts after particular modifications of this $L = 3$ system: It becomes clearly visible upon introducing a weak substrate potentials that favors the lying phase, the phenomenology of which we present in Sec. 5.5. It is also more visible in the case of longer rods ($L = 5$), which we present in Sec. 5.4. (We also see this type of transition is also visible for dimers ($L = 2$) at *attractive substrates*, see Sec. 5.7.2.) Monolayer growth is almost put to a halt when a such wetting layer forms, seen in a near "plateau" of $\rho(t^\star)$ in Fig. 5.17, where for $\epsilon \leq -3.33$

[18] We are cautious to use the phrase "free energy barrier" for these highly nonequilibrium situations.

only the onset thereof is captured, as the simulation expired upon reaching this "wetting layer".

Another phase transition scenario can be observed in ϵ-regime IIIb: As shown in Fig. 5.19, pronounced, compact islands of the lying phase may compete with standing islands. One may speculate this stage might occur upon crossing the metastable critical point $T_{\mathrm{cr,nem}}$ predicted by FMT (Fig. 5.2(b)), between two "nematic" phases, i.e. a lying–standing transition. We see a different form of three-phase demixing in what we dubbed as "regime IIIb": vapor, lying islands, and standing islands, and islands with lying–standing demixing. Some of the compact islands appear to be split between lying an standing phases, which we dubbed as "two-faced" (Fig. 5.19). In the figure, early stages of the evolution are characterized by both lying and standing compact islands appearing and competing, which we will discuss later in Sec. 5.3.9 as a typical part of phase transition scenario (C). However, at later stages of the same trajectory, the lying phase forms a (very coarse) "gel"-network with standing islands coarsening or growing at the same time (phase transition scenario (D)). This means this is likely a borderline case of (D) and (C).

Likewise in this ϵ-regime, the aforementioned "wetting layer", at nearly full packing fraction, has noticeably lower nematic order over longer periods of the growth trajectory than the arrested state seen in ϵ-regime IIIa (compare Fig. 5.14). Also, this dynamically arrested state at nearly perfectly full packing fraction $\eta \approx 1$ sets in at lower values of F/D than in regime IIIa, which attests to a higher stability of this "wetting layer". Later in Sec. 5.3.9, we will see that this low-Q-wetting layer corresponds to a different dynamical regime of the monolayer, where phase transition scenario (E) happens.

Two main "axes" controlling structure formation

We have attempted to demonstrate the effect of these two competing "axes" on the global nematic order Q by varying D/F over seven orders of magnitude and $1/|\epsilon|$ over a rather large range. Extreme cases of growth trajectories are seen best in the (η, Q)-plane, which become more disparate for lower temperatures, given the same set of parameters F/D. Just as a higher diffusion D/F (at fixed temperature) increases the bandwidth of possible events in between flux time-steps (farther reaches of space can be correlated via diffusive transport), and, thus, the complexity of the many-body processes at play, a very low reduced temperature T^* (or inverse attraction strength $1/|\epsilon|$) can have an analogous effect: As it "halts" motion locally (traps particles at first temporarily), long-ranged correlations can build up, leading to highly non-Markovian dynamics and collective, partly deterministic motion. Resulting structures are multifarious depending on the two main "axes" – $1/|\epsilon|$ and D/F – which control the likelihood and lifetimes of metastable phases, as well as the early stages of nucleation-and-growth kinetics, setting the final length-scales of phase-separated structures in the system (at any given density).

To visualize the effect of the two "axes" controlling the nonequilibrium dynamics, we have provided a map of configuration snapshots during growth in the $(\ln(1/|\epsilon|), \log(D/F))$–plane in Figs. 5.20 – 5.23. (We do not display the configurations of regime I.) Just as we have shown in Figs. 5.13 and 5.12 before, in regime III the lying dense phase (blue and yellow rods) forms network-like structures, which are favored at low D/F and can even dominate the entire monolayer. At very low reduced temperatures, compact lying islands

can form and compete with standing islands (magenta-colored clusters), where the lying phase appears to be metastable. At very high D/F, only standing clusters survive in regime III. In our categorization of ϵ-regime II, the only *compact* phase that grows in the form of islands is that of a standing orientation. In regimes II and III, higher densities imply larger length-scales in the system, as more time has passed and more power is exerted by the external deposition force (which enhances growth and ripening at late stages).

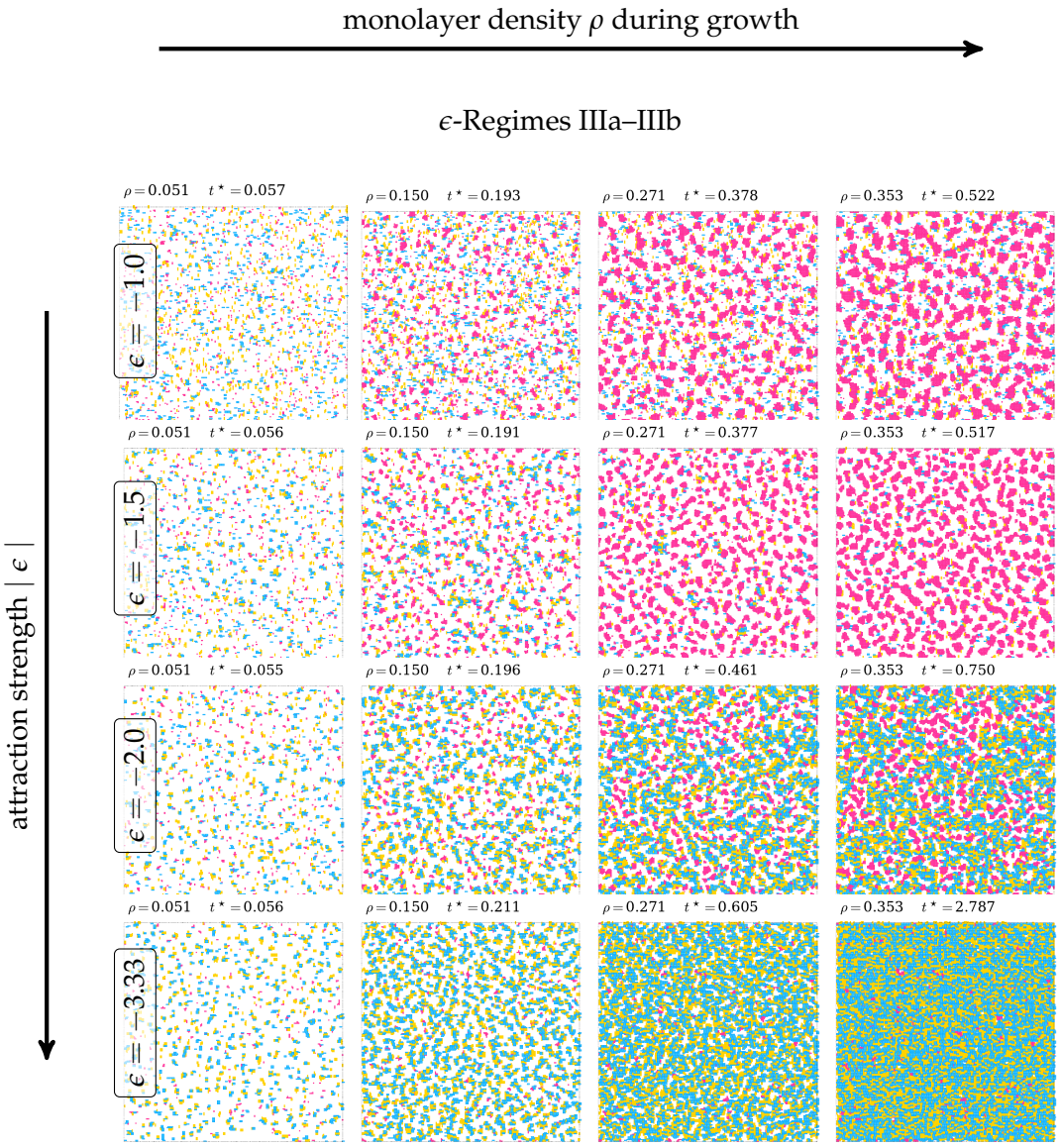

FIGURE 5.12: Configuration snapshots at three densities during monolayer growth via deposition for varying attraction strength $|\epsilon|$ within ϵ-regimes IIIa–IIIb at neutral substrates: $\epsilon \in \{-1.0, -1.5, -2.0, -3.33\}$. The dynamical parameters are fixed at $\{\gamma = 3.0, F/D = 1.67 \times 10^{-4}\}$. The "gel"-like, metastable lying liquid phase (blue and yellow) that can grow and ripen appears for stronger rod–rod attractions. It can form a wetting layer upon $\rho \gtrapprox 1/L \approx 0.33$ for strong attractions and fast deposition (see also example for $\epsilon = -2.0$ in Fig. 5.13).

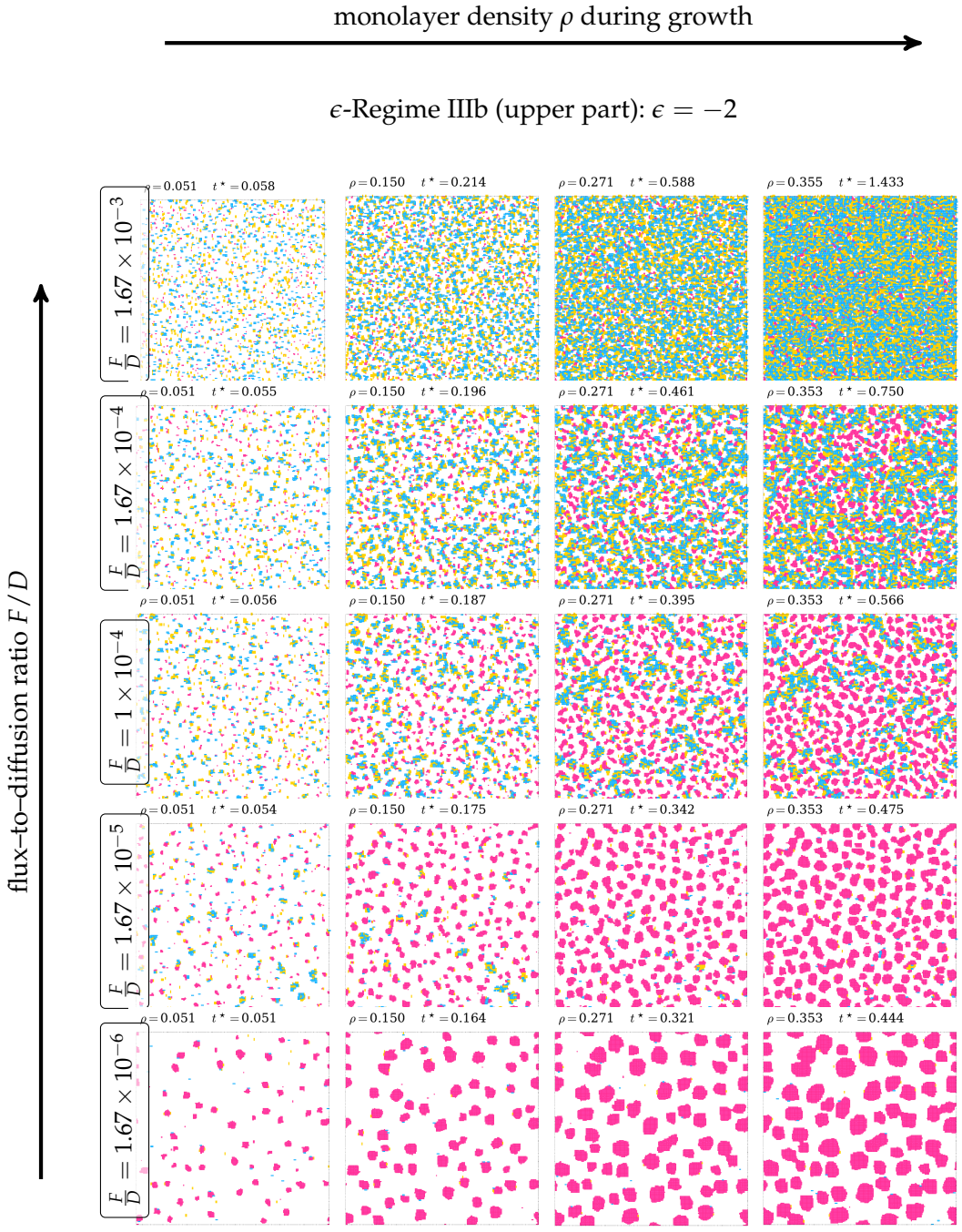

FIGURE 5.13: Configuration snapshots at four densities during monolayer growth in ϵ-regime IIIb (upper part) for varying F/D at neutral substrates. Here, $\epsilon = -2.0$ and the dynamical parameters are (top–to–bottom) $(\gamma, F/D) \in \{(3.0, 1.67 \times 10^{-3}), (3.0, 1.67 \times 10^{-4}), (0.5, 1 \times 10^{-4}), (3.0, 1.67 \times 10^{-5}), (3.0, 1.67 \times 10^{-6})\}$. A competition between lying (blue and yellow) and standing (magenta) phases is visible: An aggregating, metastable lying "gel" is favored with faster deposition rates F/D.

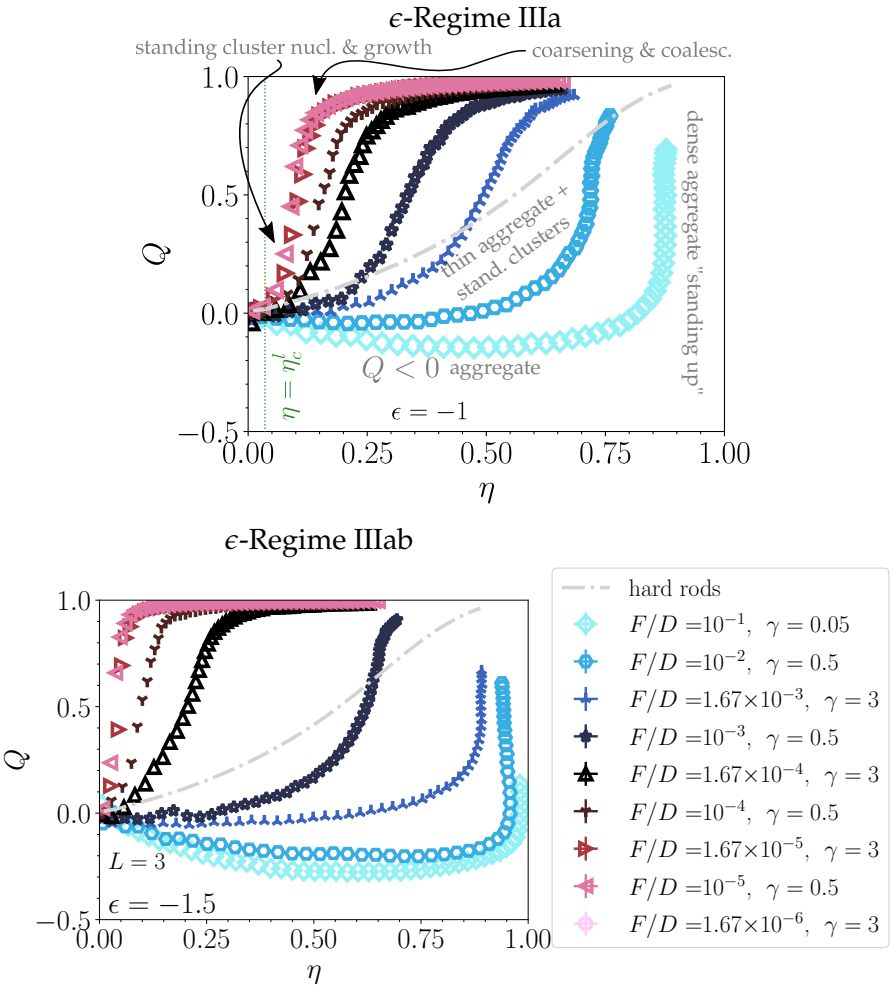

FIGURE 5.14: Nematic order parameter Q versus packing fraction (coverage) during growth of a monolayer for ϵ-regime III at varying F/D ($L = 3$): IIIa at $\epsilon = -1$ (left) and IIIab at $\epsilon = -1.5$ (right). The green lines indicate the packing fractions of the left binodals estimated by GCMC simulations (for $\epsilon < \epsilon_{\text{crit}}$). The gray dashed curve represents quasiequilibrium growth for purely hard-core rods ($\epsilon = 0$). Please compare to regime II in Fig. 5.9.

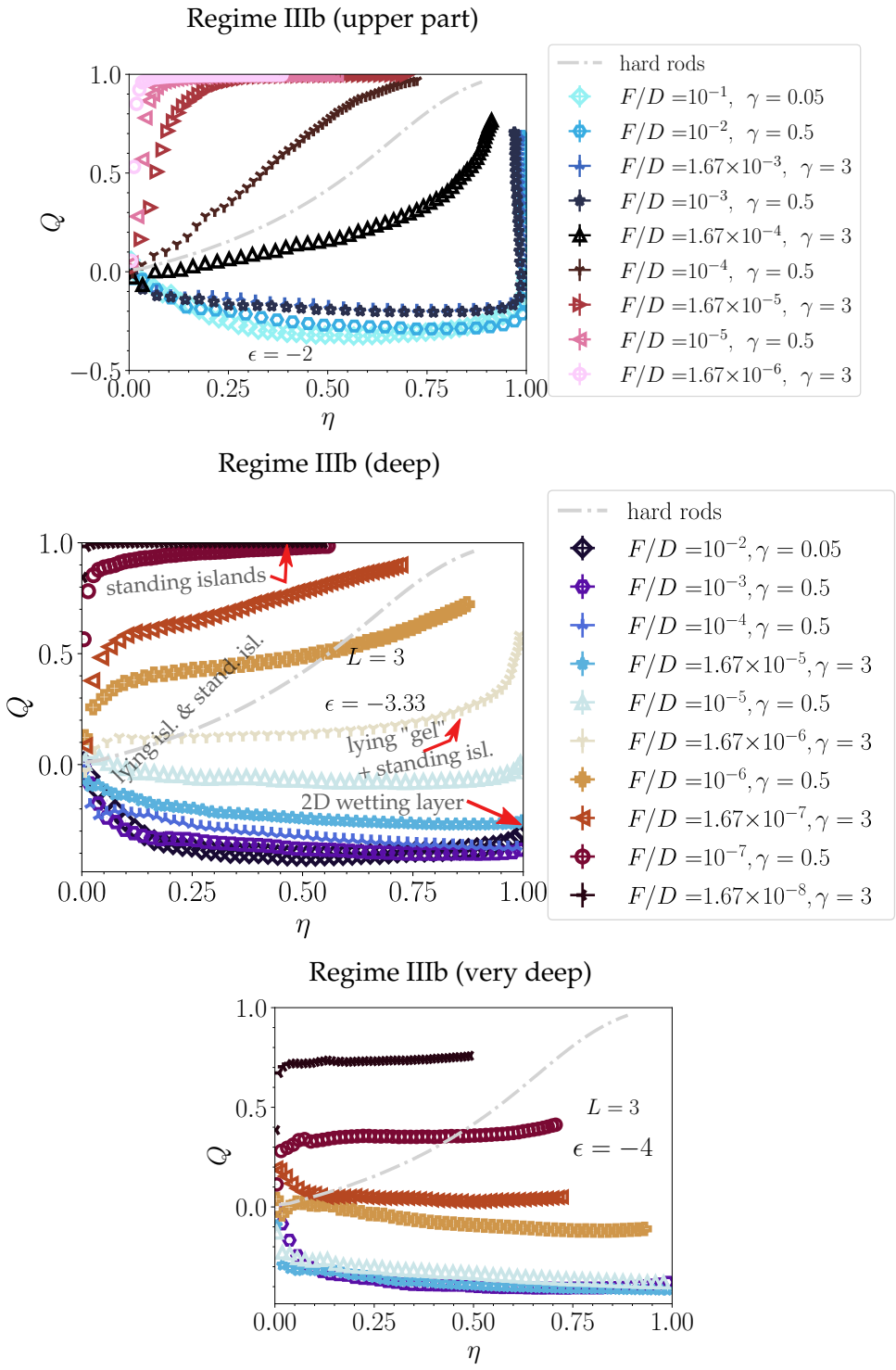

FIGURE 5.15: Nematic order parameter Q versus packing fraction (coverage) during growth of a monolayer of trimers deep in ϵ-regime III at varying F/D ($L = 3$). Trajectories are more extreme in the (Q, η)–plane compared to ϵ-regime IIIa (Fig. 5.14). For very strong ϵ ($\epsilon = -4$), Q remains nearly constant during the increase in coverage, indicating a nearly balanced, co-occurring growth of both lying and standing dense phases (discussed later, these are scenarios (C) and (D)). A nearly-2D "wetting layer" for $\eta = 1$ forms with a rapid deposition quench F/D (scenario (E)). "Only" the standing phase survives and grows ever earlier at ever smaller values of F/D (a limiting case of scenario (C)): At $\epsilon = -4$, $F/D \propto 10^{-8}$ does not yet suffice.

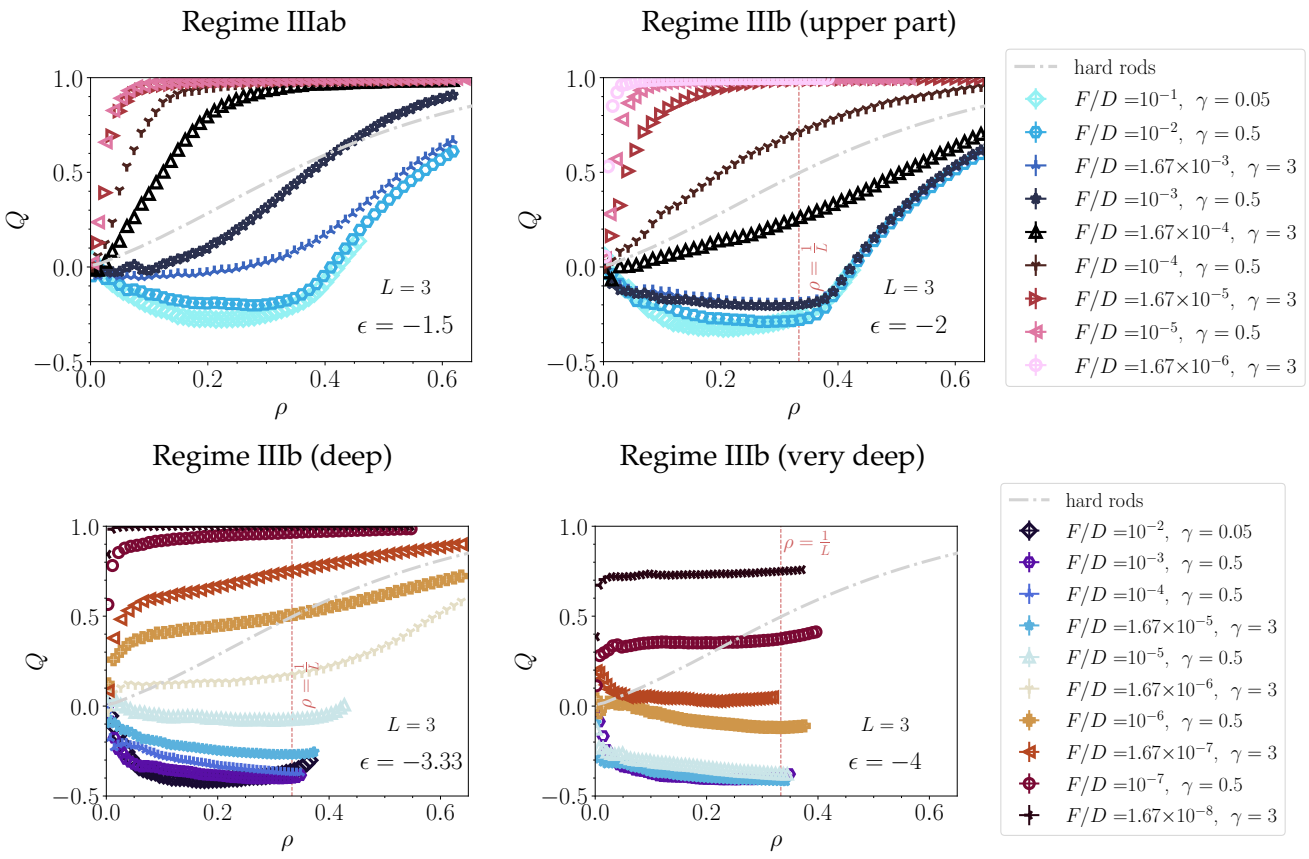

FIGURE 5.16: Global order parameter Q versus global density ρ at fixed attraction strengths for a sweep over F/D ($L = 3$) within ϵ-regimes IIIab–IIIb. Estimates of left vapor–liquid binodals are not displayed, as are very near 0. Nearly $\rho \approx 0.38$, the order parameter seems to undergo a (smeared out) "standing up" transition from a lying arrested state or "wetting layer". Later, we will see this occurrence corresponds to the dynamical regime when phase transition scenario (E) happens. The simulations were terminated around this point for deeper ϵ, they got "stuck", despite "high" F/D.

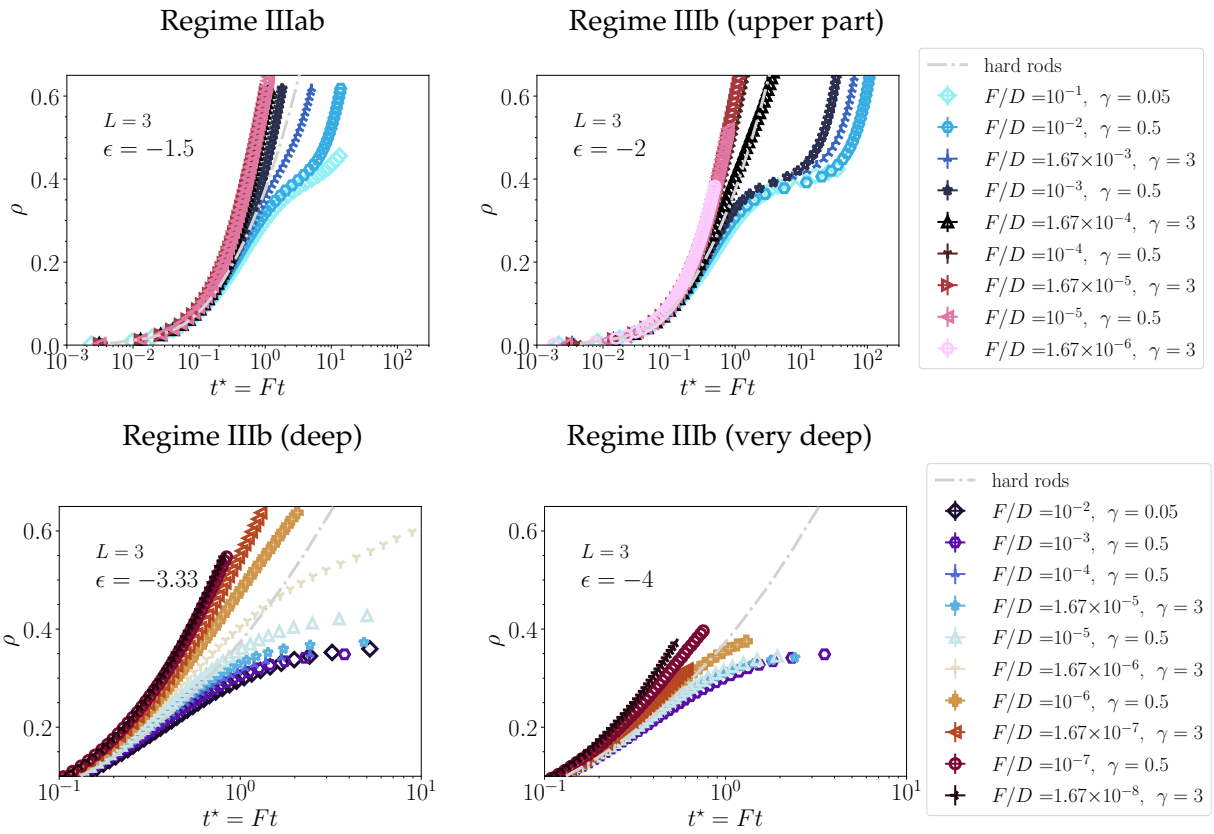

FIGURE 5.17: Global number density ρ rods versus time $t^\star$ rescaled with the attempt flux rate at fixed attraction strengths for a sweep over F/D ($L = 3$) within ϵ-regimes IIIab–IIIb. A near plateau is reached when the lying phase dominates the monolayer at nearly full packing fraction (a "wetting layer" forms). Later, we will see this occurrence corresponds to the dynamical regime when phase transition scenario (E) happens.

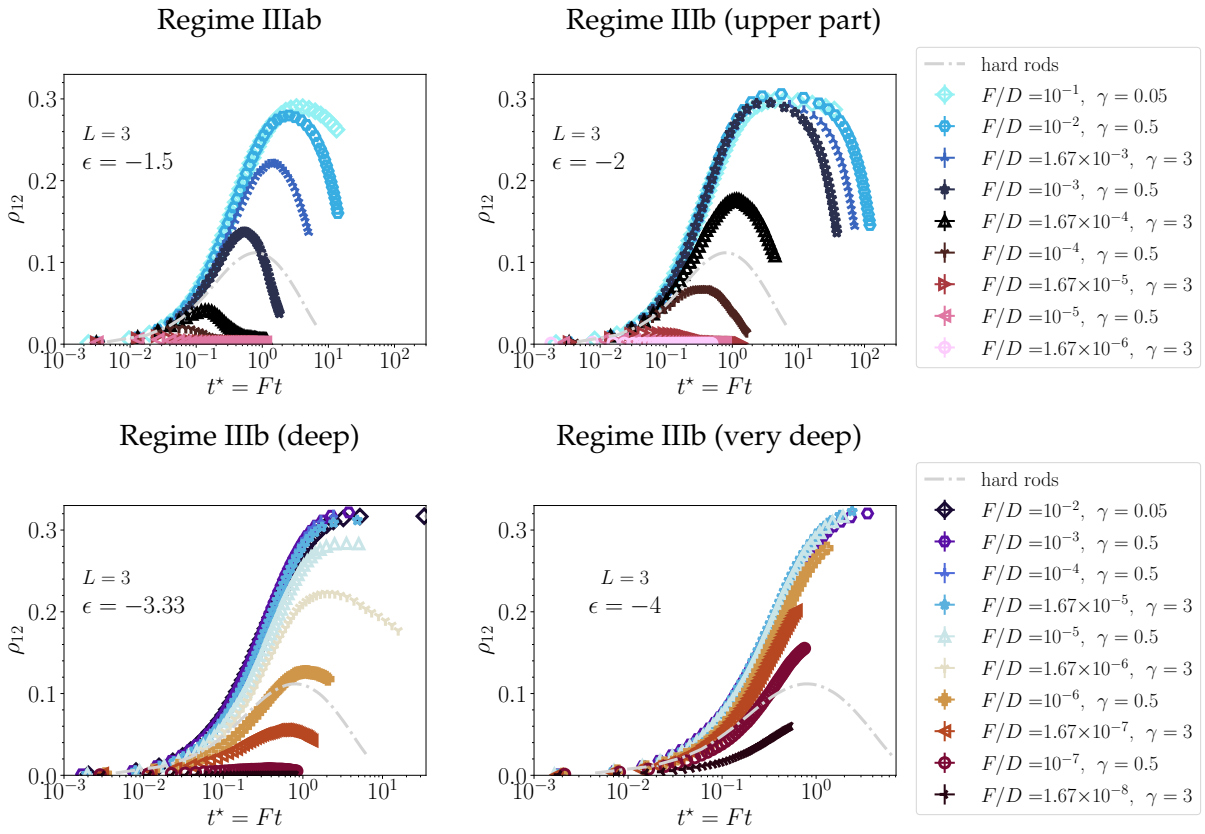

FIGURE 5.18: Global number density ρ_{12} rods versus time $t^\star$ rescaled with the attempt flux rate at fixed attraction strengths for a sweep over F/D ($L = 3$). The maximal reachable value is $\rho_{12} \leq 1/L \approx 0.33$, which is almost perfectly reached when the lying phase dominates the monolayer at nearly full packing fraction in regime IIIb. Later, we will see this occurrence corresponds to an extremely deep position in the dynamical regime when phase transition scenario (E) happens.

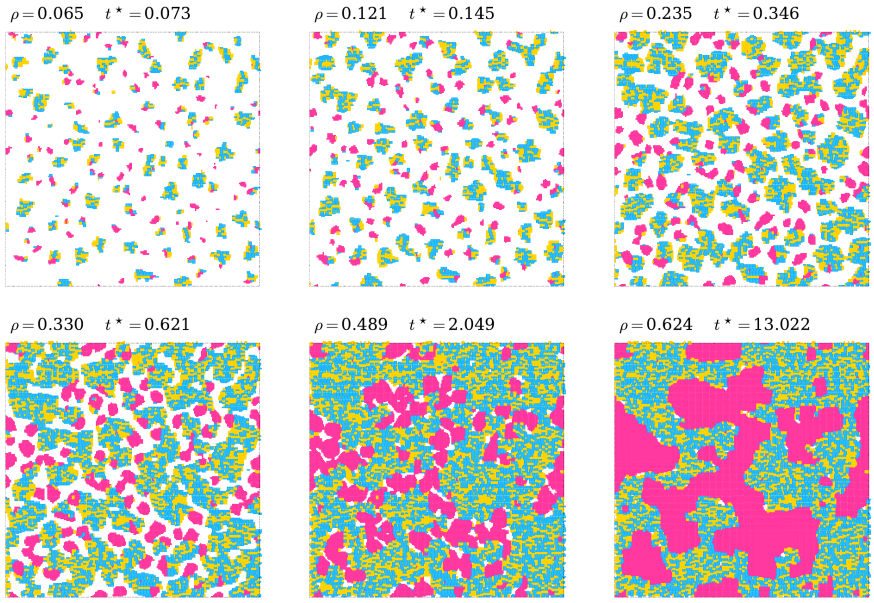

FIGURE 5.19: Snapshots during growth of a monolayer with $L = 3$ in ϵ-regime IIIb (deep), showing the existence of large, compact lying (blue–yellow) and standing (magenta) islands (a borderline case between phase transition scenarios (C) and (D)). As a subtlety, some islands become "two-faced" islands split between both phases. A network-like structure of lying rods forms later on, where eventually the vacancies are suppressed and eliminated. Thereafter, the stable standing phase begins to "eat up" the surviving lying phase. Specific parameters are $\epsilon = -3.33$, $F/D = 1.67 \times 10^{-6}$, and $\gamma = 3.0$.

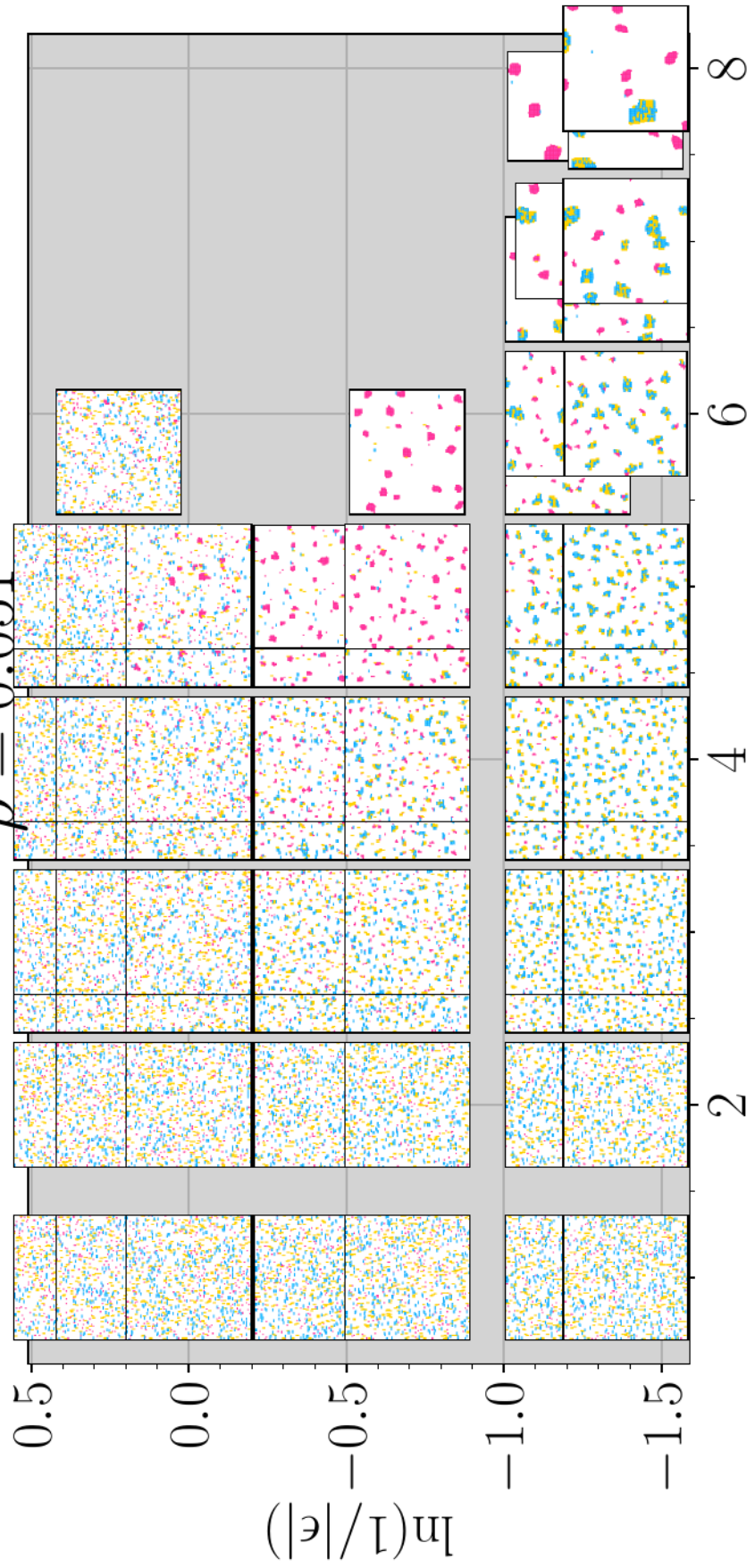

FIGURE 5.20: Schematic overview of snapshots during growth as plotted in the $(\ln(1/|\epsilon|), \log(D/F))$–plane at $\rho = 0.051$ in ϵ-regimes II and III ($L = 3$, neutral substrates), whereby the logarithm of the y-axis is taken in order to show more even spacing between sampled points. The top two rows are in regime II, the next two in regime IIIa, and the bottom two are deep in regime IIIb. Notice how regime II does not show standing (magenta) clusters, while regime IIIa, just below, does. Deep in regime III, we see large lying (green–yellow) clusters that co-occur with standing clusters at high D/F. Regime IIIa lacks large lying clusters at this density. Snapshots are approximately 128×128 unit-sized cutouts of the configurations, which are 256×256 in size. See Fig. A.16 in the appendix for the y-axis plotted as a function of ϵ instead, shown for regime III only.

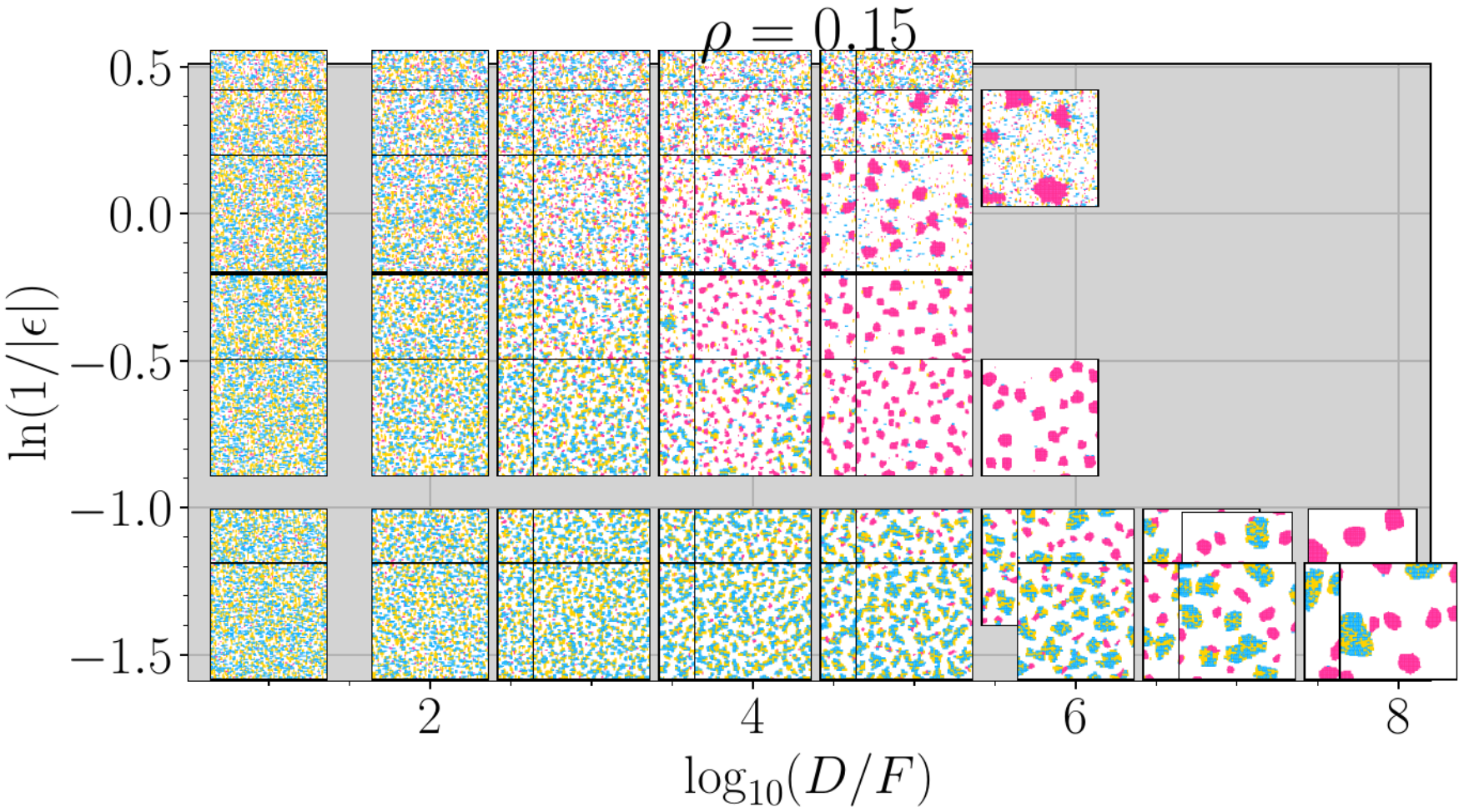

FIGURE 5.21: A continuation of Fig. 5.20 for higher densities, at $\rho = 0.15$. Notice how ϵ-regime II in the second row (corr. to $\epsilon = -0.8$) now does show standing (magenta) clusters that increase in size massively with higher D/F, once the left binodal has been crossed. Also, at this point, regime IIIa now does show lying clusters that are large, although quite aggregate-like in shape. Regime IIIb continues to show lying compact clusters co-occurring with standing ones. The coexistence of isolated lying and standing clusters in regime IIIb is quite remarkable. Deep in this regime, we can even see "two-faced" clusters, "split" between lying and standing orientations. At lower D/F, the lying phase begins to form a network. At very low D/F, the monolayer becomes covered with a majority of lying rods, forming an arrested state.

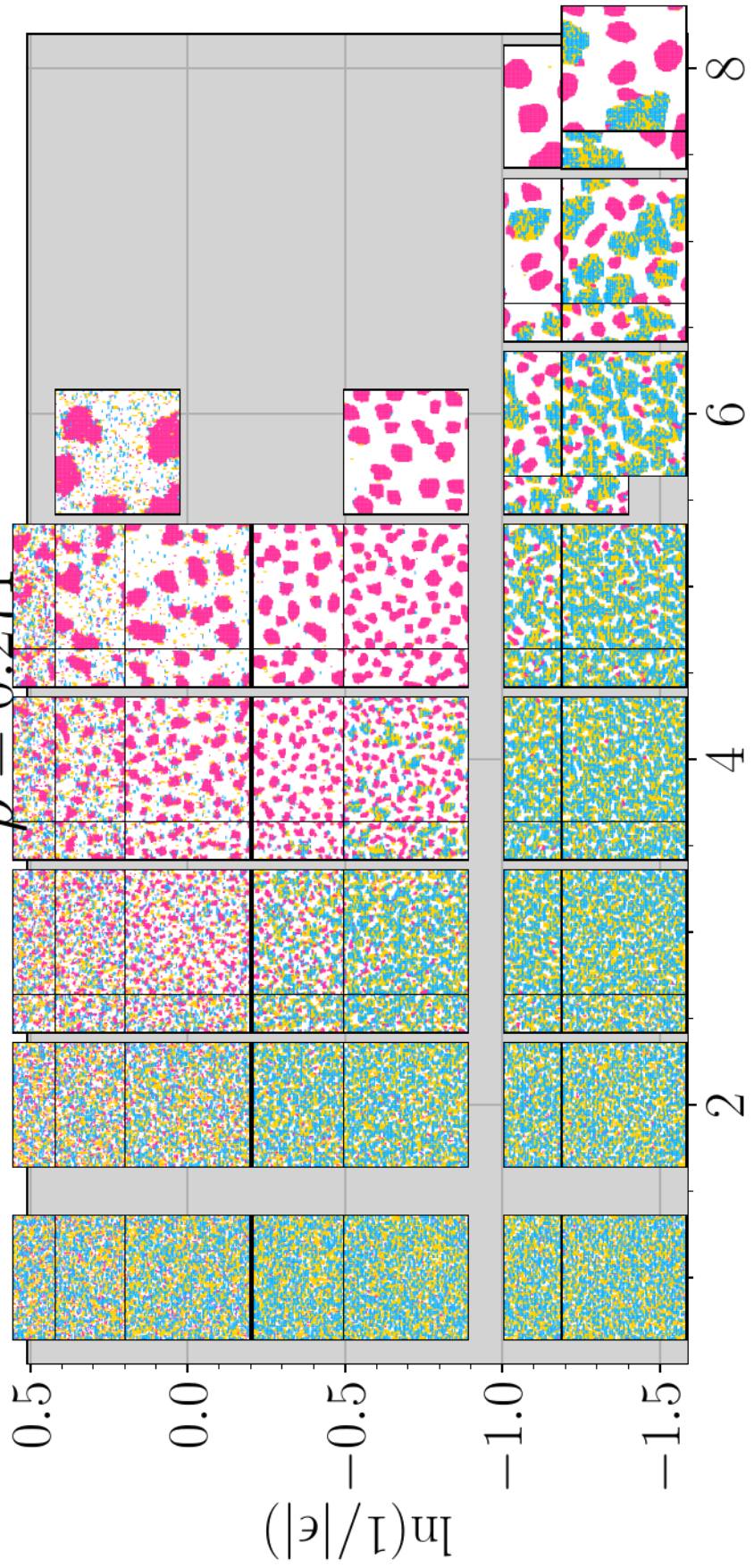

FIGURE 5.22: A continuation of Fig. 5.20 for $\rho = 0.271$. A comparison to Fig. 5.21 shows even larger cluster at high D/F, while at lower D/F, the lying phase forms a network or "gel" phase that is coarser than in the case of $\rho = 0.15$, with less vacant space for a vapor phase. At lowest D/F, the monolayer is almost fully covered with lying rods. Deep in regime IIIb, highly conspicuous "two-faced" clusters of competing lying and standing phases grow.

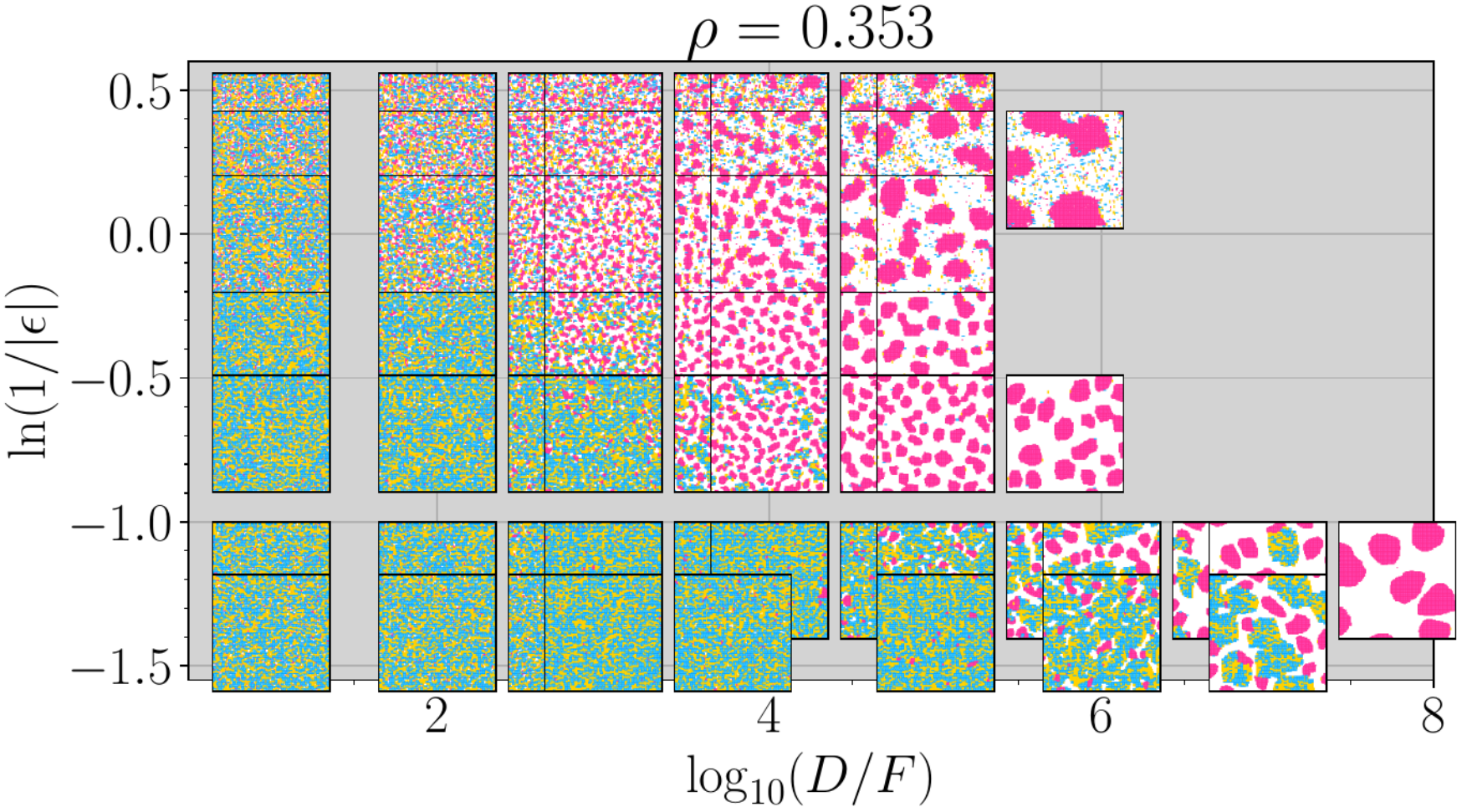

FIGURE 5.23: A continuation of Fig. 5.20 for $\rho = 0.353$. The "gel" like phase seems to continue to coarsen (possibly ripen in cluster number) compared to Fig. 5.22, see e.g. $D/F = 10^{-4}$ and $\ln(1/|\epsilon|) = -0.69$ ($\epsilon = -2$). In the extremes of low D/F, the lying phase may form a nearly-fully-packed lying arrested state or nearly-2D "wetting layer" (regime III).

5.3.6 Quantitative results: Effect of ϵ at fixed F/D on global order parameters

This section provides further quantitative results for growth of rods with length $L = 3$, showing the effect of ϵ when fixing dynamics with a particular F/D and γ. Figures 5.24–5.29 each show different aspects of the three ϵ-regimes we described before: We present here the behavior of the global nematic order parameter Q, global density ρ, lying density ρ_{12}, and the standing density ρ_3. (Note that some of the specific data-points are re-plotted from previous figures). These types of plots are found in later sections of this chapter for other cases, which is why we provide them here for our standard case of $L = 3$ at neutral substrates.

Figure 5.24 shows the effect of the reduced temperature on the global nematic order parameter during growth. Beginning with "warmer" temperatures in regimes I and II , we notice a drastic change in the behavior at $\epsilon = -1.5$ or $\epsilon = -2$ depending on the ratio F/D. These signal a pronounced appearance of a lying phase (regime III), which decreases the global order parameter. If the order parameter becomes negative, which occurs for low reduced temperatures, the monolayer can become arrested at full packing $\eta \approx 1$ with a lying global-mean orientation (the displayed simulations were cut off if the full packing fraction was reached). This is not the "end" state of the monolayer, which should be for $Q \to 1$. This fully-packed "wetting layer" is favored by low temperatures and high F/D. The nematic order parameter plotted against global density ρ is displayed in Fig. 5.25. Its time-evolution of Q is found in Fig. 5.26. The dynamics of the global density ρ, global lying density ρ_{12}, and standing density ρ_3 are plotted against a rescaled time variable $t^\star = Ft$, are likewise found in Figs. 5.27, 5.28 and 5.29, correspondingly.

* * *

Up to this point, the quantitative analysis presented included global order and number densities only. In a nonequilibrium system, especially one in which phase separation occurs, quantities that encode some information of mesoscopic-scales variables in the system provide another view on the structural evolution. We analyze and present cluster number densities, morphological measures, and percolation points in the following Sec. 5.3.7. Further, information extracted on the dynamics (motion) in the system provides complementary information about the evolution. We have constructed and analyzed particular dynamical observables from the rates of processes in the system, presented in Sec. 5.3.8.

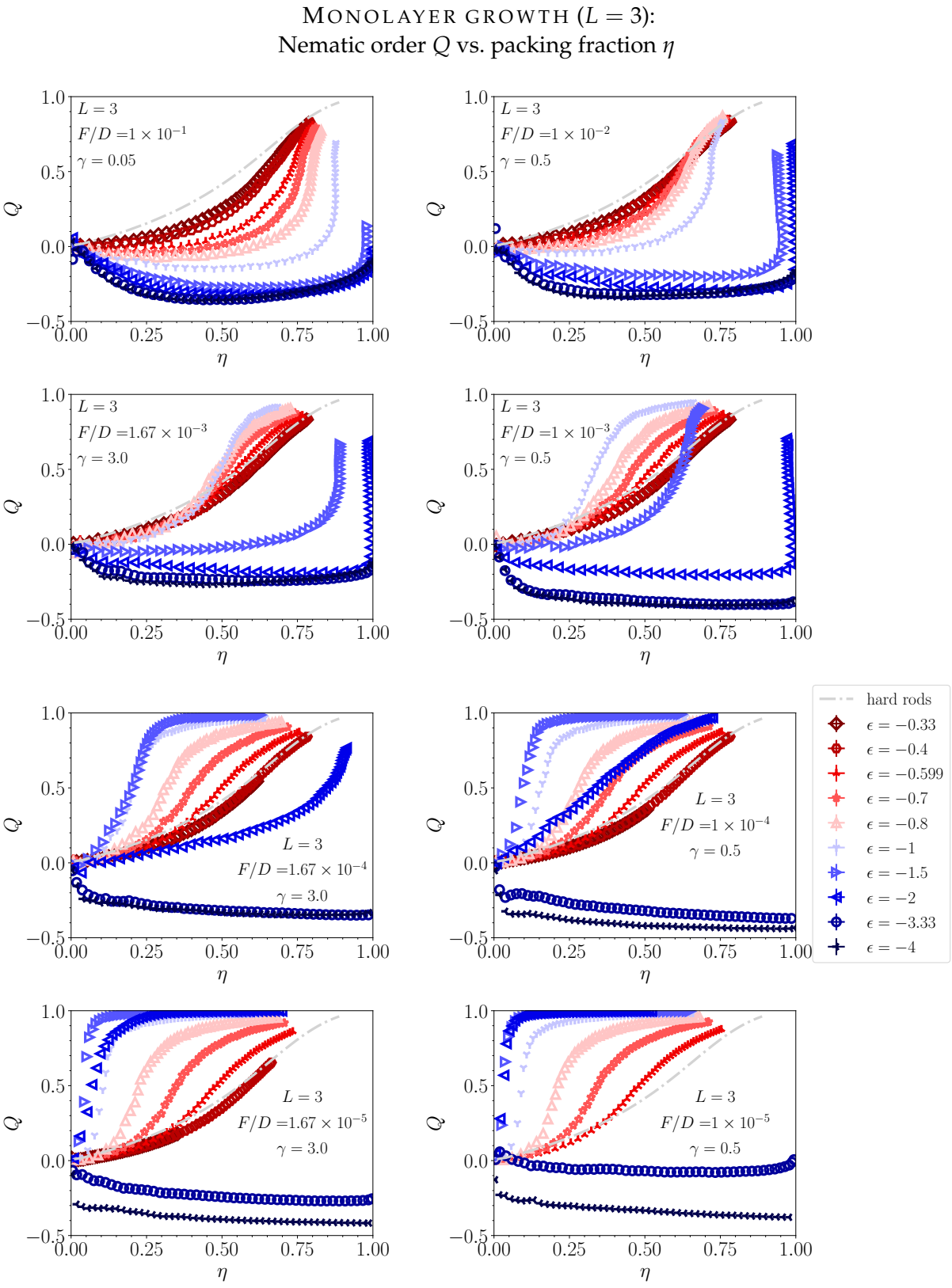

FIGURE 5.24: Nematic order parameter Q versus packing fraction (coverage) during growth of a monolayer of trimers at fixed F/D conditions: Comparison of attraction strengths ϵ. Beginning from weak $|\epsilon|$, regime II sets in around $\epsilon \lessapprox 0.6 \approx \epsilon_{\text{crit}}$ (rough estimate from GCMC simulations). Regime IIIa sets in around $\epsilon_{\text{crit, meta, denem}} \approx -1.0$, regime IIIab in $\epsilon \approx -1.5$, and regime IIIb below that. Note the striking similarity to Fig. 5.14, which was plotted in each case for varying F/D in regime IIIa–IIIab. The hard-rods curves represents quasiequilibrium growth for $\epsilon = 0$.

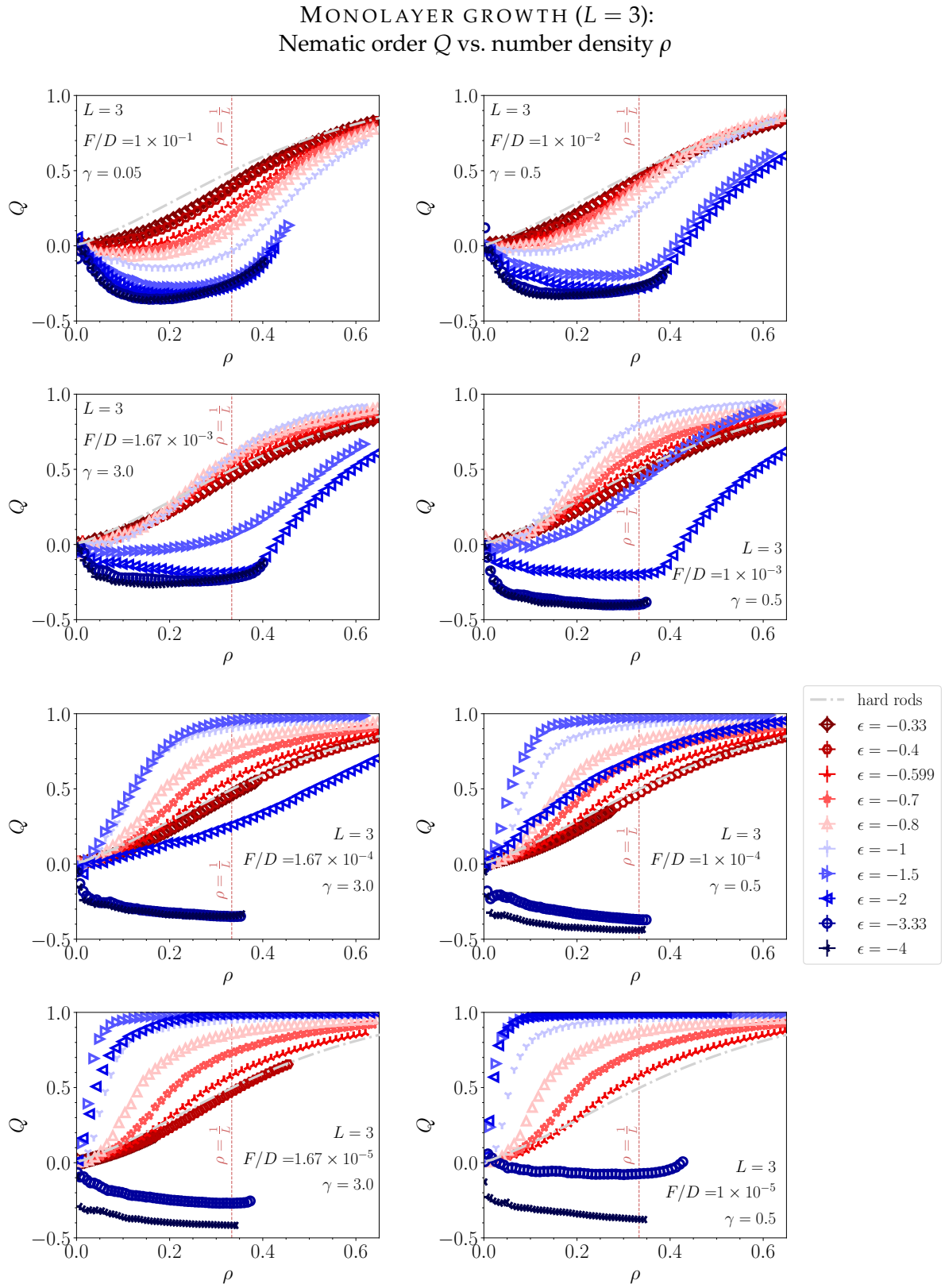

FIGURE 5.25: Global order parameter Q versus global density ρ (at a fixed F/D) for a sweep over attraction strengths ($L = 3$). Compare to Fig. 5.24.

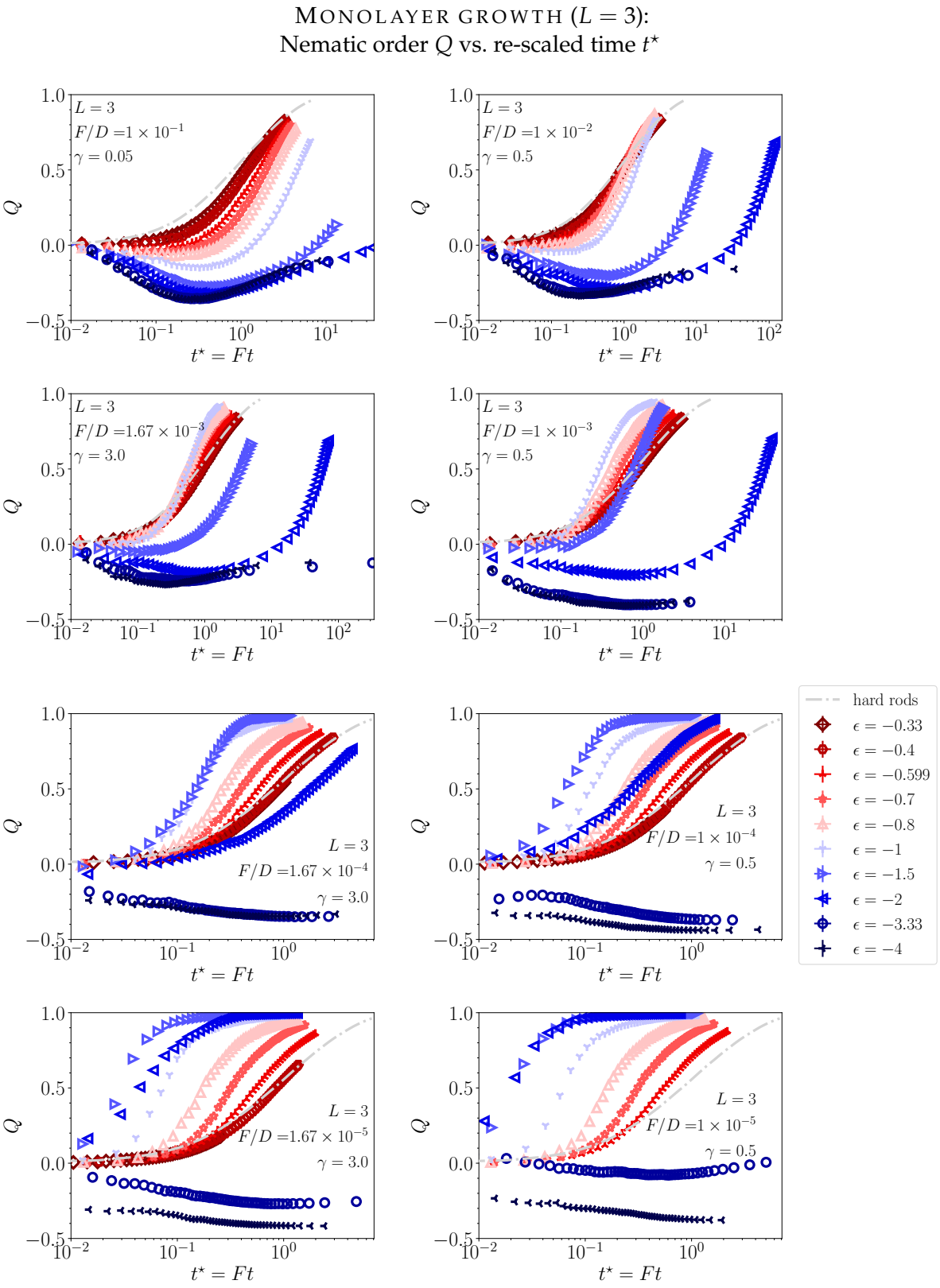

FIGURE 5.26: Global order parameter Q versus global density ρ (at a fixed F/D) for a sweep over attraction strengths ($L = 3$). Compare to Fig. 5.24.

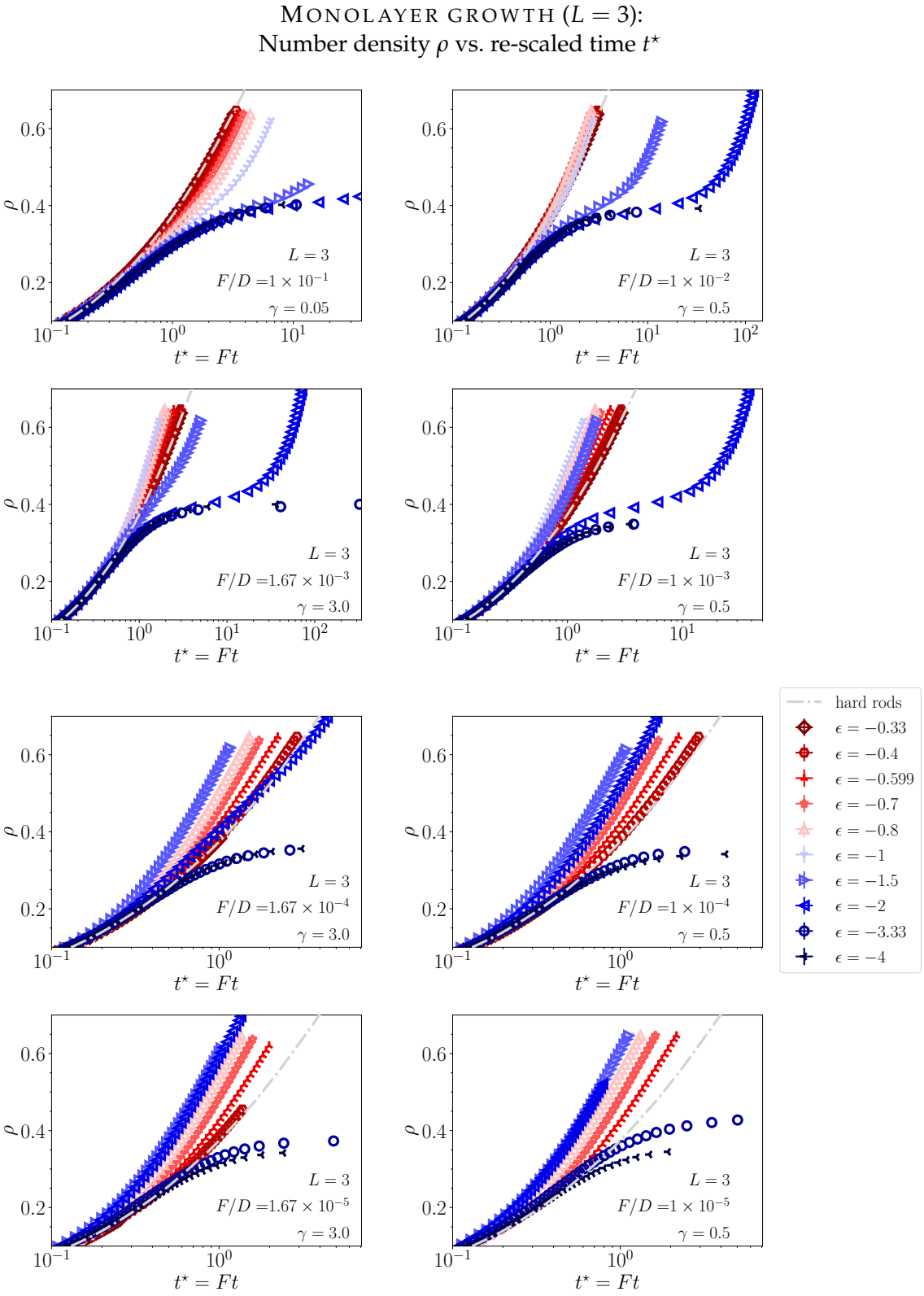

FIGURE 5.27: Global density ρ versus time $t^\star$ rescaled with the attempt flux rate (at a fixed F/D) for a sweep over attraction strengths ($L = 3$). Compare to Fig. 5.24. The log–log-scaled plots plot is found in the appendix (app. A.2, Fig. A.10).

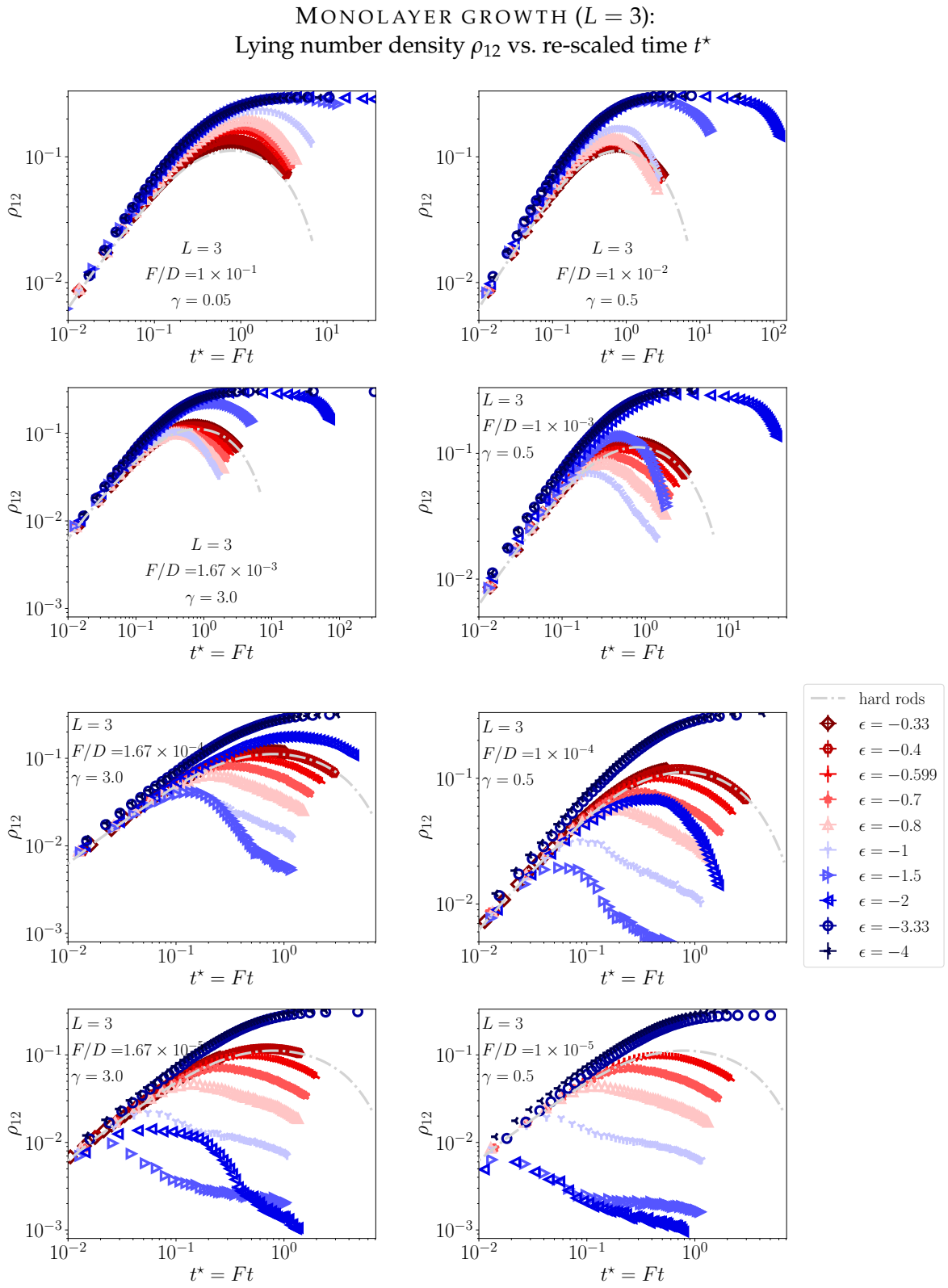

FIGURE 5.28: Global density ρ_{12} of lying rods versus time $t^\star$ rescaled with the attempt flux rate (at a fixed F/D) for a sweep over attraction strengths ($L = 3$). Compare to Fig. 5.24. The linear–log-scaled plots plot is found in the appendix (app. A.2).

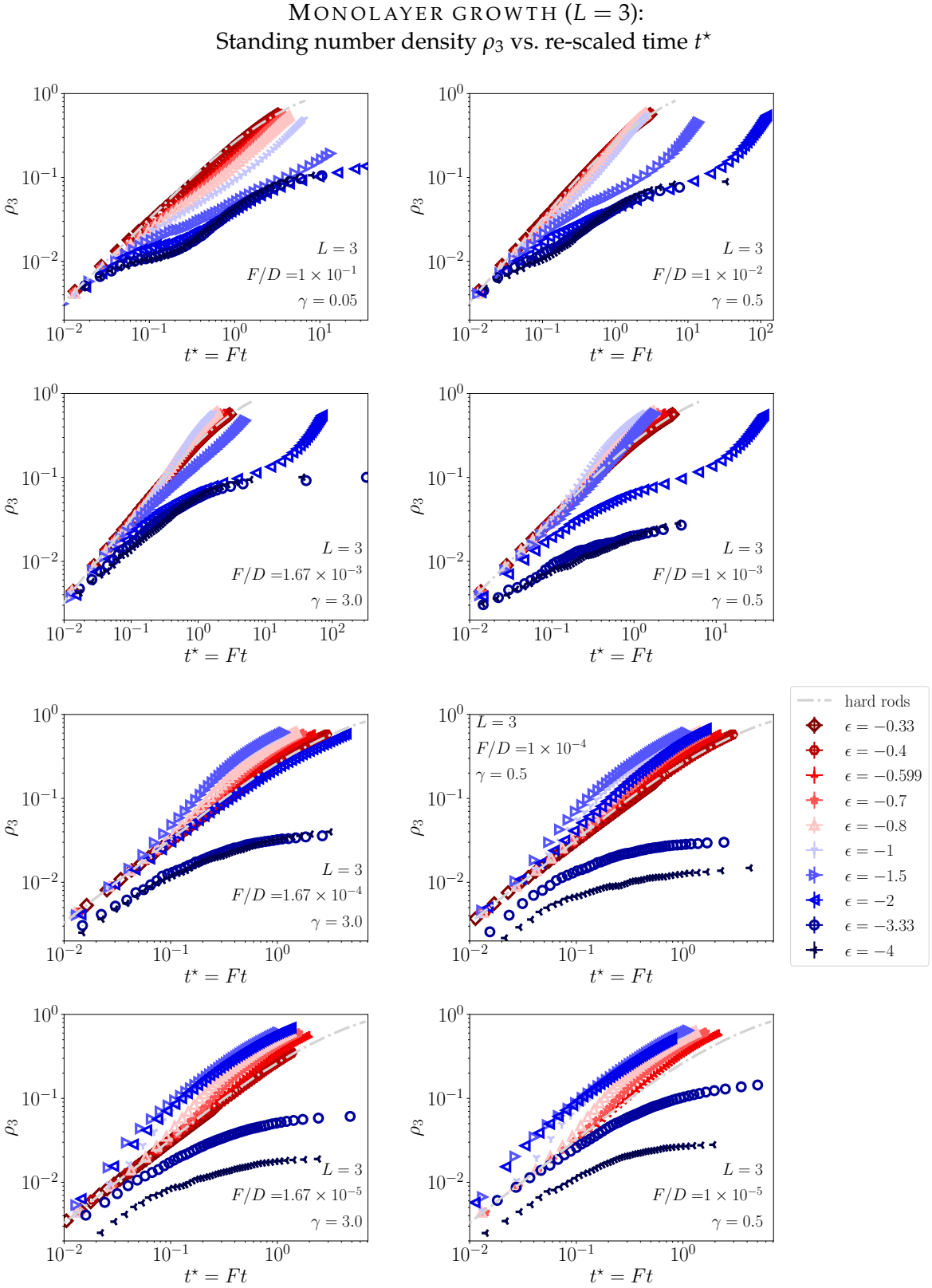

FIGURE 5.29: Global density of standing rods ρ_3 versus time $t^\star$ rescaled with the attempt flux rate (at a fixed F/D) for a sweep over attraction strengths ($L = 3$). Compare to Fig. 5.24. The linear–log-scaled plots plot is found in the appendix (app. A.2).

5.3.7 Further quantitative analysis: Clusters and morphology

In the following we shall present results of cluster statistics of (separately) lying and standing phases from simulation snapshots. We analyze growth only in ϵ-regimes II and III, where phase separation occurs. We have implemented a 2D, nearest-neighbor cluster detections scheme using the *Hoshen-Kopelman algorithm* [895] as a basis.[19] We note that we have not analyzed short-time fluctuations in the snapshots, hence a distinction between equilibrium fluctuations like in regime I and stable clusters that grow are technically difficult. We consider stable clusters after an (arbitrarily set) minimal cluster size that we reduce for stronger $|\epsilon|$: For regime II we chose $i_{\min} = 10$, for regime IIIa–IIIab[20] we chose $i_{\min} = 7$ and deep in regime IIIb we chose $i_{\min} = 4$ across any choice of orientation (lying or standing clusters). An important point of specification is that we construct or detect connected regions or clusters based on solely *lying* particles (a subset of ρ_{12}) or *standing* particles (a subset of ρ_3). We can also detect clusters defined as nearest-neighbors of *any* orientation, a few results of which we also present below. We clarify our use of notation regarding the orientation of particles is the cluster detection schemes below in Tab. 5.4.

NOTATION	MEANING FOR CLUSTER DETECTION
lying	Search for connected regions composed solely of lying rods
standing	Search for connected regions composed solely of standing rods
"any"	Search for connected regions composed of any and all rods

TABLE 5.4: Notation and meaning of orientational labels used to distinguish between different types of nearest-neighbor cluster detection cases.

We have further analyzed the clusters detected from the snapshots using Minkowski functionals W_ν,[21] which are morphological measures stemming from integral geometry, using the *marching square algorithm* of Ref. [896] (see an application thereof in Ref. [897]). As explained in the reference, such functionals can be defined by integrals of curvatures using differential geometry of smooth surfaces. Their numerical calculation is relatively "easy", especially for lattice systems: The Minkowski functionals are *additive*, so that in the detection program, a double *for*-loop over all pixels results in the overall value of the functionals.

In our quasi-2D case, the functional W_1 represents the total *area* or "mass" of clusters in configurations. The functional W_0 the total *boundary length* "surface area" of clusters[22] The topology can be further described by the Euler characteristic χ, which counts the number of clusters minus the number of holes in the system (it detects boundaries forming closed loops). In forthcoming plots, we normalize all quantities with the system size M^2, as these functionals should scale with it (for our physical system without boundary walls). Note that these

[19] We have modified this scheme to consider most cases of avoiding double-counting clusters that extend across the periodic boundary conditions.

[20] as well as $\epsilon = -2$, which is at the upper part of region IIIb

[21] The standard notation is actually "M_ν"

[22] The circumference W_0 is measured in the *1-norm*: The unit circle has circumference 8.

functionals must also be differentiated between lying, standing, and "any" as described in Tab. 5.4. All the functionals were processed *after* detecting clusters, which only count after reaching a minimal cluster sizes $i_{\min}$ that we described above.

Growth of regions of the standing, stable phase

We emphasize up-front that as we are analyzing clusters under *driven* nonequilibrium conditions. Growth laws of cluster numbers will be modified compared to at constant-density conditions, which are more typically investigated in the field of soft matter. (We have preliminarily investigated the growth laws at constant densities upon temperature-quenching, see Sec. 5.8.)

The cluster number densities of the stable, standing phase are found in Figs. 5.31 and 5.30 plotted as a function of ρ and $t^\star$, respectively. In regime II ($\epsilon = -0.7, -0.8$), the growth of standing clusters is noticeably delayed in comparison to that of regime III ($\epsilon \leq -1$). The left binodals set in at later densities in regime II, as depicted in Fig. 5.3. Fig. 5.31 clearly demonstrates how the onset of cluster growth is delayed towards higher densities, or later times in Fig. 5.30, the higher the deposition quench rate F/D. However, the minimal density (at lowest F/D at which the onset is visible should correspond to the left binodal density, which appears to be the case for regime II (for which we know the densities). In regime II, there is no significant change in the induction time of nucleation. The cluster number density shows its steepest growth rate there (compared to all other regimes), and saturates later on. Further in regime II, the cluster number densities drop rapidly after reaching a maximal value: this signifies the onset of coalescence of islands. The mean cluster size "takes off" in this region, as coalescence rapidly increases the size of clusters, see Fig. 5.32. The Minkowski functionals W_0 (total length of the standing-region borders) and W_1 (total area of the standing phase) in Figs. 5.33 and 5.34 continue to increase as the phase separation process continues with the unceasing addition of new particles.

The lying phase of regime III (which should set in at very low densities, according to the equilibrium FMT-predicted boundaries), which can later form a , aggregate or form a "wetting layer" in regime IIIb, clearly hinders the growth of the stable-phase clusters (standing clusters), see Fig. 5.32 ($\epsilon = -2, F/D = 10^{-2}$). Deep in regime IIIb, at $\rho \approx 0.05$ in Fig. 5.31 for the case of $\epsilon = -4$ seems to show rapid slowing in the growth of clusters for many cases of F/D. Visual inspection shows the appearance of both lying and standing compact islands for this density. In any case, the numbers increase again between $\rho \approx 0.3 - 0.4$, which we know from analysis in the previous sections to signify the "escape" from a nearly-fully-packed, lying "wetting layer".

One important point is that the cluster detection scheme may be picking up on quenched, random fluctuations,[23] which persist once the lying phase begins to dominate. However, discerning between classically nucleated clusters and a quenched form of density fluctuations is impossible via static analysis (of snapshots): An extended analysis in the future would correlate motion (rotational and translational fluxes) at the rim of the clusters with the structural signatures (for which we have already implemented the basic numerical scheme), possibly

[23] even though we have set a minimal cluster size cutoff ($i_{\min}$, described above)

better discerning the nature of the high-density 'clusters'. Returning our discussion to the lying "wetting layer", a standing-up transition from it signifies the rapid growth of the standing, quenched fluctuations (clusters). This may be a rather interesting phenomenon unique to the *driven* nonequilibrium dynamics of this system. We will further discuss the behavior when adding weak substrate potentials in Sec. 5.5, as the system can form vacancies (a vapor) between the lying and standing clusters, which might better signify the existence and growth of more classical "clusters" rather than quenched fluctuations. Further, preliminary analysis of temperature-quenching experiments at *constant* densities (rapidly reducing the temperature) – Sec. 5.8 – provide further evidence that the nucleation and growth of these standing clusters is clearly hindered by the lying phase in regime III, showing off a two-step process via two power laws.

We have also plotted the cluster number densities composed of *any* orientation, for completeness, in Figs. 5.35 and 5.36.

Evolution of the network-forming $Q < 0$ lying phases or $Q \approx 0$ nonequilibrium aggregates

We provide the Minkowski functionals W_0, W_1 and Euler characteristic χ of the lying phase in Figs. 5.37, 5.38 and 5.39, respectively. One might be confused by the presence of connected lying regions for regime II – at very low F/D this signifies that the vapor phase entails large enough density fluctuations in a lying orientation – the vapor phase may even entail more lying than "isotropic" domains, which might be in agreement with the FMT predictions for a "denematic" gas–liquid transition. Visual inspection verifies that the "vapor" phase does contain many lying rods that are transiently connected in a nearest-neighbor fashion. During very fast deposition, the monolayer system forms a $Q \approx 0$ aggregate, which dominates the system up to very high packing fraction. The morphological analysis for regime II in these cases are that of this highly nonequilibrium state. Even more so, the lying rods in this aggregate form a percolating network, see next subsection, which is another hint that the particle dynamics are out-of-equilibrium and *arrested*.

In ϵ-regime III, the lying phase mostly exists in the form of a liquid phase that can be described as "gel-like" (see previous discussions). The functional W_1 gives an estimate for the total area (packing fraction) of this phase, which reaches a maximal value (possibly almost 1) before eventually decaying, as it is metastable. The functional W_0 can provide an estimate to the boundary (line area) of this phase to the vapor or standing phase. For fast growth in regime III, the line area can show a loop, indicating morphological reordering processes before the phase decays. The Euler characteristic χ in this time period decays and rapidly switches sign, indicating a predominance of "holes' rather than closed clusters in the system (notice the characteristic does not consider any minimal cluster number and is purely topological and morphological in nature). The percolation of the lying phase is discussed in the next section, occurring near, but not exactly at the zero-crossing-point of the Euler characteristic.

Percolation transitions under driven nonequilibrium conditions

During growth, the topology of the dense phases becomes fundamentally different upon a percolation event, where a cluster spans the entire system. Percolation transitions are of fundamental interest for statistical-mechanical systems, and exemplify self-organized criticality found in many kinds of many-body systems. In our case, we can see evidence for a *nonequilibrium* percolation transition, in the sense that it appears during the *driven* nonequilibrium growth of a monolayer. We define the percolation "probability" as the binned average over evolving snapshots that entail *binary* values for percolating clusters (1 indicates *any* detected cluster percolates, 0 indicates that no detected cluster has percolated).[24]

If we analyze the lying phase only, the percolation transition gives crucial information about the network structure of the lying, $Q < 0$ phase of matter in regime IIIb. Figs. 5.40 and 5.41 below show our results for the percolation of the lying phase versus re-scaled time and density, respectively. After this point, the phase of matter "ripens", where local length-scales in the gel grow, which we can see via visual inspection as well as in quantitative measures like the total area (W_1 in Fig. 5.34) and the Euler characteristic (χ in Fig. 5.39). As this gel phase is transient, however, an *anti-percolation* point also appears, after which the phase of matter inevitably decays. The time-span between the percolation and anti-percolation point is an excellent measure for the lifetime of the phase in these driven nonequilibrium conditions, as its growth and decay are quite rapid.

One interesting finding is that even regime II shows a lying percolation and anti-percolation transition in Figs. 5.40 and 5.41. The anti-percolation point gives us information when the lying phase (if it had percolated) irreversibly dissolves. Unfortunately, we cannot verify this for all values of F/D, as our simulations ended prematurely.[25] Exceptions are seen for the extremely high deposition quench rate, $F/D = 1 \times 10^{-1}$. This is evidence for a highly nonequilibrium state in regime II, where only standing compact clusters can form at low enough deposition rates, and signifies arrested dynamics of (lying) rods. The percolation transition occurs soon after the estimated equilibrium left binodals that are found in Fig. 5.3. The anti-percolation transitions for a fast deposition quench $F/D = 10^{-1}$ of regime II ($\epsilon = -0.7, -0.8$) occurs around $\rho \sim 0.42 - 0.45$. This is coincidentally near the green (isotropic–isotropic) boundary line predicted by FMT in Fig. 5.2(b).

As we have discussed in this chapter and in Ch. 2.3, a fast deposition quench F/D is akin to lowering the temperature, in some respects: In regime II, where a does *not* form, the metastable transition at lower temperatures seems to be *foreshadowed* by quenching the system rapidly (via deposition). Moreover, a right thermodynamic binodals of regime II are comparable to the densities of the anti-percolation transition in this highly nonequilibrium evolution. Connections between dynamical percolation and metastable binodals in the phase diagram are not clear at all from the theoretical side, and the topic may be worthy of further attention with more focused investigations.

[24] We only analyzed single runs, which is why the probabilities are highly prone to noise.

[25] At this point we would like to communicate that the institute at which the author wrote this thesis has poor management of electricity infrastructure. Unnecessary power cuts were announced less than two weeks in advance, forcing us to stop many of our simulation runs for deep ϵ's prematurely.

Further, we analyzed the percolation behavior of connected regions formed by *any* orientation of rods, in Figs. 5.42 and 5.43. Physically, the percolation transition for very low F/D, when there is a vapor phase, can signify the anti-percolation point of the vapor itself, i.e. when it is is split into disconnected regions. In cases of very high deposition quench rates, this should also be roughly true, but we emphasize that even a "vapor" phase can be out-of-equilibrium. For high deposition quench rates, the percolation of the system occurs earlier (in time and ρ) for deeper reduced temperatures (a slight "switch" between $\epsilon = -4$ and $\epsilon = -3.33$ is visible, but may not be significant). The "sticky" attraction between rods certainly seems to favor the connectedness of the rods in the system. As the quench rate F/D is lowered, the re-scaled time-points at which this occurs begin to separate ever more depending on the reduced temperature. Many of the "late" transitions seem to occur around $t^\star = 1$, correspond to densities in the range of $\rho = 0.35 - 0.6$. At these densities, FMT predicts a load of things happening in the equilibrium phase diagram: At densities around $\rho \sim 0.3 - 0.4$, FMT predicts the system to cross a "denematic gas–liquid binodal" between two states of low degree of order. Further, the FMT predicts another metastable boundary at global densities around $\rho = 0.55$ for a reduced temperature that is probably situated in the middle of our regime II: the FMT denotes this point as the first-order transition between two differently-ordered phases (a "nematic–nematic" transition). Whether or not the percolation points only coincidentally agree with the metastable binodals or boundary lines is fully unclear, but, offers food for thought for future investigations.

To this end, the percolation points of the *standing* connected regions is shown in Figs. 5.44 and 5.45. In many low F/D cases where the simulations did not terminate prematurely, the standing percolation transitions occur around $t^\star = 1$. A "late" case is found for $F/D = 10^{-3}$, where the standing phase percolates around $t^\star \approx 30$. This happens after the lying aggregate or "wetting layer" had to be overcome, the percolation transition occurring at very high density ($\rho \sim 0.68$).

We are well aware that percolation data presented here are noisy and partly incomplete, as many simulation runs would have to be continued for higher densities. Nevertheless, we hope these results still prove a point, namely, that the percolation behavior contains crucial information on structure formation in the monolayer, depends on the dynamical parameters of the driving force, and, thus, depends on the history of each trajectory. Relationships to thermodynamics are completely open and seem worthwhile investigating, as this would be a fundamental connection between driven nonequilibrium behavior and equilibrium theory; specifically, unexpected nonequilibrium information might be contained in the FMT free energy functional. Averaging over multiple runs to obtain preciser estimates of these transitions remains out of the scope of this thesis.

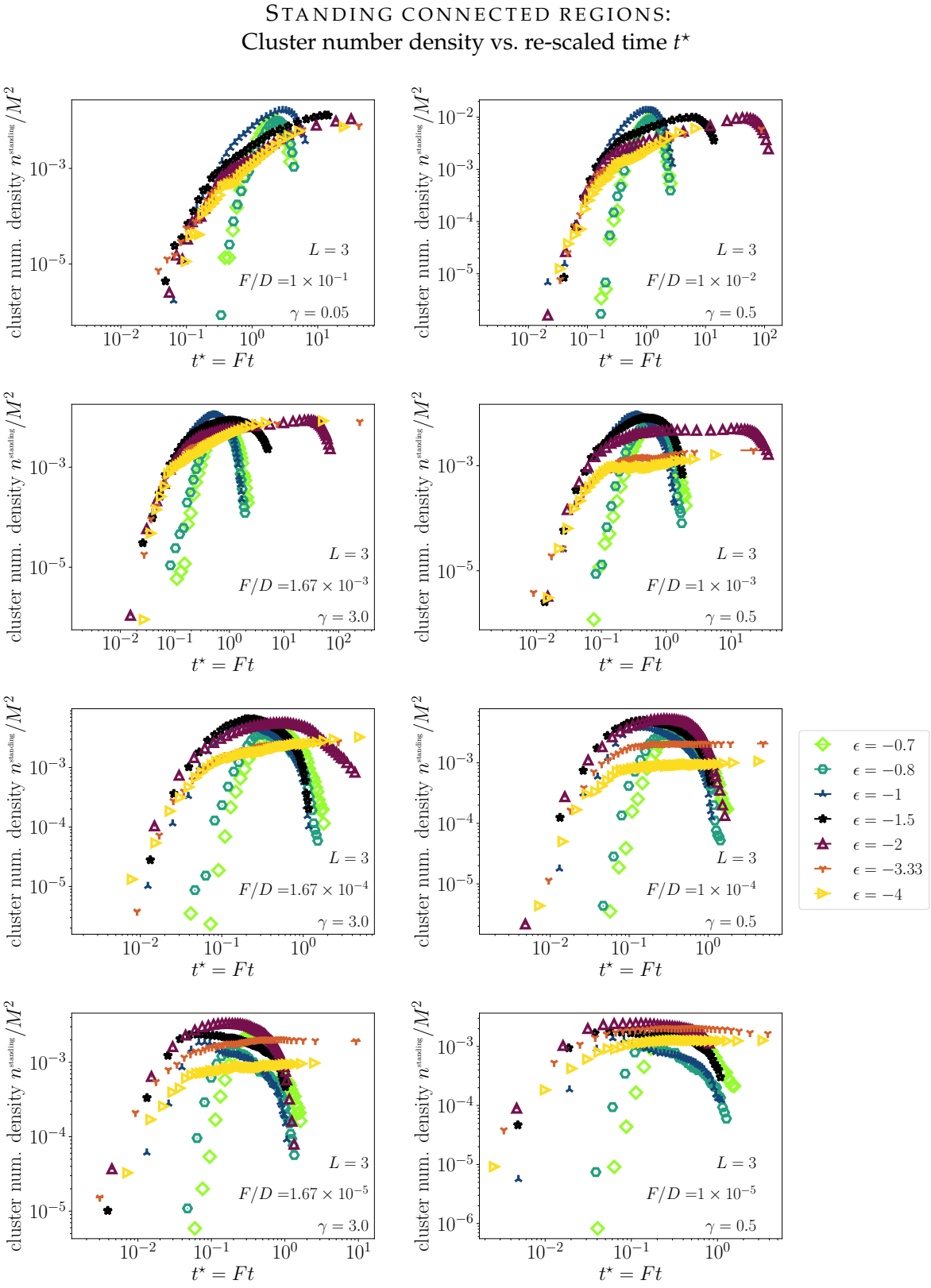

FIGURE 5.30: Cluster number density of standing clusters versus re-scaled time $t^\star$(at a fixed F/D) for a sweep over attraction strengths ($L = 3$).

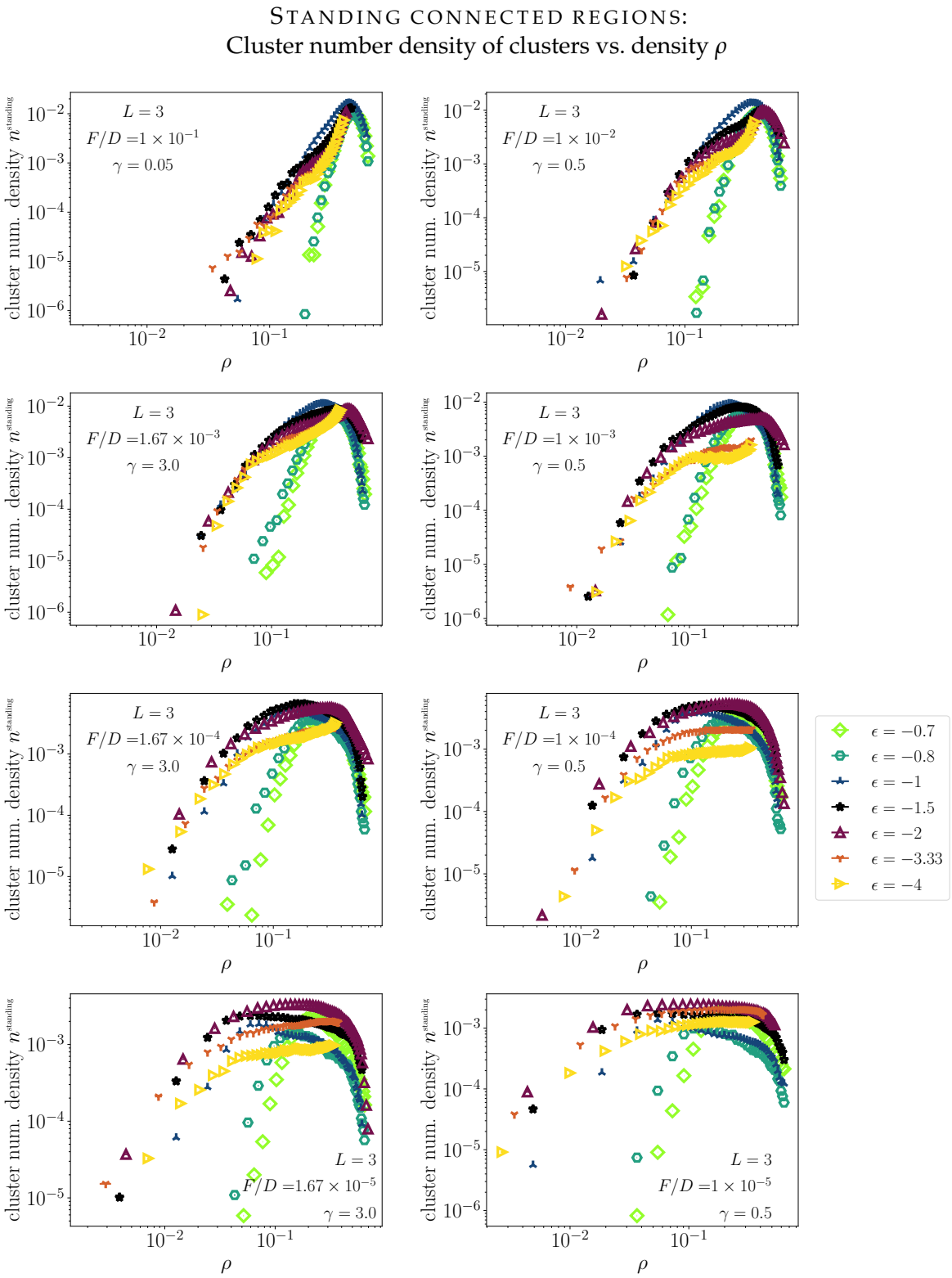

FIGURE 5.31: Cluster number density of clusters composed of standing particles versus global density ρ (at a fixed F/D) for a sweep over attraction strengths ($L = 3$).

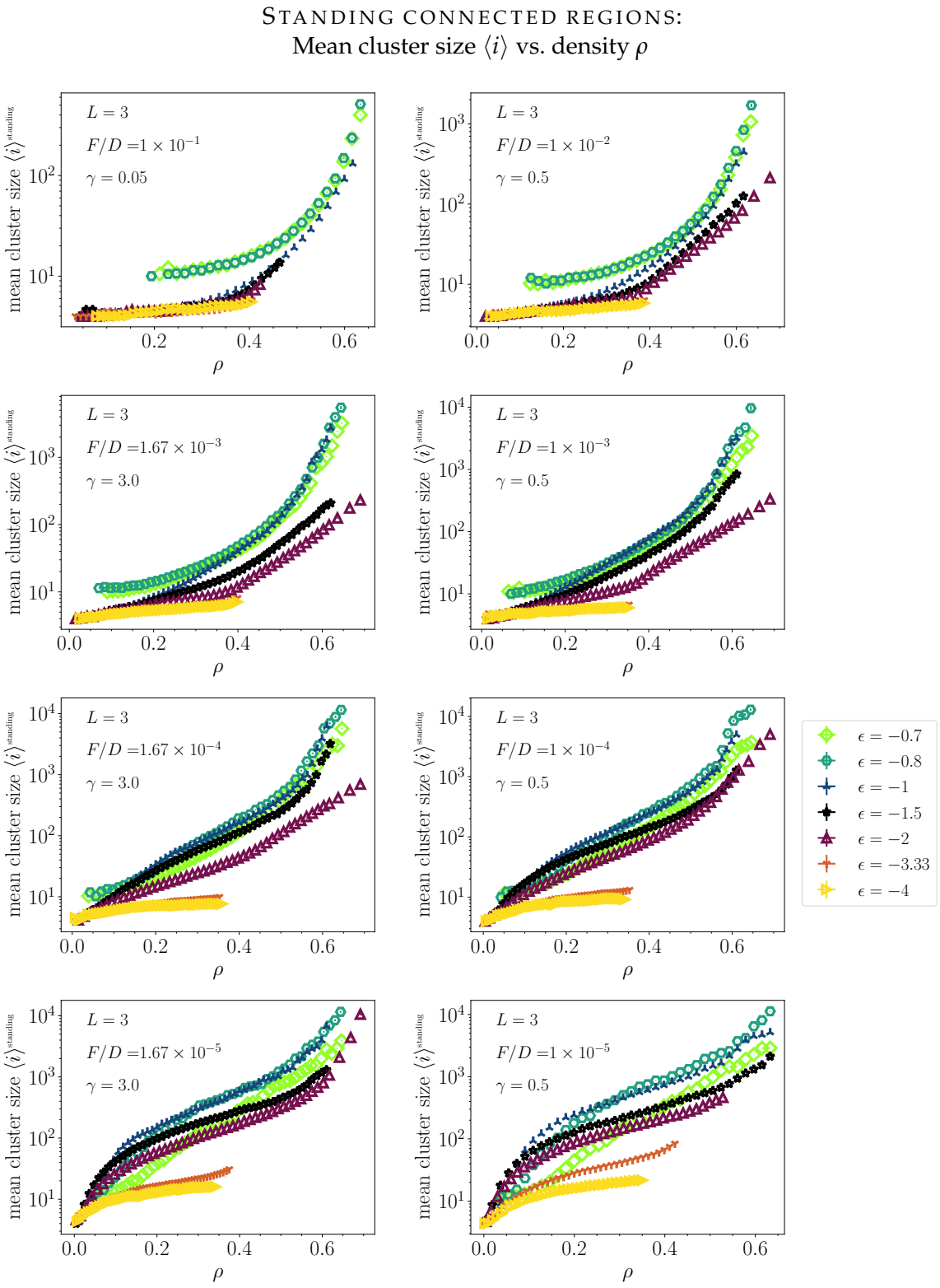

FIGURE 5.32: Mean cluster size of standing clusters versus global density ρ (at a fixed F/D) for a sweep over attraction strengths ($L = 3$).

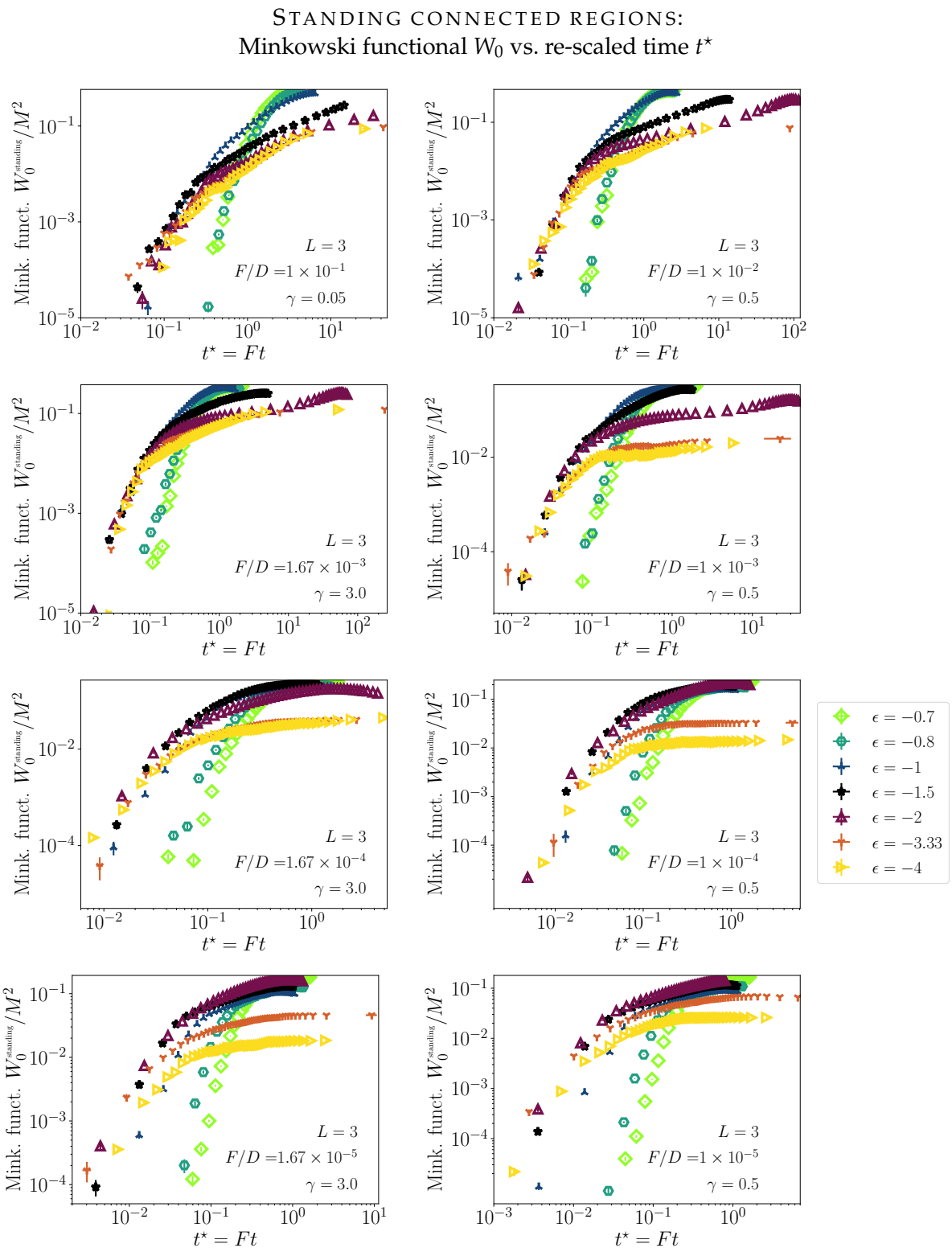

FIGURE 5.33: Minkowski functional W_0 of standing clusters versus versus re-scaled time $t^\star$ (at a fixed F/D) for a sweep over attraction strengths ($L = 3$).

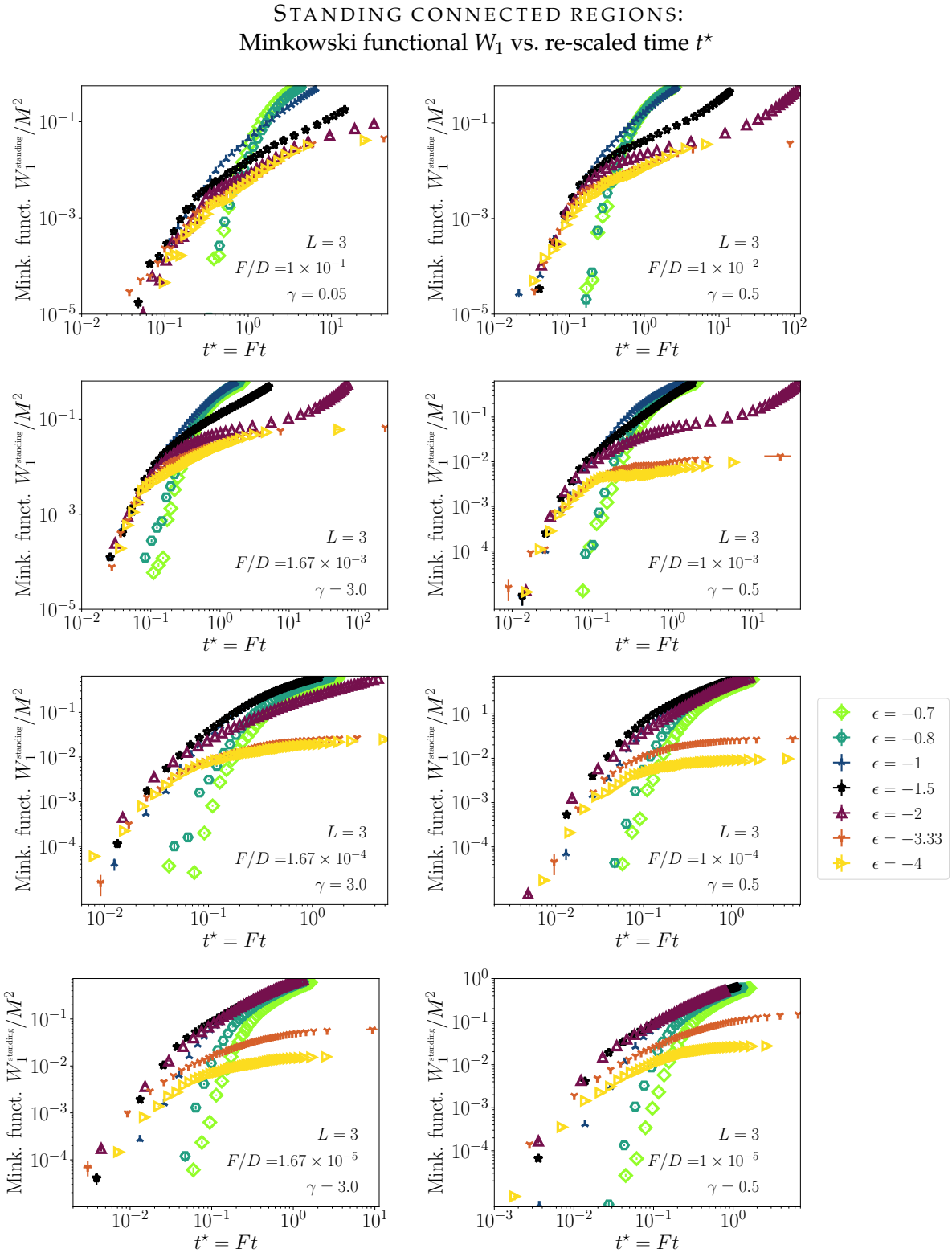

FIGURE 5.34: Minkowski functional W_1 of standing clusters versus re-scaled time $t^\star$(at a fixed F/D) for a sweep over attraction strengths ($L = 3$). Compare to Fig. 5.33.

ANY DENSE-PHASE OR CONNECTED REGION:
Cluster number density vs. re-scaled time $t^\star$

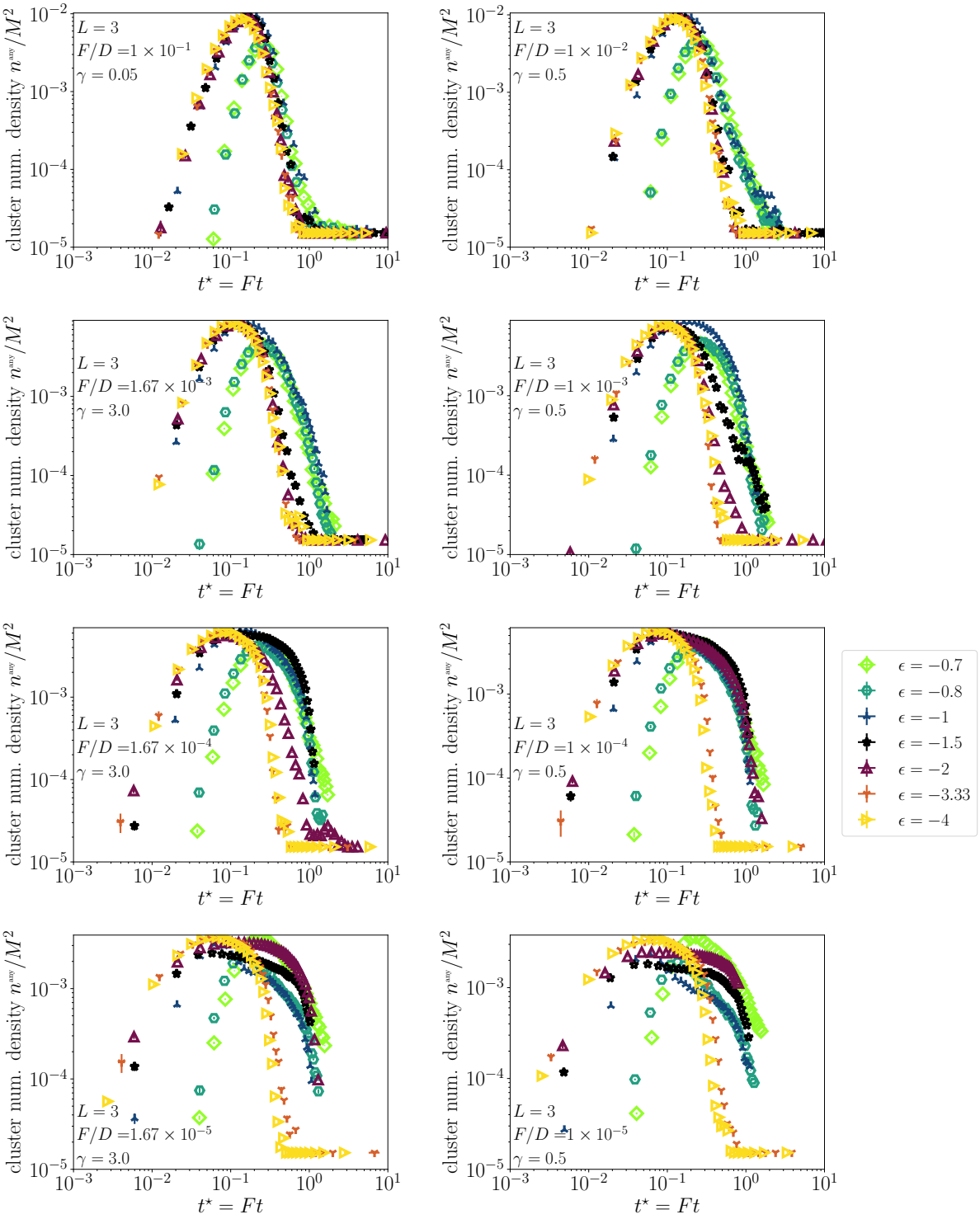

FIGURE 5.35: Cluster number density of clusters composed of particles of any orientation versus re-scaled time $t^\star$(at a fixed F/D) for a sweep over attraction strengths ($L = 3$).

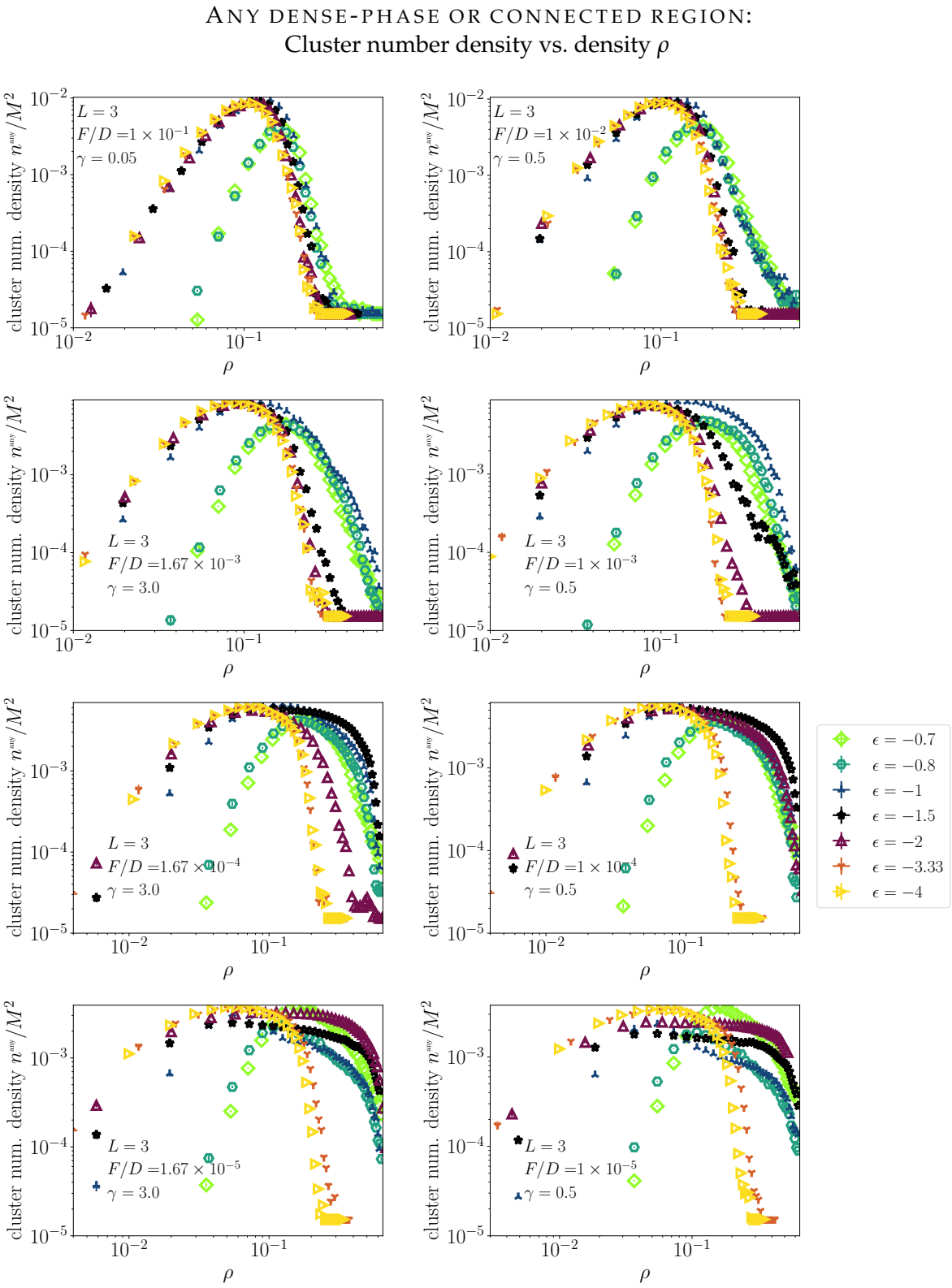

FIGURE 5.36: Cluster number density composed of particles of any orientation versus global density ρ (at a fixed F/D) for a sweep over attraction strengths ($L = 3$).

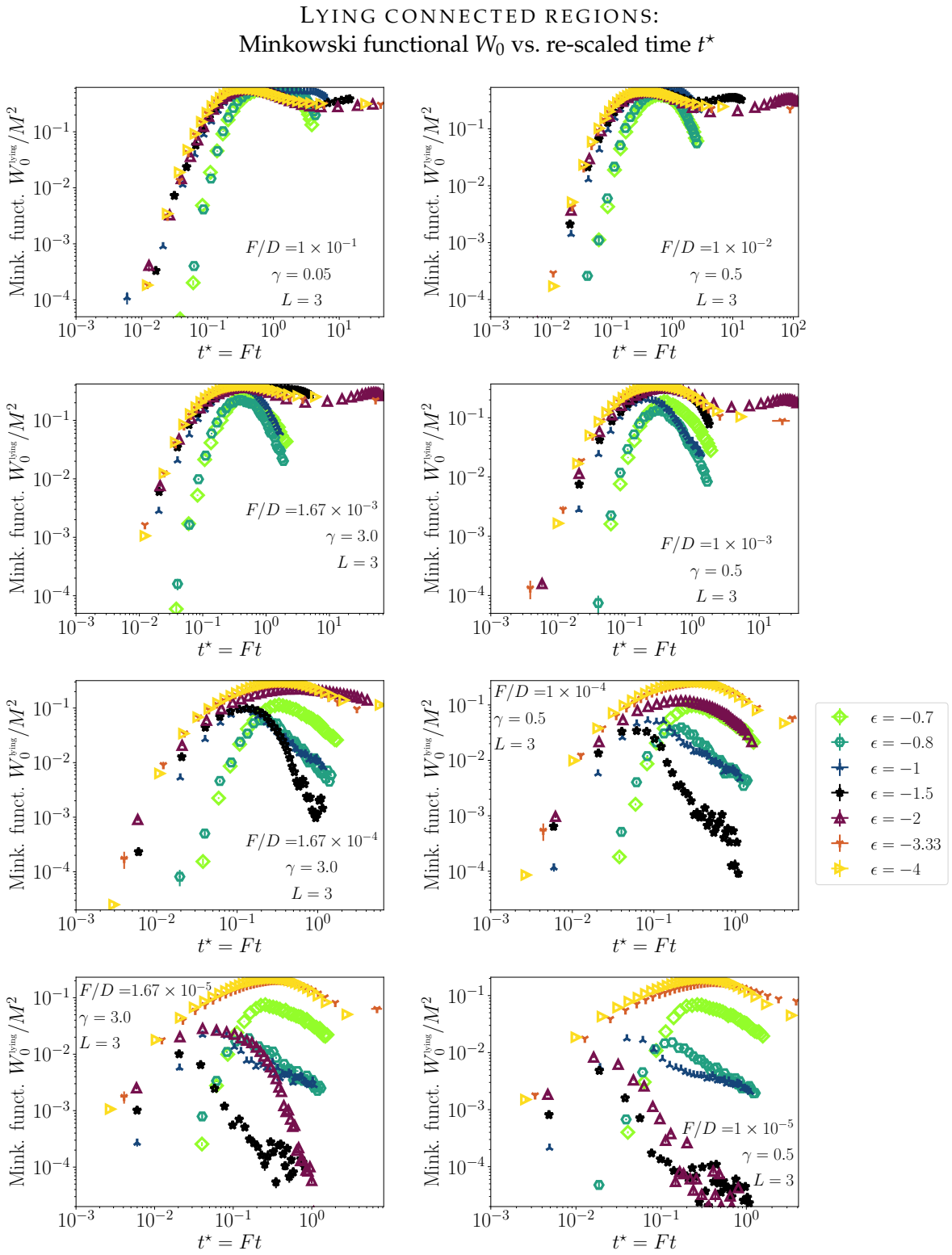

FIGURE 5.37: Minkowski functional W_0 of lying clusters versus re-scaled time $t^\star$(at a fixed F/D) for a sweep over attraction strengths ($L = 3$).

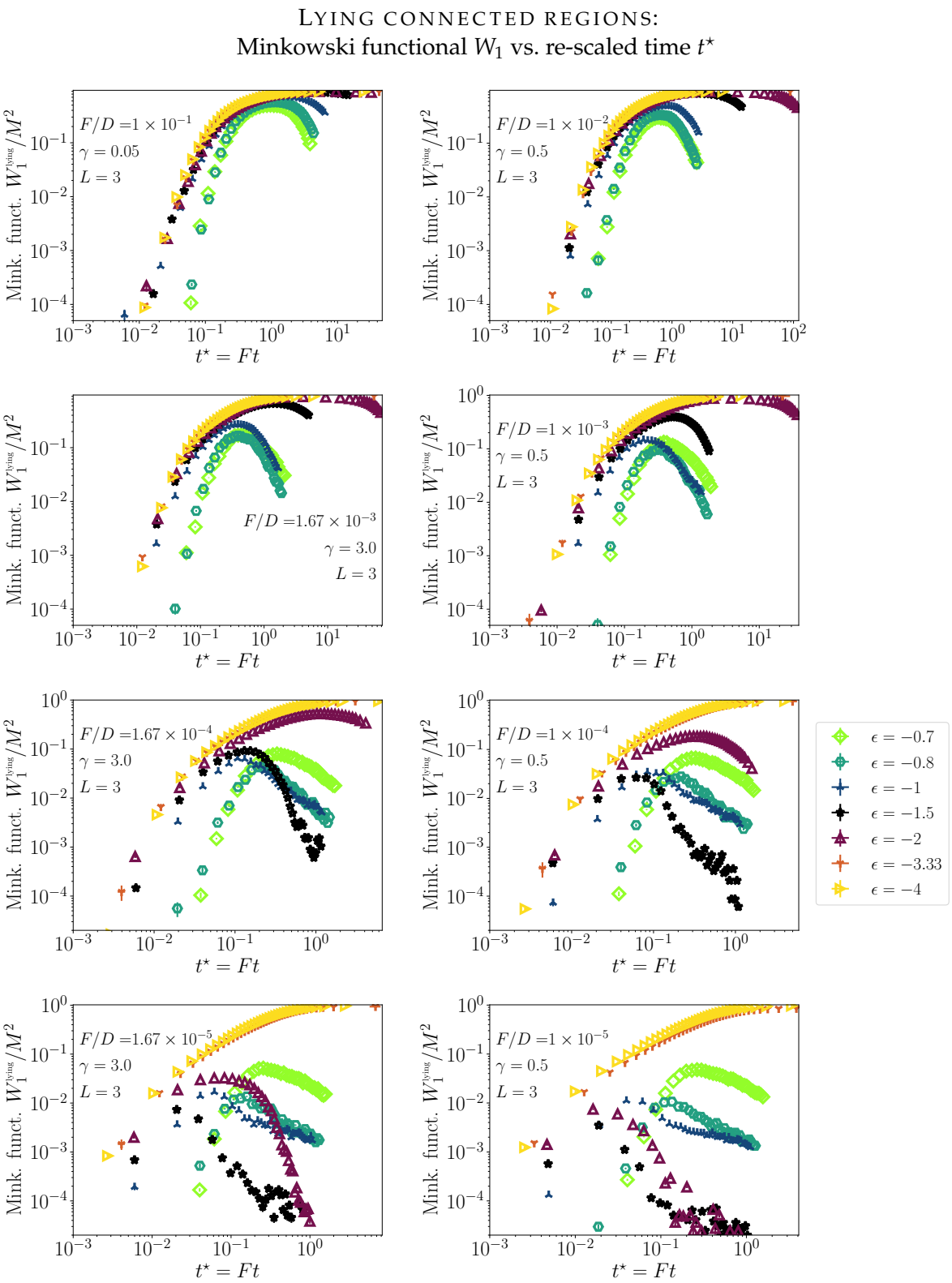

FIGURE 5.38: Minkowski functional W_1 of lying clusters versus re-scaled time $t^\star$(at a fixed F/D) for a sweep over attraction strengths ($L = 3$). Compare to Fig. 5.37.

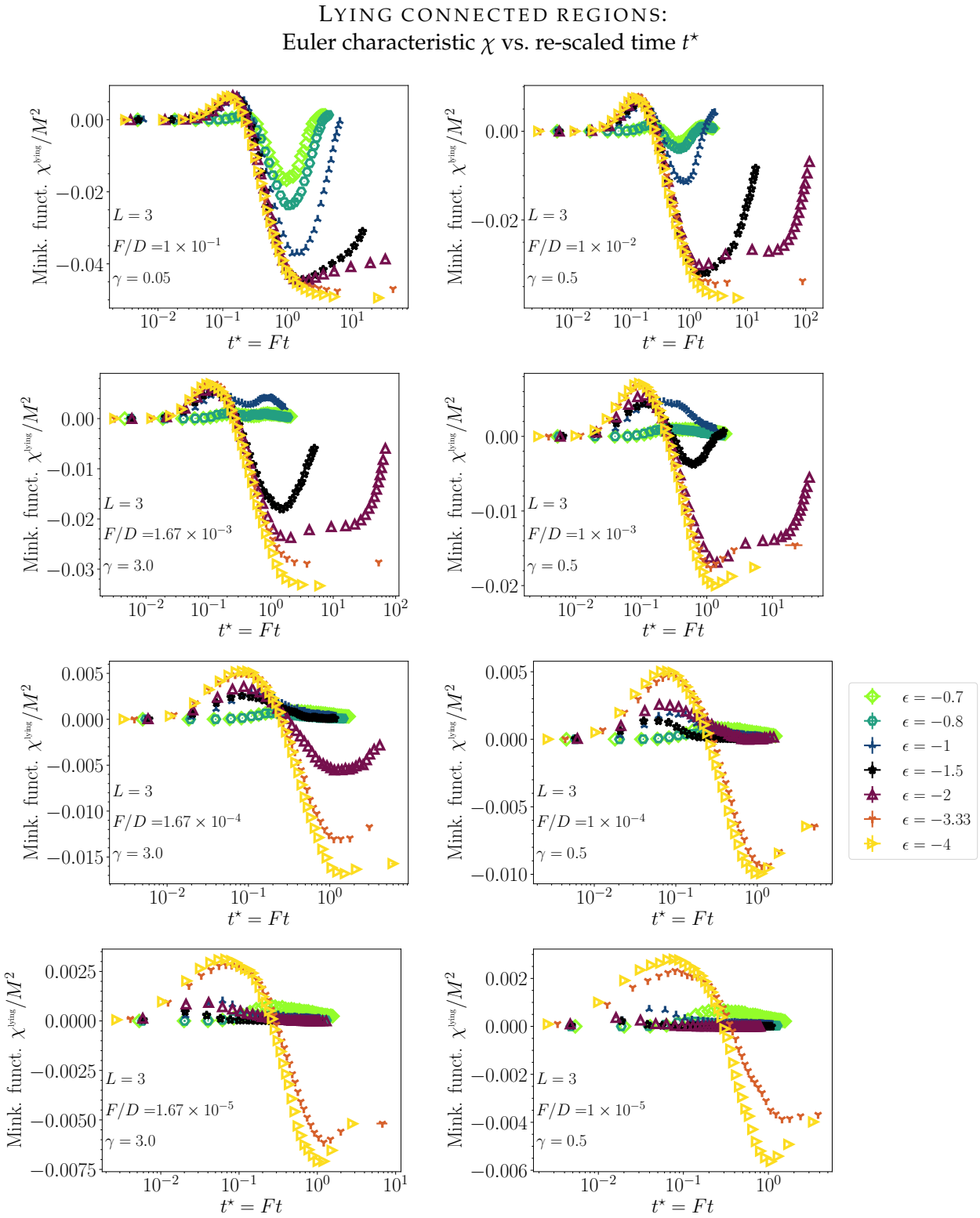

FIGURE 5.39: Euler characteristic χ of lying connected clusters versus re-scaled time $t^\star$ (at a fixed F/D) for a sweep over attraction strengths ($L = 3$). Compare to Fig. 5.38.

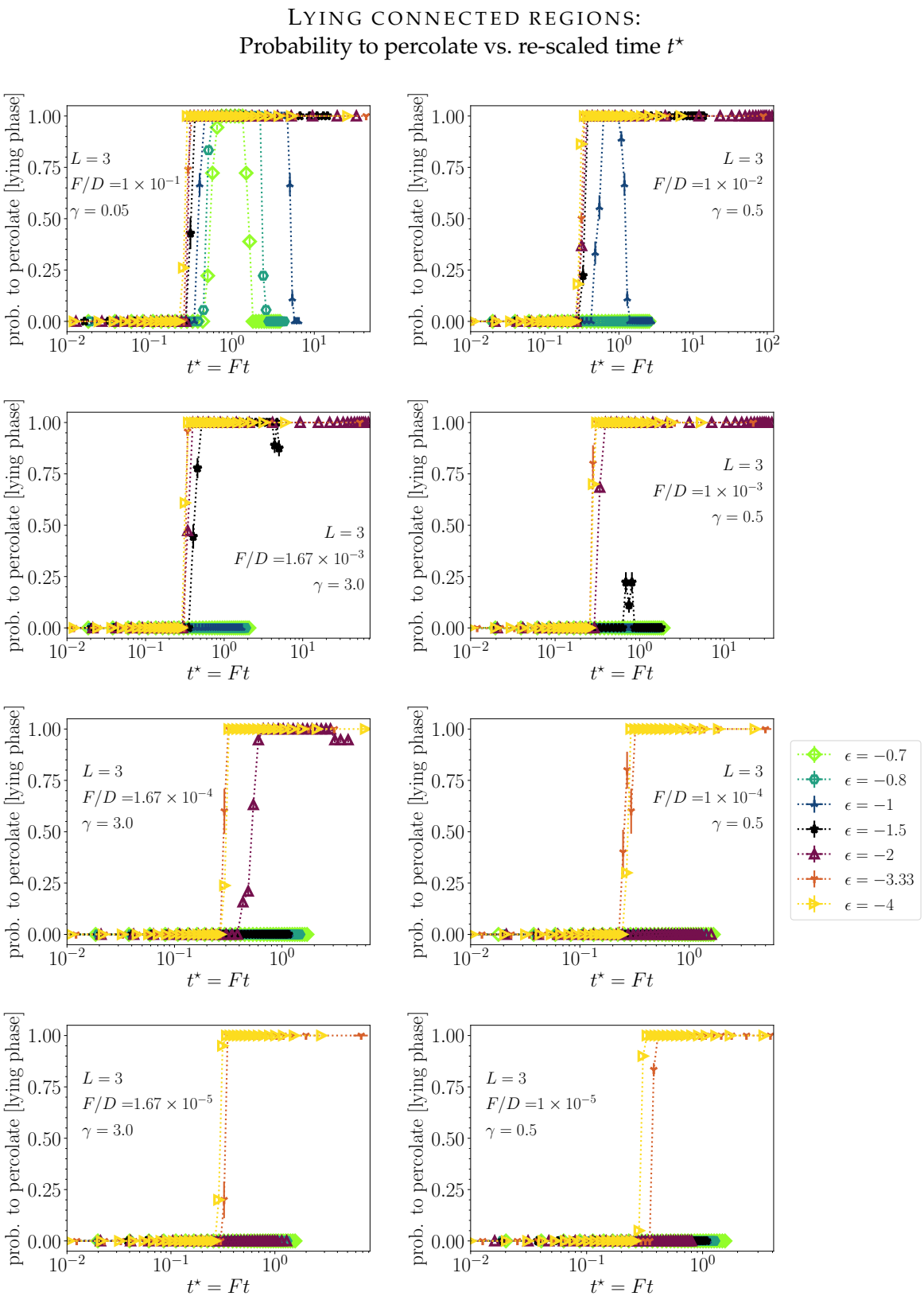

FIGURE 5.40: Probability that the lying phase percolates (a binary value for unbinned data) versus re-scaled time $t^\star$ (at a fixed F/D) for a sweep over attraction strengths ($L = 3$).

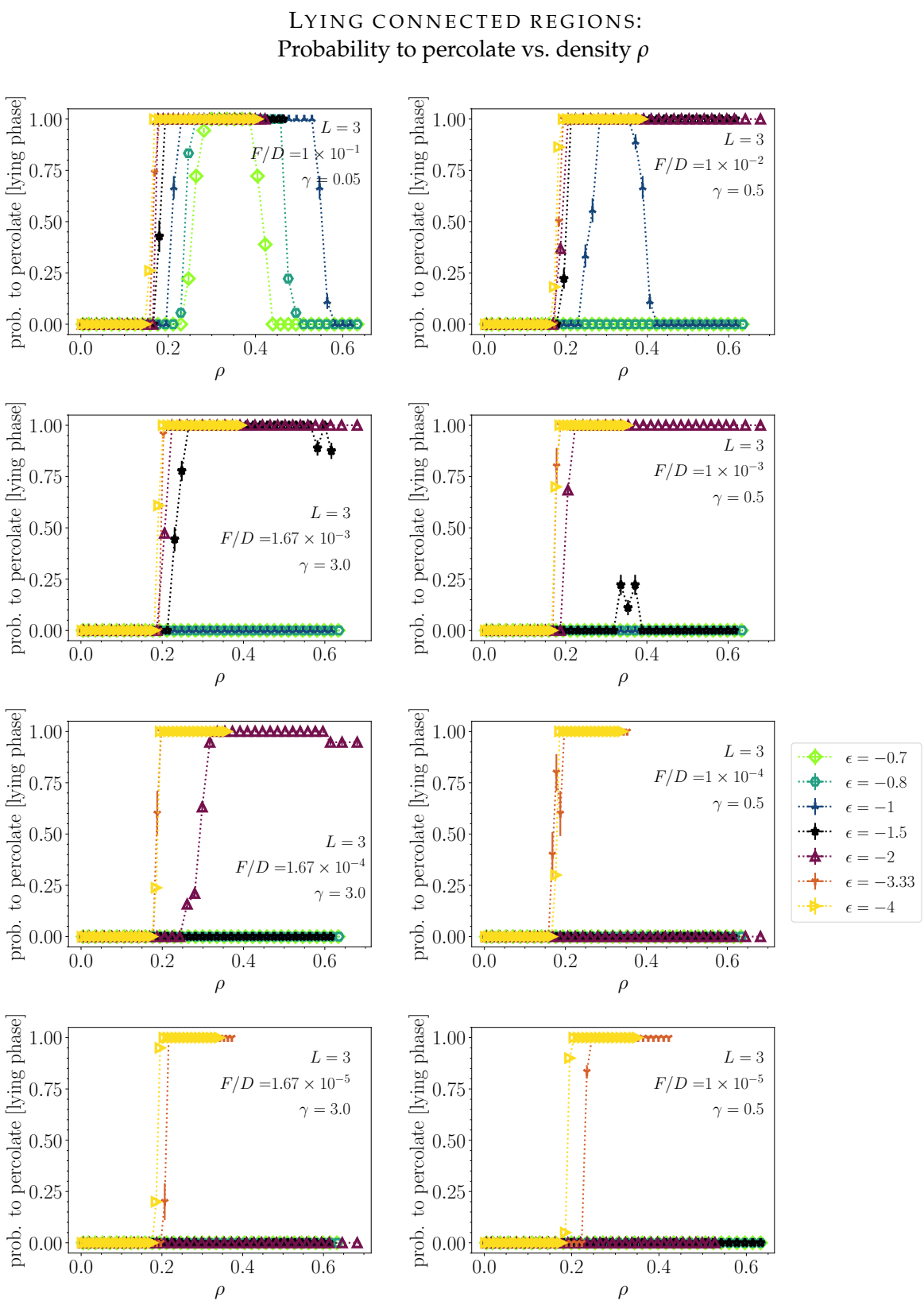

FIGURE 5.41: Probability that the lying phase percolates (a binary value for unbinned data) versus re-scaled time $t^\star$ (at a fixed F/D) for a sweep over attraction strengths ($L = 3$).

ANY DENSE-PHASE OR CONNECTED REGION:
Probability to percolate vs. re-scaled time $t^\star$

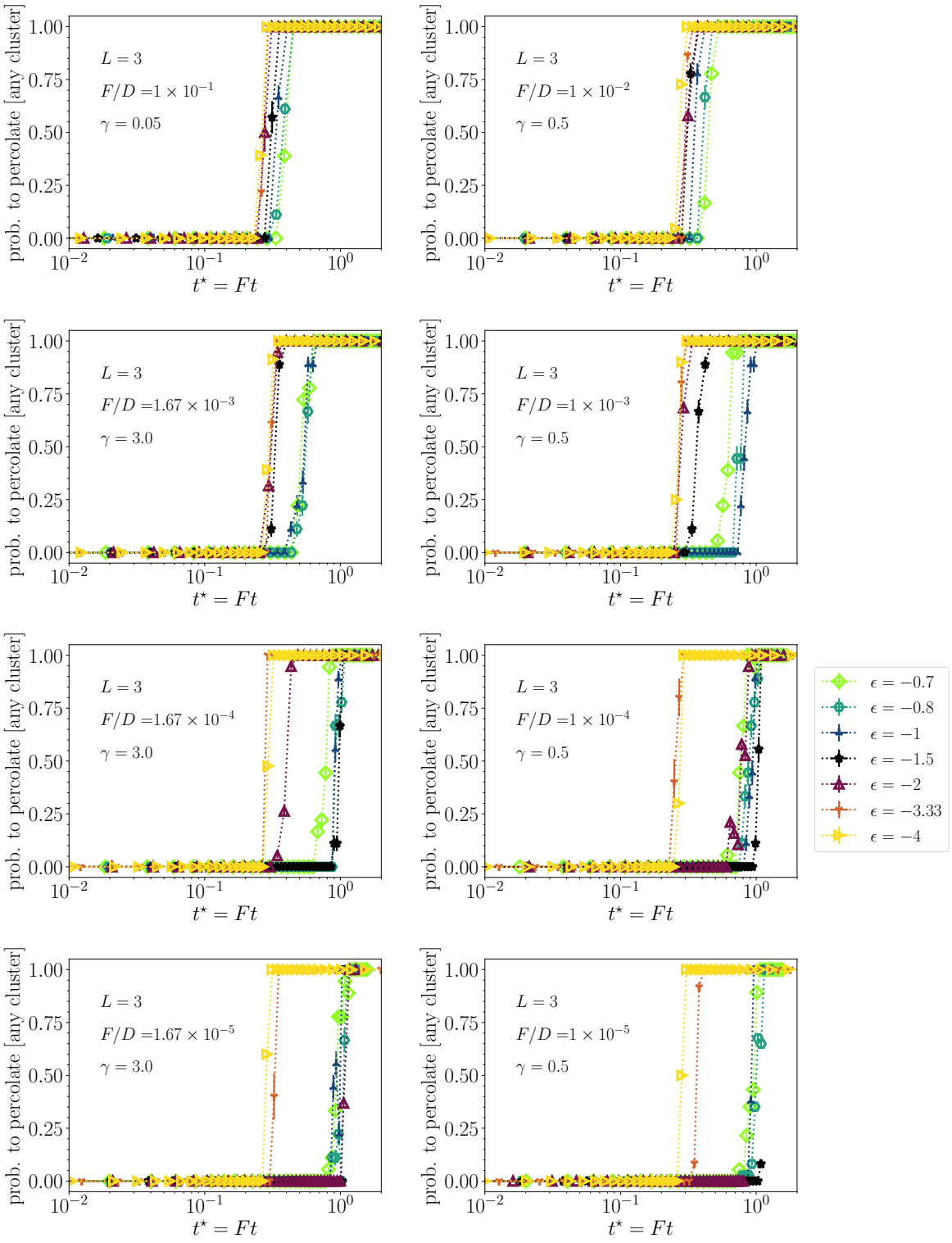

FIGURE 5.42: Probability that the any connected cluster (a dense phase formed from any rod orientation) percolates versus re-scaled time $t^\star$ (at a fixed F/D) for a sweep over attraction strengths ($L = 3$).

ANY DENSE-PHASE OR CONNECTED REGION:
Probability to percolate vs. density ρ

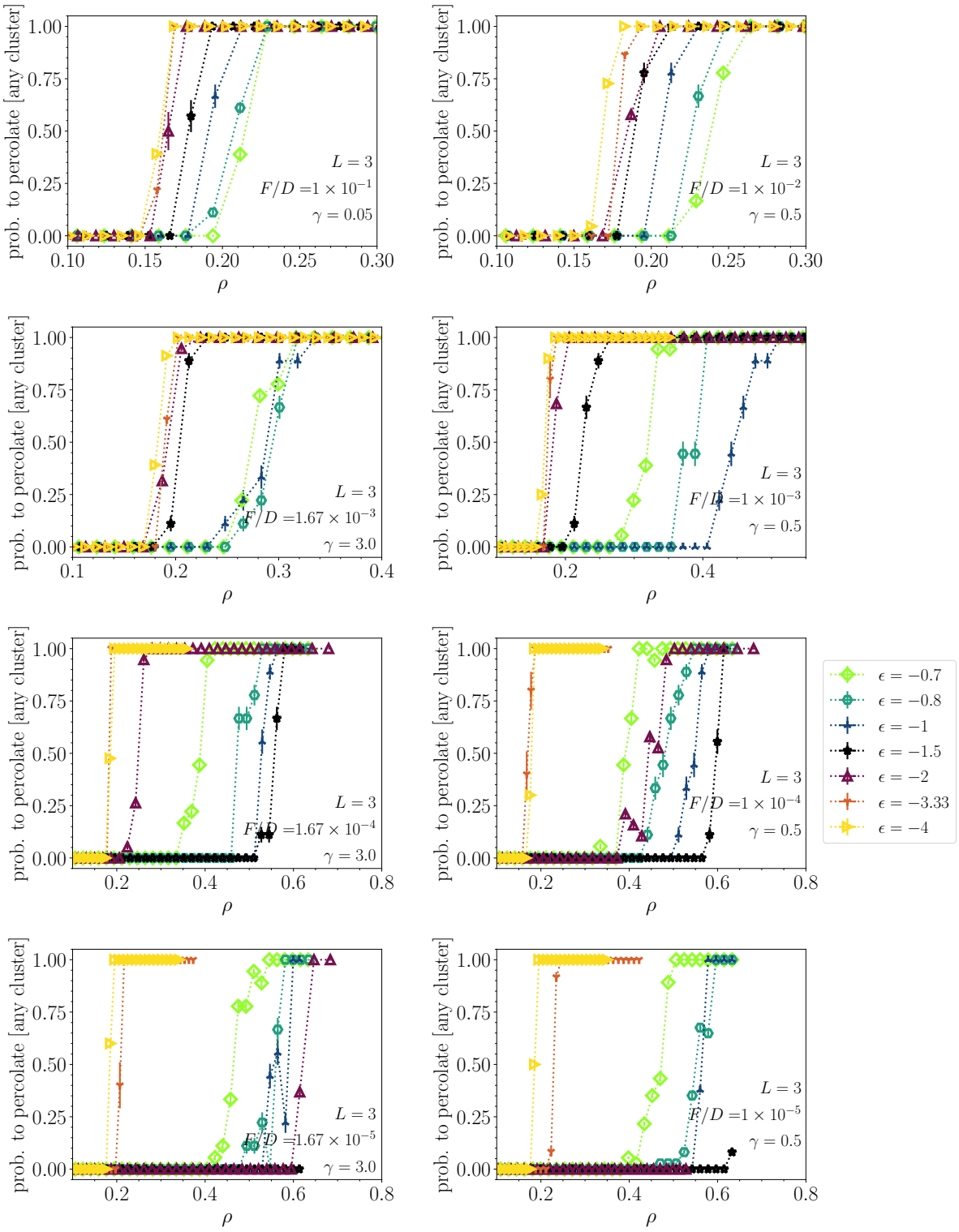

FIGURE 5.43: Probability that the any connected cluster (a dense phase formed from any rod orientation) percolates versus versus global density ρ(at a fixed F/D) for a sweep over attraction strengths ($L = 3$).

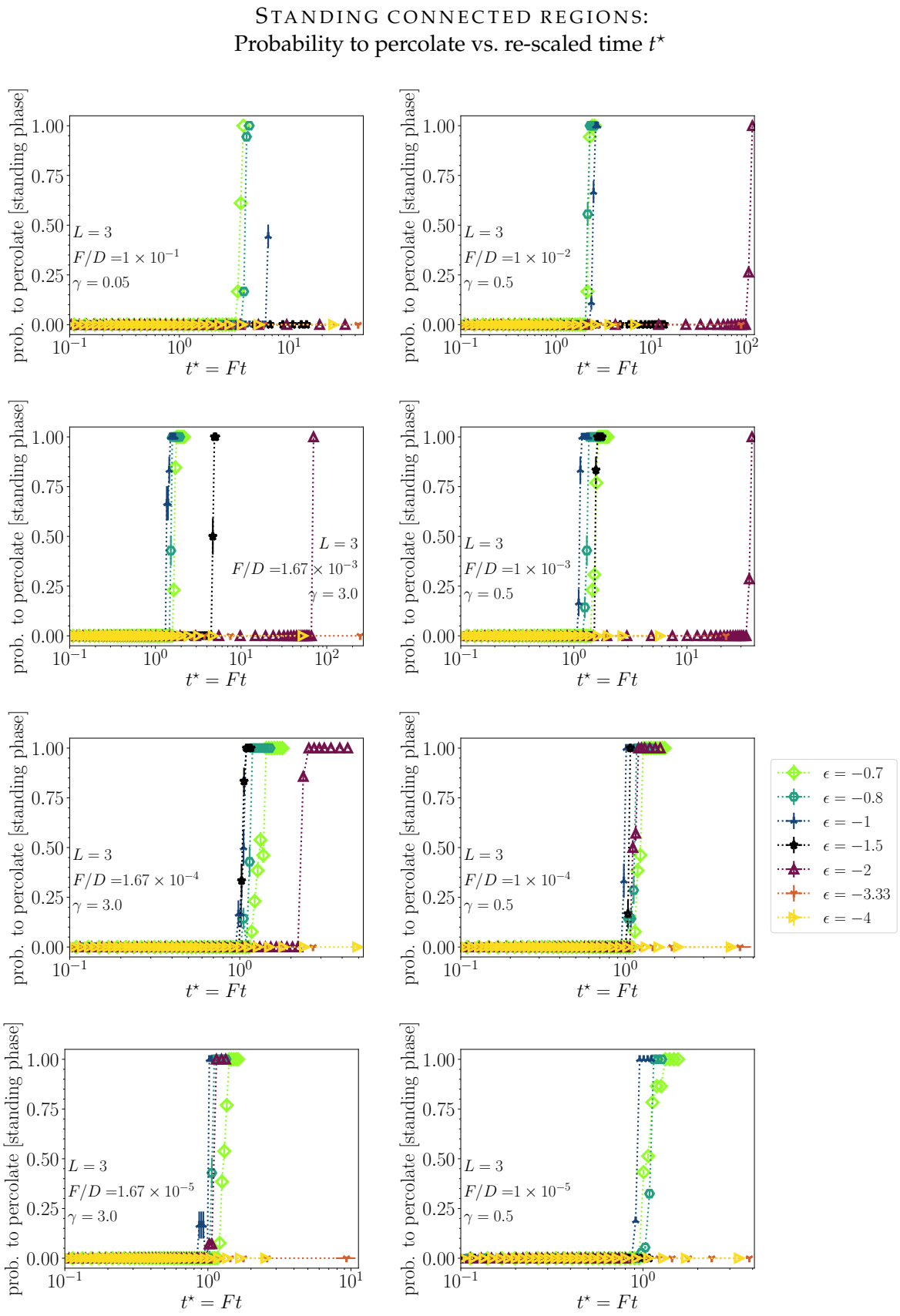

FIGURE 5.44: Probability that the standing phase percolates (a binary value for unbinned data) versus re-scaled time $t^\star$ (at a fixed F/D) for a sweep over attraction strengths ($L = 3$).

STANDING CONNECTED REGIONS:
Probability to percolate vs. density ρ

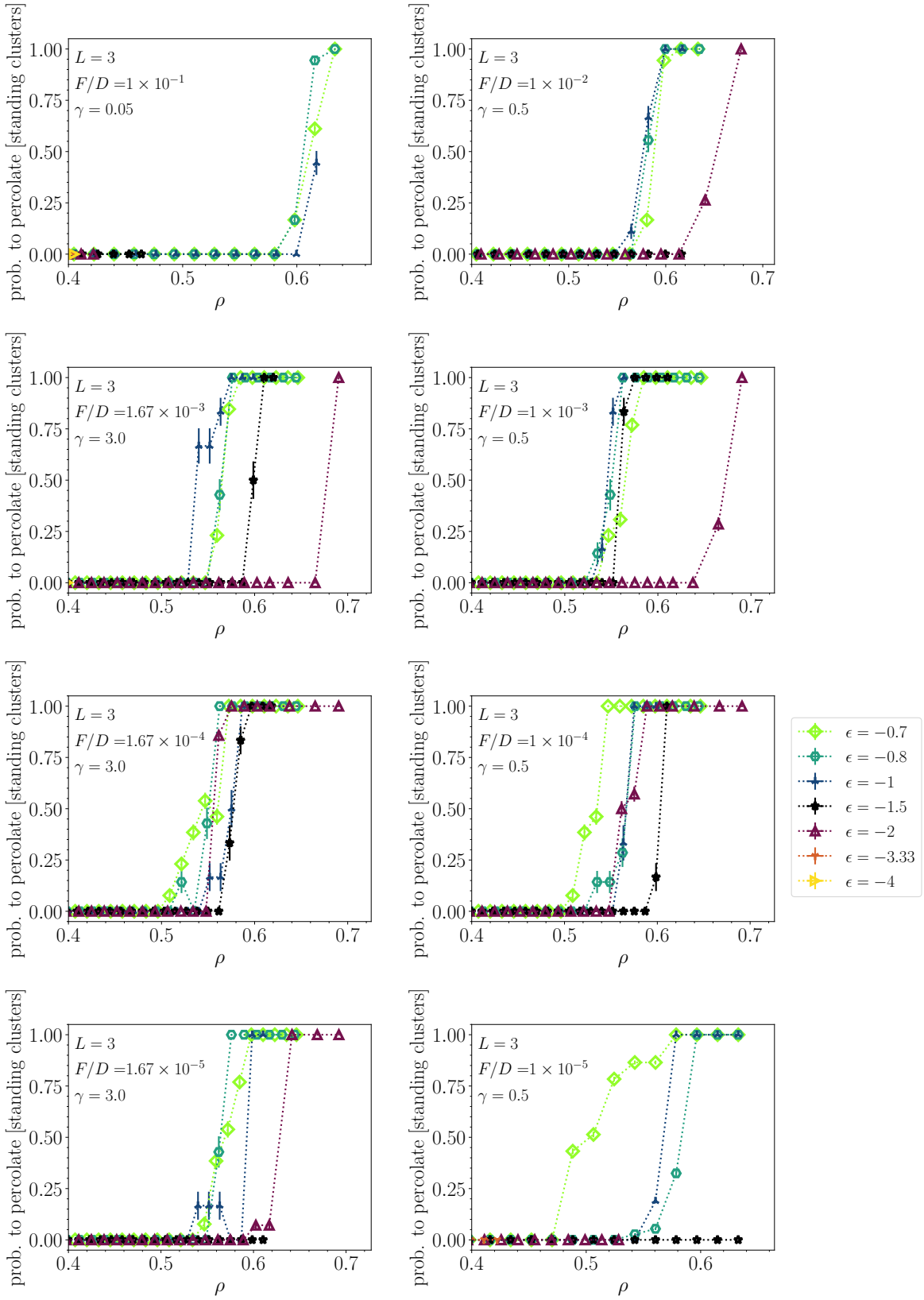

FIGURE 5.45: Probability that the standing phase percolates (a binary value for unbinned data) versus re-scaled time $t^\star$ (at a fixed F/D) for a sweep over attraction strengths ($L = 3$).

5.3.8 Further quantitative analysis: Dynamical properties

A nonequilibrium system may show dynamical heterogeneity, in general, in particular a system undergoing phase transformation processes. Information about dynamical heterogeneity is contained in quantities sensitive to dynamics such as the number of mobile particles. For the locally Markovian dynamics of hard-core particles in a lattice, the distinction between "mobile" and "immobile" is easy: The former is true when a particle is allowed to perform a "move", i.e. no hard-core repulsion is blocking it. To this end, we have analyzed configurational snapshots in a very different way comparing to the last section: We are able to reconstruct the event-lists of KMC "moves" from each snapshots, allowing us to access information on the dynamics during the simulation *ex situ*. Further, we can calculate both the "hard-core" and "hard-core + sticky-attraction" rates. We remind the reader that the KMC algorithm is a hybrid, rejection-free for steric (hard-core) repulsions and requiring an extra MC accept-or-reject step for additional "sticky" attractions.

Mobile particles

In the nonequilibrium system of the monolayer, many particles will be hindered in their individual degrees of freedom. Dynamics during global reorganization process due to a phase transformation acquire a collective character, involves many length-scales. Therefore, we have set out to quantify the mobility in the system – first, with the number of mobile particles, which we can discern between different types of moves (rotations, translational hops). From a practical point-of-view, there are no comparable observables that are defined within the unstable region inside the binodal from thermodynamic equilibrium theory, hence, quantifying this provides unique information on the state of the system.

In Fig. 5.46, we present the results of the (unique) number of *translationally* mobile particles in the system as a function of monolayer density ρ during growth. These particles can be of any orientation. In regime I ($\epsilon = -0.5988$), where growth is hard-rod-like and, thus, much closer to equilibrium, the number density of mobile particles takes on the highest value across the board, in agreement with our argumentation above. The same is true for the *rotationally* mobile particles, more specifically, for standing particles"rotating downwards" (the density of mobile particles for rotating upwards is equivalent to ρ_{12}, which has been presented in Fig. A.11), see Fig. 5.47.

Fig. 5.46 signifies a few more features worthy of attention. The point where the monolayer becomes almost completely filled (dynamically arrested) in a nonequilibrium intermediary state (in the mixed aggregate or lying "wetting layer") is now clearly visible, i.e. where $\rho_{\text{mob., trans.}}$ reaches 0 or becomes minimal or shows a near-"kink" in past regime IIIa ($\epsilon \lessapprox -1.5$) – these densities are around $\rho \sim 0.35 - 0.41$, depending on F/D. As in the discussion of Sec. 5.3.7, this region may represent a region between two metastable binodals, signifying different vapor–liquid transitions; however, this remains speculative. In any case, translationally mobile particles deep in regime III, when can be found in a vapor phase, at an interface between a vapor and dense liquid, or within a non-fully-packed nonequilibrium aggregate that is partly homogeneous. Finally, Fig. 5.46 shows regime III clearly distinguished from regime II or I: the trajectories of $\rho_{\text{mob., trans}}$ are bundled up to some transition density $\rho \sim 0.05 - 0.15$

depending on F/D, after which the trajectories "split" apart. We note that number densities of mobile particles represent *conditional probabilities* of the system entailing particle numbers, which clearly fluctuate in contrast to the global density ρ (which would only fluctuate if we were to allow for desorption moves, see Sec. 5.8). We have provided plots showing the variances of $\rho_{\text{mob., trans}}$, calculated from running bins, in App. A.2.

To assess the orientation of *translationally* mobile particle, we have calculated the nematic order

$$Q_{\text{mob., trans.}} \equiv \frac{\rho^3_{\text{mob., trans}} - \frac{1}{2}\rho^{12}_{\text{mob., trans}}}{\rho_{\text{mob., trans.}}} , \tag{5.15}$$

where $\rho^3_{\text{mob., trans.}}$ represents the number density of standing mobile particles, etc., resulting in the plots of Fig. 5.48.

Interestingly, the general form of $Q_{\text{mob., trans.}}$ looks quite familiar, like $Q(\rho)$ of Fig. 5.25. However, there are subtle differences with new information: The values of ρ at which $Q_{\text{mob., trans.}}$ "takes off" coincide with the minima or "kinks" of $\rho_{\text{mob., trans.}}$ in Fig. 5.47, and a much steeper increase is seen in the curves of $Q_{\text{mob., trans.}}$ than in Q. This implies that the proportion of *standing* mobile particles increases significantly after the nearly-fully-packing aggregate or "wetting layer" has maximized its extent. We rationalize this as follows: A lying particle in a 2D wetting layer that rotates upward instantly creates a vacant space for translational motion (that is $(L-1)\times 1$ units in lateral size). Another subtle difference we report on is that the curve of $Q_{\text{mob., trans.}}(\rho)$ can sometimes show a brief, nearly-linear increase between $\rho \sim 0.35 - 0.43$ (see e.g. cases where $F/D \in \{1\times 10^{-2}, 1.67\times 10^{-3}, 1\times 10^{-3}\}$). We are not sure how to interpret this currently.

The nematic order $Q_{\text{mob., rot.}}$ of the out-of-plane *rotationally* mobile particles (those which can lay down or stand up) of the system, which we calculate in complete analogy to Eq. 5.15, is presented in Fig. 5.49. The curves now look very different from those of the global $Q(\rho)$ plots. For plots in regime III, i.e. $\epsilon = -1.5, -2$, we see how the nematic order can change from from lying $Q_{\text{mob., rot.}} < 0$ to isotropic or standing $Q_{\text{mob., rot.}} \gtrapprox 0$ for intermediate and low F/D. We inspected the re-scaled time-points at which this occurs (not shown here): The lying–standing transition viewed from rotational mobile particles seems to coincide with the times just after the monolayer has the largest number of standing clusters, before the latter beginning to drop (Fig. 5.30). If a vapor phase surrounding clusters in thin, then standing particles have the best chance to rotate downwards when they are situated at the cluster rim. Therefore, this order parameter is probably picking up on the total curvature of standing clusters, which is likely maximal around this point in time.

Relative fluxes

We now continue our exploration of dynamical variables based on the fluxes (rates) in the system – in other words, the magnitudes of currents in the system. In Fig. 5.50, we present the total translational flux, as a relative ratio to the total motion flux in the system (of "internal" dynamics excluding deposition moves).

To clarify, the quantity of interest is

$$J_{\text{trans., rel.}} \equiv \frac{\sum\limits_{\mu \in \{k_{\text{trans}}\}} j_\mu}{\sum\limits_{\nu} j_\nu} \,, \tag{5.16}$$

where for either μ or ν,

$$j_\nu \equiv k_0(\nu) \times \min\left\{1, \mathrm{e}^{-\Delta\mathcal{H}/(k_\mathrm{B}T)}\right\} \tag{5.17}$$

represents the "true" rate of a move of a particle indexed by ν (the KMC simulation accounts for the hard-core part only before applying a Metropolis step for the "sticky" attractions). The quantity $\Delta\mathcal{H}$ is the change in the local configurational Hamiltonian around the particle, $k_0(\nu)$ is the attempt rate of the move, and "$\mu \in \{k_{\text{trans}}\}$" signifies that the particle move indexed by μ is in the set of all *translational* moves in the system.

The relative flux of translational motion in the system shows the formation of a plateau deep in regime IIIb ($\epsilon = -3.33, -4$) at very low F/D, where we see large lying and standing islands forming, reaching a peak near unity when the monolayer becomes fully packed with a "wetting layer". The plateau seems to indicate a situation in which the translational flux relative to all other kinetics in the system is *constant*. We think this might indicates that, at best, a *linear* growth of relative length-scales in the system occurs during at this time. Visual inspection shows a "scaling up" of the lying and standing clusters in the system, the former of which are less compact than the co-occurring, standing islands. A more exact exploration of this plateau may be interesting for future investigations.

"Sticky" acceptance ratio for total particle motion flux ("internal" dynamics)

We define the "sticky" acceptance ratio of the total "internal"-motion flux (not including deposition) at any one point in time as follows:

$$\alpha \equiv \frac{\sum\limits_{\nu} j_\nu}{\sum\limits_{\nu} j_\nu^{\text{hard}}} \,, \tag{5.18}$$

j_ν is the "true" rate defined by Eq. (5.17), and

$$j_\nu^{\text{hard}} \equiv k_0(\nu) \times \min\left\{1, \mathrm{e}^{-\Delta\mathcal{H}_{\text{hard}}/(k_\mathrm{B}T)}\right\} \tag{5.19}$$

represents the KMC rate updated in our simulations, which has *already* accounted for hard-core repulsions $\mathcal{H}_{\text{hard}}$, but not for the *sticky* attraction U_{sticky} ($\mathcal{H} = \mathcal{H}_{\text{hard}} + U_{\text{sticky}}$). The observable indicates the probability that *anything* (any rods) will move, given we only consider *mobile* particles: The probability is less than one because of the binding energies between rods. For hard-core rods, this ratio should always remain unity.

The results for the "sticky" acceptance ratio during growth is shown in Fig. 5.51. Clearly, the acceptance ratio shrinks for stronger attraction strengths, generally. As a system is cooled, the total motion in the system is reduced, i.e. the total currents are weaker. This ratio further picks up on singular events

in the system dynamics, such as when the system becomes arrested with the formation of a high-density aggregate or "wetting layer". In any case, the (log of the) acceptance ratio α contains crucial information on the dynamics: As each flux term j_ν is weighted with a Boltzmann factor of the *differential* local configurational energy (potential energy), the log of the ratio α quantifies an effective, differential work that can be performed by motion-inducing bath (the intrinsic, "overdamped" dynamics) within the given time-step – the part that will lead to a true change in the system. (Differential work lost within the current time-step due to the hard-core repulsion of rods is separate from this quantity).

In future work, it would be interesting to explore fluctuations of this quantity. Quantifying global nonequilibrium current fluctuations is *the* central task for a rigorous theoretical approach, where fundamental bounds on these have been derived for steady-state conditions, as mentioned in Ch. 3. However, such an undertaking remains outside of the scope of this thesis. One could also extend this analysis to an acceptance ratio based on the total "true" rate in the system, *including* the deposition flux: Rejections arise when lattice sites are occupied at the places where a particle (of a random orientation) should be inserted. This total rate would contain further structural information – about the coverage of the system.

* * *

In this section we explored observables on dynamical properties (mobility of the system, fluxes, and the forward-propagation of the system) during the driven, nonequilibrium evolution of the monolayer system. These have offered complementary insight into the monolayer growth process, in particular non-structural quantities that characterize motion in the system. Up to now, we have extensively investigated the $L = 3$ system at neutral substrates, and have attempted to identify and classify various phenomena during the self-assembly evolution. We consolidate our findings in the next section, where we outline the various phase transition scenarios that appear in ϵ-regimes II and III.

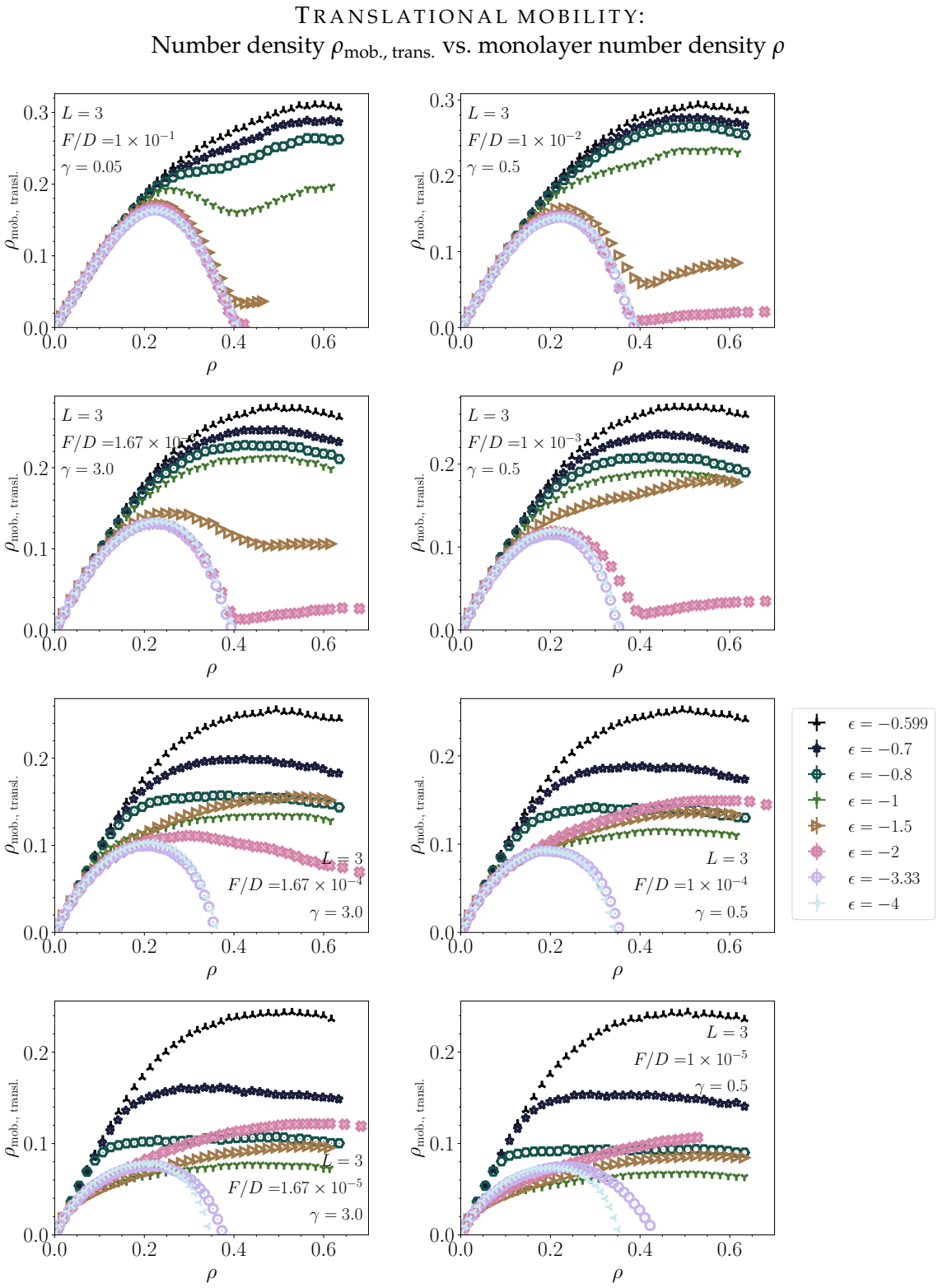

FIGURE 5.46: Translationally mobile particles: Number density $\rho_{\text{mob., trans.}}$ versus global density ρ (at a fixed F/D) for a sweep over attraction strengths ($L = 3$).

ROTATIONAL MOBILITY (downwards):
Number density $\rho^3_{\text{mob., rot. down}}$ vs. monolayer number density ρ

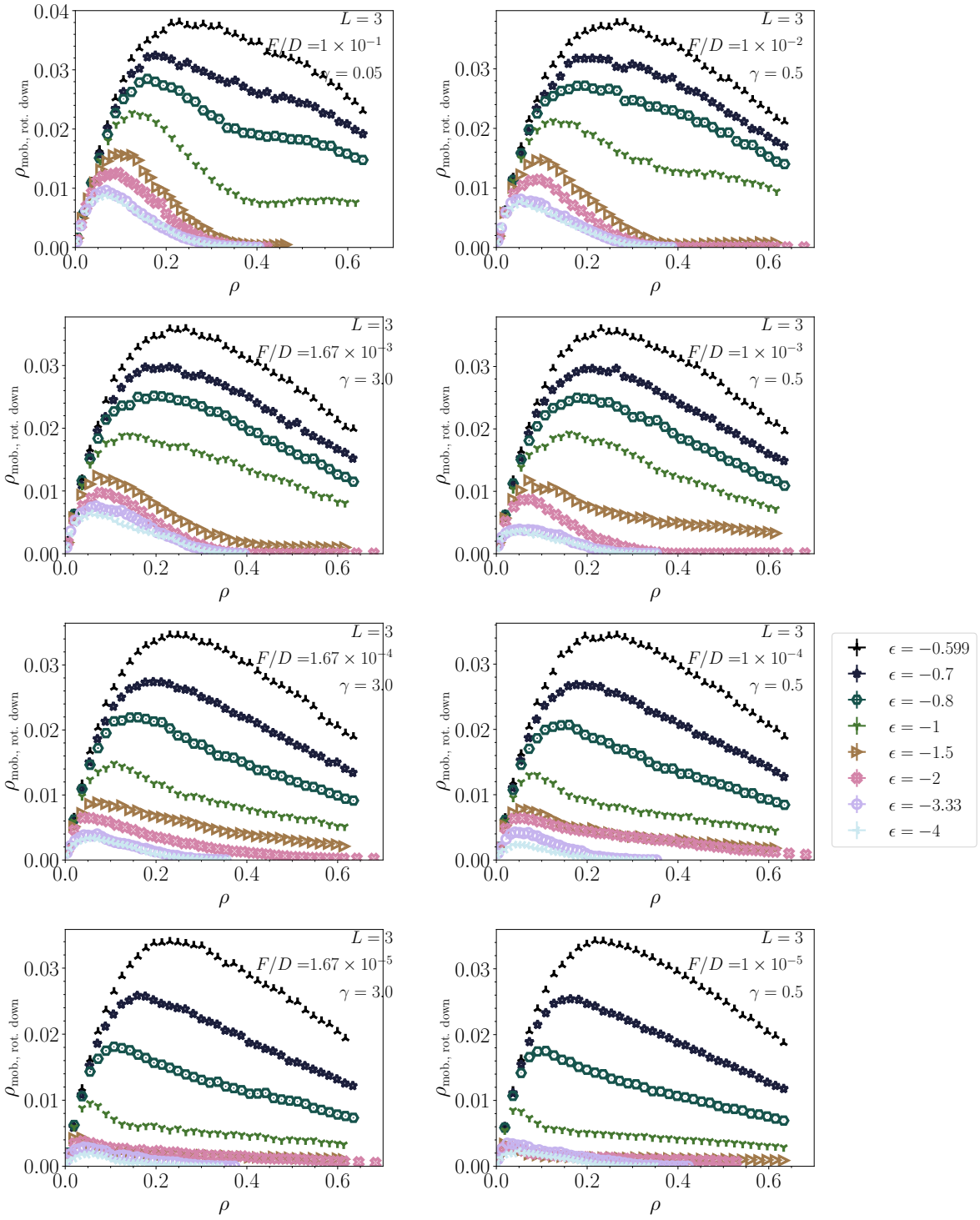

FIGURE 5.47: Rotationally mobile particles (rotations downwards): Number density $\rho^3_{\text{mob., rot. down}}$ of standing rods versus global density ρ (at a fixed F/D) for a sweep over attraction strengths ($L = 3$).

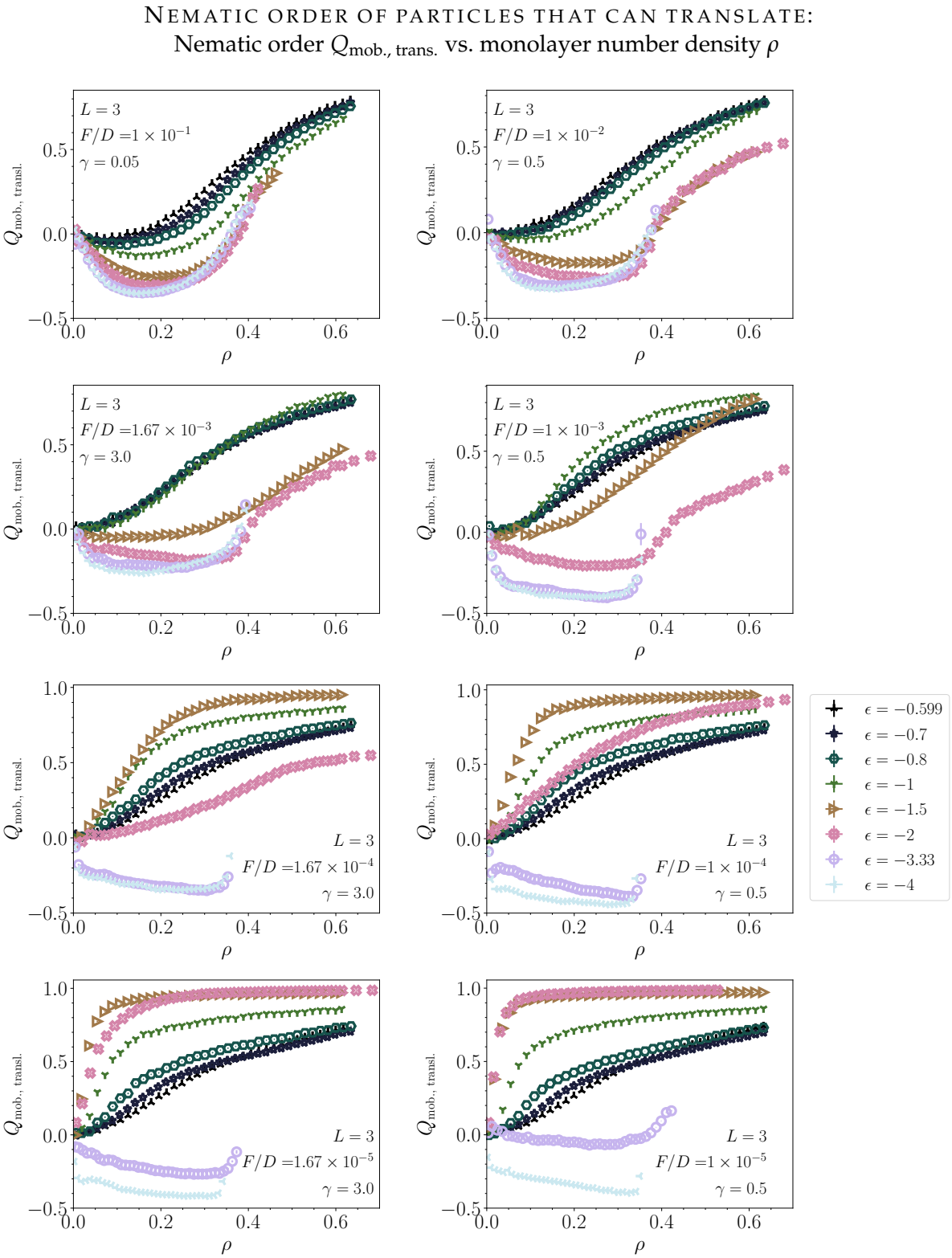

FIGURE 5.48: Translationally mobile particles: Nematic order $Q_{\text{mob., trans.}}$ versus global density ρ (at a fixed F/D) for a sweep over attraction strengths ($L = 3$).

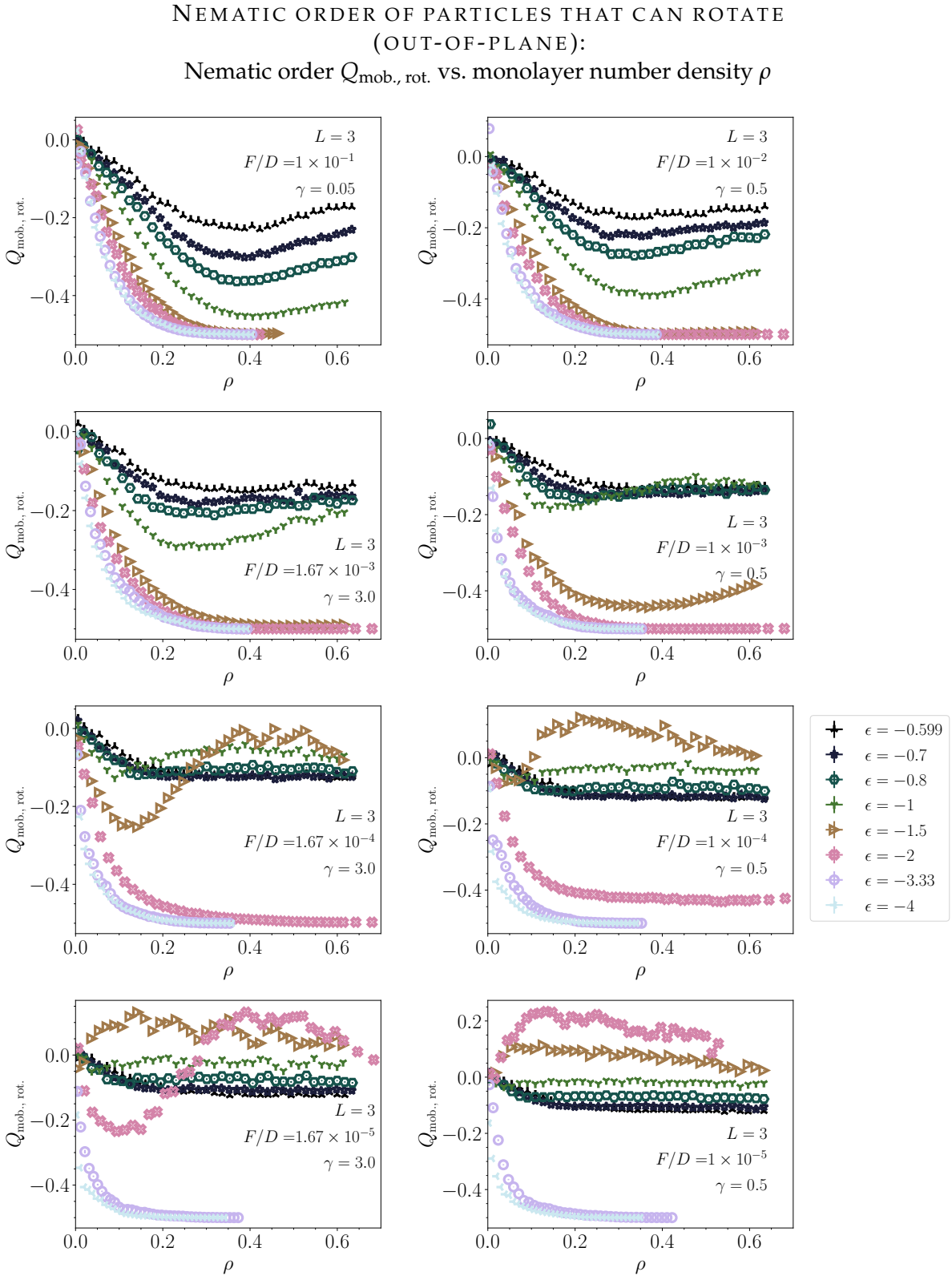

FIGURE 5.49: Rotationally mobile particles (out-of-plane rotations): Nematic order $Q_{\text{mob., rot.}}$ versus global density ρ (at a fixed F/D) for a sweep over attraction strengths ($L = 3$).

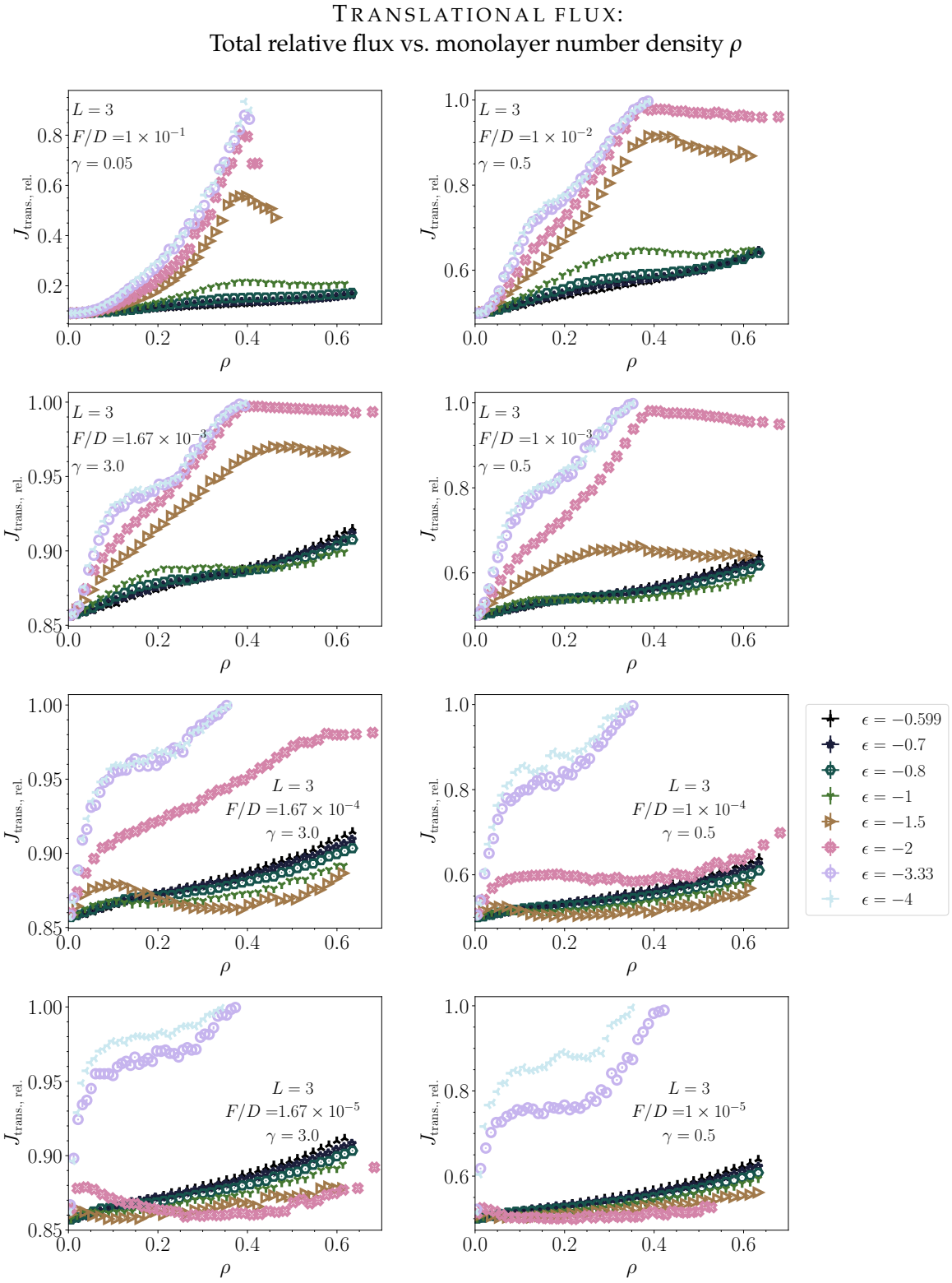

FIGURE 5.50: Total relative rate for translational motion, normalized by the total flux for all moves in the monolayer (excluding deposition events from external source) – see Eq. (5.16)– versus global density ρ (at a fixed F/D) for a sweep over attraction strengths ($L = 3$).

ROTATIONAL + TRANSLATIONAL FLUX:
"Sticky" acceptance ratio vs. monolayer number density ρ

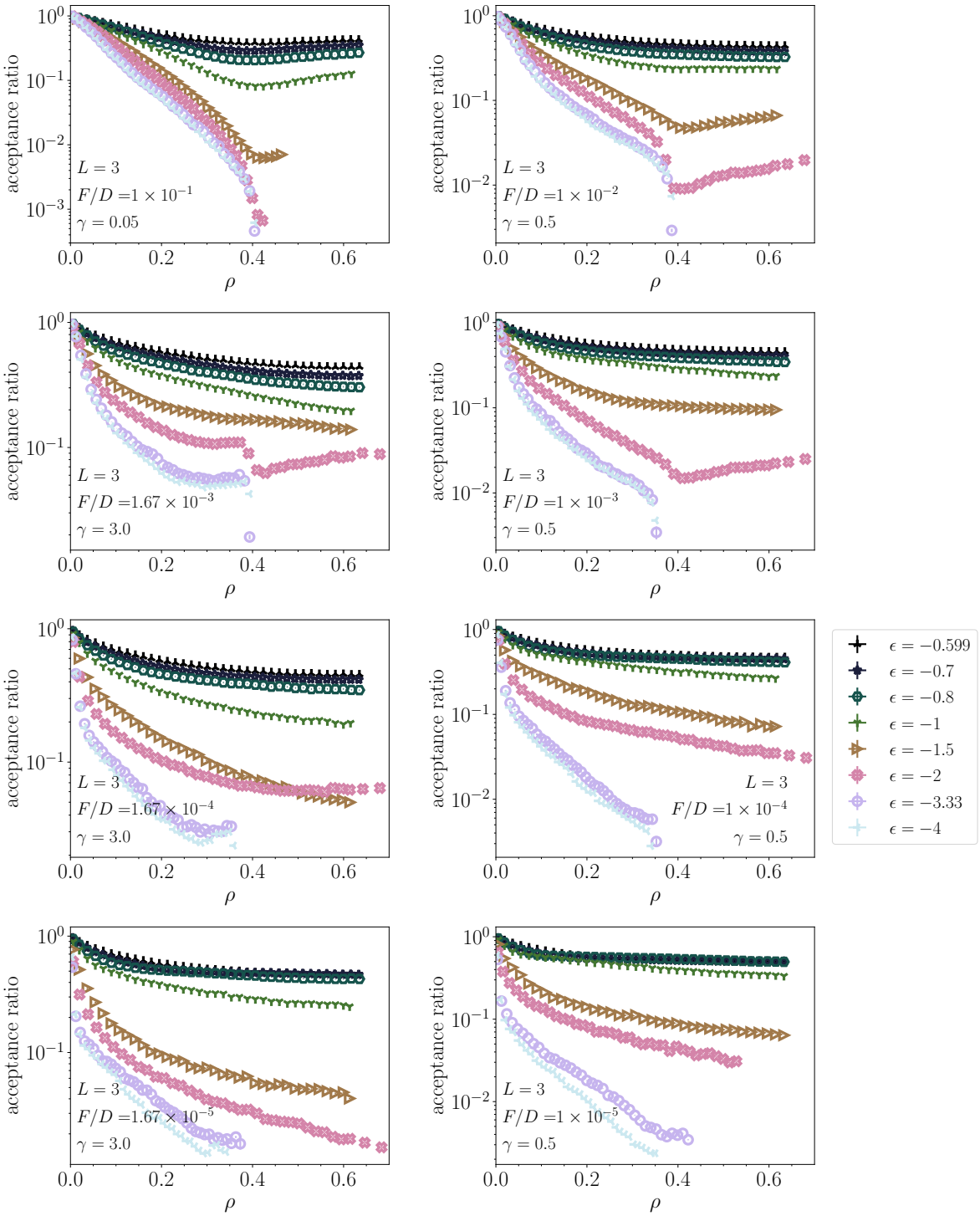

FIGURE 5.51: "Sticky" acceptance ratio for "internal" motion (all moves in the monolayer excluding deposition events from the external source), given by Eq. (5.18), versus global density ρ (at a fixed F/D) for a sweep over attraction strengths ($L = 3$). Any rejected moves only arise due to "sticky" binding energies and *not* due to hard-core repulsion. We calculated this and all dynamical observables *ex situ* from simulation snapshots by reconstructing the KMC event-lists.

5.3.9 Characterizing the main phase transition scenarios

In this section, we will summarize our findings presented so far. The large number of investigated observables combined with the microscopic pictures seen in the simulation snapshots offers us the unique possibility to characterize four different phase transition scenarios for monolayer growth differing significantly from "hard-rod-like" growth at high reduced temperatures (in scenario (A)). Importantly, these scenarios are a function of *both* the reduced temperature or attraction strength (i.e. $1/|\epsilon|$) *and* the deposition quench rate F/D. The ϵ-regimes we have used to categorize the results thus far do not tell the whole story.

(A) "Hard–rod–like" growth of a monolayer

We have not analyzed the kinetics for this scenario in high detail – please consult to Sec. 5.3.2 for a brief report and description of the observed behavior. For very fast deposition quench rates F/D, a logical consequence is a jamming transition, which represents a "hard" limit on dynamics in the monolayer growth system. Locating these transitions and characterizing their kinetics is out of the scope of this thesis.

(B) Isotropic–fluid–to–standing transition via "nucleation and growth" of clusters

The specific example of phase transition scenario (B) that we present in Figs. 5.52–5.53 is defined by the pair of parameters $(F/D = 1 \times 10^{-3}, \epsilon = -0.7)$, or $(\log_{10}(D/F) = 3, \ln(1/|\epsilon|) = 0.356)$. We now attempt to describe the kinetics of scenario (B) in forthcoming paragraphs with the data in the presented figures. Please note that we will often use the term "growth rate" for quantities plotted in a double-logarithmic scale as an alias for the *derivative* of quantities in this representation.

Up to $t^\star \approx 0.1$ ($\rho \approx 0.6$), we observe an isotropic fluid forming under the deposition protocol. The lying and standing densities, ρ_{12} and ρ_3, respectively, growth in a *power-law*-like fashion – they entail almost the same growth law (see Fig. 5.52, top figure). While the growth of ρ_{12} slows down significantly afterwards, finally saturating at $t^\star \approx 0.4$ ($\rho_{12} \approx 0.1$, $\rho \approx 0.2$), ρ_3 still follows the same power law up to $t^\star \approx 0.2$. Thereafter, the growth appears to 'change gears', taking on a second power for a slightly faster growth rate. It shifts another gear down to significantly slower power-law-like growth around $t^\star \gtrapprox 0.5$. The lying density ρ_{12} decreases continuously for $t^\star \gtrapprox 0.4$. Consequently, the nematic order parameter Q begins increasing at $t^\star \gtrapprox 0.1$ and shows its fastest growth rate when ρ_{12} reaches its maximum (at saturation).

We further deduce a number of interesting characteristics on the growth of standing clusters. They grow at the expense of a prior lying phase (which is non-compact and forms aggregate-like structures): The formation of connected regions of lying rods (number densities) can be deduced from χ^{lying}, which counts the number of clusters at low densities (Fig. 5.52, bottom figure). It sets in earlier ($t^\star \approx 0.04$) than the "nucleation" of standing clusters ($t^\star \approx 0.1$), which shown for the cluster number density n^{standing}/M^2 of only nearest-neighbor standing rods (Fig. 5.52, middle figure). The cluster number density n^{any}/M^2 of "any"-oriented nearest-neighboring particles (Fig. 5.52, bottom

figure), also shows the signature of an earlier formation of clusters that are *not* solely standing. The n^{any} increases, reaches its maximum at $t^\star \approx 0.2$, and decreases thereafter.

Lying ("any") connected clusters (nearest-neighbor structures that are larger than $i_{\min}$ in number) begin growing at $t^\star \approx 0.08$ – this can be inferred from the discrepancy between n^{any} and n^{standing}. The Minkowski functionals of this lying phase (Fig. 5.52, bottom figure), which measure the boundary "1D surface" W_0 and "total amount" W_1, display *exactly* the same dynamics: the curves overlap.[26] We rationalize this with a possibly *fractal-like* structure of the lying phase (network-like): compact clusters are not visible, visually. These two lying functionals increase rapidly upon $t^\star \approx 0.1$, ending up in a sharp maximum at $t^\star \approx 0.4$, decreasing rapidly thereafter. The absolute value of the Euler characteristic[27] of the lying phase $|\chi^{\text{lying}}|$ reaches a plateau in the interval $0.15 < t^\star < 0.8$. This indicates that the microstructure of the lying connected regions is self-similar, as ρ_{12} has saturated and ρ_3 still follows its second power law. The absolute value of the Euler characteristic starts to drop when "holes" predominate the structure of the lying phase: the growth of the standing phase happens at the expense of the lying phase.

The cluster number density of the standing phase n^{standing}/M^2 (Fig. 5.52, middle figure) initially grows in a power-law-like-manner in the interval $0.1 < t^\star < 0.2$ before the "nucleation" process slows down. It finally comes to a halt at around $t^\star \approx 0.5$. (Note that the Minkowski functional W_0^{standing} obtains an inflection point at the same time.) The growth of these clusters sets in around $t^\star \approx 0.2$ — it is *delayed* compared to the growth of the lying connected clusters, which we already explained above. Their growth rate, as can be inferred from the average cluster sizes $\langle i^{\text{standing}} \rangle$ over time, increases until the end of the simulation. We can deduce that their growth mainly stems from the standing-up of the lying connected regions: At $t^\star \approx 0.3$, the nematic order $Q_{\text{mob. rot.}}$ of rotationally mobile particles (Fig. 5.53, middle figure) decreases until it reaches a minimum at $Q \sim -0.1$, where it remains until the end of the simulation. At the same time, the probability of rotating downwards, seen in $\rho_{\text{mob. rot. down}}$, decreases continually. For $t^\star > 0.5$, the standing cluster number densities n^{standing}/M^2 drops significantly due to the growth and (or) coarsening of the standing phase. This sets in when the system begins to percolate, seen in the percolation plots for "any"-oriented connected regions in Fig. 5.53 (top figure). The standing phase percolates around $t^\star \approx 1.2$. At the same time, the absolute value of the Euler characteristic of the standing phase $|\chi^{\text{standing}}|$ reaches a sharp maximum, and W_0^{standing} (the boundary "1D area") saturates.

To summarize, we have identified four time intervals: In the first, $t^\star < 0.1$, non-compact lying connected regions (clusters) form. In the second, $0.1 < t^\star < 0.4$ standing clusters "nucleate and grow", during which the formation of lying connected clusters slows down. Growth and (or) coarsening of the standing phase occurs in the interval of $0.4 < t^\star < 1.2$. The standing phase seems to grow in expense of the lying phase (it looks like aggregate-like structures or a fluid). In the last time interval we simulated, $t^\star \gtrsim 1.2$, the

[26] Note the two curves entail separate y-axes, hence they overlap apart from a scaling factor.

[27] Note that elsewhere in this chapter (in Sec. 5.3.7), the absolute value operation was *not* applied to the Euler characteristic. Any zero-crossing of χ will be visible as a very sharp "drop" and "return" in the $|\chi|$-representation.

standing phase coarsens and percolates.

We would like to make a note that a growth trajectory for the case of $\epsilon = -0.5988$, very near the estimated critical point ϵ_{crit}, seems to display essentially the *same* kinetics described here: We have plotted some of the same quantities in the same type of overlay in Fig. A.4 in App. A.1.

(C) Competition of lying- and standing-cluster formation

The specific example of this phase transition scenario we present in Figs. 5.54–5.55 is defined by the pair of parameters $(F/D = 1 \times 10^{-4}, \epsilon = -1.5)$ or $(\log_{10}(D/F) = 4, \ln(1/|\epsilon|) = -0.405)$. We attempt to describe the kinetics in the data in forthcoming paragraphs.

Similarly to scenario (B), we observe the same power-law-type growth in the number densities ρ_{12} and ρ_3 at early times (Fig. 5.54, top figure), but, lasting for a much shorter time span (in the interval $t^\star < 0.04$, $\rho \lesssim 0.05$). The next time interval is $0.04 < t^\star < 0.1$, where we see the number density of lying rods ρ_{12} heading towards a constant value of about 0.02 all the while ρ_3 shows power-law-like growth with a larger growth rate than in the first time interval. Thereafter, in the interval $0.1 < t^\star \lesssim 0.3$, ρ_{12} drops substantially, during which the standing-rod density ρ_3 crosses over to a third power law with a slower growth rate. A last time interval is $t^\star \gtrsim 0.3$, where growth of the standing rod density ρ_3 slows down and the tiny amount of remaining lying rods ρ_{12} disappears continually (this will be split into two intervals, again, in the discussion below).

Regarding the clusters of the lying phase (Fig. 5.54, bottom figure), at the earliest times we observe lying clusters forming: The "any" cluster number density, the lying Minkowski functionals and as well as the absolute value of the lying Euler characteristic (which corresponds to the cluster number density at low densities) all grow. This growth comes to a halt, indicating the onset of the second time interval, when the formation process of the lying phases "freezes". In stark contrast, the standing phase only "nucleates" within the first time interval (Fig. 5.54, middle figure) and undergoes a mixture of "nucleation and growth" within the second interval. In the latter, the "nucleation" slows down, whereupon the number density n^{standing}/M^2 of standing clusters levels off to a nearly constant value in the third time interval. The mean cluster size $\langle i^{\text{standing}} \rangle$ shows constant growth rate (power-law-like) during this period, while the amount W_1^{lying} of the lying phase, and the sizes of the clusters decrease dramatically (which can be inferred from the mild decrease in n^{any}/M^2 and drop in $|\zeta^{\text{lying}}|$). Note that the Minkowski functionals for the lying phase W_1^{lying} and W_0^{lying} overlap almost exactly apart from a scaling factor, an effect we are not sure how to explain. In the third time interval, the standing phase "eats up" the remaining lying phase. Closer inspection reveals that the final time interval is, in fact, split into two. Up to around $t^\star \approx 0.8$, both growth and coarsening of the standing phase occurs, while in the last sub-interval, the standing phase mainly coarsens. There, the system heads towards a percolating state (for "any" and standing clusters are equivalent at that point, see Fig. 5.55, top figure), where the number of clusters drops rapidly to unity and the growth process is maximally accelerated.

These different time-intervals can be identified easily in the dynamical observables (Fig. 5.55, middle and bottom figures). Most striking is the time trace of the relative translational motion flux $J_{\text{trans., rel.}}$ (relative to the total "internal" motion flux). This quantity shows a pronounced loop: It increases in the first time interval, levels off to a nearly constant value in the second, decreases in the third, increases slightly in the first half of the fourth interval, and increases more rapidly thereafter.

(D) Low-density-lying-gel and standing-cluster formation

The specific example of phase transition scenario (D) that we present in Figs. 5.56–5.57 is defined by the pair of parameters $(F/D = 1.667 \times 10^{-4}, \epsilon = -2)$, or $(\log_{10}(D/F) = 3.778, \ln(1/|\epsilon|) = -0.693)$.

As in scenarios (B) and (C), ρ_{12} and ρ_3 in Fig. 5.56 (upper figure) display the same power-law-like growth in a first time interval ($t^\star < 0.15$, $\rho \lessapprox 0.13$) before Q begins to increase. Afterwards, the growth of ρ_{12} slows down and saturates at around $t^\star \approx 1$ ($\rho \approx 0.4$, $\rho_{12} \approx 0.2$). The standing number density ρ_3 follows the same power law until $t^\star \approx 0.5$, smoothly crossing over to a second power law that sets in at $t^\star \approx 1$.

The lying phase percolates at $t^\star \approx 0.4$ (Fig. 5.57, top figure), and forms a low-density gel when ρ_{12} approaches its maximum value. The percolation point is very near when the absolute value of the Euler characteristic $|\chi^{\text{lying}}|$ shows a sharp drop to zero (the zero-crossing of χ without the absolute value): Holes now dominate the topology of the lying phase.

Lying and standing clusters begin forming right from the beginning (Fig. 5.56, bottom two figures). We see only a very short time interval ($t^\star < 0.03$) where constant "nucleation" rates persist. While the lying phase coarsens significantly upon $t^\star > 0.07$, which can be inferred from n^{any}/M^2 and the Minkowski functionals and Euler characteristic of the lying phase, the time interval between $0.04 < t^\star < 1$ seems to be a complex interplay of "nucleation", growth and coarsening of the standing phase.

Once the lying, low-density gel has formed $t^\star \approx 0.4$, the rotational mobility of the system is carried by rods predominantly in the lying orientation, which always have a non-zero probability to stand up and are hence mobile (see $Q_{\text{mob., rot.}}$ in Fig. 5.57, middle figure). The total number of translationally mobile particles $\rho_{\text{mob., transl.}}$ decreases, the population of which is dominated by rods in the standing orientation, i.e. $Q_{\text{mob., transl.}} > 0$. At around $t^\star \approx 0.2$, the standing phase percolates (Fig. 5.57, top figure) and, consequently, the dynamics in the system slows down significantly. The standing phase coarsens at around this time.

(E) Formation of standing clusters out of a dense gel phase

The specific example of phase transition scenario (E) that we present in Figs. 5.58–5.59 is defined by the pair of parameters $(F/D = 1.67 \times 10^{-2}, \epsilon = -2)$, or $(\log_{10}(D/F) = 2, \ln(1/|\epsilon|) = -0.693)$.

In contrast to the scenarios discussed so far, the number densities of lying (ρ_{12}) and standing rods (ρ_3) do not show a synchronous power-law-type growth at earliest times ($t^\star < 0.15$, $\rho < 0.1$) (Fig. 5.58, top figure). The lying phase grows significantly more quickly than the standing phase and, consequently, the nematic order parameter Q becomes negative. Within this time interval, we

observe the formation and growth of clusters of both lying and standing phases, indicated by $|\chi^{\text{lying}}|$ and n^{any}, as well as n^{standing}/M^2, respectively (Fig. 5.58, bottom two figures).

In the second time interval ($0.15 < t^\star < 1$), the growth of ρ_{12} slows down and saturates at around 0.3, which is near the maximal possible value of $1/L \approx 0.33$. Within the same time interval, the standing-rod density ρ_3 grows with a second power law with a much slower growth rate. The nematic order parameter reaches Q reaches its minimum value of about -0.3. Moreover, the lying phase forms a percolating gel (the lying percolation point is around $t^\star \approx 0.25$ in Fig. 5.59, top figure), which becomes more dense until the end of this time interval. The "any" cluster number density n^{any} (Fig. 5.58, bottom figure) reaches a maximum at the beginning of this time interval and shows an enormous drop until reaching its minimal value of unity at the end of this second time interval. The percolated gel remains stable until the end of the simulation. The absolute value of the lying Euler characteristic $|\chi^{\text{lying}}|$ shows a sharp "dip" near the percolation point $t^\star \approx 0.25$, indicating the dominance of holes over clusters in the network-like lying phase thereafter, reaching a maximal value at the end of the second time interval. The nematic order drops down to around $Q \approx -0.3$.

In the third time interval we identify ($1 < t^\star <\sim 40$), the number density of lying rods ρ_{12} remains constant, while that of standing rods (ρ_3) continually increases its growth rate. The total number density saturates in the first "half" of the time interval ($t^\star < 5$), and increases again in the second half (Fig. 5.58, top figure). Careful inspection of all these observables and of simulation snapshots suggests that the microstructure of the gel coarsens, at first, up to times of $t^\star \approx 5$, during which W_0^{lying} decreases and W_1^{lying} increases (Fig. 5.58, bottom figure). The microstructure of the gel becomes finer, again, around $\sim 5 < t^\star <\sim 40$. Yet, it appears to remain self-similar, which we deduce from the observation that the Euler characteristic χ^{lying} does not change much during this time. The time-trace of the standing cluster number density n^{standing} (Fig. 5.58, middle figure) shows a nearly constant, low "nucleation" rate of standing clusters over the second and third time intervals ($0.15 < t^\star < 40$). The mean cluster sizes thereof $\langle i^{\text{standing}} \rangle$ indicate a slow, but constant growth rate, as well. The standing phase "nucleates" from within the lying, dense gel, and grows very slowly at the expense of the lying phase. The time-trace of the standing cluster number density n^{standing} clearly shows a "two-step-nucleation" scenario. The crossover occurs between the first and second time interval.

We identify a last time interval ($t^\star > 40$), where the lying density ρ_{12} decreases while the standing density ρ_3 increases significantly. The number density of standing clusters n^{standing}/M^2 decreases, while their mean size $\langle i^{\text{standing}} \rangle$ "explodes" (Fig. 5.58, top and middle figures). The standing phase grows and coarsens, "eating up" the lying phase. It heads towards its percolation point at around $t^\star \approx 100$ (Fig. 5.59, top figure.

Based on our observations, we propose that scenario (E) indicates the formation of a lying gel that is *stable* over long periods of time. We would expect to see that the gel phase observed in scenario (D) becomes stable for stronger deposition quench rate F/D or when the attraction strength $|\epsilon|$ becomes stronger. Indeed, we will see that this fits with the picture we will present in the next subsection, i.e. Fig. 5.60.

Extrapolation "maps" of Q in the $(\ln(1/|\epsilon|), \log(D/F))$–plane

The different scenarios can be pinpointed visually in a sequence of extrapolation maps of the global nematic order Q in the $(\ln(1/|\epsilon|), \log(D/F))$–plane at fixed densities. We present these in Fig. 5.60. We first remark that a cubic extrapolation scheme has been employed (to guarantee continuous and differentiable extrapolated functions) among the grid values.[28] Hence, some caution is necessary when considering grid-points far from supporting points or within large gaps between such points. Supporting points for the extrapolation scheme are from our simulation datasets, and their positions are indicated in small, magenta circles.

In Fig. 5.60, we see that at very high reduced temperatures or for very weak attractions, indicated by high $\ln(1/|\epsilon|$ in the "map", the nematic order becomes slightly positive at early stages of film growth $\rho = 0.051$ (top left image). The value of Q is nearly independent of the applied deposition quench rate (or, inversely, of D/F). With increasing density (progressing among the figures from left-to-right and top-to-bottom, the nematic order increases monotonically, reaching values of $Q \approx 0.3 \ldots 0.7$ at $\rho = 0.353$ (bottom right figure) at these values of $\ln(1/|\epsilon|$. The observed increase in Q is stronger for smaller deposition quench rates F/D (larger D/F). The rectangular area that is green in color at $\rho = 0.15$ (top right figure) corresponds to where *scenario (A)* is found.

At medium and strong attraction strengths ($0 < \ln(1/|\epsilon|) < -1.5$) and small–to–medium deposition quench rates F/D (large–to–medium D/F), we can identify a green–brownish–purple "blob" region in the lower right region of the diagram for $\rho = 0.051$ (top left figure), corresponding to values of $Q > 0.2$ (the standing phase dominates). Upon increasing the density to $\rho = 0.353$ (bottom right figure), values of $Q \sim 0.7 \ldots 1.0$ are reached. The "blob" region best identifiable at $\rho = 0.051$ corresponds to where phase transition *scenario (C)* is found.

At medium and strong attraction strengths ($0.2 < \ln(1/|\epsilon|) < -1.5$) medium–to–high deposition quench rates F/D (medium–to–low D/F), a triangular region of blue color can be identified: This shows the area where $Q < 0$ (i.e where the lying phase dominates), which is seen in the lower-left corner of all diagrams. This represents where *scenario (E)* will be found.

The phase transition *scenario (B)* is best identifiable in $\rho = 0.271$: It is seen for medium attraction strengths ($0.5 > \ln(1/|\epsilon|) \geq 0$) and for all deposition quench rates F/D where the values of $Q > 0.2$. This corresponds to a trapezoidal region in the map. Note that we have checked snapshots from simulations in this region to verify.

Between all these regions, a clearly visible white "coastline" connects the (x, y)–coordinates $(0.5, \sim 0.4)$ and $(\sim 6.5, -1.5)$. Along this gel-transition line is where we find phase transition *scenario (D)*.

We further propose that by extrapolating the gel line to high deposition quench rates (to even lower values of D/F), we should find a *gel–to–jamming transition*. At this point, translational motion would be effectively frozen-out by the deposition flux, where thermodynamics would find its hard limit. The corresponding temperature may give a fair estimate for the critical temperature of the isotropic–vapor–standing–transition, or critical value ϵ_{crit}. We have extrapolated the white gel line in the upper two maps up to the lowest-shown x-axis value of $x = 0.5 = \log_{10}(D/F)$, obtaining a y-axis value of $y \approx 0.4 \ldots 0.5$.

[28] We have used the *Scipy* numerical library in *Python3* for these purposes.

The corresponding value of $\epsilon \approx -0.67 \cdots - 0.61$ would increase slightly if the transition sets in at somewhat lower values of D/F. Notably, the ballpark estimates of $\epsilon_{\text{crit}} \approx -0.5988$ from our KMC simulations and $\epsilon_{\text{crit}} \approx -0.625$ from GCMC simulations (reported in Sec. 5.2) are very close to this extrapolation value.

Moreover, the gel line (scenario (D)) meets the lower end of the trapezoidal region of scenario (B) and the upper-left-corner of the region for scenario (C) in an uncertain, "triple" region. Regions (B) and (C) meet along the extrapolated line around a crossing point with (x, y)–coordinates $(2, 0.2)$. The corresponding value of $\epsilon \approx -1.2$ may provide an estimate of the position of one of the FMT-predicted metastable critical points, i.e. $\epsilon_{\text{crit, meta, denem}}$ or $\epsilon_{\text{crit, meta, nem}}$ corresponding to the reduced critical temperatures "$T_{\text{crit,2}}$" and "$T_{\text{crit,nem}}$" in the FMT phase diagram Fig. 5.2(b)). This would be situated just in-between our older categorization of ϵ-Regime IIIa ($\epsilon = -1$) and Regime IIIab ($\epsilon = -1.5$). A denser grid (with more simulation points) would be helpful to clarify these issues with more certainty.[29]

To this end, simulating this region (at low values of D/F) for larger systems and for more values of ϵ is feasible for future investigations. Particularly useful may be the same mobility plots that we have used in our analysis so far. It would be most interesting to verify this, as it would attest to a deep and theoretically unexplored connection between jamming transition, arrested states, and thermodynamic critical points. We will discuss a hunch we have about these unexplored relationships again in Chs. 6 and 8.

* * *

In the next section, we will explore rods that are somewhat longer ($L = 5$), where we will see that these systems are (very likely) characterized by the same phase transition scenarios (A)–(E). Some subtleties and other features of the phase transition scenarios that we have presented so far will become clearer for the case of longer rods.

[29] We are well aware that finite-size effects can play a significant role in out-of-equilibrium conditions. Future investigations of these scenarios for larger lattice sizes may be necessary.

SCENARIO (B):
Isotropic–fluid–to–standing transition via "nucleation and growth" of clusters

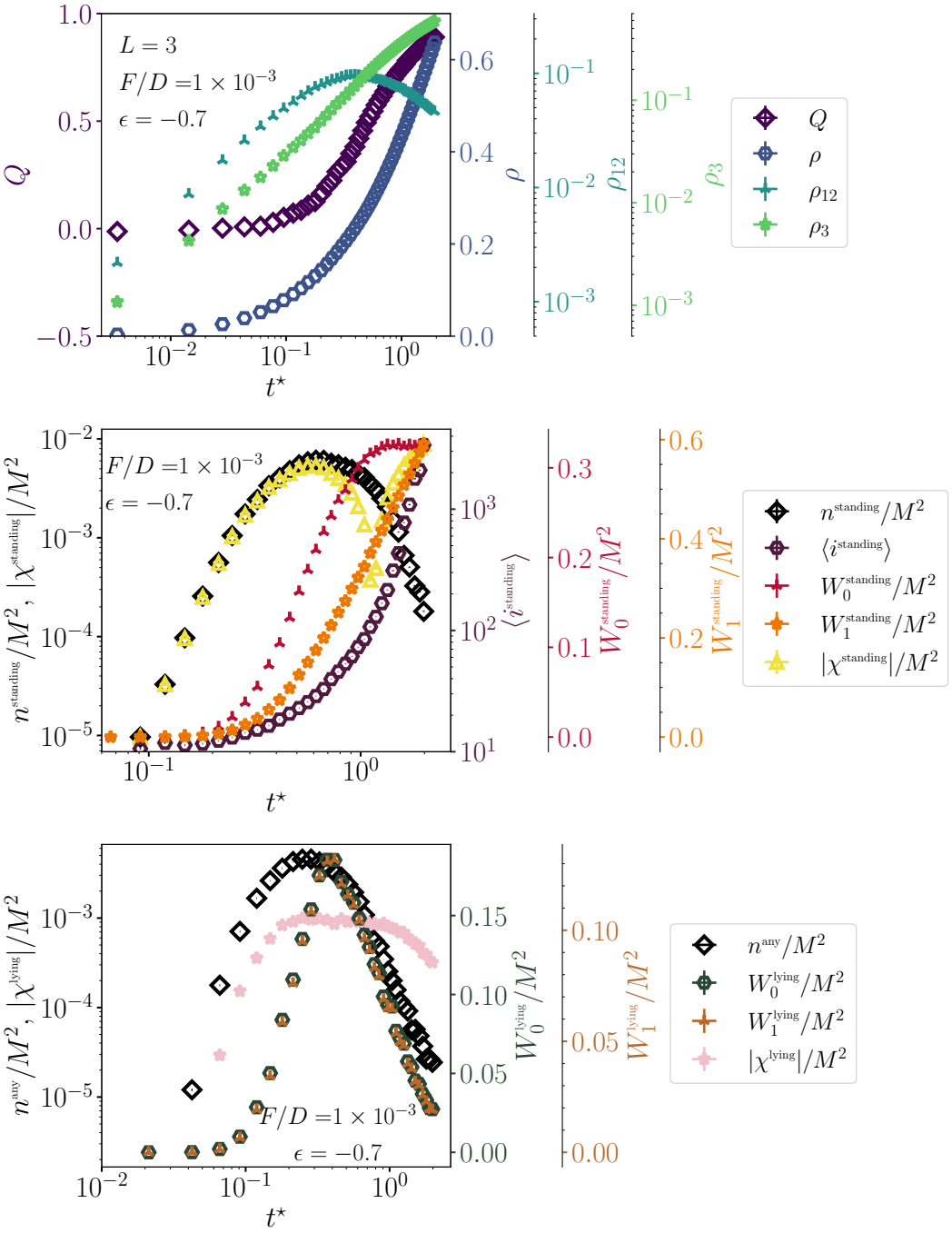

FIGURE 5.52: Exemplary case of phase transition scenario (B): First set of the time-traces of of various observables – the global order parameters and number densities in the top figure, standing clusters statistics and Minkowski functionals in the middle figure, and "any" cluster numbers and lying Minkowski functionals in the bottom figure ($L = 3$, neutral substrates). The specific example is defined by the pair of parameters $(F/D = 1 \times 10^{-3}, \epsilon = -0.7)$, or $(\log_{10}(D/F) = 3, \ln(1/|\epsilon|) = 0.356)$. Please refer to Tab. 5.3 for clarification on observables and notation, and the main text for a description of the figures.

SCENARIO (B) (continued):
Isotropic–fluid–to–standing transition via "nucleation and growth" of clusters

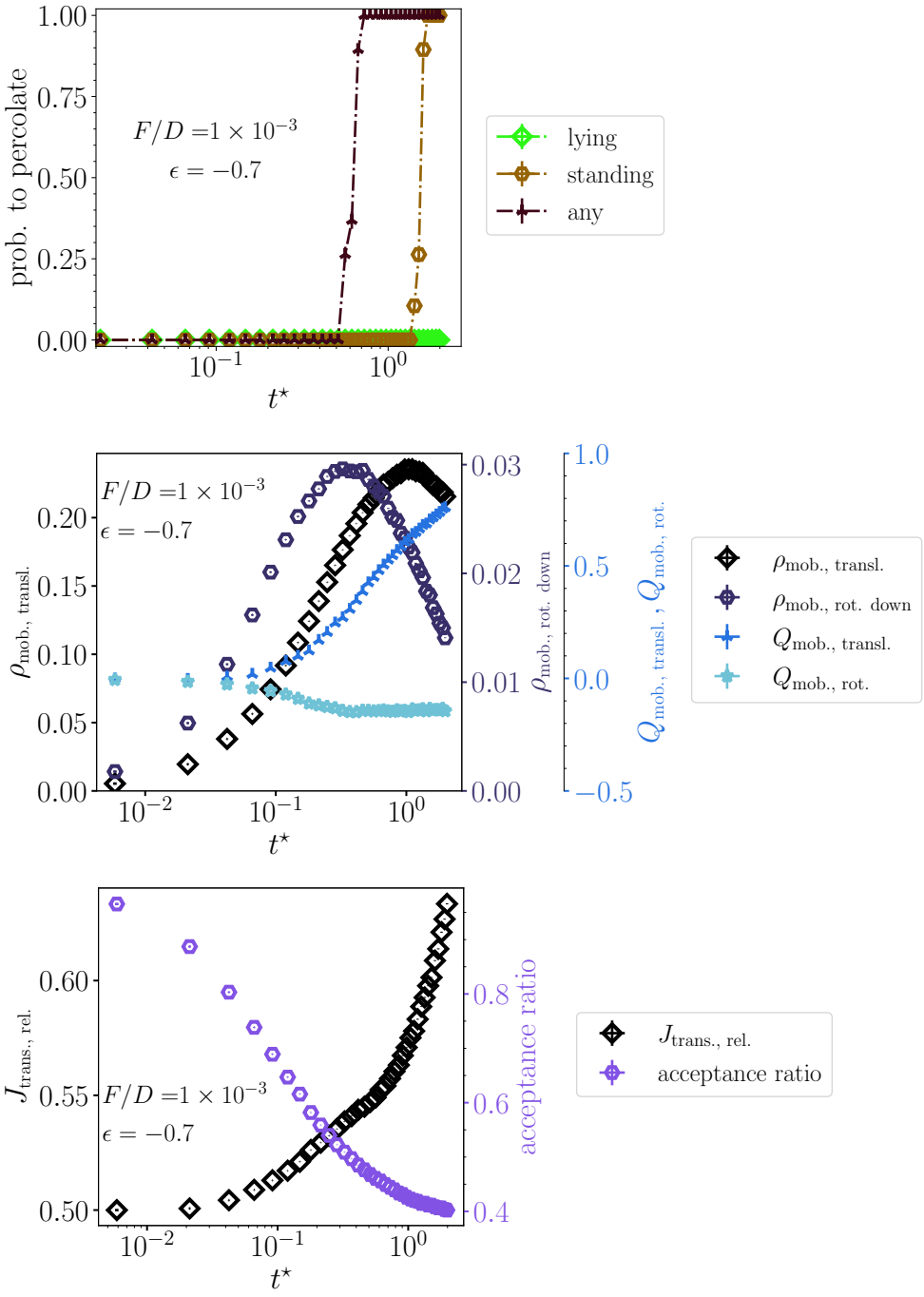

FIGURE 5.53: Exemplary case of phase transition scenario (B): Second set of the time-traces of various observables – the percolation probability for connected structures the top figure, mobilities and nematic order of mobile particles in the middle figure, and relative translational flux and "sticky" acceptance ratio in the bottom figure ($L = 3$, neutral substrates). Please see caption of Fig. 5.52.

SCENARIO (C):
Competition of lying- and standing-cluster formation

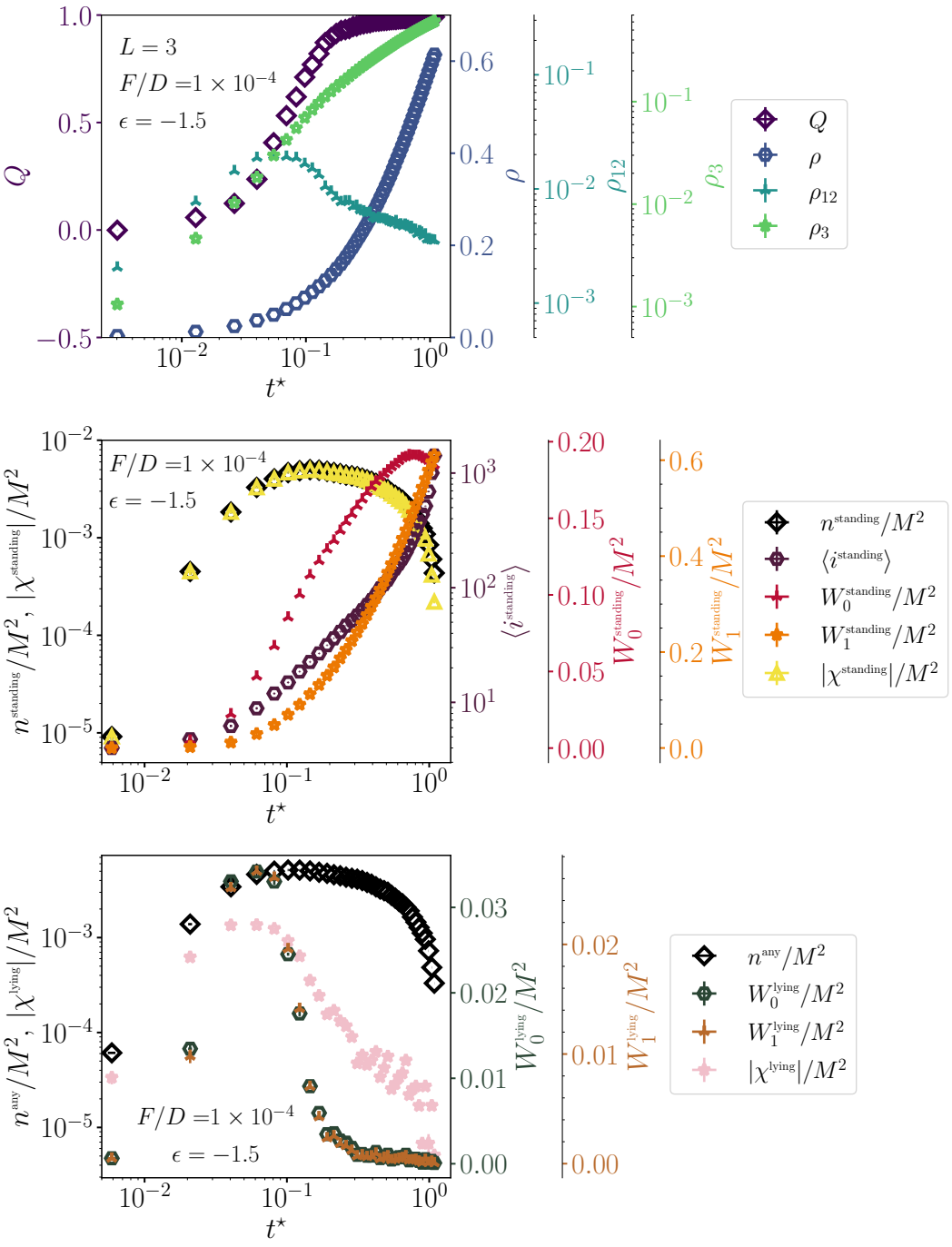

FIGURE 5.54: Exemplary case of phase transition scenario (C): First set of the time-traces of of various observables – the global order parameters and number densities in the top figure, standing clusters statistics and Minkowski functionals in the middle figure, and "any" cluster numbers and lying Minkowski functionals in the bottom figure ($L = 3$, neutral substrates). The specific example is defined by the pair of parameters $(F/D = 1 \times 10^{-4}, \epsilon = -1.5)$ or $(\log_{10}(D/F) = 4, \ln(1/|\epsilon|) = -0.405)$. Please refer to Tab. 5.3 for clarification on observables and notation, and the main text for a description of the figures.

SCENARIO (C) (continued):
Competition of lying- and standing-cluster formation

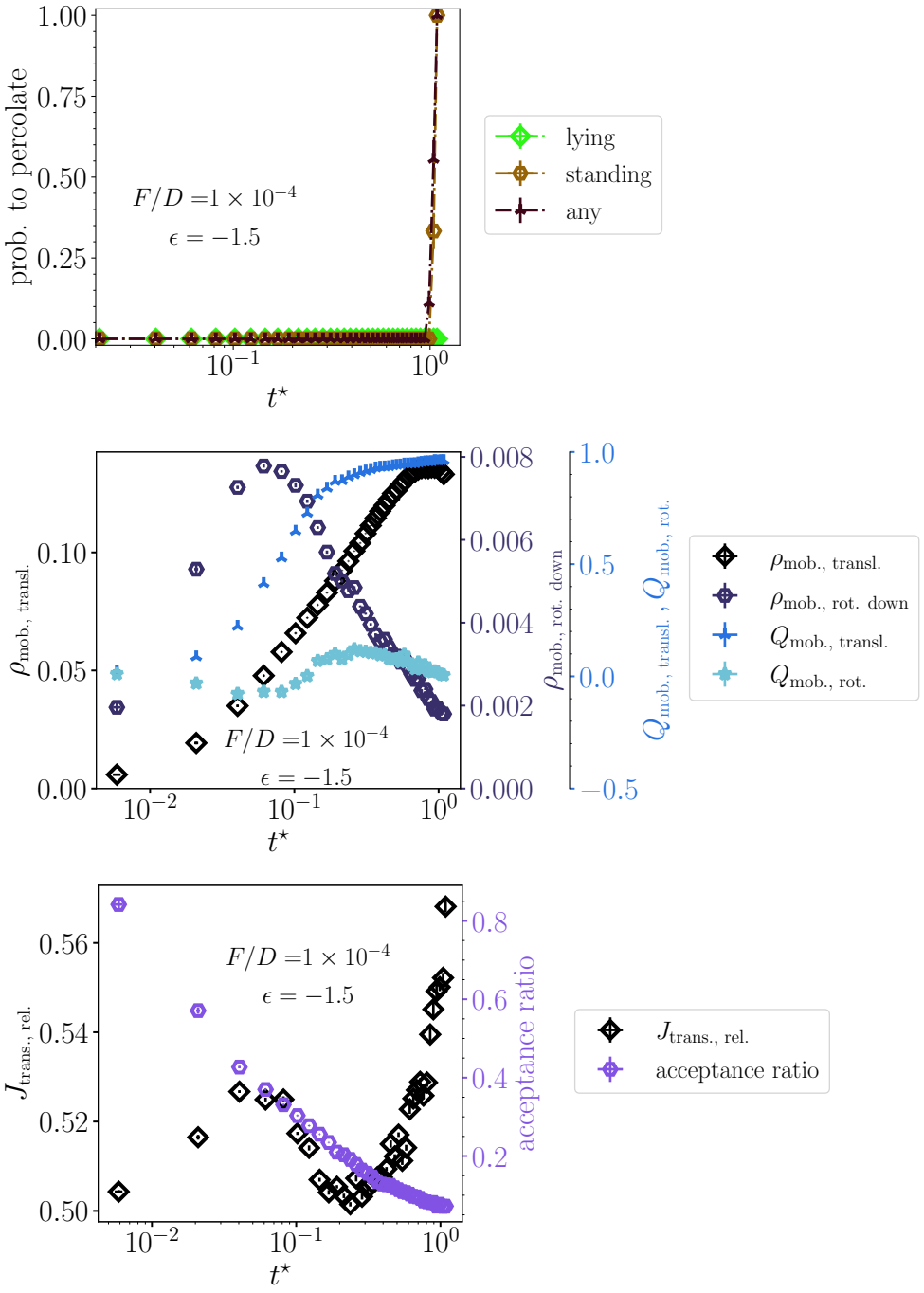

FIGURE 5.55: Exemplary case of phase transition scenario (C): Second set of the time-traces of various observables – the percolation probability for connected structures the top figure, mobilities and nematic order of mobile particles in the middle figure, and relative translational flux and "sticky" acceptance ratio in the bottom figure ($L = 3$, neutral substrates). Please see caption of Fig. 5.54.

SCENARIO (D):
Low-density-lying-gel and standing-cluster formation

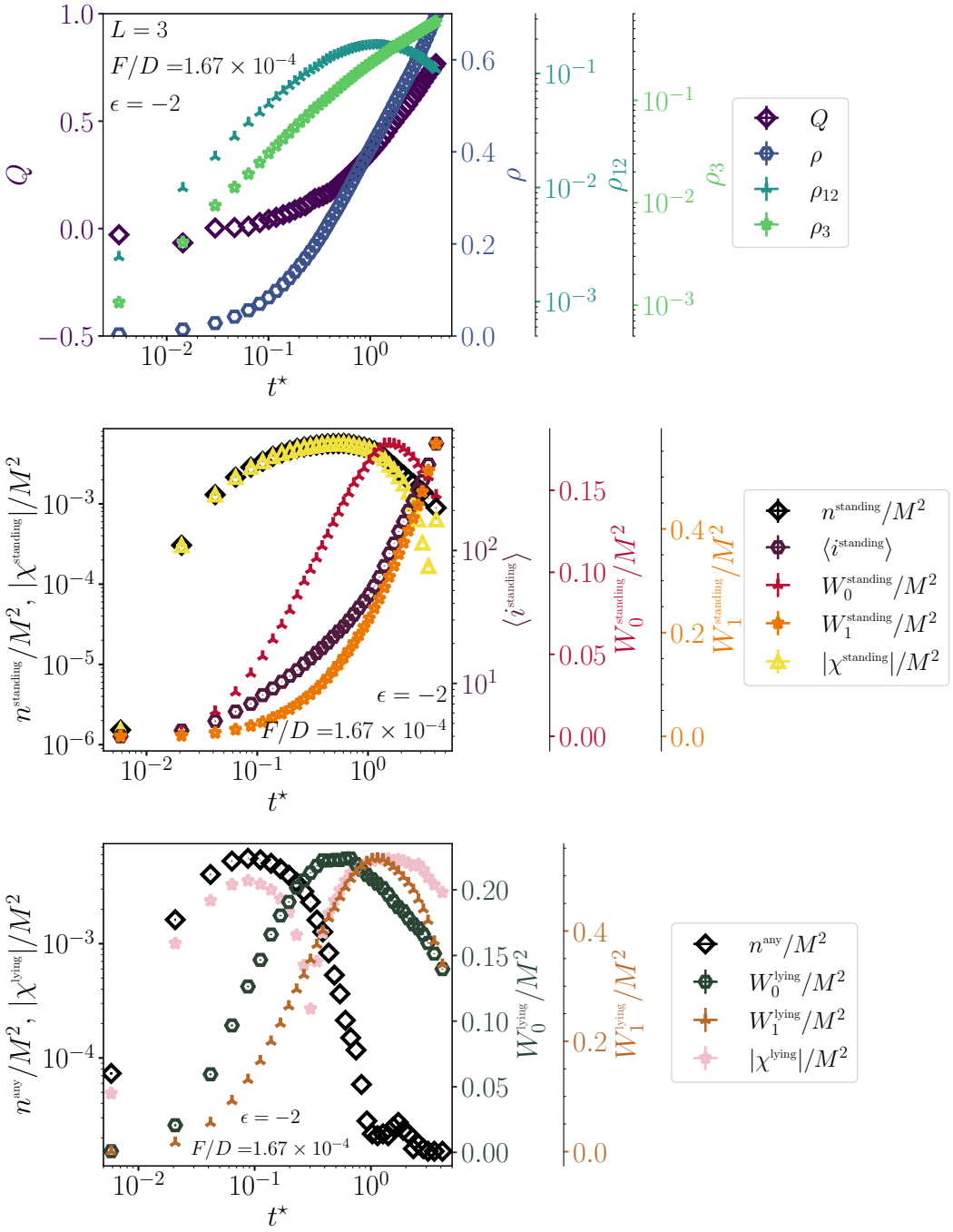

FIGURE 5.56: Exemplary case of phase transition scenario (D): First set of the time-traces of of various observables – the global order parameters and number densities in the top figure, standing clusters statistics and Minkowski functionals in the middle figure, and "any" cluster numbers and lying Minkowski functionals in the bottom figure ($L = 3$, neutral substrates). The specific example is defined by the pair of parameters $(F/D = 1.667 \times 10^{-4}, \epsilon = -2)$, or $(\log_{10}(D/F) = 3.778, \ln(1/|\epsilon|) = -0.693)$. Please refer to Tab. 5.3 for clarification on observables and notation, and the main text for a description of the figures.

SCENARIO (D) (continued):
Low-density-lying-gel and standing-cluster formation

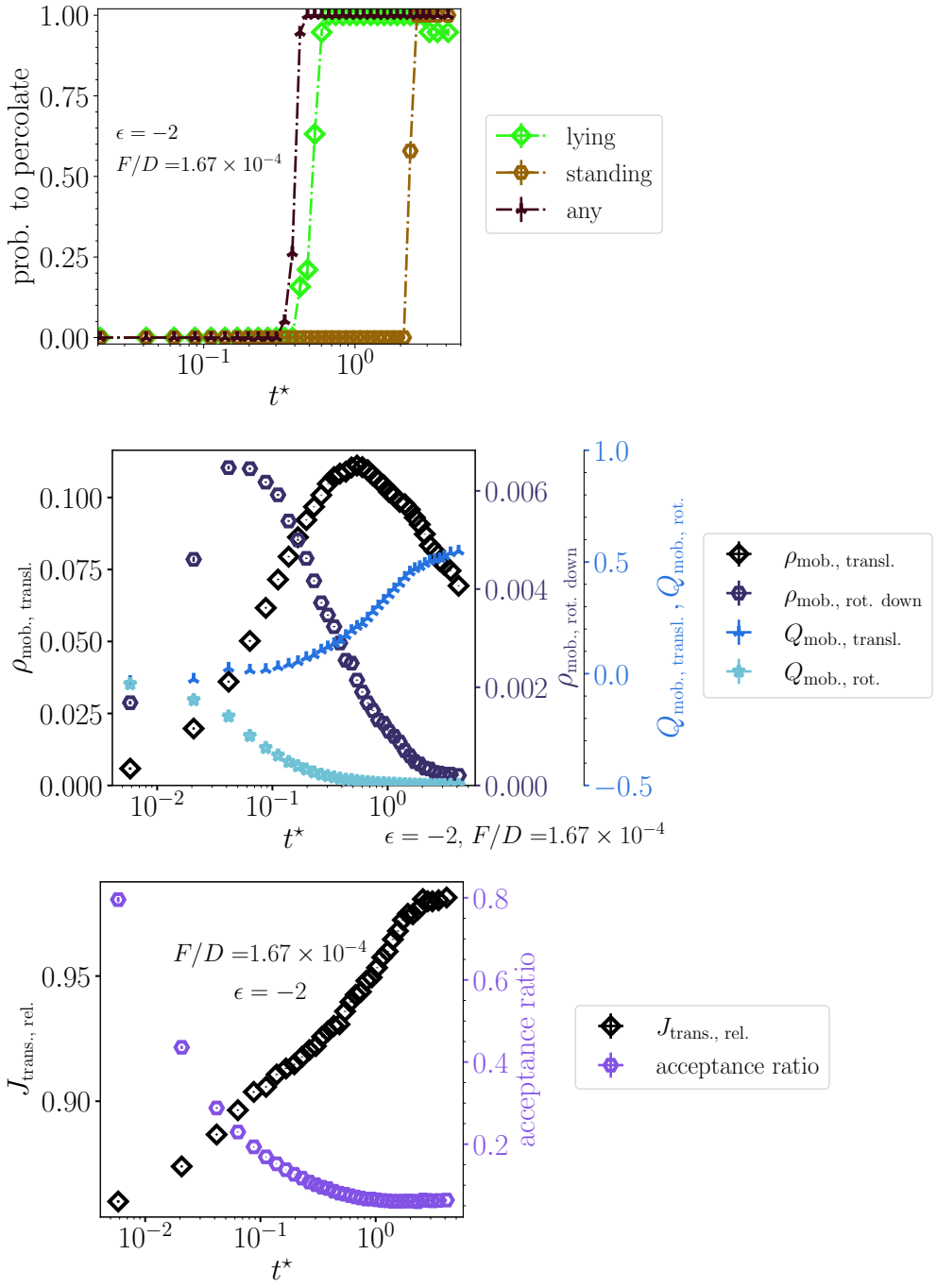

FIGURE 5.57: Exemplary case of phase transition scenario (D): Second set of the time-traces of various observables – the percolation probability for connected structures the top figure, mobilities and nematic order of mobile particles in the middle figure, and relative translational flux and "sticky" acceptance ratio in the bottom figure ($L = 3$, neutral substrates). Please see caption of Fig. 5.56.

SCENARIO (E):
Formation of standing clusters out of a dense gel phase

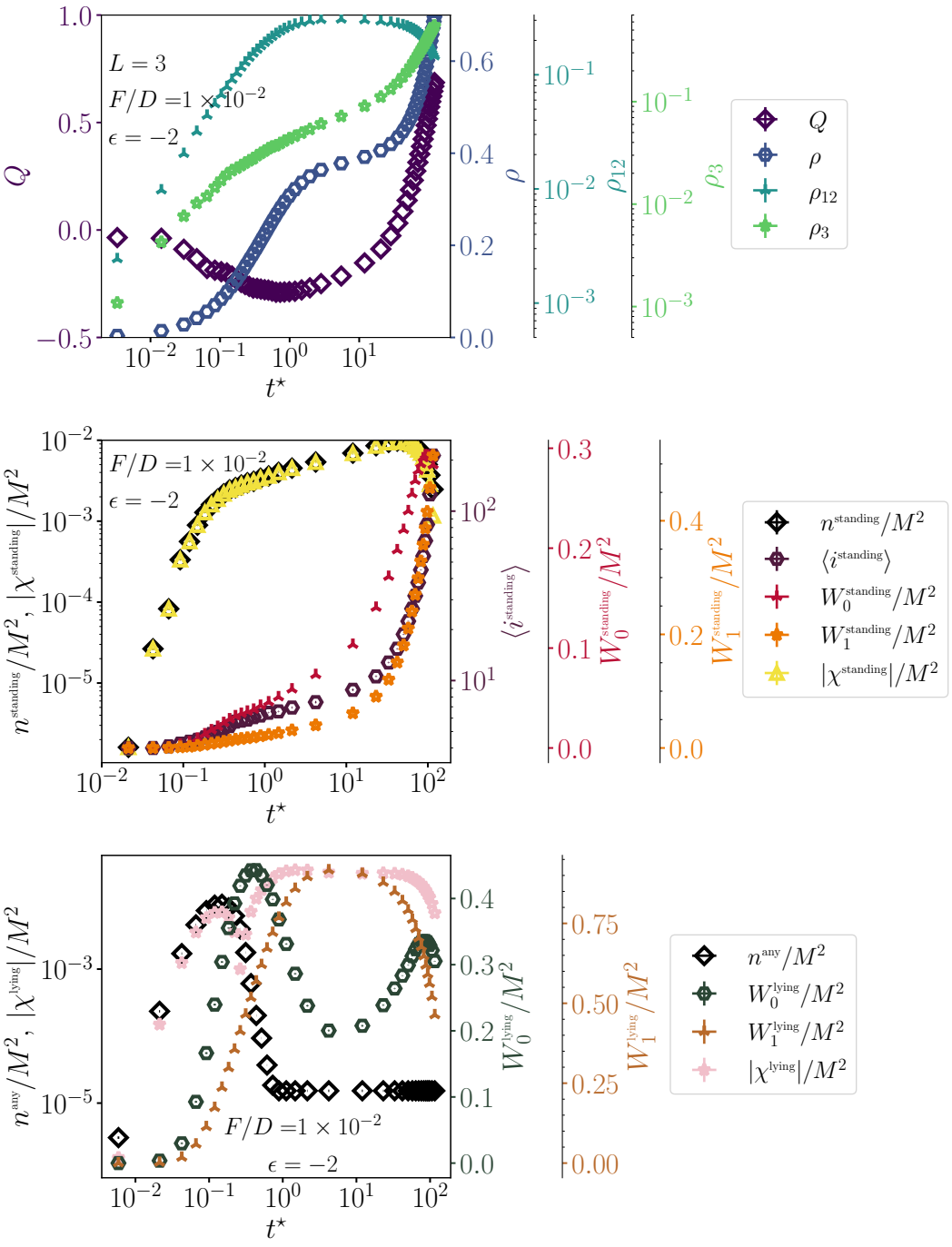

FIGURE 5.58: Exemplary case of phase transition scenario (E): First set of the time-traces of of various observables – the global order parameters and number densities in the top figure, standing clusters statistics and Minkowski functionals in the middle figure, and "any" cluster numbers and lying Minkowski functionals in the bottom figure ($L = 3$, neutral substrates). The specific example is defined by the pair of parameters $(F/D = 1 \times 10^{-2}, \epsilon = -2)$, or $(\log_{10}(D/F) = 2, \ln(1/|\epsilon|) = -0.693)$. Please refer to Tab. 5.3 for clarification on observables and notation, and the main text for a description of the figures.

SCENARIO (E) (continued):
Formation of standing clusters out of a dense gel phase

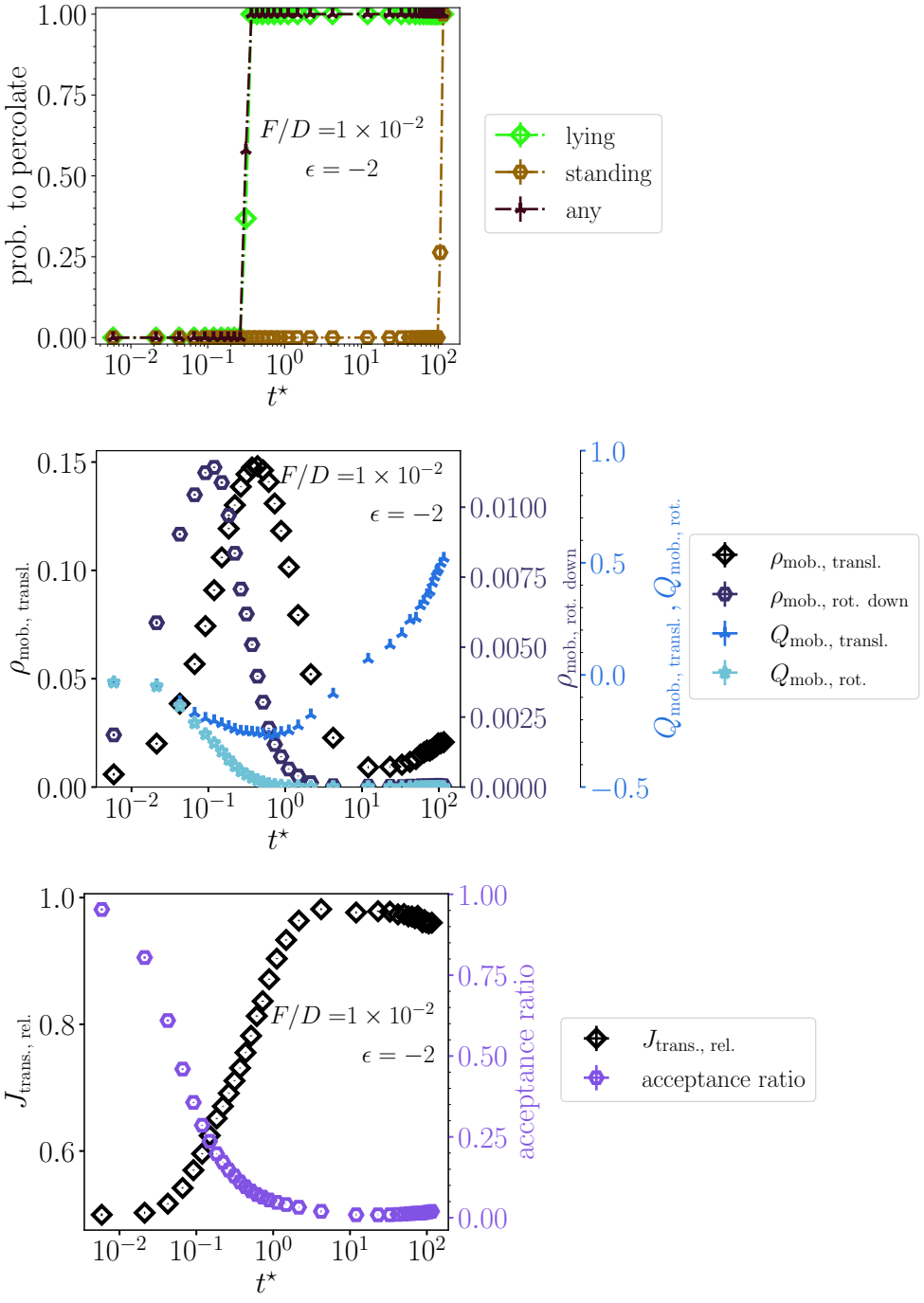

FIGURE 5.59: Exemplary case of phase transition scenario (E): Second set of the time-traces of various observables – the percolation probability for connected structures the top figure, mobilities and nematic order of mobile particles in the middle figure, and relative translational flux and "sticky" acceptance ratio in the bottom figure ($L = 3$, neutral substrates). Please see caption of Fig. 5.58.

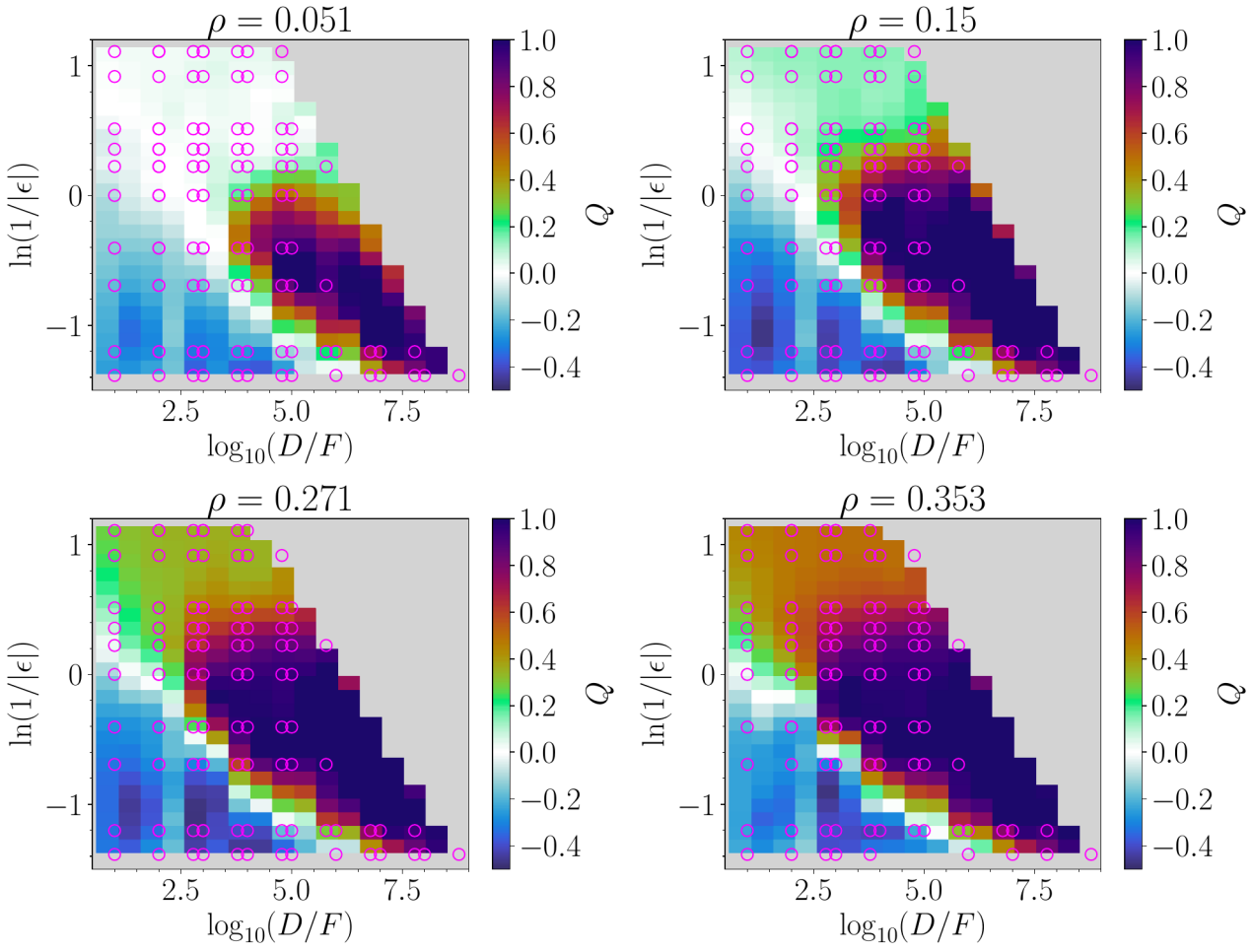

FIGURE 5.60: Extrapolated maps of the nematic order occurring during growth as plotted in the $(\ln(1/|\epsilon|), \log(D/F))$-plane at six different densities during growth ($L = 3$, neutral substrates). This includes ϵ-regimes I (top three data-point rows), II (next two data-point rows) and III (bottom five data-point rows). Magenta circles indicate supporting data points from simulation. The logarithm of the y-axis is taken in order to show more even spacing between sampled points. A cubic extrapolation scheme is employed.

5.4 Growth with longer rods

5.4.1 Results for $L = 5$

As shown by our GCMC simulations in equilibrium, the stable critical point for $L = 5$ is higher (at higher reduced temperatures) than $L = 3$, see Fig. 5.3. In our growth simulations that we elaborate on below, we can deduce that the metastable critical points, which define our "ϵ-regime III" will move towards higher reduced temperatures (weaker $|\epsilon|$). Maps of configurations in the $(\ln(1/|\epsilon|), \log(D/F))$–plane are provided in Figs. 5.62–5.65 further below, as well as as a corresponding map of the order parameter Q in Fig. 5.68. Beforehand, Fig. 5.61 presents the evolution of the order parameter Q as a function of packing fraction η, in full analogy to the analysis for $L = 3$ (Fig. 5.24). The order parameter is also plotted versus ρ and $t^\star = Ft$ in Figs. 5.66 and 5.67, accordingly. The dynamics of the global density ρ, lying density ρ_{12}, standing density ρ_3, and packing fraction η are plotted against the rescaled time $t^\star = Ft$ in Figs. 5.69, 5.70, 5.71, and 5.72, respectively.

Qualitative similarities to $L = 3$

We observe that the general behavior during monolayer growth is qualitatively very similar to the $L = 3$ case. The different phase transition scenarios as described in the previous section (Sec. 5.3.9) seem part of $L = 5$ systems, as well. However, a complete analysis of island statistics, cluster morphological analysis, and dynamical observables are outside of the scope of this thesis. We will, nevertheless, be able to infer the three basic ϵ-regimes I–III similar as for $L = 3$.

"Hard-rod-like" growth (ϵ-regime I) is seen for the topmost row of images ($\epsilon = -0.33$) in Figs. 5.62–5.63. The evolution of the nematic order parameter Q visible in Figs. 5.61, 5.66 and 5.67 also show very little change upon faster deposition quench rates F/D. At $\epsilon = -0.5$, only standing clusters grow, hinting at an "ϵ-regime II" like in the case of $L = 3$, see second row of images from the top in Figs. 5.62–5.63. We further speculate a metastable critical point $\epsilon_{\text{crit, meta, denem}} \gtrapprox -0.7$ for $L = 5$, below which the lying phase appears in aggregate-like clusters or network-like structures (possible "regime IIIa"). This is seen in the third row of images from the top in Figs. 5.62–5.63. Analogously to $L = 3$, we think a second metastable critical point might be around $\epsilon_{\text{crit, meta, 2D demix}} \lessapprox -1$, where we observe the formation of compact lying islands co-occurring with standing islands ("regime IIIb"), as well as a "wetting layer" with noticeably low nematic order (certainly for $\epsilon = -1.5$). Please consult to the fourth and fifth rows of images from the top in Figs. 5.62–5.63. The case of $\epsilon = -1.5$ (fifth row) also shows the "standing up" from a lying arrested state or wetting layer slightly past $\rho \gtrapprox 1/L = 0.2$, visible at $F/D = 10^{-2} \ldots 10^{-4}$ in Fig. 5.66. Seen in the time-trace of Q in Fig. 5.67, a prolonged period of time is required to overcome the "wetting layer", towards $Q > 0$ (in analogy to the cases we see for ϵ-regime III for $L = 3$). At even lower $F/D = 1.67 \times 10^{-5}$ a co-evolution of the lying phase (amorphous islands or very coarse "gel") and standing islands endures until very late stages.

The topology of Q in the $(\ln(1/|\epsilon|), \log(D/F))$–plane at fixed density is displayed in Fig. 5.68. This shows similarities to that of the $L = 3$ case in Fig. 5.60, yet is less detailed than the data presented here owing to less points available

in our simulation dataset. Nevertheless, in this representation the "gel line" can be identified: It connects the points $(1, 0.5)$ and $(4.5, -0.5)$ in the displayed pair of coordinates $[(\log(D/F), \ln(1/|\epsilon|))]$. Note that this gel line looks different than that for $L = 3$ in Fig. 5.60. There seems to be a "kink" at the coordinates $(2.5, 0.35)$ for $\rho = 0.15$. We propose with an argument similar to that discussed in in Sec. 5.3.9 that as this indicates the onset of arrested dynamics for a "critical" low value of D/F, that allows us to estimate a *metastable critical point*. The corresponding y-value renders $\epsilon_{\text{meta}} \approx -0.7$. For $\rho = 0.05$ the "gel line" looks almost horizontal for $\log_{10}(D/F)$ up to a value of 3. Via similar reasoning, we propose the critical point of the isotropic–standing transition may be found by extrapolating this nearly horizontal line towards very low D/F, which may be around a y-value of ~ 0.9 (although more data would be necessary), rendering $\epsilon_c \approx -0.5$. Therefore, the simulated curves for $\epsilon = -0.33, -0.5$ may be very near the critical point (above and below it), which matches to how we categorized these cases via "ϵ-regimes I and II" before. Nonetheless, more simulation points would be necessary for a better estimate and clearer "maps".

Figs. 5.62 and 5.63) show, quite intuitively, how the lying clusters or islands (regime IIIb) are noticeably larger in surface area in comparison to the $L = 3$ case of Sec. 5.3. Additionally, the higher degree of anisotropy favors the percolation of lying aggregate structures at lower densities, as different parts of space can more easily be bridged when rods are longer (requiring fewer rods to be localized in such a bridge). We report that the percolation transitions occur at earlier densities than $L = 3$ (not shown here), in alignment with the earlier "wetting layer" or lying arrested state. Figs. 5.64 and 5.65) display the system at intermediate densities, approaching the maximal-η states when the system forms a lying "wetting layer" or arrested state. They also demonstrate "two-faced" islands that occur in regime III for low F/D. Further comments on the configurations are found in the corresponding captions.

Subtle difference to $L = 3$: Pronounced loops in packing fraction

Apart from qualitative similarities, an important, subtle difference of growth with monolayers with rods of length $L = 5$ appears in comparison to those with $L = 3$. From Fig. 5.61 we can infer that the evolution entails more pronounced loops in the packing fraction for the cases of $\epsilon = -0.7, -1$, as well as the beginnings of loops for $\epsilon = -1.5$ at particular values of F/D. The loops can be seen in the time trace of the packing fraction in Fig. 5.72. We observe therein the formation of new vacancies or an expansion of the volume available to a vapor while the global nematic ordering increases. This occurs at global densities between $\rho \sim 0.1 \ldots 0.2$. We will find this kind of behavior for shorter rods at $L = 3$ at weakly attractive substrates ($u_{\text{sub}} = -0.5$) in Sec. 5.5.1 later on, as well as for even longer rods in Sec. 5.6. The loops become more pronounced for longer rods, as a *longer* lying rod that stands up leaves a much larger vacant space. The $L = 3$ case at neutral substrates does seem to entail such loops within regime III (see Fig. 5.24), but, these are very weak and thus difficult to spot. Nevertheless, such loops originate from a collective "standing up" process in the monolayer.

We further provide plots on observables sensitive to the mobility of the system in Figs. 5.73 and 5.73. In the former, we have plotted the number density of translationally mobile particle versus the packing fraction η (in contrast to ρ, which was the variable plotted for the case of $L = 3$ in Fig. 5.46). This quantity

displays a "loop" simultaneously to when a loop in the packing fraction occurs. We can additionally see that when the loop occurs *after* $\eta = 0.5$, the loop is associated with a leveling off and prompt drop of the number of translationally mobile particles thereafter (see $F/D = \mathbf{1}.67 \times 10^{-2} \ldots 1 \times 10^{-3}\}$). If the loop occurs at lower packing fraction (see $F/D \leq 1.67 \times 10^{-4}\}$), then the numbers increase for some time before eventually decreasing. If the loop occurs near $\eta = 1$ (in the case of e.g. $\epsilon = -1.5$, $F/D = 1.67 \times 10^{-4}\}$), then the system is seen to escape from the arrested state of a lying arrested state or wetting layer. The case of $\epsilon = -1.5$, very likely deep in regime IIIb, shows a nearly parabolic trajectory of $\rho_{\text{mob., trans.}}$ up to $F/D = 1 \times 10^{-4}$, indicating the formation of the above-mentioned lying arrested state or wetting layer (the same behavior is seen for $L = 3$).

The rotational mobility of standing particles (rotating downwards) is displayed in Fig. 5.74. The "cusps" and "loops" seen in the curves of $\rho^3_{\text{mob., rot. down}}$ are unique to these longer rods (they are "smeared out" for $L = 3$), and showcase the collective reordering dynamics in the system in a rather conspicuous way – those that occur when loops in the packing fraction appear (or during time-periods when the packing fraction is constant).

MONOLAYER GROWTH WITH LONGER RODS ($L = 5$):
Nematic order Q vs. packing fraction η

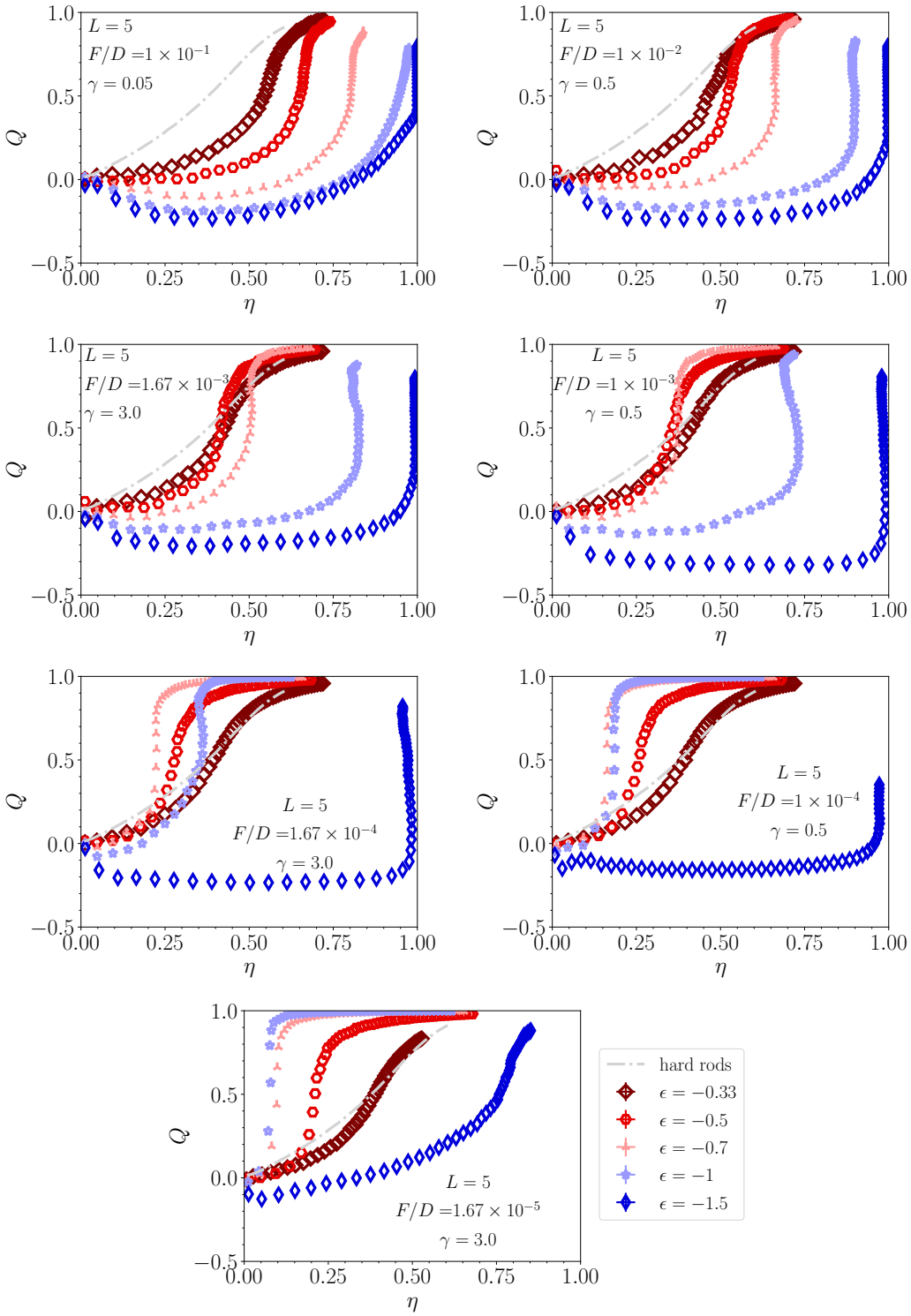

FIGURE 5.61: Nematic order parameter Q versus packing fraction (coverage) η during growth of a monolayer of $L = 5$ rods at various fixed F/D conditions: Comparison of attraction strengths ϵ. The case of $\epsilon = -0.33$ is likely very close to ϵ_{crit} (visual inspection shows strong density fluctuations: Fig. 5.63). Regime II likely sets in somewhere in the interval of $\epsilon_{\text{crit, meta, denem}} \in (\sim -0.33, -0.5]$. The case of $\epsilon = -0.7, -1$ likely belong to regime IIIa, although the latter case is likely around $\epsilon_{\text{crit, meta, denem}}2$. The case of $\epsilon = -1.5$ belongs to regime IIIb. The hard-rods curve represents quasiequilibrium growth for $\epsilon = 0$.

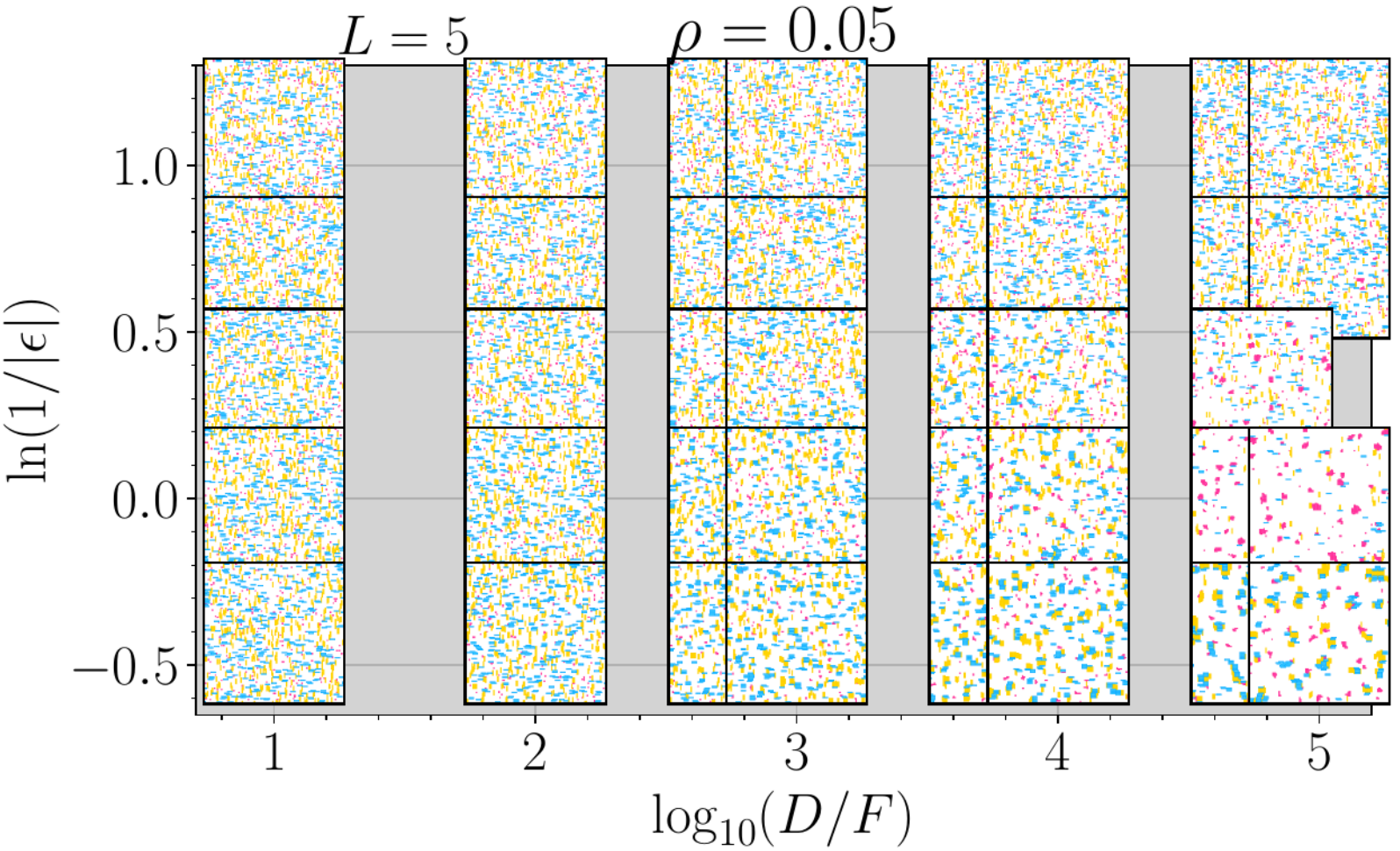

FIGURE 5.62: Schematic overview of snapshots during growth ($L = 5$, neutral substrates) as plotted in the $(\ln(1/|\epsilon|), \log(D/F))$–plane at $\rho = 0.05$ for regimes I (first row) II (second row) and III (bottom three rows), whereby the logarithm of the y-axis is taken in order to show more even spacing between sampled points. Snapshots are approximately 128×128 unit-sized cutouts of the configurations, which are 256×256 in size. The same color scheme is used here as in e.g. Fig. 5.20 Standing clusters (magenta) are seen for very high D/F and are mixed with lying clusters (blue and yellow) in regime III. A few standing clusters appear for regime II (more subtly), as we have likely already crossed the binodal (see Fig. 5.2). The long length of lying rods (yellow and blue) become apparent when comparing to Fig. 5.20, i.e. the case of $L = 3$.

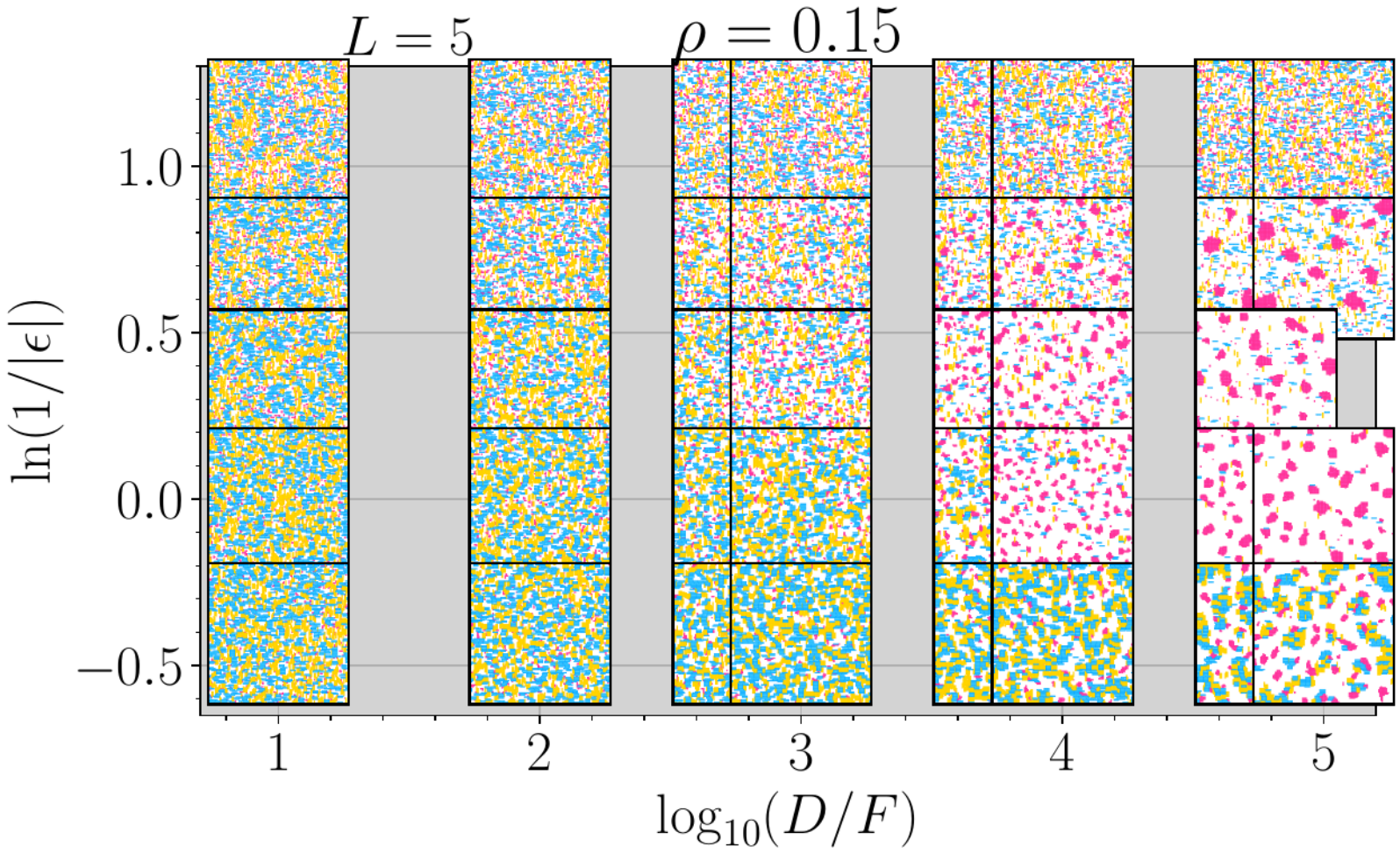

FIGURE 5.63: A continuation of Fig. 5.62 for $\rho = 0.15$. At this density the lying phase dominates the monolayer almost fully for lower D/F. Also, the islands seen at high D/F are clearly larger, and we can observe "two-faced" cases of islands with both lying and standing orientations (regime IIIb).

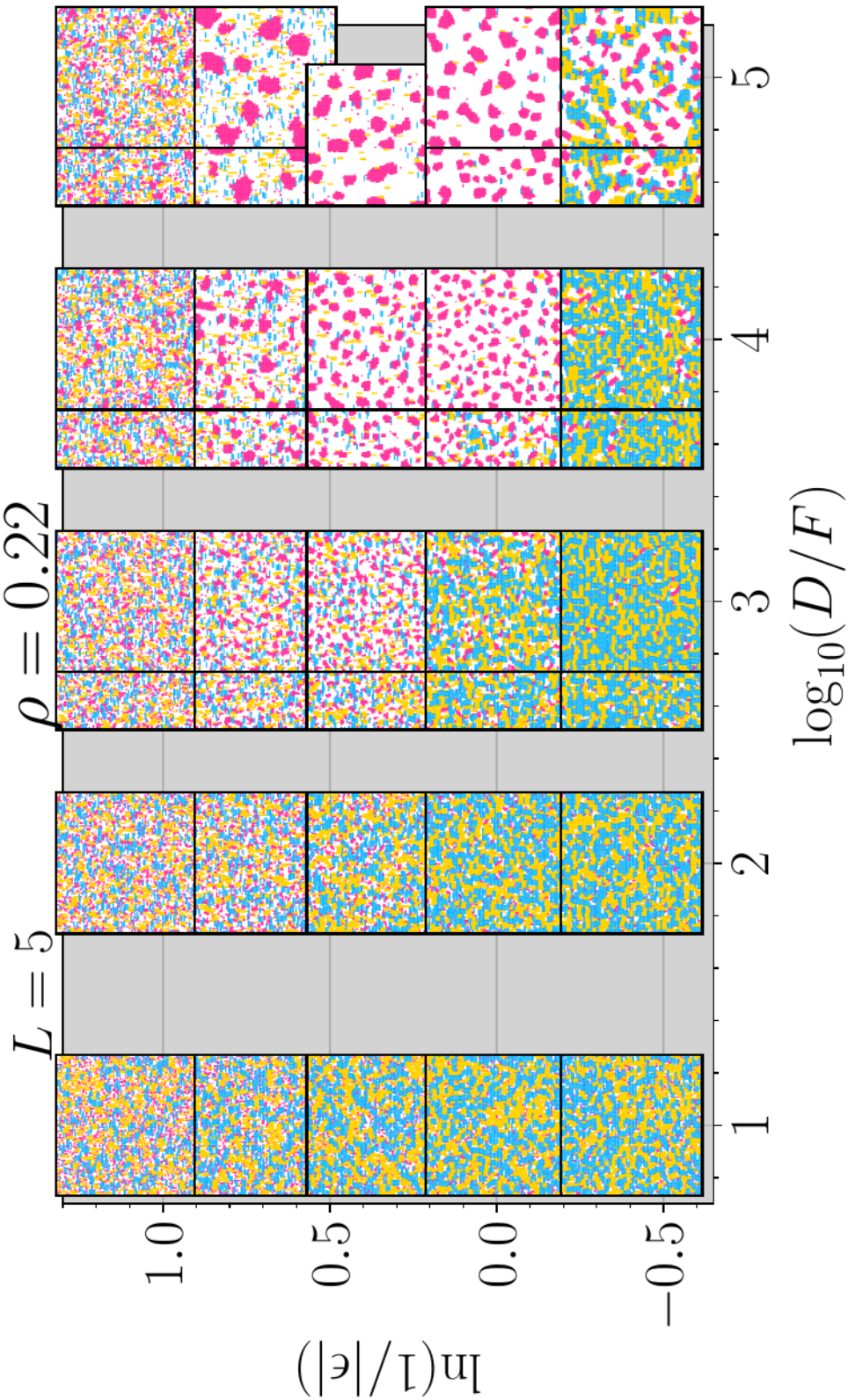

FIGURE 5.64: A continuation of Fig. 5.62 for $\rho = 0.22$, which is around the density at which the lying arrested state or wetting layer – in regime III at low to intermediate D/F – begins to stand up.

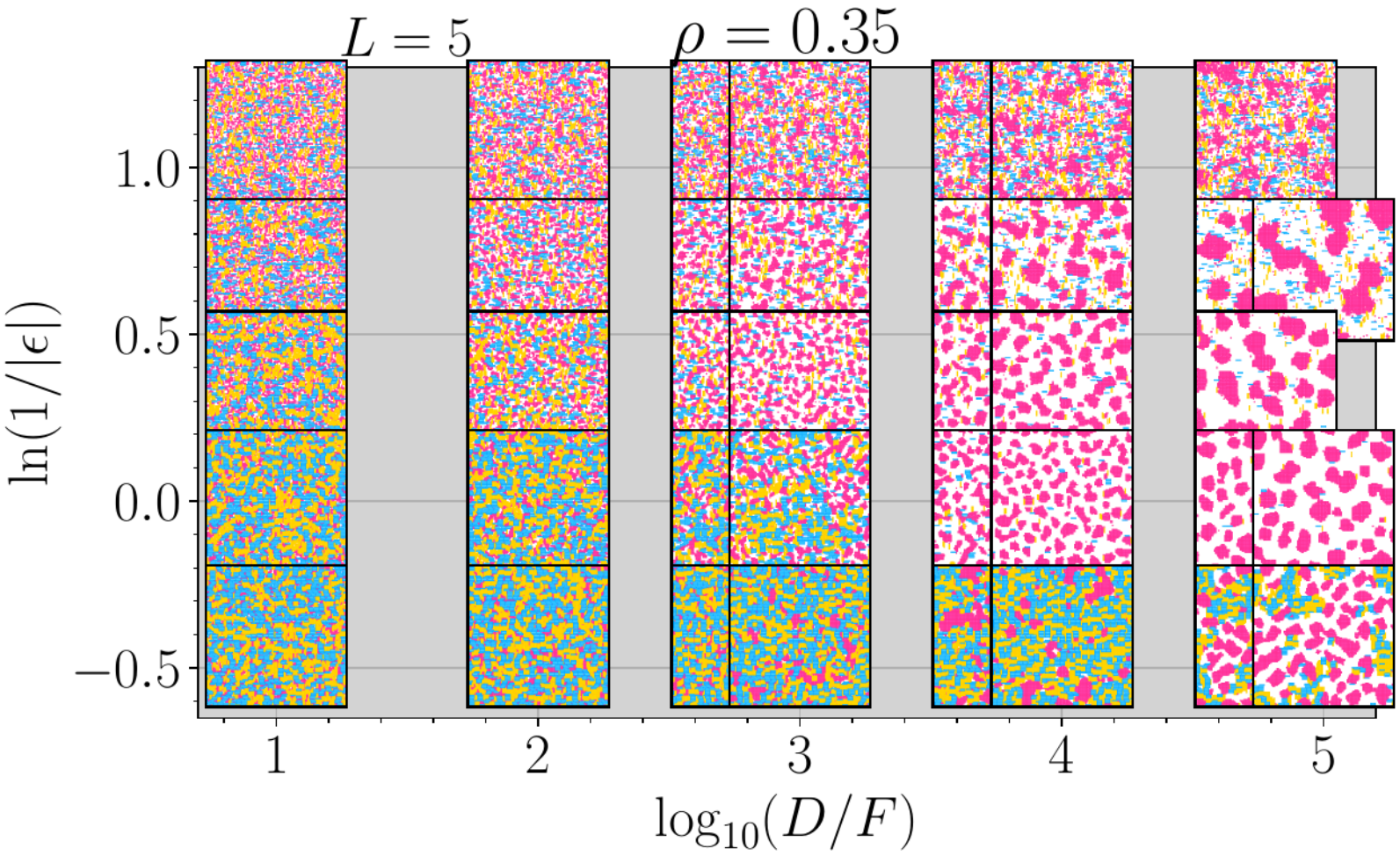

FIGURE 5.65: A continuation of Fig. 5.62 for $\rho = 0.35$. Compared to Fig. 5.64, regime III can show a co-occurrence of standing clusters surrounded completely by a lying "gel" (almost no vapor phase) at intermediate and high D/F. Regime I (top row) shows pronounced fluid density fluctuations of standing rods (magenta) at this density, which are clearly suppressed at low D/F by a higher population of lying rods, pulling the global nematic Q downwards (Fig. 5.66). Standing clusters begin to coalesce in regime II (second row) for intermediate and high D/F.

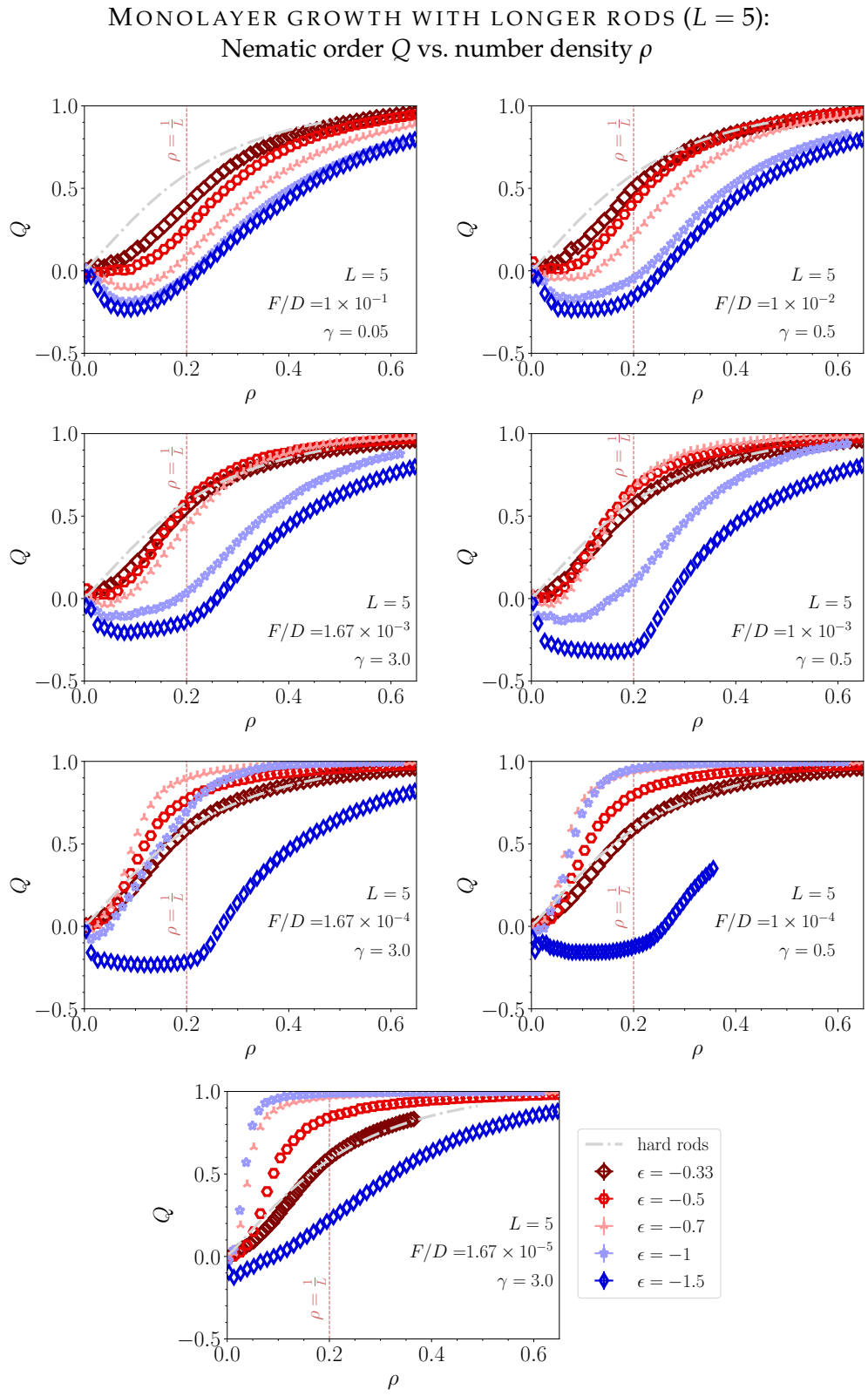

FIGURE 5.66: Global order parameter Q versus global density ρ (each plot is at various fixed F/D) for a sweep over attraction strengths ($L = 5$, neutral substrates). Compare to Fig. 5.61.

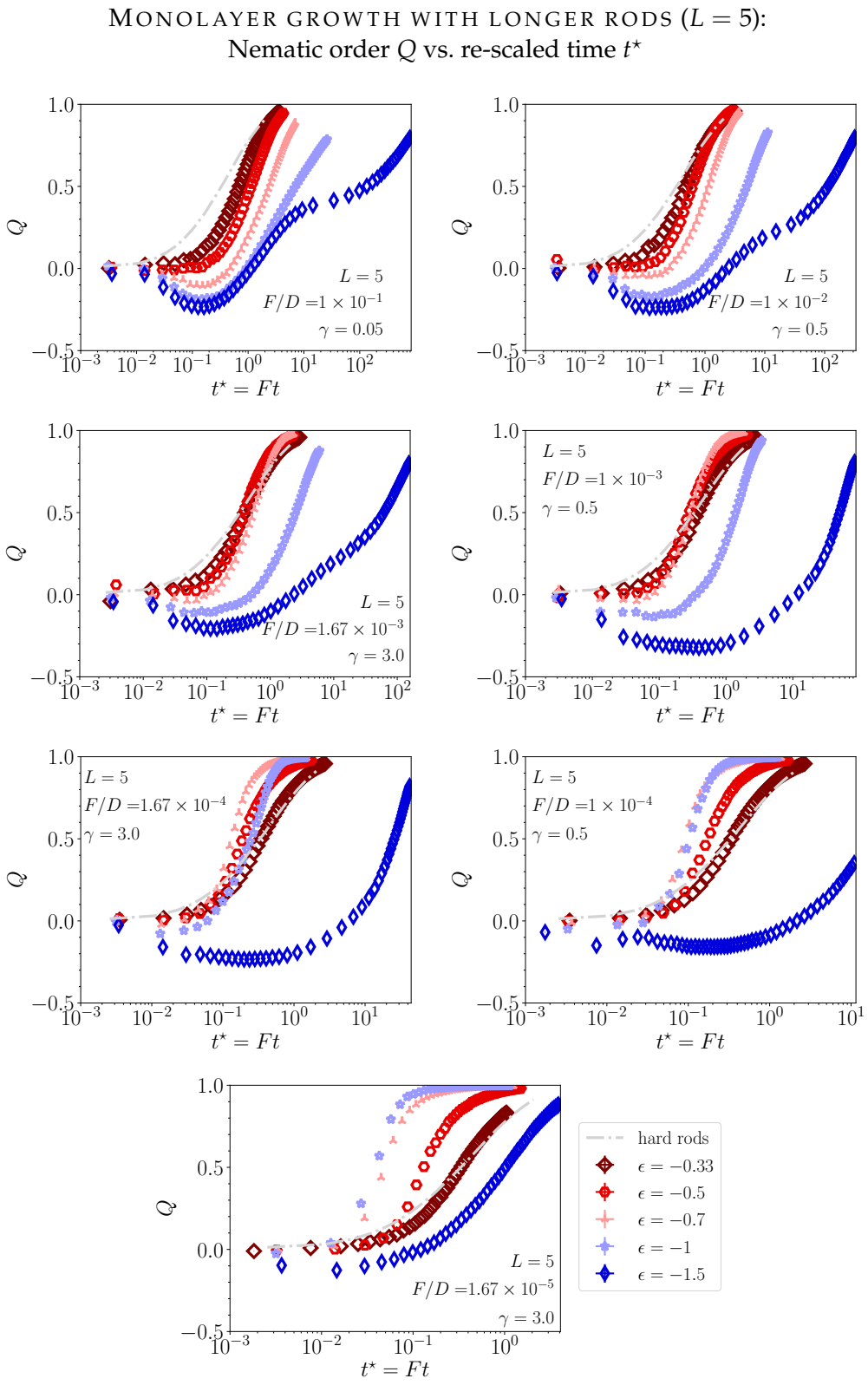

FIGURE 5.67: Global order parameter Q versus re-scaled time $t^\star$ (each plot is at various fixed F/D) for a sweep over attraction strengths ($L = 5$, neutral substrates). Compare to Fig. 5.61.

MONOLAYER GROWTH WITH LONGER RODS ($L = 5$):
Extrapolated "maps" of order parameter Q at fixed densities

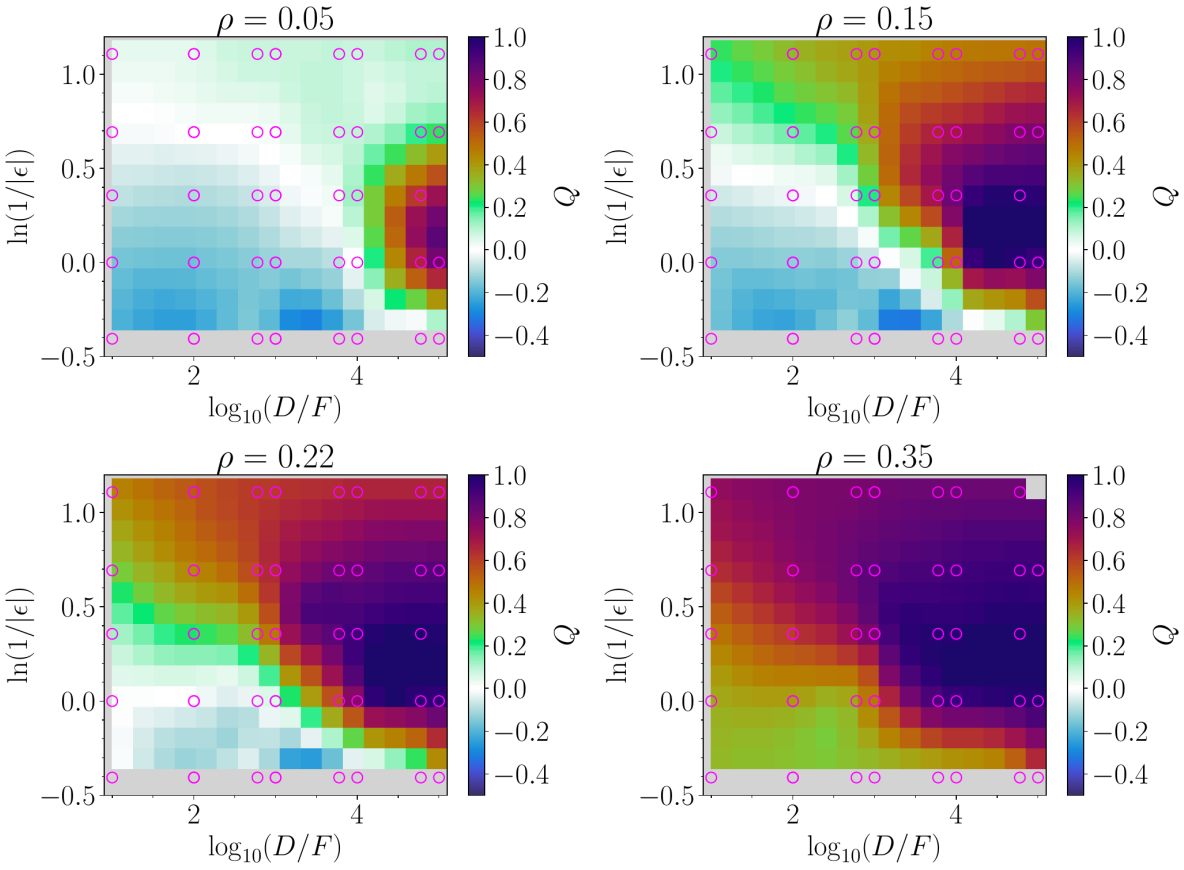

FIGURE 5.68: Extrapolated maps of the nematic order parameter in the $(\ln(1/|\epsilon|), \log(D/F))$–plane at four different densities during growth with longer rods ($L = 5$, neutral substrates). This includes ϵ-regimes I (first data-point row), II (second data-point row) and III (bottom three data-point rows). Magenta circles indicate supporting data points from simulation. A cubic extrapolation scheme is employed.

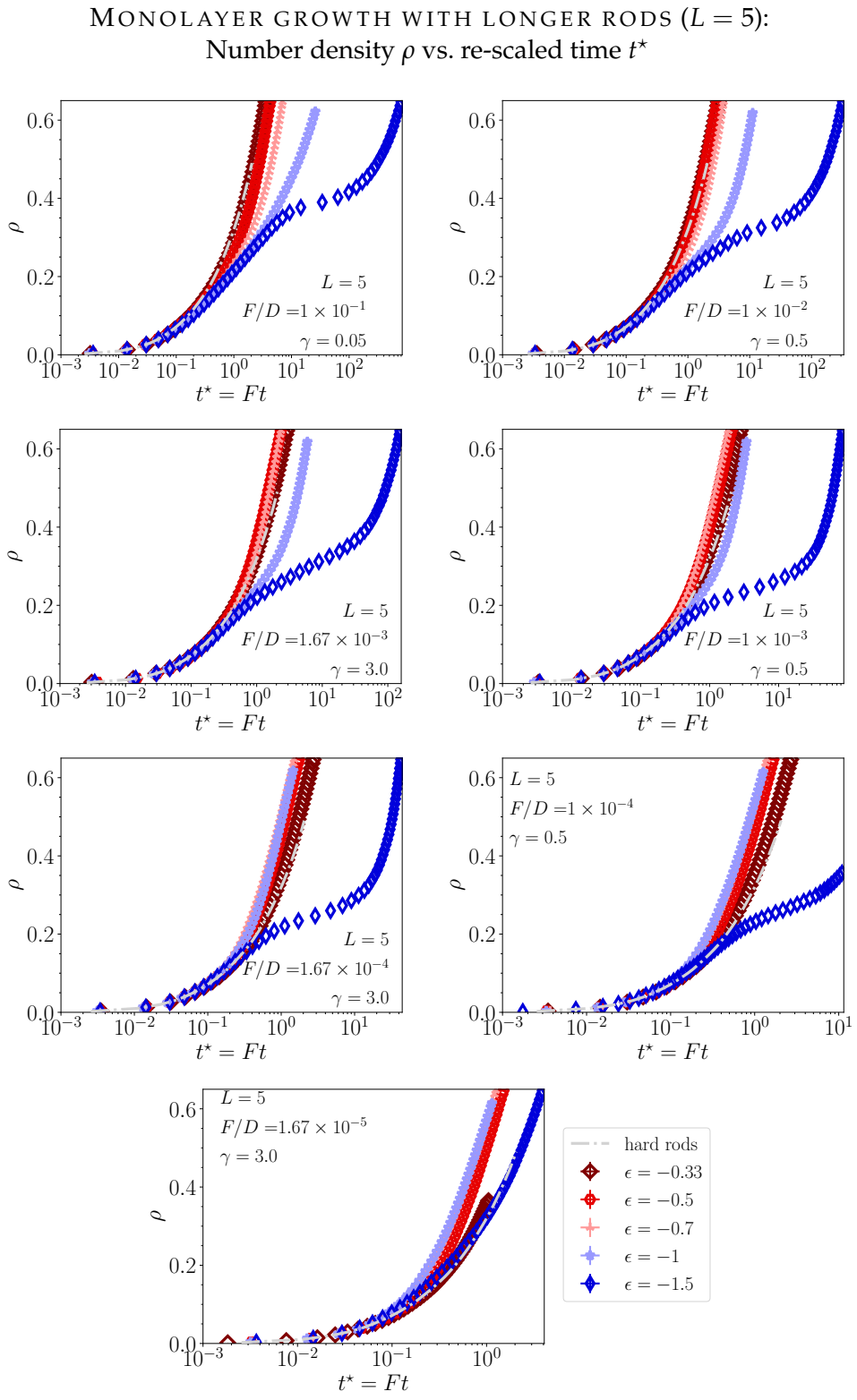

FIGURE 5.69: Global density ρ versus time $t^\star$ rescaled with the attempt flux rate (each plot is at various fixed F/D) for a sweep over attraction strengths ($L = 5$, neutral substrates). Compare to Fig. 5.61.

MONOLAYER GROWTH WITH LONGER RODS ($L = 5$):
Lying number density ρ_{12} vs. re-scaled time $t^\star$

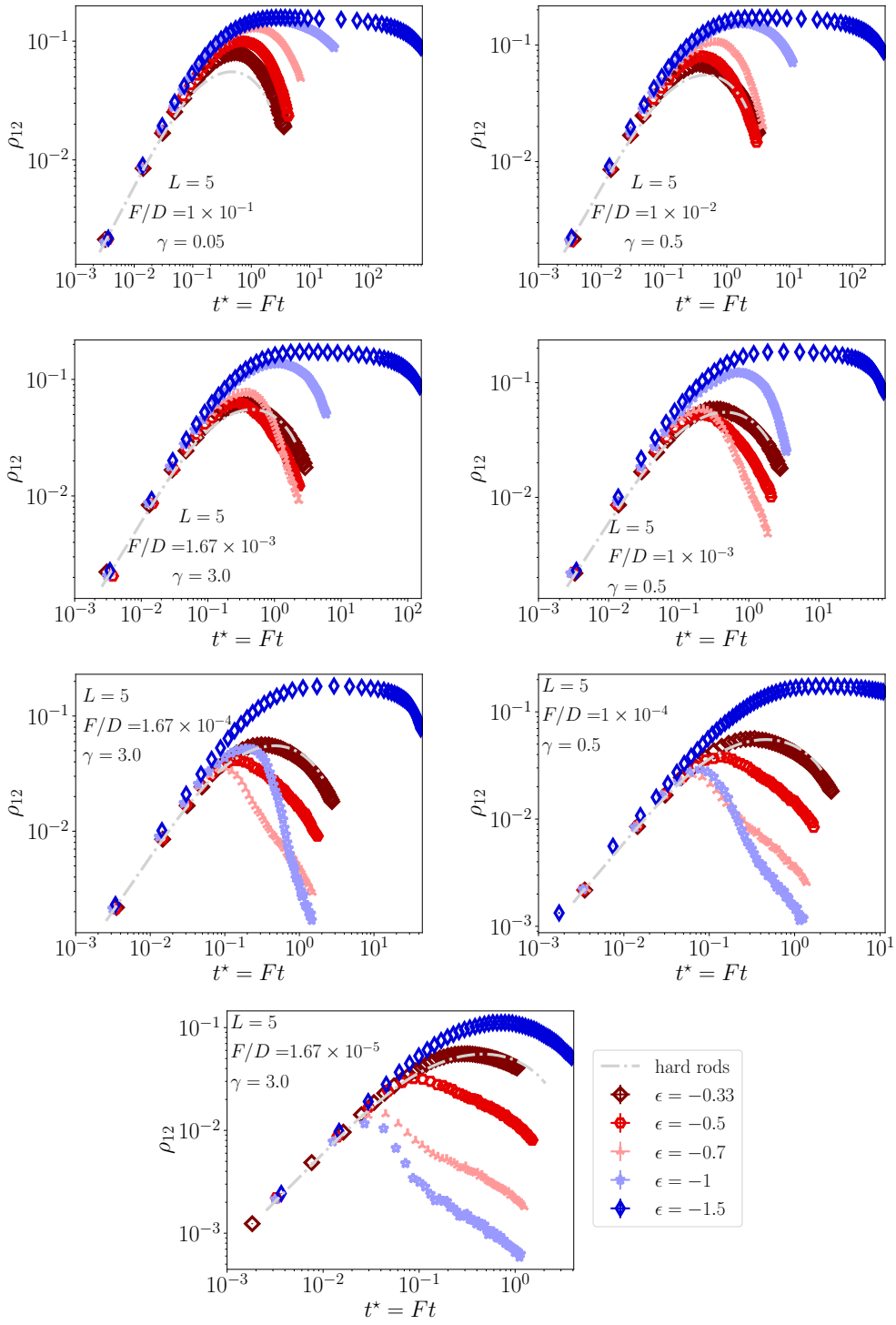

FIGURE 5.70: Global density ρ_{12} of lying rods versus time $t^\star$ rescaled with the attempt flux rate (each plot is at a fixed F/D) for a sweep over attraction strengths ($L = 5$, neutral substrates). Compare to Fig. 5.61.

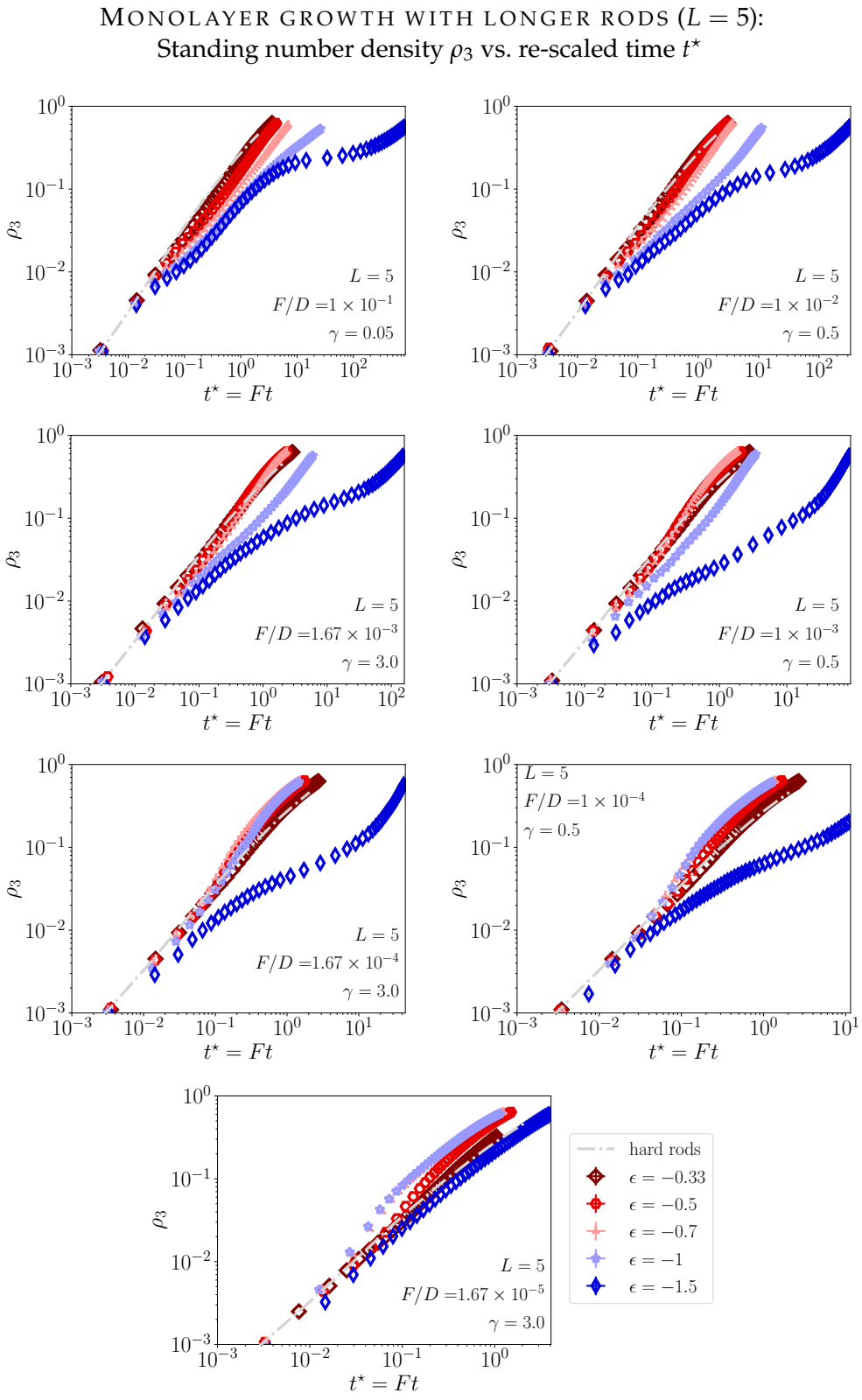

FIGURE 5.71: Global density ρ_3 of standing rods versus re-scaled time $t^\star$ for a sweep over attraction strengths ($L = 5$, neutral substrates). Compare to Fig. 5.61.

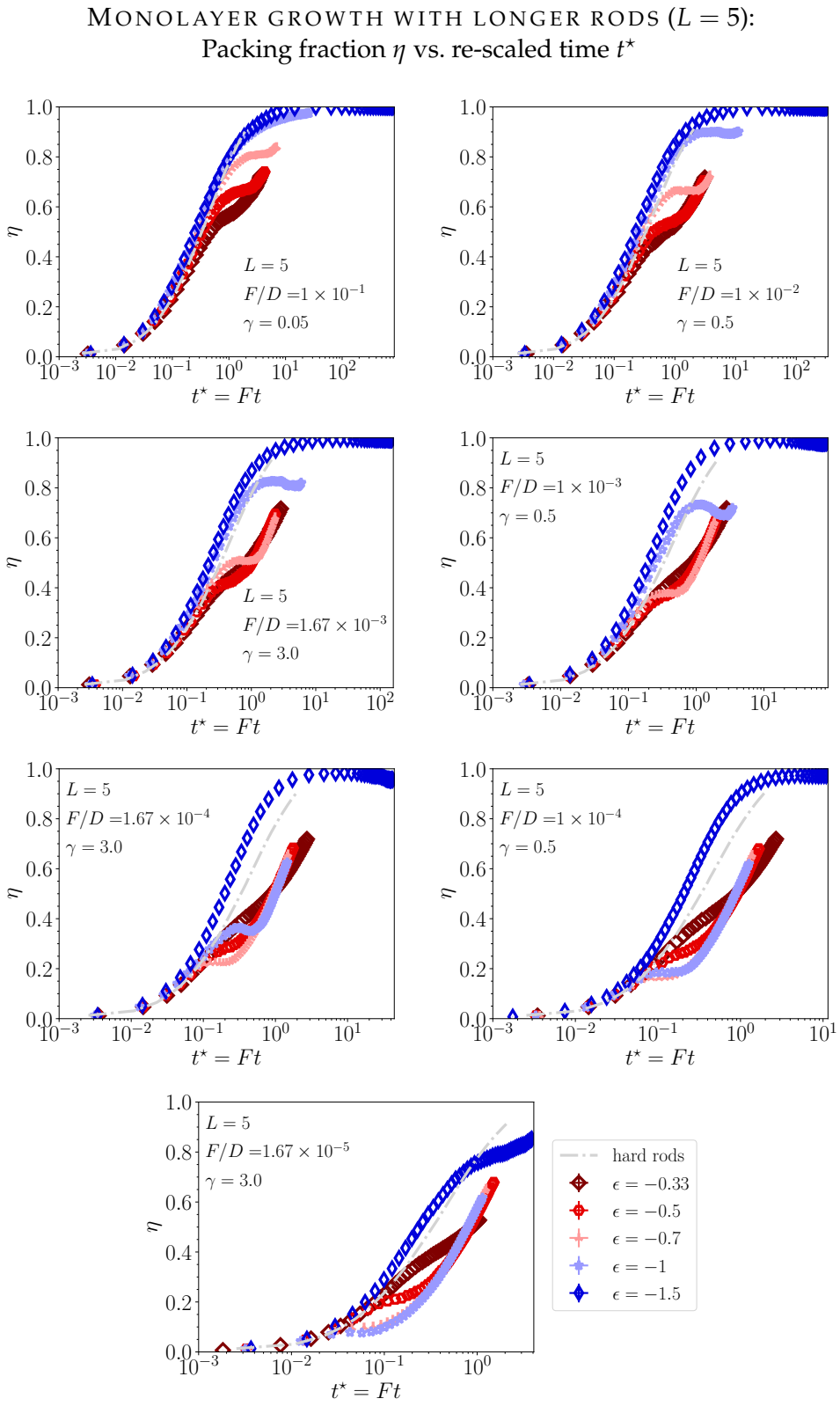

FIGURE 5.72: Global density ρ_{12} of lying rods versus re-scaled time $t^\star$ (each plot is at a fixed F/D) for a sweep over attraction strengths ($L = 5$, neutral substrates) for long times. Compare to Fig. 5.61.

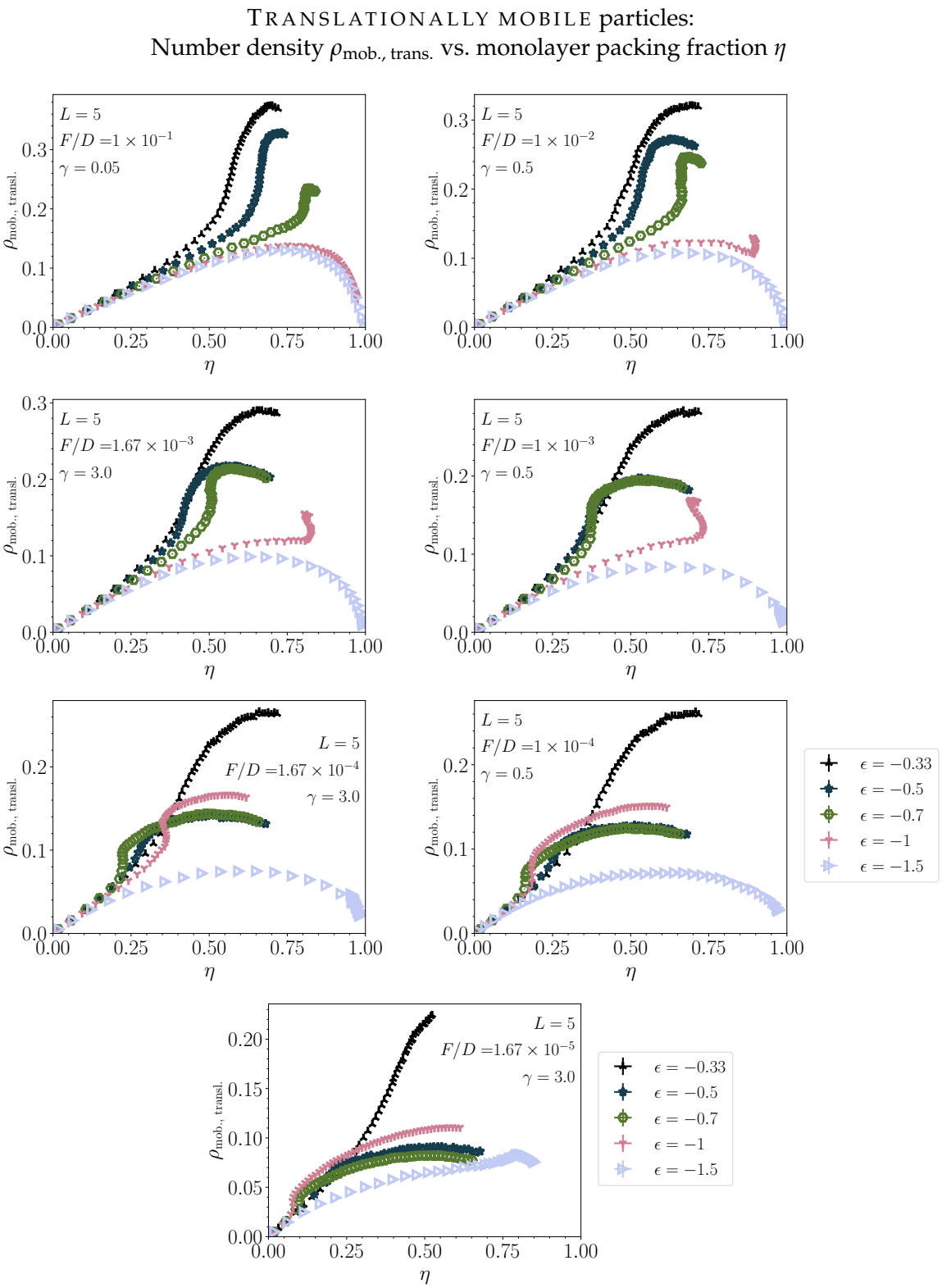

FIGURE 5.73: Translationally mobile particles: Number density $\rho_{\text{mob., trans.}}$ versus packing fraction η (at a fixed F/D) for a sweep over attraction strengths ($L = 5$).

ROTATIONALLY MOBILE particles (downwards):
Number density $\rho^3_{\text{mob., rot. down}}$ vs. monolayer packing fraction η

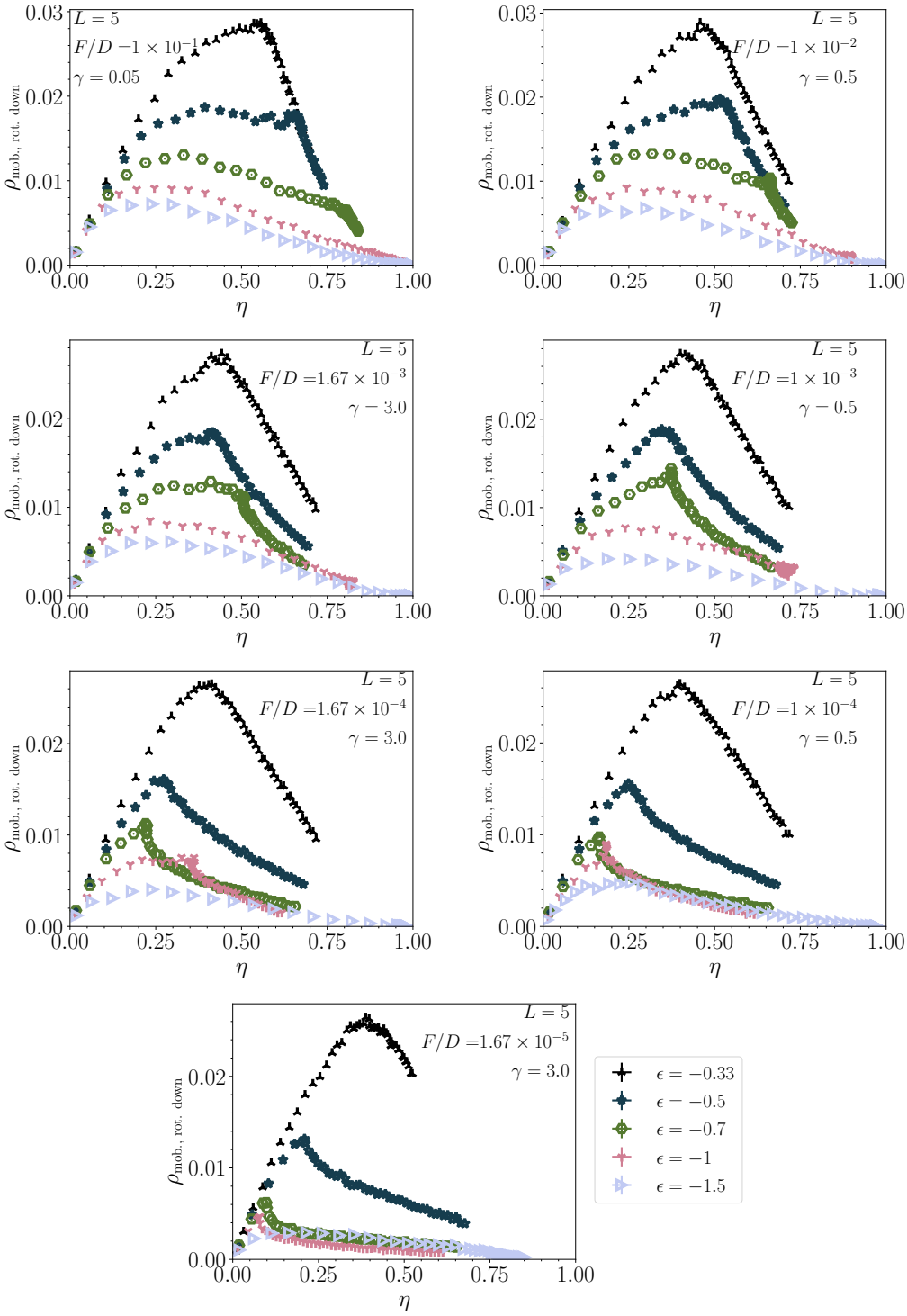

FIGURE 5.74: Rotationally mobile particles (rotations downwards): Number density $\rho^3_{\text{mob., rot. down}}$ versus packing fraction η (at a fixed F/D) for a sweep over attraction strengths ($L = 5$).

5.5 Growth at attractive substrates ($L = 3$)

The effect of substrate potentials during growth is important for understanding the full scope of morphological and dynamical evolution of these systems. In "real-world" growth experiments, the properties of the substrate can bias a particular orientation [1, 6, 16, 123, 125, 751], which may also correspond to different binding energies for either case. Indeed, we reported on estimates of this kind from the literature in part I of this thesis.

In our model system, the unit attraction strength u_{sub} is defined as described in Sec. 5.1: An additional energy barrier of $(L-1)u_{\text{sub}}$ must be overcome by a lying rod in order to stand up, which reduces the rotational rate upwards when compared with the inverse process (a rotation downwards). On the other hand, a standing rod attempting to lay down experiences no extra energy barrier. Attractive substrates that bias a lying orientation clearly favor the formation of the disorderly lying phase – both at higher temperatures and lower F/D than at neutral substrates.

Let us take a minute to reflect on the potential effect of this substrate potential on the phase diagram. Attractive substrate potentials may presumably "pull up" the metastable vapor–lying-liquid phase separation binodal, stabilizing a "2D" ($Q < 0$) or $Q \approx 0$ liquid phase, depending on the strength of $|u_{\text{sub}}|$. Indeed, a few preliminary GCMC simulations show that a lying phase can become stable for sufficiently strong $|u_{\text{sub}}|$. We see this kind of transition during monolayer growth, indeed, which we report on below.

Note that additional plots for this section are found in App. A.3.

5.5.1 Weak substrate potentials ($u_{\text{sub}} = -0.5$)

"Weak" substrate potentials ($u_{\text{sub}} = -0.5$) already induce quite a few noticeable changes to the evolution of the system, which we first present visually in Figs. 5.75–5.79. These are "maps" of configuration snapshots in the $(\ln(1/|\epsilon|), \log(D/F))$–plane in complete analogy to Figs. 5.20–5.23 for neutral substrates. For ϵ-regime III, and at lowest values of D/F, Fig. 5.75 suggests a shift of (metastable) binodal lines (last three rows), as standing clusters are barely visible. In contrast, lying rods form pronounced clusters. At higher densities of $\rho = 0.15$, Fig. 5.76, a low-Q-valued dense vapor or weak fluid spans the system for regimes II and IIIa, a feature not seen for neutral substrates. For lower reduced temperatures, this fluid forms a network or a loosely-packed gel. In the latter scenario, we observe co-occurring standing clusters for the largest D/F. This co-occurrence becomes more pronounced for $\epsilon = -1.5$ at higher densities (Figs. 5.77 and 5.78). Around $\rho = 1/L \approx 0.33$ (Fig. 5.78), the lying gel is seen to thicken, becoming the "wetting layer" we discussed in the previous sections. The case of $\epsilon = -1$ displays pronounced thinning of the 2D fluid phase surrounding the growing, standing clusters. This phase now collects at the rim of the standing clusters, resembling a "surface" fluid of sorts. We depict this scenario more clearly in Fig. 5.80. At even higher densities, Fig. 5.79, the "standing up" transition from the (nearly complete) 2D "wetting layer" is visible deeper in regime III for intermediate D/F. Fig. 5.81 shows the evolution of the monolayer for $\epsilon = -1.5$ up to $\rho = 0.638$: A competition between the lying gel and standing-phase island growth persists even past these densities. Such an elongated competition up to high densities is visible at neutral substrates for lower

reduced temperatures, i.e. $\epsilon = -2$ at $F/D = 10^{-2}$. On attractive substrates, $\epsilon = -2$ shows much clearer evidence for a first-order lying-standing transition occur after forming a lying "wetting layer" around $\rho_{\text{wet}} \approx 1/L \approx 0.33$, where the nematic order parameter almost reaches $Q = -0.5$. We show a visualization of this transition in Fig. 5.82.

We suspect, then, that regimes II and III may have shifted "upwards". This also means that the phase transitions scenarios (B)–(E) have moved upwards. Owing to a a lack of (initial) evidence for a network-forming lying phase (phase transition scenario (D)), the case of $\epsilon = -1$ (which had corresponded to "weak" regime IIIa for neutral substrates) may have moved up into "regime II", although more simulated parameters would be necessary. Further, the case of $\epsilon = -0.7$ (originally regime II) does not show pronounced, standing cluster formation from an isotropic liquid like on neutral substrates (phase transition scenario (B)). It may be that the substrate potential has shifted this case "upwards" towards the boundary of regime I. The "standing-up" transition from a 2D "wetting layer" (scenario (E)) may become stable for even stronger $|u_{\text{sub}}|$, which we will show next section.

Enhanced competition of lying and standing "liquid" phases for $\epsilon = -1.5, -2$ at low deposition quench rates

Fig. 5.83 shows, how the lying phase forms aggregate clusters, then a gel, co-occurring with the growth of standing islands. The lateral size of the structures are enhanced at the same F/D as for neutral substrates (compare Fig. 5.13): This is because of the weaker $|\epsilon|$ necessary for this scenario to occur. As weaker attractions allow for a higher mobility of particles, the structures become larger in analogy to a larger diffusion rate. Therefore, weak substrates are quite interesting for their ability to enhance and therewith highlight aspects of the phase diagram at neutral substrates. (Quantitative analysis of cluster sizes and mobility in the system remains outside of the scope of this thesis.)

Quantitative results

Quantitative results on the nematic order Q, as well as the number densities ρ and ρ_3 are found in Fig. 5.84 for a slow deposition quench rate F/D, Fig. 5.85 for a medium deposition quench rate, and in Fig. 5.86 for an even faster deposition quench. We see from Fig. 5.84 that the case of $\epsilon = -2$ for low F/D forms a very low-Q "wetting layer" (the curve of $Q(\rho)$). However, the "standing up" transition out of it is still "smeared out": The case of medium and faster deposition quench rates, Figs. 5.84 and 5.86 show a "sharp" transition. This means the transition remains *metastable* even for $\epsilon = -2$. In any case, the sharp transition for $\epsilon = -2$ occurs at $\rho = 1/L$, and the nematic order of the lying phase is nearly perfectly $Q = 0$.

Loops in the packing fraction for $\epsilon = -1, -1.5$ are are visible for slow, medium, and fast deposition quench rates F/D, but also (subtly) for $\epsilon = -2$. We had discussed such loops in Sec. 5.4, which are equally conspicuous for monolayer growth at neutral substrates with longer rods. The visualization for the cases of $\epsilon = -1, -1.5$ in Figs. 5.80 and 5.81, respectively, show the "reason" behind these loops – they are related in one case to the thinning of the 2D fluid between growing, standing rods (collecting at their rims). In the other case, vacant spaces open up between standing islands and the thick, lying gel. The

weak loop for the case of $\epsilon = -2$ also introduces vacancies between a lying gel and standing islands, see Fig. 5.82. However, in this case, the standing islands seem to grow *out of* the lying wetting layer, rather than growing in parallel to a network-forming gel (like for $\epsilon = -1.5$).

The loops in the packing fraction can be seen in the plots of packing fraction versus re-scaled time in Fig. 5.87. The evolution of the lying number densities are shown in Fig. 5.88 thereafter. These number densities show a characteristically steep drop during the times when the system shows the loops in packing fraction, meaning this phenomenon is related to sharp decay of lying rods which likely get incorporated into the lower-packing-fraction standing islands. This would certainly explain an affinity of lying rods to the rim of standing islands like in Fig. 5.80.

We remark on one more finding: Fig. 5.90 (bottom right) shows a case where early on the nematic order Q forms a dip near $Q \sim -0.5$ before rapidly increasing. Visual inspection shows the formation of lying clusters early on, where standing rods begin to enter the scene, eventually competing with the lying clusters like in Fig. 5.89 at further stages. A steady conversion of the clusters succeeds at the higher densities in Fig. 5.89. In the future, analyzing the translational and rotational fluxes in the system in the style of Sec. 5.3.8 could be of aid for interpreting this behavior.

We end our discussion of weakly attractive substrate potentials with a final plot (Fig. 5.90), showing the dependency of the $Q(\eta)$ trajectories as a function of F/D, plotted for original regimes II and III, where we indicate verbally how the regimes may have shifted (in the caption). To foreshadow the next section, regime IIIb seems to be characterized by a "sharp" transition of a 2D-liquid–standing-liquid of first order, but the transition remains metastable. The onset of stability might move upwards towards higher reduced temperatures for even stronger substrates, making the "2D" phase stable, and therewith this "standing up" transition at full packing fraction stable.

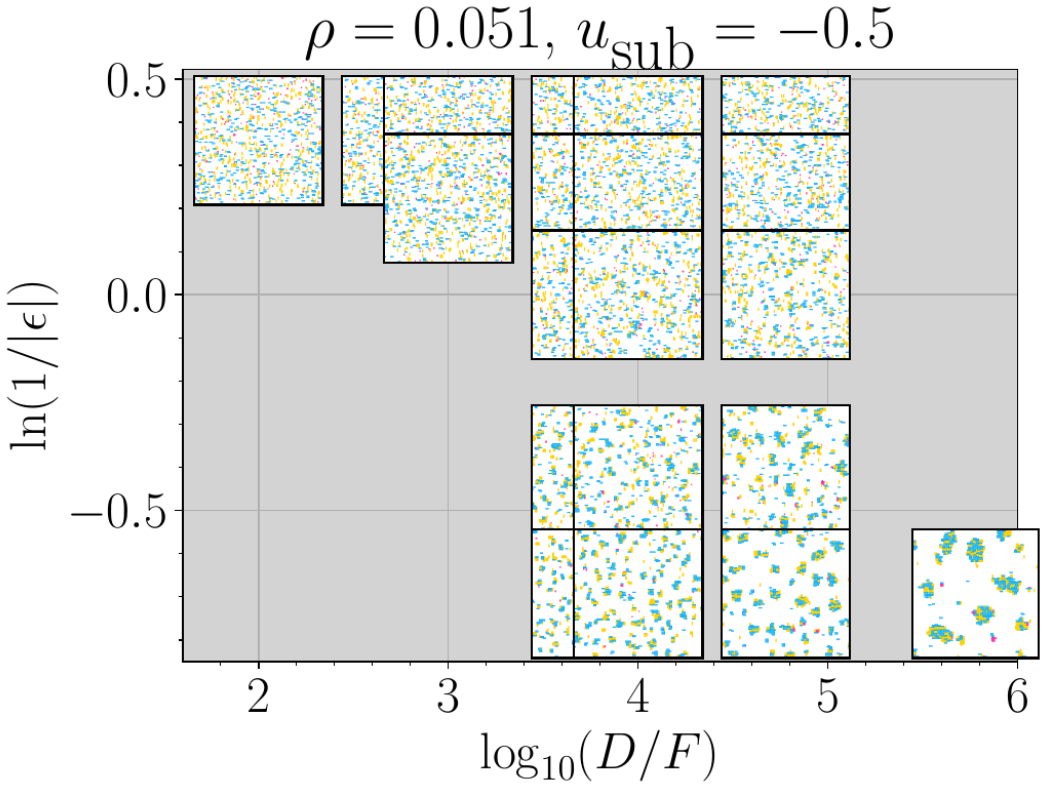

FIGURE 5.75: Effect of weak substrate potentials $u_{\mathrm{sub}} = -0.5$: Map of snapshots during growth as plotted in the $(\ln(1/|\epsilon|), \log(D/F))$–plane at $\rho = 0.051$ within ϵ-regimes II and III ($L = 3$), whereby the logarithm of the y-axis is taken in order to show more even spacing between sampled points. From top-to-bottom, the values of $\epsilon = -0.7, -0.8, -1, -1.5, -2$. Compare to Fig. 5.20 for neutral substrates. Please see Figs. 5.76–5.79: Phase transition scenario (C) seems to occur for $(5.8, -0.4)$. The coordinates $(4.75, -0.4)$, $(4, -0.52)$, $(4, -0.4)$ and $(4.75, -0.52)$ are more difficult to judge, as they may share many features characteristic of scenarios (E) and (D) or even (C). A somewhat modified phase transition scenario (B) (for standing islands separating from a $Q < 0$ fluid) seems to occur for coordinates $(4, 0)$, $(4.75, 0)$, $(4, 0.25)$ and $(4.75, 0.25)$, but possibly also above, as well.

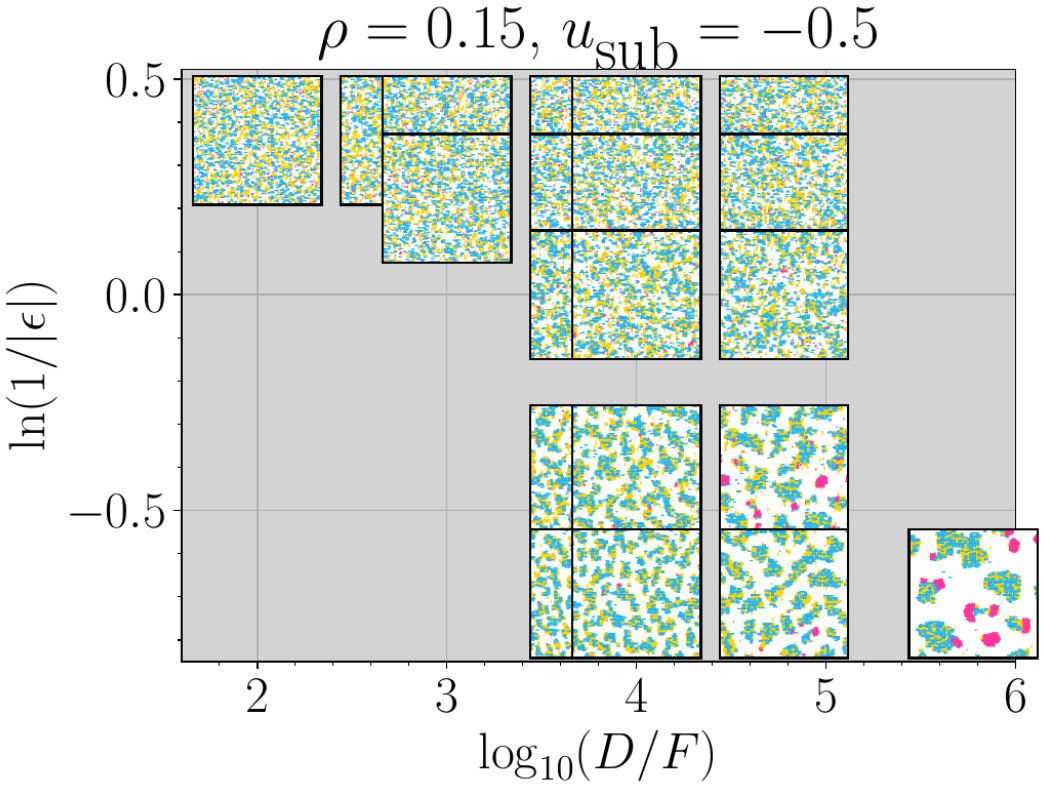

FIGURE 5.76: A continuation of Fig. 5.75 for $\rho = 0.15$. Now, a low-Q-valued fluid with intermediate packing fraction spans the system for regime II and IIIa (top three rows). For lower reduced temperatures, this lying fluid form a gel. In this regime for highest D/F, standing clusters become visible. Compare to Fig. 5.21 for neutral substrates.

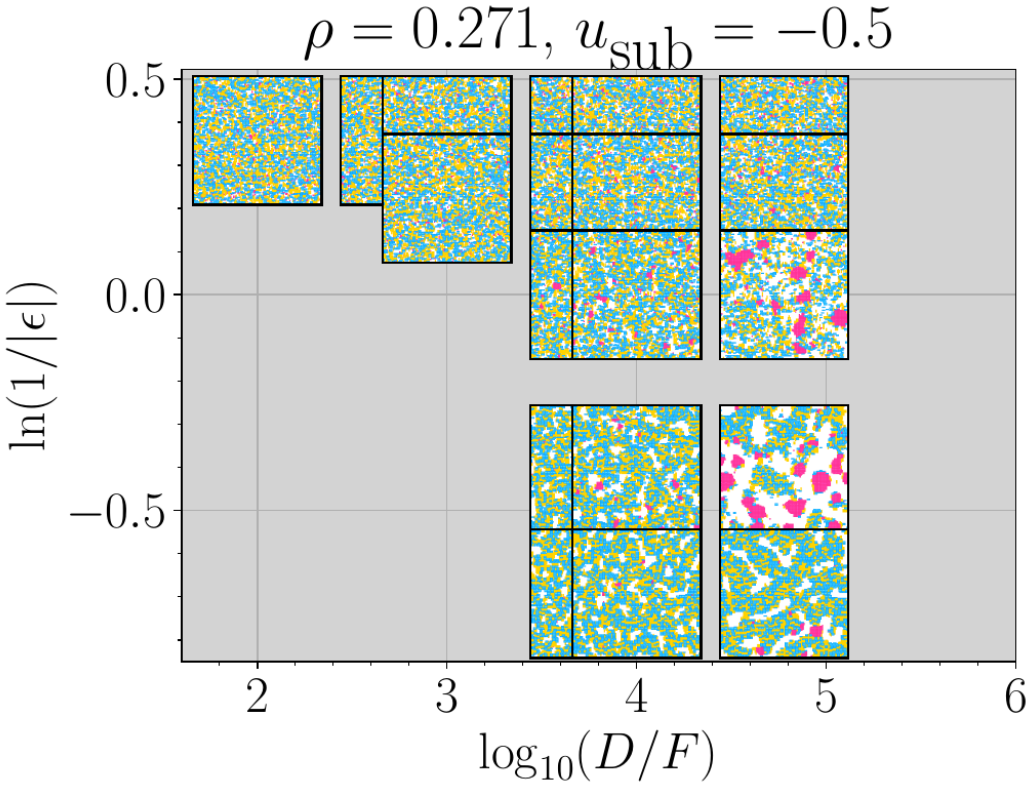

FIGURE 5.77: A continuation of Fig. 5.75 for $\rho = 0.271$. Compare to Fig. 5.22 for neutral substrates.

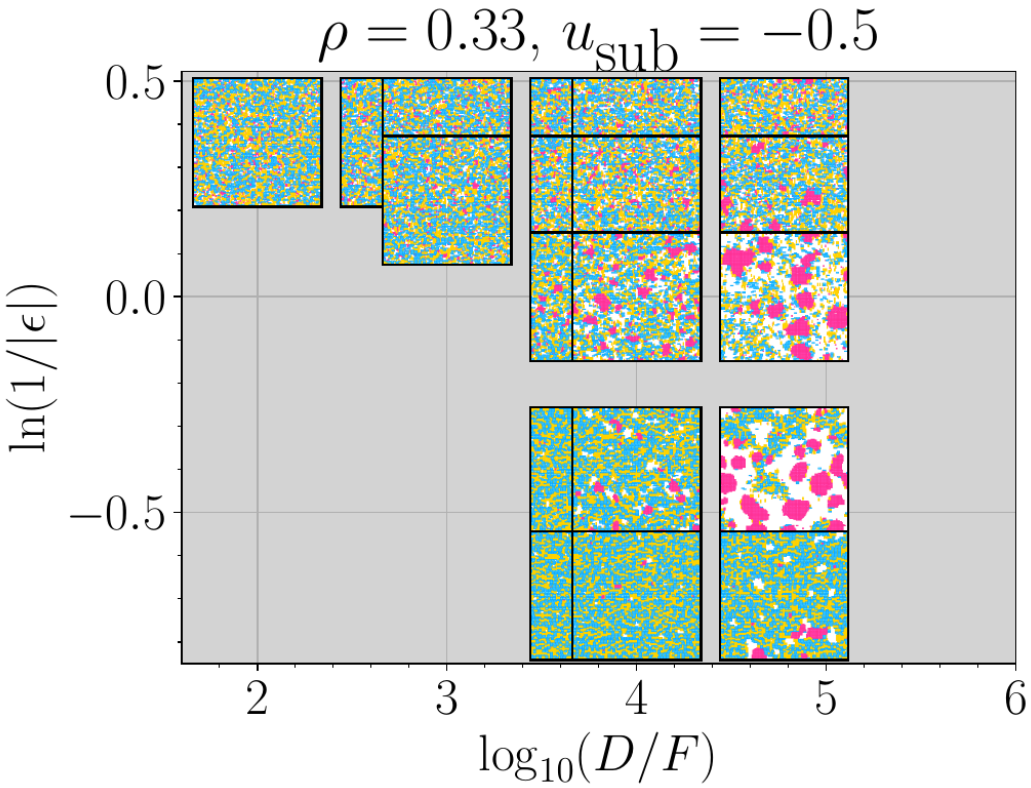

FIGURE 5.78: A continuation of Fig. 5.75 for $\rho = 0.33$.

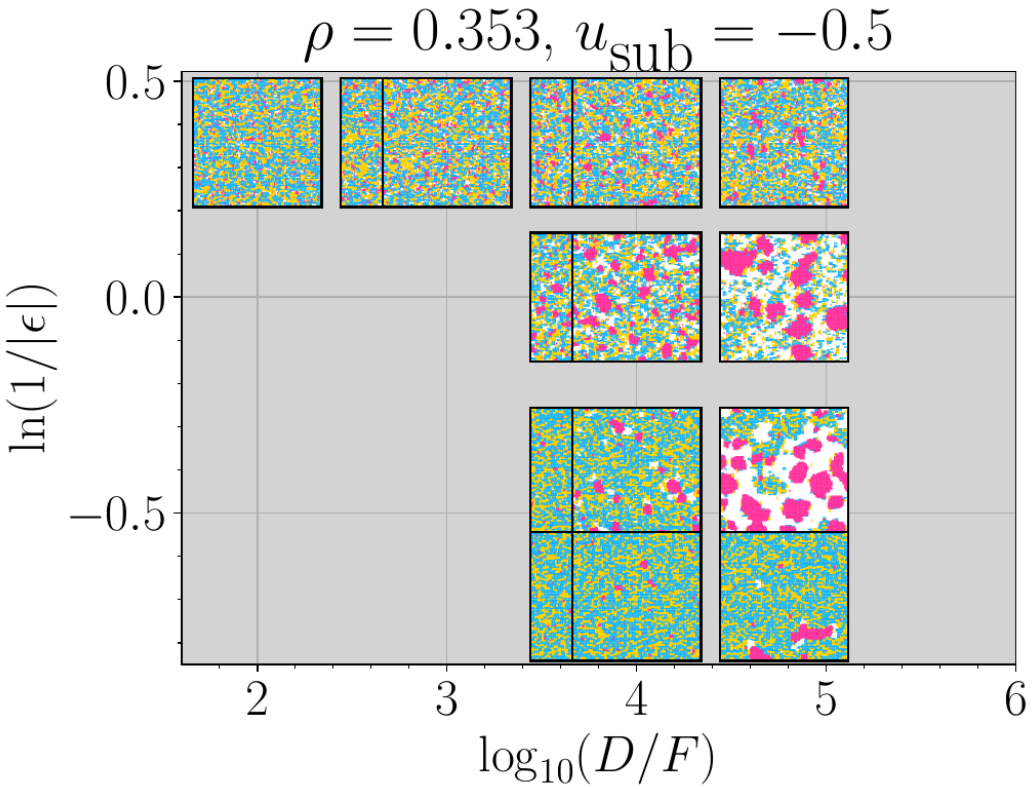

FIGURE 5.79: A continuation of Fig. 5.75 for $\rho = 0.353$. Compare to Fig. 5.23 for neutral substrates.

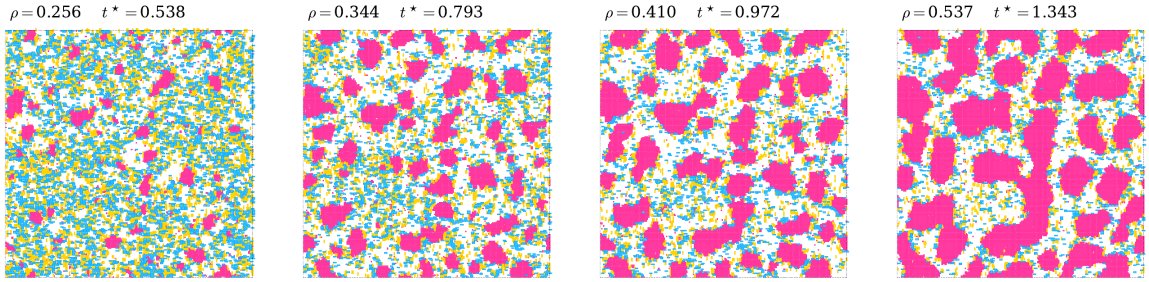

FIGURE 5.80: Visualized snapshots of standing island formation out of a $Q < 0$ dense vapor or fluid (phase transition scenario (B)), coinciding with subtle demixing of the fluid and a low-density vapor phase (the former of which collects at the island rim). The system entails a loop in the packing fraction, see Fig. 5.87, occurring for weakly attractive substrates and moderate inter-particle attractions ($u_{\mathrm{sub}} = -0.5$ and $\epsilon = -1$) ($L = 3$). The dynamical parameters are $F/D = 1.67 \times 10^{-5}$, $\gamma = 3.0$. Please take notice of the affinity of a nearly 2D fluid at the rim of the islands.

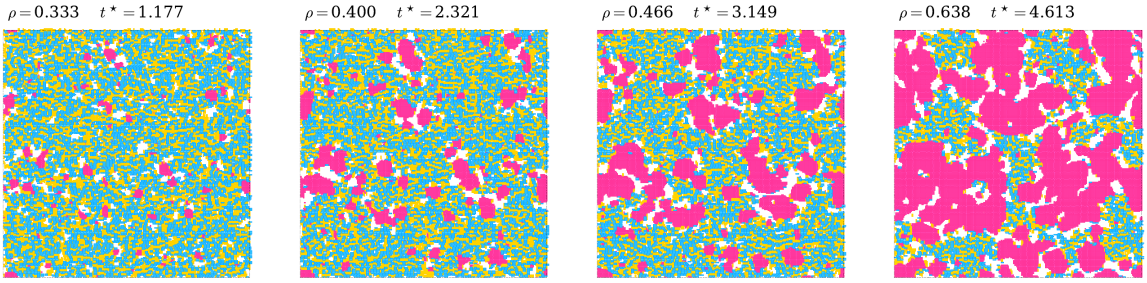

$$|u_{\text{sub}}| = 0.5 < |\epsilon| = 1.5$$

FIGURE 5.81: Visualized snapshots of standing island formation out of a dense lying gel or wetting layer (phase transition scenario (E) or marginally (D)), coinciding with subtle demixing of the lying fluid and a vapor phase (the latter of which collects at the island rim). The system entails a loop in the packing fraction, see Fig. 5.87, occurring here for weakly attractive substrates and moderate inter-particle attractions. ($u_{\text{sub}} = -0.5$ and $\epsilon = -1.5$) ($L = 3$). The dynamical parameters are $F/D = 1 \times 10^{-4}$, $\gamma = 3.0$. Notice the affinity of vacancies (the vapor) in the vicinity of the islands, which is practically the opposite case as in Fig. 5.80.

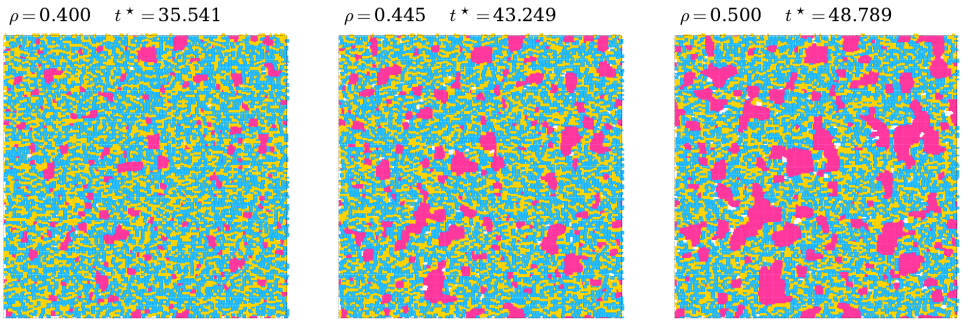

$$|u_{\text{sub}}| = 0.5 < |\epsilon| = 2$$

FIGURE 5.82: Visualized snapshots of standing islands forming out of the lying-phase (2D) wetting layer (phase transition scenario (E)), co-occurring with a phase separation process with a vapor (vacancies). This example corresponds to weakly attractive substrates and strong attractions, and is at a stage well after $\rho > 1/L$ at around $\rho \approx 0.44$ in this case. Here, $u_{\text{sub}} = -0.5$ and $\epsilon = -2$ and $L = 3$. The dynamical parameters are $F/D = 1 \times 10^{-4}$ and $\gamma = 0.5$. The right figure shows that a vapor (vacancies) form at late stages, corresponding to the subtle loop in the packing fraction of Fig. 5.87 (top right).

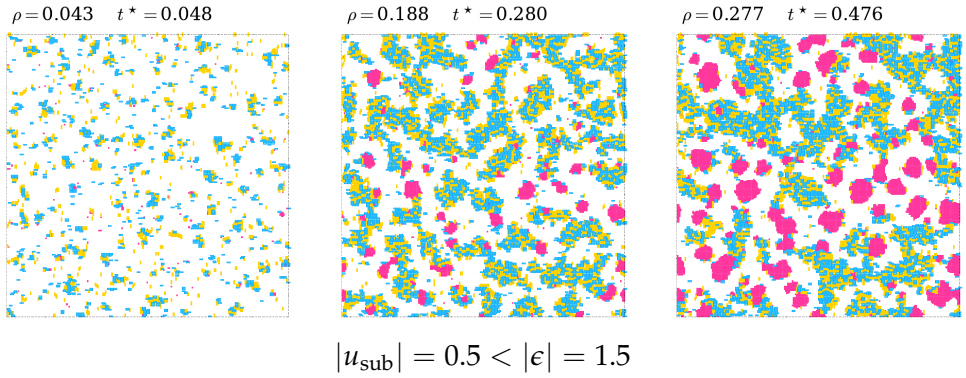

FIGURE 5.83: Visualized snapshots of competing low-density lying-phase gel and standing-phase islands (phase transition scenario (D)), occurring for weakly attractive substrates and moderately strong attractions: $u_{\text{sub}} = -0.5$ and $\epsilon = -1.5$ and $L = 3$. The dynamical parameters are $F/D = 1.67 \times 10^{-5}$, $\gamma = 3.0$. In this phase-competition scenario, larger structures form than at neutral substrates for similar values of F/D: A weaker $|\epsilon|$ is required for this type of scenario to occur.

Monolayer growth with WEAK SUBSTRATE POTENTIALS ($u_{\text{sub}} = -0.5$): Slow deposition quench rate F/D

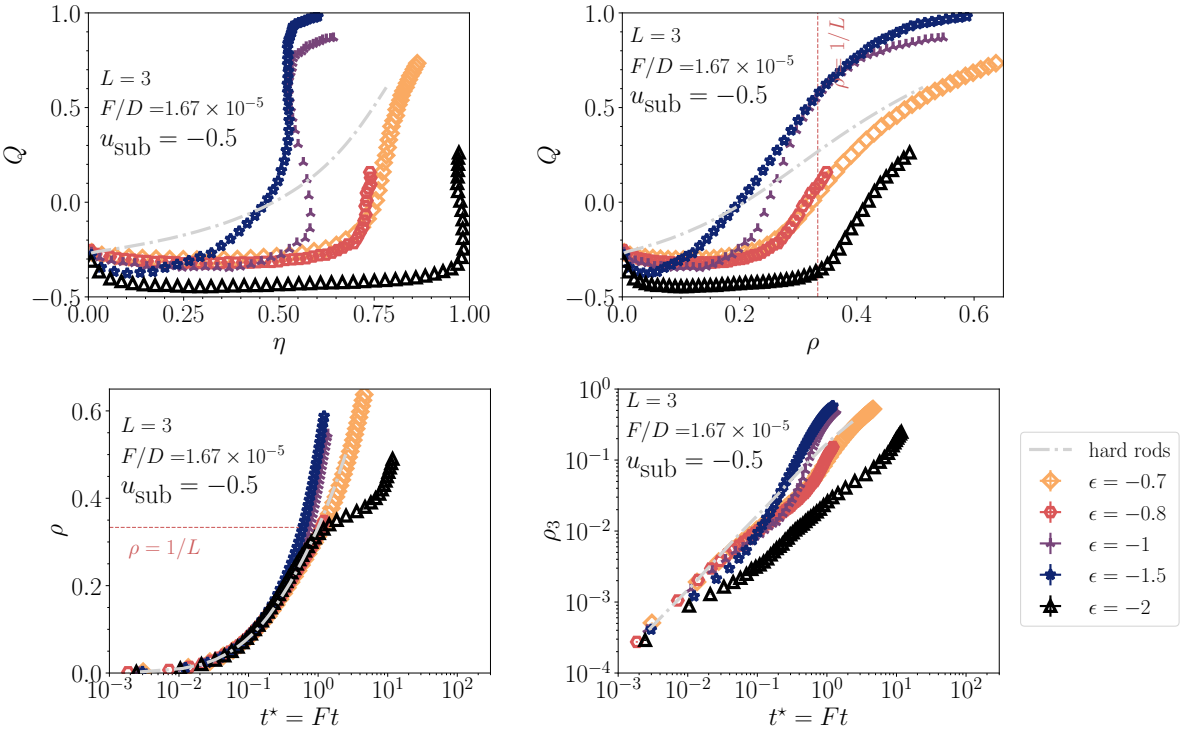

FIGURE 5.84: Effect of weak substrate potential on global observables for a sweep over ϵ during monolayer growth with fixed conditions ($F/D = 1.67 \times 10^{-5}$). Here, $\gamma = 3.0$. The gray dashed curves represent quasiequilibrium growth for purely hard-core rods ($\epsilon = 0$, $u_{\text{sub}} = -0.5$). See also Fig. A.19 in App. A.3.

Monolayer growth with WEAK SUBSTRATE POTENTIALS ($u_{\text{sub}} = -0.5$):
Medium deposition quench rate F/D

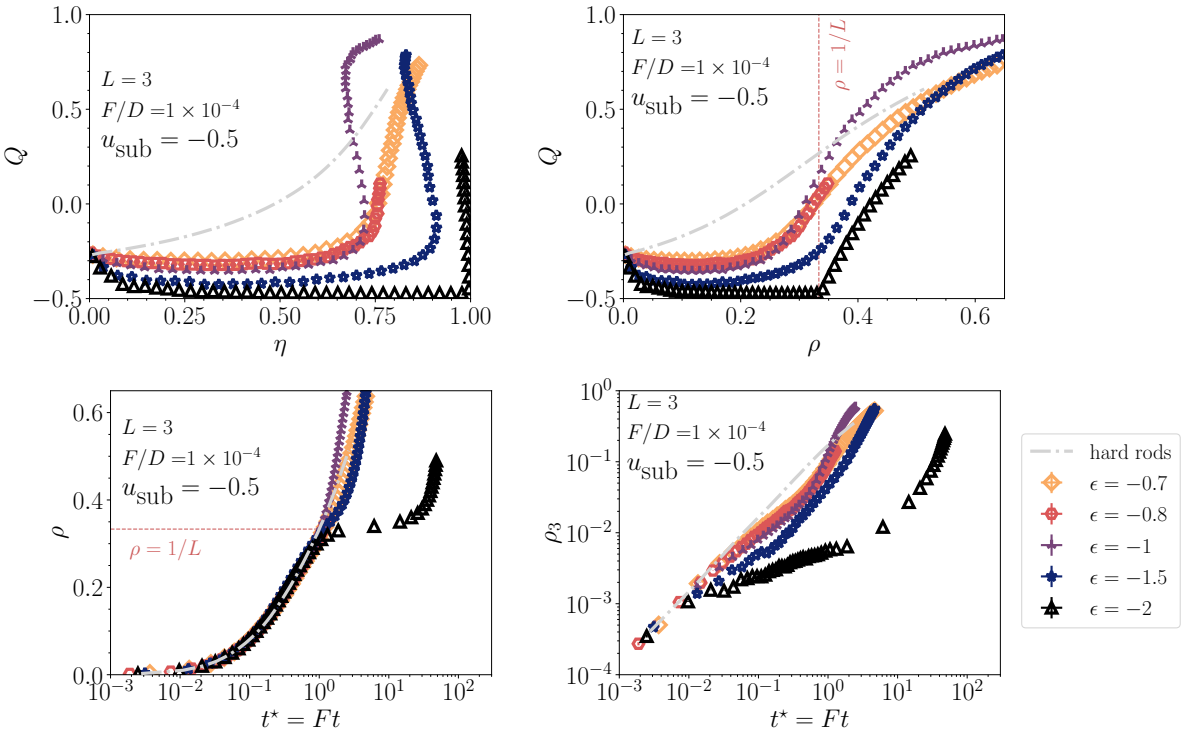

FIGURE 5.85: Effect of weak substrate potential ($u_{\text{sub}} = -0.5$) on global observables for a sweep over ϵ during monolayer growth with fixed conditions ($F/D = 1 \times 10^{-4}$). Here, $\gamma = 0.5$. The gray dashed curves represent quasiequilibrium growth for purely hard-core rods ($\epsilon = 0$, $u_{\text{sub}} = -0.5$).

Monolayer growth with WEAK SUBSTRATE POTENTIALS ($u_{\text{sub}} = -0.5$):
Somewhat faster deposition quench rate F/D

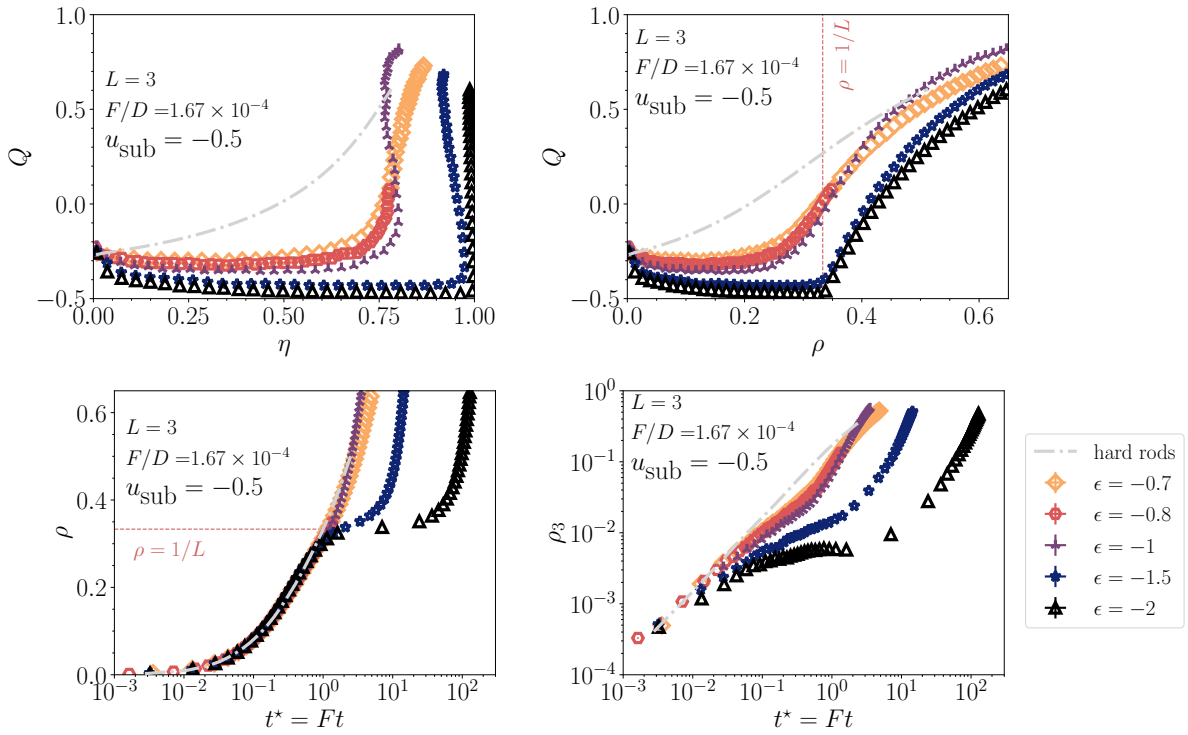

FIGURE 5.86: Effect of weak substrate potential on global observables for a sweep over ϵ during monolayer growth with fixed conditions ($F/D = 1.67 \times 10^{-5}$). Here, $\gamma = 3.0$. The gray dashed curves represent quasiequilibrium growth for purely hard-core rods ($\epsilon = 0$, $u_{\text{sub}} = -0.5$). See more figures in App. A.3.

Monolayer growth with WEAK SUBSTRATE POTENTIALS ($u_{\text{sub}} = -0.5$):
Packing fraction η vs. re-scaled time $t^\star$

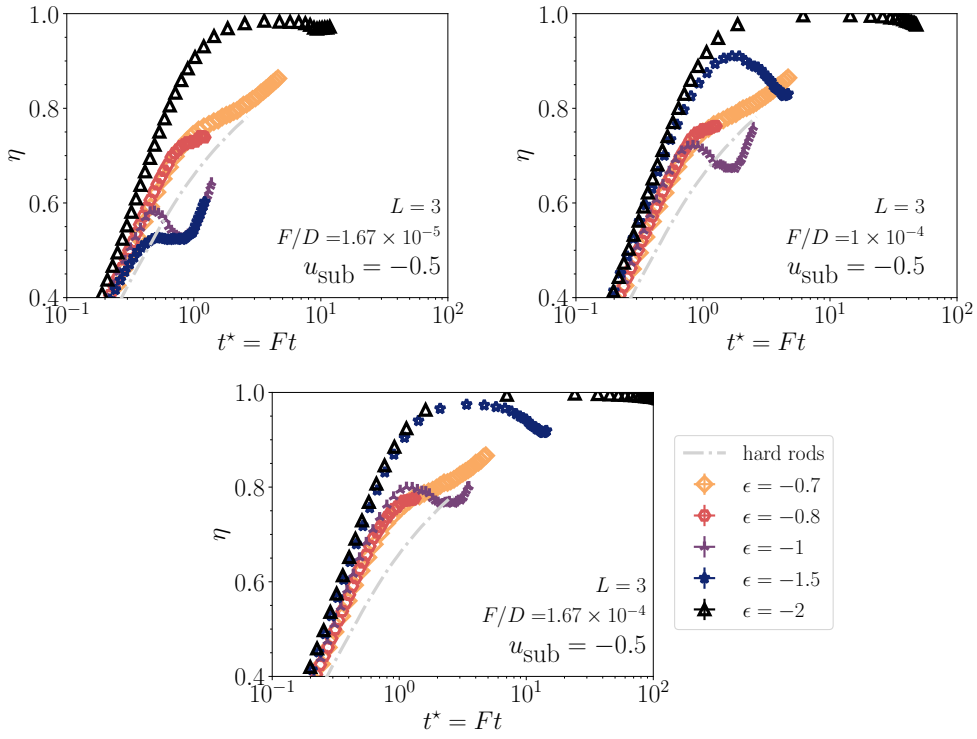

FIGURE 5.87: Global packing fraction η and ρ_{12} for a sweep over ϵ during monolayer growth for three fixed conditions with weak substrate potential $u_{\text{sub}} = -0.5$: $F/D = 1.67 \times 10^{-5}$ (left) $F/D = 1 \times 10^{-4}$ (right) and $F/D = 1.67 \times 10^{-4}$ (bottom). Loops in η are visible for $\epsilon = -1$ as well as for $\epsilon = -1.5$ at lower F/D (top left and right), while only very subtle at $F/D = 1.67 \times 10^{-4}$ (bottom). A reduction in η is associated with a vapor phase expanding or a thin lying fluid thinning. The beginning of a loop is also visible near $\eta \lesssim 1$ for $\epsilon = -2$ at very late times for lower F/D (top left and right), where later $\eta = 1$ is the final end-state, see Fig. 5.82. Here, $\gamma = 3.0$ (left and right) and $\gamma = 0.5$ (top right). See also Fig. 5.88.

Monolayer growth with WEAK SUBSTRATE POTENTIALS ($u_{\text{sub}} = -0.5$):
Lying number density ρ_{12} vs. re-scaled time $t^\star$

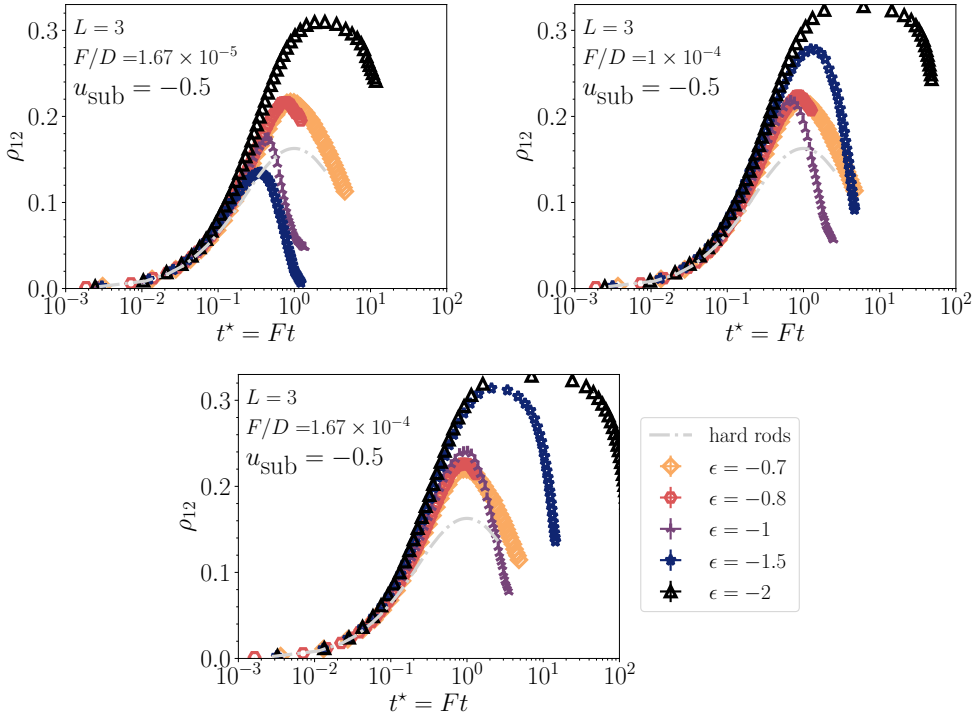

FIGURE 5.88: Global lying density ρ_{12} for a sweep over ϵ during monolayer growth for three fixed conditions with weak substrate potential $u_{\text{sub}} = -0.5$: $F/D = 1.67 \times 10^{-5}$ (top left) $F/D = 1 \times 10^{-4}$ (top right) and $F/D = 1.67 \times 10^{-4}$ (bottom). See Fig. 5.87.

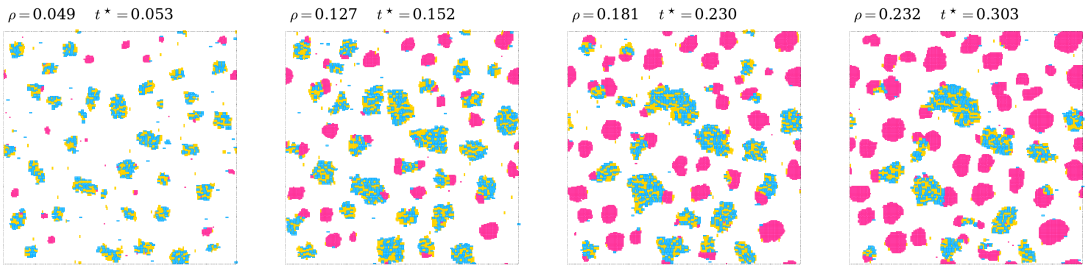

$$|u_{\text{sub}}| = 0.5 < |\epsilon| = 2$$

FIGURE 5.89: Visualized snapshots of competing, compact, lying-phase and standing-phase islands (phase transition scenario (C)), occurring here for weak attractive substrates and strong attractions for low deposition quench rate F/D. Here, $u_{\text{sub}} = -0.5$ and $\epsilon = -2$ and $L = 3$. The dynamical parameters are $F/D = 1.67 \times 10^{-6}$, $\gamma = 3.0$. This scenario clearly occurs for $u_{\text{sub}} = 0$, but, to get such large islands, much stronger attractions with values of $\epsilon = -3.33$ or $\epsilon = -4$ are required.

Monolayer growth with WEAK SUBSTRATE POTENTIALS ($u_{\text{sub}} = -0.5$):
Effect on original ϵ-regimes II and III

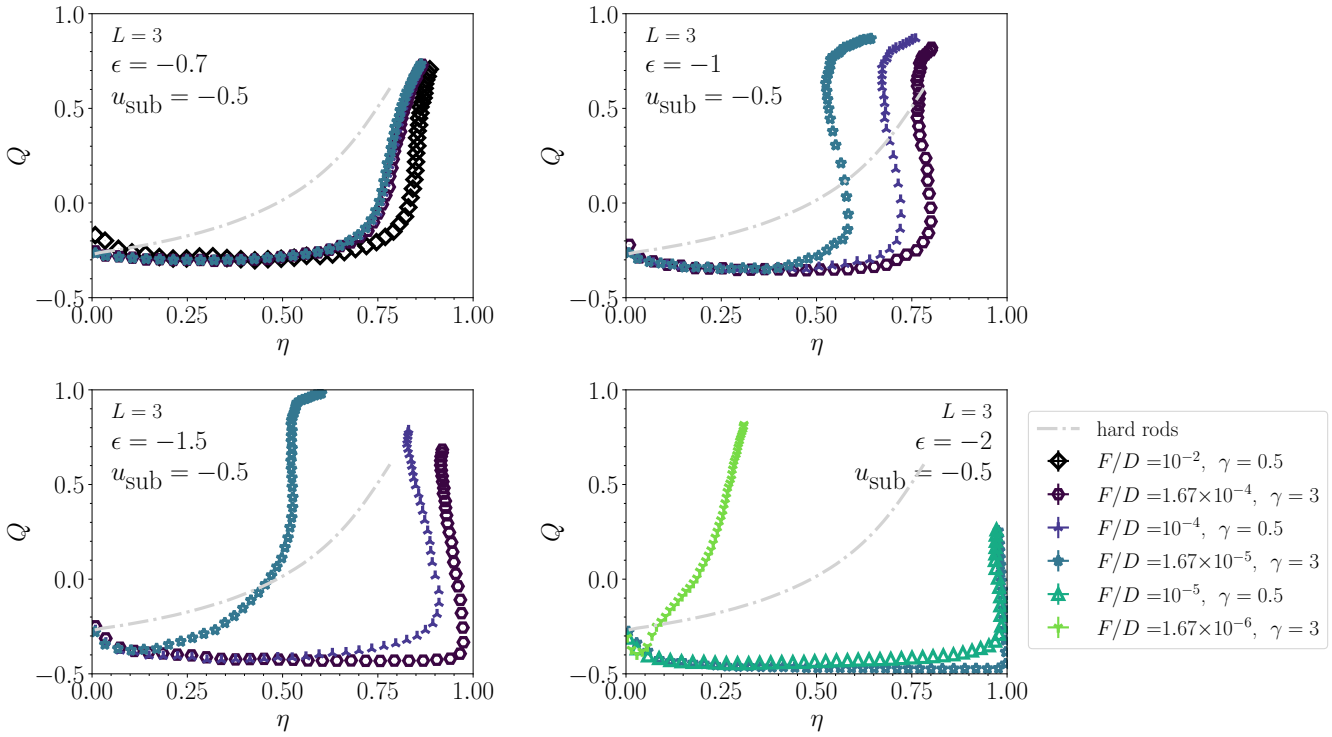

FIGURE 5.90: Effect of a weakly attractive substrate on the nematic order parameter Q versus packing fraction (coverage) during growth of a monolayer, shown for four values of $\epsilon = -0.7$ (now "higher up" in regime II) [upper left] $\epsilon = -1$ (possibly shifted to regime II (?)) [upper right], $\epsilon = -1.5$ (possibly remaining in regime III) [bottom left], and $\epsilon - 2\}$ (still regime IIIb) at varying F/D ($L = 3$, $u_{\text{sub}} = -0.5$).

5.5.2 Moderate substrate potentials ($u_{\text{sub}} = -1$)

Substrate potentials of $u_{\text{sub}} = -1$ clearly enhance the lying phase: Trajectories land in a lying, wetting layer or arrested state with $Q \approx -0.5$. This can be seen in $Q(\eta)$, $Q(\rho)$, $\rho(t^\star)$, and $\rho_3(t^\star)$ in Fig. 5.91, where we have displayed results for a "slow" deposition quench case of $F/D = 1.67 \times 10^{-5}$. At this value of F/D, these cases of $\epsilon = -1.5, -2$ (and marginally $\epsilon = -1$), this wetting layer becomes 2D, and the a "sharp" lying–standing transition occurs thereafter. We discuss more on this in forthcoming. For $\epsilon = -1, -0.8, -0.7$, visual inspection shows the lying phase behaving more "fluid-like" than for stronger ϵ. We show separate quantitative results on $Q(\eta)$ for the case of $\epsilon = -0.7$, at varying F/D in Fig. 5.92. For all values thereof, the trajectories go through a lying, arrested state at nearly full packing $\eta \approx 1$.

For the cases of ϵ originally in regime IIIb, $\epsilon = -2$ (not shown), all trajectories that we simulated go through a "sharp" standing-up transition at $\eta = 1$, for rates varying from $10^{-4} - 1.67 \times 10^{-6}$, which suggests this transition may be thermodynamically stable. We suspect that the critical point for the metastable, lying phase (the isotropic-vapor–2D-liquid transition) have now been "shifted upwards" sufficiently, leaving the left and right binodals packing fractions at these low reduced temperatures very near $\eta_l \approx 0$ and $\eta_r \approx 1$.

Standing-cluster formation from the arrested 2D phase

Yet, *all* investigated cases display the growth of standing clusters from a "sea" of a lying, arrested phase (wetting layer or dense gel) (scenario (E) from Sec. 5.3.9). The shape of the standing-up clusters varies heavily with $\epsilon = -0.7, -0.8$ and $\epsilon \leq -1$, which are much more compact and round in the latter case (higher 'surface' tension). Importantly, moderate attractive substrate potentials enforce a $Q < 0$ wetting layer even for ϵ's originally in regime II (which at neutral substrates was only characterized by standing-island growth for low F/D or a $Q \gtrapprox 0$ nonequilibrium aggregate for high F/D): We depict this lying–standing transition at full packing fraction for "higher" effective temperature ($\epsilon = -0.7$) in Fig. 5.95. We remind the reader that this behavior was not seen in the case of ϵ-regime II at neutral substrates, which formed standing clusters (no clear lying gel). At high deposition rates ($F/D \sim 10^{-1}$), a $Q \approx 0$, mixed-orientation arrested state was converted into a $Q > 0$ "aggregate" quite rapidly, see Fig. 5.11. Now, with a substrate potential of $u_{\text{sub}} = -1$, much lower rates of $F/D \sim 10^{-5}$ are sufficient to produce a globally arrested state or wetting layer. We may need to move to *much* lower F/D (possibly $F/D \sim O(10^{-8} \ldots 10^{-9})$ to see whether a co-occurrence of a lying gel and standing islands at non-full packing fraction (scenario (D) categorized in Sec. 5.3.9) is still possible (which is computationally expensive).

We did not see the above-reported "nucleation" of standing islands out of the wetting layer so prominently for neutral substrates (phase transition scenario (E)) because our simulations did not proceed long enough – they got "stuck" at the $Q < 0$–wetting layer. Regarding a mechanism to get the growth process started, we postulate that the insertion of vertical rods into rare vacancies (via the deposition flux) might suffice. It would be interesting to pinpoint the exact mechanism in future studies, particularly for understanding phase transition kinetics under these driven nonequilibrium conditions in much more general terms. The "standing up" via phase separation of a $Q = -0.5$ and

$Q = 1$ fluid will likely be very similar to the "two-step nucleation" and growth scenario that we described for scenario (E). We would have to take a closer look at the time-traces of all observables in the future. In any case, the deposition setup in these monolayer growth experiments is quite unique. In this discussed case, as soon as particles stand up, vacancies are left open for new particles to get inserted into by the incoming flux. This will keep the packing fraction full during this phase transition and very likely accelerates the growth process.

At neutral substrates, during a rapid deposition quench (high F/D), density fluctuations that render very fine, serendipitous 'clusters' of standing rods (aggregates) get "quenched" (frozen) into the globally arrested state. Much later, the "standing up" transition takes advantage of these quenched aggregates, in effect, which grow rapidly from the surrounding dense, arrested fluid. This renders non-round standing islands surrounded by the nearly-2D liquids. Thus, the arrested state stores "nuclei", in effect, for later periods. The phase transition is *two-step*, then, which corresponds to scenario (E) that we categorized in Sec. 5.3.9. More detailed analysis on kinetics both at neutral and non-neutral substrates would be highly interesting, and represent one potential outlook from this work.

Monolayer growth with MODERATE SUBSTRATE POTENTIALS ($u_{\text{sub}} = -1$)

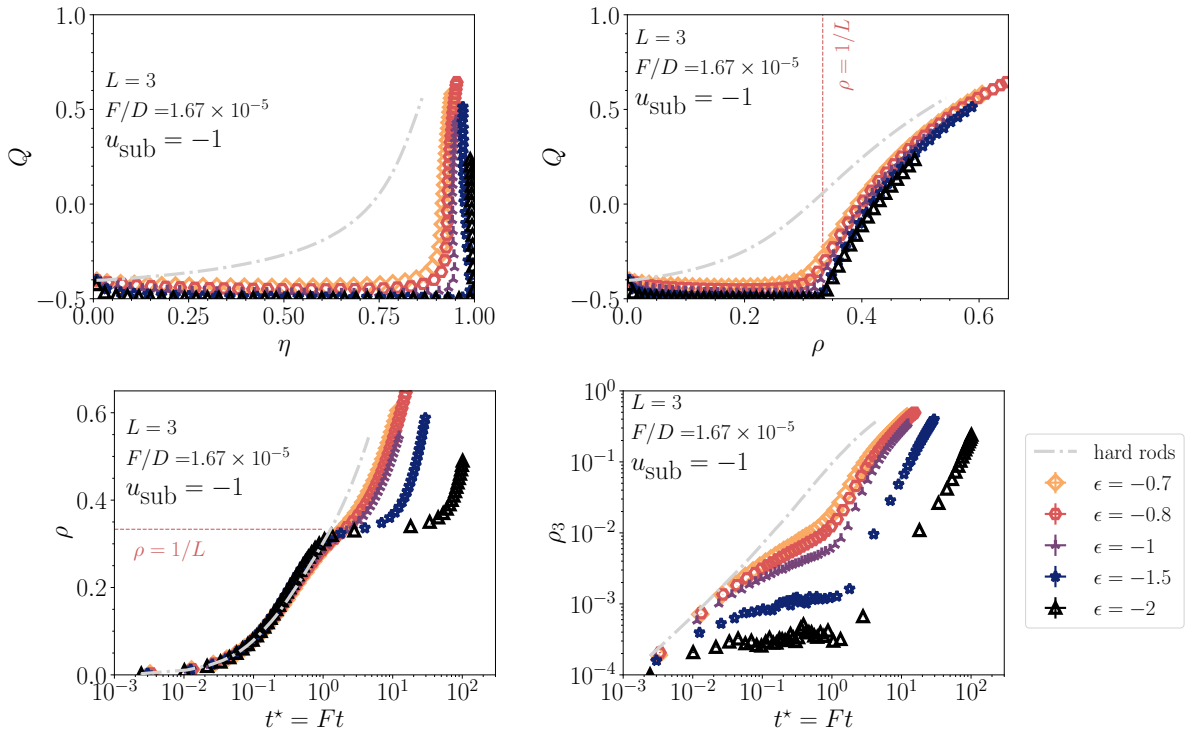

FIGURE 5.91: Effect of moderate substrate potential ($u_{\text{sub}} = -1$) on global observables for a sweep over ϵ during monolayer growth with fixed conditions ($F/D = 1.67 \times 10^{-5}$, $\gamma = 3.0$). Note that $\epsilon = -2$ and $\epsilon = -1.5$ behave differently – the former has a plateau in the density over $t^\star$. The cases of $\epsilon = -0.7, -0.8$ and mildly $\epsilon = -1$ show "softer" lying–standing transitions at $\rho \approx 0.33$. The gray dashed curves represent quasiequilibrium growth for purely hard-core rods ($\epsilon = 0$, $u_{\text{sub}} = -1$). See more figures in App. A.3.

Monolayer growth with MODERATE SUBSTRATE POTENTIALS
($u_{\text{sub}} = -1$):
Effect on original regime II

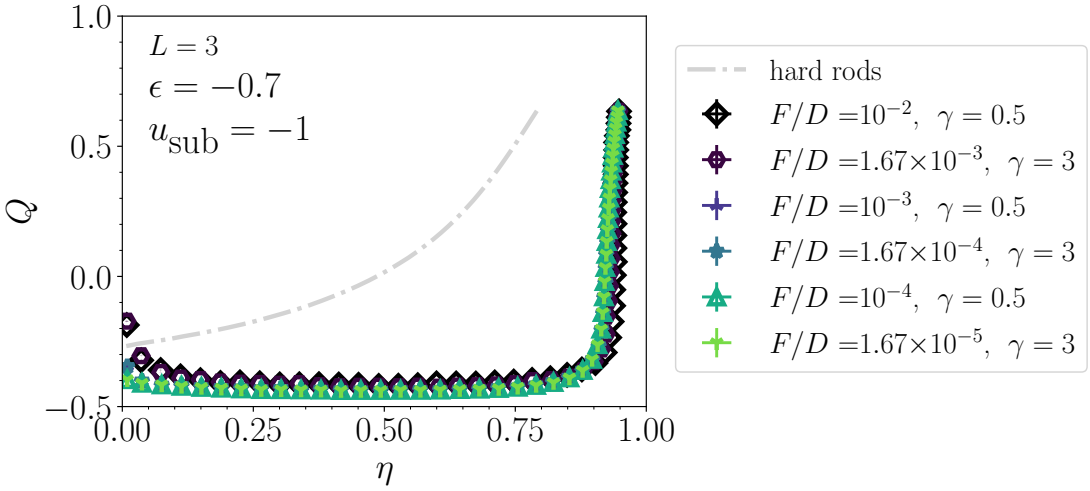

FIGURE 5.92: Effect of intermediately strong attractive substrate on the nematic order parameter Q versus packing fraction (coverage) during growth of a monolayer, shown for four values of $\epsilon = -0.7$ (originally ϵ-regime II) at varying F/D ($L = 3$, $u_{\text{sub}} = -1$).

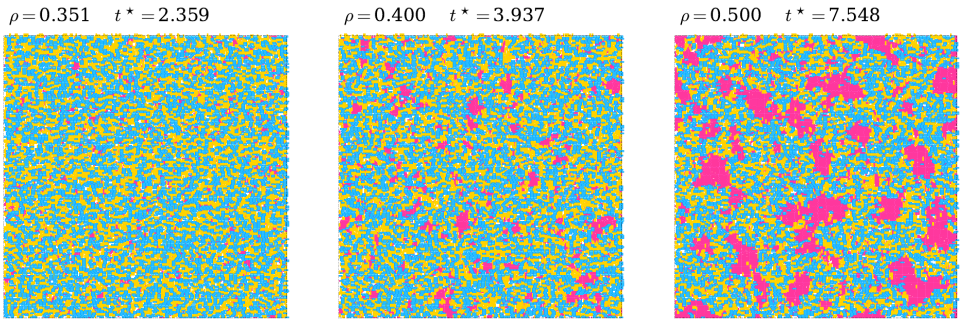

FIGURE 5.93: Visualization of the lying–standing transition at full packing, occurring here for originally ϵ-regime II ($\epsilon = -0.7$) under the influence of moderate substrate potentials ($u_{\text{sub}} = -1$)($L = 3$). The dynamical parameters are $F/D = 1.67 \times 10^{-5}$, $\gamma = 3.0$.

5.5.3 Strong substrate potentials ($u_{\text{sub}} = -2$)

As in the case of intermediately strong substrates, strong substrate potentials ($u_{\text{sub}} = -2$) strengthen the "lying–standing" transition between a lying 2D liquid or gel and a standing liquid (scenario (D) as categorized in Sec. 5.3.9). In fact, all trajectories explored in Fig. 5.94 end up at this transition, which appears noticeably "sharp". We depict an example of this transition for the "warm" case of $\epsilon = -0.7$ (originally regime II) in Fig. 5.95. For stronger attractions ($\epsilon = -1$) originally in regime IIIa, the standing phase seems to nucleate out of the lying liquid, forming round standing clusters signaling a higher surface tension than for $\epsilon = -0.7$. We depict this in Fig. 5.96.

Monolayer growth with STRONG SUBSTRATE POTENTIALS ($u_{\text{sub}} = -2$)

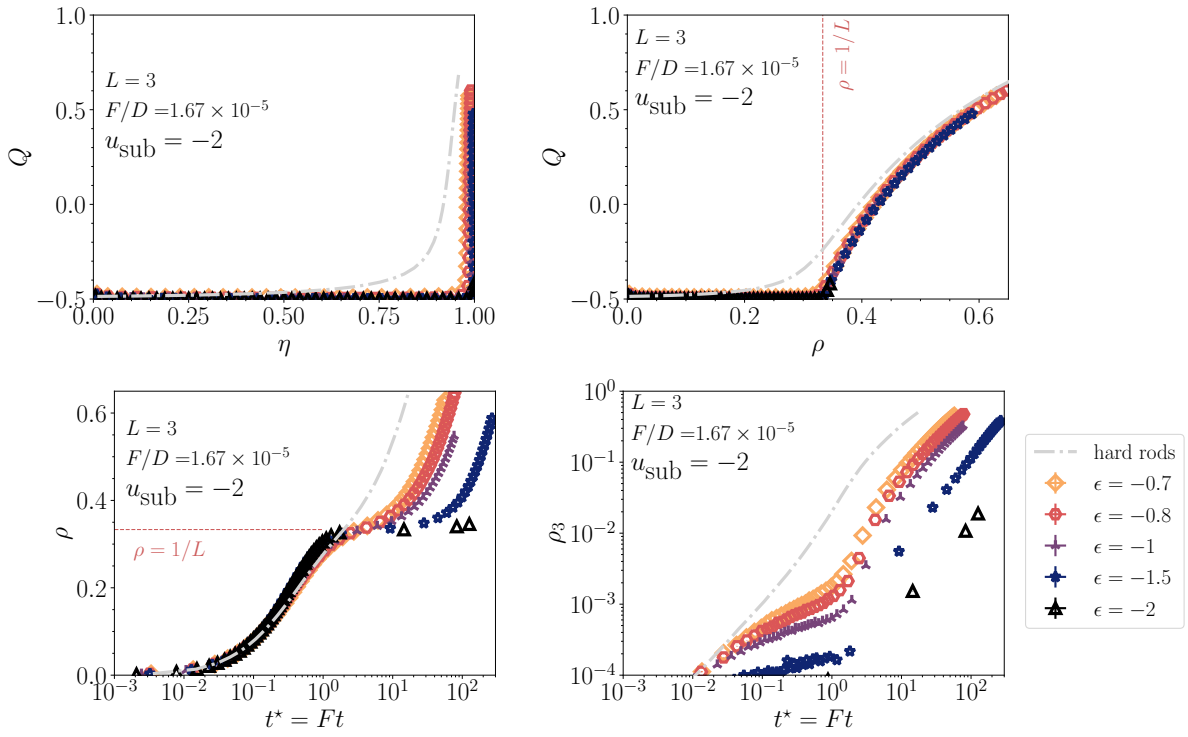

FIGURE 5.94: Effect of strong substrate potential ($u_{\text{sub}} = -2$) on global observables for a sweep over ϵ during monolayer growth with fixed conditions ($F/D = 1.67 \times 10^{-5}$, $\gamma = 3.0$). The gray dashed curves represent quasiequilibrium growth for purely hard-core rods ($\epsilon = 0$, $u_{\text{sub}} = -2$) See more figures in App. A.3.

At lower densities, we see clear evidence for a purely 2D fluid for $\epsilon = -1.5$ (originally regime IIIa (deep)). At densities around $\rho \sim 0.25$ the gel coarsens enough to form rounded cavities (vapor "bubbles"), see Fig. 5.97. These then shrink and disappear when the 2D "wetting layer" forms at $\rho = 1/L \approx 0.333$. For stronger attraction strengths $\epsilon = -2$ (originally regime IIIb) at low values of F/D, we see the formation of round, compact 2D islands separating from a vapor, which eventually coalesce see Fig. 5.98. It seems that independent of u_{sub}, the formation of *large*, compact lying clusters crucially depends on ϵ being in regime IIIb ($\lesssim -2$). $\epsilon = -1, -1.5$ form much more "amorphous" and elongated 2D islands that form a network at high enough

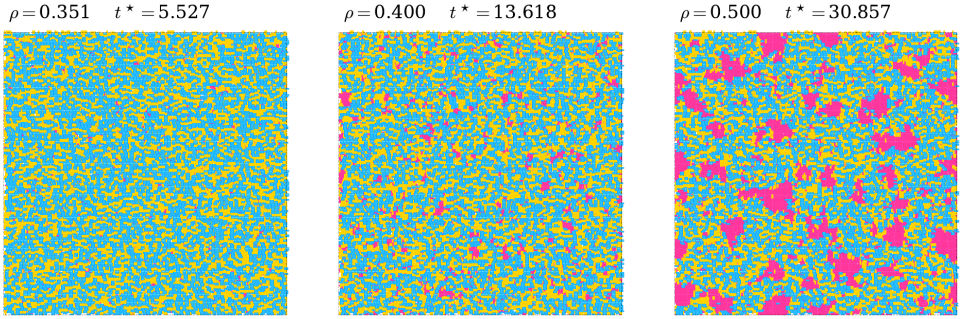

FIGURE 5.95: Visualization of the lying–standing transition at full packing, occurring here for originally regime II ($\epsilon = -0.7$) under the influence of strong substrate potentials ($u_{\mathrm{sub}} = -2$,$L = 3$). The dynamical parameters are $F/D = 1.67 \times 10^{-5}$, $\gamma = 3.0$. Compare to the case of weaker substrate potentials in Fig. 5.93.

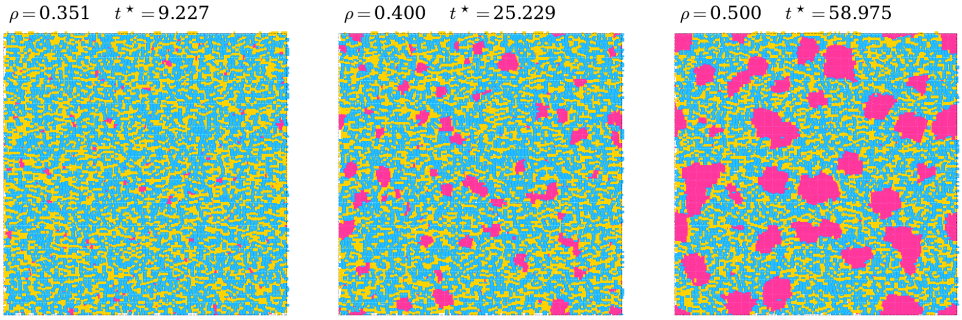

FIGURE 5.96: Visualization of the lying–standing transition at full packing, occurring here for strong substrate potentials and moderate-to-weak attractions ($\epsilon = -0.7$, $u_{\mathrm{sub}} = -2$ and $L = 3$). The dynamical parameters are $F/D = 1.67 \times 10^{-5}$, $\gamma = 3.0$. The standing-liquid clusters are more rounded than in Fig. 5.95.

densities. Nevertheless, strong substrate potentials seems to make the lying–standing transition from a 2D wetting layer stable within both regimes IIIa and IIIb; therefore, a "sharp" transition is visible, while for $\epsilon = -0.8, -0.7$ this transition is "soft". $\epsilon = -1$ seems to be the "sharp"–"soft" intermediary case. It would be interesting to map out the "soft" versus "sharp" transitions as a function of F/D and $1/|\epsilon|$, as well as u_{sub} in a more detailed way in future analysis.

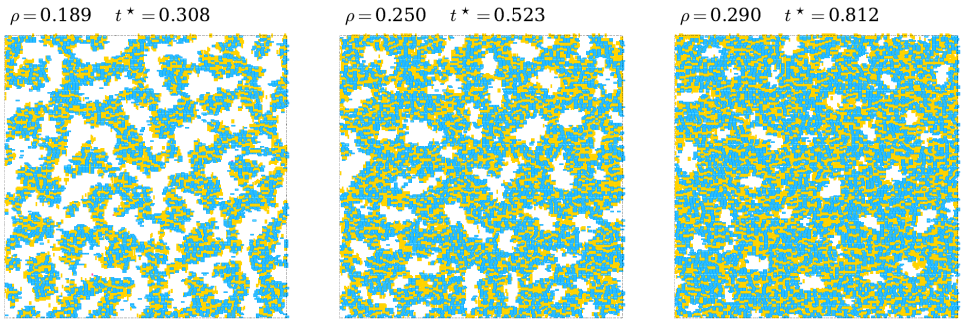

$$|u_{\text{sub}}| = 2 > |\epsilon| = 1.5$$

FIGURE 5.97: Visualized snapshots of a 2D dense gel coarsening before the lying-phase (2D) wetting layer forms, occurring here for strong attractive substrates and stronger attractions. Here, $u_{\text{sub}} = -2$ and $\epsilon = -1.5$ and $L = 3$. The dynamical parameters are $F/D = 1.67 \times 10^{-5}$, $\gamma = 3.0$.

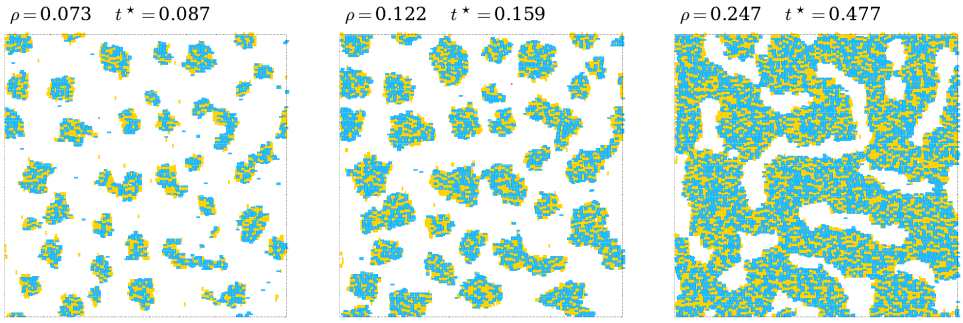

$$|u_{\text{sub}}| = 2 = |\epsilon| = 2$$

FIGURE 5.98: Visualized snapshots of solely lying-phase clusters (2D clusters) and subsequent coalescence before the lying-phase (2D) wetting layer forms, occurring for strong attractive substrates and strong attractions. Here, $u_{\text{sub}} = -2$ and $\epsilon = -2$ and $L = 3$. The dynamical parameters are $F/D = 1.67 \times 10^{-6}$, $\gamma = 3.0$.

5.5.4 Overview of effect of substrate potentials on trajectories

We show the effect of the substrate potential strength (from "none" to "strong",) on regime II (originally) in Fig. 5.99, showing the evolution of global structural – nematic order Q, particle density ρ, and standing particle density ρ_3. The same types of plots are shown for $\epsilon = -1, -1.5, -2$ (originally regime III) in Figs. 5.100, 5.101 and 5.102. A case of even lower deposition quench rate $F/D = 1.67 \times 10^{-6}$ for $\epsilon = -2$ is shown in Fig. 5.103.

* * *

The above analysis of monolayer growth with attractive substrate potentials for $L = 3$ has demonstrated a simple but powerful concept: Weak and intermediate substrate potentials elongate, in effect, the time-scales with which collective reordering processes of orientational order occur in these systems. In doing so, aspects of self-assembly that are otherwise only found very briefly at early stages of growth or for very strong inter-particle attraction strengths $|\epsilon|$

at neutral substrates can endure for a long period of time. In turn, the length-scales of structures formed with these kinetics are much larger. Another point we found is that strong or intermediate substrate potentials might cause otherwise arrested states due to nonequilibrium deposition to have a more thermodynamic character, particularly in reduced-temperature regime II. In particular, the 2D-lying-liquid–standing transition at full packing fraction appears much "sharper", in the sense of a first-order-like transition with growth of standing clusters from a lying phase in the cases of intermediate and strong substrate potentials. This scenario only happens in regime III for neutral substrates. Many questions remain unanswered, but, the phenomena are quite intriguing. Strong attractive potentials cause regime IIIa to form a large 2D liquid (standing clusters are completely absent), while regime IIIb forms large, compact 2D clusters (again without standing clusters). The "2D" phase may have become stable for strong enough attraction strengths.

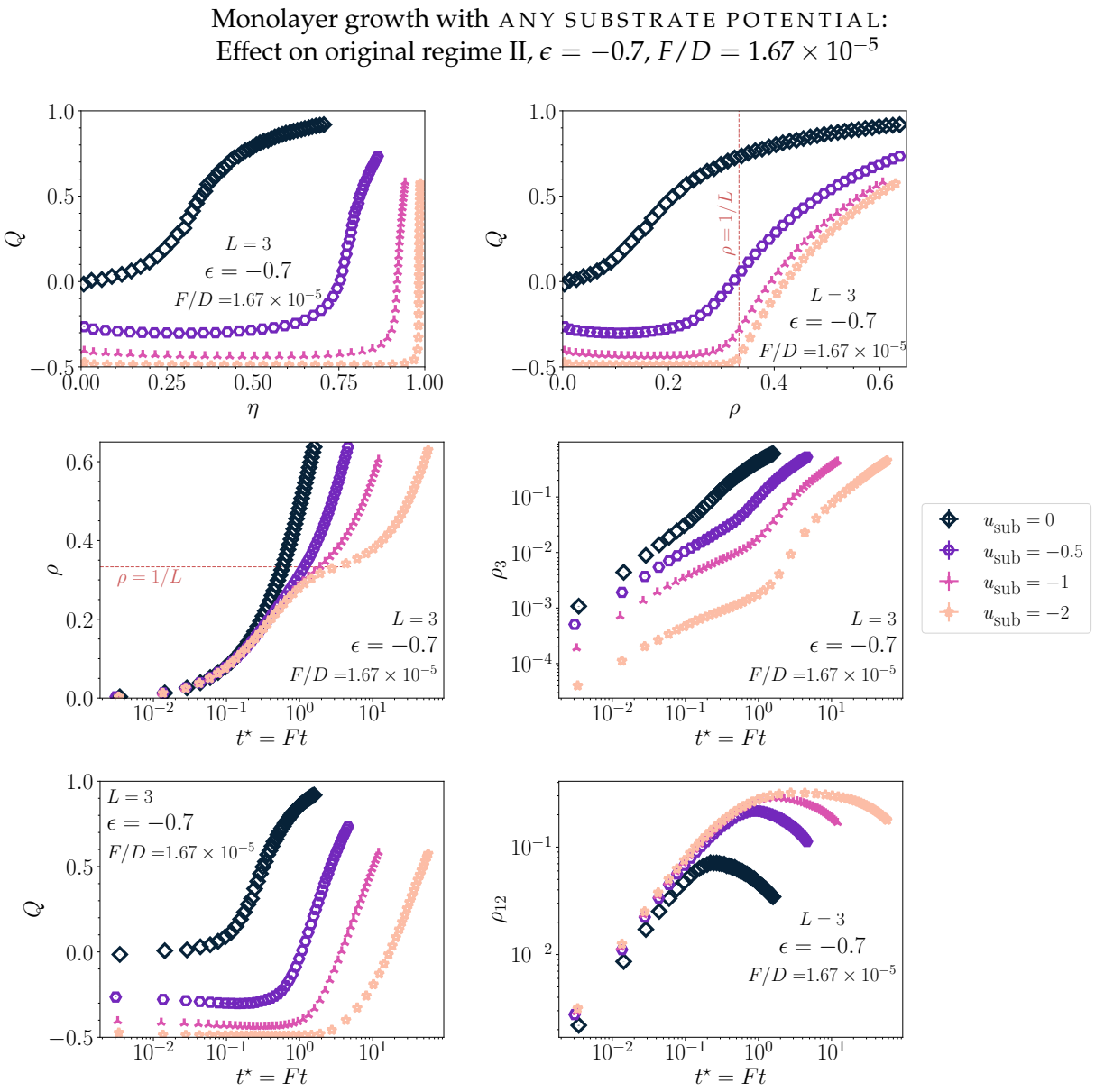

FIGURE 5.99: Effect of substrate potentials on global observables for $\epsilon = -0.7$ (originally regime II) during monolayer growth with fixed conditions ($F/D = 1.67 \times 10^{-5}$, $\gamma = 3.0$) ($L = 3$).

Monolayer growth with ANY SUBSTRATE POTENTIAL:
Effect on original regime IIIa, $\epsilon = -1$, $F/D = 1.67 \times 10^{-5}$

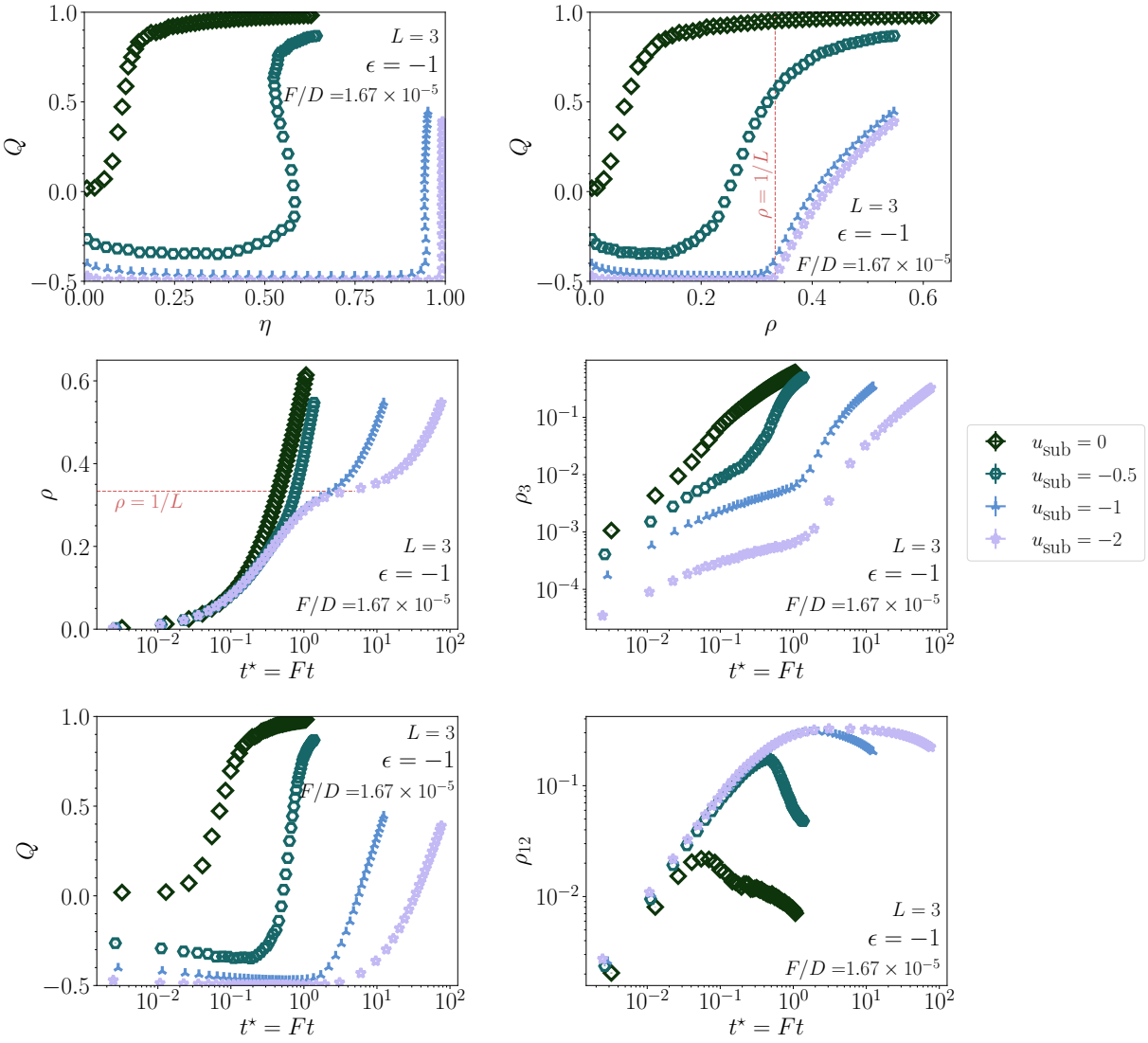

FIGURE 5.100: Effect of substrate potentials on global observables for $\epsilon = -1$ (originally regime IIIa) during monolayer growth with fixed conditions ($F/D = 1.67 \times 10^{-5}$, $\gamma = 3.0$) ($L = 3$).

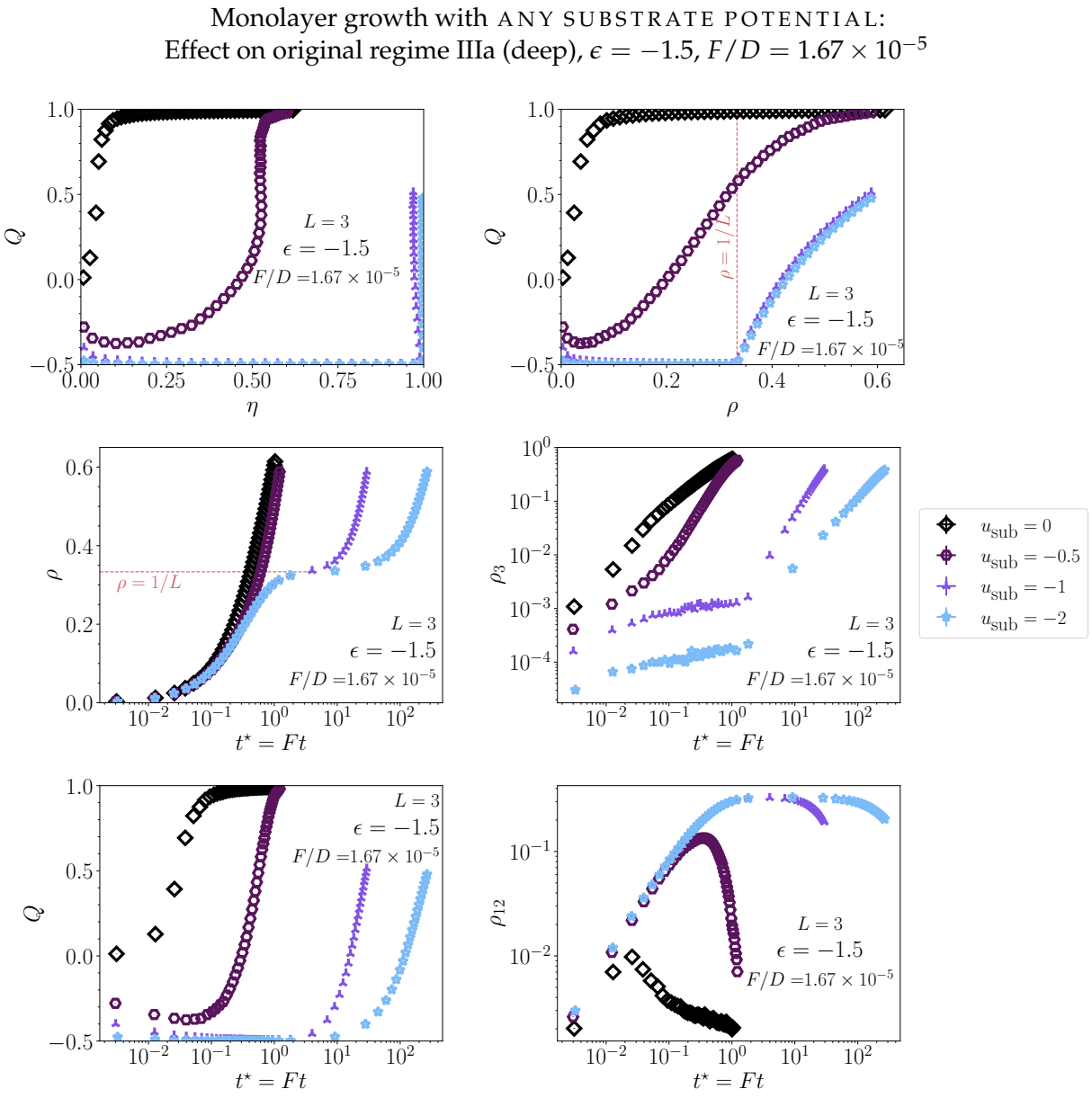

FIGURE 5.101: Effect of substrate potentials on global observables for $\epsilon = -1$ (originally "deep" in regime IIIa) during monolayer growth with fixed conditions ($F/D = 1.67 \times 10^{-5}$, $\gamma = 3.0$) ($L = 3$).

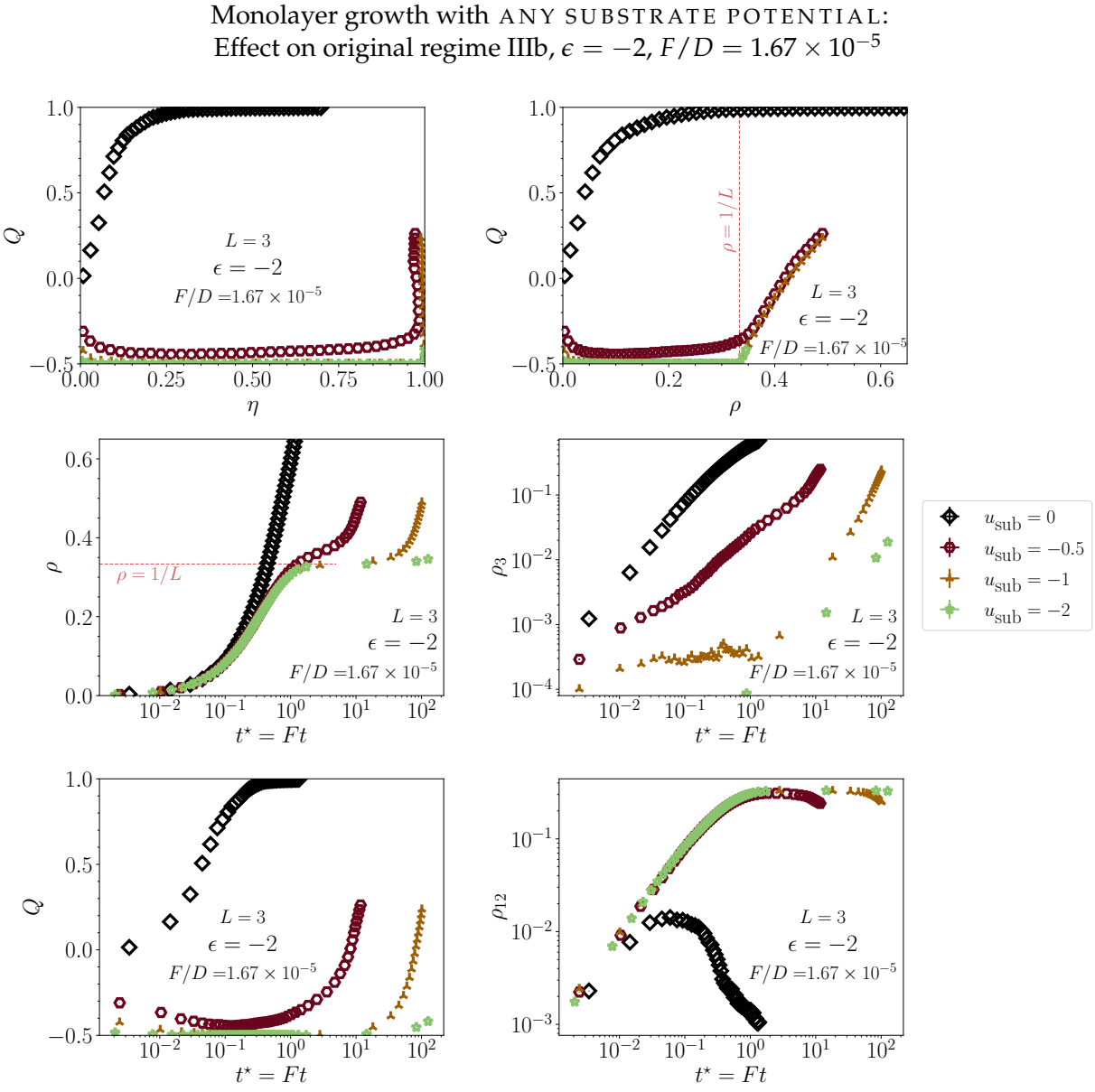

FIGURE 5.102: Effect of substrate potentials on global observables for $\epsilon = -2$ (originally regime IIIb) during growth with fixed conditions ($F/D = 1.67 \times 10^{-5}$, $\gamma = 3.0$).

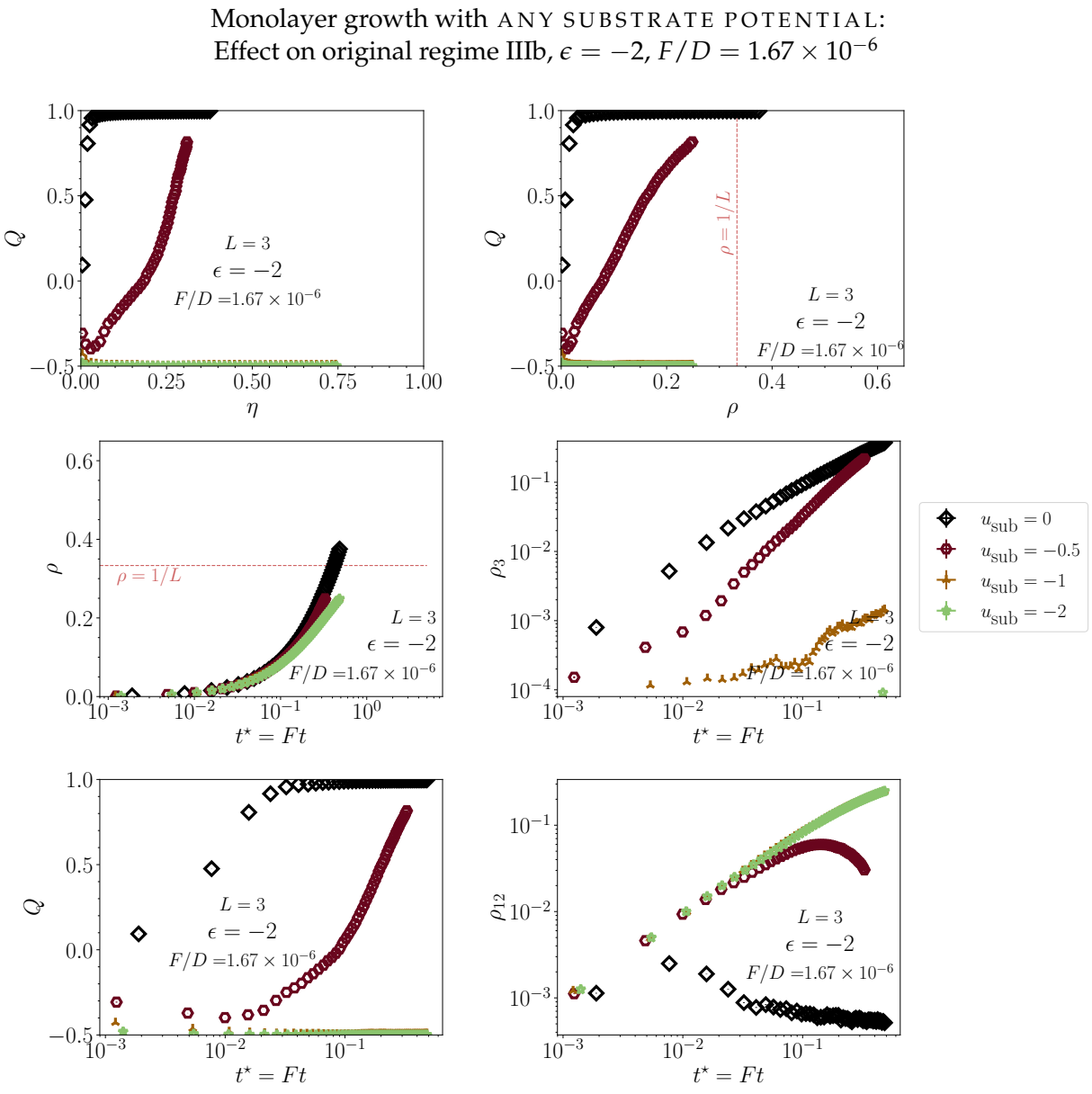

FIGURE 5.103: Effect of substrate potentials on global observables for $\epsilon = -2$ during growth with fixed conditions ($F/D = 1.67 \times 10^{-6}$,$\gamma = 3.0$) ($L = 3$). Note that data-points for $u_{\text{sub}} = -1$ often overlap exactly with those for $u_{\text{sub}} = -2$, which is why they may be hidden.

5.6 Other findings (sensitivity to choice of microscopic dynamics)

We report here on a further finding about monolayer growth with at neutral substrates for $L \geq 3$: The evolution of the monolayer depends very strongly on the specific set of rotational moves (and their rates). In this section, we show the effect of implementing tumbling-moves for out-of-plane rotations (implemented in Ch. 4 for the purely-hard-core case) instead of central rotations, about the rod center (projected onto the plane). At the very bottom of it, tumbling rotations couple the translational and rotational degrees of freedom even at the one-body level. The ideal-gas diffusion coefficient D for translational motion is modified according to Eq. 5.13. Other changes in the specifications on the out-of-plane rotational rates are that the rotational rates $k^{\mathrm{u}}_{\mathrm{tum}} = k^{\mathrm{d}}_{\mathrm{tum}} = k_{\mathrm{tum}} \equiv 1$. Note that we have changed the in-plane rotational rate (between two lying species) to $k_{1\leftrightarrow 2} \equiv 0.3$, as well,[30] but we think this should play a subordinate role.

In Fig. 5.104, we present quantitative results for $L = 3$ on the global nematic order parameter Q as a function of monolayer packing fraction η. Notably, the nematic order barely drops below zero, at best. The suppression of the lying orientation due to kinetic limitations thus avoids the formation of a $Q < 0$ "wetting layer" at intermediate F/D for ϵ-regime III ($\epsilon \lessapprox -1$). Instead, the system always forms a $Q \approx 0$ aggregate state, which was actually characteristic for regime II in our categorization of Sec. 5.3 (for our standard set of "moves"). Hence, scenario (E) categorized in Sec. 5.3.9 are absent. This can be seen, roughly, in the extrapolation "map" of Q in the $(\ln(1/|\epsilon|), \log(D/F))$–plane in Fig. 5.105, as well: No areas of (dark) blue color (low values of Q) appear, which are associated with the formation of a thick gel or wetting layer. (Please compare to Fig. 5.60 for $L = 3$ with central, out-of-plane rotations.)

On another note, we report on a small finding unique for these dynamics: we can see subtle "standing–lying–standing" loops in Q for the case of $F/D = 6 \times 10^{-3}, 6 \times 10^{-4}$ and $\epsilon = -3.33$ for $L = 3$ (regime IIIb, deep) in Fig. 5.104. We argued that these loops are signs of collective standing-up processes (kinetics) which may require more analysis with, e.g. dynamical observables on fluxes and particle mobility. Generally, then, a re-assessment and re-categorization of the growth kinetics seems necessary, as some of the phase transitions scenarios we categorized in the central-rotations case for $L = 3$ do not appear. An analysis of the time-traces of global observables and morphological measures, as well as island statistics, and so forth remains outside of the scope of this thesis, however.

Initial argumentation

This choice of tumbling dynamics means the rotational and translational degrees of freedom couple even at the one-body scale. At the microscopic level, the dynamics could be more heterogeneous, a subject which would be worth exploring in future analyses. The failure of a low-Q wetting layer forming (scenario (E)) also gives credence to the notion that the system is more strongly out-of-equilibrium, as even a globally metastable, nonequilibrium steady state (the "next" best thing to a global equilibrium state, in some sense) is completely

[30] for historical reasons

missed. Yet, the thermodynamically stable end-state – the standing phase – appears in a manner where more fractal-like islands (see Sec. 5.6.2 below) hint at aggregation-like island formation mechanism.[31]

5.6.1 Longer, tumbling rods ($L = 5, 9$): Clearly altered phase transition scenarios and kinetics

The influence of tumbling rotations versus out-of-plane rotations about the rod centers unveils itself even more visibly for longer rods. Results on the global order parameter Q versus monolayer packing fraction for monolayer growth with sticky rods of lengths $L = 5$ are shown in Fig. 5.106. Likewise, we present the results for monolayers of very long rods ($L = 9$) in Fig. 5.107.[32] It appears that the tumbling rotations hinder the formation of a high-packing-fraction $Q \approx 0$ altogether, reaching a maximal packing fraction at high deposition quench rates with $\epsilon = -2.5$ for $L = 5$. Compared to $L = 3$, however, the global order Q can dip below zero somewhat more strongly. This dip is even stronger for $L = 9$. The latter case displays strong loops in the packing fraction during growth, which is rational considering the large discrepancy between the packing fraction of a lying and standing rod (8 units of area per rod).

Finally, the trend of the trajectories of $Q(\eta)$ for various reduced temperatures in Fig. 5.106 and 5.107 hint at a *non-monotonic dependency* on F/D. These curves depend crucially on the value of γ, the ideal-gas ratio of the diffusion-to-rotational-rates ratio. Moreover, we discuss below how the ideal gas translational diffusion rate of tumbling rods may be an unsuitable dynamical parameter to describe a reduced competition "axis" comparing "internal" transport time-scales with the flux rate ("F/D").

We have provided further extrapolated "maps" of Q in the $(\ln(1/|\epsilon|), \log(D/F))$–plane for $L = 5$ in Fig. 5.108 and for $L = 9$ in Fig. 5.109 for completeness. Compared to systems with central rotations with $L = 5$ (Fig. 5.68), the case of $L = 5$ with tumbling rotations clearly shows a lack of a pronounced wetting layer or dense lying gel (dark blue in the color bar). A "gel line" is much less clear and more data points would be necessary to make the topology of the map clearer.

The case of the "map" for $L = 9$ in Fig. 5.109 looks quite different from all other "maps" we have seen so far in this chapter: First of all, the "gel line" that can be inferred from the white "coastline" seen for $\rho = 0.05, 0.08$, is curvy. One potential 'problem' may be our usage of Eq. (5.13) for a measure of D, which represents an ideal-gas limit of tumbling lateral transport. Possibly, a weighted harmonic mean of the translational and rotational degrees of freedom may represent a reduced axis "F/D", as well. We remark on this again further below. On the other hand, a curvilinear gel line may be expressing something important about dynamical arrest, and how it is manifested in the coupling between rotational and translational degrees of freedom.

Secondly, it appears as though this (curvy) gel line "hits a wall" at coordinates $(3.1, -1.2)$ to $(3.1, 1.1)$, left of which $Q \sim 0.1 - -0.2$ for $\rho = 0.05$. Q is greater than zero, but, remains lower than Q above y-values of ~ 1.5 – up to the last density displayed, $\rho = 0.15$. We propose this may be another dynamically arrested state (partial jamming at low D/F). The upper point might provide

[31] This supports the potential view of a somewhat more "energy-driven" type of self-assembly.
[32] for which we currently have no comparative results with the original move-sets.

an estimate for a critical point, i.e. $\epsilon \approx 0.33$. The hump in the "gel line" at densities $\rho = 0.05, 0.08$ may also indicate another, metastable critical point at the second peak from the left around $(4.2, 0.7)$, which would correspond to a value of $\epsilon \approx 0.5$. Future investigations with a larger number of simulation points and larger lattice sizes would be necessary to test this hypothesis.

As the coupling between rotational and translational degrees of freedom is highly nontrivial in nonequilibrium, an *empirical* measure for the transport properties, i.e. the total *translational* flux would shed more light on the coupling as well as on the general kinetics in the system. This can be done quite easily with our written routines described in Sec. 5.3.8. We comment that clarifying the role of the coupling of rotational with translational degrees of freedom may be further important when considering multi-layer growth. We refer the reader to the discussion in Sec. 5.9.

5.6.2 Diamond-like standing islands when rods tumble

The available simulation data for $L = 5$ with tumbling rotations cover lower reduced temperatures than that for out-of-plane rotations about the rod centers. We were able to discover another feature of longer rods at low reduced temperatures: The most striking difference to short rods or to higher temperatures (e.g. regime IIIa) for $L = 5$ is that standing islands tend to become fractal-like in shape. More specifically, due to the underlying symmetry of the lattice, their shape can be deemed as roughly diamond-like and pointy. We provide a visual example of these diamond-like fractal islands in Fig. 5.110.[33] The shape is in stark contrast to islands seen for $L = 5$ with central, out-of-plane rotations in Figs. 5.62–5.65. This tendency towards non-round islands is highly pronounced for very long rods ($L = 9$).

The diamond-like shape of the islands can be understood from a microscopic kinetic picture, and is geometric in nature: A round standing monomer at the center of our coordinate system can get rods attached to it at all four Cartesian directions along its boundaries. With tumbling rotations, lying rods can first get attached to the monomer in these four radial directions. A subsequent standing up via tumbling occurs within one Δt-time-step. In contrast, with central, out-of-plane rotations, the radially attached lying rods must first rotate upwards, which breaks the local bond, and subsequently hop back towards the standing monomer, which is at best a $(\Delta t)^2$-order process that additionally requires overcoming a local energy barrier (the sticky attraction bond). Therefore, the central-rotations scheme renders rather near-equilibrium, and lesser aggregation- or attachment-driven kinetics of standing island growth, roughly speaking. Therefore, the rather fractal-like shape of standing islands with tumbling rotations signals their more strongly out-of-equilibrium growth. This type of island shape is seen, weakly, for $L = 3$ at the lowest temperature investigating using the tumbling rotations ($\epsilon = -3.33$).

As to very long rods, the total binding energy between two (standing) rods scales linearly with their length. Moreover, the entropic contributions are more strongly shifted when compared contrast to central rotations: Each lying rod moving with central rotations will introduce a gap of length $(L-1)/2$ between rod and nucleus when detaching for an upwards rotation, which scales

[33] Although we have analyzed quantitatively the radius of gyration of islands, a quantitative presentation of this kind remains outside of the context of this thesis.

linearly with L. Therefore, the diamond-like shapes will be highly pronounced for $L = 9$, and the kinetics in the monolayer will be altered more strongly. Generally, longer rods will emphasize variations in the curvature of islands or other features in the monolayer more strongly.

Fig. 5.111 shows later stages of growth after such diamond-, fractal-like islands have formed and later coalesce. Notably, the lying gel that evolves in parallel to the islands leaves behind highly irregular vacant spaces once it decays. This effects the evolution and shape of nearby islands, where the zig-zag patterns at high densities (rightmost figure) appear "defective" where the lying gel once reigned. During this time, large loops appear in the packing fraction, see Fig. 5.107 (the bottommost-right corresponds to the chosen images).

"Maps" of configurations for monolayer growth with $L = 9$ in the $(1/|\epsilon|, D/F)$–plane at fixed densities is found in Figs. 5.112–5.115, where we point out some of the phenomenology in detail in the captions. Specifically, the diamond-like islands tend to elongate into strips at higher densities, within the temperature regime that presume to be a variant of "ϵ-regime III" ($\epsilon \lesssim -1$). A dense gel seems to form in this region, too, hence we speculate a connection between the formation of a network, a gel, of the lying liquid and diamond-like-shaped standing islands. Further, at higher densities, the elongated diamond-like islands begin to coalesce into approximate zig-zag patterns of the standing phase. Regarding the other regimes for $L = 9$, judging from quantitative analysis on global structural variables and visual inspection, we expect that highest value of $\epsilon = -0.1$ investigated belongs to regime I. Further, we assume something similar to "ϵ-regime II" is seen for the cases of $\epsilon = -0.33$ and $\epsilon = -0.5$ explored in our data-sets, the latter case of which may be very close to a potential "regime III", however. Specifically, for this projected "regime II", a dense-phase, lying network that mimics a gel is lacking. Further, the standing islands are much more round in shape. However, a new characterization of the phase transition scenarios seems necessary for longer rods, as various phases may become metastable (i.e. demixing in-plane, see next Sec. 5.6.3), in addition to the tumbling dynamics that further changes the game.

5.6.3 Further effect: 2D demixing for very long rods

A keen observer might notice one more prominent, new feature in Figs. 5.112–5.115, i.e. the case of monolayer growth with very long rods: The configurations hint at 2D demixing – where large domains of only one lying orientation (blue and yellow in the figures) are visible – in certain cases of density and D/F, within what presume are ϵ-regimes I–III. As the system in regimes II and III will begin to condense into standing islands, this demixing behavior may disappear once the "2D" vapor *complementary* to the standing phase becomes thin enough. A strong dependency on the dynamical parameters is imminent if the transition is transient (metastable) due to this mechanism. The specific microscopic dynamics may also play a significant role, especially if this transition competes with standing-island aggregation and growth. A comparison to results for growth with $L = 9$ with a different choice microscopic dynamics would be desirable in the future.

Preliminary quantitative analysis show evidence for 2D demixing via an abrupt nonzero mean of the reduced 2D demixing order parameter

$$|S| \equiv \frac{|\,\rho_1 - \rho_2\,|}{\rho_1 + \rho_2} \tag{5.20}$$

at quite low densities. However, we leave the quantitative results for an outlook of this thesis. Regardless, we would like to mention that the FMT predicts a first-order "reentrant demixing" transition of this kind, which is supposed to be metastable even for $L = 3$ at very low temperatures. We have not seen evidence for this transition for $L = 3$ during growth. However, FMT also predicts this transition can become *stable* once rods become longer. This may agree with our preliminary findings here. Analysis of the 2D demixing order parameter (Eq. (5.20)) for larger simulated systems will provide more certainty on these issues (we have already simulated 512×512 systems in sporadic cases of regimes I, II, and III).

* * *

We can conclude the following points from the analysis of this section about models of thin film growth with anisotropic particles: As the relaxation of Q occurs at a local, mesoscopic level in a dynamically heterogeneous system, the competition between translational and rotational degrees of freedom may be nearly as important as the competition between incoming flux F and diffusion constant D. The choice of microscopic dynamics in a model system for e.g. thin film growth will affect the outcomes. Specifically, tumbling rotational dynamics favor diamond-like, standing-island shapes at low enough reduced temperatures, an effect much more prominent for longer rods. In any case, the metastable lying phase remains an inherent part of growth within a model system of "sticky" rods, although tumbling rotations reduce its intensity or predominance. Evidence at hand suggests that 2D demixing behavior may occur for very long rods during growth before standing islands grow; a more detailed investigation may be necessary.

DYNAMICS WITH TUMBLING ROTATIONS ($L = 3$):
Nematic order Q vs. packing fraction η

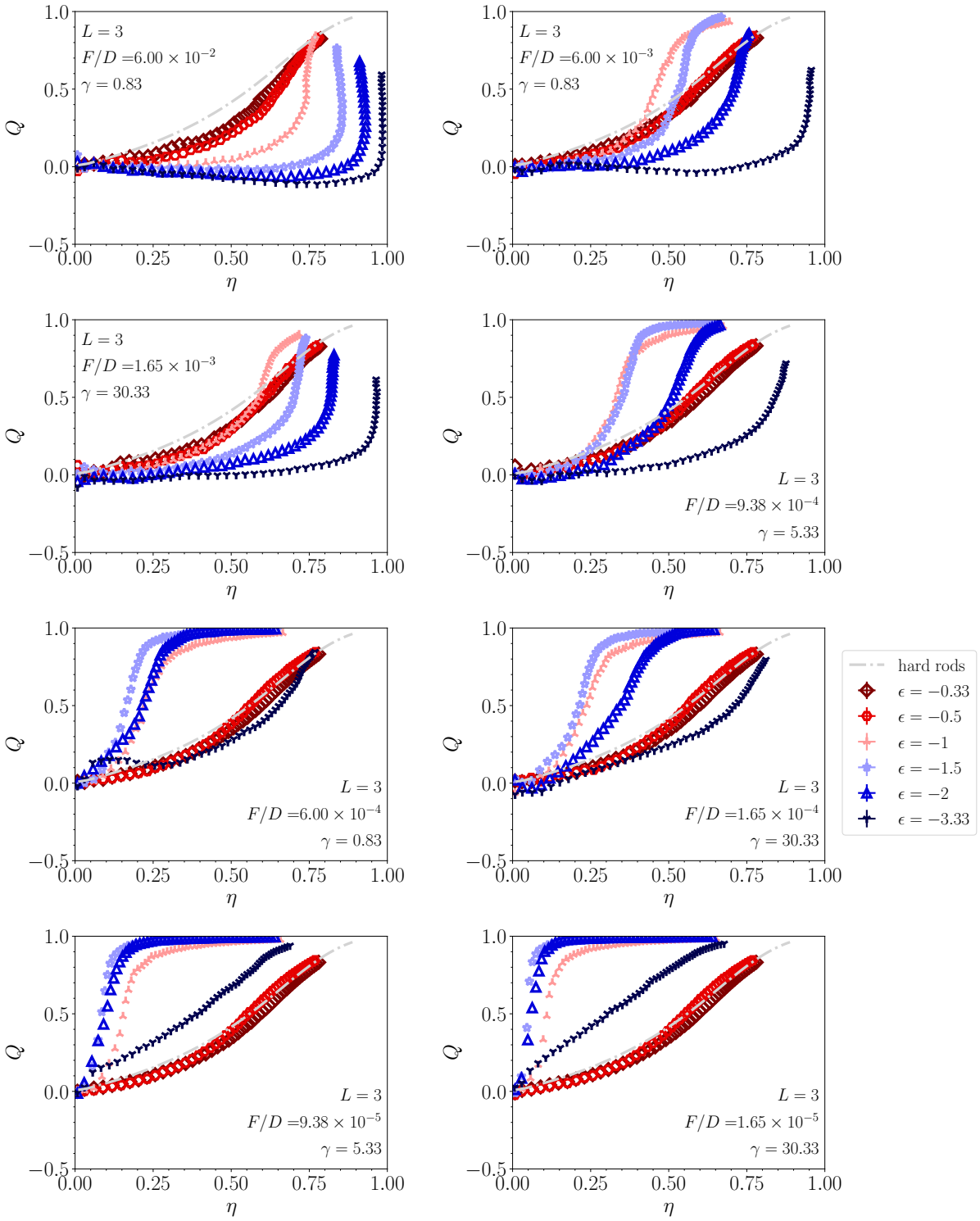

FIGURE 5.104: Nematic order parameter Q versus packing fraction (coverage) η during growth of a monolayer of $L = 3$ rods at various fixed F/D conditions with *tumbling* rotations: Comparison of attraction strengths ϵ. Here, out-of-plane rotations are implemented as tumbling moves, which changes the character of the morphological and dynamical evolution significantly, compare Fig. 5.24 [notice: mismatching legends]. The gray dashed curve represents quasiequilibrium growth with purely hard-core rods ($\epsilon = 0$).

DYNAMICS WITH TUMBLING ROTATIONS ($L = 3$):
Extrapolated "maps" of nematic order Q

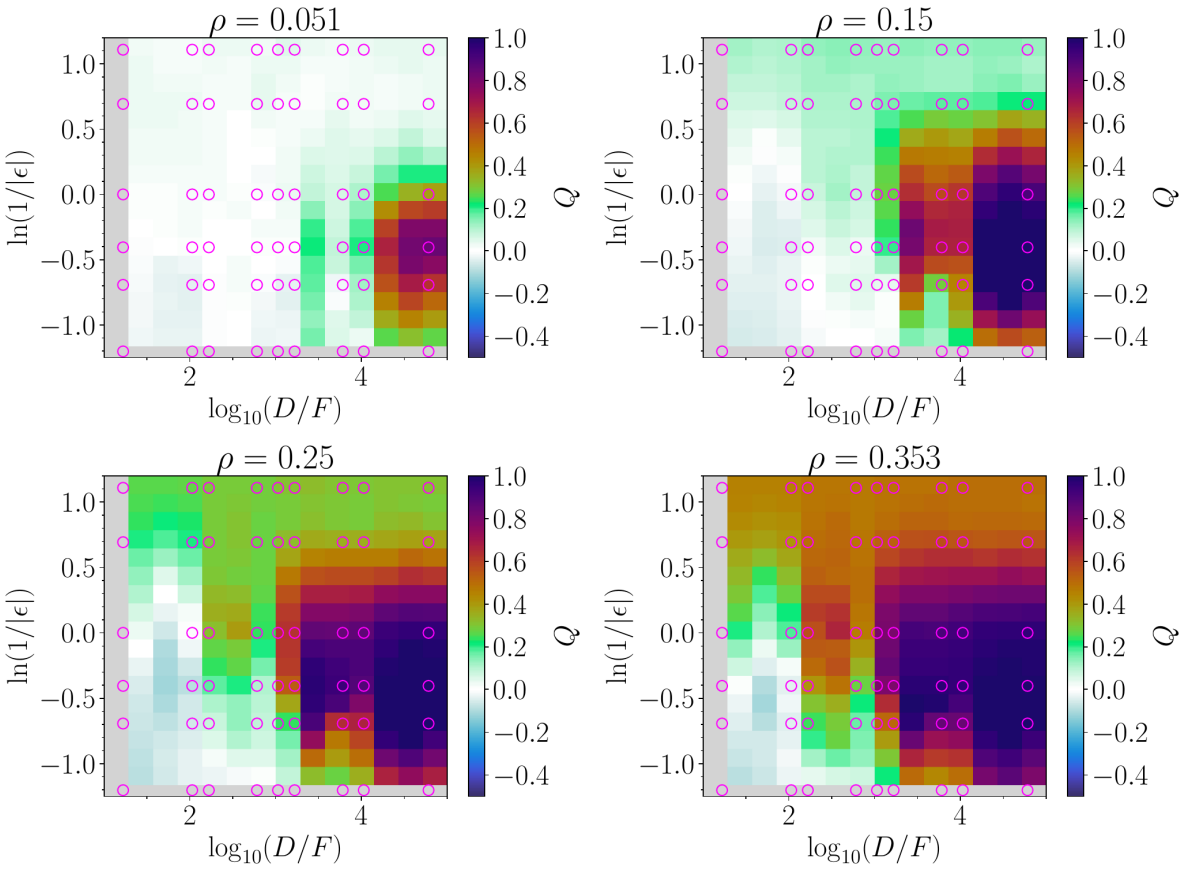

FIGURE 5.105: Extrapolated maps of the nematic order in the $(\ln(1/|\epsilon|), \log(D/F))$–plane at four different densities during growth ($L = 3$, neutral substrates), simulated with tumbling rotations. Magenta circles indicate supporting data points from simulation. A cubic extrapolation scheme is employed, hence, please consider this map as a qualitative one. This "map" shows quite different topology compared to the case of central rotations in Fig. 5.60, but, entails far fewer points than the latter.

DYNAMICS WITH TUMBLING ROTATIONS ($L = 5$):
Nematic order Q vs. packing fraction η

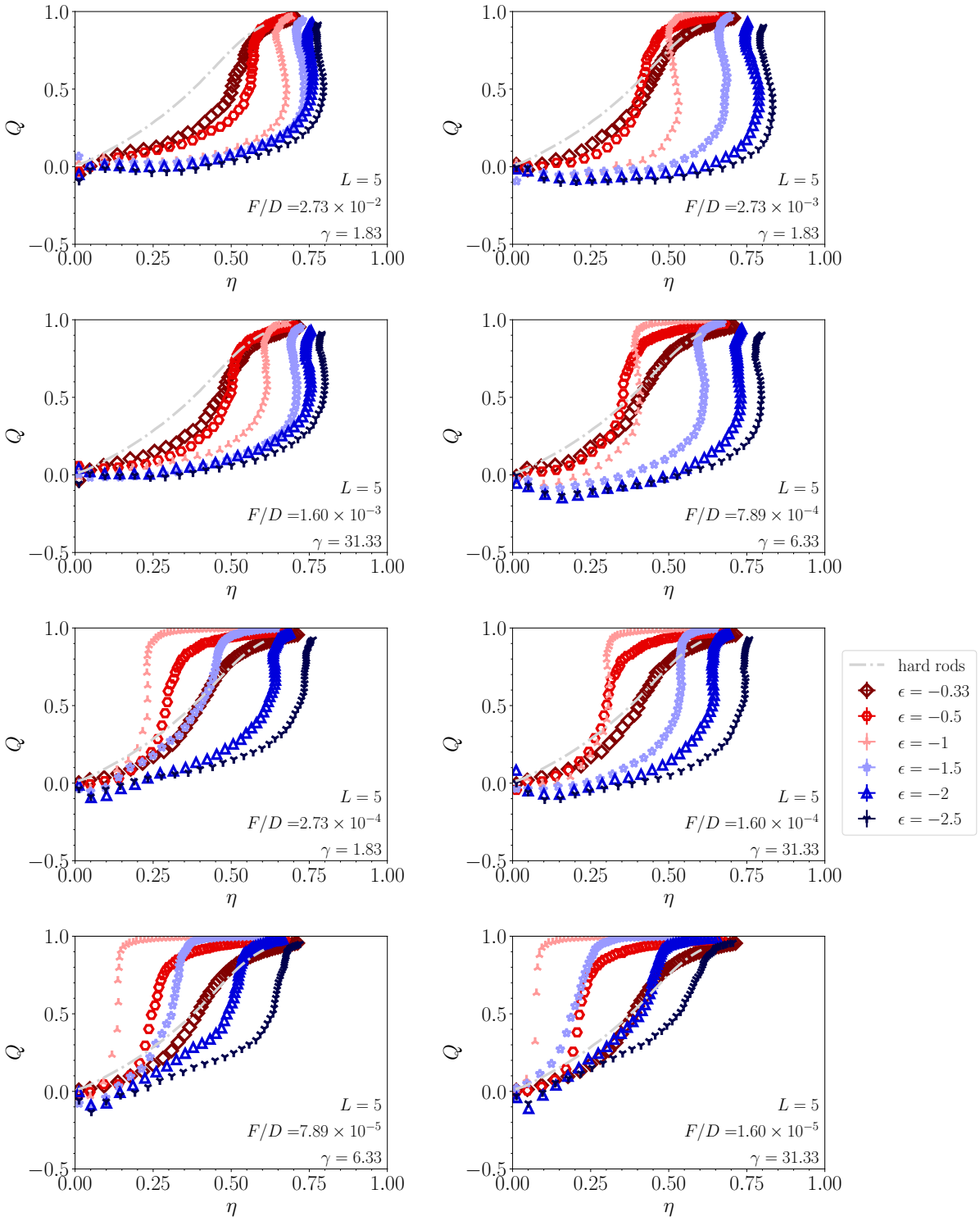

FIGURE 5.106: Nematic order parameter Q versus packing fraction (coverage) during growth of a monolayer of longer rods ($L = 5$) at various fixed F/D conditions with *tumbling* rotations: Comparison of attraction strengths ϵ. Here, out-of-plane rotations are implemented as tumbling moves, which changes the character of the morphological and dynamical evolution significantly, compare Fig. 5.61 [notice: mismatching legend]. The gray dashed curve represents quasiequilibrium growth with purely hard-core rods ($\epsilon = 0$).

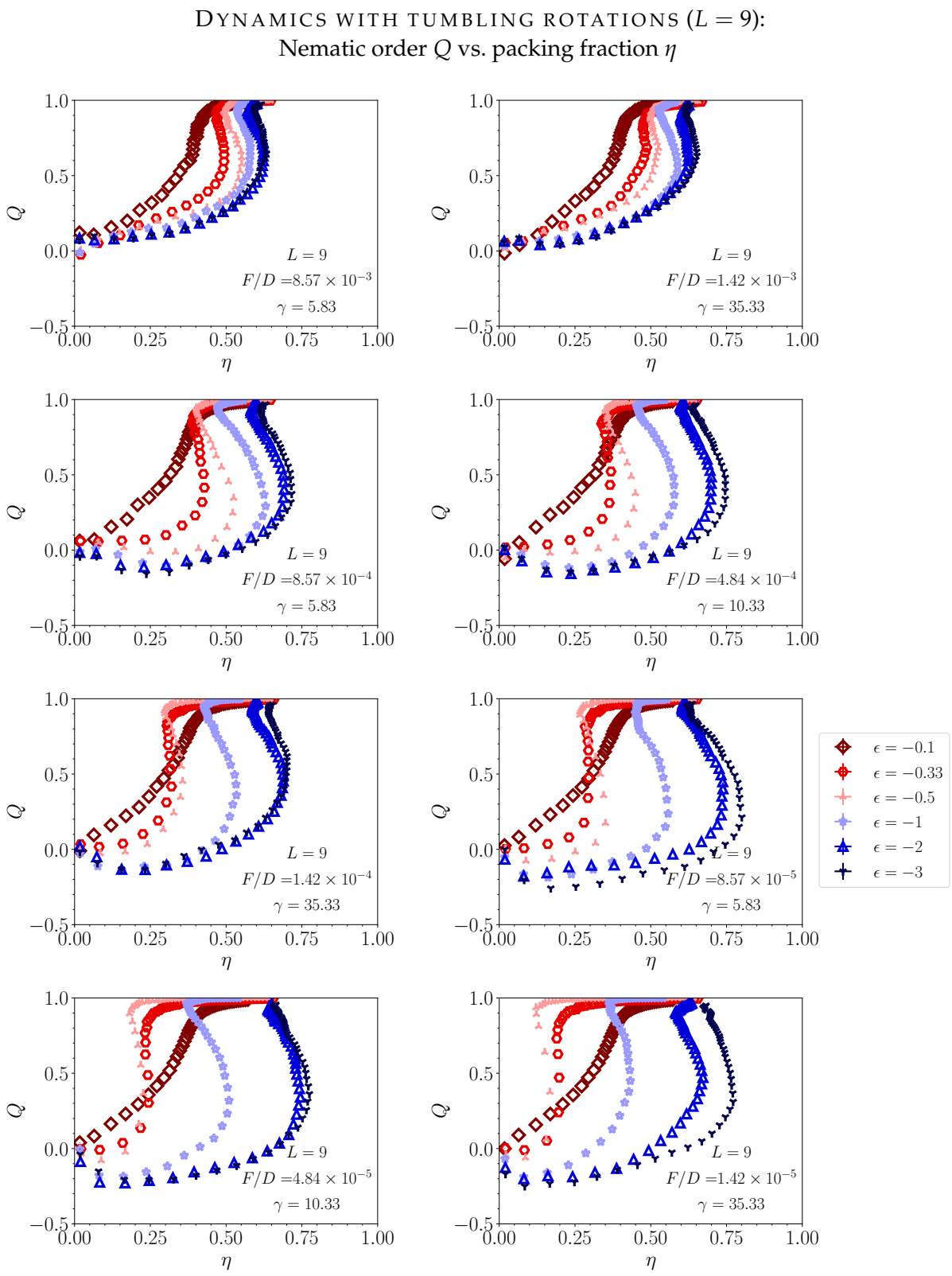

FIGURE 5.107: Nematic order parameter Q versus packing fraction (coverage) during growth of a monolayer of *very* long rods ($L = 9$) at various fixed F/D conditions with *tumbling* rotations: Comparison of attraction strengths ϵ. The case of $\epsilon = -0.1$ is likely in "regime I", while $\epsilon = -0.33, -0.5$ likely "regime II" or already "III". The topology in the $(\ln(1/|\epsilon|), \log(D/F))$–plane may be quite different, however, see Fig. 5.109 and corresponding main text.

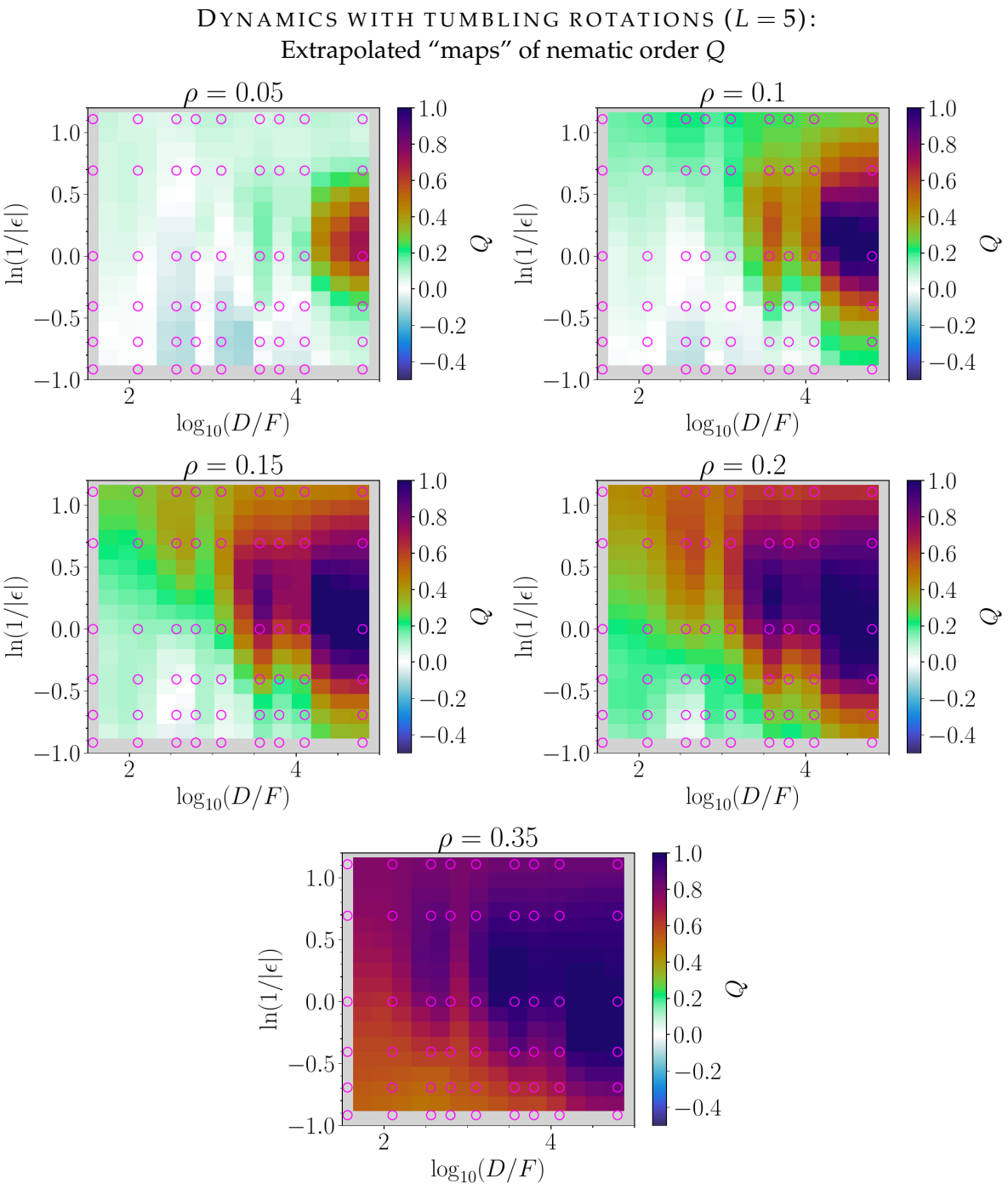

FIGURE 5.108: Extrapolated maps of the nematic order in the $(\ln(1/|\epsilon|), \log(D/F))$–plane at five different densities during growth ($L = 5$, neutral substrates), simulated with tumbling rotations. Magenta circles indicate supporting data points from simulation. A cubic extrapolation scheme is employed, hence, please consider this map as a qualitative one. This "map" shows quite different topology compared to the case of centra' rotations in Fig. 5.68.

DYNAMICS WITH TUMBLING ROTATIONS ($L = 9$):
Extrapolated "maps" of nematic order Q

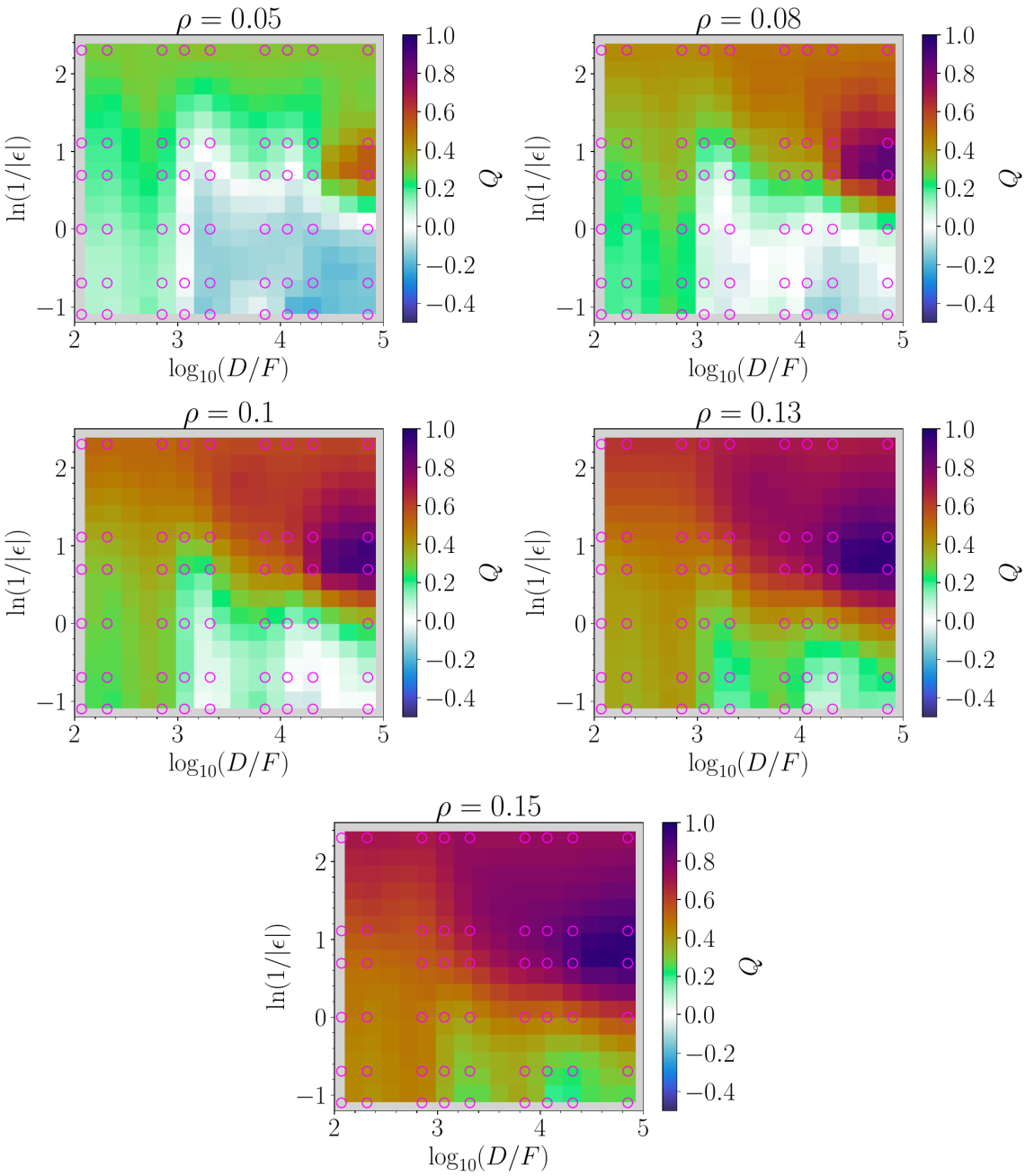

FIGURE 5.109: Extrapolated maps of the nematic order in the $(\ln(1/|\epsilon|), \log(D/F))$–plane at five different densities during growth ($L = 9$, neutral substrates), simulated with tumbling rotations. Magenta circles indicate supporting data points from simulation. A cubic extrapolation scheme is employed, hence, please consider this map as a qualitative one. The topology is very different from all other maps so far, e.g. Figs. 5.60, 5.68, 5.105, 5.108 and entails a vertical "wall" for a curvilinear "gel line", which can be inferred at the lowest two densities, spanning from coordinates $(3.1, 1.1)$ to $(4.9, 0)$.

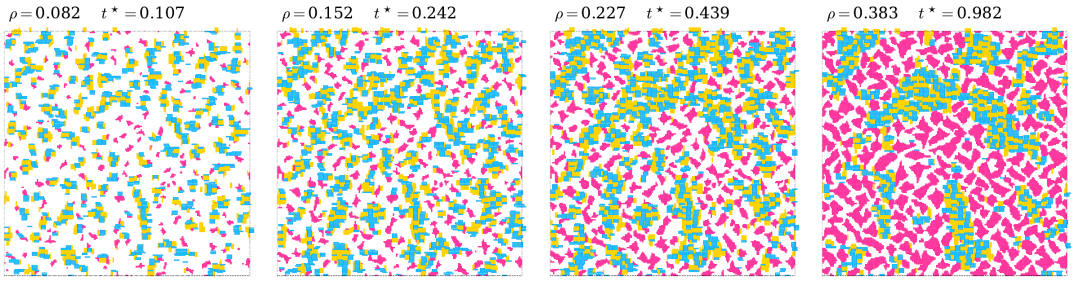

FIGURE 5.110: Visualization of "diamond-", fractal-like standing islands (magenta) forming for very long rods at low reduced temperatures ($L = 5$). Note that tumbling rotations are employed here, which seem to additionally favor this feature, apart from a very low reduced temperature.

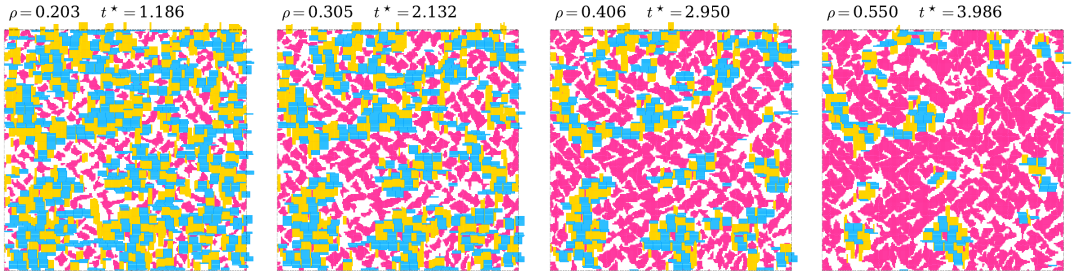

FIGURE 5.111: Visualization of late stages of the monolayer evolution after "diamond-", fractal-like standing islands (magenta) formed for very long rods at low reduced temperatures for very long rods ($L = 9$). Note that tumbling rotations are employed here, which seem to additionally favor this feature, apart from a very low reduced temperature. The associated dynamical and energetic parameters are and $\{F/D = 1.42 \times 10^{-5}, \gamma = 35.33\}$ and $\epsilon = -3$ (neutral substrates). The lying gel (blue and yellow) leaves pronounced vacant regions behind once it decays, leaving a mark on the further morphological evolution of the standing phase.

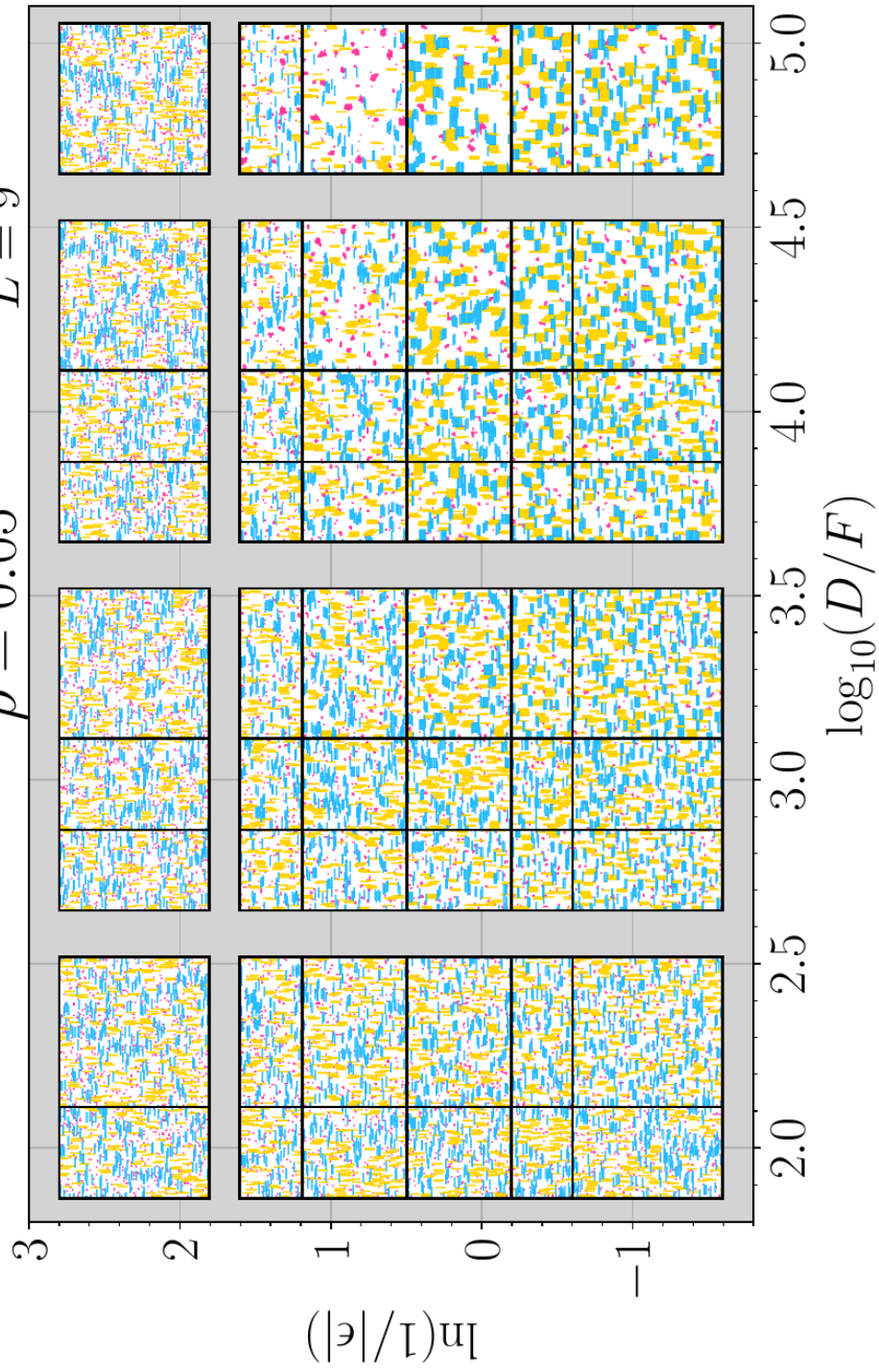

FIGURE 5.112: Configurations during growth of a monolayer with very long rods ($L = 9$) that tumble out-of-plane (for neutral substrates), displayed in the $(\ln(1/|\epsilon|), \log(D/F))$–plane (at density $\rho = 0.05$). Note that the logarithm is applied to the values on the y-axis for better scaling purposes. The same color scheme is used here as in e.g. Fig. 5.20. Snapshots are approximately 128×128 unit-sized cutouts of the configurations, which are 256×256 in size. Standing clusters (magenta) are clearly visible for high D/F, as well as lying clusters for low reduced temperatures. Please see next Figs. 5.113–5.115 for higher-ρ-cases. 2D demixing between yellow and blue species appears for certain values of $1/|\epsilon|$ and D/F (indirectly γ, as well) at these low densities (domains where only one of the two species occurs), but also at further densities.

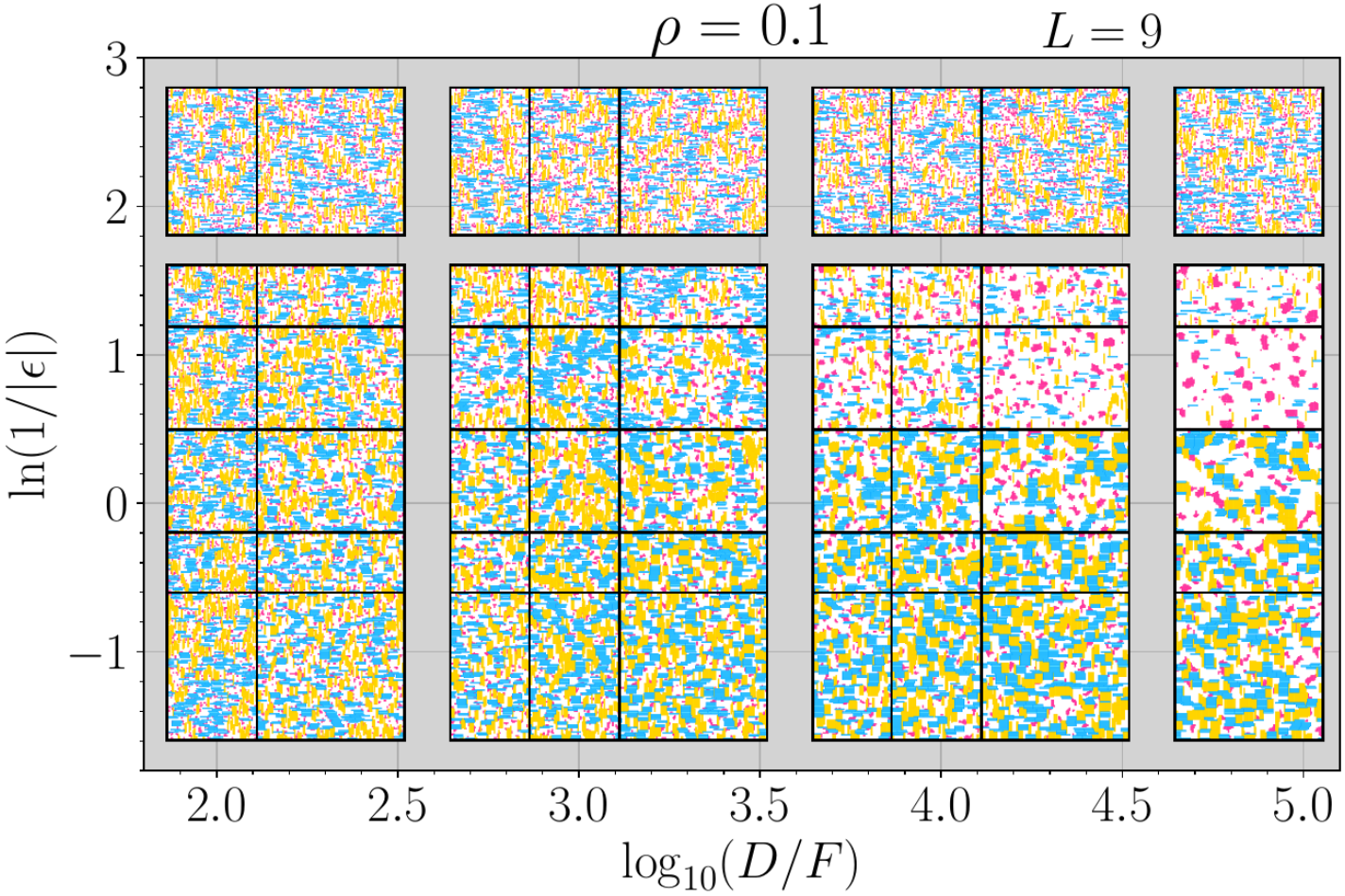

FIGURE 5.113: A continuation of Fig. 5.112 for $\rho = 0.1$. The possibility for 2D demixing can also be seen in some cases of D/F and $1/|\epsilon|$, where large domains of either yellow or blue (lying) rods appear. For deeper temperatures, a lying gel forms parallel to standing clusters, the latter of which are quite irregular in shape for large D/F in the last three rows from the top (likely a variant of "regime III"). The top row probably corresponds to a variant of "ϵ-regime I", while the next row likely to "regime II" or already near "III", but, this categorization may be misleading, see Fig. 5.109.

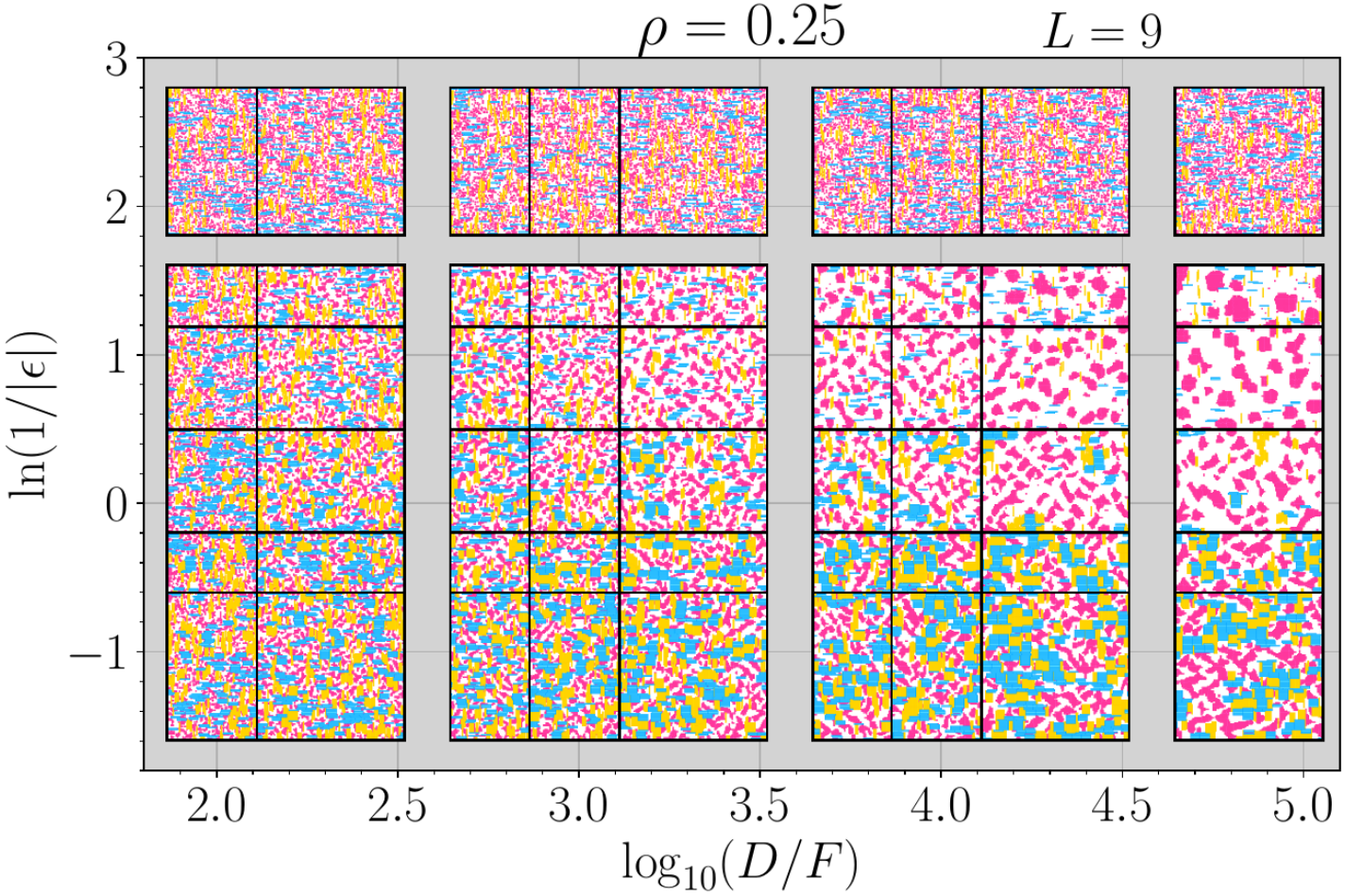

FIGURE 5.114: A continuation of Fig. 5.112 for $\rho = 0.25$. Standing clusters can be seen to form "diamond-like" islands most prominently in the last three rows from the top (likely a variant of "regime III"). At certain values of D/F within this regime (and γ, not shown here), the irregularly-shaped, standing islands of Fig. 5.113 become diamond-shaped or elongated diamond-like strips that can begin to coalesce. The latter seems to coincide with the lying gel still being present (phase transition scenario (D) categorized in Sec. 5.3.9).

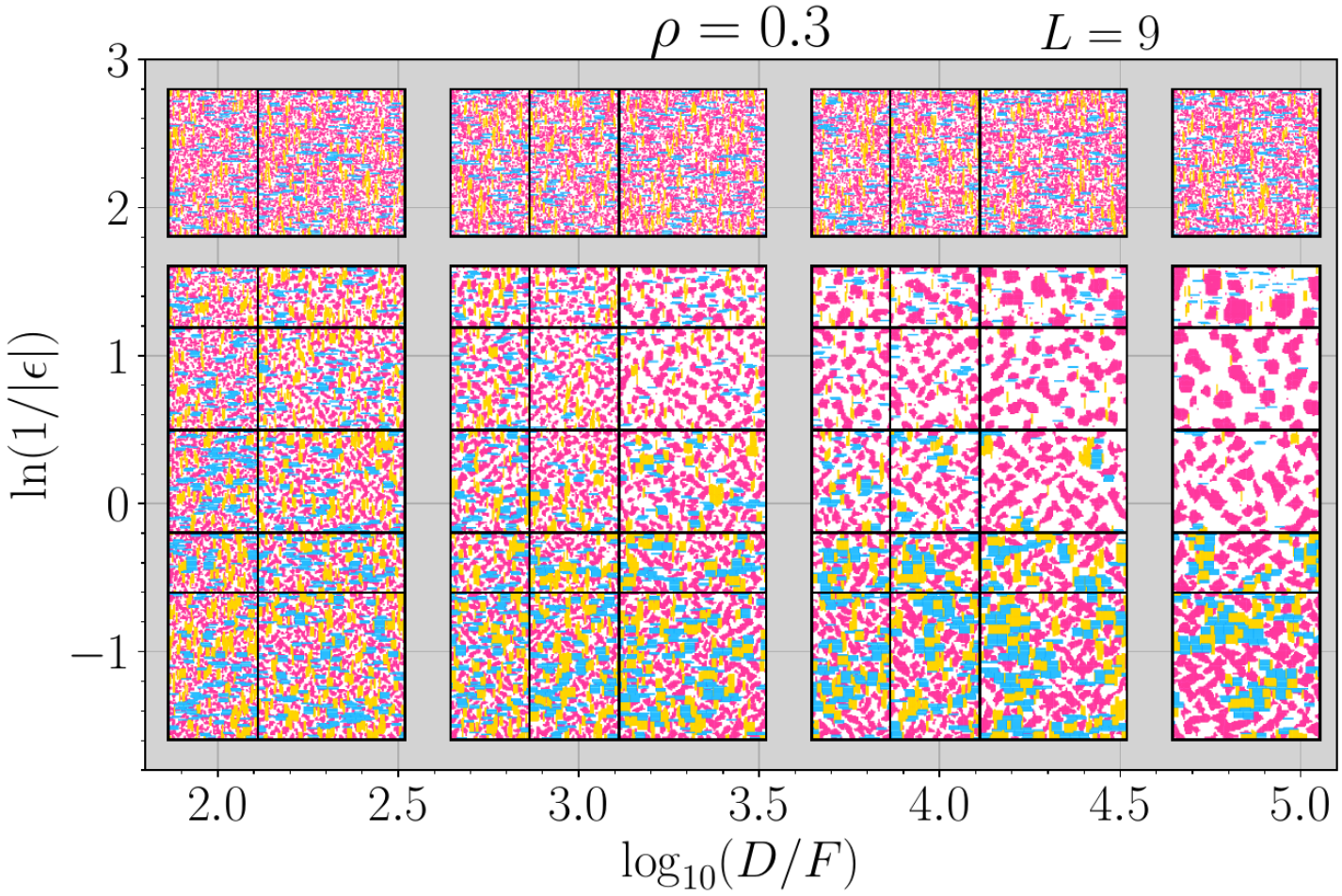

FIGURE 5.115: A continuation of Fig. 5.112 for $\rho = 0.3$. At this density, the "diamond-like", standing "strips" of Fig. 5.114 begin to form approximate zig-zag patterns. In (potentially) "ϵ-regime II" (second row from top), standing islands are large and rather round, in stark contrast.

5.7 Monolayer growth with dimers ($L = 2$)

We continue our exploration of the monolayer growth with "sticky" rods for the specific case of dimers ($L = 2$). FMT predicts that the second, metastable critical point $\epsilon_{\text{crit, meta, denem}}$ for $L = 3$ becomes stable for dimers, see Sec. 5.2. The behavior of the system for higher reduced temperatures (closer to ϵ_{crit}), therefore, should take on a quite different character in comparison. On the other hand, the phase behavior at very deep reduced temperatures should appear similar to that of $L = 3$ within regime IIIa (projected from FMT). In the subsequent Sec. 5.7.1, we will see that this argument seem to hold, indeed; moreover, we shall discover similarities between the systems of sticky dimers to that of $L = 3$ at weakly attractive substrates, which was investigated in Sec. 5.5. We shall explore the effect of attractive substrates on the dimer systems, too, in Sec. 5.7.2.

5.7.1 Dimers at neutral substrates

The general behavior of the global order parameter Q on the packing fraction over varying attraction strength ϵ is shown in Fig. 5.116, at fixed dynamical parameters. Compared to similar values of ϵ for $L = 3$ at neutral substrates, Fig. 5.24, as well as even longer rods, e.g. Fig. 5.61, the order parameter 'stands up' significantly less pronouncedly. This is certainly due to the weaker binding energies of neighboring rods that have a standing orientation, whose magnitude varies with rod length via $L\epsilon$. However, more obvious is the lack of a strongly negative global order parameter Q during growth, even for strong attraction strengths. There are only two parameter combinations where $Q < 0$ during growth: For $F/D = 6.98 \times 10^{-3}$ and $\epsilon \in \{-2, -3\}$

We will attempt to address two main issues below that will be relevant for the characteristic behavior of dimers: First, we discuss the phase behavior at higher and intermediate temperatures (relative to ϵ_{crit}). Secondly, the dimers require different microscopic dynamics owing to their even-valued L: tumbling and shuffling rotations are implemented, which can change the kinetics and morphology (we isolate this effect in Sec. 5.6).

(1) Phase behavior. The phase behavior at relatively high temperatures, but still below ϵ_{crit}, seems to entail a different character than $L = 3$ at neutral substrates. If the system is just below $\epsilon_{\text{crit,2}}$, The dimer systems should cross through three fluid regions that are stable: at low, medium, and high densities. We conjecture that the case of $\epsilon = -1$ is near $\epsilon_{\text{crit,2}}$ from the phenomenological evidence for monolayer growth . More precise information on the phase boundaries can be obtained from GCMC simulations, which, however, remains beyond the context of this thesis.

(2) Microscopic rotational dynamics. First noted in the methods section (Sec. 5.1), the microscopic dynamics we employ for the case of dimers implement out-of-plane rotations in a tumbling fashion, and in-plane-rotations in a shuffling fashion. The ideal-gas diffusion coefficients D of the long-time limit are calculated according to the formulas derived and presented in Sec. 5.1.2. Tumbling and shuffling rotations are necessary because of the *even*-valued rod-length, rendering a rod center point ill-defined on the simple cubic lattice. Sec. 5.6 describes phenomenologically how the choice of microscopic dynamics

affects the morphological and dynamical evolution of the monolayer systems. Specifically, the influence of "tumbling" out-of-plane rotations are visible when comparing observables during monolayer growth to those arising from microscopic dynamics with central rotations (done for $L = 3, 5$). Apart from energetic considerations (weaker binding energies), the altered coupling of out-of-plane rotational and translational degrees of freedom should contribute to the different character of the $Q(\eta)$-curves for $L = 2$ in a major way: These change the kinetics, which fundamentally begin at the microscopic scale.

Discussion on phenomenology

Configurations of the systems of dimers during monolayer growth are visualized in the $(1/|\epsilon|, \log(D/F))$–plane at several densities in Figs. 5.117–5.121. There, we begin with the case of $\epsilon = -1$, which appears to be near the second critical point $\epsilon_{\text{crit},2}$. Around or below this value, we see isotropic ($Q \approx 0$) clusters distinguished from a vapor, although the interface may be very broad.[34] At high densities $\rho \gtrsim 0.5$ (Figs. 5.120–5.121), standing (or $Q > 0$) clusters (or fluctuations) seem to appear out of these isotropic-fluid clusters. At lower reduced temperatures, around $1/|\epsilon| = 0.8$ ($\epsilon = -1.25$), pronounced standing clusters appear for high values of D/F at $\rho \sim 0.15$. An isotropic or lying fluid appears to collect at the rim of the islands (see Figs. 5.118–5.120), very much like the phenomenon we have observed for $L = 3$ at weakly attractive substrates in regime II. This effect is also visible for $1/|\epsilon| = 0.67$ ($\epsilon = -1.5$) and low deposition quench rates F/D.

Diamond-like shapes (elongated strips of a standing phase) are seen for the case of dimers. We discussed diamond-like *islands* in Sec. 5.6.2, in comparison. The strips appear at intermediate values of D/F and at lowest reduced temperature after ($\rho \sim 0.5$), see Figs. 5.120 and 5.121). We had found that "diamond" shapes are associated with the choice of tumbling rotations of a rod, rather than rotations out-of-plane around a rod center, the latter of which are only possible for odd rod-lengths. The effects of an irreducible coupling of rotational and translational degrees of freedom can be significant, even for the shortest possible rods (dimers). However, these diamond strips seem to disappear if we choose higher D/F – islands become compact, round and for highest D/F, even square-like. The latter represent more equilibrium island shapes. Compared to our findings on longer rods in Sec. 5.6 ($L \geq 5$), the "diamond effect" (of coupling rotational with translational degrees of freedom directly) is arguably weaker for dimers, and becomes marked at much higher densities. At these densities, previous clusters have coalesced and large strips form approximate zig-zag patterns. Transitions in shapes in the system, which are indirect indicators for fundamentally different types of dominating *force* fields in the system, are interesting topics that can be investigated in more detail the future.

At low D/F, we can observe an isotropic $Q \approx 0$ aggregate-like fluid with small spatial length-scales for the presented reduced temperatures. Yet for $1/|\epsilon| \lesssim 0.5$ ($\epsilon \lesssim -2$), a lying phase that forms aggregate-like structures become visible. This appears to be the metastable gel-phase that we have seen for longer rods. Lying clusters are visible in Fig. 5.118 at $\rho = 0.15$. Note that although easily performed, quantitative analysis of the cluster statistics, shape,

[34] Future quantitative analysis could include measuring the order parameters of clusters.

morphological quantifiers and of percolation behavior remains outside of the scope of this work.

Further quantification of the evolution of global structural quantities – Q versus the global density ρ, lying density ρ_{12} versus time re-scaled with the attempt flux, and global density versus re-scaled time – are presented in Figs. 5.122, 5.123, and 5.124, correspondingly. The time-evolution of Q is shown in Fig. 5.125. Finally, we present a (gross) projected map of the global order parameter Q versus D/F in Fig. 5.126, shown for various values of global density ρ. Compared to $L = 3$ (Fig. 5.60), Fig. 5.126 shows a less pronounced lying global order at $D/F = O(10^3)$ for relatively low temperatures (compared to ϵ_{crit}). The figure supports how a weaker lying-standing divide is realized during monolayer growth at a fixed density – this divide first becomes visible the course of increased density. In other words, the dimer systems will very likely entail weaker dynamical heterogeneity during growth, in particular to that of rotational motion. Again, although easily performed, quantitative analysis of dynamical variables (particle mobility, rotational and translational fluxes) remains outside of the scope of this thesis.

We note that the gel line – a dividing line between two main dynamical regions, where either a lying gel forms or only standing clusters – might be located in the lower left corner of the $(1/|\epsilon|, \log(D/F))$–plane, seen in Fig. 5.126 for Q, or in the images of Figs. 5.119 and 5.120.

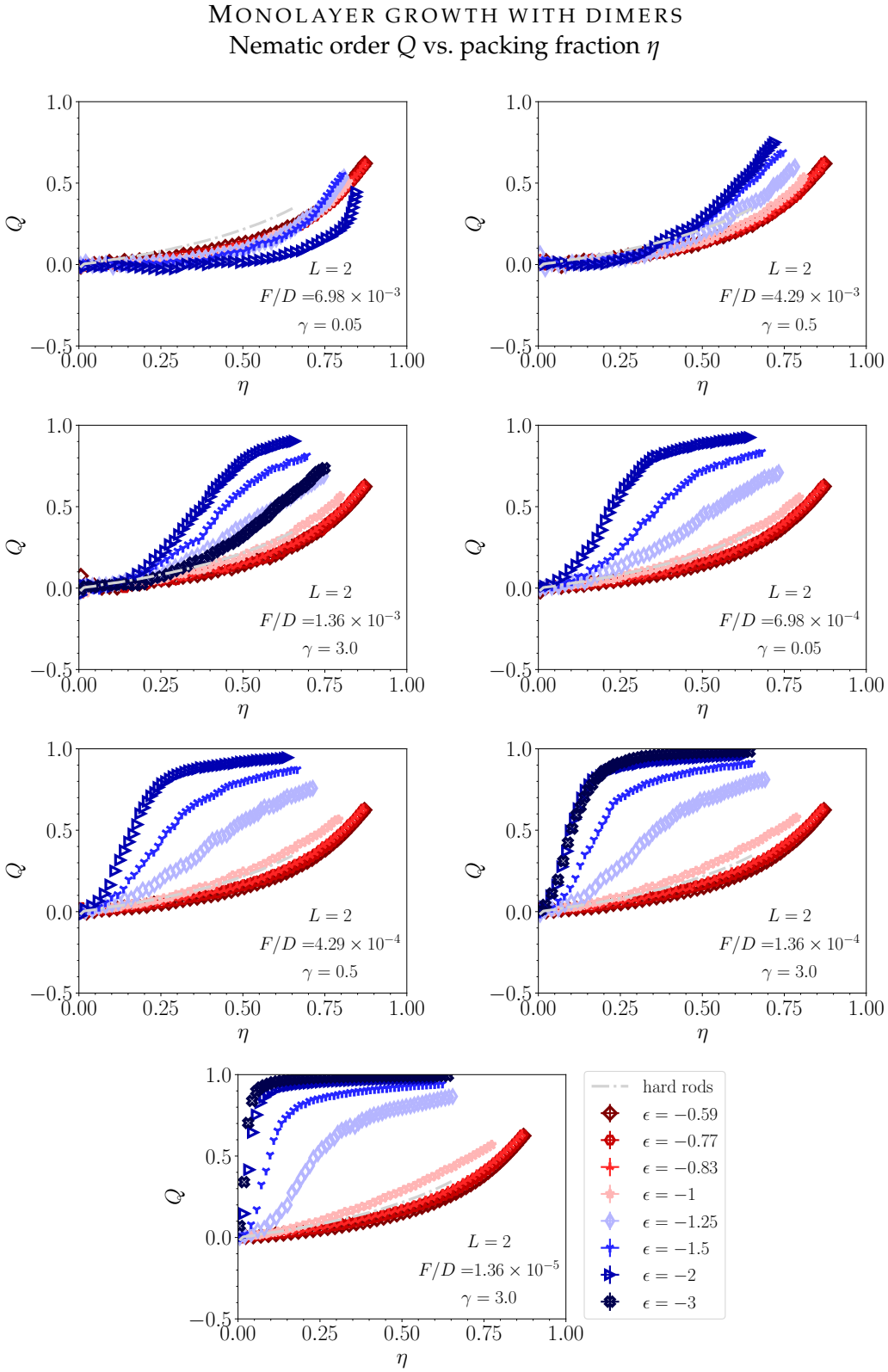

FIGURE 5.116: Nematic order parameter Q versus packing fraction (coverage) during growth of a monolayer of dimers at fixed F/D conditions: Comparison of attraction strengths ϵ. The gray, "hard rods" curve represents quasiequilibrium growth for purely hard-core rods ($\epsilon = 0$).

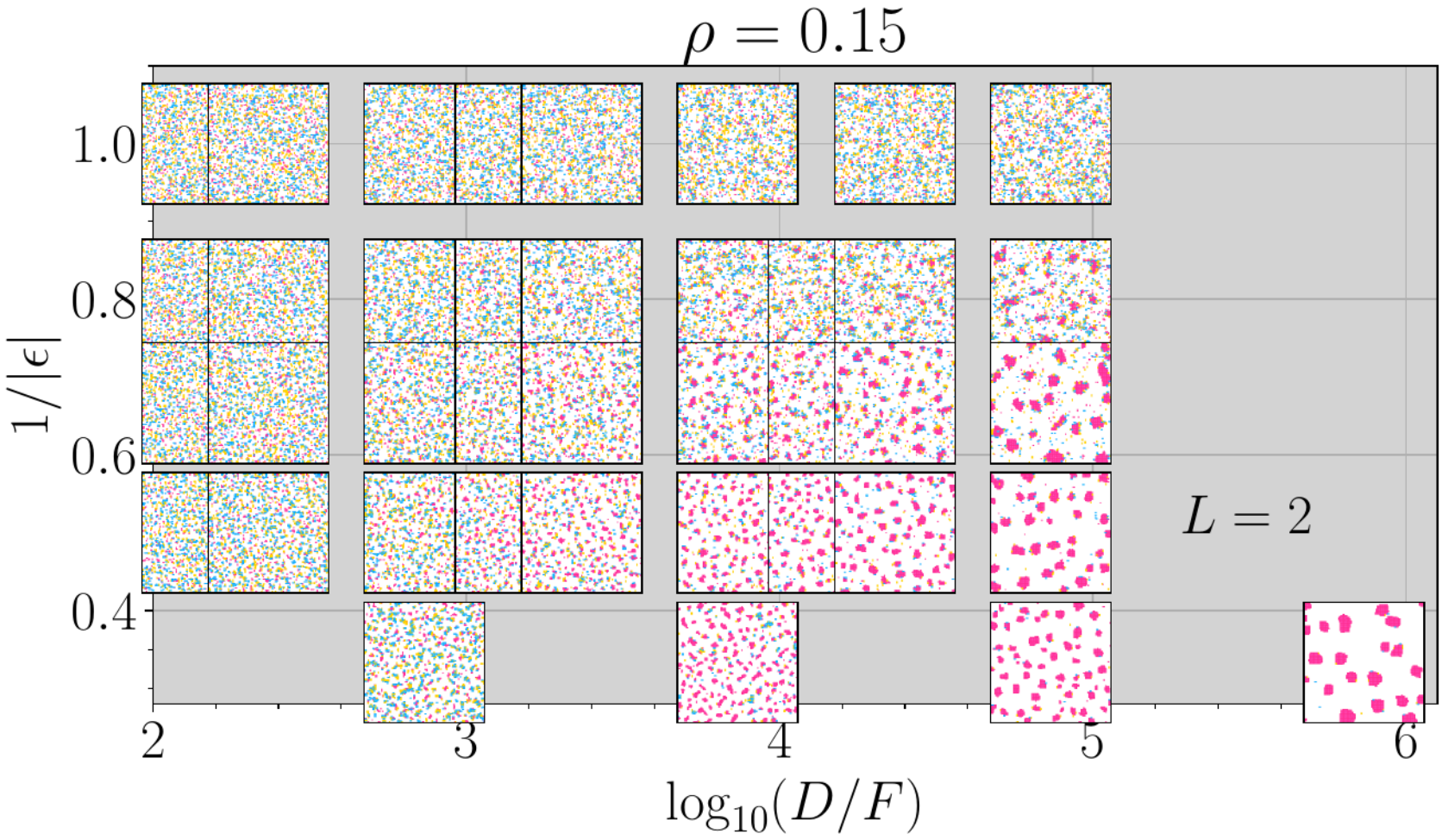

FIGURE 5.117: Visualized configurations during growth of a monolayer with sticky dimers at neutral substrates, displayed in the $(1/|\epsilon|, \log(D/F))$–plane (at density $\rho = 0.15$) for $\epsilon \leq -1$ (which is near $\epsilon_{\text{crit},2}$). Note that the y-axis is *not* scaled logarithmically here. The same color scheme is used here as in e.g. Fig. 5.20. Snapshots are approximately 128×128 unit-sized cutouts of the configurations, which are 256×256 in size. Standing clusters (magenta) are visible for $1/|\epsilon| \leq 0.8$ at high D/F.

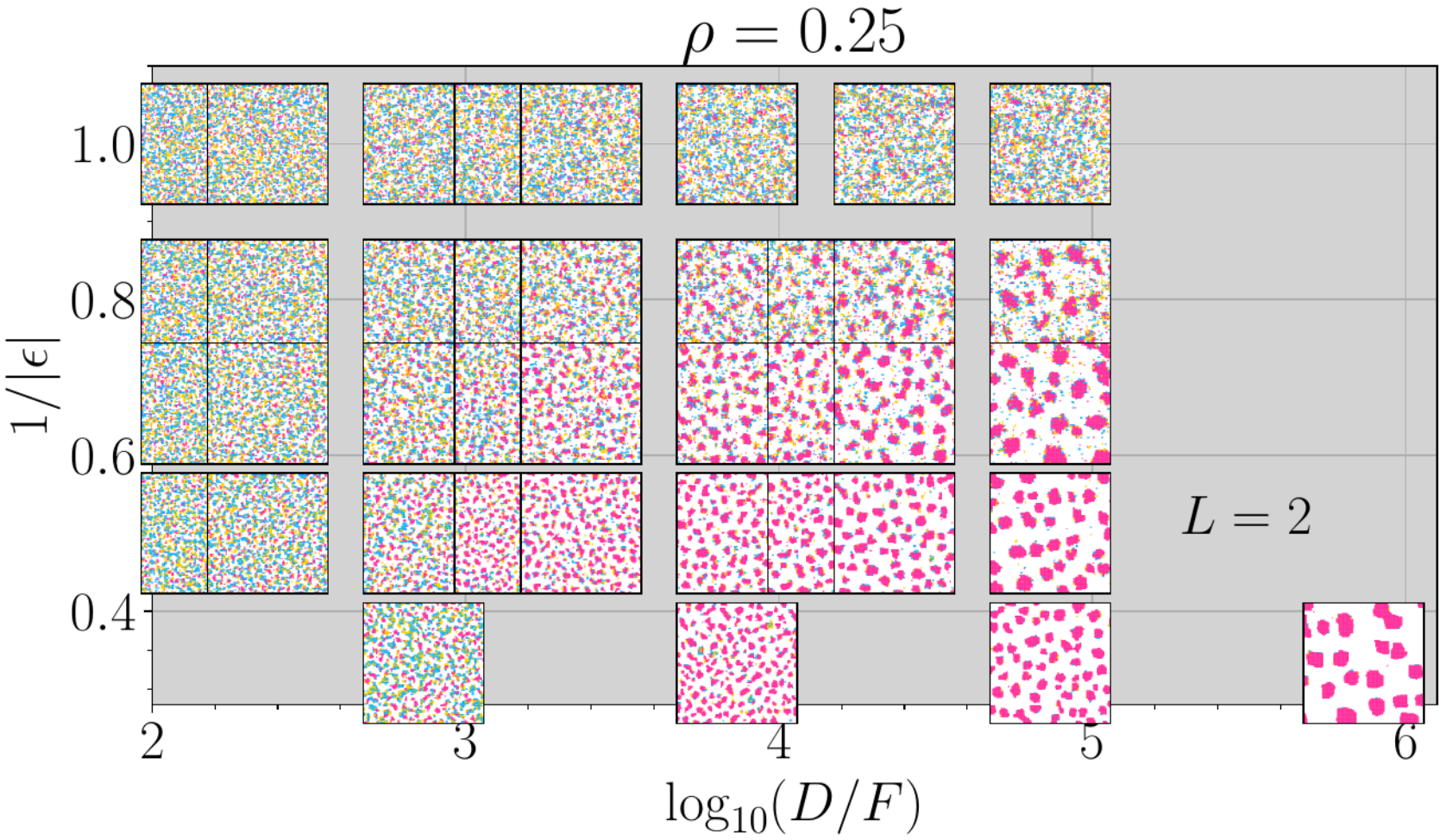

FIGURE 5.118: A continuation of Fig. 5.117 for $\rho = 0.25$. For $1/|\epsilon| = 1$, an isotropic fluid may be separating from a vapor, or strong density fluctuations of an isotropic fluid are apparent for high D/F. For lower reduced temperatures, a lying or isotropic fluid appears to collect at the rim of standing clusters, visible for high D/F. At the lowest reduced temperature $1/|\epsilon| = 0.33$ for $D/F = O(10^6)$, standing islands with near-equilibrium shapes that are square-like grow due to the underlying symmetry of the square lattice. At low D/F and low reduced temperatures, a lying phase (blue and yellow) seems to form aggregate-like clusters.

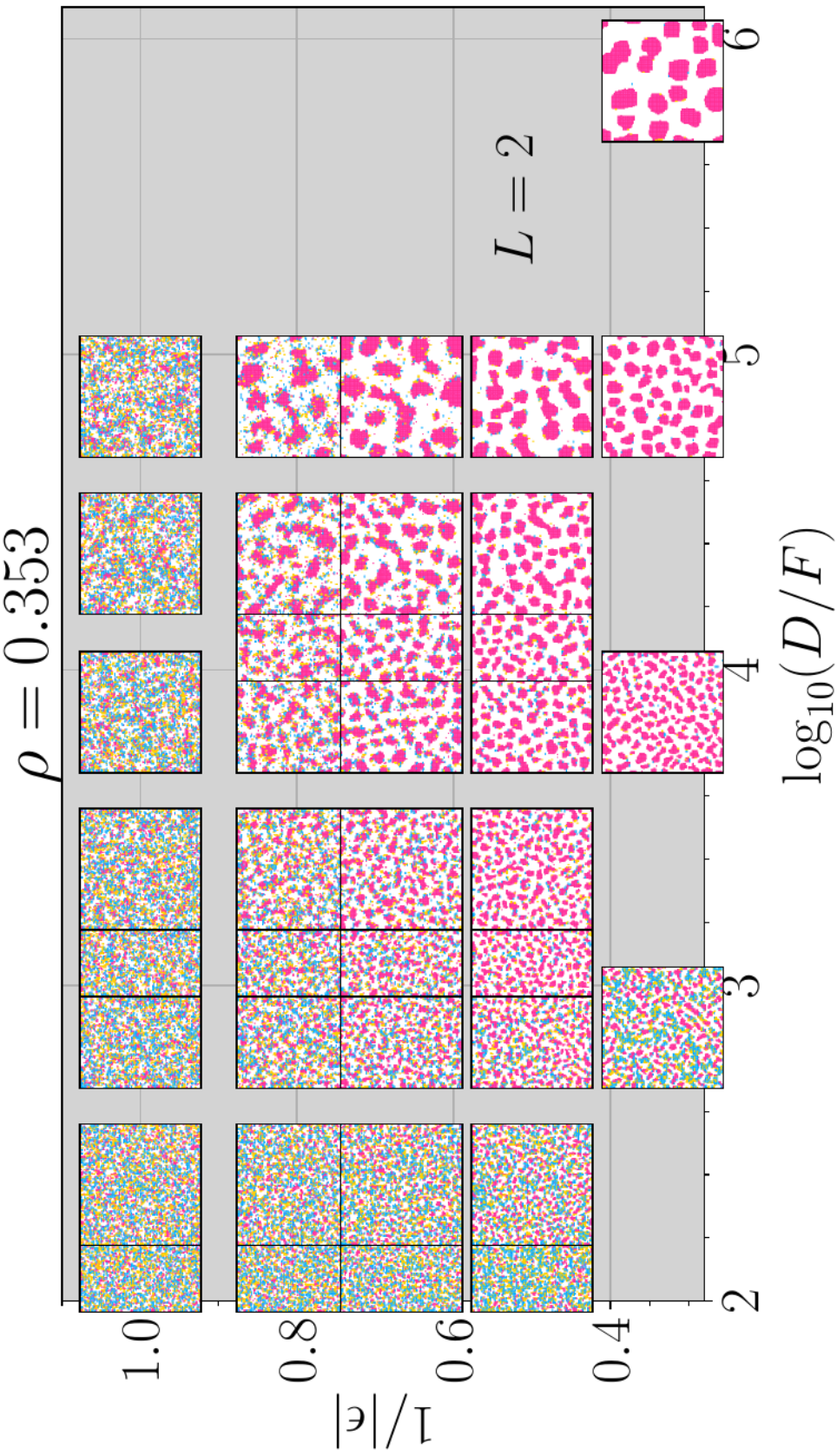

FIGURE 5.119: A continuation of Fig. 5.117 for $\rho = 0.353$. At low D/F and low reduced temperatures, the metastable lying phase (blue and yellow) can form a network parallel to clusters of the standing phase forming, just like the behavior for $L = 3$ in regime IIIb.

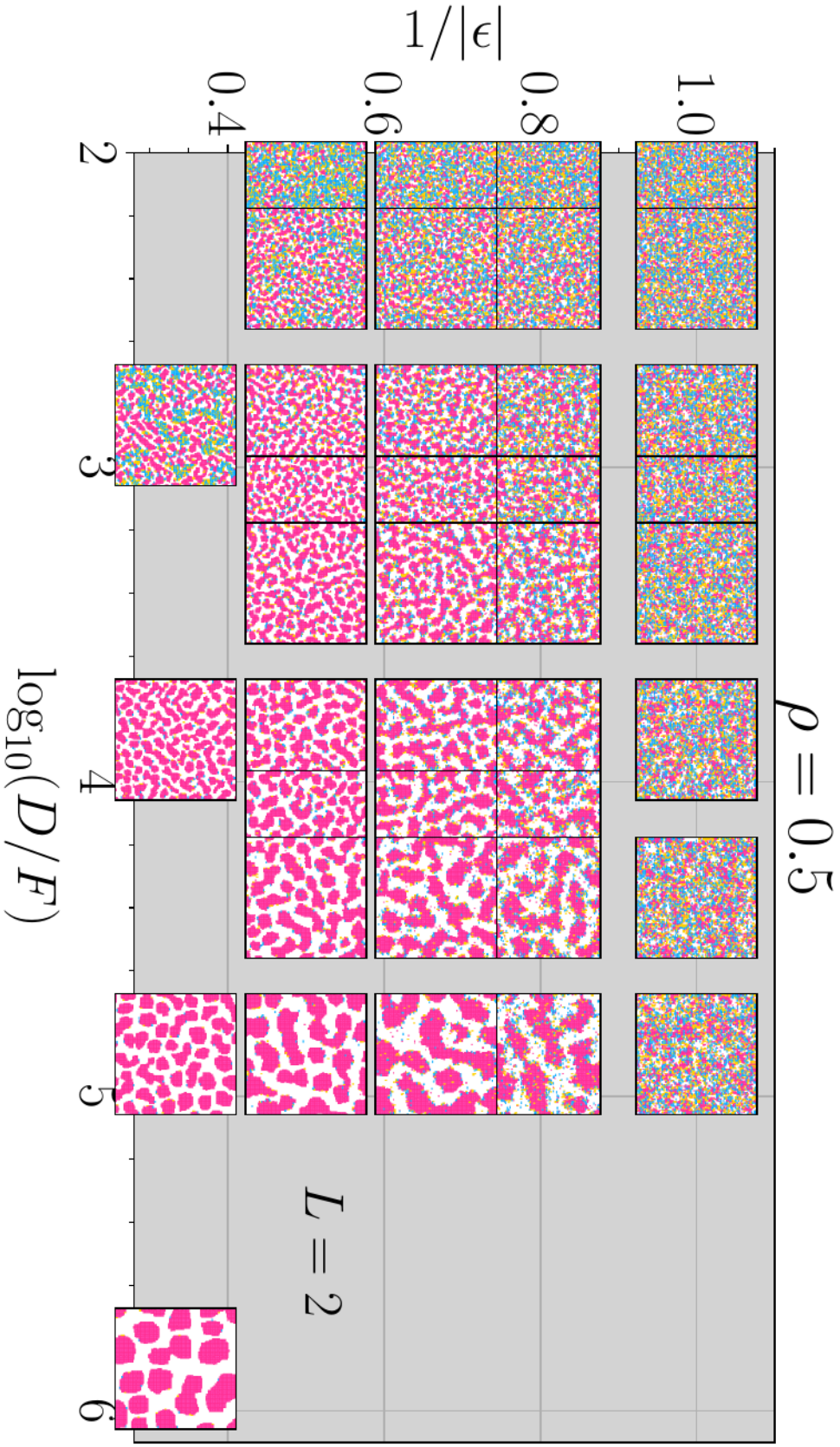

FIGURE 5.120: A continuation of Fig. 5.117 for $\rho = 0.5$, at half-full density.

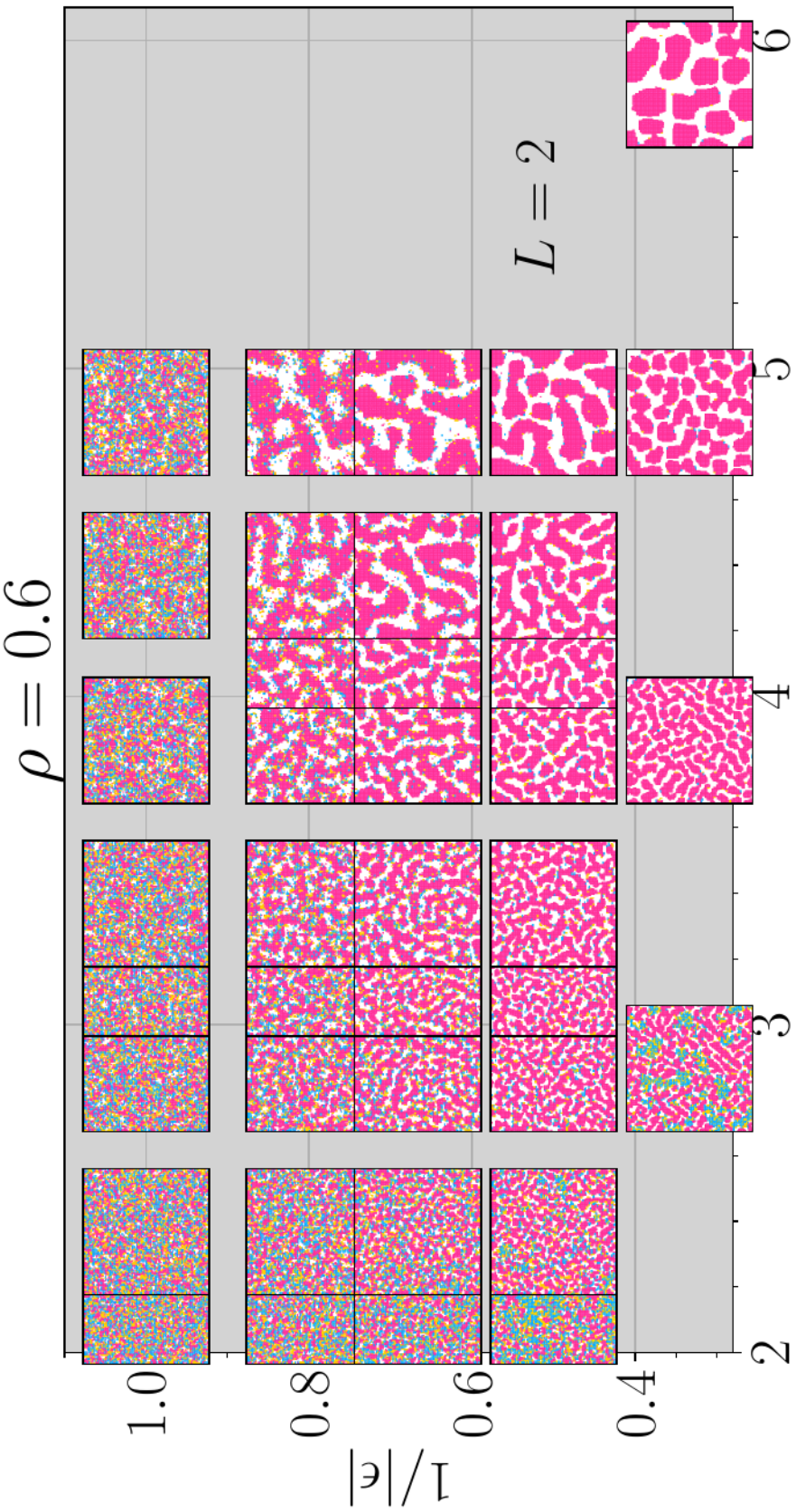

FIGURE 5.121: A continuation of Fig. 5.117 for high number density $\rho = 0.6$. The case of $1/|\epsilon| = 1$ shows a form of an isotropic or standing fluid that has become very dense, possibly separating from a vapor (weakly). The lowest reduced temperatures only render a lying liquid for the lowest values of D/F. For $1/|\epsilon| = 0.33$ around $D/F \sim 10^3$, we can see the diamond-like shapes that are signatures of "tumbling" out-of-plane rotations combined with very low temperatures (Sec. 5.6.2); here, they form elongated strips.

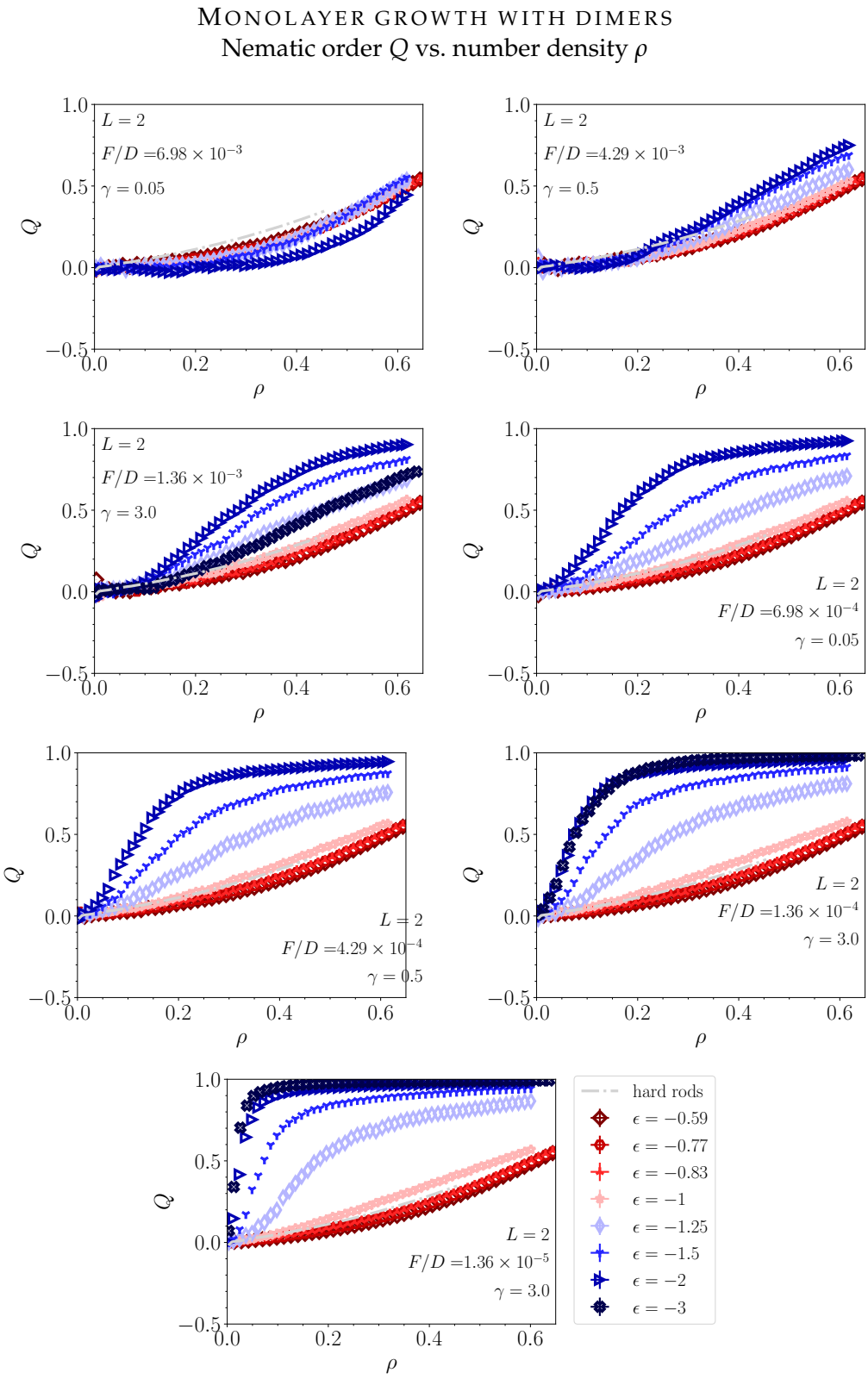

FIGURE 5.122: Nematic order parameter Q versus global density during growth of a monolayer of dimers ($L = 2$) at fixed F/D conditions (neutral substrates): Comparison of attraction strengths ϵ. See Fig. 5.116.

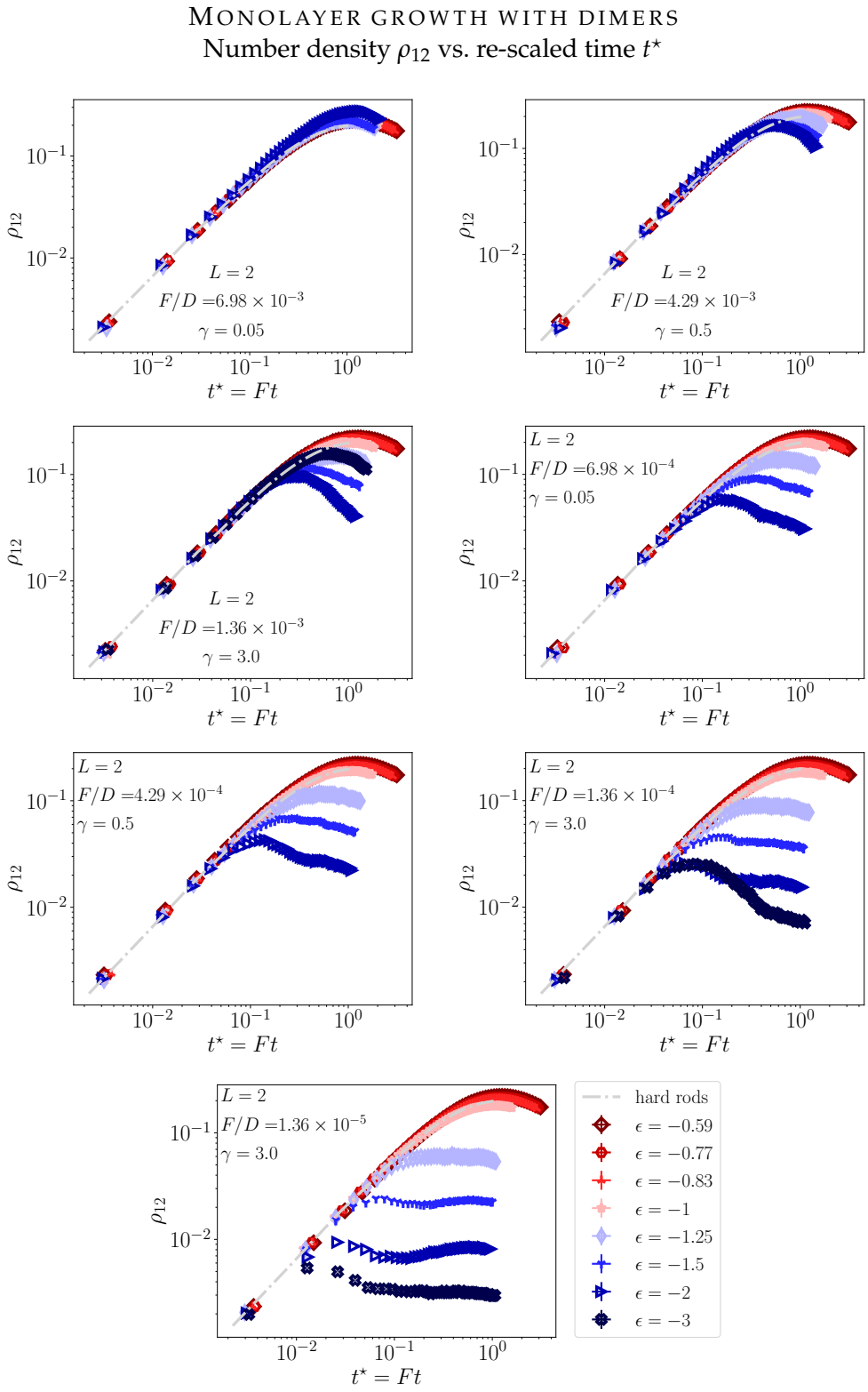

FIGURE 5.123: Global lying density ρ_{12} versus re-scaled time $t^\star$ during growth of a monolayer of dimers at fixed F/D conditions (neutral substrates): Comparison of attraction strengths ϵ. See Fig. 5.116.

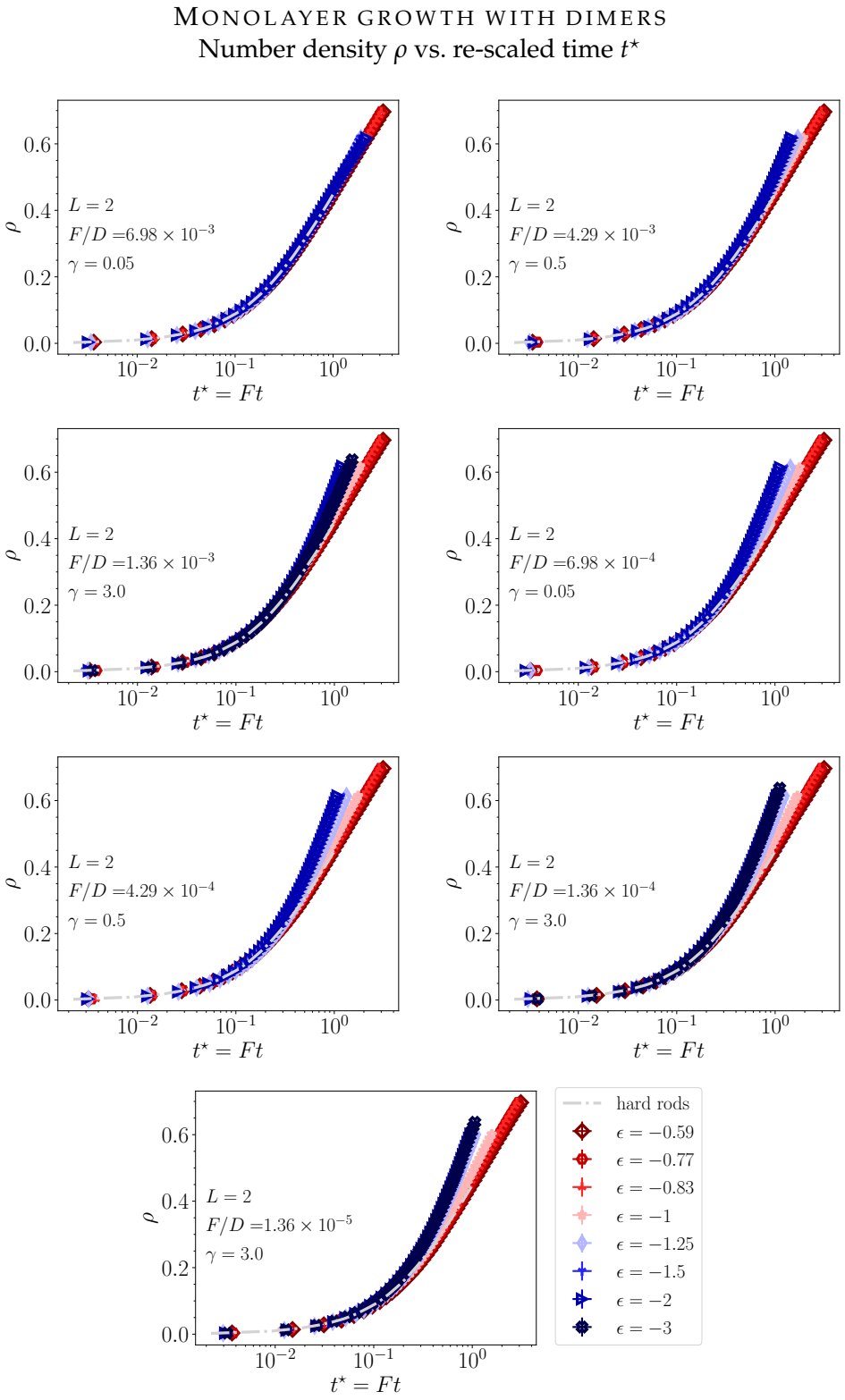

FIGURE 5.124: Global monolayer density ρ versus re-scaled time $t^\star$ during growth of a monolayer of dimers at fixed F/D conditions (neutral substrates): Comparison of attraction strengths ϵ. See Fig. 5.116.

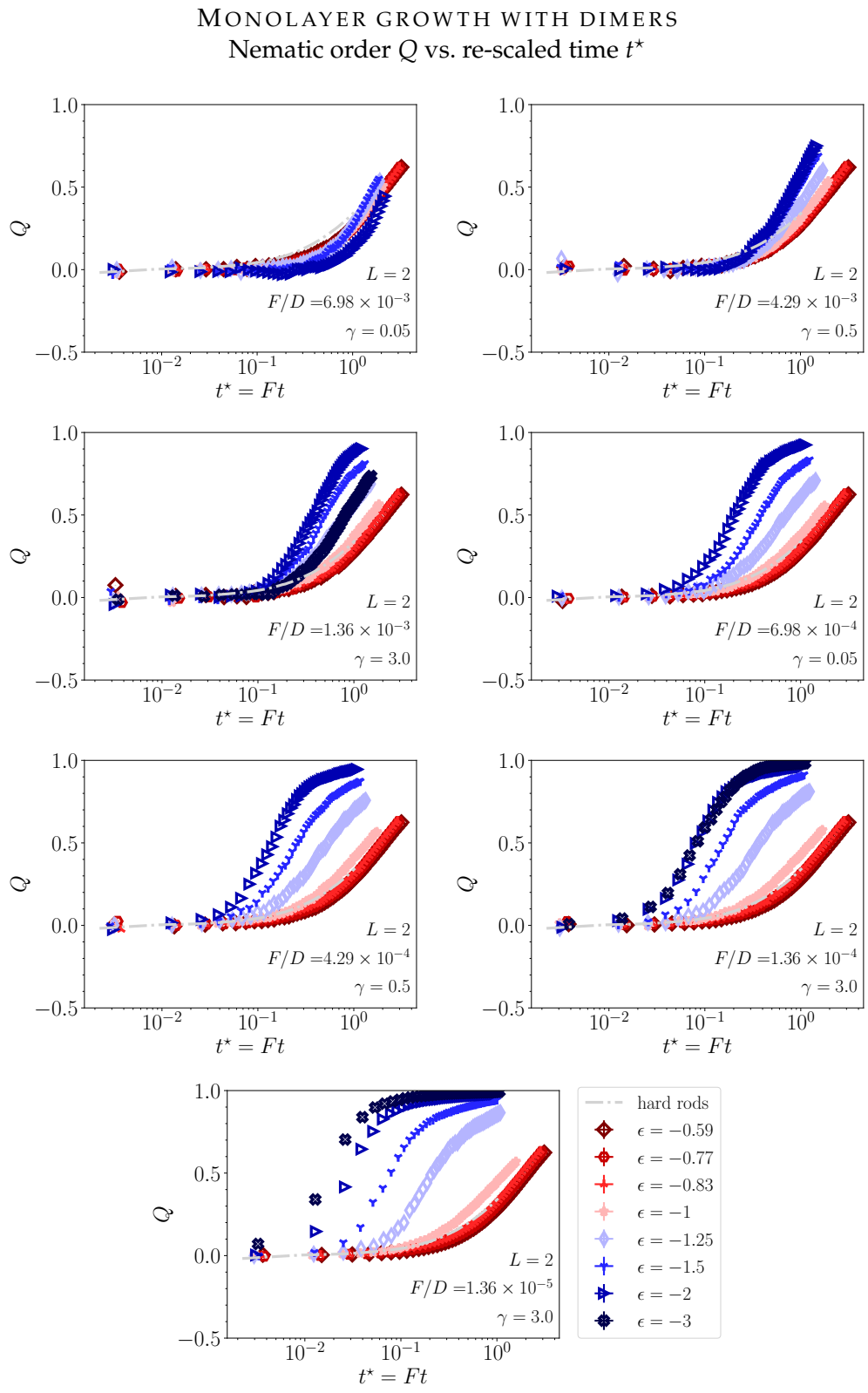

FIGURE 5.125: Global nematic order parameter Q versus re-scaled time $t^\star$ during growth of a monolayer of dimers at fixed F/D conditions (neutral substrates): Comparison of attraction strengths ϵ. See Fig. 5.116.

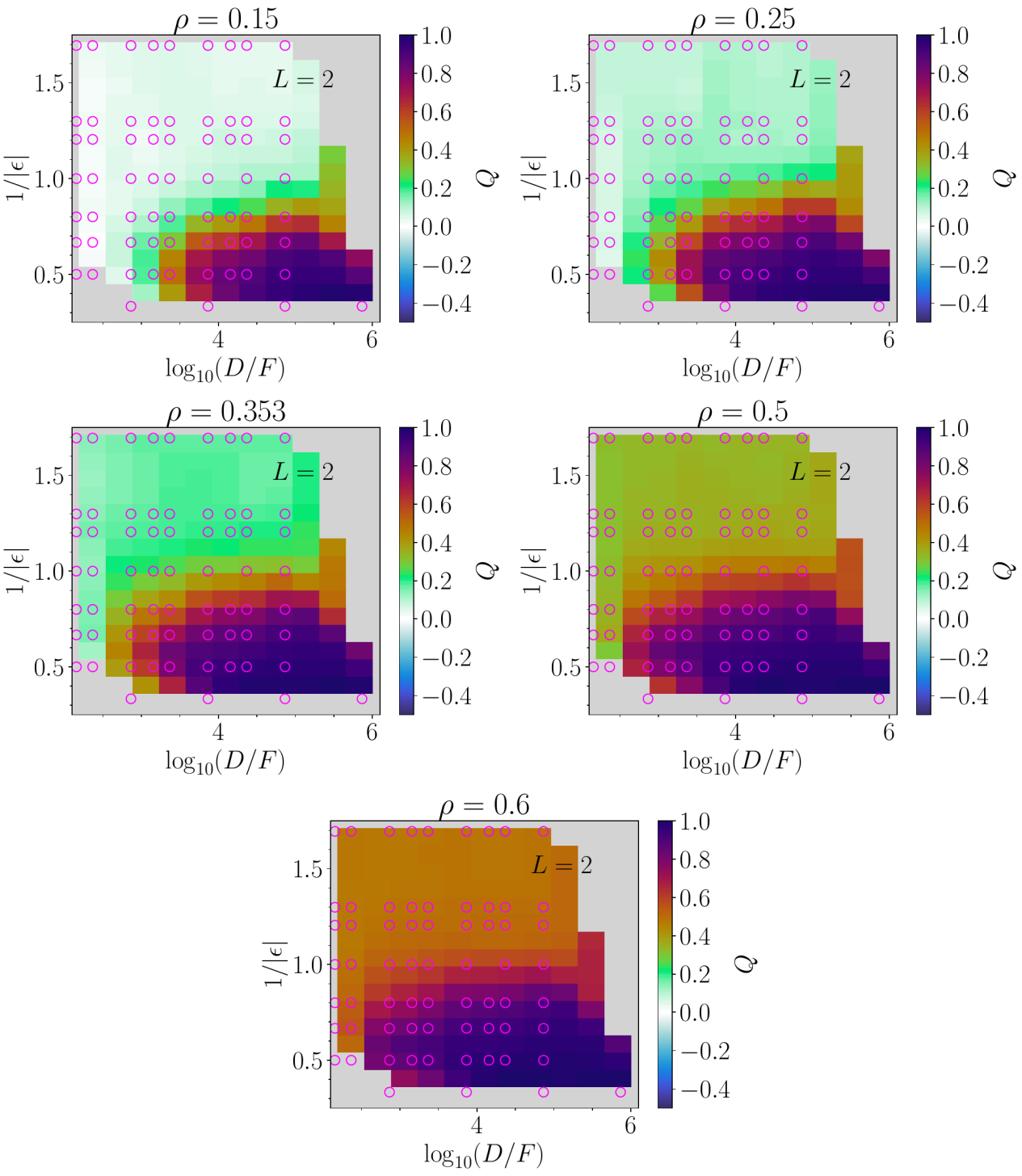

FIGURE 5.126: Extrapolated map of the nematic order Q occurring during monolayer growth as plotted in the $(1/|\epsilon|, \log(D/F))$-plane at five different densities for dimer ($L = 2$, neutral substrates). Magenta circles indicate supporting points from simulation. A cubic extrapolation scheme is employed, as well as the same color range as in Fig. 5.60. Note that the y-axis *not* scaled logarithmically here.

5.7.2 Dimers at attractive substrates

The effect of an additional attractive substrate that favors a lying orientation is explored in this section. The trajectories of $Q(\eta)$ for various $\epsilon \leq -1.25$ (where are neutral substrates we expect lying clusters to form early on) at fixed growth conditions of F/D are shown in Fig. 5.127 for the case of weak ($u_{\text{sub}} = -0.5$, top-left figure), intermediate ($u_{\text{sub}} = -1$, top right figure), and strong ($u_{\text{sub}} = -2$, bottom figure) substrate attractions. Clearly, very strong attractive substrates (bottom figure) force all trajectories at the explored values of ϵ to go through a 2D wetting layer. Weak substrate attractions bias the trajectories towards more of lying clusters or -gel at low densities, where the case of $\epsilon = -1.25$ shows a negative value of Q up to a packing fraction of about $\eta \sim 0.7$. The intermediate case of $u_{\text{sub}} = -1$ seems most interesting for the range of parameters explored here, as a noticeable competition between lying and standing phases causes a dichotomy of trajectories, where in one case, the lying phase can dominate completely, and in the other, both lying and standing phases (clusters or gel in the former case, clusters in the latter) appear and grow during monolayer growth. See also Figs. 5.128, 5.129, and 5.130 for the trajectories of global structural variables $Q(\rho)$, $\rho(t^\star)$, and $\rho_{12}(t^\star)$, respectively. The phenomenology for growth with dimers at substrates with $u_{\text{sub}} = -1$ is quite similar to that for $L = 3$ at weakly attractive substrates ($u_{\text{sub}} = -0.5$), see Sec. 5.5.1, Nonetheless, we still witness the formation of vacancies between a 2D phase and standing islands at very high packing fraction (see Figs. 5.138 and 5.139 further below), but, the effect on η is too small for this short rod length to be noticeable in the form of a loop.

MONOLAYER GROWTH WITH DIMERS ON ATTRACTIVE SUBSTRATES:
Nematic order Q vs. packing fraction η

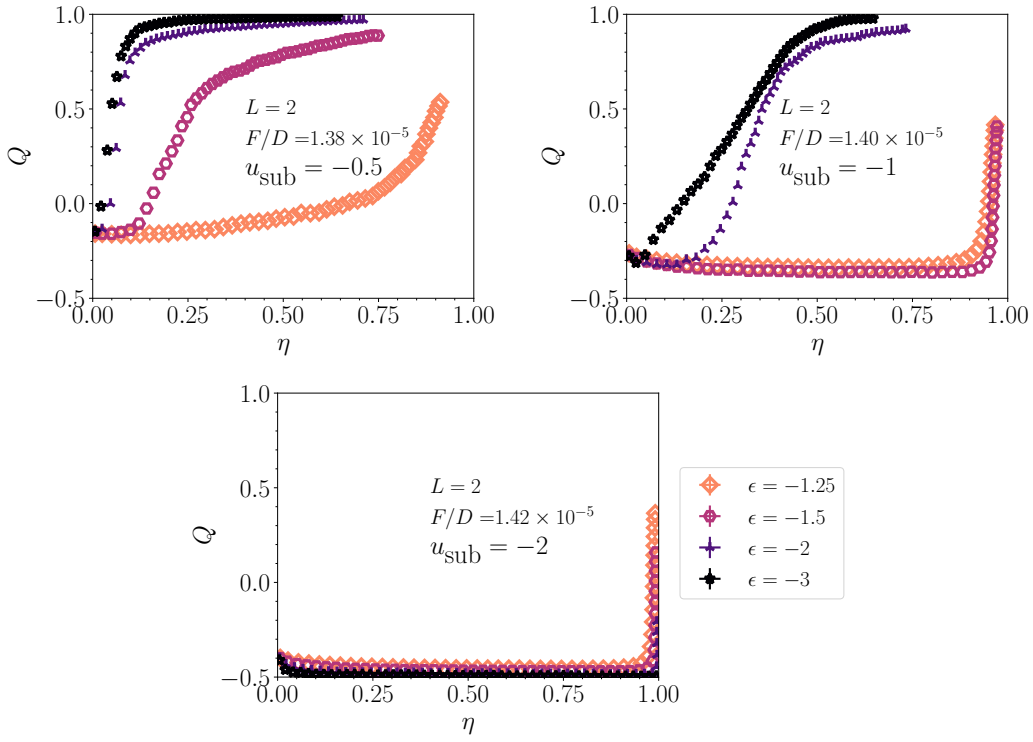

FIGURE 5.127: Nematic order parameter Q versus packing fraction η during growth of a monolayer of dimers at attractive substrates: Comparison over a sweep of ϵ at fixed F/D, shown for $u_{\text{sub}} \in \{-0.5, -1, -2\}$.

MONOLAYER GROWTH WITH DIMERS ON ATTRACTIVE SUBSTRATES:
Nematic order Q vs. monolayer density ρ

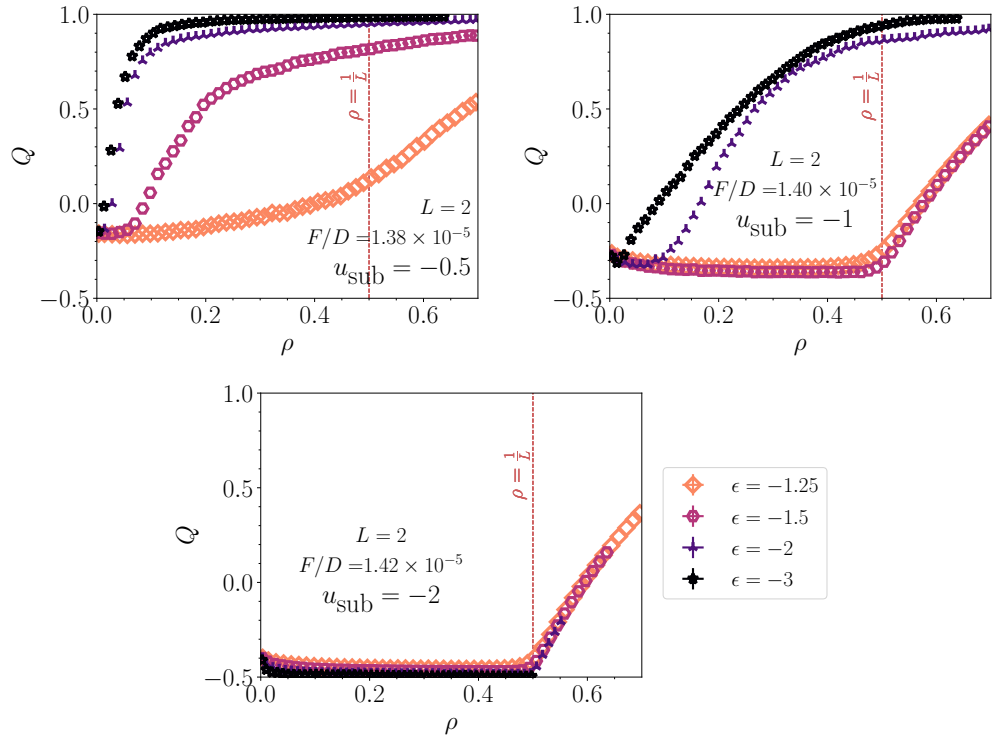

FIGURE 5.128: Nematic order parameter Q versus density ρ during growth of a monolayer of dimers at attractive substrates: Comparison over a sweep of ϵ at fixed F/D, shown for $u_{\text{sub}} \in \{-0.5, -1, -2\}$.

MONOLAYER GROWTH WITH DIMERS ON ATTRACTIVE SUBSTRATES:
Monolayer density ρ vs. re-scaled time $t^\star$

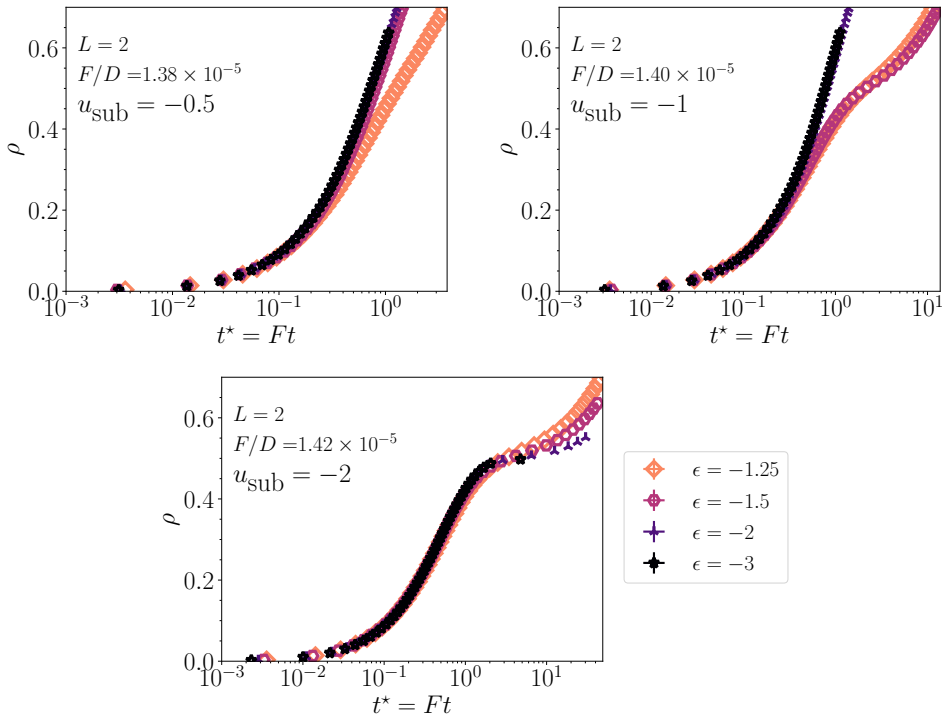

FIGURE 5.129: Global density ρ versus re-scaled time $t^\star$ during growth of a monolayer of dimers at attractive substrates: Comparison over a sweep of ϵ at fixed F/D, shown for $u_{\text{sub}} \in \{-0.5, -1, -2\}$.

MONOLAYER GROWTH WITH DIMERS ON ATTRACTIVE SUBSTRATES:
Lying density ρ_{12} vs. re-scaled time $t^\star$

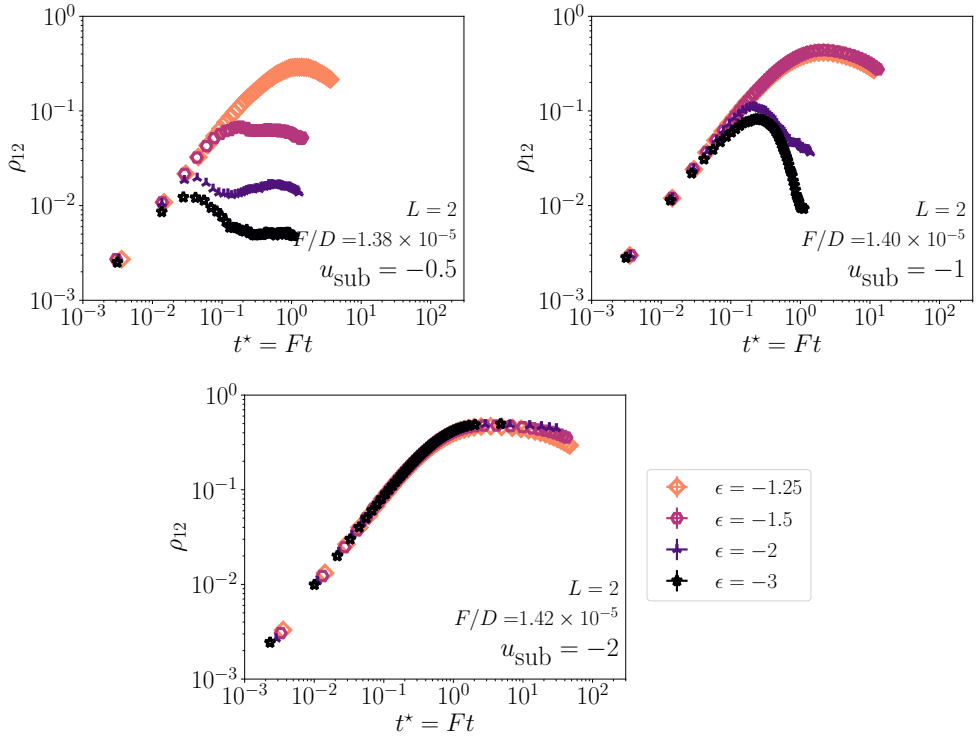

FIGURE 5.130: Global lying density ρ_{12} versus re-scaled time $t^\star$ during growth of a monolayer of dimers at attractive substrates: Comparison over a sweep of ϵ at fixed F/D, shown for $u_{\text{sub}} \in \{-0.5, -1, -2\}$.

Case of strong inter-particle attractions: $\epsilon = -3$

In this small section, we focus on the case where dimers are very sticky, i.e. $\epsilon = -3$. The substrate potential u_{sub} clearly shifts the competition between lying and standing phases for these deep reduced temperatures. For $u_{\text{sub}} = -0.5, -1$, the lying phase appears metastable, where a strong quench F/D favors its formation, seen in Fig. 5.131 (top two figures) for $Q(\eta)$. As described above, strong substrate potentials $u_{\text{sub}} = -2$ (bottom figure) force all trajectories through a 2D wetting layer, from which standing islands form in a first order transition. At $u_{\text{sub}} = -0.5$ (top left figure) such a lying aggregate does form for rapid growth, but with weaker negative order. Fig. 5.132 (top left) displays the density at which this nonequilibrium transition occurs, $\rho \approx 1/L = 0.5$. Similarly to the case of $L = 3$, we think the binodals of the vapor–2D-liquid (lying liquid) transition for strongly attractive substrates are at packing fractions (left and right) $\eta_l \approx 0$, $\eta_r \approx 1$. We provide results for $\rho(t^\star)$ and $\rho_{12}(t^\star)$ in Figs. 5.133, 5.134 as well, for completeness.

VERY STICKY DIMERS ON ATTRACTIVE SUBSTRATES:
Nematic order Q vs. packing fraction η

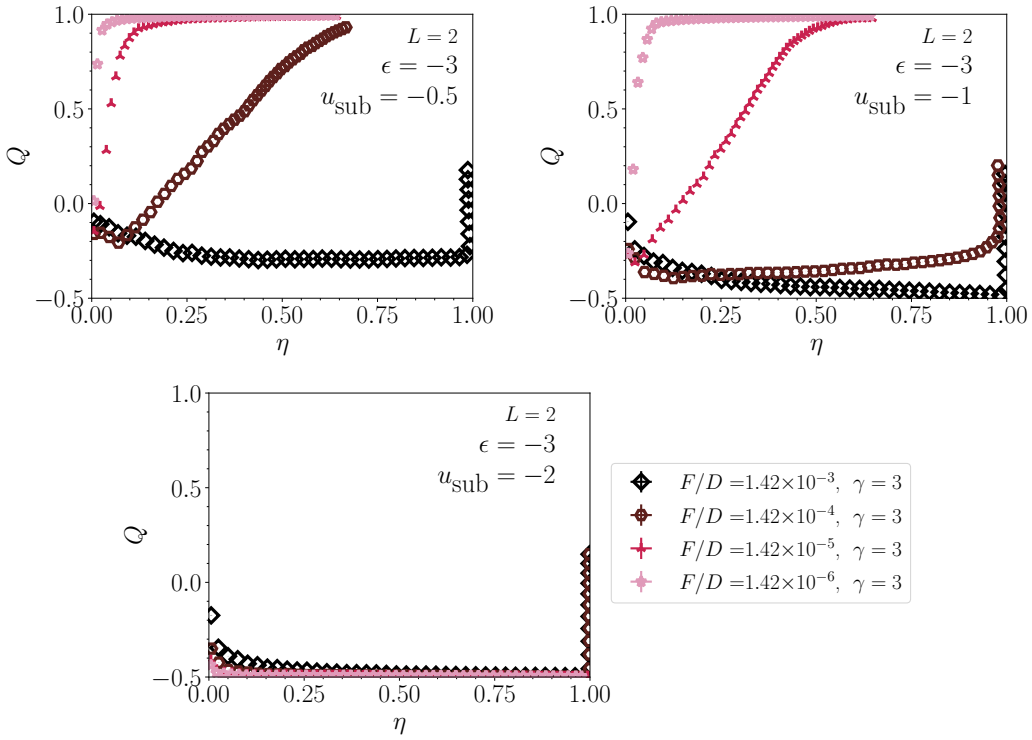

FIGURE 5.131: Nematic order parameter Q versus packing fraction η during growth of a monolayer of very sticky dimers ($\epsilon = -3$) at attractive substrates: Comparison over various values of F/D for $u_{\text{sub}} \in \{-0.5, -1, -2\}$.

Discussion

We attempt to provide a visual illustration of how the substrate potential affects structure during monolayer growth in Figs. 5.135–5.139 for the case of very sticky dimers ($\epsilon = -3$). Configurations at fixed values of the density are plotted

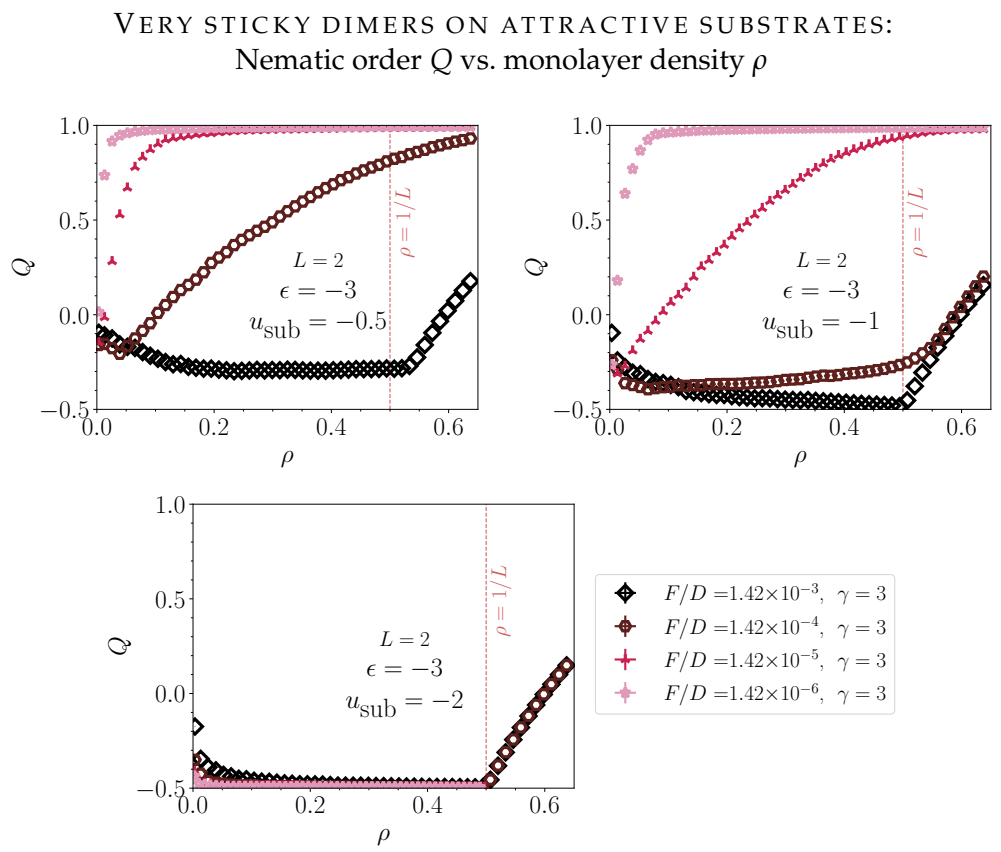

FIGURE 5.132: Nematic order parameter Q versus monolayer density ρ during growth of a monolayer of very sticky dimers ($\epsilon = -3$) at attractive substrates: Comparison over various values of F/D for $u_{\text{sub}} \in \{-0.5, -1, -2\}$.

in the (u_{sub}, D/F)–plane. On a very general note, differences between configurations are initially more subtle, especially at lower values of D/F in Fig. 5.135, where small clusters either of lying or standing kinds form. These initial differences intensify as monolayer growth proceeds, see Figs. 5.137 and 5.139 as a stark comparison. All cases with initially predominantly lying clusters begin to form a wetting layer at intermediate densities (Fig. 5.137). Even later, the standing-up transition is imminent and begins at high densities (Figs. 5.138–Figs. 5.139). In contrast, all cases with initially predominantly standing clusters form large, compact, standing islands quickly and up to around $\rho = 0.5$, where ripening and coalescence occur in many cases.

The attractive substrate potential shifts a competition between lying and standing phases in a strongly analogous way to $1/|\epsilon|$. It represents another axis determining the dynamics, kinetics, and structure formation during monolayer growth. We could clearly draw a gel line or a "competition line" diagonally through the middle of Figs. 5.135–Figs. 5.139; the difference here is that the y-axis is now u_{sub} and not $1/|\epsilon|$. Along this diagonal, we may find a phase transition scenario where the gel competes with standing clusters, i.e. possibly scenario (D) or even (C), as the 2D phase seems to form compact islands therein. We would have to analyze the kinetics is more detail to determine which scenario is proper, or if any new scenarios have arisen. In any case, this proposed gel line divides two (or possibly three, the diagonal included) dynamical regimes: below the dividing line, the system seems to end up in phase

VERY STICKY DIMERS ON ATTRACTIVE SUBSTRATES:
Monolayer density ρ vs. re-scaled time $t^\star$

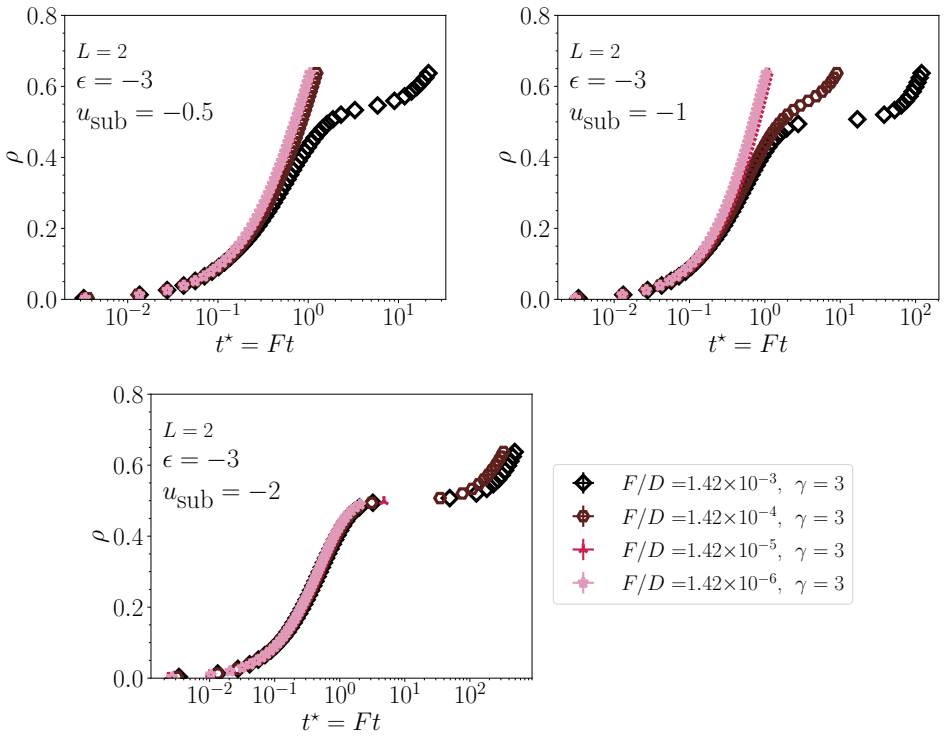

FIGURE 5.133: Monolayer density ρ versus re-scaled time $t^\star$ during growth of a monolayer of very sticky dimers ($\epsilon = -3$) at attractive substrates: Comparison over various values of F/D for $u_{\text{sub}} \in \{-0.5, -1, -2\}$.

transition scenario (E), where standing clusters eventually "nucleate" and grow out of a dense, lying gel that forms a wetting layer. Above this dividing line, the standing phase seems to win the competition very quickly and only standing clusters survive. We presume this is our previously characterized phase transition scenario (C), but, again, more detailed analysis are more data-points in the "map" are necessary.

The full attractive substrate potentials on rods scale with the rod length, i.e. adhesive energy between rod and substrate is proportional to L. Therefore, the time-scale during which the dynamics are characterized by a metastable lying phase are shifted by the substrate potential, which introduced a barrier for upward rotations. In the most simple case of an ideal gas, the time-scales of upward rotations take on a simple Arrhenius form (exponential of the barrier). Many-body or collective processes, such as the formation of a new phase, will show an elongated time-scale for the initiation of self-assembly processes involving upward rotations. (The sticky adhesion obviously forms an additional local energy barrier to stand up if within a purely 2D phase.) The total flux (current) of any self-assembly process will therefore show strong dependency on this substrate potential.

As a last remark to the standing-up transition out of the wetting layer, Fig. 5.139 at $D/F = O(10^4)$ implies that a stronger attractive potential ($u_{\text{sub}} = -2$) generates larger standing islands compared to weaker attractive potentials. However, this may be misleading, somewhat, as the monolayer density

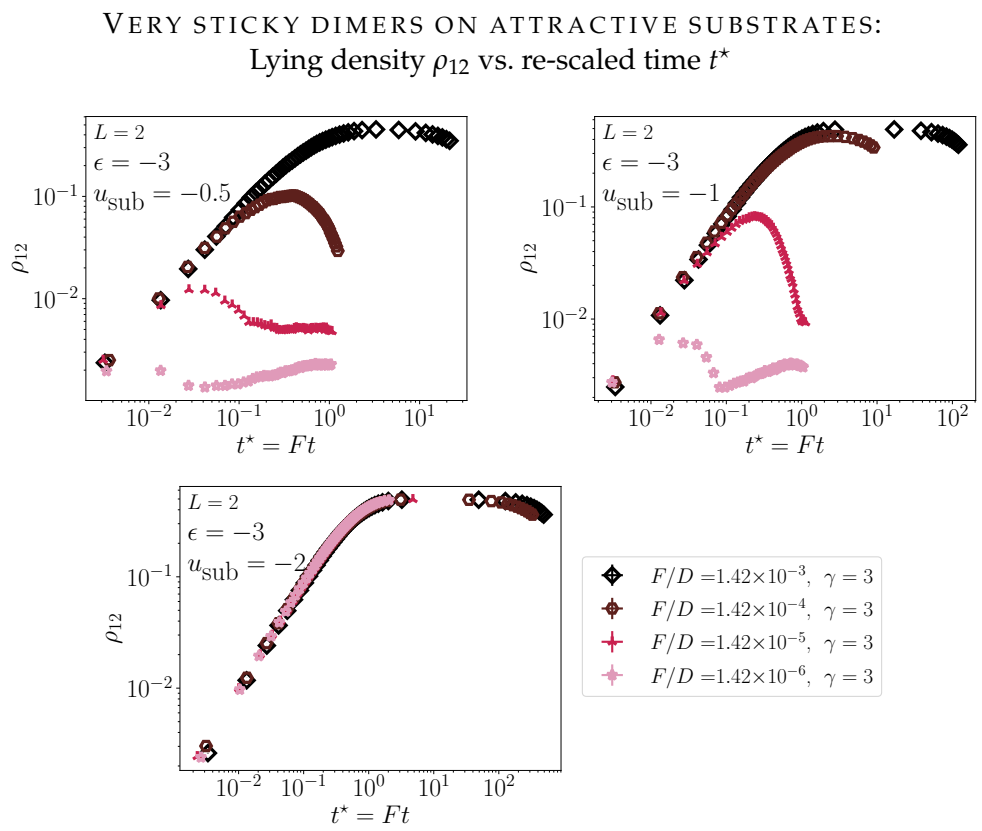

FIGURE 5.134: Nematic order parameter Q versus packing fraction η during growth of a monolayer of dimers at attractive substrates for $u_{\rm sub} \in \{-0.5, -1, -2\}$: Comparison over various values of F/D at fixed $\epsilon = -3$.

is fixed, and the time-points at which the structures appeared are mixed up. To this end, the standing-up transition for $u_{\rm sub} = -2$ should entail a larger free energy barrier – the cluster formation rate will take on an Arrhenius pre-factor that represents the rotational rate upwards for a single particle surrounded by lying rounds, in line with our discussion above. Therefore, we would have to compare the time-points after the wetting layer has formed, as well as the time-points after "nucleation" first set in. In other words, an analysis of the fluxes in the system would be beneficial here, in the style of Sec. 5.3.8. However, this shall remain outside of the scope of this thesis.

* * *

The above study case of sticky dimers at attractive substrates exemplifies the highly non-Markovian nature of large-scale structure evolution in these monolayer systems of rods. More specifically, all of them entail two competing phases with inherently different time-scales, structural order, and self-assembly mechanisms. Dimers and shorter rods like $L = 3$ are particularly nice examples, as they can form perfectly-packed lying phases (which we dubbed wetting layers) with strong enough substrate potentials – the case of attractive substrate potentials for very long rods has not been investigated, but, we suspect the wetting layer may show consistent imperfections due to steric frustration. Further, dimers can form equilibrium-shaped islands (square-like) of standing rods

VERY STICKY DIMERS ON ATTRACTIVE SUBSTRATES

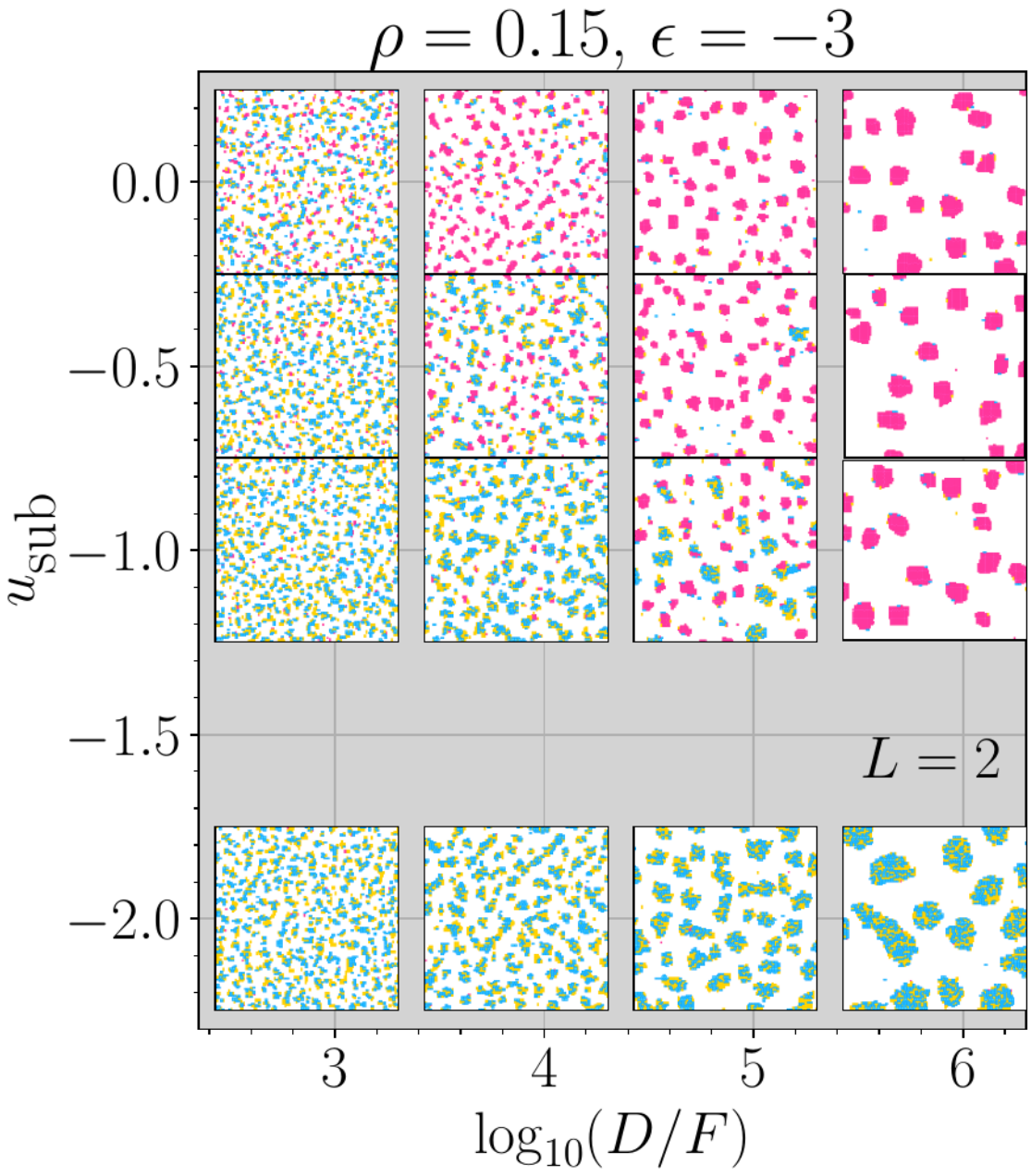

FIGURE 5.135: Visualized snapshots of the monolayer system of sticky dimers on attractive substrates in the plane of the two axes u_{sub} and D/F for density $\rho = 0.15$ and $\epsilon = -3$. Snapshots are approximately 128×128 unit-sized cutouts of the configurations, which are 256×256 in size. The same color scheme is used here as in e.g. Fig. 5.20. In all cases, we see the formation of clusters; for strong potential substrates, these are lying. For no or weak substrates, the can be standing or mixed in form.

VERY STICKY DIMERS ON VARIOUS SUBSTRATES

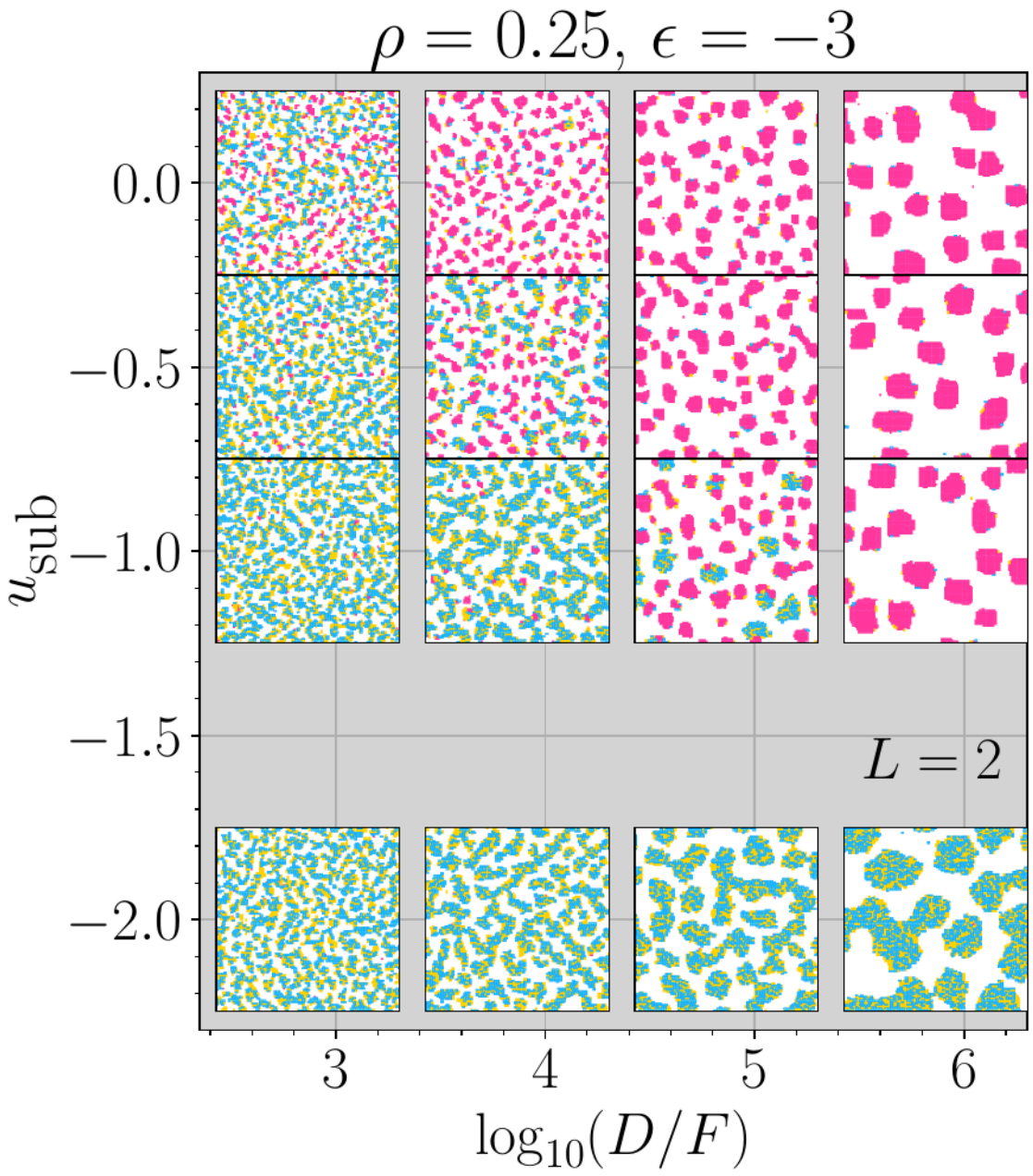

FIGURE 5.136: A continuation of Fig. 5.135 for $\rho = 0.25$. For low D/F, the lying phase begins forming a network, while at high D/F, both types of clusters become larger or begin coalescing in the case of lying clusters. In this image series (Figs. 5.135–5.139), we could draw a gel line diagonally through the image, separating two (or three, the diagonal included) main dynamical regimes.

VERY STICKY DIMERS ON VARIOUS SUBSTRATES

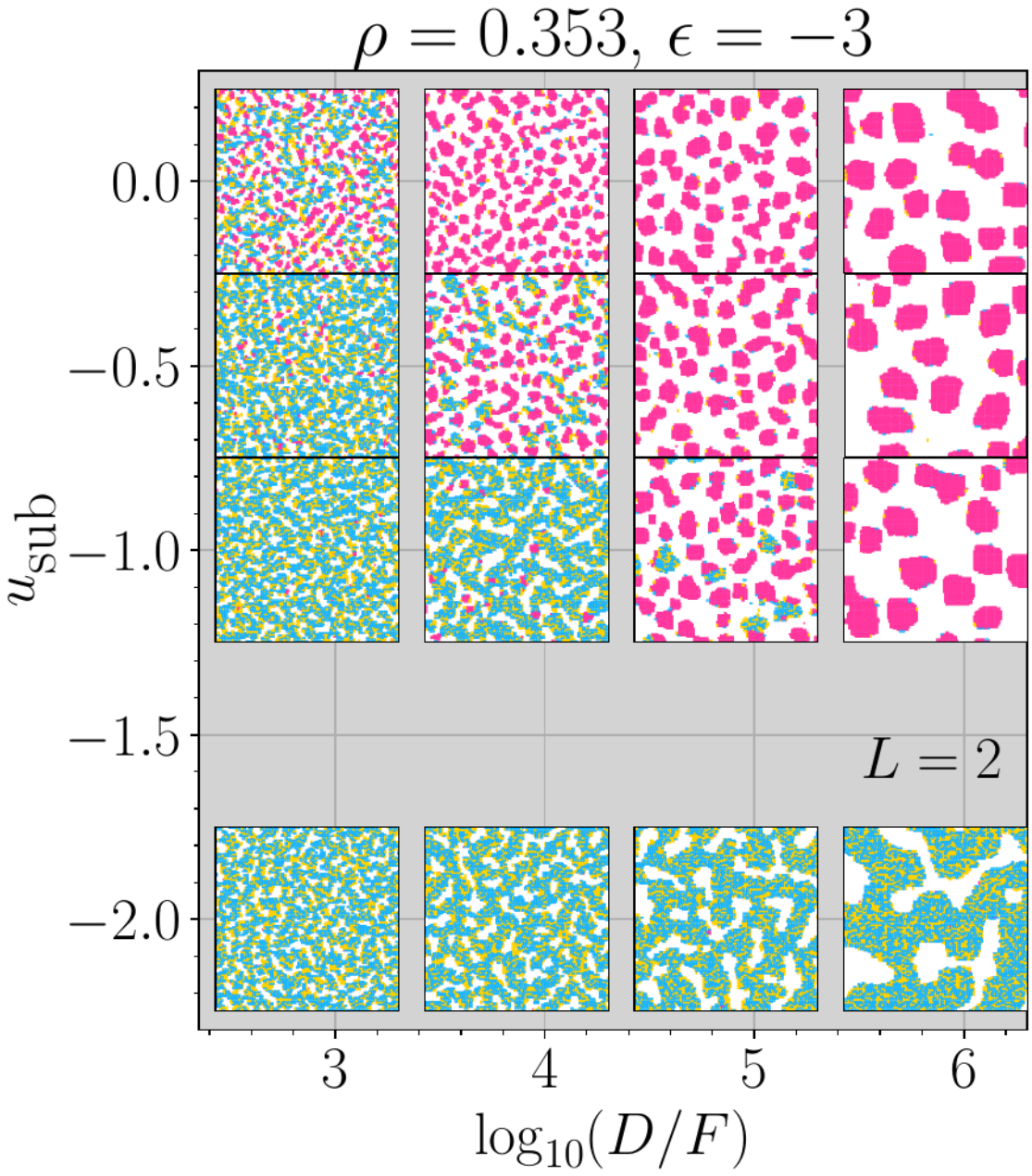

FIGURE 5.137: A continuation of Fig. 5.135 for $\rho = 0.353$. For low D/F, the lying-gel becomes increasingly dominant, while for high F/D, the lying phase has coarsened to length scales comparable to the system size. The standing islands at weaker or no substrate potentials have also coarsened and are square-like in shape owing to the underlying square lattice.

VERY STICKY DIMERS ON VARIOUS SUBSTRATES

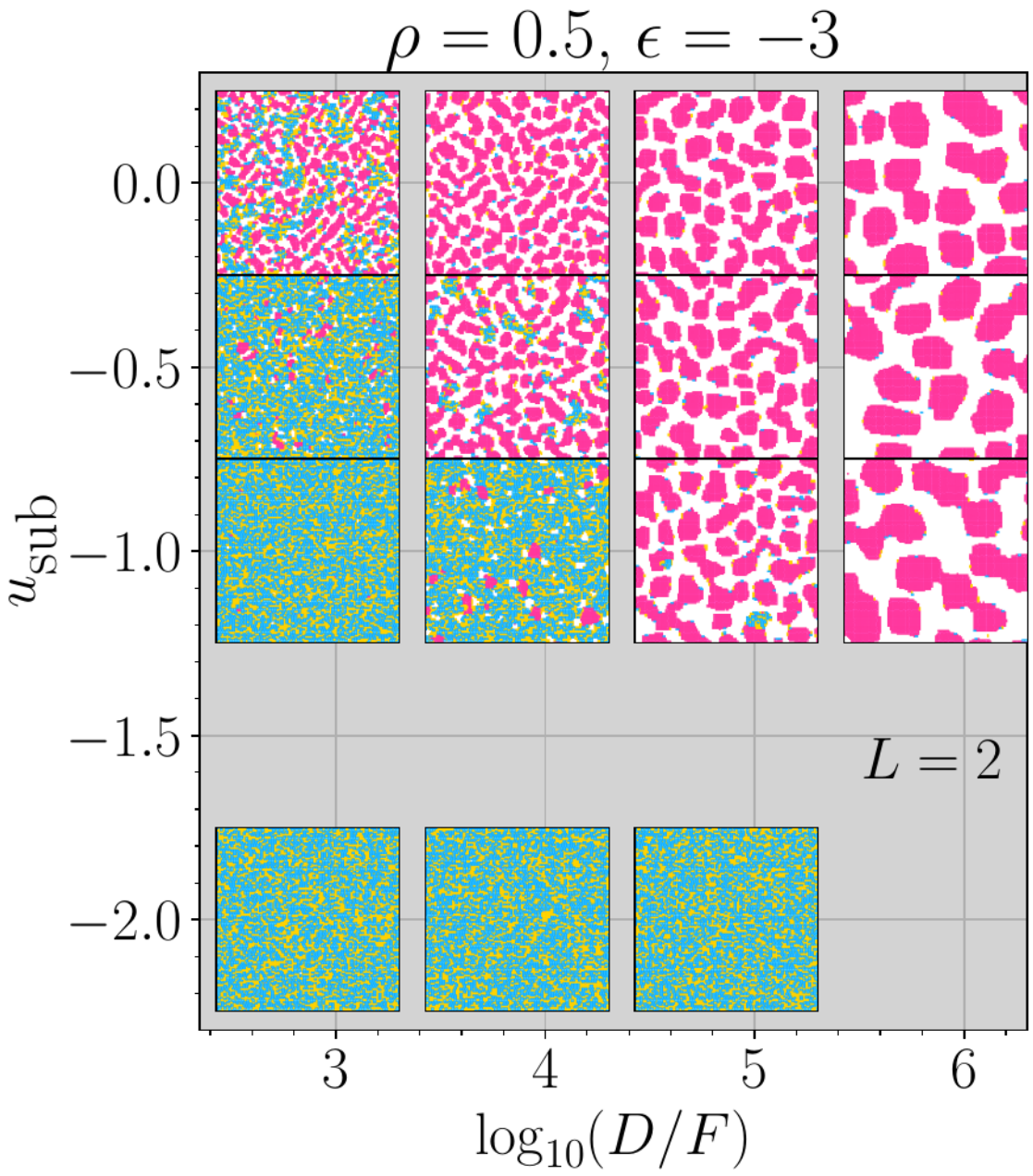

FIGURE 5.138: A continuation of Fig. 5.135 for $\rho = 0.5$. For low D/F, the wetting layer is complete for stronger substrate potentials. Some defects therein persist in the case of $u_{\mathrm{sub}} = -0.5$, as well as $u_{\mathrm{sub}} = -1$ at somewhat higher D/F. At neutral substrates at this density, the lying phase only survives in the form of large amorphous clusters. The coarsening and coalescence of standing islands continues from Fig. 5.137.

VERY STICKY DIMERS ON VARIOUS SUBSTRATES

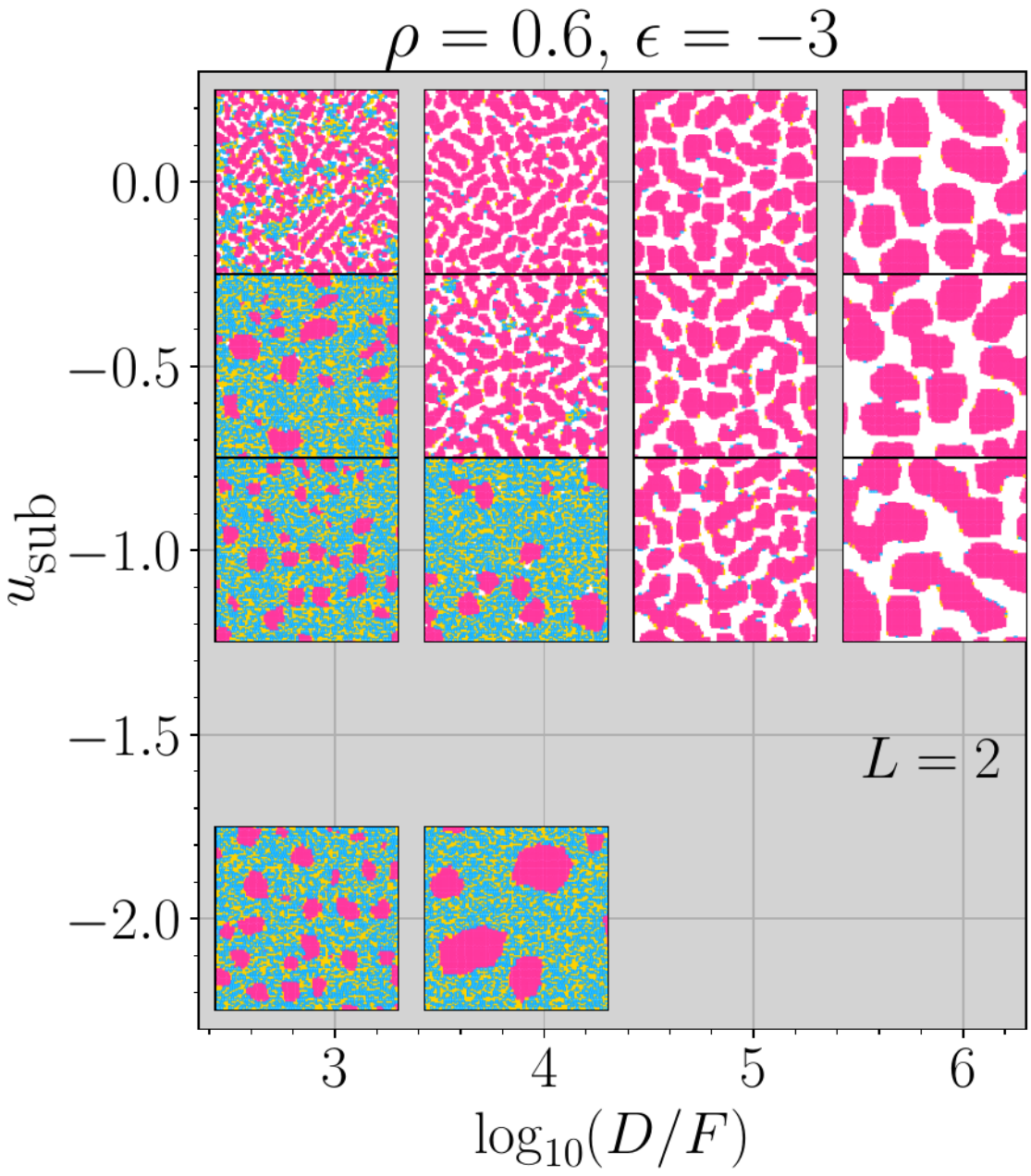

FIGURE 5.139: A continuation of Fig. 5.135 for $\rho = 0.6$. For low D/F and strong substrate potentials, the standing-up transition out of the wetting layer is visible in the form of large standing islands. In contrast, at neutral substrates, a subtle zigzag structure of the standing phase is visible, which is likely an effect of the microscopic dynamics of tumbling rotations that lead to these growth structures (discussed in the previous section). For high D/F and weak and neutral substrates, the standing islands continue to coarsen and coalesce.

more easily than longer rods, compare Figs. 5.23 ($L = 3$) and 5.65 ($L = 5$), as the binding energies are weaker.

5.8 Other experiments

We report here on general findings from other "experimental" techniques that we have employed in our studies. A quantitative presentation remains outside of the scope of this thesis.

Temperature quenches from a "hot" state and "interrupted growth"

We have preliminarily investigated phase separation kinetics at fixed densities via employing instantaneous temperature quenches from an equilibrium fluid state (the hard-rod limit). As for regime ϵ-III (with a metastable "lying phase), the formation standing islands is hindered by the metastable lying aggregate structure, providing clear evidence that the formation of the standing phase is a *two-step process*. We observe at least *two* power laws for the growth of standing clusters within ϵ-regime III.

Notably, other sources in the thin film growth literature for organic molecules have proposed the same idea: the growth of crystallites (the standing phase in our lattice model) arising via a two-step process from an aggregate precursor was discussed in Ref. [236] (see further references therein). We have motivated this possibly universal feature in many soft matter or colloidal model systems in Ch. 2. We stress that this topic is at the limit of our current understanding of crystallization in hard-core repulsive systems from a fluid phase and would be worthwhile to investigate in the context of a lattice model, particularly one that shows this feature in semi-confinement.[35]

We have also experimented with *interrupted growth*, where at a certain density or time-point the deposition is "turned off", allowing the self-assembly to continue via microscopic diffusive processes of translational and rotational type. To this end, we report that the decay or further coarsening before a decay of the metastable gel can be observed depending on the density and original growth conditions. Information on decay dynamics (possible multi-step processes) and corresponding time-scales of the decay should be theoretically of high relevance: Relaxation times and processes from each such "interrupted" configuration can provide quantifiable information about a "free energy landscape" visited during a growth trajectory. This is an outlook of the systematic work presented in this chapter.

Annealing after growth

We have implemented another "experiment" and produced a few preliminary results therewith: Upon initializing the system at an "interrupted" configuration from a growth trajectory, we are able to heat the reduced temperature of the system $T^* \equiv k_B T/\epsilon$ in a slow and steady manner (at a constant rate). Specifically, the reduced temperature T^* evolves in time t according to $T^*(t) = T^*(0) - A * t$, with A representing the annealing rate. As we have explained in the beginning of this chapter, the reduced temperature in our model affects the local interaction strength only, and not the diffusion rate. It goes into the calculation of the local Hamiltonian change $\Delta\mathcal{H}(\epsilon)/k_B T$, part of the acceptance probability of a local "move".

[35] Yet, true "nucleation" may not occur in 2D, but, these issues would have to be explored more thoroughly outside of the context of this thesis.

The usefulness of these annealing experiments are manifold. For example, observing the decay rate of the metastable phase as a function of cooling speed and density will further inform us about its metastability, and, therewith, about the "free energy" landscapes visited during growth. Preliminary results coming from these experiments further indicate that fluctuations system currents (motion fluxes) serve as better indicators for presence and disappearance of the metastable phase, compared to structural observables.[36]

On a final note, we suspect re-cooling the system after heating will show that a metastable state cannot re-appear (the metastable phase irreversibly decays), at least if we heat and cool very slowly, and as long as we remain within the "parent" liquid–vapor binodal. This may be relevant for interpreting e.g. Ref. [182], who applied heating-and-cooling cycles to thin films of pentacene (around the monolayer stage).

Growth with desorption events (evaporation–deposition dynamics)

Desorption changes the kinetics during growth quite drastically. We have developed a KMC scheme to allow for desorption events, at a fixed attempt rate k^0_{evap}, which is accepted according to the same kind of Metropolis condition as all other moves, i.e. the change in inner energy that would occur upon a desorption $p^{evap} = \{1, \exp\left(-\Delta U_{\mathrm{sticky}}/k_{\mathrm{B}}T\right)\} \equiv \exp\left(-\Delta U_{\mathrm{sticky}}/k_{\mathrm{B}}T\right)$ for "sticky" attractions, as $\Delta U_{\mathrm{sticky}} > 0$ due to the breaking of particle bonds (the "vacuum" energy is zero). (In the best possible scenario of a particle without binding nearest neighbors, this value is null, rendering an acceptance rate of 1).

Generally, the capacity for desorption equilibrates the system much more quickly and efficiently. The evaporation–deposition kinetics emulate that of a grand canonical ensemble, with additional diffusion "moves". If the system reaches a stationary state, the chemical potential is expressed by the ratio of the attempt flux and desorption rates, $\exp(\beta\mu) = F/k^0_{\mathrm{evap}}$ for $\beta = (k_{\mathrm{B}}T)^{-1}$.[37]

The deposition events represents additional currents in the system that exchange matter with a source. The addition of a near "chemical potential" "accelerates" the motion in and growth of the monolayer, the latter is important because we can reach densities of $\rho = 1$ very quickly depending on F/k^0_{evap} and ϵ. We find altered behavior of the nematic order Q in time in other ways, as well: For example, under certain conditions for regime IIIb, the nematic order obtains a pronounced peak before decaying again, a feature we did not find in the monotonic deposition.

More generally, we think that this setup will allow us to reacher longer simulated time-scales. What we find in preliminary runs is that the wetting layer (scenario (E)) can very quickly form up to full scale. The "nucleation" of standing islands can also be detected for $L = 3$ at neutral substrates, which was unreachable, in effect, with the monotonic-deposition setup. For time-periods where a semi-monotonic growth (in ρ) is observable, standing islands become very large in short periods of time, bearing some analogy to a heightened D/F in the system, and, therefore, scenarios (B) and (C) could be explored at late stages. Finally, the gel might decay much more quickly, which would allow us to pinpoint the "gel line" (scenario (D)) more "sharply" in the "maps" of Q

[36] As the cooling rate is a constant Poisson process in the system, any changes in currents can be gauged with the statistics of the cooling events.

[37] This can be shown quite easily, in a similar approach to how we derived the acceptance rate for our GCMC simulations in Ch. 3.4.2.

in the $(\ln(1/|\epsilon|), \log(D/F))$–plane. Therefore, weak-desorption experiments could aid in delineating all dynamical regimes in the monolayer with higher precision.

Further, exploring this behavior would be a systematic step for interpreting results from our full 3D model of growth, where particles may be deposited from a vapor-phase source of particles above the substrate (similar to "model II" of the previous chapter for the continuum model of spherocylinders). Monolayer–desorption will be commonplace in this semi-confinement setup.

On a last note, an extreme case could also be studied: The random desorption of particles from a fully-packed monolayer, i.e. the full jamming transitions. These findings may both be interesting for comparison to similar experiments on thin films, as well as for comparing to lattice models investigating inverse bond percolation, see e.g. Ref. [898]. We make a few remarks on the importance of these transitions again in the discussion Sec. 5.9.

5.9 Discussion

We would like to use this section to emphasize a few fundamental points on the complex nonequilibrium evolution in the "sticky" monolayer systems. This may be relevant for the thin-film growth literature on organic molecules, as well as for model approaches thereof. This discussion extends to generic self-assembly in soft matter systems, too, as well as the study of general nonequilibrium systems.

The lying vs. standing phases and dynamical asymmetry: General discussion

A lying phase or a lying wetting-layer is clearly favored by substrate potentials that bias lying rods, which may be important for understanding experimental systems of thin films. If this constitutes the "thin film phase", it should also be preferred by a high flux at later stages of growth, according to Ref. [213]. Indeed, this is what we find. If a phase is metastable, it should disappear for extremely low deposition quench rates F/D or warmer temperatures: The literature for similar molecules like pentacene [138, 182, 187], PTCDA [180, 186] or SnPc [152] show these kinds of effects. Post-growth waiting should have a similar effect [142, 899, 900].[38] These also features we can verify also using the other experiments of heating and interrupting growth.

Each type of phase structure – lying or standing – has its own inherent relaxation times. These will each depend on temperature; however, standing rods in the middle of an island will have $4L\epsilon$ binding energy, while lying rods in the middle of, say, a lying island will have $2(L+1)\epsilon < 4L\epsilon$ binding energy (for all "rods", $L > 1$): A lower (reduced) temperature (stronger attractions) widens the dynamical gap between relaxation times owing to energetic but also the entropic asymmetry between the phases – the standing phase has a higher degree of ordering than the lying phase. A substrate potential increases an effective lying-energy with $(L-1)u_{\text{sub}}$ more units. Therefore, it will further shift the energy–entropy contributions to structure formation, and broaden the

[38] Deposition with a high kinetic energy [901] may enable the system overcome such free energy barriers (even at very low temperatures).

bandwidth of relaxation times in the nonequilibrium system. One example is how the lifetime of a metastable lying phase lifetime prolonged by weak substrate potentials. Energetic and entropic contributions discussed above also depend on L: longer rods will "widen the dynamical gap" during the monolayer growth experiment, as well. As a function of binding energies, substrate potential, F/D, and rod-length, the number of processes with varying timescales will overlap. Any "sharp", thermodynamic phase transition between differently-ordered states will be "smeared out" and accompanied by a number of in-between states.

On a most general level, *asymmetry* of dynamics in the nonequilibrium system (which owes to a disbalance of generalized forces on different many-body scales) — which depend on rod orientation and position (i.e. inhomogeneities) — is the basic reason behind the complex evolution we observe. The aspect ratio of the rods and the amount of anisotropy of the interactions (between rods and substrate) are parameters that adjust this dynamical asymmetry. Under the driven deposition, F/D also shifts the competition by hindering or allowing the relaxation of slow processes. The system can become arrested in a portion of its degrees of freedom, i.e. in the lying, metastable "wetting layer" (a dense gel), or show a network-forming gel of lower density

Ref. [735] discusses (transient) gel- or network-forming phase separation processes in colloidal suspensions in detail, and we refer the reader for an expert's take on this topic. The authors claim the formation of this metastable gel may be a generic feature of short-ranged attractions in colloidal systems (see also Ref. [902]). A colloidal suspension is a mixtures of small molecules and large, heavy colloidal particles; therefore, it is a dynamically asymmetric mixture, where two components entail microscopic dynamics at disparate timescales. Further, the dynamic arrest involved with this high-density gel bears similarities to glassy behavior, i.e. particles become caged and the system is in a non-ergodic state. Notably, these discussions revolve around 3D suspensions. Gels and network structures form in many colloidal systems (3D) out of fractal-like aggregate clusters [19, 703].

In our case, we see this gel-phase in a (2+1)D (quasi-2D) confined system, which is quite intriguing. Indeed, kinetics of gel formation – which is more "aggregation-like" – may bear similarities to spinodal decomposition in that it seems to involve no energetic barriers [19]. In other contexts, early-stage phase separation kinetics of the fluid-crystal states in colloidal systems may involve a reversible form of aggregation [696, 698]. This would agree with a (necessary) appearance and decay of metastable states for the crystallization initiation. Our lattice model may be used in the future to help understand basic mechanisms of phase transformation on a general level, then. More generally, this lattice model might shed light on glassy versus arrested dynamics, which are often difficult to discern in off-lattice systems.[39] We mentioned in Sec. 5.3.8 that analyzing the cross-correlation between translational and rotational mobility in the system should shed more light on the nature of the arrested dynamics.

The effects of substrate potentials: Remarks and outlook

We would like to remark on one subtle observation on the lying phase: Whether or not the lying phase forms large-scale, compact islands (which arises due to

[39] See Refs. [662, 709, 903, 904] for additional literature on dynamics within gels.

an elongated competition time-scale for phase transition scenario (C)), compared to a loose gel co-occurring with standing islands (phase transition scenario (D)), may not be affected by a weak substrate potential u_{sub}. Weak substrate potentials elongate the time-scales with which the lying phase persists, thus seems to enhance the coarsening process. The phase transition scenario may not have changed, however. In the future, we could specify the kinetics with more precision under these conditions, and provide a further dynamical "map" with the third axis, u_{sub}.

On a related note, it would be interesting to further explore the difference between the "soft" lying–standing transitions at full packing versus "sharp" transitions we observed from a 2D wetting layer or liquid, under the influence of various substrate potentials in Sec. 5.5. These "soft" versus "sharp" transition points could be plotted in the same style of the "maps", i.e. in the plane of $(\ln(1/|\epsilon|), \log(D/F))$, which would inform us about the onset of metastability of these transitions under different conditions.

Arrested states, jamming, percolation: Remarks and outlook

We had begun to explore the percolation (and anti-percolation) behavior of both the lying phase, as well as of "any" connected region in the monolayer systems during a deposition quench. Exploring the percolation transition upon temperature quenches, i.e. spinodal decomposition, would render additional information about how this ties to the specific *driven* nonequilibrium setup. The same holds for the interrupted-growth experiments we described. We report that percolation in random sequential adsorption experiments has been explored in the context of hard-core rods in Refs. [682, 684, 898, 905–908].

Fundamentally related to these percolation models are *jamming* transitions in the same random-sequential adsorption setup [681, 683, 685, 909, 910] (see also references above). We saw a form of (partial) jamming in Ch. 4 for much longer rods at very strong substrates, as well as when the 2D wetting layer forms in the case of "sticky" rods at attractive substrates (monolayer growth halts transiently). Nevertheless, our model entails additional diffusive motion which changes the nature of these transitions, connecting them to phase separation in ways that leave many questions open. We have provided a table (Tab. 6.1) with 2D jamming and percolation transition densities in Ch. 6.8.4 in a later chapter for future reference. Most importantly, perhaps, we proposed that the crossing of a gel line in our "maps" of Q in the $(\ln(1/|\epsilon|), \log(D/F))$–plane should indicate an unavoidable jamming line at low D/F. This might offer a way to estimate (metastable) critical point(s) in the "sticky" rod system. Future exploration thereof would be most interesting, as it would tie a knot between nonequilibrium transitions like jamming with thermodynamic transitions in a system.

Caution and challenges for potential analytical approaches to monolayer growth

It seems that the growth of structures in monolayers with sticky hard rods will *not* follow universal self-assembly kinetics of one type, generally speaking. This is even true within early-time regimes of monolayer growth, i.e. "nucleation and growth" of islands. We observed a wide compendium of phase transition

scenarios: at *least* the scenarios (A)–(E) categorized for $L = 3$ at neutral substrates (Sec. 5.3.9). Depending on the main axes of growth – F/D, ϵ, as well as u_{sub}, particular phases will be favored or suppressed. Further, we have found that the systems are highly sensitive to the choice of microscopic dynamics (Sec. 5.6) – whether they couple rotational and translational motion directly (i.e. tumbling) or not. Hence this factor must also be considered when attempting to formulate e.g. rate equation models or even employing more sophisticated methods like DDFT. We have not explored the effect of γ (the ratio of the translational diffusion rate to the out-of-plane rotational rate in the ideal-gas limit) on growth systematically. Careful inspection hints that the monolayer systems are much more sensitive to γ when employing tumbling rotations, as well as for very long rods, where rotations downward are easily hindered due to crowding. Generally, any strongly nonequilibrium system will be highly sensitive to the details of the microscopic dynamics due to the nonlinear nature of the system. The nontrivial coupling of rotational and translational degrees of freedom will be much more sensitive to model details if out-of-equilibrium.

On a specific note, in our model, the character of the lying phase seems to pose a challenge for standard rate-equation approaches – those that describe island "nucleation and growth" in the submonolayer stage of thin film growth. Our observation that "nucleation" is a two-stage process is one important point. Another is that either compact islands, network-like structures, or a wetting layer of the lying phase can form, which is adjusted both by temperature and F/D. It is not clear how to incorporate the formation and competition of a gel into classical rate-equation approaches for island growth.

Island shape and internal order: Remarks on literature

As already discussed, the specific rates of moves, the length of rods, and reduced temperature in the system can strongly influence the shape of islands. Far-from-equilibrium situations, where relative time-scales matter, can mean systems are highly sensitive to such details. This highlights the importance of knowing the specific dynamics if one wants to properly emulate an experimental system of thin film growth with molecules. Indeed, many other experimental and theoretical studies have touched upon the topic of island shape. For one focused on phase separation kinetics, see Ref. [911], see also discussions in Refs. [21, 912]. Also, Ref. [913] demonstrates the role of edge-hopping on island rims. Ref. [183] (submonolayer growth with organic molecule p-6P) reports on round islands appearing at lower temperatures and fractal-like islands at higher temperatures, which is exactly in reverse of diffusion-limited aggregation models for simpler systems. We suspect that (changes in) local rotational dynamics may be at play, but leave this to speculation. Also, we can conclude from our model system that discerning the crystal phase of the clusters is crucial in these types of analyses, as metastable-phase clusters entail different morphology.

Ref. [4] had reported briefly on KMC simulations with "trimers" (unpublished elsewhere) [Fig. 6 of the reference] showing very similar diamond-, fractal-like morphology of standing islands. This morphology appears when employing our tumbling dynamical model. However, details of the simulations in the corresponding reference are not provided. Ref. [234] provides more details on their KMC simulations of "trimers" , namely, they are identical to

that of Ref. [233], which implements tumbling rotations. Yet, the type of order within islands is (completely) different than in our model, especially for the case of predominantly standing islands. The latter are characterized by a semi-homogeneous mixture of lying and standing rods – a feature we never see in our model system. Different interaction potentials are described for the "dimer" models in Ref. [233]. (The individual interaction strengths – as well as the dependencies on relative particle orientations – are varied in an exploratory fashion). Therefore, we deduce that a very different set of interaction potentials was implemented for the "trimer" models, as well, compared to our "sticky" attractions. The specific form of the interaction potentials between rods will influence the composition *and* morphology of islands in a major way, which was demonstrated in Ref. [233].

"Time" and dynamical observables: General discussion and outlook

Time in the nonequilibrium system can be rescaled with the external reference clock, namely, of the the attempt rate of the external driving force F. In this way, we have compared how much "effort" ($t^\star = Ft$) is required in order to induce a particular type of change in the system. This driven nonequilibrium setting means that state variables of the system can be plotted not against the thermodynamic parameter ρ, but, against $t^\star = Ft$, instead. In essence, the rescaled time represents a total attempt work (number of particles provided to the system) performed by the external force. Thus, $t^\star \equiv 1$ represents when the external driving force would have been able to form a full monolayer (density of 1) if the particles are non-interacting, i.e. for an ideal gas of rods. We note here one observation from our data: many "important" events during monolayer growth, such as percolation of the system ("any" connected region) or formation of the "wetting layer" seem to occur in close vicinity of this timepoint.

Dynamical quantities can distinguish equilibrium from nonequilibrium fluids in ways that are superior to structural quantifiers (observables) [104, 557, 914]. Preliminary results from our side suggest that a "sharper" detection of nonequilibrium transitions (metastable boundaries and entry into or exit from nonergodic regions) is retrieved when observing *fluctuations* of dynamical quantities like global rates (fluxes), which represent magnitudes of currents in the system. Currents and forces are the fundamental quantities in nonequilibrium, see discussions throughout Ch. 3. We had presented results on fluxes and particle mobility in Sec. 5.3.8 for the case of $L = 3$ at neutral substrates. We also mentioned there that initial efforts have been made to observe the spatial correlation and cross-correlation functions of fluxes in the system (an analysis of spatial statistics of rates reconstructed *ex situ* from simulations snapshots).

Current fluctuations are fundamentally bounded in nonequilibrium steady states [854, 855]. The arrested states in the monolayer – the gel, wetting layer, and jammed states that we reported in the previous Ch. 4 are particular examples of transient quasi-stationarity. Moreover, the total motion fluxes (probabilities) in each KMC step is related to the entropy production in the system, which we alluded to in Ch. 3.5.1. Such "easily"-measurable dynamical quantities from KMC simulations are fundamental to the nonequilibrium physics, and could be used to explore novel approaches such as power functional theory [825]. The monolayer systems studied here could serve as a workhorse model,

in this sense, especially the fact that on-lattice systems have enjoyed much less attention on this particular forefront of basic research.

* * *

All in all, the monolayer model system of hard "sticky" rods seems highly versatile for exploring nonequilibrium structure formation, kinetics and dynamics. As it is a completely generic model, the material properties and self-assembly phenomena it renders under nonequilibrium conditions may connect to many, specialized soft matter, molecular matter, and nano-particle systems. However, the combination of confinement and anisotropic particles in this driven nonequilibrium setup makes the outcomes of self-assembly highly sensitive to model details. Therefore, precaution must be taken when attempting to deduce specific protocols for custom self-assembly, for example.

5.10 Conclusions and outlook

We explored the nonequilibrium growth of monolayers composed of sticky hard rods in a lattice model, serving as an idealization for the initial growth of thin films of anisotropic particles like organic molecules. The self-assembly process of a monolayer formation is complex, entailing various metastable phases and transformation processes before reaching the stable end-state of a full monolayer. The main axes controlling the nonequilibrium competition of various (metastable) phases – their length-scales, appearance and metastable duration – are shown to be the flux-to-diffusion ration F/D (the deposition quench rate), the "sticky" inter-particle attraction strength $|\epsilon|$ (or equivalently, the reduced temperature $T^* = k_\mathrm{B}T/|\epsilon|$), the substrate potential strength $|u_\mathrm{sub}|$ biasing lying orientations, and the microscopic dynamics (tumbling- versus central-rotations). The quantities $1/|\epsilon|$ and D/F define the two main axes in various "maps" we have presented, i.e. those of Q and configurational snapshots, which have helped us discern different dynamical regimes of monolayer growth. We found at least five different phase transition scenarios that divide the $(\ln(1/|\epsilon|), \log(D/F)$–plane into corresponding regions (for our standard case of rod-length $L = 3$ at neutral substrates).

Thus, the transition to a standing, full-density monolayer from an empty monolayer has many possibilities. The aforementioned five phase transition scenarios are labeled *scenarios (A)–(E)*. In writing this chapter, we had originally categorized the phenomena in terms of "ϵ-regimes", which is somewhat suboptimal, as these do not account for the dependency on dynamical parameters (F/D). We will add a tag of this older categorization in the following reiterated list of scenarios:

- Scenario (A): "Hard-rod-like" monolayer growth for "hot" monolayers or weakly-attractive rods, in which no phase separation occurs (within "ϵ-regime I"). Jamming and dynamical arrest must occur for very low D/F, but, we have not explored these transitions or range of parameters in this thesis. The kinetics change when lowering the reduced temperatures (or $1/|\epsilon|$) close to the isotropic–standing critical point, which, in fact, seem very similar to those of scenario (B), see next item.

- Scenario (B): A transition from an isotropic fluid or vapor to a standing phase via "nucleation and growth" of standing clusters. Ripening, coalescence, and eventually coarsening of the standing phase is accompanied by the standing phase percolating at late stages. (This scenario seems to occur within "ϵ-regime II".)

- Scenario (C): A competition of lying- and standing-cluster formation (compact clusters of both phases). The formation of the lying phase precedes that of "nucleation" of standing clusters. The lying phase competes with the "nucleation and growth" process of the standing phase, slowing them down at first, but, rejuvenating growth of the standing phase at later stages, when the standing phase "eats up" the lying clusters. (This seems to occur within "ϵ-regimes IIIa, IIIab, IIIb".)

- Scenario (D): A lying phase forms amorphous, aggregate clusters, which soon form a low-density gel that percolates and coarsens thereafter. The standing phase "nucleates" after the lying phase has aggregated of formed, and begins growing in competition with the lying gel – a co-occurrence the a lying, network-forming gel and standing clusters is a poignant structural feature of this scenario. The standing clusters grow at the expense of the lying phase, eventually "eating up" the lying gel . This scenario lies in-between scenarios(C) and (E), please see next item. (This scenario occurs within "ϵ-regimes IIIa, IIIab, IIIb".)

- Scenario (E): A dense gel of lying rods dominates the system, forming a wetting layer, where the monolayer becomes fully-packed near $\eta \to 1$ at a global nematic order of $Q < 0$. The standing phase finally grows islands out of this dense gel phase, where the waiting period can be very long. (This scenario occurs within "ϵ-regimes IIIab–IIIb".) Depending on the position of $1/|\epsilon|$, this occurs at fast or "medium" F/D – it is the left-hand-side of the dynamical regimes regarding an x-axis of $\log(D/F)$.

We also report on further findings on the effect of substrate potentials u_{sub}:

- Scenario (E) is better seen (and our simulations ran long enough) for weakly attractive substrates $u_{\text{sub}} = -0.5$, which likely shift the onset of metastability of the lying phase. Loops in the packing fraction are clearly visible, as well, which are indicative of a collective standing-up process. These loops may be an inherent part of scenarios (B), (C), (D), and (E), but, are simply amplified under the influence of the substrate potential.

- Weakly attractive substrates might only shift the areas in the $(\ln(1/|\epsilon|), \log(D/F))$–plane at which each phase transitions scenario would be found.

- Strong or intermediate substrate potentials bias the orientation of the initial, isotropic fluid or vapor to a 2D fluid or vapor, which likely even becomes a thermodynamically stable 2D liquid at low enough reduced temperatures. Standing up out of a 2D wetting layer of the fully-packed 2D liquid can appear as a "sharp"; in some cases of $1/|\epsilon|$ and D/F, however, it may remain "soft". A detailed and deeper exploration on the shifting and introduction of new dynamical regimes with substrate potentials would be interesting for the future.

- As a comment, we suspect that this standing-up transition may foreshadow a dewetting transition in systems where the monolayer constraint would be removed (e.g. bilayers).

We have also provided quantitative results on the evolution of clusters or nearest-neighbor connected regions during monolayer growth – composed of standing rods, lying rods, or "any"-oriented rods. We also performed morphological analysis by means of Minkowski functionals of these connected regions, which have provided additional insight and means to discern the different phase transition scenarios. We also quantified (roughly) percolation transitions (as well as an anti-percolation transition) for these three types of nearest-neighboring connected structures. We note these transitions occur under these unique nonequilibrium conditions of a deposition quench. We have also quantified observables that render crucial dynamical information, complementary to the global (mean) and configurational observables we quantified. The mobility of particles in their translational and rotational degrees of freedom provides insight into statistics of single-particle dynamics during phase separation, when the system is dynamically heterogeneous. The orientational order of these mobile particles provides further detail on the lying–standing competition dynamics ("gymnastics"). In an exploratory manner, we also quantified the relative translational flux (motion probabilities) in the systems, as well as a "sticky" acceptance ratio during the nonequilibrium dynamics. Fluctuations and cross-correlation of motion fluxes (i.e. currents) would be a next step in future investigations.

We presented many results in the $(\ln(1/|\epsilon|), \log(D/F))$–plane, as these can be used to distinguish between the main dynamical regimes in the monolayer. In particular, we found that the "maps" of Q at fixed densities are attuned to the different dynamics, where we can trace the boundaries of the different phase transition scenarios within them – a gel line can be see for phase transition scenario (D), for example. We can also detect which dynamical regimes have *not* been explored in our datasets, for example, that extremely low-values of D/F will render crucial information on jamming transitions or further arrested states. We may marginally see these low-D/F jamming effects for $L = 5$ and $L = 9$, which we describe below. In particular, however, high deposition quench rates F/D may give us the possibility to determine a good estimate for *critical* reduced temperatures, both *metastable* and stable. We proposed how to extrapolate these from the gel line, for example, or from the place where the gel line meets a (potential) jamming transition. Further, we might be able to estimate the critical *densities* of these stable or metastable transitions from the series of maps at different values ρ – for example, at which ρ the value of Q at the "critical" point of $(\log(D/F), \ln(1/|\epsilon|)$ drops below zero. A more detailed exploration would be most interesting in the future.

We have explored monolayer growth with longer rods $L = 5$:

- The evolution with rods of length $L = 5$ shows many similarities to that with $L = 3$, although differences include pronounced loops in the packing fraction during a collective, standing-up transition, like for weakly attractive substrates with $L = 3$.

- Further, the topology of the "maps" of Q in the $(\ln(1/|\epsilon|), \log(D/F))$–plane shows subtly different features that may hint at altered relationships between dynamically arrested states and metastable critical points

that we presume exist in the system. The low-D/F "half" might have a "'kink" in the gel-line that could indicate the value of $1/|\epsilon|$ for a metastable transition. More simulated data points in the "map" would be necessary to clarify.

We reiterate here another important finding from our studies:

- We have found that the *type* of microscopic moves modeled for the single-particle motion of anisotropic rods plays a significant role, both for the evolution of structure and well as kinetics during monolayer growth. Specifically, we compared different out-of plane rotational dynamics: tumbling rather than central rotations.

- Tumbling dynamics induce diamond-like and more fractal islands of the stable, standing phase. In the central-rotations case, islands remain more round. Thus, the shape of islands is a function of the coupling between rotational and translational degrees of freedom, which are coupled directly (even at the one-body scale) for tumbling rotations.

- Further, these tumbling dynamics change the kinetics of the system. Without having explored the kinetics in detail, we have not seen the widespread dominance a *dense*, lying gel. Phase transition scenario (E) seems to be avoided – universally, even, for $L = 2, 3, 5, 9$.

Very long rods ($L = 9$) were investigated in the context of tumbling rotational dynamics, which seem to highlight and emphasize the collective, standing-up kinetics that generate loops in the packing fraction. Also, the standing island shape is diamond-like:

- The evolution at proper values of $1/|\epsilon|$ and F/D – for a phase transition scenario probably similar to (D) or (C) – is characterized by diamond-like standing islands, which later turn into strips and begin forming zig-zag patterns. These are also tied to large loops in the packing fraction during growth, which are related to steric inhibition of the lying phase and the highly irregular shape of the vacancies that open up once this phase eventually decays.

- Further, we see preliminary evidence for 2D demixing – of the two lying species of rods – at early stages of growth with very long rods. FMT predicts this transition for much lower rod-lengths, too. However, we fail to detect this clearly for $L = 3, 5$ in our growth simulations.

- Moreover, we find evidence for another kind of dynamical arrest in the case of $L = 9$, for tumbling rods, which is visible in the different topology of the "maps" of Q in the $(\ln(1/|\epsilon|), \log(D/F))$–plane. The lower-end of the D/F scale seems to entail an end-point (a "wall") for the gel line that might indicate the value of $1/|\epsilon|$ for a metastable transition, at the point of dynamical arrest of a portion of the degrees of freedom in the system.

We further explored dimers:

- Dimers show similarities to $L = 3$. At neutral substrates, we see evidence for behavior similar to phase transition scenario (B), (C), (D) in our range of parameters studied. Yet, there may be differences at higher reduced

temperatures, where FMT predicts two stable critical points. More simulation data and careful analysis over many observables would be necessary to clarify this feature.

- Owing to the even-valued length, the microscopic dynamics of rotations are of the (out-of-plane) tumbling- and (in-plane) shuffling-type, which affect the general phenomenology in a way explored for other rod-lengths: At neutral substrates, phase transition scenario (E) seems to be avoided (the wetting layer fails to form).

- At moderately strongly attractive substrates, dimers behave similarly to $L = 3$ at weakly attractive substrates, i.e. phase transition scenario (E) is recovered.

- At very strong substrates, we presume the 2D phase (lying) is stable, just like what happens for $L = 3$. The substrate potential u_{sub} is another axis controlling dynamical regimes in the monolayer, also for this case of $L = 2$.

- Regarding standing island morphology, square-like islands are seen for the dimers at high D/F, i.e. a near-equilibrium shape on the square lattice. At lower D/F, irregular standing islands that may have a diamond-like component can be spotted.

All of the phase transition scenarios discussed and their kinetics, which we are not fully explored for all cases, are unique to the nonequilibrium set-up of a *deposition quench*, i.e. to the driving force. Kinetics at constant densities could be investigated further upon reduced-temperature quenches, i.e. slow or rapid cooling (or heating), which we had begun to explore in this chapter, as well. However, owing to the new phenomenology, a deeper analysis of the large set of readily-simulated data for these other experiments – further including evaporation–deposition dynamics and interrupted growth – remains outside the scope of this thesis. Nonetheless, studies on annealing (heating) monolayers at constant densities provide further means to discover e.g. metastable phase boundaries. Relaxation of the system after interrupting the deposition process should offer a means to quantify a distance from equilibrium at any moment in time, via the relaxation time. Future work could quantify the relaxation times as a function of monolayer growth time, offering a unique window into e.g. a "free energy landscape" through which the system traverses as a function of $(F/D, 1/|\epsilon|, u_{\text{sub}}, \gamma)$. Further, evaporation–deposition dynamics emulate a system that can eventually reach grand-canonical equilibrium. The latter can "accelerate" the equilibration of the system, in that the lying, metastable phase is converted into the thermodynamically stable standing phase in lesser simulation time (scenario (D) will likely be possible in only a very narrow range of parameters). Yet, we have seen that a weak desorption rate can also quickly drive the formation of the metastable wetting layer (scenario (E)), from which we can simulate the growth of standing islands given the right conditions (a computationally difficult case to simulate with the monotonic-deposition setup). In scenarios (B) and (C), island sizes quickly increase (like the effect of a large diffusion coefficient D), as these dynamics correlate spatially separated regions efficiently. Therefore, weak-desorption experiments can aid in a fuller and preciser delineation of all dynamical regimes in the monolayer, as they will

allow us to simulate to later times, i.e. *later stages* of the phase transition kinetics, and because the system will "want" to reach the nearest quasistationary state much more quickly.

We have attempted to compare our results to the predicted phase diagrams from state-of-the-art equilibrium approaches (FMT for sticky hard rods) with the phenomena seen in our growth experiments. The FMT seems to capture some features correctly – such as the potentials for metastable phase separation involving fluids with different nematic order, as well as the "parent" vapor-liquid separation that indicates the formation of standing, stable-phase islands. However, we failed to find a metastable demixing transition between two rod-orientations in-plane for short rods. Further, we are not sure how to interpret all of the metastable transitions, e.g. one predicted to occur between two differently-ordered states at high number densities. We suspect this may correspond to the standing-up transition from the nearly-2D wetting layer (scenario (E)), but, clarification would be helpful. It would be interesting to try to extract the metastable critical densities from our simulations, at which we find the onset of different dynamical regimes (in temperature) — in the manner we proposed above using the crossing of the gel line with a jamming line, for example.

From a practical point-of-view, the work in this chapter represents a broad presentation of a novel, simple, generic model system for submonolayer growth with anisotropic molecules. Unlike many other studies of lattice models of rods with KMC simulations in the literature, we have attempted to incorporate information from thermodynamics, and discussed the the role of metastable phases. We have also found that these highly nonequilibrium systems are highly sensitive to the choice of moves in the simulation, an effect which is likely most pronounced at the submonolayer stage. The shape of islands and the morphological evolution are affected by a coupling between rotational and translational degrees of freedom at the *one-body* scale, in the (2+1)D ideal-gas limit. Further, the outcomes are dependent on the specific relative rates that include those of rotations, not only of F/D. Lastly, the nonequilibrium trajectories, and therewith the competition of various stable and metastable phases are again highly sensitive to any evaporation processes in the system (desorption). Therefore, we have shown how these model systems can be used to demonstrate the fundamental causes behind specific types of self-assembly phenomena, i.e. the phase transition kinetics. On the other hand, extreme caution must be taken in model presumptions, and experiments in the future should offer much more specific information before relying on simulation for interpretation. Specifically (and ideally), *each* system of interest should be characterized in the types of microscopic dynamics (in the vapor and at island times), their rates (order-of-magnitudes), the binding energies among particles in the quasi-2D setup, the binding energies to the substrates, and desorption rates. Otherwise, model simulations will unduly fail to provide specific parameter protocols for morphological evolution. If each system (molecule + substrate + deposition conditions) has a dramatically different phase diagram, including different (metastable) transitions, differences in outcomes of structure formation may be significant; however, we postulate that universal behavior may still be found if at least the thermodynamic properties like the multiplicity and relative positions of critical points of different systems remain similar. The proximity of a nonequilibrium evolution to equilibrium – given fixed control parameters – is a function of these critical

points. An aspect unexplored here is another choice of interaction potential, e.g. one that favors or suppresses tip-tip interactions. These will change the metastable phases (as the type of ordering can change), and therewith could, under conditions, unfold another competing phase during growth.

This work has also unveiled many points that we feel deserves further attention from a fundamental standpoint. For example, the "nucleation and growth" of the standing phase is *at least* a two-step process (seen in scenarios (B), (C), (D), and (E) – inhibited by a lying and lowly-ordered fluid phase or aggregate that in extreme cases becomes a gel, a liquid or a wetting layer. When the nucleation or growth of the standing phase occurs in terms of phase transition scenario (E) may also be a function of u_{sub}, which we would have to explore in the future. Nonetheless, *multi-step* "nucleation-and-growth" kinetics are of fundamental importance for many soft matter systems – from proteins to colloidal systems – and may occur in thin films of molecules form at surfaces, as well.

Further, we have emphasized and demonstrated the unique effects of (2+1)D confinement on systems of anisotropic particles, as well as one on a lattice, where a clear competition between lying and standing dense-phase orientations is manifested. Unlike atomistic models of submonolayer growth, the picture is much more intricate, complex and surprising: Both lying and standing phase can co-occur, wetting layers can form that may be unique to the first layer, and a 2D gel (network-forming, metastable phase) has been discovered. As the competing phases form and rearrange (and decay) at different rates and with different (power) laws, these monolayer systems show strong analogies to viscoelastic fluids that can be addressed in the future: they have the potential for two phases of matter with different intrinsic time-scales. Moreover, one of the phases is network-forming and forms a gel, a characteristic accompanying its inherent metastability. This discovery for the sticky-hard-rod model in monolayer confinement is quite intriguing, and would be most interesting to explore in other model systems (other lattices or off-lattice). We are not aware of literature addressing 2D gels in quasi-2D confinement anywhere else.

The sensitivity of the nonequilibrium systems of rods to the choice of microscopic dynamics, i.e. to the coupling of rotational and translational degrees of freedom even at the one-body level, is a somewhat surprising and fundamental point. Aspects like shape of islands and statistics thereof during growth will be altered accordingly. Unfortunately, this fact may be more than inconvenient for approaches using standard mean-field rate equations and classical nucleation models, as the microscopic degrees of freedom are "integrated out", per definition – and it is not clear how to perform such an integration for these highly correlative systems. Rod systems in confinement entail much more complexity in their behavior than point-like or atomistic model systems, generally speaking, and will represent a challenge for analytical theory. This high complexity coming from an arguably most simple model system might be a blessing, however, when venturing towards fundamentally new directions for nonequilibrium physics. For example, it would be interesting to explore this system with power functional theory. Moreover, these simulations can be seen as generator of configurations and motion, i.e. time-dependent datasets, stemming from a practically simple, *well-defined* nonequilibrium process. Therefore, we think such a model system could be very useful for fundamental questions

on machine learning, especially of inferring physical laws, as well as causality, by means of existing or new algorithms. We will explore machine learning on equilibrium data in Ch. 7, which is our first step in this direction.

Finally, the holistic view on submonolayer growth we have provided in this chapter should be very interesting for the community experimenting with growth with anisotropic organic molecules like thiophenes and conjugated molecules. Our findings in this chapter have strong places of overlap with many "unusual" reported effects of organic molecules during earliest stages of film growth – we had reviewed and discussed these in part I of this thesis.

The work presented in this chapter stands for the beginning of a number of research directions in which also more *specific* research questions around this model could also be addressed. A clear specification of the dynamical regimes in the $(\ln(1/|\epsilon|), \log(D/F))$–plane is the next logical step. Characterizing the jamming transitions and other potential arrested states at even lower D/F are important ingredients, and we proposed we may be able to determine estimates for critical points that are both stable and metastable be means of crossing points of e.g. the gel lines with the jamming transition points (or similar). Further, the percolation transitions during growth could also be charted into dynamical diagrams. The evaporation–deposition experiments, as well as heating or cooling, should aid in characterizing this diagram. As the dynamical setup is different, however, we suspect they will entail new effects and open up a whole new set of questions.

The apparent success of the FMT to capture many relevant features, at least from an equilibrium perspective, makes us hopeful that a DDFT-type approach may generate reasonable results. It would be most interesting if DDFT can model properly the formation of the network-forming gel, as analytical theories on gelation that directly incorporate many-body correlations (like the FMT) seem to be lacking in the literature.

Extended analysis of dynamical observables that we have presented like current fluctuations (correlations between fluxes), the latter of which is very feasible with the current analysis routines around simulation snapshots, are fundamental quantifiers of the nonequilibrium systems. Moreover from the technical side, we have readily implemented multilayer growth KMC simulations of sticky rods of any length. The deposition setup is similar to vapor-phase deposition experiments (see implementation in Refs. [168, 915]). This could open up a new chapter towards multi-layer growth that will very likely involve diverse dewetting transitions (i.e. of the 2D wetting layer seen in the monolayer) as well as a completely new kinetics.

This chapter has allowed us to engage with the complex, intricate, and fascinating character that many-body systems of short-ranged-attractive, hard-core-repulsive, and anisotropic particles can take on in driven nonequilibrium conditions. The particular case of a *lattice model* of hard rods for layer growth at substrate, in retrospect, seems an ideal theoretical system for investigating the role of translational and rotational degrees of freedom, as orientationally-ordered states distinguish themselves more potently in an on-lattice model, let alone one in confinement. We have seen competition of phases with two intrinsic length and time-scales. The metastable phases that enter the scene

might be inevitable precursors to the formation of compact islands. This comes in the form of lying, 2D gel or clusters. It can even form a wetting layer. As compact island formation and growth co-occurs, this model system highlights how dynamical asymmetries between differently-ordered states, accompanied by time-scale *overlap*, are an inherent part of a complex of kinetic pathways. Further, dynamical arrest and (metastable) critical points might be connected in very deep ways that are not obvious within the context of current status of statistical-mechanical theory.

Admittedly, monolayer growth of purely hard-core rods from Ch. 4 generated a much narrower variety of trajectories (or phase transition scenarios) than that of sticky hard rods. The exception we found is the case of jamming occurring under the influence of highly attractive substrate potentials. The central difference between "sticky" and purely hard-core rods is that in the former, coherent structures can form at large scales due to the phase separation processes involved. In turn, the collective dynamics entail much longer intrinsic time-scales (waiting times, relaxation times) as many more particles are directly involved.

The end of this chapter marks the end of part II of this thesis, where we have explored model systems for thin film growth of rod-like particles confined to a monolayer in an idealized lattice model. The next part of this thesis (part III) explores the *bulk* behavior of the same lattice model of hard rods – with regards to equilibrium (static) properties.

Part III

Phase Behavior of Hard Rods on Lattices in the 3D Bulk and 2D

Chapter 6

The Isotropic–Nematic Transition on Cubic and Square Lattices

It is not order only, but unexpected order, that has value.

Henri Poincaré

In this chapter, we shall present the phase behavior of lattice hard rods in the 3D (and 2D) that were mainly analyzed using GCMC simulations – a collaborative work based on two publications with multiple co-authors. We will state our contributions in Sec. 6.1 below. The introduction to this part of the thesis was provided in the introduction Ch. 1.3.

While the hard-rod system on lattices has been investigated extensively in the 2D case, an open gap in the literature persists for 3D systems. Additionally, the case of sticky rods is investigated, which has been investigated for 2D systems in a limited (weak) regime of "sticky" attractions, which we will discuss in this chapter. The 3D case has remained likewise unexplored. We focus on the isotropic–"nematic" transition, whereby we use the quotation marks because the ordering is not long-ranged. This will become clearer in the first half of this chapter. We also note that our investigations exclude a full characterization of high-density phases in 2D as well as 3D, where for both, other phase transitions or non-ergodic regions may occur.

In Ch. 4, the FMT for purely hard-core rods on lattices was presented. This constitutes a state-of-the-art theoretical approach that can also be applied to the 2D and 3D cases. We will present the results in this chapter. We note that this FMT has been further developed for short-range attractions using the depletion effect (the addition of "polymers") in Ref. [72]. This will be compared with our simulations for sticky rods in this chapter.

The scope of the research presented in this chapter addresses the following scientific questions: What are the conditions in which an isotropic–nematic transition occurs on cubic lattices, and is this comparable to that of continuum models, i.e. liquid crystal models for the bulk? What is this nature of this ordering transition, and what are the proper order parameters to describe it? What are the phase diagrams for the same systems with additional "sticky" (short-ranged) attractions between rods? How well does the lattice FMT perform, presented formally in Ch. 4, compared to the simulations? What does the addition of sticky attractions do to the ordering behavior of the system in full 2D confinement? What is the phase diagram of 2D sticky-hard-rod systems?

We have already discussed many basics on the physics of orientational ordering in the first part of this thesis, part I. More specifically, we reviewed isotropic–nematic ordering in continuum systems, as well as partially discretized systems and 2D systems in Ch. 1.3. Ordering in complex fluids of rod-like particles was discussed on a generic level in Ch. 2.1, where a coupling between rotational with translational degrees of freedom in a fluid lays behind the phase behavior, i.e. many-body, collective behavior. We provided a qualitative, preliminary discussion on the constraint of fluids (of rods) to lattices in Ch. 2.2.2. We discussed fundamentals of equilibrium statistical mechanics and Gibbs ensembles, Markov-Chain dynamics on lattices, as well as grand-canonical Monte Carlo simulations within Ch. 3.

6.1 Published work

This work and text in this chapter are based heavily on the following two publications:

> A. Gschwind, M. Klopotek, Y. Ai, and M. Oettel, "Isotropic–nematic transition for hard rods on a three-dimensional cubic lattice." In: *Physical Review E* 96.1 (July 2017), p. 012104. DOI: 10.1103/PhysRevE.96.012104.

> P. Quiring, M. Klopotek, and M. Oettel. "Nematic and gas–liquid transitions for sticky rods on square and cubic lattices". In: *Physical Review E* 100.1 (July 2019), p. 012707. DOI: 10.1103/PhysRevE.100.012707.

We state the contributions of the author of this thesis, "MK", below. We also mention that we have "moved" some of the *published* results from the publication corresponding to Ch. 4 to this chapter in Sec. 6.4, where we present all predicted results for an FMT for hard rods that correspond to 3D and 2D phase behavior.

Contributions of author (MK)

We have decided to present all of the quantitative results of the two above-mentioned publications in order to preserve the coherence of the results and scientific story. Our contributions are as follows:

Phys. Rev. E ***96****, 012104 (2017)*:
MK contributed to research in the context of co-supervision of student theses (bachelor and master), as well as supervising a summer internship with Y. Ai in the context of a *DAAD RISE* scholarship. The GCMC as well as successive umbrella sampling simulations were written and developed under the co-supervision of MK. MK wrote a portion of the discussion section of the paper (comparison to other hard-rod-like systems), and contributed to editing the manuscript. MK contributed to the planning, description, and final editing of multiple figures, and generated Figs. 6.2(b)–(c) herself.[1]

[1] MK also provided minor help in the submission process as well as in the correspondence with the editor and reviewers.

Phys Rev. E ***100****, 012707 (2019)*:
MK contributed to research in the context of co-supervision of student theses (bachelor and master). The GCMC as well as successive umbrella sampling simulations were written and developed under the co-supervision of MK (this paper represents a succession of the research presented in the previous paper.) MK wrote a portion of the introduction (on 2D systems), and contributed to editing the text and figures of the paper. MK was responsible for the full submission process and corresponded with editors and reviewers.

We have modified and added to the discussions, and have re-written the conclusions, which are contained in Secs. 6.8 and 6.9, accordingly (see next section on the organization of this chapter). We have re-written and extended significantly the introductory discussion on these topics in Ch. 1.3 of this thesis. A deeper background can be found when reading the generic discussion on the physics of hard-rod systems in Ch. 2. At an even more fundamental level, we discussed equilibrium statistical mechanics, dynamics on lattices, as well as the intimately-related Markov-Chain Monte Carlo methods in Chs. 2 and 3.

6.2 Organization of this chapter

The organization of this chapter is as follows: In Sec. 6.3 we specify the model studied in the first part of this chapter – that of purely hard-core rods, which serves as the most basic case. We present results of an FMT for purely hard-core lattice system of hard rods in Sec. 6.4, where this lattice FMT for rods was presented for the first time in Ch. 4 for the case of (2+1)D confinement. In Sec. 6.5 we present simulation results on 3D systems of purely hard-core rods, where we will discover that a lattice system of long rods entails a very weak first-order isotropic–nematic transition. We will also discover that a suitable orientational order parameter for the 3D system of rods on lattices is, in fact, *two-dimensional*, which we describe at the end of Sec. 6.5. We then move on to the same lattice systems of hard-core rods with sticky attractions in the 3D in Sec. 6.6, where the isotropic–nematic becomes strongly first-order at low reduced temperatures. We will study the phase diagrams. We will also present results on the ordering transitions and phase diagram of a 2D system of sticky hard rods, which we will see entails a tricritical point, in Sec. 6.7. (These 2D systems will be used in a study on machine learning in the next chapter, Ch. 7.) We have provided a lengthy discussion in Sec. 6.8, where we also discuss ideas and open issues as an outlook of the work presented chapter. Our conclusions are provided in Sec. 6.9.

6.3 The hard-rod model on cubic lattices

We consider a simple cubic lattice in 3D, the unit cell length is set to 1. Hard rods are parallelepipeds with extensions $L \times 1 \times 1$ and corners sitting on lattice points. The position of a rod is specified by the corner whose lattice coordinates are minimal each. They are allowed to touch (i.e., share corners or faces), but, forbidden to overlap. The cubic lattice restricts possible orientations to three, and we refer to rods oriented in x-, y-, and z-directions as species 1, 2, and 3, respectively. Species densities ρ_i are defined as number of rods of species i (N_i) per lattice site, $\rho = \rho_1 + \rho_2 + \rho_3$ is the total density and $\eta = \rho L \leq 1$ is the total

packing fraction. We introduce bulk nematic order parameters Q_i and biaxiality order parameters S_i by

$$Q_i = \frac{\rho_i - \frac{\rho_j+\rho_k}{2}}{\rho} , \tag{6.1}$$

$$S_i = \frac{\rho_j - \rho_k}{\rho_j + \rho_k} , \tag{6.2}$$

where (ijk) is a cyclic permutation of (123).

An allowed configuration of the system is given by the set of all rod positions $\mathcal{S} = \{\mathbf{s}_{j,k}\}$ where $j = 1, 2, 3$ indicates the species and $k = 1 \ldots N_j$ the rod number and in which the rods do not overlap. The total number of allowed configurations is denoted by $\mathcal{N}(\{N_j\})$. The grand partition function of the system is defined by

$$\Xi(z_i) = \sum_{i=1}^{3} \sum_{N_i=0}^{\infty} \frac{z_i^{N_i}}{N_i!} \mathcal{N}(\{N_j\}) , \tag{6.3}$$

where $z_i = \exp(\beta\mu_i)$ is the fugacity of species i ($\beta = 1/(k_\mathrm{B}T)$ is the inverse temperature and μ_i is the chemical potential of species i). In a bulk system all z_i are equal, $z_i = z$. Note that the 3 possible particle orientations can be treated as an internal property of particles such that the grand partition function in the bulk can be written alternatively as a single sum over the total number of particles:

$$\Xi(z) = \sum_{N=0}^{\infty} \frac{z^N}{N!} \mathcal{N}'(N) , \tag{6.4}$$

where $\mathcal{N}'(N)$ is the total number of allowed configurations having N particles with three possible orientations each. The grand canonical average of an observable $A(\{N_j\})$ is defined by

$$\langle A \rangle = \frac{1}{\Xi} \sum_{N=0}^{\infty} \frac{z^N}{N!} \sum_{\mathcal{S}} A(\{N_j\}) . \tag{6.5}$$

6.4 Lattice-FMT (theory) for purely hard-core rods in 2D and 3D

Note: The author of this thesis did not *contribute in a major way to the results in this section (Sec. 6.4). They are reproduced from a co-authored publication listed at the beginning of Ch. 4. We present these, nonetheless, to complete a fuller picture of lattice models of hard rods.*

A general FMT functional for hard rod mixtures on lattices with arbitrary dimensions has been derived by Lafuente and Cuesta [159, 160]. For our specific case of interest – of rods with length L and width 1 – please consult to the basic definitions provided in Ch. 4.4. Therein we presented the FMT for rods for the first time in the context of hard-rod monolayers.

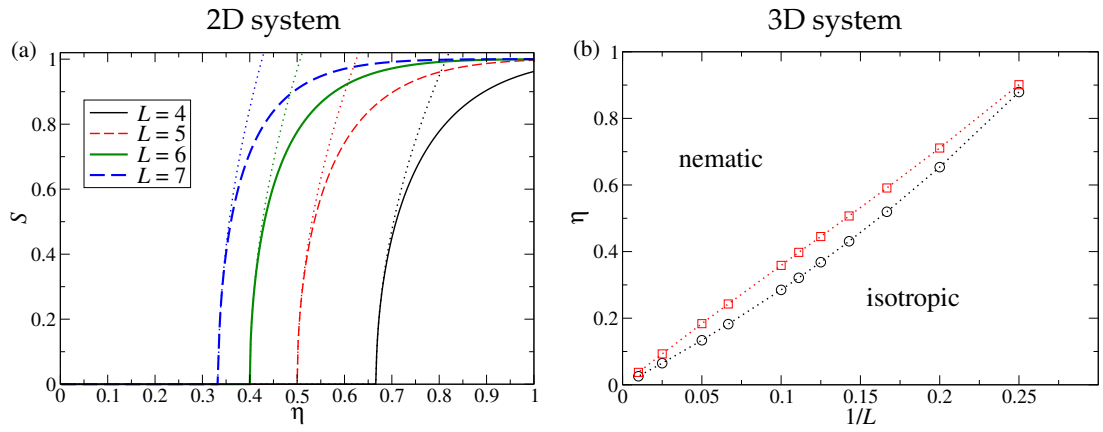

FIGURE 6.1: (a) FMT results for purely hard-core rods in 2D: Demixing order parameter S as a function of the total packing fraction for different rod lengths L. Dotted lines correspond to the approximate solution near the onset of demixing (Eq. (6.16)). (b) Corresponding results for the 3D bulk. Liquid–nematic binodal in the plane spanned by the inverse rod length $1/L$ and the packing fraction η. Square symbols show the packing fraction of the coexisting nematic state, circles the packing fraction of the coexisting liquid state.

We need the free energy density in the 3D bulk, homogeneous case for the present chapter:

$$f = f^{\mathrm{id}} + f^{\mathrm{ex}} \qquad \text{with} \tag{6.6}$$

$$\beta f^{\mathrm{id}} = \sum_{i=1}^{3} \rho_i \ln \rho_i - \rho \,, \tag{6.7}$$

$$\beta f^{\mathrm{ex}} = \Phi^{\mathrm{0D}}(L\rho) - \sum_{i=1}^{3} \Phi^{\mathrm{0D}}\left((L-1)\rho_i\right) \,. \tag{6.8}$$

Here, $\beta = 1/(k_{\mathrm{B}}T)$ is the inverse temperature which is set to 1 and

$$\Phi^{\mathrm{0D}}(\eta) = \eta + (1-\eta)\ln(1-\eta) \,. \tag{6.9}$$

is the excess free energy of a zero–dimensional cavity (which can hold no or only one particle) depending on its average occupation $\eta = [0,1]$. The equilibrium bulk state is found by minimizing f at constant total density ρ with respect to the order parameters $Q \equiv Q_i$ and $S \equiv S_i$ (for one specific i). We have found stable states only for $S = 0$ and $Q \geq 0$. Isotropic–nematic coexistence is determined by equating the chemical potential $\mu = \mu_1 = \mu_2 = \mu_3$ (with $\mu_i = \partial f/\partial\rho_i$) and pressure $p = \mu\rho - f$ between the isotropic and nematic states.

Two dimensions: the binary mixture with rod lengths $\mathbf{L}_1 = (L,1)$ and $\mathbf{L}_2 = (1,L)$

In the bulk, both densities (ρ_1 and ρ_2) and all weighted densities are constant. We introduce the total density $\rho := \rho_1 + \rho_2$ and denote by $\eta := n^{(1,1)} = L\rho$ the total packing fraction. Furthermore, $n^{(0,1)} = (L-1)\rho_1$, $n^{(1,0)} = (L-1)\rho_2$ and

$S = (\rho_1 - \rho_2)/\rho$ is an order parameter for the demixed state. We refrain from calling S a nematic order parameter, since the alignment of rods corresponds just to a demixed state between species 1 and 2, and the corresponding transition has the character of a liquid–vapor transition [356]. The bulk free energy density, $f_{2d}(\rho, S) = f_{2d}^{\mathrm{id}} + f_{2d}^{\mathrm{ex}}$, written in dependence on the variables ρ and S becomes

$$f_{2d}^{\mathrm{id}} = \sum_{i=1}^{3} \rho_i \ln \rho_i - \rho \,, \tag{6.10}$$

$$f_{2d}^{\mathrm{ex}} = \Phi^{0d}(\rho L) - \Phi^{0d}\left((L-1)\rho_1\right) - \Phi^{0d}\left((L-1)\rho_2\right) \,, \tag{6.11}$$

$$\rho_1 = \frac{\rho}{2}(1+S) \,, \tag{6.12}$$

$$\rho_2 = \frac{\rho}{2}(1-S) \,. \tag{6.13}$$

At fixed ρ, the equilibrium demixing parameter S_{eq} is found by solving $\mu_S = \partial f_{2d}/\partial S = 0$. For $L \leq 3$, the mixed state ($S_{\mathrm{eq}} = 0$) is the only solution and f is minimal there, For $L \geq 4$ there exists a critical packing fraction $\eta_c < 1$ above which three solutions $S = \{0, \pm S_{\mathrm{eq}}\}$ signal demixing: The solutions $S \neq 0$ have lower free energy. At η_c, there is no jump in the demixing parameter which is the behavior also observed at a liquid–vapor transition. One may thus expand

$$\mu_S(\eta, S) \approx \mu_{1,S}(\eta) S + \mu_{3,S}(\eta) S^3 + \ldots \tag{6.14}$$

and find the critical packing fraction by solving $\mu_{1,S}(\eta_c) = 0$, with the solution

$$\eta_c = \frac{2}{L-1} \,. \tag{6.15}$$

The equilibrium demixing $S_{\mathrm{eq}}(\eta)$ in the vicinity of η_c can be approximated by solving $\mu_S = 0$ for S using the Taylor approximation (6.14), giving

$$S_{\mathrm{eq}} = \sqrt{-\frac{\mu_{1,S}(\eta)}{\mu_{3,S}(\eta)}} \approx \sqrt{\eta - \eta_c}\,\sqrt{\frac{3}{2(L-2)}}(L-1) \,. \tag{6.16}$$

The behavior of $S_{\mathrm{eq}}(\eta)$ near η_c born out by the approximate theory is, of course, of mean-field type.

These findings can be compared with simulation work which finds the demixing transition for $L \geq 7$ [366] and a critical packing fraction $\eta_c \approx 5/L$ [363]. Thus, FMT overestimates the tendency to demix. Note, however, that the demixing follows from a *single* functional, unlike other approaches which assume distinct expressions for the isotropic and the demixed phase free energies [363]. For very high packing fractions $\eta \approx 1$, theoretical arguments predict a reentrant transitions from the demixed to a disordered state which bears some characteristics of a cubatic phase on a lattice [366]. This transition has been studied in more detail using simulations in Refs. [367, 368]. The present FMT functional, however, does not give this transition. For rods with extensions $m \times mL$ (where m, mL are integer and L may be non-integer), the phase diagram has been investigated in Ref. [365, 369], where (for $m > 1$) it is shown that a columnar phase appears between the demixed and high-density disordered phase.

Three dimensions: the ternary mixture with rod lengths $\mathbf{L}_1 = (L,1,1)$, $\mathbf{L}_2 = (1,L,1)$ and $\mathbf{L}_3 = (1,1,L)$

The total density is $\rho = \rho_1 + \rho_2 + \rho_3$ and the total packing fraction is $\eta := n^{(1,1,1)} = L\rho$. We define the order parameters

$$\begin{aligned} Q &= \frac{\rho_3 - \frac{\rho_1+\rho_2}{2}}{\rho_1+\rho_2+\rho_3}\,, \\ S &= \frac{\rho_1-\rho_2}{\rho_1+\rho_2}\,. \end{aligned} \tag{6.17}$$

$Q \neq 0$ signifies an excess ($Q > 0$) or depletion ($Q < 0$) of particles in z–direction (nematic state) while $S \neq 0$ signals order in the x–y–plane orthogonal to the nematic director (biaxial state). The bulk free energy density, $f_{3d}(\rho,Q,S) = f_{3d}^{\mathrm{id}} + f_{3d}^{\mathrm{ex}}$, written in dependence on the variables ρ, Q and S becomes

$$f_{3d}^{\mathrm{id}} = \sum_{i=1}^{3} \rho_i \ln \rho_i - \rho\,, \tag{6.18}$$

$$\begin{aligned} f_{3d}^{\mathrm{ex}} = {} & \Phi^{0d}(L\rho) - \Phi^{0d}\left((L-1)\rho_1\right) \\ & - \Phi^{0d}\left((L-1)\rho_2\right) - \Phi^{0d}\left((L-1)\rho_3\right)\,, \end{aligned} \tag{6.19}$$

$$\rho_1 = \frac{\rho}{3}(1-Q)(1+S)\,, \tag{6.20}$$

$$\rho_2 = \frac{\rho}{3}(1-Q)(1-S)\,, \tag{6.21}$$

$$\rho_3 = \frac{\rho}{3}(1+2Q)\,. \tag{6.22}$$

Minimization of the total free energy density with respect to Q and S shows that the model has a stable nematic state ($Q = Q_{\min} > 0$, $S = 0$) for $L \geq 4$. Note that the director could also be oriented along the x– or y–axis instead of the chosen z–axis. A pure nematic state with director along the $x[y]$–axis and order parameter Q' is equivalent to a minimum free energy state with $Q = -Q'/2$ and $S = \pm 3Q'/(2+Q')$ using the order parameters (6.17). This is therefore not a biaxial state. The associated liquid–nematic transition is of first order, and we have determined coexistence between the liquid and the nematic state by performing the common tangent construction for the free energy density $f_{3d}(\rho,0,0)$ (liquid phase) and $f_{3d}(\rho,Q_{\min},0)$ (nematic phase), which implies equality of the chemical potential $\mu = (\partial f_{3d})/(\partial\rho)$ and pressure $p = \mu\rho - f_{3d}$. Results are shown in Fig. 6.1(b). The packing fractions of the coexisting nematic state are very well described by $\eta_{\mathrm{c,nem}} = 3.58/L$, and the gap in packing fractions of the coexisting states has a maximum of ≈ 0.08 at $L = 8$ and tends to zero as $L \to \infty$.

Note that for off-lattice ellipse systems in 3D, the critical aspect ratio is around $L_c \approx 4$ [336].

* * *

The lattice FMT that has been presented here will be used to predict the isotropic–nematic transition at different rod-lengths L. We compare these *directly* to our GCMC simulations in forthcoming Sec. 6.5.3.

6.5 Simulation results for the isotropic–nematic transition of hard-core rods on cubic (3D) lattices

Note: The following results and discussions are almost identical to those in the corresponding publication listed at the beginning of this chapter. The author of this thesis contributed to the research method described in Sec. 6.5.1, as well as to research and results of Secs. 6.5.2, 6.5.4, and 6.5.5. The results in Sec. 6.5.3 are outside of the scope of our contribution, which we have nevertheless presented here for completeness.

6.5.1 Grand canonical Monte Carlo (GCMC) simulations for purely hard-core rods

We have simulated the model on cubic lattices with size $V = M^3$. We have worked with lattice sizes between $M = 50$ and $M = 170$, depending on rod length. In each step, a particle insertion attempt or deletion attempt was chosen with probability $1/2$. For an insertion move, the orientation and the position of the particle was picked randomly. For the deletion move, one of the particles in the system was chosen randomly. Detailed balance was obeyed: the insertion move was accepted with a probability $\min(1, 3zV/(N+1))$ if it led to an allowed configuration, and the deletion move was accepted with a probability $\min(1, N/(3zV))$. N indicates the number of particles before the insertion/deletion move was attempted.

To compute densities and orientation variables, we stored various "time" series of the rod numbers $N_i(t)$, measured every 10^7 moves (otherwise noted). In isotropic states, $N_i(t)$ fluctuated around $\langle N \rangle /3$, and equilibrium was reached promptly. On the other hand, one species having a pronounced majority was a typical sign of being in e.g. the nematic state; there, intervals of alternating majority species were observed in the time series. We assumed full equilibration of the system if of the order of 10 such intervals occurred. This criterion was of course difficult to fulfill deep in the nematic phase. The collected time series were used to calculate averages $\langle A \rangle$ and probability density distributions $P(A)$ (histograms).

The signature of a first–order transition in a GCMC simulation is usually a double peak in the probability density distribution $P(N)$, and the peaks should have equal area at coexistence (fugacity z_{coex}). In the vicinity of coexistence between an isotropic and a nematic state with excess of *one* species, the probability density distribution of one of the nematic order parameters (say $P(Q_1)$) should furthermore exhibit three peaks: one peak centered at $Q_1 \approx 0$ and two peaks centered at $Q_1 = q > 0$ and $Q_1 = -q/2$, where the second peak corresponds to the species 2 or 3 being the majority species. Consider the distribution $P(Q_{\max})$ with $Q_{\max} = \max_i(Q_i)$: it should exhibit a double–peak structure located at $Q_{\max} \approx 0$ and $Q_{\max} = q > 0$. On the other hand, a transition to a nematic state with excess of *two* species is best observed via the distribution $P(Q_{\min})$ with $Q_{\min} = \min_i(Q_i)$. It should likewise exhibit a double–peak structure located at $Q_{\min} \approx 0$ and $Q_{\min} = q < 0$.

A negative nematic order parameter in continuum models for rods would correspond to rods preferentially orienting perpendicular to a director. This has *not* been reported in the literature for *uniaxial* hard rods like those in our lattice model.

6.5.2 Main findings for rod-lengths $L = 5 \ldots 25$

To detect a first order transition, we seek to find a double peak in the histograms of particle number $P(N)$, which would be indicative of a density gap. However, for all rod lengths up to $L = 25$, it was too hard to detect any clear sign of a double peak in $P(N)$, indicating that a hypothetical density difference between isotropic and nematic states is very narrow.

For $L = 5$, the distributions $P(Q_{\min})$ and $P(Q_{\max})$ show a single peak near zero for packing fractions up to 0.9 ($z = 95$), indicating a stable isotropic phase. Yet analysis below and in further sections of this chapter shows that $L = 5$ and $L = 6$ show an "unusual" nematic phase, and for $L = 5$ this occurs at very high fractions, indeed. For $L = 6$, upon varying fugacity z between 2.2 and 2.9, $P(Q_{\min})$ transforms from one fairly sharp peak near zero, via a very broad peak (resulting from an overlap of two broad peaks), and finally to a moderately sharp peak at $Q_{\min} < 0$. The nematic transition goes from anisotropic state to a nematic state with two excess species (negative order parameter). Results for $P(Q_{\min})$ for several z (illustrating this transition) are shown in Fig. 6.2(a), and a series of snapshots in Fig. 6.2(c), which display cuts in the plane defined by the two excess species for $z = 3.8$ (in the nematic phase). The snapshots show that the system separates into weakly coupled layers that are effectively only populated by the excess species (i.e. 2D systems). Therefore, the transition is effectively a $2D$ transition, yet for $L < 7$, it is well-established that there is no 2D nematic demixing [366]. Hence the layered 2D configurations will be isotropic in-plane. We note that $Q_{\min}$ (or $Q_{\max}$)—in contrast to N—is particularly sensitive to incomplete thermalization of the system (i.e. insufficient exploration of all possible equilibrium configurations), which happens with the local algorithm used once this layering occurs.

For $L \geq 7$, upon varying z, $P(Q_{\max})$ transforms from having one peak near zero, via a broad two-peak structure, and finally to a single peak with its maximum at $Q_{\max} > 0$. This indicates a transition from an isotropic state to a nematic state with one excess species (positive order parameter). $P(Q_{\max})$ and $P(\eta)$ are shown in Fig. 6.3 for rod lengths 8 and 25, among several values of z, respectively. The vicinity of coexistence is characterized again by two peaks in $P(Q_{\max})$ smeared out broadly, yet the corresponding peaks in $P(\eta)$ show no sign of splitting or of significant broadening. Therefore, the transition must entail a very small density gap, pointing to a weak first order transition, at most.

As discussed in part I of this thesis quite generally, variances in order parameters will be indicators of phase transition points. We define the variances $\mathrm{Var}(Q_{\max}(z)) = \langle Q_{\max}^2 \rangle - \langle Q_{\max} \rangle^2$ (likewise for $\mathrm{Var}(Q_{\min})$). The maximum of $\mathrm{Var}(Q_{\max}(z))$ or $\mathrm{Var}(Q_{\min}(z))$ signals the point of strongest orientational fluctuations, and is hence used to locate the coexistence fugacity.

For $L = 8$ as an example, we have investigated finite-size effects on the behavior of $\langle Q_{\max}(z) \rangle$ and $\mathrm{Var}(Q_{\max}(z))$ more closely to examine their influence on the isotropic–nematic transition point. Fig. 6.4 shows these functions when varying the lattice extension from $M = 50$ to 168. For a first order transition, $\langle Q_{\max}(z) \rangle$ should exhibit a jump at z_{coex}, whereas z_{coex} would be a bifurcation (critical) point for a second order transition. In any case, a finite system size smears the jump or bifurcation. With increasing M, $\langle Q_{\max}(z) \rangle$ becomes steeper in the coexistence region (see Fig. 6.4(a)). The curves intersect at a common point for lattice extensions between 50 and 64, indicative of a second-order

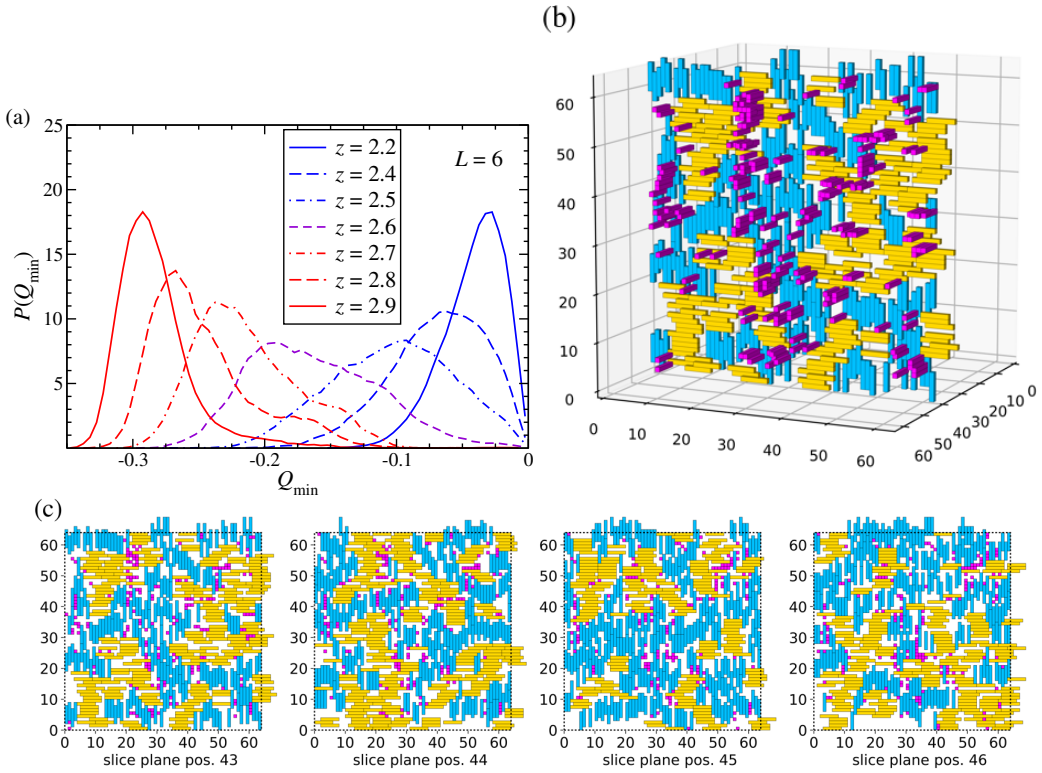

FIGURE 6.2: Purely hard-core rods: (a) The distribution $P(Q_{\min})$ from GCMC for $L = 6$ ($M = 75$, bin size $\delta Q = 0.005$) and for several fugacity values between $z = 2.2$ (isotropic state), $z = 2.6$ (near coexistence) and $z = 2.9$ (nematic state). Near coexistence the maximal relative error estimates in the middle of the histogram are (possibly exaggerated) at $\sim 40\%$, attributed to by $Q_{\min}$ de-correlating very slowly. (b) Illustration: A slice through the preferred plane in the nematic phase with negative order parameter. (c) Slices in the preferred plane at subsequent lattice points on the plane normal: One sees very few particles of the minority species and the particle positions of the majority species (patches of horizontal and vertical particles) do not correlate between the subsequent layers, thus the slices approximately correspond to independent 2D rod systems. Snapshots are for $z = 3.8$, $M = 64$.

transition. However, the intersection shifts to a lower value of z for $M = 100$ and more so for $M = 168$, pointing toward a weak first order transition, consistent with the smeared two–peak structure in $P(Q_{\max})$. The corresponding behavior of $\mathrm{Var}(Q_{\max}(z))$ is shown in Fig. 6.4(b): its peak sharpens and slightly shifts to lower z for increasing M. The peak position for the largest lattice extension $M = 168$ is what we use to define z_{coex}. The peak height in $\mathrm{Var}(Q_{\max}(z))$ shrinks with increasing M. This is not quite consistent with a first–order transition for which the peak height should stay constant. One sees that the average $\langle Q_{\max} \rangle$ at coexistence (Fig. 6.4(a)) decreases for increasing lattice size. The order parameter is below 0.1 at coexistence for $M = 168$. We additionally performed a finite-size analysis using two-dimensional order parameters known from three-state Potts models in Sec. 6.5.5 for the system with $L = 8$. It points towards a weak first-order transition, but we cannot rule out a continuous transition with certainty.

Figures 6.4(c) and (d) show $\langle Q_{\max}(z)\rangle$ and $\mathrm{Var}(Q_{\max}(z))$ in the transition region for rod length $L = 25$ and large lattice extension ($M = 170$). Here, the peak in the variance $\mathrm{Var}(Q_{\max}(z))$ is readily pronounced for this lattice size, and the average value $\langle Q_{\max}(z)\rangle$ is around 0.2 at coexistence, i.e. it is larger than for $L = 8$, but the increase is very moderate. There is no evidence that a sizeable jump in nematic order takes place at coexistence.

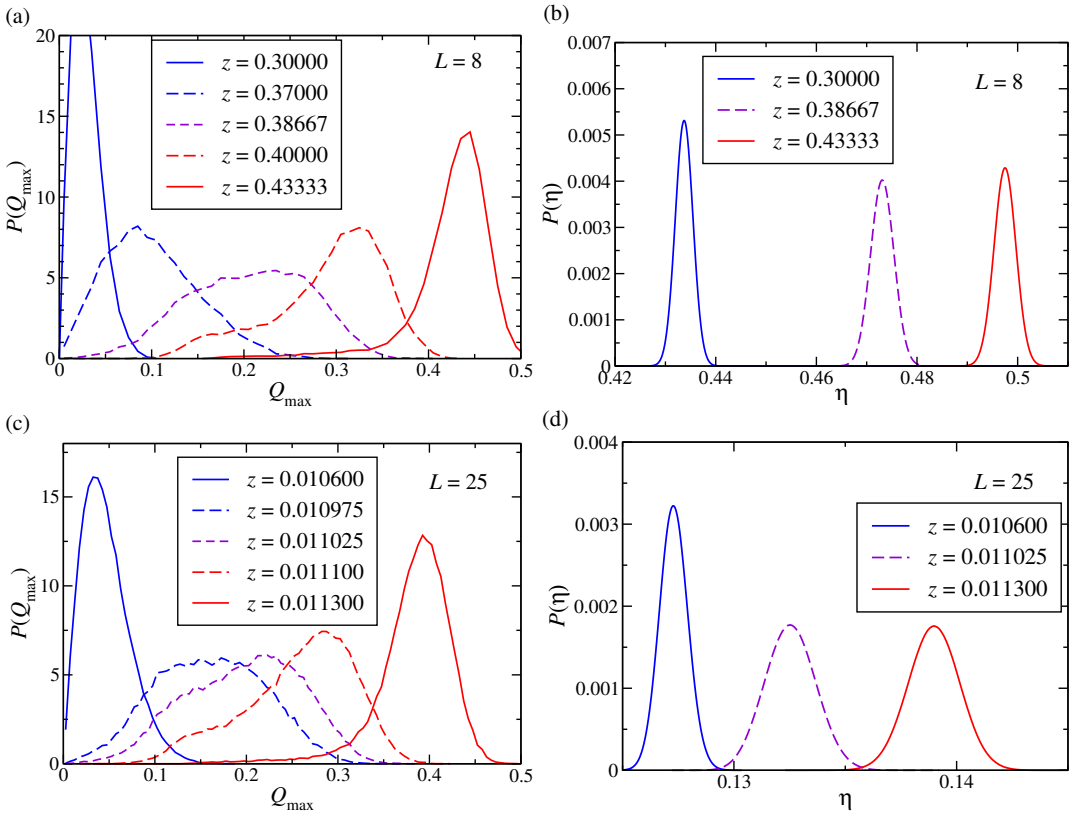

FIGURE 6.3: Purely hard-core rods: (a) The distribution $P(Q_{\max})$ from GCMC for $L = 8$ ($M = 70$, bin size $\delta Q = 0.01$, measured every $5 \cdot 10^7$ MC moves) and for several fugacity values between $z = 0.1$ (isotropic state), and $z = 0.43333$ (nematic state). The maximal relative errors in the middle of the histograms near coexistence ($z = 0.37000$, $z = 0.38667$) are estimated at $\sim 8\%$. (b) The corresponding distribution $P(\eta)$ for three fugacity values $z = 0.1$ (isotropic state), $z = 0.38667$ (near coexistence) and $z = 0.43333$ (nematic state) (all measured every MC move). The maximal error estimates at the peaks of the histograms are smaller than the line thickness. (c) The distribution $P(Q_{\max})$ from GCMC for $L = 25$ ($M = 170$, bin size $\delta Q = 0.005$, measured every 10^7 MC moves) and for several fugacity values between $z = 0.0106$ (isotropic state), and $z = 0.0113$ (nematic state). The maximal relative errors in the middle of the histograms near coexistence are estimated at $\sim 6 - 8\%$. (d) The corresponding distribution $P(\eta)$ for three fugacity values $z = 0.01$ (isotropic state), $z = 0.011025$ (near coexistence) and $z = 0.0113$ (nematic state) (all measured every MC move). The maximal error estimates at the peaks of the histograms are smaller than the line thickness.

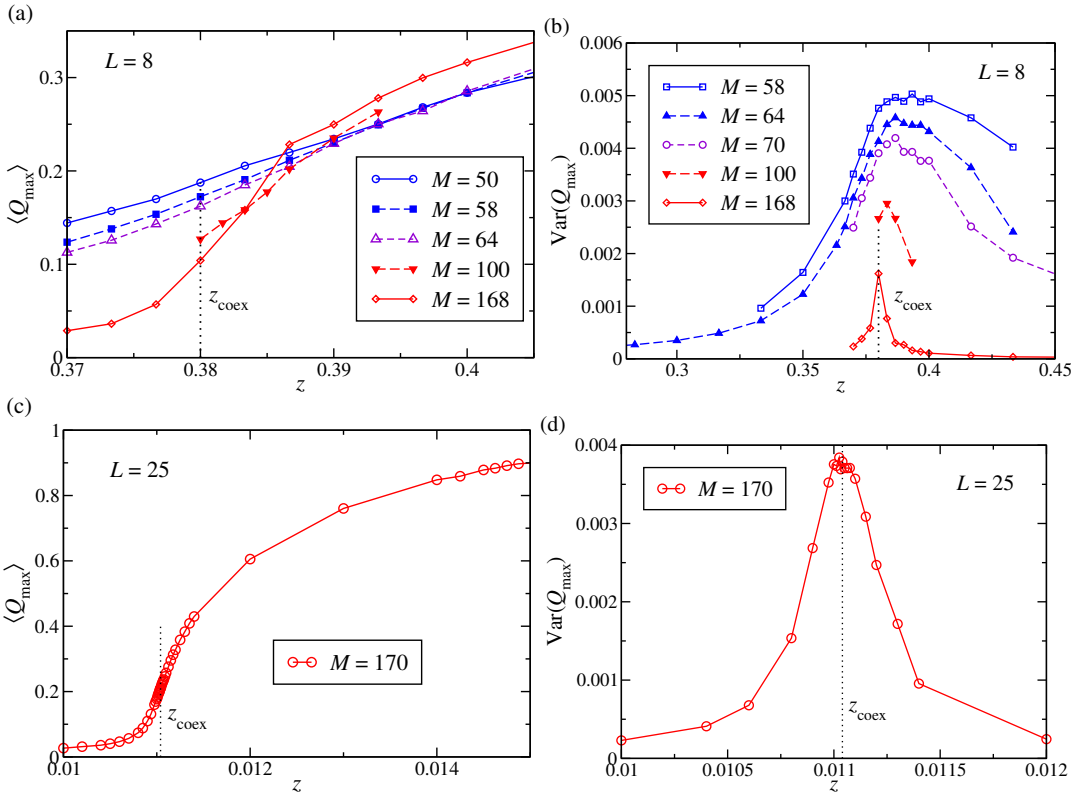

FIGURE 6.4: Purely hard core rods: (a) Average value $\langle Q_{\max}(z)\rangle$ in the transition region from GCMC for $L = 8$ and lattice extensions ranging from $M = 50$ to $M = 168$ (measured every $5 \cdot 10^7$ MC moves for $M = 64, 70, 100$, every 10^7 otherwise). The location of the coexistence fugacity z_{coex} is determined by the peak position of $\text{Var}(Q_{\max}(z))$ for the largest lattice site. The maximal relative errors for $\langle Q_{\max}\rangle$ near coexistence are estimated to less than 1% for $M = 168$, attributed to by the small variance (see (b)) at large system size. (b) The variance $\text{Var}(Q_{\max}(z))$ in the transition region for $L = 8$ and lattice extensions ranging from $M = 50$ to $M = 168$. (c) Average value $\langle Q_{\max}(z)\rangle$ in the transition region for $L = 25$ and lattice extension $M = 170$. (d) The variance $\text{Var}(Q_{\max}(z))$ in the transition region for $L = 25$.

6.5.3 Comparison to lattice FMT

Lattice FMT predicts a strong first order transition for $L \geq 4$ to a nematic state with one excess species (positive order parameter), as discussed in Sec. 6.4. We did not find stable states with a negative order parameter. The phase diagram resulting from FMT and GCMC is shown in Fig. 6.5. As described before, we were not able to detect a density gap between isotropic and nematic states in our GCMC simulations. Surprisingly, GCMC simulations and the FMT show similar packing fractions for the coexistence state. We have investigated this more closely by examining $\langle \eta(z) \rangle$ and $\langle Q_{\max} \rangle (\langle \eta \rangle)$.

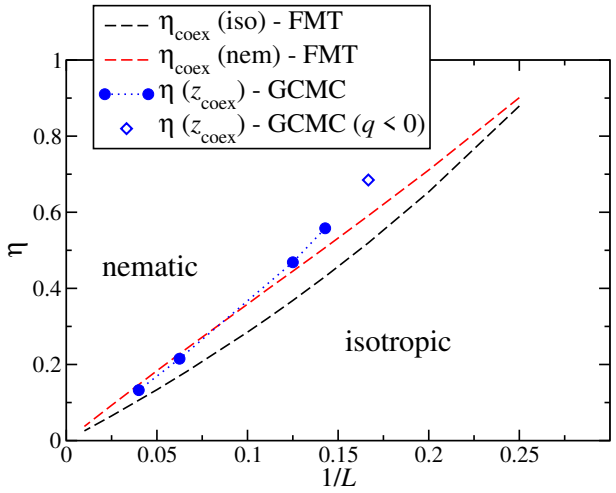

FIGURE 6.5: Phase diagram of the purely hard-core rod model in the $1/L$–η plane: Comparison between FMT (dashed lines) (coexisting nematic states in red and coexisting isotropic states in black) and GCMC simulations (blue symbols). For $L = 7, 8, 16$ and 25 the nematic state has a positive order parameter (full symbols), whereas for $L = 6$ the nematic state has a negative order parameter (open symbol).

The behavior of $\langle \eta \rangle (z)$ is captured very well by FMT, except for some mild disagreement in the coexistence region, see Fig. 6.6. A system with very short rods ($L = 2$) resembles rather a hard lattice gas (no phase transition), and so the FMT results lie on top of the GCMC data. With longer rods $L = 8$ and 25 the high- and low-density limits render good agreement with GCMC, but near coexistence the FMT data show a van der Waals loop characteristic for a first order transition (visible for $L = 8$). This is absent in the simulations.

A side-by-side comparison of $\langle Q_{\max} \rangle (\langle \eta \rangle)$ unveils stronger disagreement, see Fig. 6.7. For $L = 8$, FMT predicts much more pronounced nematic order for a given z. The closeness of the values for η_{coex} (GCMC) and η_{coex} of the nematic state (FMT) thus might only be a serendipitous accident. For $L = 25$, the FMT and GCMC results agree somewhat more. It is actually not clear whether FMT and GCMC would agree in the limit $L \to \infty$ in the vicinity of the nematic transition. FMT renders the correct second and third virial coefficient, and deviates from the fourth on. Although the nematic transition shifts to lower packing fraction with increasing L, higher virial coefficients affect the particular location of the transition, as Zwanzig analyzed in the case of a hard rod model with restricted orientational and continuous translational degrees of freedom [355]. This is not the case for hard rod models with continuous orientations,

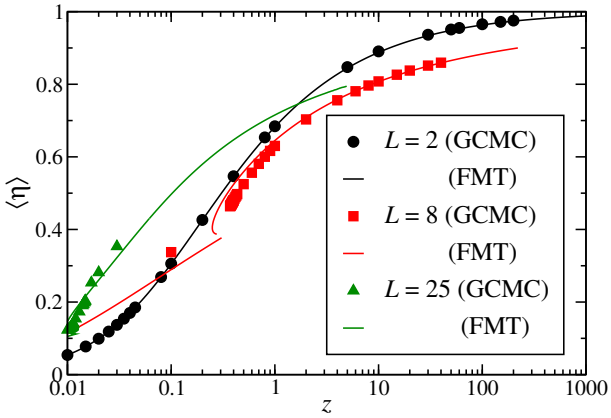

FIGURE 6.6: The expectation value of the packing fraction $\langle\eta\rangle$ as a function of the fugacity z for rod lengths $L = 2$, 8 and 25 in the purely hard-core rod model: Comparison between FMT results (full lines) and GCMC simulations (symbols)(error bars are smaller than the symbols). The van der Waals loop on the green curve is hidden near $z \approx 0.01$.

where it can be expected that a second–virial approximation is sufficient for $L \to \infty$ [355].

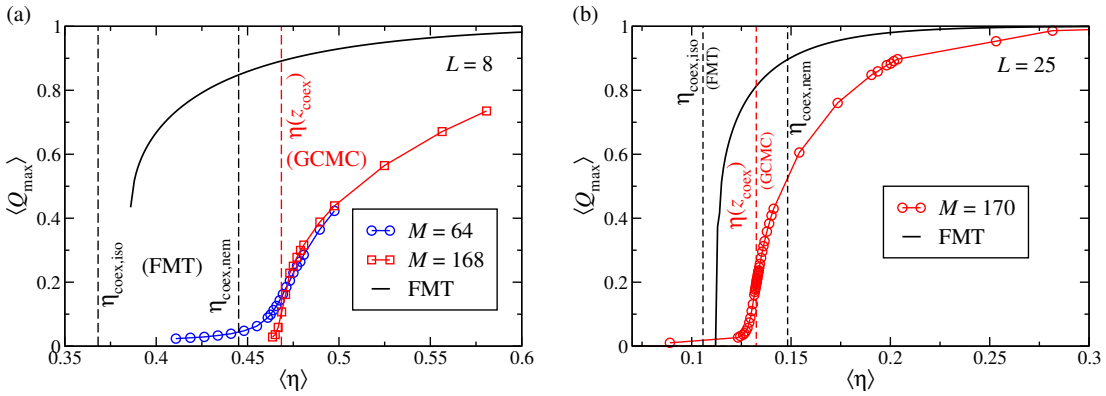

FIGURE 6.7: The expectation value $\langle Q_{\max}\rangle$ as a function of the expectation value $\langle\eta\rangle$. Black lines are FMT results, black dashed lines mark the packing fractions at coexistence from FMT and red dashed lines mark the packing fraction at coexistence from GCMC. (a) Rod length $L = 8$, symbols show GCMC results for the two lattice extensions $M = 64$ (blue) and 168 (red). (b) Rod length $L = 25$, red symbols show GCMC results for a lattice extension $M = 170$.

6.5.4 Other findings for the purely-hard-core rod systems on cubic lattices

A finite-size "layering" effect

Our simulations showed a particular finite-size effect that appeared for small systems (e.g. $M = 32$ and $L = 8$): the system was composed of stacked layers populated with preferably one species, whereby the type of species varied randomly across the layers. We estimated that the entropic gain per particle

for this layering configuration decreases inversely proportional to system size, thus this effect should vanish with larger box sizes (as confirmed by the simulations).

Successive umbrella sampling

We have also implemented biased sampling methods in addition to the standard GCMC algorithm. Specifically, we used *successive umbrella sampling* [916], which samples equilibrium configurations strictly within a particular interval or "window" of a given observable (e.g. N or Q) via biasing the ensemble, then shifting the "window" successively over the whole range of such intervals to obtain histograms $P(N)$ or $P(Q)$ with higher resolution at the tails of the distribution (the method captures the statistics of rare configurations better than standard GCMC). As $P(N)$ or $P(Q)$ did not show a clear signature for a first–order phase transition, however, these investigations did not lead to better results. This sampling method applied to observables $Q_{\max}$ or $\{\tilde{S}_i, \tilde{Q}_i\}$ (see discussion in Sec. 6.5.5) might be more promising, but preliminary trials thereof remain inconclusive.

At the end of this chapter, we will discuss how *dynamical* analysis of the Markov-Chain pseudodynamics seem to be a very promising, alternative approach to purely structural sampling analysis. We have (unfortunately) ignored the information contained in system dynamics (even if applying an equilibrium "method") in this thesis, however.

6.5.5 Two-dimensional order parameters for orientational ordering in 3D

In this section, we apply a general approach for constructing multidimensional order parameters, developed for q–state Potts models [590]. The discussion in Ref. [590], done in the canonical ensemble, can be mapped directly to the purely entropic lattice model treated in the grand–canonical ensemble. This can be done by identifying the temperature with the chemical potential, and the spin states with the rod species. Regarding the symmetries of the order parameter, our lattice model is equivalent to a three–state Potts model where the symmetry–broken phase consists of three equivalent states (each of the Cartesian axes can be a preferred direction). According to Ref. [590], the order parameter dimensionality is two, and orthogonal axes in order parameter space are formed by pairs $(\tilde{Q}_i, \tilde{S}_i)$ of *unnormalized* nematic and biaxial order parameters (Eqs. (6.1) and (6.2)):

$$\tilde{Q}_i = \rho_i - \frac{\rho_j + \rho_k}{2} , \tag{6.23}$$

$$\tilde{S}_i = \frac{\sqrt{3}}{2}(\rho_j - \rho_k) , \tag{6.24}$$

where (ijk) is a cyclic permutation of (123). In 2D histograms $P(\tilde{S}_i, \tilde{Q}_i)$, a single peak around the origin signals an isotropic state, whereas three peaks with the same distance from the origin and with a threefold symmetry signal a nematic phase. The simultaneous occurrence of all four peaks would correspond to nematic–isotropic coexistence. In Fig. 6.8, we show $P(\tilde{S}_i, \tilde{Q}_i)$ for three values

of z in a system with rod length $L = 8$ and lattice extension $M = 100$. While the isotropic and nematic state can be clearly identified, the histogram near the transition (middle graph in Fig. 6.8) shows a broad distribution. The four peaks (expected for coexistence) cannot be identified clearly.

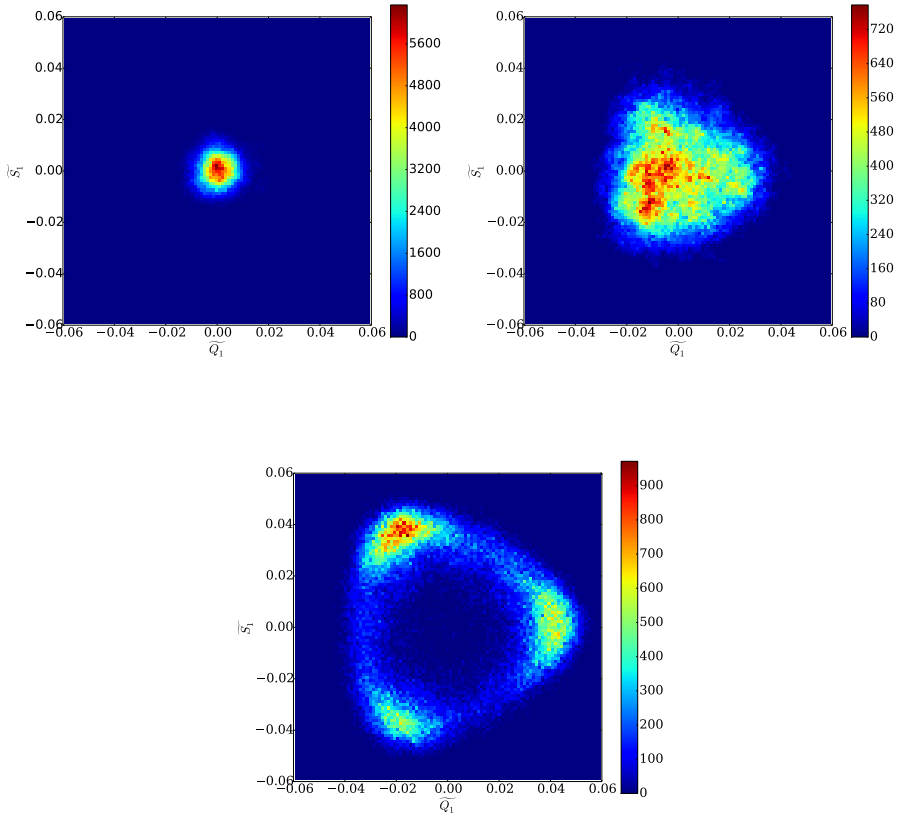

FIGURE 6.8: 2D histograms $P(\tilde{S}_1, \tilde{Q}_1)$ for three thermodynamic states in the purely hard-core rod model in 3D: (top-left) Isotropic ($z = 0.35$), (top right) near the transition ($z = 0.37667$), and (bottom) above the transition in the nematic state ($z = 0.38667$), as obtained for $L = 8$ and $M = 100$.

In order to facilitate a distinction between first order and continuous transitions, Ref. [590] introduces the reduced cumulant

$$g_M = 2 - \frac{\langle m_i^4 \rangle}{\langle m_i^2 \rangle^2} \,, \tag{6.25}$$

where m_i is the radial distance in the order parameter plane, $m_i = \sqrt{\tilde{Q}_i^2 + \tilde{S}_i^2}$. Cumulants for different lattice extensions M will intersect at z_{coex}. In the case of a first order transition, g_M will develop a minimum for increasing M below z_{coex}, and $z_{\text{coex}} - z_{\text{min}}$ (where z_{min} is the position of the minimum) scales as $1/M^3$. In Fig. 6.9 we show g_M for the system with $L = 8$. The common intersection at $z \approx 0.38$ confirms the transition activity identified via the position of the maximum in $\text{Var}(Q_{\text{max}})$ for the largest system ($M = 168$). However, our largest system $M = 168$ is just large enough to see an indication of a minimum

in g_M; therefore, we cannot do a finite size analysis for the position of the minimum. Nevertheless, the existence of the minimum would point toward a weak first order transition. Investigations much more extensive than the present one would be needed to establish the order of the transition unambiguously.

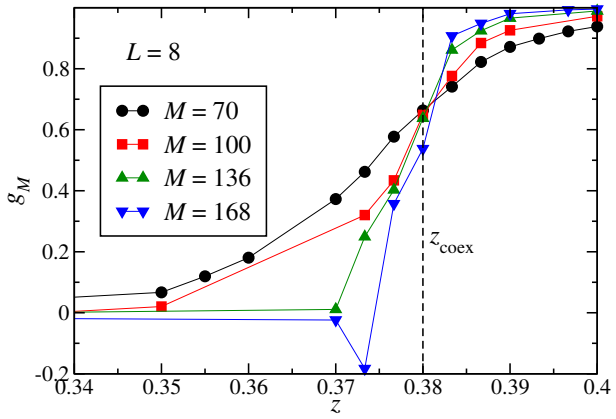

FIGURE 6.9: The reduced (Binder) cumulant g_M in a purely hard-core rod system with $L = 8$ for different lattice extensions M.

* * *

This 2D order parameter representation will be the basis for our analysis for "sticky" hard rods in Sec. 6.6.

Later in this thesis, in Ch. 7, we will also see how a two-dimensional order parameter constructed for a *two-dimensional* system of rods on lattices will be highly useful for machine learning problems, i.e. the "basis" in which configurations can be represented should represent the two global-scale order parameters of the system in 2D: the demixing parameter $\tilde{S}_{2D} \equiv \rho_1 - \rho_2$ as well as the *packing fraction* η $L(\rho_1 + \rho_2)$. Two-dimensional systems of hard, "stick" rods on square lattices is the topic of the upcoming Sec. 6.7. First, we will discuss the results we have obtained on 3D systems of "sticky" hard rods in the next section.

6.6 Phase behavior of "sticky" hard rods on cubic (3D) lattices

Note: The author of this thesis contributed to the methods, general research and presentation of results in all following subsections.

The previous section (Sec. 6.5) had considered purely hard-core rods ($T^* = \infty$) in the 3D system. In this section we extend the study to sticky hard rods.

6.6.1 Model and order parameters

We consider quadratic lattices in 2D and cubic lattices in 3D, where the unit cell length is set to 1. Hard rods are parallelepipeds with extensions $L \times 1$ (in 2D) or $L \times 1 \times 1$ (in 3D) and are defined by L consecutively-covered lattice points in one Cartesian direction. We define a binary occupancy field $O(\mathbf{s})$,

whose values are 1 for lattice points **s** covered by rods and 0 otherwise. The position of a rod is specified by the lattice point it covers having minimal coordinates (in each dimension). The rods are forbidden to overlap, i.e. there is no double occupancy of a lattice point. The quadratic lattice restricts the number of possible orientations to two, the cubic lattice to three, and we refer to rods oriented in x– resp. y– resp. z–direction as species 1 resp. 2 resp. 3. Species densities ρ_i are defined as number of rods of species i (N_i) per lattice site, $\rho = \sum_{i=1}^{D} \rho_i$ is the total density, $\eta = \rho L \leq 1$ is the total packing fraction and D is the number of dimensions.

We consider sticky attractions between rods with an energy $-\epsilon$ ($\epsilon > 0$) per touching segment of neighboring rods (see Fig. 6.10). The internal energy of a non–overlapping (valid) rod configuration ω can therefore be written as

$$U(\omega) = -\epsilon \sum_{\langle \mathbf{ss}' \rangle} O(\mathbf{s}) O(\mathbf{s}') + N(L-1)\epsilon \,, \tag{6.26}$$

where the sum is over neighboring site-pairs $\langle \mathbf{s}, \mathbf{s}' \rangle$ of the lattice and contributes whenever both sites are occupied. The second term corrects the over-counted adjacent sites *within* each rod (N is the total number of rods). With these ingredients, the grand partition function of the system is defined by

$$\Xi(z_i) = \sum_{N_1=0}^{\infty} .. \sum_{N_D=0}^{\infty} \prod_{i=1}^{D} \frac{z_i^{N_i}}{N_i!} \sum_{\omega} e^{-\beta U(\omega)}, \tag{6.27}$$

where $z_i = \exp(\beta \mu_i)$ is the fugacity of species i (with inverse temperature $\beta = 1/(k_B T)$ and chemical potential μ_i of species i). $\sum_{\omega}$ represents the sum over all non–overlapping configurations with N_i rods. In a bulk system, all z_i are equal ($z_i = z$) and the grand partition function can be written in a single–component form as

$$\Xi(z) = \sum_{N=0}^{\infty} \frac{z^N}{N!} \sum_{\tilde{\omega}} e^{-\beta U(\tilde{\omega})} \,. \tag{6.28}$$

$\sum_{\tilde{\omega}}$ is now the sum over all non–overlapping configurations with $N = \sum_{i=1}^{D} N_i$ rods. This is the considered case in this work. The phase diagram of the model is spanned by the total packing fraction η and the reduced temperature $T^* = k_B T/\epsilon$.

Order parameters

In the 2D case, we introduce the normalized order parameter

$$S = \frac{\rho_1 - \rho_2}{\rho} \tag{6.29}$$

measuring the demixing of rods oriented in x– and y– direction. Note that demixed states with S and $-S$ are equivalent since exchanging rods with x and y orientation is a symmetry of the model. The strength of demixing is characterized by $|S|$ and will be used below to determine the transition between isotropic and demixed states.

More symmetries exist in the 3D case: any permutation of the rod orientations renders an equivalent state. In this respect, our lattice model mimics

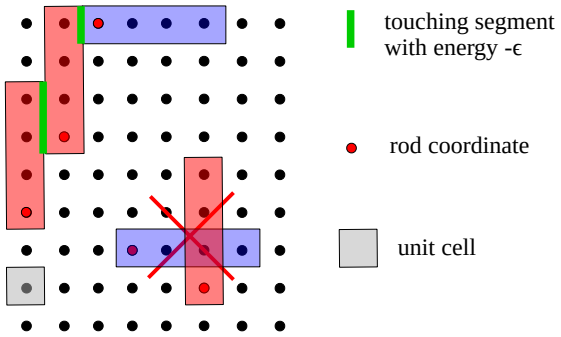

FIGURE 6.10: A 2D scheme of the model of hard rods on lattices. The two crossed out rods are representing forbidden overlap, i.e. the double occupation of a lattice cell. The common surface of touching segments of neighboring rods are shown in green.

a three-state Potts model where the symmetry-broken phase consists of three equivalent states (each of the Cartesian axes can be the preferred (or negatively-preferred) direction in the demixed phase). As we discussed in the previous Sec. 6.5.5, the order parameter dimensionality must be two, and orthogonal axes in order parameter space are formed by pairs $(\tilde{Q}_i, \tilde{S}_i)$ of unnormalized nematic and biaxial order parameters:

$$\tilde{Q}_i = \eta_i - \frac{\eta_j + \eta_k}{2} , \tag{6.30}$$

$$\tilde{S}_i = \frac{\sqrt{3}}{2}(\eta_j - \eta_k) , \tag{6.31}$$

where (ijk) is a cyclic permutation of (123). States of the system can be represented in the $\tilde{Q}$–$\tilde{S}$ order parameter plane. Fig. 6.11 shows a schematic of probability distributions (histograms) of bulk states in the order parameter plane as expected in a finite system in the grand canonical ensemble. An isotropic state is given by a peak in the origin. A nematic state with one majority species and two alike minority species (no biaxiality) renders three equivalent states, which arrange in a triangle pointed towards the right on the $\tilde{Q}_i$–axis in the order-parameter plane. This state is the "nematic$^+$" state. A nematic state with one minority species and two alike majority species renders a such triangle pointed towards the left ("nematic$^-$" state). The hypothetical case of a nematic state with *nonzero* biaxiality would render six equivalent states. We have not found stable biaxial states in all systems of 3D hard-core and hard-core "sticky" rods (next section), however.

The overall degree of nematic order can be captured by the scalar order parameter

$$m = \sqrt{\eta_1^2 + \eta_2^2 + \eta_3^2 - \eta_1\eta_2 - \eta_1\eta_3 - \eta_2\eta_3} \tag{6.32}$$

for which $m^2 = \tilde{Q}_1^2 + \tilde{S}_1^2 = \tilde{Q}_2^2 + \tilde{S}_2^2 = \tilde{Q}_3^2 + \tilde{S}_3^2$ holds.

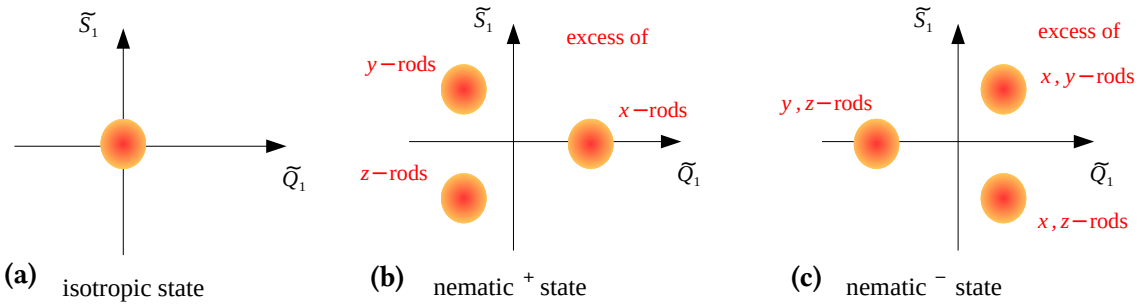

FIGURE 6.11: Schematic histograms for isotropic and nematic states in the $\tilde{Q}_1$–$\tilde{S}_1$ order parameter plane, as expected for a finite system in the grand canonical ensemble.

6.6.2 Grand canonical Monte Carlo (GCMC) simulations for "sticky" rods

The grand-canonical average of an observable $A(\tilde{\omega})$ is defined by

$$\langle A \rangle = \frac{1}{\Xi} \sum_{N=0}^{\infty} \frac{z^N}{N!} \sum_{\tilde{\omega}} A(\tilde{\omega}) e^{-\beta U(\tilde{\omega})} \tag{6.33}$$

and is computed by a grand-canonical Monte-Carlo simulation algorithm in a quadratic or cubic simulation box with linear length M. We describe the algorithm below.

Generic case of GCMC algorithm

The acceptance probability of the algorithm for inserting a "sticky" rod is denoted by α_{ins} ("$\alpha_{N\to N+1}$") and for deleting a "sticky" rod by α_{del} ("$\alpha_{N\to N-1}$"). Here, we extend the GCMC algorithm described in Sec. 6.5.1 to its *generalized form*:

$$\alpha_{\text{ins}} = \min\left(1, \frac{\pi_{N+1\to N}}{\pi_{N\to N+1}} \frac{z}{N+1} e^{-\beta(U(\tilde{\omega}_{N+1})-U(\tilde{\omega}_N)}\right) \tag{6.34}$$

$$\alpha_{\text{del}} = \min\left(1, \frac{\pi_{N-1\to N}}{\pi_{N\to N-1}} \frac{N}{z} e^{-\beta(U(\tilde{\omega}_{N-1})-U(\tilde{\omega}_N)}\right), \tag{6.35}$$

where π is a *proposal* probability for inserting ($N \to N+1$) or deleting a rod ($N \to N-1$). The ratio of the proposal probabilities in α_{ins} is equal to DM^D for D dimensions of space (in our case, 2 or 3); in α_{del}, the propsal probability is equal to $1/(DM^D)$.

For an insertion, the move is rejected automatically if it would cause an overlap of particles, i.e. the corresponding change in configurational part of the Hamiltonian would be $\Delta\mathcal{H} \equiv \mathcal{H}(\tilde{\omega}_{N+1}) - \mathcal{H}(\tilde{\omega}_N) \equiv \infty$, where $\mathcal{H}$ is the local configurational Hamiltonian. The full, local configurational Hamiltonian can be written as $\mathcal{H} = \mathcal{H}_{\text{hard}} + U$ with $\mathcal{H}_{\text{hard}} = \{0, \infty$ for non-overlapping or overlapping configurations, accordingly. We discussed the GCMC algorithm in a very generic setting and it in more detail in Ch. 3.4.2.

"Flip moves"

In this case of "sticky" hard rods, we will implement additional "flip moves" : after a successful insertion of a rod into the lattice we check if the inserted rod

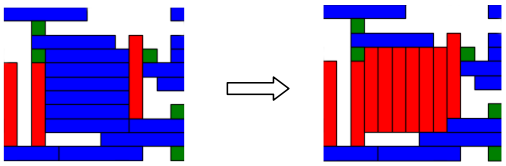

(a) (b)

FIGURE 6.12: Schematic of a "flip move" utilized in the GCMC simulations. Depicted is that of a 6×6 square of rods oriented in x–direction (a) to a 6×6 square of rods oriented in y–direction (b). The green squares are z-rods oriented perpendicular to the xy–plane.

is part of an $(L \times L)$–square fully covered by L parallel rods. The orientations of all rods within such a square are flipped randomly in-plane (please see fig. 6.12). Since there is no change in the internal energy, detailed balance holds. The flip move improves the performance of the algorithm at high densities.

In general, phase transitions in this system are accompanied by a change in packing fraction and in order ($|S|$ or m). We pinpoint the transition by the location of sharp peaks in var(η) and var($|S|$), var(m) in the z–T^* plane. Here, var denotes the variance $\mathrm{var}(A) = \langle A^2 \rangle - \langle A \rangle^2$ of an observable A. If a transition is sufficiently strongly first order, we pinpoint the transition by the location of the two peaks in $P(\eta)$ having equal area, where $P(\eta)$ is the histogram (probability distribution) of packing fractions for given z, T^*. This also renders the packing fractions of the coexisting states. For low T^* (strong attractions), we employ successive umbrella sampling (SUS) [917].

Finite-size scaling and Binder cumulant K_2

We performed a finite–size scaling (FSS) for selected systems to determine the location of critical transitions more precisely. For this, the Binder cumulant $K_2(A) = \langle A^2 \rangle / \langle |A| \rangle^2$ of an order parameter A is plotted for a few system sizes M over a temperature domain near the critical temperature T_c^*. The latter is then determined by the crossing point of the cumulants [38].

6.6.3 Results for $L = 4$: A lone, gas–liquid transition

For short rods, there is only a liquid-gas transition without nematic ordering.

Similarly as in purely-hard case, no nematic transition could be detected in the range $T^* = 1.85 \ldots \infty$ and $\eta = 0.00 \ldots 0.90$ for systems with rod-length $L = 4$. Yet, these systems show a gas–liquid transition. For a system size $M^3 = 32^3$, we have determined binodal points through double peaks in $P(\eta)$ (see Fig. 6.13(a)). The critical point was determined using FSS with the cumulant $K_2(\eta(z) - \langle \eta(z) \rangle)$, where z is the fugacity at phase coexistence (see Fig. 6.13(b)). Here, the critical temperature $T_c^* \approx 1.92$ is the T^*–coordinate of the approximate crossing point of the K_2 curves. The corresponding critical packing fraction $\eta_c \approx 0.40$ was obtained in Fig. 6.13(a) as the η–coordinate of the intersection of the horizontal line $T^* = T_c^*$ and the line connecting the mean of the coexisting liquid and gas packing fractions on the binodal, $\frac{1}{2}(\eta_l - \eta_g)$. Owing to the small system size, the histogram $P(\eta)$ shows two distinct peaks for $T^* > T_c^*$, as well.

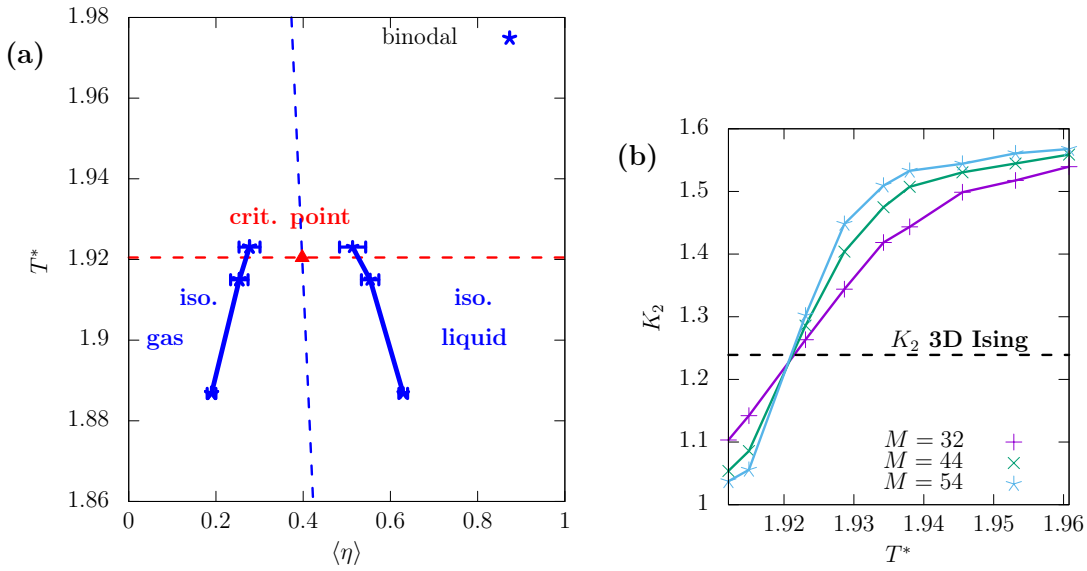

FIGURE 6.13: (a) Resulting phase diagram for $L = 4$ in 3D. Binodal points (blue symbols with error bars) are from the location of equal–area peaks in $P(\eta)$ and a system size $M^3 = 32^3$. The error was estimated from the peak-fitting procedure. The critical temperature T_c^* was obtained by FSS (see (b)) and the critical packing fraction is at the intersection of the line connecting the mean packing fraction of isothermal binodal points (blue dashed line) with horizontal line at T_c^* (red dashed line). (b) Binder cumulants K_2 for three different system sizes for temperatures near T_c^*. The critical point value of K_2 for the 3D Ising model is shown as a horizontal line.

6.6.4 Results for $L = 5, 6$: The gas–liquid and isotropic–nematic$^-$ transitions

Systems with rod-length $L = 5$ show an isotropic–nematic$^-$ transition that persists for all investigated temperatures (down to $T^* = 2.1$). The corresponding transition packing fractions $\eta^{\text{nem}}(T^*)$ become smaller with decreasing temperature, but, depend on T^* only weakly, overall. The weak-first-order character changes very little with decreasing temperatures, as can be seen in the value of var(η) at the transition. The latter increases from $1 \cdot 10^{-6}$ ($T^* = \infty$) to $8 \cdot 10^{-6}$ for $T^* = 2.1$, which points to a very small coexistence gap (see also below for estimates of the coexistence gap from var(η)). Additionally, there is a gas–liquid transition with a critical temperature above $T^* = 2.1$. We have determined coexisting states (isotropic gas and isotropic liquid) using SUS down to $T^* = 2.1$. Unfortunately, for temperatures further below we encountered equilibration problems. Therefore, we can only speculate that the line of isotropic–nematic transitions ends on the binodal, far "right" on the liquid side. Since the isotropic–nematic transition stays very weakly first order, such an end-point would amount to being a *pseudo-critical* end-point, which is presumably hard to resolve in simulations.

Systems with rod-length $L = 6$ show an isotropic–nematic$^-$ transition which shifts toward lower packing fractions as T^* decreases (similarly to $L = 5$). In contrast to the case of $L = 5$, we observe particle–number fluctuations increasing substantially with decreasing T^*. In Fig. 6.15(a) we show five

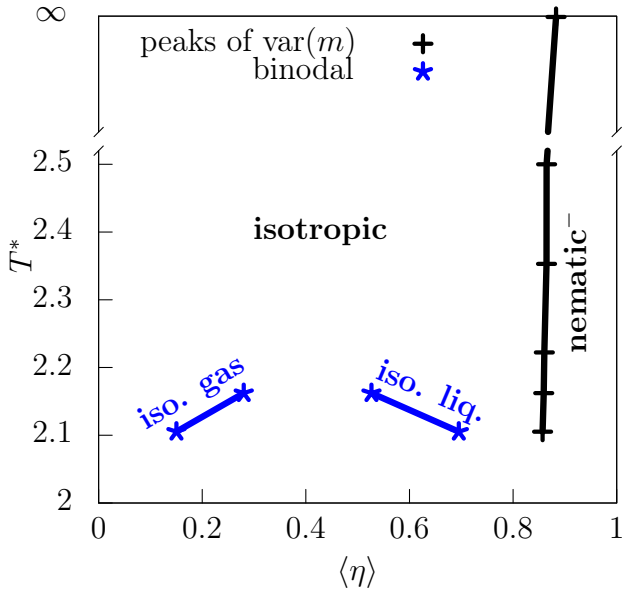

FIGURE 6.14: Resulting phase diagram for $L = 5$ in 3D for a system size $M^3 = 64^3$. The hard rod transition corresponds to $T^* = \infty$ and is located at a packing fraction $\eta_c^{\rm nem} \approx 0.88$ (in agreement with our results in Sec. 6.5 and with Ref. [918]).

isotherms for var($m(z)$) and var($\eta(z)$) in the temperature interval $T^* = 2.9...2.5$. Peak locations of var(m) and var(η) agree and signify the nematic transition in harmony. Curves of var($\eta(z)$) show a broad background signal with a sharp peak whose maximum increases from $\approx 3 \cdot 10^{-5}$ at $T^* = 2.857$ to $\approx 2 \cdot 10^{-3}$ at $T^* = 2.5$. Away from the sharp peak (in the background), the corresponding histogram $P(\eta)$ is described by a single Gaussian peak with variance σ. The grand–canonical fluctuation relation for particle numbers in a finite system with volume V expresses that

$$\mathrm{var}(\eta) = \frac{L}{V\beta}\langle\eta\rangle\chi = \sigma^2 \,, \tag{6.36}$$

where $\chi = [\eta_i(\partial p/\partial\eta_i)]^{-1}$ is the isothermal compressibility. The background noise displays a broad, secondary peak, which corresponds to a maximum in the compressibility χ, and can be viewed as the supercritical 'precursor' of the gas–liquid transition. The nematic transition contributes to var(η) at the position of the sharp peak. At the two lowest temperatures in Fig. 6.15(a) ($T^* = 2.500$ and 2.538) the corresponding histogram $P(\eta)$ displays clear double–peaks that are characteristic of the first–order nature of the transition. The peaks are approximately described by Gaussians $\exp[-(\eta - \eta_i)^2/(2\sigma_i^2)]$ where η_i is the peak position (coexistence packing fraction) and σ_i a peak width. At coexistence, contributions to var(η) arise from the compressibilities χ_i of the bulk states, from switches between the coexisting bulk states and lastly from additional fluctuations at the interface between these. At low temperatures,

these latter fluctuations are small and var(η) becomes:

$$\begin{aligned} \mathrm{var}(\eta) &= \frac{1}{4}(\eta_1-\eta_2)^2 + \frac{L}{2V\beta}(\langle\eta_1\rangle\chi_1 + \langle\eta_2\rangle\chi_2) \\ &\approx \frac{1}{4}(\eta_1-\eta_2)^2 + \frac{1}{2}(\sigma_1^2+\sigma_2^2)\ . \end{aligned} \tag{6.37}$$

The extracted coexistence gap $|\eta_1 - \eta_2|$ from Eq. (6.37) agrees well with the coexistence gap determined from the peak locations in $P(\eta)$ for low temperatures. We could not identify two well–separated peaks in $P(\eta)$ anymore for $T^* \gtrsim 2.54$. Thus, there must also be non–negligible interface fluctuations in play contributing to var(η) . Nevertheless, we can estimate an upper limit from Eq. (6.37) for the coexistence gap $|\eta_1 - \eta_2|$ from the excess (over–background) height of the peak in var($\eta(z)$) at $z = z_{\mathrm{coex}}$, as the background is described by the second term on the right-hand-side of Eq. (6.37). We assumed that the binodal with this coexistence gap is situated symmetrically around $\langle\eta\rangle(z_{\mathrm{coex}})$.

The resulting phase diagram is shown in Fig. 6.15(b) (with binodal points both from double–peaks in $P(\eta)$ and from the construction using var(η)). Upon decreasing the temperature, we observe a gradual opening of the coexistence gap. In a rather small temperature window ($T^* = 2.6...2.5$) the coexistence gap widens rapidly. The binodal describes coexistence of a low-density isotropic gas and a high-density nematic$^-$ liquid. As described, resolving the coexistence gap widening is not easy owing to the strong fluctuations in the system.

The assumption of a first-order character of the nematic transition for all temperatures is reasonable given (i) the symmetry of the model, (ii) the established weak first-order character for hard rods ($T^* \to \infty$) (presented in Sec. 6.5) and (iii) corresponding results for continuum models. Nevertheless, we investigated the finite–size behavior of the system more closely at two temperatures around $T^* = 2.6$. In Fig. 6.16, the behavior of var(m) as a function of linear system size M is shown at the two temperatures $T^* = 2.577$ and $T^* = 2.632$, at each of their coexistence fugacities z_{coex}. One may attempt to fit the data with a power law $\mathrm{var}(m) \propto M^{d-3}$. For a first order transition, $d = 3$ in three dimensions. At the lower temperature $T^* = 2.577$, we recognized two peaks in the histogram $P(\eta)$ for a system size $M = 120$ (green stars in Fig. 6.15(b)). This is consistent with the behavior of var(m) in the double-logarithmic plot in Fig. 6.16(a), which indicates a change of slope at $M \lesssim 100$. A double peak in $P(\eta)$ could not be resolved at the higher temperature $T^* = 2.632$. Consequently, the slope $d \neq 3$ up until $M \gtrsim 100$ in Fig. 6.16(b), indicating critical behavior, which, however, changes for larger M. Unfortunately, a fit would not be reliable for larger M owing to the small number of fully de-correlated Monte-Carlo samples.

The phase behavior is in contrast, quantitatively, to existing theoretical treatments of the isotropic–nematic transition both in lattice and continuum systems. For the lattice system, the phase diagram from the FMT functional derived in Ref. [72] is reproduced in Fig. 6.17. For hard rods, the FMT predicts a strong first order transition from an isotropic to a nematic$^+$ state with a coexistence gaps $\Delta\eta \approx 0.07$. With increasing attractions (lower T^*), the coexistence gap significantly widens already at high temperatures and crosses smoothly over to a transition between a thin isotropic gas and a dense nematic$^+$ liquid (thick black line in Fig. 6.17). Additionally, we show the isotropic gas–liquid binodal (green

dashed line in Fig. 6.17, obtained by a restricted minimization of the FMT functional with $m = 0$) and the onset of metastability of the nematic phase (black dot-dashed line in Fig. 6.17). The qualitative behavior of these lines is strikingly similar to the phase diagram obtained by simulations, the gas–liquid critical temperatures T_c^* are close, but the critical packing fraction η_c differs.

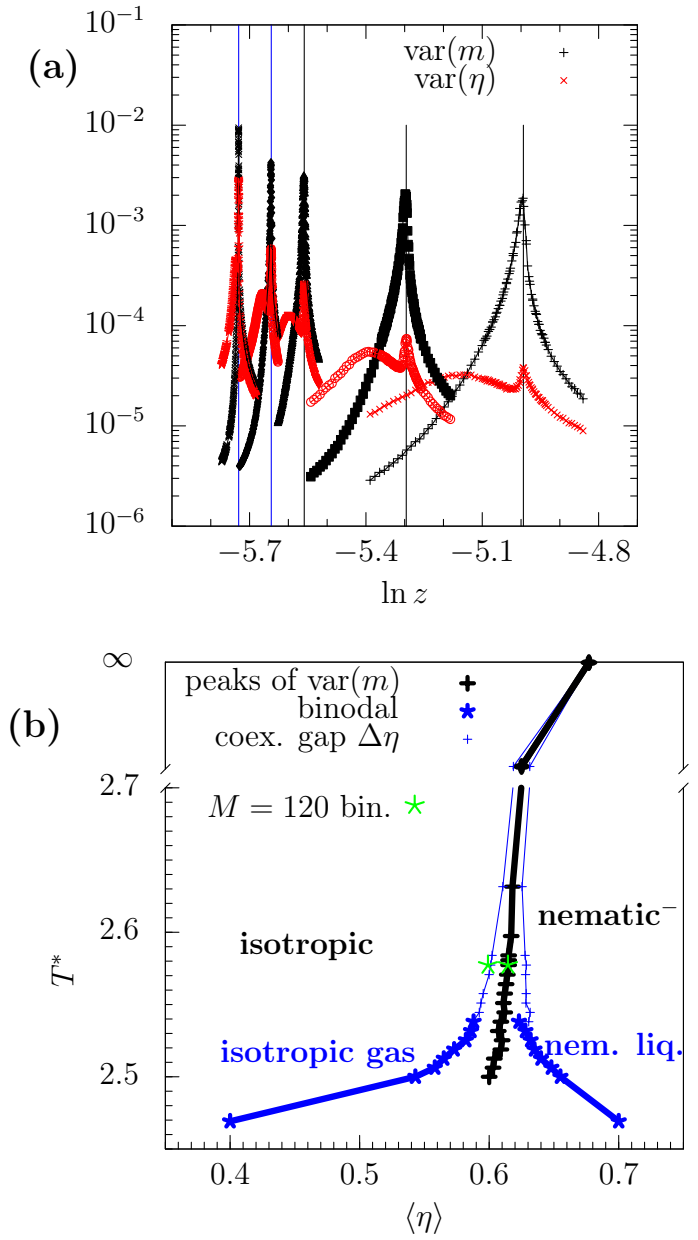

FIGURE 6.15: (a) Variances of order parameters m and η, i.e. var(m) and var(η), on isotherms as a function of $\ln z$ for a system size $M^3 = 64^3$. The temperatures (for pairs of curves from left to right) are $T^* = 2.500$, 2.538, 2.577, 2.703 and 2.857. Vertical lines indicate $\ln z$ where var(m) and var(η) are maximal. Blue vertical lines additionally indicate that at this coexistence fugacity two peaks in $P(\eta)$ were distinguishable. (b) Resulting Phase diagram for $L = 6$ in 3D for a system size $M^3 = 64^3$. Binodal points connected by thick blue lines were determined using histograms $P(\eta)$ that showed two clearly-resolvable peaks. SUS was used at the lowest temperature. An upper limit for the coexistence gap (binodal points connected by thin blue lines) were estimated from var(η), see text. Green stars are binodal points from two peaks in $P(\eta)$ at $T^* = 2.577$ for a large system size ($M^3 = 120^3$).

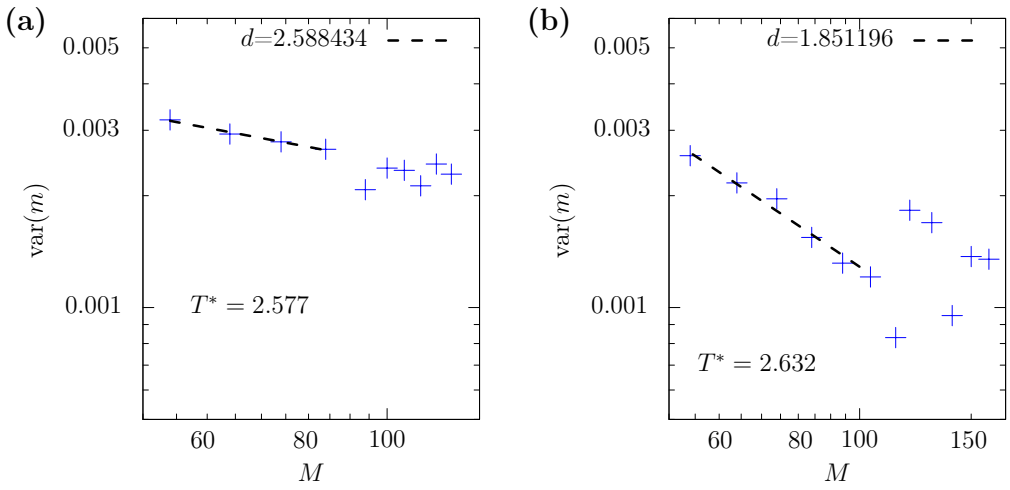

FIGURE 6.16: Variances of order parameter m, i.e. var(m) vs. linear system size M for (a) $T^* = 2.577$, $z_{\text{coex}} = 3.850 \cdot 10^{-3}$ and (b) $T^* = 2.632$, $\ln z_{\text{coex}} = 4.315 \cdot 10^{-3}$. For smaller M, data can be nicely fitted by $\ln \text{var}(m) = (d-3) \ln M + \text{const.}$ (dashed lines).

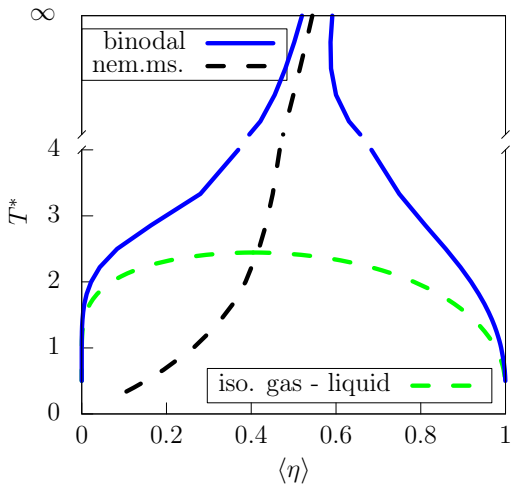

FIGURE 6.17: Phase diagram for $L = 6$ in 3D from FMT (data taken from Ref. [72]). Solid lines are binodals for the transition between isotropic and nematic$^+$ states. The green dashed line is a binodal between isotropic gas and isotropic liquid. The black dashed lines marks the onset of metastability for the nematic phase.

6.6.5 Results for $L = 8$: The gas–liquid and isotropic–nematic$^+$ transitions

The hard–rod system with rod-length $L = 8$ shows an isotropic-nematic$^+$ transition which also persists for lower temperatures. As for $L = 6$, the transition widens and becomes one between an isotropic gas and a nematic liquid within a rather short temperature interval (here at around $T^* = 3.721$). As before, we pinpoint binodal points for $T^* \lesssim 3.721$ through the locations of the two peaks in $P(\eta)$. For $T^* \gtrsim 3.721$ we obtain them from var(η) as an upper limit by Eq. (6.37). The behavior of var($\eta(z)$) and var($m(z)$) is very similar to the case of $L = 6$, see Fig. 6.15. The resulting phase diagram is shown in Fig. 6.18.

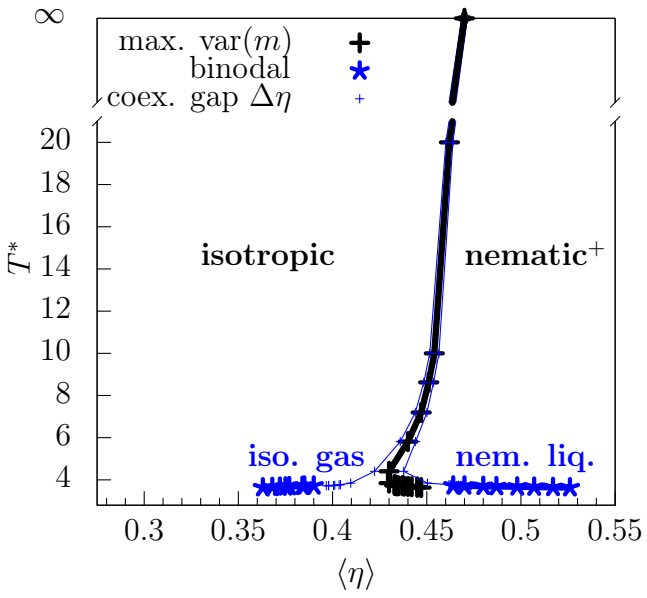

FIGURE 6.18: Resulting phase diagram for $L = 8$ in 3D for a system size 64^3. Binodal points connected by thick blue lines were determined using histograms $P(\eta)$ which showed two clearly resolvable peaks. Binodal points connected by thin blue lines were estimated from var(η) as for $L = 6$.

We illustrate the behavior of the system at coexistence for one state above $T^* = 3.721$ (where we have a weak first-order transition) and one state below $T^* = 3.721$ (where we have a strong first-order transition). Histograms in the $\tilde{Q}$–$\tilde{S}$ order parameter plane are shown in Fig. 6.19(a) for $T^* = 5.814$ and Fig. 6.19(b) for $T^* = 3.636$. At the higher temperature, two peaks in $P(\eta)$ were not discernible. This translates into a broad distribution in the $\tilde{Q}$–$\tilde{S}$ order–parameter plane. Unfortunately, this precludes an application of SUS methods on $\tilde{Q}$–$\tilde{S}$–histograms to extract the coexisting packing fractions. In contrast, we see a clear superposition of isotropic and nematic peaks at the lower temperature, i.e. a superposition of the first two histograms in the schematic Fig. 6.11.

* * *

The 3D systems of "sticky" hard rods presented in this section show a diverse array of phase diagrams, depending on rod length. For $L = 8$ the gas–liquid and isotropic–"nematic" transitions seem to "compete" at where the

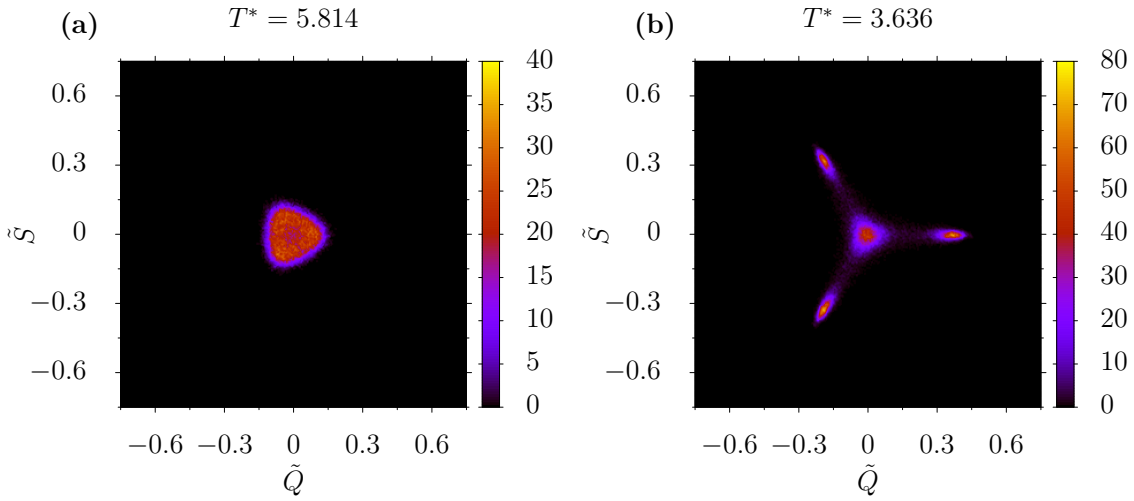

FIGURE 6.19: Two-dimensional-order-parameter $\tilde{Q}$-$\tilde{S}$ histograms taken at the isotropic-nematic$^+$ transition for two temperatures: (a) $T^* = 5.814$, showing a *weakly* first-order, and (b) $T^* = 3.636$, a *clearly* first-order transition for $L = 8$ in 3D.

binodal begins to widen. We will see that in 2D, this becomes a true tricritical point – the system that we study in the next section.

6.7 Phase behavior of "sticky" hard rods on square (2D) lattices

Note: The author of this thesis contributed to the presentation of the results in this section, as well as to general research and methods. The system presented here will be the case system studied with machine learning algorithms in Ch. 7 of this thesis.

The 2D system on square lattices has enjoyed some attention, especially the case of hard rods without attractions. The initial focus was on the onset of the second-order transition from an isotropic to a demixed state where one of the two rod species dominates. This demixing is found for $L \geq 7$ in simulations [366]. The critical packing fraction for the onset of demixing scales approximately as $4.8/L$ for large L [363, 369]. At very high packing fractions $\eta \approx 1$, theoretical arguments predict a re-entrant transition from the demixed to a disordered state bearing some characteristics of a 2D cubatic phase on a lattice [366]. This transition has been studied in more detail using simulations in Refs. [367, 368].

Some effects of sticky attractions have been characterized using simulations in Ref. [919]. On the one hand, critical temperatures T_c^* (but no critical densities) of the gas–liquid transition have been estimated from adsorption isotherms. T_c^* was shown to increase from ≈ 0.7 ($L = 2$) to ≈ 1.3 ($L = 10$). On the other hand, the demixing transition was investigated for $T^* = 2 \ldots 8$ (i.e., well above the gas–liquid transition). As for purely hard–core rods, the demixing transition was shown to be second order and sets in for $L \geq 7$. The critical packing fractions η_c^{demix} were determined using the Binder cumulant and finite-size scaling. It was shown that $\eta_c^{\text{demix}}(T^*)$ *increases* with decreasing T^* for a fixed L, a somewhat surprising result, i.e. the isotropic phase becomes more stable with increasing attractions between the rods. Naively, one would expect the opposite, namely that the tendency to demix would increase with stronger attractions since the latter favor parallel alignment.

These results leave open the question of the global phase diagram for $L \geq 7$. We have determined it for the exemplary case of $L = 10$. We locate the demixing packing fraction $\eta_c^{\text{demix}}(T^*)$ at the maxima in var($|S|$), and the gas–liquid binodal points via successive umbrella sampling. The results are shown in Fig. 6.20.

As can be seen in Fig. 6.20, starting from $T^* = \infty$ and decreasing T^* we reproduce the increase in $\eta_c^{\text{demix}}(T^*)$. There is a small shift towards lower packing fractions compared with the results of Ref. [919], which is induced by the finite system size $M = 128$ used here. Approaching T_c^*, the transition line $\eta_c^{\text{demix}}(T^*)$ changes slope and terminates on the gas-liquid binodal. Thus the terminal point is most likely a tricritical point. This entails (and is seen in our simulations) that below T_c^* the coexisting liquid is in a demixed state.

Phase diagrams in 2D for sticky rods were investigated in Ref. [72] using density functional theory (DFT) in the form of lattice fundamental measure theory (FMT). The FMT predicts the same topology of the phase diagram, i.e. a line of second-order demixing transitions for decreasing temperatures, which end in a tricritical point. However, there are serious quantitative discrepancies. The packing fractions $\eta_c^{\text{demix}}(T^*)$ are much smaller in the FMT, and the tricritical point is at a much higher temperature. In simulations, the gas–liquid binodal is very flat around T_c^*, similar to the behavior of simple liquids in 2D. The FMT

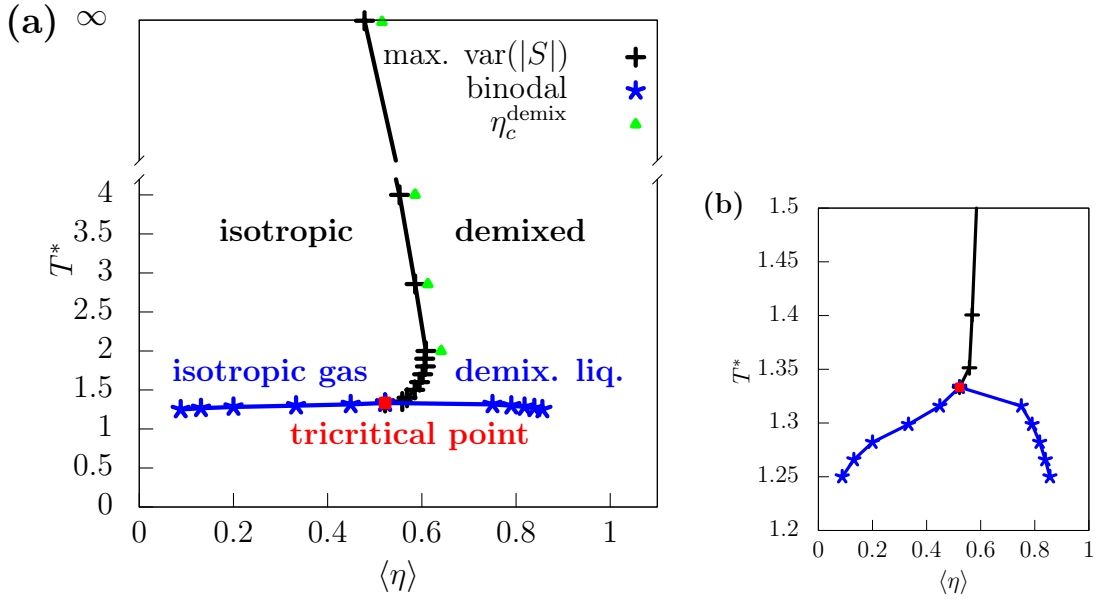

FIGURE 6.20: Phase diagram for $L = 10$ in 2D from GCMC simulations, in full in (a) and zoomed-in around the tricritical point in (b). Black symbols connected with lines show the demixing transition, obtained from var($|S|$) and a system size 128^2. Green data points for the demixing transition are obtained by finite-size-scaling in Ref. [363]. The hard rod transition corresponds to $T^* = \infty$. Blue symbols connected with lines show the gas–liquid binodal. For the system size 128^2, we estimate the location of the tricritical point at$(T_c^*, \eta_c^{\mathrm{demix}}) \approx (1.33, 0.52)$.

renders a binodal that is considerably distorted toward higher temperatures. It also does not recover the unusual behavior of increasing $\eta_c^{\mathrm{demix}}(T^*)$ with decreasing T^*.

All these discrepancies point to an important role played by larger-scale fluctuations. Simulation snapshots near $\eta_c^{\mathrm{demix}}(T^*)$ show that the system splits into larger domains where the rods are oriented in either one or the other directions, yet the order parameter $|S|$ remains small (see Fig. 6.21(a)–(c)). At high temperatures, these domains are loosely packed, but become increasingly dense for lower T^* where attractions become more important. To quantify these domains, we consider the orientation–specific binary occupancy fields $O_x(\mathbf{s})$ and $O_y(\mathbf{s})$ (which are 1 for lattice points covered by x–oriented and y–oriented rods, respectively, and 0 otherwise). We define new binary occupancy fields $O_X(\mathbf{s})$ and $O_Y(\mathbf{s})$ by the following rule:

$$O_X(\mathbf{s}) = \begin{cases} 1 & (\mathbf{s} \text{ cannot be covered by a } y\text{–oriented rod, given occupancy } O_x) \\ 0 & (\text{otherwise}) \end{cases} \tag{6.38}$$

$$O_Y(\mathbf{s}) = \begin{cases} 1 & (\mathbf{s} \text{ cannot be covered by an } x\text{–oriented rod, given occupancy } O_y) \\ 0 & (\text{otherwise}) \end{cases}$$

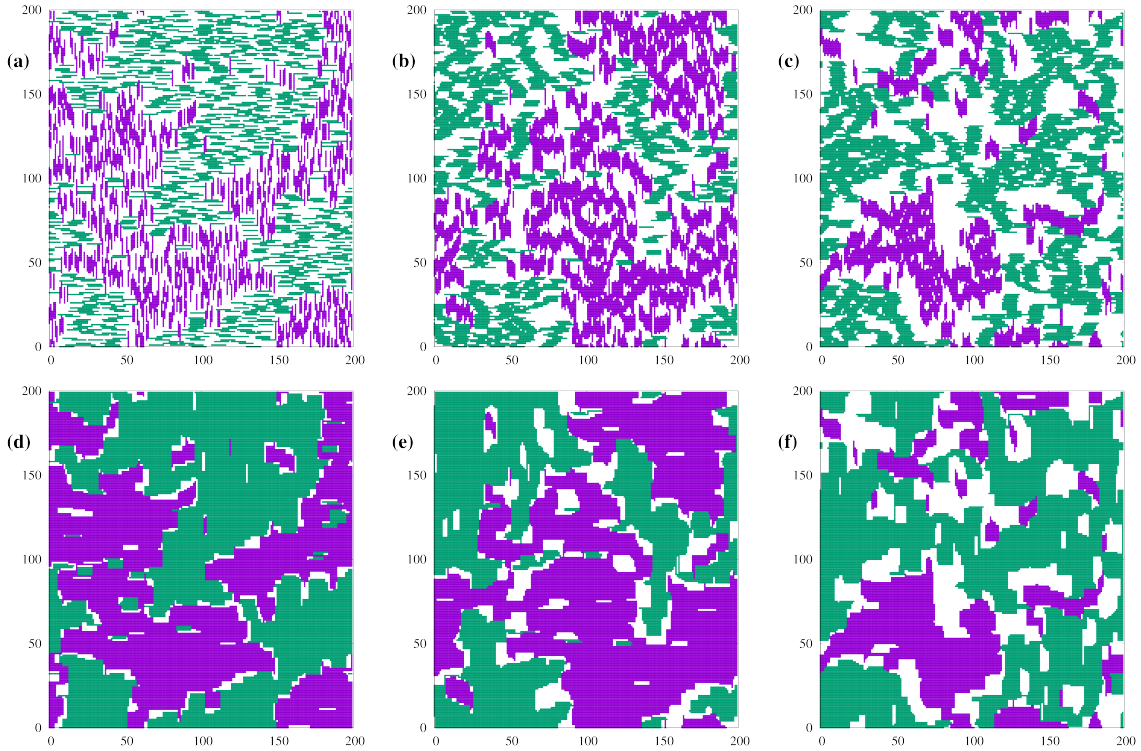

FIGURE 6.21: Snapshots of rod occupation fields at three states in the vicinity of the demixing line. Rod occupation fields O_x and O_y for (a) $T^* = \infty, z = 0.24$ ($\langle\eta\rangle = 0.48$), (b) $T^* = 2$, $z = 0.0022$ ($\langle\eta\rangle = 0.59$) and (c) $T^* = 1.5, z = 0.0004$ ($\langle\eta\rangle = 0.58$). Corresponding snapshots for O_X and O_Y in (d), (e) and (f). The system size is $M^2 = 200^2$.

In essence, O_X defines more-or-less compact X–domains (belonging to x–oriented rods) whose points cannot be covered by a y–oriented rod. Likewise O_Y defines Y–domains, see also Fig. 6.21(d)–(f). One recognizes that the system is covered to a large extent by X– and Y–domains with a few voids. One can define an order parameter S' by

$$S' = \frac{\eta_X - \eta_Y}{\eta_X + \eta_Y} , \tag{6.39}$$

where $\eta_{X[Y]} = \text{area}(X[Y])/M^2$ is the packing fraction of the $X[Y]$ domain, with M^2 being the total area of the system. Interesting is that $|S'| \approx |S|$, i.e., $|S'|$ is an equivalent order parameter. A total packing fraction $\eta_{XY} = \eta_X + \eta_Y$ of X– and Y–domains is furthermore useful to define, as well as packing fractions of rods inside these domains, i.e. $\eta_{x,X} = LN_x/\text{area}(X)$ for x–oriented rods inside X–domains and $\eta_{y,Y}$ for y–oriented rods inside Y–domains, likewise. The total packing fraction is $\eta = \eta_{x,X}\eta_X + \eta_{y,Y}\eta_Y$.

The behavior of η_c^{demix} upon variation of temperature can now be rationalized. For zero attractions, η_{XY} is rather high but the packing fractions inside the domains are moderate. Furthermore $\eta_{x,X} \approx \eta_{y,Y}$. With increasing attractions, η_{XY} is only slowly decreasing but $\eta_{x,X}$, $\eta_{y,Y}$ increase substantially. This leads to the shift of the demixing transition to higher densities. At around $T^* \lesssim 2$, η_{XY} begins to decrease substantially, whence more voids appear in the system (see

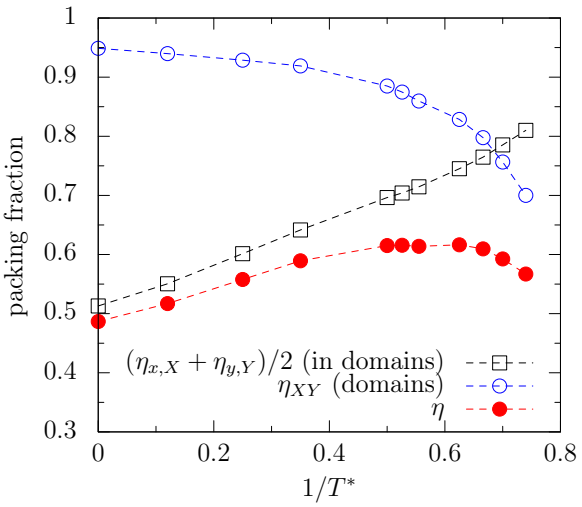

FIGURE 6.22: The behavior of the average packing fraction in the $X[Y]$ domains, the packing fraction of the domains themselves, and the rod packing fraction vs. attraction strength $1/T^*$ (for constant order parameter $|S| = 0.5$, close to the demixing transition). Data are for a system size $M^2 = 200^2$.

Figs. 6.22 and 6.21(f)). This 'signals' the approaching gas–liquid transition, and now η_c^{demix} decreases again.

* * *

In part IV, we will investigate unsupervised and generative machine learning algorithms. We will use data of configurations of this 2D model system, much like those of Fig. 6.21 as input to the machines. The fluctuating domains in 2D are important for interpreting what and how these machine learning systems learn about the 2D rod configurations.

6.8 Discussion and outlook

Note: The author of this thesis wrote parts of the discussion sections of the publications corresponding to this chapter. Below, we have included these and extended the discussions further, addressing new topics, in part, as well as discussing open issues and interesting ideas for future studies.

6.8.1 On the weak first-order isotropic–nematic transition and comparison to other models

Some of the following comparisons have already been discussed in the introduction (Ch. 1.3.1).

It is interesting to evaluate the use of lattice models of rods for a possible simplified description of continuum models. Yet, these models appear to be quite different in nature. We discussed much already in Ch. 1.3. In retrospect of the results presented here, we would like to (re-)address some findings of the isotropic-nematic transition in 3D continuum systems, as well as similarities for the "unusual" nematic phases for $L = 5, 6$ in 3D.

FMT of Zwanzig models: Martinez-Raton [239] calculated the full phase diagram of the Zwanzig model in 3D using an approximate FMT. A nematic state with negative order parameter is found in conjunction with layering, similar to our findings for $L = 5, 6$. Ref. [624] also contains Zwanzig-models of boards.

Boards and cuboids in the 3D continuum: These models release the restriction on orientation, but retain the particle anisometry and shape of the aforementioned Zwanzig models. Refs. [920–922] simulated bulk properties of hard tetragonal parallelpipeds, having found a parquet phase and smectic phases for the case of cuboids with two short, symmetrical axes (i.e. rods). These are absent in the Zwanzig models. Likewise rich phase diagrams for thin board-like colloids are mapped out in Ref. [923].[2]

Simulations of continuum hard rods (spherocylinders) in 3D: Spherocylinders have proven to be the most sought-after simulated model with regards to hard anisotropic particles in the 3D continuum. The simulation studies by Bolhuis and Frenkel [18, 42] used MC simulations with ~ 500 particles in the canonical ensemble. The isotropic–nematic transition was not detectable for small aspect ratios $L/D \leq 5.0$, i.e. it was not possible to detect a density jump between coexisting states. The order parameter $Q^{\mathrm{nem}}(\rho)$ showed weak hysteresis, but a jump in Q^{nem} between coexisting states (a clear signature of a first order transition) was not determined. The transition density is estimated from the 'kink' in the Q^{nem}–ρ–curve at the (arbitrary) value $Q^{\mathrm{nem}} = 0.4$. For $L/D \geq 15$ a density jump of $> 10\%$ had been found, the absolute value of the density jump was maximal at around $L/D = 20$. The nematic order parameter of the nematic phase at coexistence was found to be 0.784 at $L/D = 15$ and further increases when the aspect ratio lengthens. So, for $L/D \geq 15$, the transition is very strongly first order. Vink et al. [916] employed grand canonical MC techniques. For $L/D = 15$ they confirmed the sizable density jump, and at coexistence the probability distribution $P(\rho)$ showed two clearly separated peaks.

Continuum hard rods in 2D: In 2D continuum models with anisotropic particles, simulations have addressed the case of hard needles [332] and hard ellipses [328, 329]. Since the particle orientation is indeed a continuous variable—in contrast to lattice models—fluctuations in the average orientation may destroy the long–range order of a nematic state (leading to a quasinematic state); however, anisotropic hard particles (for which position and orientation degrees of freedom are highly coupled) may still exhibit true, nematic long-range order, see the discussion in Ref. [332] Thus a continuous isotropic–quasinematic transition of Kosterlitz-Thouless type is possible, as well as an isotropic–nematic transition of first order. Interestingly, both types had been found in the hard ellipse system [328] (first order for aspect ratio 4 and continuous for aspect ratio 6), though, Ref. [336] contradicts this and finds only continuous transitions. This topic may still be an open one. Nevertheless, since the 2D lattice rod model shows an Ising–type, demixing transition, we may conclude that in 2D lattice and continuum models show qualitatively very different behavior with respect to the type of phase transition.

[2] An experimental realization boards focusing on biaxial phases is reported in Ref. [924].

On the theory side, the most accurate density functionals for hard anisotropic particles have been derived from Fundamental Measure Theory (FMT) [292–298]. Wittmann et al. used mixed measures to derive a functional that is exact in the low-density limit; for higher densities, typical FMT approximations were employed [296]. The corresponding phase diagram for hard spherocylinders showed almost quantitative agreement with Ref. [42]. However, the FMT results showed an almost constant density jump between the coexisting isotropic and nematic states for aspect ratios starting from $L/D \gtrsim 3.5$. Thus the transition is strongly first order for all aspect ratios.

It hence appears that for moderate aspect ratios, strong orientational fluctuations cause the isotropic–nematic transition to be weakly first order, both on the lattice and in the continuum. The lattice model exhibits in addition the peculiarity of a nematic state with negative order parameter (for $L = 5, 6$). The lattice and the continuum stand in contrast to each other for large aspect ratios since we have not found evidence for a strong first-order transition. Moreover, it does not seem that a smooth crossover in the topology of the phase diagram is possible from the lattice to the continuum: this was shown by a study using a second-virial density functional with variable orientational degrees of freedom [925].

We would like to extend our claim that lattice models of hard rods with sticky attractions are a worthwhile complement and counterpart to existing literature on continuum models. We suggest a few similar model systems: Hard rods with non-unit width [368] and rods on triangular lattice [367] have only been studied in the hard-core case. Hard, polydisperse rods were studied in a random-sequential-adsorption-setting in Ref. [685], but it seems the equilibrium phases have not been determined even for the hard-core case.

6.8.2 Unexplored regions of the phase diagrams

On finite-size effects and proposals on surface-layering behavior in semi-confinement

The "layering" effect which we found in finite-sized systems for purely hard-core rods (Sec. 6.5.4) may be an interesting point for future simulation studies of the hard-rod systems in *semi-confinement*: We discussed in the introductory part of this thesis (part I) that so-called finite-size effects are a manifestation of confinement. Quite generally, states that are unstable in the bulk can become metastable in confinement; states that are metastable in the bulk can become thermodynamically stable in confinement (depending on the confinement condition). This "layering" may hint at a wetting/layering transition that would occur when the system is exposed to attractive walls. As these and any wetting transitions are relevant for multilayer thin film growth with long rods, it would certainly be interesting to simulate this case in the future.

To this end, we project that semi-confined system of rod lengths $L = 5, 6$ could show a layering transition very near, but slightly before the isotropic–"nematic$^-$" transition of the bulk which we have characterized. As the system already forms 2D-like "sheets", the entropic barrier to a 2D-like layering or wetting transition at the wall should be small. As to longer rods, the first layering transition may be of the kind discussed in the above paragraph, where layers switch between all three orientations – or, at least, where large lateral domains

of one predominant species "stack up". Nonetheless, our GCMC simulations can be modified easily to consider the case of a a hard, attractive wall.

Nonequilibrium transitions, metastable states and connection to (2+1)D systems

We showed example phase diagrams for simple model systems of mixtures (AB models) in Ch. 2.2.2, Fig. 2.5. The topology of the phase diagrams bear strong resemblance to the 3D systems (or, rather, the 2D systems) if we image the weak-first-order transition to be continuous instead. The reason is, probably, that the ordering transitions in the lattice model are of *demixing*-type, where in 3D the three orientational species into two subsets (one dominant species and two suppressed, or vice versa). We project that analogy may be extended in light of Fig. 2.6: very likely, various *metastable* states exist below the pseudo-tricritical points. The finite-size effects we reported and discussed above, i.e. "layering", is one example.

These metastable states are difficult to detect in the grand canonical ensemble, where particle number fluctuations compel a much more rapid dissolution thereof. Hence investigations in the canonical ensemble seem a worthwhile task. To this end, we have developed a full 3D KMC code for sticky rods on cubic lattices as an extension of the project of Ch. 5. KMC simulations model local dynamics in the same way as local-move canonical MC simulations (and is additionally event-driven). As we have further developed the code for "growth", "heating", or "quenching", as we mentioned in Ch. 5.8, a detection of metastable critical points might be possible using one, if not a combination of these dynamical experiments.

We note that the "nematic" phase for $L = 5, 6$ in 3D, where one species of rods is suppressed and the system nearly decouples into 2D systems, may be an "echo" of the monolayer system with a kinetically arrested "lying" phase rods at nearly full packing (See Ch. 5). We also note that the full 2D case of confinement represents a limiting case of (2+1)D confinement with very attractive substrates. There, we say that the "lying" phase in the monolayer can become stable. Moreover, the 2D-demixing behavior was seen in the monolayer for very long rods ($L = 9$), which is close to our studied case of $L = 10$ here for full 2D confinement.

Quantifying metastable phases is crucially important for the fundamental understanding of phase transformation kinetics which we discussed in Ch. 2.3. As we demonstrated in Ch. 5 for the sticky rod systems in monolayer confinement ((2+1)D), these metastable phases are products of partial dynamical arrest and are connected to gelation of the system. This can further connect to *percolation* processes in these systems. The major question we have not addressed is where these metastable states and nonequilibrium transitions occur for the 3D bulk. We will discuss more broadly the topic of dynamical information from MCMC simulations further below in Sec. 6.8.5.

Jamming and percolation transitions are important, generally, for the study of disordered solids (i.e. to understand the formation of rigid bodies) [661]. It would be most interesting to pass through the isotropic–demixing transition binodal for the 3D systems with the above-mentioned canonical-ensemble simulation approach. A gelation or a percolation transition could occur 'on the way' towards the demixed phase, and may be pronounced where the demixing transition sets in at very high densities (i.e. low temperatures) for $L = 5$. To

this end, we have provided a list of the reported jamming and percolation transitions of the 2D and 3D hard rod lattice models that we found in the literature in Sec. 6.8.4 below. We discuss potential relationships to the phase diagrams we characterized on a speculative level, as well. Note that nonergodic regions in the phase diagrams have been reported and discussed in Refs. [914, 926] for the two-dimensional case of lattice systems of purely hard-core rods. Hence a fuller investigation of metastable and arrested states in the "sticky" models in both the 2D and 3D settings would be quite interesting.

Reported metastable and high-density phases

We have not investigated the possibility of high-density phases in the 3D system, owing to limitations of our simple grand-canonical algorithm. These high-density phases could include a completely disordered phase of cubatic-type, which could be similar to the high-density phase in 2D [366, 367]. This problem should be treated with optimized algorithms similar to those for 2D in Ref. [367] for example.

In this regard, the preprint of Ref. [918] (`arXiv:1705.10531v1`) appeared on *aXiv.org* during the publication process of our work. They simulated purely hard-core rods in 3D higher densities using the aforementioned optimized algorithm. They find another high-density phase that is 2D-like, similar to the layered nematic phase, but that appears metastable. They could also show that the layered nematic phase with $q < 0$ not only appears for $L = 5, 6$ but also for $L = 7$ at high packing fractions of around 0.9. The corresponding findings for the isotropic–nematic($q > 0$) transition are similar to ours. The systems studied were smaller than ours, therefore this transition appeared to be critical in the size regime used.

6.8.3 On the lattice FMT (speculative discussion and outlook)

It seems that the lattice FMT does not capture the strong fluctuations in nematically-ordered domains properly, overestimating the strength of the first-order transitions in the hard-core and weak-attraction limit. We have shown (in 2D) the importance of domains with one particular orientational order for the fluctuations of the system. Large-scale clusters (domains) in the systems are thus of fundamental importance for the phenomenology: the lattice FMT of Ref. [265] is based on a finite set of lattice clusters or of partially-ordered sets in the system. Interestingly, the authors discuss similarities of their ansatz to a Bethe lattice. We have mentioned that the current FMT for the purely hard-core case, in 2D and 3D, correspond exactly to the entropy of hard rods on a Bethe-like lattice of Ref. [360], which obviously has a different lattice topology (it should be a square or cubic lattice). Understanding the inherent lattice topology of a lattice-FMT may be an interesting point worthwhile to explore in the future.

FMT for machine learning and accelerated MC algorithm

Also, in the next chapter, Ch. 7, we will see how machine learning can automatically discover such fluctuating domains in the rod systems. Therefore, combining a lattice FMT (e.g. based on a "cluster expansion") with machine

learning may represent a novel scientific endeavor in which both fundamentals of statistical mechanics as well as new, physics-inspired machine learning algorithms could be studied. This is part of a broader outlook of this thesis.

Regarding equilibrium MCMC sampling, we report at attempted at a grand-canonical cluster-algorithm that employs local (grand-canonical) equilibrium within a definable cluster in the style of Fischer and Vink [356]. However, the acceptance rates are very small due to constraining translational degrees of freedom to a lattice (unlike the case in the paper).

A more innovative idea would be modify the accelerated algorithm of Kundu, Rajesh et al., who use a 1D density functional of hard rods during the MCMC scheme. We speculate the 2D or 3D lattice FMT could possibly as a "guidance" free energy in the form of a proposal distribution for a transition along a particular reaction coordinate (e.g. the nematic order parameter). Incorporating this into a fully detailed-balance scheme might resemble the innovative methods reported in Refs. [927–929], where they used machine learning for the proposal transition. Other options include parallel tempering or simulated annealing techniques [930, 931].

6.8.4 Jamming and percolation transitions from literature and speculative comparison

2D RSA

Random sequential adsorption (RSA) of rods on square lattices has been studied quite extensively for 2D systems, see e.g. Ref. [681, 683–685, 906, 910, 932]. Percolation transitions under RSA conditions are related to the jamming transitions. We list the 2D jamming, percolation, and inverse percolation packing fractions (when percolation disappears from a fully packed system) and corresponding packing fractions for the 2D case below in Tab. 6.1, which were reported in Ref. [908].

L	$\eta_{\text{jam}}^{\text{2D}}$	$\rho_{\text{jam}}^{\text{2D}}$	$\eta_{\text{perc}}^{\text{2D}}$	$\rho_{\text{perc}}^{\text{2D}}$	$\eta_{\text{perc, inv}}^{\text{2D}}$	$\rho_{\text{perc, inv}}^{\text{2D}}$
2	0.864	0.432	0.462	0.231	0.450	0.225
3	0.824	0.275	0.423	0.141	0.415	0.138
5	0.792	0.158	0.347	0.158	0.367	0.073
6	0.785	0.131	0.315	0.053	0.350	0.058
9	0.772	0.086	0.249	0.028	0.311	0.035
10	0.769	0.077	0.231	0.023	0.301	0.030

TABLE 6.1: Jamming, percolation, and inverse percolation packing fractions η and number densities ρ for the random sequential adsorption of hard rods on 2D (square) lattices. Data are from Ref. [908].

For the 2D case we studied in this chapter, $L = 10$, the jamming transition ($\eta_{\text{jam}}^{\text{2D}} = 0.769$) appears right of the isotropic–demixing transition packing fractions for temperatures above the tricritical point (Fig. 6.20). It would meet the top of the right half of the binodal that we estimated. Notice that this jamming transition is for absolutely no diffusive motion; jamming transitions can also occur under nonequilibrium conditions with diffusive motion, where the particle attraction strength plays a role. Therefore, it would be interesting to

quantify arrested dynamical transitions in 2D for various attraction strengths in a dynamical model like KMC.

We have provided these results for a potential connection to the monolayer systems of hard, sticky rods studied in Ch. 5, where a 2D system is a limiting case of very strong substrate potentials.

3D RSA

In 3D, Refs. [686, 933] studied the RSA jamming and percolation transition of hard rods on cubic lattices (See also selected results in [934]). We summarize the reported results on transition points in Tab. 6.2.

L	$\eta_{\text{jam}}^{\text{iso,3D}}$	$\eta_{\text{perc}}^{\text{iso,3D}}$	$\eta_{\text{jam}}^{\text{para,3D}}$
4	0.780344	0.1800	0.803892
4*	0.7808	–	–
5	0.736061	0.1555	0.792284
6	0.701346	0.1364	0.784637
6*	0.7026	–	–
7	0.673355	0.1218	–
7*	0.6749	–	–
8	0.650282	0.1089	–
8*	0.5858	–	–
24	0.507750	0.0411	–

TABLE 6.2: 3D jamming and percolation packing fractions for the random sequential adsorption of hard rods on cubic lattices, in either isotropic (iso) deposition or parallel (para) deposition. Data without any notation are from Refs. [686, 933], which overlap; rows denoted with stars (*) are from Ref. [934] using quite small (18^3) lattices sizes, but both sets are subject to finite-size effects.

We discuss below a loose comparison of the data-points in Tab. 6.2 to the "isotropic–nematic" transitions in 3D studied in this chapter:

$L = 4$: the 3D RSA percolation threshold $\eta_{\text{perc}}^{\text{iso,3D}} = 0.1800$ appears to be quite close to the left demixing fraction at low temperatures ($T^* \approx 1.885$) for sticky rods in 3D (Fig. 6.13).

$L = 5$: (the "unusual" phase diagram in Fig. 6.14), the 3D jamming fractions are somewhat lower than the isotropic–demixing transition fractions, around $\eta_c \approx 0.85$ for lower temperatures (Fig. 6.14). However, it is not clear what happens in the region between the vapor–liquid binodal and the when the isotropic–demixing transition line for temperatures around $T^* \approx 2$. It would be interesting if there were a direct relation to the 3D jamming transition in this "gray area".[3] Further, just like for $L = 4$, the 3D percolation transition $\eta_{\text{perc}}^{\text{iso,3D}} \approx 0.156$ is very close to the lowest measured binodal fraction — sampling difficulties arose at lower temperatures (as far as we recall).

[3] In contrast to the RSA data, we failed to perform finite-size scaling analysis, which is something that would need to be done in order to make precise statements.

$L = 6$: (Fig. 6.15), the 3D jamming transition packing fraction is somewhat higher than the hard-rod isotropic–demixing transition density at $T^* = \infty$. Notably, our highest reported value of the isotropic–demixing demixing density at low temperatures is very near the reported $\eta_{\text{jam}}^{\text{iso,3D}} \approx 0.701$. As far as we reckon, we experienced equilibration problems in our GCMC algorithm beyond this density (at lower temperatures).

$L = 7, 8, 25$ ("long" rods where the nematic phase entails one predominant species): the 3D jamming transition packing fraction for isotropic deposition is much higher than that of the the isotropic–demixing transition at high temperatures ($T^* = \infty$). A comparison at very low temperatures would lie beyond the range we investigated for $L = 8$ (Fig. 6.18).

Possibly, then, the 3D RSA jamming and percolation limits could be foreshadowing low-temperature left- and right- binodal densities that delineate easily accessible regions for a local GCMC algorithm. We ponder whether this may be likewise the case for the "triple" region of the $L = 5$ phase diagram. All of this is speculation, however. Analyzing dynamical properties of the local-move GCMC simulation, apart from structural variables, should shed more light onto arrest and jamming behavior in the hard-rod-model. We discuss the topic of dynamical information in the next subsection.

6.8.5 Dynamical information (speculative discussion and outlook)

Recent work in Ref. [914] discussed the nonequilibrium (nonergodic) nature of a high density transition for the 2D hard rod system. This spurs on thoughts on dynamics that we alluded to further above, and wish to argue in more length in this section. Most generally, it would be useful to quantify dynamical quantities from the Markov-Chain pseudodynamics. In particular, this seems useful more accurately describing the phase behavior in regions of the phase diagram where we remain unsure about the behavior: For example, for lengths $L = 5, 6, 8$ in 3D in the region where the isotropic–nematic transition widens or where the variance of the order parameter Q meets the vapor-liquid binodal (a possible pseudo-tricritical point). Also, high-density regions for the sticky model in 2D could be explored, as well as the dynamics around the tricritical point.

As discussed throughout this thesis, dynamics are inseparable for the statistical properties of systems, and are fundamental when these are marginally ergodic or lose ergodicity. Fast compression algorithms can be employed on the Markov-Chain time-series data, for example those described in Refs. [914, 926]. Also discussed in this thesis is the notion that many-body variables (and order parameters) are heterogeneous in space and time, even in equilibrium. Therefore, local-scale order parameters could provide a better resolution of phase boundaries (see Refs. [914, 926]), analogous to how finite-size scaling behavior allows us to predict the true critical points of system. Other types of order of the hard rod systems are reported to appear at very high densities that are distinct from the nematic transitions discussed in this chapter [365, 368, 369, 918]). These would require other order parameters.

Further, as we discussed further above, there may be metastable binodals hidden underneath the stable binodals (particularly for for $L = 5, 6$) in 3D, and for the 2D systems. This is suggested by analogous two-component mixture

models that have such phase diagrams, see Ref. [677] and Fig. 2.6. Notably, such metastable binodals and further demixing lines exist for the "sticky" monolayer system we studied in Ch. 5. These metastable phases may not be resolvable in any easy way in the grand canonical ensemble, and would likely require an addition of diffusion-type moves, at minimum. Hence the extension of GCMC pseudodynamics that include local diffusion may not only help in equilibration, but also gives us new information on dynamics, especially if most of the MC-moves are predominantly diffusion-moves over insertion–deletion moves. An analysis would help clarify outstanding issues about the phase diagrams, as argued above.

In our simulations, we encountered an imminent problem of memory of the initial condition at high densities, and effects of hysteresis depending on the density at which the algorithm equilibrated. In retrospect, this ordering transition (Fig. 6.15) may actually indicate glassy dynamics or a gel, for example (See also Fig. 11 in Ref. [724]) that we indeed find in a confined system of sticky rods in Ch. 5.

We also mention that both diffusion and insertion-deletion dynamics can be implemented with kinetic Monte Carlo (KMC): We have programmed this already for sticky rods in a monolayer in Ch. 5; moreover, the KMC code has been written for fully 3D dynamics (or growth at a surface), as well. This is an outlook from this thesis. The advantage of KMC is that the dynamics are tracked directly by the algorithm, and analysis of the spatial and time correlations of these dynamics is quite straightforward.

Additionally, machine learning algorithms could aid in this process [935]. Variational autoencoders applied in the upcoming Ch. 7 – that we even applied to 2D sticky-rod systems, at intermediate densities – are shown to be able to decipher phases of matter very succinctly. They could be of help in many of the above-mentioned issues.

6.9 Conclusions

Note: This text is the author's writing (the conclusions have been re-written, when, for example, comparing to those contained in the publications).

In the first half of this chapter, we investigated purely hard-core rods of size $L \times 1 \times 1$ on a cubic (3D) lattice in a Monte Carlo simulation study. The Monte Carlo simulations are performed in the grand-canonical ensemble, where we utilized cubic lattice up to $M = 168$ in linear size. In this on-lattice model, the fully discretized degrees of freedom (rotational and translational) lead to interesting characteristics of the isotropic–nematic phase transition, which differs substantially compared to liquid-crystal-type models in the continuum.

We have observed a "nematic" transition for $L \geq 5$ (where we studied $L = 6, 8, 25$ in detail). For $L = 5, 6$, the nematic state entails a negative order parameter: ordering is realized by the dominance of *two* orientational directions simultaneously. The type of ordering changes for $L \geq 7$, where the nematic state entails a positive order parameter: one of the three orientations dominates. To detect the nematic phase, we first described the system using either a "maximum" (or "minimum") nematic order parameter; later, we found that a two-dimensional order parameter analogous to that of three-state Potts models is superior for describing the orientational ordering of the system.

We have investigated rod lengths up to $L = 25$ and have found evidence that the isotropic–nematic transition is of very weak first order for all rod lengths $5 \ldots 25$. Yet, deciding on the type of the transition is very difficult despite using large systems containing several 10^5 particles. The nematic order is very small near the transition. We deduce that these systems entail strong fluctuations in the order parameter, which broaden the probability distribution over the order parameter significantly. This near-"destruction" of the first-order transition complements results for 2D systems, where earlier studies have shown that the ordering transition is non-long-ranged ("pseudonematic") and presumably of the Ising universality class [366]. Notably, the ordering transition occurs in 2D for $L \geq 7$, which is the length at which we first observe an ordering transition with a *single* dominant orientation (see above).

We additionally compared the transition at various rod-lengths to those predicted by a lattice fundamental measure theory (FMT). This turns out to be the bulk is equivalent to the DiMarzio entropy [358] (who, in fact, described the entropy from a mean-field approach), as well as the solution of the entropy on Bethe-like lattices [360].[4] The FMT overestimates the strength of nematic ordering strongly, which we attribute to a systematic failure at capturing the strong orientational fluctuations. One way to improve the FMT may be include extending the 0D cavities (of the theory) to include more than one particle in order to capture correlations between differently-oriented particles better [160, 265].

In the second half of this chapter, we presented and described the phase diagrams of the same hard-core rods with additional "sticky" (short-ranged) attractions for 3D (cubic) lattices, as well as in 2D (square lattice). This was likewise a GCMC simulation study. The additional attractions induce a gas–liquid transition that competes with the orientational ordering transitions. The phase diagrams are both qualitatively and quantitatively different from those of comparable model systems of the continuum (e.g. spherocylinders with short-ranged attractions).

In the 3D system, the weak-attraction limit is similar to the purely-hard-core limit we studied in the first part: the isotropic–nematic transitions are weakly first order, and strong fluctuations in orientational order likewise play a significant role. (The coexistence density gap is not resolvable in histograms of the particle numbers.) As in the hard-core case, at rod-lengths $L = 5, 6$, the orientationally-ordered phase entails a *suppression* of one of three particle species (orientations), which we deemed a "nematic$^-$" transition. Longer rods likewise show one dominating species, which we deemed a "nematic$^+$" transition. Upon increasing attractions (or decreasing the reduced temperature), this weak-first-order character persists down to a transition temperature region. Thereafter, the coexistence density gap widens dramatically, i.e. the transition becomes strongly first-order in character and represents a separation of an isotropic gas and nematic liquid. Therefore, for small system sizes, where the weak-first-order transition appears continuous, the phase diagrams can be understood a line of critical isotropic–nematic transitions hitting a gas–liquid binodal at a tricritical point. We will see this is truly the case for 2D systems further below. However, the above-mentioned transition temperature region depends heavily on rod-length, and even is manifested with a different phase

[4] A related discussion can also be found in Ref. [265].

diagram topology for the case of $L = 5$: The transition to a nematic phase occurs at much higher packing fractions, and does not seem to meet the critical point of the gas–liquid binodal, which appears at lower densities.

We compared the 3D phase diagrams with those from a lattice fundamental measure theory for sticky rods: Qualitative similarities are visible; however, we think these (still) fail at properly capturing strong fluctuations in the orientational order, which are manifested in large, sterically-incompatible nematic domains. We found this behavior when observing the 2D system, in particular, which we describe below.

In the 2D system (on a square lattice), the nematic phase is manifested by the demixing of the two possible particle species (orientations). We presented results for the exemplary case of $L = 10$ (long rods). For weak attractions, the isotropic–nematic transition remains continuous, forming a line of critical points for increasing attractions that presumably terminates at a tricritical point. Thereafter, a gas–liquid binodal widens substantially. In the region just above the tricritical point, the line of critical points bends in an unexpected way: the transition moves to higher densities upon increasing the temperature before moving to lower densities again, which seems counterintuitive. However, upon visual inspection of the configuration snapshots, as well as a special quantitative analysis of the orientationally ordered domains, we have rationalized this behavior: Stronger attractions cause these domains to become more compact *internally*, but do not change the demixing order parameter significantly. Upon increasing the attractions further, the domains become so compact that they effectively pull together, leaving room for voids between them. In other words, the high steric incompatibility of the domains frustrates the packing problem and voids open up at the interfaces of the domains. This is the beginning of the gas–liquid demixing transition at the (presumed) tricritical point.

Outlook

These studies have highlighted the role of highly-discriminating orientational domains of one type of order (strong fluctuations) in the lattice models. We discussed how these may point to ways of improving the FMT – in particular, cluster-based methods or multi-particle cavities are examples.

As to the phase diagrams, novel analysis methods such as compression schemes and complexity measures on the Markov-Chain time-series – i.e. using the pseudo-dynamics of the system for dynamical information – may offer a way to decipher any "gray areas" of the phase diagrams. For example, areas near the (pseudo-)tricritical regions, as well as other nonergodic regions of the phase diagrams (i.e. macroscopically arrest states) that can occur at high densities and very strong attractions. Refs. [914, 926] have recently demonstrated such approaches for the purely hard-core 2D systems. Moreover, exploring the "internals" of the liquid–gas binodals, i.e. characterizing potential metastable critical points, would offer new (out-of-equilibrium) information about the phase diagrams. In particular, the systems of $L = 5, 6$ would likely show very different metastable phases and percolation behavior than for $L \geq 7$ in the bulk. A study of dynamical jamming and percolation transitions would likewise offer complementary, nonequilibrium information about e.g. critical behavior in these systems. (We discussed how jamming transitions in

the random-sequential-adsorption setup have received much more attention, regarding investigation of lattice models of hard rods.) Dynamical jamming transitions as well as percolation could be investigated via the KMC simulations we developed in Ch. 5.

Finally, characterizing the surface phases of these systems is the next logical step (putting the system in semi-confinement with an attractive wall), in connecting to the (2+1)D monolayer-confined systems studied in part II. These would be important for understanding structure and phase transitions in multilayer thin films.

As to the simulation side, we experimented with cluster-moves in the grand canonical ensemble for these systems of long rods. However, the constraint of the degrees of translational degrees of freedom to the lattice resulted in very low acceptance probabilities. We think a combination of the lattice FMT (possibly also for sticky rods) with the standard GCMC algorithm could possibly render a novel, DFT-inspired accelerated Monte Carlo algorithm — by employing the DFT functional for *proposal* probabilities, and guaranteeing detailed balance on the full acceptance probability. To this end, machine learning might offer another interesting method: this will become clearer after presenting our studies in machine learning in Ch. 6.

The end of this chapter marks the end of part III of this thesis, where we explored the statistical mechanics of hard-rod systems constrained to lattices in the case of 3D bulk, as well as 2D. We have characterized the latter case of 2D for sticky hard rods, which is useful for the next part of this thesis, part IV. There, we explore a machine learning algorithm by using configurations of the 2D lattice model of sticky rods as training data. In that way, we aim to understand whether an unsupervised, generative learning algorithm can recover physical principles of the coarse-grained, thermodynamic properties of these systems. We also seek to understand better the limits of the algorithm, in particular its generative properties. Thus, the characterization of the tricritical phase behavior in the 2D sticky hard-rod model system in this preceding chapter will be of fundamental importance for analysis and interpretation of the algorithm.

Part IV

Machine Learning of 2D Systems of Hard Rods on Lattices

Chapter 7

Fluctuating Collective Variables: On Variational Autoencoders Learning 2D "Sticky"-Hard-Rod Configurations

The means of obtaining as much variety as possible, but with the greatest possible order... is the means of obtaining as much perfection as possible.

Gottfried Wilhelm Leibniz

In this chapter, we shall explore the behavior of *beta-variational-autoencoders* (β-VAEs) after training them on (biased) Boltzmann-Gibbs-distributed configurations of the 2D "sticky" hard rod model characterized in Ch. 6. We had introduced this part of the thesis quite broadly in the context of machine learning in Ch. 1.4. We delved into probabilistic modeling for machine learning as well as described the basic theory behind variational autoencoders in Ch. 3.6. We described the algorithm in detail in Ch. 3.6.2.

Presented in the last chapter, the 2D sticky-hard-rod system entails two competing transitions meeting at a tricritical point: A continuous orientational ordering transition as well as a vapor–liquid transition. Therefore, representing a three-fold symmetry (a two-dimensional order parameter, see Ch. 6) will be crucial in the data *pre-processing* step. We remind the reader that we discussed the coupling of orientational and translational degrees of freedom, as well as related multidimensional order parameters, quite generally in Ch. 2.1, as well.

As the dimension of the original configurations is much larger than the latent space, we expect the β-VAEs (as well as other algorithms) to *coarse grain* the configurations. The term "coarse-graining" is used loosely; we discussed coarse-graining in Ch. 3. We will see that the VAEs find collective variables in statistical ensembles,[1] which can be regarded as "hidden features" of the fluid.

The inference model of the VAE presumes a Gaussian approximate posterior on the latent variables. This implies that latent variables fluctuate even for a *single* input data (one configuration); thus, "microstate" fluctuations are part of learning the generative model. (We discussed Gaussian field models in Ch. 3.2.) In fact, the strength of fluctuations of collective variables in *ensembles* of configurations is key to how the VAE discovers them in the optimization problem. In turn, the collective variables and the fluctuations provide important statistical

[1] we briefly discussed collective variables in Ch. 2.1.3

information on thermodynamic ensembles themselves. The statistics over the learned model parameters will become excellent detectors of phase transitions, and possibly even their order (first or second order).

We will see effects of "internal" frustration in the learning problem, inducing threshold behavior upon varying a fundamental hyperparameter β at fixed latent-space dimension. The former adjusts a trade-off between matching the approximate posterior to the prior on latent space and the quality of the image reconstruction. At a threshold state, we will discover that the character of the learned variables changes drastically, forming a kind of coarse-graining hierarchy, among other effects like the "mode collapse" of high-order variables.

7.1 Organization of this chapter

This chapter is organized as follows: Sec. 7.2 refreshes the reader of the physical model system of sticky hard rods in 2D that was investigated in Ch. 6, in case the reader had skipped the previous chapter. The input datasets, composed of configurations of the rod system, are specified in detail – including a key difference between the thermodynamic properties of the training and test datasets we employ. Further, the variational autoencoders, are described and specified. In Sec. 7.3, we discuss the importance of the choice of data representation for the hard-rod configurations, which is a first finding of this study. Sec. 7.4 discusses and presents quantitative results demonstrating how the VAEs appear to "coarse-grain" the statistical system of rods upon varying the dimension of the provided latent space. In Sec. 7.5 we discuss and interpret the latent variables of the VAE – they can find the order parameters of the physical system, as well as higher-order collective variables that fluctuate in the homogeneous hard-rod fluid. Thereafter, in Sec. 7.6, we study more carefully phenomena that we observe when varying the hyperparameter β (a parameter in the cost function fixed prior to optimization). In Sec. 7.7, we discuss how the probabilistic model of VAEs offers us an alternative characterization of equilibrium states (if provided as input) that is highly sensitive to thermodynamic properties, such as positions of phase transition points as well as the order of the transition. In Sec. 7.8, we will present a few comparative results, as well as an important preliminary finding on VAEs with deep-convolutional neural-network architectures. Thereafter in Sec. 7.9, we briefly report on a few other experiments with machine learning, for example other algorithms. A general discussion and prospective ideas are provided in Sec. 7.10 thereafter. We state our conclusions of this chapter in Sec. 7.11

7.2 Model and methods

7.2.1 Physical model system (the input data)

The definition of the 2D sticky-hard-rod model system was also presented in Ch. 6: The physical model system is that of hard rods on a quadratic lattice in 2D, where hard rods are rigid parallelepipeds with extensions $L \times 1$ and are defined by L consecutively-covered lattice points in one Cartesian direction. We fix the *rod-length* to $L = 10$ in this study. We define an occupancy field $O(\mathbf{s})$, whose values are 1 for lattice points $\mathbf{s}$ covered by rods and 0 otherwise.

The hard rods are forbidden to overlap one another, i.e. there is no double occupancy of a lattice point. The quadratic lattice restricts the number of possible orientations to two, and we refer to rods oriented in horizontal and vertical directions as species 1 and 2, respectively. Species densities ρ_i are defined as the total number of rods of species i (N_i) normalized with the system size, which is $M^2 = 128^2$ square units. The total density (which goes between 0 and 1) is $\rho = \sum_{i=1}^{2} \rho_i$, and the total packing fraction is $0 \leq \eta = \rho L \leq 1$.

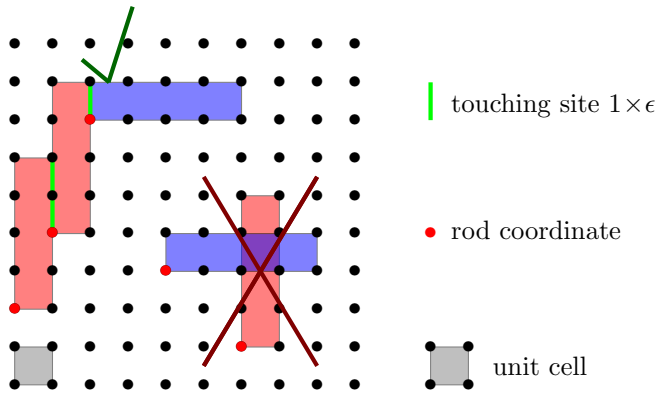

FIGURE 7.1: 2D scheme of the model. The two crossed out rods are representing forbidden overlap, i.e. the double occupation of a lattice cell. The common surface of touching segments of neighboring rods are shown in green. Reproduced from Ch. 6.

The rods in the system have additional short-ranged, "sticky" attractions on top of the hard-core repulsion between rods, the strength of which is quantified by a (fixed) ϵ, so that the unit binding energy is $-|\epsilon|$ between touching segments of nearest-neighboring rods (see Fig. 7.1). The internal energy of a valid "sticky"-rod *configuration* $\mathbf{x}$ can therefore be written as

$$U(\mathbf{x}) = \epsilon \sum_{\langle \mathbf{s}\mathbf{s}' \rangle} O(\mathbf{s})O(\mathbf{s}') - N(L-1)\epsilon, \tag{7.1}$$

for $\epsilon < 0$, where the sum is over neighboring sites $\mathbf{s}, \mathbf{s}'$ of the lattice and gives a contribution whenever both sites are occupied. The second term corrects for the over-counted adjacent cites *within* each rod, which is a rigid entity (N is the total number of rods).

Notation

An equilibrium (Boltzmann-Gibbs) distribution of rods in the grand-canonical $(\mu_{\text{chem}}, V, T)$ ensemble is defined by a fixed chemical potential μ_{chem}, volume V, and temperature T. In this study, grand-canonical ensembles in the physical system are equivalently identified by the variables (f, V, T^*). The fugacity is the variable $f \equiv \exp(\mu_{\text{chem}}/k_B T)$, k_B is the Boltzmann constant. Further, $T^* \equiv (k_B T)/|\epsilon|$ is the *reduced temperature* of the system. As the only relevant quantities are relative to $k_B T$, we can set $k_B T \equiv 1$. The volume of the 2D physical system $V = M^2 = \text{const}$ is constant in all data employed in this study.

Remark. Standard notation for the chemical potential μ, fugacity z, and inverse temperature β would be easily confused in this study: The mean variables on

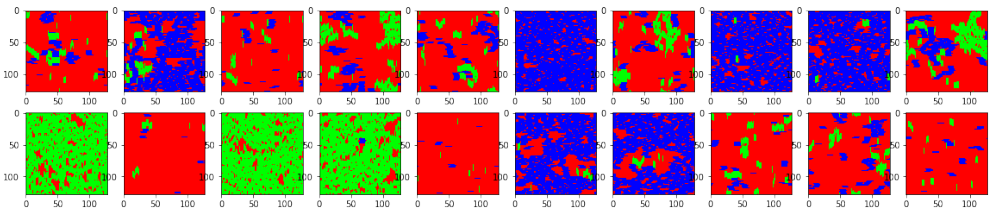

FIGURE 7.2: Example configurations of the 2D sticky rod system: Red lattice sites indicate vacant sites, green those occupied by vertical rods, and blue those by horizontal rods. The "nematic" (demixed) phase is characterized by mostly blue or green configurations, while the isotropic phase has both. A gas phase is characterized by mostly red color in the image. The rod-lengths are $L = 10$ units, their widths are unity. The area of the system is $M^2 = 128^2$

NOTATION	MEANING
$L = 10$	Rod-length (fixed!)
μ_{chem}	Chemical potential
$f = \exp(\mu_{\text{chem}}/(k_B T))$	Fugacity
V	System volume (area) $V = M^2 = 128 \times 128$
M	Linear system size (of the box) $M^2 = 128 \times 128$
ϵ	"sticky" attraction strength
T^*	Reduced temperature $= (k_B T)/\lvert\epsilon\rvert$
$\boldsymbol{s}$	Lattice site
$\boldsymbol{x}$	Configuration sample or input sample
$U(\boldsymbol{x})$	Inner energy of a configuration, see Eq. (7.1)
ρ	Number density of rods, see Eq. (7.3)
η	Packing fraction of rods $\eta \equiv L\rho$
S	Unnormalized demixing parameter, see Eq. (7.3)
$\mathbf{c}$	Complex-valued 2D (tricritical) order parameter, see Eq. (7.13)

TABLE 7.1: List of physical quantities of 2D "sticky" hard-rod model system: Notation and meaning.

latent space encoded by VAEs are denoted "μ". The latent variables are denoted by "$\boldsymbol{z}$". The hyperparameter entering the cost function (the negative evidence lower bound, see further below) is denoted β. For this reason we provide a list of the variables and their meanings in Tab. 7.1 and in Tab. 7.2 later.

Competing gas–liquid and orientational-ordering phase transitions

Let us discuss the phase behavior of the "sticky" hard rod system in 2D. This will be relevant for interpreting the behavior during and after learning. The phase diagram of the model we have quantified in Ch. 6 (Fig. 7.3) is spanned by the total (mean) packing fraction η and reduced temperature $T^* = k_{\text{B}}T/|\epsilon|$. A line of critical points (black line) separates the *isotropic* (both species are at hand at the same time) and "nematic" or, rather *demixed* phase, where one of two orientation-species dominates over a longer period of Monte-Carlo-time. In this symmetry-broken phase the system "jumps" back-and-forth between two

possible *mesostates*, in effect, and shows large, fluctuating domains with only one species, see e.g. Fig. 6.21.) The line begins at $T^* = \infty$, the limiting case of purely hard-core rods, down to a (presumed) *tricritical* point, indicated in red. Below the tricritical point, this orientational-ordering transition becomes first order: The demixing of orientational states "competes" or is *coupled with* with the separation of the fluid in a vapor (low-density) and liquid (high-density). The 2D system of very long rods is highly correlative, in the sense that we discussed in Ch. 2.2: rotational and translational degrees of freedom are strongly coupled in the 2D systems. At low temperatures, the global translational symmetry of the fluid begins to break: Vacancies (which allow for translational motion) are *rare* inside the highly-dense domains of the demixed phase (within which only one orientation-species persists); vacancies are predominant in the vapor phase. The blue points in Fig. 7.3 indicate the estimated *binodal* of this first-order transition.

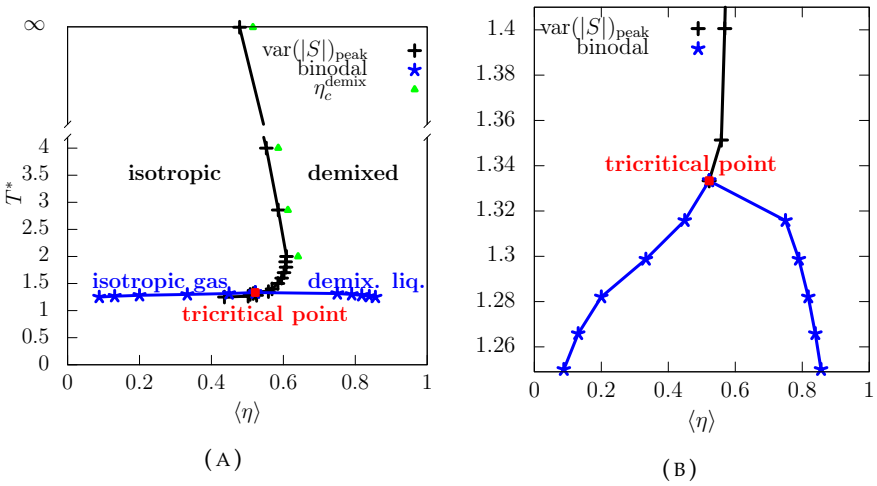

FIGURE 7.3: Phase diagram of 2D sticky hard rods on a square lattice for $L = 10$ in the reduced–temperature – packing–fraction plane, (a) reproduced from Ch. 6 and (b) zoomed in to near the tricritical point. Note the black points were obtained with a normalized version of the nematic order parameter (Eq. 7.3).

The tricritical phase behavior implies the system entails the possibility for three types of ("stable") states: (1) A high-vacancy phase $\rho \gtrsim 0$, which would correspond to many "red" areas in configurations represented in Fig. 7.2; (2) a "demixed" state with predominantly horizontal rods, $\rho \approx \rho_1 \gg 0$; and (3) the other, degenerate broken-orientational-symmetry state with predominantly vertical rods, $\rho \approx \rho_2 \gg 0$. Such a "tri-state" (at the tricritical point) is best expressed by a *two-dimensional* order parameter – a *pair* of one-dimensional, scalar order parameters: (ρ, S). Here, ρ is the total *density* and S is the *unnormalized orientation-demixing order parameter*. (Please note this difference of definition to compared to Ch. 6, where S indicated a normalized order parameter):

$$\rho \equiv \rho_1 + \rho_2 \tag{7.2}$$
$$S \equiv \rho_1 - \rho_2 \tag{7.3}$$

The degenerate demixed states with S and $-S$ are thermodynamically equivalent (equally represented over long enough Monte-Carlo-time), since exchanging of rods with horizontal and vertical orientations represents a rotational symmetry of the model. In Ch. 3.2.1, we discussed how such symmetry-broken states may be considered "metastable", in effect, especially for finite system sizes. Later, we will see that the unsupervised machine learning algorithm indeed "lumps" states with $+S$ or $-S$ together, respectively, as if these represent different stable states of the system.

7.2.2 Monte-Carlo data generation and thermodynamic properties of data-sets

We employed Markov-Chain Monte Carlo simulations in the grand canonical ensemble (GCMC) to generate all data. We described the algorithm in more detail in Ch. 6. An equilibrium ensemble is characterized by the triple (f, V, T^*) that we discussed in Sec. 7.2.1, where the simulation box size is $128 \times 128 \equiv V$. In every equilibrium ensemble, particle numbers N fluctuate.

Data-set type I: Biased Boltzmann-Gibbs ensembles (training)

After some period of experimentation, we found that employing *biased ensembles*, biased in the particle number N, for the training data is conducive for learning. Specifically, a continuous variable N that is approximately *evenly-distributed* is helpful. Variational autoencoders and many other algorithms model *continuous* variables in latent space. The technique of *successive umbrella sampling* (SUS) [916] produces an even-N-histogram of samples by confining the system successively in particle-number "windows".[2] All training data was generated in these biased ensembles, which are not equilibrium Gibbs-Boltzmann ensembles. In our empirical observations, a very important factor for success and interpretability of learning about many different phases of the hard-core rod system is that input data spans across phase boundaries – moreover, when the order parameters are nearly-evenly distributed over the samples from phase space. We will discuss this point more succinctly in Sec. 7.3.

All results on VAEs presented correspond to a training set biased ensembles at fixed reduced temperature $T^*_{\text{train}} = 1.401$. The training set comprises of $\sim 1.4 \times 10^5$ configurations. In all cases (also training data, see below) we leverage the $S \to -S$ symmetry of the rod model by rotating the configurations by 90° and adding them to the data-sets, which, however, makes them statistically dependent. Yet, we observed that the latent-space representations will become "balanced" much more easily, i.e symmetric around null. A "rotation" of input images is standard practice in the machine learning literature.

Note that as the machine learning is fully unsupervised, and no explicit information about the thermodynamic variables f and T^* is transferred to the learning system. We will propose related ideas for improvements on VAEs in Sec. 7.10.

Data-set type II: Equilibrium Boltzmann-Gibbs ensembles (only for testing)

Testing data comprises of sets of Boltzmann-Gibbs equilibrium ensembles defined by fixed (f, V, T)). In most cases, the testing data stems from simulations

[2] a technique we also employed in the studies presented in Ch. 6

below the training temperature. In fact, the test sets are situated in part *well below* the tricritical temperature: at fixed chemical potentials and temperatures at or below the training reduced temperature $T^*_{\text{test}} = 1.401 \ldots 1.266$. Each temperature entails between $\sim 1 \times 10^5 \ldots 2 \times 10^5$ configurations.

Note that in some cases, we test the VAEs in the biased ensembles, as well – either at the same training temperature, but out-of-sample compared to training data, or at different reduced temperatures. We will make a note whenever this type of data-set is employed is the case.

7.2.3 Variational autoencoders

Variational autoencoders are *generative* models, entailing a full probabilistic, inference model of data. We described these concepts and the fundamentals of the algorithm in detail Ch. 3.6. The encoding–decoding aspect of VAEs means that they bear some resemblance to deterministic autoencoders (AEs) (Fig. 1.7). (We even compared the VAEs to AEs, as well, in preliminary work. We remark on this in Sec. 7.9.) The most basic parts are reviewed here:

The *encoder* neural network maps the input into a latent space, where the encoding contains a pair on multidimentional variables $(\boldsymbol{\mu}, \boldsymbol{\sigma})$, which represent the parametrization of a posterior distribution of latent variables $\boldsymbol{z}$ over the input data $\boldsymbol{x}$ (the probability density of an encoding in latent space conditioned on each ground-truth configuration $\mathbf{x}$). Crucially, the posterior over $\boldsymbol{z}$ is approximate – it is assumed to be a *diagonal* multidimensional Gaussian following $p(\mathbf{z}|\mathbf{x}) \approx \mathcal{N}(\mu, \sigma)$. (The dimension of latent space is a hyperparameter, which is set aforehand, and which we denote $\dim(\boldsymbol{z})$.) Thus, VAEs model local *fluctuations* of each configuration in latent space, making them inherently *stochastic*, in stark contrast to deterministic autoencoders: On a repeated sampling, the random encoding is assumed, on average, to be positioned at vector μ away from the center of latent space ($\mathbf{0}$), fluctuating about this mean position with variance σ^2. Figure 7.4 shows an example of such generated samples in the original space, a set $\{\boldsymbol{x}'\}$ which are conditioned on a single ground-truth $\boldsymbol{x}$. The generated images are obtained by sending a randomly *sampled* $\boldsymbol{z}$ (distributed according to the parametrized $p(\mathbf{z}|\mathbf{x}) = \mathcal{N}(\mu, \sigma)$) through the *decoder* network. The encoder, sampler, and decoder encoder is visible in Fig. 7.5 further below. Note that the assumption of a diagonal Gaussian for the posterior distribution is a *mean-field* assumption.

As we will discover in Sec. 7.5, the sampled variables $\boldsymbol{z}$ indicate collective variables or spatial "modes" in the hard-rod configurations (analogous to local domains, etc.).

Training the parameters of the neural networks is formulated in an optimization problem. The cost function is written as a trade-off between the quality of the reconstructed or generated images, $\{\boldsymbol{x}'\}$ compared to $\boldsymbol{x}$, as well as the quality of the encoding according to an imposed probabilistic model of the latent variables $p(\mathbf{z}|\mathbf{x}) \approx \mathcal{N}(\mu, \sigma)$. The first part – the reconstruction cost – represents the "stochastic autoencoder" capability of the neural network. It ensures that a direct relationship (a map) persists between the latent variables and the physical space, and is denoted by the term $\mathcal{L}_{\text{mse}}(\boldsymbol{x}, \boldsymbol{x}')$.

The second part of the cost function enforces the faithfulness of the probabilistic (inference) model over the latent variables. As in physics, information is relative, hence the efficiency of the probabilistic encoding is judged via a relative entropy of the posterior distribution of latent variables to the model prior.

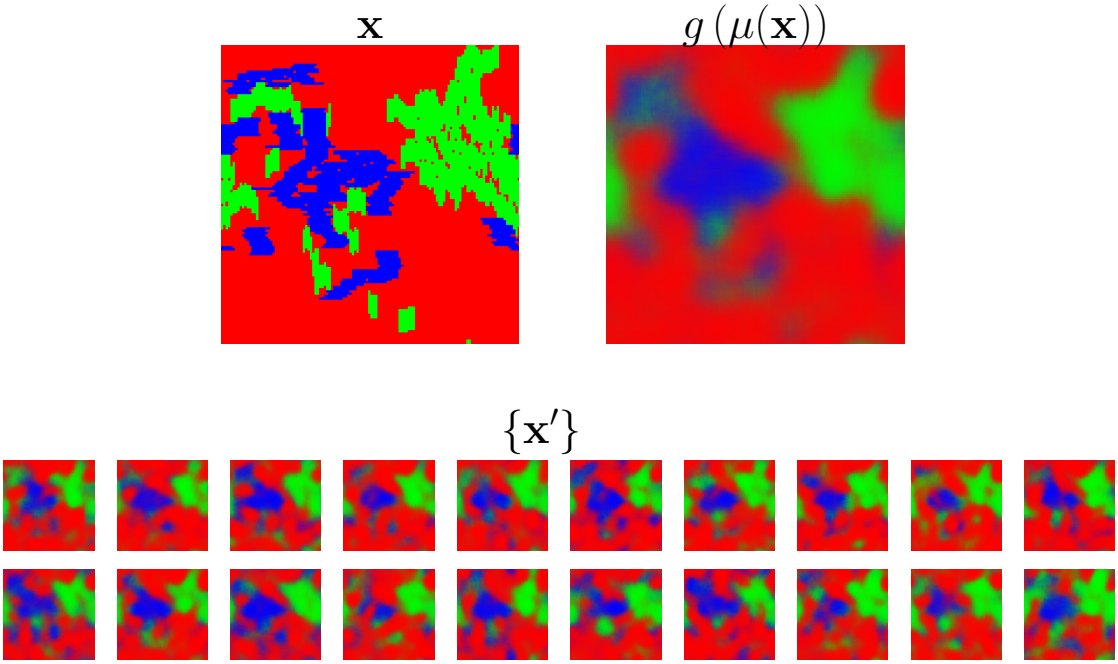

FIGURE 7.4: Generating random configurations from the Gaussian posterior model $p(\mathbf{z}|\boldsymbol{x}) = \mathcal{N}(\boldsymbol{\mu}, \boldsymbol{\sigma})$, where $(\boldsymbol{\mu}(\mathbf{x}), \boldsymbol{\sigma}(\mathbf{x}))$ are encoded variables of the single input configuration $\mathbf{x}$ (top left). (Top right): The decoded image using the means $\boldsymbol{\mu}(\mathbf{x})$ only, which we denoted "$g(\boldsymbol{\mu}(\boldsymbol{x}))$". (Bottom): Example generated samples $\{\boldsymbol{x}'\}$ by sampling $\mathbf{z} \sim \mathcal{N}(\boldsymbol{\mu}, \boldsymbol{\sigma})$ and sending the variables through the decoder. This VAE was trained with hyperparameters $\dim(\mathbf{z}) = 128$ and $\beta = 8$. The ground-truth configuration $\boldsymbol{x}$ was generated from simulations at temperature $T^* = 1.299$.

The specific form of the prior is assumed to be irrelevant, in theory, hence a simple prior that further provides a nice normalization of latent space should suffice: A multidimensional unit Gaussian $p(\mathbf{z}) = \mathcal{N}(\mathbf{0}, \mathbf{1})$ is the standard choice. The *relative entropy* or *Kullback-Leibler (KL-) divergence* between the approximate posterior and model prior is written in a term $D_{KL}\left(N(\boldsymbol{\mu}, \boldsymbol{\sigma})||\mathcal{N}(\mathbf{0}, \mathbf{1})\right)$, and represents a *variational free-energy gap* (for every $\boldsymbol{x}$) that should be minimized. Please note that we discussed topics of variational mean-field approximations in a much broader, physical context in Chs. 3.2 and 3.5.2.

The cost function is minimized during training is an expectation value of the reconstruction cost and KL-loss over random (mini-) batches of input data.

$$\mathcal{L}_{\text{VAE}} = \left\langle \mathcal{L}_{\text{mse}}(\boldsymbol{x}, \boldsymbol{x}') + \beta D_{KL}\left(N(\boldsymbol{\mu}, \boldsymbol{\sigma})||\mathcal{N}(\mathbf{0}, \mathbf{1})\right) \right\rangle_{\text{batch}(\boldsymbol{x})} \ . \tag{7.4}$$

In β-VAEs, which we study in this chapter, the KL-loss is multiplied by a factor β (Eq. (7.4)), as we are investigating the more flexible and generalized version [52, 533]. The KL-loss between the unit Gaussian prior and diagonal-Gaussian posterior is explicitly

$$D_{KL}\left(N(\boldsymbol{\mu}, \text{diag}(\boldsymbol{\sigma}))||\mathcal{N}(\mathbf{0}, \mathbb{1})\right) = \frac{1}{2} \sum_{k=1}^{\dim(\mathbf{z})} \left(\sigma_k^2 + \mu_k^2 - \ln(\sigma_k^2) - 1\right) \ , \tag{7.5}$$

NOTATION	MEANING
$\boldsymbol{x}$	Configuration sample or input sample
$\boldsymbol{x}'$	Reconstructed configuration or decoded sample $\boldsymbol{x}' \equiv g(\boldsymbol{z})$, where $\boldsymbol{z} \sim p(\boldsymbol{z}\|\boldsymbol{x})$ is sampled
$\phi(\boldsymbol{s})$	physical "field" over sites, congruent to vector $\boldsymbol{x}$, $\phi(\boldsymbol{s}) \doteq \boldsymbol{x}$. It is binary on each channel ν: $\phi(\boldsymbol{s}) = \sum_{nu=1}^{3} \phi_\nu(\boldsymbol{s}) = \sum_{\nu=1}^{3} \delta_\nu(\boldsymbol{s})$
$\phi'(\boldsymbol{s})$	output "field" over sites, congruent to vector $\boldsymbol{x}'$, $\phi'(\boldsymbol{s}) \doteq \boldsymbol{x}'$. It is a continuous distribution on each occupancy channel ν: $\phi'(\boldsymbol{s}) = \sum_{nu=1}^{3} \phi'_\nu(\boldsymbol{s}) = \sum_{\nu=1}^{3} \mathrm{Ber}_\nu(\boldsymbol{s})$
$\boldsymbol{z}$	Latent variable(s) (multidimensional)
$\dim(\mathbf{z})$	Dimension of latent space
$\boldsymbol{\mu}$	"Mean" vector of latent space encoding (multidimensional), which is a function of $\boldsymbol{x}$
$\boldsymbol{\sigma}$	"Standard deviation" vector of latent space encoding, which is a function of $\boldsymbol{x}$
$p(\boldsymbol{z}\|\boldsymbol{x})$	Approximate posterior of the model, $p(\boldsymbol{z}\|\boldsymbol{x}) \equiv \mathcal{N}(\boldsymbol{\mu}, \mathrm{diag}(\boldsymbol{\sigma}))$
$p(\boldsymbol{z})$	Prior of the model on latent space $p(\boldsymbol{z}) \equiv \mathcal{N}(\mathbf{0}, \mathbb{1})$
$p(\boldsymbol{x}\|\boldsymbol{z})$	Conditioned likelihood of $\boldsymbol{x}$
$p(\boldsymbol{x})$	Likelihood of $\boldsymbol{x}$
$\mathcal{L}_{VAE}$	Cost function of β-VAEs Eq. (7.4) or Eq. (3.280)
β	hyperparameter of β-VAEs, see Eq. (7.4) or Eq. (3.280)
$D_{KL}(\cdot\|\|\cdot)$	Kullback-Leibler divergence (relative entropy), see Eq. (3.224)
$\mathcal{L}_{MSE}$	Reconstruction cost: average mean-squared-error-term, $\mathcal{L}_{MSE} = \langle \|\boldsymbol{x} - \boldsymbol{x}'\|^2 \rangle$, Eq. (7.4) or Eq. (3.280)

TABLE 7.2: List of quantities related to the β-VAEs: Notation and meaning.

where $\boldsymbol{\mu}(\boldsymbol{x})$ and $\boldsymbol{\sigma}(\boldsymbol{x})$ are functions of each input data image $\boldsymbol{x}$. We also note that in the standard VAE implementation, only a single shot of generated images $\boldsymbol{x}'$, i.e. only a single $\boldsymbol{z}$ is sampled from the posterior, is required for a reasonable estimation of the error on the reconstruction.

In our study, we employ the mean-squared error as a reconstruction cost function:

$$\mathcal{L}_{\text{mse}} = \left\langle \left\| \boldsymbol{x} - \boldsymbol{x}' \right\|^2 \right\rangle_{\text{batch}(\boldsymbol{x})} , \tag{7.6}$$

which sums point-wise errors between $\boldsymbol{x}$ and $\boldsymbol{x}'$ over all sites $\boldsymbol{s}$. This is then averaged over a mini-batch of input data. Tab. 7.2, we provide a list on the notation of quantities surrounding the topic of the variational autoencoders.

7.2.4 Implementation of VAEs

The "vanilla" VAEs studied in this work have a shallow and wide neural network architecture. However, we will also compare this architecture to that

of deep convolutional VAEs in Sec. 7.8. The "vanilla" architecture is described below.

The "Vanilla-VAE" neural network

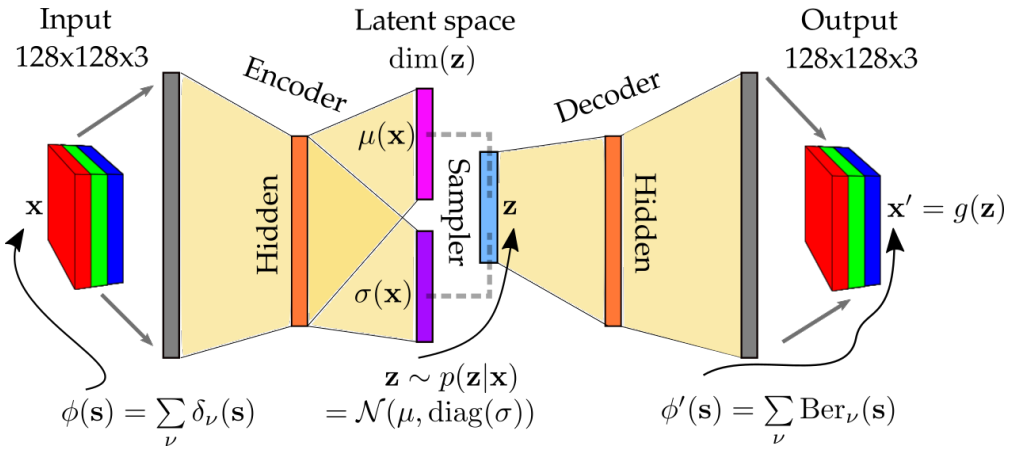

FIGURE 7.5: Sketch of the "vanilla" VAE implemented. Shown is the flattening of the data at the input side (converting a $M \times M \times 3$ matrix to a $M^2 * 3$ linear vector), and the reverse operation on the output side. The input image can be thought of as a "field" $\phi(s)$ that sums over field contributions in three channels (red–green–blue), which are binary for the "sharp" input configuration. Not shown is that the input x is subsequently transformed linearly in its range of values from $[0, 1]$ (binary values) to $[-1, 1]$. The encoder network is composed of a single hidden layer (fully connected) with a nonlinear activation function (see Tab. 7.3), where two latent vectors are encoded in parallel, $(\mu(x), \sigma(x))$, which represent the "mean" and "standard deviation" of the approximate posterior function $p(z|x)$. A single, random latent vector z is sampled from the distribution before it is sent through the decoder network, which "mirrors" the encoder in form. The final output layer employs a *Softmax* activation function, so that the output values are *probabilities* between 0 and 1 (a Bernoulli distribution, in effect). The output "field" over lattice sites $\phi'(s)$ now has a "fuzzy", probabilistic character. The random output is denoted $x' = g(z)$. Note that the relative sizes of the layers are *not to scale*. All golden areas indicate dense connections (between all nodes).

We used a standard implementation of variational autoencoders, which we denote the "vanilla-VAE" architecture, illustrated in Fig. 7.5. Tab. 7.3 lists the specifications that we will describe in this paragraph. Our "vanilla"-VAE entails a *single hidden layer* and *fully-connected* layers (no convolutional layers, for example). The binary input images of size $128 \times 128 \times 3$ (3 color channels, red–green–blue) are *flattened* to a one-dimensional array,[3] and the scalar values of the occupation probabilities are transformed to the range $-1 \ldots 1$ (this may aid learning). A fully connected layer with *PreLu* (parametric *ReLu*) activation is made to a hidden layer of dimension 256 (with an exception for when the latent space dimensions 256: then this layer is 512-wide). This is then fully

[3] i.e. the multidimensional array is now represented in an elongated, 1D array, where the original dimension fo space is lost, in effect

VAE PROPERTY	VALUE OR NOTE
Connections	*Dense* (fully-connected)
Activation functions	*PreLu* (parametric *ReLu*)
Output activation	*Softmax*
Regularization technique	Early stopping
(Optional)	*BatchNormalization* in encoder and decoder
Optimizer	*Adam* (or *RMSProp*)
Learning rate	0.00002 (or higher if *BatchNormalization* employed)
Hidden layer dimension	256 for $\dim(\mathbf{z}) \leq 128$ $2 \times \dim(\mathbf{z})$ for $\dim(\mathbf{z}) \geq 256$
Latent dimensions explored	$\dim(\mathbf{z}) = 16 \ldots 1024$
Values of β explored	Depends on $\dim(\mathbf{z})$, $\beta = 0.001 \ldots 32$
Number of trainable parameters	Depends on $\dim(\mathbf{z})$. For $\dim(\mathbf{z}) = 128$: Encoder: 12,649,216 Decoder: 12,665,344

TABLE 7.3: Specifications of "vanilla" β-VAE neural network: parameters and setting.

connected with two parallel layers, the μ and the σ layers of the Gaussian latent encoding, having dimensions $\dim(\mathbf{z})$. These are functions of $\boldsymbol{x}$, as the *encoder* network plays the role of the parametrized map. A *sampler* function then uses these as input to draw a single $\dim(\mathbf{z})$-dimensional random variable distributed as $\mathcal{N}(\mu, \sigma)$. The *decoder*, which maps a sampled $\boldsymbol{z}$ back to physical space, i.e. $\boldsymbol{x}' = g(\boldsymbol{z})$ with $\boldsymbol{x}'$ corresponding to the output image. It is essentially a "mirror" of the encoder: The output of the sampler is fully connected with the mirrored hidden layer of the encoder (with *PreLu* activation), and this is fully connected to the output layer, which has a *Softmax* activation since the input is binary (the output should be an approximate "mirror" image of the input). The output array is then be reshaped to the original image size $128 \times 128 \times 3$. We employ the *Adam* optimizer [878] with a learning rate of 0.00002 (which is increased if we employ *batch normalization*, see below). We implement the *Keras* libraries with the *Tensorflow* backend, as well as the *scikit-learn* libraries for e.g. principal component analysis complementary to the neural networks.

Reconstruction cost

The original formulation of VAEs utilizes a binary-crossentropy reconstruction cost function instead of the mean-squared error. We report that using the binary-crossentropy cost function produced qualitatively similar results on the output. The matching to the prior on latent space may have been somewhat better, under conditions, but the latent variables were less interpretable (e.g. order parameters were not well-identifiable, for example.) Careful analysis thereof remains outside of the scope of this thesis.

Regularization

We employed the technique of so-called *early stopping*, which halts the training process whenever the *generalization error* (the out-of-sample cost measure) began increasing. This is described in the literature as a type of regularization, in

effect, which prevents over-fitting (where the generalization error increases).[4]

Selection criterion of "fully-ranked" latent spaces

Most of the analysis in this chapter is done for cases of β-VAEs where the latent space preserved its *full rank* (i.e. no mode collapse), where all latent variables participate or show fluctuations when measured on the test data set. We will discuss our findings in the results later. Notably, judging whether the VAE had "full rank" was also possible by performing PCA (a linear transformation) on the (sampled) latent space codes $\boldsymbol{z}$ over test data. The importance ratio or singular values revealed the rank of the latent space.

Usage of batch normalization

We report here on our experience with employing batch normalization in both the encoder and decoder, which we began to employ late in our study. Batch normalization applied in-between layers re-centers and rescales the data coming out of the last layer to unit variance. The mean and variances are estimated from the current minibatch of input data. We found it generally stabilizes training and, crucially, avoids the need for early stopping: we found universally that the cost function levels off to a constant without increasing again (i.e. overfitting was avoided). This method is thus particularly useful for training VAEs on very large latent dimensions. In these cases, we additionally increased the size of the hidden layer in the encoder and generator, which made the fully-connected networks very large (and wide). The final cost function was typically slightly lower (about 10%) than in the case of early stopping without batch normalization. However, this method seems to fundamentally change the behavior of the VAEs, including our finding that it avoids mode collapse at given values of β where the original architecture failed to. Moreover, the "form" of the first two latent variables (which are identifiable with the physical order parameters, see Sec. 7.5) changes somewhat regarding the shape of their empirical posterior histograms. Therefore, this method is quite interesting, but, would have to be explored separately in a systematic manner outside of the scope of this thesis.

7.3 Data representations (preprocessing) and order parameter fields

As we discussed in Sec. 7.2.1, the tricritical behavior in the system implies three macroscopic states of the system: The system can be in one of two degenerate, high-density states upon an orientational demixing transition – states characterized by positive and negative in demixing order S. The systems can also be in an isotropic state – a vapor or low-density phase below a tricritical point, which separates from a high-density liquid having demixed orientational order. Hence, we may imagine the rod system as one with *three* "species", in effect: two rod species and one for vacancies. In this way, the 2D "sticky" hard-rod system has the same 'spirit' as a three-state *Potts model*, for example.

[4]Note that this "regularization" technique is different from 'standard' techniques, as no term with a Lagrange multiplier is added to the cost function.

Order parameter fields

From the point-of-view of a statistical field theory [65], let us assume that we can represent all three types of macroscopic states locally, as well. As the total probability for any three states at a single site is unity, this constrains the number of macroscopic degrees of freedom per site to two. This implies we can introduce a two-dimensional order parameter for the state of a system that we denote as $\hat{Q}$. This can conveniently be defined on the *complex plane* as

$$\hat{Q} = \sum_{\nu=1}^{3} Q_\nu e^{i\frac{2\pi}{3}(\nu-1)} . \tag{7.7}$$

Each Q_ν will be expressed terms of the two quantities: the density ρ and orientational demixing parameter S.

Following our presumptions, we now associate Q_ν at the local scale with a field $\phi(\boldsymbol{s})$ over *each site* $\boldsymbol{s}$: $Q_\nu \rightarrow \phi_\nu(\boldsymbol{s})$. The order parameters on the global, mean scale in a homogeneous, equilibrium fluid state arise from the mean over all sites:[5]

$$\overline{\phi_\nu} \equiv \frac{1}{M^2} \sum_{\mathbf{s}} \phi_\nu(\mathbf{s}) = Q_\nu . \tag{7.8}$$

In a *hard-core* particle model, these fields arise from combinations of "sharp" occupancies of horizontal or vertical rods, as well as a vacancies, all of which are mutually exclusive, i.e. they correspond to delta-functions:

$$\phi_\nu(\boldsymbol{s}) \equiv \delta_\nu(\boldsymbol{s}) \tag{7.9}$$

for any occupancy $\delta_n u$ of each "species" ν. Therefore, the order parameter $\hat{Q}$ follows

$$\hat{Q} \equiv \mathbf{c} \equiv \overline{\phi_1} + \overline{\phi_2} e^{i\frac{2\pi}{3}} + \overline{\phi_3} e^{i\frac{4\pi}{3}} . \tag{7.10}$$

Note that we have now renamed $\hat{Q}$ into $\mathbf{c}$.[6]

We can now begin to express $\hat{Q}$ or $\mathbf{c}$ in terms of the density ρ (or packing fraction $\eta = \rho L$) and orientational demixing parameter S. The complement to the "vacancy" density (species index "0")

$$1 - \overline{\phi_0(\mathbf{s})} \equiv \rho L \equiv \eta \tag{7.11}$$

is simply the full packing fraction of the rod system. Likewise, the density of rod occupancies of species "1" and "2" follow

$$\overline{\rho_1(\mathbf{s})} - \overline{\rho_2(\mathbf{s})} \equiv SL . \tag{7.12}$$

Therefore, our 2D order parameter $\mathbf{c}$ expresses the global ordering properties via

$$\mathbf{c} = \left(1 - \frac{3}{2} L\rho\right) + i\left(\frac{\sqrt{3}}{2} LS\right) , \tag{7.13}$$

[5] An ensemble average may also be implied here

[6] inspired by the word "color"

where total density ρ is found along the *real* axis, and the demixing order parameter S likewise on the *imaginary* axis:

Input data representations

We have discussed in detail the representation of 2D global order parameters in to local, 2D order parameter fields because this is highly relevant for machine-learning of configurations of a physical model system like that of "sticky" hard rods. Fundamentally, we found that the features of configurations learnt by the algorithm depend crucially on the raw-data form in which the configurations are presented.

As an example, we trained a VAE on dataset with a local (site- or pixel-wise) data representation of $\phi(\mathbf{s}) \in \{0, -1, 1\}$ for {vacancy, horizontal, vertical}-species-occupancy. Although this will correctly represent the demixing order parameter S at the local scale, an ambiguity regarding vacant sites arises, which are supposed to entail $\phi(\mathbf{s}) = 0$ – the value of 0 may be interpreted as "either -1 or 1" by the machine learning algorithms. We verified this with both additional convolutional VAEs and (linear) principal component analysis (PCA): The demixing order parameter S is easily identified as the first latent variable (approximately), while the algorithms struggled (or failed) at identifying the total density ρ or packing fraction η as a second variable that stands out from higher-order variables.

We summarize this finding on the role of choice of representation (i.e. of the dimensionality of the input data basis) in our following "rule-of-thumb": The local, site-wise data representation (usually of binary digits) should have at least as many degrees of freedom as that of the macroscopic order parameters. In our case of the "sticky" hard-rod, on-lattice system in 2D, a two- *or* three-dimensional representation of the local order parameter facilitated PCA and the VAEs in identifying two latent variables to *both* the total density and the demixing order parameter. One option we confirm is to represent *each* lattice site $\boldsymbol{s}$ with the complex vector

$$\hat{\phi}(\boldsymbol{s}) \in \left\{1, e^{i\frac{2\pi}{3}}, e^{i\frac{4\pi}{3}}\right\} , \tag{7.14}$$

which one can to convert a two-dimensional, real-valued vector with the following form:

$$\hat{\phi}(\boldsymbol{s}) \in \left\{(1,0), (-1/2, \sqrt{3}/2), (-1/2, -\sqrt{3}/2)\right\} . \tag{7.15}$$

In this chapter, we chose a three-dimensional representation as three 'RGB'-color channels for an input image, e.g.

$$\phi(\boldsymbol{s}) \in \{(1,0,0), (0,1,0), (0,0,1)\} . \tag{7.16}$$

Therefore, each index ν indicates the color channel.

Indeed, this introduces more sparsity into the data (the input data is not in a fully-compact representation, i.e. its volume is effectively expanded), which may be an arguable reason why this representation is conducive to the general stability and interpretability of the learned representations in latent space. In our own words, this expansion of the input data space contains implicitly

discernible information on fundamentally physical (and, therefore, generative) facts about the datasets – that particles are hard-core repulsive.

In fact, one could further expand the input data basis to $1 + 2L$ dimensions per lattice site in order to represent every "part" of the rod of length L in separate dimensions. However, as in our case $L = 10$, this would result in 21 dimensions per site, which would have been computationally unfeasible for this study. Nonetheless, this 21-dimensional representation should render additional, implicit information about the *rigidity* of the particles on top of the hard-core repulsion. We postulate that considering similar preprocessing "tricks" could be interesting for real-world datasets, as well.

Output data representations

The *output* images of a VAE $\boldsymbol{x}'$ are likewise expressible as local fields $\phi'(\boldsymbol{s})$. A crucial, physical difference between input and output is that at each channel v, the fields take on *continuous* values between 0 and 1 such that a summation over all channels renders unity. We attempted to explore VAEs in a standard setup, where this kind of output is most commonly propagated in the literature. In any case, this output realized with a *Softmax* activation layer is inherently smooth, which stands in stark contrast to the hard-core-repulsive nature of our physical model system. As this is a weak point in the context of our investigations, modifications – like drawing a random color according to the Bernoulli probabilities at each pixel – could be explored in future studies.

Macroscopic properties contained in the training data-sets

We also mention one more finding related to the macroscopic features contained in the training data-sets: In Sec. 7.2.2, we described how we generated training data according to a biased ensemble (SUS scheme) in to produce "even" data in the density: If the training data contained a prominent "gap" in the density (which arise from producing data from *unbiased* grand canonical ensembles below the tricritical point), the algorithms did not identify the order parameters consistently. As VAEs and PCA model *continuous* variables in latent space, the learning task seemed more difficult when the data-sets entailed "gaps" in the macroscopic features (order parameters).

7.4 "Coarse-grained" configurations

We have found that the VAEs appear to "coarse-grain" configurations of the rod systems. This term is somewhat loosely-meant, but, the idea will become clear when observing the reconstructed or generated configurations of Figs. 7.6 and 7.7.

It appears from Figs. 7.6–Fig. 7.7 that $\dim(\mathbf{z})$ sets the *maximal* spatial 'mode', i.e. the maximal the cutoff level-of-resolution representable by the VAE. In this sense, $\dim(\mathbf{z})$ is a fundamental parameter that controls the degree of coarse-graining. Another that adjusts the resolution is the hyperparameter β. It can induce *mode collapse* past a threshold value, which effectively reduces the "coarse-graining" dimension. This topic will be discussed in Sec. 7.6. We will use the term of a *fully-ranked* latent-space model for VAEs whose latent variables all showed a high level of *significance*. Specifically, the mean fluctuations of the

variables, when measured on the test data-set, remained significant (did not drop to nearly 0). We will describe this issue in more detail in Secs. 7.5 and 7.6.

An increased latent dimension allows for more and more details or local structures to come into view, resembling the allowance of more, collective (harmonic), "Fourier-like" modes. We will see in the next subsection how this analogy may entail some element of truth.

7.4.1 Maximal resolution cutoff: quantitative results

We trained the VAEs with various latent dimension sizes $\dim(\mathbf{z}) = 2 \dots 1024$; for $\dim(\mathbf{z}) = 2 \dots 256$, we trained them at the *same*, fixed value of $\beta = 4$ and compared the properties of the outputs. Only up to $\dim(\mathbf{z}) = 256$ did we find a full "rank" of latent space, which is a crucial criterion for comparable results in the following. Figure 7.8 displays larger images of the output of these VAEs for one configuration, where we have taken the means $\mu(\boldsymbol{x})$ as an input $\boldsymbol{x}$ (shown in the top row) to the decoder.

To shed light on how the dimension of latent space affects the physical properties of reconstructed configurations, we quantify their reconstruction error (mean-squared error) as well as physical errors from observables in Figs. 7.9–7.12. The test sets are cross the phase-transition fugacity at every fixed temperature. (These temperature are in every case below the training temperature $T^*_{\text{train}} = 1.401$). All averages represent (grand-canonical) ensemble averages at fixed fugacities (test data-set type II, see Sec. 7.2.2).

We observe a monotonous decrease in reconstruction error (top-left) and error in the inner energy (top-right) when increasing the latent dimension. This overall decrease appears throughout the entire range fugacities (packing fractions near 1) tested (not shown). The peak is always found at the phase transition fugacity.

In contrast, the error in the absolute value of the angle of the the complex (2D) order parameter $\mathbf{c}$ show more complicated behavior, shown in Figs. 7.9–7.12 (bottom left) for various test temperatures above and below the tricritical point. In the isotropic phase (left of the phase transition lines shown in gray), all VAEs represent the complex angle quite well. At the phase transition, the error peaks, where fluctuations in the physical system are strongest. However, just after the phase transition, in the orientationally-demixed phase, all VAEs are prone to much larger error in $|\mathbf{c}|$. We report that this observable show much stronger error than that of only the density or of $|S|$ (not shown here); the angle represents a correlation between ρ and S. Past the phase transition point, the value of S will jump back-and-forth strongly between values of $S > 0$ and $S < 0$, and the density is much lower. Therefore, the larger error in the absolute value of the angle points at an increased difficulty in capturing all relevant macroscopic information in the orientationally-demixed phase. Moreover, the error *increases* with larger spatial dimension, which hints at a fundamental tradeoff between the accuracy of macroscopic correlations versus microscopic correlations. Note that, in contrast, all VAEs accurately reproduce the *variance* of $|\arg(\mathbf{c})|$ – the curves in Figs. 7.9–7.12 (bottom right) are indiscernible from the ground truth. Yet, the increase in the error after the phase transition is also related to the value of β, which we will discuss in Sec. 7.6.

Errors of physical observables = detectors of phase transitions

At this point we draw attention to the observation that these error measures are all excellent *detectors of phase transition points* in the physical system, from the posterior side of the VAE model (given input data). In fact, the errors in "energetic" quantities like the mean-squared error and inner energy resemble physical order parameters. On the other hand, errors in order parameters resemble more fluctuations in physical order parameters. This validates other findings in the literature on this regard, in that the reconstruction error [463] – or even the error of some predicted output in a supervised setting – "detect" thermodynamic phase transition points.

Importantly, the inner energy and order parameters are calculated in fundamentally different ways: For each configuration, the real and complex parts of the order parameter $\mathbf{c}$ are obtained as sums over all lattice sites (Eq. 7.10). In contrast, the inner energy (Eq. 7.1) entails a sum over a multiplication between nearest neighbors, hence this quantity detects correlations at the single-site scale. The mean-squared error, however, does not multiply two neighboring lattice sites: It is a point-wise comparison between $\boldsymbol{x}$ and $\boldsymbol{x}'$.

Intensities of gradients of order-parameter fields

We further investigate how the VAEs perform in the gradients within each configuration (image). The gradients of fields using the first color channel are associated with the packing fraction field $\eta(\boldsymbol{s})$. We take its gradient $\nabla\eta(\mathbf{s})$, where $\mathbf{s}$ indicates each lattice position, and average over all positions, and take the squared-norm $\|\cdot\|^2$ of the result (i.e. a sum-over-squares over all lattice sites). These values are then averaged within the thermodynamic ensemble, as well. The results are shown in Fig. 7.13–7.16 (left figures), where we again varied the VAE dimension $\dim(\mathbf{z})$, and observed the gradients across test data in equilibrium thermodynamic ensembles.

The gradients in the second and third color channels represent the gradient of the orientational-demixing-order-parameter field $S(\boldsymbol{s})$; hence we calculate $\nabla S(\mathbf{s})$ and the squared-norm, as well as the ensemble-average in the same way as before. The results are shown in Fig. 7.13–7.16 (right figures).

"Harmonic-like" approximation

We can conclude from Fig. 7.13–7.16 that larger latent dimensions are tied with greater intensities of the gradient fields, which seems intuitive when looking at the example reconstructed configurations in Fig. 7.8. However, we can observe one important feature in the plots: The nearly-even spacing in the y-axis, which is presented in a logarithmic scale, indicates there is an approximately linear relationship between latent space dimension $\dim(\mathbf{z})$ and the intensity of the gradients. This further supports the picture of "coarse graining": The latent space dimension seems to restrict an upper cutoff wavelength in the images; moreover, this gives credence to how the VAE appears to follow a harmonic-like approximation model of the input space. The latter notion is also compatible with the model prior of VAEs – a unit Gaussian distribution over latent variables. We will see in Secs. 7.5 and 7.6 that the latent variables represent "collective variables" in the configurations. Under some conditions,

these seem to represent spatial "modes" that are "Fourier-" or "solid-state-like" in character.

RECONSTRUCTED (GENERATED) IMAGES for trained VAEs vs. INCREASING $\dim(\mathbf{z})$

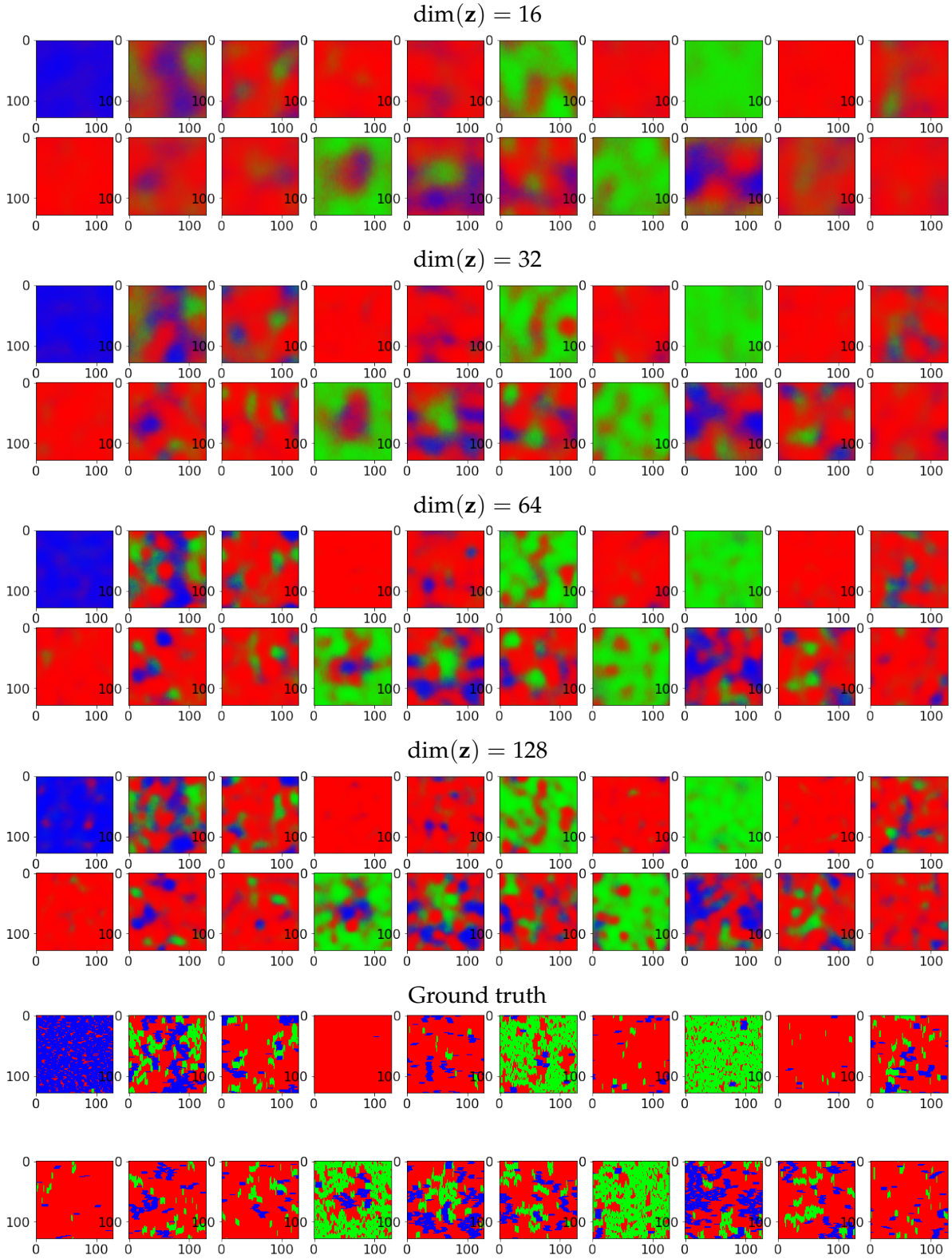

FIGURE 7.6: A series of example output (reconstructed) images from VAEs of increasing latent-space dimension $\dim(\mathbf{z}) = 16 \ldots 128$ (fully-ranked). The data correspond to the test set simulated under the conditions as the training set. All of the VAEs had a single hidden layer in encoder and decoder of dimension 256. The ground truth images are in the bottom row. See also next Fig. 7.7.

RECONSTRUCTED (GENERATED) IMAGES (continued) for trained VAEs vs. INCREASING $\dim(\mathbf{z})$

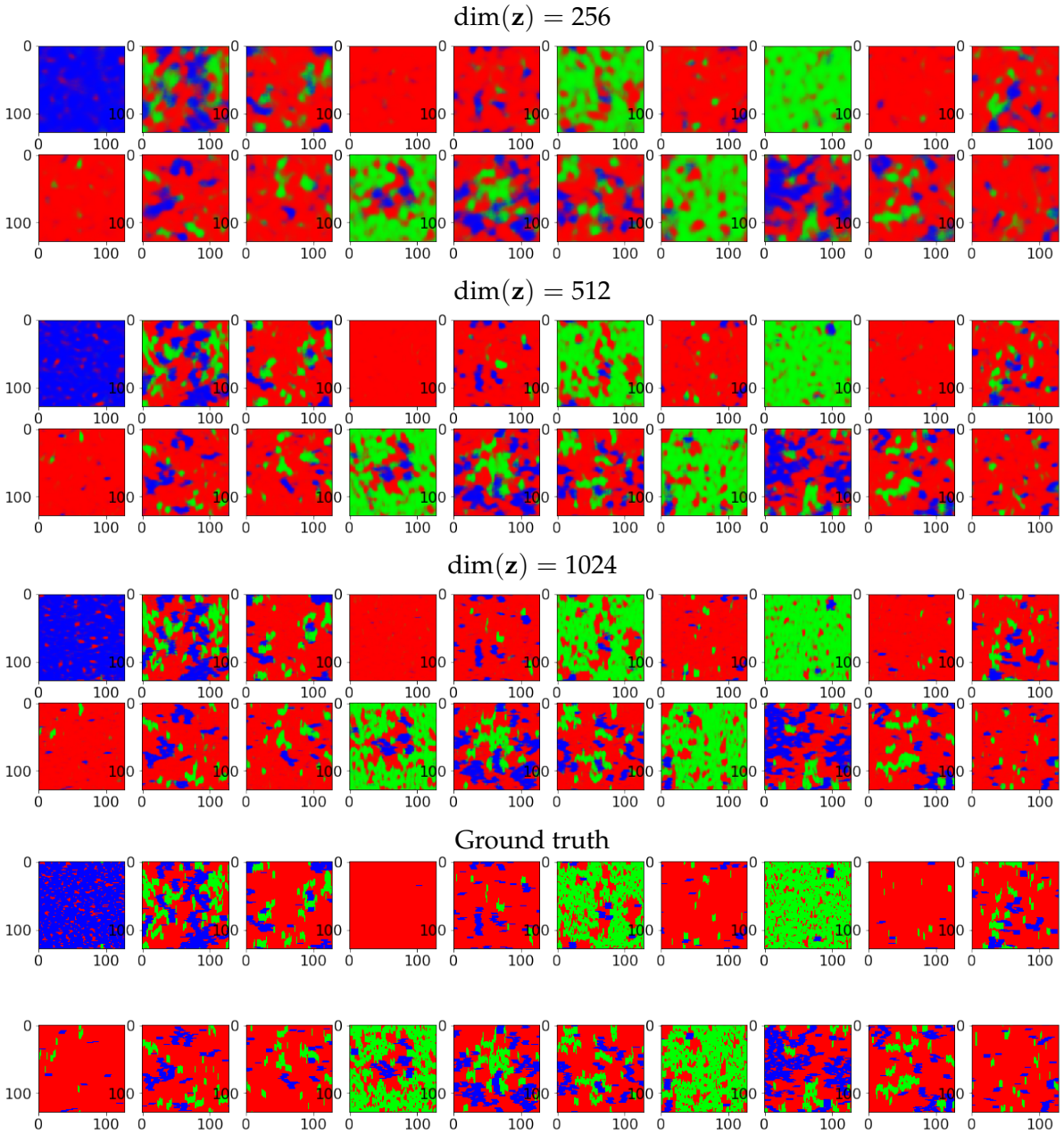

FIGURE 7.7: A series of example output (reconstructed) images from VAEs of increasing latent-space dimension $\dim(\mathbf{z}) = 256 \ldots 1024$ (of full rank). All of the VAEs entailed a single hidden layer in encoder and decoder of dimension $2 \times \dim(\mathbf{z})$ (which are larger than in Fig. 7.6), which is one reason why the colors are brighter and the images are less "fuzzy" than in Fig. 7.6.

RECONSTRUCTED (GENERATED) IMAGES (close-up) for trained VAEs vs. INCREASING $\dim(\mathbf{z})$

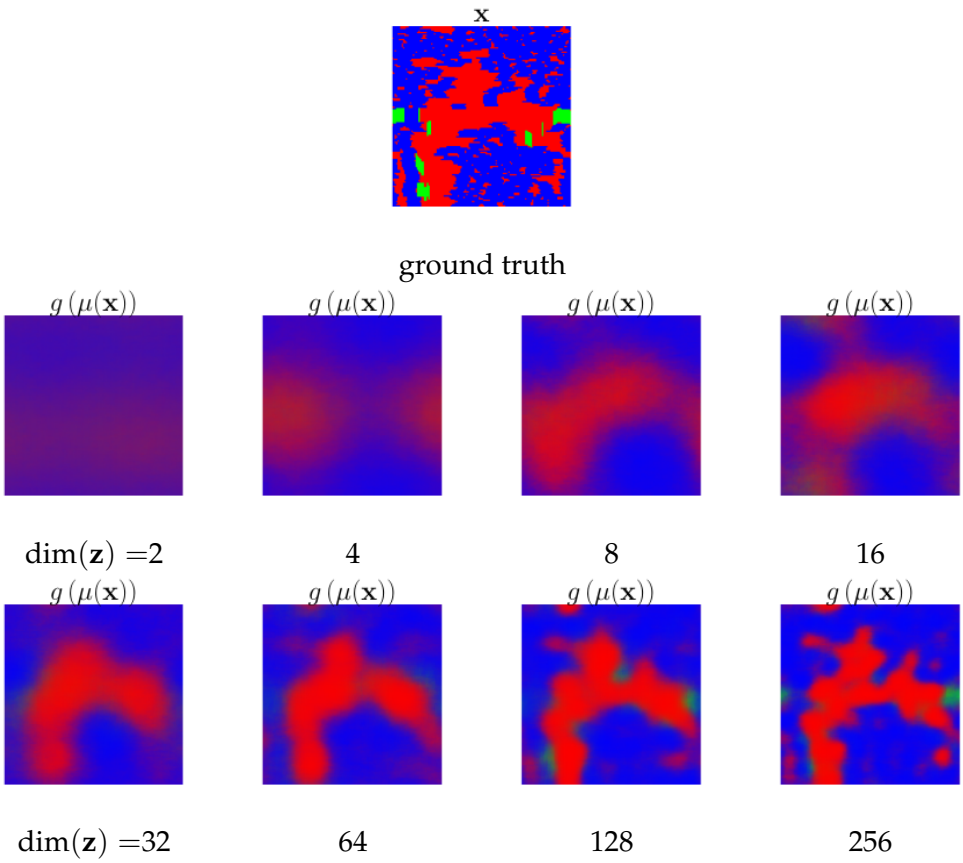

FIGURE 7.8: A more detailed look at one reconstruction: Decoded, "coarse-grained" images of the latent means $\mu(\mathbf{x})$ for an example input example $\boldsymbol{x}$, which we denoted "$g(\mu(\mathbf{x}))$", versus VAEs trained at various value of the latent space dimension $\dim(\mathbf{z})$ (bottom), increasing in powers of 2. For all VAEs, the value of $\beta = 4$ and the latent spaces are fully-ranked. (Top): Ground-truth configuration (input).

VAEs with different dim(**z**)'s tested ABOVE TRICRITICAL POINT
Errors in reconstruction, inner energy and order parameter

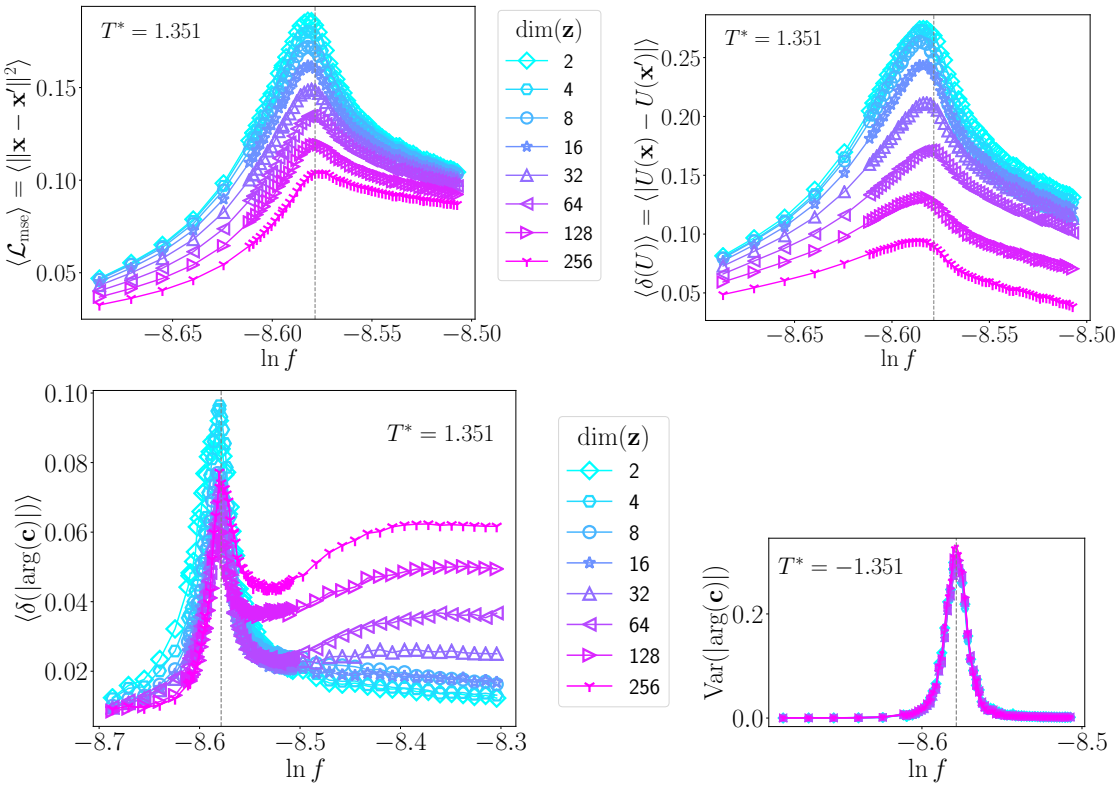

FIGURE 7.9: VAEs with different latent-space dimension dim(**z**): (Top left) reconstruction error, (top right) absolute error in reconstructed inner energy (normalized by lattice size $M^2 = 128^2$), (bottom left) errors in the angles of complex order parameter $\mathbf{c}(\mathbf{x}')$, and (bottom right) variances of the angle of the order parameter – all versus versus log-fugacity for test data at $T^* = 1.351$, above the tricritical point. The gray vertical line indicates an estimate of the transition fugacity from the peak in $\mathrm{var}(|S|/\rho)$. $\beta = 4$ for all VAEs.

VAEs with different dim($\mathbf{z}$)'s tested AROUND TRICRITICAL POINT
Errors in reconstruction, inner energy and order parameter

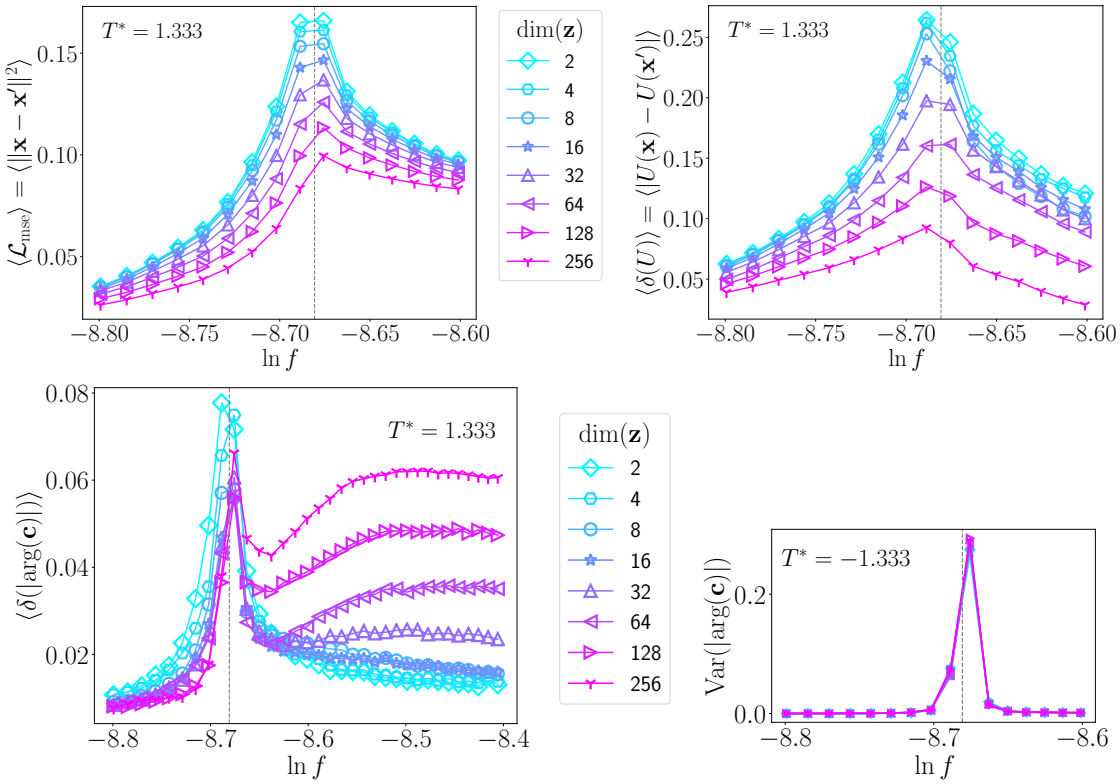

FIGURE 7.10: Same as Fig. 7.9, but for test data at $T^* = 1.333$, around the tricritical point.

VAEs with different dim(**z**)'s tested BELOW TRICRITICAL POINT
Errors in reconstruction, inner energy and order parameter

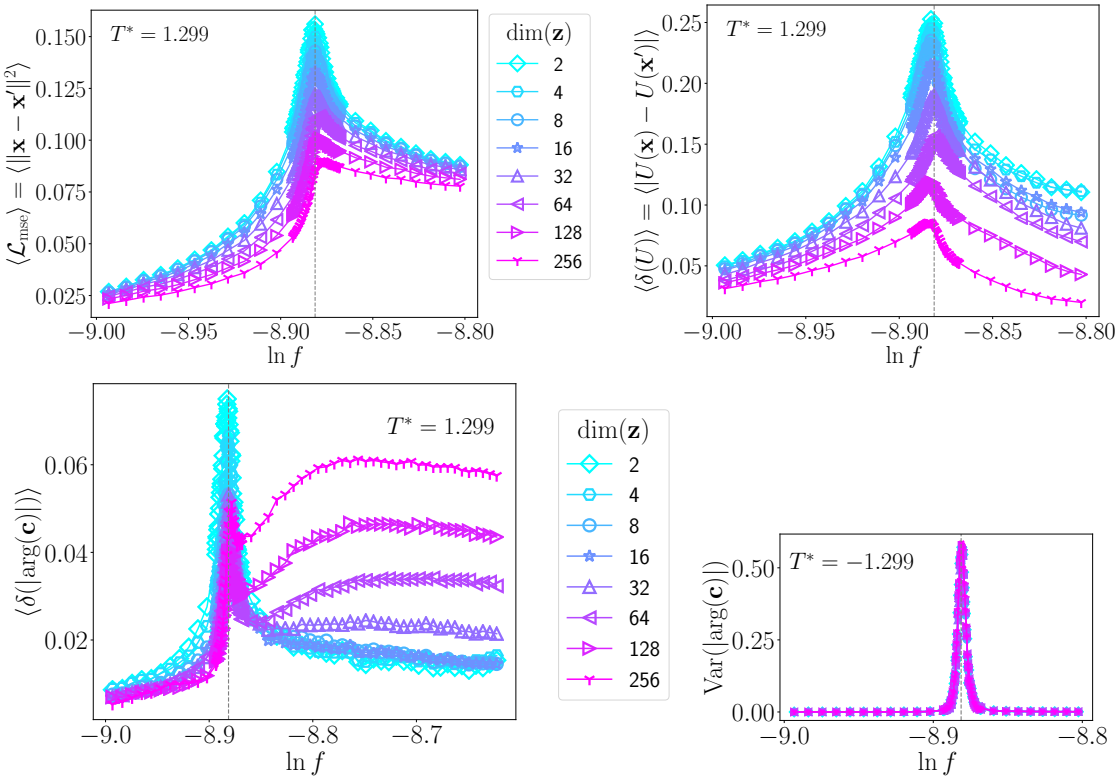

FIGURE 7.11: Same as Fig. 7.9, but for test data at $T^* = 1.299$, below the tricritical point.

VAEs with different dim(**z**)'s tested BELOW TRICRITICAL POINT
Errors in reconstruction, inner energy and order parameter

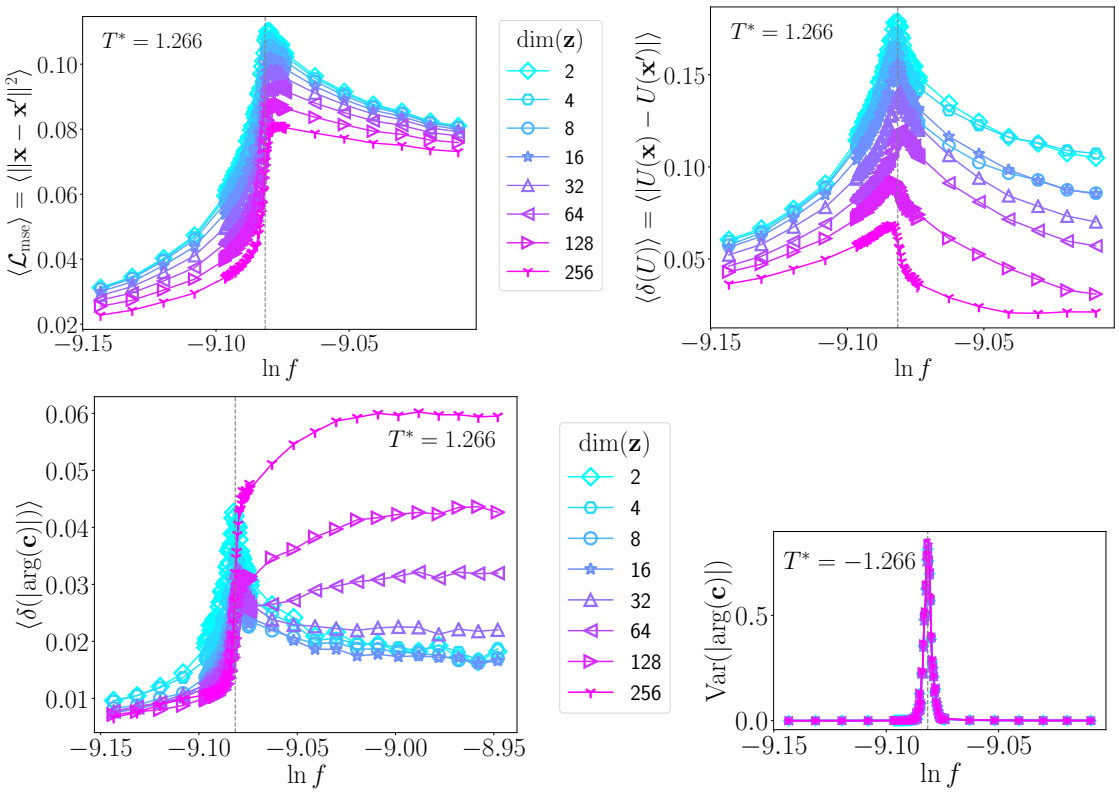

FIGURE 7.12: Same as Fig. 7.9, but for test data at $T^* = 1.282$, below the tricritical point.

VAEs with different dim(**z**)'s tested ABOVE TRICRITICAL POINT
Average square-gradients in local order-parameter fields

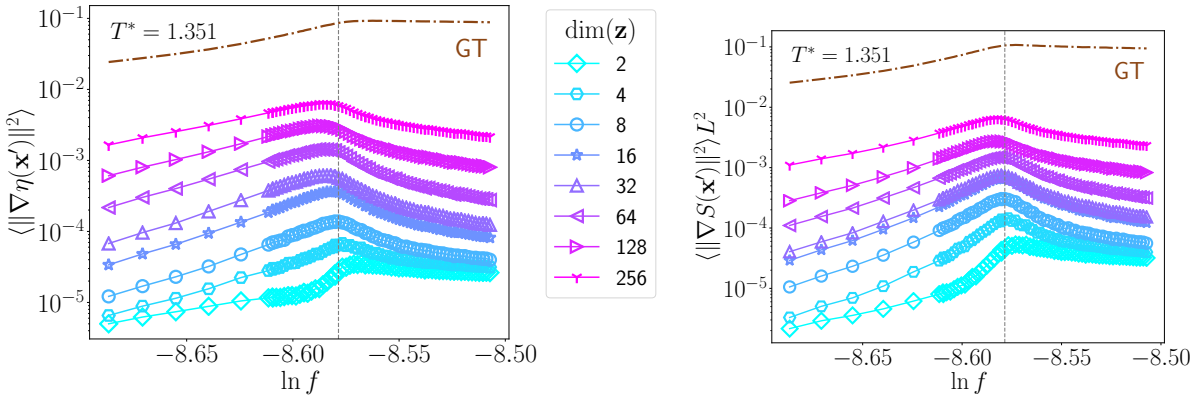

FIGURE 7.13: VAEs with different latent-space dimensions dim(**z**): Ensemble averages of the squared-norm of gradients in reconstructed order-parameter fields of the output configurations $\mathbf{x}'$, calculated using the (left) first color channel ($\sim$ packing fraction) and (right) the last two channels ($\sim$ demixing order parameter). Ground-truth values are in the dot-dashed curve ("GT"). This is for test data at $T^* = 1.351$, below the tricritical point. Note the logarithmic scale on the y-axis.

VAEs with different dim($\mathbf{z}$)'s tested AROUND TRICRITICAL POINT
Average square-gradients in local order-parameter fields

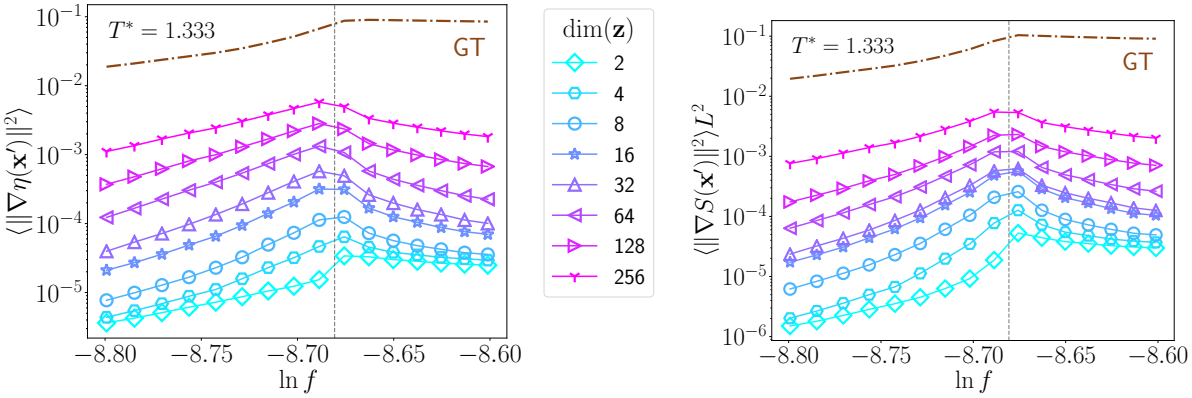

FIGURE 7.14: Same as Fig. 7.13, but for test data at $T^* = 1.333$, below the tricritical point.

VAEs with different dim($\mathbf{z}$)'s tested BELOW TRICRITICAL POINT
Average square-gradients in local order-parameter fields

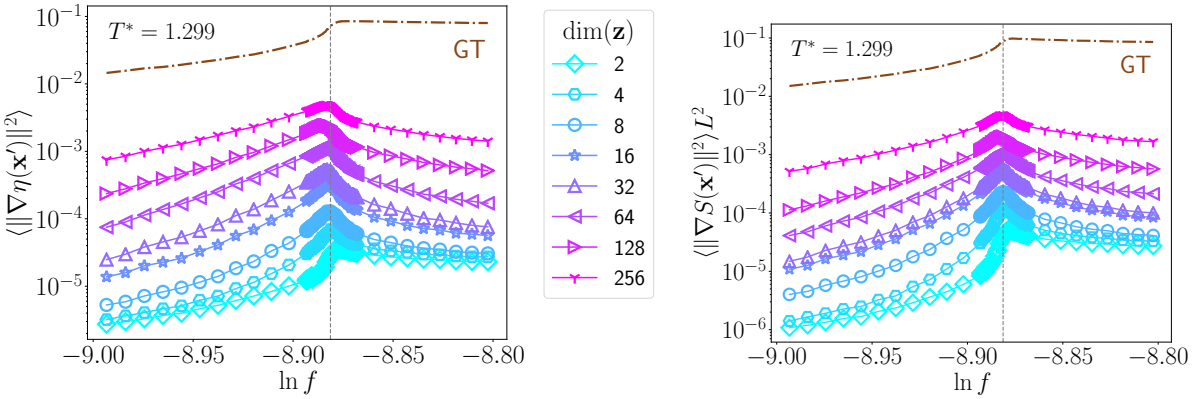

FIGURE 7.15: Same as Fig. 7.13, but for test data at $T^* = 1.299$, below the tricritical point.

VAEs with different dim($\mathbf{z}$)'s tested BELOW TRICRITICAL POINT
Average square-gradients in local order-parameter fields

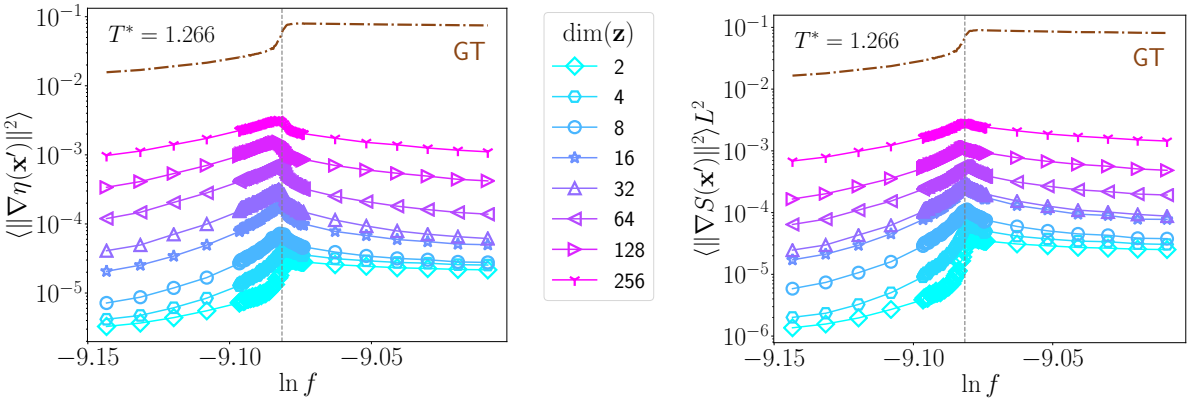

FIGURE 7.16: Same as Fig. 7.13, but for test data at $T^* = 1.282$, below the tricritical point.

7.5 Latent variables: Fluctuating "collective variables" in the hard-rod system

We find that the VAEs in the fully-connected architecture "first" learn latent variables $\{z_k\}$. $k = 1 \ldots \dim(\mathbf{z})$ that are identifiable with the 2D order parameter of the sticky-hard-rod system, i.e. similar to the order parameters ρ and S. In fact, we found that principal component analysis (PCA) on the same data-set (a method which can be considered a limiting case of VAEs with linear decoder and encoder) finds these variables *exactly*. Fig. 7.18 demonstrates this notion for

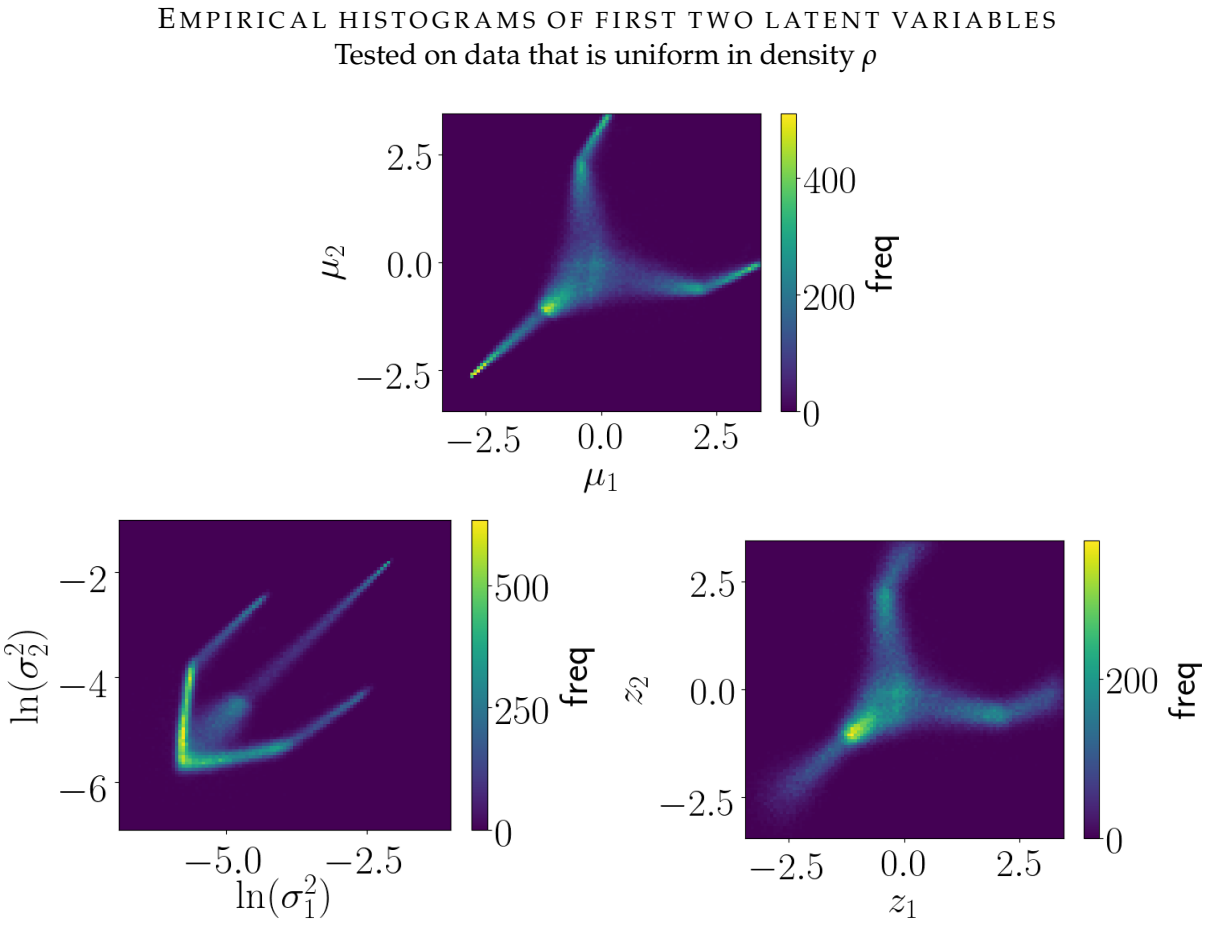

FIGURE 7.17: Empirical histograms of the first two latent variables on test data: means $(\mu 1, \mu_2)$ (top left), log-variances $(\ln(\sigma_1^2), \ln(\sigma_2^2))$ (top right) and stochastic samples (z_1, z_2), where $\boldsymbol{z} \sim p(\boldsymbol{z}|\boldsymbol{x}) = \mathcal{N}(\boldsymbol{\mu}(\boldsymbol{x}), \mathrm{diag}(\boldsymbol{\sigma}(\boldsymbol{x})))$ is drawn from the Gaussian model posterior (bottom right). The test data here are *uniform in density*, i.e. composed of *biased* Boltzmann-Gibbs equilibrium ensembles ("type I")($T^* = 1.333$). The hyperparameters $\beta = 8$ at $\dim(\mathbf{z}) = 128$ corresponds to the learning system with a strong β (see Sec. 7.6).

an example VAE. Plotted are empirical histograms over the first two latent variables, taken from test data-sets that are *uniform* in density ρ (data-set type I from Sec. 7.2.2): In the top-right, the empirical histogram over the means μ_1, μ_2 are displayed. In the bottom row, the empirical histogram over the sampled latent variables z_1, z_2, generated according to the model posterior probability distributions $p(\boldsymbol{z}|\boldsymbol{x}) = \mathcal{N}(\boldsymbol{\mu}, \mathrm{diag}(\boldsymbol{\sigma}))$ are shown. The corresponding histogram over

the logarithm of the first two σ's are shown in the bottom-left figure. When com-

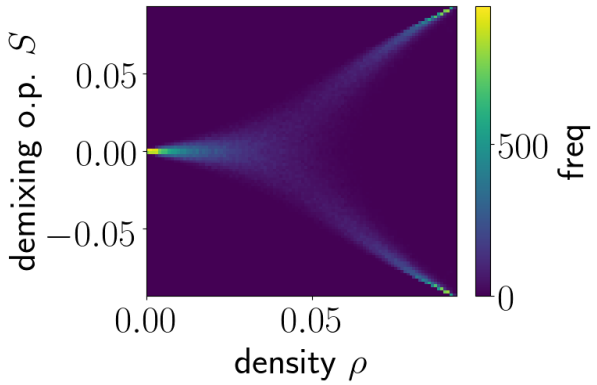

FIGURE 7.18: Empirical histograms of the *physical* 2D order parameters, ρ and S, measured on on test data uniform in density (of the same "type I" as the training set) ($T^* = 1.333$). Compare to Fig. 7.17.

paring with physical order parameters plotted in Fig. 7.18, figure 7.17 compels the notion that the first two latent variables, approximately identify with the two (scalar) order parameters of the system: the particle number ρ (or packing fraction η) and the demixing order S (rotated by about 45 degrees).

The higher-order variables $k \geq 3$ are very different in character. In Fig. 7.19, we present empirical histograms of many latent variables $k = 1 \ldots 8, 16 \ldots 128$ for three test-sets at difference reduced temperatures, all of which are uniform in density ("type I"). Apart from the first two variables $k = 1, 2$ (the "order parameters"), the VAEs learn a nearly perfectly symmetric unit-Gaussian distribution of variables (around the center of latent space, which is zero). Their alignment around zero and normalization to unit standard deviation is enforced during training by matching the posterior distribution (i.e. empirical histograms on the training set) to the prior, which is a unit Gaussian. Thus, we infer that the higher-order variables represent structural "fluctuations" in the hard-rod fluid – their symmetry is not broken in the data-sets. We note here that this VAE has a rather "high" value of β, which is related to the strong separation of the first two variables from the rest. These topics are discussed in Sec. 7.6.

In fact, the latent variables represent "collective variables" in the configurations, which will become increasingly clear in the next section, Sec. 7.6. We may also consider σ^2 as "generalized susceptibilities", as they describe the variance of the variables z at a local scale in latent space. Beforehand, however, we should point out one more aspect on Fig. 7.17: The bottom-left plot with the logarithm of the (inverse) σ's show nearly perfectly linear segments. Closer analysis has revealed that the three parallel segments correlate very strongly with the system chemical potential (or log-fugacity) – when tested on data-sets of type II (Boltzmann-Gibbs ensembles) like in Fig. 7.20 further below. This will also become more apparent in upcoming plots in Sec. 7.6. Therefore, it appears as if the VAE learns to encode *conjugate fields* to the physical order parameters – in the logarithm of the inverse σ's.

We also provide similar figures as the ones above for the case where test data-sets are "bunched together" from equilibrium Boltzmann-Gibbs ensembles (i.e. simulated at different fugacities), in Figs. 7.20, 7.21, and 7.22. Crucial

to note is that in 7.21, where the physical order parameters are plotted, we see a large "gap" in the middle, representing rarely sampled states (the number of samples in each bin is highly concentrated around three extremal points in the plane, which makes it hard to see them). If we were to reduce the temperature even further, a "forbidden" gap in the density arises due to the first-order transition. The VAEs also show these "rare places" in the middle of the first two latent variables, shown in Fig. 7.20. The rare configurations are better visualized in the histograms in Fig. 7.22, where we can clearly see at least three peaks in the first two latent variables (the "order parameters"). We also see that the higher-order variables remain "nearly Gaussian" with nearly unit variance, despite the stark contrast in the thermodynamic distribution of the data.

Sorting the latent variables

In order to speak of a *first*, *second*, or *third* latent variable, we must order them according to some protocol: We have found a (number of) a ways to judge their relative importance or "*participation*", via empirical trial-and-error. The statistics over each σ-encoding are the key to "sorting" the latent variables, indexed by k.

For the rest of this chapter, we will present results where we ordered the latent variables according to the following function $\gamma(k)$:

$$\gamma(k) \equiv \left\langle \frac{1/\sigma_k^2}{\sum_{l=1}^{\dim(\mathbf{z})} 1/\sigma_l^2} \right\rangle_{\boldsymbol{x}\sim p_{\text{data}}(\boldsymbol{x})} \tag{7.17}$$

The ordering is then chosen by sorting the variables from highest to lowest values of $\gamma(k)$. Whenever we present results of a VAE, the ordering of the variables according to $\gamma(k)$ is calculated from the *same* test set $p_{\text{data}}(\boldsymbol{x})$: The out-of-sample data complementary to the training set, i.e. configurations generated from biased ensembles ("type I") at the training reduced temperature $T^* = 1.401$. In this way, we preserve the consistency of the ordering across different test sets (for example, of "type II").

We report that we also tried the following ordering functions:
$\left\langle \frac{1/\sigma_k}{\sum_{l=1}^{\dim(\mathbf{z})} 1/\sigma_l} \right\rangle_{\boldsymbol{x}\sim p_{\text{data}}(\boldsymbol{x})}$ (highest-to-lowest),
$\left\langle \frac{1}{\sigma_k} \right\rangle_{\boldsymbol{x}\sim p_{\text{data}}(\boldsymbol{x})}$ (highest-to-lowest),
$\left\langle \frac{1}{\sigma_k^2} \right\rangle_{\boldsymbol{x}\sim p_{\text{data}}(\boldsymbol{x})}$ (highest-to-lowest),
and $\left\langle \frac{\sigma_k^2}{\sum_{l=1}^{\dim(\mathbf{z})} \sigma_l^2} \right\rangle_{\boldsymbol{x}\sim p_{\text{data}}(\boldsymbol{x})}$ (lowest to highest). The results on the ordering of the variables did *not* change significantly when applied to the same test data-set, at least for a number of VAEs we have trained (e.g. a VAE with $\dim(\mathbf{z}) = 128$ and $\beta = 8$).[7]

[7] Very few variable-numbers k in the "middle" of the ordering function (versus k) may have swapped positions, for example.

7.5.1 The generative model prior: Like at a critical point

The inference model of VAEs equips us with the possibility to generate new configurations unconditioned on input data – sampling from the prior distribution on latent space, $p(\boldsymbol{z})$. From Figs. 7.20 and 7.21, we can infer from just the first two latent variables that the unit Gaussian interval, $z_k = -1 \dots 1$, for $k = 1, 2$ is situated exactly within the rare-configuration "gap" at the center of latent space – for the case of $T^* = 1.333$, which is the estimated tricritical point. Therefore, we infer that the model prior is generating the rare, thermodynamically unstable configurations which would correspond to a critical point, possibly at an effectively higher temperature. Indeed, the same histogram provided for a much higher $T^* = 0.4$, which is above the training temperature, does show thermodynamically stable configurations therein – shown in Fig. 7.23. Therefore, we postulate that there may be a hidden relationship between the model prior and the physical reduced temperature of the system. This has led us to a startling result, which we present in the next paragraph. Beforehand, Fig. 7.24 depicts a collection of randomly generated configurations by sampling from the prior and sending the drawn variables through the decoder. Indeed, we see how all system variables fluctuate wildly within the model prior, which may appear like a critical point. The possibly "effectively higher" system temperature may be understood as a loss of information via the "coarse-graining" procedure. In the future, it would be interesting to explore this analysis for much larger VAEs, with e.g. $\dim(\mathbf{z}) = 1024$.

The physical reduced temperature and the KL-loss

We have uncovered a startling empirical result: the reduced temperature of the physical system can be gauged using the Kullback-Leibler divergence (KL-loss) of the posterior of the latent variables with the prior. The term is calculated according to Eq. (7.5). We have taken a mean over test data-sets that are uniform in density ("type I") in order to have comparable data distributions across temperatures. The results are found in Fig. 7.25. This seems rather remarkable: VAEs are capable of discerning the thermodynamic reduced temperature of the hard-rod model system, although trained at different temperatures. The mean relative entropy to the prior – for data spread widely across phase space – is thus an measure for the reduced temperature, which is one of the three fundamental parameters to indicate the particular thermodynamic ensemble of the physical system (in equilibrium), i.e. (f, V, T^*). We suspect that a comparison at different temperatures at the *critical* or *coexistence* fugacities – in Boltzmann-Gibbs ensembles – will render the same trend. Proving this remains outside of the scope of this thesis, however.

No clear interpretability

With the current form of the VAEs, we cannot reasonably test the thermodynamic truthfulness of *generated* configurations from the model *prior*. There is no explicit way to control fundamental variables that define Boltzmann-Gibbs ensembles (i.e. temperature and fugacity). The above finding is certainly encouraging, nonetheless, that the VAEs may have the *capacity* to learn to represent true ensembles, given a modified setup. We discuss some ideas at the end of this chapter in Sec. 7.10.

EMPIRICAL HISTOGRAMS OF LATENT VARIABLES
Test data-sets are uniform in density ("type I")

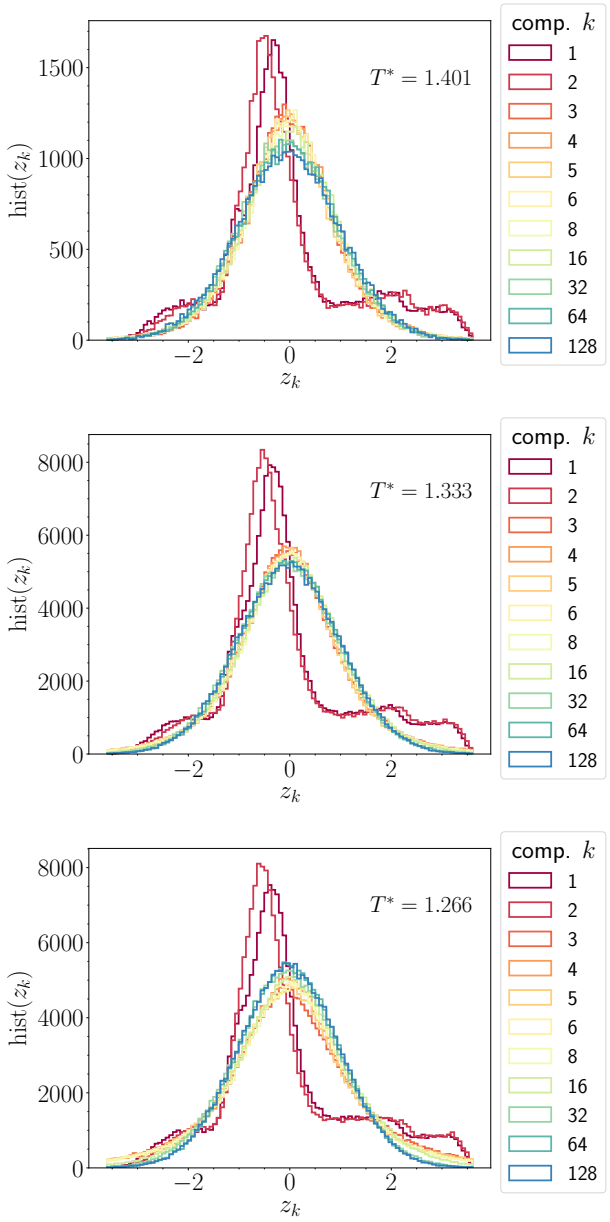

FIGURE 7.19: Empirical histograms of latent variables z_k, for various k's (the components are ordered by $\gamma(k)$) for test data that is uniform in density ("type I"). This represents the same VAE as presented in Fig. 7.18, where the first two variables are highly discernible from the rest (discussed more in Sec. 7.6). The higher-order variables are all nearly unit Gaussians. The top figure represents configurations simulated at the training reduced temperature, the middle at the tricritical temperature, and the bottom well-below the tricritical temperature in biased ensembles. Notice the high degree of similarity across the three panels.

EMPIRICAL HISTOGRAMS OF FIRST TWO LATENT VARIABLES
Tested on data that represent Boltzmann-Gibbs states ("type II")

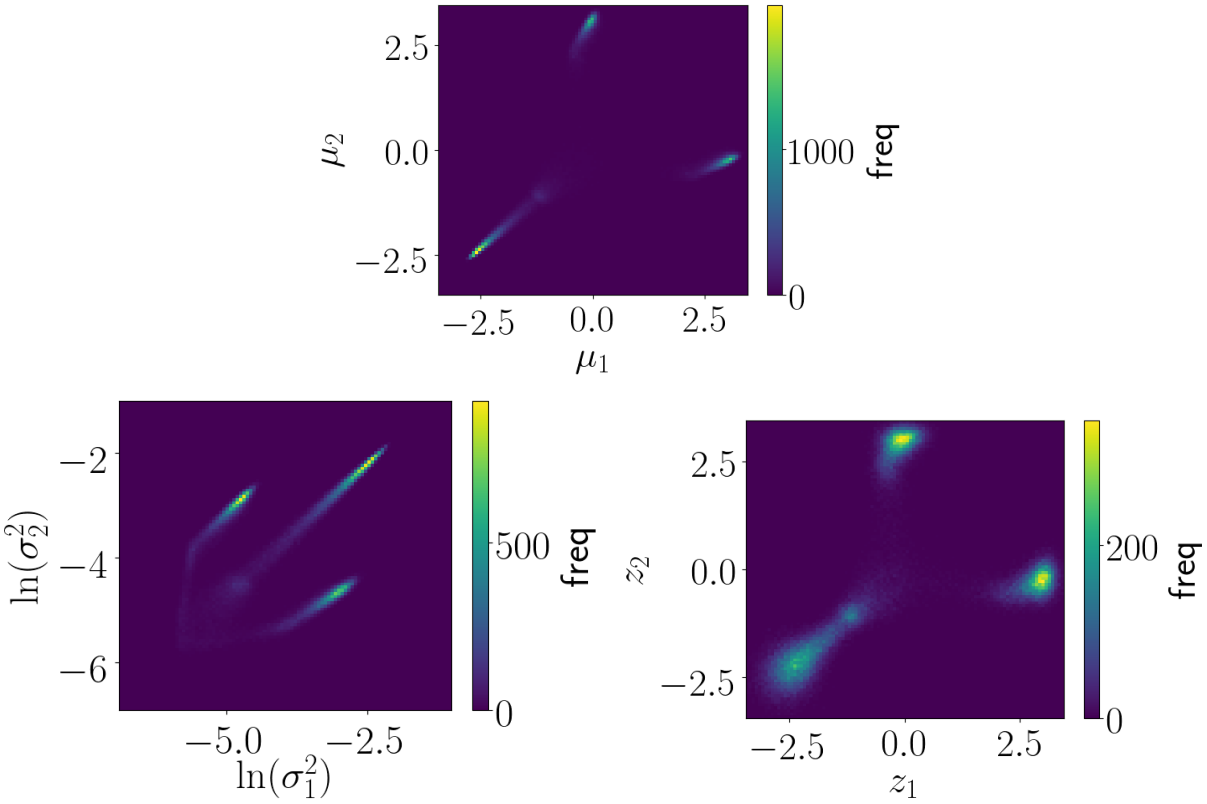

FIGURE 7.20: Empirical histograms of the first two latent variables on test data representing Boltzmann-Gibbs ensembles: means $(\mu 1, \mu_2)$ (top left), log-variances $\left(\ln(\sigma_1^2), \ln(\sigma_2^2)\right)$ (top right) and stochastic samples (z_1, z_2), where $\boldsymbol{z} \sim p(\boldsymbol{z}|\boldsymbol{x}) = \mathcal{N}(\boldsymbol{\mu}(\boldsymbol{x}), \mathrm{diag}(\boldsymbol{\sigma}(\boldsymbol{x})))$ is drawn from the Gaussian model posterior (bottom right). The test data here are *uniform in density*, i.e. composed of Boltzmann-Gibbs equilibrium ensembles ("type II")($T^* = 1.333$, which is at the tricritical point). Compare with the same observables tested on uniform data-sets in Fig. 7.17.

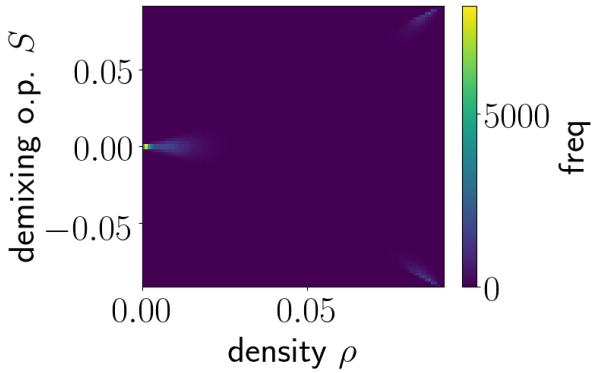

FIGURE 7.21: Empirical histograms of the *physical* 2D order parameters, ρ and S, measured on on test data representing Boltzmann-Gibbs ensembles ("type II") ($T^* = 1.333$, which is at the tricritical point). Compare to Fig. 7.18 and Fig. 7.20.

EMPIRICAL HISTOGRAMS OF LATENT VARIABLES
Test data-sets that represent Boltzmann-Gibbs states ("type II")

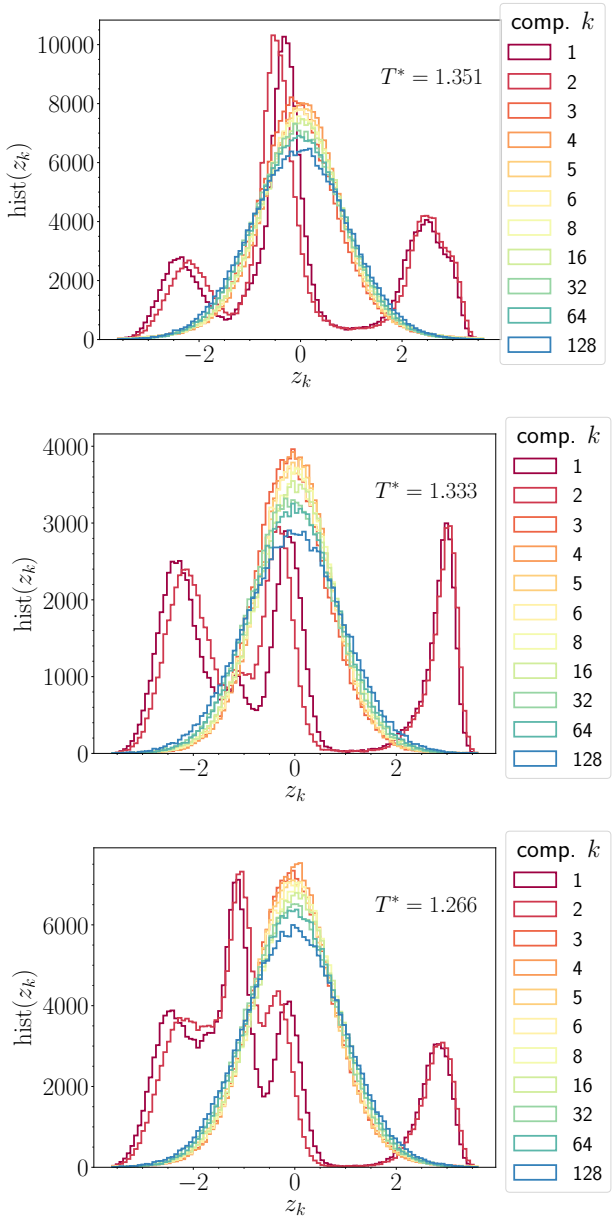

FIGURE 7.22: Empirical histograms of latent variables z_k, for various k's (the components are ordered by $\gamma(k)$) for test data representing Boltzmann-Gibbs ensembles ("type II"). The higher-order variables all remain nearly unit Gaussians. The top figure represents configurations simulated below the training reduced temperature but above the tricritical point, the middle at the tricritical temperature, and the bottom well-below the tricritical temperature in biased ensembles.

EMPIRICAL HISTOGRAMS OF FIRST TWO LATENT VARIABLES
Tested on data that represent Boltzmann-Gibbs states ("type II")

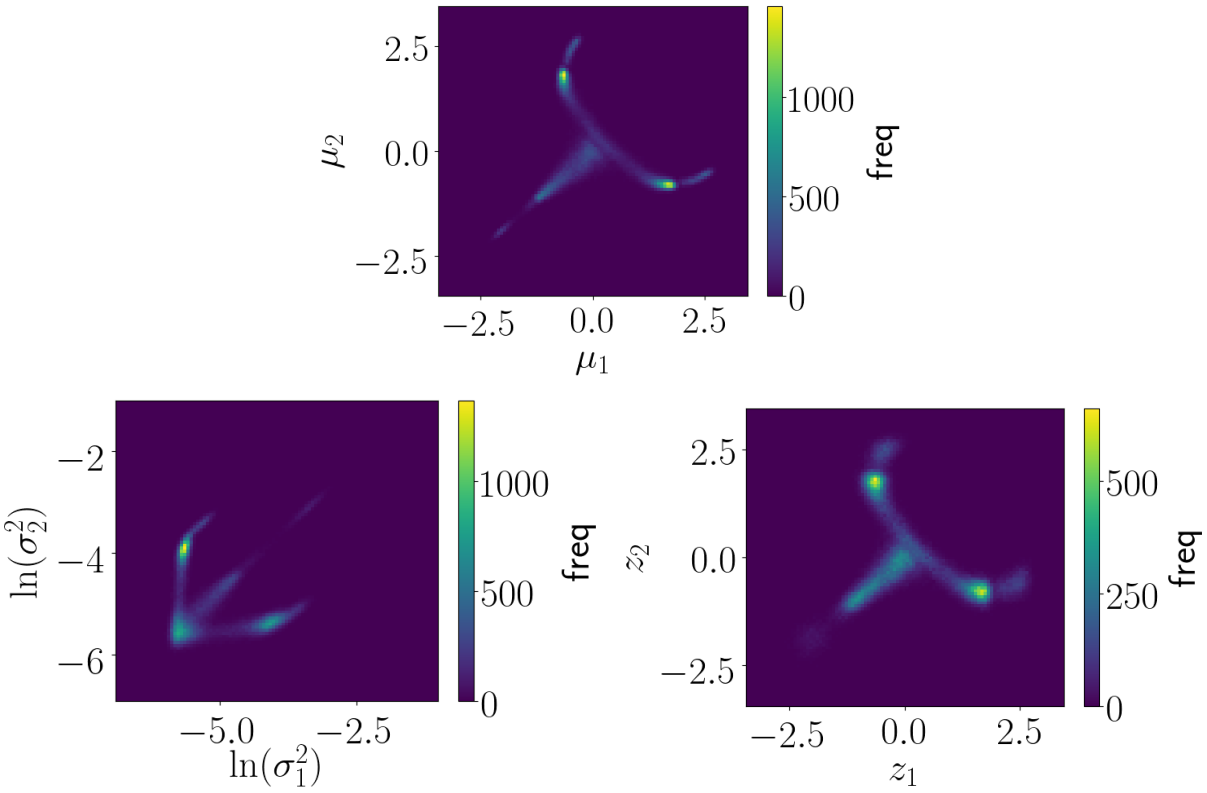

FIGURE 7.23: Empirical histograms of the first two latent variables on test data representing Boltzmann-Gibbs ensembles: means $(\mu 1, \mu_2)$ (top left), log-variances $\big(\ln(\sigma_1^2), \ln(\sigma_2^2)\big)$ (top right) and stochastic samples (z_1, z_2), where $\boldsymbol{z} \sim p(\boldsymbol{z}|\boldsymbol{x}) = \mathcal{N}(\boldsymbol{\mu}(\boldsymbol{x}), \mathrm{diag}(\boldsymbol{\sigma}(\boldsymbol{x})))$ is drawn from the Gaussian model posterior (bottom right). The test data here are *uniform in density*, i.e. composed of Boltzmann-Gibbs equilibrium ensembles ("type II")($T^* = 4$, which is well above the training temperature). We see how the thermodynamically unstable "gap" in the middle of latent space (see Fig. 7.20) is now covered by data-points at this reduced temperature.

SAMPLING FROM THE PRIOR:
Grid of 10×10 generated configurations $\{\boldsymbol{x}' = g(\boldsymbol{z})\}$
via sampling $\boldsymbol{z} \sim p(\boldsymbol{z})$ from the prior

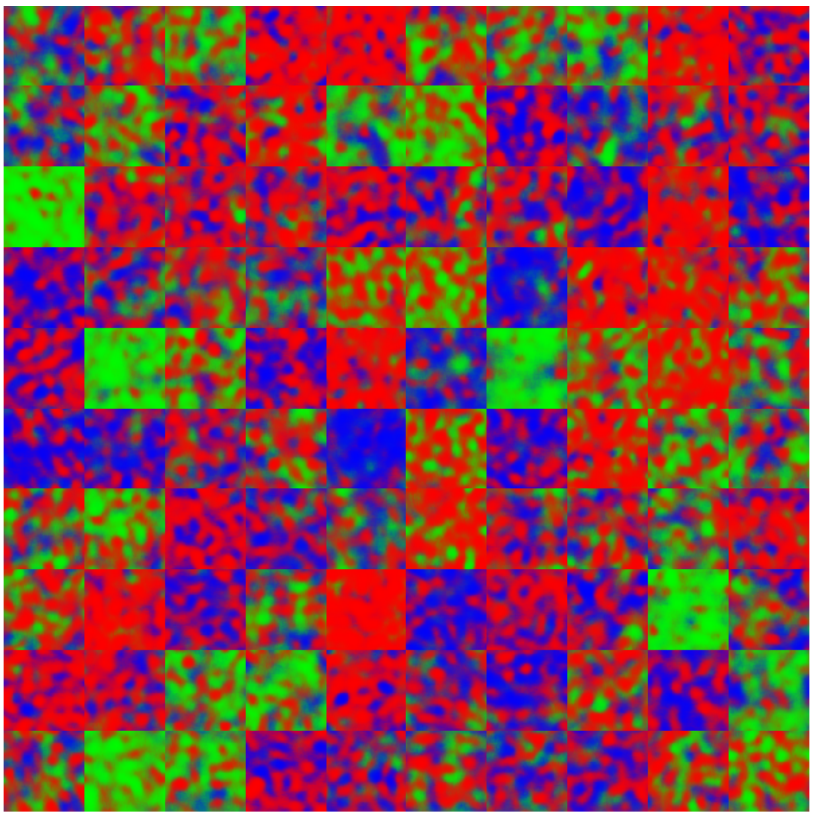

FIGURE 7.24: A grid of 10×10 sampled configurations $\boldsymbol{x}'$, where random values of $\boldsymbol{z} \sim p(\boldsymbol{z})$ were sampled from the unit Gaussian prior and subsequently sent through the decoder, denoted here by "$g(\boldsymbol{z})$".

GAUGING THE REDUCED TEMPERATURE
Kullback-Leibler divergence term D_{KL} versus reduced temperature T^* for data-sets uniform in density

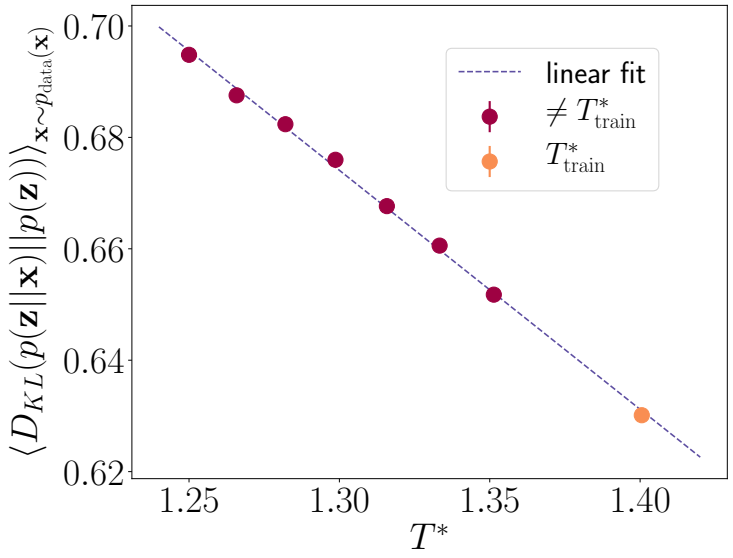

FIGURE 7.25: The empirical average of the Kullback-Leibler divergence between model posterior and prior of the latent variables versus reduced temperature of the rod system, tested over data-sets that are uniform in density, i.e. "type I". We find an approximately linear relationship between the two, where a fit is shown in the dashed line. The training reduced temperature is indicated in orange (the data is nonetheless complementary to training data). Fit parameters: slope: -0.43, y-crossing: 1.23.

7.5.2 Possible probabilistic model of VAEs

The introduction of the latent variables $\mathbf{z}$ in VAEs is equivalent to the introduction of a joint probability distribution $p(\mathbf{x}, \mathbf{z})$ with the hope that key aspects of the data distribution $p(\mathbf{x}) = \int d\mathbf{z} p(\mathbf{x}, \mathbf{z})$ can be modeled with more ease. The implementation of VAEs fixes both

$$p(\mathbf{z}) = \int d\mathbf{x} p(\mathbf{x}, \mathbf{z}) = \mathcal{N}(\mathbf{0}, \mathbf{1}) \,, \tag{7.18}$$

$$p(\mathbf{z}|\mathbf{x}) = \mathcal{N}(\boldsymbol{\mu}(\boldsymbol{x}), \mathrm{diag}(\boldsymbol{\sigma}(\boldsymbol{x}))) \tag{7.19}$$

to Gaussian distributions, so $p(\mathbf{x})$ appears to be heavily constrained. A model joint distribution fulfilling these constraints is given by

$$p(\mathbf{x}, \mathbf{z}) \propto \exp\left(-\sum_i \frac{(z_i - x_{c,i})^2}{2(\sigma_i')^2} \right) g(\mathbf{x}_\perp) \exp\left(-\sum_i \frac{z_i^2}{2} \right) \,, \tag{7.20}$$

where the configuration variables $\mathbf{x}$ are split into a set of collective variables $\mathbf{x}_c$ (with same dimensionality as $\mathbf{z}$) and "orthogonal" variables $\mathbf{x}_\perp$. The distribution in "orthogonal" variables $g(\mathbf{x}_\perp)$ remains unknown but is also of no further interest. Additionally, $\int d\boldsymbol{x} = \int d\boldsymbol{x}_c d\boldsymbol{x}_\perp$ should hold. The mean value and the variance in the distribution $p(\mathbf{z}|\mathbf{x})$ (Eq. (7.19)) are then given by

$$\mu_i = x_{c,i} \frac{\sigma_i^2}{(\sigma_i')^2} \,, \qquad \sigma_i^2 = \frac{(\sigma_i')^2}{1 + (\sigma_i')^2} \tag{7.21}$$

and the (model) data distribution is given by

$$p(\mathbf{x}) \propto \exp\left(-x_{c,i}^2 \frac{\sigma_i^2}{2(\sigma_i')^4} \right) g(\mathbf{x}_\perp) \,. \tag{7.22}$$

In essence, according to this model, the VAE approximates the data distribution by Gaussians in collective variables $\mathbf{x}_c$ which are (up to a factor) given by the mean values $\boldsymbol{\mu}$ of Eq. (7.19). The collective variables are determined by the optimization process (learning) in an unsupervised manner, i.e. no prior knowledge is actually assumed apart from the form of the Bayesian model in Eqs. (7.18) and (7.19).

In our GCMC simulation of training data, $p(\mathbf{x})$ is actually distributed according to a complicated Boltzmann distribution (the training data was further in a series of biased ensembles via the successive umbrella sampling scheme). Nevertheless, it appears to be reasonable to approximate $p(\mathbf{x})$ by Gaussians in certain collective variables by the central limit theorem, especially in equilibrium conditions. Standard, practical examples are the energy distribution in canonical simulations or the particle number distribution in grand canonical simulations. The novel aspect here is that the VAE itself identifies these variables automatically, and can even form a coarse-graining hierarchy under conditions (see Sec. 7.6).

In preliminary investigations, we see how the distributions of latent variables from reconstructed (generated) images – fed back into the VAEs – tend towards a local Gaussian. Therefore, the VAEs may model how local fluctuations eventually propagate an initial sets of collective variables (from initial configurations) towards a local 'equilibrium' distribution thereof. However,

these findings and a more precise validation of the above suggested model are out of the scope of this thesis.

7.6 The effects of β on latent variables

So far, we have not described the role of the hyperparameter β. Let us first begin with the KL-loss function, which describes how well the posterior distribution of latent variables matches to the prior. Figure 7.26 displays the KL-loss of Boltzmann-Gibbs equilibrium datasets at one exemplary temperature. In varying across different log-fugacities $\ln(f)$, we cross a phase boundary (indicated in the gray vertical line). The original motivation behind increasing β is to tax the KL-loss in the cost function, which should decrease the mismatch to the model prior. We see that across all ensembles, the KL-loss is lower for

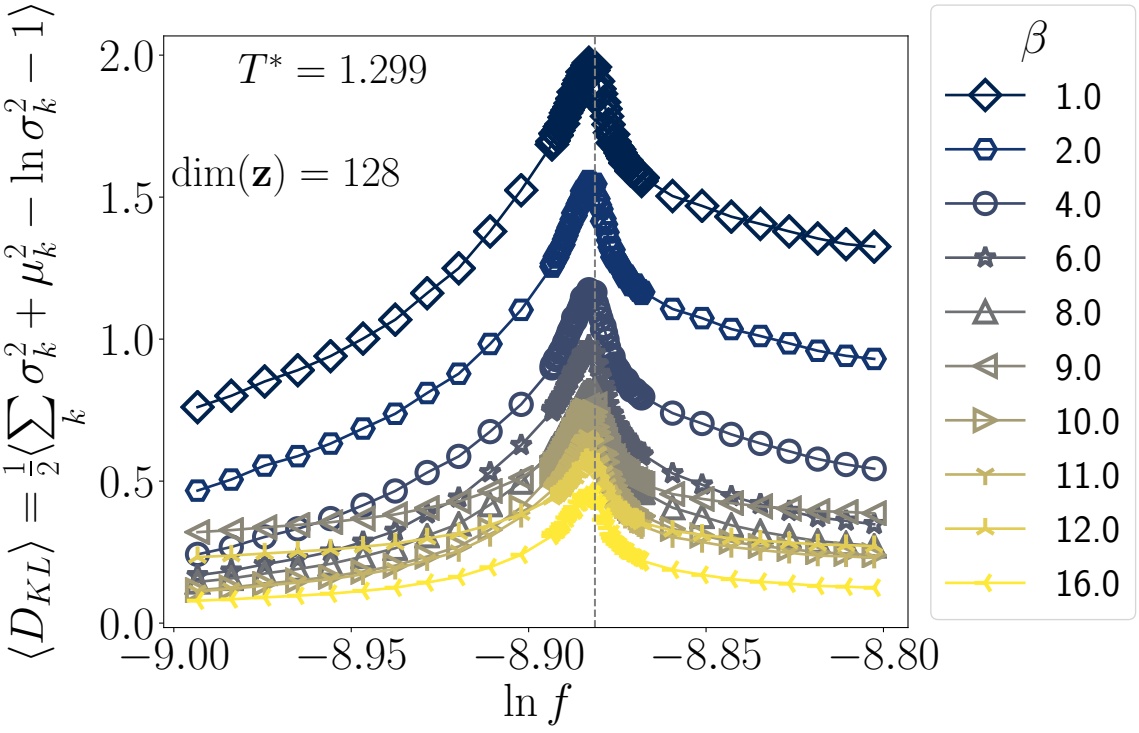

FIGURE 7.26: VAEs with different β's: Comparison of full KL-loss between approximate posterior and prior distribution, versus log-fugacity for VAEs of $\dim(\mathbf{z}) = 128$ and varying β. The data-sets are in Boltzmann-Gibbs ensembles at $T^* = 1.299$, which is below the tricritical point. The gray vertical line is the estimated position of the coexistence (phase transition) fugacity.

higher β; except for regions far left and right from the critical point, where at $\beta \approx 9$, we see a "flip" in this ordering. Indeed, we have found that $\beta \approx 9$ is a threshold value (for VAEs at $\dim(\mathbf{z}) = 128$) – it is the point of "mode collapse", where some of the highest-k variables lose their "participation" in $\gamma(k)$. In fact, we have interpreted this as a phase transition in the learning system.

7.6.1 "Mode collapse" = collapse to (uninformative) model prior

We can investigate the state of the variables by averaging their σ's over data-sets of type I, i.e. *uniform* in density, in Fig. 7.27 (top). We observe the "mode collapsed" variables at the far end of the component spectrum, occurring for $\beta \geq 9$.

We can further describe an energetic quantity: the KL-loss of each individual variable. Due to the diagonal Gaussian assumption of the approximate posterior (as well as prior), the KL-divergence can be evaluated component-wise. This is defined as

$$D_{KL}(k) = \frac{1}{2}\left(\sigma_k^2 + \mu_k^2 - \ln(\sigma_k^2) - 1\right) \ , \tag{7.23}$$

which we quantified in Fig. 7.28 over the same uniform-density data-sets as above. The values of $D_{KL}(k)$ for "mode collapsed" variables are clearly significantly lower than that for "participating" variables. The variables have collapsed to the model prior, which also matches to their maximal (root) "susceptibility" $\sigma_k \approx 1$, on average, which is the standard deviation of the unit Gaussian prior. In this sense, mode collapsed variables are "stuck" at the center of latent space – they become part of the *uninformative* prior distribution, serving as a "background" for the relative information that the model posterior generates. The effective "rank" of the latent space is reduced.

We note that this mode collapse is quite weak – effects of "mode collapse" on the reconstructed configurations is too subtle to tell by eye, as demonstrated in Fig. 7.29. Reconstructions for a particular configuration $\boldsymbol{x}$ are shown. The only thing we may be able to discern is that at $\beta = 10$, the images are a bit blurrier.

We find much stronger forms of mode collapse for very large networks, where the "rank" is reduced over a much larger range. There, we observe that there are multiple "steps" in the participation ratio $\gamma(k)$, for example. A quantitative presentation remains outside of the scope of this thesis, but, we present images of reconstructed configurations for these large networks in Fig. 7.30. There, once can better see how the reduction of the rank lowers the "coarse-graining" resolution, where we provided comparisons to fully-ranked VAEs.

7.6.2 Changing histograms of latent variables with varying β

Let us now consider the values of β *prior* to mode collapse: $\beta \leq 8$ in the examples studied above. Figure 7.31 presents the results of the distributions of a subset of all variables in latent space; a uniform data distribution is used ("type I"). We can observe how *lowering* the value of $\beta < 4$ induces a drastic change in the distributions. The "order parameters" $k = 1, 2$ are now not "alone", as higher-order variables also discern themselves from a unit Gaussian distribution. In the next section, Sec. 7.6.3, we will see how this results from an "entanglement" of the order parameters with higher-order collective variables. They become "mixed" in effect. Afterwards, we present results of the statistics of the z_k's and σ_k's over thermodynamic ensembles.

MODE COLLAPSE OF LATENT VARIABLES upon threshold β:
Mean σ_k of each latent variable and participation ratio $\gamma(k)$

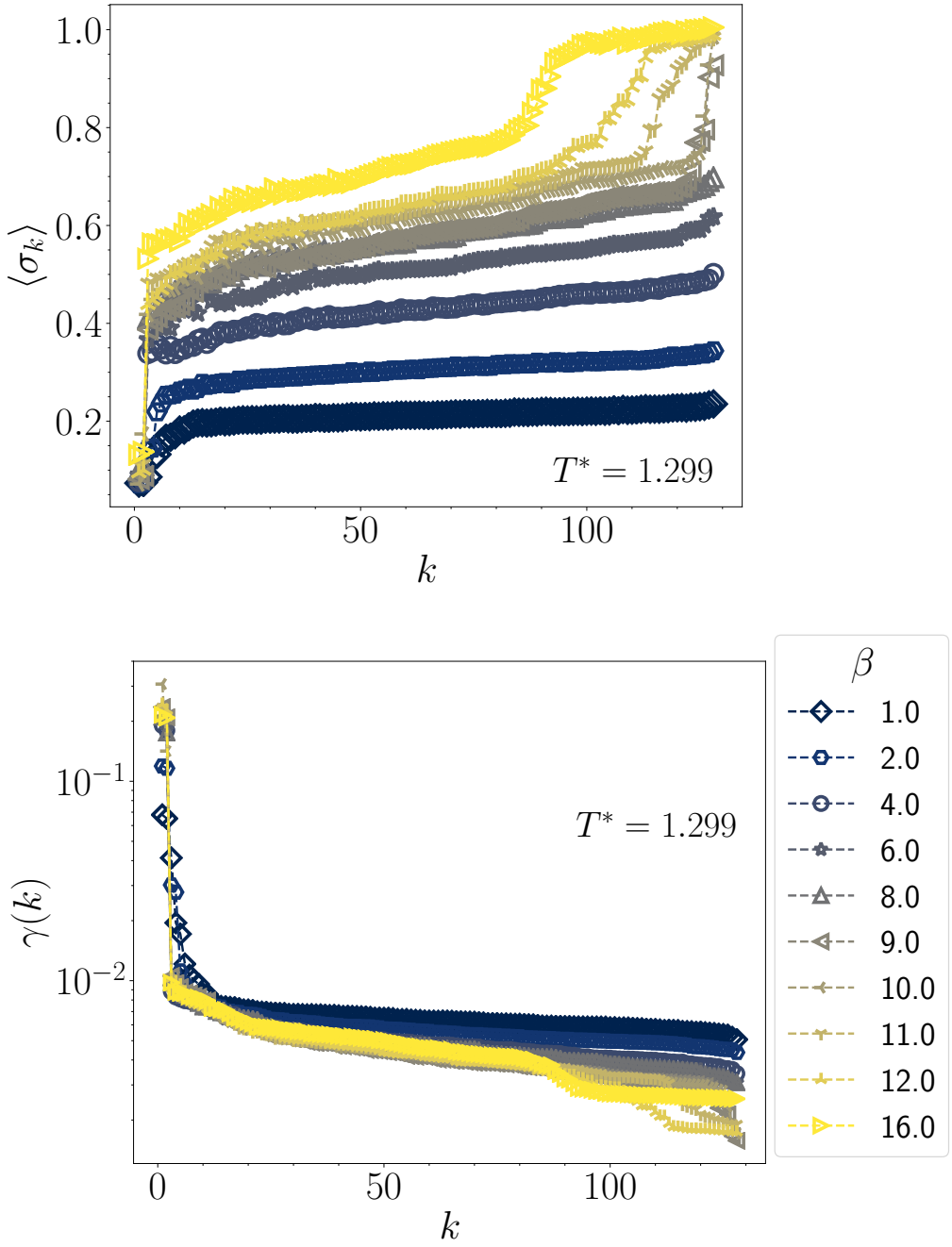

FIGURE 7.27: Dependency on β: Empirical mean over variables σ_k (top figure), estimated from the entire data-set, which is uniform in density ("type I"). The same reduced temperature $T^* = 1.299$ is employed as in Fig. 7.26. The variables are sorted according to $\gamma(k)$ at the training temperature; each curve represents a separate VAE with a different β, all have $\dim(\mathbf{z}) = 128$. The threshold value of β is approximately 9.

MODE COLLAPSE OF LATENT VARIABLES upon threshold β:
Component-wise KL-loss of each variable

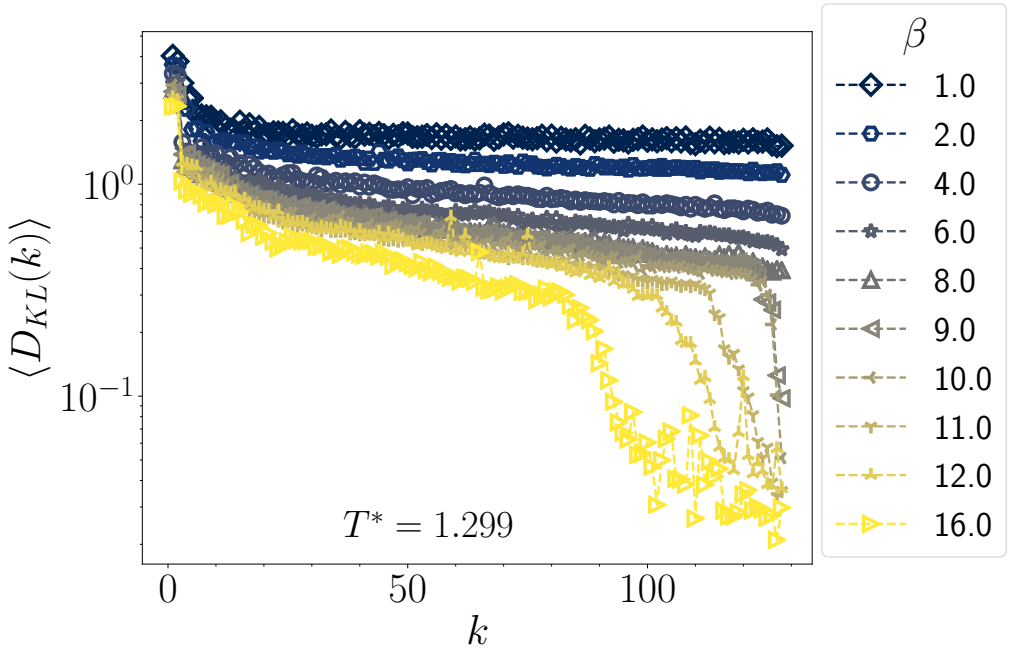

FIGURE 7.28: Dependency on β: Empirical mean over component-wise KL-loss. Please see caption of Fig. 7.27. The mode-collapsed variables entail very low KL-loss, as they effectively collapse to the uninformative prior distribution.

EFFECT OF β ON RECONSTRUCTED IMAGES

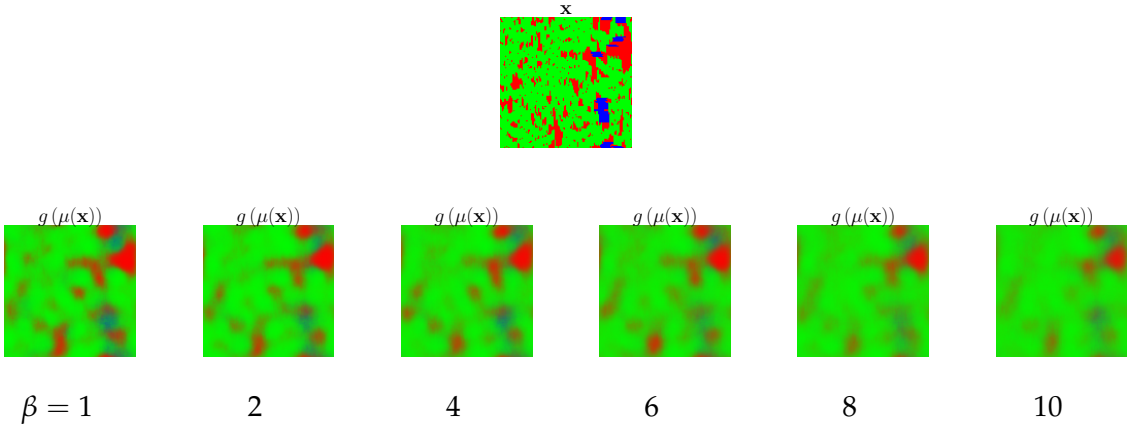

FIGURE 7.29: Effect of β on reconstructed images: Reconstructions of the means $\mu(\mathbf{x})$ versus VAEs trained with various β. (Top): ground-truth configuration. (Bottom rows): From left to right, the values are $\beta \in \{1, 2, 4, 6, 8, 10\}$. The value $\dim(\mathbf{z}) = 128$ for all VAEs, and their ranks are all 128 except for the case of $\beta = 10$, whose rank is around 100. Differences are very subtle as long as no significant mode collapse occurs: compare to Fig. 7.30

EFFECT OF "MODE COLLAPSE" ON RECONSTRUCTED (GENERATED) IMAGES for very large $\dim(\mathbf{z})$'s

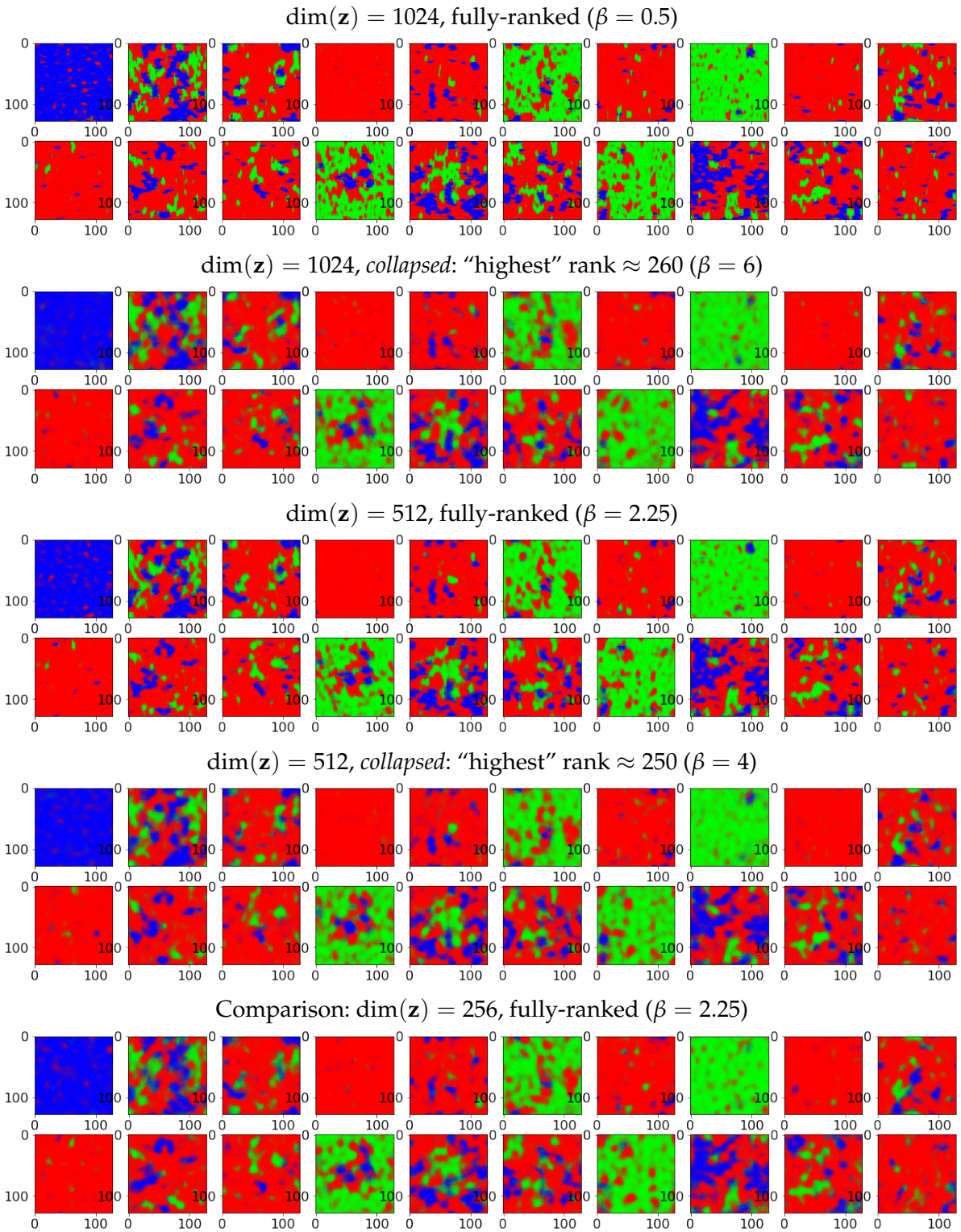

FIGURE 7.30: Effect of mode collapsed on output images, shown for VAEs with very *large* $\dim(\mathbf{z})$. All collapsed VAEs have comparable "highest" rank of around 250 or 260. A comparison to a VAE of fully-rank with $\dim(\mathbf{z}) = 256$ is shown at the bottom. All VAEs here employed batch normalization on encoder and decoder.

EFFECT OF β ON EMPIRICAL HISTOGRAMS OF LATENT VARIABLES:
Test data-sets that represent uniform data-sets states ("type I")

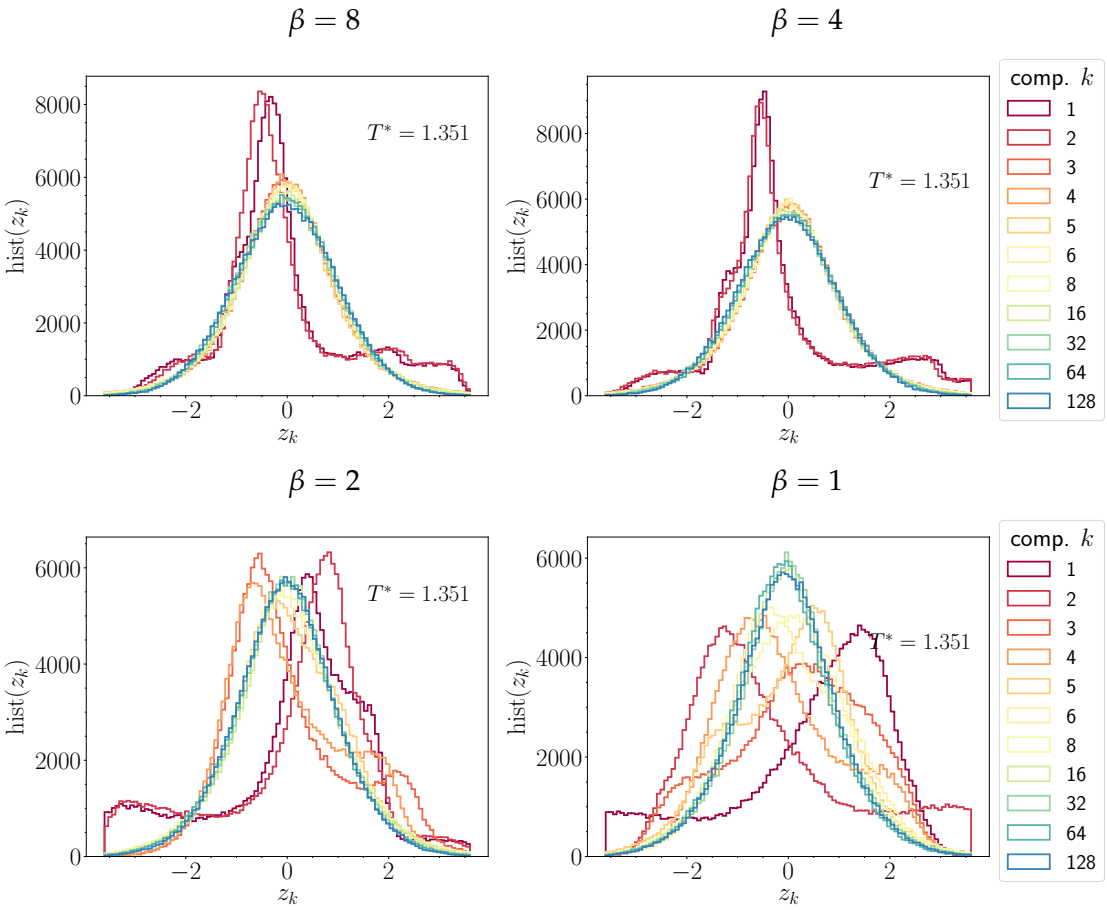

FIGURE 7.31: Effect of β: Empirical histograms of latent variables z_k, for various k's (the components are ordered by $\gamma(k)$) for test data uniform in density ("type I"). Four different VAEs are compared, each trained on a different value of β. For high β, the first two components are unique, and higher-order components form a Gaussian (top left). For low β (bottom right), many variables are not Gaussian distributed, i.e. they are skewed and deformed. On the other hand, components 1 and 2 are reflected around the zero point. The other two cases are intermediates between these two extremes. Note that not all latent component have been plotted (there are 128).

7.6.3 Effects of β on the character of the latent variables

Since the decoder allows us to visualize the latent variables, we now explore if the latent variables 'look' different upon increasing β. In this section we will use a VAE with $\dim(\mathbf{z}) = 256$, in contrast to the previous sections. We also use test sets uniform in density ("type I").

In Fig. 7.32 we visualize the "axes" of latent space, ordered by the hierarchy $\gamma(k)$, with exponential spacing between their numbers k. The first two maximal and minimal components ($k = 1, 2$, top and bottom rows) represent scalar fields: the red, green, and blue extrema of our complex physical order parameter $\mathbf{c}$. The red component represents vacancies, the green and blue represent demixing order with one particle species. The components 4 and 8 resemble low-order harmonic modes. The images become more "fuzzy" further along the line of k's, however. The reduced intensity of the modulations in within images seems to be an expression of the smaller likelihood ("energy") of these components in the system. Hence, for practical purposes, we plot the coordinates with emphasized amplitude in Figure 7.33. This can be achieved by scaling the amplitude of a latent space vector – the farther a vectors goes astray from 0, the more intense ("certain") the variables become. In other words, the distance of a vector component from the unit Gaussian prior at the center of latent space is an expression for its discernibility from most probable states.

Interestingly, then, near the threshold values, the collective variables form a "coarse-graining" hierarchy: The correlation length or characteristic length-scale within the images reduces roughly by a factor of $1/2$. The ordering of the coordinates of latent space according to their σ's ($\gamma(k)$) is thus also an indicator of a hierarchy in length-scale within decoded collective variables.

The latent space coordinates around the threshold value of β resemble strongly the eigenvectors found by principal component analysis on the same input data, which performs a linear transformation (singular value decomposition). We will not present the results here, but, comment more on this in Sec. 7.9. We only mention that this could imply the encoder (and decoder) become nearly- or partly-linear at the threshold state. These "modes" may be considered "solid-state-like" in comparison to those for weaker *beta* (see further text).

For weaker values of β, in Figs. 7.34 and Fig. 7.35, the length-scales are in the decoded latent variables become lesser separated among components (they become "entangled". The interpretability of these collective variables declines substantially as soon as this mixing dominates. Moreover, this explains the phenomenology we described in the previous section, in that the "order parameters" are mixed into different latent-space components.

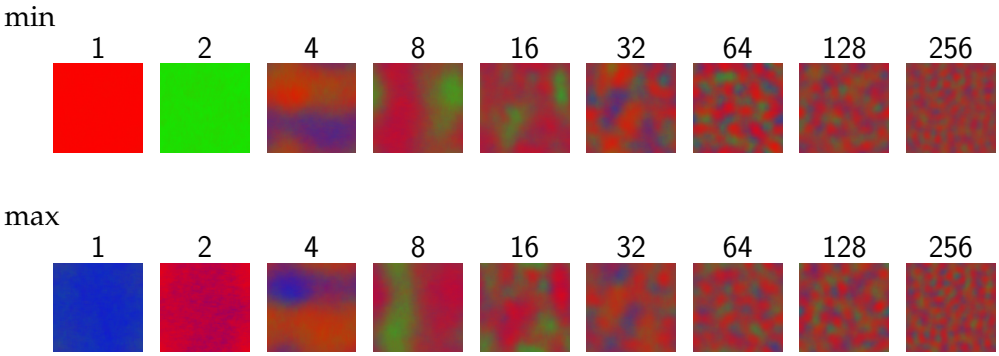

FIGURE 7.32: Coordinates of latent space: Generated images from the maximal value (top row) and minimal value (bottom row) of the coordinate z_k from the set of all configurations in the test set, where k is written above the images. The reduced temperature used to determine the minimum and maximum values of z_k in the test data is $T^* = 1.299$, although these do not significantly different for other temperatures. This VAE corresponds to $\beta = 4$ ("strong") for $\dim(\mathbf{z}) = 256$, near the threshold value.

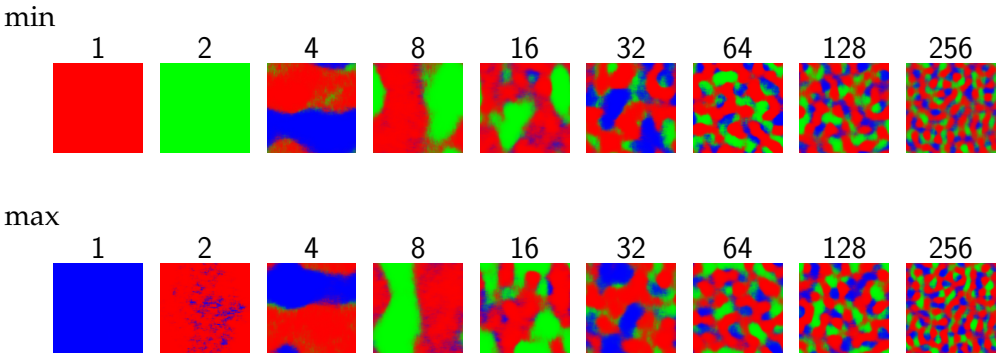

FIGURE 7.33: Coordinates of latent space: Generated images from the maximal value (top row) and minimal value (bottom row) of the coordinate z_k, *scaled by a factor of 10*. k is written above the images. See caption in Fig. 7.32.

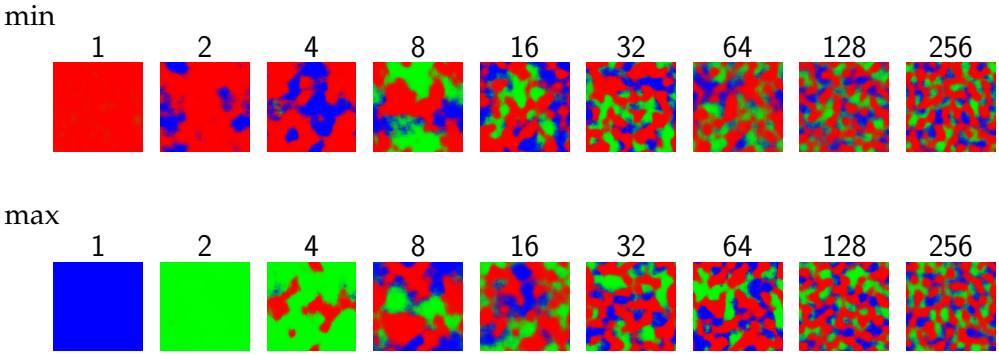

FIGURE 7.34: Coordinates of latent space with *weaker* length-scale decoupling among components, $\beta = 1.0$ for $\dim(\mathbf{z}) = 256$. Compare to Fig. 7.33.

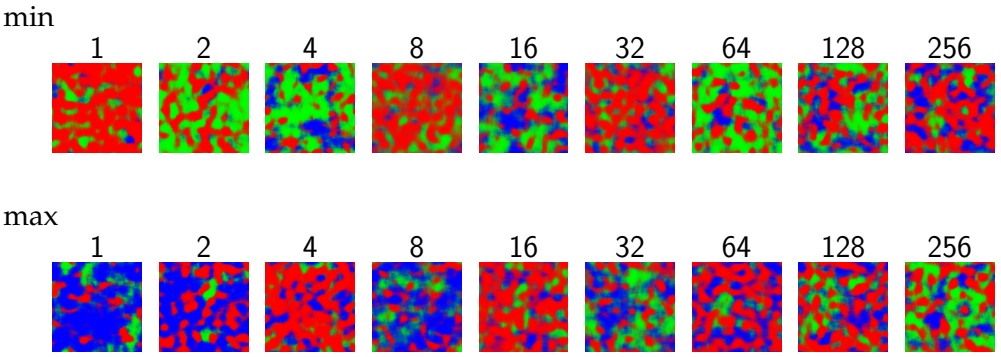

FIGURE 7.35: Coordinates of latent space with *very weak* length-scale decoupling among components (strong "entanglement"): $\beta = 0.1$ for $\dim(\mathbf{z}) = 256$. Compare to Fig. 7.34.

7.6.4 Statistics of latent variables in thermodynamic ensembles

In this section, we present a large number of plots that show the statistics of the latent variables over Boltzmann-Gibbs thermodynamic ensembles (upon varying $\ln(f)$). The plots are presented for fully-ranked VAEs with $\dim(\mathbf{z}) = 128$, having values $\beta = 8$ ("high"), $\beta = 4$ ("intermediate") and $\beta = 2$ ("low"). The threshold value for this $\dim(\mathbf{z})$ is around 9; hence, the first case represents the "threshold" state before mode collapse. As we discovered in the previous section, this implies that $\beta = 8$ will have "disentangled" latent variables, with a strong length-scale separation in the collective variables on the output side. The second case, $\beta = 4$ shows a moderate amount of "entanglement" of mixing of length-scales in the output. The last case, $\beta = 2$, shows even stronger mixing or "entanglement" of spatial length-scales in the output.

In Figs. 7.36–7.37, we can observe how the highly "disentangled" representation indeed gives all variables $k \geq 3$ a centered mean $\langle z_k \rangle \approx 0$ with mild fluctuations about, except near phase transition points (indicated in vertical gray lines). The variance in these higher-order variables peaks at the phase transition. In contrast, the variance in the first two variables obtains an inflection point. This is true across all reduced temperatures (temperatures).

In Figs. 7.38–7.39, we present the results on $\langle \sigma_k \rangle$, as well as $\langle \ln(1/\sigma_k) \rangle$ for this "high" value of β. For all k's, $\langle \sigma_k \rangle$ finds a minimum just before the phase transition fugacities. In contrast, $\langle \ln(1/\sigma_k) \rangle$ obtains its maximum just before. The distances between curves for different $k's$ remain nearly constant across all thermodynamic ensembles – reminiscent of a constant "momentum" gap in between. Moreover, we can observe that $\langle \ln(1/\sigma_k) \rangle$ is nearly linearly dependent on $\ln(f)$ (the chemical potential), as as we move farther from the phase transition points. In fact, this trend continues, but, we have cropped the range of fugacities in these plots to near the transition points. This means that $\langle \ln(1/\sigma_k) \rangle$ seems to be directly correlated to the chemical potential, which is a conjugate variable to the density ρ. Therefore, we have found evidence that VAEs "map" conjugate fields to order parameters in variables like $\langle \ln(1/\sigma_k) \rangle$. This is quite intriguing and could be thought through more deeply in the future.

In Figs. 7.40–7.43, we have presented results of the same analysis for $\beta = 4$ ("moderate"). As this system entails a slightly higher degree of "entanglement"

of latent variables, the first few components will "include" order-parameter-like behavior (i.e. like that of $k = 1, 2$ for $\beta = 8$).

In Figs. 7.44–7.47, we have presented results of the same analysis for $\beta = 2$ ("weak"). As this system entails a high degree of "entanglement" of latent variables. We have provided the full set of plots for completeness.

* * *

We have provided more analysis on the role of *beta* in the physical "faithfulness" of the output configurations, for example, as well as other empirical "experiments" in App. B.

VAE with a HIGH VALUE OF β (strong length-scale separation in collective variables)
Tested ABOVE AND AROUND TRICRITICAL POINT:
Ensemble-average of sampled variables z_k for increasing latent components k

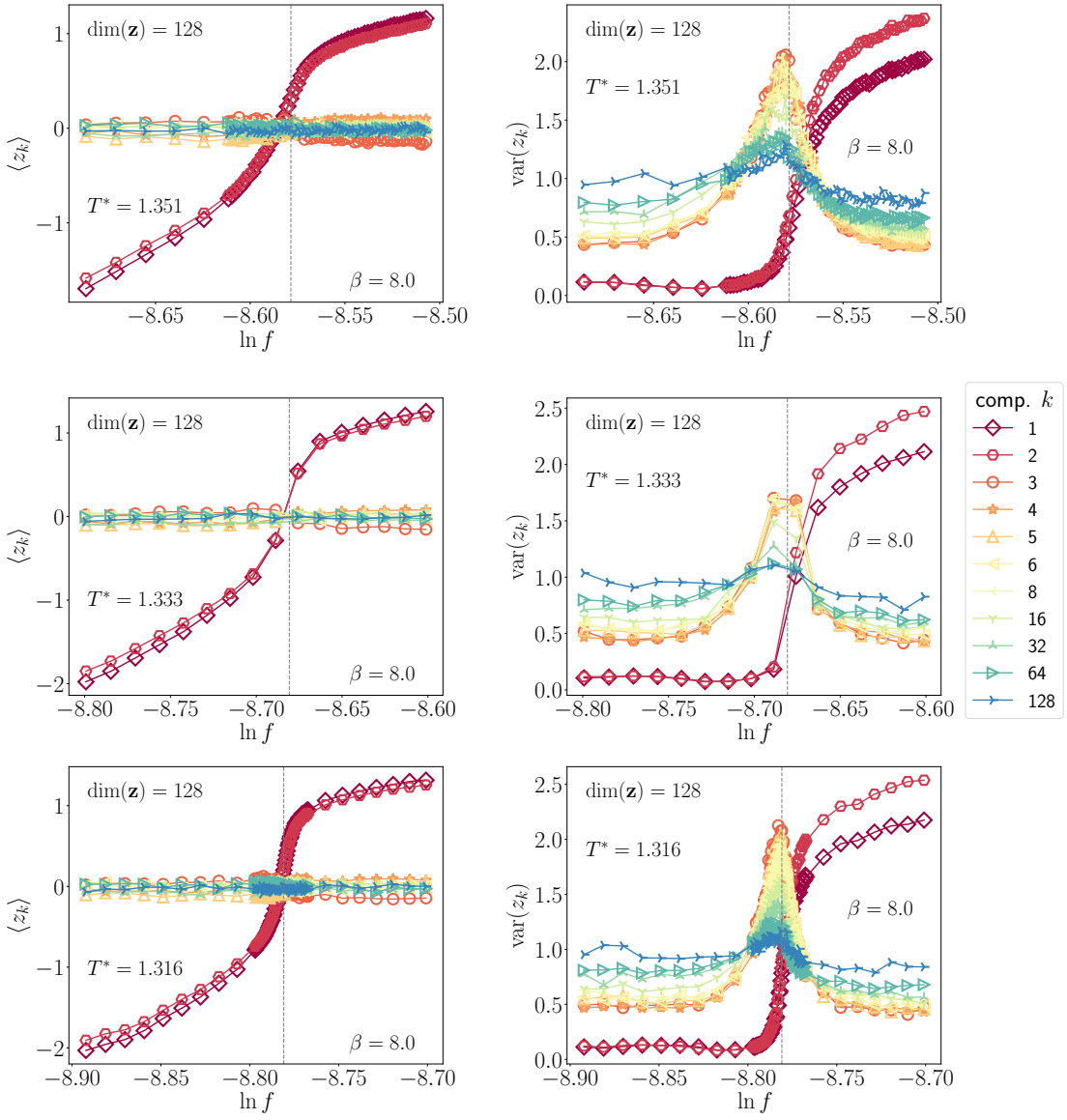

FIGURE 7.36: Ensemble-average of the sampled variables z_k (left column) and their empirical variances (right column) shown for different components k versus log-fugacity (thermodynamic ensembles): The separate VAEs are tested on thermodynamic ensembles at three different temperatures above (top) and around (bottom two) the tricritical temperature. The VAE of $\dim(\mathbf{z}) = 128$ and $\beta = 8$ was trained on the standard training temperature $T^*_{\text{train}} = 1.401$. This value of β is near the threshold value, indicating that the collective variables found by the VAE are much more "disentangled" and approximately separate spatial length-scales in a hierarchy. The components were ordered by $\gamma(k)$ evaluated at T^*_{train}. The gray vertical lines indicate approximate phase transition fugacities of the rod-model, estimated from GCMC simulations. See next Fig. 7.37.

VAE with a HIGH VALUE OF β (strong length-scale separation in collective variables)
Tested BELOW TRICRITICAL POINT:
Ensemble-average of encoded variables z_k for increasing latent components k

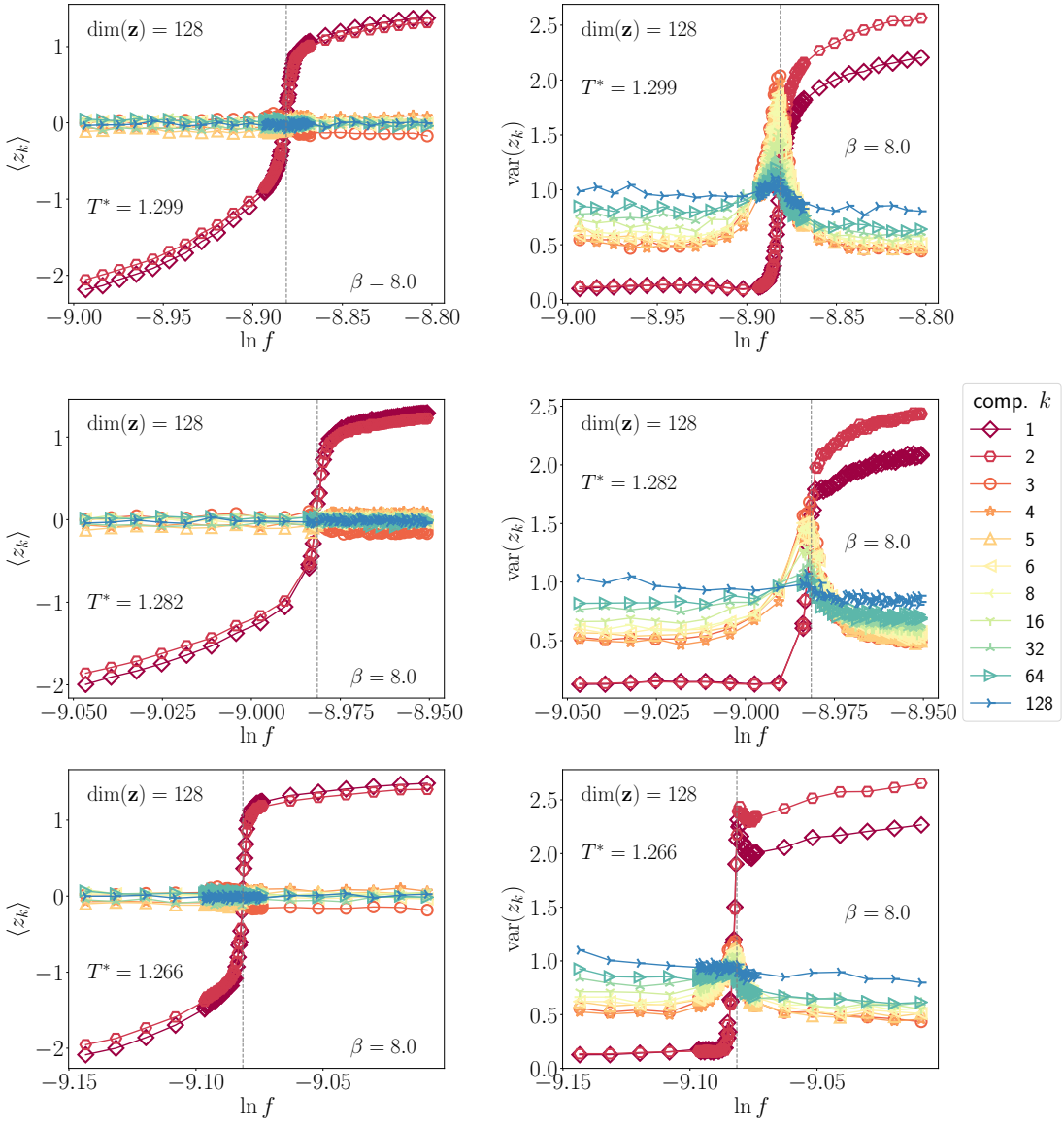

FIGURE 7.37: Ensemble-average of the sampled variables z_k (left column) and their empirical variances (right column) shown for different components k versus log-fugacity (thermodynamic ensembles): The separate VAEs are tested on thermodynamic ensembles at three different temperatures below the tricritical temperature. See also caption of Fig. 7.36.

VAE with a HIGH VALUE OF β (strong length-scale separation in collective variables)
Tested ABOVE AND AROUND TRICRITICAL POINT:
Ensemble-average of encoded variables σ_k or $\ln(1/\sigma_k)$ for increasing latent components k

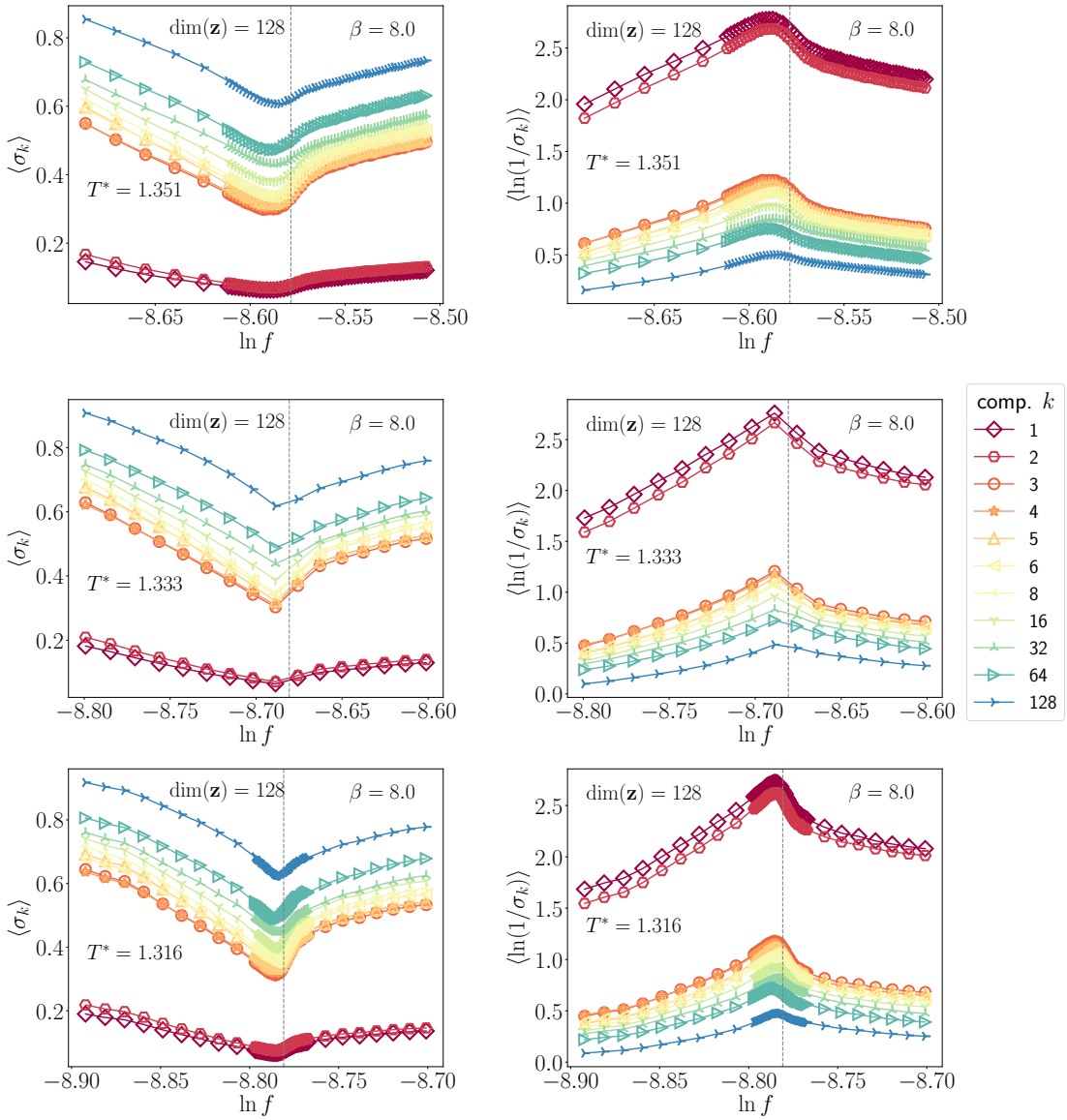

FIGURE 7.38: Ensemble-average of the encoded variables σ_k or $\ln(1/\sigma_k)$ shown for different components k versus log-fugacity (thermodynamic ensembles): The separate VAEs are tested on thermodynamic ensembles at three different temperatures above (top) and around (bottom two) the tricritical temperature. The VAE of $\dim(\mathbf{z}) = 128$ and $\beta = 8$ (near the threshold value of β) was trained on the standard training temperature $T^*_{\text{train}} = 1.401$. The components were ordered by $\gamma(k)$ evaluated at T^*_{train}. The gray vertical lines indicate approximate phase transition fugacities of the rod-model, estimated from GCMC simulations. See next Fig. 7.39.

VAE with a HIGH VALUE OF β (strong length-scale separation in collective variables)
Tested BELOW TRICRITICAL POINT:
Ensemble-average of encoded variables σ_k or $\ln(1/\sigma_k)$ for increasing latent components k

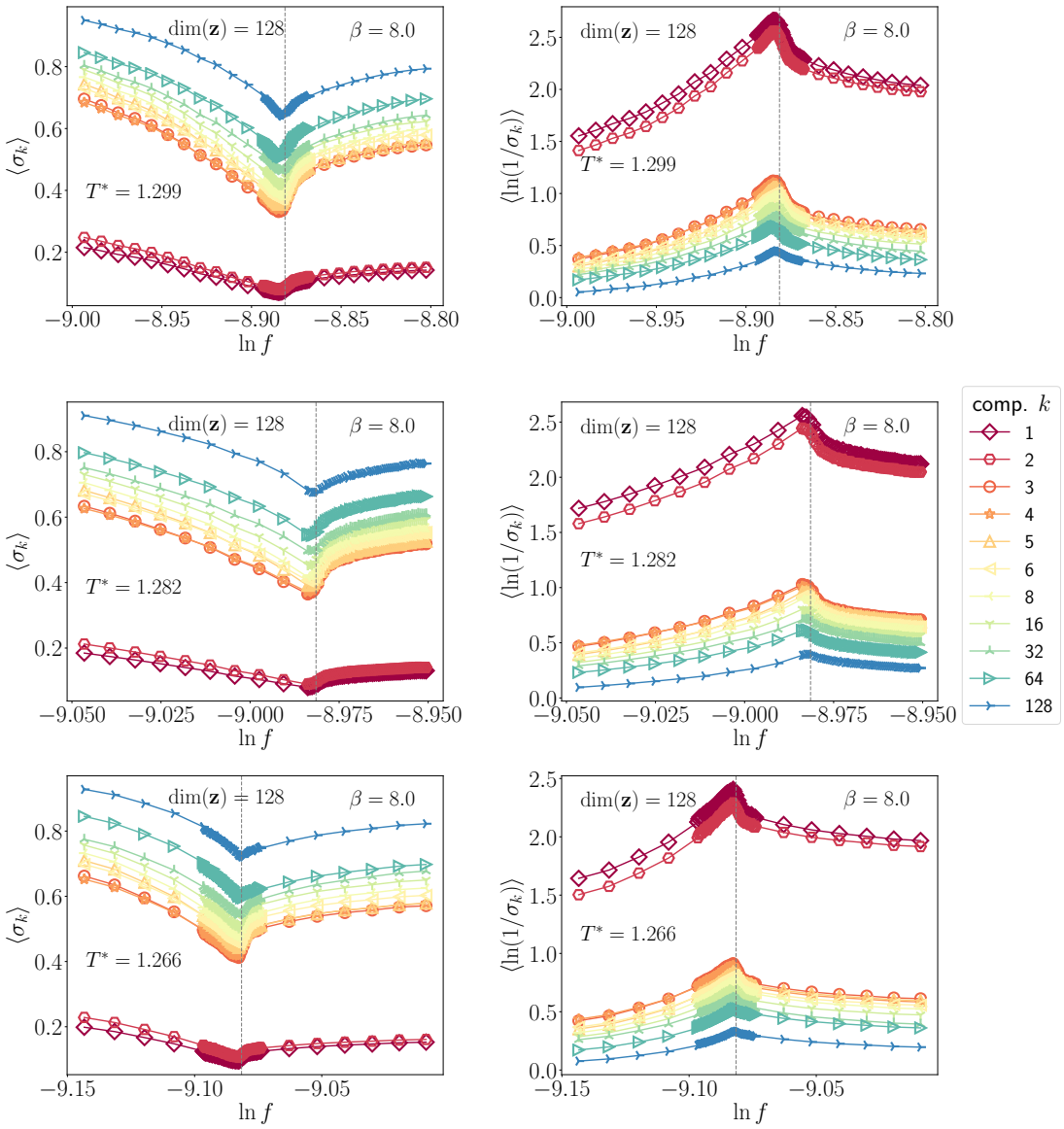

FIGURE 7.39: Same as Fig. 7.38, but tested on thermodynamic ensembles at three different temperatures below the tricritical temperature.

VAE with a MODERATE VALUE OF β (moderate length-scale separation in collective variables)
Tested ABOVE AND AROUND TRICRITICAL POINT:
Ensemble-average of sampled variables z_k for increasing latent components k

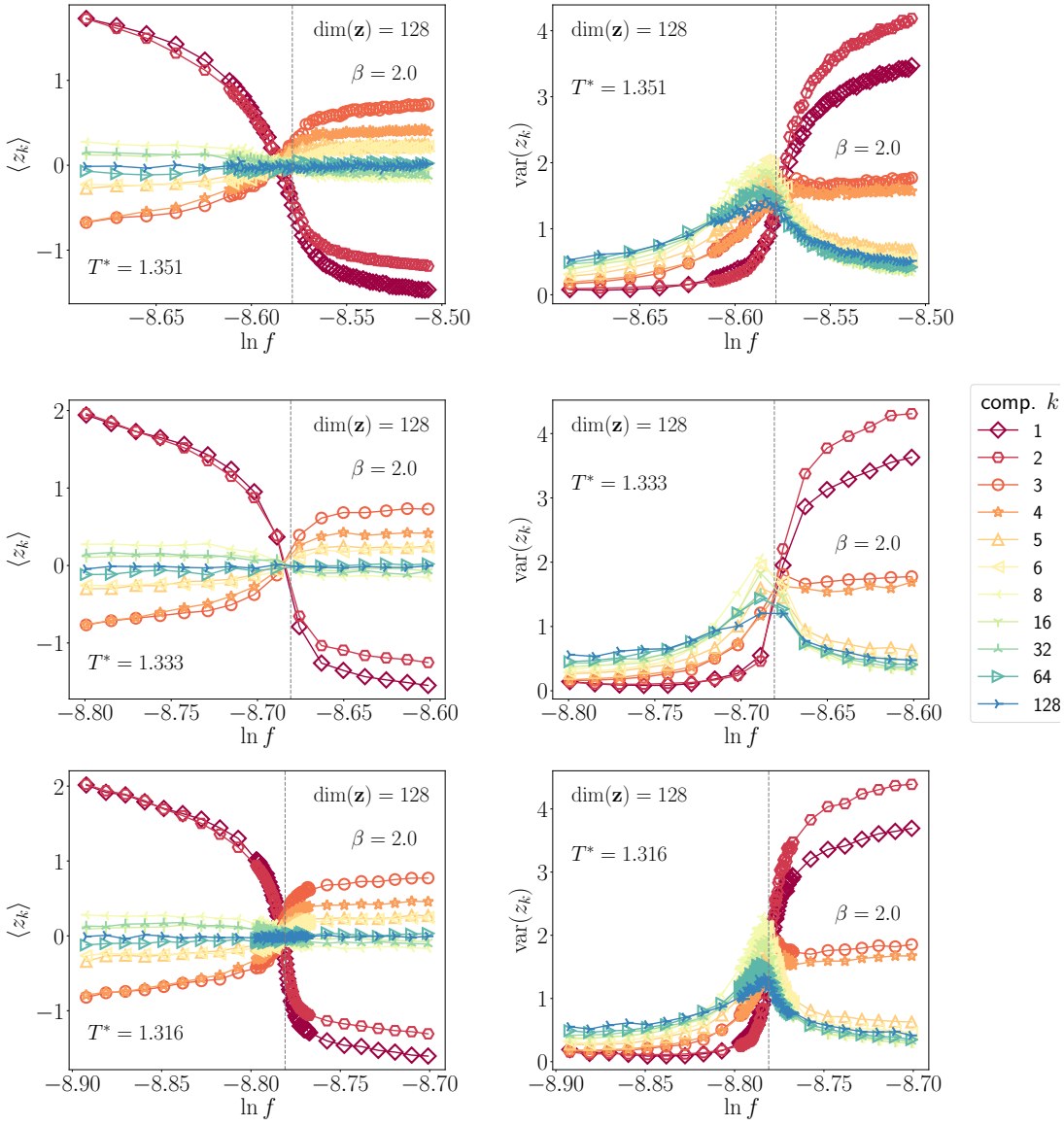

FIGURE 7.40: Ensemble-average of the sampled variables z_k (left column) and their empirical variances (right column) shown for different components k versus log-fugacity (thermodynamic ensembles): The separate VAEs are tested on thermodynamic ensembles at three different temperatures above (top) and around (bottom two) the tricritical temperature. The VAE of $\dim(\mathbf{z}) = 128$ and $\beta = 2$ was trained on the standard training temperature $T^*_{\text{train}} = 1.401$. This value of β is much lower than the threshold value, indicating that the collective variables found by the VAE are much more "entangled" and are not organized according to spatial length-scales in images. The components were ordered by $\gamma(k)$ evaluated at T^*_{train}. The gray vertical lines indicate approximate phase transition fugacities of the rod-model, estimated from GCMC simulations. See next Fig. 7.41.

VAE with a MODERATE VALUE OF β (moderate length-scale separation in collective variables)
Tested BELOW TRICRITICAL POINT:
Ensemble-average of encoded variables z_k for increasing latent components k

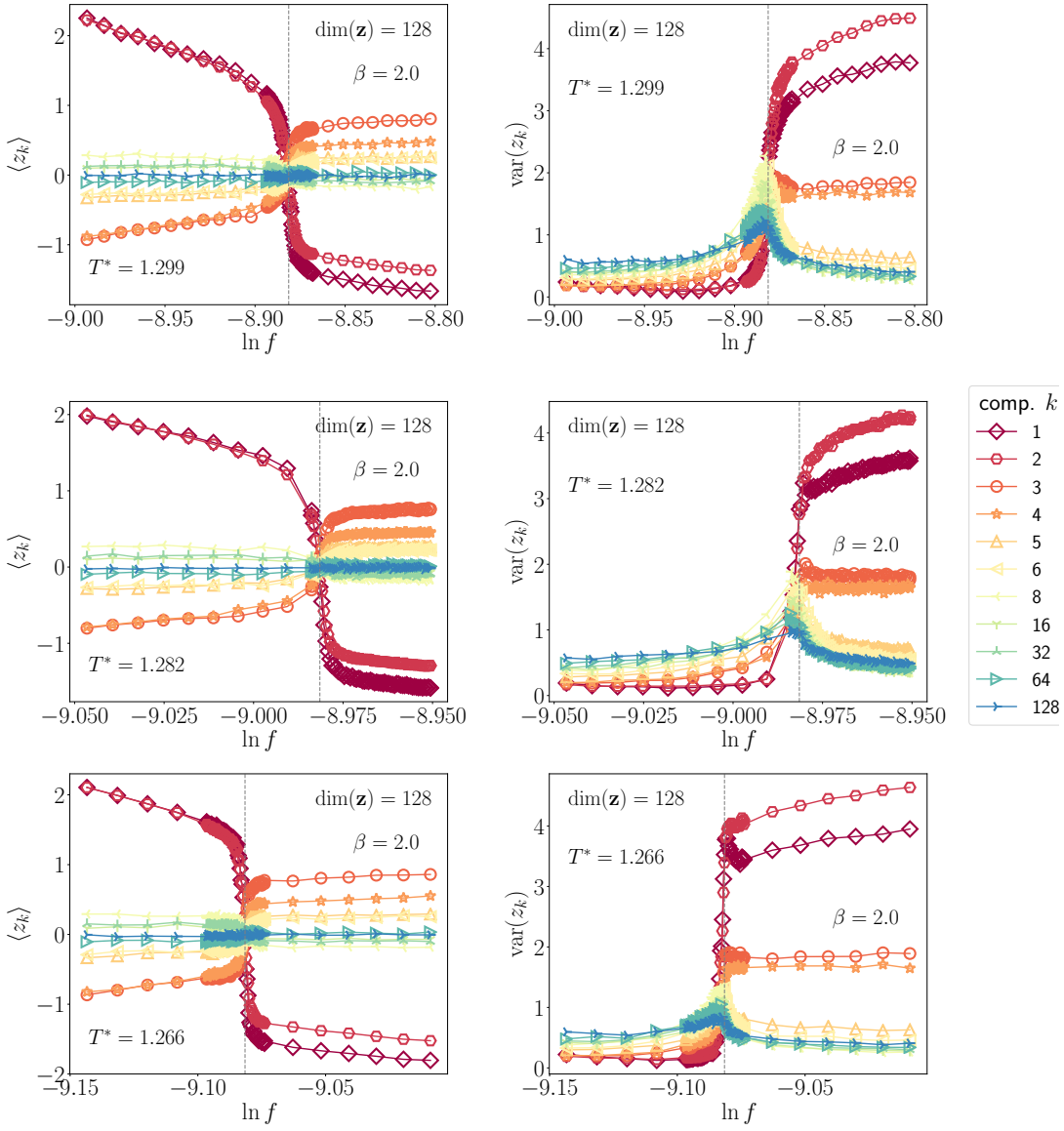

FIGURE 7.41: Ensemble-average of the sampled variables z_k (left column) and their empirical variances (right column) shown for different components k versus log-fugacity (thermodynamic ensembles): The separate VAEs are tested on thermodynamic ensembles at three different temperatures below the tricritical temperature. See also caption of Fig. 7.40.

VAE with a MODERATE VALUE OF β (moderate length-scale separation in collective variables)
Tested ABOVE AND AROUND TRICRITICAL POINT:
Ensemble-average of encoded variables σ_k or $1/\sigma_k$ for increasing latent components k

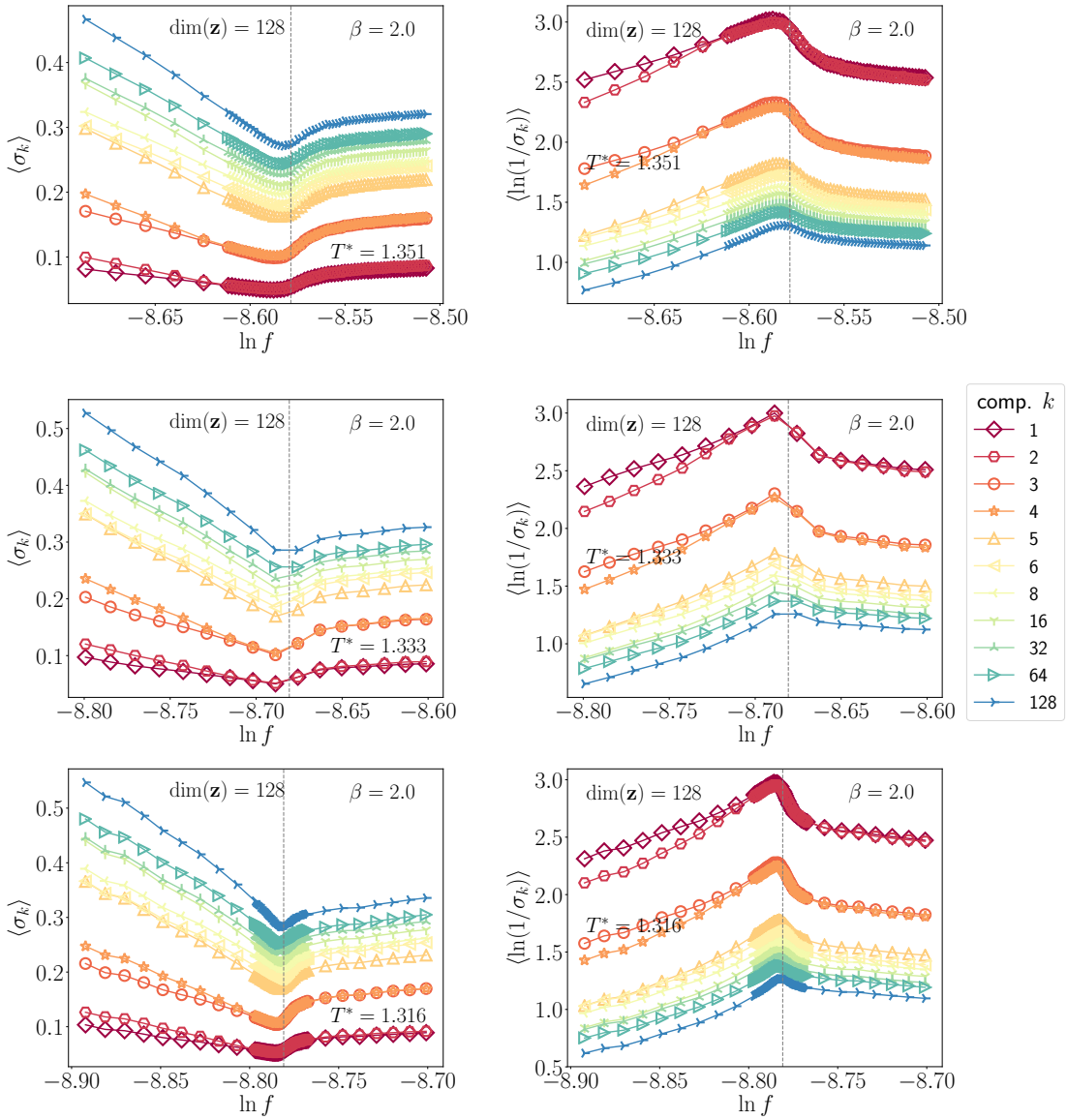

FIGURE 7.42: Ensemble-average of the encoded variables σ_k or $\ln(1/\sigma_k)$ shown for different components k versus log-fugacity (thermodynamic ensembles): The separate VAEs are tested on thermodynamic ensembles at three different temperatures above (top) and around (bottom two) the tricritical temperature. The VAE of $\dim(\mathbf{z}) = 128$ and $\beta = 2$ (well below the threshold value of β) was trained on the standard training temperature $T^*_{\text{train}} = 1.401$. The components were ordered by $\gamma(k)$ evaluated at T^*_{train}. The gray vertical lines indicate approximate phase transition fugacities of the rod-model, estimated from GCMC simulations. See next Fig. 7.43.

VAE with a MODERATE VALUE OF β (moderate length-scale separation in collective variables)
Tested BELOW TRICRITICAL POINT:
Ensemble-average of encoded variables σ_k or $1/\sigma_k$ for increasing latent components k

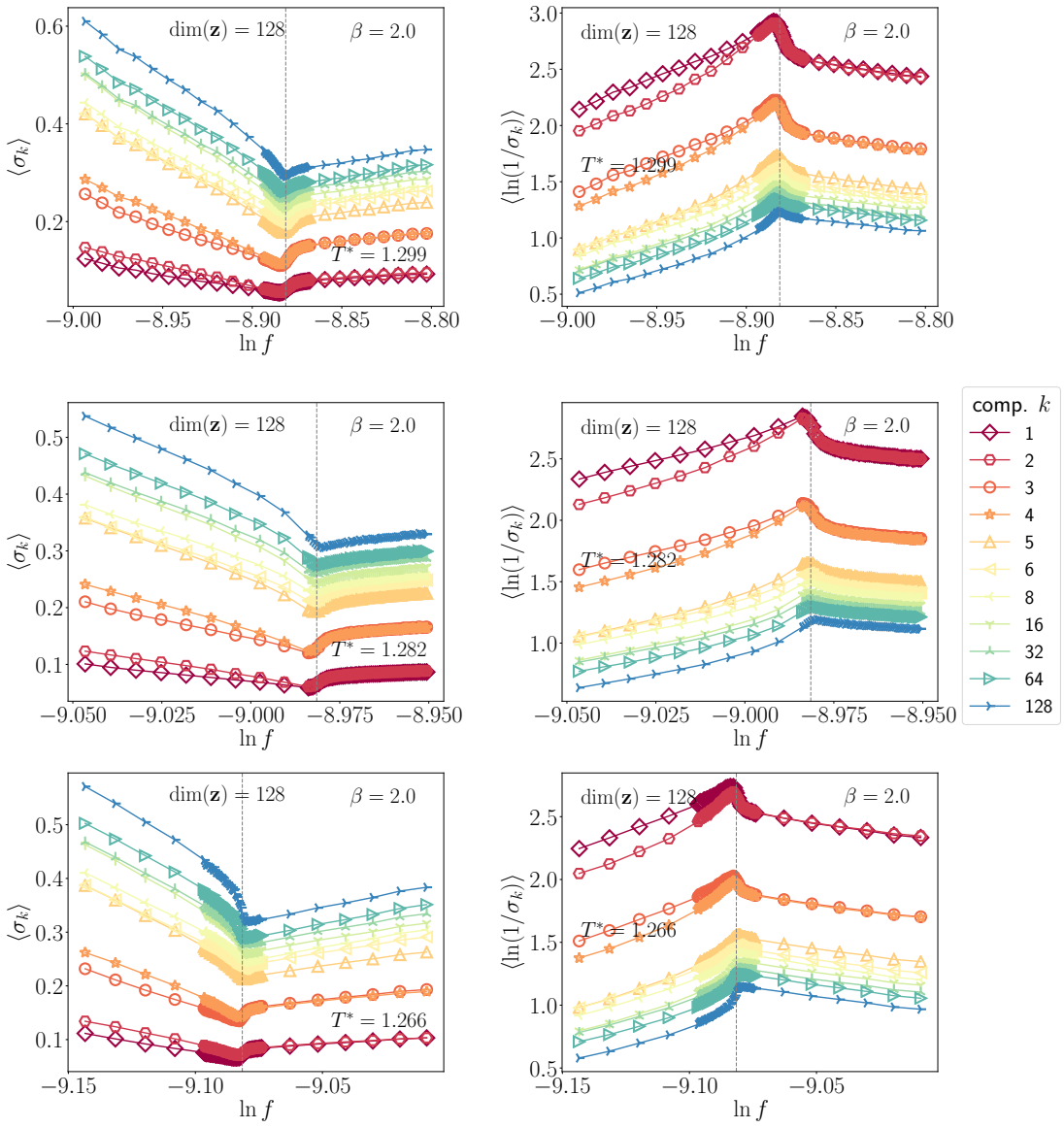

FIGURE 7.43: Ensemble-average of the encoded variables σ_k (left column) or $1/\sigma_k$ (right column) shown for different components k versus log-fugacity (thermodynamic ensembles): The separate VAEs are tested on thermodynamic ensembles at three different temperatures below the tricritical temperature. See also caption of Fig. 7.42.

VAE with a LOW VALUE OF β (weak length-scale separation in collective variables)
Tested ABOVE AND AROUND TRICRITICAL POINT:
Ensemble-average of sampled variables z_k for increasing latent components k

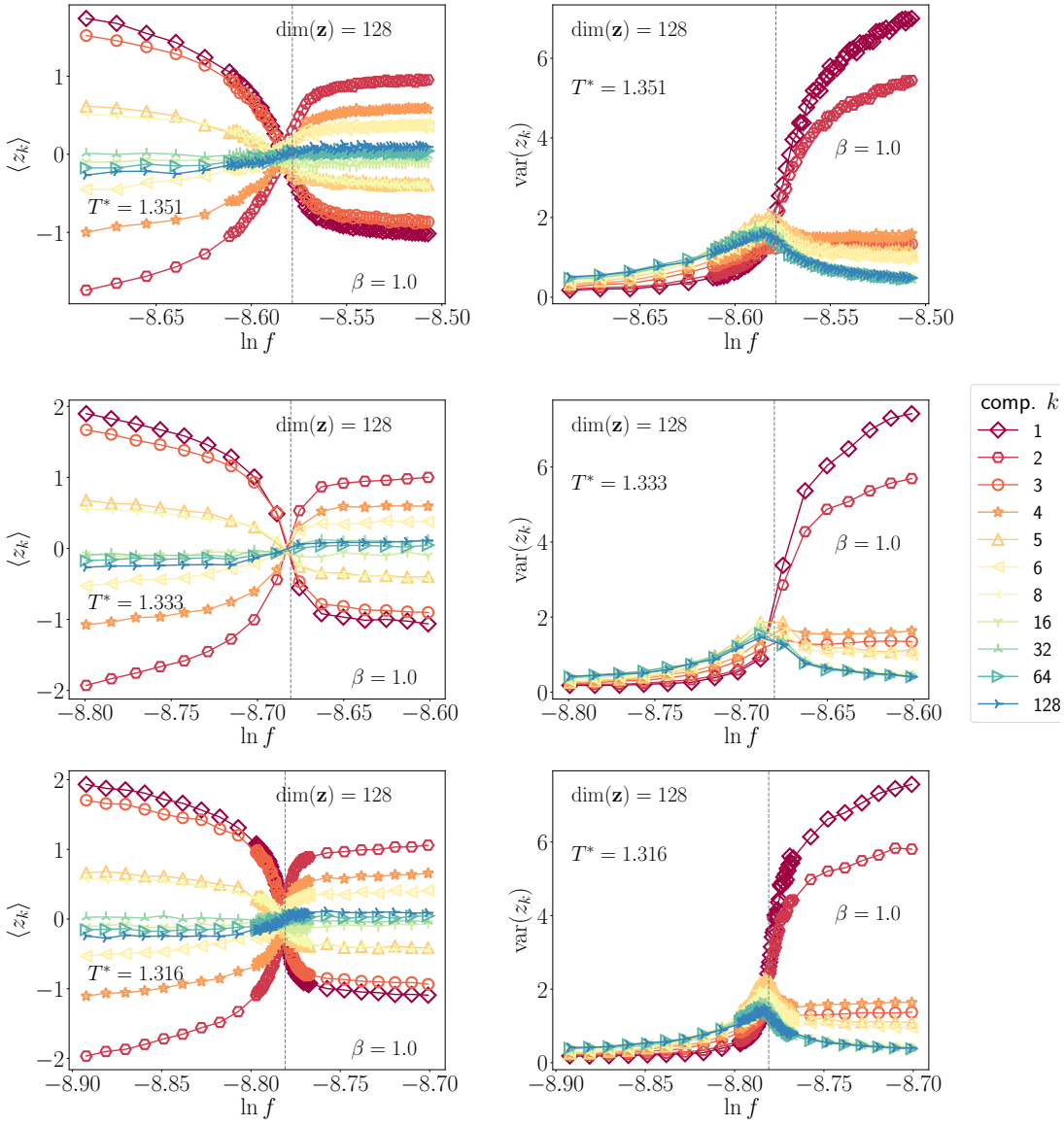

FIGURE 7.44: Ensemble-average of the sampled variables z_k (left column) and their empirical variances (right column) shown for different components k versus log-fugacity (thermodynamic ensembles): The separate VAEs are tested on thermodynamic ensembles at three different temperatures above (top) and around (bottom two) the tricritical temperature. The VAE of $\dim(\mathbf{z}) = 128$ and $\beta = 1$ was trained on the standard training temperature $T^*_{\text{train}} = 1.401$. This value of β is much lower than the threshold value, indicating that the collective variables found by the VAE are much more "entangled" and are not organized according to spatial length-scales in images. The components were ordered by $\gamma(k)$ evaluated at T^*_{train}. The gray vertical lines indicate approximate phase transition fugacities of the rod-model, estimated from GCMC simulations. See next Fig. 7.45.

VAE with a LOW VALUE OF β (weak length-scale separation in collective variables)
Tested BELOW TRICRITICAL POINT:
Ensemble-average of encoded variables z_k for increasing latent components k

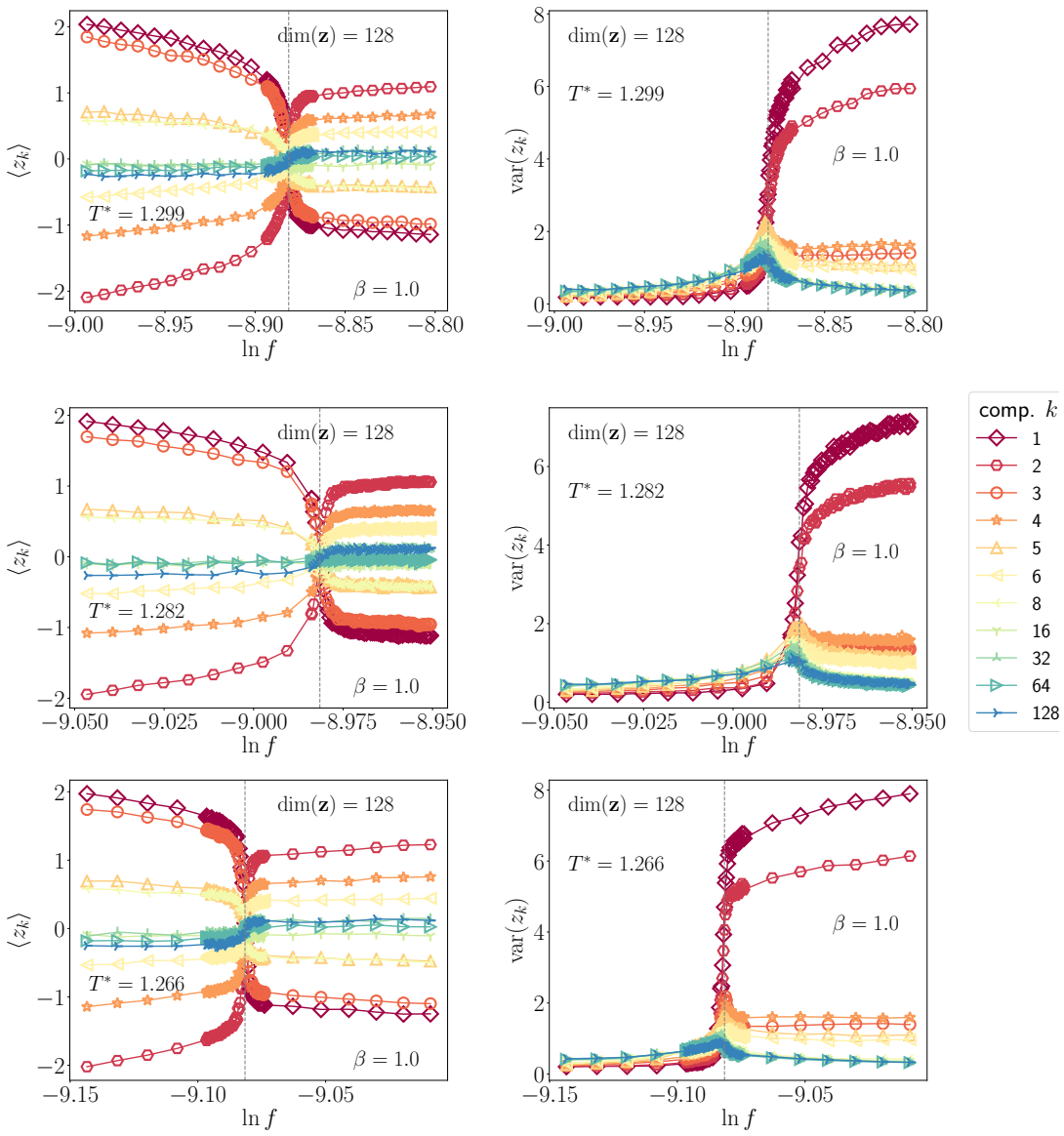

FIGURE 7.45: Ensemble-average of the sampled variables z_k (left column) and their empirical variances (right column) shown for different components k versus log-fugacity (thermodynamic ensembles): The separate VAEs are tested on thermodynamic ensembles at three different temperatures below the tricritical temperature. See also caption of Fig. 7.44.

VAE with a LOW VALUE OF β (weak length-scale separation in collective variables)
Tested ABOVE AND AROUND TRICRITICAL POINT:
Ensemble-average of encoded variables σ_k or $1/\sigma_k$ for increasing latent components k

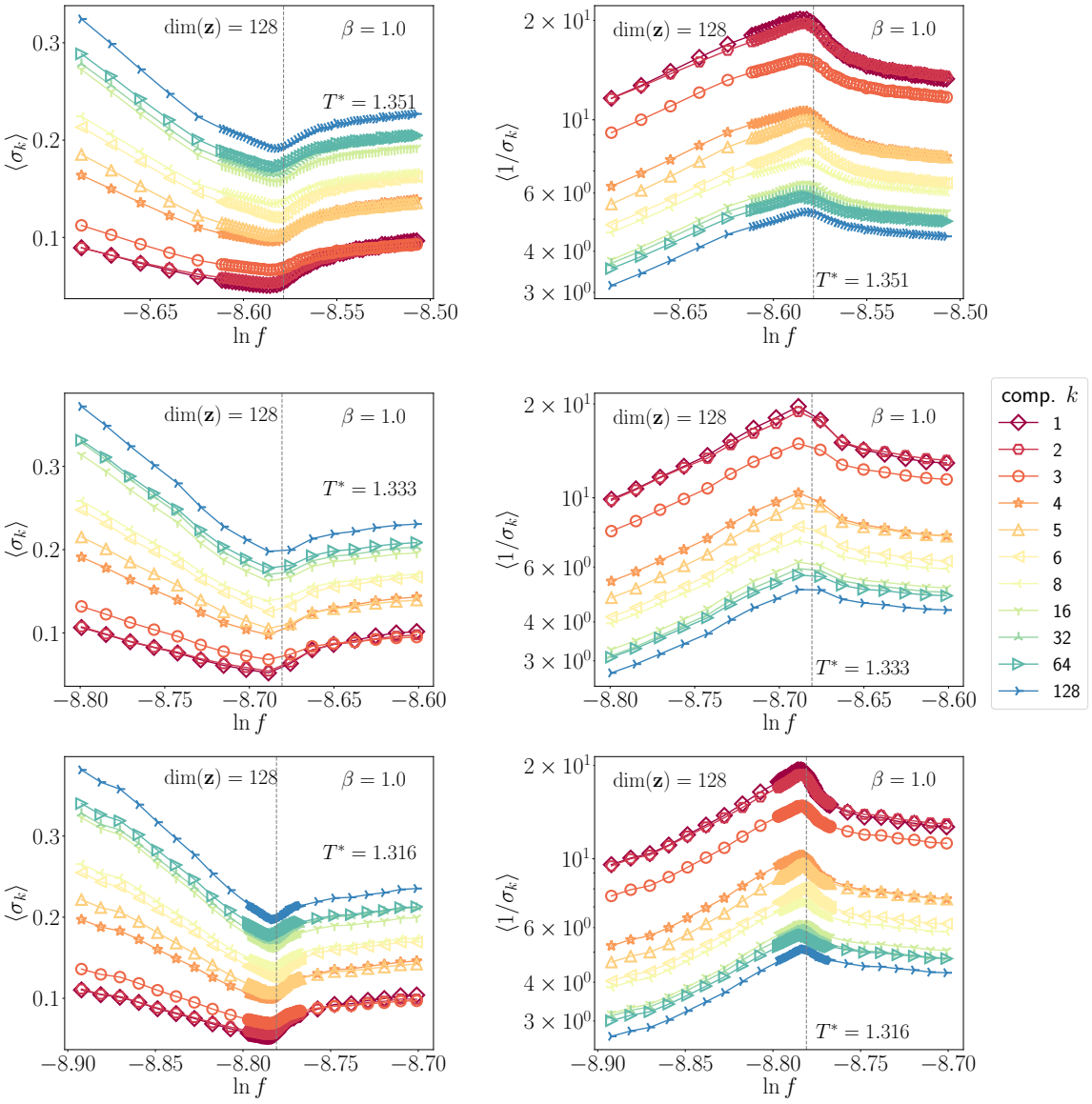

FIGURE 7.46: Ensemble-average of the encoded variables σ_k or $1/\sigma_k$ shown for different components k versus log-fugacity (thermodynamic ensembles): The separate VAEs are tested on thermodynamic ensembles at three different temperatures above (top) and around (bottom two) the tricritical temperature. The VAE of $\dim(\mathbf{z}) = 128$ and $\beta = 1$ (well below the threshold value of β) was trained on the standard training temperature $T^*_{\text{train}} = 1.401$. The components were ordered by $\gamma(k)$ evaluated at T^*_{train}. The gray vertical lines indicate approximate phase transition fugacities of the rod-model, estimated from GCMC simulations. See next Fig. 7.47.

VAE with a LOW VALUE OF β (weak length-scale separation in collective variables)
Tested BELOW TRICRITICAL POINT:
Ensemble-average of encoded variables σ_k or $1/\sigma_k$ for increasing latent components k

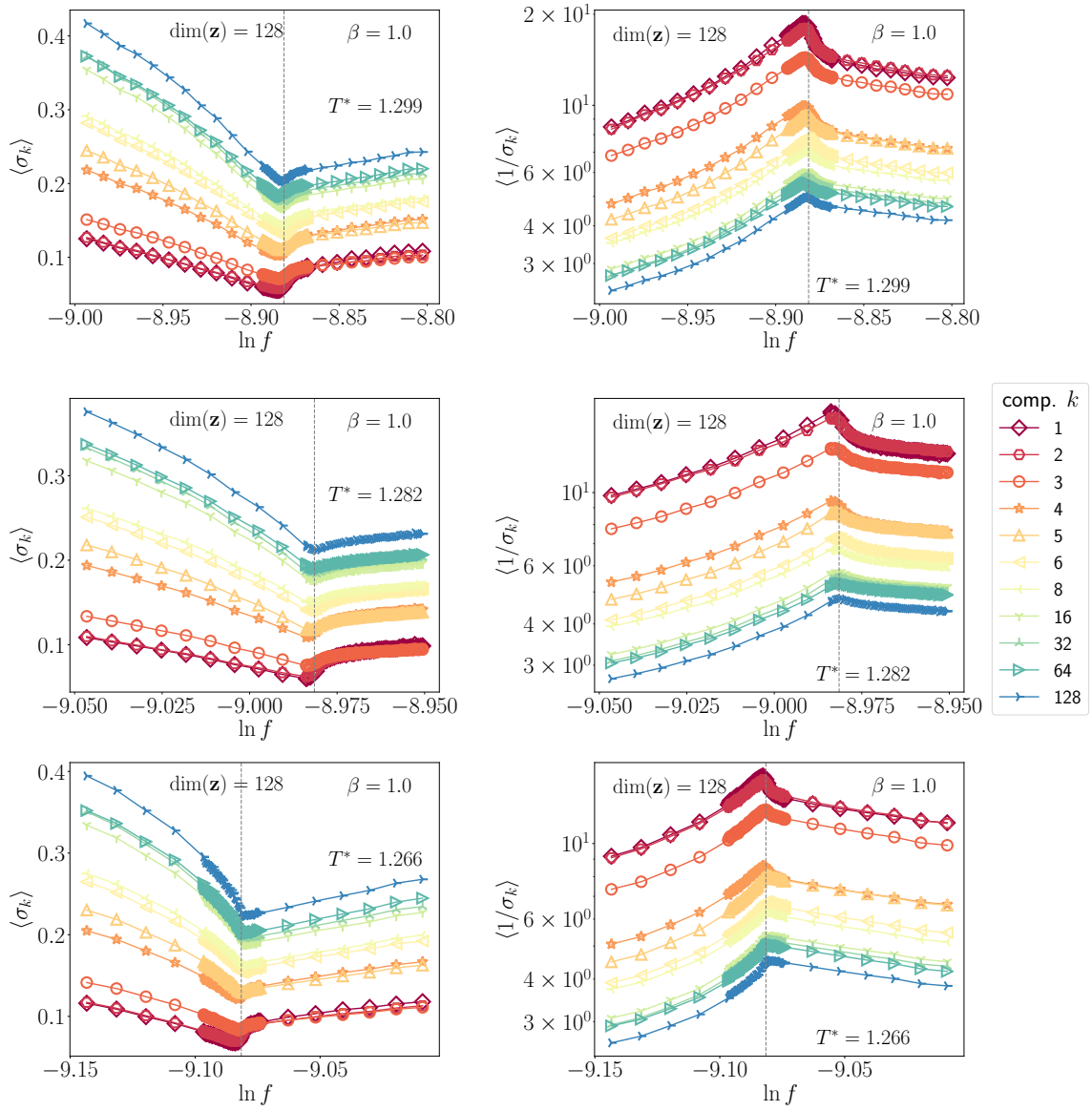

FIGURE 7.47: Ensemble-average of the encoded variables σ_k (left column) or $1/\sigma_k$ (right column) shown for different components k versus log-fugacity (thermodynamic ensembles): The separate VAEs are tested on thermodynamic ensembles at three different temperatures below the tricritical temperature. See also caption of Fig. 7.46.

7.7 Sensitivity to thermodynamic states (empirical findings)

In the coming section, we will present the statistics of the absolute values of latent variables across different thermodynamic ensembles. In sec. 7.7.2, we will explore the statistics of further quantities that are functions of thee pairwise encoding (μ, σ) such as the Kullback-Leibler divergence, along with another observable. We can also construct alternative order parameters on latent space using principal component analysis on the latent variables, which very sharply distinguish detect the phase transition fugacities. This is shown in Sec. 7.7.3. The analysis here represents a collection of empirical findings that together make one main point about VAEs: The encoded representation contains highly sensitive information about the thermodynamic states of the system in test data-sets. This even includes data at vastly different reduced temperatures than that of the training data-set. All observables presented here can be used to "detect" phase boundaries, and possibly even discern the order of a phase transition (first or second order). This may be interesting for practical applications in physics, but also attest to our finding that VAEs must learn (implicitly) important thermodynamic properties, which is necessary in order to minimize the objective function. This includes, of course, the *generative* aspects of the VAE model, which possibly mimics learning an effective, free-energy-like generating function of the hard-rod system.

The example VAE we investigate here is one with $\dim(\mathbf{z}) = 128$ and $\beta = 8$, which is near the threshold value before we observed mode collapse. Therefore, the decoded latent variables show a strong separation of spatial length-scales (they are "disentangled").

7.7.1 Absolute values of "order-parameter" and "fluctuation" collective variables

Quite generally, we might consider each "fluctuation" collective variable, indexed $k \geq 2$ as a *mesoscopic* order parameter in the fluid of rods. In theory, a spatially-*inhomogeneous* external potential imposed onto the hard-rod system would bias these variables – thus, the "fluctuation" collective variables can be considered conjugate variables to higher-order, inhomogeneous external potentials. (See Ch. 3.2 for a generic discussion of conjugate fields.) In the homogeneous fluid systems in equilibrium without such an inhomogeneous potential the variables remain "fluctuations".

In Figs. 7.48–7.51 below, we observe the behavior of both the first two "order parameter" as well as examples of higher-order "fluctuation" collective variables across thermodynamic ensembles. At first, we observe the statistics of $|z_k|$ in 7.48–7.49; thereafter, we observe the statistics of $|\mu_k|$ in 7.50–7.51. Both sets of plots look quite similar, qualitatively. However, the means $|\mu_k|$ entail much less noise, and the higher-order variables are much more closely-distributed. This is expected given the "extra" fluctuations contained in the $\boldsymbol{z}$'s due to the Gaussian variances σ^2.

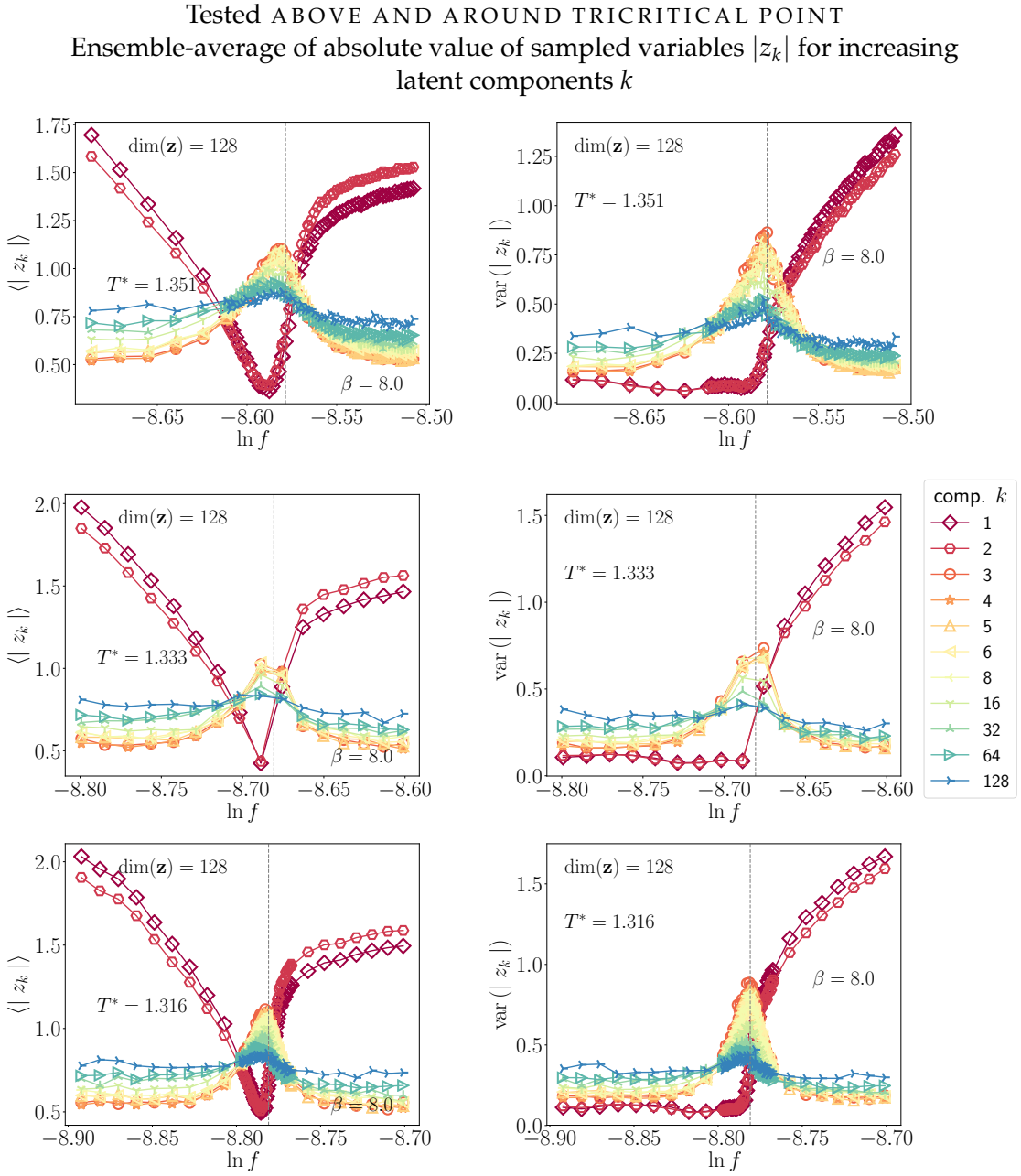

FIGURE 7.48: Ensemble-average of the absolute value of sampled variables $|z_k|$ (left column) and the variances (right column) shown for different components k versus log-fugacity (thermodynamic ensembles): The separate VAEs are tested on thermodynamic ensembles at three different temperatures above (top) and around (bottom two) the tricritical temperature. The VAE of $\dim(\mathbf{z}) = 128$ and $\beta = 8$ (near the threshold value of β) was trained on the standard training temperature $T^*_{\text{train}} = 1.401$. The components were ordered by $\gamma(k)$ evaluated at T^*_{train}. The gray vertical lines indicate approximate phase transition fugacities of the rod-model, estimated from GCMC simulations. See next Fig. 7.49.

Tested BELOW TRICRITICAL POINT
Ensemble-average of absolute value of sampled variables $|z_k|$ for increasing latent components k

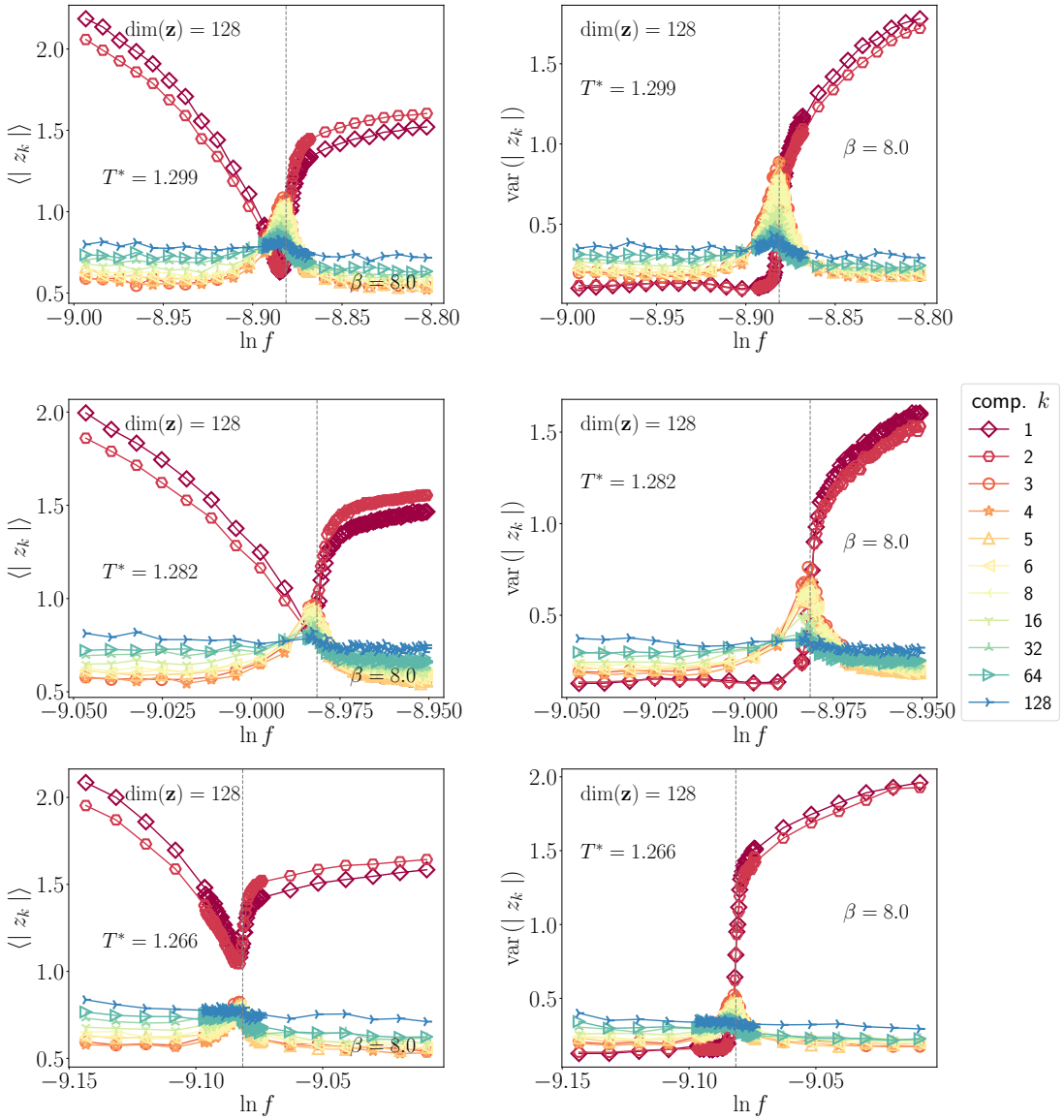

FIGURE 7.49: The same as Fig. 7.48, but tested on thermodynamic ensembles at three different temperatures below the tricritical temperature.

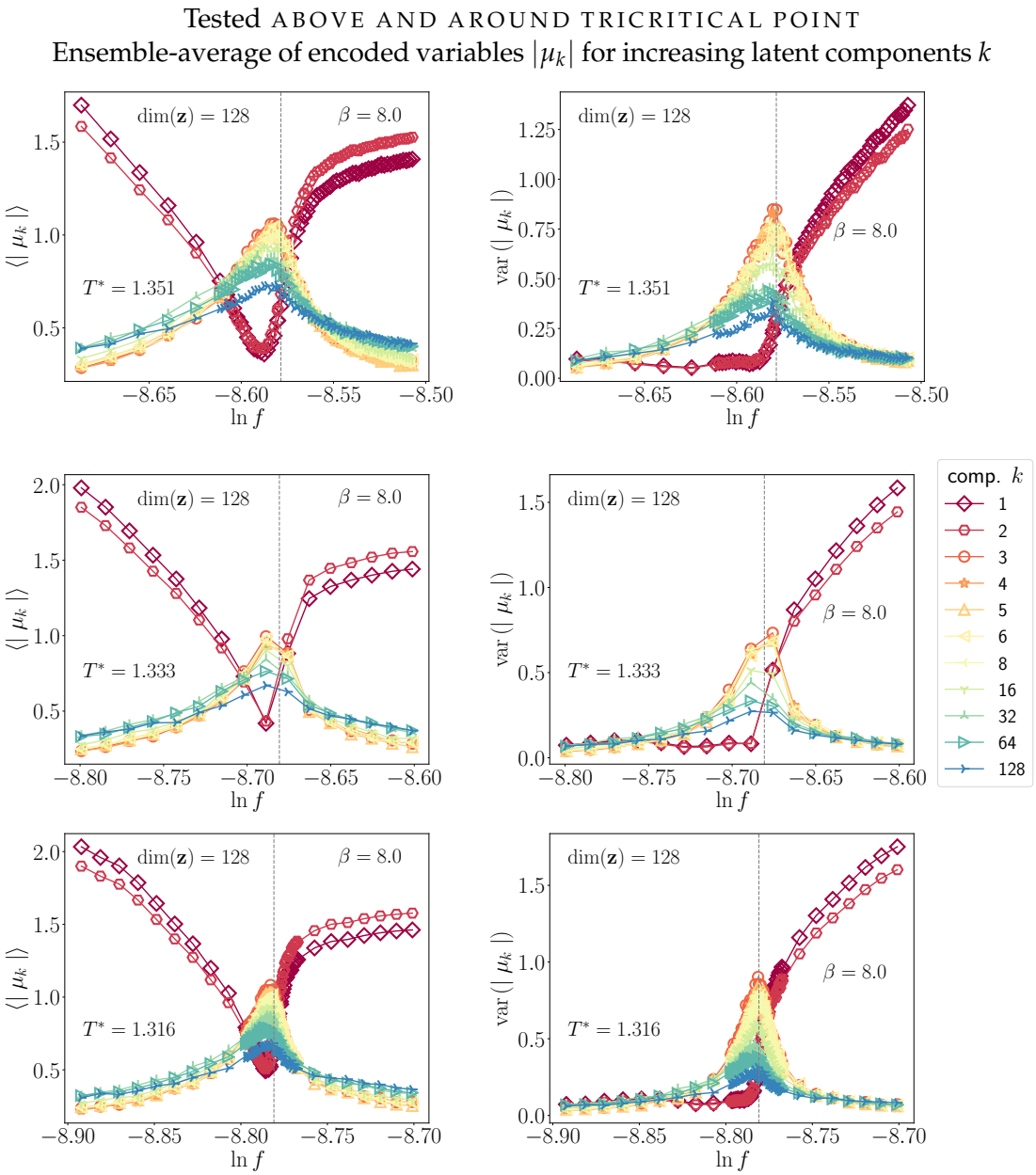

FIGURE 7.50: Ensemble-average of the absolute value of encoded means, $|\mu_k|$ (left column), and their ensemble variances (right column) shown for different components k versus log-fugacity (thermodynamic ensembles): The separate VAEs are tested on thermodynamic ensembles at three different temperatures above (top) and around (bottom two) the tricritical temperature. The VAE of $\dim(\mathbf{z}) = 128$ and $\beta = 8$ (near the threshold value of β) was trained on the standard training temperature The gray vertical lines indicate approximate phase transition fugacities of the rod-model, estimated from GCMC simulations.$T^*_{\text{train}} = 1.401$. The components were ordered by $\gamma(k)$ evaluated at T^*_{train}. See next Fig. 7.51.

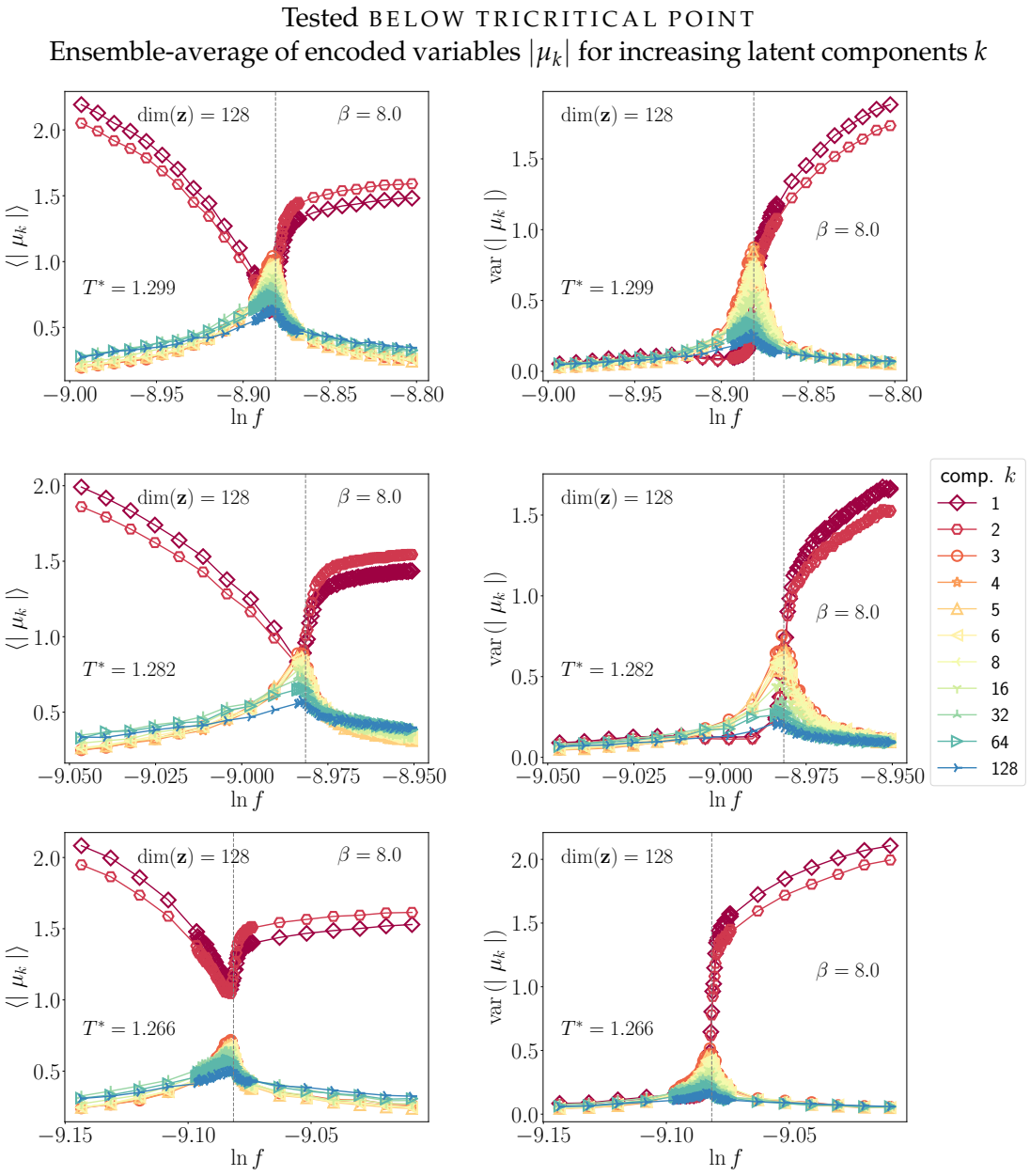

FIGURE 7.51: The same as Fig. 7.50, but tested on thermodynamic ensembles at three different temperatures below the tricritical temperature

7.7.2 Observables combining μ's and σ's

The component-wise Kullback-Leibler divergence $D_{KL}(k)$

The Kullback-Leibler (KL-) divergence in the cost function (Eq. (7.4)) defines a relative entropy between the model posterior distribution (the multivariate, diagonal Gaussian of latent variables conditioned on input) and the prior distribution– unit Gaussian on latent space. Due to the diagonal form of this model, the evaluation is a sum-over-latent-components k. We present the behavior of the component-wise $D_{KL}(k)$, defined previously in Eq. 7.23, across thermodynamic ensembles in Figs. 7.52 and 7.53 (for a single, trained VAE), whereby k is ordered according to the ordering function $\gamma(k)$.

The plots clearly show how the first two latent variables are characteristically different from the higher-order variables: Their relative entropy is always higher compared to other variables, i.e. their distribution is much less unit-Gaussian-like compared to the rest. This is intuitive, as these two variables represent the scalar order parameters of the rod model system, while higher-order variables are identifiable as "fluctuations" in the configurations (see discussion in Sec. 7.5). The higher-order variables also show peaks very near the estimated phase transition fugacities indicated in gray, vertical lines (but, somewhat before the transition for Fig. 7.52). The empirical *variances* of the KL-divergences appear to constitute another set of "order parameters" of the rod-model system: The first two components "take off" at the phase-transition fugacities like typical thermodynamic order parameters, while the higher-order components look like typical variances of thermodynamic order parameters.

It would be interesting to explore other empirical moments of these quantities in the future. For example, this and other latent "observables" could be used to construct reduced fourth-order (Binder) cumulants to distinguish between first-order and second-order transitions in the rod-model system.

Observable $R(k)$

Regarding the histograms of the means $\boldsymbol{\mu}$ and log-variances $\boldsymbol{\sigma}$ for the first two components in Fig. 7.17, we were compelled by the similarity in their general shape, if one takes the absolute value of $\boldsymbol{\mu}$. Hence, we constructed the observable

$$R(k) \equiv \left\langle \ln\left(\frac{1}{\sigma_k}\right) \right\rangle \langle |\mu_k| \rangle \tag{7.24}$$

measured for each latent variable k. The averages $\langle\cdot\rangle$ represent thermodynamic ensemble-averages (as well as further data-binning in very narrow bins of $\ln f$), resulting in Figs. 7.54 and 7.55. To our surprise, this observable seems to be able to capture the differences between first and second order transitions in a rather remarkable way: *Above* the tricritical temperature (Fig. 7.54, top figure), $R(k)$ of the first two components $k = 1, 2$ (the components identifiable with the scalar order parameters of the rod system) have an inflection point of $R(k)$ at the transition temperatures. In contrast $R(k)$ of higher-order components (which are identifiable with "fluctuations") entail their maxima around the phase transition, much like in the plots for $D_{KL}(k)$ (Fig. 7.52). However, the $R(k)$ curves "pierce through" the maxima of $R(k)$ of higher-order components when above the tricritical temperature. Near the tricritical temperature (Fig. 7.54,

bottom two figures), i.e for the cases $T^* = 1.333, 1.316$, the two sets of curves of $R(k)$ for $k = 1, 2$ and $k \geq 3$ just barely "touch" at the phase transition fugacity. Below the tricritical temperature (Fig. 7.55), the curves of $R(k)$ entail a gap between two sets $k = 1, 2$ and $k \geq 3$ at the transition fugacity. We also provided the variances of this quantity in the right columns of Figs. 7.54 and 7.55, where the change from a second-order to a first-order transition is also clearly visible in the shape of the curves of $R(k)$ for $k = 1, 2$.

The observable $R(k)$ is likely expressing an energy difference, which is why it bears strong similarities to the quantity $D_{KL}(k)$ in its empirical variances (Figs. 7.52 and 7.53). As we have already found that $\ln(1/\sigma_k)$ could represent conjugate field variables to the "order parameters" of $k = 1, 2$, which are mostly encoded in the μ_k's, we suspect that the quantity $R(k)$ is expressing important fluctuation–response relationships (the response to conjugate fields). This would be interesting to explore in the future.

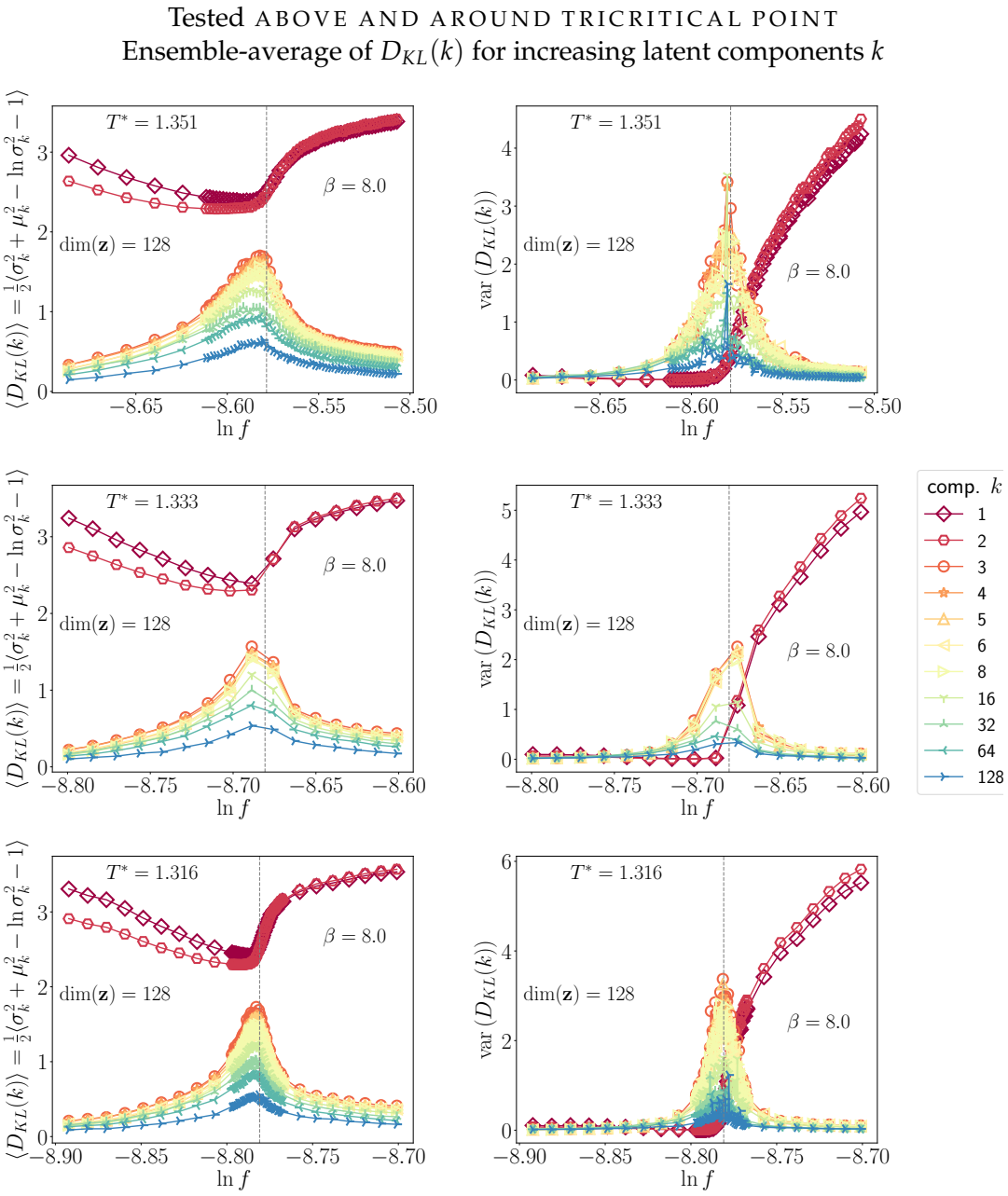

FIGURE 7.52: Behavior of $D_{KL}(k)$ defined in Eq. (7.23) *per latent component k* (left column) versus log-fugacity (thermodynamic ensembles), as well as variances thereof (right column): The separate VAEs are tested on thermodynamic ensembles at three different temperatures above (top) and around (bottom two) the tricritical temperature. The VAE of $\dim(\mathbf{z}) = 128$ and $\beta = 8$ (near the threshold value of β) was trained on the standard training temperature $T^*_{\text{train}} = 1.401$. The components were ordered by $\gamma(k)$ evaluated at T^*_{train}. The gray vertical lines indicate approximate phase transition fugacities of the rod-model, estimated from GCMC simulations.See next Fig. 7.53.

Tested BELOW TRICRITICAL POINT
Ensemble-average of $D_{KL}(k)$ for increasing latent components k

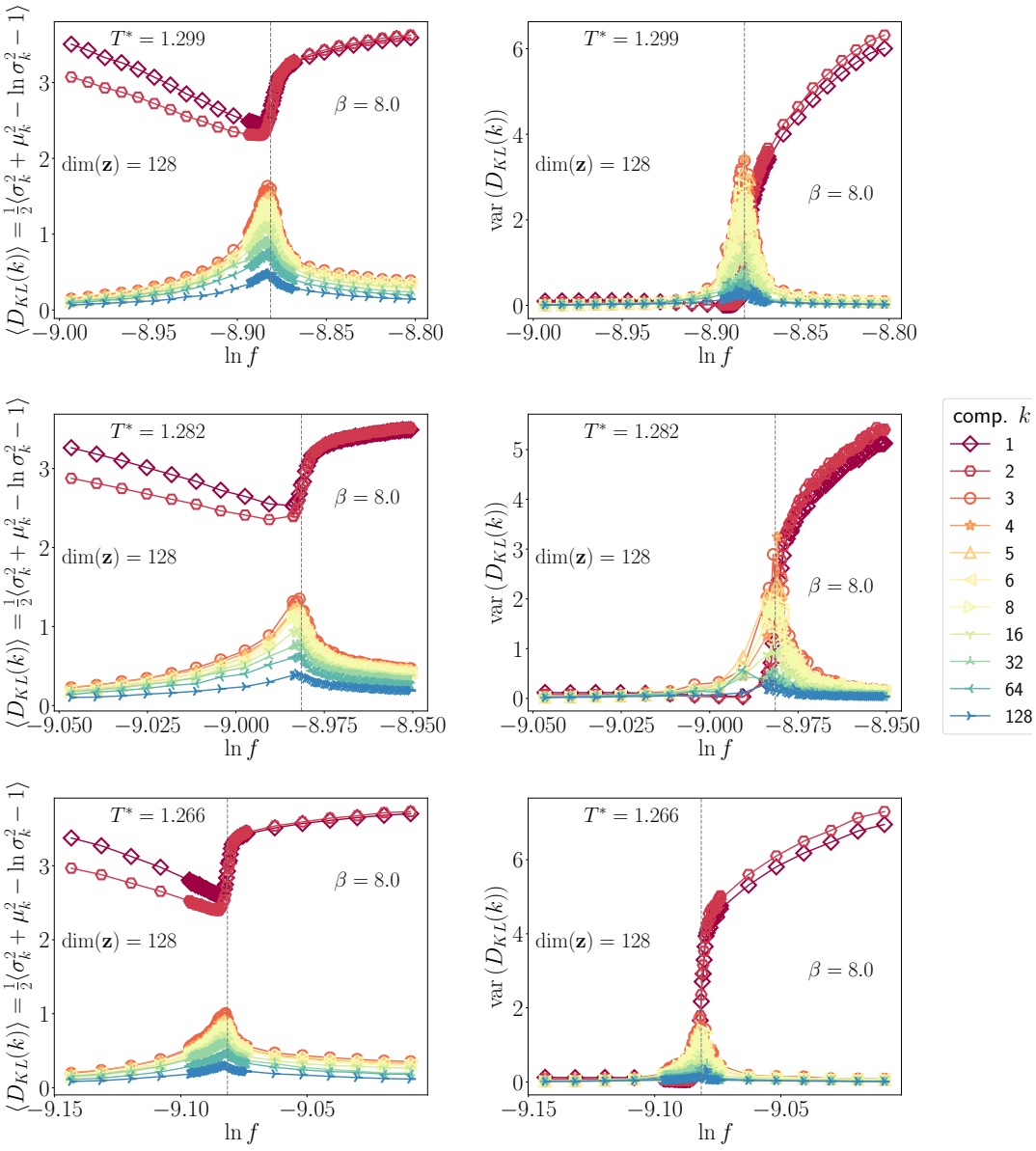

FIGURE 7.53: Behavior of $D_{KL}(k)$ defined in Eq. (7.23) *per latent component k* (left column) versus log-fugacity (thermodynamic ensembles), as well as variances thereof (right column): The separate VAEs are tested on thermodynamic ensembles at three different temperatures below the tricritical temperature. See also caption of Fig. 7.52.

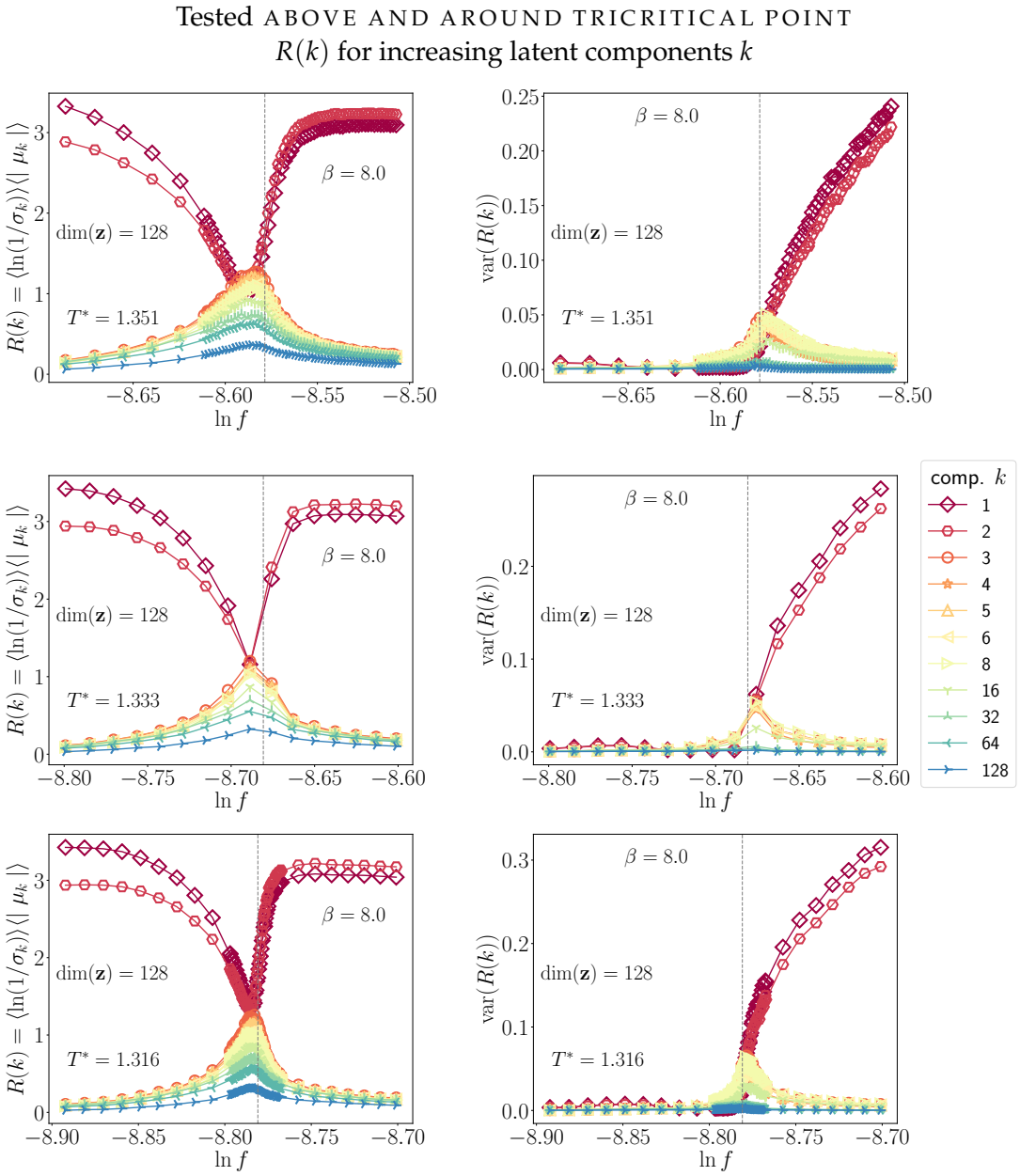

FIGURE 7.54: Behavior of $R(k)$ defined in Eq. (7.24) *per latent component* k (left column) versus log-fugacity (thermodynamic ensembles), as well as variances thereof (right column): The separate VAEs are tested on thermodynamic ensembles at three different temperatures above (top) and around (bottom two) the tricritical temperature. The VAE of dim$(\mathbf{z}) = 128$ and $\beta = 8$ (near the threshold value of β) was trained on the standard training temperature $T^*_{\text{train}} = 1.401$. The components were ordered by $\gamma(k)$ evaluated at T^*_{train}. The gray vertical lines indicate approximate phase transition fugacities of the rod-model, estimated from GCMC simulations.See next Fig. 7.55.

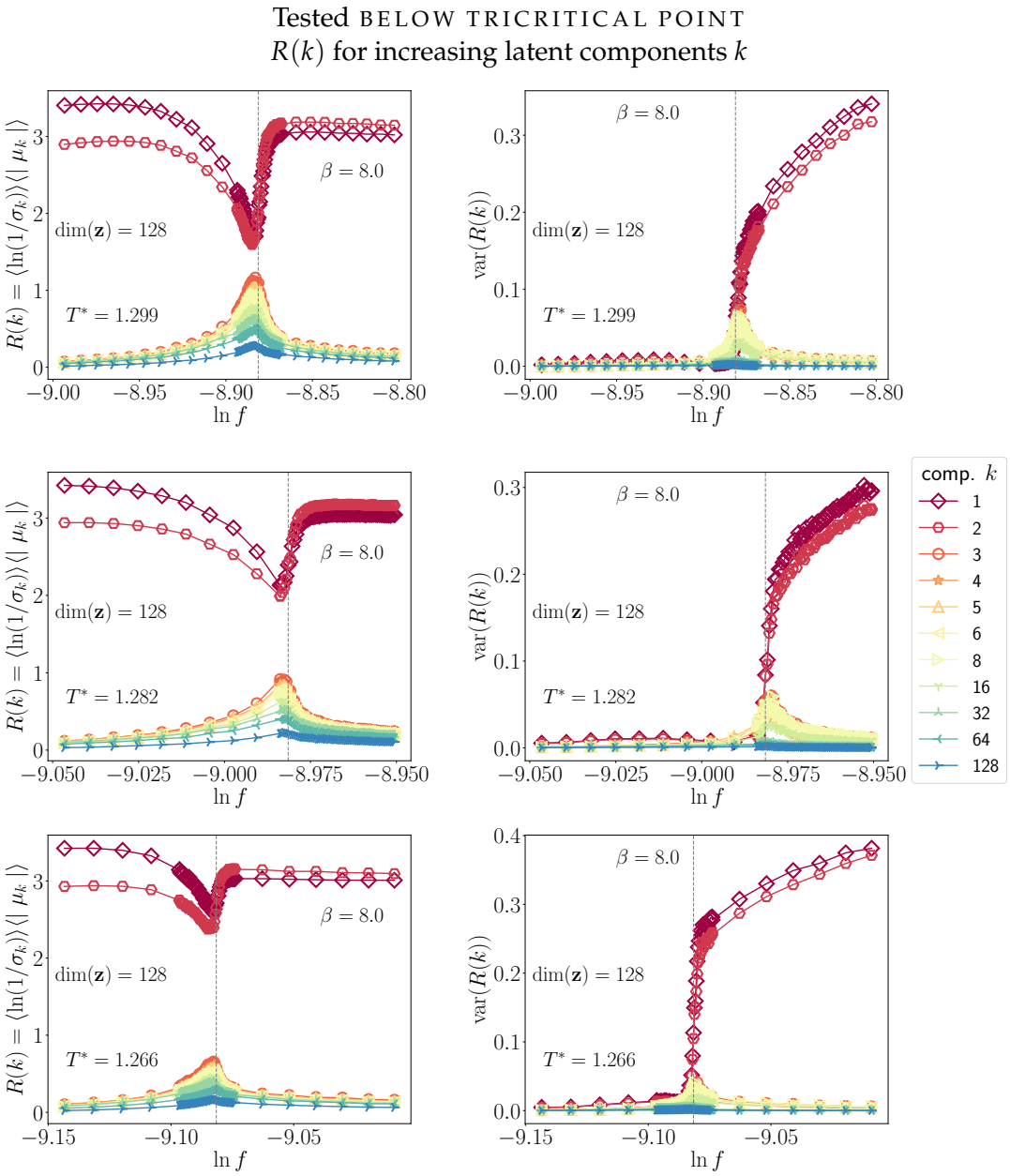

FIGURE 7.55: Behavior of $R(k)$ defined in Eq. (7.24) *per latent component* k (left column) versus log-fugacity (thermodynamic ensembles), as well as variances thereof (right column): The separate VAEs are tested on thermodynamic ensembles at three different temperatures below the tricritical temperature. See also caption of Fig. 7.54.

7.7.3 PCA on z's: Further "order parameters"

We have explored the possibility of using the first two latent variables for quantitative, reduced order parameters on latent space. We report that these can be used to "detect" phase transitions; however, as the variables are not fully orthogonal to further latent variables, this observable was somewhat suboptimal. To alleviate the problem of this residual "rotation" in latent space, we performed PCA on the latent variables and extracted the first two latent components. We then defined

$$\hat{\mathbf{q}}_{12}^{\mathrm{PCA}} \equiv z_1^{\mathrm{PCA}} + i z_2^{\mathrm{PCA}} \,, \tag{7.25}$$

which is measurable empirically over the ensembles in the training data-sets. In Figs. 7.56 and 7.57, we present the results of this order parameter across different thermodynamic ensembles, varying the latent space dimensions $\dim(\mathbf{z})$. Note that all VAEs had a fully-ranked latent space. Note that we performed PCA on the full set of grand-canonical ensembles at one testing temperature T^*, and then plotted the results of the ensemble average of the norm $\|\cdot\|$ of this complex (2D) order parameter versus the fugacity in Figs. 7.56 and 7.57.

All VAEs contain two axes in latent space that are distinguished significantly from the remaining $\dim(\mathbf{z}) - 2$ axes – we have not provided plots of the explained variable variance (eigenvalues) here. Nonetheless, the results in Figs. 7.56 and 7.57 clearly show that the reduced-representations in latent space can be used to construct an order parameter that very sharply "detects" the phase transition points – the variances all peak at the estimated critical or coexistence points in the rod model (the gray vertical lines). In fact, these may point out small errors in our estimations thereof, but, a clarification is outside the scope of this thesis. "Sharp" observables like these could have interesting practical implications for theory in many model systems of physics. In the future, one could investigate whether reduced fourth-order cumulants could be constructed out of latent variables, for example, in order to enable a highly precise method for determining the true critical points in the models. Of course, it would be necessary to evaluate these quantities on differently-sizes input configurations; this is one outlook arising from the quantitative analysis presented here.

We also note that the case of $\dim(\mathbf{z}) = 32$ seems particularly adept at detecting the phase transition (the variance is highest at the transition fugacity across all temperatures); subtle differences in the training duration and success thereof could be to blame, as we employed early-stopping techniques.

We repeated the same experiment as above for VAEs trained on different values of β, shown in Figs. 7.58 and 7.59. One can observe that an increase in β is associated with a larger amplitude of the averages $\langle \|\hat{\mathbf{q}}_{12}^{\mathrm{PCA}}\| \rangle$, as well as smaller amplitude of var $\left(\|\hat{\mathbf{q}}_{12}^{\mathrm{PCA}}\|\right)$ within the thermodynamic ensembles; the latter is particularly visible at the phase-transition fugacities (vertical gray lines) across all test reduced-temperatures. As *beta* controls how strongly the Kullback-Leibler divergence term in the cost function is enforced (Eq. (7.5)), this behavior of the latent order parameter can be rationalized as follows: As the posterior distributions must match the unit-Gaussian prior, they are "pulled" towards the unit-circle center of latent space. The "order parameters" found in the first two latent variables will thus become more distorted and less spread-out, which causes their empirical variance among data to shrink; in other words,

different phases become somewhat less discernible at the cost of a more efficient representation and obedience to the generative model prior. In fact, we have observed more evidence for this by comparing the VAEs to deterministic autoencoders (AEs) (which might be similar to the case of $\beta = 0$ (see Sec. 7.9). AEs tend to "use up" the full expanse of latent space, resulting in less compact representations.

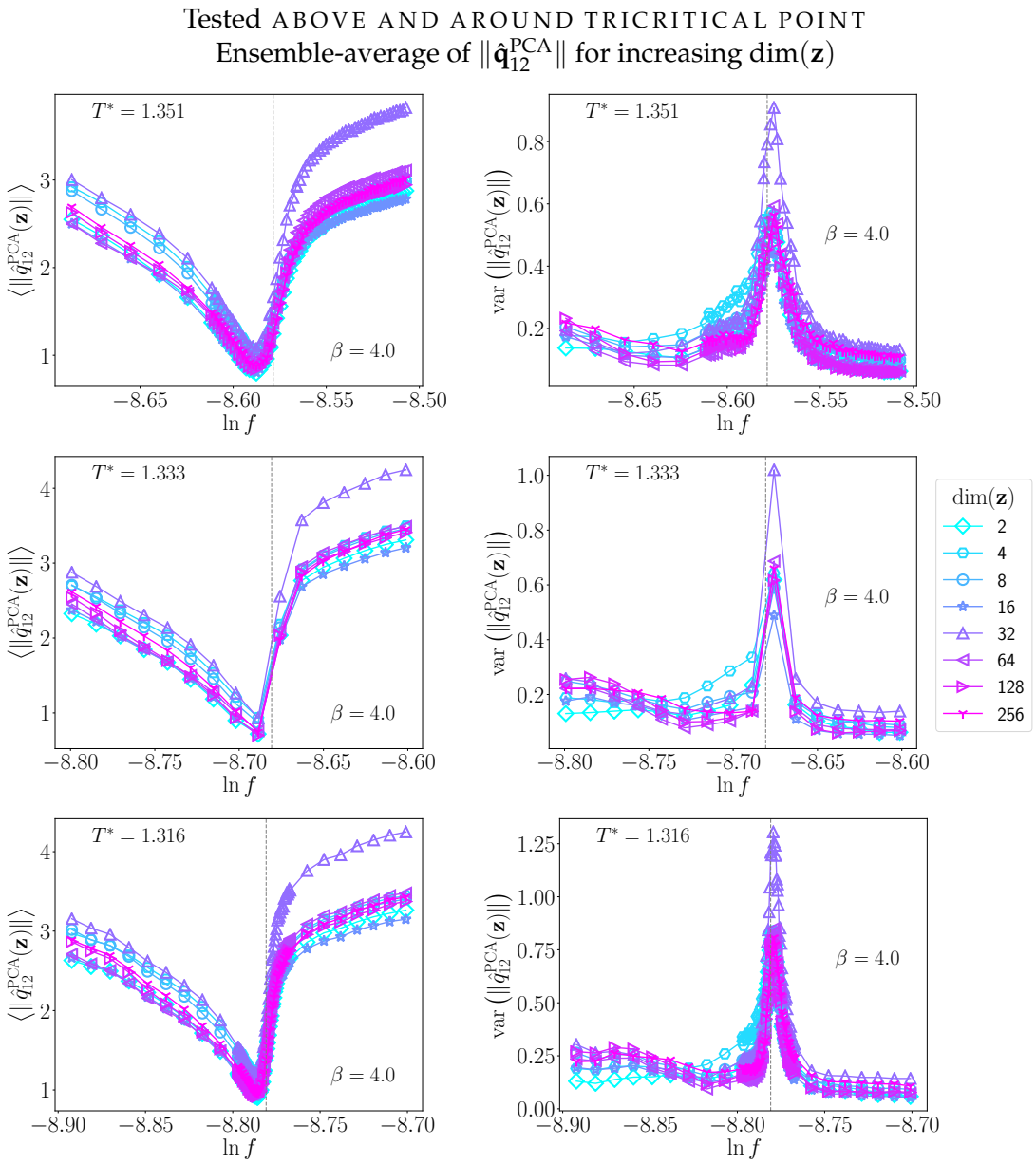

FIGURE 7.56: Behavior of $\|\hat{\mathbf{q}}_{12}^{\mathrm{PCA}}\|$ defined by Eq. (7.25) versus log-fugacity (thermodynamic ensembles) over different VAEs of sizes $\dim(\mathbf{z})$ (left column), as well as variances thereof (right column): The separate VAEs are tested on thermodynamic ensembles at three different temperatures above (top) and around (bottom two) the tricritical temperature. The VAEs of $\dim(\mathbf{z}) = 128$ and $\beta = 4$ were all trained on the standard training temperature $T^*_{\mathrm{train}} = 1.401$. The gray vertical lines indicate approximate phase transition fugacities of the rod-model, estimated from GCMC simulations. See next Fig. 7.57.

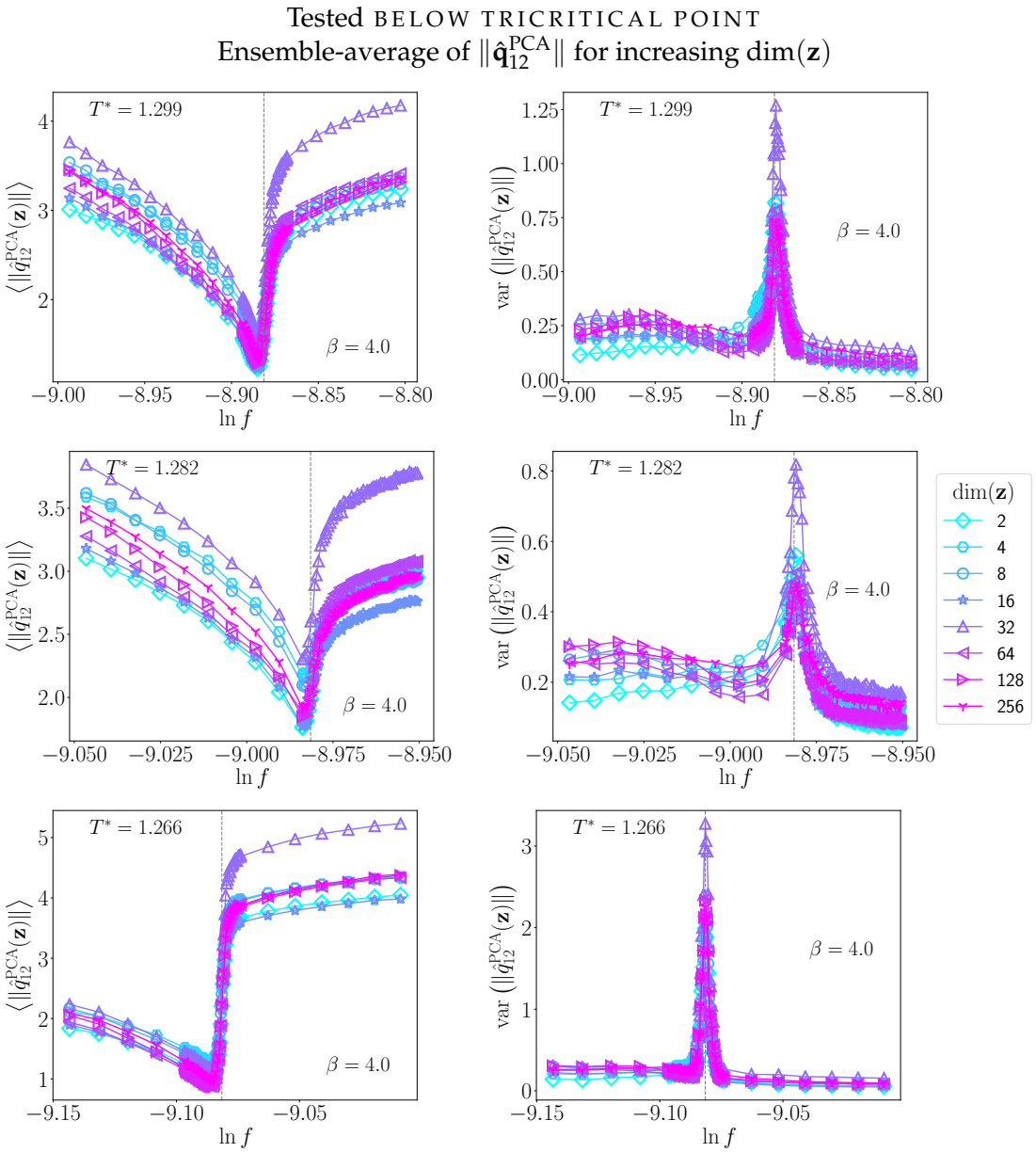

FIGURE 7.57: Behavior of $\|\hat{\mathbf{q}}_{12}^{\mathrm{PCA}}\|$ defined by Eq. (7.25) versus log-fugacity (thermodynamic ensembles) over different VAEs of sizes dim(z) (left column), as well as variances thereof: The separate VAEs are tested on thermodynamic ensembles at three different temperatures below the tricritical temperature. See also caption of Fig. 7.56.

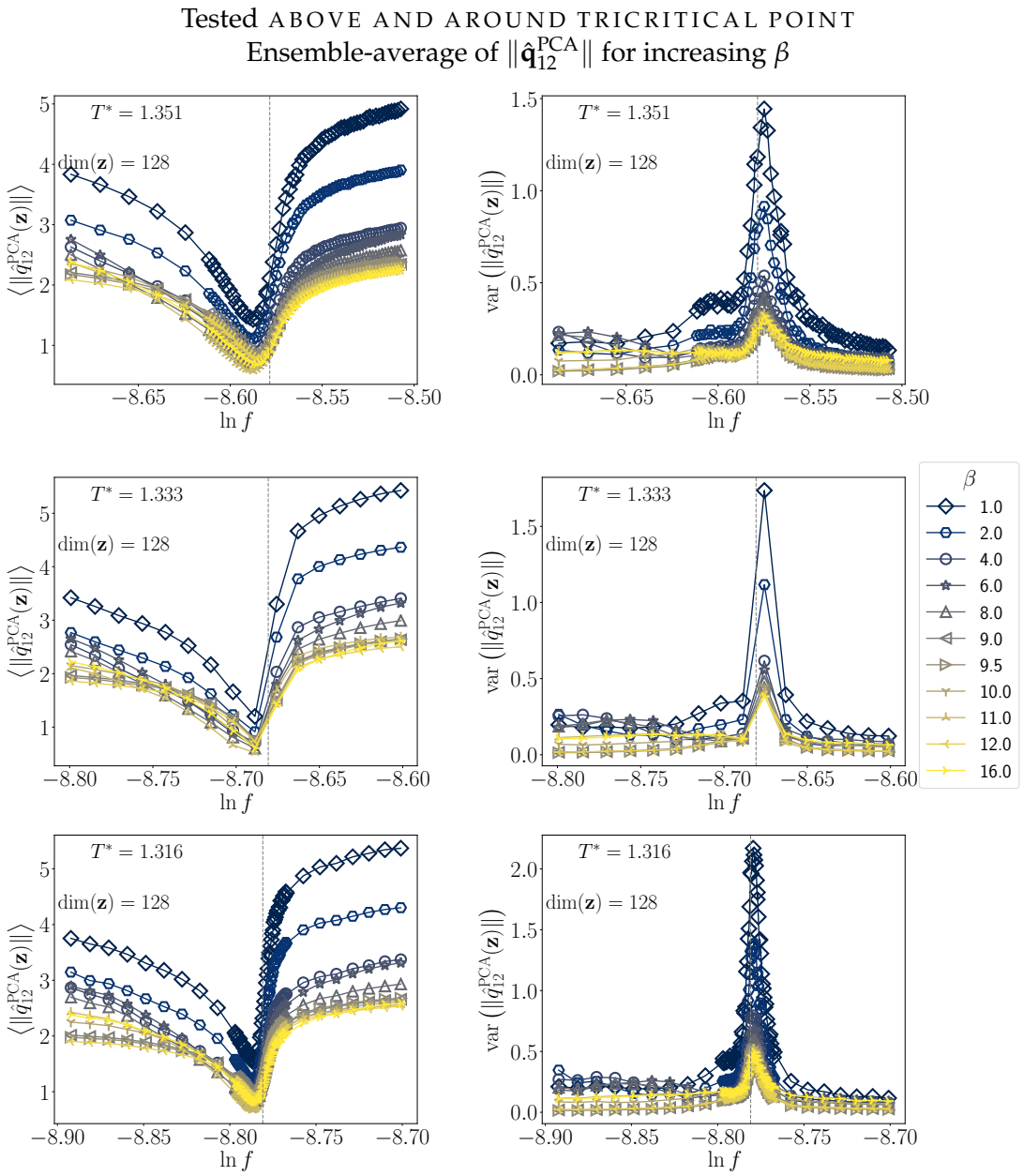

FIGURE 7.58: Behavior of $\|\hat{\mathbf{q}}_{12}^{\mathrm{PCA}}\|$ defined by Eq. (7.25) versus log-fugacity (thermodynamic ensembles) over VAEs trained on different β's (left column), as well as variances thereof (right column): The separate VAEs are tested on thermodynamic ensembles at three different temperatures above (top) and around (bottom two) the tricritical temperature. The VAEs of $\dim(\mathbf{z}) = 128$ and $\beta = 4$ were all trained on the standard training temperature $T^*_{\mathrm{train}} = 1.401$. The gray vertical lines indicate approximate phase transition fugacities of the rod-model, estimated from GCMC simulations. See next Fig. 7.59.

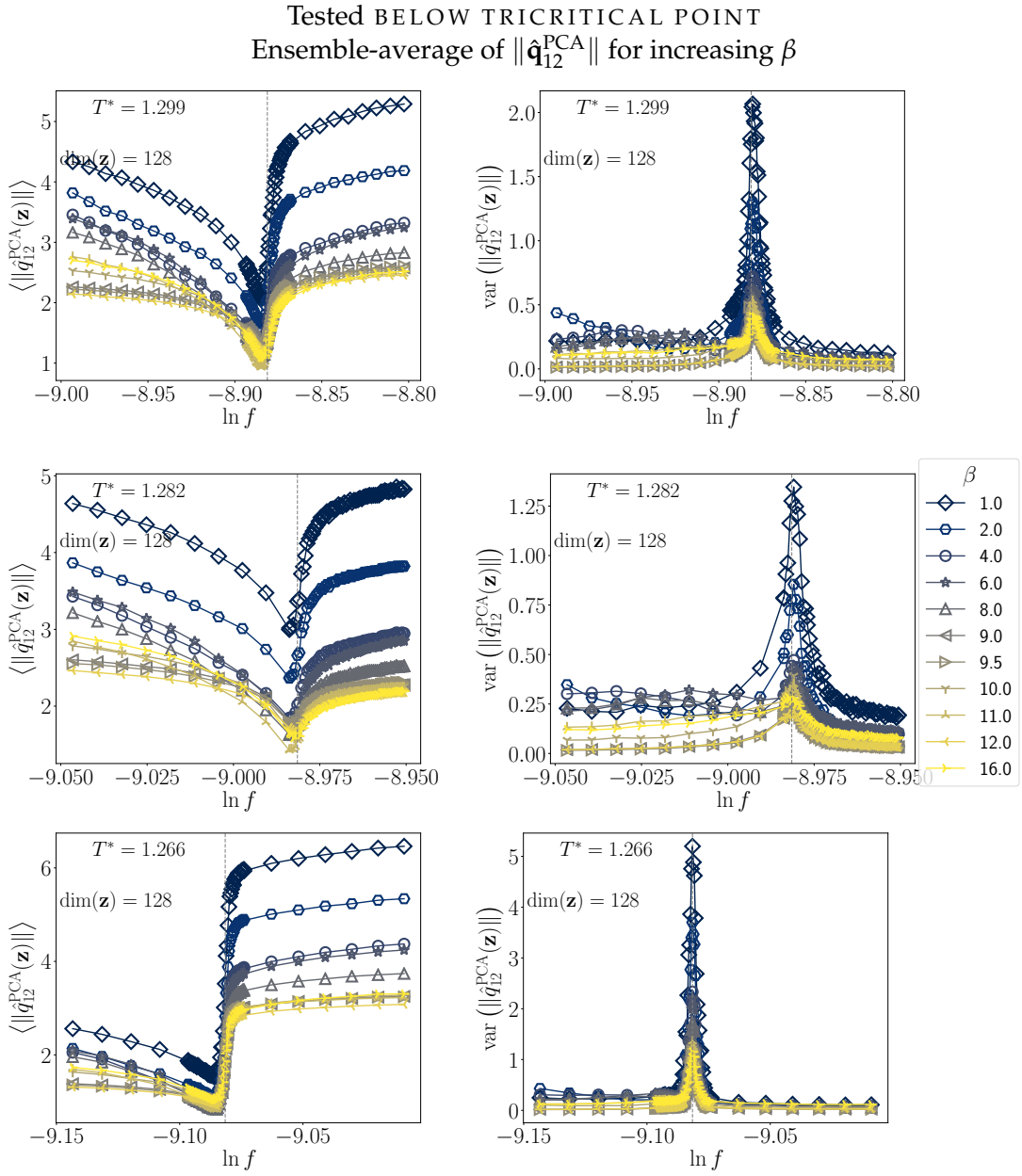

FIGURE 7.59: Behavior of $\|\hat{\mathbf{q}}_{12}^{\mathrm{PCA}}\|$ defined by Eq. (7.25) versus log-fugacity (thermodynamic ensembles) over VAEs trained on different β's (left column), as well as variances thereof: The separate VAEs are tested on thermodynamic ensembles at three different temperatures below the tricritical temperature. See also caption of Fig. 7.58.

7.8 Comparison to deep convolutional VAE

In this section, we compare the learned representations of the hard-rod system in the "vanilla"-VAE to that of a deep convolutional variational autoencoders (DC-VAEs). One motivation is that convolutional networks are esteemed efficiently extracting local features, and the two dimensional nature of the images is preserved upon applying convolution operations. On the other hand, fully-connected layers may be better-suited at global summation operations. The "vanilla"-VAEs at the center of this study used a single hidden layer, and are therefore very simple. One may, naively, expect them to have more trouble accurately capturing local-scale features in the configurations of rods. We will see whether these arguments hold in the results in Sec. 7.8.2 after presenting the neural network specifics below.

In the encoder, a series of convolution and pooling operations constitutes a processing unit *between* the input and the hidden layer(s), which are then connected to the latent layer. The "mirrored" opposite is true for the decoder, i.e. the "near-opposite" processing unit is situated between the last hidden layer and the output. Fig. 7.60 illustrates the basic set-up of the DC-VAE our implementation. The details on the convolutional blocks are described in the next subsection.

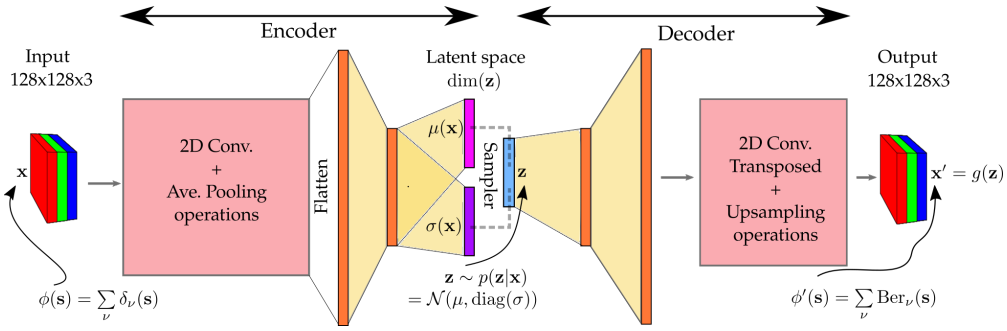

FIGURE 7.60: Basic depiction of the deep convolutional β-VAE (DC-VAE), compare to "vanilla"-VAE in Fig. 7.5. The encoder and decoder both have large convolutional and pooling processing units adjacent to the input and output, respectively. Golden areas indicate *dense* connections (fully-connected).

7.8.1 Neural network details

Each of the neural networks is composed of 6 "blocks" where 2D convolution operations are combined with a pooling operation and nonlinear activation function. We further employ two fully-connected layers coming into and out of the latent encoding, for reasons related to . For the decoder, which is almost a "mirror image" of the encoder, the "transposed" 2D convolution operation is used together with an *upsampling* operation to increase the dimension. All the operations we have employed for the results presented here can be seen in Figs. 7.61 and 7.62, which are schematics of the dimension-changing operations in the encoder and decoder, respectively.[8] Tab. 7.4 provides more specifications of the network and training protocol. Note that the decoder has about 10% more free parameters, which arose due to difficulties in matching the output

[8]Note that the length-scales of the boxes are displayed in a logarithmic fashion

dimension properly. We have experimented with a number of modifications to this network (convolution filter sizes, usage of *BatchNormalization*, optimizer functions, *dropout*), and found the results and behavior to be similar across the board. We also experimented with deterministic AEs with a very similar architecture, which we will report on briefly in Sec. 7.9.

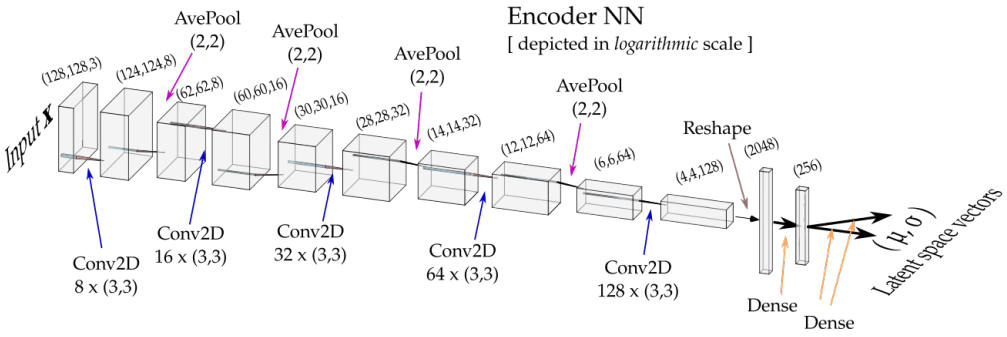

FIGURE 7.61: Detailed schematic of the deep convolutional encoder employed, showing resulting dimensions (triplet numbers) after each operation: convolutions (the number of "*Conv2D*" filters with 2D filter size is indicated), average pooling ("*AvePool*" with 2D pooling filter size) as well as fully-connected layers ("*Dense*").

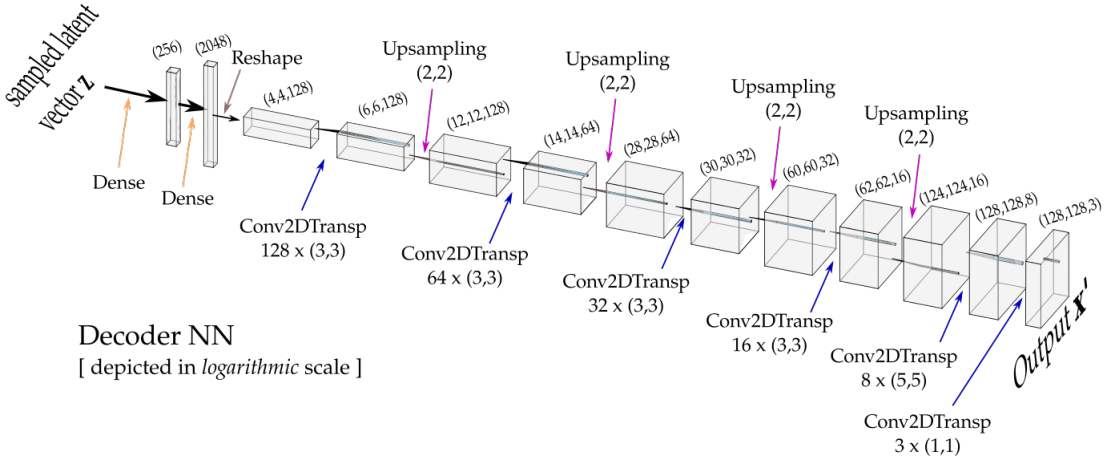

FIGURE 7.62: Detailed schematic of the deep convolutional decoder employed, showing resulting dimensions (triplet numbers) after each operation: transposed convolutions (the number of "*Conv2DTransp*" filters with 2D filter size is indicated), upsampling ("*Upsampling*" with scaling filter size) as well as fully-connected layers ("*Dense*").

7.8.2 Quantitative results: Direct comparison to "vanilla-VAE"

Figures 7.63 and 7.64 (top left) show that the DC-VAEs are superior compared to the "vanilla"-VAEs regarding the mean-squared error reconstruction cost. On the other hand, the squared-norm of the gradients in the images (bottom right figures) are more intensely represented by DC-VAEs (the values are higher). This seems intuitive, as the series of convolutional operations performed on the images should "pick up" higher frequencies in the images. When inspecting

DC-VAE PROPERTY	VALUE OR NOTE
Connection types	*Dense*, *Conv2D*, *Conv2DTransposed*, *Pooling*, *Upsampling* see Figs. 7.61 and 7.62
Activation functions	*PreLu* (parametric *ReLu*) after *Conv2D* or *Conv2DTransposed* and before *Pooling* or *Upsampling*
Convolution filter sizes	(3×3) or (5×5)
Convolution padding	'valid'
Output activation	*Softmax*
Regularization technique 1	Early stopping
Regularization technique 2	*Dropout* layers (only 8% dropout), in Encoder and Eecoder at or after 2048 (Dense) layer
(Optional, not in Sec. 7.8.2)	*BatchNormalization* between conv. and activation
Optimizer	*Adam*
Learning rate	0.00006
Hidden (Dense) layer dimensions	2048 and 256
Latent dimension	$\dim(\mathbf{z}) = 128$
Values of β	$\beta = 0.5 \ldots 8$
Number of trainable parameters	Encoder: 906,064 Decoder: 1,047,891

TABLE 7.4: Specifications of deep convolutional β-VAE neural network (DC-VAE): parameters and setting.

reconstructed images in Fig. 7.65, we see how the DC-VAE generates sharper borders between separate domains of a mean color. Therefore, DC-VAEs appear to delineate the "mesoscopic" ordering domains in the rod configurations. This could have interesting practical applications for theoretical physics– we discussed in Ch. 6 how exactly these kinds of ordering domains are crucial for the phase behavior and phenomenology of the "sticky" hard-rod systems on lattices. Current forms of analytical theory in the form of fundamental measure theory do not account for these domains properly.

Somewhat surprisingly, DC-VAEs are *not* superior to the "vanilla"-VAEs in other measures: The error in the inner energy U (top right figures) are rather comparable between both architectures in the isotropic, low-density states (left of the phase transition fugacities). After the orientational-demixing transition (and gas-liquid separation for data below the tricritical point), the vanilla-VAE outperforms the DC-VAE in the inner energy. The inner energy (Eq. 7.1) is calculated via a sum over nearest-neighbor products of pixels in the images; surprisingly, then, sums over local-scale correlations in images seem to be better represented by the vanilla-VAE. The DC-VAE seems to be underestimating the local-scale fluctuations and is over-confident about the local order parameter fields *within* domains. Contributions from smaller vacancy-pockets (red) like those in Fig. 7.65 are important for the calculation of U. The vanilla-VAE does not have the capability to fully resolve the small pockets, either, but incorporates them into weakly fluctuating "fuzz". This "insecurity" also leads to lower gradients in the images as well as lower confidence on the correlation between global S and ρ (which is captured by the angle in $\mathbf{c}$). The green patch in figure 7.65 (center) is almost unrecognizable "fuzz" for the vanilla-VAE; but, on

COMPARISON TO DC-VAE:
Test data ABOVE THE TRICRITICAL POINT:
Reconstruction error, error in inner energy, and squared-norm of gradients in order parameter fields

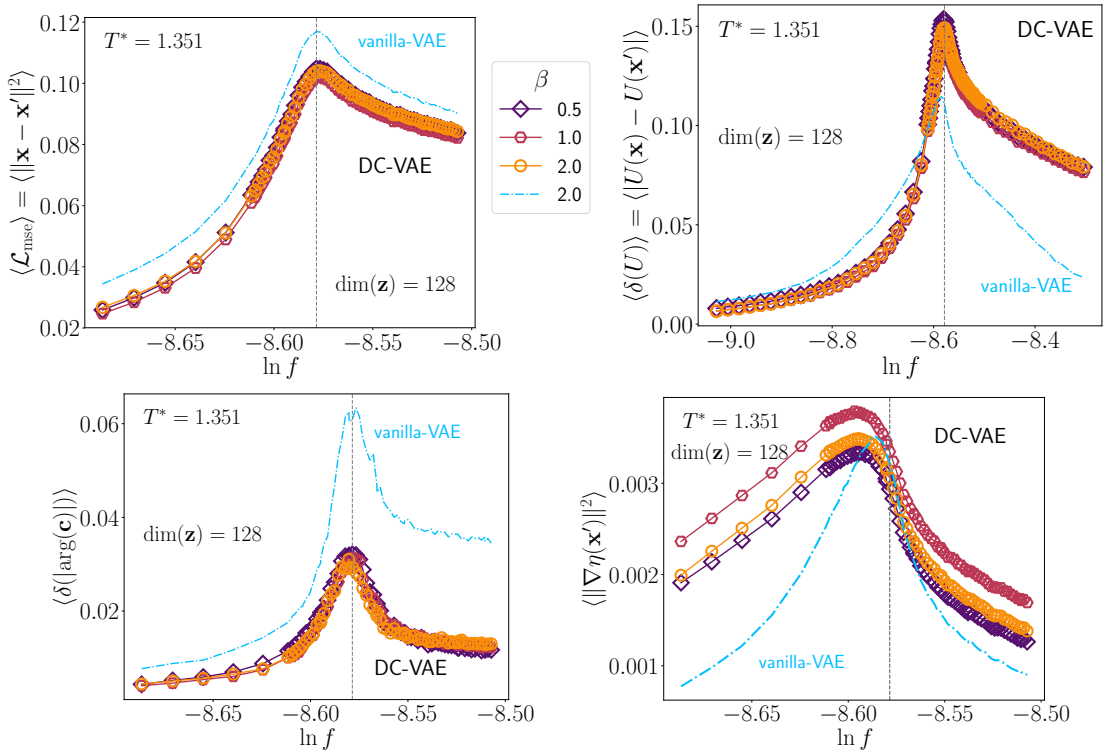

FIGURE 7.63: DC-VAEs with different β's: Reconstruction error (top left), absolute error in reconstructed inner energy (top right), that of the angle in the order parameter (bottom left), and squared-norm of the gradients of the packing fraction fields in each configuration. The test data is at $T^* = 1.351$, above the tricritical point). $\dim(\mathbf{z}) = 128$ for all VAEs. The vertical gray line indicates the thermodynamic phase transition fugacity from an isotropic ($S \approx 0$) to an orientationally-demixed state ($|S| > 0$). The blue curves indicate the results of a "vanilla"-VAE with the same value of $\dim(\mathbf{z})$, and $\beta = 2$.

average, the vanilla-VAE likely captures blue-red nearest-neighbor correlations better.

From another perspective, the value of $\beta = 2$ in the vanilla-VAE is related to a high degree of "entanglement" in the latent variables. We saw in Sec. B.1 that the strength of the "entanglement" significantly affects the quality of this particular observable. This becomes more obvious in Figs. 7.66 and 7.67 below, which show decoded latent variables in both cases. At this value of β, the "vanilla" variables appear significantly "entangled" (a weak degree of spatial length-scale separation). In contrast, the DC-VAE entails a few decoded variables that have approximately separated-out order-length-scales in the images ("demixed" order parameter fields). Therefore, the DC-VAE appears to be more efficient at finding "disentangled" order parameters than the vanilla-VAE. When decoding the empirical extremal values along each axis (in the data-sets), the decoded latent variables of the DC-VAE show a significantly

COMPARISON TO DC-VAE:
Test data BELOW THE TRICRITICAL POINT:
Reconstruction error, error in inner energy, and squared-norm of gradients in order parameter fields

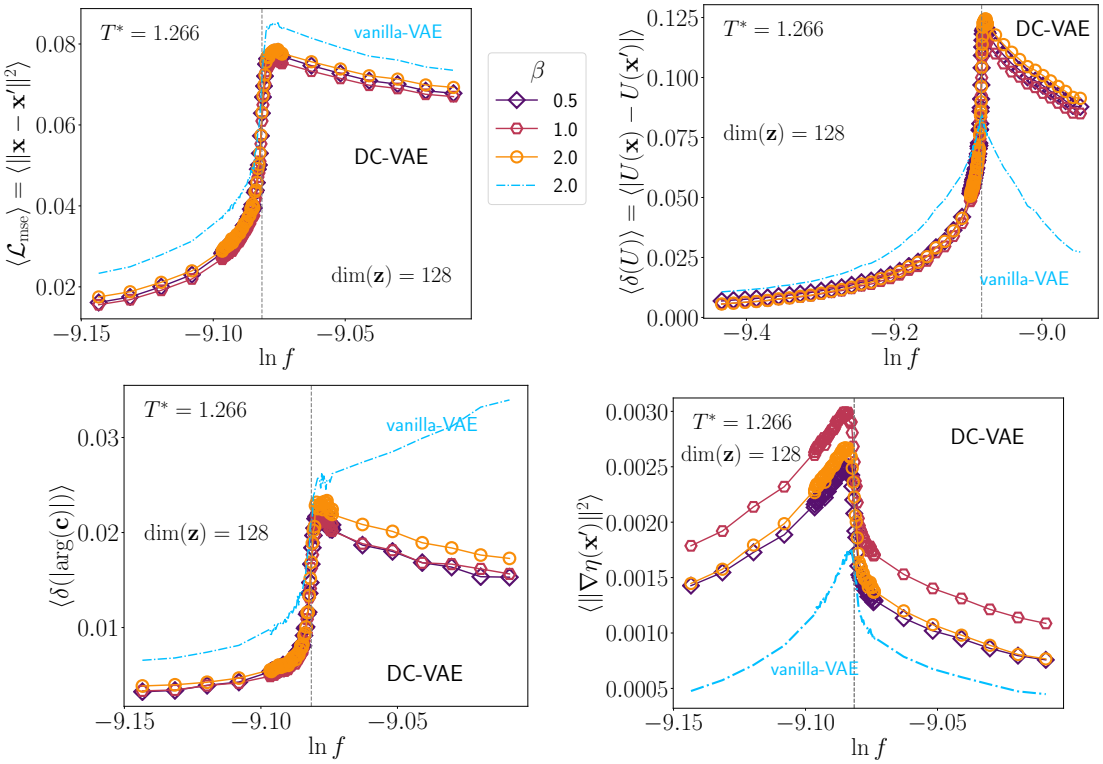

FIGURE 7.64: Same as Fig. 7.63, but for $T^* = 1.266$ (well below the tricritical point).

higher amplitude of color, which indicates that the DC-VAE is more "secure" *locally* about having found the order parameters of the hard-rod model system. It also suggests a higher level of efficiency in the learned representation.

On a side note, we found mode collapse at similar values of $\beta \sim 8 \ldots 9$ for both architectures.

High complexity of the data-sets

Altogether, however, the differences between both architectures are much more subtle than we expected. We suspect this has to do with the datasets of configurations from the sticky-hard-rod model: The culprit may be the hard-core repulsive interactions. The highly correlative nature of many-body systems with hard-core repulsive interactions is a well-known and fundamental aspect of liquid state theory and soft matter physics (see discussion in Ch. 2).

Machine learning has been successfully applied to other statistical model systems in the literature, which are most often of the lattice-"spin-type", e.g. Ising models, where generated images on the output can represent physically *valid* configurations, if we were sample each pixel on the output to an e.g. binary value. Here, we have spatially-extended particles that are hard-core repulsive, i.e. the particles exclude free volumes of space, and output configurations (even if sampled to binary values per pixel, and not continuous values between 0 and

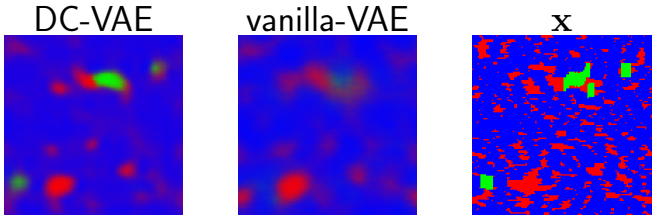

FIGURE 7.65: Comparison between DC-VAE (left) and vanilla-VAE (middle) reconstruction of an input image (right), using the means parameter μ. The image is a sample from the orientationally-demixed phase (blue, horizontal rods dominate) and entails a very high packing fraction (few total "red" pixels).

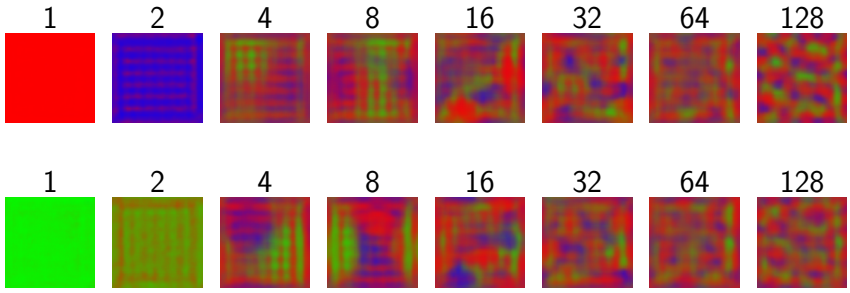

FIGURE 7.66: Decoded extremal coordinates (measured over data-sets) of latent variables for the DC-VAE: $\beta = 2$ and $\dim(\mathbf{z}) = 128$. Artifacts of the boundaries of the image, due to convolution windows, are visible. Notice that the first circa 8 variables are quite "disentangled" regarding a lack of mixing multiple length-scales of different color, and are quite bright in color (no enhancement applied).

1, as implemented currently) will not necessarily be physically valid. In effect, this interaction generates a nontrivial thermodynamic entropy (i.e. free energy in purely hard-core repulsive systems). The highly-esteemed DC-VAEs did not necessarily outperform the simple architecture massively; this may support the notion that our data-sets are more difficult to learn than e.g. spin-type model systems. The amount of information in the datasets is very likely extremely high.[9]

Preliminary finding: DC-VAEs learn "conjugate-field" representations

Preliminary evidence suggests that DC-VAEs learn a "conjugate-field" representation compared to the fully-connected, "vanilla"-VAE architecture. It appears as if DC-VAEs encode the fugacity and another field conjugate to the demixing-order-parameter S in a combination of the first few latent variables. This would be quite stimulating, as the generative model could be more "useful" by fixing the "fugacity", for example – a generating function of "ensembles".[10] A presentation of the results is outside of the scope of this thesis.

[9] This idea is also in congruency with our observation that all architectures "coarse-grain" the images according to gross length-scales, which is set by the latent space dimension, i.e. achieving a high resolution requires huge latent-space dimensions and fine-tuning of β.

[10] Not clear is the issue of "temperature", however.

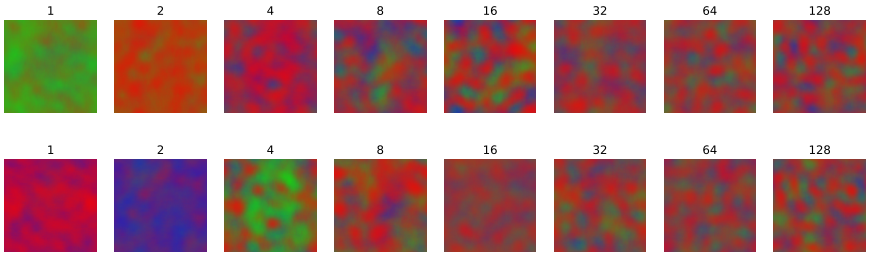

FIGURE 7.67: Same as Fig. 7.66, but for the vanilla-VAE with $\beta = 2$ and $\dim(\mathbf{z}) = 128$. Note that images entail only a weak separation of length-scales of each color (the order parameter fields are "mixed"), compared to Fig. 7.66. The colors are much less intense in these variables, indicating a higher level of "insecurity" of the predictability of the variables, as well as a lower efficiency of the representation.

Nonetheless, this "conjugate" representation may be quite rational: Convolution operations are much more "near-sighted" (local-scale) than global summations performed in fully-connected networks. Also, fundamental measure theory for hard-core particle systems provides a free energy functional based on convolution operations of density fields (distributions). Thus, convolutions may be 'mathematically correcter' operations for expressing free energies in the statistical mechanical system.

7.9 Other experiments

In this section, report on choosing different training temperatures, for the case of the "vanilla" VAEs. We also experimented with deeper VAEs, entailing two hidden layers. Thereafter, we briefly report on our experiences with other unsupervised or generative machine learning algorithms.

Training on data at different reduced temperatures

We report that comparable training data-sets at lower reduced temperatures seemed to represent an "easier" task for the VAEs to learn. The convergence was faster, particularly after applying batch normalization, and the cost function was generally lower, depending on the given hyperparameters. Results thereof remain outside of the scope of this thesis. We mention, however, that this may be intuitive: At lower reduced temperatures, configurations entail low-spatial-wavelengths more frequently, i.e. the many-body system becomes ever more "collective" or coherent at mesoscopic scales.

On a related note, we did not present results for the VAEs tested on higher temperatures than the training temperature. Preliminary investigations show that they show much higher errors, and are much less capable at "detecting" the critical points. At higher temperatures, single of few-particle degrees of freedom (variables) become more important. These are likely "out-of-range", i.e. cut-off by the latent space dimension. The lowest-order (most "macroscopic") degrees of freedom – the order parameters – are learned first.

Deeper VAEs with two hidden layers

We explored an extension of the "vanilla-VAE" architecture (Fig. 7.5), where we incorporated a second hidden layer, symmetrically in both encoder and decoder, twice the size of the smaller hidden layer (the latter of which is 256 or $2 \times zdim$). We did not change the training data-set. Learning was much more unstable, and the usage of batch normalization seems to be even more important in these respects. In particular, upon varying β, we observed *two* mode-collapse events. However, it was very difficult to obtain a fully-ranked latent-space dimension larger than 256, which still was the determining factor for the level of "coarse-grained" resolution of the hard-rod configurations. In contrast, however, the configurations were less "fuzzy" than those generated from the "vanilla" architecture – like the DC-VAE, it seems that the VAE was able to achieve a higher degree of certainty of local order-parameter fields. In the future, it would be interesting to continue this exploration on larger datasets, and to study the two successive mode collapsing events more carefully. We suspect that one of the VAE states becomes metastable after a certain value of β is crossed.

Principal component analysis

Principal component analysis is known to be related to VAEs as a limiting case of a linear VAE, see e.g. Ref. [397]. It is purely linear, unlike our neural-networks used in this study, and its generative capabilities are quite limited. Nevertheless, we have seen strong similarities between PCA and VAEs in our model study: The "reconstructed" (inverted) principal component basis vectors look quite similar to those we find for β-VAEs with large latent dimension near the threshold state, where the collective variables appeared "disentangled". We concluded conversely, then, that the VAEs become nearly-linear (showing "solid-state-like" modes in the rod system) at the threshold state.

Tested on the ferromagnetic Ising model (not shown in this thesis), we found that the principal component basis vectors identify with local gradient operators, i.e. $\nabla_{\mathbf{m}(\mathbf{s})}$, where $\mathbf{m}(\mathbf{s})$ is the local field magnetization. This makes sense in light of Gaussian field-theoretic models (Ch. 3.2), the linear nature of PCA, and the global homogeneity (global translational symmetry!) of the hard-rod model (at least in equilibrium states above the tricritical point).

Deterministic autoencoders ("vanilla" and deep-convolutional)

We explored deterministic autoencoders, regularized in the latent space encoding using a Euclidean-norm regularization term (L2-AEs). The cost function

$$\mathcal{L}_{L2-AE} = \left\langle \mathcal{L}_{\text{mse}}(\boldsymbol{x}, \boldsymbol{x}') + \lambda \|\boldsymbol{z}\|^2 \right\rangle_{\text{batch}(\boldsymbol{x})} \ , \tag{7.26}$$

entails a Lagrange multiplier λ, which represents a hyperparameter of the system that we varied between 1 and 10, along with varying $\dim(\mathbf{z}) = 16 \ldots 512$. The two architectures we explored were fully analogous to the "vanilla-VAEs" and DC-VAEs; the only difference was the lack of the σ-variables in the bottleneck, and a sampler (no random $\boldsymbol{z}$ is generated).

We report that in both cases, the AEs identified the two-dimensional order parameter of the system. In fact, the empirical distribution over the first two latent variables was very similar to that of the means $\boldsymbol{\mu}$'s in VAEs with a small

value of β. Conversely, then, a weak-β-VAE appears to behave quite similar to a deterministic autoencoder, which is quite intuitive. We observed mode collapse, as well. A quantitative presentation of the results on AEs is outside of the scope of this thesis, however.

7.10 Discussion

Possible improvements on basic choices for the learning setup

In the future, it would be important to explore more deeply the role of the reconstruction cost function: We mentioned in Sec. 7.2.3 that we employed the mean-squared error instead of the binary-cross-entropy, which could be a flaw of this study. We saw how the latent representations lose their interpretability in comparison, as the "order parameters" are less easily identifiable. However, we would have to investigate the "generalized susceptibilities" (the σ's) in more detail, as well as vary β over a larger range before making conclusions.

Further, we mentioned in Ch. 7.3 that an arguably weak point of our choice of setup was that the output data representation, the field $\phi(x')$, takes on continuous values between 0 and 1. This represents a physically different system, locally, than the input data, where pixels take on binary values owing to the hard-core repulsion between rods. In the future, it would be interesting to test a setup where the decoder is inherently stochastic, generating a binary-valued sample in the output layer. In principle, the VAE might be taxed more strongly from misrepresenting local-scale correlations, especially where pixels belong to an individual rod. However, we think that a reconstruction error in the form of a mean-squared error or binary cross-entropy are suboptimal, as they perform pixel-wise operations. In Sec. 7.10.1 further below, we will make a few suggestions for reconstructions functions that would enforce local correlations in images directly.

After having analyzed the results of the generative model, we suspect that training on the tricritical temperature of the "sticky"-hard-rod model would be beneficial both for the interpretability of the VAE, as well as quantitative results. First of all, we discussed how training at lower reduced temperatures was associated with somewhat more "ease" during training, which we attribute to the dominance of lower spatial frequencies (i.e. large, *dense* particle clusters). These, in turn, are more "coarse-grainable" by the VAEs. However, the tricritical temperature represents an inherently symmetric state where all states in the rod model – the low-density state (dominated by red in configurations), as well as the two forms of the high-density, de-mixed states – show critical behavior (i.e. these will be power-law-distributed). As the Gaussian prior appears to be approximately a critical state or coexistence state of the hard-cord system, it seems reasonable to allow the system to train around this maximally symmetric state.

"Coarse-graining", hierarchical organization principles, and critical states

We would like to highlight two aspects that we found VAEs "do": They produce "coarse-grained" configurations in a generative model and find collective variables that can even be organized according to a hierarchy. While both are theoretically interesting (and quite deep), they could be "useful", as well, offering potential applications within physics. (We will discuss a few such ideas

that tie together other topics of this thesis in the discussion Ch. 8.) We discussed how (generative) learning, in general, might be based on these principles of "coarse-graining" and hierarchical organization in Ch. 1.4. Moreover, we have seen that the learning of collective variables that form a spatial hierarchy is tied to "power-law-like" behavior and the threshold state of the machine: the "participation ratio" of the variables becomes maximally broad and flat before "mode collapse" during training. From this work, we propose that optimal learning will mean a learning machine is poised at a critical state, i.e. at an *out-of-equilibrium* state where ergodicity is (nearly)[11] lost – these ideas have been discussed much more broadly in the literature on learning, as well, which we reviewed briefly in Ch. 1.4.

Hard-core repulsive systems are "hard" to learn

As we mentioned in Sec. 7.8, the hard-core-repulsive part of the sticky-hard-rod model might pose a uniquely difficult challenge for learning systems. It generates configurational data-sets that are highly "complex" – in other words, the amount of irreducible or incompressible information in our training sets may be high. This sounds intuitive from the point of view of liquid state theory: As we discussed in Ch. 2, hard-core repulsion between particles is the basis for the complex, many-body relationships in liquids. The esteemed successes of machine learning algorithms applied to statistical-mechanical model systems from physics overwhelmingly arise from application to lattice spin-type models. (Please see the brief literature review provided in Ch. 1.4.) Therefore, hard-core model systems from physics provide excellent data sets testing the limits and capabilities of machine learning algorithms, and are complementary to prototypical model systems like Ising models. Intuitively, then, much more complex latent models would be necessary for better capturing correlations at various length-scales in the rod-model system. We discuss a number of prospective ideas within the next section.

7.10.1 Ideas and potential improvements to VAEs, generally

From our studies, we conclude that a fundamental weak point of the VAE probabilistic model is in their designed posterior model. In its current form, the posterior distribution assumes a diagonal Gaussian across all dimensions of latent space. When the VAEs are applied to configurations of hard-core particle systems, this presumption seems completely nonphysical. In order to capture many-body correlations in a generative model of the physical system, consistently and across all kinds of neural network architectures, it seems impertinent to make the posterior model on latent space more complex. We think a latent-variable model that accounts for higher-order correlations (three-, four-body correlations) among latent variables would be a promising endeavor. (Please see the discussion further below).

Employing VAEs whose posterior is a *non-diagonalized* Gaussian would be a first case to test. Certainly, the covariance matrix can be diagonalized with a unitary transformation, which, in principle, could be taken over by the encoder. Nonetheless, not clear is how the quality of physical quantities on the output

[11] For finite-sized systems, ergodicity is always restored and true power laws do not exist – they are represented by very broad distributions

would be changed, as well as the interpretability of the latent space regarding order parameters, the physical reduced temperature, etc.

On another note, *invertible* neural networks are quite interesting options. In these architectures, nonlinear maps between layers are realized by invertible functions only, which makes a decoder unnecessary, and more computational power (i.e. a deeper network) can be allocated towards the encoder. One choice of architecture that we have already begun to experiment with is *realNVP* [936]. Apart from practical appeal, this may be more amenable to interpretation as well as present interesting applications for theory development in physics [519].

Physics-inspired latent-variable models, I.

The sub-optimality of the variational approximation in VAEs has been discussed in the literature [884, 937, 938]. There seems to be general agreement that a more complex model on the latent variables would be highly desirable – i.e. a more complex approximate posterior distribution $p(\boldsymbol{z}|\boldsymbol{x})$ of the latent variables.

We propose that physics might offer some help: As mentioned afore, in soft matter physics, hard-core repulsions induce highly correlative behavior in liquids. Exactly describing the state of a liquid in equilibrium conditions, in two or three dimensions of space, represents one of the unresolved "holy grails" of statistical mechanics, which we motivated in part I of this thesis. The most sophisticated theories for purely hard-core repulsive systems of particles are found in the context of classical density functional theory – specifically, fundamental measure theory (FMT), which has been discussed (and explored) in most previous chapters of this thesis. We think that incorporating an FMT functional into the learning problem – one that governs the free energy of physical systems like hard spheres or hard rods (either in the continuum or in on-lattice models like those studied in this thesis) – would represent a novel way forward. As the modern FMT functionals attempt to capture many-body correlations in liquid systems, these could enhance the latent-space or probabilistic model of data. However, future studies would need to clarify uncertain issues like computational feasibility (the FMT functional would need to be minimized during training), as well as the role of hyperparameters of the model – like an external potential on the hard-core-particle model system (of the latent model).

Physics-inspired latent-variable models, II.

A latent model of data that emulates *physical motion* (an equation of motion pertaining to a physical system) is a potential physics-based approach that has already been initiated in the literature recently: Hamiltonian motion has been the basis for generative learning algorithms found in Refs. [401, 402]. Time-dependent data of statistical-physical model systems in out-of-equilibrium conditions could offer novel ways to test these algorithms. The kinetic Monte Carlo simulation trajectories of sticky-hard-rod-model in monolayer confinement of Ch. 5 represents one class of example systems from nonequilibrium statistical physics that could be employed for these purposes. The key challenge to learning nonequilibrium dynamics will be that coherence in time or a proper *ordering-of-events* will have to be predicted – at the relevant many-body (collective) level of description accessible and learnable by the machine. These are very interesting prospects for future research.

We propose that putting in more physics into machine learning algorithms, generally, seems important both for the interpretability of the algorithms, as well as for the quality and genericness of learning: A physics-based approach might offer unique advantages – one could define learning systems that guarantee specific conservation laws – for example, of energy in the case of Hamiltonian motion, which implies a symmetry of the direction of time (i.e. *reversibility* in (virtual) "time" of the latent model). A conservation of other physical quantities like momentum would represent fundamental, hidden symmetries in the data. On the other hand, a novel generative model could be constructed on the basis of *breaking* these symmetries – upon *perturbing* an "equilibrium" latent model via external "forces".

To this end, we propose that motion of a *many-body* system, particularly, a dissipative system coupled to a thermal bath (a local Markovian approximation of dynamics) may be better suited for many learning problems, as this would undeniably enhance the complexity (and thus capacity) of the latent model. It would also offer a clearer interpretation of convergence to an equilibrium state (a stationary solution), as well as potential possibilities to transition between different equilibrium states in a manner that would abide to physical law. Physics-inspired architectures that emulate dissipative physical systems out-of-equilibrium are not known to us. A synergy between nonequilibrium many-body physics and machine learning represents one, broader outlook of this thesis.

Physics-inspired latent-variable models, III.

Further, a latent space model that emulates Boltzmann-Gibbs distributions (i.e. grand canonical ensembles, or any other thermodynamic ensemble) would offer a higher degree of interpretability, as well as novel control on the generative model. This would require, for example, an introduction of one-dimensional "fugacities" as well as "reduced temperature" variables that condition the generative model, possibly in the form of a hierarchy of model priors (see next paragraph). In any case, latent space "phase diagrams" could be spanned by these thermodynamic conditioning parameters, and relationships between the *true* phase diagrams and those generated by the model could be explored. This would have a large number of interesting practical applications for physicists. Moreover, this would offer a unique window into the learning problem and offer formal, physics-based explanations to the learning behavior.

Other ideas to latent-variable models

On another note, the "tri-state" symmetry of a physical model system with a tricritical point leaves us questioning whether a multimodel prior may aid the learning problem for input systems with vastly different thermodynamic phases. Refs. [939, 940] explore and discuss multimodal priors; hierarchical priors are discussed in [941]. We can only speculate that the latter could aid the learning of a coarse-graining hierarchy of collective variables in complex fluids (thermodynamic physical systems).

With regards to our analysis of VAEs in this chapter, we further speculate that a *discrete* latent-space representation may be advisable for learning the fully discretized lattice model, and possibly beneficial for the 'problem' of hard-core

repulsions between the rods. Discrete-latent-space models have been discussed in e.g. Refs. [942, 943].

Physics-inspired reconstruction cost functions

We also see potential for physics-inspired reconstruction cost functions. A Landau-Ginzburg-type effective Hamiltonian (see Ch. 3.2) might constitute a mean-field approach for a cost function that includes square-order terms on "order parameter fields" in the input and output data, as well as squared *gradients* thereof, analogous to our analysis of reconstructed images in Sec. 7.4. The gradient operations can be implemented via convolutional operations, which would be computationally feasible with current libraries and GPU architectures. Moreover, a cost function that judges whether *correlations* either within or among output images are captured correctly (within mini-batches, for example) would be desirable, as well.

We found in our investigations that the error in the *inner energy* is more sensitive to physically-relevant (thermodynamic) features in the configurations. The inner energy was calculated as a sum over nearest-neighbor products over pixels, hence contains information on local correlations within images. An error thereof could be calculated on-the-fly via convolutional operations,[12] as well (which is the numerical method we utilized, in fact, in our *ex-situ* calculations thereof). We stress that an "Ising-type" of nearest-neighbor Hamiltonian over pixels could be applied for general data-sets as well, and is not necessarily bound to data-sets representing statistical model systems from physics. Investigations would be needed to clarify whether this idea is truly computationally feasible, however, and whether it would suffice to capture correlations in hidden-layer (compressed) representations, instead.

7.11 Conclusions and outlook

We have studied a popular generative, unsupervised machine learning algorithm, β-VAEs, in this chapter. By applying the algorithm to datasets of configurations of a physical system of sticky hard rods in 2D, we have explored the capabilities, limits, and interpretability of the algorithm. The VAEs were implemented in a standard way using neural networks with only one hidden layer in the encoder and decoder. We later compared this implementation with deep convolutional neural networks. We explored the more flexible variant of standard VAEs, where the hyperparameter β is adjustable – it controls the degree to which the model posterior distribution of latent variables should match to the diagonal Gaussian prior.

We trained the VAEs on one reduced temperature in a biased series of ensembles, spanning across phase boundaries. The test data we employed were Boltzmann-Gibbs equilibrium ensembles of the grand canonical type – having different reduced temperatures than the training set. In this way, we sought out to explore which thermodynamic properties the VAEs are able to capture.

We have found that the algorithms "coarse-grain" the configurations of the physical system, and the resolution is limited by the dimension of latent space $\dim(\mathbf{z})$. Roughly speaking, level of resolution scales with $\sim \log(\dim(\mathbf{z}))$.

[12] using 3×3 convolutional windows with a fixed filter which has 1's on the "+" in the middle, and 0's at the corners

However, this is only approximately true when the set of learned variables is fully-ranked. In contrast, "mode collapse" during training means some of the variables are ignored, i.e. they do not contribute to fluctuations in the dataset. In these cases, the output images have roughly the same level of coarse-graining-resolution as a fully-ranked VAE with a smaller $\dim(\mathbf{z})$. The second fundamental hyperparameter β is responsible for this mode collapse (given the training dataset does not change). We propose that the two axes could span a "phase diagram", i.e. in the $(\beta, \dim(\mathbf{z}))$–plane, representing the internal learning states of the VAE. Further transitions are possible: we found such double-transition behavior in preliminary experiments on VAEs with deeper (two-hidden-layer-), fully-connected architectures.

We interpreted the latent variables as "collective variables" in the assemblages (data-sets) of configurations – as long as the latent space remains fully-ranked (see further below). The VAE models a Gaussian posterior distribution of each variable with means $\boldsymbol{\mu}$ and variances $\boldsymbol{\sigma}^2$ for every input, i.e. it models a distribution of "similar" configurations for every single input. The information about each configuration is encoded in these pairs of variables. While most of the variance of the latent variables – measured in states *across* thermodynamic phase boundaries – is contained in the $\boldsymbol{\mu}$'s, the $\boldsymbol{\sigma}^2$'s are interpreted as "generalized susceptibilities". We have used them (or their inverses) to order the latent variables according to a "participation ratio". Both variables together seem to contain highly sensitive information to the thermodynamic state of the rod system – we have quantified a wide variety of latent "order parameters" and latent-space observables using this paired encoding. All of these "detect" phase boundaries with ease; moreover, some of them may be used to distinguish the order of the phase transition (first or second order).

The character of the learned latent variables depends strongly on β. If the VAE is fully-ranked, collective variables typically appear "liquid-like" or "entangled", judging from decoded images thereof. The first two latent variables (indexed $k = 1, 2$) are exceptions: these identifiable with the thermodynamic *order parameters* of the system. We have conducted a study on a physical model system with a *tricritical point*; therefore, the first two variables represents the two-dimensional global order parameter. Higher-order variables (indexed $k \geq 3$) seem to represent "fluctuation" collective variables in the fluid – they are distributed nearly symmetrically around the zero-point of the latent space for all thermodynamic ensembles, and their absolute values peak around all phase transition fugacities. At least, this is true for VAEs trained with sufficiently large values of β (see further below) – for lower β (in the simple architecture) the order parameters are much more weakly identifiable – in fact, only in the empirical variances (not in the means) of the latent variables.

Due to the three-fold symmetry of the system (tricritical ordering), the VAEs set the "zero" or center of latent space at a point representing tri-critical or co-existence states. This is best visible in the first two latent variables (the order parameters), as their symmetry is clearly broken in different thermodynamic states. We interpret that the full generative model, i.e. the unit Gaussian prior, is the tricritical point of the phase diagram, despite training at higher temperatures. A multivariate Gaussian might be a fair approximation for a finite-sized physical system. Yet, we can only be partly sure about this interpretation of the generative model. In particular, we cannot discern exactly how the physical temperature of the system is encoded, although the Kullback-Leibler divergence between model posterior and model prior (the relative entropy) does

show a monotonic relationship with the reduced temperature. In the fully-connected neural network, the fugacity or chemical potential seems to be encoded in the logarithm of the inverse σ's, although this can vary somewhat depending on the training conditions. This opens up prospects for the future: incorporating basic thermodynamic parameters such as the reduced temperature or fugacity (indirectly, possibly) would offer a much higher degree of interpretability as well as interesting applications.

Intriguing phenomena occur around the *threshold* value of β, before the onset of mode collapse (before the latent space is reduced in rank, in effect). Around the threshold state, the decoded latent variables form a *hierarchy* over spatial correlation-lengths in images; the collective variables now represent nearly-separate, characteristic length-scales in images. A doubling of the level-of-resolution occurs after every $\log_2(k)$ variables ($k = 1 \dots \dim(\mathbf{z})$ indicates the latent variable number), approximately. These decoded variables mimic somewhat closely the reconstructed principal components that are learned by principal component analysis, which is a linear (unsupervised) method that finds gradient-like operators in the configurations (i.e. it represents a global Gaussian theory). Heuristically, then, the distortions of learned features in the hard-cord model appear "stretched out" at this threshold state. In this way, the higher-order variables variables ($k \geq 3$) become "disentangled" and possibly "solid-state-like" in character (i.e. like Goldstone modes).

Moreover, the sorting scheme of the variables, the "participation ratio" based on the σ's, for example, shows the flattest (broadest) distribution over the variables (indexed by k's). This might be expected for self-organized critical behavior, in that power-law-like distributions are involved. Past the threshold value of β, a portion of variables do not participate in the datasets (they are ignored), and seem to represent "localized" modes, as they represent at the highest spatial frequencies (rather than low-frequency, collective modes). The critical behavior in the VAEs may be intuitive, in fact, as the training data-sets are *out-of-equilibrium*, in effect: they span across phase boundaries and, therefore, do not represent a single, equilibrium ensemble. We discussed that this behavior of VAEs might be analogous to when a liquid becomes frustrated at the onset of solidification (i.e. glassy behavior, relaxation of long-ranged tensions in a material, etc.). Detailed investigations in the future would be interesting both for machine-learning as well as for physics, as implications could be much broader.

We sought to understand whether the "hard limit" on spatial resolution via $\dim(\mathbf{z})$ is due to the shallow, simple neural network model that we used – with one hidden layer. In a direct comparison, we explored the learning behavior of a deep convolutional VAE (DC-VAE) on the same data-sets. We find that even these show the same, general type of "coarse-graining" behavior: The coarse-graining resolution of output images is limited by $\dim(\mathbf{z})$. Also, mode collapse of latent space occurs upon a critical β. Quantitative results show that both the "vanilla"-VAE and DC-VAE have advantages and disadvantages in their ability to preserve physical quantities on the output — like the inner energy, order parameters, and gradients thereof. Most intriguingly, however, preliminary findings suggest that DC-VAEs may learn a "conjugate" representation of latent variables compared to the fully-connected VAEs. More detailed investigations are needed, but, this would suggest that DC-VAEs learn a model that is theoretically more useful. Nonetheless, in the future, a generative model that

would be conditioned on thermodynamic control parameters of Boltzmann-Gibbs ensembles would make VAEs much more interpretable and guaranteed useful regarding their generative properties (at least for physics).

In order to obtain realistic output images (which is the pragmatic goal behind all generative models like VAEs), where clusters of only a few individual rods are roughly identifiable in the output images, latent space dimensions (and rank) need to exceed $\dim(\mathbf{z}) > 512$, at least. This was surprising, as the standard VAEs we found in the literature have reported much smaller latent dimensions suffice for many, real-world datasets. We deduce the following: the dataset of physical configurations of hard-core rods in 2D may present a very difficult learning problem. It may be nearly impossible to compress the information to only a few latent variables (it may be highly irreducible), especially with the simple, standard VAE probabilistic model. We propose that the hard-core part of the interaction Hamiltonian makes this model much more challenging to learn. Many other models explored in the literature of the lattice-"spin" type, which may be one reason for their general success and popularity. A more sophisticated generative model would be necessary, i.e. a more complex posterior distribution of latent variables that can better "deal with" the highly correlative nature of hard-core interactions. We have proposed a number of ways to realize (potentially) physics-inspired models for these purposes. A model that captures many-body correlations based on fundamental measure theory for hard-core particles, for example, might render improvements for real-world data-sets, as well.

Lastly, we found that the initial data preprocessing is a crucial step in the success and stability of the learning problem, as well as for the interpretability of the latent variables. Specifically, a local (pixel-wise) representation that reflects the three-state (tricritical) symmetry of the thermodynamic (global) order parameter was crucial for the particular problem at hand – of the 2D sticky-hard-rod system. In this kinds of representation, then, the lattice configurations represent order parameter *fields* – the thermodynamic order parameters are found easily by the learning system thereafter. We found this is also true for other, unsupervised machine learning algorithms we tested: principal component analysis, as well as deterministic autoencoders. This did not help our experimentation with generative adversarial networks (GANs), which remained notoriously unstable.

All in all, VAEs succeed in an ability to mimic configurations of a physical system of hard-core, sticky rods. This is true given a few collateral factors like a very large latent-space dimension, a correct value of β to avoid "mode collapse", given we pre-process the data properly. Specifically, to the latter, the "pixel-wise" data (at the local scale) should be able to represent the symmetry break occurring at the global scale during thermodynamic phase transitions.

Deep convolutional neural networks do not necessarily out-perform much simpler implementations of the encoder an decoder regarding the physical properties of reconstructed configurations. This may point to a very large amount of information contained in the datasets. In turn, these data-sets are uniquely adept for testing machine learning algorithms. We propose this high "complexity" may be attributed in part to the hard-core repulsive interactions between rods, i.e. the Hamiltonian is neither completely local nor "soft". Hard-core-repulsive systems may embody a more difficult class of problems (in the context of physical many-body systems) to learn.

Although they encode sensitive thermodynamic information implicitly, we found VAEs are not *fully* interpretable in terms of which thermodynamic aspects of the hard-rod systems they learn. In order to enhance the interpretability of the generative model, we think it would be important to construct a probabilistic model that mimics Boltzmann-Gibbs ensembles, i.e. one that incorporates fundamental thermodynamic parameters such as temperature, fugacity (chemical potential), and volume (or pressure). This could be of high interest for a number of practical applications – for example, for accelerating physical simulations. This could be useful as well as interesting for real world data-sets, as well, as it might offer a way for directly controlling statistical features within the generative model. We also propose that "pseudo"-dynamics of traversing latent space could be modeled within a quasi-stationary or adiabatic approximation –i.e. linear response theory – which could have interesting applications for both fields of study.

Physics-inspired models on latent space seem to be the next logical step. Not only are "any" higher-order correlations important – models that abide to laws of physics could capture *causal relations*, especially if the model follows an equation of motion, i.e. *dynamics*. On the side of reconstructions, cost functions that are likewise physics-based could be constructed. A Landau-Ginzburg-type effective Hamiltonian might constitute a simpler, mean-field ansatz for a cost function. However, a cost function that judges correlations between output images would be desirable, as well. Future investigations would be needed to clarify whether any such cost functions are computationally feasible – they need to be computed quickly, and compatible with GPU architectures.

An enhanced interpretability and (potentially) power of machine learning algorithms – by incorporating physics of statistical mechanics of equilibrium – is one, general outlook arising from this work for the future. We think 'putting more physics into machine learning' should include knowledge of nonequilibrium physics, as well: Nonequilibrium systems both entail a high capacity for complexity in dynamics and evolution of structures (they can be very "creative" given only a few adjustable parameters, as we saw in Ch. 5). An inherently out-of-equilibrium learning system could be better at learning very different kinds of tasks, arguably, which could allow for the development of more general forms of artificial intelligence.

This end of this chapter marks the end of part IV of this thesis. This was also the last part dedicated to presenting scientific studies. The closing part of this thesis (part V) begins at the next chapter (Ch. 8), where we will discuss outcomes of this thesis as well as open-ended issues across different chapters and on a general level. The conclusions of this thesis are written in Ch. 9.

Part V

Closing

Chapter 8

General Discussion

Chaos at the bottom means order at the top.
Order at the bottom means chaos at the top.

Stephen K. Hayes

This chapter tries to tie together general aspects of the theoretical, preparatory discussion in Chs. 2 and 3 with the results in Chs. 4–7. We also reassess the feasibility and scope of the scientific aims behind some of the research engaged in this thesis. In doing so, we arrive at a number of prospective ideas. These may reflect specific and promising routes for continuation of the research, but also more fundamental questions about many-body systems.

8.1 Employing on-lattice models as simpler aliases for complicated systems

One aim of this thesis has been to investigate to what extent we can employ lattice models as simpler "imitations" for more complex systems (soft matter or organic molecular matter). We have seen that the thermodynamic, bulk behavior is quite different in comparison to continuum models of rods, in particular with respect to the isotropic–nematic transition (Ch. 6). Systems of hard rods in monolayer confinement were compared to a continuum model with spherocylinders, which represent a system with colloidal-type dynamics and phase properties. In monolayers, these models show qualitative overlap. However, the thermodynamic phase transitions are lacking (Ch. 4). Hence despite different equation-of-states (or, rather, different virial coefficients), at the macroscopic scale, the general standing-up transition may be similar among models.

We have also explored the lattice model of rods in monolayer confinement for the purpose of modeling thin film growth with organic molecules at the initial stages. With sticky hard rods (Ch. 5), we see a large variety of effects which may shed light on phenomena reported in the literature that we reviewed in Ch. 1.2 and Ch. 2.4.

The advantages and disadvantages of the lattice model depends on which effects they are supposed to imitate, i.e. which time- and length- (and energy-)scales we are interested in. However, in nonequilibrium conditions, these time- and length-scales are generally non-separable due to a loss of ergodicity. We found in Ch. 5 that in nonequilibrium, the specific choice of microscopic dynamics is crucial for the evolution at the macroscopic scale, as well as all other mesoscopic scales "in-between". From our additional investigations on comparing lattice and continuum models in Ch. 4 we predict the following: whether

one uses a colloidal-type model with continuous degrees of freedom or a lattice model will fundamentally alter the nonequilibrium dynamics; therefore, kinetics during phase transitions. (The direct comparison we made was for the case of purely-hard-core-rod systems, which lacked thermodynamic phase transitions, i.e. showed no poignant phase separation kinetics.) From the equilibrium side, we saw in Ch. 6 how thermodynamic properties fundamentally change depending on the types of model, i.e. the strength of first-order transitions. (In the lattice model, the isotropic–nematic transition is very weakly first order, while in the continuum, this is well-known to be a strong first-order transition.)

8.2 Lessons learned from the behavior of lattice models

8.2.1 Constraint to lattices: Fluctuating domains exclusive to one orientationally-ordered state

In Ch. 6, we saw the lattice model produces large, "loose" nematic domains that exclude the other orientation, which we presented at least for the 2D case of "sticky" rods. We think this exclusive-orientation-domain-forming behavior should also apply to the 3D case, especially as we found particularly unusual phase behavior for $L = 5, 6$, where the system splits into 2D-like (transient) sheets composed of two of three orientations. Nematic ordering for longer rods is characterized by the transient dominance of only one orientation; the demixing behavior is likely of the Ising universality type. Near the transition point, this exclusive-orientation domain-forming behavior is key to the phenomenology. The dynamics of domains (fluctuations) and associated phase transition kinetics would be necessary to characterize for a fuller understanding of the many-body system. We have ignored, frankly, dynamics both in our studies on phase behavior in Ch. 6 that accessible in the Markov-Chain pseudodynamics, and in Ch. 4, where we only observed them mean motion of globally-summed quantities (thermodynamic-order-parameter means).

We mention, further, that quantifying and understanding domain fluctuations and related two-time correlation functions is important for developing better e.g. density functionals for equilibrium theory. A domain- or cluster-based (lattice-) FMT like in Ref. [265] represents one way forward. On-lattice models of hard-core particles like the rod systems like we have studied provide unique testing ground for such approaches.

Lastly, we saw that machine learning (Ch. 7) can automatically "pick up" on collective variables – those whose fluctuations among and within different thermodynamic states are most significant. These could be aliases for domains in the fluid, which have nonlinear boundaries. It would be most interesting to clarify this point in the future, as it could be useful for theory development, particularly when studying nonequilibrium transitions like jamming or the formation of arrested states. Moreover, machine learning might offer ways forward to faster equilibrium simulations: the learned model could provide a biasing potential, in terms of the encoded collective variables, for proposing new configurations during an equilibrium Monte Carlo simulation.[1] This idea represents one outlook of this thesis.

[1] The biasing potential might be expressible through the Kullback-Leibler divergence between a model posterior and model prior in the VAE, for example.

8.2.2 Constraint to lattices: Consequences for phase behavior

We saw in this thesis how phase behavior in lattice models can be unique and quite different from that of continuum models. This is due to fully constraining particle degrees of freedom to a lattice, i.e. to a discrete set. Interestingly, analogies can be found to *dimensional* confinement: The first-order isotropic–nematic transition in the 3D we studied for lattice hard rods is nearly "destroyed", become weakly first order (Ch. 6). A "destruction" of first-order transitions is known to occur in strong confinement, which we discussed in Ch. 2. In 2D, we saw how the isotropic–nematic transition (a demixing transition) is indeed "destroyed", i.e. it is critical until it reaches a tricritical point. We have not investigated as to *why* in detail, but, alluded to confinement and discretization in a general way in Ch. 2. We speculate on related issues below and in Sec. 8.6 later on.

The weakening of the isotropic–nematic transition could be tied to a general tendency towards enhanced mesoscopic ordering in the fluid: We discussed the fluctuating domains of exclusively one of three degenerate states of orientational order above. In the 3D bulk (Ch. 6), this demixing behavior is not a nematic phase transition with long-ranged ordering; rather, a dominant direction is transient, fluctuating among all possible ordered directions. In fact, this ordering can be manifested in a *suppression* of one of three directions, for rod-length $L = 5, 6$. These systems split into nearly-decoupled 2D-like systems (again, another form of mesoscopic ordering), which appears unique to fully on-lattice systems of rods. The latter is *not* a smectic phase, as the rods are not orientationally ordered within these nearly-2D sheets. Further, the nature of the 2D transition is most likely a demixing transition of two orientational species (i.e. it is *not* long-ranged, it is mesoscopic), which has been argued for 2D Zwanzig models [356].

As to the (presumed) tricritical behavior of 2D, sticky hard rods (part III), tricritical behavior occurs in other, spin-type lattice models with discrete orientational states in 2D (Potts, Blume-Emery-Griffiths, etc.) (see Chs. 1.3, 2.2.2 and 2.2). This may *not* be a unique lattice feature: In a specific short-range-attractive liquid-crystal model, Ref. [331] reports on a crossover from the Kosterlitz-Thouless-type of isotropic–quasinematic transition in 2D to tricritical behavior depending on the range of the attractive part of the pair-potential. Therefore, these features could also be inherent in other continuum models. Another feature of commonness between lattice and continuum is that ordering phase sets in for $L = 7$ in 2D, which is similar to the minimum aspect ratio required for 2D spherocylinders of ~ 7. In 3D, nematic ordering sets in for $L = 5$ on the lattice, and an aspect ratio of 3.8 for spherocylinders (see Ch. 1.3). It would be interesting to compare rods on the lattice with non-unit width (and depth).

We compared a hard-rod lattice model with a continuum model of spherocylinders in monolayer confinement (Ch. 4). They show qualitative overlap in the standing-up ordering behavior (which is entropy-driven), which, however, was compared in systems that lack thermodynamic phase transitions. They entail different "equation–of-states" regarding the dependency of the orientational order parameter ordering on the density (i.e. virial coefficients). The continuum model shows scaling behavior with regards to the rod geometry, while the lattice model does not (as far as we can tell). One cannot take a dense-lattice-limit of the lattice model, for example, to produce the continuum model.

We did not explore jamming transitions or dynamically arrested states during monolayer growth in this thesis. This would offer a sharper level of scrutiny when comparing the monolayer systems between lattice and continuum models, for example: dynamical scaling laws upon approaching a nonequilibrium (or equilibrium) critical point would be rigorous quantifiers of their fundamentally different behavior. We saw arrested behavior in our studies of purely hard-core monolayers (Ch. 4): The author of this thesis recalls that the case of simulating *attractive* substrates for the hard spherocylinders in the Monte Carlo simulations generated quite "interesting" configurations that were associated with a difficulty in equilibration (transient arrest). In our KMC lattice model, we saw dynamical arrest (a nonequilibrium jamming transition), which occurs at attractive substrates.

We demonstrated that systems of hard, sticky hard rods on lattices in (2+1)D monolayer confinement (Ch. 5) effectively split between a lowly-ordered, 2D lying phase and highly-ordered standing phase. The lying phase is metastable, a feature particular to this form of strong confinement. A direct comparison to a continuum model would be useful. To this end, Ref. [944] models continuous spherocylinders in open, semi-confinement (not monolayers) with different interaction potentials, from which it is difficult to make any concise statement regarding the monolayer phases (apart from the observations that an ordered standing phase tends to form more than one layer, and disordered phases can also occur). However, we have argued that our findings may be qualitatively consistent with experimental or simulated systems of organic molecules at substrates (Ch. 1.2). These show similar phenomenology like a "disorderly", uniquely-monolayer phase that appears metastable, forming a wetting layer in some cases; or, at least, large-scale structures that can be amorphous in shape. Further, these can co-occur with stable, crystalline structures (in analogy to our standing islands) during submonolayer growth. Hence, clarifying the role of lattice restrictions in monolayer confinement for sticky- or attractive-hard-rod systems would be important: Identifying the features in an idealized, generic dynamical model that reflect or retain the relevant physics faithfully, while remaining generic, is an ultimate aim of physics models. Moreover, understanding lattice restrictions in various forms of confinement would contribute to a deeper understanding of many-body physics, quite generally.

Lattice modifications and future exploration

We saw how "sticky" attractions widens the isotropic–nematic coexistence gap (also seen in continuum models) substantially below a pseudo-tricritical point. Inspired by this, polydisperse mixtures of rod-lengths, which can be thought to inducing effective attractions via the exclusion effect, might render more similarities to a bulk 3D systems in the continuum. A polydisperse mixture increases the number of ways to couple orientational and translation degrees of freedom. Finer lattice structures (containing for rotational states, like triangular lattices) or those containing sub-lattices, i.e. those with *multiple scales* should also increase this diversity. However, the specific choice of lattice or sub-lattice will be key for the strength and type of coupling between rotational and translational degrees of freedom. Regarding the monolayer systems, a triangular lattice or a sub-lattice model might "bridge the gap" better between our cubic-model system and organic molecules, allowing for more kinds of ordered states

to form. Regarding the 3D bulk, it would be interesting to explore the isotropic–nematic transition of hard rods on these different types of lattices, whether one of them can induce behavior mimicking that in the continuum models better.

To this end, we also discussed how the FMT derived for the 2D and 3D hard-core lattice models (the results are given in Ch. 6) renders the same entropy functional as for rods on Bethe-like lattices [360]. The latter types of lattice is (somewhat) network-like in its topology; therefore, the FMT might entail a certain degree of recursion, although we leave this notion rather unspecified in this discussion. From the point-of-view of theoretical development of functionals, it would be interesting to test whether the current FMT derived by Lafuente and Cuesta [159, 160] may actually be *better-suited* for hard-core particle models on lattices with sub-lattice structures.

8.3 Generic, on-lattice models for nonequilibrium thin film growth with anisotropic particles

We infer from our studies of monolayer growth in part II the following: In order for a lattice model system to emulate "real-world" self-assembly phenomena at surfaces, it will need to will need to capture just the 'right' variety of mesoscopic ordering phenomena, which is related to capturing the correct collective states and associated time-scales in nonequilibrium. Therefore, an (optimal) trade-off between simplicity (idealism of the model) and complexity (a high 'bandwidth' of (co-occurring) collective processes (kinetics) and resulting structures.

We have seem that a simple elongation of particle shape, from $1 \times 1 \times 1$ cubes into $L \times 1 \times 1$ rods, generates highly complex ordering phenomena, entailing with at least two, if not more competing phases growing in the monolayer[2] As we saw in Ch. 5, the specific choice of microscopic dynamics ("tumbling" versus "central" rod rotations out-of-plane) changes the phase separation kinetics and morphologic evolution in the monolayer significantly. This issue requires more care and attention than might be expected. Generally, we predict that energy scales (potential depth and width) should change the nonequilibrium kinetics, and the models thereof would need to be assessed case-by-case.

More specific models with an extra degree of particle anisotropy, i.e. "boards", should entail phases in equilibrium (see e.g. Ref. [368] for the hard-core case), and, therewith even more kinetic pathways in nonequilibrium (during layer growth). Nonetheless, these types of models could be interesting for specific organic molecular systems whose molecules have three symmetry axes.

Further, we discussed how desorption seems to play a significant role, as well (from preliminary investigations). Desorption and re-adsorption dynamics introduce a higher degree of reversibility into the model, i.e. the system finds the "next" quasistationary (metastable) or equilibrium state more quickly. This should have a dramatic effect on the kinetics and all resulting morphology, e.g. island shape and collective reordering processes. This should be taken into account when performing multi-layer, 3D growth simulations (an outlook of this thesis). A "vapor-phase deposition" model similar to model II in Ch. 4 will generate different growth results than a "solid-on-solid"-type of 3D growth model.

[2] given rods entail short-range attractions and hard-core repulsions.

In other words, the specific MC-moves matter, even for multilayer growth with much simpler, $1 \times 1 \times 1$ "point-particle" models. In an upcoming publication (Ref. [168]), we found that vapor-deposition or solid-on-solid-type growth models show different kinetics and, therewith, predict a different evolution of thin film growth.

We suspect that different models of short-ranged attractive rods or elongated particles (lattice or continuum) might find something in common in *monolayer* confinement: For long enough particles, the main orientational differences – between lying and standing – may be associated with two different phases. A pronounced competition of these phases during layer growth will be visible if the lying phase is metastable (i.e. due to an inherent dynamical asymmetry), as seen in our findings in Ch. 5. Their dynamical asymmetry is tied to their differing degrees of local order. Therefore, the combined situation of monolayer confinement and particle elongation, as well as short-ranged attractions may generate similar phenomena across different models. An exploration thereof would underscore and give credence to the genericness of the simple lattice model explored in this thesis.

Prospect: multilayer growth modeling

A motivation arising at the end of this thesis is to continue modeling thin film growth with "sticky" attractions in multilayer growth simulations. In writing the codes for sticky-hard-rod monolayer growth with various rotational moves in the context of part II of this thesis, the author has already included the possibility for simulating bulk 3D dynamics. We mentioned this in the outlook of Ch. 5. (We note that the event-driven KMC codes are complicated algorithmically for anisotropic particles when implementing full 3D dynamics; we can implement all rod-length and different choices of rotational moves, i.e.rotations around rod-centers, near-center, and at the rod-ends.) These nonequilibrium simulations would be complemented with equilibrium GCMC simulations in semi-confinement, i.e. to find out the surface phases of the 3D system of sticky hard rods. (Existing GCMC codes need only be modified to include an attractive wall).

8.4 On the phase transformation kinetics during monolayer growth with rod-like particles

We saw in Ch. 5 how the kinetic pathways to a full monolayer depend on (reduced) temperature (interaction strengths), the flux-rate–to–diffusion-rate (the deposition quench rate), as well as particle shape (rod length) and substrate potentials. In the coming paragraphs, we discuss this model as a rough analogy to a crystallization process from a fluid phase (in the bulk).

Metastable intermediate phases may be universal features of crystallization out of a fluid phase (see also discussion in Ch. 2). In fact, amorphous, liquid-like precursors are reported for colloidal crystallization [7, 669, 699, 715–721]. Moreover, these may be more 2D-like in their ordering, even though crystallization occurs in the bulk [945]. The pathways to crystallization may very often be non-classical in nature [699], i.e. not describable by means of monomer attachment.

We argued in this thesis that organic molecules forming crystal films on substrates may share these features owing to their anisotropic, extended shape and directional interaction potentials. Kinetics of cluster growth at the submonolayer stage seems to be highly "non-classical" under various conditions, deduced from our studies in Ch. 5.

Indeed, some examples from the organic-thin-film literature attests to non-classical as well as multi-step cluster growth kinetics. Liquid-like, lying precursors or "non-nucleating liquids" are reported to precede the formation of well-ordered crystal phases [10, 12, 141, 179, 181, 212, 236, 237, 751, 752, 946]. Clearly, precursor phases will change the scaling behavior of nucleation and growth of the standing (high-ordered crystal) islands, as well as the resulting morphology (island shape).[3,4] Two different Arrhenius-type rates for island formation are reported at high and low substrate temperatures [183]. Bimodal island sizes are also reported in e.g. [913].

These low-ordered, lying phases are described as forming very large-scale structures [947] (see also Refs. [13, 183]). Moreover, the standing (stable "crystal") structure may first be stable in the *second* layer, hence second-layer dewetting accompanies the growth evolution in a number of reported examples: It can occur before, but near the full packing fraction [13, 946]; at the onset of full packing [12, 182, 188, 189], or after annealing a film having full coverage [182, 187]. Further, in the literature, amorphous wetting-layers and crystal island-forming phases were reported to co-occur in rubrene [212], as well as in p-6P [13, 146, 183] and other substances [147]. This may resemble the lying–standing transition out of a wetting layer, or the occurrence of islands of different orientation that we found in our model system. A high sensitivity of kinetics to the substrate, which shifts this nonequilibrium competition, is also reported in the literature [740],

8.4.1 General remarks on rate-equation approaches

Analytical models of the kinetics at the early submonolayer stage of thin film growth have historically constructed "nucleation-and-growth"-type rate equations. These model *one-body* kinetics in the form of monomers attaching and detaching from islands [699], by means of single-particle diffusive transport [20, 113, 124, 153, 154, 163, 165, 689, 748, 948–950]. Such nucleation theories rest on the assumption that the critical nucleus is amenable to a thermodynamic description, i.e. that a free energy difference between the crystal and the vapor drives the spontaneous nucleation and growth of islands of the crystal phase, which is surrounded by a vapor. As mentioned, presuming that the kinetics are effectively one-dimensional implies they should be describable by just a single reaction coordinate. This general idea is borrowed from first-order phase transitions between phases with the same or similar translational symmetry (fluid order), most notably simple gas–liquid transitions. But the fluid–to–solid phase transition is different, as both the translational and orientational symmetries of the liquid are broken upon crystallization [551]. The hard-rod systems we investigated entail much more structural and dynamical complexity owing to the rotational degrees of freedom, which couple non-trivially to

[3] We have e.g. Refs. [178, 183, 208, 209, 212, 251] in mind, in these regards.

[4] Ref. [251] investigates "bimodal growth modes" in the submonolayer regime that different from simpler nucleation models. The results are interpreted as due to so-called "hot precursors", a population of monomers that is highly mobile.

the translational degrees of freedom in a many-body (fluid) system. An effectively one-dimensional process implies, in contrast, a gigantic gap of length and time-scales between one-body and all other variables in the system. Thus, the equations are mean in character – both in space and time: For example, no cluster-cluster correlations or memory effects are taken into account.

Seeking for a master set of kinetic equations may be dangerous, in general, but specifically for anisotropic-particle systems (i.e. monolayer growth of rod-like particles). When systems are in nonequilibrium, *a priori* assumptions about the dynamics may easily become uncontrolled. The (generally-accepted) presumption that crystal nucleation (from a liquid) can be described by purely diffusive-driven processes is up to hefty debate [951]. Indeed, many-body correlative processes (collective motion) seems to be most fundamental in hard-sphere model systems, where crystallization is purely entropy-driven [555–557]. Moreover, which variables are *relevant* in the nonequilibrium evolution are not clear up-front [952]. Our findings in Ch. 5 of a lying gel than can span the entire system, or, in other cases, a lying liquid that precedes and competes in the "nucleation" of a dense phase, bears no resemblance to that of "nucleation-and-growth" of compact islands of a stable (standing) phase from a 2D vapor. Thus, the formation of the standing phase ("crystal") goes through a disorderly intermediary state before the stable phase "nucleates" and grows. The phase transformation kinetics are *not direct* (i.e. isotropic-vapor–standing-liquid or (-crystal)) and much more subtle. Notably, the aggregation-like formation kinetics of the lying gel phase will (very likely) not involve an energy barrier [19, 696]. All of these findings attest to the striking reality of how orientational and translational degrees of freedom are non-trivially coupled in the process; this is also true, more generally, for crystallization from a bulk fluid (in 3D) [551]. A description thereof would, thus, certainly go beyond simple nucleation theories [549, 551, 699, 951, 953–955].

As mentioned before in this thesis, literature on organic molecular systems already discussed the possibility of two-step phase transition kinetics, see Ref. [236] and e.g. Refs. [256, 956].[5]

Rate equation models for multi-component systems have received little attention, as well. We have found only rare exceptions in the literature in e.g. Refs. [958, 959]. On a related note, simulation studies trimmed at the effect of "impurities" (a sparse amount of a third phase that may be mobile or positionally fixed) for monolayer growth are found in Refs. [960–963].[6] As for the ABV model,[7] the topic for monolayer and multilayer growth will be addressed in an upcoming work [915] outside of the scope of this thesis.

8.5 Applying machine learning to a statistical model system of rods

Another aim of this thesis was to apply machine learning algorithms, preferably unsupervised in nature, to statistical model systems. The model system of 2D rods was a suitable candidate, as we had explored its phase behavior in part III in addition to a fully-tested simulation system to generate data.

[5] See also Ref. [957].

[6] Also, distinguished properties of island growth when modeling *anisotropic* interactions has been addressed in Ref. [260].

[7] two-component systems plus vacancies

High complexity of data-sets: hard-core repulsive model systems from physics

The Ising and other spin-like models have been a favorite choice in the literature, which, however, entail much less inherent complexity than the hard-rod system of sticky hard rods in 2D: At the end of the day, the hard-core repulsive interactions in our sticky-hard-rod system generate pronounced many-body correlations in the fluids, where a significant portion of order-parameter fluctuations are highly non-local at even intermediate densities. The system shows a strong coupling of rotational and translational degrees of freedom (which we discussed quite generally in Ch. 2), which, arguably, makes it a much more challenging test system for modern machine learning algorithms.

Moreover, the system entails a *tricritical point*, which in our studies with machine learning has highlighted many important aspects about the role of properly representing macroscopic- versus microscopic-scale symmetries before (in data preprocessing) as well as during learning (in the nature of the learned, latent representations).

Sparse and symmetric input-data representations

To the former, we saw the importance of properly represented input data, in that data should express the (three) globally-ordered states inherent to the system – it should express this at the local scale, as if each point in space entails a 2D microscopic order parameter. This notion alludes to the concept of *locality* of a Hamiltonian, further related to whether the degrees of freedom can be decoupled even at the smallest scale of treatment (no long-ranged interactions that couple particles in a direct manner). This is a fundamental assumption behind field-theoretic, coarse-grained approaches to many-body systems, i.e. Gaussian field models that we discussed in Ch. 3. Arguably, then, we might conclude that learning with a Gaussian (local) model is easier if the *relevant* physical quantities contained in the input data are represented in a statistically independent manner. In other words, sparse input representations enhance the discernibility between macroscopic (gross) properties in the data. Further, the symmetry of the input data – by providing data from across "far reaches" of phase space – helps the VAEs identify global order parameters. These are quantities that identify with the global symmetries that are broken upon phase transitions.

8.6 Other thoughts (speculative discussion)

8.6.1 Towards mesoscopic approaches to monolayer growth (with rods)

In light of the above discussion, structure formation in the monolayer might be describable in terms collective motion (modes) that are functions of both translational and rotational degrees of freedom in the system. These may further be coupled – different from a first-order *Gaussian* theory, for example that variational autoencoders employ. Mode coupling theory may offer a theoretical framework that expresses these basic physical ideas [665]. A description of

nonequilibrium dynamics or phase transformation kinetics in a coupled-mode representation is certainly not new [964, 965].[8]

The collective variables and fluctuations found by VAEs in Ch. 7 might provide a novel and modern way to proceed. Fluid or solid systems entails different vibrational density of states and types of modes [966–969]. It would be interesting, further, to explore the learning of growth trajectories (rather than merely configurations). This would represent an interesting prospective outlook of this thesis and would tie together research on nonequilibrium statistical mechanics with machine learning.

Coarse-grained, continuum field equations-of-motion in the style of Cahn-Hilliard or phase-field modeling [225, 227, 734, 970, 971] are more popular analytical approaches to kinetics of phase transformations. These, however, retain a mean-field character [972]. As we have discussed, the FMT of sticky-hard-rod monolayers captures many relevant features of the monolayer systems unique to a nonequilibrium setting, at least in the form of metastable states. Master-equation-type equations-of-motion in the style of the DDFT approach for hard rods in Ch. 4, take account for two-body correlations from an equilibrium functional. However, the kinetics of 2D gel or wetting layer formation during the "crystallization" process to a stable thermodynamic state may need more precise analysis. As the DDFT equations-of-motion are diffusion-like in character, we are not sure what kind of kinetics it could predict, especially if aggregation is involved. To the latter, dynamics are far from diffusion-like and the kinetics do not involve energy barriers. One question is whether additional 'hydrodynamic' terms can account for some of the behavior [973], but this belongs to the realm of speculation.

Surprisingly little has been done to characterize the sublimation (vapor–crystal) kinetics on surfaces from first principles in large-scale simulations of simpler, well-known model fluids. Vapor–crystal phase transition kinetics for 2D Lennard-Jones systems were addressed only a few years ago [658]. In contrast, phase separation kinetics (nucleation, growth, spinodal decomposition, and coarsening) at constant densities ("quenches") were studied long before for ABV models in Refs. [678, 972, 974–977]; ternary systems have also been studied in in Refs. [978–980]. As to experimental investigations on the kinetics, properties at fixed coverages or chemical potentials could render crucial information – preciser relationships between the chemical potential differences and growth laws might be extractable, for example [113, 124, 748, 948].

8.6.2 Alternative approaches to nonequilibrium physics and complex systems

In Ch. 3.3.7, we opened up a discussion about potential (what we dubbed) "self-consistent" approaches for stochastic descriptions of *nonequilibrium* systems. Dynamics on the full N-body level should arise from proper accounting of (nonequilibrium) many-body forces (in their strengths as well as likelihoods or frequencies in time). These generate currents in the system. Within a formalism referred to as *Power Functional Theory* [825, 826], the nonequilibrium (reduced) one-body densities (i.e. the structure) is generated as a consequence of the continuity equation *after* the physical dynamics are determined from a variational problem. We feel the lattice model of sticky hard rods studied

[8] The idea of a modulation of spatial modes has also motivated other approaches [728].

in Ch. 5 may be an ideal candidate for theory development to this end, as it is defined by only a few free parameters. Yet, it entails a richness of testable phenomena: Metastable transient states as well as multiple *dynamical regimes* with different scaling behavior would be key effects to reproduce in a "good" theory.

Moreover, we discussed in Ch. 3.3 how a loss of the time-ordering-of-events is fundamentally tied to *dissipation*: The simplest example is coupling to a bath, which induces thermal, *random* motion of particles. In light of this, it seems ever more important to quantify dissipation or irreversibility precisely for any effective description of a nonequilibrium system. A measure of irreversibility for a time series of measurement was defined in Ref. [857] as the Kullback–Leibler divergence between the probability density of a time-series realization and that of its time-reversal conjugate; the earlier Ref. [788] uses the Jensen-Shannon divergence (a similar quantity) [849, 851] instead. We discussed these measures in Ch. 3.5.1, as well.

These topics have much common ground with modern information theory (e.g. theory on computation). For example, a transfer of information is inherently time-asymmetric, and is embodied by the so-called *transfer entropy*, which is a conditional mutual information: it can distinguish between driving and response in time-evolving systems, i.e. detect causality [981–983]. Harmonizing a theory of information exchange and general nonequilibrium dynamics would constitute a foundational endeavor (additional Refs [983–985] venture in this direction). A formalism about the conservation or loss of causal relationships in complex or many-body system (for example, via a path-integral formulations [102, 827]) would certainly be interesting for machine learning research.

8.6.3 Machine learning: Criticality and potentially "optimal" states

In the machine learning systems we studied, β-VAEs, we saw critical-like behavior manifested in two ways. First, the learning system with the highest level of interpretability – tied to the maximal discernibility between physical "order parameter" variables and "fluctuation" collective variables – is the system poised at an "internal" critical point or threshold point (of β). Scaling relationships in nonequilibrium [965, 986] – whenever they may exist – express a high correlation of events of the past with those now. Systems are subject to a broad bandwidth of characteristic length-scales and time-scales whenever power-law behavior reigns. Indeed, we saw in Ch. 7 how the participation ratio or hierarchy of the latent variables (quantified as a function of their modeled susceptibilities) was broadest around a threshold or critical state of β. Secondly, the generative model on latent space (the prior) appears to correspond to the tricritical point of the physical model system. Therefore, we infer there must be a deep relationship between critical behavior and optimal forms of learning. We alluded to this issue on a very general level in the introduction, Ch. 1.4.1, as well.

Notably, at a critical state, systems are inherently *out-of-equilibrium*. Understanding the "dynamics" (the learning dynamics) during training (via e.g. stochastic gradient descent) seems a pertinent issue both for developing better algorithms as well as for an interpretation of the learning process. We think nonequilibrium statistical mechanics – which we studied in the context of an example system in Ch. 5 – could offer insight and help in this direction.

Final note: Disorder and order – two sides of the same token

Though the lattice models were studied in this thesis for often pragmatic reasons, they confront us with the fundamental notions of symmetry and the role of disorder versus order, particularly in out-of-equilibrium situations. An affinity of nonequilibrium liquids to quantum mechanical systems has long been noticed in their vibrational density of states [967]. Nonergodic (nonequilibrium) classical many-body systems show similarities to Anderson localization [987, 988], where a many-body wave-function is localized in the presence of disorder in the solid [989, 990]. Generally, the introduction of disorder has a similar effect to both liquids and solids, where their vibrational spectra entail intriguing features [382, 639, 903, 904, 991–996] such as localized modes. Therefore, it would be interesting to clarify the connection between quenched disorder (frustration and arrested states) and phase ordering kinetics at a more fundamental level. The (2+1)D monolayer systems show an astonishingly broad variety of phase separation scenarios, which makes them well-suited for foundational questions.

We showed machine learning can learn collective variables of a physical systems: The automatized discovery of relevant variables in highly nonequilibrium systems would be highly useful, from a practical point-of-view. Moreover, it would be most interesting to see if $\beta-$VAEs may find the dynamical regimes that we discovered in monolayer growth with sticky hard rods: More specifically, one could explore whether machine learning can learn to decipher between different types of phase separation kinetics in physical systems. Even more interesting would be whether a simple, generative model of the *nonequilibrium* system like that learned by β-VAEs suffices to predict the full breadth of possible self-assembly trajectories – while retaining sufficient predictive power to precisely "simulate" trajectories. To this end, the machine learning algorithms would have to be trained in time-dependent data, which represents a clear outlook of this thesis. We note that as our monolayer model system for nonequilibrium has an extremely small amount of free parameters (diffusion rates, flux rate, rod-length and interaction strength), it seems to be highly suited for such exploratory and novel investigations.

Machine learning dynamics, which may be interpreted as the relaxation kinetics of a statistical system from an initially quenched-disordered state, should be exposed to this same "dance" between order and disorder. Understanding this in more detail and in a rigorous way would be part of a quest towards foundations on the physics of complex systems. Bringing together statistical mechanics of both equilibrium and nonequilibrium systems with machine learning seems a promising and hopeful endeavor for the next decades. As Stephen Hawking stated at the dawn of the new millennium,[9] "*I think the next century will be the century of complexity*."

[9] On January 23, 2000 (San Jose Mercury News)

Chapter 9

Summary and Final Conclusions

What we observe is not nature itself, but nature exposed to our method of questioning.

Werner Heisenberg

This thesis endeavored on understanding the statistical mechanics of highly idealized model systems of hard rods (as well as sticky hard rods) fully constrained to square or cubic-type lattices – in 2D, (2+1)D monolayer confinement, and in the 3D bulk – using Monte Carlo simulation methods. We studied orientational transitions and phase behavior of the systems in equilibrium conditions using simulations in the grand canonical ensemble. In many cases, results were compared directly to analytical theory in the form of classical density functional theory. In order to better understand early stages of thin film growth with anisotropic particles, i.e. nonequilibrium physics, we studied systems of rods in monolayer confinement using kinetic Monte Carlo simulations. We further explored the behavior of a machine learning algorithm by using the 2D hard-rod model as input data, in the form of configurations, in order to better understand the algorithm, its limits and capabilities.

Below, we review each part of this thesis, and summarize the findings and conclusions of our studies. In Sec. 9.2 afterwards, we will state our final conclusions.

9.1 Summary

In part I of this thesis (Chs. 1–3), after a general introduction, we delved into fundamentals of complex fluids of rods. We then discussed fundamentals on equilibrium statistical mechanics, and illustrated a generic treatment of dynamics on lattices by means of a master equation. We also discussed the basis of the simulations algorithm employed in this thesis – kinetic Monte Carlo (KMC) and Markov-Chain Monte Carlo methods for simulating equilibrium ensembles. Moreover, we highlighted and discussed the unresolved, theoretical difficulty of describing nonequilibrium many-body systems by analytical means. We highlighted fundamental connections between statistical mechanics and information theory, in particular with respect to concepts surrounding entropy. We also discussed machine learning and the algorithm of variational autoencoders that we later investigated in this thesis.

In part II of this thesis (Chs. 4 and 5), we studied the nonequilibrium dynamics of systems of hard-core rods in monolayer confinement ((2+1)D)) in a lattice

model. Rods have geometry $L \times 1 \times 1$, and are fully discretized in their rotational and translational degrees of freedom. We also characterized their equilibrium phase behavior, in particular for the limiting case of purely hard-core rods. The next paragraphs describe our findings.

In chapter 4, we analyzed the equilibrium properties of systems of rods in the *purely hard-core limiting case* of rod interactions. This (first) study represents a collaborate effort (*J. Chem. Phys. 145, 074902 (2016)*, please see corresponding chapter). We developed and performed formally-exact Monte-Carlo simulations in the grand canonical ensemble (GCMC), which served as a test for density functional theory (DFT) in which the equilibrium properties were explored. Specifically, lattice fundamental measure theory (FMT) was formulated for the rods system. Rods continually stand-up with increasing density, which is a purely entropic effect. Strongly attractive substrates that bias lying rods induce (only) "pseudo-"-second-order transitions, i.e. a *near*-"kink" in the order parameter upon increasing the density. In the same context, the on-lattice model was compared to a continuum model of hard spherocylinders in monolayer constraint. They show qualitative similarities in the behavior of global-scale order parameters. However, key differences (e.g. scaling behavior and different "equation-of-states" or virial coefficients) point at the fact that these models represent fundamentally different systems.

We then investigated (nonequilibrium) monolayer growth with long rods on lattices in monolayer confinement, in the same purely hard-core limit. This study was likewise a collaborate effort (*J. Chem. Phys. 146, 084903 (2017)*, please see corresponding Ch. 4). We studied the many-body, dynamical system by means of (formally-exact) KMC simulations. The simulations we wrote and developed from scratch were conceptualized, first, with a novel, *rejection-free* algorithmic implementation for hard-core, anisotropic particles. For a wide range of particle deposition rates, we found that monolayer growth with hard rods can be described by quasiequilibrium growth dynamics. The underlying reason for this affinity to equilibrium in driven conditions is very likely the lack of thermodynamic phase transitions in the monolayer (in the purely-hard-core case). Using the KMC simulations, we tested the quality of a lattice dynamical density functional theory (DDFT), which was formulated for the lattice system of purely hard-core rods. This seems to perform well as long as the system retains a near-equilibrium character, associated with a decoupling of rotational and translational degrees of freedom. In the case of strongly attractive substrates, the system loses ergodicity – dynamical arrest occurs in the form of a (possible) nonequilibrium jamming transition. We did not explore the physics of this case further, but, an explicit dependence of the macroscopic evolution on the hopping rate of particles was found. The DDFT would need extensions to capture this variability, and in its current form, appears to emulate the case of very large hopping rate. Exploring quantities relevant for the dynamics in the system such as two-time and two-point correlation functions, or currents would be important in the future.

Also using the KMC simulations, we compared the nonequilibrium evolution of the lattice model during monolayer growth to that of the continuum model of hard spherocylinders. (We realized deposition with two different protocols in the continuum model, accordingly). Qualitative agreement in the evolution of global order parameters was found between both models. Much like in the equilibrium case, differences arise mainly due to different "equation-of-states".

Further in part II, in chapter 5, we presented a broad as well as in-depth investigation into nonequilibrium systems of sticky hard rods on lattices in (2+1)D confinement. The model studied was an idealization for the initial growth of thin films of anisotropic particles like organic molecules. We wrote, developed and performed a very large number of (specifically-designed and developed) KMC simulations: We varied the relevant dynamics in the systems over seven to eight orders of magnitude and the temperature over a wide range of values (across multiple (presumed) critical points). We also varied the rod-lengths ($L = 2, 3, 5, 9$) and explored different substrate attraction strengths.

The physics of monolayer growth with sticky hard rods is very rich, showing a wide variety of possible kinetic pathways towards the stable end-state of a full monolayer of standing rods: these include (a competition with) metastable phases and collective reorganization processes. The dynamical model is defined fully only by a handful of main control parameters: the flux-to-translational-diffusion ratio F/D (the deposition quench rate) and the specific microscopic rotational dynamics. The energetics are defined by the "sticky" inter-particle attraction strength $|\epsilon|$ (or equivalently, the reduced temperature $T^* = k_B T/|\epsilon|$), as well as the rod-length L. We found at least five different phase transition scenarios (labeled (A)–(E)) that divide the $(\ln(1/|\epsilon|), \log(D/F)$–plane – the two main axes that define a dynamical "map" of the order parameter – into corresponding regions. The rod-length, the substrate potential strength, as well as the specific choice of microscopic rotational dynamics (tumbling versus central rotations in the out-of-plane direction) all shift these dynamical regimes, and can even change the topology of the "map" by excluding or introducing new phase transition scenarios.

For the best-studied case of $L = 3$ at neutral substrates, we deduced the following scenarios: (A) "Hard-rod-like" monolayer growth for weakly-attractive rods, in which no phase separation occurs. (B) A transition from an isotropic fluid or vapor to a standing phase via "nucleation" and growth of standing clusters. (C) A competition of lying- and standing-cluster formation (compact clusters of both phases appearing). (D) A lying, low-density gel competing with and accompanying the "nucleation-and-growth" of standing clusters. (E) A dense, lying gel forms a wetting layer, from which standing clusters grow.

Weak substrate potentials seem to shift the scenarios in the $(\ln(1/|\epsilon|)$, $\log(D/F)$–plane, generating large-scaled competing structures in scenario (C), and inducing scenario (E) more easily. They also enhance collective standing-up kinetics, generating loops in the (evolving) packing fraction, for example. Strong or intermediate substrate potentials (very likely) induce a thermodynamically stable 2D (lying) liquid at low enough reduced temperatures. The evolution with rods of length $L = 5$ shows many similarities to that with $L = 3$, although differences include pronounced loops in the packing fraction like those seen for weakly attractive substrates with $L = 3$. Further, their associated "maps" of Q in the $(\ln(1/|\epsilon|), \log(D/F))$–plane could indicate *two* metastable critical points more clearly (see below). Additional simulations would be needed clarify this point. We find evidence that growth with very long rods ($L = 9$) includes 2D (in-plane) demixing at early stages, as well, an effect predicted by a lattice FMT for these systems. We proposed that crossing points of e.g. the gel line (scenario (D)) with other transition lines associated with dynamical arrest could be used to estimate the position of metastable critical points – both their reduced temperature (attraction strength) as well as the

density (potentially).

The specific choice of out-of-plane rotational dynamics is another, surprisingly important factor effecting the kinetics, and therewith the morphological evolution in the growing monolayer. Tumbling dynamics generate diamond-like-shaped islands, which are even more pronounced for longer rods. Further, scenario (E) seems to be avoided completely, i.e. a wetting layer does not form (at neutral substrates), and collective standing-up processes are highly pronounced in the form of loops in the packing fraction. We also explored dimers ($L = 2$), which also avoid scenario (E) at neutral substrates. It is then recovered for moderate substrate strengths.

We provided quantitative results on the evolution of clusters or nearest-neighbor connected regions during monolayer growth – composed of standing rods, lying rods, or "any"-oriented rods. We also performed morphological analysis by means of Minkowski functionals of these connected regions, which have provided additional insight and means to discern the different phase transition scenarios. We also quantified (roughly) percolation transitions (as well as an anti-percolation transition) for these connected structures. We constructed and quantified observables like the particle *mobility* in rotational or translational degrees of freedom. These render crucial dynamical information complementary to that contained in global (mean) structural observables.

We also performed preliminary experiments with e.g. monolayer heating, temperature quenches, interrupted growth, and evaporation–deposition dynamics. These could render further, deep insight into the phase separation kinetics and nonequilibrium properties of these systems. Regarding evaporation–deposition dynamics, weak desorption can "accelerate" the system toward the next quasistationary (metastable) or stable state, which seems like an interesting prospect for future studies.

In part III (Ch. 6), we investigated hard-core rods of size $L \times 1 \times 1$ on a cubic (3D) lattice in Monte Carlo simulation studies, performed in the grand-canonical ensemble. In the fully on-lattice model, the discretized degrees of freedom (both rotational and translational) lead to interesting characteristics of the isotropic–nematic phase transition, which differs substantially compared to liquid-crystal-type models in the continuum.

We first studied purely hard-core rods. This represented a collaborate effort (*Phys. Rev. E 96, 012104 (2017)*, please see corresponding Ch. 6). We observed a nematic transition for $L \geq 5$ (where we studied $L = 6, 8, 25$ in detail). For $L = 5, 6$, the nematic state entails a negative order parameter: ordering is realized by the dominance of *two* orientational directions simultaneously. The type of ordering changes for $L \geq 7$, where the nematic entails a positive order parameter: one of the three orientations dominates. We (later) found that a two-dimensional order parameter analogous to that of three-state Potts models is superior for describing the orientational ordering. Importantly, we found evidence that the isotropic–nematic transition is *weakly* first order, which is in stark comparison to the behavior of continuum models. The weak-first-order character is hidden in even rather large system sizes, where the transition appears to be a continuous one. We found evidence first in very large systems of size $M^3 = 168^3$. Indeed, the system shows highly pronounced fluctuations in the order parameter around the transition state. Lattice fundamental measure theory (FMT) very likely fails at capturing these strong fluctuations, and

massively overestimates the strength of the (first-order) transition. In fact, the functional is equivalent to a mean-field-type entropy formulated much earlier in other contexts.

We proceeded to simulate and analyze the phase behavior of the same lattice model of hard rods with additional "sticky" attractions, first in the 3D bulk, as well as in full 2D confinement. This study likewise was performed in a collaborate context (*Phys. Rev. E 100, 012707 (2019)*, please see corresponding Ch. 6). The additional attractions induce a gas–liquid transitions that compete with the orientational ordering transitions. The phase diagrams are both qualitatively and quantitatively different from those of comparable model systems of the continuum (e.g. spherocylinders with short-ranged attractions). In the 3D system, the isotropic–nematic transitions remain weakly first-order for the limit of weak attractions. Upon increasing attractions (or decreasing the reduced temperature), this weak-first-order character persists down to a transition temperature region. Thereafter, the coexistence density gap widens dramatically, i.e. the transition becomes strongly first-order in character and represents a separation of an isotropic gas and nematic liquid. The transition-region depends heavily on rod-length, and even is manifested with a remarkably different phase diagram topology for the case of $L = 5$.

In the 2D system (on a square lattice), the nematic phase is manifested by the demixing of the two possible particle species (orientations). We presented results for the exemplary case of $L = 10$ (long rods). For weak attractions, the isotropic–nematic transition remains continuous, forming a line of critical points for increasing attractions that presumably terminates at a tricritical point. Thereafter, a gas–liquid binodal widens substantially. In the region just above the tricritical point, the line of critical points bends in an unexpected way: the transition moves to higher densities upon increasing the temperature before moving to lower densities again, which seems counterintuitive. However, we have rationalized this behavior by observing that the internal density of large nematic domains increases for stronger attractions. These domains are highly sterically-incompatible at their boundaries since they contain exclusively one rod orientation. Vacant spaces open up between domains at the onset of the gas–liquid demixing transition at the (presumed) tricritical point.

In part IV (Ch. 7), we explored the behavior of a machine learning algorithm. (Beta-) variational autoencoders (β-VAEs) are powerful neural-network architectures capable of learning abstract representations of data as well as a generative model thereof – in an unsupervised fashion. To better understand them as well as interpret their limits and generative capabilities, we applied β-VAEs to a statistical (physical) model system which we characterized in this thesis: to datasets of configuration snapshots of the 2D, sticky-hard-rod system.

We uncovered that they "coarse-grain" the configurations, and the level of coarse-graining depends crucially on the latent space dimension. The level also depends on the hyperparameter β, which can induce mode collapse upon a threshold value – a phase transition occurs. This threshold varies with the latent-space dimension provided. We interpreted the latent variables (the internal representation) as "collective variables" in the hard-rod system, whereby the first two variables are identifiable with the 2D order parameter for the tricritical phase behavior of the hard-rod system. As the probabilistic model encodes both means and variances in an approximate (Gaussian) posterior

distribution over latent variables, the variances may be interpreted as "generalized susceptibilities". These render additional information on fluctuations of the variables in the system, and can be used to rank the collective variables in the test data. Interestingly, at the threshold state of the system, just before mode collapse, we saw that the character of the collective variables changes drastically. They form a coarse-graining hierarchy, become disentangled, and their fluctuations in the data are most broadly distributed across latent dimensions. The Gaussian prior seems to represent, very roughly, a (tri-)critical or coexistence thermodynamic state, albeit one that remains uninterpretable. As the thermodynamic state parameters do not condition the generative model, it cannot sample thermodynamic states and is limited in interpretability.

We found that the specific choice of data representation during preprocessing is of central importance for the success of the algorithm as well as the (partial) interpretability of the learned representations. Ideally, the information at the *microscopic* scale of the particles should be represented in a basis that reflects the possible realizations of the relevant *global* order parameters. In this way, any broken global symmetries in the system upon thermodynamic phase transition(s) will be detected with ease. Moreover, the resulting sparse input representation may be beneficial in more general contexts. Indeed, we tested the β-VAEs on a wide range of datasets belonging to different Boltzmann-Gibbs equilibrium distributions (in grand canonical ensembles), i.e. even distributions with different temperatures than the training set. Errors in physical observables on the output like energy, order parameters, or gradients thereof each detect, quite sharply, the thermodynamic phase transition points, i.e. the critical and coexistence chemical potentials in the rod system. Further, observables on the latent encoding of the data are likewise adept at detecting phase transitions, and possibly even the order of the transitions.

We compared the "vanilla"-VAEs that we studied in much more depth to deep-convolutional β-VAEs. We found these are likewise limited by the chosen latent space dimension in their ability to "coarse-grain" configurations. They did not necessarily out-perform the "vanilla"-VAEs on various measures. Intriguingly, however, preliminary findings suggest that DC-VAEs may learn a "conjugate" representation of latent variables compared to the fully-connected VAEs. This may be more theoretically more useful. On a final note, the dataset of physical configurations of hard-core rods in 2D may present a very difficult learning problem. We argued that the highly-correlative nature of hard-core repulsions produce configurational datasets with an unusually high amount of complexity.

Finally, as part of the closing of this thesis, in Ch. 8, we provided a general discussion. We tied together findings about the effects of full lattice constraints on phase behavior as well as related phenomenology. We discussed challenges in finding a generic model for thin film growth with molecules, as well as related rate-equation approaches. We discussed our method-of-approach to better understanding and characterizing machine learning, i.e. the task of learning the configurational realizations of an idealized, many-body model system from physics. We also discussed a few prospective and speculative ideas that have arisen while writing this thesis.

9.2 Final conclusions and outlook

All in all, we saw that lattice models can be very helpful for explaining physics of systems in equilibrium and nonequilibrium conditions. This owes to their inherent simplicity, which, however, also defines their limits. Simple model systems are excellent and necessary for theoretical development. We need to find abstractions over the immense complexity contained in many-body systems. However, even seemingly simple systems can be highly intricate, in particular when in *nonequilibrium* conditions. In this thesis, we unveiled unexpected complexity generated from a very simple, dynamical model system of anisotropic particles – of a lattice model of sticky hard rods. We showed the model can be very useful for understanding basics of the nonequilibrium physics of thin film growth with anisotropic particles, which was the particular nonequilibrium setting in focus.

Each such idealization implies a separation of time-, energy-, or spatial-scales in a system (or degrees of freedom), which is either on-purpose or *not*. Understanding the full implications of each model of a many-body system is not clear up front, especially when a system is modeled under nonequilibrium conditions. Fundamentally, global energy or mean values thereof are not conserved, which is tied to the loss of ergodicity – this can result in a vast array of unexpected behavior. For example, we saw that even fine adjustments to dynamical or energetic model assumptions can lead to vastly different results in a nonequilibrium evolution. Nonequilibrium many-body systems, therefore, are inherently difficult to control theoretically, in the sense that an "all-purpose" procedure to properly coarse-grain nonequilibrium many-body systems is currently not known or well-established. Therefore, one must be cautious not to oversimplify a model for complicated systems in out-of-equilibrium conditions, where various presumptions on the dynamics can very easily break down. The long-time outcomes in the model may go vastly astray when compared to the behavior of the more complicated system in mind.

Even in equilibrium, a lattice model will not be equivalent or a (rigrously) coarse-grained counterpart to a more complicated system with fully continuous degrees of freedom. We can attest to this for the case of anisotropic, *hard-core* model systems that we compared in this thesis. We demonstrated how ordering and phase behavior in simple lattice models of hard rods is remarkably different from that of continuum counterpart models. The bulk behavior of the lattice models regarding the isotropic–nematic transition is quite different when compared to that of liquid-crystal-type models in the continuum. In the monolayer, qualitative overlap between the lattice and continuum models of anisotropic particles might persist due to the strong level of confinement, where the major, many-body events will ultimately involve a transition from a low-density isotropic (or lying) state to a high-density standing state. However, the direct comparison we presented in this thesis was for the case of purely hard-core rod systems in the monolayer, which lacked thermodynamic phase transitions. Therefore, some aspects around the comparability of lattice and continuum models of rods in strong, monolayer confinement remain open.

From our studies on VAEs, we have uncovered that a generative machine learning method applied onto configurations of a physical model system renders an intriguing, alternate model of the physical system. The model produces "coarse-grained" versions of configurations, identifies the order parameters of the physical system, and possibly even conjugate variables thereof. Further,

they discover higher-order, collective variables that represent structural fluctuations in the fluid. As the generative model appears to approximate the tricritical point of the physical model system, this form of learning appears deeply connected with critical behavior. Moreover, deep convolutional architectures may provide a higher level of interpretability and utility from a theoretical perspective, as they potentially render "conjugate" models that could mimic an approximate free energy functional.

Therefore, generative machine learning algorithms seem to have the potential to learn statistical physics. We state the following (rough) postulate: In order to organize large, complex data in abstract, compact (and useful) pieces of information in a machine with finite capacity, machine learning will ultimately have to "do" thermodynamics or statistical mechanics in one form or another – representing different "thermodynamic" states may be one of the only reasonable ways to (implicitly) group data according to gross similarities. In general, we think 'putting in' more physics into machine learning is a clear way forward, especially knowledge of the statistical mechanics of hard-core particle systems (e.g. like that of hard rods), which are highly correlative in nature. In turn, we have seen that if we apply machine learning to a complex, (hard-core) many-body system from physics, which we understand well, then we can begin to learn how machine learning works. We think this protocol may help open up the black box of many algorithms, as well as offer novel ideas. Efforts towards a closer synergy between both fields seems a promising for the future.

Appendix A

Appendix for monolayer growth with “sticky” rods

This appendix pertains to Ch. 5 of this thesis.

A.1 Growth of monolayers in ϵ-regime I or around ϵ_{crit}

Way above the critical point, we observe the dynamics of a monolayer that resemble that of hard rods, at least for the investigated parameter range of F/D (the quench rate). Figs. A.1 and A.2 display the behavior for $\epsilon = -0.33$ for neutral substrates, which is well above the vapor–liquid critical point ϵ_{crit}.

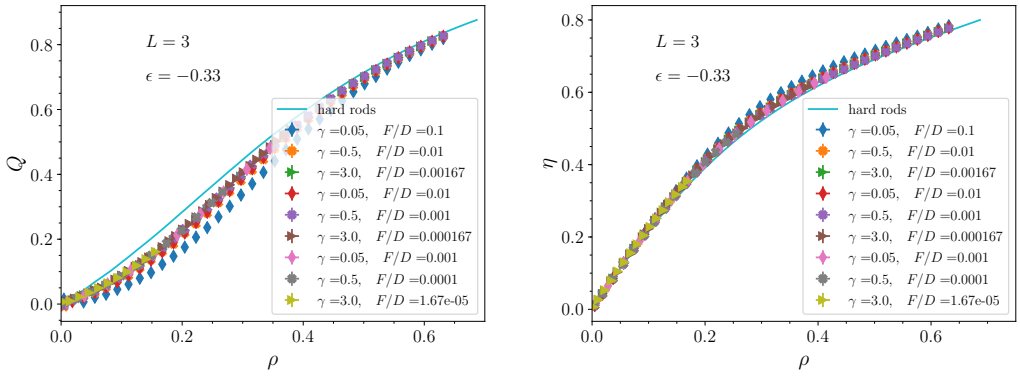

FIGURE A.1: Evolution of the order parameter Q versus number density (left) and surface packing fraction η (right) for system of hard rods with length $L = 3$ with sticky attraction $\epsilon = -0.33$, shown for various sets of kinetics parameters $\{\gamma, F/D\}$. Very fast growth with $\{\gamma = 0.05, F/D = 0.1\}$ differs from $\{\gamma = 0.5, F/D = 0.01\}$, though they are described by the same hard-rod-like-growth parameter $\alpha = \gamma F/D = 0.005$. These results were obtained with a larger lattice size of $M \times M = 512^2$. The solid curves are purely-hard rods ($\epsilon = 0$) in equilibrium.

Upon approaching the critical point for lower temperatures, the monolayer fluid entails stronger fluctuations in density and order parameters. This is natural for systems near critical points. The evolution of global quantities such as the nematic order parameter and packing fractions unveil a pronounced sensitivity of the trajectories of the system to the specific relative rate of the quench rate F/D in Fig. A.3 when compared to higher reduced temperatures (Fig. A.1).

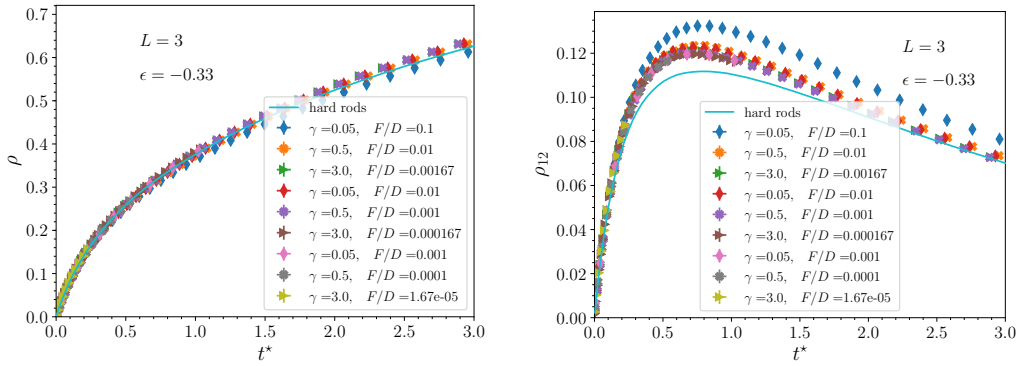

FIGURE A.2: Evolution of the density(left) and lying-rod density ρ_{12} (right) versus rescaled time for system of hard rods with length $L = 3$ with sticky attraction $\epsilon = -0.33$, shown for various sets of kinetics parameters $\{\gamma, F/D\}$. It is more apparent in the right figure that very fast growth with $\{\gamma = 0.05, F/D = 0.1\}$ differs from $\{\gamma = 0.5, F/D = 0.01\}$, though they are described by the same hard-rod-like-growth parameter $\alpha = \gamma F/D = 0.005$. The solid curves represent purely-hard rods ($\epsilon = 0$) growing in quasiequilibrium.

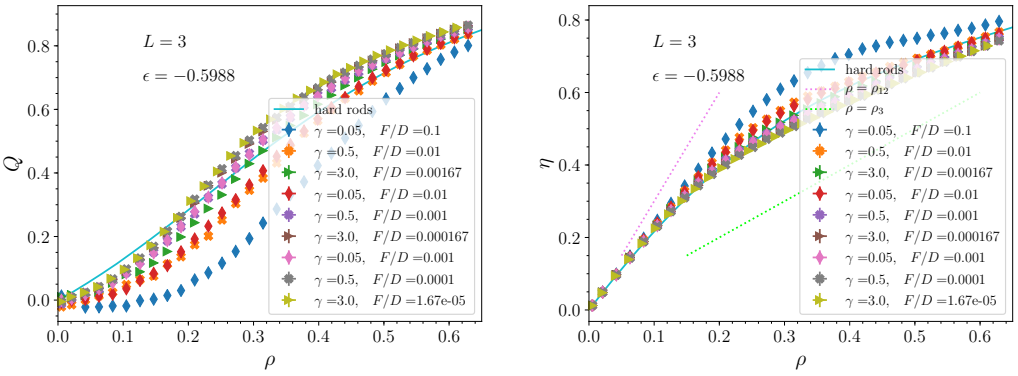

FIGURE A.3: Evolution of the order parameter Q versus number density (left) and surface packing fraction η (right) for system of hard rods with length $L = 3$ with sticky attraction $\epsilon = -0.5988$, close to the critical point, shown for various sets of kinetic parameters $\{\gamma, F/D\}$. The solid curves are purely-hard rods ($\epsilon = 0$) in quasiequilibrium.

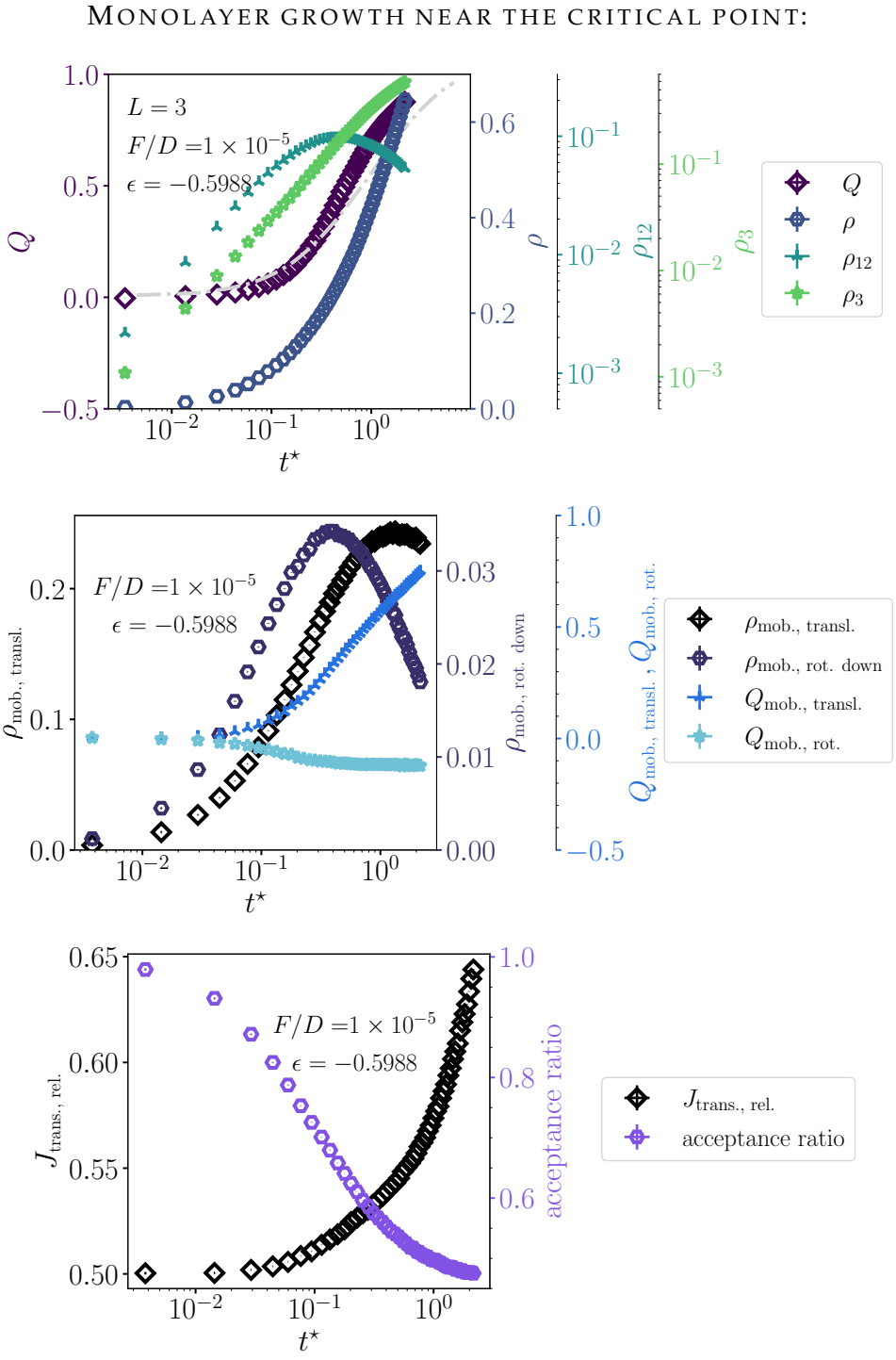

FIGURE A.4: Multiple order parameters and observables plotted over the time-trace for an exemplary case of fixed dynamics, $F/D = 1 \times 10^{-5}$, for growth of a monolayer with $\epsilon = -0.5988$ near the critical point ($L = 3$). The kinetics already have the same signature as scenario (B), see Fig. 5.52.

Structural quantification: Nearest-neighbor connected clusters

These structures can be quantified per moment in time with the help of cluster detection schemes, which detect nearest-neighboring particles from simulation snapshots. The mean "cluster" sizes of *lying* particles at high deposition rates is higher compared to that of slower F/D. The opposite is true for *standing* particles. We stress here that the structural quantities analyzed represent nearest-neighbor connected regions. The detection schemes are explained in Sec. 5.3.7.

Interestingly, both for ϵ-Regime I (Fig. A.5) and near the critical point (Fig. A.6), we find that the mean cluster size of *lying* rods peaks around $\rho \approx 0.33$, a density at which or near which (slightly after) the system can become arrested for lower reduced temperatures (regimes II and III).

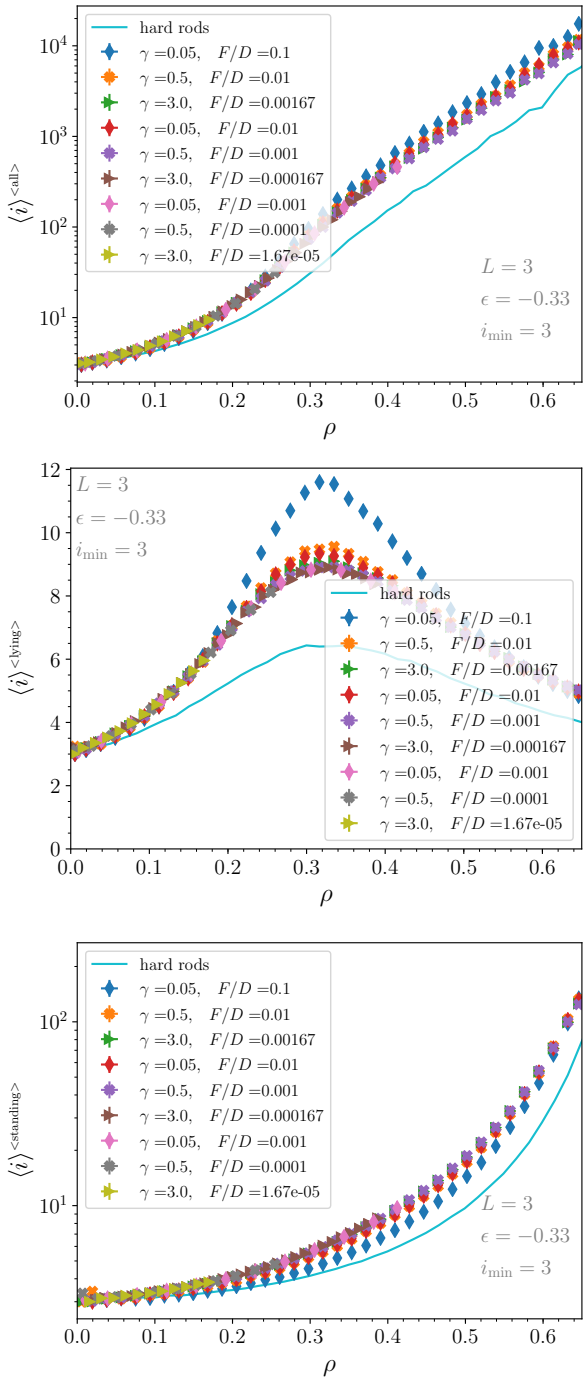

FIGURE A.5: Average measured nearest-neighbor cluster size $\langle i \rangle$ larger than the cutoff $i_{\min}$ versus monolayer density during monolayer growth via deposition at $\epsilon = -0.33$ (regime I): (Top) Nearest neighbor detection scheme using particles of *any* orientation, (middle) only *lying* nearest-neighboring particles, (bottom) only *standing* nearest-neighboring particles. Note that the $\epsilon = -0.33$ system was simulated on a larger lattice of $M \times M = 512 \times 512$.

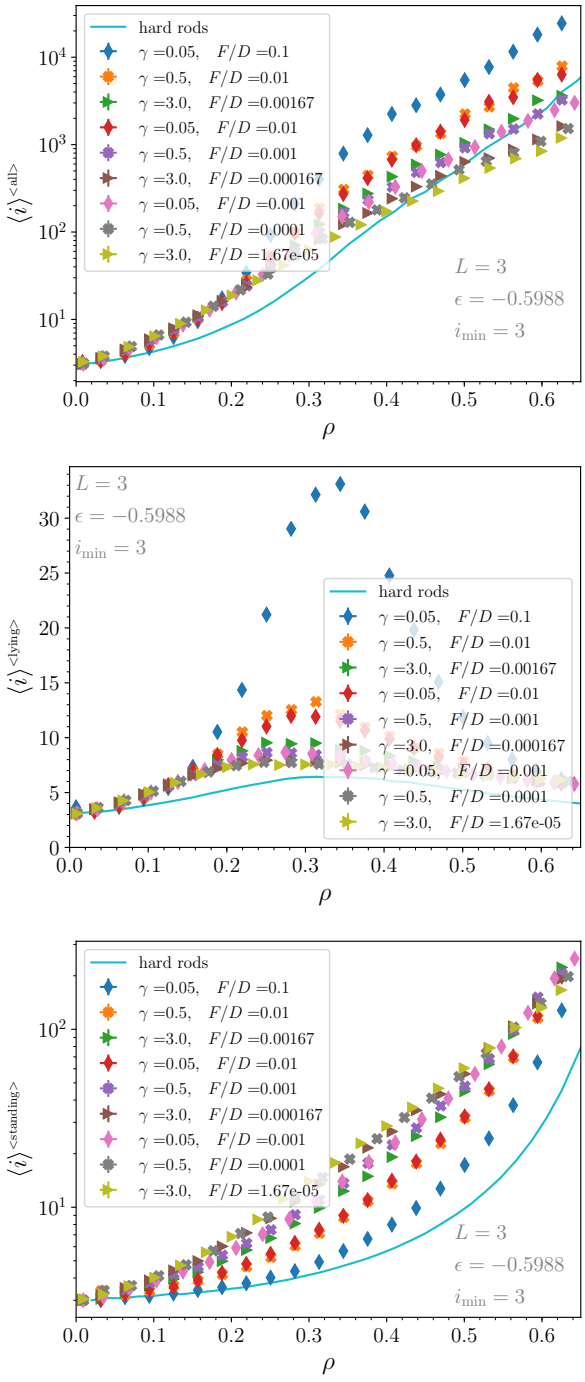

FIGURE A.6: Average measured nearest-neighbor cluster sizes $\langle i \rangle$ larger than the cutoff $i_{\min}$ versus monolayer density during monolayer growth via deposition at at $\epsilon = -0.5988$, which is close to the critical point: (Top) Nearest neighbor detection scheme using particles of *any* orientation, (middle) only *lying* nearest-neighboring particles, (bottom) only *standing* nearest-neighboring particles. Compare to Fig. A.5. Fast growth favors larger average cluster size especially when just above the critical point ϵ_{crit}.

A.2 Additional plots for neutral substrates, $L = 3$, regimes II and III

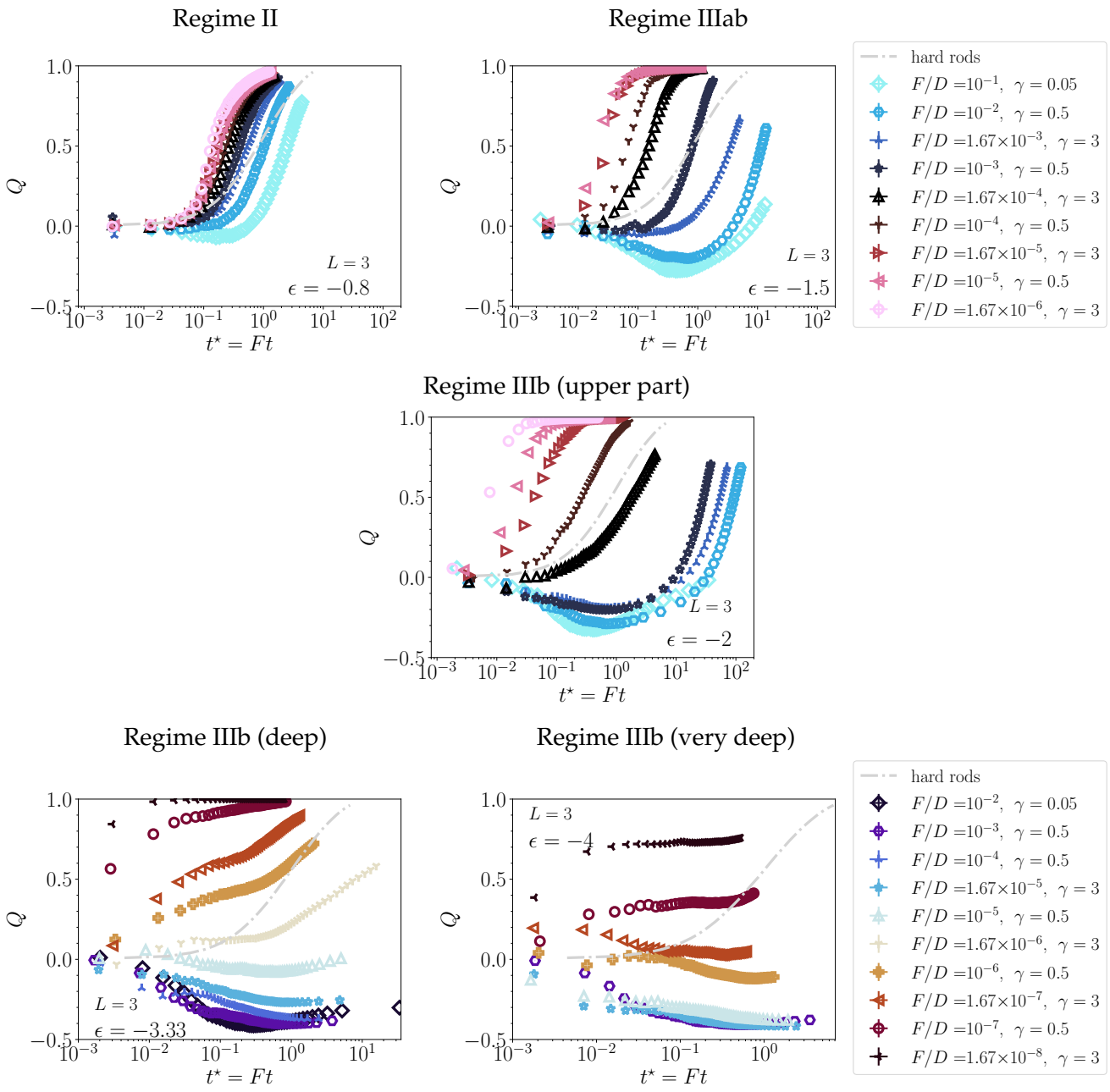

FIGURE A.7: Global order parameter Q rods versus time $t^\star$ rescaled with the attempt flux rate at fixed attraction strengths for a sweep over F/D ($L = 3$).

Below we provide an overview in Figs. A.17 and 5.12 of the growth of monolayers via deposition at temperatures below the second critical point in for the nematic order parameter and packing fraction.

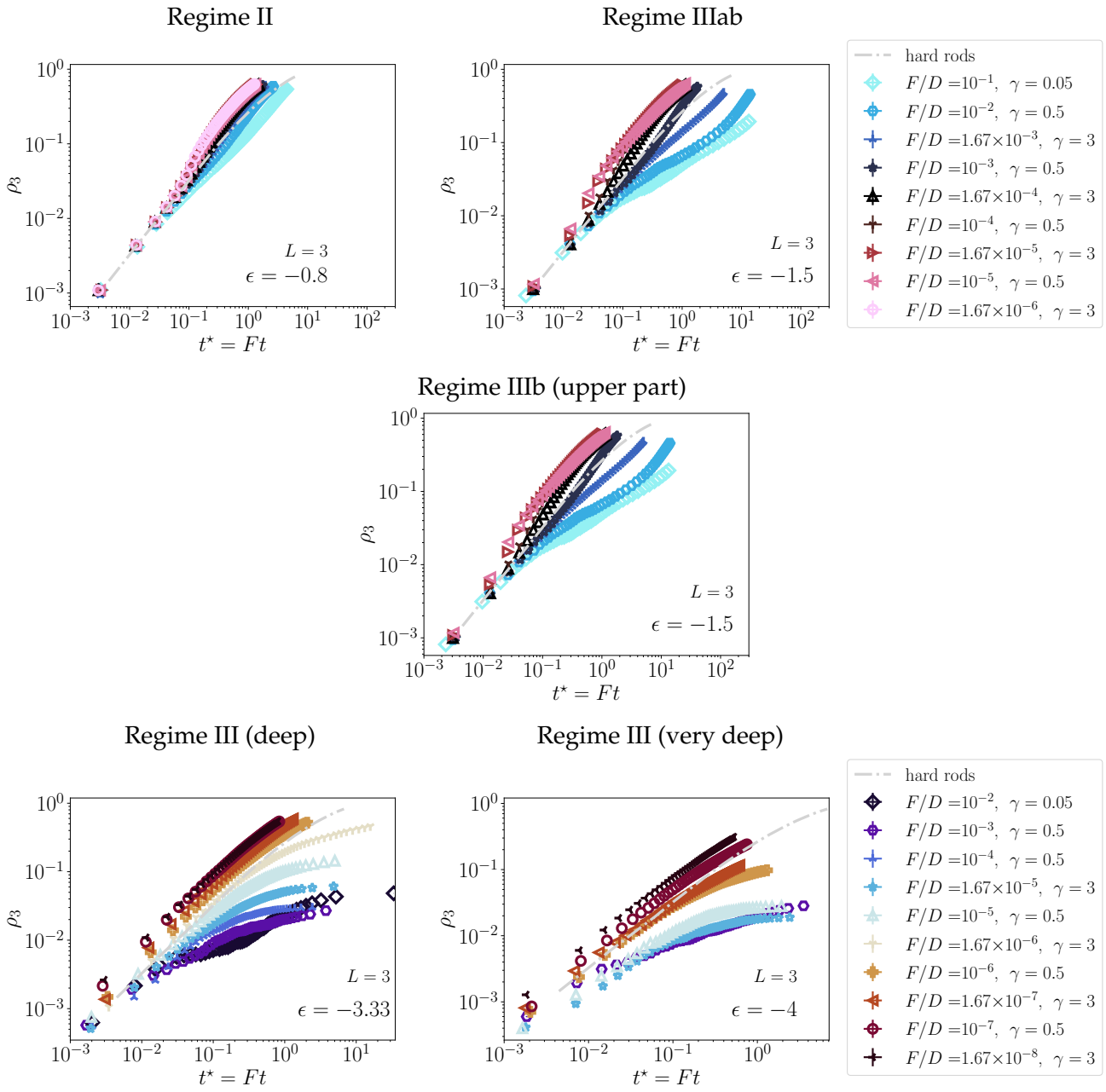

FIGURE A.8: Global number density ρ_3 rods versus time $t^\star$ rescaled with the attempt flux rate at fixed attraction strengths for a sweep over F/D ($L = 3$).

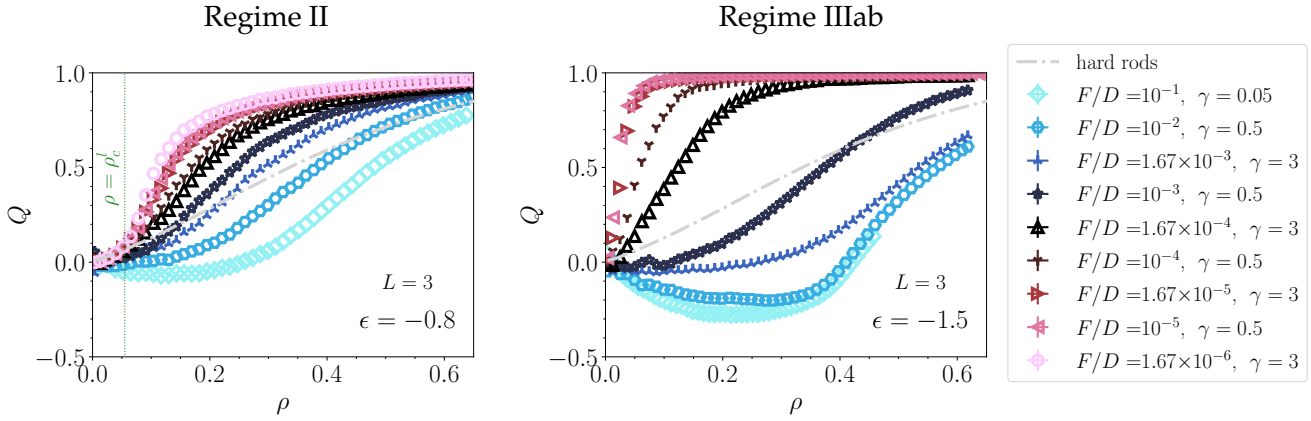

FIGURE A.9: Global order parameter Q versus global density ρ at fixed attraction strengths for a sweep over F/D ($L = 3$) for regime II and IIIab.

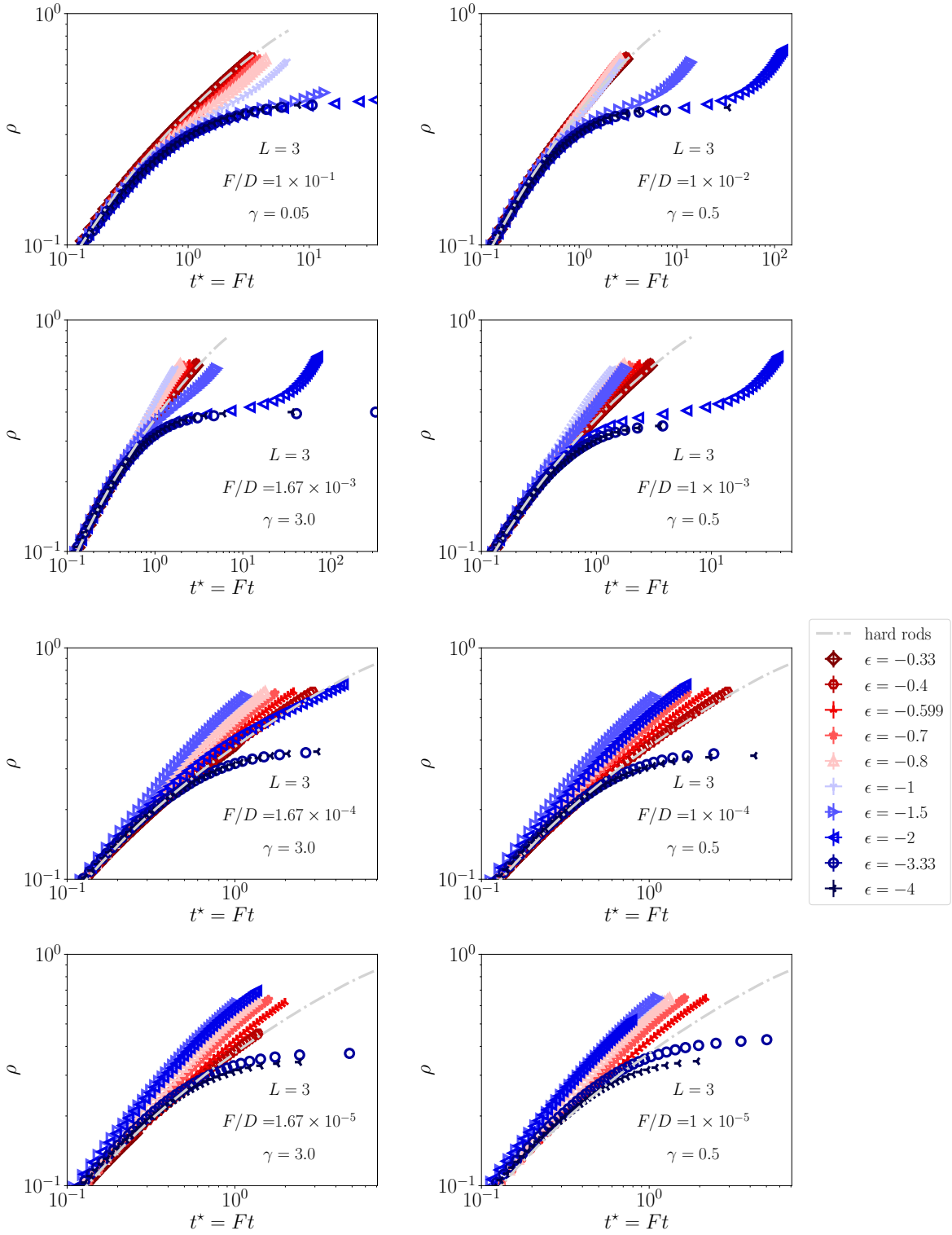

FIGURE A.10: Global density ρ versus time $t^\star$ rescaled with the attempt flux rate (at a fixed F/D) for a sweep over attraction strengths ($L = 3$) for long times. Compare to Fig. 5.24. The lin–log-scaled plots plot is found in the corresponding chapter (Fig. 5.27).

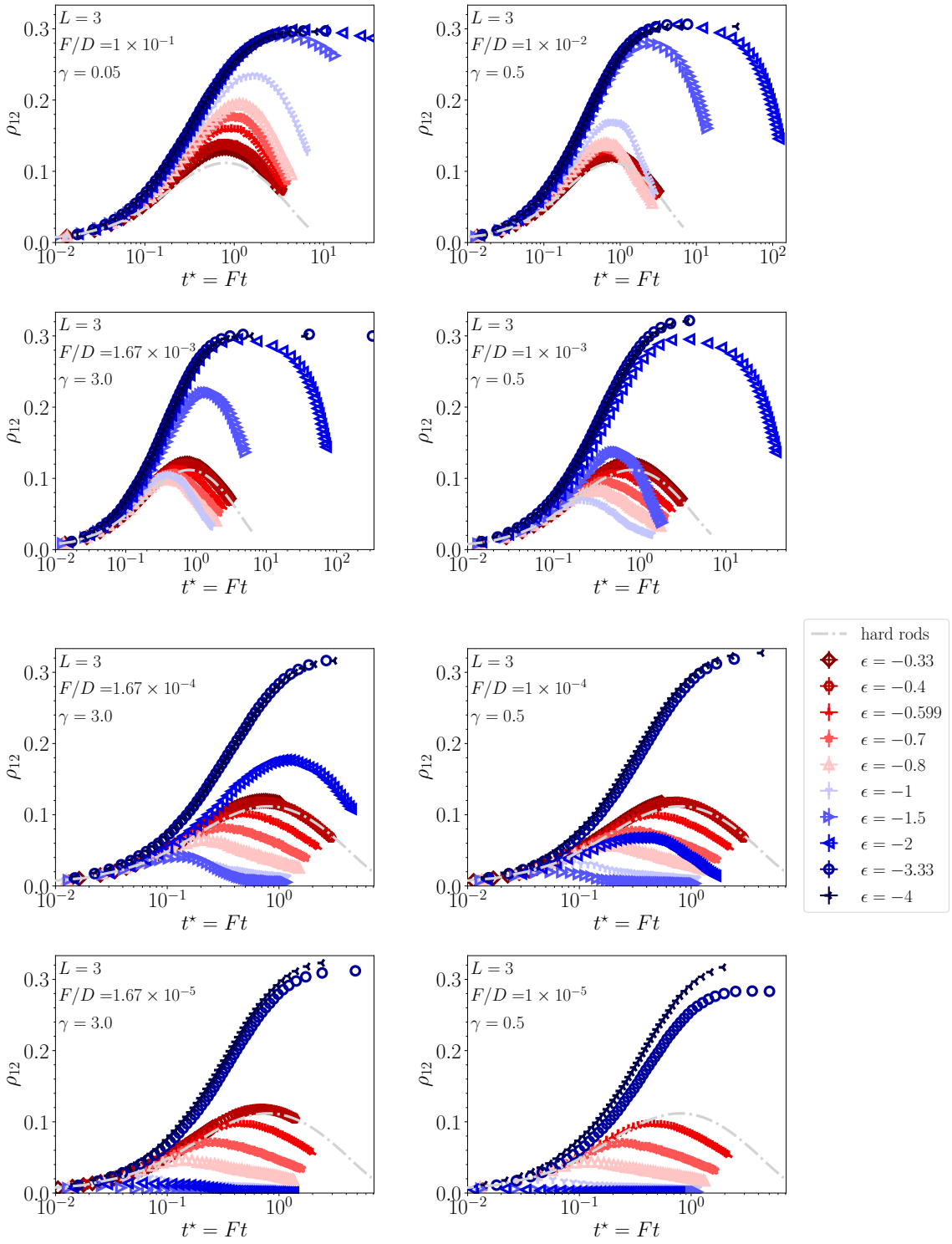

FIGURE A.11: Global density ρ_{12} of lying rods versus time $t^\star$ rescaled with the attempt flux rate (at a fixed F/D) for a sweep over attraction strengths ($L = 3$) for long times. Compare to Fig. 5.24.

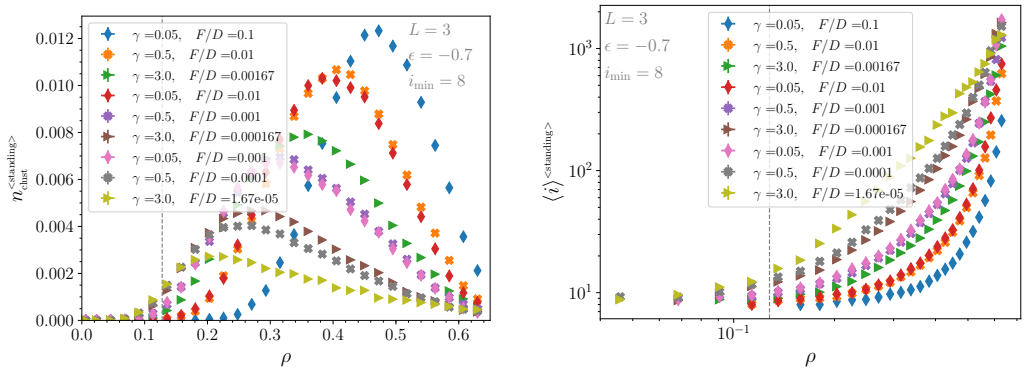

FIGURE A.12: Monolayer growth via deposition below first critical point at $\epsilon = -0.7$: Upright-cluster number density (left) and average size (right), calculated for clusters of size greater than $i_{\min}$. After hitting the binodal (dotted line), the clusters increase in number and size, though the onset for clusters larger than $i_{\min}$ is delayed for very fast F/D, which initially generates many *small* clusters.

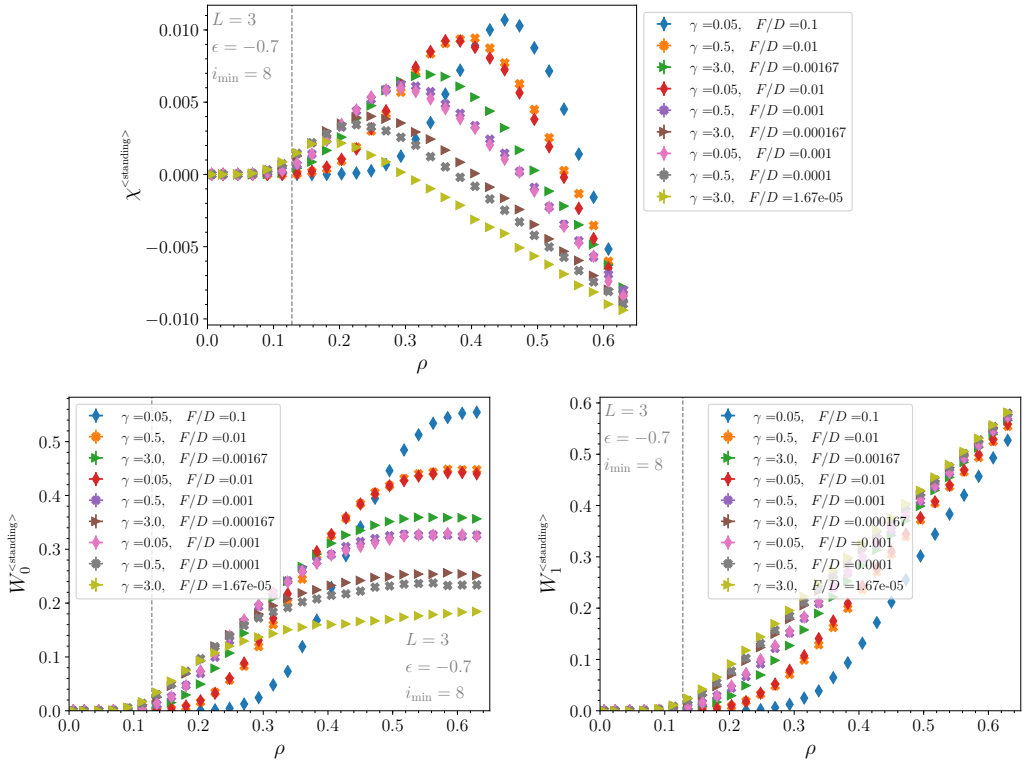

FIGURE A.13: Monolayer growth via deposition below first critical point at $\epsilon = -0.7$: Standing clusters and connected regions analyzed with Minkowski functionals: (Top) Euler characteristic of, (left) circumference of, (right) area of standing clusters. Compare Fig. A.12.

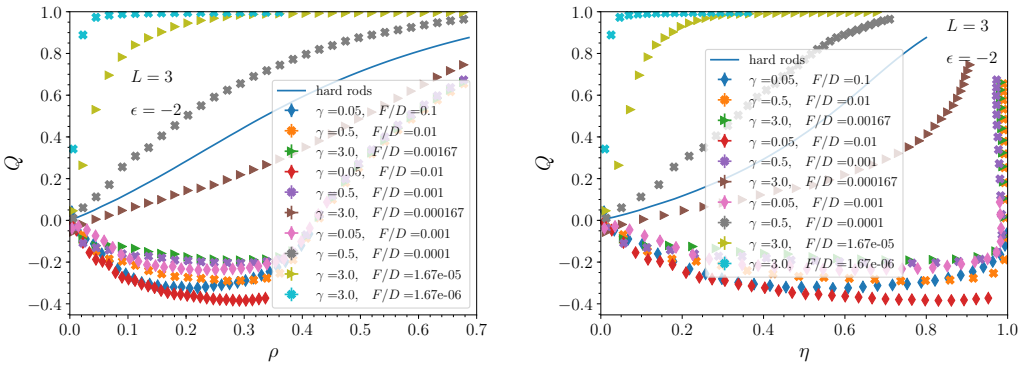

FIGURE A.14: Evolution of the order parameter Q versus number density (left) and surface packing fraction η (right) for system of hard rods with length $L = 3$ with sticky attraction $\epsilon = -2$, below the second critical point, shown for various sets of kinetics parameters $\{\gamma, F/D\}$. The solid curves are purely-hard rods ($\epsilon = 0$) in equilibrium.

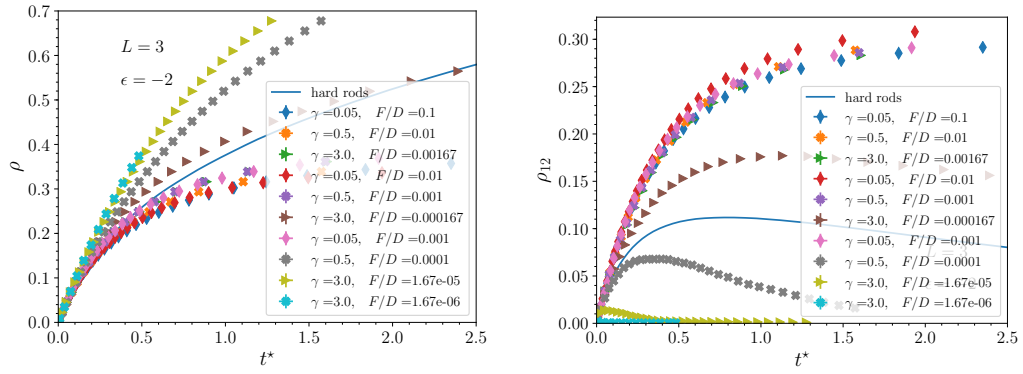

FIGURE A.15: Evolution of the density(left) and lying-rod density ρ_{12} (right) versus rescaled time for system of hard rods with length $L = 3$ with sticky attraction $\epsilon = -2$, shown for various sets of kinetics parameters $\{\gamma, F/D\}$. The solid curves represent purely-hard rods ($\epsilon = 0$) growing in quasiequilibrium.

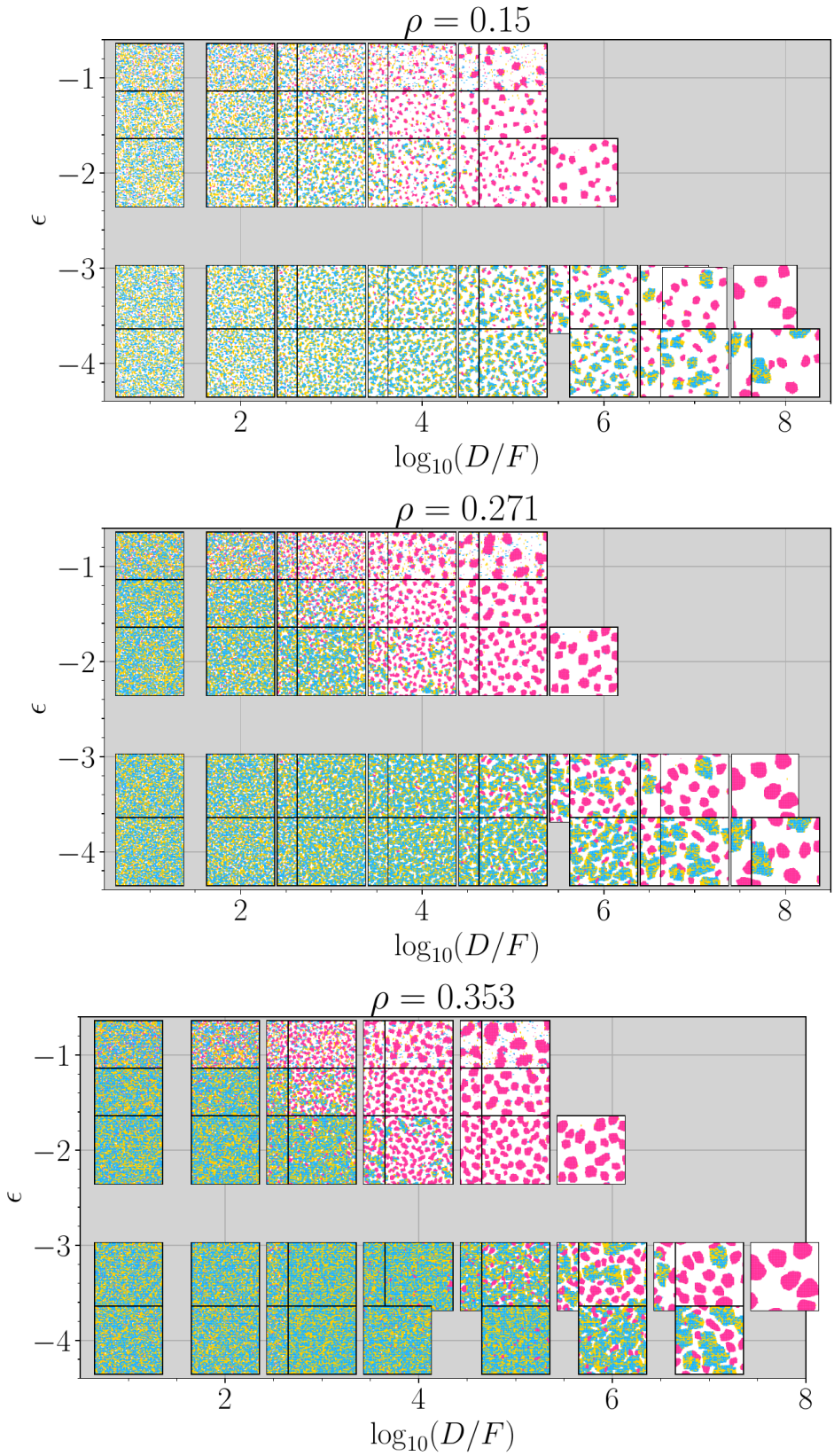

FIGURE A.16: Schematic overview of snapshots during growth as plotted in the $(\epsilon, D/F)$-plane at three different densities for regime III. This is for $L = 3$ and neutral substrates. Snapshots are approximately 128×128 unit-sized cutouts of the configurations, which are 256×256 in size.

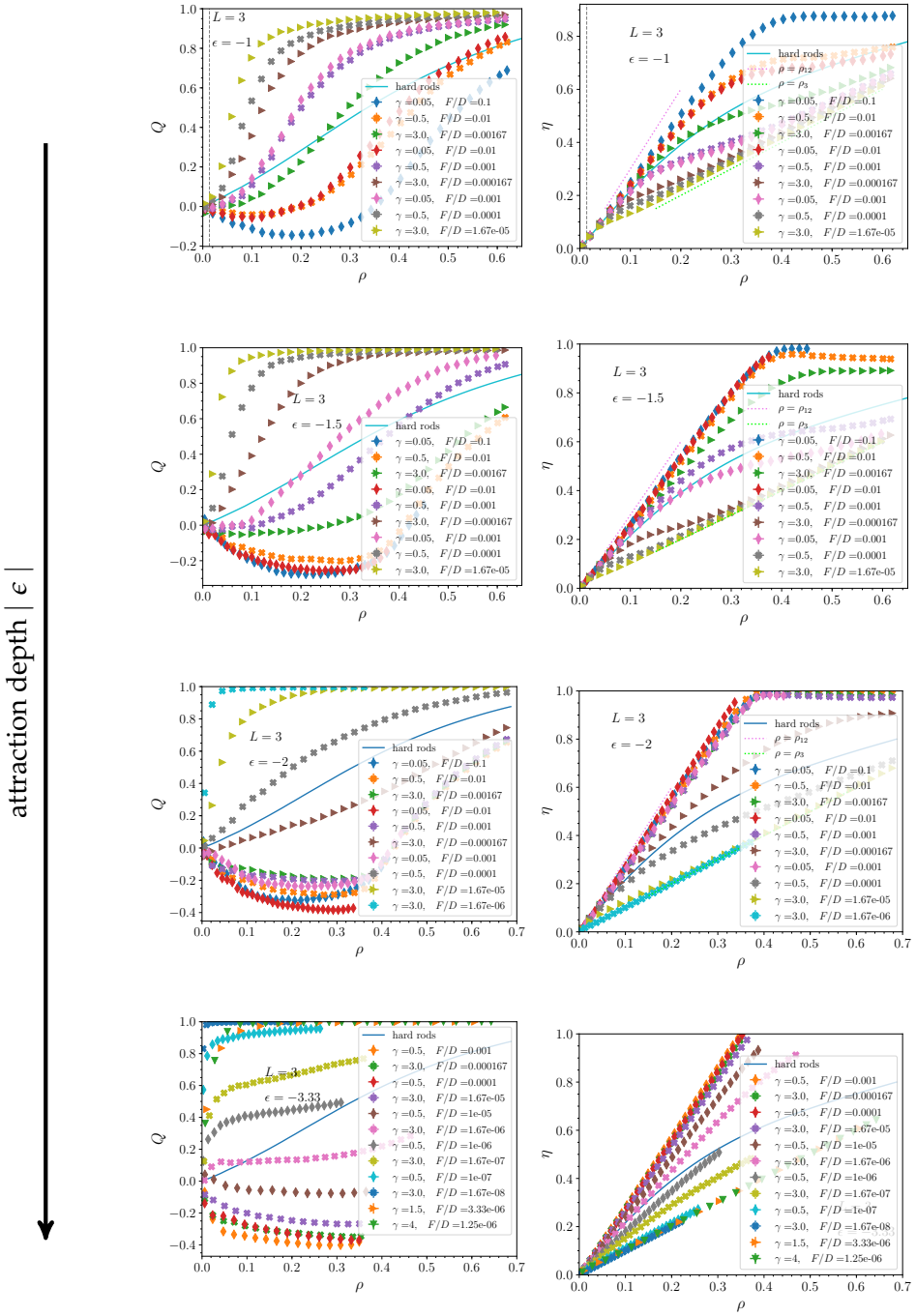

FIGURE A.17: Evolution of order parameter and packing fraction during monolayer growth for $\epsilon \in \{-1.0, -1.5, -2.0, -3.33\}$

TRANSLATIONALLY mobile particles:
variance of number density ρ_{mob} vs. monolayer number density ρ

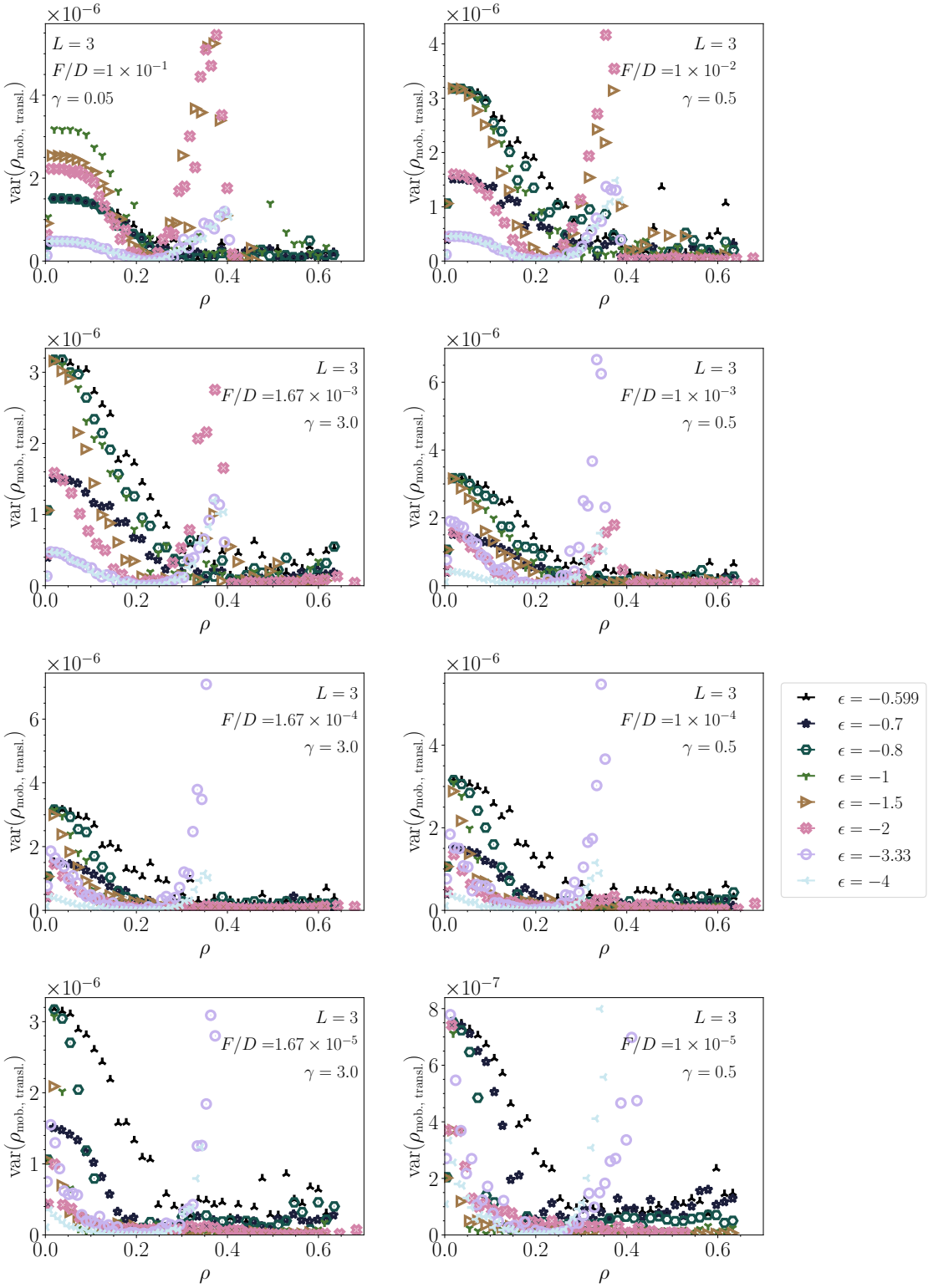

FIGURE A.18: Translationally mobile particles (out-of-plane rotations): Variance of number density ρ_{mob} versus global density ρ (at a fixed F/D) for a sweep over attraction strengths ($L = 3$). The variance was calculated from running bins of datapoints.

A.3 More results on growth at attractive substrates ($L = 3$)

We provide here additional plots in the analysis of growth of monolayers with sticky rods at attractive substrates (Ch. 5.5).

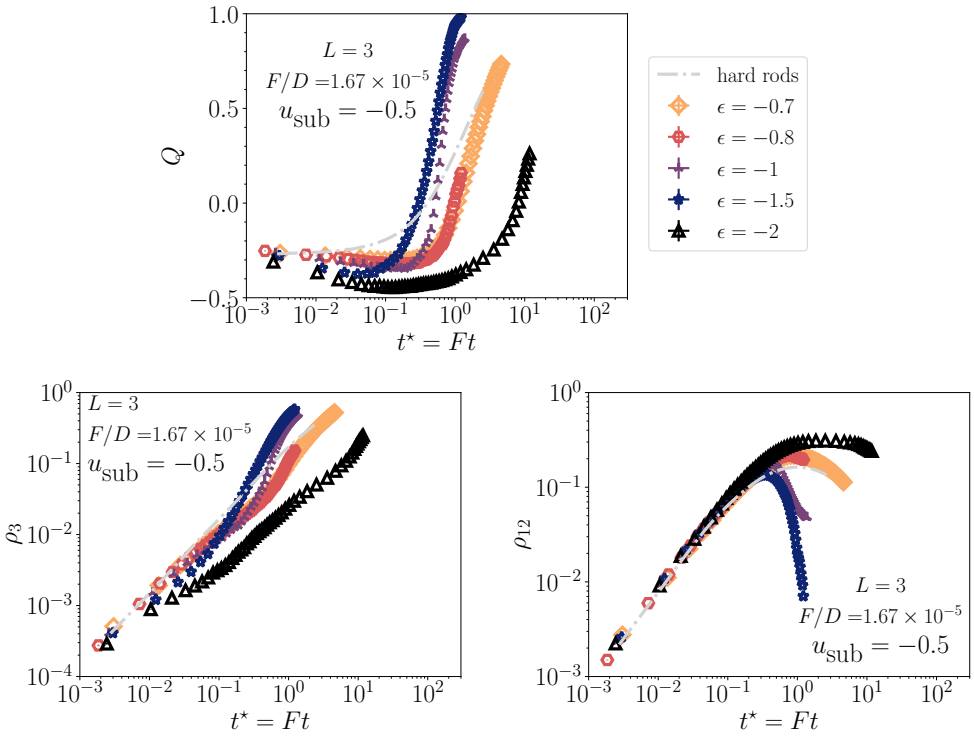

FIGURE A.19: Time-trace of global observables during growth with fixed conditions ($F/D = 1.67 \times 10^{-5}$) for weak substrate potentials $u_{\text{sub}} = -0.5$.

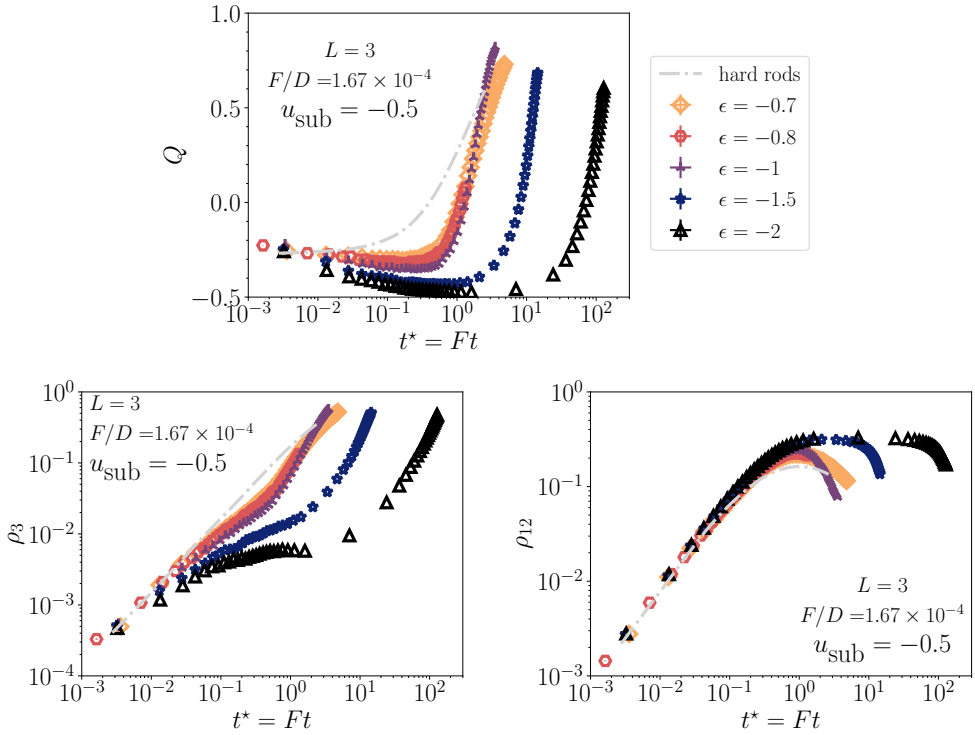

FIGURE A.20: Time-trace of global observables during growth with fixed conditions ($F/D = 1.67 \times 10^{-4}$) for weak substrate potentials $u_{\text{sub}} = -0.5$.

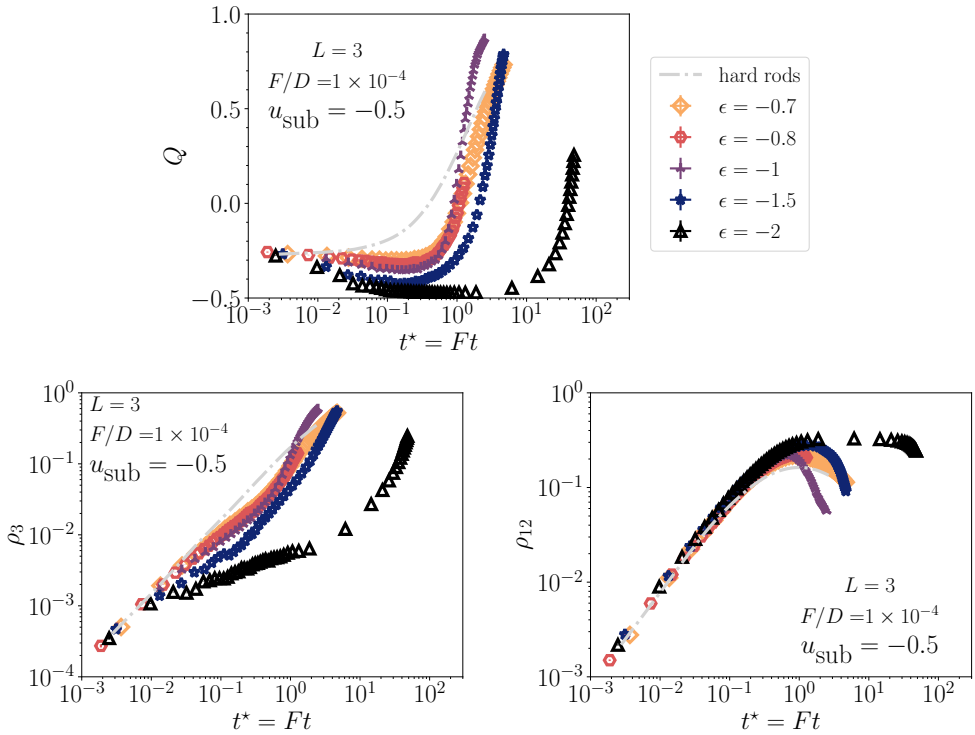

FIGURE A.21: Time-trace of global observables during growth with fixed conditions ($F/D = 1 \times 10^{-4}$) for weak substrate potentials $u_{\text{sub}} = -0.5$.

Appendix B

Appendix to study on variational autoencoders

This appendix pertains to Ch. 7.

B.1 Output space: quantitative comparisons for changing β

To quantify or gauge the 'physical' consistency of the VAE, we treat the output like true configurations of the "sticky" hard-rod system: We measure the error in quantities such as the inner energy, the fluctuations of order parameters, and gradients thereof, as all these can be calculated on the "field" quantities, i.e. pixel-wise at every channel and site, in both the output configurations as well as the input. Treating the images as local order parameter fields was key to successful and interpretable learning with VAEs, which we reported in Sec. 7.3. Therefore, in the section below we systematically probe the thermodynamic, and, therefore, physical "truthfulness" of the output data (conditioned on input) by applying the trained VAEs to test data in Gibbs-Boltzmann ensembles (just like the analysis above).

The reconstruction error, as well as error in inner energy, the angle of the 2D physical order parameter field, and the intensity of the gradients in the order-parameter fields are presented in Figure B.1. The reconstruction error (top left) does steadily suffer with higher β; the intensities of the gradients do, as well (bottom left). Yet, the error in the inner energy calculation and angle of the complex order parameter $\mathbf{c}$ do yield a more complex dependency. In particular, it appears as though $\beta = 10$ for this particular $\dim(\mathbf{z})$ is a bit "out of line". This is already *past* the threshold state, which is around $\beta = 9$ for $\dim(\mathbf{z}) = 128$.

The accuracy of the reconstructed configurations and their physical characteristics versus β depend crucially on the latent-space dimension, shown as a comparison in Fig. B.2 for a thinner and thicker network. The larger the latent-space dimension given (and the higher the capacity the network has), the more sensitive a VAE is to small changes in β.

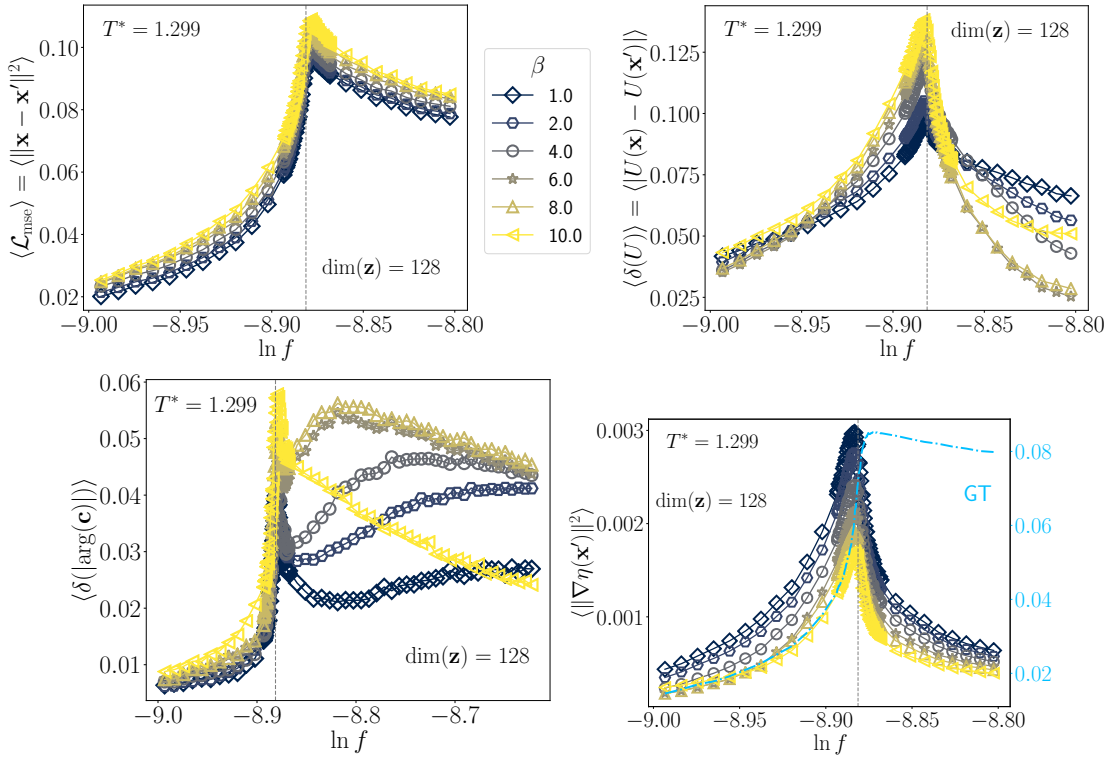

FIGURE B.1: VAEs with different β's: (Top left) reconstruction error, absolute error in reconstructed inner energy (top right) (normalized by lattice size $M^2 = 128^2$), (bottom left) that of the order parameter, and square gradient of the occupation probability in a configuration (with ground truth labeled "GT") versus log-fugacity for test data at $T^* = 1.299$, below the tricritical point. The gray lines indicates an estimate of the coexistence log-fugacity from the peak in $\text{var}(|S|/\rho)$. $\dim(\mathbf{z}) = 128$ for all VAEs.

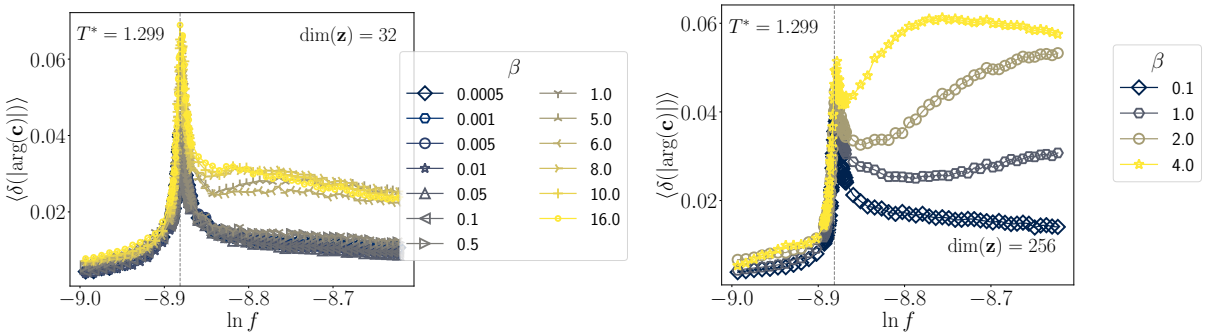

FIGURE B.2: VAEs with different β's: Comparison to Fig. B.1 (top right) for smaller and larger latent space dimension. Absolute error in reconstructed inner energy for (left) $\dim(\mathbf{z}) = 32$ and (right) $\dim(\mathbf{z}) = 256$, which has wider hidden layers (see text in Sec. 7.2.3.

B.2 Successively "turning on" latent variables (exploratory)

In this section, we present more results in an exploration of the learned latent representations. Let us consider a VAE near a threshold value of β, where the latent variables show a hierarchy, as described in Sec. 7.6. We can successively "turn on" latent variables of each image. This is possible because the latent variables over entire test data sets (i.e. over large spans of thermodynamic states) are centered around zero. (We found this in Sec. 7.5.) Figure B.3 shows quanti-

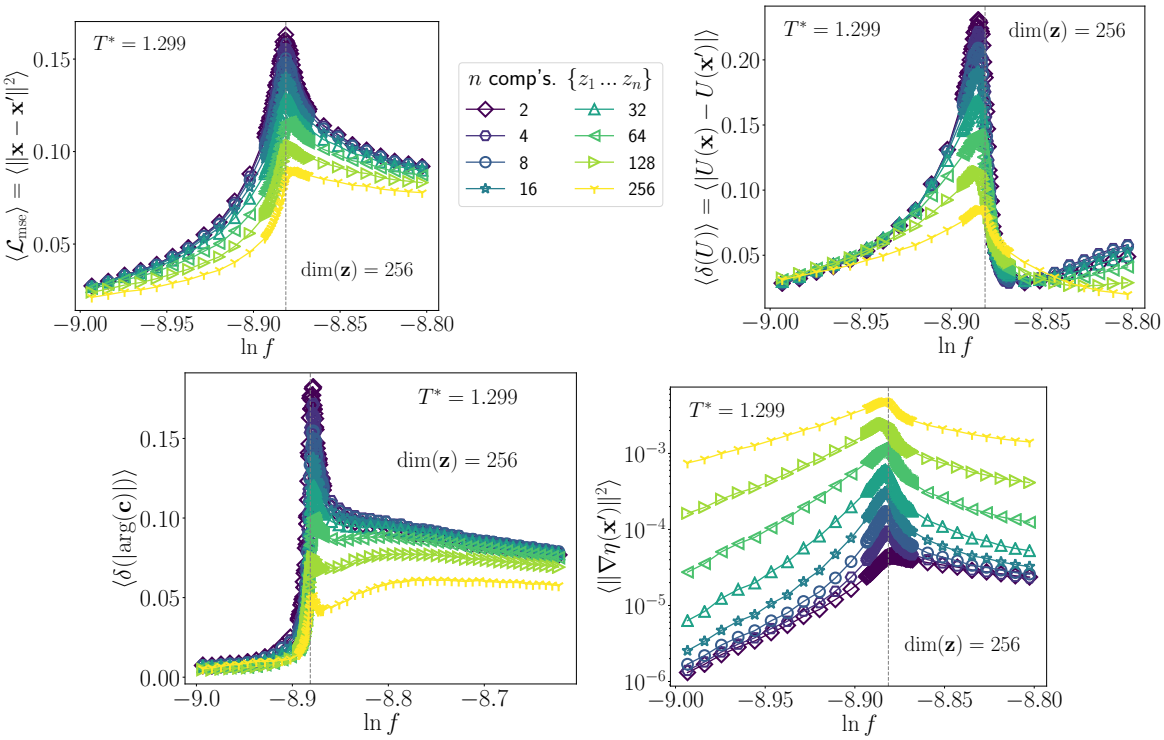

FIGURE B.3: Successively "turning on" variables in the latent space (fix others to zero) for VAEs that learned a pronounced coarse-graining hierarchy of collective variables (i.e. separated or "disentangled" spatial modes): Reconstruction error (top left), absolute error in reconstructed inner energy (top right), error in the order parameter (bottom left)and intensity of gradients (bottom right) versus log-fugacity for test data at $T^* = 1.299$, below the tricritical point. VAE with $\beta = 4$ and $\dim(\mathbf{z}) = 256$.

tative results of the *output* after applying this scheme: The reconstruction error (top left figure) behaves, remarkably, nearly identically to that contained in Fig. 7.11 which varies $\dim(\mathbf{z})$, instead. Hence, we might be "coarse-graining" the reconstructed images, at least judged by the nearly-even spacing of the curves (which represent exponential increases of the number of variables) in the mean-squared error. However, the inner energy (top right figure) reveals somewhat different behavior to the same observable found in Fig. 7.11. The same is true when observing the errors of the angle of the complex order parameter (bottom left figure) and intensity of the gradients (bottom right). Thus, this "coarse-graining" is only approximate. Visual inspection of the reconstructed

configurations after successively "turning on" variables (not shown here) attests to this. The variables are not exactly orthogonal to one another, so, the spatial modes still mix to some degree and are not cleanly separated into a hierarchy.

This mixing of spatial modes is the key feature of the latent variables for VAEs with small β, apparent in Figs. 7.34 and 7.35. We repeated the same experiment for this case of VAEs. The results of the reconstruction error in inner energy are presented in Fig. B.4. We report analogous behavior of all plots for other tested temperatures $T^* = 1.351, 1.333, 1.266$. The reconstruction error does not show near-even spacing between the curves for exponentially-increasing numbers of components. Interestingly, however, the error in the inner energy does show much more regular spacing in the demixed phase (past the phase transition point indicated in the vertical gray line). Moreover, the form of the curves is completely different compared to those in Fig. B.3 (top right). The inner energy is calculated using a multiplication operation over nearest-neighbor sites on the lattice: it contains information on correlations within each image. Hence, this error quantity seems to reflect the *total* information contained in all subsets of latent variables, while the mean-squared error (which is only a pixel-wise comparison) only does when the latent variables form a spatial coarse-graining hierarchy.

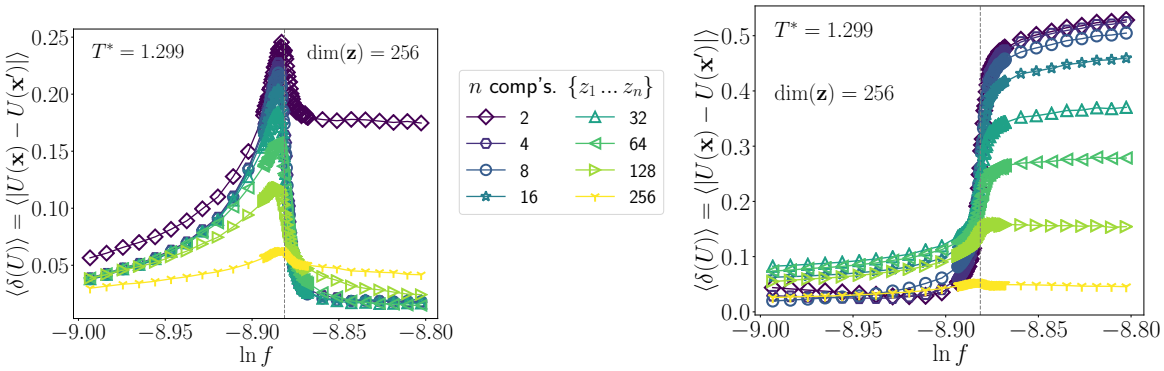

FIGURE B.4: Successively "turning on" variables in the latent space (fix others to zero) for VAEs that learned a weak coarse-graining hierarchy of collective variables (i.e. mixed of "entangled" spatial modes): Absolute error in reconstructed inner energy at $T^* = 1.299$, above the tricritical point. (left): $\beta = 1$ and (right): $\beta = 0.1$ (very weak) for $\dim(\mathbf{z}) = 256$. Contrast to Fig. B.3 (top row).

Bibliography

[1] G. Hlawacek and C. Teichert. "Nucleation and growth of thin films of rod-like conjugated molecules". In: *J. Phys. Condens. Matter* 25.14 (Mar. 2013), p. 143202. DOI: 10.1088/0953-8984/25/14/143202.

[2] G. Witte and C. Wöll. "Growth of aromatic molecules on solid substrates for applications in organic electronics". In: *J. Mater. Res.* 19.7 (Jan. 2004), pp. 1889–1916. DOI: 10.1557/JMR.2004.0251.

[3] F. Schreiber. "Organic molecular beam deposition: Growth studies beyond the first monolayer". In: *Phys. Status Solidi A* 201.6 (May 2004), pp. 1037–1054. DOI: 10.1002/pssa.200404334.

[4] P. Clancy. "Application of Molecular Simulation Techniques to the Study of Factors Affecting the Thin-Film Morphology of Small-Molecule Organic Semiconductors". In: *Chem. Mater.* 23.3 (2011), pp. 522–543. DOI: 10.1021/cm102231b.

[5] S. R. Forrest. "The Path to Ubiquitous and Low-Cost Organic Electronic Appliances on Plastic". In: *Nature* 428.6986 (2004), pp. 911–918. DOI: 10.1038/nature02498.

[6] S. Kowarik, A. Gerlach, and F. Schreiber. "Organic molecular beam deposition: fundamentals, growth dynamics, and *in situ* studies". In: *J. Phys. Condens. Matter* 20.18 (Apr. 2008), p. 184005. DOI: 10.1088/0953-8984/20/18/184005.

[7] A. O. F. Jones et al. "Substrate-Induced and Thin-Film Phases: Polymorphism of Organic Materials on Surfaces". In: *Adv. Funct. Mater.* 26.14 (2016), pp. 2233–2255. DOI: 10.1002/adfm.201503169.

[8] Q. Wang et al. "Heteromolecular Bilayers on a Weakly Interacting Substrate: Physisorptive Bonding and Molecular Distortions of Copper-Hexadecafluorophthalocyanine". In: *ACS Appl. Mater. Interfaces* 12.12 (2020). PMID: 32109044, pp. 14542–14551. DOI: 10.1021/acsami.9b22812.

[9] S. Kowarik et al. "Real-Time Observation of Structural and Orientational Transitions during Growth of Organic Thin Films". In: *Phys. Rev. Lett.* 96.12 (Mar. 2006), p. 125504. DOI: 10.1103/PhysRevLett.96.125504.

[10] S.-W. Chen et al. "Adsorption of Phenacenes on a Metallic Substrate: Revisited". In: *J. Phys. Chem. C* 121.21 (2017), pp. 11390–11398. DOI: 10.1021/acs.jpcc.7b01806.

[11] J. Niederhausen et al. "Tetracene Ultrathin Film Growth on Hydrogen-Passivated Silicon". In: *Langmuir* 36.31 (2020). PMID: 32659091, pp. 9099–9113. DOI: 10.1021/acs.langmuir.0c01154.

[12] A. J. Fleming, F. P. Netzer, and M. G. Ramsey. "Nucleation and 3D growth ofpara-sexiphenyl nanostructures from an oriented 2D liquid layer investigated by photoemission electron microscopy". In: *J. Phys. Condens. Matter* 21.44 (Oct. 2009), p. 445003. DOI: 10.1088/0953-8984/21/44/445003.

[13] J. Yang et al. "Ultrathin-Film Growth of para-Sexiphenyl (II): Formation of Large-Size Domain and Continuous Thin Film". In: *J. Phys. Chem. B* 112.26 (2008). PMID: 18529074, pp. 7821–7825. DOI: 10.1021/jp711457p.

[14] W. Belza et al. "Molecular Structure and Electronic Properties of para-Hexaphenyl Monolayer on Atomically Flat Rutile TiO2(110)". In: *J. Phys. Chem. C* 124.10 (2020), pp. 5681–5689. DOI: 10.1021/acs.jpcc.9b11533.

[15] S. E. Fritz et al. "Structural Characterization of a Pentacene Monolayer on an Amorphous SiO2 Substrate with Grazing Incidence X-ray Diffraction". In: *J. Am. Chem. Soc.* 126.13 (2004). PMID: 15053579, pp. 4084–4085. DOI: 10.1021/ja049726b.

[16] J. Götzen et al. "Growth and structure of pentacene films on graphite: Weak adhesion as a key for epitaxial film growth". In: *Phys. Rev. B* 81.8 (Feb. 2010), p. 085440. DOI: 10.1103/PhysRevB.81.085440.

[17] J. K. G. Dhont. *An Introduction to Dynamics of Colloids*. First Edition. Vol. 2. Studies in Interface Science. Elsevier Science, 1996. ISBN: 9780080535074.

[18] P.G. Bolhuis. "Liquid-like behavior in solids, solid-like behavior in liquids: computer simulation of phase transitions in colloidal dispersions". Doctoral Thesis. Utrecht University, 1996. URL: https://dspace.library.uu.nl/bitstream/handle/1874/10403/frenkeL_96_liquids-like_behavior_solids.pdf.

[19] V. J. Anderson and H. N.W. Lekkerkerker. "Insights into phase transition kinetics from colloid science". In: *Nature* 416.6883 (2002), pp. 811–815. DOI: 10.1038/416811a.

[20] Thomas Michely and Joachim Krug. *Islands, Mounds and Atoms: Patterns and Processes in Crystal Growth Far from Equilibrium*. Vol. 42. Springer Series in Surface Sciences. Springer-Verlag Berlin Heidelberg, 2004. ISBN: 978-3-642-62237-3.

[21] Alberto Pimpinelli and Jacques Villain. *Physics of Crystal Growth*. Cambridge: Cambridge University Press, 1998. ISBN: 978-0-521-55198-4.

[22] A. P. J. Jansen. *An Introduction to Kinetic Monte Carlo Simulations of Surface Reactions*. Vol. 856. Lecture Notes in Physics. Springer-Verlag Berlin Heidelberg, 2012. DOI: 10.1007/978-3-642-29488-4.

[23] A. B. Bortz, M. H. Kalos, and J. L. Lebowitz. "A new algorithm for Monte Carlo simulation of Ising spin systems". In: *J. Comput. Phys.* 17.1 (1975), pp. 10–18. ISSN: 0021-9991. DOI: 10.1016/0021-9991(75)90060-1.

[24] A. F. Voter. "Introduction to the Kinetic Monte Carlo Method". In: *Radiation Effects in Solids*. Ed. by Kurt E. Sickafus, Eugene A. Kotomin, and Blas P. Uberuaga. Dordrecht: Springer Netherlands, 2007, pp. 1–23. ISBN: 978-1-4020-5295-8.

[25] M. Dijkstra. "Entropy-Driven Phase Transitions in Colloids: From spheres to anisotropic particles". In: *Adv. Chem. Phys.* John Wiley & Sons, Ltd, 2014. Chap. 2, pp. 35–71. ISBN: 9781118949702. DOI: 10.1002/9781118949702.ch2.

[26] Jean-Pierre Hansen and Ian R. McDonald. *Theory of Simple Liquids with Applications to Soft Matter*. Fourth Edition. Oxford: Elsevier Ltd., 2013. ISBN: 978-0-12-387032-2.

[27] Y. Rosenfeld. "Scaled field particle theory of the structure and the thermodynamics of isotropic hard particle fluids". In: *J. Chem. Phys.* 89.7 (1988), pp. 4272–4287. DOI: 10.1063/1.454810.

[28] Y. Rosenfeld. "Free-energy model for the inhomogeneous hard-sphere fluid mixture and density-functional theory of freezing". In: *Phys. Rev. Lett.* 63.9 (Aug. 1989), pp. 980–983. DOI: 10.1103/PhysRevLett.63.980.

[29] Y. Rosenfeld, D. Levesque, and J.-J. Weis. "Free-energy model for the inhomogeneous hard-sphere fluid mixture: Triplet and higher-order direct correlation functions in dense fluids". In: *J. Chem. Phys.* 92.11 (1990), pp. 6818–6832. DOI: 10.1063/1.458268.

[30] R. Roth. "Fundamental measure theory for hard-sphere mixtures: a review". In: *J. Phys. Condens. Matter* 22.6 (Jan. 2010), p. 063102. DOI: 10.1088/0953-8984/22/6/063102.

[31] R. Evans. "The nature of the liquid-vapour interface and other topics in the statistical mechanics of non-uniform, classical fluids". In: *Adv. Phys.* 28.2 (1979), pp. 143–200. DOI: 10.1080/00018737900101365.

[32] H. Löwen. "Density functional theory of inhomogeneous classical fluids: recent developments and new perspectives". In: *J. Phys. Condens. Matter* 14.46 (Nov. 2002), pp. 11897–11905. DOI: 10.1088/0953-8984/14/46/301.

[33] P. Tarazona, J. A. Cuesta, and Y. Martínez-Ratón. "Density Functional Theories of Hard Particle Systems". In: *Theory and Simulation of Hard-Sphere Fluids and Related Systems*. Ed. by Ángel Mulero. Berlin, Heidelberg: Springer Berlin Heidelberg, 2008, pp. 247–341. ISBN: 978-3-540-78767-9. DOI: 10.1007/978-3-540-78767-9_7.

[34] U. M. B. Marconi and P. Tarazona. "Dynamic density functional theory of fluids". In: *J. Chem. Phys.* 110.16 (1999), pp. 8032–8044. DOI: 10.1063/1.478705.

[35] A. J. Archer and R. Evans. "Dynamical density functional theory and its application to spinodal decomposition". In: *J. Chem. Phys.* 121.9 (2004), pp. 4246–4254. DOI: 10.1063/1.1778374.

[36] A. J. Archer and M. Rauscher. "Dynamical density functional theory for interacting Brownian particles: stochastic or deterministic?" In: *J. Phys. A* 37.40 (Sept. 2004), pp. 9325–9333. DOI: 10.1088/0305-4470/37/40/001.

[37] M. te Vrugt, H. Löwen, and R. Wittkowski. "Classical dynamical density functional theory: from fundamentals to applications". In: *Adv. Phys.* 69.2 (2020), pp. 121–247. DOI: 10.1080/00018732.2020.1854965.

[38] Kurt Binder and Dieter W. Heermann. *Monte Carlo Simulation in Statistical Physics: An Introduction*. Fifth Edition. Graduate Texts in Physics. Berlin, Heidelberg: Springer, 2010. ISBN: 978-3-642-03162-5.

[39] P. G. de Gennes and J. Prost. *The Physics of Liquid Crystals*. Ed. by J. Birman et al. Second Edition. The International Series of Monographs on Physics. Oxford: Oxford Univeristy Press, 1993. ISBN: 0 19 852024 7.

[40] L. Mederos, E. Velasco, and Y. Martínez-Ratón. "Hard-body models of bulk liquid crystals". In: *J. Phys. Condens. Matter* 26.46 (Oct. 2014), p. 463101. DOI: 10.1088/0953-8984/26/46/463101.

[41] L. Onsager. "The effects of shape on the interaction of colloidal particles". In: *Ann. NY Acad. Sci.* 51.4 (May 1949), pp. 627–659. DOI: 10.1111/j.1749-6632.1949.tb27296.x.

[42] P. Bolhuis and D. Frenkel. "Tracing the phase boundaries of hard spherocylinders". In: *J. Chem. Phys.* 106.2 (1997), pp. 666–687. DOI: 10.1063/1.473404.

[43] E. Ising. "Beitrag zur Theorie des Ferromagnetismus". In: *Z. Phys.* 31.1 (Feb. 1925), pp. 253–258. ISSN: 0044-3328. DOI: 10.1007/BF02980577.

[44] L. P. Kadanoff et al. "Static Phenomena Near Critical Points: Theory and Experiment". In: *Rev. Mod. Phys.* 39.2 (Apr. 1967), pp. 395–431. DOI: 10.1103/RevModPhys.39.395.

[45] K. G. Wilson. "Problems in physics with many scales of length". In: *Sci. Am.* 241.2 (1979), pp. 158–179. DOI: 10.1038/scientificamerican0879-158.

[46] F. Y. Wu. "The Potts model". In: *Rev. Mod. Phys.* 54.1 (Jan. 1982), pp. 235–268. DOI: 10.1103/RevModPhys.54.235.

[47] James P. Sethna. *Statistical Mechanics: Entropy, Order Parameters and Complexity*. Oxford Master Series in Physics. OUP Oxford, 2006. ISBN: 9780198566779.

[48] Linda E. Reichl. *A Modern Course in Statistical Physics*. 4th revised and updated edition. Weinheim, Germany: WILEY-VCH Verlag GmbH & Co. KGaA, 2016. ISBN: 978-3-527-69046-6.

[49] David A. Lavis. *Equilibrium Statistical Mechanics of Lattice Models*. Theoretical and Mathematical Physics. Dordrecht: Springer Science+Business Media, 2015. ISBN: 978-94-017-9430-5. DOI: 10.1007/978-94-017-9430-5.

[50] D. P. Kingma and M. Welling. "Auto-Encoding Variational Bayes". In: *Proc. of the 2nd Intl. Conf. on Learning Representations, ICLR 2014, Banff, AB, Canada, April 14–16, 2014, Conference Track Proceedings*. Ed. by Y. Bengio and Y. LeCun. 2014.

[51] D. J. Rezende, S. Mohamed, and D. Wierstra. "Stochastic Backpropagation and Approximate Inference in Deep Generative Models". In: *Proc. of the 31th Intl. Conf. on Machine Learning, ICML, 21–26 June 2014*. Vol. 32. JMLR Workshop and Conference Proceedings. Beijing, China: JMLR.org, 2014, pp. 1278–1286.

[52] I. Higgins et al. "beta-VAE: Learning Basic Visual Concepts with a Constrained Variational Framework". In: *Proc. of the 5th International Conference on Learning Representations, ICLR 2017, Toulon, France, April 24-26, 2017, Conference Track Proceedings*. OpenReview.net, 2017.

[53] L. P. Kadanoff. "More is the same; phase transitions and mean field theories". In: *J. Stat. Phys.* 137.5-6 (2009), p. 777. DOI: 10.1007/s10955-009-9814-1.

[54] R. Peierls. "On Ising's model of ferromagnetism". In: *Math. Proc. Cambridge* 32.3 (1936), pp. 477–481. DOI: 10.1017/S0305004100019174.

[55] R. B. Griffiths. "Peierls Proof of Spontaneous Magnetization in a Two-Dimensional Ising Ferromagnet". In: *Phys. Rev.* 136.2A (Oct. 1964), A437–A439. DOI: 10.1103/PhysRev.136.A437.

[56] P. C. Hohenberg and B. I. Halperin. "Theory of dynamic critical phenomena". In: *Rev. Mod. Phys.* 49.3 (July 1977), pp. 435–479. DOI: 10.1103/RevModPhys.49.435.

[57] Istvan Montvay and Gernot Münster. *Quantum Fields on a Lattice*. Cambridge, UK: Cambridge University Press, 1994. ISBN: 0 521 40432 0.

[58] David A. Lavis and George M. Bell. *Statistical Mechanics of Lattice Systems: Volume 2: Exact, Series and Renormalization Group Methods*. Texts and Monographs in Physics. Springer-Verlag Berlin Heidelberg GmbH, 1999. ISBN: 978-3-642-08410-2. DOI: 10.1007/978-3-662-10020-2.

[59] H. N. W. Lekkerkerker and A. Stroobants. "Phase Behaviour of Rod-like Colloid + Flexible Polymer Mixtures". In: *Il Nuovo Cimento D* 16 (1994), p. 949. DOI: 10.1007/BF02458781.

[60] P. G. Bolhuis et al. "Numerical study of the phase behavior of rodlike colloids with attractive interactions". In: *J. Chem. Phys.* 107.5 (1997), pp. 1551–1564. DOI: 10.1063/1.474508.

[61] M. E. J. Newman and G. T. Barkema. *Monte Carlo Methods in Statistical Physics*. Oxford: Oxford University Press, 1999. ISBN: 9780198517979.

[62] D. P. Landau and K. Binder. *A Guide to Monte Carlo Simulations in Statistical Physics*. Third Edition. Cambridge: Cambridge University Press, 2009, p. 471. ISBN: 978-0-521-76848-1.

[63] Werner Krauth. *Statistical Mechanics: Algorithms and Computations*. First publ. Edition. Oxford Master Series in Statistical, Computational, and Theoretical Physics. Oxford et al.: Oxford University Press, 2006, p. 342. ISBN: 978-0-19-851536-4.

[64] Roger Balian. *From Microphysics to Macrophysics: Methods and Applications of Statistical Physics*. Study Edition. Vol. I. Theoretical and Mathematical Physics. Original French edition: *Du microscopique au macroscopiqite*, Cours de l'Ecole Polytechnique, Ellipses, 1982 Edition Marketing S.a.r.L Paris. Springer-Verlag Berlin Heidelberg, 2007. ISBN: 3-540-45469-1.

[65] Mehran Kardar. *Statistical Physics of Fields*. Cambridge: Cambridge University Press, 2007. ISBN: 978-0-521-87341-3.

[66] Jean Zinn-Justin. *Phase Transitions and Renormalization Group*. Oxford, New York: Oxford University Press, Inc., 2007. ISBN: 978-0-19-922719-8.

[67] Giorgio Parisi. *Statistical Field Theory*. Reading, MA: Addison-Wesley Publishing Company, Inc., 1988. ISBN: 0-201-05985-1.

[68] Akira Onuki. *Phase Transition Dynamics*. Cambridge: Cambridge University Press, 2004. ISBN: 0511-03974-3.

[69] R. Evans et al. "New developments in classical density functional theory". In: *J. Phys. Condens. Matter* 28.24 (Apr. 2016), p. 240401. DOI: 10.1088/0953-8984/28/24/240401.

[70] S. Asakura and F. Oosawa. "On Interaction between Two Bodies Immersed in a Solution of Macromolecules". In: *J. Chem. Phys.* 22.7 (1954), pp. 1255–1256. DOI: 10.1063/1.1740347.

[71] Kerson Huang. *Statistical Mechanics*. Second Edition. First published in 1963. New York: John Wiley & Sons, 1987. ISBN: 0471815187.

[72] M. Mortazavifar and M. Oettel. "Phase diagrams for sticky rods in bulk and in a monolayer from a lattice free-energy functional for anisotropic particles with depletion attractions". In: *Phys. Rev. E* 96.3 (Sept. 2017), p. 032608. DOI: 10.1103/PhysRevE.96.032608.

[73] P. C. W. Davies and S. I. Walker. "The hidden simplicity of biology". In: *Rep. on Prog. Phys.* 79.10 (Sept. 2016), p. 102601. DOI: 10.1088/0034-4885/79/10/102601.

[74] D. H. Wolpert. "The stochastic thermodynamics of computation". In: *J. Phys. A* 52.19 (Apr. 2019), p. 193001. DOI: 10.1088/1751-8121/ab0850.

[75] J. M. R. Parrondo, J. M. Horowitz, and T. Sagawa. "Thermodynamics of information". In: *Nat. Phys.* 11.2 (2015), p. 131. DOI: 10.1038/nphys3230.

[76] M. C. Cross and P. C. Hohenberg. "Pattern formation outside of equilibrium". In: *Rev. Mod. Phys.* 65.3 (July 1993), pp. 851–1112. DOI: 10.1103/RevModPhys.65.851.

[77] J. P. Gollub and J. S. Langer. "Pattern formation in nonequilibrium physics". In: *Rev. Mod. Phys.* 71.2 (Mar. 1999), S396–S403. DOI: 10.1103/RevModPhys.71.S396.

[78] *The Blind Watchmaker*. London: Penguin Group, 2006. ISBN: 0141026162.

[79] B. B. Machta et al. "Parameter Space Compression Underlies Emergent Theories and Predictive Models". In: *Science* 342.6158 (2013), pp. 604–607. ISSN: 0036-8075. DOI: 10.1126/science.1238723.

[80] C. R. Shalizi, K. L. Shalizi, and R. Haslinger. "Quantifying Self-Organization with Optimal Predictors". In: *Phys. Rev. Lett.* 93.11 (Sept. 2004), p. 118701. DOI: 10.1103/PhysRevLett.93.118701.

[81] J. P. Eckmann and D. Ruelle. "Ergodic theory of chaos and strange attractors". In: *Rev. Mod. Phys.* 57.3 (July 1985), pp. 617–656. DOI: 10.1103/RevModPhys.57.617.

[82] G. Nicolis and D. Daems. "Probabilistic and thermodynamic aspects of dynamical systems". In: *Chaos* 8.2 (1998), pp. 311–320. DOI: 10.1063/1.166313.

[83] G. Nicolis. "Dissipative systems". In: *Rep. Prog. Phys.* 49.8 (Aug. 1986), pp. 873–949. DOI: 10.1088/0034-4885/49/8/002.

[84] G. Nicolis and C. Nicolis. "Chaotic dynamics, Markovian coarse-graining and information". In: *Physica A* 163.1 (1990), pp. 215–231. ISSN: 0378-4371. DOI: 10.1016/0378-4371(90)90331-L.

[85] J. C. Mauro, P. K. Gupta, and R. J. Loucks. "Continuously broken ergodicity". In: *J. Chem. Phys.* 126.18 (2007), p. 184511. DOI: 10.1063/1.2731774.

[86] Ludwig Boltzmann. *Vorlesungen über Gastheorie, I. Theil: Theorie des Gase mit einatomigen Molekülen, deren dimensionen gegen die Mittlere weglänge verschwinden*. Vol. 1. JA Barth, 1896.

[87] R. H. Fowler. *Statistical Mechanics: The Theory of the Properties of Matter in Equilibrium*. 1955 reprinted from the 1936 second edition. First publication in 1929. London, New York: The Syndics of the Cambridge University Press, 1936.

[88] Richard C. Tolman. *The Principles of Statistical Mechanics*. Dover Edition (from the original 1938 Oxford University Press Edition). Dover Publications, Inc., 1979. ISBN: 0-486-63896-0.

[89] Josiah Willard Gibbs. *Elementary principles in statistical mechanics: developed with especial reference to the rational foundation of thermodynamics*. Cambridge, USA: Yale Univeristy Press, 1902.

[90] Oliver Penrose. *Foundations of Statistical Mechanics: A Deductive Treatment*. Ed. by D. Ter Haar. First Edition. Vol. 22. International Series in Monographs in Natural Philosophy. Pergamon Press Ltd., 1970. ISBN: 978-0-08-013314-0.

[91] Walter T. Grandy, Jr. *Foundations of Statistical Mechanics*. Vol. II: Nonequilibrium Phenomena. Dordecht: D. Reidel Publishing Company, 1987. ISBN: 90-277-2649-3.

[92] S. Pressé et al. "Principles of maximum entropy and maximum caliber in statistical physics". In: *Rev. Mod. Phys.* 85.3 (July 2013), pp. 1115–1141. DOI: 10.1103/RevModPhys.85.1115.

[93] Robert Zwanzig. *Nonequilibrium Statistical Mechanics*. New York: Oxford University Press, 2001. ISBN: 9781429401814.

[94] Radu Balescu. *Equilibrium and Nonequilibrium Statistical Mechanics*. New York: John Wiley & Sons, Inc., 1975. ISBN: 0-471-04600-0.

[95] Radu Balescu. *Statistical Dynamics: Matter Out of Equilibrium*. London: Imperial College Press, 1997. ISBN: 1-86094-046-3.

[96] R. Kubo, M. Toda, and N. Hashitsume. *Statistical Physics II: Nonequilibrium Statistical Mechanics*. Ed. by P. Fulde. Vol. 31. Springer Series in Solid-State Sciences, [*Series Editors:* M. Cardona and H. -J. Queisser]. Springer-Verlag Berlin Heidelberg, 1985. ISBN: 3-540-11461-0.

[97] D. Evans and G. Morris. *Statistical Mechanics of Nonequilibrium Liquids*. Second Edition. Cambridge et al.: Cambridge University Press, 2008. ISBN: 978-0-511-39864-3.

[98] L. Zdeborová and F. Krzakala. "Statistical physics of inference: Thresholds and algorithms". In: *Adv. Phys.* 65.5 (2016), pp. 453–552. DOI: 10.1080/00018732.2016.1211393.

[99] J. Barbier et al. "Optimal errors and phase transitions in high-dimensional generalized linear models". In: *Proc. Nat. Acad. Sci.* 116.12 (2019), pp. 5451–5460. ISSN: 0027-8424. DOI: 10.1073/pnas.1802705116.

[100] Stephen L. Adler. *Quantum theory as an emergent phenomenon: The statistical mechanics of matrix models as the precursor of quantum field theory*. Cambridge: Cambridge University Press, 2004. ISBN: 0-511-21655-6.

[101] Gerard 't Hooft. *The cellular automaton interpretation of quantum mechanics*. Vol. 185. Fundamental Theories of Physics. Springer New York, 2016. ISBN: ISBN 978-3-319-41285-6. DOI: 10.1007/978-3-319-41285-6.

[102] V. Vanchurin. *Towards a theory of machine learning*. arXiv e-prints. 2020. arXiv: 2004.09280 [cs.LG].

[103] W. van Megen and H. J. Schöpe. "The cage effect in systems of hard spheres". In: *J. Chem. Phys.* 146.10 (2017), p. 104503. DOI: 10.1063/1.4977523.

[104] D. Chandler and J. P. Garrahan. "Dynamics on the Way to Forming Glass: Bubbles in Space-Time". In: *Ann. Rev. Phys. Chem.* 61.1 (2010). PMID: 20055676, pp. 191–217. DOI: 10.1146/annurev.physchem.040808.090405.

[105] J. S. Langer. "Theories of glass formation and the glass transition". In: *Rep. on Prog. in Phys* 77.4 (Mar. 2014), p. 042501. DOI: 10.1088/0034-4885/77/4/042501.

[106] E. D. Zanotto and J. C. Mauro. "The glassy state of matter: Its definition and ultimate fate". In: *J. Non-Cryst. Solids* 471 (2017), pp. 490–495. ISSN: 0022-3093. DOI: 10.1016/j.jnoncrysol.2017.05.019.

[107] R. Klages, G. Radons, and I. M. Sokolov, eds. *Anomalous transport: Foundations and Applications*. Weinheim: WILEY-VCH Verlag GmbH & Co. KGaA, 2008. ISBN: 978-3-527-40722-4.

[108] Y. Bengio. "Learning Deep Architectures for AI". In: *Found. Trends Mach. Learn.* 2.1 (Jan. 2009), pp. 1–127. ISSN: 1935-8237. DOI: 10.1561/2200000006.

[109] Y. Bengio, A. Courville, and P. Vincent. "Representation Learning: A Review and New Perspectives". In: *IEEE T. Pattern Anal.* 35.8 (Aug. 2013), pp. 1798–1828. ISSN: 1939-3539. DOI: 10.1109/TPAMI.2013.50.

[110] Y. Bengio et al. "Deep Generative Stochastic Networks Trainable by Backprop". In: *Proc. of the 31th International Conference on Machine Learning, ICML 2014, Beijing, China, 21-26 June 2014*. Vol. 32. JMLR Workshop and Conference Proceedings. JMLR.org, 2014, pp. 226–234.

[111] I. Goodfellow et al. "Generative Adversarial Nets". In: *Adv. Neur. In.* Ed. by Z. Ghahramani et al. Vol. 27. Curran Associates, Inc., 2014, pp. 2672–2680.

[112] V. M. Kaganer, H. Möhwald, and P. Dutta. "Structure and phase transitions in Langmuir monolayers". In: *Rev. Mod. Phys.* 71.3 (Apr. 1999), pp. 779–819. DOI: 10.1103/RevModPhys.71.779.

[113] J. Czarniecki and M. Jaroniec. "Studies of adsorption kinetics by means of the stochastic numerical simulation". In: *Surf. Sci. Rep.* 3.6 (1983), pp. 301–353. ISSN: 0167–5729. DOI: 10.1016/0167-5729(84)90001-3.

[114] F. Schmid. "Stabilization of tilt order by chain flexibility in Langmuir monolayers". In: *Phys. Rev. E* 55.5 (May 1997), pp. 5774–5784. DOI: 10.1103/PhysRevE.55.5774.

[115] H. Kraack et al. "The structure of organic langmuir films on liquid metal surfaces". In: *Nuclear Instruments and Methods in Physics Research Section B: Beam Interactions with Materials and Atoms* 200 (2003), pp. 363–370. ISSN: 0168-583X. DOI: 10.1016/S0168-583X(02)01724-X.

[116] M. A. Kalinina. "Self-assembly of metastable Langmuir monolayers on planar solid surfaces". In: *Colloid J.* 77 (2015), pp. 537–555. DOI: 10.1134/S1061933X15050099.

[117] K. Hannikainen et al. "Surface Phase Metastability during Langmuir Evaporation". In: *Phys. Rev. Lett.* 123.18 (Nov. 2019), p. 186102. DOI: 10.1103/PhysRevLett.123.186102.

[118] A. Halperin, S. Alexander, and I. Schechter. "Mean field theory of nematic order for grafted rods". In: *J. Chem. Phys.* 86.11 (1987), pp. 6550–6555. DOI: 10.1063/1.452397.

[119] M. M. Telo Da Gama. "Phase transitions in liquid crystal films". In: *Physica A* 172.1 (1991), pp. 219–224. ISSN: 0378-4371. DOI: 0.1016/0378-4371(91)90322-4.

[120] D. Kramer et al. "Monte Carlo and mean-field studies of successive phase transitions in rod monolayers". In: *J. Chem. Phys.* 96.3 (1992), pp. 2236–2252. DOI: 10.1063/1.462074.

[121] E. M. del Río et al. "Surface-induced alignment at model nematic interfaces". In: *Phys. Rev. E* 52.5 (Nov. 1995), pp. 5028–5039. DOI: 10.1103/PhysRevE.52.5028.

[122] F. Vandenbrouck, M. P. Valignat, and A. M. Cazabat. "Thin Nematic Films: Metastability And Spinodal Dewetting". In: *Phys. Rev. Lett.* 82.13 (Mar. 1999), pp. 2693–2696. DOI: 10.1103/PhysRevLett.82.2693.

[123] E. Umbach, K. Glöckler, and M. Sokolowski. "Surface "architecture" with large organic molecules: interface order and epitaxy". In: *Surf. Sci.* 402-404 (1998), pp. 20–31. ISSN: 0039-6028. DOI: 10.1016/S0039-6028(98)00014-4.

[124] A. Patrykiejew, S. Sokołowski, and K. Binder. "Phase transitions in adsorbed layers formed on crystals of square and rectangular surface lattice". In: *Surf. Sci. Rep.* 37.6 (2000), pp. 207–344. ISSN: 0167-5729. DOI: 10.1016/S0167-5729(99)00011-4.

[125] F. Schreiber. "Structure and growth of self-assembling monolayers". In: *Prog. Surf. Sci.* 65.5 (Dec. 2000), pp. 151–257. DOI: 10.1016/S0079-6816(00)00024-1.

[126] D. K Schwartz. "Mechanisms and Kinetics of Self-Assembled Monolayer Formation". In: *Ann. Rev. Phys. Chem.* 52.1 (2001). PMID: 11326061, pp. 107–137. DOI: 10.1146/annurev.physchem.52.1.107.

[127] F. Schreiber et al. "Adsorption mechanisms, structures, and growth regimes of an archetypal self-assembling system: Decanethiol on Au(111)". In: *Phys. Rev. B* 57.19 (May 1998), pp. 12476–12481. DOI: 10.1103/PhysRevB.57.12476.

[128] H. Kallmann and M. Pope. "Photovoltaic Effect in Organic Crystals". In: *J. Chem. Phys.* 30.2 (1959), pp. 585–586. DOI: 10.1063/1.1729992.

[129] R. Ruiz et al. "Dynamic Scaling, Island Size Distribution, and Morphology in the Aggregation Regime of Submonolayer Pentacene Films". In: *Phys. Rev. Lett.* 91.13 (Sept. 2003), p. 136102. DOI: 10.1103/PhysRevLett.91.136102.

[130] R. Ruiz et al. "Pentacene Thin Film Growth". In: *Chem. Mater.* 16.23 (2004), pp. 4497–4508. DOI: 10.1021/cm049563q.

[131] A. C. Dürr et al. "Rapid Roughening in Thin Film Growth of an Organic Semiconductor (Diindenoperylene)". In: *Phys. Rev. Lett.* 90.1 (Jan. 2003), p. 016104. DOI: 10.1103/PhysRevLett.90.016104.

[132] W. Yao and Yong S. Zhao. "Tailoring the self-assembled structures and photonic properties of organic nanomaterials". In: *Nanoscale* 6.7 (2014), pp. 3467–3473. DOI: 10.1039/C3NR04654K.

[133] P. A. Korevaar et al. "Model-driven optimization of multicomponent self-assembly processes". In: *Proc .Nat. Acad. Sci.-USA* 110.43 (2013), pp. 17205–17210. ISSN: 0027-8424. DOI: 10.1073/pnas.1310092110.

[134] S. Sasi et al. "Scope of surface-modified molecular and nanomaterials in gel/liquid forms for developing mechanically flexible DSSCs/QDSSCs". In: *Photochem. Photobiol. Sci.* 18.1 (2019), pp. 15–29. DOI: 10.1039/C8PP00293B.

[135] L. Li et al. "Controllable Growth and Field-Effect Property of Monolayer to Multilayer Microstripes of an Organic Semiconductor". In: *J. Am. Chem. Soc.* 132.26 (2010), pp. 8807–8809. DOI: 10.1021/ja1017267.

[136] J. Barbasz and M. Cieśla. "Domain structure created by irreversible adsorption of dimers". In: *Acta Phys. Pol. B* 44.5 (May 2013). 25th Marian Smoluchowski Symposium on Statistical Physics, Krakow, Poland, Sep. 10-13, 2012, pp. 937–944. ISSN: 0587-4254. DOI: 10.5506/APhysPolB.44.937.

[137] M. Antonietta Loi et al. "Supramolecular organization in ultra-thin films of α-sexithiophene on silicon dioxide". In: *Nat. Mater.* 4 (2005), pp. 81–85. DOI: 10.1038/nmat1279.

[138] S. Chiodini et al. "Self-organization of complete organic monolayers via sequential post-deposition annealing". In: *Prog. Org. Coat.* 138 (2020), p. 105408. ISSN: 0300–9440. DOI: 10.1016/j.porgcoat.2019.105408.

[139] Y. Zeng, B. Tao, and Z. Yin. "Molecular orientation transformation of pentacene on amorphous SiO2: A computational study on the initial growth stage of physical vapor deposition". In: *J. Cryst. Growth* 405 (2014), pp. 73–80. ISSN: 0022-0248. DOI: 10.1016/j.jcrysgro.2014.07.038.

[140] N. Kleppmann and S. H. L. Klapp. "Nonequilibrium surface growth in a hybrid inorganic-organic system". In: *Phys. Rev. B* 94.24 (Dec. 2016), p. 241404. DOI: 10.1103/PhysRevB.94.241404.

[141] A. Moser et al. "A disordered layered phase in thin films of sexithiophene". In: *Chem. Phys. Lett.* 574 (2013), pp. 51–55. ISSN: 0009-2614. DOI: 10.1016/j.cplett.2013.04.053.

[142] F. Chiarella et al. "Post-Deposition Wetting and Instabilities in Organic Thin Films by Supersonic Molecular Beam Deposition". In: *Sci. Rep.* 8.1 (2018), pp. 1–11. DOI: 10.1038/s41598-018-30567-7.

[143] F. Lin et al. "Temperature-tuned organic monolayer growth: N,N′-di(n-butyl)quinacridone on Ag(110)". In: *Phys. Rev. B* 73.23 (June 2006), p. 235420. DOI: 10.1103/PhysRevB.73.235420.

[144] L. Kilian et al. "The commensurate-to-incommensurate phase transition of an organic monolayer: A high resolution LEED analysis of the superstructures of NTCDA on Ag(111)". In: *Surf. Sci.* 602.14 (2008), pp. 2427–2434. ISSN: 0039-6028. DOI: 10.1016/j.susc.2008.05.025.

[145] A. Soukopp et al. "Superstructure formation of large organic adsorbates on a metal surface: A systematic approach using oligothiophenes on Ag(111)". In: *Phys. Rev. B* 58.20 (Nov. 1998), pp. 13882–13894. DOI: 10.1103/PhysRevB.58.13882.

[146] J. Yang et al. "Weak Epitaxy Growth of Metal-Free Phthalocyanine on p-Sexiphenyl Monolayer and Double-Layer Films". In: *J. Phys. Chem. B* 112.10 (2008). PMID: 18281981, pp. 3132–3137. DOI: 10.1021/jp711161f.

[147] Y. Tang et al. "Vacuum-Deposited Submonolayer Thin Films of a Three-Ring Bent-Core Compound". In: *J. Phys. Chem. B* 108.34 (2004), pp. 12921–12926. DOI: 10.1021/jp048607f.

[148] P. Guaino et al. "Scanning tunneling microscopy study of pentacene adsorption on Ag/Si(1 1 1)-($\sqrt{3} \times \sqrt{3}$)$R30°$". In: *Appl. Surf. Sci.* 212-213 (2003), pp. 537–541. ISSN: 0169-4332. DOI: 10.1016/S0169-4332(03)00052-7.

[149] H. Marchetto et al. "Direct observation of epitaxial organic film growth: temperature-dependent growth mechanisms and metastability". In: *Phys. Chem. Chem. Phys.* 17.43 (2015), pp. 29150–29160. DOI: 10.1039/C5CP05124J.

[150] N. Kawakita et al. "Metastable phase of lead phthalocyanine films on graphite: Correlation between geometrical and electronic structures". In: *Phys. Rev. B* 95.4 (Jan. 2017), p. 045419. DOI: 10.1103/PhysRevB.95.045419.

[151] C. Rolin et al. "Vapor Phase Growth of Functional Pentacene Films at Atmospheric Pressure". In: *Adv. Funct. Mater.* 22.23 (2012), pp. 5050–5059. DOI: 10.1002/adfm.201200896.

[152] C. Stadler et al. "Structural investigation of the adsorption of SnPc on Ag(111) using normal-incidence x-ray standing waves". In: *Phys. Rev. B* 74.3 (July 2006), p. 035404. DOI: 10.1103/PhysRevB.74.035404.

[153] J. A. Venables, G. D. T. Spiller, and M. Hanbucken. "Nucleation and growth of thin films". In: *Rep. Prog. Phys.* 47.4 (Apr. 1984), pp. 399–459. DOI: 10.1088/0034-4885/47/4/002.

[154] M. Einax, W. Dieterich, and P. Maass. "Colloquium: Cluster growth on surfaces: Densities, size distributions, and morphologies". In: *Rev. Mod. Phys.* 85.3 (2013), pp. 921–939. DOI: 10.1103/RevModPhys.85.921.

[155] T. Wang and D. Yan. "Ultrathin organic semiconductor films — Soft matter effect". In: *Adv. Colloid Interfac.* 207 (2014), pp. 332–346. ISSN: 0001-8686. DOI: 10.1016/j.cis.2014.01.012.

[156] Q. Wang et al. "Bilayer Formation vs Molecular Exchange in Organic Heterostructures: Strong Impact of Subtle Changes in Molecular Structure". In: *J. Phys. Chem. C* 122.17 (2018), pp. 9480–9490. DOI: 10.1021/acs.jpcc.8b01529.

[157] J. M. Fish and R. L. C. Vink. "Isotropic-to-nematic transition in confined liquid crystals: An essentially nonuniversal phenomenon". In: *Phys. Rev. E* 81.2 (Feb. 2010), p. 021705. DOI: 10.1103/PhysRevE.81.021705.

[158] M. González-Pinto et al. "Effect of shape biaxiality on the phase behavior of colloidal liquid-crystal monolayers". In: *Phys. Chem. Chem. Phys.* 17.9 (Jan. 2015), pp. 6389–6400. DOI: 10.1039/C4CP04812A.

[159] L. Lafuente and J. A. Cuesta. "Fundamental measure theory for lattice fluids with hard-core interactions". In: *J. Phys. Condens. Matter* 14.46 (Nov. 2002), pp. 12079–12097. DOI: 10.1088/0953-8984/14/46/314.

[160] L. Lafuente and J. A. Cuesta. "Density Functional Theory for General Hard-Core Lattice Gases". In: *Phys. Rev. Lett.* 93.13, 130603 (Sept. 2004), p. 130603. DOI: 10.1103/PhysRevLett.93.130603.

[161] Robert Evans. *Density Functional Theory for Inhomogeneous Fluids I: Simple Fluids in Equilibrium*. Lectures at the 3rd Warsaw School of Statistical Physics, Kazimierz Dolny. 27 June – 3 July. 2009.

[162] Matthias Schmidt. *Functional Many-Body Dynamics*. Lecture notes of the first Spring School on Classical Density Functional Theory, University of Freiburg (im Breisgau), 18–21 March. 2019.

[163] A. C. Levi and M. Kotrla. "Theory and simulation of crystal growth". In: *J. Phys. Condens. Matter* 9.2 (1997), p. 299. DOI: 10.1088/0953-8984/9/2/001.

[164] J. Rottler and P. Maass. "Second Layer Nucleation in Thin Film Growth". In: *Phys. Rev. Lett.* 83.17 (Oct. 1999), pp. 3490–3493. DOI: 10.1103/PhysRevLett.83.3490.

[165] F. Family. "Scaling, percolation and coarsening in epitaxial thin film growth". In: *Physica A* 266.1 (1999), pp. 173–185. ISSN: 0378-4371. DOI: 10.1016/S0378-4371(98)00589-5.

[166] A. Sassella et al. "Tuning the growth mode in organic molecular-beam epitaxy". In: *Phys. Rev. B* 71.20 (May 2005), p. 201311. DOI: 10.1103/PhysRevB.71.201311.

[167] B. Krause et al. "Temperature dependence of the 2D-3D transition in the growth of PTCDA on Ag(111): A real-time X-ray and kinetic Monte Carlo study". In: *Europhys. Lett.* 65.3 (Feb. 2004), pp. 372–378. DOI: 10.1209/epl/i2003-10090-6.

[168] E. Empting et al. "Lattice gas study of thin-film growth scenarios and transitions between them: Role of substrate". In: *Phys. Rev. E* 103.2 (Feb. 2021), p. 023302. DOI: 10.1103/PhysRevE.103.023302.

[169] R. Banerjee et al. "Evidence for Kinetically Limited Thickness Dependent Phase Separation in Organic Thin Film Blends". In: *Phys. Rev. Lett.* 110.18 (May 2013), p. 185506. DOI: 10.1103/PhysRevLett.110.185506.

[170] C. Frank et al. "Analysis of island shape evolution from diffuse x-ray scattering of organic thin films and implications for growth". In: *Phys. Rev. B* 90.20 (Nov. 2014), p. 205401. DOI: 10.1103/PhysRevB.90.205401.

[171] M. T. Alkhafaji and A. D. Migone. "Heat-capacity study of the melting of submonolayer butane films adsorbed on graphite". In: *Phys. Rev. B* 48.3 (July 1993), pp. 1761–1764. DOI: 10.1103/PhysRevB.48.1761.

[172] Y. Wu et al. "Controlling the Early Stages of Pentacene Growth by Supersonic Molecular Beam Deposition". In: *Phys. Rev. Lett.* 98.7 (Feb. 2007), p. 076601. DOI: 10.1103/PhysRevLett.98.076601.

[173] A. Hauschild et al. "Normal-incidence x-ray standing-wave determination of the adsorption geometry of PTCDA on Ag(111): Comparison of the ordered room-temperature and disordered low-temperature phases". In: *Phys. Rev. B* 81.12 (Mar. 2010), p. 125432. DOI: 10.1103/PhysRevB.81.125432.

[174] C. Wagner et al. "Repulsion between molecules on a metal: Monolayers and submonolayers of hexa-peri-hexabenzocoronene on Au(111)". In: *Phys. Rev. B* 81.3 (Jan. 2010), p. 035423. DOI: 10.1103/PhysRevB.81.035423.

[175] James Kerfoot. "The growth and fluorescence of organic monolayers and heterostructures". PhD thesis. University of Nottingham, 2018. URL: http://eprints.nottingham.ac.uk/50673/1/Thesis_Corrections_1.pdf.

[176] K. Sun, T.-N. Shao, and J.-Z. Wang. "Orientation transition of pentacene molecule on Bi(111)". In: *Surf. Sci.* 636 (2015), pp. 31 –35. ISSN: 0039-6028. DOI: 10.1016/j.susc.2014.10.005.

[177] T. Djuric et al. "Epitaxially Grown Films of Standing and Lying Pentacene Molecules on Cu(110) Surfaces". In: *Crystal Growth & Design* 11.4 (2011). PMID: 21479111, pp. 1015–1020. DOI: 10.1021/cg101230j.

[178] T. Potocar et al. "Initial stages of a para-hexaphenyl film growth on amorphous mica". In: *Phys. Rev. B* 83.7 (Feb. 2011), p. 075423. DOI: 10.1103/PhysRevB.83.075423.

[179] F. Bischoff et al. "How Surface Bonding and Repulsive Interactions Cause Phase Transformations: Ordering of a Prototype Macrocyclic Compound on Ag(111)". In: *ACS Nano* 7.4 (2013). PMID: 23521075, pp. 3139–3149. DOI: 10.1021/nn305487c.

[180] L. Kilian et al. "Role of Intermolecular Interactions on the Electronic and Geometric Structure of a Large π-Conjugated Molecule Adsorbed on a Metal Surface". In: *Phys. Rev. Lett.* 100.13 (Apr. 2008), p. 136103. DOI: 10.1103/PhysRevLett.100.136103.

[181] A. Langner et al. "Structural properties of tetracene films on Ag(111) investigated by SPA-LEED and TPD". In: *Surf. Sci.* 574.2 (2005), pp. 153–165. ISSN: 0039-6028. DOI: 10.1016/j.susc.2004.10.031.

[182] L. Zhang et al. "Kinetic Barrier Against Standing Up of Pentacene Molecules Upon a Pentacene Monolayer". In: *Phys. Status Solidi-R.* 12.8 (2018), p. 1800230. DOI: 10.1002/pssr.201800230.

[183] J. Yang et al. "Ultrathin-Film Growth of para-Sexiphenyl (I): Submonolayer Thin-Film Growth as a Function of the Substrate Temperature". In: *J. Phys. Chem. B* 112.26 (2008). PMID: 18512887, pp. 7816–7820. DOI: 10.1021/jp711455u.

[184] T. Yamada and T. Munakata. "Spectroscopic and microscopic investigations of organic ultrathin films: Correlation between geometrical structures and unoccupied electronic states". In: *Prog. Surf. Sci.* 93.4 (2018), pp. 108–130. ISSN: 0079-6816. DOI: 10.1016/j.progsurf.2018.09.003.

[185] J. Schaffert et al. "Imaging the dynamics of individually adsorbed molecules". In: *Nature Mater.* 12 (2013), pp. 223–227. DOI: 10.1038/nmat3527.

[186] L. Kilian, E. Umbach, and M. Sokolowski. "Molecular beam epitaxy of organic films investigated by high resolution low energy electron diffraction (SPA-LEED): 3,4,9,10-perylenetetracarboxylicacid-dianhydride (PTCDA) on Ag(111)". In: *Surf. Sci.* 573.3 (2004), pp. 359–378. ISSN: 0039-6028. DOI: 10.1016/j.susc.2004.10.004.

[187] L. Zhang et al. "Growth of pentacene on $\alpha-\mathbf{Al_2O_3}$(0001) studied by in situ optical spectroscopy". In: *Phys. Rev. Materials* 1.4 (Sept. 2017), p. 043401. DOI: 10.1103/PhysRevMaterials.1.043401.

[188] S. Rangan et al. "Growth of a highly ordered inhomogeneous kinetically trapped molecular monolayer". In: *Phys. Rev. B* 100.24 (Dec. 2019), p. 245411. DOI: 10.1103/PhysRevB.100.245411.

[189] A. Al-Mahboob et al. "Real-Time Microscopy of Reorientation Driven Nucleation and Growth in Pentacene Thin Films on Silicon Dioxide". In: *Adv. Funct. Mater.* 23.20 (2013), pp. 2653–2660. DOI: 10.1002/adfm.201203427.

[190] B. Stadtmüller et al. "Submonolayer growth of CuPc on noble metal surfaces". In: *Phys. Rev. B* 83.8 (Feb. 2011), p. 085416. DOI: 10.1103/PhysRevB.83.085416.

[191] H. Wang et al. "High mobility vanadyl-phthalocyanine polycrystalline films for organic field-effect transistors". In: *Appl. Phys. Lett.* 90.25 (2007), p. 253510. DOI: 10.1063/1.2751103.

[192] M. Hodas et al. "Real-Time Monitoring of Growth and Orientational Alignment of Pentacene on Epitaxial Graphene for Organic Electronics". In: *ACS Appl. Nano Mater.* 1.6 (2018), pp. 2819–2826. DOI: 10.1021/acsanm.8b00473.

[193] Matthias Lexow et al. "Stability and Exchange Processes in Ionic Liquid/Porphyrin Composite Films on Metal Surfaces". In: *J. Phys. Chem. C* 123.49 (2019), pp. 29708–29721. DOI: 10.1021/acs.jpcc.9b08531.

[194] B. Stadtmüller et al. "Unexpected interplay of bonding height and energy level alignment at heteromolecular hybrid interfaces". In: *Nat. Commun.* 5, 3685 (Apr. 2014), p. 3685. DOI: 10.1038/ncomms4685.

[195] E. Goiri et al. "Multi-Component Organic Layers on Metal Substrates". In: *Adv. Mater.* 28.7 (2016), pp. 1340–1368. DOI: 10.1002/adma.201503570.

[196] B. Stadtmüller et al. "Commensurate Registry and Chemisorption at a Hetero-organic Interface". In: *Phys. Rev. Lett.* 108.10 (Mar. 2012), p. 106103. DOI: 10.1103/PhysRevLett.108.106103.

[197] C. Lorch et al. "Controlling length-scales of the phase separation to optimize organic semiconductor blends". In: *Appl. Phys. Lett.* 107.20 (2015), p. 201903. DOI: 10.1063/1.4935545.

[198] C. Lorch et al. "Growth and annealing kinetics of α-sexithiophene and fullerene C60 mixed films". In: *J. Appl. Cryst.* 49.4 (2016), pp. 1266–1275.

[199] C. Lorch et al. "Influence of C60 co-deposition on the growth kinetics of diindenoperylene–From rapid roughening to layer-by-layer growth in blended organic films". In: *J. Chem. Phys.* 146.5 (2017), p. 052807. DOI: 10.1063/1.4966583.

[200] R. Banerjee et al. "Structure and Morphology of Organic Semiconductor–Nanoparticle Hybrids Prepared by Soft Deposition". In: *J. Phys. Chem. C* 119.9 (2015), pp. 5225–5237. DOI: 10.1021/acs.jpcc.5b00480.

[201] Z. Liu et al. "Electronic Decoupling of Organic Layers by a Self-Assembled Supramolecular Network on Au(111)". In: *J. Phys. Chem. Lett.* 10.15 (2019). PMID: 31318568, pp. 4297–4302. DOI: 10.1021/acs.jpclett.9b01167.

[202] G. van Straaten et al. "Role of the Central Metal Atom in Substrate-Mediated Molecular Interactions in Phthalocyanine-Based Heteromolecular Monolayers". In: *J. Phys. Chem. C* 122.15 (2018), pp. 8491–8504. DOI: 10.1021/acs.jpcc.8b02689.

[203] K. Akaike et al. "Structural Disordering upon Formation of Molecular Heterointerfaces". In: *J. Phys. Chem. C* 123.19 (2019), pp. 12242–12248. DOI: 10.1021/acs.jpcc.9b01123.

[204] T. Niu et al. "Submolecular Imaging of Parallel Offset π-π Stacking in Nonplanar Phthalocyanine Bilayers". In: *J. Phys. Chem. C* 123.12 (2019), pp. 7178–7184. DOI: 10.1021/acs.jpcc.8b12523.

[205] S. Thussing and P. Jakob. "Thermal Stability and Interlayer Exchange Processes in Heterolayers of CuPc and PTCDA on Ag(111)". In: *J. Phys. Chem. C* 121.25 (2017), pp. 13680–13691. DOI: 10.1021/acs.jpcc.7b02377.

[206] A. Haags et al. "Growth and Evolution of TCNQ and K Coadsorption Phases on Ag(111)". In: *New J. Phys.* 22.6 (June 2020), p. 063028. DOI: 10.1088/1367-2630/ab825f.

[207] B. Stadtmüller et al. "Tailoring metal–organic hybrid interfaces: heteromolecular structures with varying stoichiometry on Ag(111)". In: *New J. Phys.* 17.2 (Feb. 2015), p. 023046. DOI: 10.1088/1367-2630/17/2/023046.

[208] Y. Hattori Y.and Kimura and M. Kitamura. "Nucleation Density and Shape of Submonolayer Two-Dimensional Islands of Diphenyl Dinaphthothienothiophene in Vacuum Deposition". In: *J. Phys. Chem. C* 124.1 (2020), pp. 1064–1069. DOI: 10.1021/acs.jpcc.9b08628.

[209] G. S. Bales and D. C. Chrzan. "Transition from Compact to Fractal Islands during Submonolayer Epitaxial Growth". In: *Phys. Rev. Lett.* 74.24 (June 1995), pp. 4879–4882. DOI: 10.1103/PhysRevLett.74.4879.

[210] R. Pimpinelli A.and Ferrando. "Reentrant morphological instability of epitaxial islands". In: *Phys. Rev. B* 60.24 (Dec. 1999), pp. 17016–17022. DOI: 10.1103/PhysRevB.60.17016.

[211] M. Kratzer et al. "Temperature dependent growth morphologies of parahexaphenyl on SiO2 supported exfoliated graphene". In: *J. Vac. Sci. Technol. B* 31.4 (2013), p. 04D114. DOI: 10.1116/1.4813895.

[212] Marcello Campione et al. "Kinetic Phase Selection of Rubrene Heteroepitaxial Domains". In: *J. Phys. Chem. C* 113.49 (2009), pp. 20927–20933. DOI: 10.1021/jp905752r.

[213] R. K. Nahm and J. R. Engstrom. "Who's on first? Tracking in real time the growth of multiple crystalline phases of an organic semiconductor: Tetracene on SiO2". In: *J. Chem. Phys.* 146.5 (2017), p. 052815. DOI: 10.1063/1.4971288.

[214] Christian Hermann Frank. "Real-time x-ray scattering studies on organic thin films". Doctoral Thesis. Department of Physics: University of Tübingen, 2014.

[215] P. Gurin et al. "Ordering of hard rectangles in strong confinement". In: *J. Chem. Phys.* 146.13 (2017), p. 134503. DOI: 10.1063/1.4979497.

[216] R. K. Nahm et al. "Faster Is Smoother and So Is Lower Temperature: The Curious Case of Thin Film Growth of Tetracene on SiO2". In: *J. Phys. Chem. C* 121.15 (2017), pp. 8464–8472. DOI: 10.1021/acs.jpcc.7b01369.

[217] I. Kröger et al. "Submonolayer growth of H_2-phthalocyanine on Ag(111)". In: *Phys. Rev. B* 86.19 (Nov. 2012), p. 195412. DOI: 10.1103/PhysRevB.86.195412.

[218] I. Kröger et al. "Submonolayer growth of copper-phthalocyanine on Ag(111)". In: *New J. Phys.* 12.8 (Aug. 2010), p. 083038. DOI: 10.1088/1367-2630/12/8/083038.

[219] C. Stadler et al. "Tuning intermolecular interaction in long-range-ordered submonolayer organic films". In: *Nature Phys.* 5.2 (2009), pp. 153–158. DOI: 10.1038/nphys1176.

[220] C. Henneke et al. "Controlling the growth of multiple ordered heteromolecular phases by utilizing intermolecular repulsion". In: *Nature Mater.* 16.6 (June 2017), pp. 628–633. DOI: 10.1038/nmat4858.

[221] J. van der Lit et al. "Modeling the Self-Assembly of Organic Molecules in 2D Molecular Layers with Different Structures". In: *J. Phys. Chem. C* 120.1 (2016), pp. 318–323. DOI: 10.1021/acs.jpcc.5b09889.

[222] M. Häming et al. "Coverage dependent organic–metal interaction studied by high-resolution core level spectroscopy: SnPc (sub)monolayers on Ag(111)". In: *J, Electron Spectrosc.* 174.1 (2009), pp. 59–64. ISSN: 0368-2048. DOI: 10.1016/j.elspec.2009.03.023.

[223] J. Ziroff et al. "Hybridization of Organic Molecular Orbitals with Substrate States at Interfaces: PTCDA on Silver". In: *Phys. Rev. Lett.* 104.23 (June 2010), p. 233004. DOI: 10.1103/PhysRevLett.104.233004.

[224] F. S. Tautz. "Structure and bonding of large aromatic molecules on noble metal surfaces: The example of PTCDA". In: *Prog. Surf. Sci.* 82.9 (2007), pp. 479–520. ISSN: 0079-6816. DOI: 10.1016/j.progsurf.2007.09.001.

[225] D. Walgraef. "Nanostructure initiation during the early stages of thin film growth". In: *Physica E Low Dimens. Syst. Nanostruct.* 15.1 (2002), pp. 33 –40. ISSN: 1386-9477. DOI: 10.1016/S1386-9477(01)00492-1.

[226] M. Müller and D.-W. Sun. "Directing the Self-Assembly of Block Copolymers into A Metastable Complex Network Phase via A Deep and Rapid Quench". In: *Phys. Rev. Lett.* 111.26 (Dec. 2013), p. 267801. DOI: 10.1103/PhysRevLett.111.267801.

[227] U. Thiele et al. "Modelling approaches to the dewetting of evaporating thin films of nanoparticle suspensions". In: *J. Phys. Condens. Matter* 21.26 (June 2009), p. 264016. DOI: 10.1088/0953-8984/21/26/264016.

[228] V. Thapar, T. Hanrath, and F. A. Escobedo. "Entropic self-assembly of freely rotating polyhedral particles confined to a flat interface". In: *Soft Matter* 11.8 (2015), pp. 1481–1491. DOI: 10.1039/C4SM02641A.

[229] D. Orsi et al. "2D dynamical arrest transition in a mixed nanoparticle-phospholipid layer studied in real and momentum spaces". In: *Sci. Rep.* 5, 17930 (Dec. 2015), p. 17930. DOI: 10.1038/srep17930.

[230] A. Della Villa et al. "Localized modes in photonic quasicrystals with Penrose-type lattice". In: *Opt. Express* 14.21 (Oct. 2006), pp. 10021–10027. DOI: 10.1364/OE.14.010021.

[231] P. Z. Hanakata, J. F. Douglas, and F. W. Starr. "Interfacial mobility scale determines the scale of collective motion and relaxation rate in polymer films." In: *Nat. Commun.* 5 (2014), p. 4163. DOI: 10.1038/ncomms5163.

[232] Z. Mao et al. "The mechanism of morphogenesis in a phase-separating concentrated multicomponent alloy". In: *Nature Mater.* 6.3 (2007), pp. 210–216. DOI: 10.1038/nmat1845.

[233] D. Choudhary et al. "A Computational Study of the Sub-monolayer Growth of Pentacene". In: *Adv. Func. Mater.* 16.13 (2006), pp. 1768–1775. DOI: 10.1002/adfm.200500148.

[234] M. Haran et al. "Multiscale Modeling of Self-Assembled Monolayers of Thiophenes on Electronic Material Surfaces". In: *Langmuir* 23.9 (2007). PMID: 17397195, pp. 4897–4909. DOI: 10.1021/la063059d.

[235] L. Muccioli, G. D'Avino, and C. Zannoni. "Simulation of vapor-phase deposition and growth of a pentacene thin film on C60 (001)". In: *Adv. Mater.* 23.39 (Oct. 2011), pp. 4532–4536. DOI: 10.1002/adma.201101652.

[236] O. Roscioni et al. "Pentacene Crystal Growth on Silica and Layer-Dependent Step-Edge Barrier From Atomistic Simulations". In: *J. Phys. Chem. Lett.* 9.23 (Nov. 2018), pp. 6900–6906. DOI: 10.1021/acs.jpclett.8b03063.

[237] A. Lorenzoni, M. Muccini, and F. Mercuri. "A Computational Predictive Approach for Controlling the Morphology of Functional Molecular Aggregates on Substrates". In: *Adv. Theory Simul.* 2.12 (2019), p. 1900156. DOI: 10.1002/adts.201900156.

[238] T. Heinemann et al. "Equilibrium structures of anisometric, quadrupolar particles confined to a monolayer". In: *J. Chem. Phys.* 144.7 (2016), p. 074504. DOI: 10.1063/1.4941585.

[239] Y. Martínez-Ratón. "Bulk inhomogeneous phases of anisotropic particles: A fundamental measure functional study of the restricted orientations model". In: *Phys. Rev. E* 69.6 (June 2004), p. 061712. DOI: 10.1103/PhysRevE.69.061712.

[240] R. van Roij, M. Dijkstra, and R. Evans. "Interfaces, wetting, and capillary nematization of a hard-rod fluid: Theory for the Zwanzig model". In: *J. Chem. Phys.* 113.17 (2000), pp. 7689–7701. DOI: 10.1063/1.1288903.

[241] B. S. John, C. Juhlin, and F. A. Escobedo. "Phase behavior of colloidal hard perfect tetragonal parallelepipeds". In: *J. Chem. Phys.* 128.4 (Jan. 2008), p. 044909. DOI: 10.1063/1.2819091.

[242] G. Antczak et al. "Complex Surface Diffusion Mechanisms of Cobalt Phthalocyanine Molecules on Ag(100)". In: *J. Am. Chem. Soc.* 137.47 (2015). PMID: 26584143, pp. 14920–14929. DOI: 10.1021/jacs.5b08001.

[243] M. Miletic et al. "Impact of Polarity on Anisotropic Diffusion of Conjugated Organic Molecules on the $(10\bar{1}0)$ Zinc Oxide Surface". In: *J. Phys. Chem. C* 123.11 (2019), pp. 6549–6559. DOI: 10.1021/acs.jpcc.8b12112.

[244] S. Hahne and P. Maass. "Diffusion Coefficients from Signal Fluctuations: Influence of Molecular Shape and Rotational Diffusion". In: *J. Phys. Chem. A* 118.12 (2014). PMID: 24640969, pp. 2237–2243. DOI: 10.1021/jp500479a.

[245] S. Hahne, P. Rahe, and P. Maass. "Determination of diffusion tensors from oscillating and circulating scanning probe tips". In: *Europhys. Lett.* 110.6 (June 2015), p. 66003. DOI: 10.1209/0295-5075/110/66003.

[246] K. D. Dobbs and D. J. Doren. "Dynamics of molecular surface diffusion: Energy distributions and rotation–translation coupling". In: *J.Chem. Phys.* 99.12 (1993), pp. 10041–10051. DOI: 10.1063/1.465508.

[247] P. Rotter et al. "Coupling between diffusion and orientation of pentacene molecules on an organic surface". In: *Nature Mater.* 15.4 (2016), pp. 397–400.

[248] C. Reichhardt and C. J. Olson Reichhardt. "Dynamical Ordering and Directional Locking for Particles Moving over Quasicrystalline Substrates". In: *Phys. Rev. Lett.* 106.6 (Feb. 2011), p. 060603. DOI: 10.1103/PhysRevLett.106.060603.

[249] C. Reichhardt and C. J. Olson Reichhardt. "Depinning and nonequilibrium dynamic phases of particle assemblies driven over random and ordered substrates: a review". In: *Rep. Prog. Phys.* 80.2 (Dec. 2016), p. 026501. DOI: 10.1088/1361-6633/80/2/026501.

[250] S. Frieder Hopp and A. Heuer. "Anisotropic behavior of organic molecules on prepatterned surfaces". In: *J. Chem. Phys.* 136.15 (2012), p. 154106. DOI: 10.1063/1.3692289.

[251] Adolf W. "On the nucleation and initial film growth of rod-like organic molecules". In: *Surf. Sci.* 652 (2016). Insights into Surface Phenomena: In Honor of John T. Yates Jr, pp. 367–377. ISSN: 0039-6028. DOI: 10.1016/j.susc.2016.02.015.

[252] M. H. Köpf et al. "Substrate-mediated pattern formation in monolayer transfer: a reduced model". In: *New J. Phys.* 14.2 (Feb. 2012), p. 023016. DOI: 10.1088/1367-2630/14/2/023016.

[253] U. Thiele et al. "First order phase transitions and the thermodynamic limit". In: *New J. Phys.* 21.12 (Dec. 2019), p. 123021. DOI: 10.1088/1367-2630/ab5caf.

[254] R. Banerjee et al. "Interrupted Growth to Manipulate Phase Separation in DIP:C60 Organic Semiconductor Blends". In: *J. Phys. Chem. C* 122.3 (2018), pp. 1839–1845. DOI: 10.1021/acs.jpcc.7b09637.

[255] J. E. Goose and P. Clancy. "Exploring the Energetic Deposition of Pentacene on Pentacene through Molecular Dynamics Simulations". In: *J. Phys. Chem. C* 111.43 (2007), pp. 15653–15659. DOI: 10.1021/jp074124a.

[256] G. D'Avino, L. Muccioli, and C. Zannoni. "From Chiral Islands to Smectic Layers: A Computational Journey Across Sexithiophene Morphologies on C60". In: *Adv. Funct. Mater.* 25.13 (2015), pp. 1985–1995. DOI: 10.1002/adfm.201402609.

[257] N. Kleppmann and S. H. L. Klapp. "A scale-bridging modeling approach for anisotropic organic molecules at patterned semiconductor surfaces". In: *J. Chem. Phys.* 142.6 (2015), p. 064701. DOI: 10.1063/1.4907037.

[258] Nicola Kleppmann. "Simulation of growth and self-assembly of complex molecules on surfaces". PhD thesis. Fakultät II - Mathematik und Naturwissenschaften: Technische Universität Berlin, Sept. 2015. DOI: 10.14279/depositonce-4693.

[259] V. F. Fefelov et al. "The simplest model of adsorption of molecules with different orientations in adlayer on the stepped surface". In: *Appl. Surf. Sci.* 256.17 (2010), pp. 5298 –5304. ISSN: 0169-4332. DOI: 10.1016/j.apsusc.2009.12.065.

[260] T. Martynec and S. H. L. Klapp. "Impact of anisotropic interactions on nonequilibrium cluster growth at surfaces". In: *Phys. Rev. E* 98.4 (Oct. 2018), p. 042801. DOI: 10.1103/PhysRevE.98.042801.

[261] N. Vigneshwar et al. “Phase diagram of a system of hard cubes on the cubic lattice”. In: *Phys. Rev. E* 99.5 (May 2019), p. 052129. DOI: 10.1103/PhysRevE.99.052129.

[262] L. Lafuente and J. A. Cuesta. “Elusiveness of Fluid-Fluid Demixing in Additive Hard-Core Mixtures”. In: *Phys. Rev. Lett.* 89 (14 Sept. 2002), p. 145701. DOI: 10.1103/PhysRevLett.89.145701.

[263] L. Lafuente and J. A. Cuesta. “Phase behavior of hard-core lattice gases: A fundamental measure approach”. In: *J. Chem. Phys.* 119.20 (2003), pp. 10832–10843. DOI: 10.1063/1.1615511.

[264] L. Lafuente and J. A. Cuesta. “Density functional theory for nearest-neighbor exclusion lattice gases in two and three dimensions”. In: *Phys. Rev. E* 68.6 (Dec. 2003), p. 066120. DOI: 10.1103/PhysRevE.68.066120.

[265] L. Lafuente and J. A. Cuesta. “Cluster density functional theory for lattice models based on the theory of Möbius functions”. In: *J. Phys. A* 38.34 (Aug. 2005), pp. 7461–7482. DOI: 10.1088/0305-4470/38/34/002.

[266] J. A. Cuesta, L. Lafuente, and M. Schmidt. “Lattice density functional for colloid-polymer mixtures: Comparison of two fundamental measure theories”. In: *Phys. Rev. E* 72.3 (Sept. 2005), p. 031405. DOI: 10.1103/PhysRevE.72.031405.

[267] A. Robledo and C. Varea. “On the relationship between the density functional formalism and the potential distribution theory for nonuniform fluids”. In: *J. Stat. Phys.* 26 (1981), pp. 513–525. DOI: 10.1007/BF01011432.

[268] M. Nieswand, W. Dieterich, and A. Majhofer. “Density-functional method for lattice-gas problems”. In: *Phys. Rev. E* 47.1 (Jan. 1993), pp. 718–720. DOI: 10.1103/PhysRevE.47.718.

[269] M. Nieswand, A. Majhofer, and W. Dieterich. “Lattice-gas analog of density-functional theory: Application to ordering transitions”. In: *Phys. Rev. E* 48.4 (Oct. 1993), pp. 2521–2527. DOI: 10.1103/PhysRevE.48.2521.

[270] D. Reinel, W. Dieterich, and A. Majhofer. “Interfacial properties in lattice gases: A density functional approach”. In: *Phys. Rev. E* 50.6 (Dec. 1994), pp. 4744–4749. DOI: 10.1103/PhysRevE.50.4744.

[271] J. Buschle, P. Maass, and W. Dieterich. “Exact density functionals in one dimension”. In: *J. Phys. A: Math. Gen.* 33.4 (2000), p. L41.

[272] J. Buschle, P. Maass, and W. Dieterich. “Wall-induced density profiles and density correlations in confined takahashi lattice gases”. In: *J. Stat. Phys.* 99.1 (2000), pp. 273–312.

[273] S. Prestipino and P. V. Giaquinta. “Density-functional theory of a lattice-gas model with vapour, liquid, and solid phases”. In: *J. Phys. Condens. Matter* 15.23 (2003), p. 3931.

[274] S. Prestipino. “Lattice density-functional theory of surface melting: the effect of a square-gradient correction”. In: *J. Phys. Condens. Matter* 15.47 (2003), p. 8065.

[275] D. Woywod and M. Schoen. "Topography of phase diagrams in binary fluid mixtures: A mean-field lattice density functional study". In: *Phys. Rev. E* 73.1 (Jan. 2006), p. 011201. DOI: 10.1103/PhysRevE.73.011201.

[276] M. Schmidt, L. Lafuente, and J. A. Cuesta. "Freezing in the presence of disorder: a lattice study". In: 15.27 (June 2003), p. 4695. DOI: 10.1088/0953-8984/15/27/304.

[277] L. Lafuente and J. A. Cuesta. "First-principles derivation of density-functional formalism for quenched-annealed systems". In: *Phys. Rev. E* 74.4 (Oct. 2006), p. 041502. DOI: 10.1103/PhysRevE.74.041502.

[278] B. Bakhti, S. Schott, and P. Maass. "Exact density functional for hard-rod mixtures derived from Markov chain approach". In: *Phys. Rev. E* 85.4, 042107 (Apr. 2012), p. 042107. DOI: 10.1103/PhysRevE.85.042107.

[279] B. Bakhti, Gerhard Müller, and P. Maass. "Interacting hard rods on a lattice: Distribution of microstates and density functionals". In: *J. Chem. Phys.* 139.5 (2013), p. 054113. DOI: 10.1063/1.4816379.

[280] Benaoumeur Bakhti. "Development of lattice density functionals and applications to structure formation in condensed matter systems". PhD thesis. University of Osnabrück, 2013.

[281] M. J. Stephen and J. P. Straley. "Physics of liquid crystals". In: *Rev. Mod. Phys.* 46.4 (Oct. 1974), pp. 617–704. DOI: 10.1103/RevModPhys.46.617.

[282] D. Demus et al., eds. *Handbook of Liquid Crystals*. Vol. 2A: Low Molecular Weight Liquid Crystals I. Weinheim: WILEY-VCH Verlag GmbH, 1998. ISBN: 3-527-29271-3.

[283] D. Demus et al., eds. *Handbook of Liquid Crystals*. Vol. 2B: Low Molecular Weight Liquid Crystals II. Weinheim: WILEY-VCH Verlag GmbH, 1998. ISBN: 3-527-29296-9.

[284] J. Buitenhuis et al. "Phase Separation of Mixtures of Colloidal Boehmite Rods and Flexible Polymer". In: *J. Colloid Interf. Sci.* 175.1 (1995), pp. 46–56. ISSN: 0021-9797. DOI: 10.1006/jcis.1995.1427.

[285] S. V. Savenko and M. Dijkstra. "Phase behavior of a suspension of colloidal hard rods and nonadsorbing polymer". In: *J. Chem. Phys.* 124.23 (2006), p. 234902. DOI: 10.1063/1.2202853.

[286] A. Kuijk et al. "Phase behavior of colloidal silica rods". In: *Faraday Discuss.* 159.0 (2012), pp. 181–199. DOI: 10.1039/C2FD20084H.

[287] A. Kuijk, A. van Blaaderen, and A. Imhof. "Synthesis of Monodisperse, Rodlike Silica Colloids with Tunable Aspect Ratio". In: *J. Am. Chem. Soc* 133.8 (2011). PMID: 21250633, pp. 2346–2349. DOI: 10.1021/ja109524h.

[288] Y. Gao et al. "Directed self-assembly into low-density colloidal liquid crystal phases". In: *Phys. Rev. Materials* 2.1 (Jan. 2018), p. 015601. DOI: 10.1103/PhysRevMaterials.2.015601.

[289] Carla Fernández-Rico et al. "Synthesis of Colloidal SU-8 Polymer Rods Using Sonication". In: *Adv. Mater.* 31.17 (2019), p. 1807514. DOI: 10.1002/adma.201807514.

[290] D. Mukhija and M. J. Solomon. "Nematic order in suspensions of colloidal rods by application of a centrifugal field". In: *Soft Matter* 7.2 (2011), pp. 540–545. DOI: 10.1039/C0SM00493F.

[291] A. Kuijk et al. "Effect of external electric fields on the phase behavior of colloidal silica rods". In: *Soft Matter* 10.33 (2014), pp. 6249–6255. DOI: 10.1039/C4SM00957F.

[292] H. Hansen-Goos and K. Mecke. "Fundamental Measure Theory for Inhomogeneous Fluids of Nonspherical Hard Particles". In: *Phys. Rev. Lett.* 102.1 (Jan. 2009), p. 018302. DOI: 10.1103/PhysRevLett.102.018302.

[293] H. Hansen-Goos and K. Mecke. "Tensorial density functional theory for non-spherical hard-body fluids". In: *J. Phys. Condens. Matter* 22.36 (Aug. 2010), p. 364107. DOI: 10.1088/0953-8984/22/36/364107.

[294] R. Wittmann, M. Marechal, and K. Mecke. "Fundamental measure theory for smectic phases: Scaling behavior and higher order terms". In: *J. Chem. Phys.* 141.6 (2014), p. 064103. DOI: 10.1063/1.4891326.

[295] R. Wittmann and K. Mecke. "Surface tension of isotropic-nematic interfaces: Fundamental measure theory for hard spherocylinders". In: *J. Chem. Phys.* 140.10 (2014), p. 104703. DOI: 10.1063/1.4867277.

[296] R. Wittmann, M. Marechal, and K. Mecke. "Fundamental mixed measure theory for non-spherical colloids". In: *Europhys. Lett.* 109.2 (Jan. 2015), p. 26003. DOI: 10.1209/0295-5075/109/26003.

[297] R. Wittmann, M. Marechal, and K. Mecke. "Fundamental measure theory for non-spherical hard particles: predicting liquid crystal properties from the particle shape". In: *J. Phys. Condens. Matter* 28.24 (Apr. 2016), p. 244003. DOI: 10.1088/0953-8984/28/24/244003.

[298] René Wittmann. "Density Functional Theory for Liquid Crystals : Refining Fundamental Measure Theory for anisotropic bodies". Doctoral Thesis. Friedrich-Alexander Universität Erlangen-Nürnberg, University Press, July 2015, xii, 395 S. ISBN: 978-3-944057-37-8. URL: https://opus4.kobv.de/opus4-fau/frontdoor/index/index/docId/6737.

[299] M. A. Cotter and D. E. Martire. "Statistical Mechanics of Rodlike Particles. I. A Scaled Particle Treatment of a Fluid of Perfectly Aligned Rigid Cylinders". In: *J. Chem. Phys.* 52.4 (1970), pp. 1902–1908. DOI: 10.1063/1.1673231.

[300] M. A. Cotter and D. E. Martire. "Statistical Mechanics of Rodlike Particles. II. A Scaled Particle Investigation of the Aligned $\rightarrow$ Isotropic Transition in a Fluid of Rigid Spherocylinders". In: *J. Chem. Phys.* 52.4 (1970), pp. 1909–1919. DOI: 10.1063/1.1673232.

[301] M. A. Cotter. "Hard-rod fluid: Scaled particle theory revisited". In: *Phys. Rev. A* 10.2 (Aug. 1974), pp. 625–636. DOI: 10.1103/PhysRevA.10.625.

[302] G. Lasher. "Nematic Ordering of Hard Rods Derived from a Scaled Particle Treatment". In: *J. Chem. Phys.* 53.11 (1970), pp. 4141–4146. DOI: 10.1063/1.1673914.

[303] K. M. Timling. "Scaled particle theory of hard spherocylindrical fluids". In: *J. Chem. Phys.* 61.2 (1974), pp. 465–469. DOI: 10.1063/1.1681919.

[304] J. Vieillard-Baron. "The equation of state of a system of hard spherocylinders". In: *Mol. Phys.* 28.3 (1974), pp. 809–818. DOI: 10.1080/00268977400102161.

[305] G. J. Vroege and H. N. W. Lekkerkerker. "Phase transitions in lyotropic colloidal and polymer liquid crystals". In: *Rep. Prog. Phys.* 55.8 (Aug. 1992), pp. 1241–1309. DOI: 10.1088/0034-4885/55/8/003.

[306] R. van Roij. "The isotropic and nematic liquid crystal phase of colloidal rods". In: *Eur. J. Phys.* 26.5 (July 2005), S57–S67. DOI: 10.1088/0143-0807/26/5/s07.

[307] D. A. Ward and F. Lado. "Structure, thermodynamics, and orientational correlations of the nematogenic hard ellipse fluid from the Percus-Yevick equation". In: *Mol. Phys.* 63.4 (1988), pp. 623–638. DOI: 10.1080/00268978800100431.

[308] M. A. Cotter. "Hard spherocylinders in an anisotropic mean field: A simple model for a nematic liquid crystal". In: *J. Chem. Phys.* 66.3 (1977), pp. 1098–1106. DOI: 10.1063/1.434044.

[309] J. P. Straley. "Ordered phases of a liquid of biaxial particles". In: *Phys. Rev. A* 10.5 (Nov. 1974), pp. 1881–1887. DOI: 10.1103/PhysRevA.10.1881.

[310] R. Alben. "Phase Transitions in a Fluid of Biaxial Particles". In: *Phys. Rev. Lett.* 30.17 (Apr. 1973), pp. 778–781. DOI: 10.1103/PhysRevLett.30.778.

[311] M. J. Freiser. "Ordered States of a Nematic Liquid". In: *Phys. Rev. Lett.* 24.19 (May 1970), pp. 1041–1043. DOI: 10.1103/PhysRevLett.24.1041.

[312] V. T. Rajan and C.-W. Woo. "Orientation-averaged pair correlations in a molecular theory of nematic liquid crystals". In: *Phys. Rev. A* 17.1 (Jan. 1978), pp. 382–389. DOI: 10.1103/PhysRevA.17.382.

[313] A. M. Somoza and P. Tarazona. "Density functional approximation for hard-body liquid crystals". In: *J. Chem. Phys.* 91.1 (1989), pp. 517–527. DOI: 10.1063/1.457487.

[314] A. M. Somoza and P. Tarazona. "Nematic and smectic liquid crystals of hard spherocylinders". In: *Phys. Rev. A* 41.2 (Jan. 1990), pp. 965–970. DOI: 10.1103/PhysRevA.41.965.

[315] Z. Dogic et al. "Isotropic-nematic phase transition in suspensions of filamentous virus and the neutral polymer Dextran". In: *Phys. Rev. E* 69 (2004), p. 051702. DOI: 10.1103/PhysRevE.69.051702.

[316] Z. Dogic and S. Fraden. "Cholesteric Phase in Virus Suspensions". In: *Langmuir* 16.20 (2000), pp. 7820–7824. DOI: 10.1021/la000446t.

[317] Z. Dogic and S. Fraden. "Smectic Phase in a Colloidal Suspension of Semiflexible Virus Particles". In: *Phys. Rev. Lett.* 78.12 (Mar. 1997), pp. 2417–2420. DOI: 10.1103/PhysRevLett.78.2417.

[318] X. Wen, R. B. Meyer, and D. L. D. Caspar. "Observation of smectic-A ordering in a solution of rigid-rod-like particles". In: *Phys. Rev. Lett.* 63.25 (Dec. 1989), pp. 2760–2763. DOI: 10.1103/PhysRevLett.63.2760.

[319] E. Grelet. "Hexagonal Order in Crystalline and Columnar Phases of Hard Rods". In: *Phys. Rev. Lett.* 100.16 (Apr. 2008), p. 168301. DOI: 10.1103/PhysRevLett.100.168301.

[320] J. P. Straley. "Liquid Crystals in Two Dimensions". In: *Phys. Rev. A* 4.2 (Aug. 1971), pp. 675–681. DOI: 10.1103/PhysRevA.4.675.

[321] N. D. Mermin and H. Wagner. "Absence of Ferromagnetism or Antiferromagnetism in One- or Two-Dimensional Isotropic Heisenberg Models". In: *Phys. Rev. Lett.* 17.22 (Nov. 1966), pp. 1133–1136. DOI: 10.1103/PhysRevLett.17.1133.

[322] S. Chakravarty and C.-W. Woo. "Short-range correlations in two-dimensional liquid crystals". In: *Phys. Rev. A* 11.2 (Feb. 1975), pp. 713–720. DOI: 10.1103/PhysRevA.11.713.

[323] S. Chakravarty and C.-W. Woo. "Short-range correlations in two-dimensional liquid crystals. II. Smectic and crystalline phases". In: *Phys. Rev. A* 12.1 (July 1975), pp. 245–253. DOI: 10.1103/PhysRevA.12.245.

[324] J. A. Cuesta, C. F. Tejero, and M. Baus. "Isotropic-nematic transition of hard ellipses". In: *Phys. Rev. A* 39.12 (June 1989), pp. 6498–6506. DOI: 10.1103/PhysRevA.39.6498.

[325] Y. Shnidman and E. Domany. "Destruction of a first-order transition by dimensional crossover". In: *J. Phys. C Solid State* 14.26 (Sept. 1981), pp. L773–L779. DOI: 10.1088/0022-3719/14/26/001.

[326] P. G. Ferreira et al. "The hard ellipse liquid: An integral equation study". In: *J. Chem. Phys.* 95.10 (1991), pp. 7591–7602. DOI: 10.1063/1.461385.

[327] M. A. Bates and D. Frenkel. "Phase behavior of two-dimensional hard rod fluids". In: *J. Chem. Phys.* 112.22 (2000), pp. 10034–10041. DOI: 10.1063/1.481637.

[328] J. A. Cuesta and D. Frenkel. "Monte Carlo simulation of two-dimensional hard ellipses". In: *Phys. Rev. A* 42.4 (Aug. 1990), pp. 2126–2136. DOI: 10.1103/PhysRevA.42.2126.

[329] W.-S. Xu et al. "Hard ellipses: Equation of state, structure, and self-diffusion". In: *J. Chem. Phys.* 139.2 (July 2013), pp. 024501–024501. DOI: 10.1063/1.4812361.

[330] H. H. Wensink and R. L. C. Vink. "First-order phase transitions in two-dimensional off-lattice liquid crystals". In: *J. Phys. Condens. Matter* 19.46, 466109 (Nov. 2007), p. 466109. DOI: 10.1088/0953-8984/19/46/466109.

[331] R. L. C. Vink. "Crossover from a Kosterlitz-Thouless phase transition to a discontinuous phase transition in two-dimensional liquid crystals". In: *Phys. Rev. E* 90.6, 062132 (Dec. 2014), p. 062132. DOI: 10.1103/PhysRevE.90.062132.

[332] D. Frenkel and R. Eppenga. "Evidence for algebraic orientational order in a two-dimensional hard-core nematic". In: *Phys. Rev. A* 31.3 (Mar. 1985), pp. 1776–1787. DOI: 10.1103/PhysRevA.31.1776.

[333] J. M. Kosterlitz and D. J. Thouless. "Ordering, metastability and phase transitions in two-dimensional systems". In: *J. Phys. C Solid State* 6.7 (Apr. 1973), pp. 1181–1203. DOI: 10.1088/0022-3719/6/7/010.

[334] J. M. Kosterlitz. "The critical properties of the two-dimensional XY model". In: *J. Phys. C Solid State* 7.6 (Mar. 1974), pp. 1046–1060. DOI: 10.1088/0022-3719/7/6/005.

[335] J. M. Kosterlitz. "Kosterlitz–Thouless physics: a review of key numbers". In: *Rep. Prog. Phys.* 79.2 (Jan. 2016), p. 026001. DOI: 10.1088/0034-4885/79/2/026001.

[336] A. M. Luo, L. M. C. Sagis, and P. Ilg. "The Landau free energy of hard ellipses obtained from microscopic simulations". In: *J. Chem. Phys.* 140.12, 124901 (Mar. 2014), p. 124901. DOI: 10.1063/1.4868988.

[337] R. L. C. Vink. "The isotropic-to-nematic transition in a two-dimensional fluid of hard needles: a finite-size scaling study." In: *Eur. Phys. J. B* 72 (2009), 225–231. DOI: 10.1140/epjb/e2009-00333-x.

[338] S. Davatolhagh and S. Foroozan. "Structural origin of enhanced translational diffusion in two-dimensional hard-ellipse fluids". In: *Phys. Rev. E* 85.6 (June 2012), p. 061707. DOI: 10.1103/PhysRevE.85.061707.

[339] M. Moradi, S. Hashemi, and F. Taghizadeh. "Monte Carlo simulation of a confined hard ellipse fluid". In: *Physica A* 389.21 (2010), pp. 4510–4519. ISSN: 0378-4371. DOI: 10.1016/j.physa.2010.06.046.

[340] Z. Zheng and Y. Han. "Self-diffusion in two-dimensional hard ellipsoid suspensions". In: *J. Chem. Phys.* 133.12 (2010), p. 124509. DOI: 10.1063/1.3490669.

[341] R. Radhakrishnan, K. E. Gubbins, and M. Sliwinska-Bartkowiak. "Existence of a Hexatic Phase in Porous Media". In: *Phys. Rev. Lett.* 89.7 (July 2002), p. 076101. DOI: 10.1103/PhysRevLett.89.076101.

[342] D. R. Nelson and B. I. Halperin. "Dislocation-mediated melting in two dimensions". In: *Phys. Rev. B* 19.5 (Mar. 1979), pp. 2457–2484. DOI: 10.1103/PhysRevB.19.2457.

[343] W. Janke and H. Kleinert. "Monte Carlo study of two-step defect melting". In: *Phys. Rev. B* 41.10 (Apr. 1990), pp. 6848–6863. DOI: 10.1103/PhysRevB.41.6848.

[344] J. Tobochnik and G. V. Chester. "Monte Carlo study of the planar spin model". In: *Phys. Rev. B* 20.9 (Nov. 1979), pp. 3761–3769. DOI: 10.1103/PhysRevB.20.3761.

[345] M. Suzuki. "Relationship among Exactly Soluble Models of Critical Phenomena. I*): 2D Ising Model, Dimer Problem and the Generalized XY-Model". In: *Prog. Theor. Phys.* 46.5 (Nov. 1971), pp. 1337–1359. ISSN: 0033-068X. DOI: 10.1143/PTP.46.1337.

[346] P. A. Lebwohl and G. Lasher. "Nematic-Liquid-Crystal Order–A Monte Carlo Calculation". In: *Phys. Rev. A* 6.1 (July 1972), pp. 426–429. DOI: 10.1103/PhysRevA.6.426.

[347] L. A. S. Mól et al. "Monte Carlo study of 2D generalized XY-models". In: *Eur. Phys. J. B* 50.4 (Apr. 2006), pp. 541–548. ISSN: 1434-6036. DOI: 10.1140/epjb/e2006-00172-3.

[348] P. G. de Gennes. "Soft matter". In: *Rev. Mod. Phys.* 64.3 (July 1992), pp. 645–648. DOI: 10.1103/RevModPhys.64.645.

[349] D. Frenkel. "Soft condensed matter". In: *Physica A* 313.1 (2002), pp. 1–31. ISSN: 0378-4371. DOI: 10.1016/S0378-4371(02)01032-4.

[350] H. C. Andersen, D. Chandler, and J. D. Weeks. "Roles of Repulsive and Attractive Forces in Liquids : The Equilibrium Theory of Classical Fluids". In: *Adv. Chem. Phys.* John Wiley & Sons, Ltd, 2007. Chap. 2, pp. 105–156. ISBN: 9780470142530. DOI: 10.1002/9780470142530.ch2.

[351] D. Frenkel. "Entropy-driven phase transitions". In: *Physica A* 263.1 (1999), pp. 26–38. ISSN: 0378-4371. DOI: 10.1016/S0378-4371(98)00501-9.

[352] H. Tanaka et al. "Revealing key structural features hidden in liquids and glasses". In: *Nat. Rev. Phys.* 1 (2019), pp. 333–348. DOI: 10.1038/s42254-019-0053-3.

[353] S. Torquato. "Perspective: Basic understanding of condensed phases of matter via packing models". In: *J. Chem. Phys.* 149.2 (2018), p. 020901. DOI: 10.1063/1.5036657.

[354] J. M. Brader. "Nonlinear rheology of colloidal dispersions". In: *J. Phys. Condens. Matter* 22.36 (Aug. 2010), p. 363101. DOI: 10.1088/0953-8984/22/36/363101.

[355] R. Zwanzig. "First-Order Phase Transition in a Gas of Long Thin Rods". In: *J. Chem. Phys.* 39.7 (1963), pp. 1714–1721. DOI: 10.1063/1.1734518.

[356] T. Fischer and R. L. C. Vink. "Restricted orientation "liquid crystal" in two dimensions: Isotropic-nematic transition or liquid-gas one(?)" In: *Europhys. Lett.* 85.5 (Mar. 2009), p. 56003. DOI: 10.1209/0295-5075/85/56003.

[357] J. Y. Denham et al. "Computer Simulation Studies of Anisotropic Systems, III. Two-Dimensional Nematic Liquid Crystals". In: *Mol. Cryst. and Liquid Crystals* 60.3 (1980), pp. 185–205. DOI: 10.1080/00268948008072399.

[358] E. A. DiMarzio. "Statistics of Orientation Effects in Linear Polymer Molecules". In: *J. Chem. Phys.* 35.2 (1961), pp. 658–669. DOI: 10.1063/1.1731986.

[359] R. Alben. "Pretransition Effects in Nematic Liquid Crystals: Model Calculations". In: *Mol. Cryst. and Liquid Crystals* 13.3 (1971), pp. 193–231. DOI: 10.1080/15421407108083541.

[360] D. Dhar, R. Rajesh, and J. F. Stilck. "Hard rigid rods on a Bethe-like lattice". In: *Phys. Rev. E* 84.1 (July 2011), p. 011140. DOI: 10.1103/PhysRevE.84.011140.

[361] M. A. Cotter and D. E. Martire. "A Quasi-Chemical Lattice Treatment of Rod-like Molecules. Application to the Nematic-lsotropic Transition". In: *Mol. Cryst.* 7.1 (1969), pp. 295–323. DOI: 10.1080/15421406908084880.

[362] D. H. Linares, F. Romá, and A. J. Ramirez-Pastor. "Entropy-driven phase transition in a system of long rods on a square lattice". In: *J. Stat. Mech.: Theory Exp.* 2008.3 (Mar. 2008), p. 03013. DOI: 10.1088/1742-5468/2008/03/P03013.

[363] D. A. Matoz-Fernandez, D. H. Linares, and A. J. Ramirez-Pastor. "Critical behavior of long straight rigid rods on two-dimensional lattices: Theory and Monte Carlo simulations". In: *J. Chem. Phys.* 128.21 (June 2008), pp. 214902–214902. DOI: 10.1063/1.2927877.

[364] D. A. Matoz-Fernandez, D. H. Linares, and A. J. Ramirez-Pastor. "Determination of the critical exponents for the isotropic-nematic phase transition in a system of long rods on two-dimensional lattices: Universality of the transition". In: *Europhys. Lett.* 82.5 (May 2008), p. 50007. DOI: 10.1209/0295-5075/82/50007.

[365] J. Kundu and R. Rajesh. "Asymptotic behavior of the isotropic-nematic and nematic-columnar phase boundaries for the system of hard rectangles on a square lattice". In: *Phys. Rev. E* 91.1, 012105 (Jan. 2015), p. 012105. DOI: 10.1103/PhysRevE.91.012105.

[366] A. Ghosh and D. Dhar. "On the orientational ordering of long rods on a lattice". In: *Europhys. Lett.* 78.2 (Apr. 2007), p. 20003. DOI: 10.1209/0295-5075/78/20003.

[367] J. Kundu et al. "Nematic-disordered phase transition in systems of long rigid rods on two-dimensional lattices". In: *Phys. Rev. E* 87.3, 032103 (Mar. 2013), p. 032103. DOI: 10.1103/PhysRevE.87.032103.

[368] J. Kundu and R. Rajesh. "Phase transitions in a system of hard rectangles on the square lattice". In: *Phys. Rev. E* 89.5, 052124 (May 2014), p. 052124. DOI: 10.1103/PhysRevE.89.052124.

[369] J. Kundu and R. Rajesh. "Phase transitions in systems of hard rectangles with non-integer aspect ratio". In: *Eur. Phys. J. B* 88.5, 133 (May 2015), p. 133. DOI: 10.1140/epjb/e2015-60210-7.

[370] A. Bellemans and R. K. Nigam. "Phase Transitions in the Hard-Square Lattice Gas". In: *Phys. Rev. Lett.* 16.23 (June 1966), pp. 1038–1039. DOI: 10.1103/PhysRevLett.16.1038.

[371] A. Bellemans and R. K. Nigam. "Phase Transitions in Two-Dimensional Lattice Gases of Hard-Square Molecules". In: *J. Chem. Phys.* 46.8 (1967), pp. 2922–2935. DOI: 10.1063/1.1841157.

[372] J. Kundu, J. F. Stilck, and R. Rajesh. "Phase diagram of a bidispersed hard-rod lattice gas in two dimensions". In: *Europhys. Lett.* 112.6 (Dec. 2015), p. 66002. DOI: 10.1209/0295-5075/112/66002.

[373] Joyjit Kundu. "Phase transitions in systems of hard anisotropic particles on lattices". PhD thesis. Homi Bhaba National Institute, 2015. URL: https://www.imsc.res.in/xmlui/bitstream/handle/123456789/367/HBNI%20Th82.pdf.

[374] R. Dickman. "Discontinuous phase transition in a dimer lattice gas". In: *J. Chem. Phys.* 136.17 (2012), p. 174105. DOI: 10.1063/1.4709617.

[375] O. J. Heilmann and E. H. Lieb. "Theory of monomer-dimer systems". In: *Commun. Math. Phys.* 25.3 (Sept. 1972), pp. 190–232. ISSN: 1432-0916. DOI: 10.1007/BF01877590.

[376] O. J. Heilmann and E. H. Lieb. "Lattice models for liquid crystals". In: *J. Stat. Phys.* 20.6 (June 1979), pp. 679–693. ISSN: 1572-9613. DOI: 10.1007/BF01009518.

[377] M. Disertori and A. Giuliani. "The Nematic Phase of a System of Long Hard Rods". In: 323 (2013), pp. 143–175. DOI: 10.1007/s00220-013-1767-1.

[378] I. Jauslin and E. H. Lieb. "Nematic Liquid Crystal Phase in a System of Interacting Dimers and Monomers". In: *Commun. Math. Phys.* 363.3 (Nov. 2018), pp. 955–1002. ISSN: 1432-0916. DOI: 10.1007/s00220-018-3237-2.

[379] D. Alberici. "A Cluster Expansion Approach to the Heilmann–Lieb Liquid Crystal Model". In: *J. Stat. Phys.* 162.3 (Feb. 2016), pp. 761–791. ISSN: 1572-9613. DOI: 10.1007/s10955-015-1421-8.

[380] D. Ioffe, Y. Velenik, and M. Zahradník. "Entropy-Driven Phase Transition in a Polydisperse Hard-Rods Lattice System". In: *J. Stat. Phys.* 122.4 (Feb. 2006), pp. 761–786. ISSN: 1572-9613. DOI: 10.1007/s10955-005-8085-8.

[381] L. Gartner and E. Lerner. "Nonlinear modes disentangle glassy and Goldstone modes in structural glasses". In: *SciPost Phys.* 1.2 (2016), p. 016. DOI: 10.21468/SciPostPhys.1.2.016.

[382] E. Lerner and E. Bouchbinder. "Frustration-induced internal stresses are responsible for quasilocalized modes in structural glasses". In: *Phys. Rev. E* 97.3 (Mar. 2018), p. 032140. DOI: 10.1103/PhysRevE.97.032140.

[383] Trevor Hastie, Robert Tibshirani, and Jerome Friedman. *The Elements of Statistical Learning: Data Mining, Inference, and Prediction*. Second Edition, online corrected 12th printing (Springer Science+Business Media, LLC, 2017). Springer Series in Statistics. New York: Springer-Verlag, 2009. ISBN: 9780387848587. DOI: 10.1007/978-0-387-84858-7. eprint: https://web.stanford.edu/~hastie/ElemStatLearn/printings/ESLII_print12.pdf.

[384] Ethem Alpaydin. *Introduction to Machine Learning*. Ed. by Thomas Dietterich. Second Edition. Adaptive Computation and Machine Learning. Cambridge, London: Massachusetts Institute of Technology, 2010. ISBN: 978-0-262-01243-0.

[385] Alexander J. Smola and S. V. N. Vishwanathan. *Introduction to Machine Learning*. Cambridge: Cambridge University Press, 2008. ISBN: 0-521-82583-0.

[386] Ian Goodfellow, Yoshua Bengio, and Aaron Courville. *Deep Learning*. MIT Press, 2016. URL: http://www.deeplearningbook.org.

[387] Tom M. Mitchell. *Machine Learning*. McGraw-Hill series in computer science. McGraw-Hill, 1997. ISBN: 9780070428072.

[388] David Barber. *Bayesian Reasoning and Machine Learning*. New York, NY, USA: Cambridge University Press, 2012. ISBN: 9780521518147.

[389] Christopher M. Bishop. *Pattern Recognition and Machine Learning*. Information Science and Statistics. New York: Springer Science+Business Media, LLC, 2006. ISBN: 0-387-31073-8.

[390] Z. Ghahramani. "Probabilistic machine learning and artificial intelligence". In: *Nature* 521 (2015), pp. 452–459. DOI: 10.1038/nature14541.

[391] Y. LeCun, Y. Bengio, and G. Hinton. "Deep learning". In: *Nature* 521 (2015), pp. 436–444. DOI: 10.1038/nature14539.

[392] Marcus Hutter. *Universal Artificial Intelligence: Sequential Decisions Based on Algorithmic Probability*. Texts in Theoretical Computer Science, An EATCS Series. Berlin, Heidelberg New York: Springer-Verlag, 2005. ISBN: 3-540-22139-5.

[393] S. Ben-David et al. "Learnability can be undecidable". In: *Nat. Mach. Intell.* 1 (2019), pp. 44–48. DOI: 10.1038/s42256-018-0002-3.

[394] P. Mehta et al. "A high-bias, low-variance introduction to Machine Learning for physicists". In: *Phys. Rep.* 810 (2019). A high-bias, low-variance introduction to Machine Learning for physicists, pp. 1–124. ISSN: 0370-1573. DOI: 10.1016/j.physrep.2019.03.001.

[395] M. Z. Alom et al. "A State-of-the-Art Survey on Deep Learning Theory and Architectures". In: *Electronics* 8.3 (2019). Article No. 292. ISSN: 2079-9292. DOI: 10.3390/electronics8030292.

[396] M. I. Jordan and T. M. Mitchell. "Machine learning: Trends, perspectives, and prospects". In: *Science* 349.6245 (2015), pp. 255–260. ISSN: 0036-8075. DOI: 10.1126/science.aaa8415.

[397] M. Rolinek, D. Zietlow, and G. Martius. "Variational Autoencoders Recover PCA Directions (by Accident)". In: *Proc. of the IEEE/CVF Conference on Computer Vision and Pattern Recognition (CVPR)*. June 2019, pp. 12406–12415.

[398] K. Kansky et al. "Schema Networks: Zero-Shot Transfer with a Generative Causal Model of Intuitive Physics". In: *Proc. of the 34th Intl. Conf. on Machine Learning - Volume 70*. ICML'17. Sydney, NSW, Australia: JMLR.org, 2017, pp. 1809–1818.

[399] K. Singh et al. *Deep Convolutional Neural Networks for Pairwise Causality*. arXiv e-prints. 2017. arXiv: 1701.00597.

[400] M. Tegmark and T. Wu. "Pareto-Optimal Data Compression for Binary Classification Tasks". In: *Entropy* 22.1 (2019). Article No. 7. ISSN: 1099-4300. DOI: 10.3390/e22010007.

[401] P. Toth et al. "Hamiltonian Generative Networks". In: *Proc. of the 8th International Conference on Learning Representations, ICLR 2020, Addis Ababa, Ethiopia, April 26-30, 2020*. OpenReview.net, 2020. arXiv: 1909.13789 [cs.LG].

[402] S. Greydanus, M. Dzamba, and J. Yosinski. "Hamiltonian Neural Networks". In: *Advances in Neural Information Processing Systems*. Ed. by H. Wallach et al. Curran Associates, Inc., 2019, pp. 15379–15389. URL: http://papers.nips.cc/paper/9672-hamiltonian-neural-networks.pdf.

[403] S. Kirkpatrick, C. D. Gelatt, and M. P. Vecchi. "Optimization by Simulated Annealing". In: *Science* 220.4598 (1983), pp. 671–680. ISSN: 0036-8075. DOI: 10.1126/science.220.4598.671.

[404] N. Metropolis et al. "Equation of State Calculations by Fast Computing Machines". In: *J. Chem. Phys.* 21.6 (1953), pp. 1087–1092. DOI: 10.1063/1.1699114.

[405] Marc Mezard, Giorgio Parisi, and Virasoro Miguel Angel. *Spin Glass Theory and Beyond*. Vol. 9. World Scientific Lecture Notes in Physics. Singapore, New Jersey, Hong Kong: World Scientific Publishing Co. Pte. Ltd., 1987. ISBN: 9971-50-115-5.

[406] L. G. Valiant. "A Theory of the Learnable". In: *Commun. ACM* 27.11 (Nov. 1984), pp. 1134–1142. ISSN: 0001-0782. DOI: 10.1145/1968.1972.

[407] W. Krauth and M. Mezard. "Learning algorithms with optimal stability in neural networks". In: *J. Phys. A* 20.11 (Aug. 1987), pp. L745–L752. DOI: 10.1088/0305-4470/20/11/013.

[408] E. Gardner. "Maximum storage capacity in neural networks". In: *Europhys. Lett.* 4 (Sept. 1987), p. 481. DOI: 10.1209/0295-5075/4/4/016.

[409] E. Gardner and B. Derrida. "Optimal storage properties of neural network models". In: *J. Phys. A* 21.1 (1988), pp. 271–284. DOI: 10.1088/0305-4470/21/1/031.

[410] E. Gardner and B. Derrida. "Three unfinished works on the optimal storage capacity of networks". In: *J. Phys. A.* 22.12 (1989), p. 1983. DOI: 10.1088/0305-4470/22/12/004.

[411] M. Opper and D. Haussler. "Generalization performance of Bayes optimal classification algorithm for learning a perceptron". In: *Phys. Rev. Lett.* 66.20 (1991), p. 2677.

[412] H. S. Seung, H. Sompolinsky, and N. Tishby. "Statistical mechanics of learning from examples". In: *Phys. Rev. A* 45.8 (Apr. 1992), pp. 6056–6091. DOI: 10.1103/PhysRevA.45.6056.

[413] L. Reimers and A. Engel. "Generalization from educated teachers". In: *J. Phys. A* 25.24 (Dec. 1992), pp. 6649–6668. DOI: 10.1088/0305-4470/25/24/018.

[414] A. Engel and C. Van den Broeck. "Systems That Can Learn from Examples: Replica Calculation of Uniform Convergence Bounds for Perceptrons". In: *Phys. Rev. Lett.* 71.11 (1993), pp. 1772–1775. DOI: 10.1103/PhysRevLett.71.1772.

[415] T. L. H. Watkin, A. Rau, and M. Biehl. "The statistical mechanics of learning a rule". In: *Rev. Mod. Phys.* 65.2 (Apr. 1993), pp. 499–556. DOI: 10.1103/RevModPhys.65.499.

[416] S. Lahiri, J. Sohl-Dickstein, and S. Ganguli. *A universal tradeoff between power, precision and speed in physical communication*. arXiv e-prints. 2016. arXiv: 1603.07758 [cond-mat.stat-mech].

[417] H. W. Lin, M. Tegmark, and D. Rolnick. "Why Does Deep and Cheap Learning Work So Well?" In: *J. Stat. Phys.* 168.6 (Sept. 2017), pp. 1223–1247. ISSN: 1572-9613. DOI: 10.1007/s10955-017-1836-5.

[418] M. Koch-Janusz and Z. Ringel. "Mutual information, neural networks and the renormalization group". In: *Nature Phys.* 14.6 (2018), p. 578. DOI: 10.1038/s41567-018-0081-4.

[419] Y. Bahri et al. "Statistical Mechanics of Deep Learning". In: *Annu. Rev. Condens. Matter Phys.* 11.1 (2020), pp. 501–528. DOI: 10.1146/annurev-conmatphys-031119-050745.

[420] S. Geman and D. Geman. "Stochastic Relaxation, Gibbs Distributions, and the Bayesian Restoration of Images". In: *IEEE T. Pattern Anal.* PAMI-6.6 (Nov. 1984), pp. 721–741. ISSN: 1939-3539. DOI: 10.1109/TPAMI.1984.4767596.

[421] C. Haldeman and J. M. Beggs. "Critical Branching Captures Activity in Living Neural Networks and Maximizes the Number of Metastable States". In: *Phys. Rev. Lett.* 94.5 (Feb. 2005), p. 058101. DOI: 10.1103/PhysRevLett.94.058101.

[422] S. Yu et al. "Universal organization of resting brain activity at the thermodynamic critical point". In: *Front. Behav. Neurosci.* 7 (2013), p. 42. DOI: 10.3389/fnsys.2013.00042.

[423] Miguel A. Muñoz. "Colloquium: Criticality and dynamical scaling in living systems". In: *Rev. Mod. Phys.* 90.3 (July 2018), p. 031001. DOI: 10.1103/RevModPhys.90.031001.

[424] T. Mora and W. Bialek. "Are Biological Systems Poised at Criticality?" In: *J. Stat. Phys.* 144.2 (July 2011), pp. 268–302. ISSN: 1572-9613. DOI: 10.1007/s10955-011-0229-4.

[425] B. C. Daniels et al. "Criticality Distinguishes the Ensemble of Biological Regulatory Networks". In: *Phys. Rev. Lett.* 121.13 (Sept. 2018), p. 138102. DOI: 10.1103/PhysRevLett.121.138102.

[426] C. Zanoci, N. Dehghani, and M. Tegmark. "Ensemble inhibition and excitation in the human cortex: An Ising-model analysis with uncertainties". In: *Phys. Rev. E* 99.3 (Mar. 2019), p. 032408. DOI: 10.1103/PhysRevE.99.032408.

[427] P. M. Lenggenhager et al. "Optimal Renormalization Group Transformation from Information Theory". In: *Phys. Rev. X* 10.1 (Feb. 2020), p. 011037. DOI: 10.1103/PhysRevX.10.011037.

[428] J. Song, M. Marsili, and J. Jo. "Resolution and relevance trade-offs in deep learning". In: *J. Stat. Mech.: Theory Exp.* 2018.12 (Dec. 2018), p. 123406. DOI: 10.1088/1742-5468/aaf10f.

[429] T. Wu et al. "Learnability for the Information Bottleneck". In: *Entropy* 21.10 (Sept. 2019), p. 924. DOI: 10.3390/e21100924.

[430] Jorma Rissanen. *Stochastic Complexity in Statistical Inquiry*. Vol. 15. World Scientific Series in Computer Science. Singapore: World Scientific Publishing Co Pte Ltd., 1989. ISBN: 9971-50-859-1.

[431] R. J. Cubero, M. Marsili, and Y. Roudi. "Minimum Description Length Codes Are Critical". In: *Entropy* 20.10 (2018). Article No. 755. ISSN: 1099-4300. DOI: 10.3390/e20100755.

[432] R. J. Cubero et al. "Statistical criticality arises in most informative representations". In: *J. Stat. Mech.: Theory Exp.* 2019.6 (June 2019), p. 063402. DOI: 10.1088/1742-5468/ab16c8.

[433] Ryan John Cubero. "Statistical mechanics of samples, efficient representations and criticality". PhD thesis. Scuola Internazionale Superiore di Studi Avanzati, Trieste, Italy, Oct. 2018. URL: http://hdl.handle.net/20.500.11767/90676.

[434] L. Aitchison, N. Corradi, and P. E. Latham. *Zipf's law arises naturally in structured, high-dimensional data*. arXiv e-prints. 2014. arXiv: 1407.7135 [q-bio.NC].

[435] W. Bialek, I. Nemenman, and N. Tishby. "Predictability, complexity, and learning". In: *Neural Comput.* 13.11 (2001), pp. 2409–2463. DOI: 10.1162/089976601753195969.

[436] S. Still et al. "Thermodynamics of Prediction". In: *Phys. Rev. Lett.* 109.12 (Sept. 2012), p. 120604. DOI: 10.1103/PhysRevLett.109.120604.

[437] S. Still. "Thermodynamic Cost and Benefit of Memory". In: *Phys. Rev. Lett.* 124.5 (Feb. 2020), p. 050601. DOI: 10.1103/PhysRevLett.124.050601.

[438] A. A. Alemi and I. Fischer. *TherML: Thermodynamics of Machine Learning*. arXiv e-prints. 2018. arXiv: 1807.04162 [cs.LG].

[439] S. Still. "Information Bottleneck Approach to Predictive Inference". In: *Entropy* 16.2 (2014), pp. 968–989. ISSN: 1099-4300. DOI: 10.3390/e16020968.

[440] H. Hafez-Kolahi, S. Kasaei, and M. Soleymani-Baghshah. *Do Compressed Representations Generalize Better?* arXiv e-prints. 2019. arXiv: 1909.09706.

[441] N. Tishby, F. C. N. Pereira, and W. Bialek. *The information bottleneck method*. arXiv e-prints. 2000. arXiv: physics/0004057.

[442] G. Chechik et al. "Information Bottleneck for Gaussian Variables". In: *J. Mach. Learn. Res.* Vol. 6. 2005, pp. 165–188.

[443] O. Shamir, S. Sabato, and N. Tishby. "Learning and generalization with the information bottleneck". In: *Theoretical Computer Science* 411.29 (2010). Algorithmic Learning Theory (ALT 2008), pp. 2696–2711. ISSN: 0304-3975. DOI: 10.1016/j.tcs.2010.04.006.

[444] R. Shwartz-Ziv and N. Tishby. *Opening the Black Box of Deep Neural Networks via Information*. arXiv e-prints. 2017. arXiv: 1703.00810.

[445] T. Wu and I. Fischer. "Phase Transitions for the Information Bottleneck in Representation Learning". In: *Proc. of the 8th International Conference on Learning Representations, ICLR 2020, Addis Ababa, Ethiopia, April 26-30, 2020*. OpenReview.net, 2020. arXiv: 2001.01878.

[446] A. Zaidi, I. Estella-Aguerri, and S. Shamai (Shitz). "On the Information Bottleneck Problems: Models, Connections, Applications and Information Theoretic Views". In: *Entropy* 22.2 (2020). Article No. 151. ISSN: 1099-4300. DOI: 10.3390/e22020151.

[447] A. M. Saxe et al. "On the information bottleneck theory of deep learning". In: *J. Stat. Mech.: Theory Exp.* 2019.12 (Dec. 2019), p. 124020. DOI: 10.1088/1742-5468/ab3985.

[448] B. Rodríguez Gálvez, R. Thobaben, and M. Skoglund. "The Convex Information Bottleneck Lagrangian". In: *Entropy* 22.1 (2020). Article No. 98. ISSN: 1099-4300. DOI: 10.3390/e22010098.

[449] G. Carleo et al. "Machine learning and the physical sciences". In: *Rev. Mod. Phys.* 91.4 (Dec. 2019), p. 045002. DOI: 10.1103/RevModPhys.91.045002.

[450] C. Bény. *Deep learning and the renormalization group*. arXiv e-prints. Jan. 2013. arXiv: 1301.3124 [quant-ph].

[451] S. Saremi and T. J. Sejnowski. "Hierarchical model of natural images and the origin of scale invariance". In: *P. Natl. Acad. Sci. USA* 110.8 (2013), pp. 3071–3076. ISSN: 0027-8424. DOI: 10.1073/pnas.1222618110.

[452] P. Mehta and D. J. Schwab. *An exact mapping between the Variational Renormalization Group and Deep Learning*. arXiv e-prints. 2014. arXiv: 1410.3831 [stat.ML].

[453] C. Bény and T. J. Osborne. "Information-geometric approach to the renormalization group". In: *Phys. Rev. A* 92.2 (Aug. 2015), p. 022330. DOI: 10.1103/PhysRevA.92.022330.

[454] S. Bradde and W. Bialek. "PCA Meets RG". In: *J. Stat. Phys.* 167.3 (May 2017), pp. 462–475. ISSN: 1572-9613. DOI: 10.1007/s10955-017-1770-6.

[455] S.-H. Li and L. Wang. "Neural Network Renormalization Group". In: *Phys. Rev. Lett.* 121.26 (Dec. 2018), p. 260601. DOI: 10.1103/PhysRevLett.121.260601.

[456] S. Iso, S. Shiba, and S. Yokoo. "Scale-invariant feature extraction of neural network and renormalization group flow". In: *Phys. Rev. E* 97.5 (2018), p. 053304. DOI: 10.1103/PhysRevE.97.053304.

[457] D. Liu et al. "Machine learning by unitary tensor network of hierarchical tree structure". In: *New J. Phys.* 21.7 (July 2019), p. 073059. DOI: 10.1088/1367-2630/ab31ef.

[458] L. Zdeborová. "New tool in the box". In: *Nat. Phys.* 13 (2017), pp. 420–421. DOI: 10.1038/nphys4053.

[459] G. Torlai and R. G. Melko. "Learning thermodynamics with Boltzmann machines". In: *Phys. Rev. B* 94.16 (Oct. 2016), p. 165134. DOI: 10.1103/PhysRevB.94.165134.

[460] L. Wang. "Discovering phase transitions with unsupervised learning". In: *Phys. Rev. B* 94.19 (Nov. 2016), p. 195105. DOI: 10.1103/PhysRevB.94.195105.

[461] N. Portman and I. Tamblyn. "Sampling algorithms for validation of supervised learning models for Ising-like systems". In: *J. Comput. Phys.* 350 (Dec. 2017), pp. 871–890. DOI: 10.1016/j.jcp.2017.06.045. arXiv: 1611.05891 [cond-mat.stat-mech].

[462] C. Wang and H. Zhai. "Machine learning of frustrated classical spin models. I. Principal component analysis". In: *Phys. Rev. B* 96.14 (Oct. 2017), p. 144432. DOI: 10.1103/PhysRevB.96.144432.

[463] S. J. Wetzel. "Unsupervised learning of phase transitions: From principal component analysis to variational autoencoders". In: *Phys. Rev. E* 96.2 (Aug. 2017), p. 022140. DOI: 10.1103/PhysRevE.96.022140.

[464] W. Hu, R. R. P. Singh, and R. T. Scalettar. "Discovering phases, phase transitions, and crossovers through unsupervised machine learning: A critical examination". In: *Phys. Rev. E* 95.6 (June 2017), p. 062122. DOI: 10.1103/PhysRevE.95.062122.

[465] K. Ch'ng et al. "Machine Learning Phases of Strongly Correlated Fermions". In: *Phys. Rev. X* 7.3 (Aug. 2017), p. 031038. DOI: 10.1103/PhysRevX.7.031038.

[466] J. Carrasquilla and R. G. Melko. "Machine learning phases of matter". In: *Nat. Phys.* 13.5 (2017), pp. 431–434. DOI: 10.1038/nphys4035.

[467] E. P. L. Van Nieuwenburg, Y.-H. Liu, and S. D. Huber. "Learning phase transitions by confusion". In: *Nat. Phys.* 13.5 (2017), pp. 435–439. DOI: 10.1038/nphys4037.

[468] P. Suchsland and S. Wessel. "Parameter diagnostics of phases and phase transition learning by neural networks". In: *Phys. Rev. B* 97.17 (May 2018), p. 174435. DOI: 10.1103/PhysRevB.97.174435.

[469] R. A. Vargas-Hernández et al. "Extrapolating Quantum Observables with Machine Learning: Inferring Multiple Phase Transitions from Properties of a Single Phase". In: *Phys. Rev. Lett.* 121.25 (Dec. 2018), p. 255702. DOI: 10.1103/PhysRevLett.121.255702.

[470] Y.-H. Liu and E. P. L. van Nieuwenburg. "Discriminative Cooperative Networks for Detecting Phase Transitions". In: *Phys. Rev. Lett.* 120.17 (Apr. 2018), p. 176401. DOI: 10.1103/PhysRevLett.120.176401.

[471] C. Wang and H. Zhai. "Machine learning of frustrated classical spin models (II): Kernel principal component analysis". In: *Front. Phys.* 13.5 (June 2018), p. 130507. ISSN: 2095-0470. DOI: 10.1007/s11467-018-0798-7.

[472] K. Mills and I. Tamblyn. "Deep neural networks for direct, featureless learning through observation: The case of two-dimensional spin models". In: *Phys. Rev. E* 97.3 (Mar. 2018), p. 032119. DOI: 10.1103/PhysRevE.97.032119.

[473] W. Zhang, J. Liu, and T.-C. Wei. "Machine learning of phase transitions in the percolation and *XY* models". In: *Phys. Rev. E* 99.3 (Mar. 2019), p. 032142. DOI: 10.1103/PhysRevE.99.032142.

[474] H. Y. Kwon et al. "Searching magnetic states using an unsupervised machine learning algorithm with the Heisenberg model". In: *Phys. Rev. B* 99.2 (Jan. 2019), p. 024423. DOI: 10.1103/PhysRevB.99.024423.

[475] Xin Xu et al. "Recognition of polymer configurations by unsupervised learning". In: *Phys. Rev. E* 99.4 (Apr. 2019), p. 043307. DOI: 10.1103/PhysRevE.99.043307.

[476] Xiao-Yu Dong, Frank Pollmann, and Xue-Feng Zhang. "Machine learning of quantum phase transitions". In: *Phys. Rev. B* 99.12 (Mar. 2019), p. 121104. DOI: 10.1103/PhysRevB.99.121104.

[477] A. Decelle, V. Martin-Mayor, and B. Seoane. "Learning a local symmetry with neural networks". In: *Phys. Rev. E* 100.5 (Nov. 2019), p. 050102. DOI: 10.1103/PhysRevE.100.050102.

[478] Albert A. Shirinyan et al. "Self-organizing maps as a method for detecting phase transitions and phase identification". In: *Phys. Rev. B* 99.4 (Jan. 2019), p. 041108. DOI: 10.1103/PhysRevB.99.041108.

[479] T. Ohtsuki and T. Mano. "Drawing Phase Diagrams of Random Quantum Systems by Deep Learning the Wave Functions". In: *J. Phys. Soc. Jpn.* 89.2 (2020), p. 022001. DOI: 10.7566/JPSJ.89.022001.

[480] N. Yoshioka, Y. Akagi, and H. Katsura. "Learning disordered topological phases by statistical recovery of symmetry". In: *Phys. Rev. B* 97.20 (May 2018), p. 205110. DOI: 10.1103/PhysRevB.97.205110.

[481] P. Zhang, H. Shen, and H. Zhai. "Machine Learning Topological Invariants with Neural Networks". In: *Phys. Rev. Lett.* 120.6 (Feb. 2018), p. 066401. DOI: 10.1103/PhysRevLett.120.066401.

[482] R. Kaubruegger, L. Pastori, and J. C. Budich. "Chiral topological phases from artificial neural networks". In: *Phys. Rev. B* 97.19 (May 2018), p. 195136. DOI: 10.1103/PhysRevB.97.195136.

[483] I. Glasser et al. "Neural-Network Quantum States, String-Bond States, and Chiral Topological States". In: *Phys. Rev. X* 8.1 (Jan. 2018), p. 011006. DOI: 10.1103/PhysRevX.8.011006.

[484] J. F. Rodriguez-Nieva and M. S. Scheurer. "Identifying topological order through unsupervised machine learning". In: *Nature Phys.* 15.8 (2019), pp. 790–795.

[485] R. B. Jadrich, B. A. Lindquist, and T. M. Truskett. "Unsupervised machine learning for detection of phase transitions in off-lattice systems. I. Foundations". In: *J. Chem. Phys.* 149.19 (2018), p. 194109. DOI: 10.1063/1.5049849.

[486] R. B. Jadrich et al. "Unsupervised machine learning for detection of phase transitions in off-lattice systems. II. Applications". In: *J. Chem. Phys.* 149.19 (2018), p. 194110. DOI: 10.1063/1.5049850.

[487] V. Dunjko and H. J. Briegel. "Machine learning & artificial intelligence in the quantum domain: a review of recent progress". In: *Rep. Prog. Phys.* 81.7 (June 2018), p. 074001. DOI: 10.1088/1361-6633/aab406.

[488] X. Gao and L Duan. "Efficient representation of quantum many-body states with deep neural networks". In: *Nat. Commun.* 8.662 (2017). DOI: 10.1038/s41467-017-00705-2.

[489] G. Carleo and M. Troyer. "Solving the quantum many-body problem with artificial neural networks". In: *Science* 355.6325 (2017), pp. 602–606. ISSN: 0036-8075. DOI: 10.1126/science.aag2302.

[490] Y. Nomura et al. "Restricted Boltzmann machine learning for solving strongly correlated quantum systems". In: *Phys. Rev. B* 96.20 (Nov. 2017), p. 205152. DOI: 10.1103/PhysRevB.96.205152.

[491] Z. Cai and J. Liu. "Approximating quantum many-body wave functions using artificial neural networks". In: *Phys. Rev. B* 97.3 (Jan. 2018), p. 035116. DOI: 10.1103/PhysRevB.97.035116.

[492] H. Saito and M. Kato. "Machine Learning Technique to Find Quantum Many-Body Ground States of Bosons on a Lattice". In: *J. Phys. Soc. Jpn.* 87.1, 014001 (Jan. 2018), p. 014001. DOI: 10.7566/JPSJ.87.014001.

[493] K. Choo et al. "Symmetries and Many-Body Excitations with Neural-Network Quantum States". In: *Phys. Rev. Lett.* 121.16 (Oct. 2018), p. 167204. DOI: 10.1103/PhysRevLett.121.167204.

[494] G. Torlai et al. "Neural-network quantum state tomography". In: *Nat. Phys.* 14.5 (2018), pp. 447–450. DOI: 10.1038/s41567-018-0048-5.

[495] A. Rocchetto et al. "Learning hard quantum distributions with variational autoencoders". In: *npj Quantum Inf.* 4.1 (2018), pp. 1–7. DOI: 10.1038/s41534-018-0077-z.

[496] G. Torlai and R. G. Melko. "Latent Space Purification via Neural Density Operators". In: *Phys. Rev. Lett.* 120.24 (June 2018), p. 240503. DOI: 10.1103/PhysRevLett.120.240503.

[497] J. Carrasquilla et al. "Reconstructing quantum states with generative models". In: *Nat. Mach. Intell.* 1.3 (2019), pp. 155–161. DOI: 10.1038/s42256-019-0028-1.

[498] M. J. S. Beach et al. "QuCumber: wavefunction reconstruction with neural networks". In: *SciPost Phys.* 7.1 (2019), p. 9. DOI: 10.21468/SciPostPhys.7.1.009.

[499] O. Sharir et al. "Deep Autoregressive Models for the Efficient Variational Simulation of Many-Body Quantum Systems". In: *Phys. Rev. Lett.* 124.2 (Jan. 2020), p. 020503. DOI: 10.1103/PhysRevLett.124.020503.

[500] A. Haim, R. Kueng, and G. Refael. *Variational-Correlations Approach to Quantum Many-body Problems*. arXiv e-prints. 2020. arXiv: 2001.06510 [cond-mat.str-el].

[501] R. Iten et al. "Discovering Physical Concepts with Neural Networks". In: *Phys. Rev. Lett.* 124.1 (Jan. 2020), p. 010508. DOI: 10.1103/PhysRevLett.124.010508.

[502] R. T. D'Agnolo and A. Wulzer. "Learning new physics from a machine". In: *Phys. Rev. D* 99.1 (Jan. 2019), p. 015014. DOI: 10.1103/PhysRevD.99.015014.

[503] A. De Simone and T. Jacques. "Guiding new physics searches with unsupervised learning". In: *Eur. Phys. J. C* 79.4 (Mar. 2019), p. 289. ISSN: 1434-6052. DOI: 10.1140/epjc/s10052-019-6787-3.

[504] A. A. Melnikov et al. "Active learning machine learns to create new quantum experiments". In: *P. Natl. Acad. Sci. USA* 115.6 (2018), pp. 1221–1226. ISSN: 0027-8424. DOI: 10.1073/pnas.1714936115.

[505] T. Wu and M. Tegmark. "Toward an artificial intelligence physicist for unsupervised learning". In: *Phys. Rev. E* 100.3 (Sept. 2019), p. 033311. DOI: 10.1103/PhysRevE.100.033311.

[506] S.J. Wetzel and M. Scherzer. "Machine learning of explicit order parameters: From the Ising model to SU(2) lattice gauge theory". In: *Phys. Rev. B* 96.18 (Nov. 2017), p. 184410. DOI: 10.1103/PhysRevB.96.184410.

[507] P. Ponte and R. G. Melko. "Kernel methods for interpretable machine learning of order parameters". In: *Phys. Rev. B* 96.20 (Nov. 2017), p. 205146. DOI: 10.1103/PhysRevB.96.205146.

[508] C. Giannetti, B. Lucini, and D. Vadacchino. "Machine Learning as a universal tool for quantitative investigations of phase transitions". In: *Nucl. Phys. B* 944 (2019), p. 114639. ISSN: 0550-3213. DOI: 10.1016/j.nuclphysb.2019.114639.

[509] K. Liu, J. Greitemann, and L. Pollet. "Learning multiple order parameters with interpretable machines". In: *Phys. Rev. B* 99.10 (Mar. 2019), p. 104410. DOI: 10.1103/PhysRevB.99.104410.

[510] C. Casert et al. "Interpretable machine learning for inferring the phase boundaries in a nonequilibrium system". In: *Phys. Rev. E* 99.2 (Feb. 2019), p. 023304. DOI: 10.1103/PhysRevE.99.023304.

[511] J. Greitemann, K. Liu, and L. Pollet. "Probing hidden spin order with interpretable machine learning". In: *Phys. Rev. B* 99.6 (Feb. 2019), p. 060404. DOI: 10.1103/PhysRevB.99.060404.

[512] S. Blücher et al. "Towards novel insights in lattice field theory with explainable machine learning". In: *Phys. Rev. D* 101.9 (May 2020), p. 094507. DOI: 10.1103/PhysRevD.101.094507.

[513] T. Geigenfeind and D. de las Heras. "Principal component analysis of the excluded area of two-dimensional hard particles". In: *J. Chem. Phys.* 150.18 (2019), p. 184906. DOI: 10.1063/1.5092865.

[514] S.-C. Lin and M. Oettel. "A classical density functional from machine learning and a convolutional neural network". In: *SciPost Phys.* 6.2 (2019), p. 25. DOI: 10.21468/SciPostPhys.6.2.025.

[515] S.-C. Lin, G. Martius, and M. Oettel. "Analytical classical density functionals from an equation learning network". In: *J. Chem. Phys.* 152.2 (2020), p. 021102. DOI: 10.1063/1.5135919.

[516] P. E. Shanahan, D. Trewartha, and W. Detmold. "Machine learning action parameters in lattice quantum chromodynamics". In: *Phys. Rev. D* 97.9 (May 2018), p. 094506. DOI: 10.1103/PhysRevD.97.094506.

[517] K. Zhou et al. "Regressive and generative neural networks for scalar field theory". In: *Phys. Rev. D* 100.1 (July 2019), p. 011501. DOI: 10.1103/PhysRevD.100.011501.

[518] D. Wu, L. Wang, and P. Zhang. "Solving Statistical Mechanics Using Variational Autoregressive Networks". In: *Phys. Rev. Lett.* 122.8 (Feb. 2019), p. 080602. DOI: 10.1103/PhysRevLett.122.080602.

[519] F. Noé et al. "Boltzmann generators: Sampling equilibrium states of many-body systems with deep learning". In: *Science* 365.6457 (2019). ISSN: 0036-8075. DOI: 10.1126/science.aaw1147.

[520] J. Köhler, L. Klein, and F. Noé. *Equivariant Flows: sampling configurations for multi-body systems with symmetric energies*. arXiv e-prints. 2019. arXiv: 1910.00753.

[521] K. Sprague et al. "Watch and learn—a generalized approach for transferrable learning in deep neural networks via physical principles". In: *Mach. Learn.: Sci. Technol.* 2.2 (Feb. 2021), 02LT02. DOI: 10.1088/2632-2153/abc81b.

[522] Z. Li, M. Luo, and X. Wan. "Extracting critical exponents by finite-size scaling with convolutional neural networks". In: *Phys. Rev. B* 99.7 (Feb. 2019), p. 075418. DOI: 10.1103/PhysRevB.99.075418.

[523] S. Efthymiou, M. J. S. Beach, and R. G. Melko. "Super-resolving the Ising model with convolutional neural networks". In: *Phys. Rev. B* 99.7 (Feb. 2019), p. 075113. DOI: 10.1103/PhysRevB.99.075113.

[524] K. Mills et al. "Extensive deep neural networks for transferring small scale learning to large scale systems". In: *Chem. Sci.* 10.15 (2019), pp. 4129–4140. DOI: 10.1039/C8SC04578J.

[525] Julien Despois. *Autoencoders — Deep Learning bits #1*. [Blog] https://hackernoon.com/autoencoders-deep-learning-bits-1-11731e200694. Accessed on August 20, 2020. Feb. 2017.

[526] Lilien Wang. *From Autoencoder to Beta-VAE*. [Blog] https://lilianweng.github.io/lil-log/2018/08/12/from-autoencoder-to-beta-vae.html. Accessed on August 19, 2020. July 2019.

[527] B. Dai et al. "Connections with Robust PCA and the Role of Emergent Sparsity in Variational Autoencoder Models". In: *J. Mach. Learn. Res.* 19.41 (2018), pp. 1–42.

[528] B. Dai and D. P. Wipf. "Diagnosing and Enhancing VAE Models". In: *Proc. of the 7th International Conference on Learning Representations, ICLR 2019, New Orleans, LA, USA, May 6-9, 2019*. OpenReview.net, 2019. arXiv: 1903.05789 [cs.LG].

[529] M. D. Hoffman and M. J. Johnson. "Elbo surgery: yet another way to carve up the variational evidence lower bound". In: *Proc. of the Workshop in Advances in Approximate Bayesian Inference, NIPS*. Vol. 1. 2016, p. 2.

[530] J. He et al. "Lagging Inference Networks and Posterior Collapse in Variational Autoencoders". In: *Proc. of the 7th International Conference on Learning Representations, ICLR 2019, New Orleans, LA, USA, May 6–9, 2019*. OpenReview.net, 2019.

[531] A. Asperti. "Variational Autoencoders and the Variable Collapse Phenomenon". In: *Sensors & Transducers* 234.6 (2019), pp. 1–8.

[532] I. Higgins et al. *Towards a Definition of Disentangled Representations*. arXiv e-prints. 2018. arXiv: 1812.02230.

[533] E. Mathieu et al. "Disentangling Disentanglement in Variational Autoencoders". In: *Proc. of the 36th International Conference on Machine Learning, ICML 2019, 9-15 June 2019, Long Beach, California, USA*. Ed. by K. Chaudhuri and R. Salakhutdinov. Vol. 97. Proceedings of Machine Learning Research. PMLR, 2019, pp. 4402–4412.

[534] F. D'Angelo and L. Böttcher. "Learning the Ising model with generative neural networks". In: *Phys. Rev. Research* 2.2 (June 2020), p. 023266. DOI: 10.1103/PhysRevResearch.2.023266.

[535] W. Zhong et al. *Learning about learning by many-body systems*. arXiv e-prints. 2020. arXiv: 2001.03623 [cond-mat.stat-mech].

[536] Ilia A. Luchnikov et al. "Variational Autoencoder Reconstruction of Complex Many-Body Physics". In: *Entropy* 21.11 (2019). Article No. 1091. ISSN: 1099-4300. DOI: 10.3390/e21111091.

[537] C. X. Hernández et al. "Variational encoding of complex dynamics". In: *Phys. Rev. E* 97.6 (June 2018), p. 062412. DOI: 10.1103/PhysRevE.97.062412.

[538] C. Wehmeyer and F. Noé. "Time-lagged autoencoders: Deep learning of slow collective variables for molecular kinetics". In: *J. Chem. Phys.* 148.24 (2018), p. 241703. DOI: 10.1063/1.5011399.

[539] W. Man et al. "Experiments on Random Packings of Ellipsoids". In: *Phys. Rev. Lett.* 94.19 (May 2005), p. 198001. DOI: 10.1103/PhysRevLett.94.198001.

[540] P. F. Damasceno, M. Engel, and S. C. Glotzer. "Predictive Self-Assembly of Polyhedra into Complex Structures". In: *Science* 337.6093 (2012), pp. 453–457. ISSN: 0036-8075. DOI: 10.1126/science.1220869.

[541] U. Agarwal and F. A. Escobedo. "Mesophase behaviour of polyhedral particles". In: *Nat. Mater.* 10.3 (2011), pp. 230–235. DOI: 10.1038/nmat2959.

[542] E. S. Harper, B. Waters, and S. C. Glotzer. "Hierarchical self-assembly of hard cube derivatives". In: *Soft Matter* 15.18 (2019), pp. 3733–3739. DOI: 10.1039/C8SM02619J.

[543] Z. Sumer and A. Striolo. "Nanoparticles shape-specific emergent behaviour on liquid crystal droplets". In: *Mol. Syst. Des. Eng.* (2020). DOI: 10.1039/C9ME00153K.

[544] H. Malmir, M. Sahimi, and M. R. R. Tabar. "Microstructural characterization of random packings of cubic particles". In: *Sci. Rep.* 6.1 (2016), pp. 1–9. DOI: 10.1038/srep35024.

[545] S. C. Glotzer and M. J. Solomon. "Anisotropy of building blocks and their assembly into complex structures". In: *Nat. Mater.* 6.8 (2007), pp. 557–562. DOI: 10.1038/nmat1949.

[546] M. E. Irrgang et al. "Virial Coefficients and Equations of State for Hard Polyhedron Fluids". In: *Langmuir* 33.42 (2017), pp. 11788–11796. DOI: 10.1021/acs.langmuir.7b02384.

[547] W. Man et al. "Experimental measurement of the photonic properties of icosahedral quasicrystals". In: *Nature* 436 (2005), pp. 993–996. DOI: 10.1038/nature03977.

[548] A. Della Villa et al. "Band Gap Formation and Multiple Scattering in Photonic Quasicrystals with a Penrose-Type Lattice". In: *Phys. Rev. Lett.* 94.18 (May 2005), p. 183903. DOI: 10.1103/PhysRevLett.94.183903.

[549] H. Tanaka. "Importance of many-body orientational correlations in the physical description of liquids". In: *Faraday Discuss.* 167.0 (2013), pp. 9–76. DOI: 10.1039/C3FD00110E.

[550] B. O'Malley and I. Snook. "Structure of hard-sphere fluid and precursor structures to crystallization". In: *J. Chem. Phys.* 123.5 (2005), p. 054511. DOI: 10.1063/1.1992475.

[551] J. Russo and H. Tanaka. "Crystal nucleation as the ordering of multiple order parameters". In: *J. Chem. Phys.* 145.21 (2016), p. 211801. DOI: 10.1063/1.4962166.

[552] É. Roldán et al. "Universal features in the energetics of symmetry breaking". In: *Nature Phys.* 10.6 (2014), pp. 457–461. DOI: 10.1038/nphys2940.

[553] J. M. R. Parrondo. "The Szilard engine revisited: Entropy, macroscopic randomness, and symmetry breaking phase transitions". In: *Chaos* 11.3 (2001), pp. 725–733. DOI: 10.1063/1.1388006.

[554] M. P. Allen et al. "Hard Convex Body Fluids". In: *Adv. Chem. Phys.* John Wiley & Sons, Ltd, 2007. Chap. 1, pp. 1–166. ISBN: 9780470141458. DOI: 10.1002/9780470141458.ch1.

[555] W. van Megen and H. J. Schöpe. "The cage effect in systems of hard spheres". In: *J. Chem. Phys.* 146.10 (2017), p. 104503. DOI: 10.1063/1.4977523.

[556] G. Schöpe H. J.and Bryant and W. van Megen. "Small changes in particle-size distribution dramatically delay and enhance nucleation in hard sphere colloidal suspensions". In: *Phys. Rev. E* 74.6 (Dec. 2006), p. 060401. DOI: 10.1103/PhysRevE.74.060401.

[557] W. van Megen and H. J. Schöpe. "Entropic Identification of the First Order Freezing Transition of a Suspension of Hard Sphere Particles". In: *Phys. Rev. Lett.* 124.20 (May 2020), p. 205701. DOI: 10.1103/PhysRevLett.124.205701.

[558] Y. Levin et al. "Nonequilibrium statistical mechanics of systems with long-range interactions". In: *Phys. Rep.* 535.1 (2014). Nonequilibrium statistical mechanics of systems with long-range interactions, pp. 1–60. ISSN: 0370-1573. DOI: 10.1016/j.physrep.2013.10.001.

[559] D. Mukamel, S. Ruffo, and N. Schreiber. "Breaking of Ergodicity and Long Relaxation Times in Systems with Long-Range Interactions". In: *Phys. Rev. Lett.* 95.24 (Dec. 2005), p. 240604. DOI: 10.1103/PhysRevLett.95.240604.

[560] F. Bouchet et al. "Phase space gaps and ergodicity breaking in systems with long-range interactions". In: *Phys. Rev. E* 77.1 (Jan. 2008), p. 011125. DOI: 10.1103/PhysRevE.77.011125.

[561] A. Figueiredo, T. M. Rocha Filho, and M. A. Amato. "Ergodicity and central-limit theorem in systems with long-range interactions". In: *Europhys. Lett.* 83.3 (July 2008), p. 30011. DOI: 10.1209/0295-5075/83/30011.

[562] F. P. da C. Benetti et al. "Ergodicity Breaking and Parametric Resonances in Systems with Long-Range Interactions". In: *Phys. Rev. Lett.* 108.14 (Apr. 2012), p. 140601. DOI: 10.1103/PhysRevLett.108.140601.

[563] R. Mahnke, J. Kaupuźs, and I. Lubashevsky. *Physics of Stochastic Processes: How Randomness Acts in Time*. Weinheim: WILEY-VCH Verlag GmbH & Co. KGaA, 2009. ISBN: 978-3-527-40840-5.

[564] S. Roy et al. "Aging phenomena during phase separation in fluids: decay of autocorrelation for vapor–liquid transitions". In: *Soft Matter* 15.23 (2019), pp. 4743–4750. DOI: 10.1039/C9SM00366E.

[565] A. G. Cherstvy, A. V. Chechkin, and R. Metzler. "Ageing and confinement in non-ergodic heterogeneous diffusion processes". In: *J. Phys. A* 47.48 (Nov. 2014), p. 485002. DOI: 10.1088/1751-8113/47/48/485002.

[566] K. Binder. "Theory of first-order phase transitions". In: *Rep. Prog. Phys.* 50.7 (July 1987), pp. 783–859. DOI: 10.1088/0034-4885/50/7/001.

[567] S. Martiniani, P. M. Chaikin, and D. Levine. "Quantifying Hidden Order out of Equilibrium". In: *Phys. Rev. X* 9.1 (Feb. 2019), p. 011031. DOI: 10.1103/PhysRevX.9.011031.

[568] H. J. Schöpe. *Translational and orientational ordering in hard sphere systems*. Private communication. Aug. 2020.

[569] G. A. Mansoori and S. A. Rice. "Confined Fluids: Structure, Properties and Phase Behavior". In: *Adv. Chem. Phys.* John Wiley & Sons, Ltd, 2014. Chap. 5, pp. 197–294. ISBN: 9781118949702. DOI: 10.1002/9781118949702.ch5.

[570] H. Nakanishi and M. E. Fisher. "Multicriticality of Wetting, Prewetting, and Surface Transitions". In: *Phys. Rev. Lett.* 49.21 (Nov. 1982), pp. 1565–1568. DOI: 10.1103/PhysRevLett.49.1565.

[571] M. E. Fisher and H. Nakanishi. "Scaling theory for the criticality of fluids between plates". In: *J. Chem. Phys.* 75.12 (1981), pp. 5857–5863. DOI: 10.1063/1.442035.

[572] P. G. de Gennes. "Wetting: statics and dynamics". In: *Rev. Mod. Phys.* 57.3 (July 1985), pp. 827–863. DOI: 10.1103/RevModPhys.57.827.

[573] K. Binder, D. Landau, and M. Müller. "Monte Carlo studies of wetting, interface localization and capillary condensation". In: *J. Stat. Phys.* 110.3-6 (2003), pp. 1411–1514. DOI: 10.1023/A:1022173600263.

[574] K. Binder et al. "Confinement effects on phase behavior of soft matter systems". In: *Soft Matter* 4.8 (2008), pp. 1555–1568. DOI: 10.1039/B802207K.

[575] K. Binder et al. "Phase Separation in Confined Geometries". In: *J. Stat. Phys.* 138.1–3 (Feb. 2010), pp. 51–84. DOI: 10.1007/s10955-010-9924-9.

[576] H. Emmerich et al., eds. *Heterogenous Nucleation and Microstructure Formation: Steps Towards a System and Scale Bridging Understanding*. Feb. 2014, pp. 337–608.

[577] F. Turci et al. "Solid phase properties and crystallization in simple model systems". In: *Eur. Phys. J.-Spec. Top.* 223.3 (Feb. 2014), pp. 421–438. DOI: 10.1140/epjst/e2014-02100-8.

[578] M. Schmidt and H. Löwen. "Phase diagram of hard spheres confined between two parallel plates". In: *Phys. Rev. E* 55.6 (June 1997), pp. 7228–7241. DOI: 10.1103/PhysRevE.55.7228.

[579] T. Shioda, B. Wen, and C. Rosenblatt. "Continuous nematic anchoring transition due to surface-induced smectic order". In: *Phys. Rev. E* 67.4 (Apr. 2003), p. 041706. DOI: 10.1103/PhysRevE.67.041706.

[580] M. E. Fisher and P. G. de Gennes. "Wall phenomena in a critical binary mixture". In: *C. R. Acad. Sci. Paris Ser. B* 287 (1978), p. 207.

[581] H. BG Casimir. "On the attraction between two perfectly conducting plates". In: *Proc. Kon. Ned. Akad. Wet.* Vol. 51. 1948, p. 793.

[582] F. Schlesener, A. Hanke, and S. Dietrich. "Critical Casimir forces in colloidal suspensions". In: *J. Stat. Phys.* 110 (2003), pp. 981–1013. DOI: 10.1023/A:1022184508016.

[583] A. Maciołek and S. Dietrich. "Collective behavior of colloids due to critical Casimir interactions". In: *Rev. Mod. Phys.* 90.4 (Oct. 2018), p. 045001. DOI: 10.1103/RevModPhys.90.045001.

[584] C. Hertlein et al. "Direct measurement of critical Casimir forces". In: *Nature* 451.7175 (2008), pp. 172–175. DOI: 10.1038/nature06443.

[585] S. Balibar. "The force of fluctuations". In: *Nature* 451 (2008), pp. 136–137. DOI: doi:10.1038/451136a.

[586] S. Paladugu et al. "Nonadditivity of critical Casimir forces". In: *Nat. Commun,* 7 (2016), p. 11403. DOI: doi.org/10.1038/ncomms11403.

[587] O. A. Vasilyev, S. Dietrich, and S. Kondrat. "Nonadditive interactions and phase transitions in strongly confined colloidal systems". In: *Soft Matter* 14.4 (2018), pp. 586–596. DOI: 10.1039/C7SM01363A.

[588] M. Krech. "Fluctuation-induced forces in critical fluids". In: *J. Phys. Condens. Matter* 11.37 (Sept. 1999), R391–R412. DOI: 10.1088/0953-8984/11/37/201.

[589] M. E. Fisher and M. N. Barber. "Scaling Theory for Finite-Size Effects in the Critical Region". In: *Phys. Rev. Lett.* 28.23 (June 1972), pp. 1516–1519. DOI: 10.1103/PhysRevLett.28.1516.

[590] K. Vollmayr et al. "Finite size effects at thermally-driven first order phase transitions: a phenomenological theory of the order parameter distribution". In: *Z. Phys. B Con. Mat.* 91 (1993), p. 113. DOI: 10.1007/BF01316713.

[591] K. Binder. "Finite size scaling analysis of Ising model block distribution functions". In: *Z. Phys. B Con. Mat.* 43.2 (June 1981), pp. 119–140. ISSN: 1431-584X. DOI: 10.1007/BF01293604.

[592] K. Binder. "Critical Properties from Monte Carlo Coarse Graining and Renormalization". In: *Phys. Rev. Lett.* 47.9 (Aug. 1981), pp. 693–696. DOI: 10.1103/PhysRevLett.47.693.

[593] M. E. Fisher. "The renormalization group in the theory of critical behavior". In: *Rev. Mod. Phys.* 46.4 (Oct. 1974), pp. 597–616. DOI: 10.1103/RevModPhys.46.597.

[594] A. Fortini and M. Dijkstra. "Phase behaviour of hard spheres confined between parallel hard plates: manipulation of colloidal crystal structures by confinement". In: *J. Phys. Condens. Matter* 18.28 (June 2006), pp. L371–L378. DOI: 10.1088/0953-8984/18/28/l02.

[595] E. P. Bernard and W. Krauth. "Two-Step Melting in Two Dimensions: First-Order Liquid-Hexatic Transition". In: *Phys. Rev. Lett.* 107.15 (Oct. 2011), p. 155704. DOI: 10.1103/PhysRevLett.107.155704.

[596] A. B. G. M. Leferink op Reinink et al. "Phase behaviour of lyotropic liquid crystals in external fields and confinement". In: *Eur. Phys. J. Spec. Top.* 222 (2013), 3053–3069. DOI: 10.1140/epjst/e2013-02075-x.

[597] M. Cosentino Lagomarsino, M. Dogterom, and M. Dijkstra. "Isotropic-nematic transition of long, thin, hard spherocylinders confined in a quasi-two-dimensional planar geometry". In: *J. Chem. Phys.* 119.6 (2003), pp. 3535–3540. DOI: 10.1063/1.1588994.

[598] H. H. Wensink et al. "Differently shaped hard body colloids in confinement: From passive to active particles". In: *Eur. Phys. J. Spec. Top.* 222 (2013), pp. 3023–3037. DOI: 10.1140/epjst/e2013-02073-0.

[599] P. Sharma et al. "Hierarchical organization of chiral rafts in colloidal membranes". In: 513 (2014), pp. 77–80. DOI: 10.1038/nature13694.

[600] B. Jerome. "Surface effects and anchoring in liquid crystals". In: *Rep. Prog. Phys.* 54.3 (Mar. 1991), pp. 391–451. DOI: 10.1088/0034-4885/54/3/002.

[601] M. M. Telo da Gama. "Phase diagrams and interfacial properties of nematic liquid crystals". In: *Physica A* 244.1 (1997), pp. 389–401. ISSN: 0378-4371. DOI: 10.1016/S0378-4371(97)00223-9.

[602] M. P. Allen. "Molecular simulation and theory of the isotropic-nematic interface". In: *J. Chem. Phys.* 112.12 (2000), pp. 5447–5453. DOI: 10.1063/1.481112.

[603] C. Bahr and D. Fliegner. "Behavior of a first-order smectic-A–smectic-C transition in free-standing liquid-crystal films". In: *Phys. Rev. A* 46.12 (Dec. 1992), pp. 7657–7663. DOI: 10.1103/PhysRevA.46.7657.

[604] D. A. Olson et al. "Determination of symmetry and molecular arrangements of free-standing liquid crystal films using null-transmission ellipsometry". In: *Liq. Cryst.* 29.12 (2002), pp. 1521–1528. DOI: 10.1080/0267829021000017979.

[605] L.D. Pan, C. S. Hsu, and C. C. Huang. "Surface-Surface Interaction in Smectic Liquid Crystal Films". In: *Phys. Rev. Lett.* 108.2 (Jan. 2012), p. 027801. DOI: 10.1103/PhysRevLett.108.027801.

[606] M. Dijkstra, R. van Roij, and R. Evans. "Wetting and capillary nematization of a hard-rod fluid: A simulation study". In: *Phys. Rev. E* 63.5 (Apr. 2001), p. 051703. DOI: 10.1103/PhysRevE.63.051703.

[607] H. Steuer, S. Hess, and M. Schoen. "Phase behavior of liquid crystals confined by smooth walls". In: *Phys. Rev. E* 69.3 (Mar. 2004), p. 031708. DOI: 10.1103/PhysRevE.69.031708.

[608] M. Greschek, M. Melle, and M. Schoen. "Isotropic–nematic phase transitions in confined mesogenic fluids. The role of substrate anchoring". In: *Soft Matter* 6.9 (2010), pp. 1898–1909. DOI: 10.1039/B924417D.

[609] F. N. Braun, T. J. Sluckin, and E. Velasco. "Director distortion in a nematic wetting layer". In: *J. Phys. Condens. Matter* 8.16 (Apr. 1996), pp. 2741–2754. DOI: 10.1088/0953-8984/8/16/003.

[610] I. Rodríguez-Ponce et al. "Interplay between Anchoring and Wetting at a Nematic-Substrate Interface". In: *Phys. Rev. Lett.* 82.13 (Mar. 1999), pp. 2697–2700. DOI: 10.1103/PhysRevLett.82.2697.

[611] I. Rodríguez-Ponce et al. "Anchoring and nematic-isotropic transitions in a confined nematic phase". In: *J. Phys. Condens. Matter* 12.8A (Feb. 2000), A363–A367. DOI: 10.1088/0953-8984/12/8a/349.

[612] S. Singh. "Reentrant phase transitions in liquid crystals". In: *Phase Transit.* 72.3 (2000), pp. 183–209. DOI: 10.1080/01411590008228989.

[613] M. P. Allen. "Molecular simulation and theory of liquid crystal surface anchoring". In: *Mol. Phys.* 96.9 (1999), pp. 1391–1397. DOI: 10.1080/00268979909483083.

[614] J. Quintana and A. Robledo. "Phase properties of nematics confined by competing walls". In: *Physica A* 248.1 (1998), pp. 28–43. ISSN: 0378-4371. DOI: 10.1016/S0378-4371(97)00523-2.

[615] Z. Zhang et al. "Substrate-induced bulk alignment of liquid crystals". In: *Phys. Rev. E* 53.3 (Mar. 1996), pp. 2461–2465. DOI: 10.1103/PhysRevE.53.2461.

[616] T. Gruhn and M. Schoen. "Substrate-induced order in confined nematic liquid-crystal films". In: *J. Chem. Phys.* 108.21 (1998), pp. 9124–9136. DOI: 10.1063/1.476359.

[617] F. N. Braun et al. "Oblique anchoring at a free nematic surface". In: *Phys. Rev. E* 53.1 (Jan. 1996), pp. 706–713. DOI: 10.1103/PhysRevE.53.706.

[618] P. I. C. Teixeira. "Structure of a nematic liquid crystal between aligning walls". In: *Phys. Rev. E* 55.3 (Mar. 1997), pp. 2876–2881. DOI: 10.1103/PhysRevE.55.2876.

[619] I. Rodríguez-Ponce, J. M. Romero-Enrique, and L. F. Rull. "Orientational transitions in a nematic liquid crystal confined by competing surfaces". In: *Phys. Rev. E* 64.5 (Oct. 2001), p. 051704. DOI: 10.1103/PhysRevE.64.051704.

[620] D. de las Heras, E. Velasco, and L. Mederos. "Effects of wetting and anchoring on capillary phenomena in a confined liquid crystal". In: *J. Chem. Phys.* 120.10 (2004), pp. 4949–4957. DOI: 10.1063/1.1646374.

[621] D. de las Heras, E. Velasco, and L. Mederos. "Capillary Smectization and Layering in a Confined Liquid Crystal". In: *Phys. Rev. Lett.* 94.1 (Jan. 2005), p. 017801. DOI: 10.1103/PhysRevLett.94.017801.

[622] I. Rodríguez-Ponce, J. M. Romero-Enrique, and L. F. Rull. "Density functional theory study of the nematic-isotropic transition in an hybrid cell". In: *J. Chem. Phys.* 122.1 (2005), p. 014903. DOI: 10.1063/1.1829041.

[623] S. V. Savenko and M. Dijkstra. "Sedimentation and multiphase equilibria in suspensions of colloidal hard rods". In: *Phys. Rev. E* 70.5 (Nov. 2004), p. 051401. DOI: 10.1103/PhysRevE.70.051401.

[624] Tara M. Drwenski. "Colloidal liquid crystals: phase behavior, sedimentation, and percolation of rods, boomerangs, and cuboids". Doctoral Thesis. Utrecht University, 2018. ISBN: 978-90-393-7021-6. URL: http://dspace.library.uu.nl/handle/1874/368235.

[625] A. J. Archer et al. "Generation of Defects and Disorder from Deeply Quenching a Liquid to Form a Solid". In: *Mathematical Challenges in a New Phase of Materials Science*. Ed. by Yasumasa Nishiura and Motoko Kotani. Tokyo: Springer Japan, 2016, pp. 1–26. ISBN: 978-4-431-56104-0.

[626] A. Poniewierski and A. Samborski. "Anchoring of a nematic liquid crystal on an anisotropic substrate". In: *Liq. Cryst.* 27.10 (2000), pp. 1285–1293. DOI: 10.1080/026782900423322.

[627] H. Takezoe, E. Gorecka, and M. Čepič. "Antiferroelectric liquid crystals: Interplay of simplicity and complexity". In: *Rev. Mod. Phys.* 82.1 (Mar. 2010), pp. 897–937. DOI: 10.1103/RevModPhys.82.897.

[628] T. J. Sluckin. "Anchoring transitions at liquid crystal surfaces". In: *Physica A* 213.1 (1995), pp. 105–109. ISSN: 0378-4371. DOI: 10.1016/0378-4371(94)00151-I.

[629] E. Allahyarov, A. Voigt, and H. Löwen. "Smectic monolayer confined on a sphere: topology at the particle scale". In: *Soft Matter* 13.44 (2017), pp. 8120–8135. DOI: 10.1039/C7SM01704A.

[630] R. van Roij, M. Dijkstra, and R. Evans. "Orientational wetting and capillary nematization of hard-rod fluids". In: *Europhys. Lett.* 49.3 (Feb. 2000), pp. 350–356. DOI: 10.1209/epl/i2000-00155-0.

[631] K. Shundyak and R. van Roij. "Hard colloidal rods near a soft wall: Wetting, drying, and symmetry breaking". In: *Europhys. Lett.* 74.6 (June 2006), pp. 1039–1045. DOI: 10.1209/epl/i2006-10062-4.

[632] T. Geigenfeind et al. "Confinement of two-dimensional rods in slit pores and square cavities". In: *J. Chem. Phys.* 142.17 (2015), p. 174701. DOI: 10.1063/1.4919307.

[633] W. Janke and H. Kleinhert. "From First-Order to Two Continuous Melting Transitions: Monte Carlo Study of a New 2D Lattice-Defect Model". In: *Phys. Rev. Lett.* 61.20 (Nov. 1988), pp. 2344–2347. DOI: 10.1103/PhysRevLett.61.2344.

[634] C.-F. Chou et al. "Multiple-Step Melting in Two-Dimensional Hexatic Liquid-Crystal Films". In: *Science* 280.5368 (1998), pp. 1424–1426. ISSN: 0036-8075. DOI: 10.1126/science.280.5368.1424.

[635] Y. Martínez-Ratón, S. Varga, and E. Velasco. "Phase behaviour of liquid-crystal monolayers of rod-like and plate-like particles". In: *J. Chem. Phys.* 140.20, 204906 (May 2014), p. 204906. DOI: 10.1063/1.4876719.

[636] R. Aliabadi et al. "Ordering transitions of weakly anisotropic hard rods in narrow slitlike pores". In: *Phys. Rev. E* 97.1 (Jan. 2018), p. 012703. DOI: 10.1103/PhysRevE.97.012703.

[637] S. M. Pittman, G. G. Batrouni, and R. T. Scalettar. "Monte Carlo study of an inhomogeneous Blume-Capel model: A case study of the local density approximation". In: *Phys. Rev. B* 78.21 (Dec. 2008), p. 214208. DOI: 10.1103/PhysRevB.78.214208.

[638] J. M. Polson and E. E. Burnell. "Nematic-isotropic phase coexistence in a Lebwohl–Lasher model binary liquid crystal mixture". In: *Chem. Phys. Lett.* 281.1 (1997), pp. 207–211. ISSN: 0009-2614. DOI: 10.1016/S0009-2614(97)01185-8.

[639] L. Zhang et al. "Experimental studies of vibrational modes in a two-dimensional amorphous solid". In: *Nat. Commun.* 8.67 (2017). DOI: 10.1038/s41467-017-00106-5.

[640] F. Höfling et al. "Entangled dynamics of a stiff polymer". In: *Phys. Rev. E* 77.6 (June 2008), p. 060904. DOI: 10.1103/PhysRevE.77.060904.

[641] F. Höfling, E. Frey, and T. Franosch. "Enhanced Diffusion of a Needle in a Planar Array of Point Obstacles". In: *Phys. Rev. Lett.* 101.12 (Sept. 2008), p. 120605. DOI: 10.1103/PhysRevLett.101.120605.

[642] S. Leitmann, F. Höfling, and T. Franosch. "Tube Concept for Entangled Stiff Fibers Predicts Their Dynamics in Space and Time". In: *Phys. Rev. Lett.* 117.9 (Aug. 2016), p. 097801. DOI: 10.1103/PhysRevLett.117.097801.

[643] X. Ma et al. "Test of the Universal Scaling Law of Diffusion in Colloidal Monolayers". In: *Phys. Rev. Lett.* 110.7 (Feb. 2013), p. 078302. DOI: 10.1103/PhysRevLett.110.078302.

[644] S. Jiang et al. "Orientationally Glassy Crystals of Janus Spheres". In: *Phys. Rev. Lett.* 112.21 (May 2014), p. 218301. DOI: 10.1103/PhysRevLett.112.218301.

[645] T. Munk et al. "Effective Perrin theory for the anisotropic diffusion of a strongly hindered rod". In: *Europhys. Lett.* 85.3 (Feb. 2009), p. 30003. DOI: 10.1209/0295-5075/85/30003.

[646] M. Doi and S. F. Edwards. "Dynamics of rod-like macromolecules in concentrated solution. Part 1". In: *J. Chem. Soc., Faraday Trans. 2* 74.0 (1978), pp. 560–570. DOI: 10.1039/F29787400560.

[647] M. Doi and S. F. Edwards. "Dynamics of rod-like macromolecules in concentrated solution. Part 2". In: *J. Chem. Soc., Faraday Trans. 2* 74.0 (1978), pp. 918–932. DOI: 10.1039/F29787400918.

[648] Kenneth L. Kearns et al. "Hiking down the Energy Landscape: Progress Toward the Kauzmann Temperature via Vapor Deposition". In: *J. Phys. Chem. B* 112.16 (2008). PMID: 18386872, pp. 4934–4942. DOI: 10.1021/jp7113384.

[649] A. Gambassi and S. Dietrich. "Critical Casimir forces steered by patterned substrates". In: *Soft Matter* 7.4 (2011), pp. 1247–1253. DOI: 10.1039/C0SM00635A.

[650] J. J. Gray and R. T. Bonnecaze. "Adsorption of colloidal particles by Brownian dynamics simulation: Kinetics and surface structures". In: *J. Chem. Phys.* 114.3 (2001), pp. 1366–1381. DOI: 10.1063/1.1319317.

[651] J. Bleibel, A. Domínguez, and M. Oettel. "Onset of anomalous diffusion in colloids confined to quasimonolayers". In: *Phys. Rev. E* 95.3 (Mar. 2017), p. 032604. DOI: 10.1103/PhysRevE.95.032604.

[652] Y. Gao et al. "Structural disorder, filament growth and self-poisoning in short rods confined onto a flat wall". In: *Soft Matter* 13.46 (2017), pp. 8678–8683. DOI: 10.1039/C7SM01761H.

[653] Z. Zheng et al. "Structural signatures of dynamic heterogeneities in monolayers of colloidal ellipsoids". In: *Nat. Commun.* 5, 3829 (May 2014), p. 3829. DOI: 10.1038/ncomms4829.

[654] C. K. Mishra, A. Rangarajan, and R. Ganapathy. "Two-Step Glass Transition Induced by Attractive Interactions in Quasi-Two-Dimensional Suspensions of Ellipsoidal Particles". In: *Phys. Rev. Lett.* 110.18 (Apr. 2013), p. 188301. DOI: 10.1103/PhysRevLett.110.188301.

[655] Z. Zheng, F. Wang, and Y. Han. "Glass Transitions in Quasi-Two-Dimensional Suspensions of Colloidal Ellipsoids". In: *Phys. Rev. Lett.* 107.6 (Aug. 2011), p. 065702. DOI: 10.1103/PhysRevLett.107.065702.

[656] S. K. Das et al. "Initial correlation dependence of aging in phase separating solid binary mixtures and ordering ferromagnets". In: *J. Phys. Condens. Matter* 32.18 (Feb. 2020), p. 184005. DOI: 10.1088/1361-648x/ab6d10.

[657] Jiarul Midya and Subir K. Das. "Droplet growth during vapor-liquid transition in a 2D Lennard-Jones fluid". In: *J. Chem. Phys.* 146.2 (2017), p. 024503. DOI: 10.1063/1.4973617.

[658] J. Midya and S. K. Das. "Kinetics of Vapor-Solid Phase Transitions: Structure, Growth, and Mechanism". In: *Phys. Rev. Lett.* 118.16 (Apr. 2017), p. 165701. DOI: 10.1103/PhysRevLett.118.165701.

[659] C. Chatelain et al. "Softening of first-order transition in three-dimensions by quenched disorder". In: *Phys. Rev. E* 64.3 (Aug. 2001), p. 036120. DOI: 10.1103/PhysRevE.64.036120.

[660] H. G. Ballesteros et al. "Critical behavior in the site-diluted three-dimensional three-state Potts model". In: *Phys. Rev. B* 61.5 (Feb. 2000), pp. 3215–3218. DOI: 10.1103/PhysRevB.61.3215.

[661] A. J. Liu and S. R. Nagel. "The Jamming Transition and the Marginally Jammed Solid". In: *Annu. Rev. Condens. Matter Phys* 1.1 (2010), pp. 347–369. DOI: 10.1146/annurev-conmatphys-070909-104045.

[662] L. Rovigatti, W. Kob, and F. Sciortino. "The vibrational density of states of a disordered gel model". In: *J. Chem. Phys.* 135.10 (2011), p. 104502. DOI: 10.1063/1.3626869.

[663] E. Bertin, J.-P. Bouchaud, and F. Lequeux. "Subdiffusion and Dynamical Heterogeneities in a Lattice Glass Model". In: *Phys. Rev. Lett.* 95.1 (June 2005), p. 015702. DOI: 10.1103/PhysRevLett.95.015702.

[664] G. Biroli and M. Mézard. "Lattice Glass Models". In: *Phys. Rev. Lett.* 88.2 (Dec. 2001), p. 025501. DOI: 10.1103/PhysRevLett.88.025501.

[665] R. Schilling. "Mode-coupling theory for translational and orientational dynamics near the ideal glass transition". In: *J. Phys. Condens. Matter* 12.29 (July 2000), pp. 6311–6322. DOI: 10.1088/0953-8984/12/29/303.

[666] R. C. Kramb and C. F. Zukoski. "Yielding in dense suspensions: cage, bond, and rotational confinements". In: *J. Phys. Condens. Matter* 23.3 (Dec. 2010), p. 035102. DOI: 10.1088/0953-8984/23/3/035102.

[667] S.-H. Chong and W. Götze. "Idealized glass transitions for a system of dumbbell molecules". In: *Phys. Rev. E* 65.4 (Apr. 2002), p. 041503. DOI: 10.1103/PhysRevE.65.041503.

[668] Hu Cang et al. "Dynamical signature of two "ideal glass transitions" in nematic liquid crystals". In: *J. Chem. Phys.* 119.19 (2003), pp. 10421–10427. DOI: 10.1063/1.1618215.

[669] H. J. Schöpe, G. Bryant, and W. van Megen. "Two-Step Crystallization Kinetics in Colloidal Hard-Sphere Systems". In: *Phys. Rev. Lett.* 96.17 (May 2006), p. 175701. DOI: 10.1103/PhysRevLett.96.175701.

[670] J. P. Straley and M. E. Fisher. "Three-state Potts model and anomalous tricritical points". In: *J. Phys. A* 6.9 (Sept. 1973), pp. 1310–1326. DOI: 10.1088/0305-4470/6/9/007.

[671] M. Deserno. "Tricriticality and the Blume-Capel model: A Monte Carlo study within the microcanonical ensemble". In: *Phys. Rev. E* 56.5 (Nov. 1997), pp. 5204–5210. DOI: 10.1103/PhysRevE.56.5204.

[672] A. N. Berker and M. Wortis. "Blume-Emery-Griffiths-Potts model in two dimensions: Phase diagram and critical properties from a position-space renormalization group". In: *Phys. Rev. B* 14.11 (Dec. 1976), pp. 4946–4963. DOI: 10.1103/PhysRevB.14.4946.

[673] Y.-L. Wang, F. Lee, and J. D. Kimel. "Phase diagrams of the spin-1 Ising Blume-Emery-Griffiths model: Monte Carlo simulations". In: *Phys. Rev. B* 36.16 (Dec. 1987), pp. 8945–8947. DOI: 10.1103/PhysRevB.36.8945.

[674] M. Hasenbusch and E. Vicari. "Anisotropic perturbations in three-dimensional O(N)-symmetric vector models". In: *Phys. Rev. B* 84.12 (Sept. 2011), p. 125136. DOI: 10.1103/PhysRevB.84.125136.

[675] J. P. Straley. "Three-dimensional Potts model". In: *J. Phys. A* 7.17 (Nov. 1974), pp. 2173–2180. DOI: 10.1088/0305-4470/7/17/012.

[676] W. Janke and R.Villanova. "Three-dimensional 3-state Potts model revisited with new techniques". In: *Nucl. Phys. B* 489.3 (1997), pp. 679 –696. ISSN: 0550-3213. DOI: 10.1016/S0550-3213(96)00710-9.

[677] N. B. Wilding, F. Schmid, and P. Nielaba. "Liquid-vapor phase behavior of a symmetrical binary fluid mixture". In: *Phys. Rev. E* 58.2 (Aug. 1998), pp. 2201–2212. DOI: 10.1103/PhysRevE.58.2201.

[678] K. Tafa, S. Puri, and D. Kumar. "Kinetics of phase separation in ternary mixtures". In: *Phys. Rev. E* 64.5 (Oct. 2001), p. 056139. DOI: 10.1103/PhysRevE.64.056139.

[679] M. I. Guerrero, J. S. Rowlinson, and G. Morrison. "Model fluid mixture which exhibits tricritical points.—Part 1". In: *J. Chem. Soc., Faraday Trans. 2* 72.0 (1976), pp. 1970–1979. DOI: 10.1039/F29767201970.

[680] A. Scacchi, M. Krüger, and J. M. Brader. "Driven colloidal fluids: construction of dynamical density functional theories from exactly solvable limits". In: *J. Phys. Condens. Matter* 28.24 (Apr. 2016), p. 244023. DOI: 10.1088/0953-8984/28/24/244023.

[681] N. I. Lebovka et al. "Random sequential adsorption of partially oriented linear k-mers on a square lattice". In: *Phys. Rev. E* 84.6 (Dec. 2011), p. 061603. DOI: 10.1103/PhysRevE.84.061603.

[682] N. I. Lebovka et al. "Jamming and percolation in generalized models of random sequential adsorption of linear k-mers on a square lattice". In: *Phys. Rev. E* 92.6 (Dec. 2015), p. 062116. DOI: 10.1103/PhysRevE.92.062116.

[683] Grzegorz Kondrat, Zbigniew Koza, and Piotr Brzeski. "Jammed systems of oriented needles always percolate on square lattices". In: *Phys. Rev. E* 96.2 (Aug. 2017), p. 022154. DOI: 10.1103/PhysRevE.96.022154.

[684] M. G. Slutskii, L. Y. Barash, and Y. Y. Tarasevich. "Percolation and jamming of random sequential adsorption samples of large linear k-mers on a square lattice". In: *Phys. Rev. E* 98.6 (Dec. 2018), p. 062130. DOI: 10.1103/PhysRevE.98.062130.

[685] R. C. Hart and F. D. A. Aarão Reis. "Random sequential adsorption of polydisperse mixtures on lattices". In: *Phys. Rev. E* 94.2 (Aug. 2016), p. 022802. DOI: 10.1103/PhysRevE.94.022802.

[686] G. D. Garcia et al. "Percolation of polyatomic species on a simple cubic lattice". In: *Euro. Phys. J. B* 86.9, 403 (Sept. 2013), p. 403. DOI: 10.1140/epjb/e2013-40509-1.

[687] J. W. Evans. "Random and cooperative sequential adsorption". In: *Rev. Mod. Phys.* 65.4 (Oct. 1993), pp. 1281–1329. DOI: 10.1103/RevModPhys.65.1281.

[688] P. L. Krapivsky, S. Redner, and E. Ben-Naim. *A Kinetic View of Statistical Physics*. Cambridge and New York: Cambridge University Press. ISBN: 978-0-521-85103-9.

[689] E. P. Feldman, L. I. Stefanovich, and Yu. V. Terekhova. "Influence of adsorption or desorption and surface diffusion on the formation kinetics of open half-monolayer coverage". In: *Phys. Rev. E* 89.6 (June 2014), p. 062406. DOI: 10.1103/PhysRevE.89.062406.

[690] Z. Adamczyk, B. Siwek, and M. Zembala. "Reversible and irreversible adsorption of particles on homogeneous surfaces". In: *Colloid Surface* 62.1 (1992), pp. 119–130. ISSN: 0166-6622. DOI: 10.1016/0166-6622(92)80043-2.

[691] M. Campione et al. "Role of Desorption in the Growth Process of Molecular Organic Thin Films". In: *J. Phys. Chem. B* 109.16 (2005). PMID: 16851915, pp. 7859–7864. DOI: 10.1021/jp0453616.

[692] A. Sassella et al. "Strategies for two-dimensional growth of organic molecular films". In: *Chem. Phys.* 325.1 (2006). Electronic Processes in Organic Solids, pp. 193–206. ISSN: 0301-0104. DOI: 10.1016/j.chemphys.2005.12.008.

[693] P. V. Liddicoat et al. "Nanostructural hierarchy increases the strength of aluminium alloys". In: *Nat. Commun.* 1.1 (2010), pp. 1–7. DOI: 10.1038/ncomms1062.

[694] G. M. Whitesides and B. Grzybowski. "Self-Assembly at All Scales". In: *Science* 295.5564 (2002), pp. 2418–2421. ISSN: 0036-8075. DOI: 10.1126/science.1070821.

[695] M. P. Lettinga. "Phase Separation Kinetics". In: *Soft Matter: Complex Materials on Mesoscopic Scales*. Ed. by J. K. G. Dhont, G. Gompper, and D. Richer. Vol. 10. Schriften des Forschungszentums Jülich: Reihe Materie und Material/Matter and Materials. Lecture manuscripts of the 33rd IFF winter school. Jülich: Forschungszentrum Jülich GmbH, 2002, pp. C7.1–C7.38.

[696] E. K. Hobbie. "Metastability and Depletion-Driven Aggregation". In: *Phys. Rev. Lett.* 81.18 (Nov. 1998), pp. 3996–3999. DOI: 10.1103/PhysRevLett.81.3996.

[697] W. C. K. Poon et al. "Colloid-Polymer Mixtures at Triple Coexistence: Kinetic Maps from Free-Energy Landscapes". In: *Phys. Rev. Lett.* 83.6 (Aug. 1999), pp. 1239–1242. DOI: 10.1103/PhysRevLett.83.1239.

[698] E. K. Hobbie. "Depletion-Driven Phase Separation and Reversible Aggregation in Confined Colloidal Mixtures". In: *Langmuir* 15.26 (1999), pp. 8807–8812. DOI: 10.1021/la990397o.

[699] D. Gebauer and H. Cölfen. "Prenucleation Clusters and Non-classical Nucleation". In: *Nano Today* 6.6 (2011), pp. 564–584. ISSN: 1748-0132. DOI: 10.1016/j.nantod.2011.10.005.

[700] K. N. Pham et al. "Multiple Glassy States in a Simple Model System". In: *Science* 296.5565 (2002), pp. 104–106. ISSN: 0036-8075. DOI: 10.1126/science.1068238.

[701] R. M. L. Evans, W. C. K. Poon, and F. Renth. "Classification of ordering kinetics in three-phase systems". In: *Phys. Rev. E* 64.3 (Aug. 2001), p. 031403. DOI: 10.1103/PhysRevE.64.031403.

[702] M. van Schmoluchowski. "Versuch einer Mathermatischen Theorie der Koagulationkinetik Losungen". In: *Z. Phys. Chem.* 92 (1917), pp. 129–168. DOI: 10.1515/zpch-1918-9209.

[703] W. C. K. Poon, A. D. Pirie, and P. N. Pusey. "Gelation in colloid–polymer mixtures". In: *Faraday Discuss.* 101.0 (1995), pp. 65–76. DOI: 10.1039/FD9950100065.

[704] M. C. Grant and W. B. Russel. "Volume-fraction dependence of elastic moduli and transition temperatures for colloidal silica gels". In: *Phys. Rev. E* 47.4 (Apr. 1993), pp. 2606–2614. DOI: 10.1103/PhysRevE.47.2606.

[705] C. P. Royall, S. R. Williams, and H. Tanaka. "Vitrification and gelation in sticky spheres". In: *J. Chem. Phys.* 148.4 (2018), p. 044501. DOI: 10.1063/1.5000263.

[706] E. Zaccarelli. "Colloidal gels: equilibrium and non-equilibrium routes". In: *J. Phys. Condens. Matter* 19.32 (July 2007), p. 323101. DOI: 10.1088/0953-8984/19/32/323101.

[707] J. R. Weeks, J. S. van Duijneveldt, and B. Vincent. "Formation and collapse of gels of sterically stabilized colloidal particles". In: *J. Phys. Condens. Matter* 12.46 (Oct. 2000), pp. 9599–9606. DOI: 10.1088/0953-8984/12/46/307.

[708] L. Starrs et al. "Collapse of transient gels in colloid-polymer mixtures". In: *J. Phys. Condens. Matter* 14.10 (Mar. 2002), pp. 2485–2505. DOI: 10.1088/0953-8984/14/10/302.

[709] R. M. L. Evans and L. Starrs. "Emergence of a stress transmission length-scale in transient gels". In: *J. Phys. Condens. Matter* 14.10 (Mar. 2002), pp. 2507–2529. DOI: 10.1088/0953-8984/14/10/303.

[710] H. Tanaka and T. Araki. "Simulation Method of Colloidal Suspensions with Hydrodynamic Interactions: Fluid Particle Dynamics". In: *Phys. Rev. Lett.* 85.6 (Aug. 2000), pp. 1338–1341. DOI: 10.1103/PhysRevLett.85.1338.

[711] P. N. Segrè et al. "Glasslike Kinetic Arrest at the Colloidal-Gelation Transition". In: *Phys. Rev. Lett.* 86.26 (June 2001), pp. 6042–6045. DOI: 10.1103/PhysRevLett.86.6042.

[712] R. Ni et al. “Glassy Dynamics, Spinodal Fluctuations, and the Kinetic Limit of Nucleation in Suspensions of Colloidal Hard Rods”. In: *Phys. Rev. Lett.* 105.8 (Aug. 2010), p. 088302. DOI: 10.1103/PhysRevLett.105.088302.

[713] J. W. Cahn. “The Metastable Liquidus and Its Effect on the Crystallization of Glass”. In: *J. Am. Ceram. Soc.* 52.3 (1969), pp. 118–121. DOI: 10.1111/j.1151-2916.1969.tb11194.x.

[714] K. G. Soga, J. R. Melrose, and R. C. Ball. “Metastable states and the kinetics of colloid phase separation”. In: *J. Chem. Phys.* 110.4 (1999), pp. 2280–2288. DOI: 10.1063/1.477881.

[715] T. Schilling et al. “Precursor-Mediated Crystallization Process in Suspensions of Hard Spheres”. In: *Phys. Rev. Lett.* 105.2 (July 2010), p. 025701. DOI: 10.1103/PhysRevLett.105.025701.

[716] S. Iacopini, T. Palberg, and H. J. Schöpe. “Crystallization kinetics of polydisperse hard-sphere-like microgel colloids: Ripening dominated crystal growth above melting”. In: *J. Chem. Phys.* 130.8 (2009), p. 084502. DOI: 10.1063/1.3078310.

[717] J. F. Lutsko and G. Nicolis. “Theoretical Evidence for a Dense Fluid Precursor to Crystallization”. In: *Phys. Rev. Lett.* 96.4 (Feb. 2006), p. 046102. DOI: 10.1103/PhysRevLett.96.046102.

[718] X. Wei, P. B. Miranda, and Y. R. Shen. “Surface Vibrational Spectroscopic Study of Surface Melting of Ice”. In: *Phys. Rev. Lett.* 86.8 (Feb. 2001), pp. 1554–1557. DOI: 10.1103/PhysRevLett.86.1554.

[719] J. G. Dash. “Surface melting”. In: *Contemp. Phys* 30.2 (1989), pp. 89–100. DOI: 10.1080/00107518908225509.

[720] J. W. M. Frenken, P. M. J. Marée, and J. F. van der Veen. “Observation of surface-initiated melting”. In: *Phys. Rev. B* 34.11 (Dec. 1986), pp. 7506–7516. DOI: 10.1103/PhysRevB.34.7506.

[721] C. S. Jayanthi, E. Tosatti, and L. Pietronero. “Surface melting of copper”. In: *Phys. Rev. B* 31.6 (Mar. 1985), pp. 3456–3459. DOI: 10.1103/PhysRevB.31.3456.

[722] K. J. Strandburg. “Two-dimensional melting”. In: *Rev. Mod. Phys.* 60.1 (Jan. 1988), pp. 161–207. DOI: 10.1103/RevModPhys.60.161.

[723] Stefan Ulrich. “Aggregation and Gelation in Random Networks”. Doctoral Thesis. Georg-August-Universit"at G"ottingen, 2010. URL: http://hdl.handle.net/11858/00-1735-0000-0006-B4C7-A.

[724] H. Tanaka. “Viscoelastic phase separation”. In: *J. Phys. Condens. Matter* 12.15 (Mar. 2000), R207–R264. DOI: 10.1088/0953-8984/12/15/201.

[725] E. Lerner and E. Bouchbinder. “Effect of instantaneous and continuous quenches on the density of vibrational modes in model glasses”. In: *Phys. Rev. E* 96.2 (Aug. 2017), p. 020104. DOI: 10.1103/PhysRevE.96.020104.

[726] M. E. Cates and P. S. Clegg. “Bijels: a new class of soft materials”. In: *Soft Matter* 4.11 (2008), pp. 2132–2138. DOI: 10.1039/B807312K.

[727] J. A. Witt, D. R. Mumm, and A. Mohraz. "Bijel reinforcement by droplet bridging: a route to bicontinuous materials with large domains". In: *Soft Matter* 9.29 (2013), pp. 6773–6780. DOI: 10.1039/C3SM00130J.

[728] M. Seul and D. Andelman. "Domain Shapes and Patterns: The Phenomenology of Modulated Phases". In: *Science* 267.5197 (1995), pp. 476–483. ISSN: 0036-8075. DOI: 10.1126/science.267.5197.476.

[729] Markus Wilczek. "Pattern Formation in Driven Thin Layers of Simple and Complex Liquids". Doctoral Thesis. Westfälische Wilhelms-Universität Münster, 2016.

[730] Erik K. Hobbie. "Kinetics of size segregation in quasi-two-dimensional nearly-hard-sphere mixtures". In: *Phys. Rev. E* 55.5 (May 1997), pp. 6281–6284. DOI: 10.1103/PhysRevE.55.6281.

[731] P. Tierno. "Depinning and Collective Dynamics of Magnetically Driven Colloidal Monolayers". In: *Phys. Rev. Lett.* 109.19 (Nov. 2012), p. 198304. DOI: 10.1103/PhysRevLett.109.198304.

[732] T. Bohlein and C. Bechinger. "Experimental Observation of Directional Locking and Dynamical Ordering of Colloidal Monolayers Driven across Quasiperiodic Substrates". In: *Phys. Rev. Lett.* 109.5 (July 2012), p. 058301. DOI: 10.1103/PhysRevLett.109.058301.

[733] A. Stannard. "Dewetting-mediated pattern formation in nanoparticle assemblies". In: *J. Phys. Condens. Matter* 23.8 (Feb. 2011), p. 083001. DOI: 10.1088/0953-8984/23/8/083001.

[734] O. J. J. Ronsin et al. "A phase-field model for the evaporation of thin film mixtures". In: *Phys. Chem. Chem. Phys.* 22.12 (2020), pp. 6638–6652. DOI: 10.1039/D0CP00214C.

[735] H. Tanaka, Y. Nishikawa, and T. Koyama. "Network-forming phase separation of colloidal suspensions". In: *J. Phys. Condens. Matter* 17.15 (Apr. 2005), pp. L143–L153. DOI: 10.1088/0953-8984/17/15/l02.

[736] R. Ganapathy et al. "Direct Measurements of Island Growth and Step-Edge Barriers in Colloidal Epitaxy". In: *Science* 327.5964 (2010), pp. 445–448. ISSN: 0036-8075. DOI: 10.1126/science.1179947.

[737] N. Kleppmann and S. H. L. Klapp. "Particle-resolved dynamics during multilayer growth of C_{60}". In: *Phys. Rev. B* 91.4 (Jan. 2015), p. 045436. DOI: 10.1103/PhysRevB.91.045436.

[738] N. Kleppmann, F. Schreiber, and S. H. L. Klapp. "Limits of size scalability of diffusion and growth: Atoms versus molecules versus colloids". In: *Phys. Rev. E* 95.2 (Feb. 2017), p. 020801. DOI: 10.1103/PhysRevE.95.020801.

[739] W.-S. Xu, Z.-Y. Sun, and L.-J. An. "Heterogeneous crystallization of hard spheres on patterned substrates". In: *J. Chem. Phys.* 132.14 (2010), p. 144506. DOI: 10.1063/1.3383239.

[740] S. Dorosz and T. Schilling. "On the influence of a patterned substrate on crystallization in suspensions of hard spheres". In: *J. Chem. Phys.* 136.4 (2012), p. 044702. DOI: 10.1063/1.3679385.

[741] K. E. Jensen et al. "Rapid growth of large, defect-free colloidal crystals". In: *Soft Matter* 9.1 (2013), pp. 320–328. DOI: 10.1039/C2SM26792F.

[742] T. Dasgupta, J. R. Edison, and M. Dijkstra. "Growth of defect-free colloidal hard-sphere crystals using colloidal epitaxy". In: *J. Chem. Phys.* 146.7 (2017), p. 074903. DOI: 10.1063/1.4976307.

[743] B. Li et al. "Modes of surface premelting in colloidal crystals composed of attractive particles". In: *Nature* 531 (2016), pp. 485–488. DOI: 10.1038/nature16987.

[744] A. Baule. "Shape Universality Classes in the Random Sequential Adsorption of Nonspherical Particles". In: *Phys. Rev. Lett.* 119.2 (July 2017), p. 028003. DOI: 10.1103/PhysRevLett.119.028003.

[745] R. C. Kramb et al. "Glass Formation and Shear Elasticity in Dense Suspensions of Repulsive Anisotropic Particles". In: *Phys. Rev. Lett.* 105.5 (July 2010), p. 055702. DOI: 10.1103/PhysRevLett.105.055702.

[746] Maryam Beigmohamadi. "Growth, structure and morphology of organic thin films". Doctoral Thesis. Rheinisch-Westfälische Technische Hochschule Aachen, 2007. URL: http://publications.rwth-aachen.de/record/62341/files/Beigmohamadi_Maryam.pdf.

[747] B. Scherwitzl, R. Resel, and A. Winkler. "Film growth, adsorption and desorption kinetics of indigo on SiO2". In: *J. Chem. Phys.* 140.18 (2014), p. 184705. DOI: 10.1063/1.4875096.

[748] S. J. Mitchell, G. Brown, and P. A. Rikvold. "Static and dynamic Monte Carlo simulations of Br electrodeposition on Ag(100)". In: *Surf. Sci.* 471.1 (2001), pp. 125–142. ISSN: 0039-6028. DOI: 10.1016/S0039-6028(00)00892-X.

[749] H.-F. Xiang et al. "Method for measurement of the density of thin films of small organic molecules". In: *Rev. Sci. Instrum.* 78.3 (2007), p. 034104. DOI: 10.1063/1.2712932.

[750] V. Marcon and G. Raos. "Free Energies of Molecular Crystal Surfaces by Computer Simulation: Application to Tetrathiophene". In: *J. Am. Chem. Soc.* 128.5 (2006). PMID: 16448085, pp. 1408–1409. DOI: 10.1021/ja056548t.

[751] D. Käfer, L. Ruppel, and G. Witte. "Growth of pentacene on clean and modified gold surfaces". In: *Phys. Rev. B* 75.8 (Feb. 2007), p. 085309. DOI: 10.1103/PhysRevB.75.085309.

[752] G. Duva et al. "Template-Free Orientation Selection of Rod-Like Molecular Semiconductors in Polycrystalline Films". In: *J. Phys. Chem. Lett.* 10.5 (2019), pp. 1031–1036. DOI: 10.1021/acs.jpclett.9b00304.

[753] J. Felter et al. "Two-dimensional growth of dendritic islands of NTCDA on Cu(001) studied in real time". In: *Nanoscale* 11.4 (2019), pp. 1798–1812. DOI: 10.1039/C8NR08943D.

[754] C. Toninelli, G. Biroli, and D. S. Fisher. "Jamming Percolation and Glass Transitions in Lattice Models". In: *Phys. Rev. Lett.* 96.3 (Jan. 2006), p. 035702. DOI: 10.1103/PhysRevLett.96.035702.

[755] T. Chou, K. Mallick, and R. K. P. Zia. "Non-equilibrium statistical mechanics: from a paradigmatic model to biological transport". In: *Rep. Prog. Phys.* 74.11 (Oct. 2011), p. 116601. DOI: 10.1088/0034-4885/74/11/116601.

[756] R. Balian, Y. Alhassid, and H. Reinhardt. "Dissipation in many-body systems: A geometric approach based on information theory". In: *Phys. Rep.* 131.1-2 (Jan. 1986), pp. 1–146. DOI: 10.1016/0370-1573(86)90005-0.

[757] P. W. Anderson. "More Is Different". In: *Science* 177.4047 (1972), pp. 393–396. ISSN: 0036-8075. DOI: 10.1126/science.177.4047.393.

[758] J. L. Lebowitz. "Macroscopic laws, microscopic dynamics, time's arrow and Boltzmann's entropy". In: *Physica A* 194.1 (Mar. 1993), pp. 1–27. DOI: 10.1016/0378-4371(93)90336-3.

[759] J. L. Lebowitz. "Boltzmann's entropy and time's arrow". In: *Phys. Today* 46 (1993), pp. 32–32.

[760] G. E. Uhlenbeck and G. W. Ford. *Lectures in Statistical Mechanics*. Ed. by Mark Kac. Vol. 1. Lectures in Applied Mathematics: Proceedings of the Summer Seminar, Boulder, Colorado, 1960. Providence, Rhode Island: American Mathematical Society, 1963.

[761] R. Zwanzig. "Ensemble Method in the Theory of Irreversibility". In: *J. Chem. Phys.* 33.5 (1960), pp. 1338–1341. DOI: 10.1063/1.1731409.

[762] H. Mori. "Transport, Collective Motion, and Brownian Motion". In: *Prog. Theor. Phys.* 33.3 (Mar. 1965), pp. 423–455. ISSN: 0033-068X. DOI: 10.1143/PTP.33.423.

[763] E. Darve, J. Solomon, and A. Kia. "Computing generalized Langevin equations and generalized Fokker–Planck equations". In: *P. Natl. Acad. Sci. USA* 106.27 (2009), pp. 10884–10889. ISSN: 0027-8424. DOI: 10.1073/pnas.0902633106.

[764] R. Balian. "Information in statistical physics". In: *Stud. Hist. Philos. M. P.* 36.2 (2005), pp. 323–353. ISSN: 1355-2198. DOI: 10.1016/j.shpsb.2005.02.001.

[765] Roger Balian. *From Microphysics to Macrophysics: Methods and Applications of Statistical Physics*. Study Edition. Vol. II. Theoretical and Mathematical Physics. Original French edition: *Du microscopique au macroscopiqite*, Cours de l'Ecole Polytechnique, Ellipses, 1982 Edition Marketing S.a.r.L Paris. Springer-Verlag Berlin Heidelberg, 2007. ISBN: 3-540-45478-0.

[766] E. T. Jaynes. *Probability Theory: The Logic of Science*. Ed. by Larry G. Bretthorst. Cambridge, New York: Cambridge University Press, 2003. ISBN: 978-0-521-59271-0.

[767] Craig S. Lent [Ed.] et al. *Energy Limits in Computation: A Review of Landauer's Principle, Theory and Experiments*. Springer International Publishing AG, part of Springer Nature, 2019. ISBN: 978-3-319-93458-7. DOI: 10.1007/978-3-319-93458-7.

[768] L. P. Kadanoff. "Relating theories via renormalization". In: *Stud. Hist. Philos. M. P.* 44.1 (2013), pp. 22–39. DOI: 10.1016/j.shpsb.2012.05.002.

[769] Alexander Altland and Ben Simons. *Condensed Matter Field Theory*. Second Edition. Cambridge: Cambridge University Press, 2010. ISBN: 978-0-511-78928-1.

[770] Jean Zinn-Justin. *Quantum Field Theory and Critical Phenomena*. Fourth Edition. Vol. 113. International Series of Monographcs on Physics. Oxford, New York: Oxford University Press, Inc., 2002.

[771] R. Shankar. *Quantum Field Theory and Condensed Matter: An Introduction*. Cambrdige: Cambridge University Press, 2017. ISBN: 978-0-521-59210-9.

[772] E. T. Olsen. "Classical mechanics and entropy". In: *Found. Phys. Lett.* 6 (1993). contains Poincare's 1889 paper in the appendix in English, pp. 327–337. DOI: 10.1007/BF00665652.

[773] H. Poincaré. "Sur le problème des trois corps et les équations de la dynamique". In: *Acta Mathematica* 13.1 (1890), A3–A270.

[774] Josef Honerkamp. *Statistical Physics: An Advanced Approach with Applications*. Second Edition. Berlin et al.: Springer, 2002. ISBN: 3-540-43020-2.

[775] Dmitrii Zubarev, Vladimir Morozov, and Gerd Röpke. *Statistical Mechanics of Nonequilibrium Processes*. Vol. 1: "Basic Concepts, Kinetic Theory". Berlin: Akademie Verlag GmbH, 1996. ISBN: 3-05-501708-0.

[776] C. V. Heer. *Statistical Mechanics, Kinetic Theory, and Stochastic Processes*. New York and London: Academic Press, Inc., 1972.

[777] M. P. Allen and D. J. Tildesley. *Computer Simulation of Liquids*. Oxford Science Publications. Oxford: Oxford University Press, 1987. ISBN: 0-19-855645-4.

[778] N. C. Stone and N. W. C. Leigh. "A statistical solution to the chaotic, non-hierarchical three-body problem". In: *Nature* 576.7787 (2019), pp. 406–410. DOI: 10.1038/s41586-019-1833-8.

[779] O. Penrose. "Foundations of statistical mechanics". In: *Rep. Prog. Phys.* 42.12 (Dec. 1979), pp. 1937–2006. DOI: 10.1088/0034-4885/42/12/002.

[780] D. A. Lavis and P. J. Milligan. "The Work of E. T. Jaynes on Probability, Statistics and Statistical Physics". In: *Brit. J. Philos. Sci.* 36.2 (1985), pp. 193–210. ISSN: 00070882, 14643537. URL: http://www.jstor.org/stable/687036.

[781] B. Gaveau and L. S. Schulman. "Is ergodicity a reasonable hypothesis for macroscopic systems?" In: *Eur. Phys. J. Spec. Top.* 224.5 (2015), pp. 891–904. DOI: 10.1140/epjst/e2015-02434-7.

[782] P. Gaspard. "Cycles, randomness, and transport from chaotic dynamics to stochastic processes". In: *Chaos* 25.9 (2015), p. 097606. DOI: 10.1063/1.4916922.

[783] J. M. R. Parrondo and L. Granger. "Maxwell demons in phase space". In: *Eur. Phys. J. Spec. Top.* 224.5 (2015), pp. 865–878.

[784] D. J. Evans and D. J. Searles. "The Fluctuation Theorem". In: *Adv. Phys.* 51.7 (2002), pp. 1529–1585. DOI: 10.1080/00018730210155133.

[785] K. Sturm. "Statistical Mechanics". In: *Soft Matter: Complex Materials on Mesoscopic Scales*. Ed. by J. K. G. Dhont, G. Gompper, and D. Richer. Vol. 10. Schriften des Forschungszentums Jülich: Reihe Materie und Material/Matter and Materials. Lecture manuscripts of the 33rd IFF winter school. Jülich: Forschungszentrum Jülich GmbH, 2002, B1.1–B1.26.

[786] D. Kannan. *Introduction to Stochastic Processes*. New York: Elsevier North Holland, Inc., 1979. ISBN: 0-444-00301-0.

[787] Denis J. Evans, Debra J. Searles, and Stephen R. Williams. *Fundamentals of Classical Statistical Thermodynamics: Dissipation, Relaxation and Fluctuation Theorems*. Weinheim: Wiley-VCH Verlag GmbH & Co., 2016. ISBN: 978-3-527-69576-8.

[788] E. H. Feng and G. E. Crooks. "Length of Time's Arrow". In: *Phys. Rev. Lett.* 101.9 (Aug. 2008), p. 090602. DOI: 10.1103/PhysRevLett.101.090602.

[789] Kip S. Thorne and Roger D. Blandford. *Modern Classical Physics: Optics, Fluids, Plasmas, Elasticity, Relativity, and Statistical Physics*. Princeton, Oxford: Princeton University Press, 2017. ISBN: 0691159025.

[790] E. T. Jaynes. "Information Theory and Statistical Mechanics". In: *Phys. Rev.* 106.4 (May 1957), pp. 620–630. DOI: 10.1103/PhysRev.106.620.

[791] E. T. Jaynes. "Information Theory and Statistical Mechanics. II". In: *Phys. Rev.* 108.2 (Oct. 1957), pp. 171–190. DOI: 10.1103/PhysRev.108.171.

[792] H. Löwen. "Melting, freezing and colloidal suspensions". In: *Phys. Rep.* 237.5 (1994), pp. 249–324. ISSN: 0370-1573. DOI: 10.1016/0370-1573(94)90017-5.

[793] Roland Roth. *"Introduction to Density Functional Theory of Classical Systems: Theory and Applications"*. Lecture notes, Kyushu University, Fukuoka, Japan. Nov. 2006. URL: https://bytebucket.org/knepley/cdft-git/wiki/papers/Lecture_Notes_on_DFT__Roland_Roth.pdf.

[794] David Chandler. *Introduction to Modern Statistical Mechanics*. New York and Oxford: Oxford University Press, Inc., 1987. ISBN: 0-19-504276-X.

[795] J. K. Percus. "Equilibrium state of a classical fluid of hard rods in an external field". In: *J. Stat. Phys.* 15 (1976), pp. 505–511. DOI: 10.1007/BF01020803.

[796] C. Jarzynski. "Stochastic and Macroscopic Thermodynamics of Strongly Coupled Systems". In: *Phys. Rev. X* 7.1 (Jan. 2017), p. 011008. DOI: 10.1103/PhysRevX.7.011008.

[797] N. Goldenfeld. *Lectures on Phase Transitions and the Renormalization Group*. Vol. 85. Frontiers in Physics. Boulder, Colorado: Westview Press, 1992.

[798] M. E. Fisher. "Renormalization group theory: Its basis and formulation in statistical physics". In: *Rev. Mod. Phys.* 70.2 (Apr. 1998), pp. 653–681. DOI: 10.1103/RevModPhys.70.653.

[799] K. G. Wilson. "The renormalization group and critical phenomena". In: *Rev. Mod. Phys.* 55.3 (July 1983), pp. 583–600. DOI: 10.1103/RevModPhys.55.583.

[800] A. J. Bray. "Theory of phase-ordering kinetics". In: *Adv. Phys.* 51.2 (Mar. 2002), pp. 481–587. DOI: 10.1080/00018730110117433.

[801] R. Kubo. "The fluctuation-dissipation theorem". In: *Rep. Prog. Phys.* 29.1 (Jan. 1966), pp. 255–284. DOI: 10.1088/0034-4885/29/1/306.

[802] C. Nicolis and G. Nicolis. "The Fluctuation–Dissipation Theorem Revisited: Beyond the Gaussian Approximation". In: *J. Atmos. Sci.* 72.7 (July 2015), pp. 2642–2656. ISSN: 0022-4928. DOI: 10.1175/JAS-D-14-0391.1.

[803] A. L. Kuzemsky. "Theory of transport processes and the method of the nonequilibrium statistical operator". In: *Int. J. Mod. Phys. B* 21.17 (2007), pp. 2821–2949. DOI: 10.1142/S0217979207037417.

[804] T. R. Gingrich et al. "Near-optimal protocols in complex nonequilibrium transformations". In: *Proc. Nat. Acad. Sci.-USA* 113.37 (2016), pp. 10263–10268. ISSN: 0027-8424. DOI: 10.1073/pnas.1606273113.

[805] T. R. Gingrich et al. "Dissipation Bounds All Steady-State Current Fluctuations". In: *Phys. Rev. Lett.* 116.12 (Mar. 2016), p. 120601. DOI: 10.1103/PhysRevLett.116.120601.

[806] T. R. Gingrich, G. M. Rotskoff, and J. M. Horowitz. "Inferring dissipation from current fluctuations". In: *J. Phys. A* 50.18 (Apr. 2017), p. 184004. DOI: 10.1088/1751-8121/aa672f.

[807] P. C. Hohenberg and A. P. Krekhov. "An introduction to the Ginzburg-Landau theory of phase transitions and nonequilibrium patterns". In: *Phys. Rep.* 572 (Apr. 2015), pp. 1–42. DOI: 10.1016/j.physrep.2015.01.001.

[808] P. Ehrenfest. "Phase changes in the ordinary and extended sense classified according to the corresponding singularities of the thermodynamic potential". In: *Proc. Acad. Sci. Amsterdam*. Vol. 36. Amsterdam, 1933, pp. 153–157.

[809] S. Lübeck. "Universal scaling behavior of non-equilibrium phase transitions". In: *Int. J. Mod. Phys. B* 18.31n32 (2004), pp. 3977–4118. DOI: 10.1142/S0217979204027748.

[810] M. Niss. "History of the Lenz–Ising model 1965–1971: the role of a simple model in understanding critical phenomena". In: *Arch. Hist. Exact Sci.* 65.6 (Aug. 2011), p. 625. ISSN: 1432-0657. DOI: 10.1007/s00407-011-0086-1.

[811] L. P. Kadanoff. "Scaling laws for Ising models near T_c". In: *Physics Physique Fizika* 2.6 (June 1966), pp. 263–272. DOI: 10.1103/PhysicsPhysiqueFizika.2.263.

[812] L. P. Kadanoff. "Spin-spin correlations in the two-dimensional ising model". In: *Il Nuovo Cimento B (1965-1970)* 44.2 (Aug. 1966), pp. 276–305. ISSN: 1826-9877. DOI: 10.1007/BF02710808.

[813] Nicolaas G. van Kampen. *Stochastic Processes in Physics and Chemistry*. Rev. and enlarged Edition. The Netherlands: North-Holland, 1992, p. 465. ISBN: 0-444-89349-0.

[814] C. W. Gardiner. *Handbook of Stochastic Methods: For Physics, Chemistry and the Natural Sciences*. Third Edition. Berlin et. al: Springer, 2004, p. 415. ISBN: 3-540-20882-8.

[815] Roberto Livi and Paolo Politi. *Nonequilibrium Statistical Physics: A Modern Perspective*. Cambridge: Cambridge University Press, 2017. ISBN: 978-1-107-04954-3.

[816] J. L. Lebowitz and H. A. Spohn. "Gallavotti–Cohen-Type Symmetry in the Large Deviation Functional for Stochastic Dynamics". In: *J. Stat. Phys.* 95 (1999), pp. 333–365. DOI: 10.1023/A:1004589714161.

[817] Gavin E. Crooks. "Entropy production fluctuation theorem and the nonequilibrium work relation for free energy differences". In: *Phys. Rev. E* 60.3 (Sept. 1999), pp. 2721–2726. DOI: 10.1103/PhysRevE.60.2721.

[818] J. Kurchan. "Fluctuation theorem for stochastic dynamics". In: *J. Phys. A* 31.16 (Apr. 1998), pp. 3719–3729. DOI: 10.1088/0305-4470/31/16/003.

[819] U. Seifert. "Entropy Production along a Stochastic Trajectory and an Integral Fluctuation Theorem". In: *Phys. Rev. Lett.* 95.4 (July 2005), p. 040602. DOI: 10.1103/PhysRevLett.95.040602.

[820] C. Jarzynski. "Nonequilibrium Equality for Free Energy Differences". In: *Phys. Rev. Lett.* 78.14 (Apr. 1997), pp. 2690–2693. DOI: 10.1103/PhysRevLett.78.2690.

[821] M. Michel, S. C. Kapfer, and W. Krauth. "Generalized event-chain Monte Carlo: Constructing rejection-free global-balance algorithms from infinitesimal steps". In: *J. Chem. Phys.* 140.5 (2014), p. 054116. DOI: 10.1063/1.4863991.

[822] R. Bamler et al. "Tightening bounds for variational inference by revisiting perturbation theory". In: *J. Stat. Mech.: Theory Exp.* 2019.12 (Dec. 2019), p. 124004. DOI: 10.1088/1742-5468/ab43d3.

[823] T. Tsuruyama. "The Conservation of Average Entropy Production Rate in a Model of Signal Transduction: Information Thermodynamics Based on the Fluctuation Theorem". In: *Entropy* 20.4 (2018). Article No. 303. ISSN: 1099-4300. DOI: 10.3390/e20040303.

[824] D. A. Sivak and G. E. Crooks. "Thermodynamic geometry of minimum-dissipation driven barrier crossing". In: *Phys. Rev. E* 94.5 (Nov. 2016), p. 052106. DOI: 10.1103/PhysRevE.94.052106.

[825] M. Schmidt and J. M. Brader. "Power functional theory for Brownian dynamics". In: *J. Chem. Phys.* 138.21 (2013), p. 214101. DOI: 10.1063/1.4807586.

[826] J. M. Brader and M. Schmidt. "Dynamic correlations in Brownian many-body systems". In: *J. Chem. Phys.* 140.3 (2014), p. 034104. DOI: 10.1063/1.4861041.

[827] A. D. Wissner-Gross and C. E. Freer. "Causal Entropic Forces". In: *Phys. Rev. Lett.* 110.16 (Apr. 2013), p. 168702. DOI: 10.1103/PhysRevLett.110.168702.

[828] R. Kawai, J. M. R. Parrondo, and C. Van den Broeck. "Dissipation: The Phase-Space Perspective". In: *Phys. Rev. Lett.* 98.8 (Feb. 2007), p. 080602. DOI: 10.1103/PhysRevLett.98.080602.

[829] K. A. Fichthorn and W. H. Weinberg. "Theoretical foundations of dynamical Monte Carlo simulations". In: *J. Chem. Phys.* 95.2 (1991), pp. 1090–1096. DOI: 10.1063/1.461138.

[830] E. Adam, L. Billard, and F. Lanccon. "Class of Monte Carlo algorithms for dynamic problems leads to an adaptive method". In: *Phys. Rev. E* 59.1 (Jan. 1999), pp. 1212–1216. DOI: 10.1103/PhysRevE.59.1212.

[831] W. K. Hastings. "Monte Carlo sampling methods using Markov chains and their applications". In: *Biometrika* 57.1 (Apr. 1970), pp. 97–109. DOI: 10.1093/biomet/57.1.97.

[832] J.-S. Wang and R. H. Swendsen. "Cluster Monte Carlo algorithms". In: *Physica A* 167.3 (1990), pp. 565–579. ISSN: 0378-4371. DOI: 10.1016/0378-4371(90)90275-W.

[833] U. Wolff. "Collective Monte Carlo Updating for Spin Systems". In: *Phys. Rev. Lett.* 62.4 (Jan. 1989), pp. 361–364. DOI: 10.1103/PhysRevLett.62.361.

[834] P. Tamayo, R. C. Brower, and W. Klein. "Single-cluster Monte Carlo dynamics for the Ising model". In: *J. Stat. Phys.* 58 (1990), pp. 1083–1094. DOI: 10.1007/BF01026564.

[835] G. V. Chester. "The theory of irreversible processes". In: *Rep. Prog. Phys.* 26.1 (Jan. 1963), pp. 411–472. DOI: 10.1088/0034-4885/26/1/311.

[836] G. Nicolis, S. Martínez, and E. Tirapegui. "Finite coarse-graining and Chapman-Kolmogorov equation in conservative dynamical systems". In: *Chaos Soliton. Fract.* 1.1 (1991), pp. 25–37. ISSN: 0960-0779. DOI: 10.1016/0960-0779(91)90053-C.

[837] J. L. Lebowitz. "Microscopic origins of irreversible macroscopic behavior". In: *Physica A* 263.1 (1999), pp. 516–527. ISSN: 0378-4371. DOI: 10.1016/S0378-4371(98)00514-7.

[838] H. R. Brown, W. Myrvold, and J. Uffink. "Boltzmann's H-theorem, its discontents, and the birth of statistical mechanics". In: *Stud. Hist. Philos. M. P.* 40.2 (2009), pp. 174–191. ISSN: 1355-2198. DOI: 10.1016/j.shpsb.2009.03.003.

[839] Y. Elskens and I. Prigogine. "From instability to irreversibility". In: *Proc. Nat. Acad. Sci.-USA* 83.16 (1986), pp. 5756–5760. ISSN: 0027-8424. DOI: 10.1073/pnas.83.16.5756.

[840] J. R. Dorfman. "Deterministic chaos and the foundations of the kinetic theory of gases". In: *Phys. Rep.* 301.1 (1998), pp. 151–185. ISSN: 0370-1573. DOI: 10.1016/S0370-1573(98)00009-X.

[841] B. Misra and I. Prigogine. "On the Foundations of Kinetic Theory". In: *Prog. Theor. Phys. Supp.* 69 (Mar. 1980), pp. 101–110. ISSN: 0375-9687. DOI: 10.1143/PTP.69.101.

[842] B. Misra. "Nonequilibrium entropy, Lyapounov variables, and ergodic properties of classical systems". In: *Proc. Nat. Acad. Sci.-USA* 75.4 (1978), pp. 1627–1631. DOI: 10.1073/pnas.75.4.1627.

[843] B. Misra, I. Prigogine, and M. Courbage. "From deterministic dynamics to probabilistic descriptions". In: *Proc. Nat. Acad. Sci.-USA* 76.8 (1979), pp. 3607–3611. DOI: 10.1073/pnas.76.8.3607.

[844] J. S. Nicolis. "Chaotic dynamics applied to information processing". In: *Rep. Prog. Phys.* 49.10 (Oct. 1986), pp. 1109–1196. DOI: 10.1088/0034-4885/49/10/002.

[845] Scott J. Muller. *Asymmetry: The Foundation of Information*. The Frontiers Collection. Springer-Verlag Berlin Heidelberg, 2007. ISBN: 978-3-540-69883-8.

[846] W. Ebeling. "Entropy and information in processes of self-organization: uncertainty and predictability". In: *Physica A* 194.1 (1993), pp. 563–575. ISSN: 0378-4371. DOI: 10.1016/0378-4371(93)90386-I.

[847] R. Balian. "Incomplete descriptions and relevant entropies". In: *Am. J. Phys.* 67.12 (1999), pp. 1078–1090. DOI: 10.1119/1.19086.

[848] C. E. Shannon. "A Mathematical Theory of Communication". In: *Bell Syst. Tech. J.* 27.3 (1948), pp. 379–423. DOI: 10.1002/j.1538-7305.1948.tb01338.x.

[849] Thomas M. Cover and Joy A. Thomas. *Elements of Information Theory*. Ed. by D. L. Schilling. Wiley Series in Communications. New York: John Wiley & Sons, Inc., 1991. ISBN: ISBN 0-471-20061-1.

[850] David J. C. MacKay. *Information Theory, Inference, and Learning Algorithms*. Version 7.2 (fourth printing). Cambridge University Press, Mar. 2003.

[851] Solomon Kullback. *Information Theory and Statistics*. Dover edition, an unabridged republication of the Dover 1968 edition which was an unabridged republication of the original 1959 work published by John Wiley & Sons, New York. Dover Publications, Inc., 1997. ISBN: 9780486696843.

[852] S. Kullback and R. A. Leibler. "On Information and Sufficiency". In: *Ann. Math. Statist.* 22.1 (Mar. 1951), pp. 79–86. DOI: 10.1214/aoms/1177729694.

[853] W. Ebeling. "Physical basis of information and the relation to entropy". In: *Eur. Phys. J.-Spec. Top.* 226.2 (Jan. 2017), pp. 161–176. ISSN: 1951-6401. DOI: 10.1140/epjst/e2016-60366-5.

[854] P. Gaspard. "Random paths and current fluctuations in nonequilibrium statistical mechanics". In: *J. Math. Phys.* 55.7 (2014), p. 075208. DOI: 10.1063/1.4881534.

[855] V. Lecomte, C. Appert-Rolland, and F van Wijland. "Thermodynamic Formalism for Systems with Markov Dynamics". In: *J. Stat. Phys.* 127 (2007), pp. 51–106. DOI: 10.1007/s10955-006-9254-0.

[856] S. Pigolotti et al. "Generic Properties of Stochastic Entropy Production". In: *Phys. Rev. Lett.* 119.14 (Oct. 2017), p. 140604. DOI: 10.1103/PhysRevLett.119.140604.

[857] É. Roldán and J. M. R. Parrondo. "Entropy production and Kullback-Leibler divergence between stationary trajectories of discrete systems". In: *Phys. Rev. E* 85.3 (Mar. 2012), p. 031129. DOI: 10.1103/PhysRevE.85.031129.

[858] V. G. Morozov and G. Röpke. In: *Condens. Matter Phys.* 1.4(16) (1998), pp. 673–686. DOI: 10.5488/CMP.1.4.673.

[859] U. Seifert. "From stochastic thermodynamics to thermodynamic inference". In: *Annu. Rev. Condens. Matter Phys.* 10 (2019), pp. 171–192. DOI: 10.1146/annurev-conmatphys-031218-013554.

[860] H. Dekker. "Nonisothermal activation: Nonequilibrium thermodynamics of metastable mesoscopic systems". In: *Phys. Rev. A* 43.8 (Apr. 1991), pp. 4224–4230. DOI: 10.1103/PhysRevA.43.4224.

[861] G. Biroli and J.-P Bouchaud. "Diverging length scale and upper critical dimension in the Mode-Coupling Theory of the glass transition". In: *Europhys. Lett.* 67.1 (July 2004), pp. 21–27. DOI: 10.1209/epl/i2004-10044-6.

[862] E. T. Jaynes. "Prior Probabilities". In: *IEEE T. Syst. Sci. Cyb.* 4.3 (Sept. 1968), pp. 227–241. ISSN: 2168-2887. DOI: 10.1109/TSSC.1968.300117.

[863] J. Shore and R. Johnson. "Axiomatic derivation of the principle of maximum entropy and the principle of minimum cross-entropy". In: *IEEE T. Inform. Theory* 26.1 (Jan. 1980), pp. 26–37. ISSN: 1557-9654. DOI: 10.1109/TIT.1980.1056144.

[864] J. Shore and R. Johnson. "Properties of cross-entropy minimization". In: *IEEE T. Inform. Theory* 27.4 (July 1981), pp. 472–482. ISSN: 1557-9654. DOI: 10.1109/TIT.1981.1056373.

[865] E. T. Jaynes. "The Minimum Entropy Production Principle". In: *Annu. Rev. Phys. Chem.* 31.1 (1980), pp. 579–601. DOI: 10.1146/annurev.pc.31.100180.003051.

[866] R. Dewar. "Information theory explanation of the fluctuation theorem, maximum entropy production and self-organized criticality in non-equilibrium stationary states". In: *J. Phys. A* 36.3 (Jan. 2003), pp. 631–641. DOI: 10.1088/0305-4470/36/3/303.

[867] G. E. Crooks. "Measuring Thermodynamic Length". In: *Phys. Rev. Lett.* 99.10 (Sept. 2007), p. 100602. DOI: 10.1103/PhysRevLett.99.100602.

[868] E. H. Feng and G. E. Crooks. "Far-from-equilibrium measurements of thermodynamic length". In: *Phys. Rev. E* 79.1 (Jan. 2009), p. 012104. DOI: 10.1103/PhysRevE.79.012104.

[869] I. Prigogine and J. Géhéniau. "Entropy, matter, and cosmology". In: *Proc. Natl. Acad. Sci.-USA* 83.17 (Sept. 1986), pp. 6245–6249. DOI: 10.1073/pnas.83.17.6245.

[870] B. Bonnier, D. Boyer, and P. Viot. "Pair correlation function in random sequential adsorption processes". In: *J. Phys. A* 27.11 (June 1994), pp. 3671–3682. DOI: 10.1088/0305-4470/27/11/017.

[871] J. Klafter and I. M. Sokolov. *First Steps in Random Walks: From Tools to Applications*. Oxford: Oxford University Press, 2011. ISBN: 978-0-19-875409-1.

[872] D. de las Heras and M. Schmidt. "Flow and Structure in Nonequilibrium Brownian Many-Body Systems". In: *Phys. Rev. Lett.* 125.1 (June 2020), p. 018001. DOI: 10.1103/PhysRevLett.125.018001.

[873] A. Onuki. "On fluctuations in μ-space". In: *J. Stat. Phys.* 18.5 (May 1978), pp. 475–499. DOI: 10.1007/BF01014519.

[874] M. H. Ernst and E. G. D. Cohen. "Nonequilibrium fluctuations in μ space". In: *J. Stat. Phys.* 25.1 (May 1981), pp. 153–180. DOI: 10.1007/BF01008484.

[875] T. R. Kirkpatrick, E. G. D. Cohen, and J. R. Dorfman. "Fluctuations in a nonequilibrium steady state: Basic equations". In: *Phys. Rev. A* 26.2 (Aug. 1982), pp. 950–971. DOI: 10.1103/PhysRevA.26.950.

[876] K. Kawasaki. "Kinetic equations and time correlation functions of critical fluctuations". In: *Annals of Physics* 61.1 (1970), pp. 1–56. ISSN: 0003-4916. DOI: 10.1016/0003-4916(70)90375-1.

[877] H. W. Lin and M. Tegmark. "Critical Behavior in Physics and Probabilistic Formal Languages". In: *Entropy* 19.7 (2017). Article No. 299. ISSN: 1099-4300. DOI: 10.3390/e19070299.

[878] Diederick P. Kingma. "Variational inference & deep learning: A new synthesis". PhD thesis. Informatics Institute (IVI), Faculty of Science (FNWI): University of Amsterdam, Oct. 2017. URL: https://hdl.handle.net/11245.1/8e55e07f-e4be-458f-a929-2f9bc2d169e8.

[879] Vladimir N. Vapnik. *Statistical Learning Theory*. Adaptive and Learning Systems for Signal Processing, Communications, and Control. New York: John Wiley & Sons, Inc., 1998. ISBN: 0-471-03003-1.

[880] Sumio Watanabe. *Mathematical Theory of Bayesian Statistics*. Boca Raton: Taylor & Francis Group, LLC, 2018. ISBN: 978-1-482-23806-8.

[881] A. Srivastava et al. "VEEGAN: Reducing Mode Collapse in GANs using Implicit Variational Learning". In: *Adv. Neur. In.* Ed. by I. Guyon et al. Vol. 30. Curran Associates, Inc., 2017, pp. 3308–3318.

[882] M. Tschannen, O. F. Bachem, and M. Lučić. "Recent Advances in Autoencoder-Based Representation Learning". In: *Proc. of the Bayesian Deep Learning Workshop, NeurIPS*. 2018. arXiv: 1812.05069 [cs.LG].

[883] Gareth James et al. *An Introduction to Statistical Learning: with Applications in R*. (Corrected at 8th printing 2017). Springer Texts in Statistics. New York: Springer Science+Business Media, 2013. ISBN: ISBN 978-1-4614-7138-7. DOI: 10.1007/978-1-4614-7138-7.

[884] D. P. Kingma et al. "Improved Variational Inference with Inverse Autoregressive Flow". In: *Proc. of the 30th International Conference on Neural Information Processing Systems*. NIPS'16. Barcelona, Spain: Curran Associates Inc., 2016, pp. 4743–4751. ISBN: 9781510838819.

[885] T. K. Vanderlick, H. T. Davis, and J. K. Percus. "The statistical mechanics of inhomogeneous hard rod mixtures". In: *J. Chem. Phys.* 91.11 (Dec. 1989), pp. 7136–7145. DOI: 10.1063/1.457329.

[886] R. F. Kayser and H. J. Raveché. "Bifurcation in Onsager's model of the isotropic-nematic transition". In: *Phys. Rev. A* 17.6 (June 1978), pp. 2067–2072. DOI: 10.1103/PhysRevA.17.2067.

[887] R. Eppenga and D. Frenkel. "Monte Carlo study of the isotropic and nematic phases of infinitely thin hard platelets". In: *Mol. Phys.* 52.6 (Jan. 1984), pp. 1303–1334. DOI: 10.1080/00268978400101951.

[888] S. Varga et al. "Effect of orientational restriction on monolayers of hard ellipsoids". In: *Phys. Chem. Chem. Phys.* 18.6 (Jan. 2016), pp. 4547–4556. DOI: 10.1039/C5CP05702G.

[889] M. A Saum, T. P Schulze, and C. Ratsch. "Inverted List Kinetic Monte Carlo with Rejection Applied to Directed Self-Assembly of Epitaxial Growth". In: *Commun. Comput. Phys.* 6.3 (2009), p. 553.

[890] H. Hansen-Goos and M. Weigt. "A hard-sphere model on generalized Bethe lattices: dynamics". In: *J. Stat. Mech.: Theory Exp.* 2005.08 (Aug. 2005), P08001–P08001. DOI: 10.1088/1742-5468/2005/08/p08001.

[891] L. Berthier and W. Kob. "The Monte Carlo dynamics of a binary Lennard-Jones glass-forming mixture". In: *J. Phys. Condens. Matter* 19.20 (Apr. 2007), p. 205130. DOI: 10.1088/0953-8984/19/20/205130.

[892] A. Patti and A. Cuetos. "Brownian dynamics and dynamic Monte Carlo simulations of isotropic and liquid crystal phases of anisotropic colloidal particles: A comparative study". In: *Phys. Rev. E* 86.1 (July 2012), p. 011403. DOI: 10.1103/PhysRevE.86.011403.

[893] E. Sanz and D. Marenduzzo. "Dynamic Monte Carlo versus Brownian dynamics: A comparison for self-diffusion and crystallization in colloidal fluids". In: *J. Chem. Phys.* 132.19 (2010), p. 194102. DOI: 10.1063/1.3414827.

[894] D. Frenkel and B. Smit. *Understanding Molecular Simulation: From Algorithms to Applications*. Ed. by D. Frenkel et al. Second Edition. Vol. 1. Computational Science: From Theory to Applications. San Diego, London: Academic Press, 2002. ISBN: 0-12-267351-4.

[895] J. Hoshen and R. Kopelman. "Percolation and cluster distribution. I. Cluster multiple labeling technique and critical concentration algorithm". In: *Phys. Rev. B* 14.8 (Oct. 1976), pp. 3438–3445. DOI: 10.1103/PhysRevB.14.3438.

[896] H. Mantz, K. Jacobs, and K. Mecke. "Utilizing Minkowski functionals for image analysis: a marching square algorithm". In: *J. Stat. Mech.: Theory Exp.* 2008.12 (Dec. 2008), P12015. DOI: 10.1088/1742-5468/2008/12/p12015.

[897] J. Bleibel et al. "Collective dynamics of colloids at fluid interfaces." In: *Eur. Phys. J. E* 34.125 (2011). DOI: 10.1140/epje/i2011-11125-5.

[898] L. S. Ramirez, P. M. Centres, and A. J. Ramirez-Pastor. "Inverse percolation by removing straight rigid rods from square lattices in the presence of impurities". In: *J. Stat. Mech.: Theory Exp.* 2019.3 (Mar. 2019), p. 033207. DOI: 10.1088/1742-5468/ab054d.

[899] B. Krause et al. "Late growth stages and post-growth diffusion in organic epitaxy: PTCDA on Ag(111)". In: *Surf. Sci.* 572.2 (2004), pp. 385–395. ISSN: 0039-6028. DOI: 10.1016/j.susc.2004.09.011.

[900] G. Berlanda et al. "Evidence of postdeposition nucleation in organic molecular thin films". In: *Phys. Rev. B* 69.8 (Feb. 2004), p. 085409. DOI: 10.1103/PhysRevB.69.085409.

[901] L. Casalis et al. "Hyperthermal Molecular Beam Deposition of Highly Ordered Organic Thin Films". In: *Phys. Rev. Lett.* 90.20 (May 2003), p. 206101. DOI: 10.1103/PhysRevLett.90.206101.

[902] S. Buzzaccaro, R. Rusconi, and R. Piazza. ""Sticky" Hard Spheres: Equation of State, Phase Diagram, and Metastable Gels". In: *Phys. Rev. Lett.* 99.9 (Aug. 2007), p. 098301. DOI: 10.1103/PhysRevLett.99.098301.

[903] M. A. Lohr et al. "Vibrational and structural signatures of the crossover between dense glassy and sparse gel-like attractive colloidal packings". In: *Phys. Rev. E* 90.6 (Dec. 2014), p. 062305. DOI: 10.1103/PhysRevE.90.062305.

[904] Z. Varga and J. W. Swan. "Normal modes of weak colloidal gels". In: *Phys. Rev. E* 97.1 (Jan. 2018), p. 012608. DOI: 10.1103/PhysRevE.97.012608.

[905] M. Dolz, F. Nieto, and A. J. Ramirez-Pastor. "Site-bond percolation of polyatomic species". In: *Phys. Rev. E* 72.6 (Dec. 2005), p. 066129. DOI: 10.1103/PhysRevE.72.066129.

[906] Y. Yu. Tarasevich et al. "Impact of defects on percolation in random sequential adsorption of linear *k*-mers on square lattices". In: *Phys. Rev. E* 91.1 (Jan. 2015), p. 012109. DOI: 10.1103/PhysRevE.91.012109.

[907] I. Lončarević et al. "The study of percolation with the presence of extended impurities". In: *J. Stat. Mech.: Theory Exp.* 2017.9 (Sept. 2017), p. 093202. DOI: 10.1088/1742-5468/aa82c0.

[908] L. S. Ramirez, P. M. Centres, and A. J. Ramirez-Pastor. "Standard and inverse bond percolation of straight rigid rods on square lattices". In: *Phys. Rev. E* 97.4 (Apr. 2018), p. 042113. DOI: 10.1103/PhysRevE.97.042113.

[909] C. K. Gan and J.-S. Wang. "Series-expansion studies of random sequential adsorption with diffusional relaxation". In: *Phys. Rev. E* 55.1 (Jan. 1997), pp. 107–123. DOI: 10.1103/PhysRevE.55.107.

[910] C. Fusco et al. "Random sequential adsorption and diffusion of dimers and k-mers on a square lattice". In: *J. Chem. Phys.* 114.17 (2001), pp. 7563–7569. DOI: 10.1063/1.1359740.

[911] T. T. Rautiainen and A. P. Sutton. "Influence of the atomic diffusion mechanism on morphologies, kinetics, and the mechanisms of coarsening during phase separation". In: *Phys. Rev. B* 59.21 (June 1999), pp. 13681–13692. DOI: 10.1103/PhysRevB.59.13681.

[912] Y. Saito. "Two-dimensional nucleation with edge and corner diffusions". In: *J. Phys. Soc. Jpn.* 72.8 (2003), pp. 2008–2014. DOI: 10.1143/jpsj.72.2008.

[913] L. Tumbek et al. "Origin of the bimodal island size distribution in ultrathin films of para-hexaphenyl on mica". In: *Phys. Rev. B* 86.8 (Aug. 2012), p. 085402. DOI: 10.1103/PhysRevB.86.085402.

[914] E. E. Vogel et al. "Alternative characterization of the nematic transition in deposition of rods on two-dimensional lattices". In: *Phys. Rev. E* 101.2 (Feb. 2020), p. 022104. DOI: 10.1103/PhysRevE.101.022104.

[915] Eelco Empting. "Kinetic Monte Carlo Simulations of Binary Thin Film Growth". Supervisor: Martin Oettel. MA thesis. Department of Physics: University of Tübingen, 2017.

[916] R. L. C. Vink, S. Wolfsheimer, and T. Schilling. "Isotropic-nematic interfacial tension of hard and soft rods: Application of advanced grand canonical biased-sampling techniques". In: *J. Chem. Phys.* 123.7 (2005), p. 074901. DOI: 10.1063/1.2000237.

[917] P. Virnau and M. Müller. "Calculation of free energy through successive umbrella sampling". In: *J. Chem. Phys.* 120.23 (2004), p. 10925. DOI: 10.1063/1.1739216.

[918] N. Vigneshwar, D. Dhar, and R. Rajesh. "Different phases of a system of hard rods on three dimensional cubic lattice". In: *J. Stat. Mech.: Theory Exp.* 2017.11 (Nov. 2017), p. 113304. DOI: 10.1088/1742-5468/aa967d.

[919] P. Longone, D. H. Linares, and A. J. Ramirez-Pastor. "Critical behavior of attractive rigid rods on two-dimensional lattices". In: *J. Chem. Phys.* 132.18 (2010), p. 184701. DOI: 10.1063/1.3424775.

[920] B. S. John, A. Stroock, and F. A. Escobedo. "Cubatic liquid-crystalline behavior in a system of hard cuboids". In: *J. Chem. Phys.* 120.19 (2004), pp. 9383–9389. DOI: 10.1063/1.1711594.

[921] B. S. John and F. A. Escobedo. "Phase Behavior of Colloidal Hard Tetragonal Parallelepipeds (Cuboids): A Monte Carlo Simulation Study". In: *J. Phys. Chem. B* 109.48 (2005). PMID: 16853998, pp. 23008–23015. DOI: 10.1021/jp0551521.

[922] B. S. John, C. Juhlin, and F. A. Escobedo. "Phase behavior of colloidal hard perfect tetragonal parallelepipeds". In: *J. Chem. Phys.* 128.4 (2008), p. 044909. DOI: 10.1063/1.2819091.

[923] S. D. Peroukidis and A. G. Vanakaras. "Phase diagram of hard boardlike colloids from computer simulations". In: *Soft Matter* 9.31 (2013), pp. 7419–7423. DOI: 10.1039/C3SM51165K.

[924] E. van den Pol et al. "Experimental Realization of Biaxial Liquid Crystal Phases in Colloidal Dispersions of Boardlike Particles". In: *Phys. Rev. Lett.* 103.25 (Dec. 2009), p. 258301. DOI: 10.1103/PhysRevLett.103.258301.

[925] K. Shundyak and R. van Roij. "Isotropic-nematic transition in hard-rod fluids: Relation between continuous and restricted-orientation models". In: *Phys. Rev. E* 69.4 (Apr. 2004), p. 041703. DOI: 10.1103/PhysRevE.69.041703.

[926] E. E. Vogel, G. Saravia, and A. J. Ramirez-Pastor. "Phase transitions in a system of long rods on two-dimensional lattices by means of information theory". In: *Phys. Rev. E* 96.6 (Dec. 2017), p. 062133. DOI: 10.1103/PhysRevE.96.062133.

[927] J. Liu et al. "Self-learning Monte Carlo method". In: *Phys. Rev. B* 95.4 (Jan. 2017), p. 041101. DOI: 10.1103/PhysRevB.95.041101.

[928] J. Liu et al. "Self-learning Monte Carlo method and cumulative update in fermion systems". In: *Phys. Rev. B* 95.24 (June 2017), p. 241104. DOI: 10.1103/PhysRevB.95.241104.

[929] L. Huang and L. Wang. "Accelerated Monte Carlo simulations with restricted Boltzmann machines". In: *Phys. Rev. B* 95.3 (Jan. 2017), p. 035105. DOI: 10.1103/PhysRevB.95.035105.

[930] W. Wang, J. Machta, and Helmut G. Katzgraber. "Comparing Monte Carlo methods for finding ground states of Ising spin glasses: Population annealing, simulated annealing, and parallel tempering". In: *Phys. Rev. E* 92.1 (July 2015), p. 013303. DOI: 10.1103/PhysRevE.92.013303.

[931] J. Machta. "Population annealing with weighted averages: A Monte Carlo method for rough free-energy landscapes". In: *Phys. Rev. E* 82.2 (Aug. 2010), p. 026704. DOI: 10.1103/PhysRevE.82.026704.

[932] N. Lebovka et al. "Barrier properties of k-mer packings". In: *Physica A* 408 (2014), pp. 19–27. ISSN: 0378-4371. DOI: 10.1016/j.physa.2014.04.019.

[933] "Random sequential adsorption of straight rigid rods on a simple cubic lattice". In: *Physica A* 436 (2015), pp. 558–564. ISSN: 0378-4371. DOI: 10.1016/j.physa.2015.05.073.

[934] I. Lončarević et al. "Random sequential adsorption of lattice animals on a three-dimensional cubic lattice". In: *Phys. Rev. E* 101.1 (Jan. 2020), p. 012119. DOI: 10.1103/PhysRevE.101.012119.

[935] E. D. Cubuk et al. "Identifying Structural Flow Defects in Disordered Solids Using Machine-Learning Methods". In: *Phys. Rev. Lett.* 114.10 (Mar. 2015), p. 108001. DOI: 10.1103/PhysRevLett.114.108001.

[936] L. Dinh, J. Sohl-Dickstein, and S. Bengio. "Density estimation using Real NVP". In: *Proc. of the 5th International Conference on Learning Representations, ICLR 2017, Toulon, France, April 24-26, 2017, Conference Track Proceedings*. OpenReview.net, 2017. URL: https://openreview.net/forum?id=HkpbnH9lx.

[937] C. Cremer, X. Li, and D. Duvenaud. "Inference Suboptimality in Variational Autoencoders". In: *Proc. of the 35th International Conference on Machine Learning, ICML 2018, Stockholmsmässan, Stockholm, Sweden, July 10-15, 2018*. Ed. by J. G. Dy and A. Krause. Vol. 80. Proceedings of Machine Learning Research. PMLR, 2018, pp. 1086–1094. arXiv: 1801.03558 [cs.LG].

[938] S. Zhao, J. Song, and S. Ermon. "InfoVAE: Balancing Learning and Inference in Variational Autoencoders". In: *Proceedings of the Thirty-Third AAAI Conference on Artificial Intelligence*. Vol. 33. 1. AAAI-19, IAAI-19, EAAI-20. AAAI Press, 2019, pp. 5885–5892. DOI: 10.1609/aaai.v33i01.33015885.

[939] V. Abrol, P. Sharma, and A. Patra. "Improving Generative Modelling in VAEs using Multimodal Prior". In: *IEEE Transactions on Multimedia* (2020), pp. 1–1. DOI: 10.1109/TMM.2020.3008053.

[940] F. Lavda, M. Gregorová, and A. Kalousis. "Improving VAE Generations of Multimodal Data Through Data-Dependent Conditional Priors". In: *ECAI 2020 - 24th European Conference on Artificial Intelligence, 29 August-8 September 2020, Santiago de Compostela, Spain, August 29 - September 8, 2020 - Including 10th Conference on Prestigious Applications of Artificial Intelligence (PAIS 2020)*. Ed. by Giuseppe De Giacomo et al. Vol. 325. Frontiers in Artificial Intelligence and Applications. IOS Press, 2020, pp. 1254–1261. DOI: 10.3233/FAIA200226. arXiv: 1911.10885 [cs.LG].

[941] A. Klushyn et al. "Learning Hierarchical Priors in VAEs". In: *Advances in Neural Information Processing Systems 32*. Ed. by H. Wallach et al. Curran Associates, Inc., 2019, pp. 2870–2879. URL: http://papers.nips.cc/paper/8553-learning-hierarchical-priors-in-vaes.pdf.

[942] A. van den Oord, O. Vinyals, and K. Kavukcuoglu. "Neural Discrete Representation Learning". In: *Advances in Neural Information Processing Systems 30*. Ed. by I. Guyon et al. Curran Associates, Inc., 2017, pp. 6306–6315.

[943] J. T. Rolfe. "Discrete Variational Autoencoders". In: *Proc. of the 5th International Conference on Learning Representations, ICLR 2017, Toulon, France, April 24-26, 2017, Conference Track Proceedings*. OpenReview.net, 2017. arXiv: 1609.02200 [stat.ML].

[944] M. Dixit, T. Schilling, and M. Oettel. "Growth of films with anisotropic particles: Simulations and rate equations". In: *J. Chem. Phys.* 149.6 (2018), p. 064903. DOI: 10.1063/1.5031217.

[945] D. Oxtoby. "Catching crystals at birth". In: *Nature* 406 (2000), pp. 464–465. DOI: 10.1038/35020163.

[946] M. Hu, S. Noda, and H. Komiyama. "Amorphous-to-crystalline transition during the early stages of thin film growth of Cr on SiO2". In: *J. Appl. Phys.* 93.11 (2003), pp. 9336–9344. DOI: 10.1063/1.1571214.

[947] L. Tumbek and A. Winkler. "Attachment limited versus diffusion limited nucleation of organic molecules: Hexaphenyl on sputter-modified mica". In: *Surf. Sci.* 606.15 (2012), pp. L55–L58. ISSN: 0039-6028. DOI: 10.1016/j.susc.2012.03.018.

[948] B. Dünweg, A. Milchev, and P. A. Rikvold. "A model for adsorption of O on Mo(110): Phase transitions with nonuniversal behavior". In: *J. Chem. Phys.* 94.5 (1991), pp. 3958–3973. DOI: 10.1063/1.460673.

[949] C. Ratsch and J. A. Venables. "Nucleation theory and the early stages of thin film growth". In: *J. Vac. Sci. Technol. A* 21.5 (2003), S96–S109. DOI: 10.1116/1.1600454.

[950] H. Brune. "Microscopic view of epitaxial metal growth: nucleation and aggregation". In: *Surf. Sci. Rep.* 31.4 (1998), pp. 125–229. ISSN: 0167-5729. DOI: 10.1016/S0167-5729(99)80001-6.

[951] A. Kuhnhold et al. "Derivation of an exact, nonequilibrium framework for nucleation: Nucleation is a priori neither diffusive nor Markovian". In: *Phys. Rev. E* 100.5 (Nov. 2019), p. 052140. DOI: 10.1103/PhysRevE.100.052140.

[952] H. Meyer, T. Voigtmann, and T. Schilling. "On the dynamics of reaction coordinates in classical, time-dependent, many-body processes". In: *J. Chem. Phys.* 150.17 (2019), p. 174118. DOI: 10.1063/1.5090450.

[953] L. Gránásy and D. W. Oxtoby. "Cahn–Hilliard theory with triple-parabolic free energy. II. Nucleation and growth in the presence of a metastable crystalline phase". In: *J. Chem. Phys.* 112.5 (2000), pp. 2410–2419. DOI: 10.1063/1.480807.

[954] V. Talanquer and D. W. Oxtoby. "Crystal nucleation in the presence of a metastable critical point". In: *J. Chem. Phys.* 109.1 (1998), pp. 223–227. DOI: 10.1063/1.476554.

[955] J. F. Lutsko. "How crystals form: A theory of nucleation pathways". In: *Sci. Adv.* 5.4 (2019). DOI: 10.1126/sciadv.aav7399.

[956] F. Ito et al. "Direct Visualization of the Two-step Nucleation Model by Fluorescence Color Changes during Evaporative Crystallization from Solution". In: *Sci. Rep.* 6 (2016). DOI: doi.org/10.1038/srep22918.

[957] A. Zangwill and D. D. Vvedensky. "Novel Growth Mechanism of Epitaxial Graphene on Metals". In: *Nano Lett.* 11.5 (2011). PMID: 21495700, pp. 2092–2095. DOI: 10.1021/nl2006005.

[958] M. Kotrla and J. Krug. "Effects of Atomic Interactions in Two-Component Submonolayer Growth". In: *Atomistic Aspects of Epitaxial Growth*. Ed. by M. Kotrla et al. Dordrecht: Springer Netherlands, 2002, pp. 489–498. ISBN: 978-94-010-0391-9. DOI: 10.1007/978-94-010-0391-9_38.

[959] M. Einax, P. Maass, and W. Dieterich. "Self-consistent rate theory for submonolayer surface growth of multicomponent systems". In: *Phys. Rev. B* 90.3 (July 2014), p. 035441. DOI: 10.1103/PhysRevB.90.035441.

[960] M. Kotrla, J. Krug, and P. Šmilauer. "Submonolayer growth with decorated island edges". In: *Surf. Sci.* 454-456 (2000), pp. 681–685. ISSN: 0039-6028. DOI: 10.1016/S0039-6028(00)00251-X.

[961] M. Kotrla, J. Krug, and P. Šmilauer. "Submonolayer epitaxy with impurities: Kinetic Monte Carlo simulations and rate-equation analysis". In: *Phys. Rev. B* 62.4 (July 2000), pp. 2889–2898. DOI: 10.1103/PhysRevB.62.2889.

[962] M. Kotrla, J. Krug, and P. Šmilauer. "Effects of mobile and immobile impurities on two-dimensional nucleation". In: *Surf. Sci.* 482-485 (2001), pp. 840–843. ISSN: 0039-6028. DOI: 10.1016/S0039-6028(01)00819-6.

[963] R. Sathiyanarayanan et al. "Role of codeposited impurities during growth. II. Dependence of morphology on binding and barrier energies". In: *Phys. Rev. B* 83.3 (Jan. 2011), p. 035424. DOI: 10.1103/PhysRevB.83.035424.

[964] P. C. Martin, E. D. Siggia, and H. A. Rose. "Statistical Dynamics of Classical Systems". In: *Phys. Rev. A* 8.1 (July 1973), pp. 423–437. DOI: 10.1103/PhysRevA.8.423.

[965] R. Bausch, H.K. Janssen, and H. Wagner. "Renormalized field theory of critical dynamics". In: *Z. Physik B* 24 (1976), pp. 113–127. DOI: 10.1007/BF01312880.

[966] D. W Oxtoby. "Vibrational population relaxation in liquids". In: *Adv. Chem. Phys.* 47 (1981), pp. 487–519.

[967] D. W. Oxtoby. "Vibrational relaxation in liquids: quantum states in a classical bath". In: *J. Phys. Chem.* 87.16 (1983), pp. 3028–3033. DOI: 10.1021/j100239a014.

[968] R. M. Stratt. "The Instantaneous Normal Modes of Liquids". In: *Accounts of Chemical Research* 28.5 (1995), pp. 201–207. DOI: 10.1021/ar00053a001.

[969] H. Chen et al. "Intermolecular vibrational energy transfers in liquids and solids". In: *Phys. Chem. Chem. Phys.* 16.27 (2014), pp. 13995–14014. DOI: 10.1039/C4CP01300J.

[970] U. Thiele. "Thin film evolution equations from (evaporating) dewetting liquid layers to epitaxial growth". In: *J. Phys. Condens. Matter* 22.8 (Feb. 2010), p. 084019. DOI: 10.1088/0953-8984/22/8/084019.

[971] H. Löwen. "A phase-field-crystal model for liquid crystals". In: *J. Phys. Condens. Matter* 22.36 (Aug. 2010), p. 364105. DOI: 10.1088/0953-8984/22/36/364105.

[972] J.-F. Gouyet et al. "Description of far-from-equilibrium processes by mean-field lattice gas models". In: *Adv. Phys.* 52.6 (2003), pp. 523–638. DOI: 10.1080/00018730310001615932.

[973] B. D. Goddard et al. "General Dynamical Density Functional Theory for Classical Fluids". In: *Phys. Rev. Lett.* 109.12 (Sept. 2012), p. 120603. DOI: 10.1103/PhysRevLett.109.120603.

[974] K. Yaldram and K. Binder. "Monte Carlo simulation of phase separation and clustering in the ABV model". In: *J. Stat. Phys.* 62.1-2 (1991), pp. 161–175. DOI: 10.1007/BF01020864.

[975] M. Plapp and J.-F. Gouyet. "Surface Modes and Ordered Patterns during Spinodal Decomposition of an ABv Model Alloy". In: *Phys. Rev. Lett.* 78.26 (June 1997), pp. 4970–4973. DOI: 10.1103/PhysRevLett.78.4970.

[976] M. Plapp and J.-F. Gouyet. "Spinodal decomposition of an ABv model alloy: Patterns at unstable surfaces". In: *Eur. Phys. J. B* 9.2 (1999), pp. 267–282. DOI: 10.1007/s100510050766.

[977] S. Puri and R. Sharma. "Phase ordering dynamics in binary mixtures with annealed vacancies". In: *Phys. Rev. E* 57.2 (Feb. 1998), pp. 1873–1885. DOI: 10.1103/PhysRevE.57.1873.

[978] D. Puri S.and Kumar. "Autocorrelation functions for phase separation in ternary mixtures". In: *Phys. Rev. E* 70.5 (Nov. 2004), p. 051501. DOI: 10.1103/PhysRevE.70.051501.

[979] D. Puri S.and Kumar. "Aging and Equilibrium Fluctuations for domain Growth in Ternary Mixtures". In: *Phys. Rev. Lett.* 93.2 (July 2004), p. 025701. DOI: 10.1103/PhysRevLett.93.025701.

[980] K. C. Lakshmi and P. B. Sunil Kumar. "Scale invariance in coarsening of binary and ternary fluids". In: *Phys. Rev. E* 67.1 (Jan. 2003), p. 011507. DOI: 10.1103/PhysRevE.67.011507.

[981] T. Schreiber. "Measuring Information Transfer". In: *Phys. Rev. Lett.* 85.2 (July 2000), pp. 461–464. DOI: 10.1103/PhysRevLett.85.461.

[982] S. Ito. "Backward transfer entropy: Informational measure for detecting hidden Markov models and its interpretations in thermodynamics, gambling and causality". In: *Sci. Rep.* 6, 36831 (Nov. 2016), p. 36831. DOI: 10.1038/srep36831.

[983] Y.-C. Hung and C.-K. Hu. "Chaotic Communication via Temporal Transfer Entropy". In: *Phys. Rev. Lett.* 101.24 (Dec. 2008), p. 244102. DOI: 10.1103/PhysRevLett.101.244102.

[984] P. Strasberg et al. "Quantum and Information Thermodynamics: A Unifying Framework Based on Repeated Interactions". In: *Phys. Rev. X* 7.2 (Apr. 2017), p. 021003. DOI: 10.1103/PhysRevX.7.021003.

[985] A. C. Barato and U. Seifert. "Cost and Precision of Brownian Clocks". In: *Phys. Rev. X* 6.4 (Dec. 2016), p. 041053. DOI: 10.1103/PhysRevX.6.041053.

[986] U. C. Täuber. "Field-Theory Approaches to Nonequilibrium Dynamics". In: *Ageing and the Glass Transition*. Ed. by M. Henkel, M. Pleimling, and R. Sanctuary. Berlin, Heidelberg: Springer Berlin Heidelberg, 2007, pp. 295–348. ISBN: 978-3-540-69684-1. DOI: 10.1007/3-540-69684-9_7.

[987] S. S. Kondov et al. "Three-Dimensional Anderson Localization of Ultracold Matter". In: *Science* 334.6052 (2011), pp. 66–68. ISSN: 0036-8075. DOI: 10.1126/science.1209019.

[988] A. Lukin et al. "Probing entanglement in a many-body–localized system". In: *Science* 364.6437 (2019), pp. 256–260. ISSN: 0036-8075. DOI: 10.1126/science.aau0818.

[989] D. A. Abanin et al. "Colloquium: Many-body localization, thermalization, and entanglement". In: *Rev. Mod. Phys.* 91.2 (May 2019), p. 021001. DOI: 10.1103/RevModPhys.91.021001.

[990] T. Schwartz et al. "Transport and Anderson localization in disordered two-dimensional photonic lattices". In: *Nature* 446.7131 (2007), pp. 52–55. DOI: 10.1038/nature05623.

[991] M. L. Manning and A. J. Liu. "Vibrational Modes Identify Soft Spots in a Sheared Disordered Packing". In: *Phys. Rev. Lett.* 107.10 (Aug. 2011), p. 108302. DOI: 10.1103/PhysRevLett.107.108302.

[992] M. D. Gratale et al. "Vibrational properties of quasi-two-dimensional colloidal glasses with varying interparticle attraction". In: *Phys. Rev. E* 94.4 (Oct. 2016), p. 042606. DOI: 10.1103/PhysRevE.94.042606.

[993] E. Lerner, G. Düring, and E. Bouchbinder. "Statistics and Properties of Low-Frequency Vibrational Modes in Structural Glasses". In: *Phys. Rev. Lett.* 117.3 (July 2016), p. 035501. DOI: 10.1103/PhysRevLett.117.035501.

[994] Y. Fan, T. Iwashita, and T. Egami. "Energy landscape-driven non-equilibrium evolution of inherent structure in disordered material". In: *Nat. Commun.* 8.1 (2017), pp. 1–7. DOI: 10.1038/ncomms15417.

[995] E. Bouchbinder and E. Lerner. "Universal disorder-induced broadening of phonon bands: from disordered lattices to glasses". In: *New J. Phys.* 20.7 (July 2018), p. 073022. DOI: 10.1088/1367-2630/aacef4.

[996] D. Han et al. "Statistical complexity of potential energy landscape as a dynamic signature of the glass transition". In: *Phys. Rev. B* 101.6 (Feb. 2020), p. 064205. DOI: 10.1103/PhysRevB.101.064205.